Isotopic tracing of silicate and carbonate weathering in the Himalayan erosional system

Jesse Davenport

Isotopic tracing of silicate and carbonate weathering in the Himalayan erosional system

Jesse David Davenport

Thèse
présentée pour l'obtention du grade de
DOCTEUR DE L'UNIVERSITÉ DE LORRAINE
Spécialité géosciences

par

Jesse DAVENPORT

Traçage isotopique de l'altération du silicate et du carbonate dans le système érosif de l'Himalaya

Soutenue publiquement le 18 décembre 2018
devant le jury composé de :

Rapporteurs	François CHABAUX	Professeur, LHyGeS, Strasbourg, FR
	Nathalie VIGIER	DR, Laboratoire d'Océanographie, Villefrance-sur-Mer, FR
Examinatrices	Catherine CHAUVEL	DR, IGPG, Paris, FR
	Laurie REISBERG	DR, CRPG, Nancy, FR
Invité	Jérôme LAVÉ	DR, CRPG, Nancy, FR
Directeur	Christian France-LANORD	DR, CRPG, Nancy, FR
Directeur	Guillaume CARO	CR, CRPG, Nancy, FR

CRPG – CNRS
Centre de Recherches Pétrographiques et Géochimiques
15 rue Notre Dame des Pauvres, 54500 Vandoeuvre-les-Nancy, FRANCE

Abstract

During the latter part of the Cenozoic Era, weathering of Himalayan lithologies potentially impacted a number of geochemical and biogeochemical cycles, which together comprise the global carbon cycle. To be able to constrain and understand the processes that occurred in the Himalayas that affected these cycles, we must be able to distinguish between the signatures of silicate and carbonate weathering in the dissolved load of Himalayan rivers. Previous studies have attempted to do this using a variety of methods, which include major element and Sr isotope budget modeling as well as more non-traditional isotopic techniques. However, there is still not a clear consensus on the magnitude and flux of silicate weathering in the Himalaya. This thesis proposes the use of ^{40}Ca, a decay product of ^{40}K, as a tracer that could improve the quantification of the silicate and carbonate weathering flux in the dissolved load of Himalayan rivers. Previous work has shown that the ^{40}Ca budget of seawater is dominated by a mantle source, such that marine carbonates have a homogeneous ε^{40}Ca signature indistinguishable, or slightly elevated, from the mantle value (i.e., ε^{40}Ca = 0). In contrast, the upper silicate crust, with a K/Ca ratio of approximately 1, is expected to have developed a radiogenic composition of approximately +2–3 ε-units. The difference between the radiogenic Ca signature of carbonate and silicate lithologies can be therefore used to differentiate between carbonate and silicate weathering in the dissolved load of rivers.

Here, we present a geochemical survey, including radiogenic Ca analyses, of rivers draining the main lithological units of the Himalaya, as well as results from sediments, bedrock, soil, and gravel. Our results show that Himalayan carbonates/dolomites exhibit no radiogenic ^{40}Ca excesses (i.e., ε^{40}Ca = 0) despite highly variable ^{87}Sr/^{86}Sr signatures (0.73–0.85), whereas silicate bed rock and sediments are variably radiogenic (ε^{40} = +0.9 to +4). This suggests that for Ca, unlike for Sr, isotopic exchange between the silicate and carbonate lithologies has been minimal. The radiogenic Ca composition of river water ranges from +0.1 in carbonate dominated catchments to +11 ε-units in rivers draining silicate catchments. For large rivers, silicate and carbonate weathering budget estimates based on major elements and radiogenic Ca compositions tend to agree. However, for some smaller rivers, especially those draining silicate dominated basins in the High Himalayan Crystalline (HHC) and Lesser Himalaya (LH) formations, some discrepancies are observed. These

cannot be attributed to poor definition of the chemical or radiogenic Ca composition of the endmembers used for budget modeling, as the values required to bring the estimates into agreement are unreasonable. They also cannot be explained by precipitation of secondary carbonates in the rivers as the non-radiogenic composition of the carbonate fraction of sediments suggests that this process is only minor. Rather, these discrepancies may be due to the dissolution/weathering of trace amounts of radiogenic calcite contained within HHC and LH silicate lithologies. Similar to what has previously been suggested for Sr, the weathering of such material, which represents only a tiny fraction of the area of the silicate catchment, could yield a substantial proportion of the radiogenic Ca and may thus have a significant influence on the isotopically based weathering budgets of these basins. Nevertheless, as this effect is observed primarily in basins with low silicate erosion rates, its influence on estimates of the overall silicate weathering flux will be minor. More generally, the results of this thesis imply that the ^{40}K–^{40}Ca system can resolve issues that cannot be successfully addressed using Sr isotopes in the Himalaya. Further work is needed to define the full range of radiogenic Ca compositions in the Himalaya in order to clearly answer questions regarding silicate weathering fluxes.

Résumé

Au cours de la dernière partie de l'ère cénozoïque, l'altération des lithologies himalayennes a potentiellement impacté un certain nombre de cycles géochimiques et biogéochimiques, qui constituent ensemble le cycle global du carbone. Pour pouvoir contraindre et comprendre les processus qui se sont produits dans l'Himalaya et qui ont affecté ces cycles, nous devons être en mesure de distinguer les signatures de l'altération du silicate et du carbonate dans la charge dissoute des fleuves de l'Himalaya. Des études antérieures ont tenté de le faire en utilisant diverses méthodes, qui incluent la modélisation du budget en isotopes des éléments majeurs et Sr, ainsi que des techniques isotopiques non traditionnelles. Cependant, il n'existe toujours pas de consensus clair sur l'ampleur et le flux de l'altération du silicate dans l'Himalaya. Cette thèse propose l'utilisation du ^{40}Ca, un produit de désintégration de ^{40}K, comme traceur pouvant améliorer la quantification du flux d'altération du silicate et du carbonate dans la charge dissoute des rivières himalayennes. Des travaux antérieurs ont montré que le budget de l'eau de mer ^{40}Ca est dominé par une source de manteau, de sorte que les carbonates marins ont une signature homogène de ε^{40}Ca indiscernable ou légèrement élevée par rapport à la valeur du manteau (c'est-à-dire ε^{40}Ca = 0). En revanche, la croûte supérieure de silicate, avec un rapport K/Ca d'environ 1, devrait avoir développé une composition radiogénique d'environ +2–3 ε-units. La différence entre la signature en Ca radiogénique des lithologies de carbonate et de silicate peut donc être utilisée pour différencier l'altération du carbonate et du silicate dans la charge dissoute des rivières.

Nous présentons ici une étude géochimique comprenant des analyses de Ca radiogénique des rivières drainant les principales unités lithologiques de l'Himalaya, ainsi que des résultats provenant de sédiments, de substrat rocheux, de sol et de gravier. Nos résultats montrent que les carbonates/dolomites de l'Himalaya ne présentent pas d'excès de ^{40}Ca radiogénique (ε^{40}Ca = 0) malgré des signatures très variables ^{87}Sr/^{86}Sr (0.73–0.85), alors que les sédiments et les roches sédimentaires sont radiogènes (ε^{40}Ca = +0.9 à +4). Ceci suggère que pour Ca, contrairement à Sr, l'échange isotopique entre les lithologies silicate et carbonate a été minime. La composition en Ca radiogène de l'eau des rivières va de +0.1 dans les captages à prédominance carbonatée à +11 unités dans les rivières drainant des bassins versants silicatés. Pour les grandes rivières, les estimations du budget relatives à l'altération

du silicate et du carbonate sur la base des éléments principaux et la composition en Ca radiogénique tendent à concorder. Cependant, pour certaines rivières plus petites, en particulier celles drainant des bassins à dominance silicatée dans les formations cristallines de l'Himalaya supérieur (HHC) et du Petit Himalaya (LH), certaines divergences sont observées. Celles-ci ne peuvent pas être attribuées à une définition imprécise de la composition chimique ou radiogénique en Ca des pôles de mélange utilisés pour la modélisation budgétaire, car les valeurs requises pour résoudre le modèle ne sont pas raisonnables. Ils ne peuvent pas non plus être expliqués par la précipitation de carbonates secondaires dans les rivières car la composition non radiogénique de la fraction de carbonates dans les sédiments suggère que ce processus n'est que mineur. Au contraire, ces différences peuvent être dues à la dissolution/altération des traces de calcite radiogénique contenues dans les lithologies de silicate HHC et LH. Semblable à ce qui a été suggéré précédemment pour Sr, le vieillissement de ce matériau, qui ne représente qu'une infime partie de la surface du captage du silicate, pourrait produire une proportion substantielle du Ca radiogénique et pourrait ainsi avoir une influence significative sur le calcul des budgets de ces bassins à partir des données isotopiques. Néanmoins, comme cet effet est observé principalement dans les bassins à faible taux d'érosion des silicates, son influence sur les estimations du flux global de vieillissement du silicate sera mineure. Plus généralement, les résultats de cette thèse impliquent que le système ^{40}K–^{40}Ca permet une résolution de problématiques qui ne peuvent pas être approfondies avec succès à l'aide d'isotopes Sr dans l'Himalaya. Des travaux supplémentaires sont nécessaires pour définir la gamme complète des compositions de Ca radiogénique dans l'Himalaya afin de répondre clairement aux questions concernant les flux d'altération des silicates.

Extended Abstract

The uplift and erosion of the Himalayan-Tibetan Plateau has long been thought to play a key role in modifying the $^{87}Sr/^{86}Sr$ evolution of seawater throughout the geologic past. This could either be due to the: 1) increase in the radiogenic Sr isotopic composition of water delivered to the oceans because of the radiogenic nature of both silicate and carbonate lithologies in the Himalayan or 2) an increased flux of Sr to the oceans from the Himalayan orogen. Distinguishing between whether this dissolved load flux in the Himalaya derives from silicate or carbonate weathering is important when attempting to understand the interactions between weathering, erosion, climate, and geomorphology but also the for the long-term CO_2 cycle and seawater chemistry. However, Himalayan rivers have distinct water characteristics, i.e., high Sr concentrations and radiogenic $^{87}Sr/^{86}Sr$ signatures, that exclude a simple mixing relationship between silicate and carbonate lithologies because both silicates and carbonates carry radiogenic ^{87}Sr, and, thus, these signatures are difficult to differentiate in the dissolved load. Previous studies have attempted to do this using a variety of methods, which include major elemental and Sr isotopic budget modelling as well as more non-traditional isotopic techniques. However, there is still not a clear consensus on the magnitude and flux of silicate weathering in the Himalaya.

This thesis proposes the use of ^{40}Ca, a decay product of ^{40}K, as a tracer to potentially improve the quantification of the silicate and carbonate weathering flux in the dissolved load of Himalayan rivers. Previous analytical studies using the ^{40}K–^{40}Ca system were hampered by several geochemical and analytical limitations that significantly reduced the accuracy and reproducibility of radiogenic Ca analyses. However, with the Thermo Triton Thermal Ionization Mass Spectrometer (TIMS) we are able to conduct high precision (approximately 30 ppm S.D.) radiogenic Ca isotopic measurements, which represents an improvement by a factor of 3–5 compared with previous studies and generation of instruments.

The ^{40}K–^{40}Ca decay scheme has geochemical properties similar to the $^{87}Rb/^{87}Sr$ and similar interest when studying silicate weathering because K, similar to Rb, is an incompatible element during crustal extraction processes and is therefore concentrated in the upper continental crust, where it decays to Ca. Previous work has shown that the ^{40}Ca budget of seawater is dominated by a mantle source, such that marine carbonates have a homogeneous $\varepsilon^{40}Ca$ signature indistinguishable, or

slightly elevated, from the mantle value (i.e., $\varepsilon^{40}Ca = 0$). In contrast, the upper silicate crust, with a K/Ca ratio of approximately 1, is expected to have developed a radiogenic composition of approximately +2–3 ε-units. Previous studies have shown that this dichotomy between silicate and carbonate also exists in river water, e.g., the Mississippi (carbonate dominated) and the Columbia (young basalts) rivers have unradiogenic water compositions, whereas the Ganga and Brahmaputra have radiogenic Ca compositions. Therefore, the difference between the radiogenic Ca signature of carbonate and silicate lithologies can be used to differentiate between carbonate and silicate weathering in the dissolved load of rivers. We can also circumvent problems associated with the Rb–Sr system when quantifying weathering budgets due to the metamorphic redistribution of radiogenic Sr between silicates and carbonates in the Himalaya.

This thesis is the first of its kind to perform an extensive investigation of ^{40}K–^{40}Ca systematics in the Himalayan erosional system. We show that during Himalayan metamorphism, ^{40}Ca, unlike ^{87}Sr, remained remarkably resistant to metamorphism/dolomitization. Analyses reveal that carbonate whole-rock and sediments have nonradiogenic Ca signatures whereas silicate whole-rock and sediments have ^{40}Ca excesses that depend on their age and K/Ca ratios allowing us to distinguish carbonate and silicate sources in the dissolved load of the major Himalayan rivers. This dichotomy therefore applies to rivers, i.e., rivers that drain predominantly carbonate lithologies have unradiogenic signatures, whereas rivers that drain predominantly silicate lithologies have radiogenic signatures.

Here, we present a geochemical survey, including radiogenic Ca analyses, of rivers draining the main lithological units of the Himalaya, as well as results from sediments, bedrock, soil, and gravel. Our results show that Himalayan carbonates/dolomites exhibit no radiogenic ^{40}Ca excesses (i.e., $\varepsilon^{40}Ca = 0$) despite highly variable $^{87}Sr/^{86}Sr$ signatures (0.73–0.85), whereas silicate bed rock and sediments are variably radiogenic (+0.9 to +4). This suggests that for Ca, unlike for Sr, isotopic exchange between the silicate and carbonate lithologies has been minimal. The radiogenic Ca composition of river water ranges from +0.1 in carbonate dominated catchments to +11 ε-units in rivers draining silicate catchments.

For large rivers, silicate and carbonate weathering budget estimates based on major elements and radiogenic Ca compositions tend to agree. However, for some smaller rivers, especially those draining silicate dominated basins in the High Himalayan Crystalline (HHC) and Lesser Himalaya (LH) formations, some discrepancies are observed. These cannot be attributed to poor definition of the chemical or radiogenic Ca composition of the endmembers used for budget modeling, as the values required to bring the estimates into agreement are unreasonable. They

also cannot be explained by precipitation of secondary carbonates in the rivers as the non-radiogenic composition of the carbonate fraction of sediments suggests that this process is only minor. Rather, these discrepancies are probably due to the dissolution/weathering of miniscule hydrothermal calcite veins contained within HHC and LH silicate lithologies. Similar to what has previously been observed for Sr, the weathering of these veins, which represent only a miniscule fraction of the area of the silicate catchment, can yield a potentially large proportion of the radiogenic Ca and will thus dominate the isotopically based weathering budgets of these basins. Nevertheless, as this effect is observed primarily in basins with low silicate erosion rates, its influence on estimates of the overall silicate weathering flux will be minor.

More generally, the results of this thesis imply that the ^{40}K–^{40}Ca system can resolve issues that cannot be successfully addressed using Sr isotopes in the Himalaya. Nevertheless, further work is needed to define the full range of radiogenic Ca compositions in the Himalaya in order to clearly answer questions regarding silicate weathering fluxes.

Résumé Élargi

On pense depuis longtemps que le soulèvement et l'érosion du plateau himalayen-tibétain jouent un rôle clé dans la modification de l'évolution de l'eau de mer à travers le passé géologique. Cela pourrait être dû: 1) à l'augmentation de la composition isotopique du Sr dans l'eau transmise aux océans en raison de la nature radiogénique des lithologies de silicate et de carbonate dans l'Himalaya ou 2) à un flux accru de Sr dans les océans à partir du Orogène himalayen. Il est important de distinguer entre le flux de charge dissous dans l'Himalaya et l'altération du silicate ou du carbonate pour tenter de comprendre les interactions entre altération, érosion, climat et géomorphologie, mais aussi pour le cycle à long terme CO_2 et chimie de l'eau de mer. Toutefois, les rivières himalayennes présentent des caractéristiques distinctes, c'est-à-dire des concentrations de Sr élevées et des signatures radiogéniques $^{87}Sr/^{86}Sr$, qui excluent une simple relation de mélange entre les lithologies de silicate et de carbonate, car les silicates et les carbonates radiogenic ^{87}Sr, et donc, ces signatures sont difficiles à différencier dans la charge dissoute. Des études antérieures ont tenté de le faire en utilisant diverses méthodes, qui incluent une modélisation majeure du budget isotopique élémentaire et Sr, ainsi que des techniques isotopiques non traditionnelles. Cependant, il n'existe toujours pas de consensus clair sur l'ampleur et le flux de l'altération du silicate dans l'Himalaya.

Cette thèse propose l'utilisation de ^{40}Ca, un produit de désintégration de ^{40}K, comme traceur pour potentiellement améliorer la quantification du flux d'altération du silicate et du carbonate dans la charge dissoute des rivières himalayennes. Des études analytiques antérieures utilisant le système ^{40}K-^{40}Ca étaient gênées par plusieurs limitations géochimiques et analytiques qui réduisaient considérablement la précision et la reproductibilité des analyses de Ca radiogénique. Cependant, avec le spectromètre de masse à ionisation thermique Thermo Triton (TIMS), nous pouvons effectuer des mesures isotopiques de Ca radiogénique de haute précision (environ 30 ppm S.D.), ce qui représente une amélioration d'un facteur de 3 à 5 par rapport aux précédentes études et génération d'instruments.

Le schéma de désintégration ^{40}K-^{40}Ca a des propriétés géochimiques similaires à celles du $^{87}Rb/^{87}Sr$ et présente un intérêt similaire pour l'étude de l'altération du silicate car K, similaire à Rb, est un élément incompatible lors des processus d'extraction de la croûte et se concentre donc dans la croûte continentale supérieure,

où il se désintègre en Ca. Des travaux antérieurs ont montré que le budget de l'eau de mer ^{40}Ca est dominé par une source mantellique, de sorte que les carbonates marins ont une signature homogène ε^{40}Ca indiscernable, ou légèrement surélevée, de la valeur de manteau (c'est-à-dire ε^{40}Ca = 0). En revanche, la croûte supérieure de silicate, avec un rapport K/Ca d'environ 1, devrait avoir développé une composition radiogénique d'approximativement + 2 à 3 unités. Des études antérieures ont montré que cette dichotomie entre le silicate et le carbonate existait également dans l'eau des rivières, par exemple les rivières Mississippi (dominée par les carbonates) et Columbia (jeunes basaltes) avaient une composition en eau non radiogène, tandis que les rivières Ganga et Brahmaputra avaient une composition en Ca radiogène. Par conséquent, la différence entre la signature Ca radiogénique des lithologies de carbonate et de silicate peut être utilisée pour différencier l'altération du carbonate et du silicate dans la charge dissoute des rivières. Nous pouvons également contourner les problèmes associés au système Rb–Sr lors de la quantification des bilans climatiques dus à la redistribution métamorphique du Sr radiogénique entre silicates et carbonates dans l'Himalaya.

Malgré son potentiel en tant que traceur dans le cycle du Ca exogène, le système ^{40}K-^{40}Ca reste peu utilisé en raison de la difficulté analytique à mesurer les enrichissements radiogéniques sur l'isotope ^{40}Ca. Cela est dû en partie à l'abondance des isotopes pertinents du Ca (^{40}Ca: 96,94%; ^{42}Ca: 0,647%; ^{44}Ca: 2,086%), c'est-à-dire que l'isotope ^{40}Ca domine le système, ce qui rend difficile la mesure des isotopes moins abondants de Ca. Il est important de minimiser les erreurs sur les petits faisceaux d'ions ^{42}Ca et ^{44}Ca, car le rapport mesuré de ^{42}Ca/^{44}Ca est utilisé pour la correction du fractionnement en masse instrumentale. À l'aide du Finnigan MAT-262, des études antérieures indiquaient une précision externe de $\pm$ 0,6 à 1,5 ε-unités (2σ). Les spectromètres de masse à ionisation thermique (TIMS) plus modernes, notamment le Thermo Triton, permettent l'analyse de variations radiogéniques moins importantes sur l'isotope ^{40}Ca. En utilisant le Triton pour analyser des échantillons de cratons archéens, une étude a permis d'obtenir une reproductibilité de $\pm$ 0,5 ε-unité (2σ) et des données ^{40}Ca/^{44}Ca rapportées plus récemment dans des carbonates marins avec une précision externe de $\pm$ 0,35 ε-unité. Ces progrès en précision résultent de deux améliorations apportées à la nouvelle génération de TIMS: 1) la possibilité de mesurer des faisceaux d'ions plus importants par rapport aux instruments TIMS antérieurs (< 50 V contre < 10 V avec le MAT262) et 2) la possibilité d'utiliser le Système optique "Zoom" du Triton pour analyser les isotopes de calcium en mode multidynamique.

Le fractionnement instrumental en masse au cours d'une analyse TIMS a un impact significatif sur la composition isotopique mesurée de Ca. Par conséquent, il est important d'utiliser une loi de fractionnement appropriée pour corriger ce

fractionnement. La plupart des chercheurs ont conclu que la loi exponentielle convenait mieux à la correction du fractionnement instrumental. Cependant, plusieurs études ont signalé un comportement non exponentiel, en particulier à des niveaux élevés de fractionnement en masse. Les mesures isotopiques du calcium peuvent donc être gênées par des corrections de fractionnement de masse inappropriées dues à des écarts par rapport à la loi exponentielle. Cela pourrait résulter d'un certain nombre de processus comprenant l'évaporation de différents domaines ou régions du filament qui se sont fractionnés à des degrés différents avant ou pendant une analyse ou une transmission incomplète des ions Ca du filament aux collecteurs.

Dans cette thèse, nous rapportons les résultats d'analyses répétées du standard SRM915a du NIST effectuées au CRPG sur une période de trois ans en utilisant une approche spectrométrique de masse multi-dynamique. Nous décrivons également une technique de chargement améliorée qui élimine essentiellement 1) les phénomènes de mélange de "réservoir" de filament précédemment signalés lors des analyses TIMS des isotopes de Ca et 2) des effets de fractionnement massique important au cours d'une mesure individuelle. Ces améliorations techniques et les niveaux de reproductibilité nous permettent d'appliquer le système de Ca radiogénique au système d'érosion de l'Himalaya.

Cette thèse est la première du genre à mener une enquête approfondie sur la systématique ^{40}K-^{40}Ca dans le système d'érosion himalayen. Nous montrons qu'au cours du métamorphisme himalayen, ^{40}Ca, contrairement à ^{87}Sr, est resté remarquablement résistant au métamorphisme/dolomitisation. Les analyses révèlent que les roches et les sédiments carbonatés ont des signatures de Ca non radioactives, tandis que les sédiments des roches et des sédiments silicatés présentent des excès de ^{40}Ca qui dépendent de leur âge et de leurs rapports K/Ca, ce qui nous permet de distinguer les sources de carbonate et de silicate dans les sources dissoutes. charge des principaux fleuves himalayens. Cette dichotomie s'applique donc aux rivières, c'est-à-dire que les rivières qui drainent principalement des lithologies carbonatées ont des signatures non radiogènes, alors que les rivières qui drainent principalement des lithologies silicatées ont des signatures radiogéniques.

Ici, nous présentons un levé géochimique, incluant des analyses de Ca radiogénique, des rivières drainant les principales unités lithologiques de l'Himalaya, ainsi que des résultats de sédiments, de substrat rocheux, de sol et de gravier. Nos résultats montrent que les carbonates/dolomites de l'Himalaya ne présentent pas d'excès radiogéniques ^{40} Ca (c'est-à-dire que ε^{40}Ca = 0) malgré des variables très variables ^{87}Sr/^{86}Sr (0,73–0,85), alors que les roches et les sédiments de silicate sont radiogènes de façon variable (+0,9 à +4). Ceci suggère que pour Ca, contrairement

à Sr, l'échange isotopique entre les lithologies silicate et carbonate a été minime. La composition en Ca radiogénique de l'eau des rivières va de +0,1 dans les captages à prédominance carbonatée à +11 ε-unités dans les rivières drainant des captages de silicate.

Dans cette thèse, nous avons entrepris une étude détaillée de Khudi Khola, un petit bassin versant situé dans le bassin de Narayani, au centre du Népal. Il a été choisi en raison de sa longue histoire d'investigation et de sa nature contraignante en termes de lithologie, d'intempéries, d'érosion, de climat, de végétation et de dynamique des rivières. Sur cette base, nous montrons que les compositions d'eau radiogénique en Ca varient fortement entre la LH, en dessous du MCT, et le HHC, au-dessus du MCT. Dans la LH, à l'exception des échantillons prélevés lors d'importantes tempêtes, la composition de l'eau est non radioactive et reflète une source provenant des affleurements massifs de dolomie et de calcaire situés sous le MCT. Au-dessus du MCT dans le HHC, les compositions de Ca radiogénique sont plus élevées que le LH en raison de la nature silicate du HHC. Comme le proposaient des études antérieures, les glissements de terrain dans la partie HHC du bassin de Khudi représentent une source importante de matériaux érodés. Les analyses de poudres faites de cailloux agrégés provenant du glissement de terrain montrent que les valeurs de ε^{40}Ca varient considérablement mais sont en grande partie radiogènes. Dans le Khudi, les tempêtes de la mousson ont donné des valeurs de décharge et de charge en sédiments élevées, des pics de concentration de K, Ca, et de SO_4 et des conditions fluviales généralement turbulentes. Lors de la tempête de 2013, documentée par des études précédentes, nous observons, avec les pics de concentration d'éléments, une forte augmentation des valeurs de ε^{40}Ca, de +0 à +1,78 au plus fort de la tempête. Sur la base de la géologie et de la structure du Khudi, cette signature de Ca radiogénique ne peut provenir que du HHC. L'augmentation concomitante des concentrations de SO_4^{2-}, de K, et de Ca au cours de la tempête de 2013 implique que ces espèces ont peut-être été relâchées par l'altération du silicate et l'oxydation des sulfures associée. Sur la base de ces observations et conclusions, nous suggérons que la décomposition et le lessivage/vieillissement des cailloux et du gravier dans les glissements de terrain au HHC constituent l'explication la plus plausible des pics de concentration et de la composition radiogène en Ca observés pendant les tempêtes.

Pour les grandes rivières, les estimations budgétaires du vieillissement en silicate et en carbonate basées sur les éléments principaux et les compositions de Ca radiogénique ont tendance à concorder. Cependant, pour certaines rivières plus petites, en particulier celles drainant des bassins à dominance silicatée dans les formations cristallines de l'Himalaya supérieur (HHC) et de l'Himalaya inférieur (LH), certaines différences sont observées. Celles-ci ne peuvent pas être attribuées

à une définition médiocre de la composition chimique ou radiogénique en Ca des membres finaux utilisés pour la modélisation budgétaire, car les valeurs requises pour mettre les estimations en accord sont déraisonnables. Ils ne peuvent pas non plus être expliqués par la précipitation de carbonates secondaires dans les rivières car la composition non radiogénique de la fraction de carbonate des sédiments suggère que ce processus est seulement mineur. Au contraire, ces différences sont probablement dues à la dissolution/dégradation des veines minuscules de calcite hydrothermale contenues dans les lithologies de silicate HHC et LH. Semblable à ce qui a été observé précédemment pour Sr, l'altération de ces veines, qui ne représente qu'une infime fraction de la surface du captage de silicate, peut générer une proportion potentiellement importante de Ca radiogénique et va donc dominer les budgets de vieillissement basés sur l'isotope ces bassins. Néanmoins, cet effet étant observé principalement dans les bassins à faible taux d'érosion du silicate, son influence sur les estimations du flux global d'altération du silicate sera mineure.

Plus généralement, les résultats de cette thèse impliquent que le système ^{40}K-^{40}Ca peut résoudre des problèmes qui ne peuvent pas être traités avec succès à l'aide d'isotopes Sr dans l'Himalaya. Néanmoins, des travaux supplémentaires sont nécessaires pour définir la gamme complète des compositions de Ca radiogénique dans l'Himalaya afin de répondre clairement aux questions concernant les flux d'altération des silicates. Cette thèse présente un premier aperçu de la systématique des rapports isotopiques de Ca radiogénique dans l'Himalaya. Les idées et interprétations présentées dans cette thèse peuvent fournir un cadre pour mieux comprendre le comportement des rapports isotopiques de Ca radiogénique, mais les idées et la modélisation futures bénéficieront d'analyses plus poussées du ^{40}Ca dans le substrat rocheux, les sédiments, l'eau de rivière, les fluides hydrothermaux et d'autres échantillons terrestres dans l'Himalaya et dans le monde entier.

À l'avenir, davantage d'analyses sont nécessaires pour répondre aux questions concernant la systématique et la réduction à grande échelle des rapports isotopiques de Ca radiogénique pour son utilisation en tant que traceur géochimique. La contrainte du ^{40}Ca fluvial moyen et la composition des autres flux du système global de Ca radiogénique sont importantes pour limiter l'évolution du Ca radiogénique dans les océans. Afin de mieux comprendre la systématique de Ca radiogénique dans les rivières, nous devons étudier des bassins versants bien limités, tels que Khudi Khola, et utiliser des approches multi-proxy. Le couplage des mesures d'isotopes radiogènes de Ca (sensibles au vieillissement carbonaté et silicaté) avec d'autres systèmes isotopiques, tels que les rapports isotopiques Sr, s'est révélé avantageux dans cette thèse. Cependant, le couplage des isotopes radiogènes de Ca avec d'autres systèmes isotopiques, tels que les systèmes isotopiques de Li et Si (sensibles aux

procédés au silicate, au carbonate et aux processus biologiques), pourrait s'avérer encore plus avantageux. Beaucoup de travail reste à faire, mais les données de cette thèse confirment que les isotopes radiogéniques de Ca, mesurés par TIMS, pourraient potentiellement éclairer certaines des questions les plus importantes de la géochimie et des sciences de la Terre: les interactions entre climat, érosion, intempéries, etc. et le cycle global du carbone.

Author's Declaration

I declare that this thesis has been composed solely by myself and that it has not been submitted, either in whole or in part, in any previous application for a degree. Except where otherwise acknowledged, the work presented is entirely my own.

Jesse Davenport

2018

Acknowledgments

First point, this section is going to be long, sorry about that. Second point, maybe some will read this, maybe not, but I still appreciate your friendship, help, guidance, and all the fun times we have had together.

At the end of my Master's thesis and after painstakingly applying for numerous positions not many options were available to me. Then came an opportunity to work in quite a different discipline of geology in the Himalaya. I was accepted for the position and I decided to embark on an adventure of a lifetime.

It is certainly not an easy task to move to a foreign country thousands of kilometers away from everyone and everything you know, not in the least bit that the said country was France. A place where good food (and bread) flows freely, the wine flows thickly, and the paperwork even thicker. Despite the difficulties I've endured as a foreigner in France, I have highly come to appreciate and respect the people I've met here and the relationships I've forged here, the life here and everything in-between. This appreciation would certainly not have been possible without the help of an endless list of people who I will not be able to thank all here, but know that I am forever indebted to you.

First, and most importantly, I wish to acknowledge and thank my parents (Doug and Cindy), my grandparents (Jesse and Kathy), my sister (Rebekah) and all my family (far and near) back in the good ole U.S.A., without whose support and continual encouragement, I would have never come this far in my education and life, let alone be here in this position at the end of my thesis. It was always very difficult to explain to you how hard it has been and for you to understand, but, depsite that, you always stuck by my side. I don't think that I will be ever able to repay the debt that I owe all of you for all of this help and encouragement, but I hope (and know) that you recognize that I am forever grateful for you.

When I arrived in France, the first person that I met was Guillaume Morin (and the first French person I ever met in my life) and Guillaume buddy, I don't think I could ever express how much your friendship, guidance and aid has meant to me throughout these past five years. You are now far from Nancy, doing awesome things and living a great life in the mountains, but I will never forget the experencies that we have shared, no matter how far apart we are or no matter how long it has been since we've seen each other the last time.

Damien... you are the first person in Nancy (besides Guillaume) who made

me really feel like I was welcome here and that I have a place here. There were no pretenses, no judegements. It was "Oh, dude, you like metal?", "Yea, I do," "Awesome, come to my concert next week!" And the rest is history! We've had our good times and we've had bad times, but these experiences equally mean so much to me and I am exited for the good experiences to continue!

Aurelian... well you were only in Nancy for a year, but wow, that was a crazy year. We did some really dumb things, but man I wouldn't change anything about it!

Aimeryc... finish your house so we can have a party in it! But honestly, Aimeryc, you are a great guy and a great friend. Watching soccer, drinking beers, etc. I hope it continues.

To Remi B: We really didn't interact much during the first two years of my thesis, you told me that "you were afraid to speak to me." But when your friends starting moving on to better places, we discovered our mutual passion for music and vinyl. And frankly, Remi, I really don't know what my life would be like here in France without you. You are an amazing friend and even though you have your fancy job at Arcelor Mittal, I hope that we will continue to have such a meaningful friendship.

To Martin and Camille: Well it has been a really long time since we've spoken to each other, but really, you guys are awesome! I can't even count the number of times we did things together, but I always had a fun time, whether it was rock climbing or watching GOT, or looking at comics when we should have been working. Doesn't matter, always had fun, always laughing. Now, you guys are far away, with your sheep, doing whatever you do. I hope you guys are well and that I have the opportunity to see you soon!

To all the thesards and post-docs throughout the many years that I've been at CRPG: Yumi, Christine, Lea, Precillia, Paul, Imine, Nina, Lionel, Arjan, Sebastien (Big and small), all the Guillaumes, Leo, Romain, Yara, Remi, David, Elodie, Sara, Nicholas, Florian, Julien, Isabella x2, Michael, Antoine, Ruben and to the newer thesards/post-docs who maybe I don't know as well and any people I have forgotten. Whether we had many interactions or very few, your presence in my life has profoundly effected me and made me a better person!

To all the technicians/administration at CRPG: Catherine, Aurelie, Cati, Joelle, Isabelle, Corinne, Christiane, (encore) Aimeryc, (encore) Damien, Nordine, Pierre, Abdallah, Manu, Delphine, Julien, Bouch, all of the wonderful people of the SARM...thank you! YOU all are the people who make research possible, who make PhDs possible, who make CRPG possible. I don't think people thank you enough at all, but I thank all of you from the bottom of my heart because you made it possible for me to be able to live here in Nancy and work at CRPG. Whether you helped me book a trip for a conference, or helped me with my carte de sejour or helped me with an

analysis or did analyses for me I have learned many valuable things from all of you.

To Thomas R.: We survived Nepal during the monsoon together, well mostly. I think that is all there needs to be said about our friendship. Thank you!

To all of the researchers at CRPG thank you! I have learned many valuable life lessons through my expereinces with you.

To all of my friends, far and wide, whether in France, the U.S.A. or in some far part of the world...thank you! Friends like you make life worth living and striving to be better.

To all of the members of iTECC, whether student, post-doc, professor or collaborator. The relationships forged in this group I think will last a lifetime and I will always cherish the memories that I have of this group at meetings, conferences, and on field trips. I wish you all luck in whatever adventures life will take you on!

To Gwladys Govin: It is still hard, even after more than a year, to understand and process that you are gone. You were, without a doubt, one of the most energetic, enthusiastic, and complex people I have ever met, and honestly that made it hard to be your friend sometimes. Despite this, you were a good friend and I will always cherish the too short time that we had together. I never had the opportunity to say good-bye... I miss you Gwladys.

Finally, thank you Laurie for all of your help, guidance, and just the fact that you were willing to sit down and listen. I know that you were very busy, but I really appreciate how you've taken the time to help me get to the point where I am now.

To my parents, Doug and Cindy, without whose support and dedication,
love and sacrifice
none of this would mean anything...

Contents

List of Figures

List of Tables

CHAPTER 1

INTRODUCTION AND BACKGROUND

> "Ah!" I cried, springing up. "But no! no! My uncle shall never know it. He would insist upon doing it too. He would want to know all about it. Ropes could not hold him, such a determined geologist as he is! He would start, he would, in spite of everything and everybody, and he would take me with him, and we should never get back. No, never! never!" My over-excitement was beyond all description.
> *Jules Verne*

When we think of mountains, rivers, and volcanoes, we usually think of sports, cold or hot weather, the outdoors, maybe even the dangers associated with volcanic explosions. But do we ever think that these structures, among others, play crucial roles in governing the climate and Earth's habitability over geological timescales (i.e., millions and billions of years)? Mountains, rivers, the oceans and atmosphere, volcanoes, erosion, weathering, and plate tectonic movement are some of the structures and processes that are all encompassed within the larger process known as the global carbon cycle. The global carbon cycle is a current topic of heated debate because of its significance in the process of climate change and its implications for Earth's future habitability. The realization that the global carbon cycle and climate change are connected is, in fact, not new but dates to 1896 when Svante Arrhenius first showed that the burning of fossil fuels, which intensified with the beginning of the Industrial Revolution, was actually increasing the amount of carbon dioxide in the atmosphere. Based on observations of the interactions between CO_2 and infrared radiation, he concluded that increases in the Earth's surface temperature are a consequence of increasing atmospheric CO_2 concentrations. This eventually led to the birth of the idea of the "greenhouse effect" and the global carbon cycle.

The mechanisms that influence the climate and climate's response occur over many different time-scales. Geologists and climatologists have made numerous observations about the interactions between Earth's atmosphere and the global climate system on timescales ranging from decades to millions of years. Through time, Earth's climate has been changed and influenced by both external and internal forcing mechanisms. External forcing mechanisms can include changes in solar energy levels, Earth's orbit, land-use, volcanism, and atmospheric composition. Internal forcing mechanisms include variations in El Nino and/or the Indian Summer Monsoon (ISM). Geochemistry has continuously been interested in attempting to understand these processes and their connections with and influences on Earth's global climate over geological timescales. The recent spike in public interest in short-term anthropogenic climate change has provided a significant push to study all aspects of the global climate and climate change over all timescales.

1.1 The Global Carbon Cycle

The global carbon cycle can be divided into two different cycles that work at two different timescales: 1) the deep, geological carbon cycle (millions to billions of years) (see Figure 1.1 and 1.2) and 2) the short-term cycle (days to thousands of years). At its core, the global carbon cycle is the movement, exchange, and transfer of carbon between reservoirs that consume (sinks) and produce CO_2 (i.e., biological, geological, chemical, and physical), otherwise known as sources.

Processes such as photosynthesis, plant respiration, the formation and decay of carbonate-bearing oceanic organisms, and the decay of continental organic material, among others, occur in the short-term carbon cycle (and are not of direct interest to this thesis). The long-term carbon cycle is the sum of the processes that exchange carbon between rocks and the atmosphere, oceans, and biosphere. This exchange controls Earth's climate over millions to billions of year.

The process of silicate weathering plays a crucial role in regulating this transfer of carbon between rocks and the Earth's surface, the concentration of atmospheric CO_2, and the global climate (Walker et al., 1981; Garrels, 1983). Ebelmen (1845) and Urey (1952) were the first to speculate on this transfer of carbon but the ability to quantify these processes and their complex interactions has proven to be difficult. When a silicate rock experiences weathering, atmospheric CO_2 is transformed into dissolved bicarbonate (HCO_3^-):

$$2CO_2 + H_2O + CaSiO_3 \leftrightarrow Ca^{2+} + 2HCO_3^- + SiO_2 \tag{1.1}$$

Rivers then transport the Ca^{2+} and HCO_3^- to the oceans where they precipitate as $CaCO_3$ in marine sediments (Figure 1.2):

$$Ca^{2+} + 2HCO_3^- \leftrightarrow CaCO_3 + CO_2 + H_2O \tag{1.2}$$

Equations 1.1 and 1.2, can be combined into equation 1.3, which describes the general total reaction and consequence of silicate weathering and carbonate precipitation:

$$CO_2 + CaSiO_3 \leftrightarrow CaCO_3 + SiO_2 \tag{1.3}$$

When silicate minerals, which contain Ca and Mg, are weathered 1 mole of CO_2 is consumed for every mole of Ca or Mg liberated during weathering. Carbonate weathering, at long time scales, results in no CO_2 consumption since the CO_2 removed by marine carbonate precipitation simply balances the CO_2 released during

weathering.

Marine sediments that contain precipitated carbonate (Equation 1.2) are eventually buried deep and undergo burial metamorphism and are stored in the deep, oceanic carbonate reservoir for millions of years. This carbon eventually returns to the atmosphere, either through metamorphic reactions during orogenesis or through degassing at mid-ocean ridges and volcanic arcs if the sediments are subducted into the mantle, thus renewing the carbon cycle.

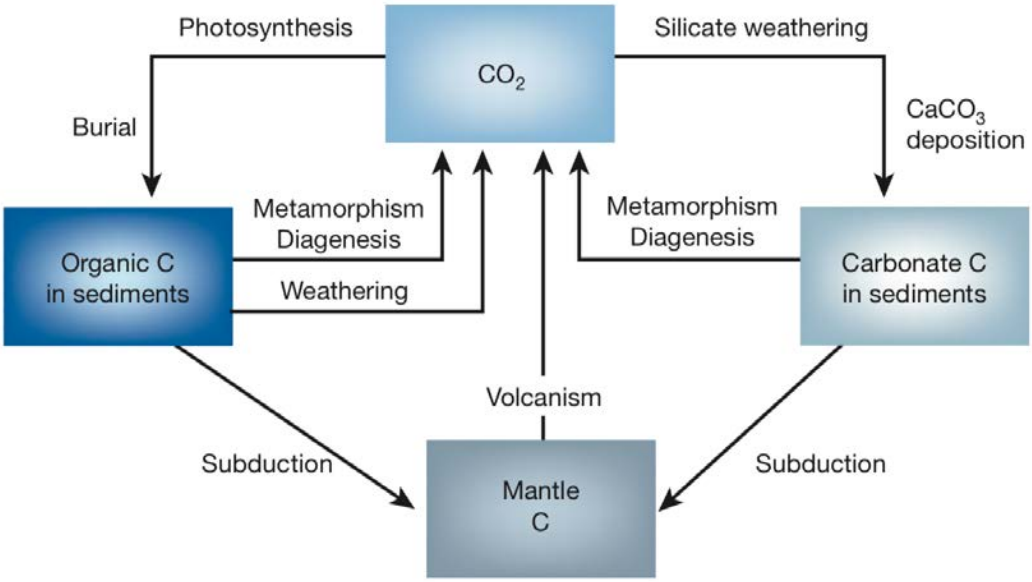

Figure 1.1 – *A model of the long-term carbon cycle and the major processes that occur within it, from Berner et al. (2003).*

Another important component of the long-term carbon cycle is the cycle of organic carbon, which, similar to silicate weathering, has a significant impact on the removal of atmospheric CO_2. The process of organic carbon burial is represented by the following reaction:

$$CO_2 + H_2O \leftrightarrow CH_2O + O_2 \tag{1.4}$$

In the forward reaction, organic carbon is buried and results in the removal of CO_2 from the atmosphere. In the reverse reaction, organic material is oxidized, resulting in the release of CO_2.

Other sinks in the global carbon cycle include the oceans. In the oceans, carbon removal occurs in cooler regions because colder temperatures increase the solubility of CO_2, whereas warmer temperatures release CO_2 to the atmosphere. The oceans are

a major reservoir of carbon, which is provided, in large part, by rivers that transport dissolved Ca and organic matter from the continents. As mentioned above, the final step of marine carbonate precipitation removes CO_2 from the atmosphere. Marine carbonates can form by either biologic or inorganic processes. Biologically, small oceanic organisms, such as foraminifera, use Ca to build carbonate exoskeletons. When these organisms die their shells sink to the ocean floor forming sedimentary carbonate, which is eventually buried deep in the oceanic carbonate reservoir. Inorganically, dissolved calcium and bicarbonate are transported from the continents to the oceans, sink to the ocean floor, and directly form carbonate in sediments. These processes do not consume CO_2 rapidly but, over geological timescales, they contribute to the significant removal of CO_2 from the atmosphere.

Tectonic activity, such as volcanism, subduction, orogenic uplift, and plate motions, also drives changes in the long-term carbon cycle. Each individual process affects the long-term carbon cycle in different ways. For example, ocean currents and circulation are strongly affected by continental position and climate. Volcanism directly provides CO_2 to the atmosphere but also affects terrestrial organisms by increasing soil nutrients. Uplift increases the magnitude of continental erosion and weathering, which, in turn, increases the supply of cations, anions, and other nutrients to the oceans.

Rivers provide the link between the continents and the oceans, transporting solutes and solids that play a key role in determining the composition and functioning of the oceans and its chemistry. At Earth's surface, the processes of erosion, alteration, and weathering redistribute mass and chemical elements from bedrock to rivers, thus determining the composition of river waters.

At the catchment scale, erosion produces sediments from soil and bedrock, whereas chemical alteration and weathering break down bedrock, soils, and sediment even further, which are then delivered as dissolved inorganic cations and anions to rivers and eventually to the oceans. The effects of weathering and erosion on each element within a rock are difficult to quantify because different processes affect each element in various ways. However, erosion and alteration are equally important because the intensity of each determine the interactions and equilibrium between the continents, rivers, and oceans.

Increases in erosion provoke increases in weathering, as erosion acts to resurface and break down the continental crust into sediments exposing fresh mineral surfaces that are not stable at surface conditions. Weathering acts to modify these minerals into a stable form and, at the same time, releases dissolved cations and anions. Several studies have shown that a delicate relationship between erosion and weathering exists but is dependent on the characteristics of the basin under consideration (White and

Blum, 1995; Millot et al., 2002).

The relationship between erosion and weathering can be simplified to two specific cases: 1) transport-limited and 2) kinetically-limited. Transport-limited processes correspond to situations where soils and sediments are produced faster than erosion can remove them from the system. This results in thickening soils and sediment deposits that cover bedrock and thus allow the possibility of increased weathering. Kinetically-limited processes refer to a situation where erosion rates far exceed the rates at which soils and sediments are produced, which results in the immediate removal of material, and thus limit weathering. These relationships are especially important in the Himalaya where unique lithologic, climatic, and landscape conditions provide a situation where it is sometimes difficult to establish clear relationships between river chemistry and erosion and weathering processes.

The rates and magnitude of the various processes mentioned above control the amounts and balance of carbon within each of Earth's reservoirs (Garrels, 1983; Berner et al., 2003). These authors argue that over a 100 Myr time scale, carbon fluxes are balanced, leading to a long-term 'steady-state' condition (Garrels, 1983; Berner, 2006). Carbon fluxes are not independent but rather are complexly connected, which leads to positive and negative feedbacks that affect the climate. The carbon budget is a synthesis of all of these reservoirs (sources and sinks): the quantity of carbon in each and the amount of carbon coming in and out of these reservoirs.

The ability to trace or understand the reactions discussed above is important when attempting to understand the carbon cycle and how it affects the climate. However, this is not an easy task. In this thesis, we focus on one important aspect of this problem, tracing the intensity of silicate weathering. Many attempts have been made to find the most appropriate proxy of silicate weathering, which in general is provided by the analysis of some aspect of river chemistry. The appropriate proxy, however, depends on many factors that vary significantly by region and, thus, it is not straightforward to find a proxy that is suitable for all regions. This is an important caveat in our attempt to constrain the carbonate and silicate weathering budgets in the Himalaya. To illustrate this point, we can take, as an example, the use of proxies such as $\delta^{18}O$ and $^{87}Sr/^{86}Sr$ (from approximately 0.7078 to 0.7092) (McArthur et al., 2001). The marine values of these proxies increased simultaneously during the Cenozoic, from approximately 0.3 to 3.5 percent per mil for $\delta^{18}O$ (Lear et al., 2000) and 0.7078 to 0.7092 for $^{87}Sr/^{86}Sr$ (since approximately 40 Ma) (McArthur et al., 2001), which is thought to be a consequence of the cooler climatic conditions that dominated towards the end of the Cenozoic. Sr isotopes have been used extensively to trace the process of silicate weathering and to try to quantify the consumption of CO_2 in the global carbon cycle due to the marked contrast of Sr isotopic compositions between carbonate

and silicate, as well as between crustal and mantle sources. However, interpreting the marine Sr isotopic record and its implications for the global carbon cycle is complicated, and these complications are particularly evident when Sr isotopes are used to study silicate weathering in the Himalaya. In the following discussion, we focus on the use of Sr isotopes to trace past changes in silicate weathering, both because this system has been extensively exploited and because of the chemical similarities between Sr and Ca.

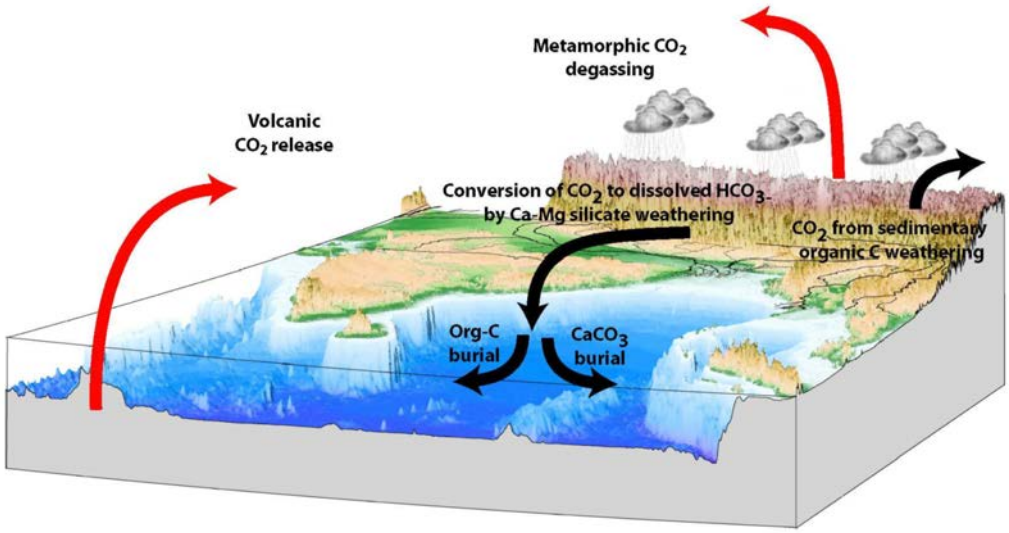

Figure 1.2 – *A representation of the global carbon cycle and the processes that occur within it, such as silicate and carbonate weathering, marine carbonate sediment formation, volcanism, and metamorphic degassing from Berner et al. (1999).*

1.2 Tracing silicate weathering: clues from Sr isotopes

The Rb–Sr system has long been used as a proxy to trace the magnitude and extent of silicate weathering. This is due to the fact that the upper continental crust has a more radiogenic composition than the mantle because Rb is more incompatible than Sr, and Rb thus concentrates in the upper crust, decaying to radiogenic Sr. This is what led to the idea that radiogenic Sr could be used to trace silicate weathering processes. Strontium also has a long residence time in the oceans (approximately 2 million years). This implies that when we analyze the isotopic evolution of Sr in the oceans across geological timescales, we observe global processes rather than smaller, short time-scale processes. Thus, it was proposed that the increase and decrease in the marine $^{87}Sr/^{86}Sr$ record could provide information on past changes in weathering, erosion, mountain building, plate tectonics, and the climate. In fact, it was Wickman (1948) that first proposed that, with the steady decay of ^{87}Rb in the Earth's crust, the Sr isotope signature in seawater would increase at a steady rate through time. Unfortunately, Wickman (1948) not only overestimated the average Rb/Sr of the crust but also did not possess knowledge of seafloor spreading, subduction, and plate tectonics (which was ten to twenty years in the future), all processes that have led to the very increases and decreases in the marine Sr record that provide important information (Palmer and Edmond, 1989; Hodell et al., 1991; Richter et al., 1992; Palmer and Edmond, 1992; DePaolo and Ingram, 1985; Hess et al., 1986; Jones and Jenkyns, 2001).

1.2.1 The marine Sr isotope record

Between 1948 and the 1970s many analytical advancements were made in the fields of isotope geochemistry and isotope ratio mass spectrometry, which led to new discoveries with increasing levels of precision. Peterman et al. (1970) were able to measure the $^{87}Sr/^{86}Sr$ compositions of macro-fossil shell carbonates with an order of magnitude increase in precision (0.0005 compared with 0.004 previously). They found that the $^{87}Sr/^{86}Sr$ values decreased throughout the Paleozoic, with a minimum in the Mesozoic, and subsequently increased towards present-day values. Additional data were compiled by Dasch and Biscaye (1971) and Veizer and Compston (1974) from Cretaceous to recent pelagic foraminifera and sedimentary carbonate, respectively. Their results generally agreed with those of Peterman et al. (1970). Veizer and Compston (1974) found that sedimentary carbonate could possibly be an unreliable tracer of the Sr isotope composition of seawater due to possible post-depositional exchange with pore waters, which would increase the $^{87}Sr/^{86}Sr$ ratios. They noted that the minimum ratio values would, therefore, be a better estimate of the Sr isotope composition of seawater. Using the reasoning above, Veizer and Compston

(1976), using Precambrian carbonates, reconstructed the PreCambrian Sr evolution of seawater. In these samples, they found unradiogenic values of Sr isotopes, only slightly elevated from mantle values. They found a significant rise in $^{87}Sr/^{86}Sr$ values during the Proterozoic that reached a maximum in the Cambrian similar to present-day values of seawater. A major effort, between 1982 and the early 90's, was made to better define the Sr isotope curve of the PreCambrian by using continuous records that were previously unattainable (Burke et al., 1982; Derry et al., 1989; Asmerom et al., 1991; Kaufman et al., 1993) (see Figure 1.3).

Further research was focused on issues associated with improving the precision on very small segments of the Sr isotope curve as well as improving techniques for sample preparation and analysis. Various types of samples were used, including brachiopods, foraminifera, belemnites, and other types of fossils. DePaolo and Ingram (1985) were able to reconstruct a precise curve for the past 100 Myr using samples from the Deep Sea Drilling Project (DSDP). These cores presented a well-preserved record of microfossils with fairly constant sedimentation rates calibrated by techniques such as biostratigraphy and magnetostratigraphy.

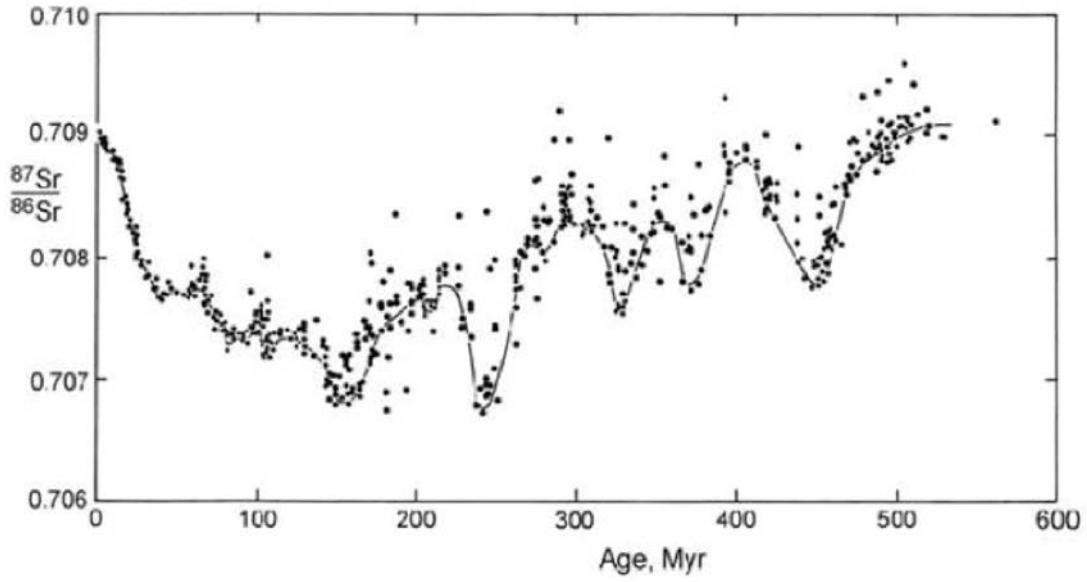

Figure 1.3 – *The Sr isotope evolution of seawater throughout the Phanerozoic from Burke et al. (1982). The solid line indicates the lower bound of errors and most likely represents the best estimate of marine Sr isotopic evolution.*

1.2.2 The fluxes of Sr

In order to interpret the marine Sr record, it is essential to consider the fluxes of Sr to the ocean and their isotopic compositions. The most obvious flux of Sr to the oceans is river-borne Sr derived from continental weathering. Current weathering fluxes

are relatively straightforward to ascertain, but information about ancient weathering fluxes is more elusive. Spooner (1976) proposed a major advance in Sr modeling when he suggested that a significant flux of unradiogenic Sr originates from submarine hydrothermal exchange and alteration of basalt on the seafloor. Spooner (1976) calculated this Sr flux to be 6 times the magnitude of the Sr flux from rivers to the oceans. This was later proven to be much too high, due to overly radiogenic estimates for Sr isotopic ratios from rivers and hydrothermal alteration. Analyses from East Pacific Rise hydrothermal vents (Albarède et al., 1981) showed that the hydrothermal Sr flux was approximately one-fourth of the riverine flux, in agreement with the conclusions of Brass (1976). The magnitudes of Sr fluxes were further updated by Palmer and Edmond (1989) and more recently by Gaillardet et al. (1999). After Spooner (1976) proposed the hydrothermal Sr flux, two more sources of Sr to the oceans were proposed. A very small flux due to the diagenetic recrystallization of seafloor carbonates was proposed by Elderfield and Gieskes (1982). In addition, a still relatively unknown source of Sr from continental groundwater flux was proposed by Chaudhuri and Clauer (1986). These proposed fluxes are shown in the illustration of Figure 1.4.

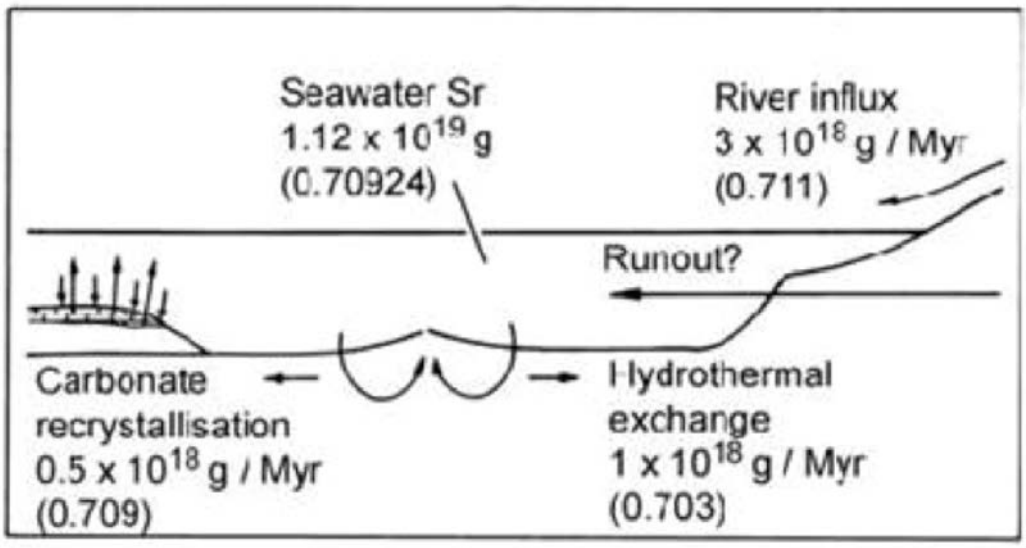

Figure 1.4 – *A simplified cartoon circulation model of the "well"-constrained fluxes of Sr to the oceans from DePaolo and Ingram (1985).*

The globally averaged flux of groundwater, as well as its composition, remains

a largely unconstrained component of the global mass balance of oceanic Sr. In the Himalaya, the potential importance of the groundwater flux for elements such as Sr into the Bay of Bengal was first proposed by Moore (1997). Galy et al. (1999) argued that the groundwater Sr flux, though poorly known, was at most, only a minor component in the Himalayan system. In contrast, Basu et al. (2001) concluded that the flux of Sr to the Bay of Bengal was a major, missing piece of the so-called Himalayan/oceanic Sr puzzle. Dowling et al. (2003) proposed quantitative estimates to the Sr flux following Basu et al. (2001). However, an extensive hydrogeological modeling study conducted by Michael and Voss (2009a,b), contradicted the findings of Dowling et al. (2003), concluding that the groundwater flux of radiogenic Sr is likely to be relatively minor.

A number of studies have set out to seek potential missing fluxes of Sr to the oceans. This search is motivated by the fact that the known hydrothermal Sr flux is too low to balance the more radiogenic Sr from riverine fluxes, suggesting the need for an additional unradiogenic flux. Over the Neogene and Pleistocene, the oceanic $^{87}Sr/^{86}Sr$ ratio has increased at a rate of 0.000054 Myr^{-1} (Hodell et al., 1989; Henderson et al., 1994). This creates a discrepancy in Sr mass balance calculations that show that the radiogenic riverine Sr flux (approximately 0.7136) (Allègre et al., 2010) is not balanced by the unradiogenic hydrothermal flux (approximately 0.7029) (Albarède et al., 1981). For a balance to occur, the magnitude of the hydrothermal flux must be 4–20 times greater than current estimates (Davis et al., 2003; Hodell et al., 1989; Palmer and Edmond, 1989; Vance et al., 2009; Jones et al., 2014). To compensate for this imbalance, several unradiogenic Sr fluxes have been proposed, such as an unradiogenic groundwater component from volcanic regions (Allègre et al., 2010) or the occurrence of off-axis hydrothermal exchanges at mid-ocean ridges (Elderfield and Gieskes, 1982).

A more recent proposition suggests that riverine particulate matter delivered to the oceans, especially from unradiogenic volcanic terrains, could help provide the required additional flux of unradiogenic Sr (Oelkers et al., 2011; Jones et al., 2012, 2014; Jeandel and Oelkers, 2015). Oelkers et al. (2011) investigated the role of particulate fluxes in various river systems throughout the world. They found that particulate fluxes dominate over dissolved elemental fluxes in river water. This particulate matter is transferred to the oceans and may include several isotopically distinct phases. The effect on seawater depends on the dissolution rate of the matter, which strongly depends on the surface area of the particles. Their main conclusion is that the dissolution of isotopically distinct particulate material, such as basalt from young volcanic islands, can significantly alter the Sr isotopic composition of seawater.

Jones et al. (2012) continued studies on particulate matter fluxes to the oceans

by conducting laboratory experiments in which they developed particulate material with differing Sr isotopic compositions and let them dissolve in batches of seawater for periods of up to 6 months. They found that all particulate material changed the Sr isotopic composition of seawater significantly within 24 hours. This highlights a possible, significant source of Sr to the oceans unaccounted for in the oceanic budget until recently.

1.2.3 Modeling the evolution of Sr

Over the years, there have been many attempts to model the Sr isotopic composition of seawater, using the Sr fluxes understood at the time. Faure et al. (1965) proposed the first model for the evolution of Sr in seawater but only used this model to try to explain modern seawater compositions. This model used a balance of Sr fluxes between young volcanics (unradiogenic Sr), older crustal rocks (radiogenic Sr) and erosion of carbonates (intermediate Sr). Peterman et al. (1970) adapted this model to try to account for the increase and decrease of Sr isotope ratios throughout the Phanerozoic. And finally, this model was also used by Armstrong (1971) in which he suggested that the peaks of Sr isotope ratios correlate well with peaks in glacial intensity during the Carboniferous and Tertiary, when glacial activity eroded crustal material with radiogenic ^{87}Sr (Figure 1.5).

Looking at Cenozoic geochemical evolution, François and Goddéris (1998) constructed a geochemical model based on the carbon and alkalinity budgets of the ocean. For inputs, they used C and Sr isotope data from seawater as well as seafloor spreading rates. They found that Cenozoic evolution was marked by the succession of a warm mode, a cooling transition, and then a cold mode. During the warm mode, a classical silicate weathering feedback regulated the atmospheric CO_2 content and the input of CO_2 from volcanoes was balanced by the silicate weathering sink. This was followed by a transitional period during during which their model also suggests a substantial increase in the riverine $^{87}Sr/^{86}Sr$ ratio between 40 and 15 Ma. The model suggests that the Cenozoic was marked by a transition from a 'chemically' to a 'physically' controlled weathering regime, reflecting changes in temperature from warm to cold.

1.2.4 The rapid increase of the $^{87}Sr/^{86}Sr$ marine record during the Cenozoic: Effects of Himalayan uplift

The past 60 Myr present a particularly good period to study the contribution of different fluxes of Sr due to the extremely rapid rise of the $^{87}Sr/^{86}Sr$ ratio of seawater during this time. This time period is characterized by a number of orogenic events, such as the rise of the Swiss Alps, the New Zealand Alps, the Andes in South America, and the Laramide orogeny of the southwestern United States. But most importantly,

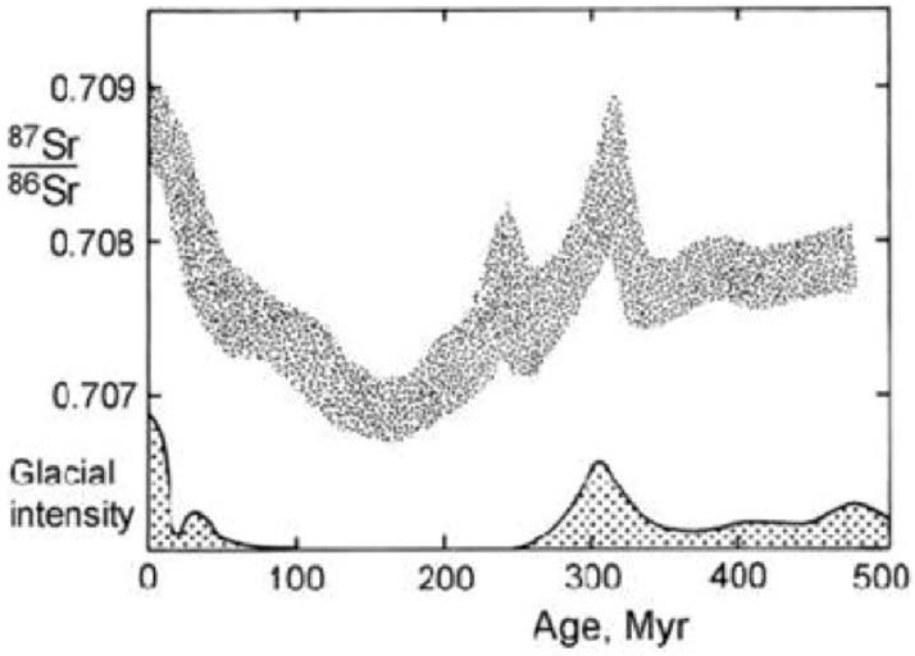

Figure 1.5 – *The evolution of Sr in seawater for the last 500 Myr with the corresponding glacial intensity during the same time period from Peterman et al. (1970). Peaks of glacial intensity seem to correlate with periods of rapid Sr growth from Armstrong (1971).*

this rise in Sr isotope ratio coincides with the collision of India and Asia and the uplift of the Himalaya.

During the Late Precambrian and into the Paleozoic, India was part of the Gondwana supercontinent and separated from Eurasia by the Tethys ocean. A number of various rifting events slowly began to initiate the closure of the Tethys ocean. India broke away from Australia and Antarctica in the Early Cretaceous creating the southern Indian Ocean. India then, in the Upper Cretaceous, began its fast ascent northward towards Asia, covering a distance of 6,000 km with the first signs of continent-continent collision/tectonic activity at approximately 65 Ma. Evidence for this comes from the relative speed of the Indian and Asian plates: 18–20 cm/yr prior to 55 Ma to approximately 4 cm/yr (Dèzes, 1999; Yin, 2006; Patriat and Achache, 1984).

During the 1990s, the debate on the role of the Himalaya in the evolution of oceanic Sr was centered around two sides: (1) those claiming that Himalayan erosion has increased the flux of dissolved Sr to the oceans (Richter et al., 1992; Raymo et al., 1988; Raymo and Ruddiman, 1992) and (2) those that claim that the flux remained stable but that the isotopic signature of the dissolved Sr being delivered to the oceans increased (Edmond, 1992; France-Lanord et al., 1993; Derry and France-Lanord, 1997,

1996).

Raymo et al. (1988) and Hodell et al. (1989) proposed that the increasingly radiogenic character of seawater Sr during the last 40 Myr (Figure 1.6) is a consequence of increasing uplift rates of the Himalayas, Tibet, and the Andes throughout this time period. The rivers that drain these areas, i.e., the Ganges-Brahmaputra, Yangtze, and Amazon, are some of the biggest in the world (20% of the total solid load to the oceans) and have some of the largest global solute and sediment fluxes, which could have supplied a substantial flux of radiogenic Sr to the ocean. Added to this, the hydrothermal Sr flux is thought to have remained constant throughout this period because oceanic spreading rates have remained relatively static since the beginning of the Neogene. Moreover, with an increase in relief, the rapid mechanical exposure/breakdown of rocks, as well as high runoff from orographic effects on mountainous regions (i.e., monsoonal effects), may have favored increased chemical weathering. Furthermore, alpine glaciation initiated the grinding of rocks to fine grain size, increasing the surface area for chemical attack and weathering.

Underlying the debate about whether the increasingly radiogenic composition of seawater Sr is due to an augmentation of the riverine Sr flux or an increase in its $^{87}Sr/^{86}Sr$ ratio is the question of how this flux is related to the intensity of silicate weathering. Both carbonate and silicate rocks contribute to the riverine Sr budget, but only silicate weathering leads to net removal of CO_2 from the atmosphere. It is thus important to determine the proportion of the dissolved load of rivers that is derived from silicate weathering. Wadleigh et al. (1985) first proposed that Sr isotopes could be used, along with Ca/Sr ratios of river water, to quantify the amount of silicate weathering and identify the sources of Ca^{2+} and Sr^{2+}. Palmer and Edmond (1992) and Krishnaswami et al. (1992) undertook an extensive geochemical survey of modern rivers that demonstrated a general worldwide correlation between $^{87}Sr/^{86}Sr$ and 1/Sr. They found, however, that Himalayan rivers fall off this worldwide trend. For the worldwide trend, rivers dominated by carbonate input display low $^{87}Sr/^{86}Sr$ with high [Sr], whereas rivers dominated by silicate inputs have high $^{87}Sr/^{86}Sr$ and low [Sr] (Gaillardet et al., 1997, 1999). Himalayan rivers, however, show an inverse relationship, where carbonates can also exhibit radiogenic $^{87}Sr/^{86}Sr$ signatures.

Using $^{87}Sr/^{86}Sr$ ratios to trace Himalayan silicate weathering is not straightforward because (1) the formations of the Himalaya have different crustal ages, hence contrasting bulk $^{87}Sr/^{86}Sr$ compositions and (2) recent metamorphism redistributed radiogenic ^{87}Sr among silicate phases and towards carbonates (France-Lanord et al., 1993). Edmond (1992) and others (Palmer and Edmond, 1989, 1992; Derry and France-Lanord, 1996) proposed that, during metamorphism, there was a redistribution of Sr between coexisting silicate phases.

For example, the Sr isotopic composition of relatively resistant and very radiogenic biotites was redistributed to less resistant and less radiogenic plagioclase. An even more important complicating factor is that radiogenic Sr from silicates can also be redistributed to carbonates (France-Lanord et al., 1993). For this reason, the relative magnitudes of silicate and carbonate weathering cannot be simply inferred from the Sr isotopic composition of the dissolved load, as both rock types have very similar isotope signatures.

Whilst it is accepted that the input of Himalayan rivers to the ocean has made a significant contribution to the marine Sr isotope record during the Cenozoic (Richter et al., 1992), there is a continuing controversy over how much Sr is derived from radiogenic carbonate and silicate lithologies (Bickle et al., 2001, 2005, 2015; Edmond, 1992; English et al., 2000; Galy et al., 1999; Harris et al., 1998; Krishnaswami et al., 1992; Oliver et al., 2003; Palmer and Edmond, 1992; Quade et al., 1997; Singh et al., 1998). The various estimates range from < 20 to > 50% of dissolved Sr being derived from silicate weathering. This greatly complicates the use of the marine Sr record to try to reconstruct how the intensity of silicate weathering has varied in the past.

1.2.5 *Tracing silicate weathering in the Himalayas: Sr isotope versus major element approaches*

In the late 1980s and early 1990s, several studies focused on the overall geochemistry of the Ganga and Brahmaputra and the general geochemical variations from the headwaters to the floodplains (Sarin et al., 1989; Sarin and Krishnaswami, 1984). They found that river sources are characterized by higher TDS (Total Dissolved Solids, approximately 350 mg/L) and that, moving from north to south, river geochemistry and elemental fluxes highly depend on the lithology of the basin under consideration (Sarin et al., 1989; Galy and France-Lanord, 1999; Sarin et al., 1992). Other studies began to use Sr isotopes more extensively in the Himalaya to try to quantify silicate weathering (Quade et al., 1997; Singh et al., 1998; Galy et al., 1999; McCauley and DePaolo, 1997). These studies, however, prompted more questions than answers, and, since then, numerous additional studies have been devoted to more specific analysis of the tributaries of the Indus and Ganga-Brahmaputra river systems located in the Lesser Himalaya (LH), the High Himalayan Crystalline series (HHC), the Tethyan Sedimentary Series (TSS), and the Siwaliks (see Chapter 2).

For example, Blum et al. (1998) analysed the Sr isotope composition of river sediment, water, and whole rocks from the Raikot watershed in northern Pakistan, which drains the HHC (see Chapter 2). Combined with the Ca/Sr ratio, they found that river water defines a positive trend between unradiogenic marbles and a possible radiogenic, hydrothermally altered vein calcite source (Figure 1.7). This implies

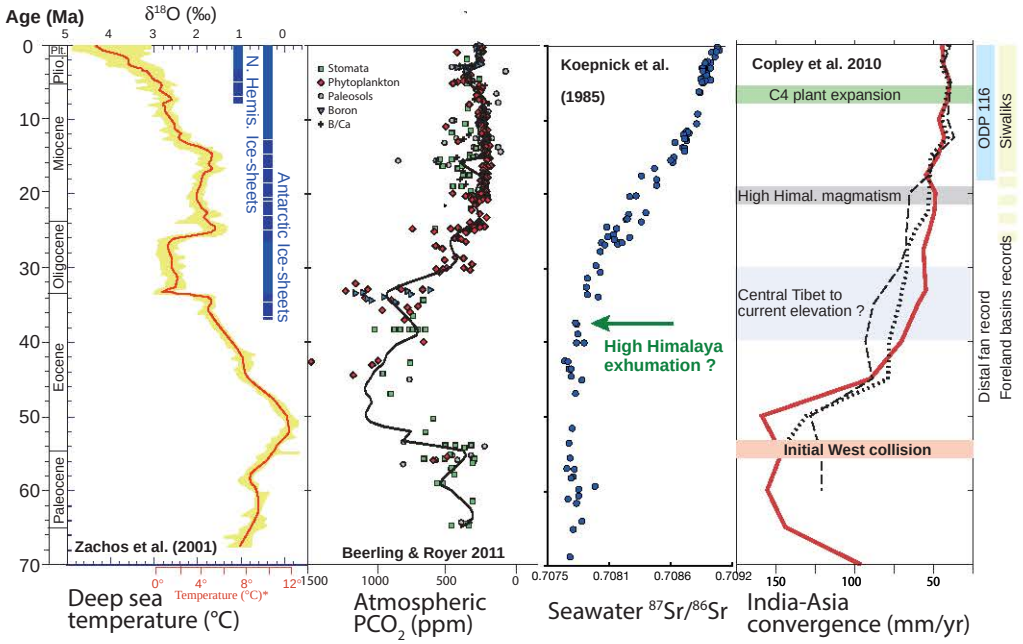

Figure 1.6 – *Record of the $\delta^{18}O$ and deep sea temperature from Zachos et al. (2001), atmospheric pCO_2 concentrations in ppm from Beerling and Royer (2011), and the evolution of the seawater Sr isotope composition from Koepnick et al. (1985) compared with the timing of the convergence of the Indian and Eurasian plates and the rise of the Himalaya from Copley et al. (2010). The increase in $\delta^{18}O$ along with the decrease in atmospheric pCO_2 indicates that global cooling is controlled by silicate weathering among other processes. However, the rise of the seawater Sr curve represents two scenarios, both of which are dependent on Sr transported from the Himalayas to the ocean: 1) If the flux of ^{87}Sr to the oceans has increased over this time period and the composition has remained the same or 2) the flux has not changed and the composition of ^{87}Sr has become increasingly radiogenic consistent with the erosion of highly radiogenic silicate and carbonate lithologies contained within the Himalayas.*

that approximately 82% of the weathering that occurs in the Raikot is carbonate weathering and 18% is silicate weathering, despite the fact that the Raikot catchment has a dominant gneiss and granite lithology (approximately 1% carbonate lithology). This was the first study to underline the important effects that trace amounts of calcite have on weathering budgets and the fluxes of Sr. Chamberlain et al. (2005) found that in areas experiencing elevated rates of rock uplift, such as collisional mountain belts like the Himalayas, weathering of only a small amount of hydrothermal vein calcite (e.g., approximately 3%) produces nearly 60% of the total Sr flux released via chemical weathering. During both congruent and incongruent silicate weathering, the magnitude of this radiogenic Sr flux will be at least one order of magnitude larger in tectonically active areas compared with inactive regions. They conclude that, if

calcite is present, riverine Sr isotopic systematics cannot quantitatively or qualitatively be used to infer the amount of silicate weathering that is occurring in tectonically active orogens. The influence of hydrothermal calcite veins on radiogenic Ca isotope systematics is discussed in Chapter 5.

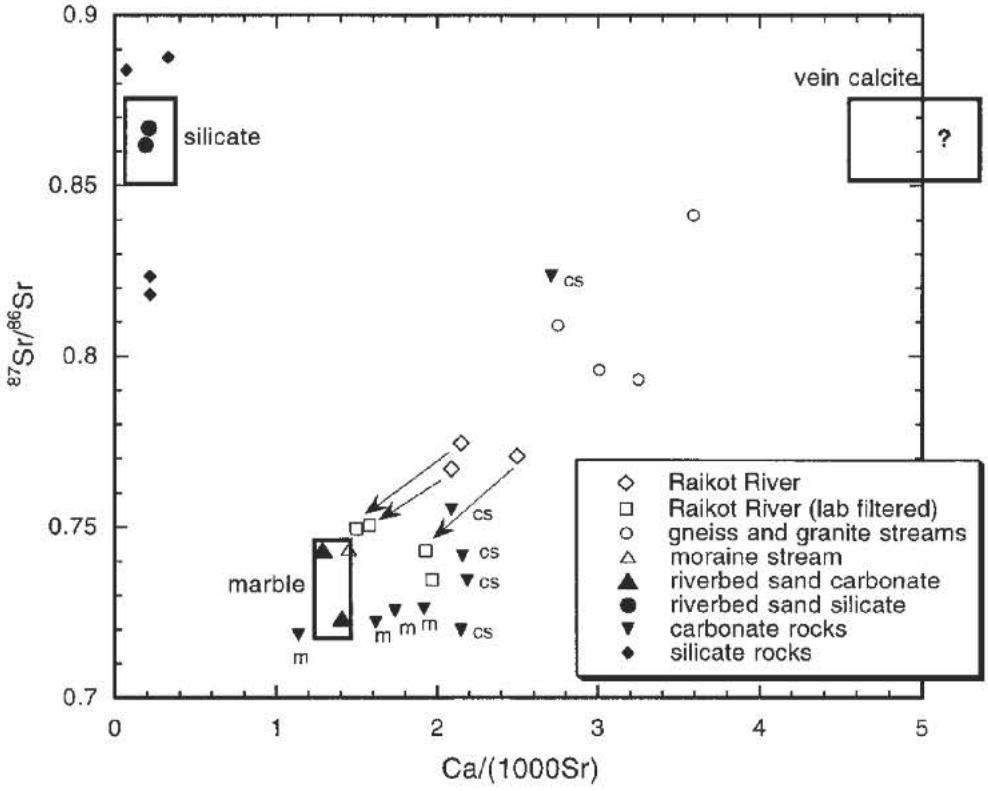

Figure 1.7 – *A plot of $^{87}Sr/^{86}Sr$ versus Ca/Sr for rivers in the Raikot watershed, Pakistan, displaying a trend between two carbonate end-members from Blum et al. (1998).*

Galy et al. (1999), after analyzing numerous river and bedrock samples, proposed several different sources of radiogenic and unradiogenic Sr. Based on hydrological and budget models, they found that riverine Sr derives mostly from a mixture between slightly radiogenic TSS carbonate sources (approximately 0.715) and highly radiogenic Sr derived from LH silicates (> 0.8), despite the presence of highly radiogenic carbonates in the LH. Galy et al. (1999) state that radiogenic LH carbonates are not a significant part of the budget because they are scarce and have low Sr concentrations.

Galy and France-Lanord (1999) proposed that carbonates are the main source of dissolved elements in the dissolved load of rivers. The cations derived from carbonate dissolution represent 80 to 90% of the total cationic charge in all parts of the basin, except in purely silicate drainage basins (Figure 1.8). They also underscored the potential importance of the then unstudied groundwater flux from the Himalayas to

the Bay of Bengal.

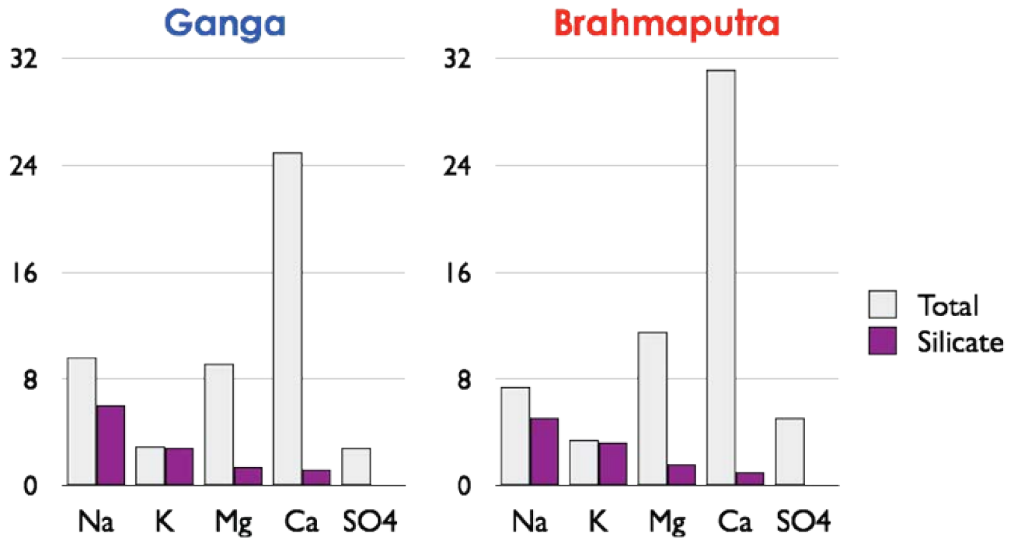

Figure 1.8 – *The relative contributions of silicate and carbonate material for several major cations and anions in the Ganges and Brahmaputra basins from Galy and France-Lanord (1999).*

Jacobson et al. (2002) agreed with the conclusions of Galy and France-Lanord (1999) and Blum et al. (1998), stating that mass balance calculations based on elemental ratios in rocks and river water provide a much better estimate of silicate weathering in the Himalaya than do calculations based on Sr isotopes. Strontium isotope approaches to determine the sources of the dissolved load in Himalayan stream waters have previously underestimated the overall input from carbonate dissolution primarily because carbonate bedrock in the Himalaya has a wide range of Ca/Sr and $^{87}Sr/^{86}Sr$ ratios that cannot be adequately defined by a single end member in conventional mass-balance equations. Also, Ca^{2+} behaves non-conservatively during transport in Himalayan stream waters.

West et al. (2002) quantified the weathering fluxes from various catchments in the Himalaya and used a modal-mineral mass balance to calculate the fluxes of silicate and carbonate weathering. They found that LH catchments have the highest silicate weathering fluxes, whereas the silicate fluxes for small HHC catchments are similar to those of adjacent larger rivers. One of the more important findings from West et al. (2002) is the fact that the silicate weathering intensity in the Ganga plain is up to six times higher than what occurs in the Higher Himalayas.

Quade (2003) studied the Seti and Arun watersheds because of their distinct

lithologies, i.e., the Seti is predominantly composed of LH carbonate and the Arun drains predominantly silicate rocks from the HHC and LH. They found that, despite the presence of silicate rocks, the river geochemistry between the Arun and Seti are dominated by carbonate weathering. For Sr isotopes, they show that the Arun has very little variation despite draining HHC and LH silicate rocks. The Seti, however, has large Sr isotopic variations, especially when passing through LH metacarbonate sequences, which they postulate as having had a possible key role in elevating the marine $^{87}Sr/^{86}Sr$ ratio.

France-Lanord et al. (2003) carried out an extensive river survey of central Nepal rivers to understand the variations in elemental fluxes as well as chemical erosion processes. They found that both runoff and physical erosion play a key role in controlling chemical erosion processes.

An alternative perspective is given by Singh et al. (2005) and Singh (2006), who proposed that silicate weathering contributes about half of the total dissolved Sr to the Brahmaputra system, and the other half originates from evaporites in the Tibetan basin (see Figure 1.9). Bickle et al. (2005) also stressed the importance of silicate weathering, concluding that this process is responsible for > 70% of the ^{87}Sr flux in the Himalayas to the oceans (Figure 1.10). Most recently, Bickle et al. (2015) undertook an extensive study of the dissolved load, bedload sediments, and their constituent minerals from the Dhauli Ganga and Alaknanda, headwaters of the Ganges in Garhwal, and the Marsyandi in Nepal and its tributaries. They used the data from these rivers to try to discriminate between the inputs of major cations and Sr from silicate and carbonate sources. They estimate that up to 60% of the Sr in High Himalayan catchments and 20 to 30% of Sr in Lesser Himalayan catchments are derived from silicates. However, they note that the story is still far from clear, especially when using elemental budgets that require estimates of bedrock-element ratios. Such ratios are subject to large uncertainties, as also pointed out by Galy and France-Lanord (1999) and discussed later in this thesis (Chapter 5).

A number of previous studies have postulated that one possible reason for the large discrepancies between weathering budget models is the occurrence of secondary calcite precipitation. These studies suggest that this process is a first-order control on riverine chemistry in the Himalaya. It has been suggested that up to 70% of dissolved Ca can be removed from the dissolved load, leading to high Sr/Ca and Mg/Ca river ratios (Galy et al., 1999; Jacobson et al., 2002; Bickle et al., 2005, 2015). Thus, secondary calcite deposition has the opposite effect of hydrothermal calcite veins described by Blum et al. (1998). These add Ca to the dissolved load, while secondary calcite deposition removes Ca from the dissolved load.

Furthermore, Evans et al. (2001, 2004, 2008) have shown that central Nepal hot

springs are an important solute and radiogenic Sr source. These studies emphasize the findings of Blum et al. (1998) and Chamberlain et al. (2005) on the importance of radiogenic hydrothermal carbonates that release Sr to the dissolved load. They also emphasize that this radiogenic contribution biases estimates of the consumption of CO_2 during the weathering of Himalayan silicate lithologies.

We know that CO_2 is consumed by Himalayan silicate rock weathering, but as the foregoing discussion implies, the amount is not well-constrained. This is especially true because the Himalaya is characterized by limited weathering, i.e., the intensity of chemical weathering is much lower than that of physical weathering. Furthermore, carbonates experience chemical weathering much more easily than silicates, thus producing a greater flux of weathered carbonates as compared with silicates. Meanwhile, there is an ongoing debate on the effect of the Himalayan organic carbon cycle, which results in a large net burial of organic carbon. This flux has been postulated to be a significantly larger sink of CO_2 than silicate weathering (France-Lanord and Derry, 1997).

The general consensus on whether silicate or carbonate weathering or even organic carbon burial dominates processes in the Himalaya appears to change every few years. For example, Galy and France-Lanord (1999) and Galy et al. (1999) found that the fluxes of silicate weathering are small in the Narayani watershed of central Nepal. Here, carbonate weathering is a more important source of cations in the dissolved load than silicate weathering. Other studies have shown that silicate weathering rates and radiogenic Sr release are higher in the Siwaliks and floodplain of central Nepal (English et al., 2000). More generally, Sr is a poor proxy for quantifying the magnitude of silicate weathering because, at best, it traces old crustal erosion whereas the most active source of silicate weathering is volcanic rocks that are unradiogenic in Sr and rich in easily weatherable minerals (such as glass and mafic phases). These easily weatherable minerals release Ca and Mg when eroded that are efficient consumers of CO_2. Old, crustal rocks, however, have lost their cations during recycling events and are poor consumers of CO_2 (Louvat and Allègre, 1997; Schopka et al., 2011; Schopka, 2011).

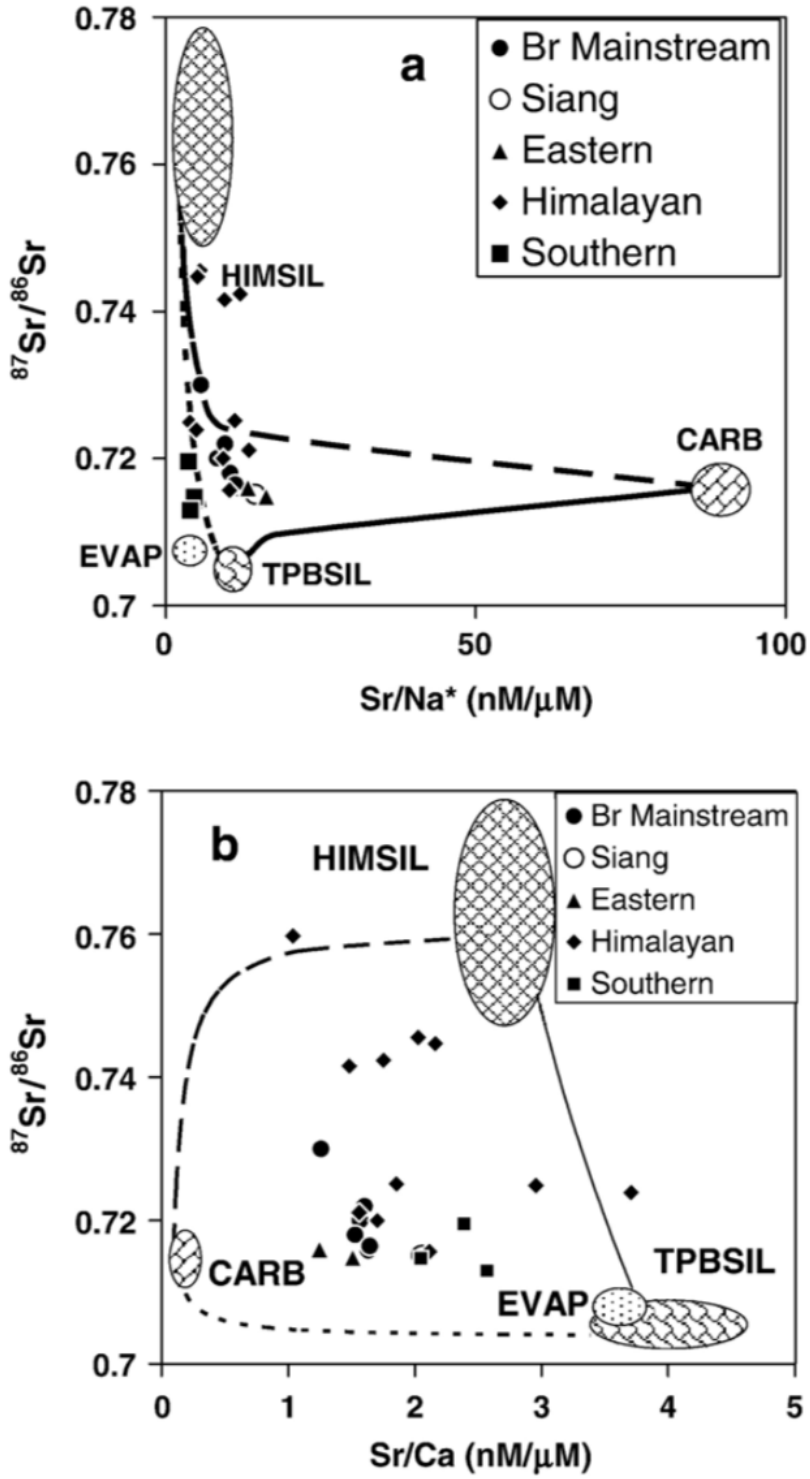

Figure 1.9 – *a)* $^{87}Sr/^{86}Sr$ *vs. Sr/Na* ratio and b)* $^{87}Sr/^{86}Sr$ *vs. the Sr/Ca ratio. According to Singh (2006), these diagrams show that Sr originates from different sources, but that the radiogenic Sr mainly originates from Himalayan silicates. Na* indicates Na concentrations corrected for the contribution of precipitation. CARB = carbonate, EVAP = evaporites, HIMSIL = Himalayan silicate, and TPBSIL = Transhimalayan silicates.*

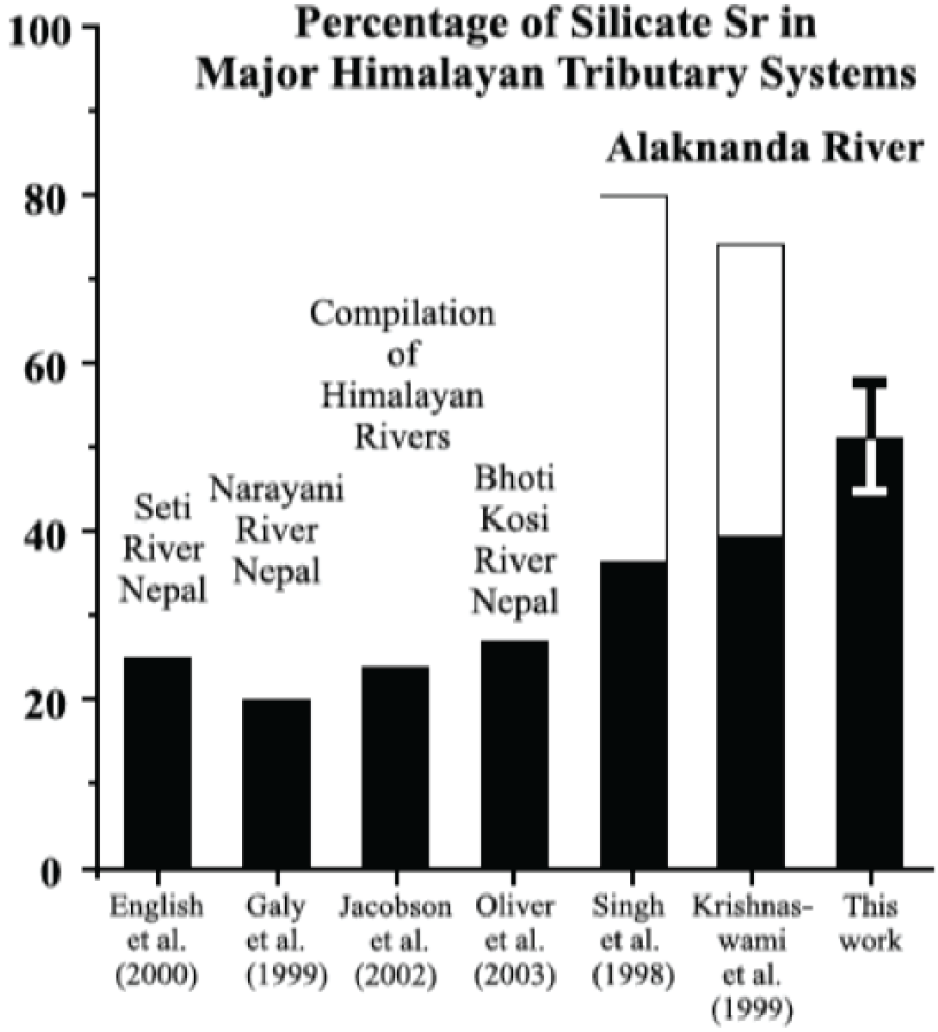

Figure 1.10 – *A graph showing the relative contributions of silicate and carbonate weathering in the dissolved river load for various watersheds from a number of different geochemical and isotopic studies from Bickle et al. (2005).*

1.3 The radiogenic calcium isotope tracer

The ambiguity concerning the interpretation of the Sr isotopic record emphasizes the need for new geochemical tracers, in particular tracers that can succinctly distinguish between carbonate and silicate sources in Himalayan rivers and elsewhere. One particularly promising tracer is possibly the radiogenic Ca isotopic system.

Compared with the Rb–Sr system, the K–Ca system has not been pursued extensively. Nevertheless, this system is interesting because, similar to the Rb–Sr system, the upper continental crust has a more radiogenic composition than the mantle because K is more incompatible than Ca during crustal extraction processes. The upper crust thus has high K/Ca ratios, which, over geological time, lead to elevated ^{40}Ca compositions. This is interesting because the K–Ca system can be used in a similar manner to the Rb–Sr system due to the distinct characteristics between the Ca composition of the mantle and upper continental crust.

The ^{40}K–^{40}Ca decay scheme is geochemically similar to the ^{87}Sr/^{86}Sr system. However, unlike Sr, calcium is a major element that plays a pivotal role in the global carbon cycle and other biogeochemical cycles. Potassium-40 (λ = 5.543 x 10^{-10} year^{-1}) (White, 2013) decays to both ^{40}Ar (11% of the decay via electron capture; λ_e = 0.581 x 10^{-10} year^{-1}) (White, 2013) and to ^{40}Ca (89% of the total decay via β^- decay; λ_β = 4.962 x 10^{-10} year^{-1}) (Nägler and Villa, 2000). Radiogenic Ca isotopes, however, are difficult to measure due to the fact that the ^{40}Ca isotope is the most abundant isotope and thus produces a large peak during analysis compared with smaller peaks for the other relevant isotopes of Ca, which are equally important during analysis (^{40}Ca: 96.94%, ^{42}Ca: 0.647%, ^{43}Ca: 0.135%, and ^{44}Ca: 2.086%). Measurements are also made difficult due to small variations and interference from ^{40}K.

The radiogenic ^{40}Ca composition is expressed, after internal normalization, in epsilon (ε) notation (parts per ten thousand) relative to the mantle reservoir or NIST standard SRM915a (Marshall and DePaolo, 1982):

$$\varepsilon^{40}Ca = \left[\frac{Y_{sample}}{Y_{SRM915a}} - 1\right] \times 10^4 \tag{1.5}$$

where Y is the ^{40}Ca/^{44}Ca ratio (^{40}Ca/^{44}Ca$_{SRM915a}$ = 47.153) (Russell et al., 1978).

Radiogenic Ca isotopes, however, are not to be confused with the stable isotopes of Ca, which have had much more widespread use in the past decade due to significant developments with plasma mass spectrometers (see Figure 1.11). From Figure 1.11, we begin with two analyses, a sample (A) and a standard (B), which both have identical ^{44}Ca/^{42}Ca values but different ^{40}Ca/^{42}Ca values indicated by the ε in the figure. The sample has experienced natural mass fractionation that changes its ^{44}Ca/^{42}Ca and

$^{40}Ca/^{42}Ca$ values to A'. Both the sample and standard then experience instrumental mass fractionation during analysis, which modifies their $^{44}Ca/^{42}Ca$ and $^{40}Ca/^{42}Ca$ values to A_{meas} and B_{meas}, respectively. These values are then corrected using the exponential law and a $^{42}Ca/^{44}Ca$ value of 0.31221 to $A_{corrected}$ and $B_{corrected}$. After correction, we see that both the standard and sample have an identical $^{44}Ca/^{42}Ca$ value but different $^{40}Ca/^{42}Ca$ values, which shows that there is a clear difference between stable and radiogenic isotopic analyses. Samples will always show an enrichment or depletion in radiogenic ^{40}Ca when normalized to a standard but stable isotopes will not show this when normalized to the standard. This can be seen in the inset of Figure 1.11 where the stable isotopes of Himalayan carbonate whole-rock and seawater vary significantly with respect to their stable isotopes of Ca, whereas the radiogenic isotopic composition of these samples do not show any radiogenic enrichments in ^{40}Ca.

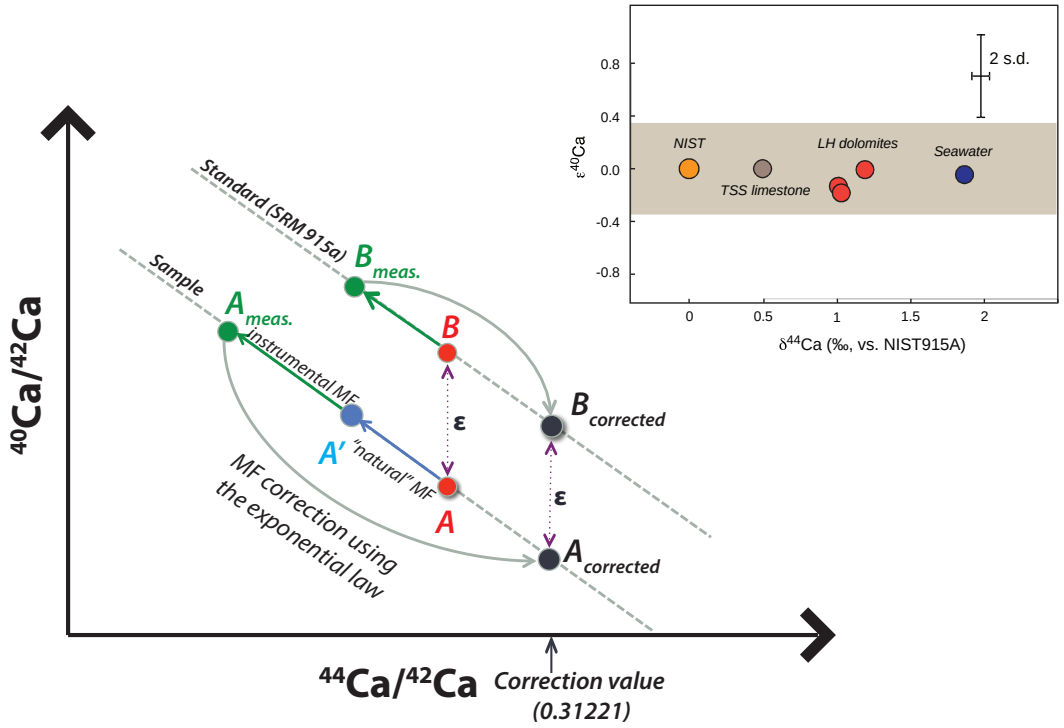

Figure 1.11 – *The differences between radiogenic and stable Ca isotope systematics. See text for description (used with permission from Guillaume Caro).*

A critical part of this thesis has been the improvement of radiogenic Ca analyses, using and improving methods that have been previously established (Caro et al., 2010). In particular, this has focused on the improvement of analytical mass spectrometric methods to obtain higher precision and reproducibility when analyzing

river, rock, and sediment samples (see Chapter 3). In addition, we use the radiogenic Sr system to complement the radiogenic Ca analyses.

1.3.1 Isotopic Logic

Until recently, research interests about radiogenic Ca isotope ratios have concentrated on developing the system as a geochronometer or tracer of petrogenesis. The few papers in the literature that have taken advantage of the ^{40}K–^{40}Ca geochronometer and petrogenetic tracer have clearly demonstrated the validity of this system, especially for rocks and minerals that have elevated K/Ca ratios. However, this system has not seen widespread use in the geochemical and geochronology communities due to complex sample preparation and limitations on the precision and reproducibility of the previous generations of mass spectrometers. Furthermore, there have been no investigations into riverine geochemical weathering properties except for an exploratory study from Caro et al. (2010).

In 1932, Holmes was the first to propose the use of the ^{40}K–^{40}Ca system as a geochemical tracer to decipher granite origins. However, Holmes (1932) thought that the ^{41}K isotope radioactively decays to ^{40}Ca, which was later proven to not be the case and studies on the radiogenic Ca system were left by the wayside because scientists believed that ^{40}Ca excesses would be much too small to be analyzed with accuracy due to poor sensitivity at this time. Ahrens (1951) suggested that the ^{40}K–^{40}Ca system could be used to date K-rich minerals, and Polevaya et al. (1958) were the first to use this technique, dating samples of sylvite (an evaporite mineral) that revealed ages that were closer to the actual sedimentation age than what was found when using K–Ar dating techniques. Furthermore, Coleman (1971) used the decay of ^{40}K to ^{40}Ca to analyze pegmatitic micas, verifying that K–Ca dating results were within approximately 10% of ages found using the Rb–Sr system. Other studies used the radiogenic Ca system to date various mineral phases but, due to poor instrument sensitivity, analyses were only done on minerals with large K/Ca ratios (Wilhelm and Ackermann, 1972; Heumann et al., 1979).

In the 1960s and 1970s, investigations into the Ca isotopic system were mainly focused on the stable isotopes of Ca and the use of the double spike technique or double or triple filament loading techniques during TIMS analysis to reduce instrumental mass fractionation effects (Coleman, 1971; Hirt and Epstein, 1964; Stahl, 1968; Stahl and Wendt, 1968; Heumann and Lieser, 1973; Heumann and Luecke, 1973). Besides concerns over reducing or eliminating instrumental fractionation, these studies mainly focused on observing the natural isotopic variations in geological samples, especially between carbonate and sulfate lithologies, such as fossil shells, limestones, hydrothermal carbonates, carbonatites, and gypsum (Hirt and Epstein,

1964; Stahl and Wendt, 1968; Stahl, 1968; Heumann and Luecke, 1973; Heumann and Lieser, 1973).

Russell et al. (1978) were the first to report the isotopic compositions of the isotopes of Ca with reliable precision. In fact, the values reported in this study are still used today for mass fractionation corrections and these developments in high-precision mass spectrometry opened a new avenue for future studies using the ^{40}K–^{40}Ca system. Since then, a number of studies have attempted to use radiogenic calcium isotopes when investigating Earth Science problems, which is especially the case in geochronologic studies. For example, Marshall and DePaolo (1982) applied the new mass spectrometry techniques, which were reported in Russell et al. (1978), to observe if the ^{40}K–^{40}Ca system could yield precise ages of geological samples. They also were the first to show that the mantle has retained a nearly constant radiogenic calcium isotopic composition throughout geologic time. Marshall et al. (1986) used the K–Ar and K–Ca dating techniques to understand elemental diffusion characteristics between K, Ca, and Ar during recrystallization processes in feldspars. Marshall and DePaolo (1989) studied ^{40}Ca enrichments in continental granitic rocks, island arc rocks, and mid-ocean ridge basalts. They showed that the enrichment or depletion in the initial composition of radiogenic calcium-40 reveals a story of the origin and evolution of igneous rocks (Marshall and DePaolo, 1989).

In the early 1990s, several studies focused on applying the K–Ca system to lunar rocks (Bogard et al., 1992, 1994; Shih et al., 1994). These studies were mainly concerned about defining the ages of lunar granites, defining the initial ^{40}Ca/^{44}Ca ratios for lunar samples, and understanding the petrogenetic processes involved during lunar formation. These studies focused on the K–Ca system because this system was shown to be more resistant, compared with the Rb–Sr or K–Ar systems, to reheating during impact events, which implies that K–Ca ages may reflect more precisely the age of the original formation event.

Fletcher et al. (1997b,a) proposed several new analytical techniques, i.e., sample loading techniques, that improved the reproducibility and sensitivity of radiogenic Ca measurements and applied these improvements to understand the formation and petrogenesis of Archean micas from the Jack Hills in Australia. More recently, Kreissig and Elliott (2005) used the new, at the time, ThermoFinnigan Triton to analyze plagioclase and whole rocks from Archaean cratons, such as Zimbabwe and western Greenland. A study from Harrison et al. (2010) was the first, due to the very high mass resolution required to separate ^{40}K$^+$ from ^{40}Ca$^+$, to analyze the K–Ca system using a microprobe to resolve a debate centered around feldspar in syenite formations from southern Greenland. Based on an extensive study of standards, Naumenko-Dèzes et al. (2015) proposed new analytical techniques as well as improved fractionation

corrections for analyses performed in static collection mode on the Triton.

These studies have demonstrated the potential for using radiogenic Ca isotopes as a geochronometer and as a petrogenetic tracer. However, as the small number of previous studies shows, technical and analytical challenges have limited the use of the potentially promising ^{40}K–^{40}Ca system. Early efforts to determine the abundance of ^{40}Ca did not yield results with a precision of better than 1 ε-unit (Marshall and DePaolo, 1982, 1989; Nelson and McCulloch, 1989; Niederer and Papanastassiou, 1984; Russell et al., 1978; Shih et al., 1994; Fletcher et al., 1997b,a). This is due to the fact that Ca isotope measurements are plagued by significant mass-spectrometry problems: 1) the large isotopic dispersion makes it hard to simultaneous collect isotope signals (Fletcher et al., 1997a), 2) the large ratios between the various isotopes have a high dynamic range (^{40}Ca/^{44}Ca $\approx$ 47, ^{40}Ca/^{42}Ca $\approx$ 151), and 3) analyzing the small radiogenic portion of the entire ^{40}Ca ion signal requires precise and accurate measurements.

These earlier studies were performed using earlier generation mass spectrometers, particularly the Finnigan MAT262. However, due to the more recent Thermo™ Triton© Thermal Ionization Mass Spectrometer (TIMS), the analysis of small variations in the abundance of the dominant ^{40}Ca isotope is more feasible. Using the Triton to analyze samples from Archean cratons, Kreissig and Elliott (2005) obtained a reproducibility of $\pm$ 0.5 ε-units (2σ) and Caro et al. (2010) reported ^{40}Ca/^{44}Ca data in marine carbonates with an external precision of $\pm$ 0.35 ε-units. These advances in external precision are a result of two improvements in the newer generation of TIMS instruments: 1) the ability to measure significantly larger ^{40}Ca ion beams, due to the option of using 10^{10} Ω feedback amplifiers, compared with the previous generation of TIMS (< 50V, against < 10V using the MAT262) and 2) using the "Zoom" optical system when measuring in multi-dynamic mode. The Zoom optical system allows the user to remain focused and to obtain correct centering of the ion beams into the appropriate cages when peak jumping is performed during multi-dynamic isotope analysis. The Zoom optical system allows us to attain higher levels of sensitivity that are required to analyze small variations in the abundant ^{40}Ca isotope (Caro et al., 2010). Furthermore, the Triton is equipped with larger Faraday cups that allow us to analyze both smaller and larger ion beams, which are dependent on the abundance of each isotope, i.e., the large ^{40}Ca ion beam versus the smaller ^{42}Ca ion beam.

Another problem plaguing ^{40}Ca analyses, in addition to that of producing reproducible, high precision data, is that isobars (e.g., ^{40}K^{+}) can interfere with the measurement of Ca isotopes. Instrumental mass fractionation during a TIMS measurement also has a significant impact on the isotopic composition of Ca

(Wasserburg et al., 1981; Hart and Zindler, 1989). Therefore, it is important to use a suitable fractionation law to correct this fractionation. Most researchers have concluded that the exponential law best suits the correction of instrumental fractionation during Ca analysis (Russell et al., 1978; Hart and Zindler, 1989). However, other researchers (Hart and Zindler, 1989; Fantle and Bullen, 2009; Lehn and Jacobson, 2015) have proposed that not all analyses follow the exponential law but actually deviate from the law due to mixing of heterogeneous isotopic reservoirs on the filament (Hart and Zindler, 1989; Roth et al., 2014; Caro et al., 2017) (see Chapter 3).

1.3.2 Why use radiogenic Ca to study the Himalaya?

Of all the elements carried by rivers, one of the most important is calcium. Calcium's abundance in the continental crust (Taylor, 1964), its place as a major elemental constituent of both silicate and carbonate rock, and its importance in biogeochemical cycles makes it one of the most important elements for planet Earth. Calcium is also directly implicated in the global carbon cycle, as the weathering of Ca-bearing silicate rocks and the precipitation and burial of calcium carbonate play a crucial role in the consumption of CO_2.

Improvements in analytical techniques allowed Caro et al. (2010) to obtain precise and reproducible data from various samples such as meteorites, marine carbonates, crustal and volcanic rocks, and sea and river water. Despite being geochemically similar to the Rb–Sr system, Caro et al. (2010) showed that the $^{40}Ca/^{44}Ca$ composition of seawater has remained constant (and indistinguishable from the mantle) since > 3.5 Ga, which is very different from what is observed in radiogenic Sr isotopes (Figure 1.12). This is due to the fact that the mantle and ultramafic rocks have very low K/Ca ratios (i.e., approximately 0.01) and have not decayed sufficiently to be detected within the current analytical capabilities. In contrast, Taylor and McLennan (1985) estimated that the upper continental crust has a K/Ca (molar) ratio of approximately 0.95. If we assume that crustal growth began at 3.8 Ga, the decay of ^{40}K to ^{40}Ca would produce an approximate 2.5–3 ε-unit growth in the $\varepsilon^{40}Ca$ composition of the upper continental crust (Marshall and DePaolo, 1982; Caro et al., 2010). However, this value is just an average. The upper crust can contain certain felsic (silicate) lithologies, which have high K/Ca ratios between 1 and 4 (and greater), thus producing large abundances of ^{40}Ca (Marshall and DePaolo, 1982; Caro et al., 2010).

Rivers dominated by carbonate or mantle (basaltic) inputs (e.g., the Mississippi and Columbia Rivers, respectively) should have $\varepsilon^{40}Ca = 0$, whereas Himalayan rivers have $\varepsilon^{40}Ca$ excesses (Figure 1.13) (Caro et al., 2010). This dichotomy, similar to global Sr systematics, may allow the easier distinction between carbonate and silicate

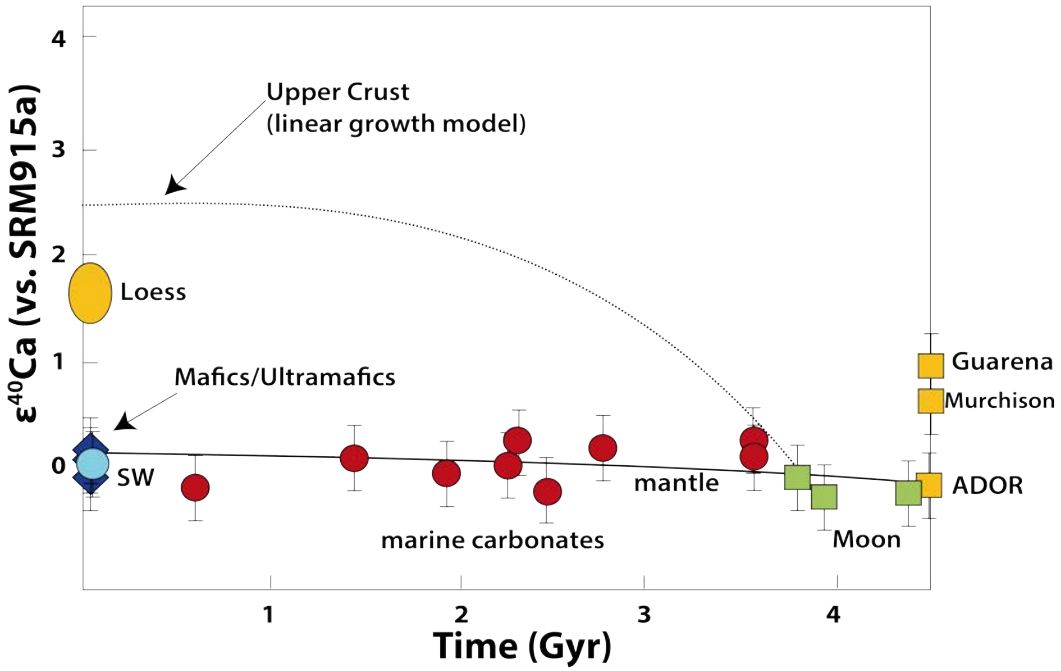

Figure 1.12 – *$\varepsilon^{40}Ca$ vs. time showing the evolution of ^{40}Ca in the mantle and the present compositions of various other samples. The main point of this graph is to illustrate that carbonates and seawater have retained indistinguishable calcium isotopic values throughout the past 3.5 billion years, whereas the continental crust has a higher K/Ca, which yields average ^{40}Ca excesses of +2–3 ε-units allowing clear distinctions between the radiogenic Ca compositions of silicate and carbonate lithologies. Figure modified from Caro et al. (2010).*

signatures in the dissolved load. Thus, a more expanded riverine, sedimentological, and lithologic dataset of radiogenic Ca values for the Himalaya may help to resolve discrepancies between Himalayan carbonate and silicate weathering budgets as described in section 1.2.5.

Caro et al. (2010) showed that the weathering input from shales and granitic sources to seawater has remained small compared to the contributions from hydrothermal fluxes over much of Earth's history. Mass balance constraints require that the present hydrothermal flux of calcium exceeds the silicate weathering flux by at least one order of magnitude. This indicates that important exchanges of calcium take place at off-axis hydrothermal sites. Thus, the hydrothermal exchange between oceanic crust and seawater appears to have governed the chemistry of the oceans through geological times. This is in stark contrast to the dynamics of Sr fluxes, where Sr input from riverine sources has dominated over hydrothermal input over much of Earth's history.

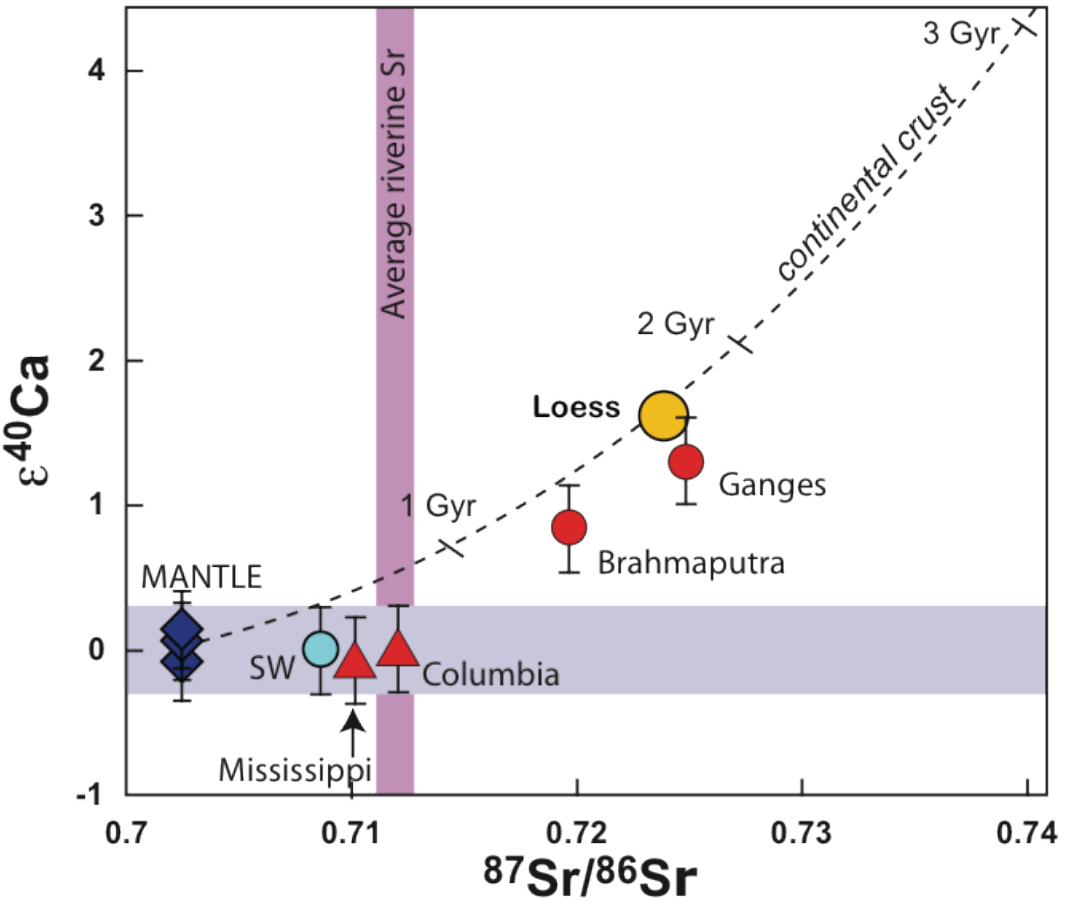

Figure 1.13 – *$\varepsilon^{40}Ca$ vs. $^{87}Sr/^{86}Sr$ showing that rivers that drain carbonate (i.e., the Mississippi) or basaltic (i.e., the Columbia) lithologies have no detectable radiogenic excesses of ^{40}Ca, while Himalayan rivers, which drain older, silicate crustal rock, have radiogenic excesses. This indicates that there may be a more dominant influence of silicate material in this region compared with carbonate sources, which may allow for simpler distinction between the two signatures in the dissolved load compared with complicated Sr isotope systematics. Figure from Caro et al. (2010).*

More recently, studies have questioned the hypothesis that the radiogenic Ca composition of the oceans has remained equivalent to that of the mantle (i.e., ε^{40}Ca = 0) (Antonelli et al., 2018). Antonelli et al. (2018) found that, relative to igneous rock standards (i.e., the bulk silicate earth represented by oceanic basalts or meteorites), seawater and the standard SRM915a have radiogenic compositions, which implies that: 1) SRM915a is not an acceptable standard to estimate ^{40}Ca excesses and 2) that seawater may be slightly more radiogenic than the mantle over the past 3.5 Ga. However, radiogenic Ca analyses from Schiller et al. (2012) and Simon et al. (2009) show that the ε^{40}Ca values of several standards and basalts are identical to the value of

the SRM915a standard. Despite these discrepancies, we can hypothesize that seawater has remained indistinguishable from or slightly more radiogenic than the modern mantle over the past 3.5 Ga (Caro et al., 2010; Schiller et al., 2012; Simon et al., 2009; Antonelli et al., 2018). In either case, the definition of the bulk silicate earth value and its agreement with SRM915a has no influence on the interpretation of the results of this thesis.

1.4 Objectives/Aims

This thesis presents a substantial new data set of radiogenic Ca isotopic ratios in Himalayan rivers, rock, and sediments. Detailed case studies are presented from Himalayan rivers, considering the controls on river chemistry, and Ca and Sr isotope systematics. In particular, this thesis addresses the influence that lithology has on the dissolved Ca isotope ratios. We aim to determine whether Ca isotopes can be used to improve on estimates based on Sr isotopes and major elements of the proportions of silicate and carbonate weathering occurring at the catchment and basin scale. To do this, we focus on small and large Himalayan basins whose major and trace elements and Sr isotopes geochemistry and dynamics have been previously studied. Chapter 2 of this thesis describes the geology, structure, hydrology, and climate of the Himalayan arc as a whole. Chapter 3 describes the analytical techniques used in this thesis.

This thesis focuses on chemical weathering in the Himalaya, and on the controls on the radiogenic Ca and Sr isotope ratios in Himalayan catchments (Chapters 4 and 5) in order to constrain the magnitude of silicate and carbonate weathering. This thesis is divided into investigations of radiogenic Ca isotopes at the small scale (i.e., the Khudi Khola) and medium scale (i.e., the Narayani Basin). The Himalayan field sites are introduced in each respective chapter and the geological, climatic, and vegetation settings are discussed. The major element and Sr isotope chemistry of the rivers are described in detail and interpreted, which provides the framework for understanding radiogenic Ca isotope ratios in these catchments.

Finally, the General Discussion and Perspectives (Chapter 6) provides a general outlook on the findings of this thesis.

CHAPTER 2

HIMALAYAN GEOLOGY, STRUCTURE, AND CLIMATE

For at least the past 40 million years, the Indian subcontinent has been continually penetrating into Asia. In the process, it has lifted the Himalaya and the Tibetan plateau in front of it and squeezed bits and pieces of China and Mongolia out of its way. The Tibetan plateau, the world's largest and highest, is by no means a tribute to the subcontinent's strength and persistence, but the most spectacular consequence of the collision between the subcontinent and the rest of Asia as the world's tallest mountain range – the Himalaya. Buttressed at its rear by the Tibetan plateau, the mass of rock comprising the Himalaya is constantly forced farther up and onto the plains of India. With each great earthquake, a segment of the Himalaya, perhaps two or three hundred kilometers in length, lurches several meters farther onto the plains; or from another perspective, the Indian subcontinent surges several meters more below the Himalaya. (Molnar, 1986)

The Himalayas (Figure 2.1 and 2.2) have been extensively investigated throughout the last century because of their importance to debates centered around biogeochemical cycles and the interactions between uplift, erosion, weathering, climate, and the global carbon cycle (see a more detailed discussion in Chapter 1) (France-Lanord and Derry, 1997; Raymo, 1994; Richter et al., 1992). The combined drainage of all the major Himalayan rivers, i.e., the Ganga, Brahmaputra, Indus, Salween, Mekong, and Yangtze, represent approximately 15% of the global riverine discharge to the oceans (Gaillardet et al., 1999). Thus, the Himalaya exert an important control on oceanic geochemistry due to the vast amount of dissolved and solid phases that Himalayan rivers export to the Bay of Bengal (Figure 2.2) and eventually to the global oceans.

The Himalayas, a product of approximately 55 million years of collision, are the largest and highest mountain range on Earth (Figure 3.3). The Himalayas stretch for nearly 2,500 km from Nanga Parbat in Pakistan in the west to Namche Barwa in the east (Dhital, 2015). The chain stretches from Tibet in the north to India in the south, varying in width from 250 to 400 km, and encompasses a total area of approximately 600,000 km^2 (Dhital, 2015). The average altitude in the Himalaya is 5,000 meters above sea level (asl) with its highest point at Mount Everest, which lies at 8,810 meters asl (Fielding et al., 1994). The Indo-Gangetic plain, lying between 0 and 300 meters asl, is the world's largest, flat surface, and occupies an area of 2.55 million km^2.

Figure 2.1 – *The Himalayan Chain and the Ganges plain. The perspective is oriented towards the NW and the Nanga Parbath. On the left is the Indian craton, and the Tibetan plateau on the right (picture taken from "The Himalayas from Space," copyright Christoff Hormann onebigphoto.com).*

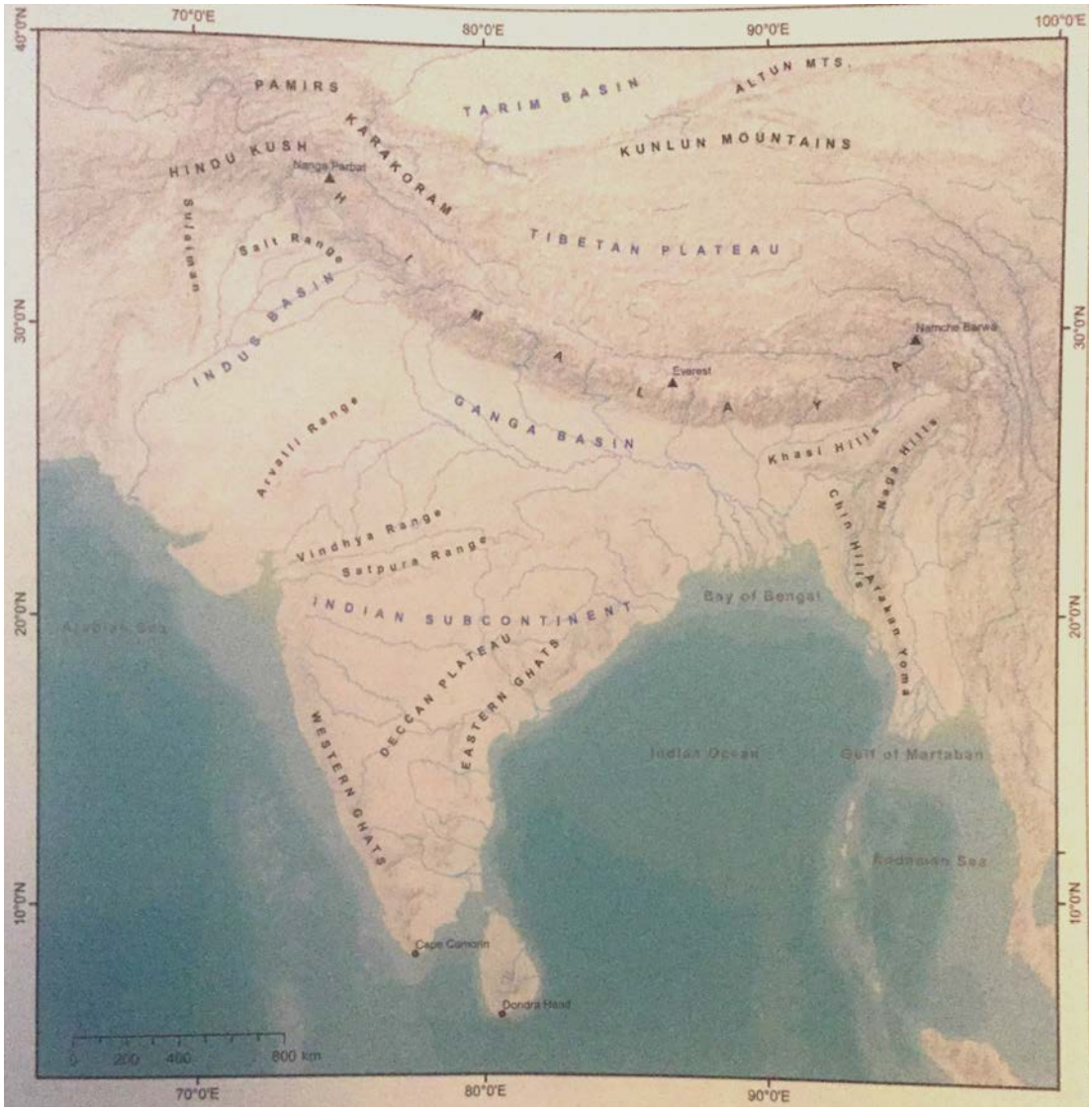

Figure 2.2 – *A view of the Tibetan Plateau, Himalaya, Indian subcontinent, and adjacent regions (map comiled from SRTM DEM, USGS, NOAA, USDA, and GIS User Community sources, and taken from Dhital (2015)).*

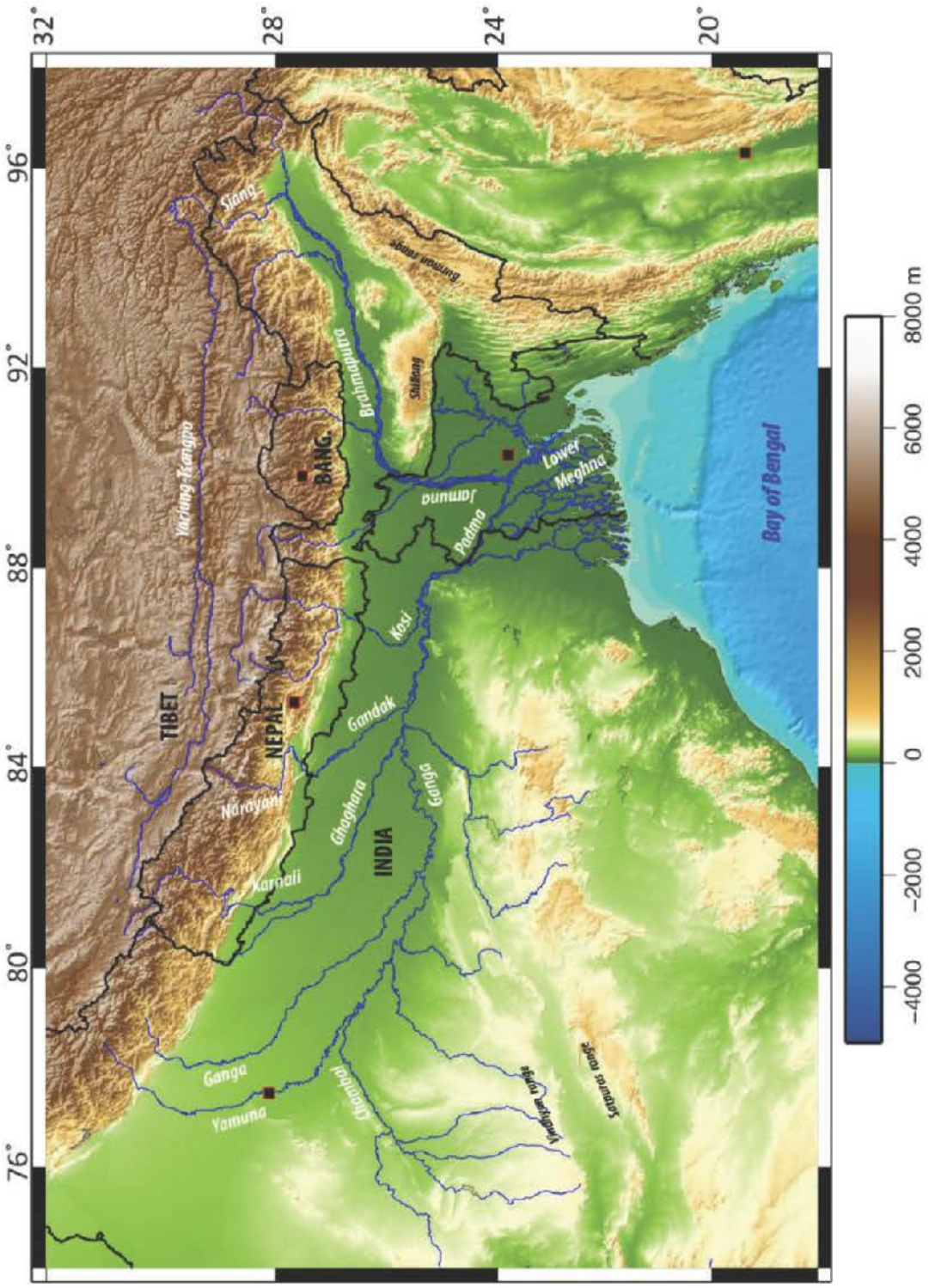

Figure 2.3 – *The topography of the Tibetan Plateau, Himalaya, Indian subcontinent, and adjacent regions (map compiled from GEOTOP30 and USGS sources, and taken from Morin (2015)).*

2.1 The Himalaya Collision

The Himalayas, as we know them today, originate from the collision between the Indian and Eurasian plates (Figure 2.4), and the subsequent subduction of the Indian plate beneath the Eurasian plate. The separation of Gondwanaland (approximately 250 Ma) prompted the northward movement of the Indian plate during the Cretaceous (Dhital, 2015). The first contact between the Indian and Eurasian plates took place in what is now the northwestern Himalaya at either 65 Ma (Jaeger et al., 1989) or 55 Ma (Klootwijk et al., 1984). The Indian plate then rotated counterclockwise and collided with the eastern portion of the Eurasian plate at either 50 Ma (Besse et al., 1984) or 45 Ma (Dewey et al., 1989). Evidence for the beginning of the collision was first proposed by Molnar and Tapponnier (1975), whose results showed that there was a significant decrease in the velocity of the Indian plate from 100–112 mm/year to 45–65 mm/year at approximately 40 Ma. Presently, the Indian plate continues to collide with the Eurasian plate, at an estimated rate of 36–38 mm/year (Wang et al., 2001; White and Lister, 2012). Figure 2.4 shows the northward movement and timing of the Indian plate towards Asia, and that the first collision took place in the northwestern regions of the Himalaya before the Indian plate rotated, colliding with the Eurasian plate in the northeastern region of the Himalaya.

Currently, debates centered around the timing of collision focus on two possibilities (White and Lister, 2012): 1) Several studies suggest that the Himalaya formed via several distinct accretionary phases (Aitchison et al., 2007; Lister et al., 2001) while 2) still others suggest that there was a single collisional event that was followed by a long uplift history (Beaumont et al., 2001, 2004; Jamieson et al., 2006; Leech, 2008; Noble et al., 2001; Searle et al., 1992, 1999; Vance and Harris, 1999; Walker et al., 2001).

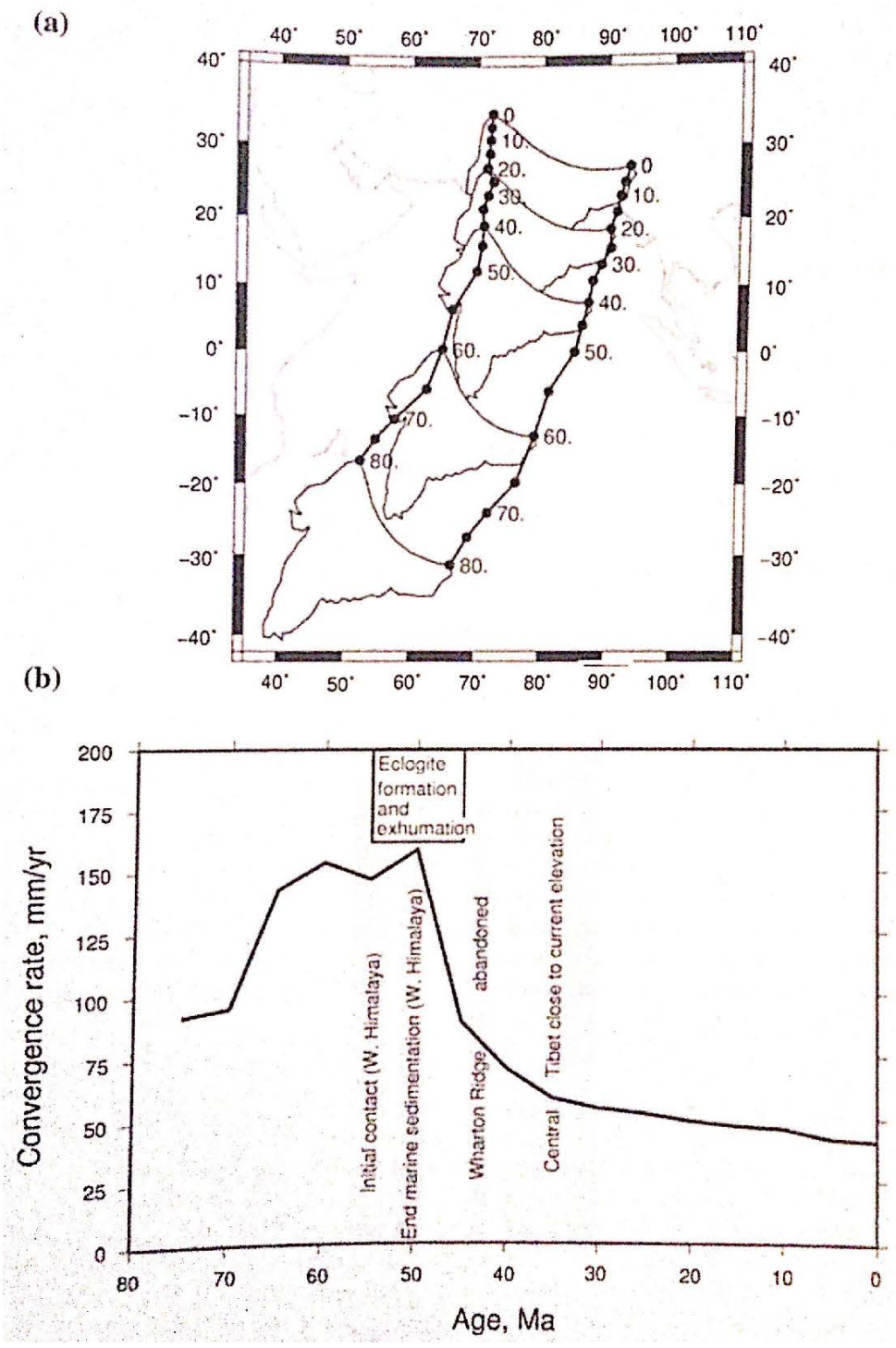

Figure 2.4 – *(a) Sketches showing the northward movement of the Indian tectonic plate at various times across the Neo-Tethys Ocean and its eventual collision with Asia and formation of the Himalayas. (b) The convergence rate (mm/year) between the Indian and Eurasian plates plotted as a function of time, showing several important tectonic events during the uplift of the Himalaya (from Dhital (2015).*

2.2 Structure and Geology of the Himalayas

The current geology and structure of the Himalaya are a consequence of the unique conditions that originate from the collision between the Indian and Eurasian plates. The main Himalayan arc lies between the Indus-Tsangpo suture in the north and the Indian shield in the south. In between, three Cenozoic-aged fault systems form the divisions between the main Himalayan lithotectonic units, i.e., from north to south, the South Tibetan Detachment System (STDS), the Main Central Thrust (MCT), and the Main Boundary Thrust (MBT) (see Figure 2.5 and 2.6). From north to south, the main Himalayan arc is composed of the following lithotectonic units:

- **The Indus-Tsangpo Stuture Zone** – A 'suture zone' is a tectonic line along which two continental plates collide and join. Hence, the Indus-Tsangpo Suture Zone marks the boundary between the Indian and Asian plates (Dhital, 2015). This zone consists of ocean-floor volcanic rocks, subduction-related high-pressure metamorphic rocks (greenschist rocks), and deep-sea sediments from the Tethys ocean (Dürr, 1996). The Tibetan segment of the Brahmaputra, known as the Yarling Tsango, generally follows along the suture zone.

- **The Tethyan (Tibetan) Himalaya** – The Tethyan Himalaya or Tethyan Sedimentary Series (TSS) is a series of sediments that have been strongly folded, imbricated, and weakly metamorphosed. The TSS preserves a nearly complete stratigraphic record that ranges from the Upper Proterozoic to the Eocene, which has generally low-grade metamorphic characteristics. Stratigraphic analyses of these sediments provide important indicators concerning the geological history of India's northern continental margin from before and during the continental collision with Eurasia. With a width of approximately 100 km, the Tethyan Himalaya is the widest zone of the Himalaya. The stratigraphic thickness of sediments in this zone reaches up to 12 km (Dhital, 2015).

- **The Higher (Greater) Himalaya Crystallines (HHC)** – The STDS separates the TSS from the HHC, where the highest summits of the Himalaya (over 7,000 m) lie. The HHC (approximately 30 different names exist in the literature to describe this unit; the most frequently found equivalents are Greater Himalayan Sequence, Tibetan Slab, and High Himalayan Crystalline Series) is composed of 10–20 km-thick sequences of medium- to high-grade metamorphic rock (schist and gneiss) and granites situated at altitudes of 3,000 to over 8,000 m (Brouand, 1989; Barbey et al., 1996; Le Fort, 1981, 1975; Vidal et al., 1982; France-Lanord

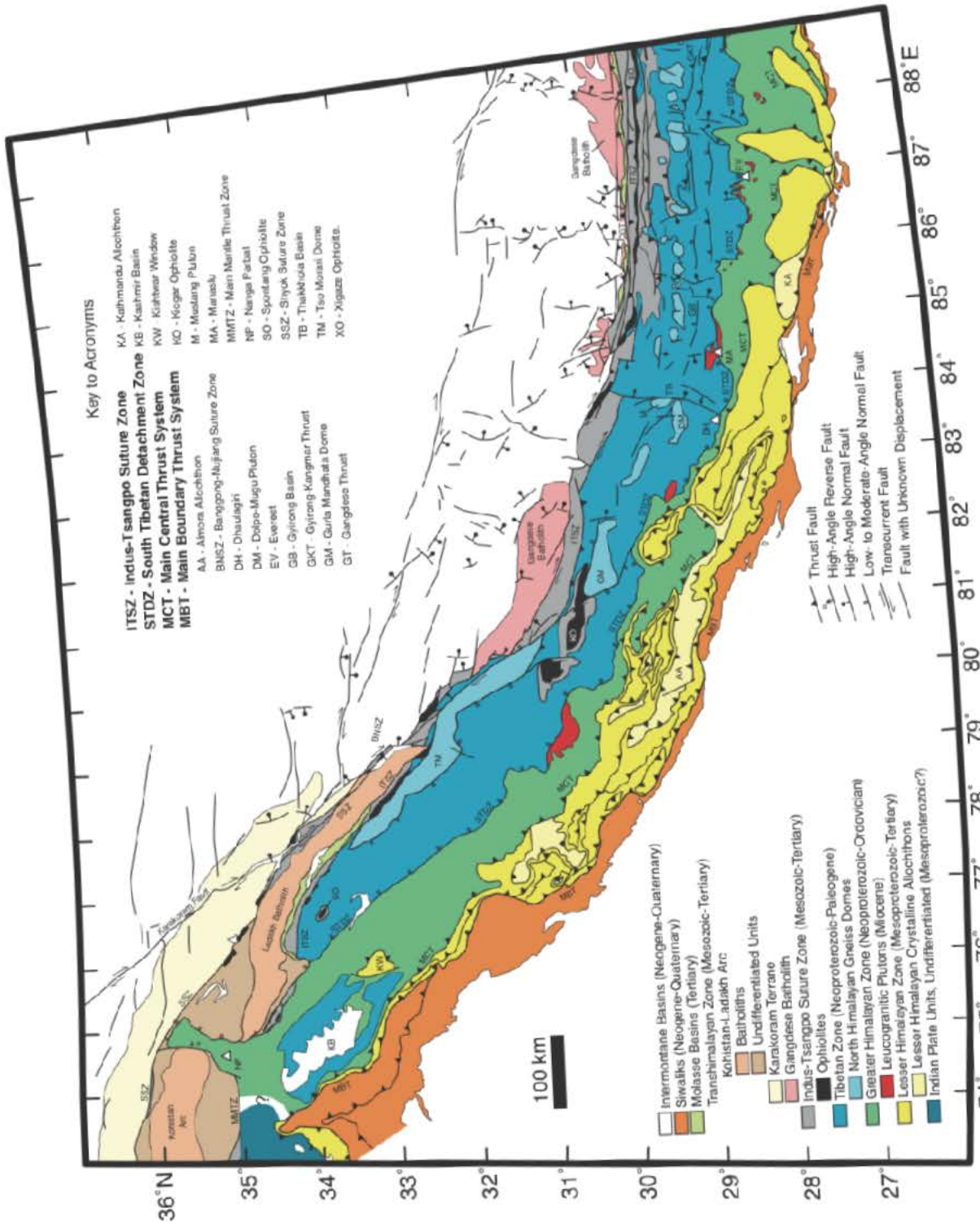

Figure 2.5 – *The structure and geology of the main Himalayan arc (from Hodges (2000).*

and Fort, 1988; Le Fort, 1986; Le Fort et al., 1987; Guillot and Le Fort, 1995; Guillot et al., 1995). The protoliths of these rocks are Proterozoic–Cambrian in age (2,000–500 Ma) and derive from Indian continental crust. The HHC is intruded in many areas by Ordovician (500 Ma) and early Miocene (22 Ma) leucogranites, which are known as the High Himalayan Leucogranites (HHL) (Le Fort, 1975; Deniel et al., 1987; France-Lanord and Fort, 1988; Barbey et al., 1996; Le Fort et al., 1987).

- **The Lesser (Lower) Himalaya** – The MCT, which thrusts the HHC over the Lesser Himalaya (LH), marks the boundary between the HHC and the LH. The LH consists of metamorphosed sedimentary rock (quartzite, marble, slate, phyllite, schist, and gneiss) and minor volcanic and granitic rocks of Proterozoic–Cambrian age (2,000–500 Ma). The stratigraphic thickness in this zone ranges from 10 to 20 km. The LH was originally a part of India's northern margin. Unlike the rich, fossiliferous TSS sediments, LH sedimentary rocks have very few fossils partly due to their much older age as well as the high degree of metamorphism. Nevertheless, metamorphism in the Lesser Himalaya was less severe (i.e., lower temperatures) compared with that of metamorphic rocks from the HHC. Compared with the TSS and HHC, LH lithostratigraphy is much more varied and complicated than other Himalayan formations. The LH also suffers from a problem of nomenclature, i.e., the same LH formation may bear different names in the various localities where it is exposed. Fully describing the LH is also limited due to a lack of constant and characteristic stratigraphic horizons and the scarcity of well-dated fossils (Dhital, 2015). Far from the MCT, LH rocks are non-metamorphosed and undeformed, whereas LH rocks are highly deformed and metamorphosed to the north near the MCT (Kohn et al., 2005). However, generally speaking, the LH can be divided into two major lithological groups:

  1. A lower, thick detrital unit that is predominantly (95%) composed of Proterozoic sandstones and metamorphosed felsic volcanogenic sediments, interbedded with amphibolite lenses (Kohn et al., 2010).
  2. A stratigraphically higher, more variable unit with several carbonaceous schists, dolomites, and limestones that are likely Upper Proterozoic to Carboniferous-Permian in age but have been generally poorly dated (Kohn et al., 2010; Upreti, 1999).

  Within the Lesser Himalaya, geologists have also mapped isolated instances of HHC rocks: these rocks are known as the 'outer crystalline zone' or the Higher

Himalayan 'klippe'. These rocks were thrust, by the MCT, over LH lithologies but were later isolated from the HHC root zone (Dhital, 2015). The LH ranges in elevation from 200 to 3,000 m and, apart from Kathmandu, is the most densely populated region in Nepal.

- **The Sub-Himalaya or Siwalik Range** – The MBT separates the LH from the Sub-Himalaya or Siwaliks. The Siwaliks are a series of foothills that range in elevation from 0 to 1,000 m. The Siwaliks are composed of 10-km thick sandstone and mudstone sequences that derive from the erosion of the High Himalaya, whose erosional products have been carried by rivers and deposited there, especially since the Miocene (i.e., the past 24 million years) (France-Lanord et al., 1993; Mukherjee, 1964; Burbank, 1992; Schelling and Arita, 1991). The Siwaliks represent a typical fluvial succession that fines upward beginning with the lower unit (the Lower Siwaliks), which consists of fluvial channel sandstones that alternate with oxidized calcareous paleosols. The Middle Siwaliks contain thick channel sandstones and neutral colored histosols and the Upper Siwaliks are comprised of predominantly gravely, braided river deposits (DeCelles and Giles, 1996; Nakayama and Ulak, 1999). However, this input diminished with the initiation of the LH Thrust System at approximately 12 Myr, after which point the LH has provided approximately 30% of the input to the Siwalik Foreland (Huyghe et al., 2001). At approximately 1 Ma, the Siwaliks were uplifted along a high-angle reverse fault (still active), which is known as the Main Frontal Thrust (MFT; also known as the Himalayan Frontal Fault or Thrust). The MFT marks the boundary between the Siwalik Range and the northern Indian plains.

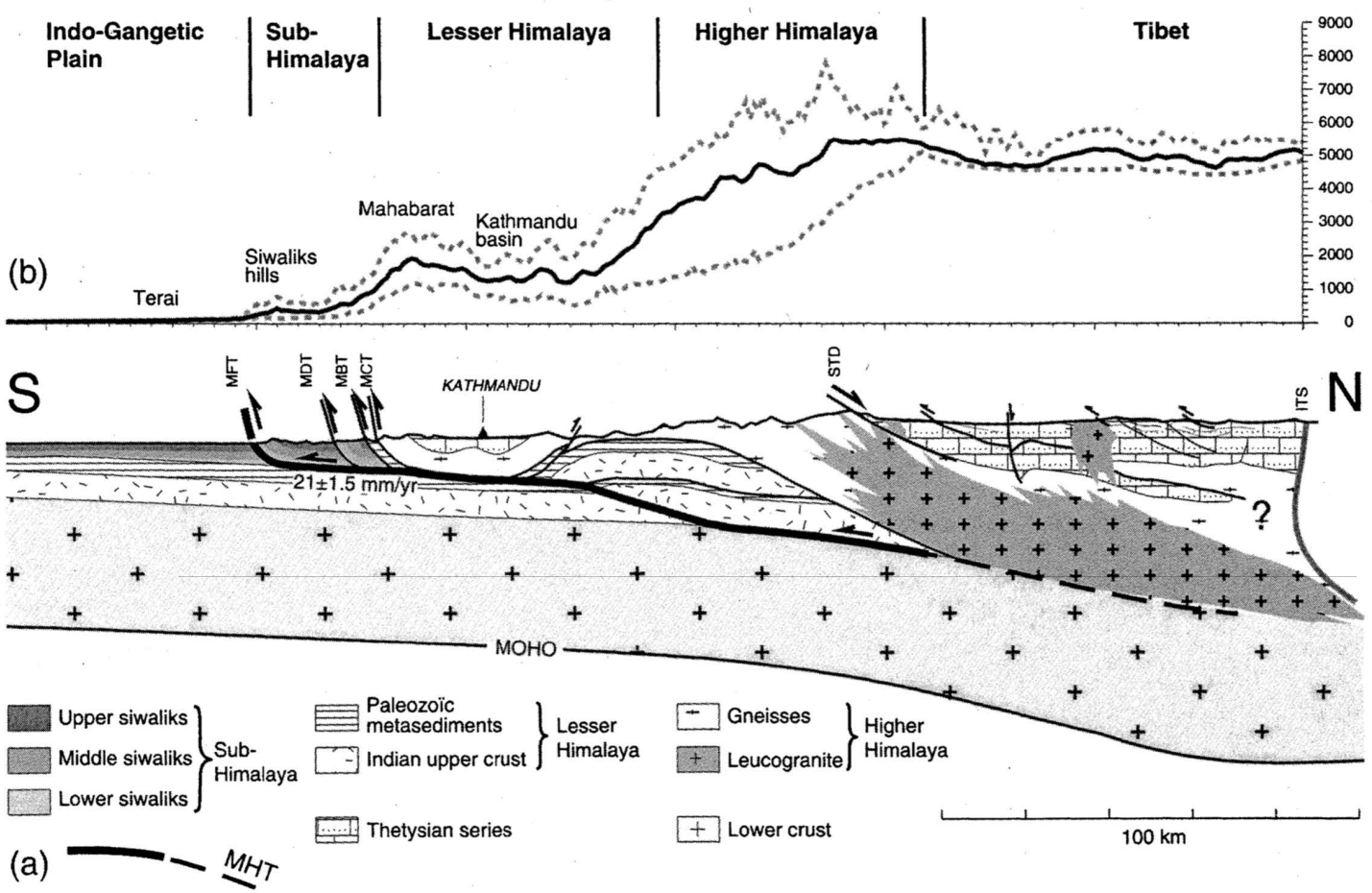

Figure 2.6 – *A geological/structural cross section of the Himalaya showing major boundaries, thrust systems and lithological units (from Lavé and Avouac (2001).*

2.3 The Hydrological Network

The Ganga-Brahmaputra-Meghna (GBM) basin covers a total area of 1.7 million km^2 (Figure 2.7) Rao (1979) and includes the countries of India, Nepal, China, Bhutan, and Bangladesh. The GBM basin is incredibly important not only in terms of hydrology and geochemistry but are also important socially, economically, and politically, as well as for water resources. Following the Congo and Amazon river systems, the GBM basin represents the third largest river system in the world in terms of river discharge to the oceans (Chowdhury and Ward, 2004).

The source of the Ganga is at Devprayag in the Indian state of Uttarakhandand near the Gangotri Massif at 7,010 m. The source of the Brahmaputra is in China near the Kalias Massif (Galy, 2007). The total area of the Ganga basin is approximately 1.06 x 10^6 km^2 (Rao, 1979). The Ganga flows southeast from its source into the plain where it is joined by rivers from both the north, i.e. from central Nepal (such as the Ghaghara, Kosi, and Gandak), and the south, i.e., from northern India (such as the Yamuna, Gomati, Chambal, and Son). The Brahmaputra, also known as the Yarlung Tsangpo in China, has a total surface area of approximately 0.58 x 10^6 km^2 (Rao, 1979). The Brahmaputra flows to the east parallel to the Indus-Tsangpo suture zone for approximately 1,700 km (Galy, 2007; Valdiya, 1993). At Namche Barwa, the Siang flows from China to Nepal. As it flows through Nepal, to the northwest of the Shillong Plateau, and into Bangladesh, rivers such as the Assam, the Manas, the Subansiri, and the Tista join the Brahmaputra before it flows directly south to meet the Ganga at Aricha. Here, the Padma forms, which eventually flows into the Bay of Bengal. Originating from south of the Shillong Plateau and the Indo-Burmese chain, the Meghna joins the Padma. Further downstream, the Padma changes to the Lower Meghna, divides into numerous small tributaries south of Bhola, and then drains into the Bay of Bengal (Galy, 2007).

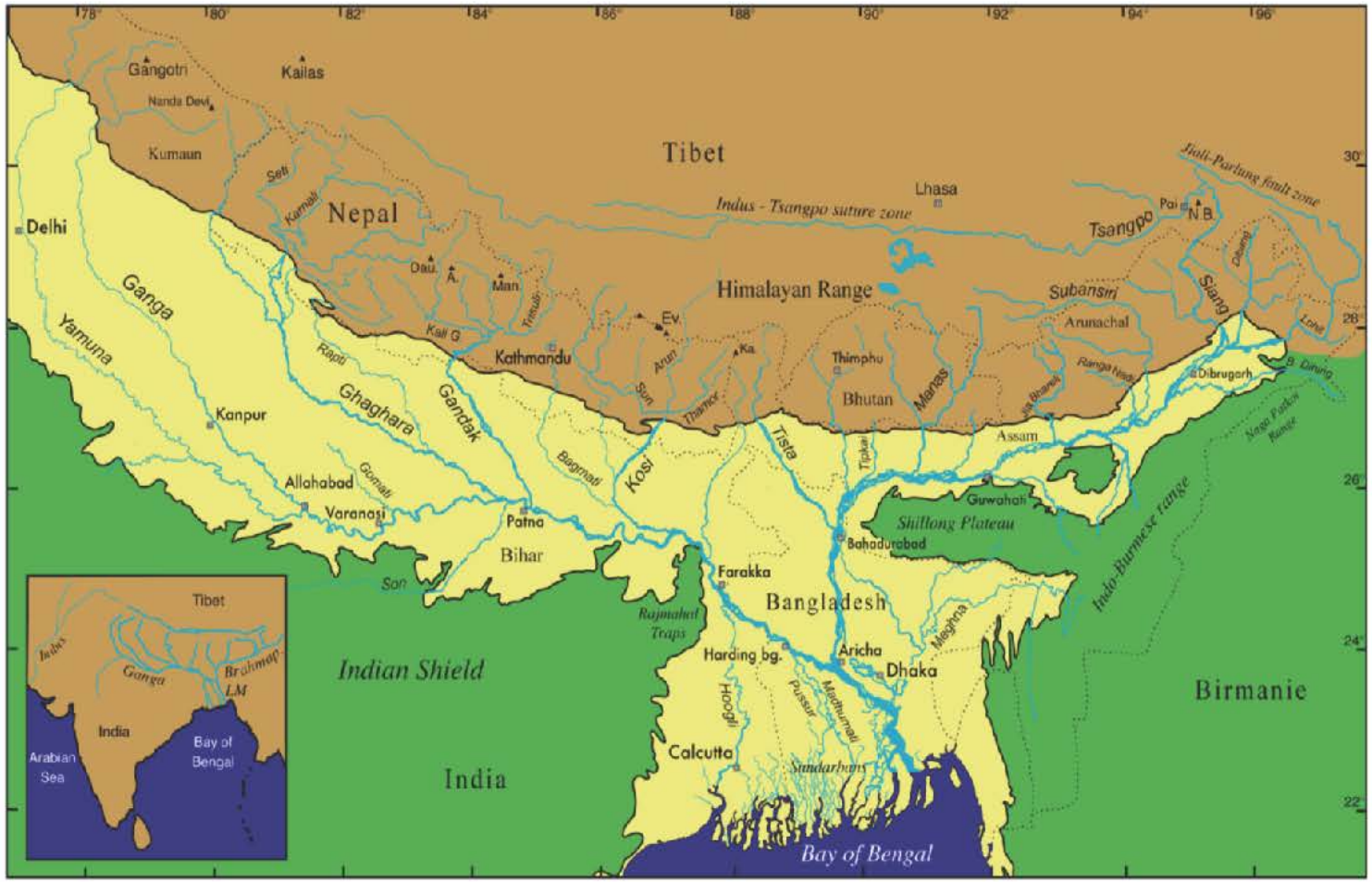

Figure 2.7 – *The Ganga-Brahmaputra-Meghna basin and its hydrological network in Nepal, India, China, and Bangladesh. The map shows the Himalayan chain (in brown), the Ganga plain (in yellow), and the Indian subcontinent and Indo-Burmese Range (in green). A: Annapurna, Dau: Daulaghiri, Ev: Everest, Ka: Kangchenjunga, Man: Manaslu, NB: Namche Barwa (figure taken from Galy (2007).*

2.4 Himalayan Climate

Climate in the Himalaya varies significantly from hot temperatures and extreme rainfall in the summer to cold temperatures, very little rainfall, and high amounts of snowfall in certain areas of the Higher Himalaya in the winter. The combination of intense monsoonal rainfall and extreme relief create situations for flooding, high erosion, landsliding, and other mass wasting movements. The Indian or South Asian monsoon plays a critical role in the Himalaya not only on these processes but also significantly impacts the infrastructure and human population throughout the habitable regions of the Himalaya.

Essentially, the monsoon is a seasonal change in wind directions. In fact, the main cause of the monsoon is a difference between the annual temperature on land and in the oceans. Solar heating over land, i.e., the Indian subcontinent, creates a low pressure zone, where the northeast and southeast trade winds converge. This zone of convergence is also known as the Inter-Tropical Convergence Zone (ITCZ) (Galy, 2007; Roe, 2005; Shrestha, 1998). This low pressure regions is characterized by a continuous rise of moist wind that originates from the ocean's surface. The wind progressively cools as it continues to rise to the upper layers of the atmosphere. At a certain point, the air masses are no longer able to hold moisture, which results in precipitation over the continent (Galy, 2007; Roe, 2005; Shrestha, 1998).

The opposite process occurs during the winter, where the continents become cooler more rapidly than the oceans, which causes the formation of a high-pressure zone on land. This zone acts to move dry air masses from the land to the oceans. These process is shown by Figure 2.8, where, in the winter months (at the bottom), the ocean is warmer than India/Nepal/Tibet, creating a high pressure area on land (a classic Hadley cell), which pushes precipitation further into the ocean. In the summer (at the top), due to increased solar radiation, the Himalayan land mass is warmer than the ocean, creating a low pressure area on land (an inversed Hadley cell), which pushes precipitation over the oceans onto the continent and begins the monsoon season.

In the summer, the monsoon begins in late May and continues until September. During the monsoon period, especially in July and August, a significant amount of rainfall occurs over the Bay of Bengal, the Indo-Gangetic plain, and the southern flank of the Himalayas. The average value of integrated precipitation over the entire range is estimated to be approximately 1.5 m/year, where more than 90% of this amount falls during the summer monsoon (Bookhagen et al., 2005b,a). However, this value can vary between 1 and 4 m/year in central Nepal, less than 0.5 m/year in the Tibetan Plateau, between 2 and 4 m/year in the east along the Ganga plain, and between 0.5 and 1 m/year in the western regions of the Ganga plain (Anders et al., 2006;

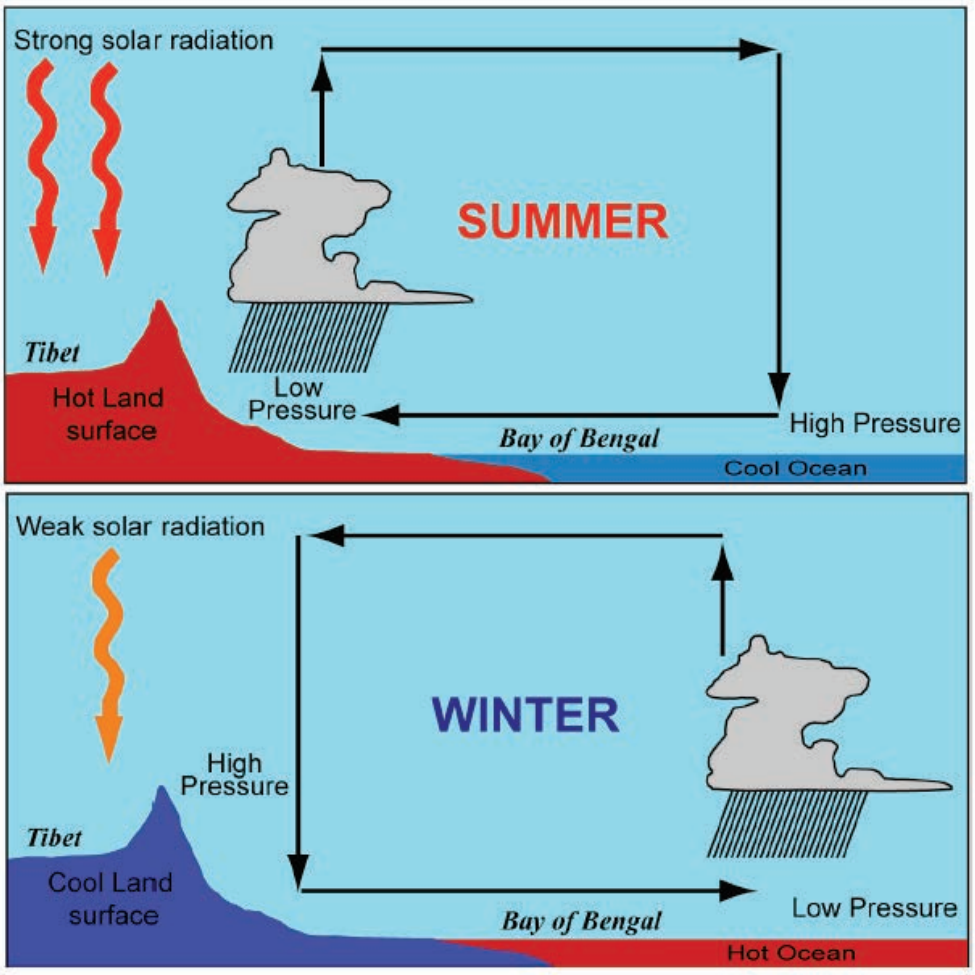

Figure 2.8 – *The differences between weather dynamics in the summer and winter in southeast Asia and the creation of the monsoon. In the winter months (at the bottom), the ocean is warmer than India/Nepal/Tibet, creating a high pressure area on land (a classic Hadley cell), which pushes precipitation further into the ocean. In the summer (at the top), due to increased solar radiation, the Himalayan land mass is warmer than the ocean, creating a low pressure area on land (an inversed Hadley cell), which pushes precipitation over the oceans onto the continent and begins the monsoon season (taken from Galy (2007)).*

Bookhagen and Burbank, 2010, 2006). Moist air masses that originate from over the Indian Ocean travel in an overall SW–NE trajectory but are then deflected to the west by the Himalayan range. North of the high chain, the Tibetan plateau is protected from monsoon influences and experiences relatively little rainfall.

This deflection, in fact, occurs because the Himalayan range creates a large, orographic barrier that blocks the path of air masses. Consequently, strong summer monsoon rainfall is concentrated along the southern flank of the Himalaya and in the Indo-Gangetic plain (Roe, 2005). This phenomena is shown in Figure 2.9, which shows

a TRMM (rainfall data collected by the Tropical Rainfall Measuring Mission satellite) rainfall image of the amount of precipitation (in m/year) from May to October between 1998 and 2007. Studies from Anders et al. (2006) and Bookhagen and Burbank (2010) show the effects of relief on the significant contrast between weak precipitation throughout the Tibetan Plateau and strong precipitation at the Himalayan Front, as well as differences in the precipitation between the east and the west. The transects in Figure 2.9 clearly show that precipitation is quite strong until monsoon air masses encounter significant increases in relief and elevation.

Throughout the geological past, numerous studies have found that monsoonal intensity has varied significantly (Shrestha, 2000; Gadgil et al., 2004; Bookhagen et al., 2005b). Bookhagen et al. (2005b) reported that monsoon intensity was particularly high at the end of the Pleistocene (29–24 ka) and Holocene (10–4 ka). These particular increases in monsoonal intensity consequently yielded more intense periods of erosion in the Himalaya, especially in the HHC and LH (Bookhagen et al., 2005a; Clift et al., 2008). Licht et al. (2014) proposed that the Eocene (55–34 Ma) was characterized by a significant increase in monsoon intensity, which has continued into the present.

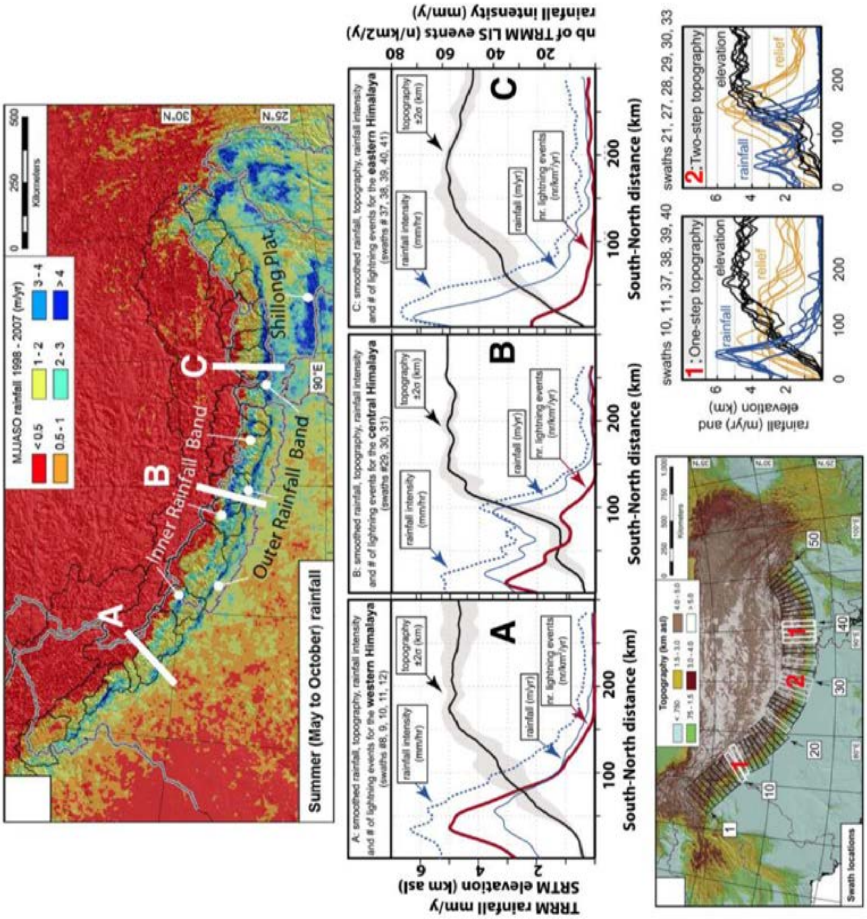

Figure 2.9 – *The effects of Himalayan orographic barriers on monsoonal precipitation and the distribution of precipitation throughout central Nepal (from Anders et al. (2006) and Bookhagen and Burbank (2010) and taken from Morin (2015)). The figure at the top represents the distribution of monsoonal rainfall based on measurement from the Tropical Rainfall Measuring Mission satellite from 1998 to 2007. This image shows that there are two bands of rainfall distribution in central Nepal. The transects A, B, and C show the relationship between precipitation intensity and relief/elevation when traversing the range from south to north. This relationship shows that, as moist air masses move from east to west, the amount of rainfall is significant until the air masses encounter significant increases in relief and elevation. This demonstrates the importance of the orographic effect and the dichotomy between the amount of precipitation in the north and south of the Himalayan range.*

2.5 Field Sites

Except for a preliminary study from Caro et al. (2010), the radiogenic Ca isotopic system has never been used in the Himalaya (see Chapter 1 for a more detailed discussion of the radiogenic Ca system). Therefore, this study began as a general attempt to assess the radiogenic Ca composition of dissolved load, sediment, pebble, and soil samples within each major Himalayan lithological unit (i.e., the TSS, HHC, and LH). As we acquired more data about radiogenic Ca in the Himalaya, we began to focus on specific lithologies and watersheds within central Nepal.

The processes of altering the continental crust to a riverine solute load is a complex function of lithology, temperature, runoff, and vegetation (Walker et al., 1981; Gaillardet et al., 1999; West et al., 2005), all of which may impact the Ca isotopic ratio of the dissolved load. River chemistry is defined by mixtures of waters with distinct chemical compositions, inherited from rock dissolution and fractionation processes. Working in small catchments where as many parameters as possible are constrained allows us to understand the controls on Ca isotope ratios in rivers. By reducing the field locations to small catchments that drain single lithologies, understanding geochemical signatures becomes significantly simpler, which is an important reason for choosing the Khudi Khola.

2.5.1 The Khudi Khola

The Khudi Khola (Figure 2.10) is a tributary of the Marsyandi located on the southern flank of the Lamjung massif, just to the east of the Annapurnas. The basin, with an area of 138 km^2, has an extreme topographical gradient, with elevations ranging from 800 to 5,000 meters asl within a lateral distance of 20 km (the average altitude is 2,558 meters). The Khudi Khola is characterized by a number of features that are typical of basins located along the southern flank of the Himalayas: steep slopes, strongly developed vegetation, and intense precipitation, which can reach 5,000 mm/year (Putkonen, 2004). Presently, the Khudi has no glaciers and field observations show that there was limited glacial coverage and glacial erosion in the past.

For at least the past 50 years, the Khudi Khola has experienced active slip due, in large part, to the active Saituti landslide located in the HHC (Gallo and Lavé, 2014) (see Figure 2.11). Average erosion rates are among the highest in central Nepal, estimated at between 2.5 and 3 mm/year (suspended load measurements) (Gallo and Lavé, 2014; Gabet et al., 2008), between 2 and 4.5 mm/year (cosmogenic isotopes) (Niemi et al., 2005; Godard et al., 2012; Puchol et al., 2014; Gallo and Lavé, 2014), and between 2 and 4 mm/year during the Quaternary (thermochronology techniques) (Blythe et al., 2007; Whipp et al., 2007). The Khudi drains almost exclusively HHC gneisses above the

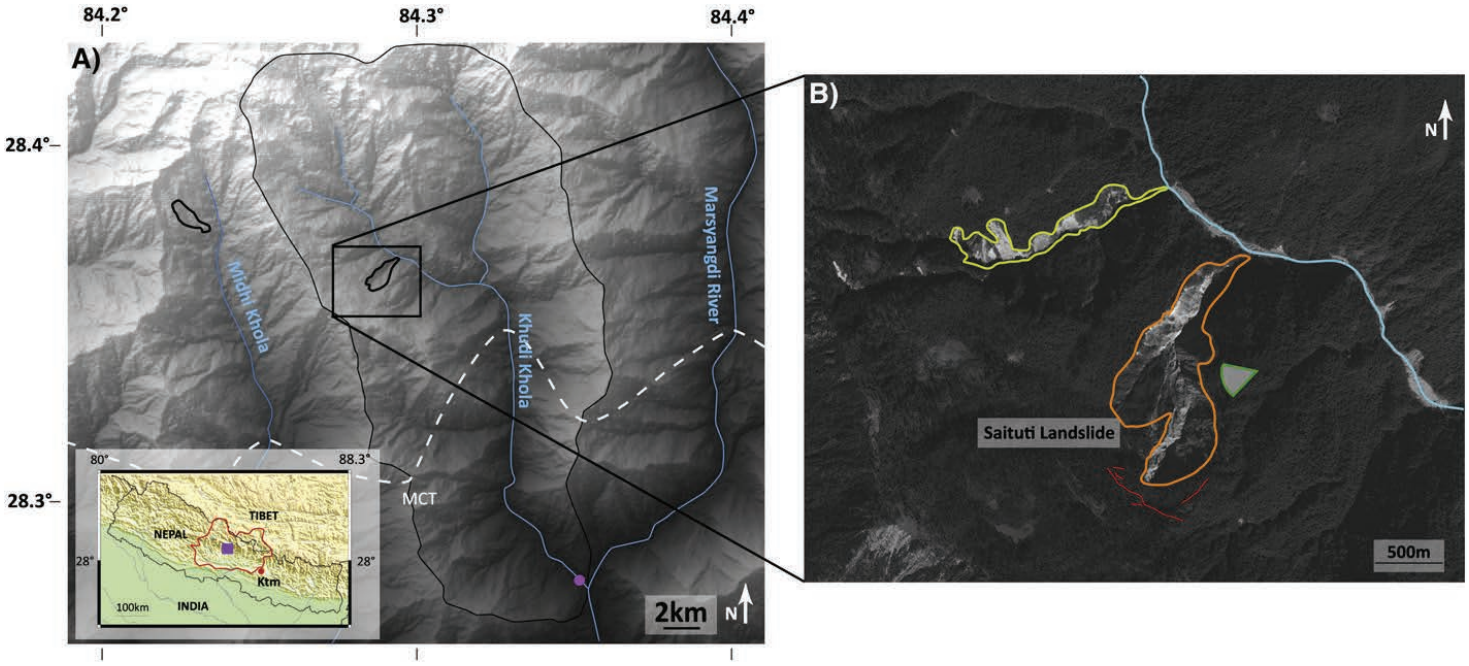

Figure 2.10 – *Topography of the Khudi Khola Basin, Lamjung Massif, and the present extent of the landslide zones (Gallo and Lavé, 2014). In the figure on the left, white dashes represent the MCT that separates HHC gneisses to the north from LH metaplites and carbonates to the south. The Khudi has two active landslides. The Saituti landslide has been active for at least the past 40 to 50 years (shown in orange). This survey and image is from the study of Gallo and Lavé (2014).*

Figure 2.11 – *View of the Saituti landslide from Gallo and Lavé (2014)*

MCT, while LH carbonates and dolomites dominate below the LH. Thus, the limited and well-constrained geology of the Khudi Khola allows a slightly less complicated study of alteration, weathering, and erosion at the small catchment scale.

Furthermore, just below the MCT, the Nepali government has installed a hydro-power electric plant and allowed the installation of equipment for sampling and riverine discharge/turbidity measurements (Figure 2.12). Due to its climatic, geological, and geomorphological properties, the Khudi is a field site well adapted for studies concerning erosion, weathering, and the dynamics of active landslides. The sediments, soils, pebbles, and water collected in the Khudi are presented in Chapter 4 of this thesis.

2.5.2 The Narayani

The major river system that traverses central Nepal is the Narayani, draining an area of 32,000 km^2, from the Tibetan Plateau (TSS) in the north through the HHC, LH, and Siwaliks to the south, where it eventually enters the Gangetic plain as the Gandak (see Figure 2.13). With such a large drainage area, the Narayani contains a plethora of terrains, lithologies, climatic conditions, and vegetation.

The Narayani is the wettest basin in all of Nepal with, on average, 1.4 m/year of precipitation, which can increase to more than 4 m/year in specific zones (Putkonen, 2004; Bookhagen and Burbank, 2010). Certain areas in the Narayani are also heavily affected by monsoon storms, especially in the Annapurna massif (Bookhagen and Burbank, 2010; Andermann et al., 2012a). The main Narayani tributaries from west to east are the Kali Gandaki, the Seti, the Marsyandi, the Bhuri Gandaki, and the Trisuli.

The geology of the Narayani basin is similar to that of the Himalayan chain as a whole, i.e., the geological units traverse the basin in west to east bands. The bedrock

Figure 2.12 – *A view of the water station at the hydro-electric power plant located approximately 4.5 km upstream from the Khudi's confluence with the Marsyandi. This is the location of the hourly water sampling that was completed in 2013 and 2015 (see Chapter 4). The long drainage system is the entry point for water from the Khudi to enter into the hydro-electric power plant.*

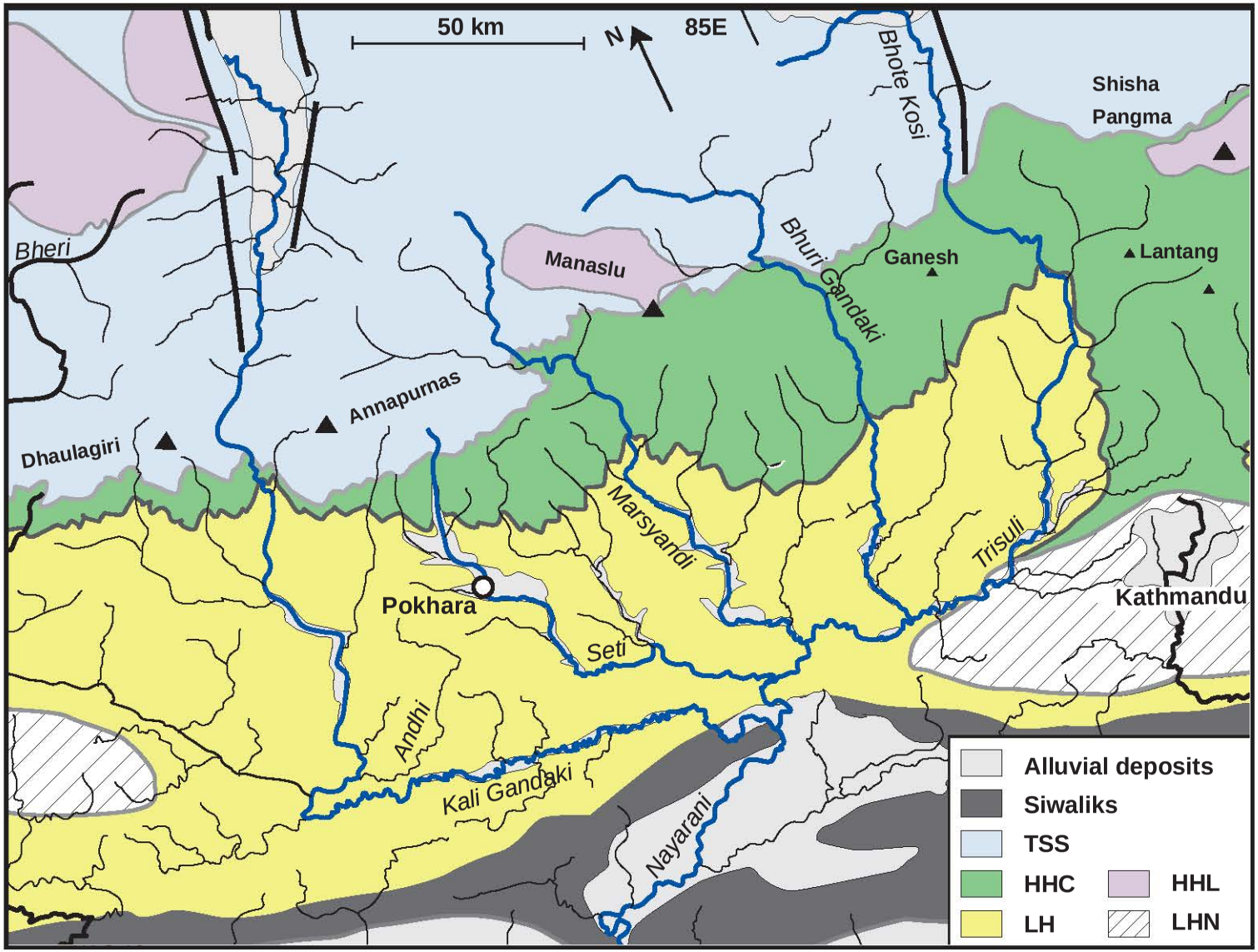

Figure 2.13 – *The Narayani-Gandak watershed, showing the geological units derived from Colchen et al. (1986) (modified after Galy and France-Lanord (1999). TSS = Tethyan Sedimentary Series, HHC = High Himalayan Crystallines, LH = Lesser Himalaya, HHL = High Himalayan Leucogranites, and LHN = Lesser Himalayan Knappes.*

composition of the Narayani is: 33% TSS, 23% HHC, 40% LH, and less than 5% for the Siwaliks (see Figure 2.13) (Morin, 2015). One of the important aspects of the Narayani is that it provides samples of the LH, which contains some of the oldest Himalayan rocks. These LH rocks and sediments, and their weathering products dissolved in river water, are some of the most radiogenic material that exists in the Himalaya and are thus important to constraining the mass balance of carbonate and silicate weathering in the dissolved load, and its effect on CO_2 consumption in the Narayani. Results from the Narayani are presented in Chapter 5 of this thesis.

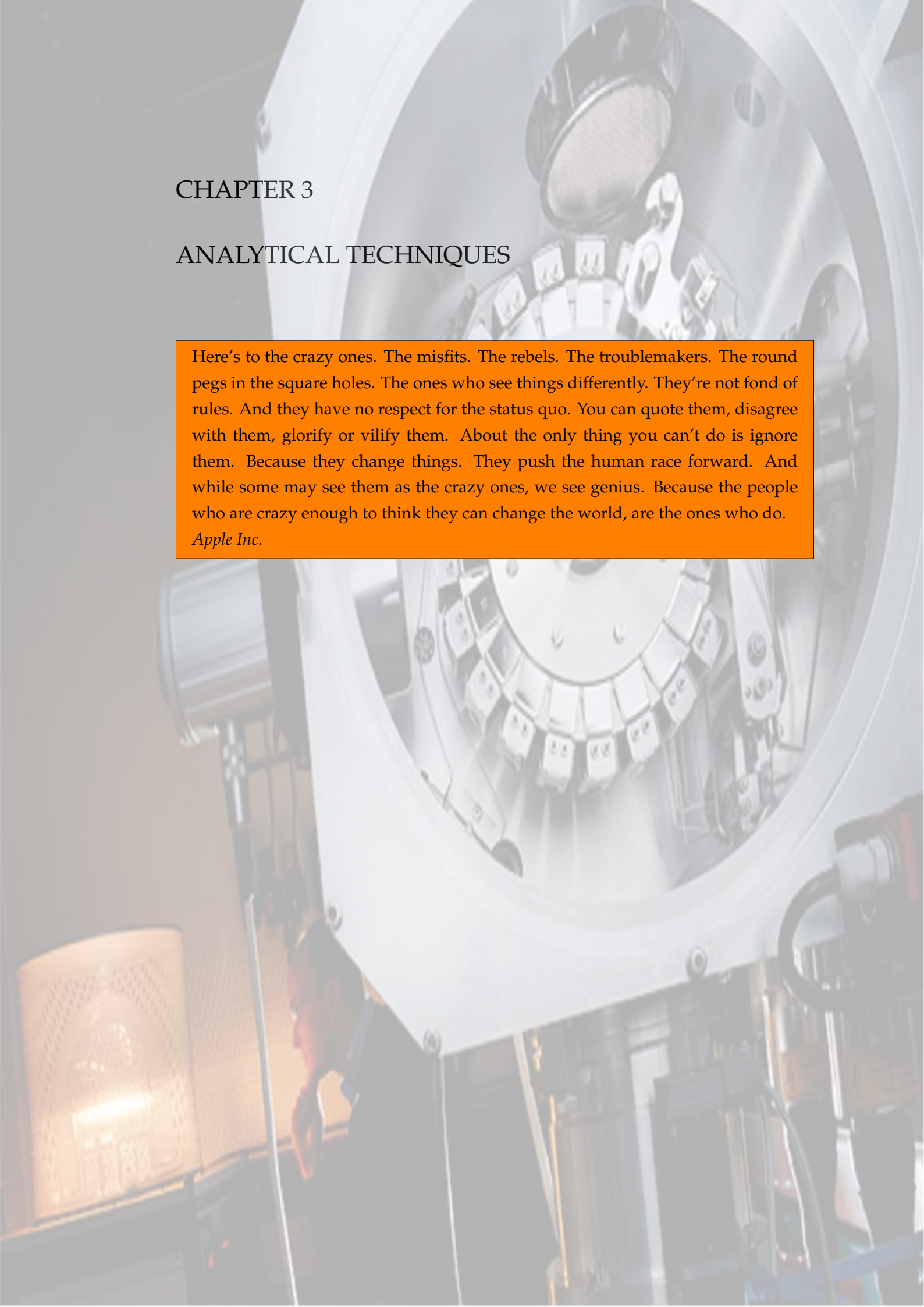

CHAPTER 3

ANALYTICAL TECHNIQUES

Here's to the crazy ones. The misfits. The rebels. The troublemakers. The round pegs in the square holes. The ones who see things differently. They're not fond of rules. And they have no respect for the status quo. You can quote them, disagree with them, glorify or vilify them. About the only thing you can't do is ignore them. Because they change things. They push the human race forward. And while some may see them as the crazy ones, we see genius. Because the people who are crazy enough to think they can change the world, are the ones who do.
Apple Inc.

This chapter discusses briefly the various analytical techniques used throughout the course of this thesis. These techniques include Inductively Coupled Plasma-Oxygen Emission Spectrometry (ICP-OES) and Inductively Coupled Plasma-Mass Spectrometry (ICP-MS) for major and trace element analysis, ionic chromatography for anion concentrations, and the analysis of Sr and Ca isotopes using the Triton thermo-ionization mass spectrometer (TIMS). These techniques were performed on water, bank and suspended load sediments, whole rock, soils, and pebbles from across the Himalayan chain.

3.1 Major and trace element analysis

Water samples were filtered at 0.2 microns and then acidified in 2% HNO_3 at the time of collection. For both water and powdered sediment and whole-rock samples, major element concentrations were measured by Inductively Coupled Plasma-Oxygen Emission Spectrometry (ICP-OES) and by Inductively Coupled Plasma-Mass Spectrometry (ICP-MS) for trace elements at the Service d'Analyse des Roches et des Minéraux (SARM) at CRPG, Nancy, France. The uncertainty on the major elemental analyses is less than 5% and in some cases less than 2%. For the trace elements (specifically Sr), uncertainty is less than 5%. Anions in water samples were measured by ionic chromatography (Chromatograph Dionex ICS 3000; AS11-HC and AS20 columns) at the Laboratoire Interdisciplinaire des Environnements Continentaux (LIEC), Nancy, France.

3.2 Chemical preparation for Ca and Sr isotope analysis

3.2.1 Preparation of materials

Sample preparation was conducted in the clean laboratory of the Centre de Recherches Pétrographiques et Géochimiques (CRPG), Nancy, France. All acids for sample preparation (HNO_3 and HCl) were single distilled before use by in-house sub-boiling distillation of analytical reagent grade acids. Suprapure hydrofluoric acid (HF) was purchased from Seastar. The concentration of all new batches of acid was checked by titration with 1M NaOH using a few drops of a phenolphthalein solution (1% in ethanol) as the indicator. Acid dilutions were performed volumetrically. Ultrapure water (18.2 MΩ; 'MQ water') was used during cleaning procedures and sample preparation. Teflon beakers (Savillex; 5, 10, 15, 30, and 60 mL) were used for column chemistry work and sample dissolutions. Teflon beakers used in column chemistry work were cleaned by filling the beaker with cHNO_3 (hereafter, the 'c' denotes that undiluted concentrated acids were used), closing the beaker, and leaving it on a hot plate at 120°C for 24 hours. The beakers were then rinsed copiously with MQ water, filled with MQ water, and then placed on the hot plate at 120°C for another 24 hours. The beakers were then dried inside a fume hood. For beakers which had been used to digest samples, a few drops of cHF were added to the first step (addition of cHNO_3). Afterwards, the HNO_3/HF mixture was discarded and a few mL of HCl were added to the beaker and again left on the hotplate for several days. The cleaning procedure was then identical to that previously described. Polypropylene centrifuge tubes (60 mL) were used to store samples as well as for performing leaching tests and leaching of sediment samples. The tubes, including the caps, were cleaned in a bath of cold 5% HNO_3 for several days. The tubes were then rinsed copiously with MQ water and left to dry inside a fume hood. Water samples were collected in HDPE bottles (60 mL and 1 L). The bottles for cation analysis were cleaned using 2% HNO_3 and those for anion analysis were cleaned using MQ water. The bottles were filled with the respective cleaning reagent and left to stand for several days. The bottles were subsequently emptied and rinsed three times with MQ water.

3.2.2 Sample digestion

Before column chemistry, we prepared both water and rock/sediment samples first by calculating the amount of sample needed based on the Ca concentration of the sample with the goal to attain 100 µg of Ca and 1 µg of Sr in the final solution after the completion of column chemistry. If Sr isotope analysis had already been completed for a sample, we only calculated the amount of sample needed for Ca analysis. Otherwise, we first performed Sr column chemistry on the sample (see below) and collected the

wash from the Sr column chemistry to use for Ca column chemistry.

After calculating the amount of sample needed, the required amount of water sample was collected and placed in a Teflon beaker. The sample was then placed on a hot plate at 120°C with the lid off and left there until the sample had completely evaporated, leaving a small residue at the bottom of the beaker. Afterward, the sample was taken off the hot plate, left to cool at room temperature for several minutes. Immediately afterward, we added 5 mL of 2N HCl to the beaker, which was shaken slightly by hand, and then placed in an ultrasonic bath at 55°C for 15 minutes to completely homogenize the solution. After this step, water samples were ready for Ca and/or Sr column chemistry.

For whole rock and sediment samples, we calculated the amount of crushed sample needed to obtain a Ca concentration of 1 mg in the final dissolved solution before Ca column chemistry. After calculation, the amount of sample (in g) was weighed out carefully and placed in 60 mL Teflon beakers and closed firmly to prevent the escape of any powder. We only performed leaching on sediment samples, where we leached the amount of sediment required in 5mL of 2N HCl for 24 hours at 120°C. After leaching, the sample was separated via centrifuge and the respective leachate and residue were placed into separate beakers and prepared for HF attack.

The HF attack was performed on all sediment (after leaching) and whole rock samples. In addition to dissolving the silicate phases, this technique destroys any organic matter in the sample. To the powder, we added a mixture of cHF (3 mL) and $cHNO_3$ (2 mL). The Teflon beaker was then closed, shaken by hand, and placed on a hot plate at 120°C for 24 hours. After 24 hours, we removed the beaker from the hot plate, let it cool at room temperature, and then placed the open beaker on the hot plate at 120°C until the mixture had completely evaporated. After evaporation, we placed 5 mL of cHCl in the beaker, shook the sample vigorously until the residue had dissolved, and then placed the closed beaker on the hot plate at 120°C for 24 hours. After 24 hours, the beaker was removed and completely evaporated at 120°C. This process, with cHCl, was repeated until no HF precipitates remained in the residue.

3.3 Chromatographic Separation of Sr and Ca

The most common extraction technique for both Ca and Sr is ion chromatography on a cation exchange column. Molecules attach themselves chemically onto the resin and are then eluted by dilution with varying concentrations of acids.

3.3.1 Sr Extraction and Analysis

Sr was extracted from the residues and leachates using EIChroM Sr Spec resin using routine techniques based on those developed by Pin and Bassin (1992). The separated Sr fractions were then deposited on simple, single assembly, rhenium filaments for analysis by thermo-ionization mass spectrometry (TIMS). Approximately 250 ng of Sr was loaded in nitric form together with 1 µL of $TaCl_5$ activator solution onto degassed single rhenium filaments.

Strontium isotopic measurements were performed on a Triton Plus (ThermoFischer Scientific) TIMS instrument in static mode. The different ratios measured are corrected for mass fractionation via the exponential law, using $^{86}Sr/^{88}Sr_{Natural}$ = 0.1194. Similarly, the $^{87}Sr/^{86}Sr$ ratios are corrected for a possible contribution of rubidium measured on mass 85 (natural ratio: $^{87}Rb/^{85}Rb$ = 0.385517). The NBS 987 liquid standard was analyzed in each session to monitor machine drift. All runs of this standard yielded a $^{87}Sr/^{86}Sr$ value of 0.710249 $\pm$ 0.000042 (2 S.D., 176 analyses) over the time period (2014–2016) of this study. In-run precisions (2 S.E.) were typically less than 0.000020. Typical total procedural Sr blanks were less than 1 ng.

3.3.2 Ca Extraction

If the sample had already been analyzed for Sr isotopes, it was directly prepared for Ca isotopic analyses. If it had not been analyzed for Sr, Sr separation was done first and the wash aliquots from Sr separation were recuperated and prepared for Ca separation. All samples were first evaporated and then redissolved in 5 mL of 2N HCl (see above). The separation of K from Ca was performed in a 20 cm long, 1 cm diameter column, containing a cation resin (AG50-X8, 200–400 mesh), following the methods described by Tera et al. (1970), which were modified slightly by Caro et al. (2010) (see Table 3.1 – procedures used in this study). The Ca column chemistry techniques used in this study roughly follow the methods of Caro et al. (2010).

Briefly, the sample was introduced into the column in 5 mL of 2N HCl. Most major cations were removed in aliquots of 10, 40, and 100 mL of 2N HCl. Calcium was then collected in 10 mL of 3N HCl and 50 mL of 4N HCl. This protocol efficiently separated Mg and Fe from Ca but in high Al samples, not all of the Al was removed by the 2 N HCl. The presence of Al results in a decrease in Ca ionization efficiency and yields short-term beam instabilities, as observed during analysis of Al-rich samples.

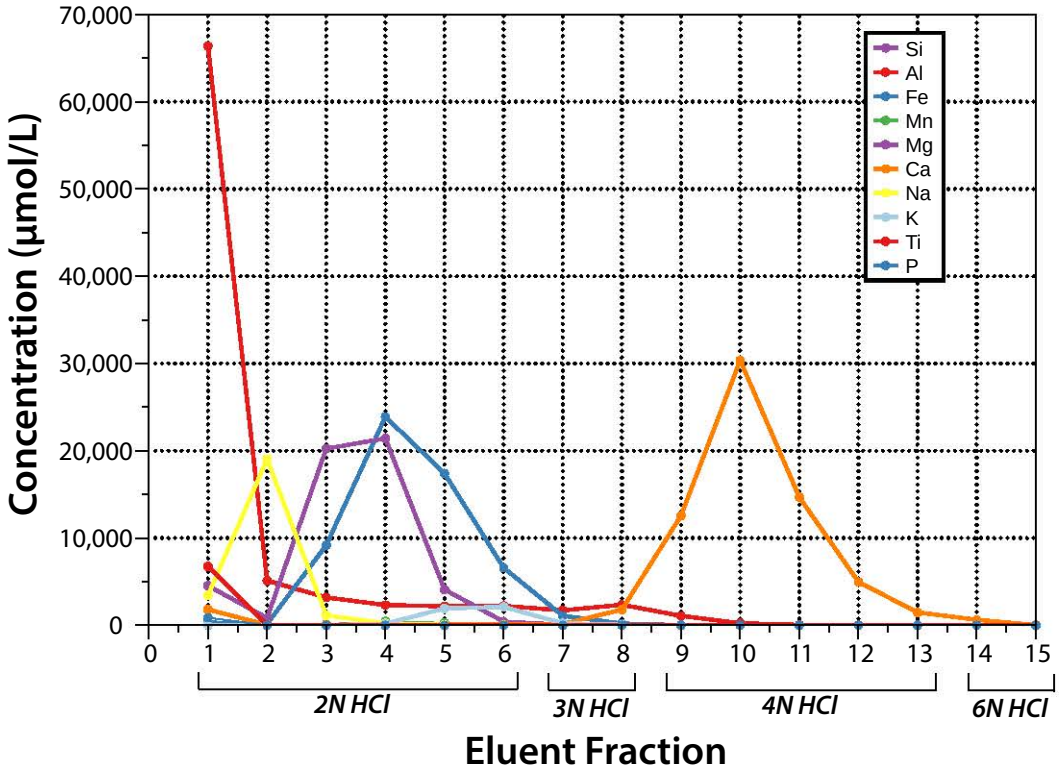

Figure 3.1 – *A Ca column calibration test to observe the concentration of each eluent in each fraction. These data follow the procedures for large columns listed in Table 3.1. After each elution stage, the waste was not discarded but collected for major element analysis. Each fraction shown on the x-axis represents the analysis of the waste collected after each elution step described in Table 3.2. The concentrations of the acids used during the elution test were 2N, 3N, 4N, and 6N HCl.*

To eliminate any remaining Al, a small cationic column was used (4 cm in length, 0.5 cm diameter). Aluminum was first eluted in 3 mL of 4 N HCl and Ca was then recovered in 3–4 mL of 4N HCl. The total chemistry yield was 70–85% (see Figure 3.1 and Table 3.2) for Ca and the procedural blank was < 1 ng. Since mass-dependent fractionation is corrected during analysis, this relatively low yield is of no consequence for the determination of the radiogenic ^{40}Ca composition.

3.3.3 ESI PrepFast

Traditional chromatography techniques in isotope geochemistry usually utilize gravity-driven column configurations. However, gravity columns impose limitations on the column length and resin particle size that can be used, due to long elution times. This makes the column setup less than ideal for very high-resolution separations, such as separating Ca from K and Al. High-performance liquid chromatography (HPLC) is an improved form of liquid chromatography that allows pressurized eluents to

Table 3.1 – *Specific steps, directions, and eluents for Ca extraction.*

Large Columns		
Eleunt	Volume Eluted	Elements
Step 1:		
2N HCl	10	Conditioning
Step 2: Sample Introduction		
2N HCl	5	Ca + Matrix
Step 3:		
2N HCl	2	
Step 4:		
2N HCl	10	
2N HCl	40	Al, K, Na
2N HCl	100	
Step 5: Rinse		
3N HCl	10	
Step 6: Final Elution		
3N HCl	10	Ca, Al
4N HCl	50	
Step 7: Wash Columns		
6N HCl	2x100	
Small Columns (Ultra-Purification)		
Step 1:		
4N HCl	5	Conditioning
Step 2: Sample Introduction		
4N HCl	1	Ca + Matrix
Step 3:		
4N HCl	200 µL	
Step 4:		
4N HCl	3	Al, K, Na
Step 5: Final Elution		
4N HCl	7	Ca
Step 6: Wash Columns		
6N HCl	10	

Table 3.2 – *A Ca calibration to test the elution efficiency of the Ca columns and resin. These data are plotted in Figure 3.1 and follow the procedures for large columns listed in Table 3.1. After each elution stage, the waste was collected for major element analysis. The concentrations of the acids used during the elution test were 2N, 3N, 4N, and 6N HCl. The table shows the eluent fractions in µmol/L. Each fraction shown on the x-axis in Figure 3.1 represents the collection/analysis of the waste after each elution step described in Table 3.1.*

	Si	Al	Fe	Mn	Mg	Ca	Na	K	Ti	P
					µmol/L					
Fraction1 - 2N HCl 10 mL	0.00	0.00	0.00	0.00	0.00	0.00	0.00	0.00	0.00	0.00
Fraction2 - 2N HCl 5 mL	bdl	5114.90	165.64	0.90	824.93	43.39	19051.76	bdl	19.70	bdl
Fraction3 - 2N HCl 2 mL	bdl	3192.74	9169.20	127.92	20238.63	55.54	1138.76	bdl	6.56	bdl
Fraction4 - 2N HCl 10 mL	bdl	2316.53	23885.41	458.68	21419.46	64.90	229.93	174.36	bdl	bdl
Fraction5 - 2N HCl 40 mL	bdl	2177.54	17401.97	281.12	4097.51	76.92	48.33	1933.58	bdl	bdl
Fraction6 - 2N HCl 100 mL	bdl	2217.75	6587.29	55.62	420.90	111.31	19.23	2105.76	bdl	bdl
Fraction7 - 3N HCl 10 mL	bdl	1709.23	1089.88	3.67	53.45	144.59	6.66	234.19	bdl	bdl
Fraction8 - 3N HCl 10 mL	bdl	2348.41	198.57	0.41	34.97	1796.25	4.44	55.09	bdl	bdl
Fraction9 - 4N HCl 10 mL	bdl	1077.84	15.74	bdl	15.96	12560.51	bdl	6.52	bdl	bdl
Fraction10 - 4N HCl 10 mL	bdl	236.29	2.52	bdl	7.20	30365.79	bdl	bdl	bdl	bdl
Fraction11 - 4N HCl 10 mL	bdl	48.26	bdl	bdl	bdl	14676.38	bdl	bdl	bdl	bdl
Fraction12 - 4N HCl 10 mL	bdl	23.35	bdl	bdl	bdl	4960.33	bdl	bdl	bdl	bdl
Fraction13 - 4N HCl 10 mL	bdl	15.72	bdl	bdl	bdl	1480.36	bdl	bdl	bdl	bdl
Fraction14 - 6N HCl 100 mL	11.32	32.88	bdl	bdl	4.24	630.77	bdl	bdl	bdl	bdl
Fraction15 - 6N HCl 100 mL	7.98	16.60	bdl	bdl	bdl	24.75	bdl	bdl	bdl	bdl

be passed through the column, eliminating problems with length and resin mesh size. To maximize the separation between Ca and other elements, especially K, Al, Sr, and Mg, we tested different column configurations and elution conditions using the PrepFAST automated low-pressure column chemistry system manufactured by Elemental Scientific (ESI; Figure 3.2). Unfortunately, the prepFAST was not delivered and installed until close to the end of the analytical period of my thesis and was therefore not implemented into my standard analytical protocol. However, the tests that were performed seemed promising for its future use at CRPG for a number of different systems and applications and several samples were separated using the PrepFast (this includes both Sr and Ca extraction for samples from the Ganga, Brahmaputra, Bay of Bengal region, and from the Garwhal Himalaya, i.e., the source of the Ganga).

Figure 3.2 – *The ESI PrepFast.*

3.4 High precision isotopic measurements of radiogenic calcium by thermal ionization mass spectrometry

To be submitted to Geostandards and Geoanalytical Research.

Keywords: radiogenic calcium isotopes, ^{40}K–^{40}Ca, mass fractionation, TIMS, exponential law, domain mixing.

Keywords: isotopes radiogenique de calcium, ^{40}K–^{40}Ca, fractionnement de masse, TIMS, loi exponentielle, domaine mélange.

Abstract We report a novel approach for the highly precise isotopic analysis of radiogenic ^{40}Ca utilizing thermal ionization mass spectrometry (TIMS). We measured the Ca isotope composition of standard NIST915a over a period of three years at CRPG, Nancy. The new sample loading and mass spectrometric techniques eliminate the filament "reservoir" mixing phenomena previously described during TIMS analysis and greatly diminishes mass fractionation over the course of a measurement. Due to this very limited fractionation, corrections using power, linear and Rayleigh laws yield results that are indistinguishable from those obtained using the exponential law, with the same level of precision. With this tightly controlled multi-dynamic analytical approach we have achieved an external precision over a three-year analytical period of $\pm$ 40 ppm (2 S.D.) for the ^{40}Ca/^{44}Ca ratio with the Thermo Triton Plus. This level of external reproducibility allows discrimination of small radiogenic ^{40}Ca effects in terrestrial and extra-terrestrial samples at precisions that were previously unattainable.

Resume Nous rapportons de nouvelles approches pour l'analyse isotopique très précise de ^{40}Ca radiogénique en utilisant la spectrométrie de masse à ionisation thermique (TIMS). Nous avons mesuré la composition en isotopes de Ca du standard NIST915a sur une période de trois ans au CRPG, Nancy. Les nouvelles techniques de spectrométrie de masse éliminent les phénomènes de mélange 'réservoir' de filaments précédemment observés lors de l'analyse TIMS et éliminent essentiellement les effets décrits par de nombreux chercheurs de fractionnement de masse au cours d'une mesure. Nous constatons également que, en raison du très peu d'écart par rapport à la loi exponentielle, nos données standard peuvent être corrigées avec les lois de puissance, linéaires et/ou de Rayleigh, tout en offrant le même niveau de précision et justesse. Ainsi, avec cette approche analytique multidynamic étroitement contrôlée, nous avons atteint une précision externe, sur une période analytique de trois ans, de $\pm$ 40 ppm (2 S.D.) pour le rapport ^{40}Ca/^{44}Ca avec le ThermoFischer Triton. Ce niveau de reproductibilité externe permet la discrimination précise de petits

effets ^{40}Ca radiogéniques dans des échantillons terrestres et extraterrestres qui étaient auparavant inaccessibles.

3.4.1 Introduction

Calcium, Earth's fifth most abundant element, has six isotopes: ^{40}Ca, ^{42}Ca, ^{43}Ca, ^{44}Ca, ^{46}Ca, and ^{48}Ca. Calcium-40, the most abundant isotope (96.9%) is produced by the β^- decay of ^{40}K (λ = 1.248 x 10^9 yr^{-1}) (Nägler and Villa, 2000). The abundance of ^{40}Ca in planetary reservoirs is thus dependent upon the source region's K/Ca ratio and the residence time of Ca in these reservoirs. Radiogenic calcium isotopes are expressed in ε notation, normalized to the NIST SRM915a standard, which was previously shown to be indistinguishable from the mantle value (Caro et al., 2010):

$$\varepsilon^{40}Ca = \left[\frac{Y_{sample}}{Y_{standard}} - 1\right] \times 10^4 \tag{3.1}$$

where Y is the ^{40}Ca/^{44}Ca ratio of the sample or standard.

Mantle rocks usually have low K/Ca ratios, on the order of 0.01, and thus have experienced negligible radiogenic Ca ingrowth over the Earth's history in terms of current detection limits. However, the upper crust, characterized predominantly by felsic lithologies with high K/Ca ratios between 1 and 4, produce large abundances of ^{40}Ca (Caro et al., 2010). The estimated K/Ca of the upper continental crust is approximately 0.95 (Taylor, 1964), placing an approximately +2–3 ε-unit limit on ^{40}Ca ingrowth in the upper continental crust (Caro et al., 2010).

Since the pioneering work of Russell et al. (1978), attempts have been made to apply the ^{40}K–^{40}Ca system as a geochronological tool (Marshall and DePaolo, 1982; Marshall et al., 1986) and as a petrogenetic tracer (Marshall and DePaolo, 1989). However, the use of this system has remained marginal, partly due to the difficulty of precisely analyzing very small relative differences in ^{40}Ca. More recently, Caro et al. (2010) used the ^{40}K–^{40}Ca to place constraints on the evolution of radiogenic Ca in the oceans and Davenport et al. (2014) attempted to use the radiogenic calcium system as a provenance tracer of silicate and carbonate rock in the dissolved load of Himalayan rivers. See Chapter 1 for a more complete review of the work that has been done on the radiogenic Ca system.

Despite its potential as a tracer in the exogenic Ca cycle, the ^{40}K–^{40}Ca system remains little used due to the analytical difficulty of measuring radiogenic enrichments on the ^{40}Ca isotope (Fletcher et al., 1997a; Marshall and DePaolo, 1982, 1989; Nelson and McCulloch, 1989; Niederer and Papanastassiou, 1984; Russell et al., 1978; Shih et al., 1994). This, in part, is due to the abundances of the relevant Ca isotopes (^{40}Ca: 96.94%; ^{42}Ca: 0.647%; ^{44}Ca: 2.086%) (Caro et al., 2010), i.e., the ^{40}Ca

isotope dominates the system making it difficult to measure the less abundant isotopes of Ca. It is important to minimize error on the small ^{42}Ca and ^{44}Ca ion beams, because the measured ratio of ^{42}Ca/^{44}Ca is used for the correction of instrumental mass fractionation (Caro et al., 2010). Marshall and DePaolo (1982) Marshall and DePaolo (1989), and Marshall et al. (1986), using the Finnigan MAT-262, reported an external precision of $\pm$ 0.6–1.5 ε-units (2σ). More modern Thermal Ionization Mass Spectrometers (TIMS), notably the Thermo Triton, permit the analysis of smaller radiogenic variations on the ^{40}Ca isotope. Using the Triton to analyze samples from Archean cratons, Kreissig and Elliott (2005) obtained a reproducibility of $\pm$ 0.5 ε-units (2σ) and Caro et al. (2010) reported ^{40}Ca/^{44}Ca data in marine carbonates with external precision of $\pm$ 0.35 ε-units. These advances in precision are a result of two improvements on the newer generation of TIMS: 1) the ability to measure larger ion beams compared to earlier TIMS instruments (< 50V, against < 10V using the MAT262) and 2) the possibility to use the "Zoom" optical system of the Triton to analyze calcium isotopes in multidynamic mode.

Instrumental mass fractionation during a TIMS analysis has a significant impact on the measured isotopic composition of Ca (Wasserburg et al., 1981; Hart and Zindler, 1989). Therefore, it is important that a suitable fractionation law be used to correct for this fractionation. Most researchers have concluded that the exponential law is best suited for the correction of instrumental fractionation (Russell et al., 1978; Hart and Zindler, 1989). However, several studies (Hart and Zindler, 1989; Fantle and Bullen, 2009; Lehn and Jacobson, 2015; Roth et al., 2014; Caro et al., 2017) reported non-exponential behavior, especially at high levels of mass fractionation. Calcium isotopic measurements may thus be hindered by inappropriate mass fractionation corrections due to deviations from the exponential law. This could result from a number of processes including the evaporation of different domains or regions on the filament that have fractionated to different degrees before or during an analysis (Hardie, 1996) or incomplete transmission of Ca ions from the filament to the collectors.

Here, we report the results of replicate analyses of NIST standard SRM 915a performed at CRPG Nancy over a period of three years utilizing a multi-dynamic mass spectrometric approach. We also describe an improved loading technique that essentially eliminates 1) the filament "reservoir" mixing phenomena previously reported during TIMS analyses of Ca isotopes (Hart and Zindler, 1989) and 2) large mass fractionation effects over the course of an individual measurement.

3.4.2 Experimental

Calcium was measured as a positive metal ion (Ca^{2+}) using a Thermo Triton Plus thermal ionization mass spectrometer at the Centre de Recherches Pétrographiques

et Géochimiques (CRPG), Nancy, France. Approximately 1 µL of a 10,000 ppm standard solution of NIST SRM915a dissolved in 10N HNO_3 (equivalent to 10 µg Ca) was loaded onto a zone refined Re filament of a double filament assembly (filament dimensions: 0.04 mm thick by 0.76 mm wide zone refined Re ribbon from HCross). The solutions were evaporated on the filament at an applied current of approximately 0.8 A. After complete loading, the current was slowly increased to approximately 1.8 A and kept at this level for 5 to 10 seconds until the filament was glowing. As the filament is heated to evaporate the solution, the combination of heat and acidity leaches Rhenium out of the filament. Calcium then precipitates as a heavy Calcium Rhenate salt that evaporates with limited mass fractionation in the thermal-ionization source. After loading, the filament turret was immediately inserted into the TIMS to avoid rehydration of the Ca-nitrate salt due to humidity.

During TIMS analysis, the ionization filament current was heated to approximately 2500 mA at a rate of 200 mA per minute and the evaporation filament current was heated to 100 to 200 mA at a rate of 50 mA per minute. The ionization filament was then increased or decreased appropriately until a $^{40}Ca^{2+}$ ion current corresponding to 10–12 V over a 10^{11} Ω amplifier was obtained. The evaporation filament, as well as the ^{40}Ca and ^{42}Ca ion beam, was continually monitored throughout the measurement. The ionization filament was automatically reheated between every two measurement blocks when signal intensity dropped below or went above 20% of its initial intensity. Isobaric interferences from ^{40}K were monitored by measuring ^{41}K and corrected online using a $^{41}K/^{40}K$ = 1.73 x 10^{-3}. The $^{41}K/^{40}Ca$ mean values for analyses of standards never exceeded 1.08 x 10^{-4} so that the $^{40}Ca/^{42}Ca$ ratio did not require significant interference correction during the course of our measurements. A multi-dynamic acquisition scheme using two magnet settings (corresponding to ^{40}Ca and ^{42}Ca in the axial detector; see above and Table 3.3) was used to reduce the effects of Faraday Cup variations on measured isotopes ratios. The first of these two settings was also used to provide a static analysis that could be directly compared with the multi-dynamic results. Each magnet setting was integrated 30 times with an integration time of 1.049 seconds each, thus a total integration time of 31.47 seconds for each acquisition line. The acquisition lines were separated by an idle time of 15 and 7 s on Line 1 and 2, respectively. To align the ion beams into the detectors for the second magnet setting, the zoom quadrupole was modified from approximately 0 V to a value between 10 and 12 V. A Ca measurement consisted of 10–12 blocks with 10 cycles per block, lasting between 4 and 6 hours. Amplifiers were rotated to the left after each block (unless otherwise noted). Peaks were centered in the axial detector every two blocks using the ^{40}Ca- (Line 1) and ^{42}Ca- (Line 2) ion beams. An automatic focusing protocol

was implemented every two blocks (after peak centering) involving the Condenser, Extraction Left, Right, X-Symmetry, and Z-Focus electrodes with the ^{40}Ca beam in the axial detector. Baselines were measured at the beginning of every measurement day with 120 baseline measurements, each lasting 60 seconds. An amplifier gain was done each time the turret was changed with new samples/standards.

3.4.3 Data processing

3.4.3.1 Correction of instrumental mass fractionation

Mass fractionation was corrected offline with the exponential law using $^{42}Ca/^{44}Ca$ = 0.31221 (Russell et al., 1978). Several models for isotope mass fractionation have been proposed: the linear, power, Rayleigh, and exponential laws (Russell et al., 1978; Hart and Zindler, 1989; Ranen and Jacobsen, 2008). Russell et al. (1978) and others (Hart and Zindler, 1989; Schiller et al., 2012; Naumenko-Dèzes et al., 2015; Zhu et al., 2015) have previously shown that the exponential law is the closest empirical representation for the behavior of isotope fractionation in the thermal-ionization source.

Equation 3.2 describes the mass fractionation correction used in this study:

$$\frac{R_M}{R_C} = \left(\frac{S_M}{S_T}\right)^A \tag{3.2}$$

where R is the isotopic ratio of interest ($^{40}Ca/^{42}Ca$ or $^{43}Ca/^{44}Ca$) and S is the normalization ratio ($^{42}Ca/^{44}Ca$). Subscripts M, C, and T represent the measured ratio, the corrected ratio, and the "true" value of the normalization ratio ($^{42}Ca/^{44}Ca$ = 0.31221) (Russell et al., 1978). The constant A is a function of mass only and varies depending on the fractionation law in question (Russell et al., 1978; Hart and Zindler, 1989; Ranen and Jacobsen, 2008). The "generalized fractionation law" provides a convenient general expression for A, which is:

$$A = \frac{40^n - 42^n}{42^n - 44^n} \tag{3.3}$$

where n is a function of the specific fractionation law. For the exponential law n > 0, and taking the natural log of equation 3.3 yields:

$$A = \frac{\ln\left(\frac{40}{42}\right)}{\ln\left(\frac{42}{44}\right)} \tag{3.4}$$

In static mode, all isotopes were measured on Line 1 and the $^{40}Ca/^{42}Ca$ and $^{43}Ca/^{42}Ca$ ratios are corrected online using $^{42}Ca/^{44}Ca$= 0.31221 as the normalization ratio. In multidynamic mode, $^{40}Ca/^{42}Ca$ was measured on Line 1 and corrected

Table 3.3 – *Collector configurations and analytical conditions for the present study.*

Present Study													
Magnet Setting	Faraday Collectors					Integration time [s]	Number of Integrations	Idle time [s]	Peak Centre	Lens Focus	Zoom Optics	
	L3*	L2	C	H1	H2						Focus [V]	Dispersion [V]
1	–	^{40}Ca	^{42}Ca	^{43}Ca	^{44}Ca	1.049	30	15.0	^{42}Ca	none	7.0	-28.5
2	–	–	^{40}Ca	^{41}K	^{42}Ca	1.049	30	7.0	^{40}Ca	^{40}Ca	0.0	0.0

Measurement Conditions:
10 cycles per block
Peak center every 2 blocks
Lens focus every 2 blocks
Amplifier rotation left every block
Baseline at beginning of every measurement day, 120 integrations of 60 s

* Faraday cups are labeled L3 (light side) to H2 (heavy side). C: central cup.

using the $^{42}Ca/^{44}Ca$ ratio measured on Line 2. This multidynamic approach, while more time consuming, allows elimination of drift and non-reproducible behaviors associated with Faraday cup efficiencies, ultimately resulting in higher reproducibility compared to the static acquisition approach (See Supplementary Tables 3.4, 3.5, 3.6, and 3.7). However, this method also introduces a bias when the evaporating sample is undergoing continuous mass fractionation during the time gap between the measurement of $^{42}Ca/^{44}Ca$ at one magnet setting and the next measurement cycle of $^{42}Ca/^{44}Ca$. During this time gap, the mass fractionation correction of $^{40}Ca/^{42}Ca$ using $^{42}Ca/^{44}Ca$ is biased by a factor that depends on the rate (and sign) of change in $^{42}Ca/^{44}Ca$. This bias is also dependent on the time gap between S1 (when $^{42}Ca/^{44}Ca$ is measured) and S2 (when $^{40}Ca/^{44}Ca$ is measured) (see Table 3.3). In the method used here, the midpoints of S1 and S2 are separated by a lag time (τ) of 37 seconds. Thus, we can rewrite equation 3.2 to account for this line switching in multidynamic mode:

$$R_C = R_M^{S2} \times \left(\frac{S_T}{S_M^{S1}} \right) \tag{3.5}$$

If the rate of mass fractionation is fast over the timescale used to switch the magnetic field between the two measurement lines, a systematic bias will be generated between R_C (the value of $^{40}Ca/^{44}Ca$ corrected using the $^{42}Ca/^{44}Ca$ measured at S1) and RT (the "true" $^{40}Ca/^{44}Ca$ ratio corrected using the expected value of $^{42}Ca/^{44}Ca$ at S2). Defining S_M^* as the "true" value of the $^{42}Ca/^{44}Ca$ ratio measured in magnet setting S2, and ϕ as the rate of mass fractionation, we have:

$$S_M^* = S_M^{S1} \times \phi \tag{3.6}$$

Therefore,

$$R_T = R_M^{S2} \times \left(\frac{S_T}{S_M^*} \right)^A = R_M^{S2} \times \left(\frac{S_T}{Z \times S_M^{S1}} \right)^A \tag{3.7}$$

which simplifies to:

$$R_C = R_T \times \phi^A \tag{3.8}$$

ϕ cannot be measured directly but can be approximated by calculating the magnitude of mass fractionation (ϕ^*) between two cycles (N and N+1):

$$\phi^* = \frac{S_M^{N+1}}{S_M^N} \tag{3.9}$$

Using τ as the time gap between the midpoint of acquisitions in magnet setting S1

and S2 (i.e., τ = 37 seconds), we can calculate that the magnitude of mass fractionation between S1 and S2 (ϕ) is equal to:

$$\phi = 1 + \frac{\Delta t}{\tau} \times (\phi^* - 1) \tag{3.10}$$

We can also express the mass fractionation rate in ppm per second as:

$$\phi = \frac{1}{\tau} \times (\phi^* - 1) \times 10^6 \tag{3.11}$$

Figure 3.3 compares the results of R_T and R_C (i.e., ΔR^C) for analyses of the NIST standard. ΔR_C is defined as the relative deviation between the corrected and true value of the $^{40}Ca/^{42}Ca$ ratio in multidynamic mode:

$$\Delta R_C = \left[\frac{R_C}{R_T} - 1\right] \times 10^6 \tag{3.12}$$

R_T is obtained after correction of instrumental mass fractionation using S^* (i.e., the interpolated value of the $^{42}Ca/^{44}Ca$ ratio at magnet setting S2, Eq. 3.12). R_C is obtained after correction of instrumental mass fractionation using S^{S1}. In Figure 3.3, ϕ is plotted against ΔR_C for all the analyses. Results show that this method of interpolation produces no significant difference between the $^{40}Ca/^{44}Ca_{MD}$ ratio and the $^{40}Ca/^{44}Ca_{INT}$ ratio. ΔR_C can reach approximately 15 ppm for a mass fractionation rate of approximately 0.4 ppm/s. Mass fractionation rates for both samples and standards typically range from –0.2 to –0.3 ppm/s, such that the $^{40}Ca/^{44}Ca_{MD}$ calculated using the conventional multidynamic method should be underestimated by 8.5–17 ppm, which is significantly less than the internal reproducibility. Thus, we can see large effects within a run, but averages of each standard analysis produce no significant variation (Figure 3.3). We thus conclude that continuous mass fractionation in the multidynamic scheme does not introduce significant bias on the corrected value of the $^{40}Ca/^{44}Ca$ ratio, given the acquisition parameters used in this study.

3.4.4 Results

Figure 3.4 shows the variations in A) $^{40}Ca/^{44}Ca$ for both static and multidynamic mode (MD), B) $\varepsilon^{40}Ca$ (MD) and C) $^{43}Ca/^{44}Ca$ in static mode (ST) throughout the three year analytical period. Figure 3.4 separates each analytical session and displays the individual reproducibility for each ratio within each session. Figure 3.5 shows a comparison of $^{40}Ca/^{44}Ca$ ratio values from this study (by session) and those from the literature. The repeated measurements of the NIST SRM915a standard over a period of three years (n = 111) yielded an average external precision (in multidynamic mode) of $\pm$ 40 ppm (2 S.D.) with a mean $^{40}Ca/^{44}Ca_{MD}$ value of 47.15072 $\pm$ 0.00118. The mean

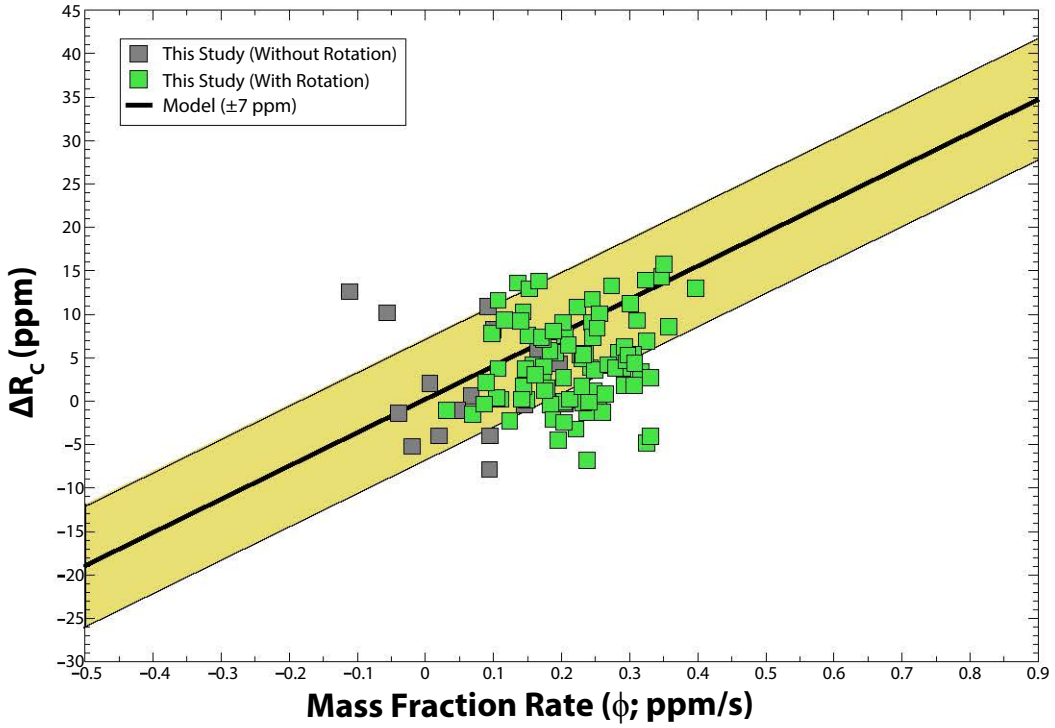

Figure 3.3 – *Relative differences between the $^{40}Ca/^{44}Ca$ ratios corrected using the conventional multi-dynamic routine and those corrected using an interpolated value of the $^{42}Ca/^{44}Ca$ ratio (ΔR_C, see text for definition of notations), plotted against the mass fractionation rate (R). The solid line represents the predicted relationship between R and ΔR_C (Equation 3.12). The magnitude of ΔR_C for all analyses performed in this study averages 4 $\pm$ 10 ppm for a mass fractionation rate of 0.18 $\pm$ 0.17 ppm/s. The magnitude of this correction is therefore negligible compared with the typical internal error of individual measurements (30–50 ppm, 2 S.D.).*

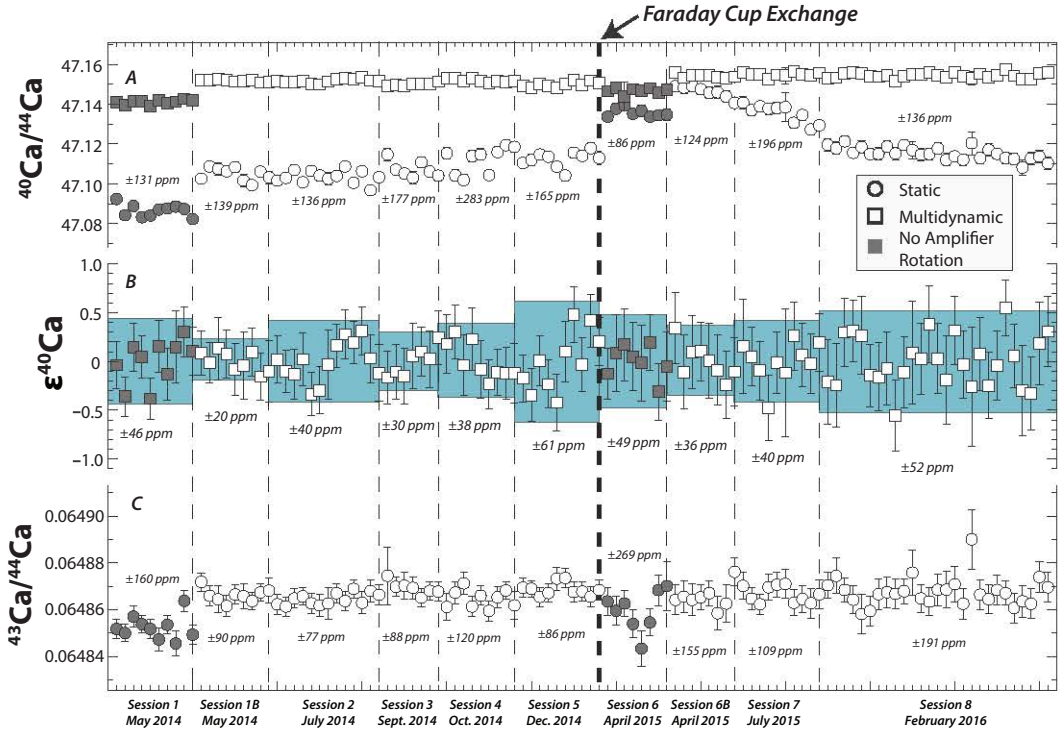

Figure 3.4 – *Calcium isotopic measurements of the NIST standard SRM 915a (N = 111) performed during the 3-year course of this study. Numbers in italics show the external reproducibility (± 2 S.D.) obtained within each analytical session. White and grey symbols represent measurements performed with and without amplifier rotation, respectively. A) $^{40}Ca/^{44}Ca$ ratios corrected for mass fractionation in static mode, B) $\varepsilon^{40}Ca$ in multi-dynamic mode. Here the $^{40}Ca/^{44}Ca$ ratio is expressed using the conventional $\varepsilon^{40}Ca$ notation, $\varepsilon^{40}Ca = \left[\frac{^{40}Ca/^{44}Ca_{STD}}{^{40}Ca/^{44}Ca_{Session}} - 1\right] \times 10^4$, where $(^{40}Ca/^{44}Ca)_{Session}$ represents the average value for all standard measurements performed during a given session of analyses, C) $^{43}Ca/^{44}Ca$ ratios corrected for mass fractionation using the exponential law with $^{42}Ca/^{44}Ca$ = 0.31221 as the normalizing ratio. Data corrected in static mode are shown as circles and those corrected in multi-dynamic mode as squares.*

$^{40}Ca/^{44}Ca_{ST}$ value was 47.11594 ± 0.00704 yielding an average external precision of ± 157 ppm (2 S.D.). The mean value of $^{41}K/^{40}Ca$ was 1.08 x 10^{-4} ± 2.29 x 10^{-3} (2 S.D.). $^{40}Ca/^{44}Ca$ variations are normalized to the average value of the relevant Ca session and expressed using the conventional $\varepsilon^{40}Ca$ notation (see Equation 3.1). Tables 3.4, 3.5, 3.6, and 3.7 in the Supplementary materials give the complete data set for all of the standard analyses discussed here and additional Triton acquisition parameters.

Figure 3.6 displays the $\varepsilon^{40}Ca$ value of each analysis performed in this study as well as standards analysed in Caro et al. (2010) and Naumenko-Dèzes et al. (2015) against its corresponding mass fractionation factor (F; % per a.m.u; calculated as

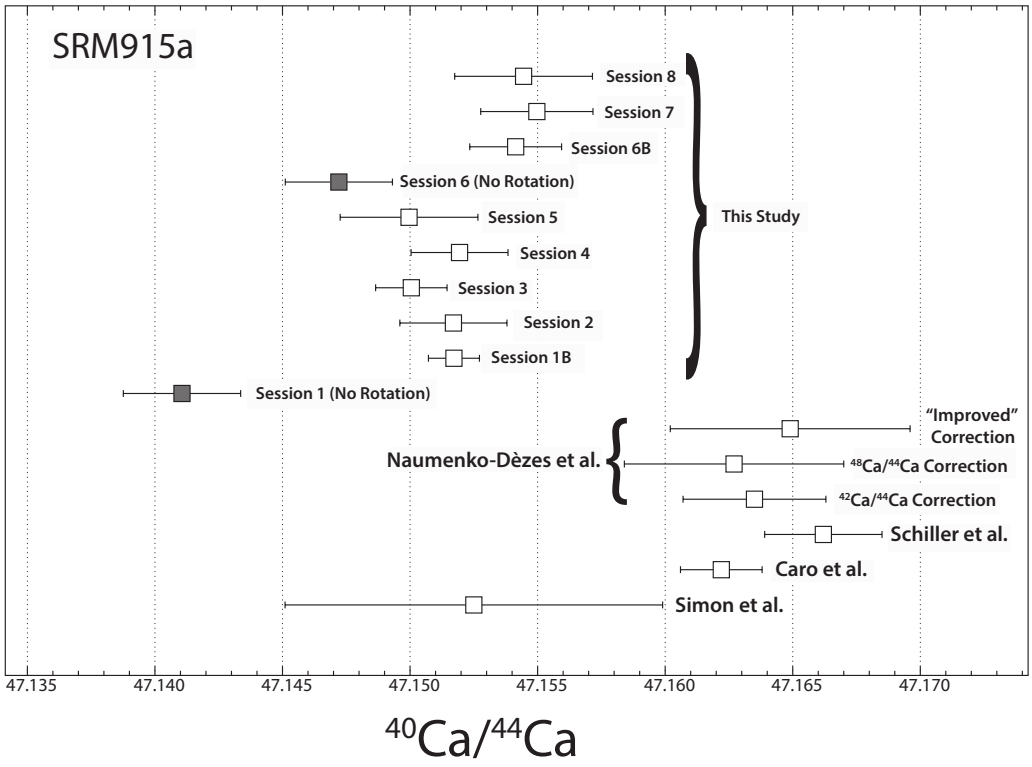

Figure 3.5 – *Comparison of published $^{40}Ca/^{44}Ca$ values for standard NIST SRM 915a (Simon et al., 2009; Caro et al., 2010; Schiller et al., 2012; Naumenko-Dèzes et al., 2015). Unless noted otherwise, all data are corrected for instrumental mass fractionation using the exponential law, with $^{42}Ca/^{44}Ca$ = 0.31221 as the normalizing ratio (Russell et al., 1978).*

$\left[\frac{^{42}Ca/^{44}Ca}{0.31221} - 1\right] \times 10^3$). We can observe, for data presented in Caro et al. (2010) and Naumenko-Dèzes et al. (2015), in Figure 3.6 that lower values of the $^{40}Ca/^{44}Ca$ ratio correspond to highly fractionated, negative values of F with a trend of increasing F values with increasing $^{40}Ca/^{44}Ca$ values. Caro et al. (2010) argued that the most significant deviations from the exponential law can produce biases on the $^{40}Ca/^{44}Ca$ of up to approximately 4 ε-units (and more, in the case of Naumenko-Dèzes et al. (2015)), creating a significant source of error. However, the F factors of the analyses in this study have a mean F value of –0.033 $\pm$ 0.086. The order of magnitude decrease in scatter of the F factor between data presented here and that of Caro et al. (2010) is a consequence of the modified loading technique, which results in the formation of a heavy Ca-Rhenate compound. When this compound breaks down during evaporation as the filament is heated in the TIMS source, the small relative mass difference between its various isotopologues limits the extent of calcium isotope fractionation.

3.4.5 Discussion

3.4.5.1 Faraday Collector Efficiencies

One of the important observations throughout the course of this study is the significant difference between the level of reproducibility between static ($\pm$ 157 ppm, 2 S.D.) and multidynamic mode ($\pm$ 40 ppm, 2 S.D.), which likely reflects non-reproducible behavior of the Faraday cups (i.e.. long-term changes in Faraday cup efficiencies). As noted by Roth et al. (2014), Faraday cups are not 100% efficient and we can review the dynamics of collector efficiencies to illustrate why static and multidynamic modes produce differing levels of precision. A simple equation to define the efficiency (E) of cup (X) is as follows:

$$E_X = \frac{I_M}{I_T} \tag{3.13}$$

where I_M is the measured ion input and I_T is the true ion input.

Ideally, the E of cup X would be 1, i.e., the ion beam that leaves the sample chamber after the entrance slit is the same as is measured by the Faraday cups. However, this is generally not the case, due to several reasons: 1) Surface radiation damage of the cups, due to the ion beam, can result in different, erratic behavior for each cup and 2) the accumulation of surface charge on the cups that can change the response time of the cup as it degrades over time (Wieser and Schwieters, 2005). In static mode, based on Table 3.3, ^{40}Ca is collected in cup L2, ^{42}Ca is collected in the central cup (C) and ^{44}Ca is collected in cup H2. Thus, we can reconstruct equation 3.2 to account for Faraday cup efficiencies:

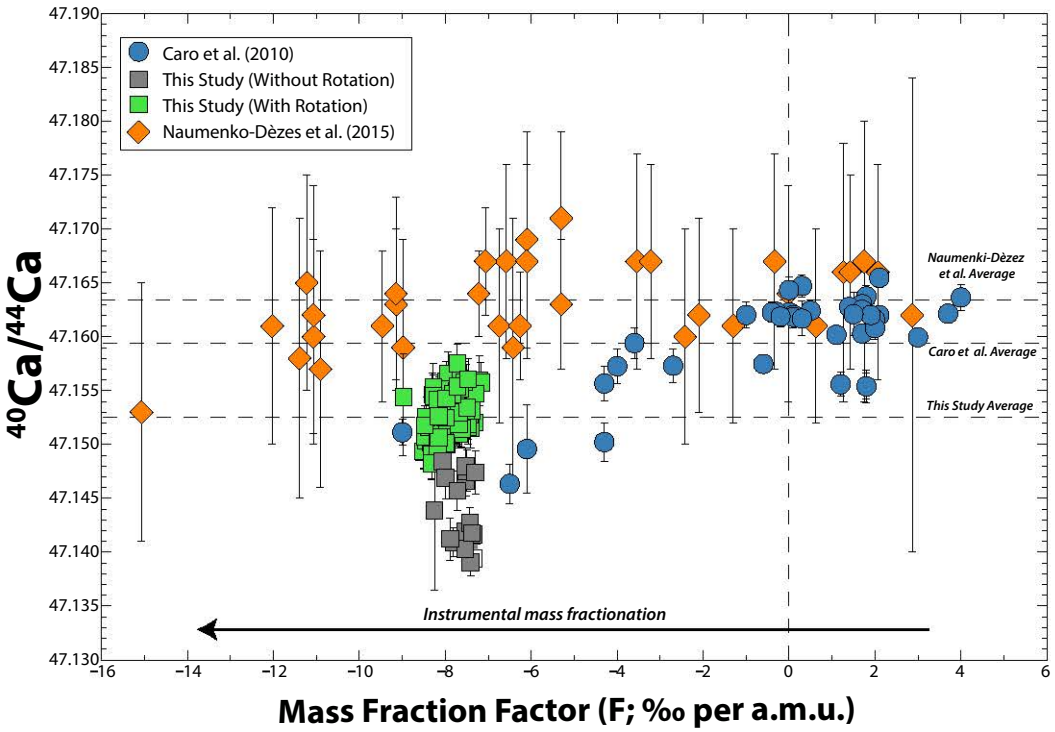

Figure 3.6 – *Multi-dynamic $^{40}Ca/^{44}Ca$ values obtained from repeated analyses of the NIST standard SRM915a (grey and green squares, N = 111) plotted against their respective mass fractionation factor (F). The standard analyses of Caro et al. (2010) (blue circles, N = 30) and Naumenko-Dèzes et al. (2015) (orange diamonds; N = 35) are shown for comparison. The mass fractionation factor is defined as* $F = 0.5 \times \left[\frac{S_M}{S_T} - 1\right] \times 10^3$*, where S_M is the measured $^{42}Ca/^{44}Ca$ ratio and S_T = 0.31221 (Russell et al., 1978). Compared with previous studies, our analyses exhibit a limited range of mass fractionation, which is a consequence of loading calcium in concentrated HNO_3 instead of H_3PO_4 (Caro et al., 2010), HCl (Schiller et al., 2012; Naumenko-Dèzes et al., 2015), or halides (Fletcher et al., 1997b,a). Loading calcium in concentrated HNO_3 induces partial dissolution of the Re filament and subsequent formation of a heavy Ca-Rhenate compound. While this heavy compound breaks down during ionization, the small relative mass difference between its various isotopologues limits the extent of calcium isotope fractionation during the course of evaporation.*

$$R_T = \frac{E_C}{E_{L2}} \times R_M \times \left(\frac{S_T}{\frac{E_{H2}}{E_C} \times S_M} \right)^A \tag{3.14}$$

which simplifies to:

$$R_T = \frac{E_C}{E_{L2}} \times \left(\frac{E_C}{E_{H2}} \right)^A \times R_C \tag{3.15}$$

Assuming that $|\frac{E_C}{E_{L2}}| \approx |\frac{E_C}{E_{H2}}|$, we can rewrite equation 3.10 as:

$$R_T \approx \left(\frac{E_C}{E_{H2}} \right)^{A+1} \times R_C \tag{3.16}$$

Since A $\approx$ 1 (exponential law), the ratio R_C deviates from the ratio RT by a factor that is proportional to the square of the Faraday efficiency ratio. We can thus define the parameter ΔR_D as the relative deviation (in ppm) between the corrected and true value of the $^{40}Ca/^{42}Ca$ ratio in static mode:

$$\Delta R_D = \left[\left(\frac{E_{H2}}{E_C} \right)^{A+1} - 1 \right] \times 10^6 \tag{3.17}$$

where D represents the deviation.

In multidynamic mode, ^{40}Ca is collected in cup C and ^{42}Ca is collected in cup H2 (Magnet setting 1). Afterward, ^{42}Ca is collected in cup C and ^{44}Ca is collected in cup H2 (Magnet setting 2). Thus, a separate equation can be made for multidynamic mode, where A + 1 is replaced by A - 1 from equation 3.16:

$$R_T \approx \left(\frac{E_C}{E_{H2}} \right)^{A-1} \times R_C \tag{3.18}$$

Since A is approximately 1, A - 1 is approximately 0, meaning that $\frac{E_{H2}}{E_C}$ is equal to 1 and thus $R_T \approx R_C$, i.e., there is very little difference between the true $^{40}Ca/^{42}Ca$ ratio and the measured.

During an analysis in static mode, 2 S.D. errors for the $^{40}Ca/^{42}Ca$ ratio are typically between 100 and 200 ppm. If this range in error is entirely caused by variations due to the efficiencies of the Faraday cups, this corresponds to a relative error between 50 and 100 ppm for the ratio $\frac{E_{H2}}{E_C}$. This in turn would translate into a 2–5 ppm error in multidynamic mode, meaning that biases caused by Faraday cup efficiencies are almost entirely negligible in multidynamic mode (see Figure 3.7, which displays the relationship between the Faraday cup efficiencies and relative

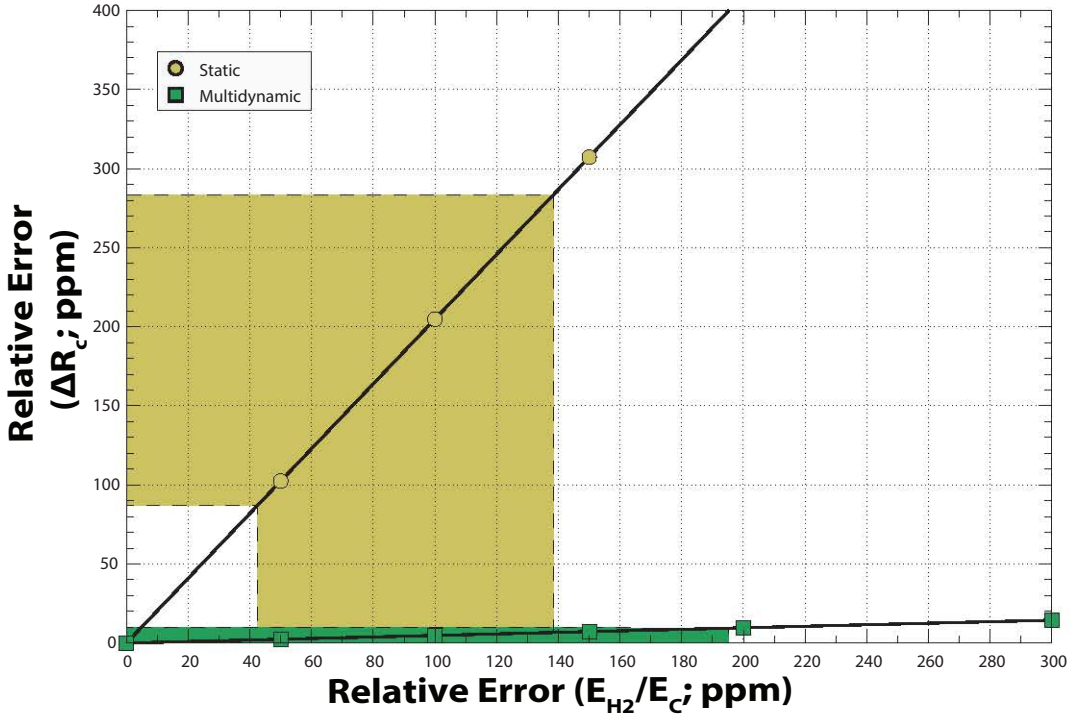

Figure 3.7 – *Relative error on the $^{40}Ca/^{44}Ca$ ratios (ΔR_C, see text for definition of notations) associated with variations of Faraday cup efficiencies $\left(\frac{E_{H2}}{E_C}\right)$ for the static (circles) and multi-dynamic (squares) acquisition schemes. The shaded areas represent the typical error (2 S.D.) for measurements in multi-dynamic (green) and static mode (yellow) within a given analytical session. Note that errors resulting from variations of Faraday cup efficiencies do not entirely cancel out in multi-dynamic mode, but have a reduced effect on the corrected $^{40}Ca/^{44}Ca$ ratio compared to the static acquisition scheme.*

error in static and multidynamic mode). Since the error/efficiency associated with $\frac{E_{H2}}{E_C}$ and $\frac{E_{L2}}{E_C}$ (where $\frac{E_{H2}}{E_C}$ corresponds to multidynamic measurements and $\frac{E_{L2}}{E_C}$ corresponds to static measurements) are treated as independent, we do not account for the possibility that error could originate from a dependent relationship between these two Faraday cup ratios. Furthermore, this calculation shows that in order to exceed the level of internal error of approximately 40 ppm on the $^{40}Ca/^{42}Ca$ ratio estimated in multidynamic mode, the uncertainty associated with $\frac{E_{H2}}{E_C}$ should exceed approximately 2‰, which is not the case in this study (see Figure 3.6). These calculations show that, even though Faraday collector efficiencies do not completely cancel when using the exponential law during dynamic measurements, the relative Faraday collector efficiencies probably cause only a slight deviation during dynamic $^{40}Ca/^{44}Ca$ measurements in the conditions of this study.

3.4.5.2 Non-Exponential Law Behavior

Deviations from the exponential law can occur as a consequence of sample loading on the filament and subsequent heterogeneous evaporation (Hart and Zindler, 1989) or incomplete transmission of Ca ions from the filament to the collectors. Based on early work performed on Mg and Ca isotope systematics, a number of authors suggested the possibility of fractionation of different reservoirs, domains or regions of a sample load on a filament during TIMS analysis (Esat et al., 1986; Papanastassiou and Wasserburg, 1987; Hart and Zindler, 1989). The cracking of the sample as it is dried down from a solution or the uneven or dispersed loading of the solution were thought to be one cause of this phenomenon. Furthermore, during measurement, there is a difference between the surface emissivity of the sample compared to that of the rhenium filament. This difference can produce temperature gradients across the sample, whereas a clean filament or one with the same emissivity as the loaded sample will attain a homogenous temperature distribution (Roth et al., 2014). During analysis, if two or more fractionated regions are simultaneously evaporating, ionizing and contributing to the ion beam, the resulting measurements will be an isotopic mixture that does not lie on the exponential curve, but rather off to its concave side (see Fig. 4 of Hart and Zindler (1989)). However, the respective isotopic compositions of each of the regions will fall along a mass fractionation curve going through the true ratios (Roth et al., 2014). A number of publications have also observed an end-run trend in fractionation that was not corrected by the exponential law (Caro et al., 2010; Kunchithapadam et al., 2007; Lehn and Jacobson, 2015). Other factors, not well understood, include Rayleigh distillation of the evaporating sample/standard and optical anomalies (when ions are transmitted in non-axial directions and then are deflected back to the axis) (Naumenko-Dèzes et al., 2015).

In this section, we construct a series of equation to define a parameter, δ, that describes if and by how much mass fractionation deviates from the exponential law. Using the generalized power law (Equation 3.27), we define δ as a deviation from the exponential law as follows:

$$\delta = \frac{M_{40}^{n+\varepsilon} - M_{42}^{n+\varepsilon}}{M_{42}^{n+\varepsilon} - M_{44}^{n+\varepsilon}} - \frac{M_{40}^{n} - M_{42}^{n}}{M_{42}^{n} - M_{44}^{n}} \tag{3.19}$$

We consider a third isotopic ratio, $^{43}Ca/^{44}Ca$ (noted X), and apply the generalized power law to construct the following equations:

$$\frac{R_M}{R_C} = \left(\frac{S_M}{S_T}\right)^A, \quad \frac{X_M}{X_C} = \left(\frac{S_M}{S_T}\right)^{A'} \tag{3.20}$$

where, as in equation 3.2, R is the $^{40}Ca/^{42}Ca$ ratio and S is the $^{42}Ca/^{44}Ca$ ratio. M represents a measured ratio, C represents a corrected ratio, and T represents the true ratio. Assuming that the mass dependent factor (A) of the mass fractionation law deviates from that of the exponential law, we can rewrite equation 3.20 as follows:

$$\frac{R_M}{R_T} = \left(\frac{S_M}{S_T}\right)^{A+\delta}, \quad \frac{X_M}{X_T} = \left(\frac{S_M}{S_T}\right)^{A'+\delta'} \tag{3.21}$$

In this case, we can note that $R_T \neq R_C$. Instead, we can write:

$$\ln\frac{R_M}{R_T} = A \times \ln\left(\frac{S_M}{S_T}\right) + \delta \times \ln\frac{S_M}{S_T} = \ln\frac{R_M}{R_C} + \delta \times \ln\left(\frac{S_M}{S_T}\right), \quad \ln\frac{X_M}{X_T} = \ln\frac{X_M}{X_C} + \delta \times \ln\left(\frac{X_M}{X_T}\right) \tag{3.22}$$

From which follows equation 3.23:

$$\ln\left(\frac{R_C}{R_T}\right) = \delta \times \ln\left(\frac{S_M}{S_T}\right), \quad \ln\left(\frac{X_C}{X_T}\right) = \delta' \times \ln\left(\frac{S_M}{S_T}\right) \tag{3.23}$$

This ultimately leads to:

$$\ln\left(\frac{R_C}{R_T}\right) = \frac{\delta}{\delta'} \times \ln\left(\frac{X_C}{X_T}\right) \tag{3.24}$$

Equation 3.24 shows that if mass fractionation deviates from the exponential law, data will define a straight line with a slope of $\frac{\delta}{\delta'}$ in a plot of the natural log of $\frac{R_C}{R_T}$ versus the natural log of $\frac{X_C}{X_T}$. This parameter can be expressed as a function of isotope masses only, using the second order expansion of the general mass fractionation law (i.e., equation 3.20):

$$\frac{\delta}{\delta'} = \frac{\ln\frac{40}{44}\left(\frac{n}{2} - \frac{n+\varepsilon}{2}\right)\left(\ln(40\times44) - \ln(42\times44)\right)}{\ln\frac{43}{44}\left(\frac{n}{2} - \frac{n+\varepsilon}{2}\right)\left(\ln(43\times44) - \ln(42\times44)\right)} = \frac{\ln\frac{40}{44}\times\ln\frac{42}{40}}{\ln\frac{43}{44}\times\ln\frac{42}{43}} \tag{3.25}$$

As shown by Eq 3.25, $\frac{\delta}{\delta'}$ is solely a function of the masses of ^{40}Ca, ^{42}Ca, ^{43}Ca, and ^{44}Ca and, therefore, is independent of the extent to which instrumental mass discrimination deviates from the exponential law. Thus, as shown in Figure 3.8, based on this relationship, we can predict the slope defined by the corrected ratios in a $^{40}Ca/^{42}Ca$ versus $^{43}Ca/^{42}Ca$ plot if fractionation deviates from the exponential law.

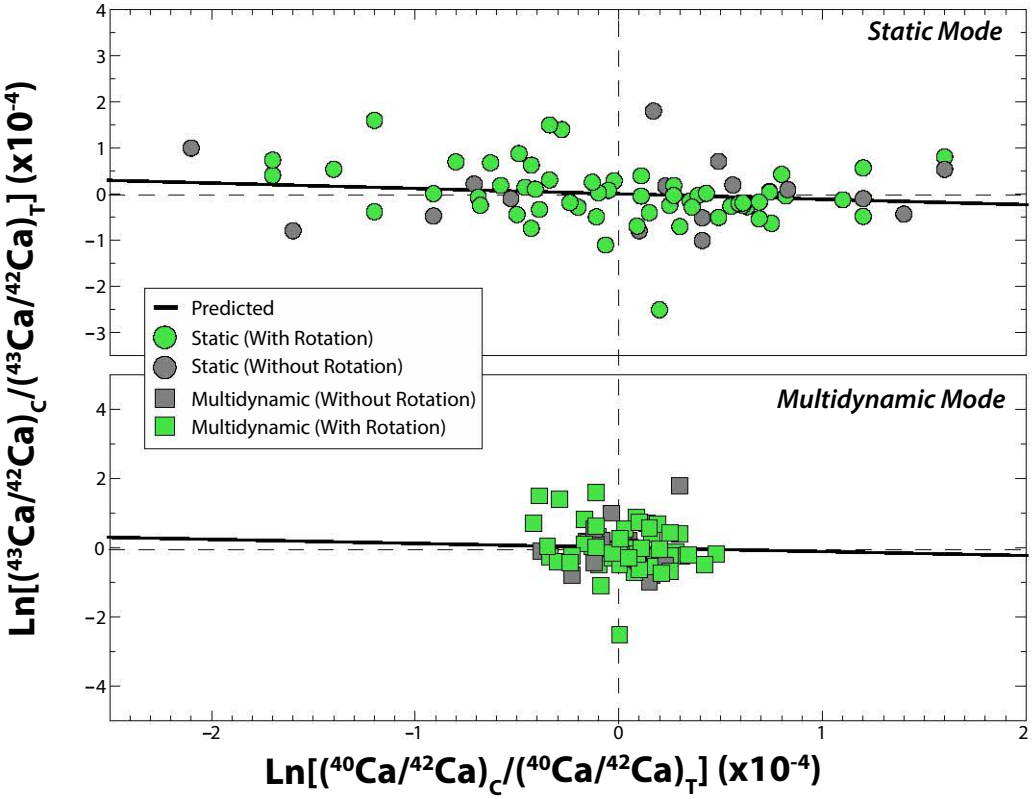

Figure 3.8 – *Natural log of* $\frac{^{43}Ca/^{42}Ca_C}{^{43}Ca/^{42}Ca_T}$ *plotted against the natural log of* $\frac{^{40}Ca/^{42}Ca_C}{^{40}Ca/^{42}Ca_T}$ *for the data produced in this study.* $^{i}Ca/^{42}Ca_C$ *is the ratio corrected from mass fractionation for each individual measurement, while* $^{i}Ca/^{42}Ca_T$ *represents the average value for a given analytical session. The solid black line represents the predicted relationship between normalized* $^{40}Ca/^{42}Ca_C$ *and* $^{43}Ca/^{42}Ca_C$ *ratios, which would result from any deviation from the ideal (exponential) fractionation law (Equation 3.25). Data for this study show no detectable correlation between* $^{40}Ca/^{42}Ca_C$ *and* $^{43}Ca/^{42}Ca_C$ *that would suggest the existence of non-exponential behavior and/or a mixing effect.*

Figure 3.8 shows no correlation between the natural log of $\frac{R_C}{R_T}$ and the natural log of $\frac{X_C}{X_T}$ (i.e., no detectable deviations from the exponential law due to mixing processes or other artefacts), indicating that any biases are smaller than typical analytical errors, which is a consequence of the improved loading techniques.

As we can observe in Figure 3.8, our data do not define a significant correlation in a $\ln(^{40}Ca/^{42}Ca)$ versus $\ln(^{43}Ca/^{42}Ca)$ plot therefore showing no evidence that instrumental mass fractionation deviates from the exponential law. In fact, the fractionation law chosen to correct Ca isotopic ratios is of secondary importance given the relatively narrow mass fractionation range observed during the course of our analyses. Figures 3.9 displays $^{40}Ca/^{44}Ca$ data corrected using the linear and power

laws along with the results from Figure 3.8 for the exponential law. The power law is given by:

$$\frac{R_M}{R_C} = \left(\frac{S_M}{S_T}\right)^A \tag{3.26}$$

where

$$A = \frac{40^n - 42^n}{42^n - 44^n} \tag{3.27}$$

giving a value of A as 1.99958 for the $^{40}Ca/^{44}Ca$ ratio and 0.49914 for the $^{43}Ca/^{44}Ca$ ratio. The linear law is given by:

$$\frac{R_M}{R_C} = (1-A) + A \times \frac{S_M}{S_T} \tag{3.28}$$

where A is the same as in the power law (equation 3.27).

In Figure 3.9, we observe that it does not matter which fractionation correction law is used, we obtain identical results for the exponential power, linear, and Rayleigh laws. In other words, given the narrow range of mass fractionation observed during analyses, any common mass discrimination laws can be used without significantly affecting the reproducibility of the results.

3.4.6 Implications and Conclusions

Using methods and techniques that have been developed in this contribution on the high precision TIMS measurements of NIST SRM 915a standard we show that: 1) A level of reproducibility in standard measurements is attained that, compared to previous ^{40}Ca analytical attempts, allows for the precise determination of small radiogenic ^{40}Ca effects in terrestrial and extraterrestrial materials, 2) An improved technique for filament sample loading can largely suppress the effects of filament reservoir mixing, and eliminate large mass fractionation effects over the course of an individual analysis, problems that have been encountered in previous studies. Our results show that the $^{40}Ca/^{44}Ca$ ratio can be determined with a reproducibility of $\pm$ 40 ppm (2 S.D.) using the Thermo Triton, which represents a significant improvement compared with the former generation of instruments and with previous results.

The ability to use dynamic acquisition schemes and amplifier rotation during TIMS measurements enables the user to automatically and simply correct for efficiency differences between the collectors. Reducing the time interval of the measurement of $^{42}Ca/^{44}Ca$ in one cycle and the measurement of $^{42}Ca/^{44}Ca$ in the next cycle is important when considering rates of mass fractionation during this time gap. Minimizing rates of mass fractionation and differences of rates of mass fractionation

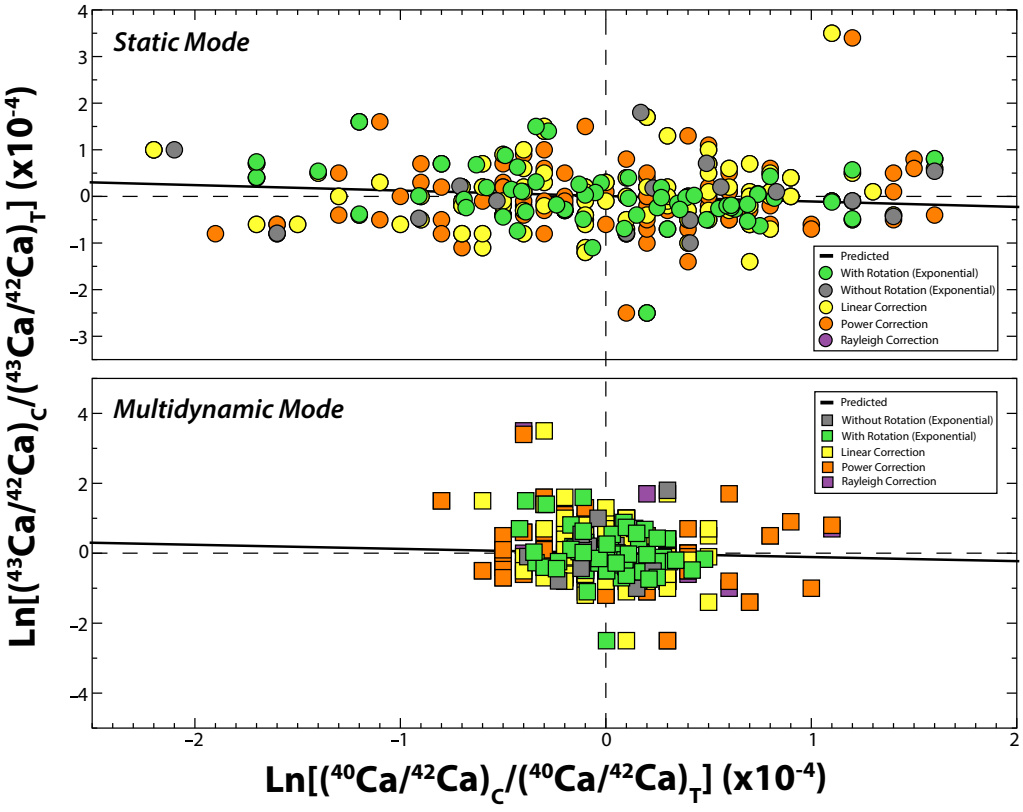

Figure 3.9 – *Natural log of* $\frac{^{43}Ca/^{42}Ca_C}{^{43}Ca/^{42}Ca_T}$ *plotted against the natural log of* $\frac{^{40}Ca/^{42}Ca_C}{^{40}Ca/^{42}Ca_T}$ *for the data produced in this study.* $^{i}Ca/^{42}Ca_c$ *is the ratio corrected for mass fractionation for each individual measurement, while* $^{i}Ca/^{42}Ca_T$ *represents the average value for a given analytical session. The solid black line represents the predicted relationship between normalized* $^{40}Ca/^{42}Ca_C$ *and* $^{43}Ca/^{42}Ca_C$ *ratios, which would result from any deviation from the ideal (exponential) fractionation law (Equation 3.25). Data for this study show no detectable correlation between* $^{40}Ca/^{42}Ca_C$ *and* $^{43}Ca/^{42}Ca_C$ *that would suggest the existence of non-exponential behavior and/or mixing effect. Circles represent data analyzed in static mode and squares represent data analyzed in multi-dynamic mode corrected by the exponential law. Grey represents data acquired without amplifier rotation and green represents data acquired with amplifier rotation. Yellow circles and squares represent measurements corrected by the linear law, the power law by red circles and squares, and purple circles and squares for the Rayleigh law. Fractionation corrections made using the different mass fractionation laws do not show any significant deviations from each other.*

between standards and samples can, in part, be accomplished by carefully controlling the filament loading process (e.g., amount and purity of Ca and consistency of loading method).

3.5 Supplementary Materials

Table 3.4 – *Results for NIST standard SRM915a. Measurements were performed between 2014 and 2016 on the TIMS Triton+ at CRPG (Centre de Recherches Pétrographiques et Géochimiques) Nancy, France. On Line 1 (Static Mode), ^{40}Ca, ^{42}Ca, ^{43}Ca, and ^{44}Ca were measured in Faraday cups L2, C, H1 and H2, respectively. On Line 2 (Multidynamic Mode) ^{40}Ca, ^{41}K, and ^{42}Ca were measured in Faraday cups c, H1 and H2, respectively. There was an idle time of 15 s and 7 s between each line and each line contained 30 integrations of 1.049 s each for a total 31.47 s per line. A measurement consisted of 12 blocks with 10 cycles per block. A peak center and lens focus were completed every 2 blocks. A baseline was done at the beginning of each with a total of 120 integrations at 60 s each. A gain was done each time that a new sample turret was placed in the TIMS.*

	# Cycles	^{40}Ca	^{42}Ca	Line 1: Static Mode						Line 2: Multidynamic Mode			
				$^{40}Ca/^{44}Ca$	±	$^{42}Ca/^{44}Ca$	$^{43}Ca/^{44}Ca$	±	$^{40}Ca/^{42}Ca$ (raw)	$^{40}Ca/^{40}Ca$	$^{40}Ca/^{42}Ca$ (raw)	$^{40}Ca/^{42}Ca$ (MD corr.)	$^{41}K/^{40}Ca$
Session 1 May 2014													
2014_05_08_Ca-STD1	120	0.10	15.26	47.09234	0.00199	0.30977	0.064852	0.0000039	149.60087	1.01244	149.75521	150.99109	0.000150
2014_05_09_Ca-STD2	120	0.10	14.85	47.08427	0.00175	0.30992	0.064850	0.0000037	149.64996	1.01599	149.82518	150.98619	0.000012
2014_05_09_Ca-STD3	120	0.09	14.30	47.08886	0.00187	0.30990	0.064857	0.0000045	149.65568	1.01294	149.82316	150.99311	0.000089
2014_05_10_Ca-STD4	120	0.11	16.28	47.08320	0.00180	0.30992	0.064854	0.0000037	149.64537	1.01448	149.83112	150.99338	0.000026
2014_05_10_Ca-STD5	120	0.10	14.61	47.08409	0.00187	0.30990	0.064852	0.0000040	149.63823	1.01236	149.81299	150.98516	0.000416
2014_05_11_Ca-STD6	80	0.10	15.62	47.08703	0.00212	0.30986	0.064847	0.0000049	149.62726	1.01410	149.80162	150.99421	0.000051
2014_05_11_Ca-STD7	110	0.10	14.50	47.08766	0.00201	0.30986	0.064854	0.0000040	149.62909	1.01728	149.79643	150.98915	0.000079
2014_05_12_Ca-STD8	60	0.10	15.11	47.08850	0.00253	0.30975	0.064846	0.0000053	149.57546	1.01612	149.74294	150.99205	0.000229
2014_05_12_Ca-STD9	70	0.10	15.84	47.08737	0.00229	0.30989	0.064864	0.0000044	149.64434	1.01418	149.82026	150.99683	0.000055
2014_05_15_Ca-STD12	90	0.10	15.05	47.08229	0.00215	0.30990	0.064849	0.0000043	149.63599	0.99992	149.82508	150.99382	0.000071
Session 2 May 2014													
2014_05_16_Ca-STD16	120	0.11	16.52	47.10256	0.00205	0.30990	0.06487	0.0000039	149.69792	1.01135	149.85533	151.02684	0.00008
2014_05_16_Ca-STD17	120	0.11	0.00	47.10871	0.00236	0.30987	0.06487	0.0000043	149.70407	1.01623	149.84150	151.02641	0.00003
2014_05_17_Ca-STD18	80	0.10	0.00	47.10746	0.00297	0.30986	0.06486	0.0000056	149.69579	1.01054	149.83889	151.02813	0.00004
2014_05_18_Ca-STD19	120	0.11	0.00	47.10626	0.00222	0.30992	0.06486	0.0000046	149.72124	1.01730	149.86675	151.02669	0.00002
2014_05_21_Ca-STD20	80	0.09	0.00	47.10836	0.00272	0.30976	0.06487	0.0000041	149.64570	1.01533	149.78229	151.02448	0.00046
2014_05_21_Ca-STD21	70	0.09	13.93	47.10164	0.00292	0.30990	0.06487	0.0000054	149.69286	1.01086	149.85146	151.02509	0.00008
2014_05_22_Ca-STD23	120	0.10	15.16	47.09938	0.00224	0.30975	0.06486	0.0000039	149.61430	1.01046	149.78133	151.02642	0.00041
2014_05_23_Ca-STD24	120	0.10	14.95	47.10615	0.00234	0.30975	0.06487	0.0000038	149.63581	1.01405	149.77798	151.02305	0.00014
2014_05_24_Ca-STD25	90	0.10	14.83	47.10328	0.00317	0.30976	0.06487	0.0000053	149.62795	1.01169	149.78011	151.02392	0.00029
Session 3 July 2014													
2014_07_04_Ca-std-8	110	0.10	15.70	47.10161	0.00224	0.30987	0.06486	0.0000042	149.67891	1.01428	149.83843	151.02594	0.00003
2014_07_04_Ca-std-9	120	0.10	15.72	47.10296	0.00210	0.30980	0.06486	0.0000040	149.64913	1.01483	149.80192	151.02351	0.00002
2014_07_05_Ca-std-10	120	0.09	14.33	47.10694	0.00259	0.30982	0.06486	0.0000041	149.67003	1.01222	149.81013	151.02346	0.00002
2014_07_06_Ca-std-11	120	0.11	16.34	47.10075	0.00246	0.30988	0.06487	0.0000036	149.68194	1.01342	149.84348	151.02523	0.00004
2014_07_08_Ca-std-14	120	0.10	14.59	47.10642	0.00279	0.30972	0.06486	0.0000043	149.62111	1.01505	149.75962	151.02025	0.00014

Table 3.4 continued from previous page

	# Cycles	^{40}Ca	^{42}Ca	Line 1: Static Mode						Line 2: Multidynamic Mode				
				$^{40}Ca/^{44}Ca$	±	$^{42}Ca/^{44}Ca$	$^{43}Ca/^{44}Ca$	±	$^{40}Ca/^{42}Ca$ (raw)	$^{40}Ca/^{40}Ca$	$^{40}Ca/^{42}Ca$ (raw)	$^{40}Ca/^{42}Ca$ (MD corr.)	$^{41}K/^{40}Ca$
2014_07_11_Ca-std-16	80	0.11	16.40	47.10416	0.00267	0.30966	0.06486	0.0000046	149.58263	1.01434	149.72811	151.02006	0.00112
2014_07_11_Ca-std-17	60	0.09	13.99	47.10253	0.00329	0.30971	0.06486	0.0000066	149.60135	1.01452	149.75637	151.02442	0.00016
2014_07_11_Ca-std-18	120	0.10	15.86	47.10397	0.00226	0.30985	0.06487	0.0000040	149.67642	1.01258	149.83138	151.02891	0.00003
2014_07_12_Ca-std-19	120	0.10	14.67	47.10870	0.00225	0.30982	0.06486	0.0000041	149.67812	1.01315	149.81876	151.02964	0.00008
2014_07_12_Ca-std-20	120	0.11	17.38	47.10052	0.00213	0.30989	0.06487	0.0000039	149.68445	1.01419	149.85044	151.02894	0.00003
2014_07_13_Ca-std-21	120	0.10	14.58	47.10634	0.00244	0.30990	0.06486	0.0000048	149.71130	1.01265	149.86082	151.03101	0.00001
2014_07_15_Ca-std-23	120	0.10	15.81	47.09675	0.00231	0.30987	0.06487	0.0000047	149.66630	1.01418	149.84155	151.02623	0.00004
2014_07_15_Ca-std-24	120	0.10	15.06	47.10335	0.00245	0.30980	0.06487	0.0000042	149.65010	1.01522	149.80323	151.02512	0.00002
Session 4 September 2014													
2014_09_25_Ca-std-1	120	0.10	15.70	47.11478	0.00304	0.30956	0.06487	0.0000124	149.56423	1.01377	149.67390	151.01799	0.00143
2014_09_26_Ca-std-3	120	0.10	15.71	47.10707	0.00252	0.30965	0.06487	0.0000042	149.58766	1.01327	149.72292	151.01907	0.00059
2014_09_26_Ca-std-4	120	0.09	13.84	47.10516	0.00229	0.30955	0.06487	0.0000057	149.53184	1.01741	149.67218	151.01814	0.00239
2014_09_26_Ca-std-5	120	0.10	14.74	47.10303	0.00301	0.30958	0.06487	0.0000048	149.53581	1.00339	149.68602	151.02124	0.00192
2014_09_28_Ca-std-7	120	0.10	15.50	47.11083	0.00245	0.30961	0.06487	0.0000040	149.57741	1.01768	149.70232	151.02070	0.00109
2014_09_30_Ca-std-10	120	0.10	15.35	47.10616	0.00249	0.30964	0.06487	0.0000039	149.57583	1.02306	149.71548	151.02060	0.00012
2014_10_02_Ca-std-12	110	0.10	14.90	47.10412	0.00260	0.30962	0.06487	0.0000042	149.55952	1.02178	149.70946	151.02445	0.00016
Session 5 October 2014													
2014_10_03_Ca-std-14	110	0.11	17.09	47.11531	0.00284	0.30990	0.06486	0.0000056	149.73977	1.01252	149.86009	151.03031	0.00001
2014_10_04_Ca-std-15	110	0.10	15.29	47.10425	0.00277	0.30973	0.06487	0.0000048	149.61736	1.01451	149.77276	151.03029	0.00008
2014_10_04_Ca-std-17	110	0.10	15.56	47.10195	0.00266	0.30969	0.06487	0.0000047	149.59159	1.01452	149.74914	151.02514	0.00006
2014_10_05_Ca-std-18	110	0.10	15.47	47.11399	0.00292	0.30986	0.06486	0.0000043	149.71534	1.01545	149.83963	151.03008	0.00002
2014_10_05_Ca-std-19	110	0.11	15.97	47.11471	0.00293	0.30969	0.06487	0.0000041	149.62930	1.01576	149.74600	151.02481	0.00036
2014_10_06_Ca-std-21	120	0.10	15.67	47.10441	0.00228	0.30957	0.06486	0.0000043	149.53689	1.01666	149.68380	151.02234	0.00008
2014_10_10_Ca-std-22	120	0.10	15.42	47.11596	0.00267	0.30959	0.06487	0.0000045	149.58597	1.01536	149.69912	151.02528	0.00044
2014_10_12_Ca-std-23	110	0.09	14.12	47.11942	0.00279	0.30966	0.06487	0.0000038	149.63037	1.01517	149.73158	151.02428	0.00029
2014_10_12_Ca-std-24	120	0.09	13.61	47.11860	0.00266	0.30983	0.06486	0.0000060	149.71506	1.01160	149.81951	151.02484	0.00247
Session 6 December 2014													
2014_12_05_Ca-std-7	120	0.10	15.40	47.11049	0.00243	0.30966	0.06487	0.0000041	149.60213	1.01551	149.72520	151.01773	0.00015
2014_12_05_Ca-std-8	120	0.11	16.73	47.11194	0.00277	0.30961	0.06487	0.0000036	149.58269	1.01718	149.69829	151.01486	0.00008
2014_12_06_Ca-std-9	120	0.11	16.17	47.11474	0.00278	0.30965	0.06487	0.0000041	149.61244	1.01666	149.72444	151.02017	0.00022
2014_12_06_Ca-std-10	120	0.10	15.30	47.11361	0.00233	0.30961	0.06487	0.0000040	149.58760	1.01556	149.70023	151.01721	0.00055
2014_12_06_Ca-std-11	120	0.11	16.21	47.10864	0.00235	0.30961	0.06487	0.0000049	149.57199	1.01580	149.69778	151.01456	0.00020
2014_12_06_Ca-std-12	120	0.10	15.60	47.10418	0.00257	0.30971	0.06487	0.0000041	149.60899	1.03713	149.75483	151.02046	0.00004
2014_12_07_Ca-std-13	120	0.11	15.96	47.11566	0.00276	0.30973	0.06487	0.0000044	149.65155	1.01528	149.76774	151.02733	0.00010
2014_12_07_Ca-std-14	120	0.10	15.68	47.11406	0.00254	0.30966	0.06487	0.0000042	149.61087	1.01399	149.72436	151.01952	0.00003
2014_12_08_Ca-std-15	120	0.09	13.75	47.11789	0.00260	0.30981	0.06487	0.0000043	149.70255	1.01269	149.81047	151.02608	0.00003
2014_12_09_Ca-std-16	120	0.11	16.50	47.11294	0.00245	0.30967	0.06487	0.0000042	149.61313	1.01412	149.73296	151.02232	0.00005

Table 3.4 continued from previous page

	# Cycles	^{40}Ca	^{42}Ca	Line 1: Static Mode					Line 2: Multidynamic Mode				
				$^{40}Ca/^{44}Ca$	±	$^{42}Ca/^{44}Ca$	$^{43}Ca/^{44}Ca$	±	$^{40}Ca/^{42}Ca$ (raw)	$^{40}Ca/^{40}Ca$	$^{40}Ca/^{42}Ca$ (raw)	$^{40}Ca/^{42}Ca$ (MD corr.)	$^{41}K/^{40}Ca$
Session 7 April 2015 Faraday Cup Change (No Rotation)													
2015_04_15_Ca-STD5	120	0.07	10.90	47.13374	0.00220	0.30986	0.06486	0.0000060	149.77785	1.01516	149.81869	151.00923	0.00013
2015_04_16_Ca-STD7	120	0.07	10.49	47.13762	0.00256	0.30969	0.06486	0.0000062	149.70308	1.01433	149.73609	151.01381	0.00053
2015_04_16_Ca-STD8	120	0.07	10.55	47.13957	0.00247	0.30963	0.06486	0.0000058	149.68091	1.01765	149.70813	151.01419	0.00036
2015_04_17_Ca-STD9b	120	0.07	10.46	47.13620	0.00245	0.30987	0.06485	0.0000060	149.78855	1.01488	149.82737	151.01506	0.00007
2015_04_17_Ca-STD10	120	0.06	9.39	47.13671	0.00271	0.30972	0.06484	0.0000078	149.71341	1.01770	149.74584	151.01030	0.00085
2015_04_18_Ca-STD11	120	0.07	11.03	47.13373	0.00248	0.30986	0.06485	0.0000058	149.77655	1.00376	149.82175	151.01359	0.00008
2015_04_20_Ca-STD13	120	0.08	11.60	47.13445	0.00207	0.30980	0.06487	0.0000067	149.74966	1.01744	149.78543	151.00639	0.00105
2015_04_21_Ca-STD14	120	0.06	9.51	47.13417	0.00293	0.30993	0.06487	0.0000104	149.81362	1.01282	149.85100	151.00711	0.00004
Session 8 April 2015 (Ampli. Rotation Left)													
2015_04_24_Ca-STD19	120	0.07	10.41	47.149088	0.002721	0.309718	0.064864	0.0000064	149.75399	1.01290	149.77538	151.03880	0.00014
015_04_28_Ca-STD22	120	0.07	10.18	47.148365	0.003060	0.309726	0.064866	0.0000068	149.75578	1.01528	149.77145	151.03070	0.00026
2015_04_28_Ca-STD24	120	0.06	9.54	47.149179	0.002997	0.309619	0.064864	0.0000068	149.70393	1.01654	149.72120	151.03494	0.00029
2015_04_29_Ca-STD25b	120	0.07	11.17	47.147586	0.002559	0.309668	0.064865	0.0000054	149.72388	1.01349	149.74588	151.03461	0.00036
2015_04_30_Ca-STD26	120	0.07	11.11	47.145693	0.002859	0.309743	0.064867	0.0000054	149.75550	1.01221	149.78344	151.03453	0.00014
2015_05_01_Ca-STD27	120	0.07	11.21	47.146008	0.003028	0.309677	0.064859	0.0000072	149.72308	1.01549	149.74750	151.03199	0.00005
2015_05_02_Ca-STD28	120	0.07	10.27	47.143950	0.003032	0.309669	0.064863	0.0000081	149.71245	1.01827	149.74097	151.02953	0.00011
2015_05_03_Ca-STD29	120	0.08	11.61	47.140651	0.002486	0.309768	0.064876	0.0000060	149.75225	1.01233	149.79388	151.03217	0.00010
Session 9 July 2015													
2015_07_02_Ca-STD2	120	0.08	12.48	47.14076	0.00312	0.30996	0.06487	0.0000057	149.84937	1.01103	149.89757	151.03913	0.00002
2015_07_02_Ca-STD3	120	0.10	14.48	47.13703	0.00259	0.30974	0.06486	0.0000048	149.72455	1.01306	149.78217	151.03671	0.00004
2015_07_02_Ca-STD4	120	0.10	14.64	47.13896	0.00234	0.30990	0.06486	0.0000043	149.81322	1.01358	149.86405	151.03600	0.00001
2015_07_03_Ca-STD5	120	0.08	12.48	47.13778	0.00282	0.30958	0.06487	0.0000056	149.64609	1.01356	149.69289	151.02821	0.00015
2015_07_06_Ca-STD7	120	0.08	12.20	47.13813	0.00282	0.30991	0.06487	0.0000055	149.81413	1.02332	149.86687	151.03526	0.00002
2015_07_11_Ca-STD10	120	0.07	11.25	47.13854	0.00732	0.30941	0.06487	0.0000061	149.56402	1.02551	149.61431	151.03422	0.00170
2015_07_12_Ca-STD12	120	0.09	13.06	47.13067	0.00265	0.30973	0.06486	0.0000056	149.70206	1.00699	149.78420	151.04106	0.00018
2015_07_13_Ca-STD13	120	0.08	12.09	47.13457	0.00259	0.30975	0.06486	0.0000057	149.72363	1.02028	149.78892	151.03656	0.00002
2015_07_14_Ca-STD14	120	0.08	11.83	47.12731	0.00273	0.30984	0.06486	0.0000064	149.74595	1.01110	149.83261	151.03480	0.00005
2015_07_15_Ca-STD15	120	0.08	12.09	47.12941	0.00264	0.30997	0.06487	0.0000061	149.81974	1.01216	149.90349	151.03858	0.00001
Session 10 February/March 2016													
2016_02_01_CaSTD2	120	0.07	10.76	47.11963	0.00314	0.30974	0.06487	0.0000057	149.67372	1.01653	149.77965	151.02967	0.00004
2016_02_01_CaSTD5	120	0.07	10.51	47.11784	0.00314	0.30974	0.06487	0.0000076	149.66754	1.01522	149.78014	151.03069	0.00005
2016_02_02_CaSTD7	120	0.08	12.07	47.12136	0.00251	0.30986	0.06487	0.0000051	149.73994	1.01767	149.84879	151.03811	0.00000
2016_02_04_CaSTD14	120	0.08	12.61	47.11557	0.00267	0.30983	0.06486	0.0000058	149.70662	1.01506	149.83469	151.03898	0.00031
2016_02_04_CaSTD15	120	0.07	10.65	47.11844	0.00307	0.30962	0.06486	0.0000082	149.60926	1.01515	149.72642	151.03725	0.00020
2016_02_05_CaSTD17	120	0.08	11.49	47.11494	0.00268	0.30973	0.06486	0.0000063	149.64962	1.01443	149.77353	151.03281	0.00023
2016_02_05_CaSTD18	120	0.08	11.61	47.11509	0.00307	0.30966	0.06487	0.0000066	149.61839	1.01501	149.74120	151.03219	0.00050
2016_02_05_CaSTD19	120	0.08	11.73	47.11865	0.00285	0.30962	0.06487	0.0000065	149.61002	1.01445	149.72375	151.03445	0.00011

Table 3.4 continued from previous page

	# Cycles	^{40}Ca	^{42}Ca	Line 1: Static Mode						Line 2: Multidynamic Mode			
				$^{40}Ca/^{44}Ca$	±	$^{42}Ca/^{44}Ca$	$^{43}Ca/^{44}Ca$	±	$^{40}Ca/^{42}Ca$ (raw)	$^{40}Ca/^{40}Ca$	$^{40}Ca/^{42}Ca$ (raw)	$^{40}Ca/^{42}Ca$ (MD corr.)	$^{41}K/^{40}Ca$
2016_02_07_CaSTD21	120	0.08	11.89	47.11526	0.00303	0.30956	0.06487	0.0000063	149.56734	1.01522	149.68326	151.02582	0.00011
2016_02_08_Ca_STD22	120	0.08	11.74	47.11946	0.00276	0.30976	0.06487	0.0000052	149.68032	1.01477	149.79035	151.03328	0.00003
2016_02_09_Ca_STD23	80	0.07	10.83	47.11690	0.00439	0.30980	0.06488	0.0000096	149.69521	1.01916	149.81652	151.03643	0.00004
2016_02_11_Ca_STD24	110	0.08	12.23	47.11468	0.00306	0.30979	0.06486	0.0000060	149.68213	1.01626	149.81015	151.03608	0.00006
2016_02_12_Ca_STD25	110	0.08	12.65	47.11497	0.00299	0.30982	0.06486	0.0000060	149.69860	1.02137	149.82931	151.03976	0.00009
2016_02_13_Ca_STD26	110	0.08	12.11	47.11777	0.00278	0.30993	0.06487	0.0000068	149.76212	1.01218	149.87956	151.03524	0.00003
2016_02_15_Ca_STD27	110	0.08	11.75	47.11207	0.00313	0.30970	0.06487	0.0000078	149.62846	1.00936	149.76021	151.03153	0.00013
2016_02_17_Ca_STD28	110	0.08	11.61	47.11383	0.00274	0.30985	0.06487	0.0000074	149.70930	1.01403	149.84264	151.03871	0.00002
2016_02_18_Ca_STD29	110	0.08	12.12	47.11211	0.00294	0.30966	0.06486	0.0000065	149.60604	1.01436	149.73947	151.03338	0.00106
2016_02_19_Ca_STD30	80	0.08	11.79	47.12045	0.00578	0.30981	0.06489	0.0000128	149.71019	1.01771	149.81359	151.02973	0.00002
2016_02_26_Ca_STD33	110	0.08	11.81	47.11295	0.00292	0.30982	0.06487	0.0000063	149.69042	1.01638	149.82477	151.03690	0.00002
2016_03_01_Ca_STD36	110	0.08	12.16	47.11717	0.00310	0.30987	0.06486	0.0000063	149.73006	1.01802	149.84531	151.03115	0.00001
2016_03_02_Ca_STD37	110	0.08	12.19	47.11506	0.00273	0.30977	0.06487	0.0000064	149.67012	1.01662	149.79592	151.03507	0.00003
2016_03_02_Ca_STD38	110	0.08	12.71	47.11299	0.00274	0.30980	0.06487	0.0000051	149.67994	1.01536	149.82147	151.04428	0.00003
2016_03_04_Ca_STD39	110	0.08	11.92	47.11248	0.00295	0.30972	0.06486	0.0000063	149.63765	1.01524	149.77043	151.03386	0.00008
2016_03_07_Ca_STD40	110	0.08	11.91	47.10818	0.00402	0.30972	0.06486	0.0000068	149.62306	1.01741	149.76375	151.02806	0.00012
2016_03_08_Ca_STD41	110	0.08	11.71	47.11275	0.00300	0.30966	0.06486	0.0000064	149.61118	1.02101	149.73786	151.02861	0.00022
2016_03_09_Ca_STD42	110	0.08	12.10	47.11366	0.00321	0.30980	0.06487	0.0000067	149.68217	1.01698	149.81483	151.03749	0.00004
2016_03_10_Ca_STD43	110	0.08	12.57	47.11034	0.00295	0.30988	0.06487	0.0000063	149.71132	1.01712	149.85656	151.03950	0.00004
Standards May 2014 (rotation)				47.08656	130.94	0.30987	0.06485	159.85	149.6302247		149.80340	150.99150	0.00012
Standards May 2014				47.10487	138.94	0.30983	0.06487	89.86	149.6334865		149.81951	150.99154	0.00011
Standards July 2014				47.10346	135.93	0.30981	0.06486	76.61	149.6314278		149.81109	150.99221	0.00013
Standards September 2014				47.10731	175.57	0.30960	0.06487	88.41	149.6279639		149.69747	150.99209	0.00013
Standards October 2014				47.11207	282.89	0.30973	0.06486	120.19	149.625063		149.76685	150.99187	0.00015
Standards December 2014				47.11242	165.19	0.30967	0.06487	85.54	149.6350102		149.73363	150.99882	0.00009
Standards April 2015 (no rotation)				47.13577	90.05	0.30979	0.06486	260.75	149.6478118		149.78679	151.00419	0.00009
Standards April 2015 (rotation)				47.14632	124.06	0.30970	0.06487	154.97	149.6589282		149.75996	151.01068	0.00008
Standards July 2015				47.13532	195.69	0.30978	0.06487	108.77	149.6832237		149.80271	151.01645	0.00005
Standards February 2016				47.11536	135.70	0.30976	0.06487	191.44	149.6834504		149.79275	151.02106	0.00012
Three Year Averages	114	0.09	13.08	47.11594	157.49	0.30975	0.06486	133.64	149.64566		149.77742	151.00104	0.00011

Table 3.5 – *Results for NIST standard SRM915a. Measurements were performed between 2014 and 2016 on the TIMS Triton+ at CRPG (Centre de Recherches Pétrographiques et Géochimiques) Nancy, France. On Line 1 (Static Mode), ^{40}Ca, ^{42}Ca, ^{43}Ca, and ^{44}Ca were measured in Faraday cups L2, C, H1 and H2, respectively. On Line 2 (Multidynamic Mode) ^{40}Ca, ^{41}K, and ^{42}Ca were measured in Faraday cups c, H1 and H2, respectively. There was an idle time of 15 s and 7 s between each line and each line contained 30 integrations of 1.049 s each for a total 31.47 s per line. A measurement consisted of 12 blocks with 10 cycles per block. A peak center and lens focus were completed every 2 blocks. A baseline was done at the beginning of each with a total of 120 integrations at 60 s each. A gain was done each time that a new sample turret was placed in the TIMS.*

	Factor L2-L1 $^{40}Ca/^{44}Ca$ (MD corr)	±	$^{40}Ca/^{44}Ca$ (MD inter)	±	$\varepsilon^{40}Ca$ (Multidynamic)	±	$\varepsilon^{40}Ca$ (Static)	±	$\varepsilon^{42}Ca$	$\varepsilon^{43}Ca$	±	Mass Fract. Factor	Mass Fract. Rate
Session 1 May 2014													
2014_05_08_Ca-STD1	-1030.64	47.14093	0.00134	47.14072	0.00113	-0.04	0.24	1.23	0.42 -3.04	-0.10	0.61	-7.81	0.20
2014_05_09_Ca-STD2	-1169.54	47.13940	0.00118	47.13920	0.00097	-0.36	0.20	-0.49	0.37 1.72	-0.37	0.57	-7.34	0.11
2014_05_09_Ca-STD3	-1117.88	47.14156	0.00136	47.14157	0.00116	0.14	0.25	0.49	0.40 1.16	0.71	0.69	-7.39	0.20
2014_05_10_Ca-STD4	-1239.72	47.14164	0.00123	47.14113	0.00102	0.05	0.22	-0.71	0.38 1.65	0.22	0.57	-7.34	0.09
2014_05_10_Ca-STD5	-1166.53	47.13908	0.00129	47.13909	0.00098	-0.38	0.21	-0.53	0.40 1.01	-0.10	0.61	-7.41	0.15
2014_05_11_Ca-STD6	-1163.98	47.14190	0.00142	47.14163	0.00127	0.16	0.27	0.10	0.45 -0.28	-0.79	0.75	-7.54	0.16
2014_05_11_Ca-STD7	-1117.10	47.14032	0.00143	47.14030	0.00126	-0.13	0.27	0.23	0.43 -0.29	0.18	0.61	-7.54	0.07
2014_05_12_Ca-STD8	-1118.41	47.14123	0.00197	47.14160	0.00175	0.15	0.37	0.41	0.54 -3.89	-1.05	0.82	-7.89	0.09
2014_05_12_Ca-STD9	-1174.18	47.14272	0.00147	47.14233	0.00120	0.30	0.25	0.17	0.49 0.74	1.75	0.68	-7.43	0.10
2014_05_15_Ca-STD12	-1262.02	47.14178	0.00139	47.14140	0.00117	0.11	0.25	-0.91	0.46 1.23	-0.47	0.66	-7.38	0.19
Session 2 May 2014													
2014_05_16_Ca-STD16	-1050.43	47.15209	0.00128	47.15191	0.00108	0.09	0.23	-0.49	0.44 2.21	0.88	0.59	-7.40	0.24
2014_05_16_Ca-STD17	-917.17	47.15196	0.00115	47.15145	0.00097	-0.01	0.21	0.82	0.50 1.36	-0.04	0.67	-7.49	0.22
2014_05_17_Ca-STD18	-955.03	47.15249	0.00191	47.15212	0.00151	0.13	0.32	0.55	0.63 1.08	-0.26	0.87	-7.51	0.10
2014_05_18_Ca-STD19	-970.93	47.15204	0.00132	47.15185	0.00115	0.08	0.24	0.30	0.47 2.95	-0.70	0.71	-7.33	0.27
2014_05_21_Ca-STD20	-911.89	47.15135	0.00144	47.15110	0.00126	-0.08	0.27	0.74	0.58 -2.30	0.06	0.63	-7.85	0.23
2014_05_21_Ca-STD21	-1058.40	47.15154	0.00187	47.15128	0.00162	-0.05	0.34	-0.69	0.62 2.07	-0.06	0.83	-7.41	0.19
2014_05_22_Ca-STD23	-1115.18	47.15196	0.00141	47.15195	0.00115	0.10	0.24	-1.17	0.48 -2.48	-0.38	0.60	-7.87	0.22
2014_05_23_Ca-STD24	-949.20	47.15091	0.00139	47.15076	0.00116	-0.16	0.25	0.27	0.50 -2.48	0.19	0.59	-7.87	0.17
2014_05_24_Ca-STD25	-1015.85	47.15118	0.00176	47.15102	0.00149	-0.10	0.32	-0.34	0.67 -2.40	0.31	0.82	-7.86	0.32
Session 3 July 2014													
2014_07_04_Ca-std-8	-1064.62	47.15181	0.00135	47.15158	0.00115	0.02	0.24	-0.39	0.48 1.72	-0.33	0.65	-7.50	0.23
2014_07_04_Ca-std-9	-1019.92	47.15105	0.00120	47.15102	0.00102	-0.10	0.22	-0.11	0.44 -0.45	-0.49	0.62	-7.72	0.26
2014_07_05_Ca-std-10	-935.14	47.15104	0.00136	47.15086	0.00120	-0.13	0.25	0.74	0.55 0.07	0.05	0.63	-7.67	0.29
2014_07_06_Ca-std-11	-1078.07	47.15159	0.00151	47.15159	0.00126	0.02	0.27	-0.58	0.52 2.09	0.19	0.56	-7.47	0.20
2014_07_08_Ca-std-14	-924.89	47.15003	0.00135	47.14990	0.00105	-0.34	0.22	0.63	0.59 -2.94	-0.27	0.66	-7.96	0.20
2014_07_11_Ca-std-16	-971.58	47.14997	0.00148	47.15008	0.00114	-0.30	0.24	0.15	0.57 -4.95	-0.40	0.70	-8.16	0.12
2014_07_11_Ca-std-17	-1035.09	47.15133	0.00211	47.15132	0.00167	-0.03	0.35	-0.20	0.70 -3.41	-0.28	1.02	-8.01	0.11
2014_07_11_Ca-std-18	-1034.19	47.15274	0.00125	47.15225	0.00104	0.16	0.22	0.11	0.48 1.08	0.40	0.62	-7.57	0.14
2014_07_12_Ca-std-19	-938.73	47.15296	0.00141	47.15279	0.00119	0.28	0.25	1.11	0.48 0.23	-0.12	0.63	-7.65	0.25

Table 3.5 continued from previous page

	Factor L2-L1	$^{40}Ca/^{44}Ca$ (MD corr)	±	$^{40}Ca/^{44}Ca$ (MD inter)	±	$\varepsilon^{40}Ca$ (Multidynamic)	±	$\varepsilon^{40}Ca$ (Static)	±	$\varepsilon^{42}Ca$	$\varepsilon^{43}Ca$	±	Mass Fract. Factor	Mass Fract. Rate
2014_07_12_Ca-std-20	-1107.64	47.15275	0.00122	47.15239	0.00103	0.19	0.22	-0.63	0.45	2.30	0.68	0.60	-7.44	0.15
2014_07_13_Ca-std-21	-997.72	47.15339	0.00144	47.15295	0.00116	0.31	0.25	0.61	0.52	2.83	-0.24	0.73	-7.39	0.12
2014_07_15_Ca-std-23	-1169.57	47.15190	0.00146	47.15163	0.00116	0.03	0.25	-1.42	0.49	1.90	0.54	0.73	-7.48	0.28
2014_07_15_Ca-std-24	-1022.20	47.15155	0.00156	47.15093	0.00137	-0.12	0.29	-0.02	0.52	-0.47	0.29	0.64	-7.72	0.27
Session 4 September 2014														
2014_09_25_Ca-std-1	-732.73	47.14933	0.00154	47.14913	0.00126	-0.17	0.27	1.59	0.64	-1.36	0.81	1.90	-8.49	0.27
2014_09_26_Ca-std-3	-903.38	47.14966	0.00149	47.14940	0.00130	-0.11	0.28	-0.05	0.53	1.71	0.08	0.65	-8.19	0.23
2014_09_26_Ca-std-4	-937.61	47.14937	0.00164	47.14918	0.00135	-0.15	0.29	-0.46	0.49	-1.50	0.15	0.88	-8.51	0.16
2014_09_26_Ca-std-5	-1003.47	47.15034	0.00181	47.15016	0.00158	0.05	0.33	-0.91	0.64	-0.80	0.01	0.74	-8.44	0.28
2014_09_28_Ca-std-7	-834.39	47.15017	0.00149	47.15038	0.00120	0.10	0.25	0.75	0.52	0.28	-0.63	0.62	-8.33	0.20
2014_09_30_Ca-std-10	-932.72	47.15014	0.00160	47.15001	0.00137	0.02	0.29	-0.24	0.53	1.15	-0.18	0.61	-8.25	0.33
2014_10_02_Ca-std-12	-1001.48	47.15134	0.00164	47.15107	0.00131	0.25	0.28	-0.68	0.55	0.52	-0.24	0.64	-8.31	0.18
Session 5 October 2014														
2014_10_03_Ca-std-14	-802.90	47.15317	0.00169	47.15265	0.00142	0.18	0.30	0.69	0.60	5.70	-0.53	0.86	-7.39	0.30
2014_10_04_Ca-std-15	-1037.50	47.15317	0.00158	47.15323	0.00130	0.30	0.28	-1.66	0.59	0.13	0.41	0.73	-7.94	0.24
2014_10_04_Ca-std-17	-1052.12	47.15156	0.00173	47.15162	0.00145	-0.04	0.31	-2.15	0.56	-1.04	1.01	0.73	-8.06	0.26
2014_10_05_Ca-std-18	-829.51	47.15310	0.00160	47.15288	0.00150	0.23	0.32	0.41	0.62	4.41	-0.51	0.67	-7.52	0.29
2014_10_05_Ca-std-19	-779.31	47.15146	0.00161	47.15140	0.00140	-0.08	0.30	0.56	0.62	-1.23	0.20	0.63	-8.08	0.25
2014_10_06_Ca-std-21	-981.43	47.15069	0.00140	47.15070	0.00118	-0.23	0.25	-1.62	0.48	-5.03	-0.79	0.66	-8.46	0.18
2014_10_10_Ca-std-22	-755.86	47.15160	0.00143	47.15127	0.00112	-0.11	0.24	0.83	0.57	-4.24	0.10	0.69	-8.38	0.17
2014_10_12_Ca-std-23	-675.90	47.15129	0.00151	47.15122	0.00124	-0.12	0.26	1.56	0.59	-2.11	0.54	0.59	-8.17	0.18
2014_10_12_Ca-std-24	-697.11	47.15147	0.00166	47.15121	0.00143	-0.12	0.30	1.39	0.57	3.42	-0.43	0.92	-7.62	0.23
Session 6 December 2014														
2014_12_05_Ca-std-7	-821.98	47.14925	0.00139	47.14882	0.00114	-0.17	0.24	-0.41	0.52	-0.39	0.11	0.63	-8.17	0.24
2014_12_05_Ca-std-8	-772.23	47.14835	0.00153	47.14800	0.00129	-0.35	0.27	-0.10	0.59	-1.92	0.03	0.55	-8.32	0.17
2014_12_06_Ca-std-9	-748.06	47.15001	0.00146	47.14965	0.00120	0.00	0.26	0.49	0.59	-0.60	-0.50	0.63	-8.19	0.20
2014_12_06_Ca-std-10	-752.34	47.14908	0.00144	47.14853	0.00117	-0.23	0.25	0.25	0.49	-1.96	-0.24	0.61	-8.32	0.24
2014_12_06_Ca-std-11	-840.34	47.14826	0.00156	47.14765	0.00138	-0.42	0.29	-0.80	0.50	-1.94	0.70	0.76	-8.32	0.40
2014_12_06_Ca-std-12	-973.80	47.15010	0.00165	47.15011	0.00149	0.10	0.32	-1.75	0.55	1.32	0.74	0.64	-8.00	0.23
2014_12_07_Ca-std-13	-775.81	47.15224	0.00157	47.15190	0.00135	0.48	0.29	0.69	0.59	1.71	-0.17	0.68	-7.96	0.25
2014_12_07_Ca-std-14	-758.00	47.14980	0.00150	47.14948	0.00132	-0.03	0.28	0.35	0.54	-0.56	-0.15	0.65	-8.18	0.32
2014_12_08_Ca-std-15	-720.36	47.15185	0.00145	47.15160	0.00128	0.42	0.27	1.16	0.55	4.51	-0.48	0.66	-7.68	0.31
2014_12_09_Ca-std-16	-800.31	47.15068	0.00132	47.15059	0.00118	0.20	0.25	0.11	0.52	-0.19	-0.04	0.65	-8.15	0.29
Session 7 April 2015 Faraday Cup Change (No Rotation)														
2015_04_15_Ca-STD5	-272.61	47.14659	0.00142	47.14664	0.00122	-0.11	0.26	-0.43	0.47	2.16	0.63	0.92	-7.52	0.05
2015_04_16_Ca-STD7	-220.48	47.14802	0.00199	47.14754	0.00185	0.08	0.39	0.39	0.54	-3.39	-0.03	0.95	-8.07	-0.06
2015_04_16_Ca-STD8	-181.78	47.14814	0.00183	47.14833	0.00163	0.25	0.37	0.80	0.52	-5.20	0.43	0.89	-8.25	0.09
2015_04_17_Ca-STD9b	-259.06	47.14841	0.00192	47.14832	0.00166	0.25	0.35	0.09	0.52	2.35	-0.69	0.92	-7.50	0.01
2015_04_17_Ca-STD10	-216.56	47.14693	0.00197	47.14717	0.00184	0.00	0.39	0.20	0.57	-2.56	-2.48	1.20	-7.99	-0.02
2015_04_18_Ca-STD11	-301.65	47.14795	0.00175	47.14814	0.00136	0.21	0.29	-0.43	0.53	2.08	-0.74	0.90	-7.53	0.02

Table 3.5 continued from previous page

	Factor L2-L1	$^{40}Ca/^{44}Ca$ (MD corr)	±	$^{40}Ca/^{44}Ca$ (MD inter)	±	$\varepsilon^{40}Ca$ (Multidynamic)	±	$\varepsilon^{40}Ca$ (Static)	±	$\varepsilon^{42}Ca$	$\varepsilon^{43}Ca$	±	Mass Fract. Factor	Mass Fract. Rate
2015_04_20_Ca-STD13	-238.79	47.14571	0.00166	47.14577	0.00124	-0.29	0.26	-0.28	0.44	0.21	1.38	1.03	-7.72	-0.04
2015_04_21_Ca-STD14	-249.41	47.14593	0.00261	47.14533	0.00228	-0.39	0.48	-0.34	0.62	4.35	1.50	1.60	-7.30	-0.11
Session 8 April 2015 (Ampli. Rotation Left)														
2015_04_24_Ca-STD19	-142.80	47.15582	0.00188	47.15578	0.00173	0.34	0.37	0.59	0.58	0.64	-0.20	0.99	-7.98	0.26
015_04_28_Ca-STD22	-104.55	47.15330	0.00205	47.15366	0.00179	-0.11	0.38	0.43	0.65	0.90	0.02	1.05	-7.96	
2015_04_28_Ca-STD24	-115.34	47.15462	0.00204	47.15461	0.00177	0.09	0.38	0.61	0.64	-2.57	-0.19	1.04	-8.30	0.15
2015_04_29_Ca-STD25b	-146.92	47.15451	0.00178	47.15467	0.00142	0.11	0.30	0.27	0.54	-0.98	-0.02	0.83	-8.14	0.22
2015_04_30_Ca-STD26	-186.56	47.15449	0.00204	47.15420	0.00183	0.01	0.39	-0.13	0.61	1.43	0.26	0.83	-7.90	0.29
2015_05_01_Ca-STD27	-163.09	47.15370	0.00197	47.15375	0.00170	-0.09	0.36	-0.07	0.64	-0.70	-1.07	1.11	-8.11	0.03
2015_05_02_Ca-STD28	-190.46	47.15293	0.00194	47.15303	0.00162	-0.24	0.34	-0.50	0.64	-0.96	-0.44	1.24	-8.14	0.19
2015_05_03_Ca-STD29	-277.86	47.15375	0.00190	47.15367	0.00164	-0.11	0.35	-1.20	0.53	2.24	1.65	0.93	-7.82	0.31
Session 9 July 2015														
2015_07_02_Ca-STD2	-321.53	47.15593	0.00236	47.15549	0.00227	0.15	0.48	1.16	0.66	5.85	0.57	0.87	-7.21	0.14
2015_07_02_Ca-STD3	-384.65	47.15517	0.00159	47.15499	0.00143	0.05	0.30	0.36	0.55	-1.35	-0.28	0.74	-7.92	0.11
2015_07_02_Ca-STD4	-339.19	47.15495	0.00168	47.15431	0.00142	-0.10	0.30	0.77	0.50	3.91	-0.65	0.66	-7.40	0.14
2015_07_03_Ca-STD5	-312.65	47.15252	0.00187	47.15252	0.00158	-0.47	0.33	0.52	0.60	-6.50	0.46	0.86	-8.44	0.24
2015_07_06_Ca-STD7	-351.87	47.15472	0.00183	47.15470	0.00149	-0.01	0.32	0.60	0.60	4.14	0.64	0.85	-7.38	0.10
2015_07_11_Ca-STD10	-336.08	47.15439	0.00401	47.15421	0.00308	-0.12	0.65	0.68	1.55	-11.91	0.69	0.94	-8.97	0.17
2015_07_12_Ca-STD12	-548.38	47.15653	0.00206	47.15598	0.00165	0.26	0.35	-0.99	0.56	-1.49	-0.56	0.86	-7.94	0.11
2015_07_13_Ca-STD13	-435.84	47.15512	0.00176	47.15507	0.00152	0.07	0.32	-0.16	0.55	-0.91	-0.31	0.87	-7.88	0.18
2015_07_14_Ca-STD14	-578.32	47.15458	0.00177	47.15465	0.00145	-0.02	0.31	-1.70	0.58	1.99	-0.58	0.98	-7.59	0.07
2015_07_15_Ca-STD15	-558.71	47.15576	0.00182	47.15568	0.00139	0.19	0.30	-1.25	0.56	6.26	0.01	0.94	-7.17	0.14
Session 10 February/March 2016														
2016_02_01_CaSTD2	-707.22	47.15297	0.00245	47.15320	0.00205	-0.21	0.43	0.91	0.67	-0.53	0.43	0.87	-7.90	0.32
2016_02_01_CaSTD5	-751.76	47.15329	0.00214	47.15304	0.00202	-0.25	0.43	0.53	0.67	-0.57	1.05	1.17	-7.90	0.30
2016_02_02_CaSTD7	-726.34	47.15561	0.00183	47.15560	0.00164	0.30	0.35	1.27	0.53	3.34	0.13	0.78	-7.51	0.21
2016_02_04_CaSTD14	-854.71	47.15588	0.00174	47.15567	0.00149	0.31	0.32	0.05	0.57	2.38	-0.52	0.90	-7.61	0.31
2016_02_04_CaSTD15	-782.47	47.15534	0.00217	47.15546	0.00187	0.27	0.40	0.66	0.65	-4.40	-1.45	1.27	-8.28	0.20
2016_02_05_CaSTD17	-827.34	47.15395	0.00181	47.15352	0.00153	-0.14	0.32	-0.09	0.57	-1.12	-1.25	0.97	-7.96	0.31
2016_02_05_CaSTD18	-820.08	47.15376	0.00179	47.15346	0.00164	-0.16	0.35	-0.06	0.65	-3.15	-0.15	1.02	-8.16	0.21
2016_02_05_CaSTD19	-759.64	47.15447	0.00202	47.15386	0.00178	-0.07	0.38	0.70	0.61	-4.40	-0.02	1.00	-8.28	0.15
2016_02_07_CaSTD21	-774.38	47.15177	0.00187	47.15160	0.00172	-0.55	0.36	-0.02	0.64	-6.43	-0.13	0.97	-8.48	0.15
2016_02_08_Ca_STD22	-734.55	47.15410	0.00200	47.15367	0.00173	-0.11	0.37	0.87	0.59	-0.08	0.04	0.80	-7.85	0.20
2016_02_09_Ca_STD23	-809.70	47.15508	0.00279	47.15461	0.00248	0.09	0.53	0.33	0.93	1.39	1.27	1.49	-7.71	0.26
2016_02_11_Ca_STD24	-854.55	47.15497	0.00201	47.15432	0.00171	0.03	0.36	-0.14	0.65	1.00	-0.43	0.93	-7.74	0.17
2016_02_12_Ca_STD25	-872.38	47.15612	0.00220	47.15598	0.00187	0.38	0.40	-0.08	0.63	1.99	-0.63	0.92	-7.65	0.16
2016_02_13_Ca_STD26	-783.54	47.15471	0.00192	47.15433	0.00169	0.03	0.36	0.51	0.59	5.48	0.14	1.05	-7.30	0.19
2016_02_15_Ca_STD27	-879.71	47.15356	0.00244	47.15330	0.00216	-0.19	0.46	-0.70	0.67	-1.89	0.14	1.19	-8.03	
2016_02_17_Ca_STD28	-889.87	47.15580	0.00192	47.15569	0.00166	0.32	0.35	-0.32	0.58	2.91	0.51	1.14	-7.56	0.09
2016_02_18_Ca_STD29	-891.05	47.15413	0.00195	47.15405	0.00162	-0.03	0.34	-0.69	0.62	-3.34	-0.78	1.00	-8.18	0.23
2016_02_19_Ca_STD30	-690.20	47.15299	0.00331	47.15298	0.00289	-0.26	0.61	1.08	1.23	1.63	3.46	1.97	-7.68	0.14

Table 3.5 continued from previous page

	Factor L2-L1	$^{40}Ca/^{44}Ca$ (MD corr)	±	$^{40}Ca/^{44}Ca$ (MD inter)	±	$\varepsilon^{40}Ca$ (Multidynamic)	±	$\varepsilon^{40}Ca$ (Static)	±	$\varepsilon^{42}Ca$	$\varepsilon^{43}Ca$	±	Mass Fract. Factor	Mass Fract. Rate
2016_02_26_Ca_STD33	-896.72	47.15523	0.00212	47.15455	0.00177	0.08	0.38	-0.51	0.62	1.88	-0.18	0.97	-7.66	0.35
2016_03_01_Ca_STD36	-769.12	47.15344	0.00195	47.15303	0.00160	-0.25	0.34	0.39	0.66	3.55	-0.49	0.97	-7.49	0.36
2016_03_02_Ca_STD37	-839.83	47.15466	0.00191	47.15400	0.00167	-0.04	0.35	-0.06	0.58	0.16	0.13	0.99	-7.83	0.32
2016_03_02_Ca_STD38	-944.64	47.15753	0.00176	47.15679	0.00137	0.55	0.29	-0.50	0.58	1.21	-0.08	0.79	-7.72	0.35
2016_03_04_Ca_STD39	-886.52	47.15428	0.00198	47.15447	0.00152	0.06	0.32	-0.61	0.63	-1.39	-1.06	0.97	-7.98	0.33
2016_03_07_Ca_STD40	-939.38	47.15247	0.00275	47.15279	0.00217	-0.30	0.46	-1.52	0.85	-1.45	-0.62	1.05	-7.99	0.24
2016_03_08_Ca_STD41	-845.97	47.15264	0.00210	47.15266	0.00176	-0.33	0.37	-0.55	0.64	-3.13	-0.79	0.98	-8.15	0.09
2016_03_09_Ca_STD42	-885.44	47.15541	0.00236	47.15505	0.00200	0.18	0.42	-0.36	0.68	1.21	0.98	1.03	-7.72	
2016_03_10_Ca_STD43	-969.12	47.15604	0.00192	47.15564	0.00199	0.31	0.36	-1.06	0.63	3.74	0.30	0.98	-7.47	0.25
Standards May 2014 (rotation)		47.14106	48.72	47.14090	45.59	0.00	0.46	0.10	1.31	0.10	3.92	0.16	-7.51	0.14
Standards May 2014		47.15172	21.60	47.15149	20.49	0.00	0.20	0.10	1.31	0.11	3.49	0.22	-7.62	0.22
Standards July 2014		47.15170	44.94	47.15148	40.10	0.00	0.40	0.10	1.36	0.10	3.56	0.23	-7.67	0.20
Standards September 2014		47.15005	29.57	47.14991	30.25	0.00	0.30	0.11	1.76	0.11	3.75	0.94	-8.36	0.24
Standards October 2014		47.15194	39.92	47.15180	37.58	0.00	0.38	0.11	2.83	0.10	3.79	0.21	-7.96	0.23
Standards December 2014		47.14996	56.80	47.14963	61.05	0.00	0.61	0.10	1.65	0.08	4.21	0.11	-8.13	0.27
Standards April 2015 (no rotation)		47.14721	45.02	47.14716	48.98	0.00	0.49	0.12	0.90	0.08	4.35	0.49	-7.74	-0.01
Standards April 2015 (rotation)		47.15414	38.75	47.15417	35.99	0.00	0.36	0.12	1.24	0.14	4.36	0.28	-8.04	0.21
Standards July 2015		47.15497	46.01	47.15476	41.33	0.00	0.40	0.08	1.96	0.14	1.65	0.19	-7.79	0.14
Standards February 2016		47.15445	56.39	47.15420	52.37	0.00	0.52	0.08	1.36	0.15	3.61	0.48	-7.84	0.24
Three Year Averages		**47.15072**	**42.77**	**47.15055**	**41.37**	**0.00**	**0.41**	**0.10**	**1.57**	**0.11**	**3.67**	**0.33**	**-7.87**	**0.19**

Table 3.6 – *Results for NIST standard SRM915a. Measurements were performed between 2014 and 2016 on the TIMS Triton+ at CRPG (Centre de Recherches Pétrographiques et Géochimiques) Nancy, France. On Line 1 (Static Mode), ^{40}Ca, ^{42}Ca, ^{43}Ca, and ^{44}Ca were measured in Faraday cups L2, C, H1 and H2, respectively. On Line 2 (Multidynamic Mode) ^{40}Ca, ^{41}K, and ^{42}Ca were measured in Faraday cups c, H1 and H2, respectively. There was an idle time of 15 s and 7 s between each line and each line contained 30 integrations of 1.049 s each for a total 31.47 s per line. A measurement consisted of 12 blocks with 10 cycles per block. A peak center and lens focus were completed every 2 blocks. A baseline was done at the beginning of each with a total of 120 integrations at 60 s each. A gain was done each time that a new sample turret was placed in the TIMS.*

	F	Δ^{40}Ca	Δ^{40}Ca Theoretical	Difference	LN(($^{40}Ca/^{42}Ca)_c/(^{40}Ca/^{42}Ca)_T$) (MD)	LN(($^{40}Ca/^{42}Ca)_c/(^{40}Ca/^{42}Ca)_T$) (Static)	LN(($^{43}Ca/^{42}Ca)_C/(^{43}Ca/^{42}Ca)_T$)
Session 1 May 2014							
2014_05_08_Ca-STD1	1.000007308	4.32	7.66	-3.34	-0.0000037	0.0001228	-0.0000095
2014_05_09_Ca-STD2	1.000004121	4.22	4.32	-0.10	-0.0000361	-0.0000487	-0.0000366
2014_05_09_Ca-STD3	1.000007602	-0.36	7.97	-8.32	0.0000143	0.0000488	0.0000711
2014_05_10_Ca-STD4	1.000003398	10.88	3.56	7.32	0.0000049	-0.0000713	0.0000222
2014_05_10_Ca-STD5	1.000005393	-0.39	5.65	-6.04	-0.0000383	-0.0000526	-0.0000096
2014_05_11_Ca-STD6	1.000006113	5.73	6.41	-0.68	0.0000156	0.0000100	-0.0000791
2014_05_11_Ca-STD7	1.000002501	0.58	2.62	-2.04	-0.0000128	0.0000234	0.0000176
2014_05_12_Ca-STD8	1.000003491	-7.88	3.66	-11.54	0.0000149	0.0000413	-0.0001045
2014_05_12_Ca-STD9	1.000003702	8.26	3.88	4.38	0.0000304	0.0000171	0.0001752
2014_05_15_Ca-STD12	1.000007181	7.97	7.53	0.44	0.0000107	-0.0000908	-0.0000470
Session 2 May 2014							
2014_05_16_Ca-STD16	1.000009943	3.89	10.42	-6.54	0.0000088	-0.0000489	0.0000877
2014_05_16_Ca-STD17	1.000009138	10.83	9.58	1.25	-0.0000010	0.0000816	-0.0000037
2014_05_17_Ca-STD18	1.000003982	7.82	4.17	3.65	0.0000133	0.0000550	-0.0000258
2014_05_18_Ca-STD19	1.000011220	4.11	11.76	-7.65	0.0000076	0.0000297	-0.0000701
2014_05_21_Ca-STD20	1.000009331	5.30	9.78	-4.48	-0.0000083	0.0000741	0.0000058
2014_05_21_Ca-STD21	1.000007826	5.59	8.20	-2.62	-0.0000045	-0.0000685	-0.0000065
2014_05_22_Ca-STD23	1.000008820	0.16	9.25	-9.09	0.0000097	-0.0001165	-0.0000379
2014_05_23_Ca-STD24	1.000007086	3.06	7.43	-4.37	-0.0000155	0.0000273	0.0000192
2014_05_24_Ca-STD25	1.000012966	3.35	13.59	-10.24	-0.0000101	-0.0000337	0.0000313
Session 3 July 2014							
2014_07_04_Ca-std-8	1.00000787	4.84	8.25	-3.41	0.0000020	-0.0000393	-0.0000332
2014_07_04_Ca-std-9	1.00000876	0.57	9.18	-8.61	-0.0000098	-0.0000107	-0.0000486
2014_07_05_Ca-std-10	1.00000994	3.80	10.42	-6.61	-0.0000133	0.0000739	0.0000047
2014_07_06_Ca-std-11	1.00000697	-0.03	7.31	-7.34	0.0000022	-0.0000575	0.0000191
2014_07_08_Ca-std-14	1.00000695	2.69	7.29	-4.60	-0.0000335	0.0000628	-0.0000271
2014_07_11_Ca-std-16	1.00000424	-2.26	4.45	-6.71	-0.0000298	0.0000149	-0.0000405
2014_07_11_Ca-std-17	1.00000379	0.24	3.97	-3.73	-0.0000034	-0.0000199	-0.0000282
2014_07_11_Ca-std-18	1.00000491	10.29	5.15	5.14	0.0000163	0.0000108	0.0000396
2014_07_12_Ca-std-19	1.00000852	3.60	8.93	-5.32	0.0000278	0.0001112	-0.0000123

Table 3.6 continued from previous page

	F	Δ^{40}Ca	Δ^{40}Ca Theoretical	Difference	LN(($^{40}Ca/^{42}Ca)_c/(^{40}Ca/^{42}Ca)_T$) (MD)	LN(($^{40}Ca/^{42}Ca)_c/(^{40}Ca/^{42}Ca)_T$) (Static)	LN(($^{43}Ca/^{42}Ca)_C/(^{43}Ca/^{42}Ca)_T$)
2014_07_12_Ca-std-20	1.00000517	7.57	5.42	2.15	0.0000192	-0.0000625	0.0000676
2014_07_13_Ca-std-21	1.00000399	9.32	4.18	5.14	0.0000311	0.0000612	-0.0000238
2014_07_15_Ca-std-23	1.00000975	5.66	10.22	-4.56	0.0000031	-0.0001425	0.0000539
2014_07_15_Ca-std-24	1.00000937	13.28	9.82	3.46	-0.0000119	-0.0000023	0.0000288
Session 4 September 2014							
2014_09_25_Ca-std-1	1.00000921	4.22	9.66	-5.44	-0.0000165	0.0001585	0.0000807
2014_09_26_Ca-std-3	1.00000805	5.48	8.44	-2.97	-0.0000106	-0.0000051	0.0000084
2014_09_26_Ca-std-4	1.00000540	4.11	5.66	-1.55	-0.0000154	-0.0000456	0.0000150
2014_09_26_Ca-std-5	1.00000957	3.82	10.03	-6.21	0.0000054	-0.0000909	0.0000012
2014_09_28_Ca-std-7	1.00000670	-4.50	7.02	-11.52	0.0000101	0.0000747	-0.0000634
2014_09_30_Ca-std-10	1.00001133	2.71	11.87	-9.16	0.0000023	-0.0000243	-0.0000184
2014_10_02_Ca-std-12	1.00000629	5.77	6.59	-0.82	0.0000247	-0.0000676	-0.0000235
Session 5 October 2014							
2014_10_03_Ca-std-14	1.00001033	11.19	10.83	0.37	0.0000180	0.0000690	-0.0000535
2014_10_04_Ca-std-15	1.00000815	-1.26	8.54	-9.80	0.0000303	-0.0001660	0.0000408
2014_10_04_Ca-std-17	1.00000892	-1.30	9.36	-10.65	-0.0000038	-0.0002148	0.0001011
2014_10_05_Ca-std-18	1.00001011	4.65	10.59	-5.94	0.0000230	0.0000407	-0.0000510
2014_10_05_Ca-std-19	1.00000848	1.23	8.89	-7.66	-0.0000085	0.0000561	0.0000201
2014_10_06_Ca-std-21	1.00000629	-0.39	6.60	-6.99	-0.0000232	-0.0001625	-0.0000793
2014_10_10_Ca-std-22	1.00000594	7.13	6.23	0.90	-0.0000113	0.0000827	0.0000099
2014_10_12_Ca-std-23	1.00000614	1.48	6.43	-4.95	-0.0000122	0.0001561	0.0000543
2014_10_12_Ca-std-24	1.00000794	5.36	8.32	-2.96	-0.0000124	0.0001386	-0.0000426
Session 6 December 2014							
2014_12_05_Ca-std-7	1.00000838	9.08	8.79	0.29	-0.0000173	-0.0000409	0.0000109
2014_12_05_Ca-std-8	1.00000585	7.33	6.13	1.20	-0.0000345	-0.0000101	0.0000031
2014_12_06_Ca-std-9	1.00000702	7.58	7.36	0.22	0.0000004	0.0000493	-0.0000499
2014_12_06_Ca-std-10	1.00000840	11.72	8.81	2.92	-0.0000234	0.0000254	-0.0000244
2014_12_06_Ca-std-11	1.00001362	12.96	14.27	-1.31	-0.0000421	-0.0000802	0.0000701
2014_12_06_Ca-std-12	1.00000796	-0.17	8.34	-8.51	0.0000101	-0.0001747	0.0000742
2014_12_07_Ca-std-13	1.00000843	7.37	8.84	-1.47	0.0000480	0.0000689	-0.0000174
2014_12_07_Ca-std-14	1.00001114	6.92	11.68	-4.76	-0.0000033	0.0000350	-0.0000147
2014_12_08_Ca-std-15	1.00001048	5.39	10.98	-5.59	0.0000417	0.0001161	-0.0000480
2014_12_09_Ca-std-16	1.00001002	1.82	10.51	-8.69	0.0000204	0.0000112	-0.0000040
Session 7 April 2015 Faraday Cup Change (No Rotation)							
2015_04_15_Ca-STD5	1.0000017	-1.06	1.79	-2.85	-0.0000109	-0.0000432	0.0000634
2015_04_16_Ca-STD7	0.9999980	10.18	-2.14	12.32	0.0000082	0.0000393	-0.0000025
2015_04_16_Ca-STD8	1.0000034	-3.99	3.60	-7.59	0.0000249	0.0000805	0.0000434
2015_04_17_Ca-STD9b	1.0000002	2.06	0.25	1.80	0.0000246	0.0000090	-0.0000694
2015_04_17_Ca-STD10	0.9999993	-5.21	-0.74	-4.47	0.0000003	0.0000199	-0.0002478
2015_04_18_Ca-STD11	1.0000007	-3.97	0.74	-4.72	0.0000209	-0.0000433	-0.0000745

Table 3.6 continued from previous page

	F	$\Delta^{40}Ca$	$\Delta^{40}Ca$ Theoretical	Difference	LN(($^{40}Ca/^{42}Ca)_c/(^{40}Ca/^{42}Ca)_T$) (MD)	LN(($^{40}Ca/^{42}Ca)_c/(^{40}Ca/^{42}Ca)_T$) (Static)	LN(($^{43}Ca/^{42}Ca)_C/(^{43}Ca/^{42}Ca)_T$)
2015_04_20_Ca-STD13	0.9999986	-1.39	-1.51	0.12	-0.0000294	-0.0000282	0.0001377
2015_04_21_Ca-STD14	0.9999960	12.61	-4.24	16.85	-0.0000386	-0.0000340	0.0001497
Session 8 April 2015 (Ampli. Rotation Left)							
2015_04_24_Ca-STD19	1.0000093	0.80	9.70	-8.90	0.0000342	0.0000588	-0.0000197
015_04_28_Ca-STD22					-0.0000108	0.0000435	0.0000020
2015_04_28_Ca-STD24	1.0000052	0.17	5.47	-5.30	0.0000093	0.0000607	-0.0000195
2015_04_29_Ca-STD25b	1.0000077	-3.21	8.12	-11.33	0.0000105	0.0000270	-0.0000025
2015_04_30_Ca-STD26	1.0000103	6.25	10.75	-4.50	0.0000006	-0.0000132	0.0000255
2015_05_01_Ca-STD27	1.0000011	-1.03	1.15	-2.18	-0.0000090	-0.0000065	-0.0001072
2015_05_02_Ca-STD28	1.0000066	-2.12	6.88	-9.00	-0.0000242	-0.0000502	-0.0000437
2015_05_03_Ca-STD29	1.0000107	1.84	11.26	-9.43	-0.0000107	-0.0001202	0.0001649
Session 9 July 2015							
2015_07_02_Ca-STD2	1.0000049	9.23	5.16	4.07	0.0000155	0.0001156	0.0000566
2015_07_02_Ca-STD3	1.0000037	3.77	3.92	-0.15	0.0000050	0.0000365	-0.0000279
2015_07_02_Ca-STD4	1.0000047	13.59	4.98	8.62	-0.0000095	0.0000772	-0.0000649
2015_07_03_Ca-STD5	1.0000084	-0.12	8.83	-8.94	-0.0000474	0.0000522	0.0000464
2015_07_06_Ca-STD7	1.0000037	0.38	3.84	-3.46	-0.0000013	0.0000596	0.0000638
2015_07_11_Ca-STD10	1.0000061	3.98	6.38	-2.39	-0.0000117	0.0000685	0.0000691
2015_07_12_Ca-STD12	1.0000037	11.60	3.93	7.67	0.0000260	-0.0000986	-0.0000558
2015_07_13_Ca-STD13	1.0000062	1.22	6.45	-5.23	0.0000065	-0.0000158	-0.0000311
2015_07_14_Ca-STD14	1.0000024	-1.47	2.56	-4.03	-0.0000024	-0.0001699	-0.0000578
2015_07_15_Ca-STD15	1.0000050	1.69	5.29	-3.60	0.0000194	-0.0001253	0.0000015
Session 10 February/March 2016							
2016_02_01_CaSTD2	1.0000114	-4.80	11.93	-16.73	-0.0000212	0.0000906	0.0000435
2016_02_01_CaSTD5	1.0000104	5.29	10.94	-5.64	-0.0000245	0.0000528	0.0001047
2016_02_02_CaSTD7	1.0000074	0.20	7.80	-7.60	0.0000297	0.0001274	0.0000128
2016_02_04_CaSTD14	1.0000108	4.39	11.30	-6.91	0.0000313	0.0000046	-0.0000518
2016_02_04_CaSTD15	1.0000071	-2.42	7.48	-9.90	0.0000267	0.0000655	-0.0001452
2016_02_05_CaSTD17	1.0000109	9.28	11.43	-2.15	-0.0000144	-0.0000088	-0.0001254
2016_02_05_CaSTD18	1.0000074	6.49	7.71	-1.22	-0.0000157	-0.0000056	-0.0000153
2016_02_05_CaSTD19	1.0000053	12.93	5.60	7.33	-0.0000072	0.0000699	-0.0000015
2016_02_07_CaSTD21	1.0000052	3.69	5.41	-1.72	-0.0000551	-0.0000021	-0.0000126
2016_02_08_Ca_STD22	1.0000071	9.06	7.44	1.62	-0.0000111	0.0000872	0.0000043
2016_02_09_Ca_STD23	1.0000090	10.06	9.40	0.66	0.0000088	0.0000328	0.0001270
2016_02_11_Ca_STD24	1.0000059	13.82	6.15	7.67	0.0000027	-0.0000144	-0.0000433
2016_02_12_Ca_STD25	1.0000057	3.04	5.94	-2.90	0.0000378	-0.0000081	-0.0000632
2016_02_13_Ca_STD26	1.0000066	8.06	6.90	1.17	0.0000029	0.0000512	0.0000139
2016_02_15_Ca_STD27					-0.0000190	-0.0000697	0.0000144
2016_02_17_Ca_STD28	1.0000031	2.16	3.28	-1.12	0.0000317	-0.0000323	0.0000506
2016_02_18_Ca_STD29	1.0000081	1.74	8.44	-6.71	-0.0000032	-0.0000688	-0.0000777
2016_02_19_Ca_STD30	1.0000050	0.22	5.20	-4.98	-0.0000258	0.0001081	0.0003458

Table 3.6 continued from previous page

	F	Δ^{40}Ca	Δ^{40}Ca Theoretical	Difference	LN(($^{40}Ca/^{42}Ca)_c/(^{40}Ca/^{42}Ca)_T$) (MD)	LN(($^{40}Ca/^{42}Ca)_c/(^{40}Ca/^{42}Ca)_T$) (Static)	LN(($^{43}Ca/^{42}Ca)_C/(^{43}Ca/^{42}Ca)_T$)
2016_02_26_Ca_STD33	1.0000122	14.34	12.75	1.59	0.0000076	-0.0000512	-0.0000182
2016_03_01_Ca_STD36	1.0000125	8.59	13.14	-4.56	-0.0000247	0.0000385	-0.0000486
2016_03_02_Ca_STD37	1.0000114	13.95	11.90	2.05	-0.0000042	-0.0000063	0.0000133
2016_03_02_Ca_STD38	1.0000123	15.73	12.86	2.87	0.0000550	-0.0000503	-0.0000085
2016_03_04_Ca_STD39	1.0000116	-4.07	12.14	-16.22	0.0000058	-0.0000611	-0.0001060
2016_03_07_Ca_STD40	1.0000083	-6.81	8.74	-15.56	-0.0000298	-0.0001523	-0.0000623
2016_03_08_Ca_STD41	1.0000030	-0.34	3.16	-3.51	-0.0000326	-0.0000552	-0.0000785
2016_03_09_Ca_STD42					0.0000181	-0.0000360	0.0000980
2016_03_10_Ca_STD43	1.0000088	8.40	9.27	-0.87	0.0000307	-0.0001064	0.0000299
Standards May 2014 (rotation)	1.0000051	3.33	5.33	-1.99	-0.00000000023	-0.00000000193	-0.00000000287
Standards May 2014	1.0000048	4.90	9.35	-4.45	-0.00000000005	-0.00000000214	-0.00000000090
Standards July 2014	1.0000049	4.58	7.28	-2.69	-0.00000000019	-0.00000000213	-0.00000000068
Standards September 2014	1.0000045	3.09	8.47	-5.38	-0.00000000010	-0.00000000330	-0.00000000084
Standards October 2014	1.0000047	3.12	8.42	-5.30	-0.00000000016	-0.00000000889	-0.00000000161
Standards December 2014	1.0000055	7.00	9.57	-2.57	-0.00000000042	-0.00000000307	-0.00000000082
Standards April 2015 (no rotation)	1.0000060	1.15	-0.28	1.43	-0.00000000026	-0.00000000089	-0.00000000744
Standards April 2015 (rotation)	1.0000062	0.38	7.62	-7.24	-0.00000000014	-0.00000000168	-0.00000000263
Standards July 2015	1.0000075	4.39	5.13	-0.74	-0.00000000019	-0.00000000431	-0.00000000133
Standards February 2016	1.0000085	5.32	8.65	-3.33	-0.00000000033	-0.00000000222	-0.00000000441
Three Year Averages	**1.0000058**	**3.73**	**6.95**	**-3.23**	**-0.00000000021**	**-0.00000000306**	**-0.00000000235**

Table 3.7 – *Results for NIST standard SRM915a. Measurements were performed between 2014 and 2016 on the TIMS Triton+ at CRPG (Centre de Recherches Pétrographiques et Géochimiques) Nancy, France.*

Acuisition parameters	Rotation	Idle1	Line1	Idle2	Line 2	t (sec)	Dt (sec)
Standards May 2014 (rotation)	No	15	31.47	7	31.47	84.94	38.47
Standards May 2014	Yes	7	31.47	7	31.47	76.94	38.47
Standards July 2014	Yes	22	31.47	7	31.47	91.94	38.47
Standards Sept 2014	Yes	22	31.47	7	31.47	91.94	38.47
Standards October 2014	Yes	22	31.47	7	31.47	91.94	38.47
Standards December 2014	Yes	22	31.47	7	31.47	91.94	38.47
Standards Aprill 2015 (no rotation)	No	17	31.47	7	31.47	86.94	38.47
Standards Aprill 2015 (rotation)	Yes	20	31.47	7	31.47	89.94	38.47
Standards July 2015	Yes	20	31.47	7	31.47	89.94	38.47
Standards February 2016	Yes	20	31.47	7	31.47	89.94	38.47

CHAPTER 4

RADIOGENIC CA SYSTEMATICS IN THE KHUDI KHOLA BASIN, CENTRAL NEPAL

"The pursuit of science has often been compared to the scaling of mountains, high and not so high. But who amongst us can hope, even in imagination, to scale the Everest and reach its summit when the sky is blue and the air is still, and in the stillness of the air survey the entire Himalayan range in the dazzling white of the snow stretching to infinity? None of us can hope for a comparable vision of nature and of the universe around us. But there is nothing mean or lowly in standing in the valley below and awaiting the sun to rise over Kinchinjunga."

Subrahmanijan Chandrasekhar, *Truth and Beauty: Aesthetics and Motivations in Science*

4.1 Introduction

Small catchments worldwide are well adapted for conducting research on factors that influence the rates and magnitude of weathering and erosion. Knowledge of the factors that affect erosion and weathering, such as climate, vegetation, lithology, and solute fluxes are normally better constrained, or at least measured more accurately in these smaller catchments, as opposed to larger river basins (Mackenzie et al., 1967; Pačes, 1983; Velbel, 1985). Larger Himalayan catchments, such as the Narayani (see Chapter 5), the Karnali, the Kosi, or more broadly the entire Ganga-Brahmaputra system, traverse larger areas and more diverse lithology, vegetation, and climates (West et al., 2002). Thus, the weathering budget at these large scales averages the lithologic and climate diversity allowing more accurate estimates of the overall silicate to carbonate proportions of weathering. On the other hand, the well-constrained nature of small-scale basins makes them ideally suited to the study of weathering processes and their impact on the overall dynamics of such a large and diverse system as the Himalaya (West et al., 2002). Pačes (1983) proposed that the annual weathering flux in a small catchment is equal to total annual stream discharge. If so, analyzing the discharge of small Himalayan catchments can provide direct weathering flux estimates that are then comparable with those of both major Himalayan and global rivers (West et al., 2002). The links between erosion and chemical weathering are not currently known on a 'micro-scale' or mechanical scale, but any advances in this field will likely be made while studying small catchments where parameters such as local climate, vegetation, and lithology are well-constrained (West et al., 2002).

Past studies reveal that climatic parameters such as precipitation/runoff, temperature, and vegetation exert important controls on the chemical weathering of silicates (Dessert et al., 2001; Velbel, 1993; Bluth and Kump, 1994; White et al., 1999; West et al., 2005). However, physical erosion has also been found to be closely linked to chemical weathering (Bluth and Kump, 1994; Gaillardet et al., 1999; France-Lanord et al., 2003; Stallard, 1995; Riebe et al., 2001). Finally, the role of lithology in climate forcing may be important as well (Stallard and Edmond, 1983; Bluth and Kump, 1994; English et al., 2000; Dessert et al., 2003; Edmond et al., 1996; Louvat and Allègre, 1997). Consequently, more recent studies propose a combined approach in which silicate weathering is governed by climatically controlled chemical denudation under circumstances of high material supply and fast removal processes (kinetically limited) or by erosionally controlled chemical weathering in times of low material supply and slow removal processes (transport limited) (Riebe et al., 2004; West et al., 2005; Gabet and Mudd, 2009). Riebe et al. (2004) found that chemical weathering rates are particularly sensitive to changes in climate at higher-altitude sites and fall virtually

to zero at the highest altitudes in their study.

The Himalayas provide an ideal backdrop for weathering-related studies because they combine steep temperature and precipitation gradients with marked morphological relief and the juxtaposition of varying lithological terrains. They also pose the formidable task of interpreting stream chemistry data as a function of these varying parameters, especially when considering the temporal variations in major element (and isotope) chemistry due to seasonal precipitation and spatial variations in lithology.

The Khudi Khola is a small Himalayan catchment located in the Annapurna-Lamjung Massif. It has been studied throughout the past 10 years (2008–2018) by various researchers and is thus well constrained in terms of lithology, vegetation, climate, and solute fluxes (Gabet et al., 2008; Wolff-Boenisch et al., 2009; Puchol et al., 2014; Gallo and Lavé, 2014; Morin, 2015). The Khudi Khola is a catchment characterized by extreme monsoonal flood events, which presents a unique opportunity to study the delivery of cations to the dissolved load after landslide activation or through other processes. Previous field seasons in the Khudi during the monsoon have documented these thunderstorm events, which begin in the evening and continue throughout the night (Morin, 2015; Morin et al., 2014). Knowledge gained from studies of small catchments such as the Khudi Khola can be applied to larger catchments, both in the Himalaya and globally, to understand the processes and mechanisms at work.

Despite the fact that numerous studies have attempted to constrain weathering budgets in the Himalaya, as well as trying to understand the climatic, erosional, and tectonic processes at play via a number of methods (see Chapter 1), there is still a lack of understanding associated with these processes and how they interact. Therefore, this study develops a new application of the ^{40}K–^{40}Ca radiogenic isotope system to explore radiogenic calcium's potential to trace the relative inputs of weathered carbonate and silicate rocks as well as understand the physical and chemical weathering processes at work in the Khudi Khola.

The Khudi Khola presents a unique opportunity to study the interactions between factors affecting the magnitude of silicate weathering and its influence on stream chemistry. It includes an active landslide, which imposes periods of intense physical and chemical weathering. We study weathering and erosion processes in the Khudi Khola for the following specific reasons:

1. Lithology, precipitation, fluxes, sediment transport, and stream chemistry are well constrained by previous studies (Putkonen, 2004; Gabet et al., 2008; Wolff-Boenisch et al., 2009; Gallo and Lavé, 2014; Morin, 2015).

2. Strong seasonal variation caused by monsoon precipitation presents an exceptional opportunity to examine silicate and carbonate weathering processes and the differences between erosion/weathering and soil leaching processes in a small catchment.

3. And finally, an active landslide presents the opportunity to study physical erosion processes and the delivery of dissolved material to the river during storm events that occur in the monsoon.

4.2 Sampling and Geological/Hydrological Setting

4.2.1 Geological and Hydrological Setting

The Khudi Khola is a small (146 km^2) tributary of the Marsyandi river and is located in central Nepal to the northeast of Pokhara and to the northwest of Gorkha. The Khudi is situated just to the southeast of the Lamjung and Annapurna Massif (Figure 4.1). At Khudi Bazaar (the confluence of the Khudi and the Marsyandi), the elevation is 800 m and, to the northwest below the massifs, elevation reaches 4,930 m. This region of Nepal experiences intense rainfall, which, based on a study from Putkonen (2004), can vary between 2.6 m/year at 800 m (i.e., Khudi Bazaar) and up to 4.2 m/year at elevations of 3,200 m, which yields a high river discharge that Gabet et al. (2008) estimated at 3.54 m/year. Most (i.e., approximately 65%) of this precipitation occurs during the monsoon (Putkonen, 2004). No glaciers or snow cover occur anywhere in the catchment, which seems to have been the case at least throughout the recent Holocene (Niemi et al., 2005; Pratt-Sitaula et al., 2011; Burbank et al., 2003).

The Khudi Khola only drains the HHC (to the north) and the LH (to the south), which are separated by the Main Central Thrust (MCT). The exact position of the MCT is not known but may pass near Probi village (see Figure 4.1, red dashed line). In the HHC, there is very little human and agricultural activity as slopes become steep quite rapidly above Probi village. Approximately 75% of the catchment's area is in the HHC (Morin, 2015), which is predominantly Formation I paragneisses (Colchen et al., 1986). This gneiss contains abundant biotite, garnet, kyanite, and sillimanite, which indicates an intermediate to high metamorphic grade. In the LH, the Khudi drains medium to high-grade metapelites, micaschist, quartzite, and a massive section of dolomitic limestone just below the MCT at the hydrothermal springs ("Tatopani" in Figure 4.1; see below for its description). The LH accounts for approximately 25% of the total area of the Khudi (Morin, 2015).

A number of previous studies have estimated erosion rates in the Khudi using terrestrial cosmogenic nuclides (TCN), yielding values between 2 and 3.5 mm/year (Niemi et al., 2005; Godard et al., 2012; Puchol et al., 2014; Godard et al., 2014). These estimates are similar to estimates based on suspended load (SL) flux measurements (Gabet et al., 2008). Current erosion rates in the Khudi are approximately two times greater than erosion rates for the entire Narayani basin (Andermann et al., 2012a; Lupker et al., 2012).

Two landslides, located in the NW part of the basin in the HHC (see Figure 4.1), have been active for at least the past 40 years and contribute significantly to dissolved load geochemistry and sediment production in the Khudi (Gallo and Lavé, 2014;

Puchol et al., 2014; Morin, 2015; Niemi et al., 2005; Gallo, 2014). The larger landslide is known as the Saituti Landslide (see Figure 4.1). Landslides are largely the source of high erosion rates in this catchment, and most of the decadal-timescale mass flux has been attributed to the Saituti Landslide (Gallo and Lavé, 2014). Erosion in the LH in the Khudi Khola does produce sediments but these are immediately washed away by the Khudi's characteristically strong discharge and do not remain in the catchment (Morin et al., 2014; Morin, 2015).

A detailed review of bedrock compositions in the Khudi Khola can be found in Morin (2015). Due to the fact that the rocks, sediments, and soils analyzed in this study were collected in the same areas as the study of Morin (2015), the major elemental compositions (see Figure 4.3) are in good agreement with the compositional variations defined by Morin (2015) for these sample types. A short summary follows:

- **Bedrock**: Bedrock geochemistry is derived from extensive field campaigns and studies from 1970 to 2014 (Pecher, 1978; Colchen et al., 1986; Brouand, 1989; Barbey et al., 1996; Morin, 2015). Bedrock from the Khudi Khola can be defined as meta-sedimentary with varying lithologies and compositions including sandstones, pelites, quartzites, and marbles (Pecher, 1978; Colchen et al., 1986). Rocks from the LH and HHC portions of the basin have quite similar Fe/Al, K/Al, and Mg/Al ratios, despite less compositional variability in the HHC compared with the LH. On the other hand, there are clear differences between the concentrations of Na, Ca, and H_2O^+ in the LH and HHC (Morin, 2015). The concentrations of Ca and Na in the HHC are 3–4 times higher than in the LH (Morin, 2015), and $[H_2O^+]$ is significantly lower in the HHC compared with the LH, probably due to water loss during high-temperature metamorphism of the HHC.

- **Bank Sediment and Pebbles**: According to Morin (2015), bank sediments and pebbles, in most cases, display very little alteration and are comparable, compositionally, to bedrock compositions (Figure 4.3 here and Figure 4.2.2 in Morin (2015)). While some elements (i.e., Fe, K, Mg, and Na) are found in concentrations similar to those of suspended sediments, some pebbles have significantly higher Ca concentrations, due probably to the pristine nature of the pebbles compared with the suspended sediments or the presence of small amounts of metamorphic carbonate (Morin, 2015).

- **Soils**: Weathering in soils is generally characterized by a continuous loss of mobile elements (i.e., Ca, Na, K, and Mg) (Kump et al., 2000; White and Brantley, 2003; Morin, 2015; Gardner and Walsh, 1996; Brantley and Lebedeva, 2011) from

the basement rock to the surface. The loss of these mobile elements also induces certain changes in mineralogy such as vermiculisation, goethite formation, and the transformation of feldspar into smectite (Morin, 2015; Lorphelin, 1986). In the Khudi, soils are all depleted with respect to the mobile elements mentioned but do not follow a distinct trend of depletion from the basement rock to the soil horizon (see Figure 4.2.5 in Morin (2015)). Morin (2015) suggests several reasons why this trend in depletion does not exist: 1) initial bedrock compositional heterogeneity dominates weathering-induced cation losses, 2) colluvial and soil creep can possibly generate perturbed soil profiles, and 3) the weathering front may be too deep to actually sample real protolith.

- **Landslide Pebbles and Sediment**: Both pebbles and sediment that derive exclusively from the Saituti Landslide have major elemental compositions similar to the suspended load in the Khudi Khola, except for slightly elevated Na and Ca concentrations (Morin, 2015). Pebbles and sediments formed on the hill slope of the landslide represent the most accurate estimate of HHC bedrock in the Khudi Khola and have compositions that are very similar to the composition of HHC Formation I gneisses, which indicates that the magnitude of alteration is quite low (Morin, 2015).

The Khudi is mainly composed of deciduous forest below elevations of 3,500 m. Above this elevation the Khudi is characterized mainly by shrubby or barren landscapes. Most human habitation occurs at or below the village of Probi (Figure 4.1).

4.2.2 Sampling and Geochemical Characteristics

Figure 4.1 shows the location of each sample analyzed in this study and Table 4.1 gives detailed information about the collection of each sample. The Khudi Khola was chosen because it has been studied quite extensively by researchers at CRPG (Evans et al., 2004; Garzanti et al., 2007; Gallo and Lavé, 2014; Puchol et al., 2014; Morin, 2015; Attal and Lavé, 2006; Gallo, 2014) and thus is well constrained in terms of fluxes, lithology, vegetation, climate, and landslide dynamics. The Khudi has also received attention from researchers outside of CRPG (Gabet et al., 2008, 2004; Wolff-Boenisch et al., 2009; Craddock et al., 2007; Martin et al., 2007).

4.2.2.1 Geochemistry of sediments, pebbles, and soils

Table 4.2 displays the major element compositions for sediments, landslide pebbles, and soils discussed below (these data are from Morin (2015) and were analyzed at the Service d'Analyses des Roches et des Mineraux, SARM, CRPG, Nancy, France;

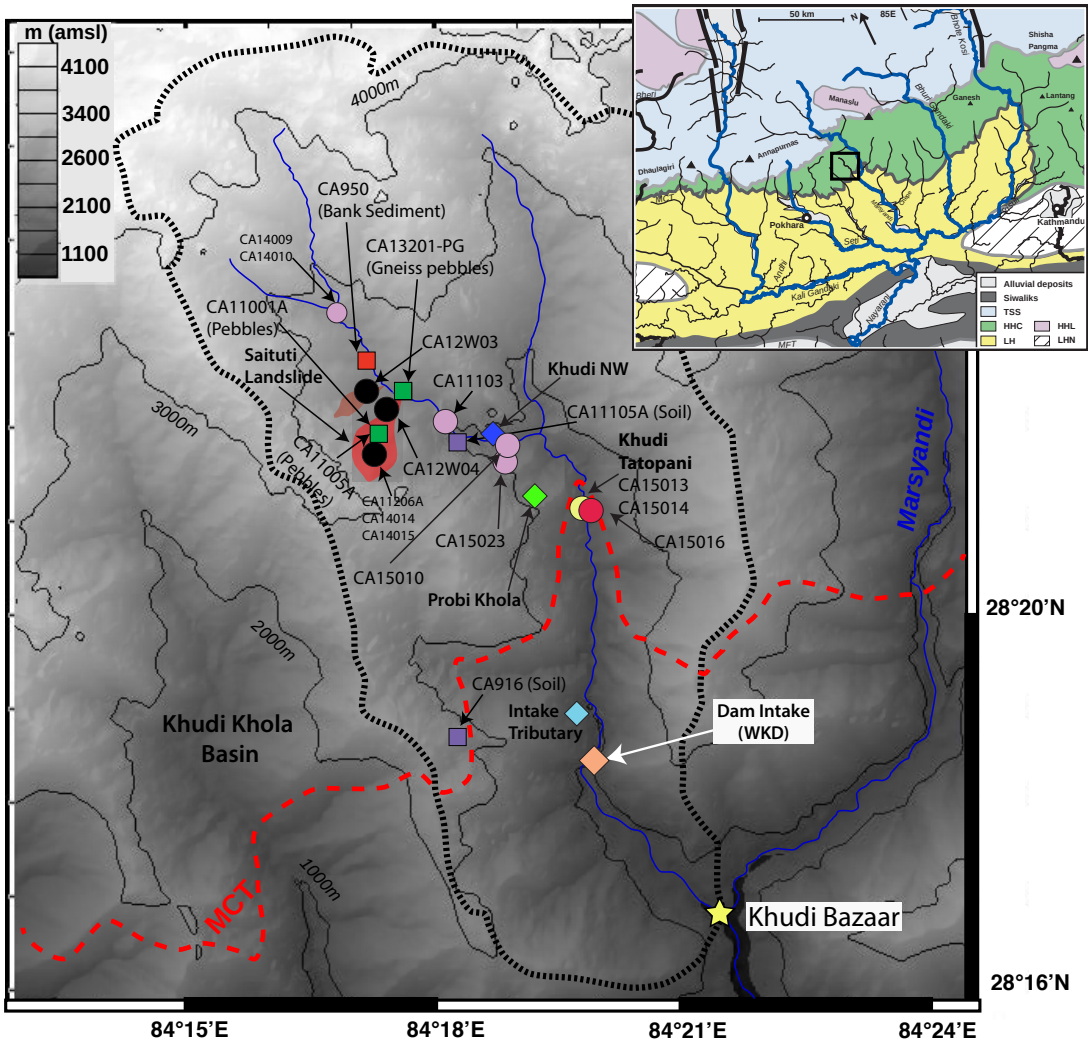

Figure 4.1 – *Location of the Khudi Khola in the Marsyandi basin, Central Nepal (modified after Morin (2015)). Detailed sampling locations in the Khudi basin: red and brown areas show the active landslide areas and the dashed red line shows the position of the MCT (Main Central Thrust). Also shown (as diamonds) are the locations for hourly time series sampling from this and previous studies (i.e., the Dam Intake – WKD, Intake Tributary, Probi Khola, and Khudi NW). Circles represent water samples and square samples represent sediment, pebble, and soil samples. The sample color-code is as follows: pink circles indicate dissolved load HHC samples (above the MCT), black circles denote dissolved load samples taken from the landslides (i.e., hydrothermal springs and small streams that traverse the landslide), light-yellow circles show two hydrothermal samples collected at the Tatopani (hot spring) close to the Khudi river, while the red circle indicates the nearby river water sample, and red, purple, and green squares respectively denote sediment, soil, and landslide pebble samples collected at several locations in the Khudi Khola basin. This color-code scheme is used in all following figures.*

Table 4.1 – *Sample Locations and descriptions for the samples analyzed in this study.*

Sample	Formation	Type	Date	Time	Longitude	Latitude	Altitude
Dissolved Load							
Khudi Intake - 2013							
WKD34606[a]	HHC+LH	River Water	July 24, 2013	16h50	84.194836	28.181961	975
WKD34701[a]	HHC+LH	River Water	July 25, 2013	0h30	84.194836	28.181961	975
WKD34702[a]	HHC+LH	River Water	July 25, 2013	02h45	84.194836	28.181961	975
WKD34703[a]	HHC+LH	River Water	July 25, 2013	04h00	84.194836	28.181961	975
WKD34704[a]	HHC+LH	River Water	July 25, 2013	05h20	84.194836	28.181961	975
WKD34707[a]	HHC+LH	River Water	July 25, 2013	10h30	84.194836	28.181961	975
Khudi Intake - 2015							
1	HHC+LH	River Water	July 29, 2015	11h00	84.194836	28.181961	975
2	HHC+LH	River Water	July 29, 2015	16h00	84.194836	28.181961	975
3	HHC+LH	River Water	July 29, 2015	21h00	84.194836	28.181961	975
4	HHC+LH	River Water	July 30, 2015	00h00	84.194836	28.181961	975
5	HHC+LH	River Water	July 30, 2015	01h00	84.194836	28.181961	975
6	HHC+LH	River Water	July 30, 2015	02h00	84.194836	28.181961	975
7	HHC+LH	River Water	July 30, 2015	03h00	84.194836	28.181961	975
8	HHC+LH	River Water	July 30, 2015	04h00	84.194836	28.181961	975
9	HHC+LH	River Water	July 30, 2015	05h00	84.194836	28.181961	975
10	HHC+LH	River Water	July 30, 2015	06h00	84.194836	28.181961	975
11	HHC+LH	River Water	July 30, 2015	07h00	84.194836	28.181961	975
12	HHC+LH	River Water	July 30, 2015	08h00	84.194836	28.181961	975
13	HHC+LH	River Water	July 30, 2015	09h00	84.194836	28.181961	975
14	HHC+LH	River Water	July 30, 2015	10h00	84.194836	28.181961	975
15	HHC+LH	River Water	July 30, 2015	11h00	84.194836	28.181961	975
Intake Tributary							
1	HHC+LH	River Water	August 1, 2015	18h00-19h00	84.194896	28.18219	983
2	HHC+LH	River Water	August 2, 2015	00h00-01h00	84.194896	28.18219	983
3	HHC+LH	River Water	August 2, 2015	07h00-08h00	84.194896	28.18219	983
Khudi -Tatopani (Hydrothermal Springs)							
CA15013	HHC+LH	Spring Water	July 30, 2015	–	84.33151	28.34912	1005
CA15014	HHC+LH	Spring Water	July 30, 2016	–	84.33151	28.34912	1005
CA15016	HHC+LH	River Water	July 30, 2017	–	84.33151	28.34912	1005
Probi Khola							
July 31 - 17:30-18:30	HHC	River Water	July 31, 2015	17h30-18h30	84.34480	28.33483	1800
July 31 - 23:30-00:30	HHC	River Water	July 31, 2015	23h30-00h30	84.34480	28.33483	1800
August 1 - 5:30-06:30	HHC	River Water	August 1, 2015	05h30-06h30	84.34480	28.33483	1800
August 1 - 9:30-10:30	HHC	River Water	August 1, 2015	09h30-10h30	84.34480	28.33483	1800
Khudi NW							
1	HHC	River Water	July 29, 2015	12h20-14h20	84.30515	28.36517	1961
2	HHC	River Water	July 29, 2015	14h20-16h20	84.30515	28.36517	1961
3	HHC	River Water	July 29, 2015	16h20-18h20	84.30515	28.36517	1961
4	HHC	River Water	July 29, 2015	18h20-20h20	84.30515	28.36517	1961
5	HHC	River Water	July 29, 2015	20h20-22h20	84.30515	28.36517	1961
6	HHC	River Water	July 29, 2015	22h20-00h20	84.30515	28.36517	1961
7	HHC	River Water	July 30, 2015	00h20-2h20	84.30515	28.36517	1961
8	HHC	River Water	July 30, 2015	02h20-04h20	84.30515	28.36517	1961
9	HHC	River Water	July 30, 2015	04h20-06h20	84.30515	28.36517	1961
10	HHC	River Water	July 30, 2015	06h20-8h20	84.30515	28.36517	1961
11	HHC	River Water	July 30, 2015	8h20-10h20	84.30515	28.36517	1961
12	HHC	River Water	July 30, 2015	10h20-12h20	84.30515	28.36517	1961
13	HHC	River Water	July 30, 2015	12h20-14h20	84.30515	28.36517	1961
Khudi - HHC							
CA11103[a]	HHC	River Water	July 31, 2011	–	84.30515	28.36517	1961
CA15010	HHC	River Water	July 29, 2015	–	84.30515	28.36517	1961
CA15023	HHC	Soil Water	July 29, 2016	–	84.183011	28.210221	2514
CA14009	HHC	River Water	November 16, 2014	–	84.295567	28.37135	2231
CA14010	HHC	River Water	November 16, 2014	–	84.295567	28.37135	2231
Khudi - HHC - Landslide							
CA11206A[a]	HHC	Landslide Stream	November 8, 2011	–	84.28762	28.36248	2770
CA12w03[a]	HHC	Landslide Spring	May 2, 2012	–	84.28773	28.36248	2991
CA12w04[a]	HHC	Landslide Spring	May 2, 2013	–	84.28780	28.36226	2992
CA14014	HHC	Landslide Stream	November 17, 2014	–	84.287317	28.3623	2759
CA14015	HHC	Landslide Stream	November 17, 2014	–	84.288233	28.36232	2793
Khudi Sediment and Soil				–			
CA950[a]	HHC	Bank Sediment - Khudi NW		–	84.173861	28.222874	2449
CA11005A[a]	HHC	Lanslide Pebbles		–	84.173226	28.221844	2322
CA11001A[a]	HHC	Landslide Pebbles		–	84.173226	28.221844	2322
CA13201-PG[a]	HHC	Fine-grained gneiss pebbles		–	84.29403	28.37177	2290
CA11105A[a]	HHC	Soil		–	84.182492	28.215122	1982
CA916 (0-10)[a]	HHC	Soil Profile		–	84.2984	28.30948	2171
CA916 (410-440)[a]	HHC	Soil Profile		–	84.2984	28.30948	2171

a: Morin (2015)

see Chapter 3). Sample CA950 (see Chapter 5) was selected for Ca isotope analysis because its Nd and Sr isotopic characteristics are characteristic of sediments from the HHC (Figure 4.2) (Morin, 2015). Figure 4.2 also shows that the LH in the Khudi has distinct Sr and Nd isotopic characteristics, which allow us to distinguish between silicates in the north of the HHC and carbonate in the south of the LH. These characteristics suggest that radiogenic Ca isotopic compositions in the LH and HHC of the Khudi will be distinct and allow us to use these compositions to more accurately differentiate between silicate and carbonate weathering. Furthermore, Figure 4.2 also shows that sediments from LH streams such as the Thulo Khola near the MCT have isotopic compositions reflecting a mixture between HHC and LH sources.

The following paragraphs provide an overview of the specific solid samples that were analyzed in this study, i.e., CA950, CA11105A, CA11005A, CA1001A, CA13201-PG, and CA916 (0–10 and 410–440 cm). These samples were taken from the existing CRPG collection. Their geochemical characteristics are described in Table 4.2 and in Figure 4.3 taken from Morin (2015).

- **Sample CA950**: CA950 is a bank sediment sample collected along the NW branch of the Khudi river upstream of the landslides. It has a geochemical signature that is quite similar to HHC FI bedrock (see Figure 4.3). CA950 is characterized by Ca and Sr concentrations and K/Ca and Ca/Si ratios of 1.55 wt. %, 82.45 ppm, 1.7, and 0.023, respectively. CA 950 has a bulk ε^{143}Nd of –16 and Sr isotopic compositions of 0.75880 and 0.75280 for the silicate and leachate fraction, respectively.

- **Samples CA11001A and CA11005A**: Samples CA11001A and CA11005A were collected as two separate samples in two different locations near the middle of the Saituti landslide (see Figure 4.4, photos of both samples). Samples CA11005 and CA11001 were sorted based on their gravel sizes. Fraction "A" represents the pebbles that are in the 2–5 cm fragment range. The pebbles have different physical appearances. CA11001A appears as more weathered with reddish surface stains. It is dominantly composed of oxidized, migmatitic gneisses, with traces of sulfide oxidation. Sample CA11005A is dominantly composed of fine grain gneisses, which are slightly more calcic than the migmatitic type, with no significant traces of oxidation. CA11001A is characterized by Ca and Sr concentrations and K/Ca and Ca/Si ratios of 1.13 wt. %, 151.2 ppm, 3.26, and 0.018, respectively. CA11005A is characterized by Ca and Sr concentrations and K/Ca and Ca/Si ratios of 2.65 wt. %, 105.9 ppm, 1.3, and 0.041, respectively.

- **Sample CA13201-PG**: Sample CA13201 is a collection of more than 250 gneissic

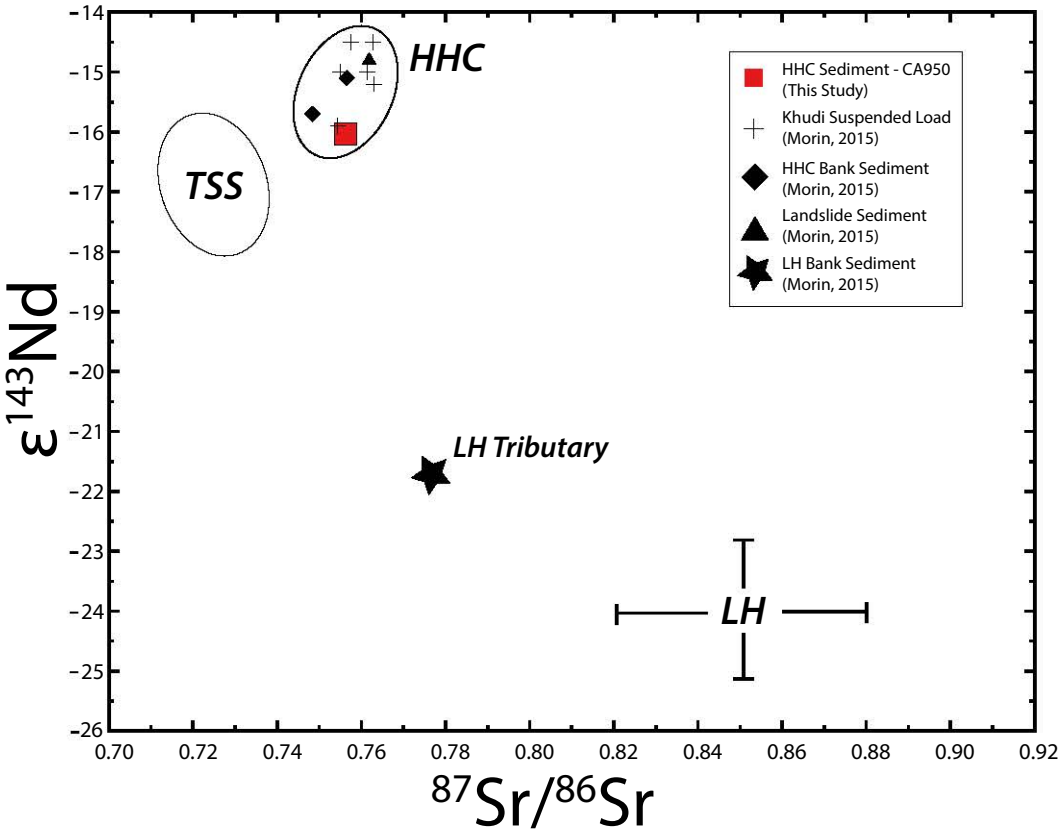

Figure 4.2 – *Sr and Nd isotopic compositions of HHC sediment (CA950) indicated by a red square with suspended load (black crosses), bank sediment (black diamonds), and landslide sediment (black triangle) derived from the HHC in the Khudi Khola shown for comparison (Morin, 2015). Sr and Nd isotopic analyses show that these river sediments have quite an exclusive range in compositions for each formation, and thus allow detailed provenance tracing. Also shown are the average compositions for the TSS (Tethyan Sedimentary Series) and LH defined by their distinct Sr and Nd isotopic characteristics (fields defined in (Galy et al., 1999, 2010; Singh and France-Lanord, 2002; Morin, 2015). The star represents a sediment sample from the Thulo Khola located in the LH near the MCT, which has an isotopic composition that reflects a mixture between HHC and LH sources.*

pebbles collected from the edge of Satiuti landslide (see Table 4.2 in Morin (2015)). Three specific types of pebbles were identified and separated into 3 groups based on their appearance and petrographic characteristics, i.e., migmatitic (MI), intermediate, and a fine-grained FI gneiss ("petit gris" = PG). A collection of pebbles of each type was collected and each type was ground together to produce three homogeneous samples. Due to beam instability during analysis, it was not possible to obtain Ca isotope data for the migmatitic and intermediate CA13201 samples. CA13201-PG is characterized by the most elevated Ca concentration at 2.87 wt. %, a K/Ca ratio of 1.0, and a Ca/Si ratio of 0.044.

- **CA11105A and CA916 (0–10 and 410–440 cm)**: These samples are soil samples collected in the Khudi. CA11105A is a surface soil sample collected near Khudi NW just south of the landslide. CA11105A has a Ca concentration at 0.55 wt. %, a K/Ca ratio of 2.47, and a Ca/Si ratio of 0.009. CA916 is a soil profile collected from the western crest of the Khudi above the MCT in the HHC. CA916 (0–10 cm) has a Ca concentration at 0.56 wt. %, a K/Ca ratio of 2.64, a Ca/Si ratio of 0.0094, and a Sr concentration of 45.41 ppm. CA916 (410–440 cm) has a Ca concentration at 1.17 wt. %, a K/Ca ratio of 1.88, a Ca/Si ratio of 0.017, and a Sr concentration of 47.46 ppm.

Figure 4.3 displays key major elements ratios in the sediment, soil, and pebble samples (CA11001A, CA11005A, CA11105A, CA13201-PG, CA950, and CA916) studied by Morin (2015), with those used in our study highlighted (i.e., Figure 4.2.2 and 4.2.4 in Morin (2015)). These data can be used to evaluate the variation and extent of weathering and mineral sorting experienced by the samples. Comparing elemental ratios as shown in Figure 4.3 provides insights into mineral sorting because quartz fragments are generally associated with coarse grain sediments whereas fine grain sediments are mainly composed of phyllosilicates such as mica and clay minerals (Lupker et al., 2011; Morin, 2015; Bouchez et al., 2011). The Al/Si ratio indicates the amount of quartz compared with phyllosilicates and is generally well correlated to grain size as coarse grains are dominated by quartz (i.e., lower Al/Si ratios), whereas fine grain sediments are enriched in micaceous and clay minerals (i.e., elevated Al/Si ratios). Furthermore, normalizing the mobile elemental ratios (i.e., Mg, Fe, K, Na, and Ca) to Al can give an idea of the degree of weathering in samples because, in most environments such as soils (Gardner and Walsh, 1996) or sediments (France-Lanord and Derry, 1997; Bouchez et al., 2012; Viers et al., 2009; Dellinger et al., 2014; Morin, 2015), Al is considered an immobile element. Larger values for mobile element to Al ratios indicate less weathering in sediments, whereas smaller values indicate more

weathering. Poorly sorted sediments, i.e., grains with differing sizes, are characteristic of the Khudi due to its turbulent nature and suggest that sediments are deposited quickly.

4.2.2.2 River water sampling and major element geochemistry

Water samples analyzed in this study were collected during various field campaigns over the past ten years, detailed in France-Lanord et al. (2003) and Morin (2015) by scientists, students and research staff members including Jerome Lave, Florian Gallo, Nicholas Puchol, Christian France-Lanord, Ananta Gajureel, Pierre Baillot, Thomas Rigaudier, Guillaume Morin, Maarten Lupker, and the Khudi Hydropower Plant (KHP) team. One of the objectives of these studies was to monitor the changes in hydrological conditions and stream chemistry during intense, daily thunderstorms that occur throughout the monsoon season. To accomplish this, detailed hourly sampling was done before, during, and after an intense rain event. In these studies, bulk water samples collected from springs, the Khudi Khola river and its tributaries were filtered through 0.2 µm PES membranes on the day of sampling, with a pressurized filtration unit coated with Teflon. These samples were stored in sealed Nalgene containers protected from light. Monsoon 2013 time series samples (WKD) were collected at the intake station of the Khudi hydropower station by trained plant-workers and stored in 2-liter containers. WKD samples containing water and sediments were stored sealed and protected from light until their monthly collection and filtration at Tribhuvan University in Kathmandu, as described in Morin (2015).

During the monsoon season of 2015, I participated in a field campaign with Christian France-Lanord, Thomas Rigaurdier, and Ananta Gajurel. The objective of this field season was to take hourly samples of the Khudi Khola and its tributaries and springs during intense rainfall events, as was previously done between 2010 and 2014. Water samples were collected from the riverside at various points throughout the catchment (see Figure 4.1), filtered through 0.2 µm PES Millipore filters, and stored in bottles free of air. One drop of 15N-distilled HNO_3 was added to each bottle to acidify the water. With the help of workers at the KHP, we were able to simultaneously collect samples at both Khudi NW and the Intake Station. Samples at Khudi NW were collected using an autosampler device that was placed on the banks of the river with a pipe that extended into the water. The autosampler was programmed to collected several milliliters every 20 minutes over the course of a 2 hour period, which began at 12h20 on July 29, 2015 and continued until July 30, 2015 at 14h20. Samples at the intake station at KHP were collected by workers in 2 L bottles from the side of the river.

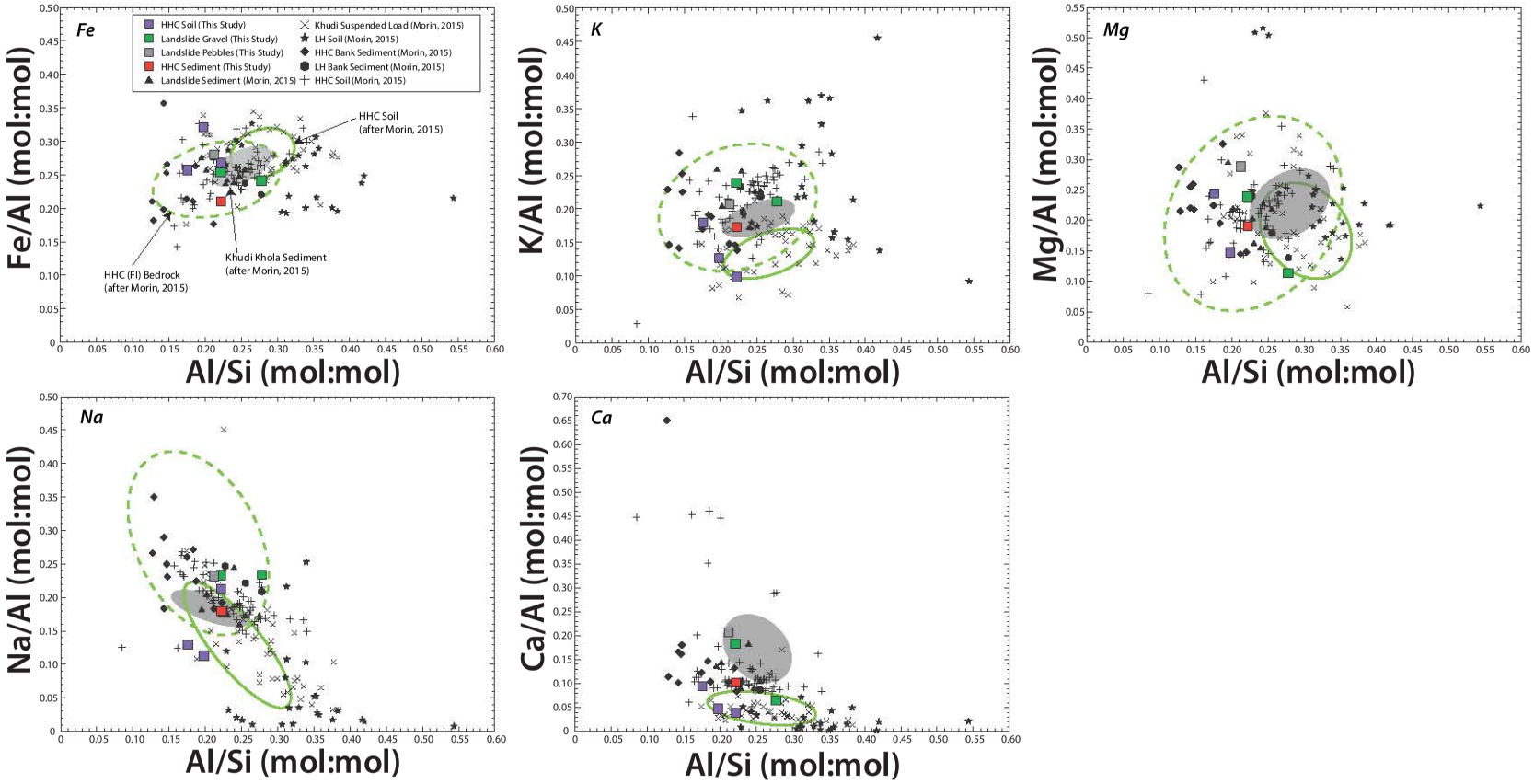

Figure 4.3 – *Compositions of soils and landslide sediments, river sediments from small stream, tributaries and the Khudi Khola based on mobile molar elemental ratios, normalized to Al (Fe/Al, K/Al, Mg/Al, Na/Al, and Ca/Al), plotted against the Al/Si ratio. The figure is taken from Morin (2015). The Al/Si ratio is a good indicator of the amount of quartz compared with phyllosilicates and is generally well correlated to grain size as coarse grains are dominated by quartz (i.e., lower Al/Si ratios), whereas fine grain sediments are enriched in micaceous and clays minerals (i.e., elevated Al/Si ratios). Symbols are as follows: suspended load (black X), LH soil (black stars), HHC bank sediment (black diamonds), LH bank sediment (black circles), HHC soils (black crosses), landslide sediment (black triangles), HCC soil (this study; purple squares), landslide gravel (samples CA11001A and CA11005A, this study; green squares), landslide pebbles (sample CA13201-PG, this study; gray square), HHC sediment (this study; red square). All black symbols are data from Morin (2015). Ellipses display 1σ standard deviation (68% confidence interval) after Morin (2015).*

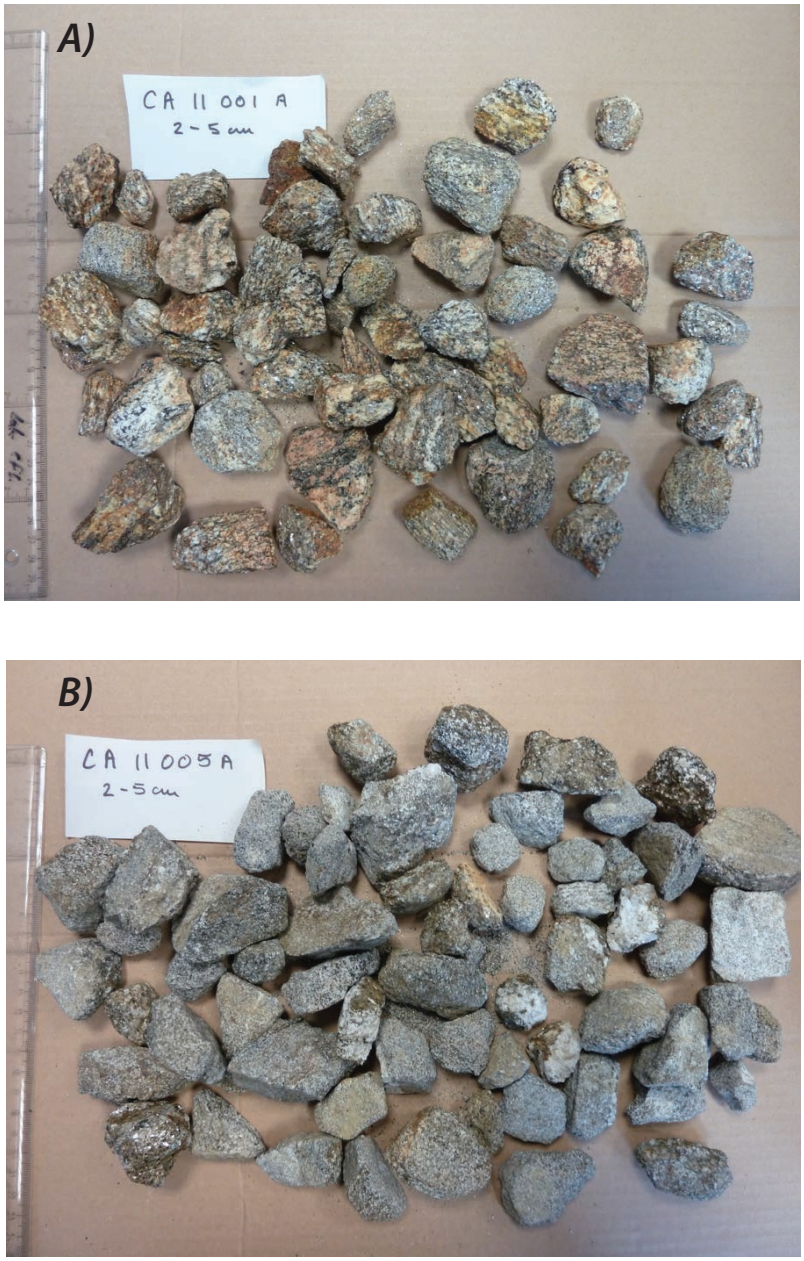

Figure 4.4 – *Pictures of pebbles/landslide sediment of samples CA11001 and CA11005. These samples are pebbles collected at two different locations near the middle of the Saituti landslide. Each was sorted based on grain size with the 2-5 cm fractions (the "A" fractions) shown here. CA11001A is dominantly composed of oxidized, migmatitic gneisses, with traces of sulfide oxidation, while CA11005A is mostly composed of fine grain gneisses, which are slightly more calcic than the migmatitic type, with no significant traces of oxidation. Each of these samples were then ground together and homogenized, which is a possible reason for heterogeneities observed in radiogenic Ca analyses (see section 4.3.1).*

Table 4.2 – *The geochemical compositions of the whole-rocks and sediments analyzed in this study.*

Sample	Type	Formation	SiO_2	Al_2O_3	Fe_2O_3	MnO	MgO	CaO	Na_2O	K_2O	TiO_2	P_2O_5	Total	Al/Si	Ca/Si	Na/Al	Ca/Al	K/Al	Fe/Al	Mg/Al	K/Ca	Sr
			wt. %											mol:mol								ppm
CA950	Bank Sediment	HHC	73.40	13.85	4.57	0.09	2.08	1.55	1.51	2.21	0.48	0.11	99.85	0.22	0.02	0.18	0.10	0.17	0.21	0.19	1.70	82.45
CA11005A	2-5 cm gneiss pebbles	Landslide	69.89	13.14	5.23	0.09	2.48	2.65	1.87	2.90	0.62	0.18	99.06	0.22	0.04	0.23	0.18	0.24	0.25	0.24	1.30	105.9
CA11001A	2-5 cm gneiss pebbles	Landslide	67.38	15.88	6.00	0.12	1.43	1.13	2.26	3.10	0.70	0.16	98.16	0.28	0.02	0.23	0.07	0.21	0.24	0.11	3.26	151.2
CA13201-PG	Fine-grained gneiss pebbles	Landslide	69.66	12.55	5.51	0.09	2.86	2.87	1.77	2.4	0.68	0.23	98.62	0.21	0.04	0.23	0.21	0.21	0.28	0.29	1.00	–
CA11105A	Soil	HHC	66.27	12.49	5.24	0.03	2.35	0.55	1.62	1.13	0.68	0.13	90.48	0.22	0.01	0.21	0.04	0.10	0.27	0.05	2.47	–
CA916 (0-10)	Soil	HHC	63.78	10.71	5.39	0.04	1.25	0.56	0.74	1.25	0.68	0.15	84.54	0.20	0.01	0.11	0.05	0.13	0.32	0.15	2.64	45.41
CA916 (410-440)	Soil	HHC	74.45	11.12	4.48	0.07	2.15	1.17	0.88	1.84	0.65	0.15	96.94	0.18	0.02	0.13	0.10	0.18	0.26	0.24	1.88	47.46

In Figure 4.1, there are a number of different types of water samples. Samples include river water samples from the main Khudi Khola River at the Khudi Dam Intake (WKD34606, WKD34701, WKD34702, WKD34703, WKD34704, and WKD34707), at the Intake Tributary (time series sampling, Table 4.1), at Probi Khola (time series sampling, Table 4.1) at Khudi NW (time series sampling, Table 4.1), and above the MCT in the HHC (CA11103, CA15010, CA14009, and CA14010). A sample of soil water (CA15023) was collected in 2015 near Khudi NW. Hydrothermal spring water was collected just below the MCT in the LH at "Tatopani" (see description below; CA15013 and CA15014) as well as a sample of the main Khudi Khola at the hydrothermal spring. In the landslide, water was collected from landslide streams (CA11206A, CA14014, and CA14015) as well as from cold water springs in the landslide (see description below; CA12w03 and CA12w04).

Tables 4.3 (water samples analyzed for radiogenic Ca) and 4.4 (2015 monsoon time series sampling not analyzed for radiogenic Ca) list the major element geochemistry of the dissolved load for the Khudi Khola. The dissolved load of the Khudi, as a result of the interaction between physical and chemical erosion, exhibits geochemical compositions that reflect the geology of the HHC in the upper Khudi and a mix of HHC and LH in the southern part of the basin, below the MCT. An interesting observation, more elaborately described in Morin (2015) , is that both the sediment flux and the concentrations in the dissolved load measured by Gabet et al. (2008) and Wolff-Boenisch et al. (2009) are dilute (although this is not systematic) compared with concentrations reported for the dissolved load between 2010 and 2014 by Morin (2015). This is due, in part, to the activation of the Saituti landslide, a consequence of an intensifying monsoon, which significantly increased the flux of suspended sediment and increased the amount of sediment available for alteration and dissolution into the dissolved load (Gallo and Lavé, 2014; Morin, 2015).

Figure 4.5 plots the geochemical composition of the dissolved load analyzed in this study in classic major element ratio diagrams (Gaillardet et al., 1997, 1999). The compositions of the Khudi intake samples analyzed in this study resemble those of Khudi intake samples reported in Morin (2015) for earlier years. Apart from samples collected at springs located near the MCT (i.e., at Khudi Tatopani; see the following paragraph) or in the Satiuti Landslide (see below), the dissolved load [Ca] of the mainstem Khudi is highly variable and dilute when compared with those of rivers draining the Tethyan Sedimentary Series (TSS) (see Chapter 5), ranging from 50 to 600 µmol/L (Figure 4.5C). Despite a large range of scatter (Figure 4.5A–B), dissolved load samples tend to form two pole mixing lines between a silicate and carbonate end-member (Figure 4.5A–B). Dissolved load samples collected from above the MCT tend to cluster towards the silicate end-member whereas samples collected from below the

MCT tend to cluster closer to the carbonate end-member. Ca/Na ratios range from 0.1 to approximately 10, where most dissolved load samples from the Intake Station are characterized by Ca/Na ratios between 2 and 8. Sr/Ca ratios (Fig. 4.5D) are mostly less than 0.002. Mg/Na ratios (Fig. 4.5B) range from 0.2–5 but are mostly concentrated between 0.5 and 2.

Tatopani (hot water) (see Figure 4.1) is a generic name, in Nepali, that refers to hot springs that are usable by travelers. Here, we use Tatopani to signify the location of hydrothermal springs in the Khudi. The tatopani in the Khudi Khola is located just below the MCT in the LH, and is characterized by 1) high, or higher than ambient, temperatures and 2) elevated carbonate content, which is connected to CO_2 enrichment at depth (Evans et al., 2004). Surface water in these hot springs is characterized by elevated levels of CO_2 that have a metamorphic origin. This is not the case for springs in the landslide, which are cold water springs.

On average, the chlorine and sulfate concentrations in the Khudi are between 3 and 7 µmol/l (and up to 34 µmol/l) and between 60 and 200 µmol/l (and up to 3,300 µmol/l), respectively. These dissolved load Cl^- values are similar but depleted relative to the values from previous studies, such as Galy and France-Lanord (1999) and Wolff-Boenisch et al. (2009) and similar for the $SO_4{}^{2-}$ concentrations. Riverine chlorine originates from one of three sources: 1) An atmospheric contribution, 2) hydrothermal springs (Tatopani) on the bank of the Khudi near the village of Probi near the MCT and 3) cold water springs in the landslide. Cold water landslide springs are not an adequate source of riverine chlorine nor are atmospheric contributions (Galy and France-Lanord, 1999; Wolff-Boenisch et al., 2009). Hydrothermal springs at Tatopani, however, produce water that is highly elevated in chlorine, i.e., between 350 and 1,224 µmol/l, with even higher concentrations reported in work from Evans et al. (2001, 2004, 2008).

Riverine SO_4 originates from the latter two sources, i.e., at hydrothermal and cold water springs. The hydrothermal springs produce water with $SO_4{}^{2-}$ concentrations between 200 and 575 µmol/l, whereas the cold water landslide springs produce water with $SO_4{}^{2-}$ concentrations between 200 and 3,300 µmol/l, and even higher $SO_4{}^{2-}$ have been reported in Galy and France-Lanord (1999) and Evans et al. (2001, 2004, 2008). In the Khudi, $SO_4{}^{2-}$ balances nearly 30% of the cationic charge. The main source of $SO_4{}^{2-}$ is likely sulfide oxidation occurring at landslide springs (Galy and France-Lanord, 1999; Turchyn et al., 2013). Morin (2015) concluded that despite the highly elevated concentrations of Cl^- and $SO_4{}^{2-}$, landslide and hydrothermal springs do not affect the dissolved load of the Khudi Khola and thus play an insignificant role in the geochemistry of the Khudi dissolved load.

Figure 4.6 shows the Khudi dissolved load samples plotted in a ternary diagram.

Samples from above the MCT have compositions similar to those of rivers eroding HHC gneisses defined by Galy and France-Lanord (1999), and plot between the limestone and silicate springs fields (Quade, 2003), indicating mixing between silicate and carbonate end-members, similar to Figure 4.5. Figure 4.6 shows that, in general, samples above the MCT (i.e., in the HHC) plot closer to the pure Na + K and Si poles, whereas samples from below the MCT (i.e., the Khudi Dam Intake and the Intake tributary) plot closer to the pure Mg + Ca and Ca poles.

As noted above, during field campaigns in 2013 and 2015, hourly sampling of the Khudi was conducted at the Intake Station and in the upper Khudi during the monsoon, over a period of several days. The geochemistry of hourly sampling in 2013 shows that there is a correlation between high amounts of rainfall and high discharge, at least in the studied rain event (Morin, 2015). Furthermore, this rain event, which was exceptionally intense, was characterized by significantly elevated concentrations of K, Ca, HCO_3, and SO_4 (Fig. 4.7). Initially, in the late evening, dissolved load concentrations were characterized by a normal range of values, i.e., a baseline. As the storm continued, the concentrations of K, Ca, HCO_3 and SO_4 increased and peaked between 3 and 4h. Between 10h and 12h the next morning, concentrations returned to normal, pre-storm baseline concentrations. Other elements, such as Na, Si, Cl, and Mg do not show elevated concentrations during the storm peak but rather are stable or diluted as would be expected during more intense runoff events (Morin, 2015). In contrast, hourly sampling conducted in 2015 shows no noticeable increases in elemental concentrations despite sampling through a number of rainfall events (this is discussed in more detail below; see Supplementary Tables 4.10, 4.11, and 4.12 for rainfall and discharge data from 2013 and 2015). Hourly samples taken in 2015 (Table 4.4) were thus not analyzed for their ε^{40}Ca compositions.

The process(es) that release these elements, i.e., Ca, K, Si, HCO_3 and SO_4, into the dissolved load are unknown, however, it is clear that the 2013 peak is related to direct runoff and increased suspended load transport following intense rainfall (Morin, 2015). We suspect that the high suspended load and concentration peaks could be related to the alteration of freshly ground bedrock at the edge of the landslide or a consequence of soil leaching (this is discussed in more detail below) (Morin, 2015; Morin et al., 2014).

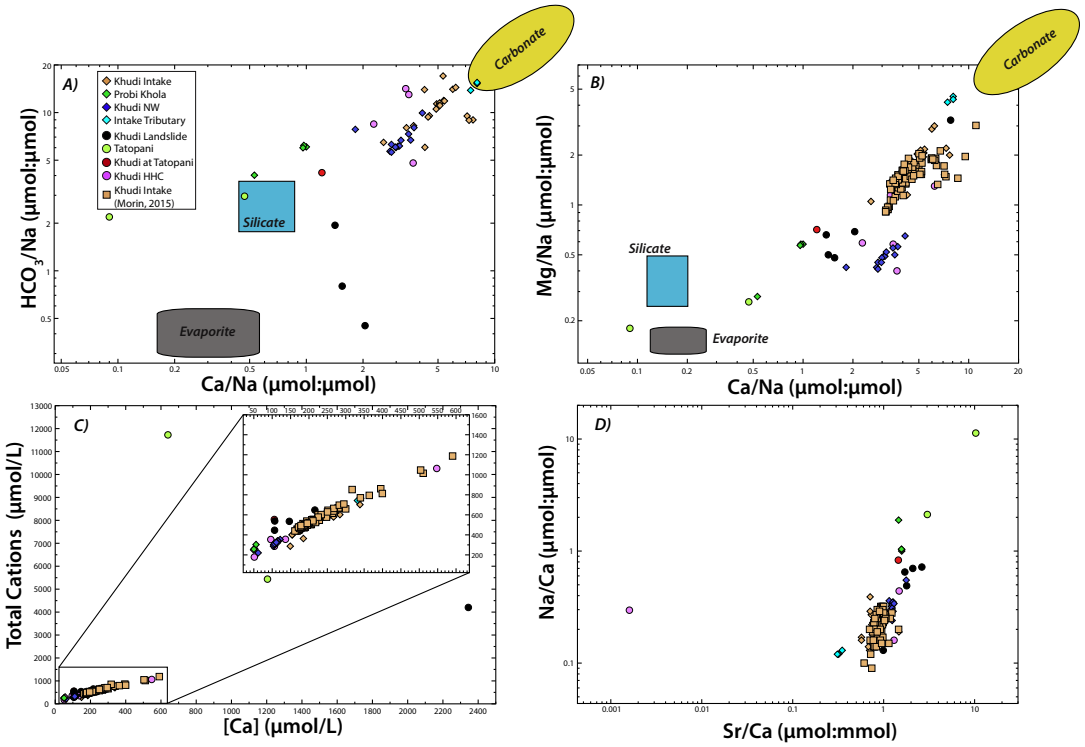

Figure 4.5 – *A) and B) Mixing diagrams using Na-normalized molar ratios in the dissolved phase of the Khudi Khola. End-member reservoirs were estimated using data on small, global rivers draining single lithologies, i.e., carbonates, silicates, and evaporites, taken from Gaillardet et al. (1999). C) Total cations (µmol/L) plotted against [Ca], where we observe that dissolved load concentrations in the HHC and below the MCT generally have [Ca] ≤ 500 µmol/L and Total cation concentrations less than 1,500 µmol/L, in contrast to several dissolved load samples collected from hydrothermal springs at the MCT and cold water springs in the Khudi Landslide, which have highly elevated concentrations of Ca and total dissolved cations. D) The Na/Ca ratio plotted against the Sr/Ca ratio for samples analyzed in this study. The sample color scheme is as follows: pink circles indicate dissolved load HHC samples (above the MCT), green circles represent the Tatopani, red circle represents the Khudi Khola main stem at the Tatopani, and black circles denote dissolved load samples taken from the landslides including both springs and streams. Also shown as diamonds are the samples collected hourly from this and previous studies, i.e., the Dam Intake – WKD (burnt orange diamonds), Intake Tributary (teal diamonds), Probi Khola (green diamonds), and Khudi NW (blue diamonds). Burnt orange squares are Dam Intake dissolved load samples from Morin (2015) for comparison.*

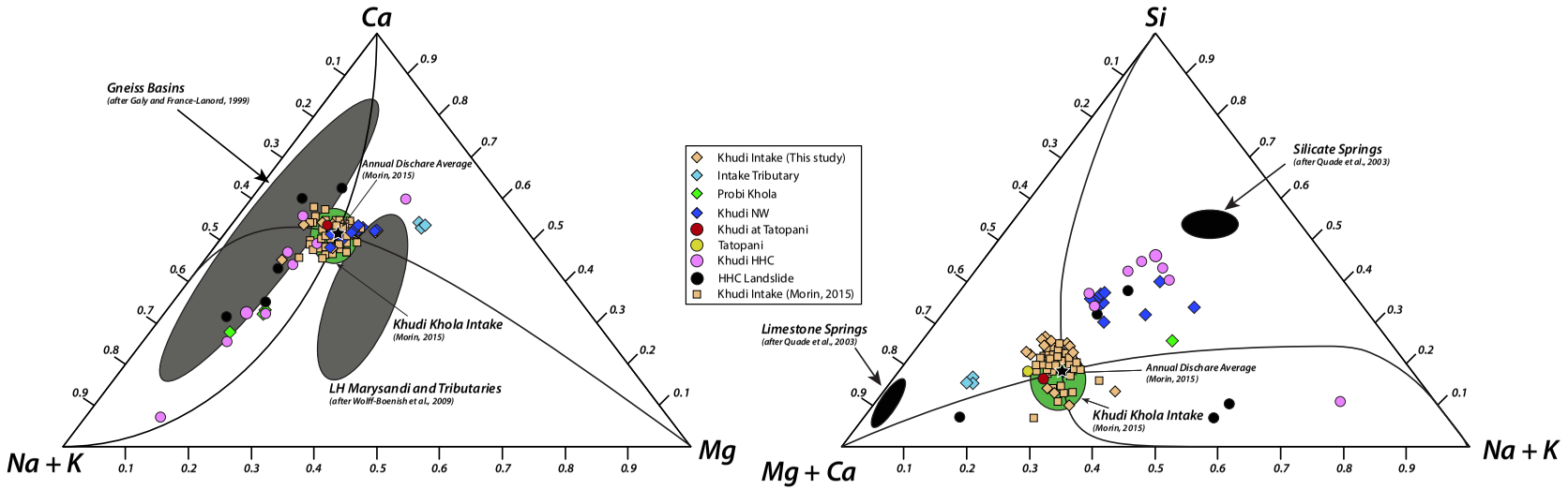

Figure 4.6 – *Triangular plots representing the relative abundances of major elements in the dissolved load of the Khudi Khola. Compositions are similar to those of other Nepalese rivers draining gneiss, silicates, and carbonates. Silicate and limestone spring compositions are from Quade (2003), Marsyandi water compositions from Wolff-Boenisch et al. (2009), and gneiss basin waters are from Galy and France-Lanord (1999). Ca and Mg are the dominant cations below the MCT, whereas Ca, Mg, K, and Na are more dominant above the MCT in the HHC. The sample color scheme is as follows: pink circles indicate dissolved load HHC samples (above the MCT), green circles represent the Tatopani hydrothermal samples, red circles represent the Khudi Khola main stem at the Tatopani. Also shown are the hourly time series samples from this and previous studies, i.e., the Dam Intake – WKD (burnt orange diamonds), Intake Tributary (teal diamonds), Probi Khola (green diamonds), and Khudi NW (blue diamonds). Burnt orange squares are Intake dissolved load samples from Morin (2015) for comparison.*

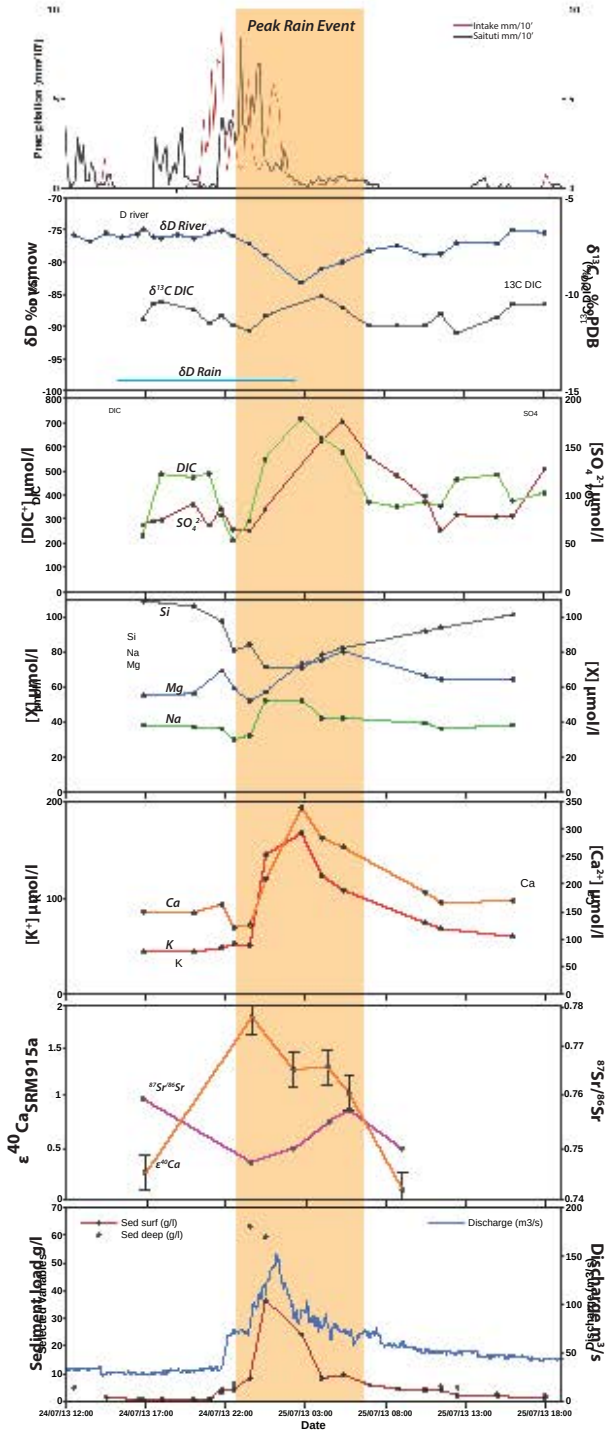

Figure 4.7 – *The dissolved load and river characteristics for the monsoon rain event in 2013 at Khudi Intake. The 2013 event was characterized by significant increases in precipitation, concentrations of DIC, SO_4^{2-}, Si, Mg, Na, Ca, and K, as well as radiogenic Sr and Ca isotopic signature, sediment load, and discharge. Despite the occurrence of a rain event in the 2015 monsoon field season (see Table 4.4), we did not observe similar increases in the dissolved load and river characteristics.*

Table 4.3 – *Dissolved load geochemistry of samples analyzed in this study for samples collected before 2015 and samples collected in 2015 that were analyzed for radiogenic Ca (see Table 4.6).*

Sample	Type	HCO_3^-	Cl^-	SO_4^{2-}	Si	Mg	Ca	Na	K	Sr
						µmol/L				
Khudi Intake - LH										
WKD34606 (July 24, 2013 16:50)	River Water	418.60				55.27	149.10	37.99	44.30	0.12
WKD34701 (July 25, 2013 0:30)	River Water	264.78	4.63	137.06	71.17	56.71	208.93	51.91	144.68	0.18
WKD34702 (July 25, 2013 2:45)	River Water	421.83	6.22	179.05	70.21	73.29	338.65	52.35	167.34	0.24
WKD34703 (July 25, 2013 4:00)	River Water	307.16	4.59	159.17	78.26	74.57	284.04	42.17	122.69	0.18
WKD34704 (July 25, 2013 5:20)	River Water	299.60	4.79	144.78	82.10	79.96	266.83	41.51	107.67	0.17
WKD34707 (July 25, 201310:30)	River Water	521.04				65.84	184.80	38.60	74.00	0.24
Khudi -Tatopani										
CA15013	Spring Water	7414.45	346.29	206.89	462.83	667.35	1204.51	2514.23	584.67	3.57
CA15014	Spring Water	15275.05	1223.58	573.55	1087.48	1276.28	639.50	6984.44	1732.04	6.36
CA15016	River Water	289.53	10.86	62.45	214.25	55.17	105.80	77.46	100.85	0.12
Khudi - HHC - Landslide										
CA11206A	River Water	169.87	2.56	124.56	193.48	49.66	146.58	95.65	49.41	0.26
CA12w03	Landslide Spring	42.54	2.31	221.56	197.64	71.10	216.07	102.61	60.13	0.35
CA12w04	Landslide Spring	783.19	2.41	3256.59	223.03	977.45	2344.31	306.66	348.59	2.31
CA14014	Landslide Stream	43.77	2.07	118.80	192.18	32.25	106.43	62.57	52.62	0.14
CA14015	Landslide Stream		2.08	209.08	222.71	46.86	106.93	69.39	92.26	0.22
Khudi - HHC										
CA11103	River Water	312.10			92.00	20.00	106.00	32.00	36.00	0.10
CA15010	River Water	215.83	9.51	3.96	9.23	17.49	51.39	15.24	84.97	0.08
CA15023	Soil Water	275.68	2.72	18.21	144.08	25.49	96.19	40.59	47.25	0.11
CA14009	River Water	148.47	2.16	82.80	124.95	18.48	136.16	38.96	37.10	0.12
CA14010	River Water		2.18	644.20	174.42	116.00	547.50	92.52	132.06	0.69

Table 4.4 – *Geochemical compositions of the dissolved load from time series sampling in the Khudi Khola from the 2015 monsoon season (these samples were not analyzed for their radiogenic Ca composition).*

Sample	HCO_3^-	Cl^-	SO_4^{2-}	Si	Mg	Ca	K	Na	Sr	IC
					µmol/L					mg/L
Intake										
July 29 - 11:00	422.28	12.69	62.28	143.44	85.37	217.62	60.77	56.49	0.14	0.4722
July 29 - 16:00	405.99	4.25	62.08	144.81	86.30	216.11	51.16	54.35	0.14	0.4627
July 29 - 21:00	391.10	4.27	62.05	144.31	81.68	210.25	50.46	53.08	0.14	0.4387
July 30 - 00:00	426.05	5.24	41.07	112.45	91.56	200.20	37.74	55.50	0.10	0.4436
July 30 - 01:00	420.04	4.13	41.14	112.54	91.91	199.44	36.57	53.95	0.10	0.6151
July 30 - 02:00	321.62	4.50	47.74	97.98	51.82	154.47	34.92	60.43	0.12	0.4605
July 30 - 03:00	312.45	3.29	50.36	99.75	52.24	154.18	33.89	60.59	0.12	0.4014
July 30 - 04:00	353.61	3.70	50.32	111.68	64.88	172.46	37.49	61.02	0.12	0.4305
July 30 - 05:00	345.39	3.55	50.62	107.56	63.15	170.36	35.68	60.37	0.11	0.4621
July 30 - 06:00	347.46	3.42	50.95	109.45	68.05	176.26	36.54	55.57	0.11	0.4057
July 30 - 07:00	371.86	5.07	53.51	116.84	73.64	188.57	41.18	56.99	0.12	0.4021
July 30 - 08:00	365.64	3.75	54.39	118.76	75.49	187.96	40.40	56.18	0.12	0.3865
July 30 - 09:00	364.10	5.01	56.10	119.05	75.58	189.70	42.26	55.32	0.12	0.4342
July 30 - 10:00	407.02	15.16	56.62	122.53	78.19	198.35	59.93	60.06	0.12	0.407
July 30 - 11:00	421.45	33.28	58.09	124.23	78.76	199.24	77.07	60.02	0.13	0.4084
Intake Tributary										
August 1 - 18:00-19:00	584.99	6.27	84.82	135.09	184.73	340.75	50.79	53.53	0.11	0.5634
August 2 - 00:00-01:00	581.61	4.28	77.01	133.49	179.92	331.77	46.43	51.29	0.10	0.5566
August 2 - 07:00-08:00	529.19	3.70	69.16	121.48	155.54	299.40	42.44	47.68	0.09	0.4888
Khudi NW										
July 29 - 12:20-14:20	192.36	7.18	59.49	125.12	21.06	121.64	43.83	41.80	0.11	0.3784
July 29 - 14:20-16:20	174.14	3.95	55.92	125.69	20.61	113.45	37.80	38.54	0.11	0.3649
July 29 - 16:20-18:20	174.18	5.34	58.61	123.79	20.86	115.83	41.15	38.55	0.12	0.3505
July 29 - 18:20-20:20	176.27	3.66	56.97	124.41	20.69	115.74	38.06	38.77	0.11	0.3654
July 29 - 20:20-22:20	176.90	3.86	56.48	125.58	20.96	114.86	39.02	38.74	0.12	0.4784
July 29 - 22:20-24:20	173.64	3.00	50.92	119.98	20.07	107.38	34.87	38.34	0.11	0.3359
July 30 - 00:20-02:20	173.94	6.40	21.07	71.59	15.22	61.87	29.92	41.72	0.07	0.3699
July 30 - 02:20-04:20	207.41	2.92	41.53	88.22	19.00	103.51	27.72	48.57	0.10	0.3824
July 30 - 04:20-06:20	183.64	2.62	47.77	103.15	18.86	106.52	30.68	41.56	0.10	0.3538
July 30 - 06:20-08:20	168.53	2.74	48.69	108.61	19.05	103.83	31.46	37.69	0.10	0.3226
July 30 - 08:20-10:20	178.09	9.11	49.50	109.83	18.41	106.50	37.82	37.84	0.11	0.3297
July 30 - 10:20-12:20	166.28	2.72	56.75	116.35	19.02	113.90	33.67	37.48	0.11	0.3288
July 30 - 12:20-14:20	171.91	5.46	54.86	117.57	19.43	110.92	37.92	38.32	0.12	0.3509
Probi Khola										
July 31 - 17:30-18:30	178.21	5.11	16.66	106.88	23.67	52.13	38.11	42.89	0.05	0.3695
July 31 - 23:30-00:30	224.16	33.87	18.04	103.76	23.86	56.04	72.41	46.87	0.05	0.3546
August 1 - 5:30-06:30	170.20	5.21	15.74	100.57	22.51	49.36	36.13	41.25	0.04	0.3388
August 1 - 9:30-10:30	170.79	5.53	16.67	104.99	22.76	50.14	37.37	41.55	0.04	0.3176

4.3 Ca isotopic composition results

Analytical techniques for Sr and Ca isotope geochemistry are presented in Chapter 3. Results for the Sr and Ca isotopic compositions for all samples are summarized in Tables 4.5 (landslide gravel, sediment, and soils) and 4.6 (water samples). Figure 4.8 displays the location and radiogenic Ca composition for each sample analyzed on the Khudi basin map presented in Figure 4.1. Following previously established conventions, we report $^{40}Ca/^{44}Ca$ measurements normalized to the calcium standard NIST SRM915a, using the "epsilon" notation ($\varepsilon^{40}Ca$):

$$\varepsilon^{40}Ca = \left[\frac{^{40}Ca/^{44}Ca_{Sample}}{^{40}Ca/^{44}Ca_{Standard}} - 1 \right] \times 10^4 \tag{4.1}$$

Repeated analyses (N = 111) of the NIST SRM 915a standard over the three-year period of this study yielded $^{40}Ca/^{44}Ca_{SRM915a}$ = 47.15072 ± 0.00118 (2 S.D. = 40 ppm). The Supplementary Materials (Tables 4.7, 4.8, and 4.9) contain a more extensive dataset for each Ca analysis.

4.3.1 Sediment, pebble and soil samples

Figure 4.9 shows the variation in the $\varepsilon^{40}Ca$ composition of the sediment, landslide pebbles, and soil samples and Figure 4.10 plots the average $\varepsilon^{40}Ca$ compositions of each of these samples against their major elemental ratios (only the silicate fraction is shown for sediment sample CA950). For sediment sample CA950, Ca and Sr isotopic analyses were performed on both the carbonate fraction, obtained by leaching with HCl, and the silicate fraction, comprising the residue. The $^{87}Sr/^{86}Sr$ of the silicate fraction is 0.75880, which is more radiogenic than the carbonate fraction, which has a ratio of 0.75280. The carbonate $^{87}Sr/^{86}Sr$ ratio is significantly out of error from the silicate value, but nevertheless is much more radiogenic than marine carbonate values, which never exceed 0.71 in the Phanerozoic (Veizer et al., 1997). The Sr in the carbonate comes much closer to reequilibration with the silicate than the Ca does, but that reequilibration was not complete. The carbonate fraction of CA950 is non-radiogenic in Ca ($\varepsilon^{40}Ca$ = –0.06) while the silicate fraction is radiogenic ($\varepsilon^{40}Ca$ = +1.85) (see also Chapter 5 for a more complete discussion). The presence of non-radiogenic Himalayan carbonates confirms the conclusions made by Caro et al. (2010), i.e., that carbonates have retained the $\varepsilon^{40}Ca$ signature of the mantle (= 0) over geological time.

For the pebble, soil, and sediment samples analyzed in this study, mainly from the upper Khudi, figures 4.9 and 4.10 show that the $\varepsilon^{40}Ca$ composition is variable (ranging from +0.01 to +3.45) and thus, similar to Nd isotopes, depends on protolith age and time-averaged K/Ca ratio. No clear correlations are observed, but the sample with the highest K/Ca and Al/Si ratios and second highest K/Al ratio has

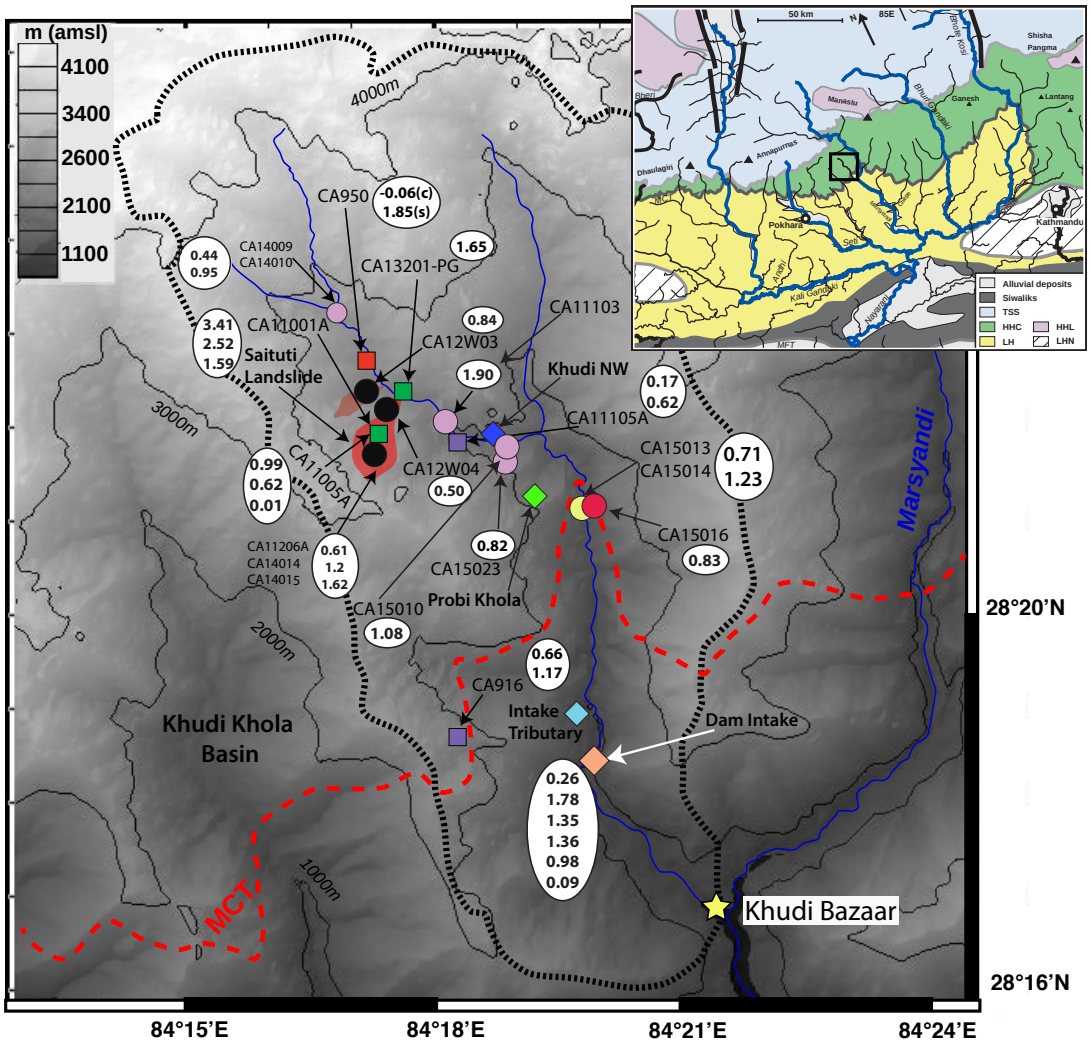

Figure 4.8 – *Map of the Khudi Khola catchment showing $\varepsilon^{40}Ca$ compositions of water, sediments, pebbles, and soil samples. Sampling locations in the Khudi basin: red areas show the active landslide areas and the dashed red line the MCT position. Also shown are the sampling locations for hourly time series sampling from this and previous studies (i.e., the Dam Intake – WKD, Intake Tributary, Probi Khola, and Khudi NW). Circles represent water samples and squares represent sediment, pebble, and soil samples. The sample color-code is as follows: light pink circles indicate dissolved load HHC samples (above the MCT) and the dark pink circle indicates the soil water sample (CA15010) from above the MCT, yellow circles represent the Tatopani hydrothermal springs, red circles represent the Khudi Khola main stem at the Tatopani, black circles denote dissolved load samples taken from the landslides (both springs and streams), and red, purple, and green squares respectively denote sediment, soil, and pebble samples collected at various locations in the Khudi Khola basin.*

Table 4.5 – *$\varepsilon^{143}Nd$, $^{87}Sr/^{86}Sr$, and $\varepsilon^{40}Ca$ compositions of whole-rock and bed load sediments.*

Sample	Type	Formation	ε^{143}Nd	^{87}Sr/^{86}Sr Silicate	^{87}Sr/^{86}Sr Carbonate	ε^{Ca}Ca WR	$\pm^a$	Average ε^{Ca}Ca	$\pm^a$	ε^{Ca}Ca Silicate	$\pm^a$	ε^{Ca}Ca Carbonate	$\pm^a$
CA950	Bank Sediment	HHC	-16	0.75880	0.75280	–	–	–	–	1.85	0.30	-0.06	0.30
CA11005A	Gneiss Pebbles	Landslide	–	–	–	0.01	0.27			–	–	–	–
			–	–	–	0.62	0.36	0.54	0.57	–	–	–	–
			–	–	–	0.99	0.35			–	–	–	–
CA11001A	Gneiss Pebbles	Landslide	–	–	–	1.59	0.28			–	–	–	–
			–	–	–	2.52	0.4	2.51	0.62	–	–	–	–
			–	–	–	3.41	0.38			–	–	–	–
CA13201-PG	Fine-grained gneiss pebbles	Landslide	–	–	–	1.65	0.4	–	–	–	–	–	–
CA11105A	Soil	HHC	–	–	–	0.17	0.33	0.40	0.50	–	–	–	–
			–	–	–	0.62	0.37			–	–	–	–
CA916 (0-10)	Soil	HHC	–	–	–	1.17	0.49	–	–	–	–	–	–
CA916 (410-440)	Soil	HHC	–	–	–	0.66	0.38	–	–	–	–	–	–

a: Uncertaintes are at 2 S.D.

Table 4.6 – *$^{87}Sr/^{86}Sr$ and $\varepsilon^{40}Ca$ compositions of water samples, including dissolved load, hydrothermal springs and soil water.*

Sample	Type	$^{87}Sr/^{86}Sr$	$\varepsilon^{40}Ca$	±	Average $\varepsilon^{40}Ca$	±
Khudi Intake - LH						
WKD34606 (July 24, 2013 16:50)	River Water	0.75947	0.21	0.3	0.26	0.38
			0.30	0.23		
WKD34701 (July 25, 2013 0:30)	River Water	0.74495	1.78	0.29	–	–
WKD34702 (July 25, 2013 2:45)	River Water	0.74995	1.35	0.26	–	–
WKD34703 (July 25, 2013 4:00)	River Water	0.75437	1.36	0.24	–	–
WKD34704 (July 25, 2013 5:20)	River Water	0.75865	1.01	0.3	0.98	0.47
			0.94	0.36		
WKD34707 (July 25, 201310:30)	River Water	0.74995	0.01	0.35		
			0.13	0.28	0.09	0.64
			0.14	0.37		
Khudi -Tatopani (Hydrothermal Springs)						
CA15013	Spring Water	0.75389	1.23	0.37	–	–
CA15014	Spring Water	0.75464	0.71	0.41	–	–
CA15016	River Water	0.74555	0.83	0.33	–	–
Khudi - HHC - Landslide						
CA11206A	River Water	0.74650	1.62	0.32	–	–
CA12w03	Landslide Spring	0.74767	0.93	0.29	0.84	0.40
			0.75	0.28		
CA12w04	Landslide Spring	0.75189	0.38	0.34		
			0.52	0.3	0.50	0.65
			0.59	0.38		
CA14014	Landslide Stream	–	1.2	0.32	–	–
CA14015	Landslide Stream	0.74626	0.61	0.39	–	–
Khudi - HHC						
CA11103	River Water	0.74767	1.90	0.3	–	–
CA15010	River Water	0.72882	1.08	0.29	–	–
CA15023	Soil Water	0.73568	0.82	0.34	–	–
CA14009	River Water	–	0.44	1.03	–	–
CA14010	River Water	–	0.95	0.45	–	–

the most radiogenic Ca value (as is logical since this sample is rich in phyllosilicates). Unfortunately, the Sr isotopic compositions for these samples have not been analyzed.

ε^{40}Ca values of material derived exclusively from the landslide vary between +0.01 (least radiogenic analysis of CA11005A) and +3.41 (most radiogenic analysis of CA11001A). Unfortunately, these extreme values are not confirmed by the replicates (Figure 4.9 and Table 4.5). Both CA11001A and CA11005A are 2–5 cm pebble samples. Despite being collected in almost the same location, these samples have substantially different major element compositions (Table 4.2) and are visually distinguishable (see above and Figure 4.4). CA11005A, the less weathered sample (see Figure 4.4) has more than twice the amount of Ca for similar concentrations of K in the samples. Each sample is composed of 50–60 pieces of gneiss, and therefore has an internal heterogeneity. We would not expect the presence of this heterogeneity in isotopic compositions, due to homogenization during powdering of the rock. This, however, may be the case if the pebbles included in each sample exhibit a large range in Ca isotopic composition. This also depends on the mass of the powder that was analyzed, which was 0.12 g for each aliquot of CA11001A, and 0.06 g for each aliquot of CA11005A. These quantities were calculated based on the amount of Ca needed for an analysis. According to Morin (2015), samples from the landslide, especially the pebbles, represent the most accurate compositional estimate of HHC crust in the Khudi area.

For soils, radiogenic Ca compositions are +0.40 $\pm$ 0.50 (CA11105A), +1.17 $\pm$ 0.49 (CA916 - 0–10 cm), and +0.66 $\pm$ 0.38 (CA916 – 410–440 cm). Given the uncertainties, these values could be considered indistinguishable. It is interesting, however, to note that for the soil profile CA916, the deepest sample (410–440 cm; +0.66) is less radiogenic than the sample collected at the surface (+1.17; 0–10 cm). This is consistent with the elevated K/Ca ratio at the top of the soil profile (2.64) as compared with the base of the soil profile (1.88). For sample CA916, [CaO] decreases from 1.17 wt. % at 4 meters depth to 0.56 wt. % at the surface and [K_2O] increases from 1.84 to 2.14 wt. % (from 4 to approximately 1 m depth) (Morin, 2015) and then decreases to 1.25 wt. % at the surface. This may be due to internal heterogeneity in the rock before weathering caused by radiogenic ingrowth, such that the loss of phases with low K/Ca ratios also led to loss of unradiogenic Ca. In Table 4.2, the total wt. % for the sediment and pebble samples all total to > 98 wt. %. For the soil samples, the totals vary from 84.5 (CA916 0–10) to 97 wt. % (CA916 410–440), which is possibly due to organic matter dilution (i.e., this would become more significant towards the soil horizon) or the presence of carbonates (resulting in high loss on ignition, LOI).

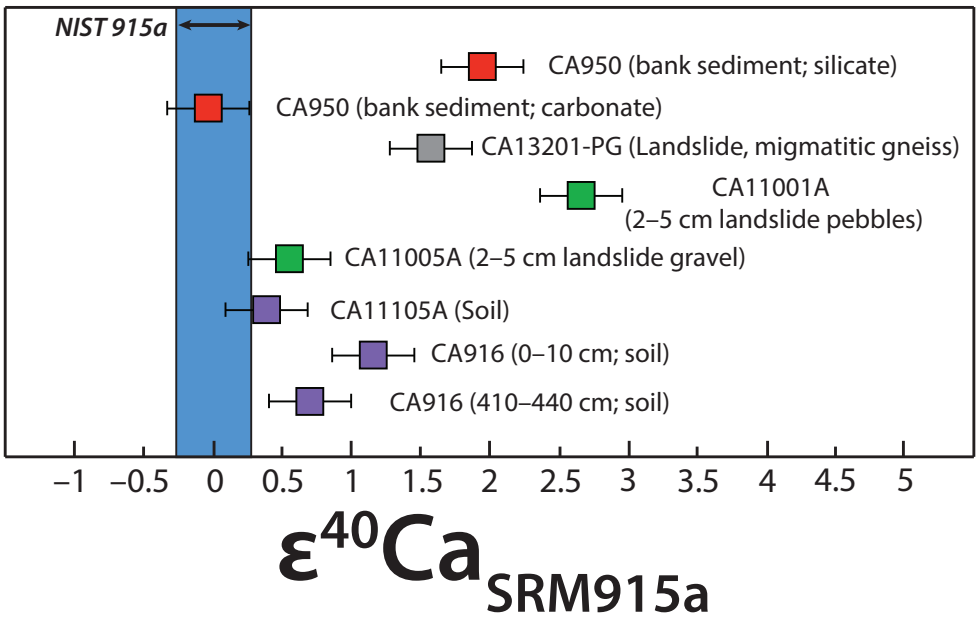

Figure 4.9 – *ε^{40}Ca results for landslide gravel, sediment, and soil samples. Typical external reproducibility is 0.39 ε-unit (2 S.D.).*

4.3.2 Dissolved Load of the Khudi Khola

Figure 4.11 shows the variation of the ε^{40}Ca composition of dissolved load samples, Figure 4.12 plots the ε^{40}Ca against the $^{87}Sr/^{86}Sr$ of all dissolved load samples, and Figure 4.13 plots ε^{40}Ca and $^{87}Sr/^{86}Sr$ of the dissolved load against, respectively, Na^*/Ca^*, and $1/Ca^*$ (where * indicates elemental concentration after correction for the contribution derived from rainwater based on analyses from Wolff-Boenisch et al. (2009)), and Na^*/Sr^* and $1/Sr^*$. In the Khudi, we observe no correlation between ε^{40}Ca and $^{87}Sr/^{86}Sr$ when all dissolved load samples are considered together. At the Khudi Intake Station (see Figure 4.8) the ε^{40}Ca composition of the dissolved load ranges from +0.13 (WKD34707) to +1.78 (WKD34701). Despite the quite radiogenic nature of several of these samples, the baseline ε^{40}Ca composition, i.e., the composition before and after the 2013 storm, at the Intake Station is at or near ε^{40}Ca = 0.

WKD samples are those that were collected hourly in 2013 and that show elevated concentrations in the dissolved load for certain elements during this intense precipitation event. For these samples, ε^{40}Ca values are roughly correlated with Ca and K concentrations, with all three parameters increasing during the peak of the 2013 storm event (Fig. 4.7). Before and after the event, the compositions are +0.26 ± 0.38 and +0.09 ± 0.64, respectively. During the event, the ε^{40}Ca composition rises to a

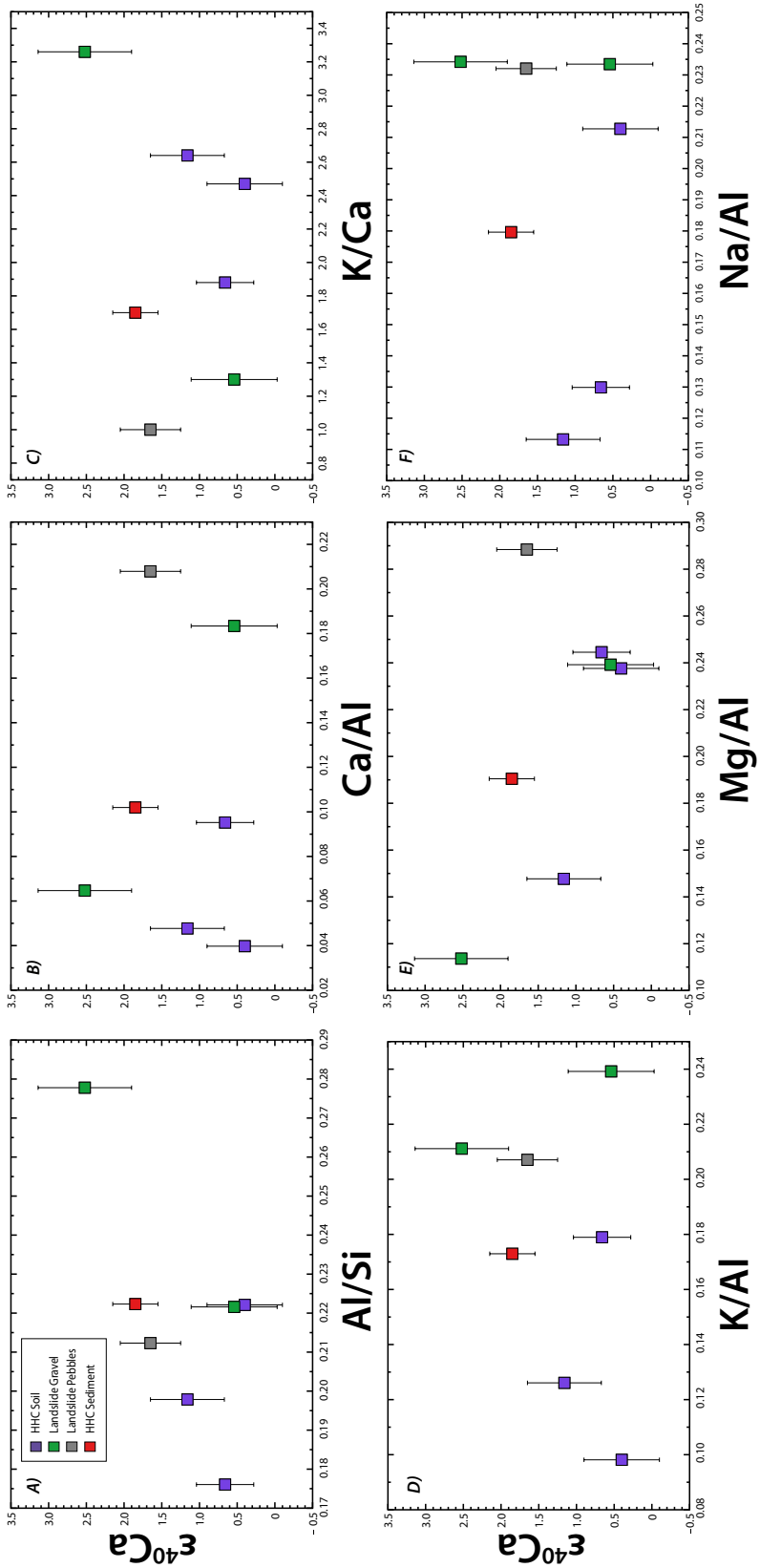

Figure 4.10 – $\varepsilon^{40}Ca$ results plotted against the major elemental ratios (*A – Al/Si, B – Ca/Al, C – Fe/Al, D – K/Al, E – Mg/Al, F – Na/Al*). *HHC soil (purple squares), Landslide pebbles (green squares), and silicate fraction of HHC sediment (red square).*

maximum of +1.78 at 0h30 and descends to +0.94–1.01 at 5h20 before returning to baseline values.

At the Tatopani, despite a carbonate major elemental signature, the hydrothermal spring samples are somewhat radiogenic, having values of +0.71 (CA15014) and +1.23 (CA15013), which indicates a more silicate origin for these springs as opposed to a carbonate/limestone spring. The geochemical signature of hydrothermal springs, such as the Tatopani at the MCT, originates from groundwater weathering that is influenced by temperature, depth, and deep metamorphic CO_2. The $^{87}Sr/^{86}Sr$ signature at the Tatopani hydrothermal springs depends on the source of the groundwater (i.e., HHC versus LH), which varies with depth (Evans et al., 2004). The Khudi is characterized by Sr ratios that are similar to the HHC or possibly a mix between HHC silicate and LH carbonates lithologies. Since the $\varepsilon^{40}Ca$ signature at the Tatopani is similar to that of the HHC dissolved load, it is likely that this signature originates from the HHC. Water from Tatopani also has elevated Na and K concentrations relative to Ca and compared with these concentrations in river water and soils. This indicates that silicate weathering is the dominant process despite the close proximity to dolostones along the MCT. The more radiogenic Ca isotopic compositions also corroborate these assumptions. Nevertheless, an alternative scenario to a HHC source could be proposed, in which the observed intermediate $\varepsilon^{40}Ca$ composition results from hydrothermal circulation through both nonradiogenic LH carbonates, and very radiogenic LH silicates, producing a mixed signature.

Springs and streams originating from the landslide have $\varepsilon^{40}Ca$ compositions ranging from +0.38 (CA12w04; landslide spring) to 1.62 (CA11206A; landslide stream). Samples CA12w03 and CA12w04 were both collected from landslide springs and are most likely strongly influenced by sulfate weathering. The radiogenic Ca composition of landslide streams and sediment/pebbles are in quite good agreement (compare samples CA11001A and CA11005A with these water samples in Figs. 4.9 and 4.11). Finally, the dissolved $\varepsilon^{40}Ca$ compositions of Khudi river samples taken above the MCT (i.e., where the river has traversed only HHC terrain) range from +0.44 (CA14009) to +1.90 (CA11103).

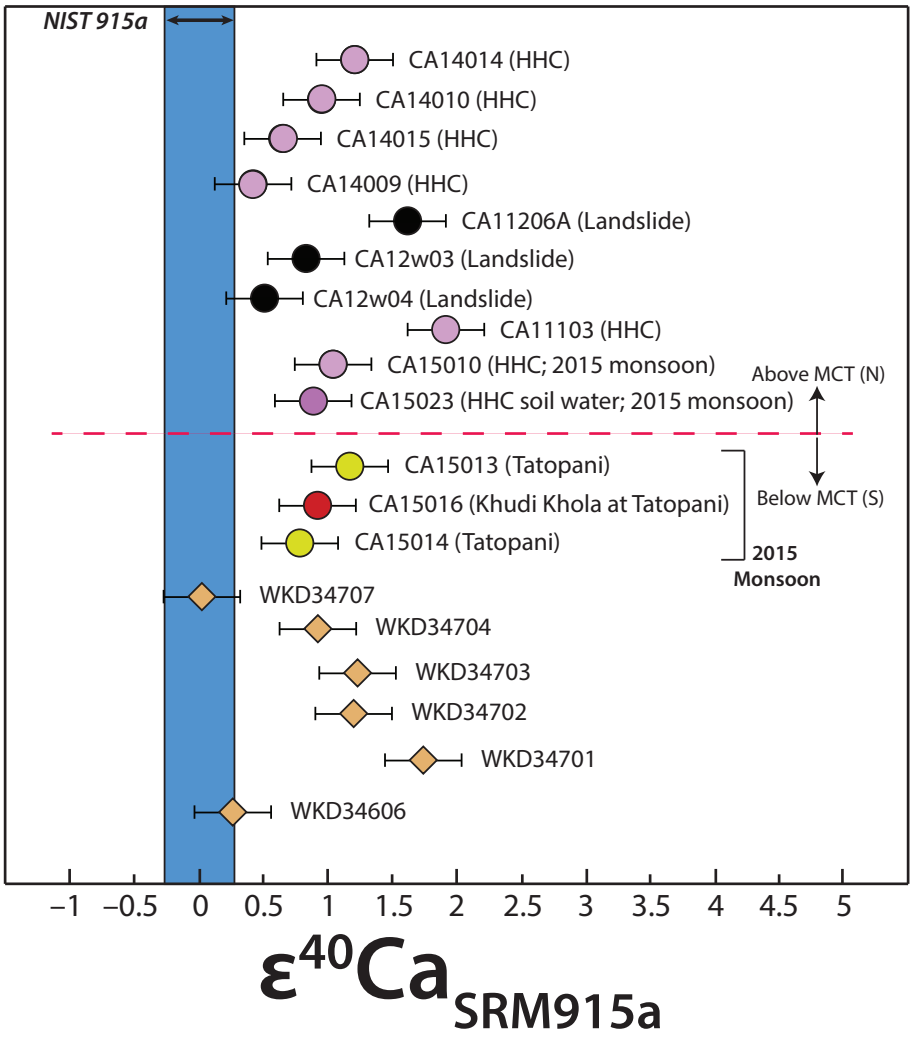

Figure 4.11 – *$\varepsilon^{40}Ca$ results for dissolved load samples analyzed in this study. Typical internal precision for sample analyses is 0.20 ε-unit, while external reproducibility (used to define error bars) is 0.39 ε-unit (2 S.D.). Burnt orange diamonds = Khudi Intake Station, yellow circles = Tatopani hydrothermal springs, the red circle is the Khudi Khola at the Tatopani, black circles = landslide streams and springs, purple circles = HHC streams.*

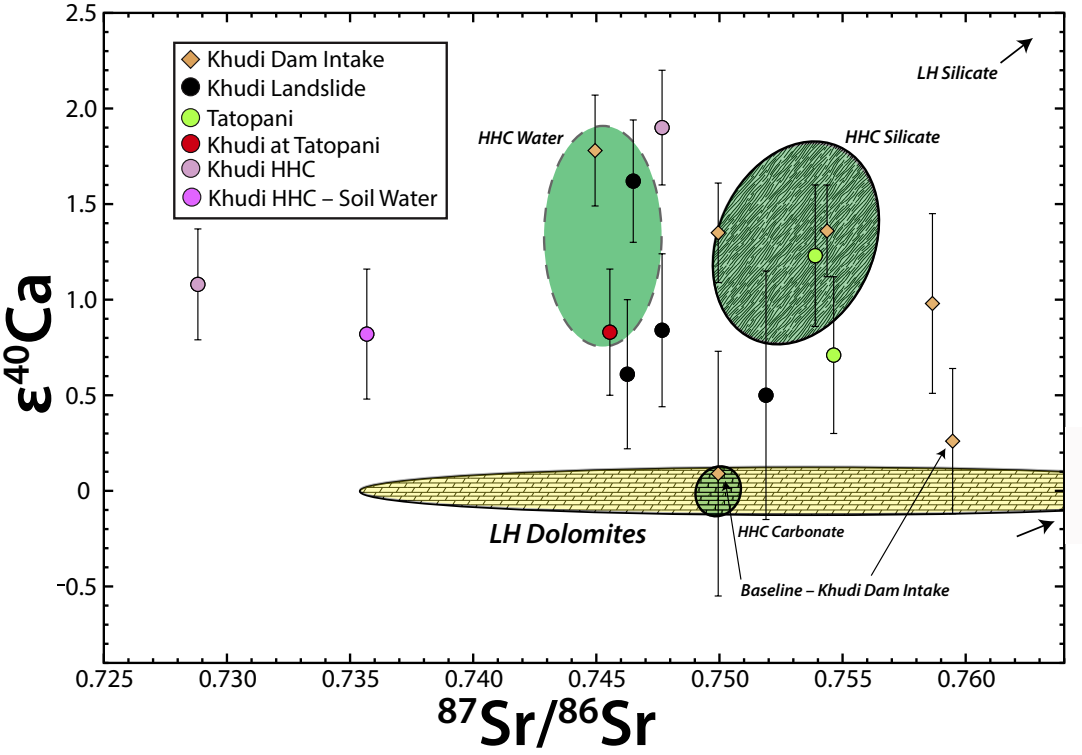

Figure 4.12 – *$\varepsilon^{40}Ca$ vs $^{87}Sr/^{86}Sr$ of the dissolved load from the Khudi Khola. Burnt orange diamonds = Khudi Intake Station, yellow circles = Tatopani hydrothermal springs, red circle = the Khudi Khola main stem at the Tatopani, black circles = landslide springs and streams, light pink circles = Khudi Khola in the HHC, and the dark pink circle is soil water from the HHC. Fields with the wavy line pattern and brick pattern are silicate and carbonate compositions, respectively, defined by the radiogenic Ca compositions of the silicate and carbonate fractions of sediments and dolomites defined in Chapter 5 for the LH and HHC.*

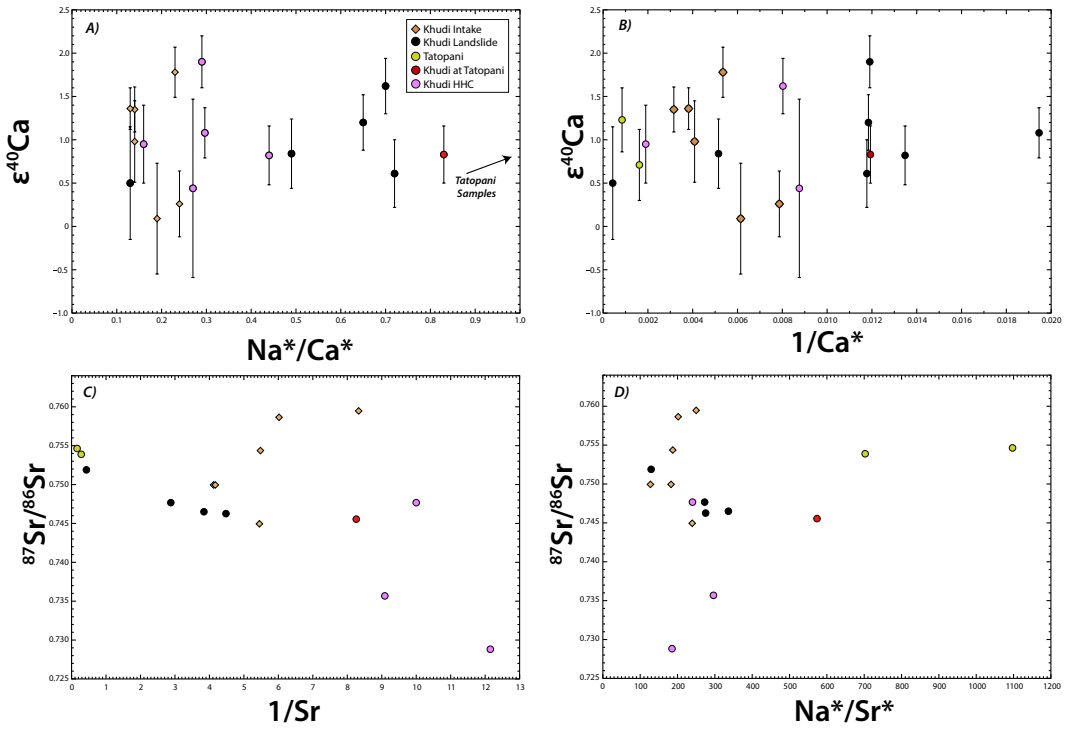

Figure 4.13 – *The relationship between the cyclic contribution (*) corrected major element ratios and Sr and Ca isotope ratios in the Khudi Khola. Burnt orange diamonds = Khudi Intake Station, yellow circles = Tatopani springs, red circles = the Khudi Khola main stem at the Tatopani, black circles = landslide, and purple circles = HHC streams. A) $\varepsilon^{40}Ca$ vs. A) Na*/Ca* and B) 1/Ca*. C) and D) Sr isotope compositions versus the Na*/Sr* and 1/Sr* ratios, respectively.*

4.4 Discussion

4.4.1 Main observations from sediment, pebbles, and soil

Based on analyses presented here (sediment sample CA950) and in Chapter 5, we observe that Himalayan carbonates have non-radiogenic compositions consistent with those found for marine limestones (ε^{40}Ca = 0) from throughout geological time (Caro et al., 2010). This implies that, unlike for Sr isotopes, Ca isotopes in carbonates have not re-equilibrated with adjacent radiogenic silicate rocks during metamorphism related to Himalayan orogenesis.

In the HHC of the Khudi Khola, we analyzed river bedload sediment and soils, as well as gravel from the Saitutu landslide. Landslide material can be taken as the most accurate estimate of typical HHC crust for both major elemental compositions (Morin, 2015) and its radiogenic Ca composition, i.e., an observed maximum of +3.41 ε-units. The three analyses of the pebble sample (CA11005), which has an elevated Ca concentration (and correspondingly low K/Ca ratio), had low or non-radiogenic ε^{40}Ca compositions whereas the analyses of the sample (CA11001A), with a low Ca concentration (high K/Ca), had high ε^{40}Ca values.

As shown by Morin (2015), soil profiles in the Khudi basin generally do not correspond to well-organized weathering patterns. The ratios of K/Al, Na/Al, and Ca/Al show no progressive depletion trends across soil horizons Morin (2015). This is possibly due to the very deep weathering front in Khudi soils, thus real protolith was not sampled. We also observe this disconnect in Ca isotopes for soil profile sample CA916 (0–10 cm versus 410–440 cm). The deeper sample has an ε^{40}Ca composition (+0.66) that is significantly less radiogenic than that of the surface sample (+1.17. However, radiogenic phases such as mica are more easily weathered compared with less radiogenic and less weatherable phases such as orthoclase or K-feldspar. So, it is surprising that the surface sample has both a higher K/Ca ratio and a more radiogenic Ca composition compared with the deep sample. This may indicate that there was an initial heterogeneity in the profile. Nevertheless, given the reproducibility of standard analyses ($\pm$ 0.40, 2 S.E.), Ca isotope compositions of these samples are not fully distinguishable so these interpretations may be questioned.

4.4.2 Dissolved Load

4.4.2.1 Contrast between dissolved load above and below MCT

At the Intake station, which represents the dissolved load of the Khudi below the MCT, the Ca isotopic signature of samples unaffected by the storm event (i.e., the baseline samples WKD34606 and WKD34707) is unradiogenic, which suggests a

dominant carbonate signature. This signature is generally due to small tributaries, such as the Thulo Khola, located just above the Intake Tributary (not analyzed in this study), that drain significant amounts of LH lithology. In this area, the LH lithology comprises predominantly thick dolomitic limestone formations located right below the MCT (Pecher, 1978), which could explain the unradiogenic Ca isotopic compositions observed in the baseline samples at the Dam Intake (Figure 4.12). Above the MCT, in the HHC, the dissolved load is characterized by more radiogenic Ca compositions due to the dominant presence of HHC FI gneisses, which have higher K/Ca ratios than LH lithologies below the MCT.

4.4.2.2 Landslide Triggered Erosion and its effect on the Dissolved Load during the Monsoon

Based on an extensive geochemical and isotopic (Sr–Nd) study of sedimentary products from the Khudi Khola, Morin (2015) showed that approximately 95 to 100% of the physical erosion in the Khudi Khola occurs above the MCT in the HHC. Despite the fact that the area covered by landslides in this basin is minor, approximately 0.45%, and the remaining 99.5% are very steep slopes exposed to approximately 3 m of annual rainfall, the landslides represent the dominant source of sediments in the Khudi Khola catchment (Niemi et al., 2005; Gabet et al., 2008; Puchol et al., 2014; Gallo and Lavé, 2014; Morin, 2015).

In-situ cosmogenic ^{10}Be measured on 10 bank samples of the river between 1997 and 2013 indicate quite variable erosion rates, between 0.7 and 2.5 mm/yr (Gallo, 2014). This suggests that there is a heterogeneity in the origin of sediments. Modeling from Morin (2015), based on the major element and isotope geochemistry, shows that the landslide provides approximately 75–80% of the river sediment while soil erosion provides only 4.5–12.5% with the upper basin providing 5–12.5%. A second model, based on organic carbon data, shows that 0–10% of erosional products originate from top soils and 90–100% from the landslide itself (Morin, 2015). Therefore, Morin (2015) concludes that soil erosion represents a minor source of sediment when compared to landslide derived sediment. This model is in agreement with data obtained by TCN (Terrestrial cosmogenic nuclides), which shows that 96% of sediment in the Khudi Basin is derived from the landslide (Niemi et al., 2005). Since the Saituti landslide area is approximately 0.5 km^2, and 75–90% of Khudi sediments have their source in the landslide, calculated local erosion rates are approximately 1,900–2,300 mm/y, which is 400 times the mean erosion rate in the basin. Conversely, calculated topsoil erosion is 0.2–0.8 mm/yr. Erosion from upper basin tributaries is of the same order of magnitude, approximately 0.2 mm/yr, which is in agreement with erosion rates of

approximately 0.14 mm/yr measured by TCN (Niemi et al., 2005).

Hourly sampling at various locations throughout the catchment in 2013 and 2015 document the evolution of the dissolved load compositions from before, during, and after storm events (e.g., the 2013 flood event in Figure 4.7). The 2013 storm event was particulary violent and is characterized by concentrations spikes in the dissolved load at Khudi Dam Intake. This is currently the only event in the Khudi Khola that exhibits this behavior. Daily sampling from 2010 in the Khudi Khola shows a possible correlation between high discharge and sediment load and high K/Na ratios (Morin et al., 2014).

In the particular example of the July 24, 2013 flood event, there is a marked increase in the sediment load and discharge which correlates with an increase in the dissolved inorganic carbon (DIC) and the concentrations of SO_4, Na, K, Ca, and Mg, which all return to their respective baseline levels after the flood event. These storm events, especially the 2013 event, are marked by extreme river turbulence, a significantly different color to the river water, and overall extreme conditions in the catchment.

Early studies of the geochemistry of the Khudi, in particular, France-Lanord et al. (2003) and Wolff-Boenisch et al. (2009), did not observe these increases in certain species of the dissolved load during storm events. This may be due to effects related to the specific time and place of sampling or, perhaps, to overall lower rates of physical erosion in the catchment as well as less intense monsoon seasons, which led to a significant decrease in the baseline values of certain elements, such as K and Ca, in 2002 compared with 2010–2014 (Wolff-Boenisch et al., 2009). This, however, is just speculation as the objective of Wolff-Boenisch et al. (2009) was not to conduct hourly sampling in the Khudi, and, therefore, concentration spikes during storm events could have certainly been occurring but not observed. Similarly, France-Lanord et al. (2003) only sampled the Khudi Khola at one time and location throughout the entire monsoon season.

In general, flood events act to dilute the cation and anion concentrations in the dissolved load via direct runoff, so a specific explanation is needed for the spikes in concentrations of certain elements. One possibility is that the leachable, upper soil layer released certain elements to the dissolved load, such as Ca and Mg. However, the upper soil layers are unlikely to have been a source of K and Ca, because, at the time of sampling, heavy, monsoonal rainfall had already acted to thoroughly saturate the soil in the Khudi (i.e., this usually occurs within the first several weeks of the monsoon, which usually starts in May or June). Hydrothermal springs, such as the studied Tatopani samples, are also an unlikely source for the increase in elemental concentrations at the Dam Intake site as they are characterized by particularly high Na

concentrations and Na increased less than the other elements during the 2013 storm event.

Thus, the most likely remaining explanation for the elevated concentrations of elements in the dissolved load during storm events is the release of these dissolved elements via physical erosion occurring in the landslide. Fresh mineral surfaces, derived from physical rock crushing, are exposed at the edge of the landslide. These surfaces are partially ground and undergo weathering for extended periods of time until they are flushed into the river during a flood event. These ground, fresh surfaces are predominantly composed of HHC gneisses, rich in K and Ca, which come in the form of gneissic pebbles, i.e., exactly the same type of samples shown in Figure 4.4 that can be quite radiogenic (Table 4.5). Delivering elements from these fresh mineral surfaces to the river requires rapid dissolution kinetics or leaching of exchangeable/mobile cations, which possibly derive from the breakdown of pebbles that are highly weathered and oxidized (Morin et al., 2014). In other words, landslides unearth abundant rock that is weathered and stored for periods that vary significantly. When unearthed, the dissolution of the most reactive (i.e., mobile) phases controls the weathering (Emberson et al., 2017). The intense, storm events provided the mechanistic "push" to deliver these mobile ions, i.e., Si, K, Ca, and SO_4 into the Khudi. In New Zealand catchments dominated by bedrock landsliding, Emberson et al. (2016a) observed that landslide events can control the variability of the dissolved load chemistry. Furthermore, Emberson et al. (2016b) cite carbonate-sulfuric-acid-driven weathering as a key factor in the enhanced delivery of reactive phases to the solute chemistry during bedrock landsliding. This may also occur in the Saituti landslide, but its magnitude is unknown. However, based on Figure 4.7, we do observe a rise in sulfate during the 2013 storm event.

On the night of the storm, a significant increase in discharge and sediment load occurred between 22h and 3h, which correlates with an increase in the ε^{40}Ca value of the dissolved load, as well as the increase in K, Ca, and SO_4 concentrations. The ε^{40}Ca value jumps from the baseline to +1.78 (Figure 4.7) and continues to be radiogenic (at approximately +1.3) until 13h the next day, after which the Ca isotopic composition drops back to baseline (Figure 4.7). As discussed above, the unradiogenic nature of the baseline composition reflects the influence of carbonates below the MCT that are drained by the Khudi and tributaries such as the Thulo Khola. As with the increase in K and Ca abundances, the increase in ε^{40}Ca during the storm event may be derived from the weathering of freshly ground surfaces of gneiss pebbles in the landslide.

Strontium isotopes vary only moderately throughout the storm event and do not follow the Ca isotopes, providing very little useful information. The first measured $^{87}Sr/^{86}Sr$ value prior to the storm is approximately 0.7595, which then drops

significantly to 0.74495 at the beginning of the event. This value then rises steadily throughout the event before dropping down to 0.74995 after the storm. The radiogenic Sr base level before the storm could be related to radiogenic dolomites that occur just beneath the MCT. This has a proportionately higher effect when the discharge is lower before the event with low Sr concentrations. Nevertheless, the interpretation of the Sr isotopic data is complicated because both the LH dolomites and the freshly ground surfaces of landslide pebbles are likely to provide rather similar radiogenic Sr. Emberson et al. (2017) stated, with reference to Sr isotopes, that when dealing with regions that are dominated by erosive landslide processes, there may be biases associated with the use of isotope proxies to understand erosion dynamics if the most mobile phases that dissolve in the landslide unequally contribute to the proxy being used. In other words, if we use Sr isotopes to understand landslide erosion processes in a setting where biotite is radiogenic in Sr, and is one of the most reactive phases, then this biotite is the first phase to release dissolved Sr and may lead to biases in the data. This could also be the case with radiogenic Ca isotopes because the most reactive phases at the edge of the landslide are the phases that are the most radiogenic in Ca, at least in the upper Khudi Khola (i.e., the gneiss pebbles depicted in Fig. 4.4). However, in the Khudi, we have no knowledge of which phases in the landslide are the most radiogenic or the Ca isotopic compositions of the different phases. Therefore, this hypothesis needs to be verified with future sampling of the different phases present in the landslide.

Based on these results, there are three possible explanations for the observed spike during the 2013 storm event: 1) An increase in the flux of water from the HHC that is characterized by elevated concentrations of K, Ca, and SO_4, 2) soil leaching processes that would produce the spikes observed for K but should also increase the riverine Si concentration, and 3) the breakdown and leaching/weathering of pebbles and gravel in the landslide and throughout the Khudi Khola during periods of peak discharge.

The third hypothesis could be the possible mechanism that yields the concentration spikes in the 2013 storm events. It is important to note that pebble and gravel occur throughout the Khudi Khola basin and not just in the landslide, i.e., samples CA11001A and CA11005A occur in the landslide but sample CA13201(-PG) occurs downstream of Khudi Intake. In fact, the river bed in the LH portion of the Khudi, as well as in the HHC, is littered with pebbles and gravel that originate from the HHC due to their gneissic appearance. These pebbles and gravel are generally highly weathered and, therefore, have damaged mineral sites that can quite possibly release the elements of interest during a storm event, i.e., K, Ca, Si, and SO_4. This implies that, despite the influence of the landslide, basin-wide weathering of these

pebbles acts as a significant process that increases the dissolved load concentrations of certain elements and must be taken into account, along with other fluxes, to assess the carbonate and silicate weathering budget in the Khudi Khola.

4.5 Conclusions

For many years, geologists have studied the Khudi because it presents a natural laboratory where the interactions between climate, erosion, and silicate and carbonate weathering can be observed first hand, especially since the Khudi's geomorphology, lithology, climatic, and vegetation characteristics are well constrained. Despite these constraints, many questions remain concerning the sources of sediment and how these sediments are delivered to the river, as well as how they may contribute to the complex geochemical signature of the dissolved load. There are several sources of dissolved solutes in the Khudi and deciphering between these sources is the key to understanding the magnitude and flux of carbonate and silicate weathering that is occurring in this catchment.

In this study, we have shown that, below the MCT in the LH, ε^{40}Ca values, excluding highly radiogenic samples from the 2013 storm event, are unradiogenic and reflect the massive outcrops of dolostone and limestone that are situated below the MCT. Above the MCT in the HHC, ε^{40}Ca values are elevated compared with those of the LH due to the silicate nature of the HHC. As proposed by previous studies, landslides in the HHC represent a significant source of erosion (Gallo and Lavé, 2014; Morin, 2015). Analyses of material from the Saituti landslide show that the Ca isotope compositions vary but are in large part radiogenic, which is corroborated by the high K/Ca ratios of these samples.

Storm events during the monsoon, particularly the strong event documented in 2013, yield high discharge and sediment load values, spikes in the concentrations of elements, such as K, Ca, Si, Mg, and SO_4, and generally turbulent riverine conditions. This is the opposite of what would normally be observed, i.e., storm events are expected to dilute the elemental concentrations in river water. Along with the element concentration spikes, we also observe a sharp increase in the ε^{40}Ca values, from +0 to +1.78 at the peak of the storm. This strongly suggests that this radiogenic Ca signature originated in the HHC. Concurrent increases in several major elements and $SO_4{}^{2-}$ concentrations during the 2013 storm event also suggest that these elements have been released via weathering of silicates or associated sulfides. We propose that these spikes may be derived from the leaching or weathering of freshly ground surfaces on gneiss pebbles in the landslide and throughout the catchment.

4.6 Supplementary Materials

Table 4.7 – *Individual analysis analytical data for each sample analyzed in this study.*

	# Cycles	^{42}Ca (V)	^{40}Ca (V)	^{41}K/^{40}Ca	Raw ratios (Line 1)			(Line 2)	Corrected ratios (static mode)			
					^{40}Ca/^{44}Ca	^{42}Ca/^{44}Ca	^{43}Ca/^{44}Ca	^{40}Ca/^{42}Ca	^{40}Ca/^{44}Ca (ST)	± (2S.D.)	^{43}Ca/^{44}Ca (ST)	± (2S.D.)
Session 1B May 2014												
2014_05_19_Ca-CA11206A	80	0.10	10.23	1.49E-04	46.42651236	0.30983	0.06462	149.84432	47.10739	3.05E-03	0.06486	5.01E-06
2014_05_20_Ca-CA12W3	90	0.10	14.46	6.70E-04	46.40484849	0.30977	0.06461	149.80370	47.10408	2.83E-03	0.06486	4.55E-06
2014_05_21_Ca-CA12w3	120	0.09	14.08	1.43E-03	46.37684718	0.30968	0.06460	149.75612	47.10578	2.52E-03	0.06486	5.45E-06
Session 2 July 2014												
2014_07_11_Ca-CA34606a	80	0.10	14.63	5.52E-04	46.34956979	0.30960	0.06459	149.70613	47.09740	2.90E-03	0.06486	5.61E-06
2014_07_12_Ca-CA34606b	120	0.10	14.72	2.59E-04	46.41139461	0.30980	0.06462	149.80905	47.09838	2.27E-03	0.06487	4.15E-06
2014_07_15_Ca-CA34707	80	0.09	13.65	2.19E-03	46.36822451	0.30966	0.06460	149.73715	47.09449	3.07E-03	0.06486	5.94E-06
Session 6 April 2015												
2015_04_15_Ca-CA12w4-1	120	0.07	10.53	3.49E-04	46.36647535	0.30967	0.06459	149.72958	47.14340	2.19E-03	0.06486	6.68E-06
2015_04_16_Ca-34701-1	120	0.07	10.52	1.19E-04	46.42289839	0.30983	0.06462	149.83294	47.14503	2.68E-03	0.06486	5.41E-06
2015_04_16_Ca-CA11103-2	120	0.08	11.96	2.27E-03	46.35631816	0.30961	0.06460	149.72329	47.14632	2.14E-03	0.06487	5.24E-06
2015_04_18_Ca-CA12w4	120	0.06	9.87	1.71E-04	46.36039477	0.30965	0.06459	149.72089	47.13897	2.62E-03	0.06486	6.65E-06
2015_04_19_Ca-347-02	120	0.07	10.18	1.55E-03	46.41758905	0.30983	0.06461	149.81798	47.14020	2.86E-03	0.06486	6.02E-06
2015_04_19_Ca-347-03	120	0.06	9.82	2.80E-05	46.42939799	0.30986	0.06462	149.84083	47.14609	2.60E-03	0.06487	7.60E-06
2015_04_19_Ca-347-04	100	0.07	10.74	1.70E-04	46.39089318	0.30973	0.06460	149.77940	47.14298	2.66E-03	0.06486	5.59E-06
2015_04_20_Ca-CA12w4d	120	0.07	10.54	3.89E-04	46.40013296	0.30977	0.06460	149.79096	47.14492	2.18E-03	0.06486	6.21E-06
2015_04_21_Ca-347-04b	120	0.06	9.56	2.43E-04	46.36914156	0.30967	0.06460	149.73883	47.14148	2.80E-03	0.06487	5.97E-06
Session 6B April 2015												
2015_04_24_Ca-CA12w4	120	0.07	10.26	3.48E-04	46.30949749	0.30946	0.06458	149.64731	47.15220	3.10E-03	0.06487	6.75E-06
2015_05_03_Ca-CA11001A-1	120	0.07	10.36	1.02E-04	46.43200222	0.30981	0.06461	149.87116	47.15691	3.04E-03	0.06486	6.44E-06
2015_05_03_Ca-CA11005A-1	120	0.08	11.47	2.53E-04	46.34293071	0.30956	0.06460	149.70608	47.14792	2.67E-03	0.06488	5.24E-06
2015_05_03_Ca-CA11105A-1	120	0.07	10.88	9.35E-04	46.31696504	0.30949	0.06458	149.65692	47.14533	2.75E-03	0.06487	5.72E-06
Session 7 July 2015												
2015_07_04_Ca-34703-2	120	0.09	14.20	4.59E-04	46.35703656	0.30962	0.06460	149.72296	47.13689	2.55E-03	0.06487	5.15E-06
2015_07_04_Ca-CA11001A-2	120	0.08	12.62	6.30E-04	46.35473483	0.30959	0.06459	149.73071	47.14845	3.44E-03	0.06487	7.65E-06
2015_07_06_Ca-CA11105A-2	120	0.09	13.46	2.28E-04	46.38053487	0.30969	0.06461	149.76561	47.14056	3.23E-03	0.06487	5.18E-06
2015_07_07_Ca-CA11005A-2	120	0.09	13.41	1.16E-03	46.31449224	0.30948	0.06459	149.65238	47.13570	2.39E-03	0.06487	5.17E-06
2015_07_13_Ca-CA11001A	120	0.09	13.01	2.82E-04	46.36426495	0.30960	0.06459	149.75318	47.14310	3.30E-03	0.06486	7.95E-06
2015_07_13_Ca-CA11005A	120	0.09	14.08	5.33E-04	46.37247858	0.30966	0.06460	149.75311	47.13651	3.03E-03	0.06486	6.85E-06
2015_07_14_Ca-34701	120	0.07	11.46	9.91E-05	46.31683423	0.30949	0.06458	149.65554	47.13120	2.64E-03	0.06486	6.43E-06
Session 8 February 2016												
2016_02_15_Ca_CA13201-PG	110	0.07	11.05	2.50E-03	46.64105632	0.31052	0.06469	150.20291	47.13074	3.24E-03	0.06486	7.28E-06
2016_02_16_Ca_CA916 0-10	110	0.08	11.57	7.59E-04	46.33307845	0.30953	0.06459	149.69070	47.12553	3.41E-03	0.06487	7.09E-06
2016_02_17_Ca_CA916 410-440	110	0.08	11.44	1.51E-03	46.38156566	0.30969	0.06461	149.76672	47.11612	3.32E-03	0.06487	7.03E-06

Table 4.7 continued from previous page

	# Cycles	^{42}Ca (V)	^{40}Ca (V)	^{41}K/^{40}Ca	Raw ratios (Line 1)			(Line 2)	Corrected ratios (static mode)			
					^{40}Ca/^{44}Ca	^{42}Ca/^{44}Ca	^{43}Ca/^{44}Ca	^{40}Ca/^{42}Ca	^{40}Ca/^{44}Ca (ST)	± (2S.D.)	^{43}Ca/^{44}Ca (ST)	± (2S.D.)
2016_02_20_Ca-CA15010	110	0.06	9.32	7.81E-04	46.3655717	0.30964	0.06460	149.74257	47.12549	9.72E-03	0.06487	2.34E-05
2016_02_23_Ca_CA15013	110	0.08	12.38	2.18E-04	46.43050628	0.30984	0.06462	149.85193	47.11585	2.90E-03	0.06486	6.97E-06
2016_02_23_Ca_CA15014	110	0.08	11.54	2.21E-04	46.31553812	0.30947	0.06458	149.65852	47.11754	3.88E-03	0.06486	6.95E-06
2016_02_27_Ca_CA14014	110	0.08	11.84	4.47E-05	46.42643907	0.30983	0.06462	149.84534	47.12149	3.01E-03	0.06487	5.96E-06
2016_02_27_Ca_CA15023	110	0.09	13.70	2.11E-04	46.43309624	0.30986	0.06462	149.85357	47.11888	2.73E-03	0.06486	5.50E-06
2016_02_29_Ca_CA15016	110	0.08	11.93	1.29E-04	46.38699451	0.30970	0.06461	149.77805	47.11835	2.87E-03	0.06487	6.15E-06
2016_03_01_Ca_CA14010	110	0.07	10.90	8.85E-05	46.41013749	0.30978	0.06463	149.81594	47.11691	3.10E-03	0.06488	6.77E-06
2016_03_08_Ca-CA15010	110	0.07	11.27	5.91E-04	46.31293908	0.30948	0.06458	149.64635	47.11168	2.84E-03	0.06487	6.15E-06
2016_03_09_Ca_CA14009	110	0.07	11.43	5.85E-05	46.4343084	0.30987	0.06463	149.85290	47.11876	7.74E-03	0.06487	9.63E-06
2016_03_10_Ca_CA14015	110	0.08	12.04	4.03E-05	46.3941169	0.30973	0.06461	149.78785	47.11743	3.38E-03	0.06487	7.77E-06

Table 4.8 – *Individual analysis analytical data for each sample analyzed in this study.*

	Corrected ratios (multidynamic mode)					ε^{40}Ca (I-MD) ± (2S.D.)		ε^{40}Ca (ST) ± (2S.D.)		ε^{43}Ca (ST) ± (2S.D.)		Mass Fract. Factor (‰)	Mass Fract. Rate (ppm.s^{-1})	F	ΔR_c (ppm)
	^{40}Ca/^{42}Ca (MD)	^{40}Ca/^{44}Ca (MD)	± (2S.D.)	^{40}Ca/^{44}Ca (I-MD)	± (2S.D.)										
Session 1B May 2014															
2014_05_19_Ca-CA11206A	151.05034	47.15943	1.92E-03	47.15914	1.50E-03	1.62	0.32	0.54	0.65	-0.18	0.77	-3.81	0.10	1.000004	6.12
2014_05_20_Ca-CA12W3	151.04022	47.15627	1.68E-03	47.15587	1.37E-03	0.93	0.29	-0.17	0.60	-0.67	0.70	-3.91	0.16	1.000006	8.39
2014_05_21_Ca-CA12w3	151.03732	47.15536	1.55E-03	47.15503	1.33E-03	0.75	0.28	0.19	0.53	-0.54	0.84	-4.05	0.29	1.000011	7.08
Session 2 July 2014															
2014_07_11_Ca-CA34606a	151.02741	47.15227	1.79E-03	47.15239	1.41E-03	0.19	0.30	-1.29	0.62	-1.16	0.86	-4.17	0.22	1.000008	-2.68
2014_07_12_Ca-CA34606b	151.02905	47.15278	1.26E-03	47.15280	1.11E-03	0.28	0.23	-1.08	0.48	0.79	0.64	-3.85	0.20	1.000008	-0.39
2014_07_15_Ca-CA34707	151.02736	47.15225	1.95E-03	47.15204	1.74E-03	0.12	0.37	-1.91	0.65	0.06	0.92	-4.08	0.16	1.000006	4.57
Session 6 April 2015															
2015_04_15_Ca-CA12w4-1	151.01819	47.14939	1.79E-03	47.14907	1.58E-03	0.41	0.34	1.62	0.46	-0.23	1.03	-4.07	-0.09	0.999996	6.84
2015_04_16_Ca-34701-1	151.03918	47.15594	1.94E-03	47.15594	1.49E-03	1.86	0.31	1.96	0.57	0.84	0.83	-3.81	-0.01	1.000000	0.04
2015_04_16_Ca-CA11103-2	151.03938	47.15600	1.66E-03	47.15624	1.43E-03	1.93	0.30	2.24	0.45	0.91	0.81	-4.16	0.13	1.000005	-4.98
2015_04_18_Ca-CA12w4	151.02105	47.15028	1.73E-03	47.14972	1.42E-03	0.54	0.30	0.68	0.56	0.24	1.03	-4.11	0.08	1.000003	11.82
2015_04_19_Ca-347-02	151.02602	47.15183	1.75E-03	47.15202	1.41E-03	1.03	0.30	0.94	0.61	-0.30	0.93	-3.82	-0.03	0.999999	-3.94
2015_04_19_Ca-347-03	151.03331	47.15411	1.70E-03	47.15364	1.24E-03	1.37	0.26	2.19	0.55	1.42	1.17	-3.77	0.19	1.000007	10.07
2015_04_19_Ca-347-04	151.03779	47.15551	1.78E-03	47.15567	1.35E-03	1.81	0.29	1.53	0.56	0.36	0.86	-3.97	0.04	1.000002	-3.49
2015_04_20_Ca-CA12w4d	151.03007	47.15310	1.66E-03	47.15292	1.53E-03	1.22	0.32	1.94	0.46	-0.67	0.96	-3.91	0.01	1.000000	3.68
2015_04_21_Ca-347-04b	151.02822	47.15252	2.13E-03	47.15171	1.71E-03	0.97	0.36	1.21	0.59	1.48	0.92	-4.07	0.03	1.000001	17.25
Session 6B April 2015															
2015_04_24_Ca-CA12w4	151.04285	47.15709	1.98E-03	47.15692	1.80E-03	0.58	0.38	1.25	0.66	0.31	1.04	-4.41	0.10	1.000004	3.52
2015_05_03_Ca-CA11001A-1	151.08704	47.17089	2.17E-03	47.17042	1.78E-03	3.45	0.38	2.25	0.64	-0.40	0.99	-3.84	0.12	1.000004	9.84
2015_05_03_Ca-CA11005A-1	151.05007	47.15934	1.94E-03	47.15880	1.63E-03	0.98	0.35	0.34	0.57	1.75	0.81	-4.24	0.15	1.000006	11.39
2015_05_03_Ca-CA11105A-1	151.03703	47.15527	1.92E-03	47.15494	1.56E-03	0.16	0.33	-0.21	0.58	0.36	0.88	-4.36	0.03	1.000001	7.11
Session 7 July 2015															
2015_07_04_Ca-34703-2	151.03670	47.15517	1.64E-03	47.15522	1.31E-03	0.10	0.28	0.33	0.54	0.23	0.79	-4.15	0.19	1.000007	-0.99
2015_07_04_Ca-CA11001A-2	151.06056	47.16262	1.63E-03	47.16225	1.30E-03	1.59	0.28	2.79	0.73	-0.13	1.18	-4.20	0.15	1.000006	7.80
2015_07_06_Ca-CA11105A-2	151.04465	47.15765	1.92E-03	47.15767	1.75E-03	0.62	0.37	1.11	0.69	0.52	0.80	-4.04	0.10	1.000004	-0.37
2015_07_07_Ca-CA11005A-2	151.03603	47.15496	1.60E-03	47.15482	1.26E-03	0.01	0.27	0.08	0.51	1.13	0.80	-4.37	0.13	1.000005	3.01
2015_07_13_Ca-CA11001A	151.07451	47.16697	2.18E-03	47.16664	1.87E-03	2.52	0.40	1.65	0.70	-1.17	1.23	-4.17	0.29	1.000011	6.94
2015_07_13_Ca-CA11005A	151.04626	47.15815	1.86E-03	47.15768	1.69E-03	0.62	0.36	0.25	0.64	-0.64	1.06	-4.08	0.20	1.000008	10.03
2015_07_14_Ca-34701	151.03484	47.15459	2.04E-03	47.15479	1.65E-03	0.01	0.35	-0.87	0.56	-0.40	0.99	-4.36	0.01	1.000000	-4.25
Session 8 February 2016															
2016_02_15_Ca-CA13201-MI	151.06179	47.16300	2.68E-03	47.16688	2.41E-03	2.69	0.51	2.30	0.86	0.75	1.45	-4.02	0.11	1.000004	-82.22
2016_02_15_Ca_CA13201-PG	151.05920	47.16219	2.13E-03	47.16198	1.89E-03	1.65	0.40	3.27	0.69	-0.45	1.12	-2.71	0.05	1.000002	4.58
2016_02_16_Ca_CA916 0-10	151.05182	47.15989	2.52E-03	47.15967	2.30E-03	1.16	0.49	2.16	0.72	-0.02	1.09	-4.30	0.04	1.000002	4.68
2016_02_17_Ca_CA916 410-440	151.04309	47.15716	2.10E-03	47.15730	1.81E-03	0.66	0.38	0.16	0.70	0.43	1.08	-4.03	0.21	1.000008	-2.79

Table 4.8 continued from previous page

	Corrected ratios (multidynamic mode)					ε^{40}Ca (I-MD) ± (2S.D.)	ε^{40}Ca (ST) ± (2S.D.)	ε^{43}Ca (ST) ± (2S.D.)	Mass Fract. Factor (‰)	Mass Fract. Rate (ppm.s^{-1})	F	ΔR_c (ppm)		
	$^{40}Ca/^{42}Ca$ (MD)	$^{40}Ca/^{44}Ca$ (MD) ± (2S.D.)		$^{40}Ca/^{44}Ca$ (I-MD) ± (2S.D.)										
2016_02_20_Ca-CA15010	151.04801	47.15870	1.12E-02	47.15930	1.07E-02	1.08	2.28	2.15	2.06	0.47	3.61	-4.12	-0.11	0.999996	-12.72
2016_02_23_Ca_CA15013	151.05240	47.16007	1.96E-03	47.15998	1.76E-03	1.23	0.37	0.11	0.62	-0.56	1.07	-3.79	0.17	1.000006	1.86
2016_02_23_Ca_CA15014	151.04540	47.15788	2.34E-03	47.15753	1.96E-03	0.71	0.41	0.46	0.82	-0.51	1.07	-4.38	0.17	1.000006	7.57
2016_02_27_Ca_CA14014	151.05272	47.16017	1.81E-03	47.15985	1.52E-03	1.20	0.32	1.30	0.64	0.37	0.92	-3.81	0.14	1.000005	6.88
2016_02_27_Ca_CA15023	151.04696	47.15837	1.93E-03	47.15804	1.60E-03	0.81	0.34	0.75	0.58	-0.44	0.85	-3.77	0.24	1.000009	7.10
2016_02_29_Ca_CA15016	151.04832	47.15880	1.93E-03	47.15808	1.54E-03	0.82	0.33	0.64	0.61	0.82	0.95	-4.01	0.17	1.000007	15.16
2016_03_01_Ca_CA14010	151.04760	47.15857	2.45E-03	47.15866	2.11E-03	0.95	0.45	0.33	0.66	1.63	1.04	-3.89	0.11	1.000004	-1.89
2016_03_08_Ca-CA15010	151.02902	47.15277	1.99E-03	47.15273	1.72E-03	-0.31	0.36	-0.78	0.60	-0.12	0.95	-4.37	0.02	1.000001	0.88
2016_03_09_Ca_CA924 (0-10)	151.05907	47.16215	1.41E+00	47.16267	2.25E-03	1.80	0.48	0.72	298.81	1.00	298.82	-4.35	0.17	1.000006	-11.04
2016_03_09_Ca_CA14009	151.04153	47.15668	6.51E-03	47.15626	4.85E-03	0.44	1.03	0.72	1.64	0.62	1.48	-3.75	0.31	1.000012	8.82
2016_03_10_Ca_CA14015	151.04428	47.15753	2.16E-03	47.15706	1.83E-03	0.61	0.39	0.44	0.72	0.43	1.20	-3.97	0.04	1.000001	10.03

Table 4.10 – *2013 Discharge at Khudi Intake, calculated from pressure gage (J. Lavé).*

Date	Julian Day	m^3/s
24/07/2013 12:00	204.50	34.09
24/07/2013 12:05	204.50	34.09
24/07/2013 12:09	204.51	32.43
24/07/2013 12:14	204.51	33.57
24/07/2013 12:20	204.51	32.51
24/07/2013 12:25	204.52	32.5
24/07/2013 12:29	204.52	32.49
24/07/2013 12:35	204.52	32.62
24/07/2013 12:40	204.53	32.46
24/07/2013 12:45	204.53	33.63
24/07/2013 12:49	204.53	31.87
24/07/2013 12:55	204.54	33.15
24/07/2013 13:00	204.54	32.79
24/07/2013 13:04	204.55	33.17
24/07/2013 13:09	204.55	33.04
24/07/2013 13:15	204.55	33.37
24/07/2013 13:20	204.56	33.05
24/07/2013 13:24	204.56	32.25
24/07/2013 13:30	204.56	33.81
24/07/2013 13:35	204.57	33.83
24/07/2013 13:39	204.57	33.79
24/07/2013 13:44	204.57	33.29
24/07/2013 13:50	204.58	33.43
24/07/2013 13:55	204.58	33.2
24/07/2013 13:59	204.58	33.95
24/07/2013 14:05	204.59	34.75
24/07/2013 14:10	204.59	35.33
24/07/2013 14:15	204.59	25.65
24/07/2013 14:19	204.60	27.68
24/07/2013 14:25	204.60	27
24/07/2013 14:30	204.60	27.54
24/07/2013 14:34	204.61	29.38
24/07/2013 14:39	204.61	29.97
24/07/2013 14:45	204.61	28.57

Table 4.10 continued from previous page

Date	Julian Day	m^3/s
24/07/2013 14:50	204.62	29.52
24/07/2013 14:54	204.62	29.64
24/07/2013 15:00	204.63	29.93
24/07/2013 15:05	204.63	29.22
24/07/2013 15:09	204.63	29.23
24/07/2013 15:14	204.64	28.9
24/07/2013 15:20	204.64	30.27
24/07/2013 15:25	204.64	30.23
24/07/2013 15:29	204.65	29.11
24/07/2013 15:35	204.65	29.03
24/07/2013 15:40	204.65	28.12
24/07/2013 15:45	204.66	27.38
24/07/2013 15:49	204.66	30.87
24/07/2013 15:55	204.66	28.95
24/07/2013 16:00	204.67	29.73
24/07/2013 16:04	204.67	27.81
24/07/2013 16:09	204.67	28.83
24/07/2013 16:15	204.68	29.2
24/07/2013 16:20	204.68	29.44
24/07/2013 16:24	204.68	28.24
24/07/2013 16:30	204.69	27.85
24/07/2013 16:35	204.69	27.85
24/07/2013 16:39	204.69	28.6
24/07/2013 16:44	204.70	28.6
24/07/2013 16:50	204.70	29.32
24/07/2013 16:55	204.70	27.09
24/07/2013 16:59	204.71	27.74
24/07/2013 17:05	204.71	27.28
24/07/2013 17:10	204.72	28.6
24/07/2013 17:15	204.72	28.4
24/07/2013 17:19	204.72	28.4
24/07/2013 17:25	204.73	29.12
24/07/2013 17:30	204.73	27.24
24/07/2013 17:34	204.73	27.62
24/07/2013 17:39	204.74	29.04

Table 4.10 continued from previous page

Date	Julian Day	m^3/s
24/07/2013 17:45	204.74	29.13
24/07/2013 17:50	204.74	29.41
24/07/2013 17:54	204.75	29.46
24/07/2013 18:00	204.75	28.13
24/07/2013 18:05	204.75	32.07
24/07/2013 18:09	204.76	30.17
24/07/2013 18:14	204.76	28.26
24/07/2013 18:20	204.76	30.81
24/07/2013 18:25	204.77	29.55
24/07/2013 18:29	204.77	31.12
24/07/2013 18:35	204.77	32.54
24/07/2013 18:40	204.78	31.74
24/07/2013 18:45	204.78	31.74
24/07/2013 18:49	204.78	31.97
24/07/2013 18:55	204.79	31.58
24/07/2013 19:00	204.79	31.76
24/07/2013 19:04	204.80	33.07
24/07/2013 19:09	204.80	30.3
24/07/2013 19:15	204.80	30.1
24/07/2013 19:20	204.81	31.39
24/07/2013 19:24	204.81	32.15
24/07/2013 19:30	204.81	32.34
24/07/2013 19:35	204.82	29.67
24/07/2013 19:39	204.82	31.42
24/07/2013 19:44	204.82	30.06
24/07/2013 19:50	204.83	31
24/07/2013 19:55	204.83	31.57
24/07/2013 19:59	204.83	29.83
24/07/2013 20:05	204.84	32.03
24/07/2013 20:10	204.84	31.51
24/07/2013 20:15	204.84	30.65
24/07/2013 20:19	204.85	31.61
24/07/2013 20:25	204.85	32.74
24/07/2013 20:30	204.85	33.67
24/07/2013 20:34	204.86	31.46

Table 4.10 continued from previous page

Date	Julian Day	m^3/s
24/07/2013 20:39	204.86	33.5
24/07/2013 20:45	204.86	32.55
24/07/2013 20:50	204.87	33.93
24/07/2013 20:54	204.87	33.38
24/07/2013 21:00	204.88	34.75
24/07/2013 21:05	204.88	35.88
24/07/2013 21:09	204.88	32.36
24/07/2013 21:14	204.89	33.88
24/07/2013 21:20	204.89	34.88
24/07/2013 21:25	204.89	34.94
24/07/2013 21:29	204.90	32.8
24/07/2013 21:35	204.90	31.6
24/07/2013 21:40	204.90	34.93
24/07/2013 21:45	204.91	36.35
24/07/2013 21:49	204.91	38.66
24/07/2013 21:55	204.91	46.97
24/07/2013 22:00	204.92	53.63
24/07/2013 22:04	204.92	67.59
24/07/2013 22:09	204.92	68.52
24/07/2013 22:15	204.93	67.48
24/07/2013 22:20	204.93	67.42
24/07/2013 22:24	204.93	70.1
24/07/2013 22:30	204.94	73.95
24/07/2013 22:35	204.94	69.68
24/07/2013 22:39	204.94	72.72
24/07/2013 22:44	204.95	71.72
24/07/2013 22:50	204.95	70.19
24/07/2013 22:55	204.95	73.4
24/07/2013 22:59	204.96	74.13
24/07/2013 23:05	204.96	72.25
24/07/2013 23:10	204.97	70.25
24/07/2013 23:15	204.97	71.97
24/07/2013 23:19	204.97	69.35
24/07/2013 23:25	204.98	68.75
24/07/2013 23:30	204.98	77.51

Table 4.10 continued from previous page

Date	Julian Day	m^3/s
24/07/2013 23:34	204.98	84.2
24/07/2013 23:39	204.99	92.62
24/07/2013 23:45	204.99	102.72
24/07/2013 23:50	204.99	97.47
24/07/2013 23:54	205.00	95.82
25/07/2013 00:00	205.00	98.12
25/07/2013 00:05	205.00	111.68
25/07/2013 00:09	205.01	107.15
25/07/2013 00:14	205.01	106.07
25/07/2013 00:20	205.01	119.86
25/07/2013 00:25	205.02	117.79
25/07/2013 00:29	205.02	110.82
25/07/2013 00:35	205.02	124.17
25/07/2013 00:40	205.03	125.73
25/07/2013 00:45	205.03	126.77
25/07/2013 00:49	205.03	135.93
25/07/2013 00:55	205.04	137.33
25/07/2013 01:00	205.04	140.01
25/07/2013 01:04	205.05	140.09
25/07/2013 01:09	205.05	151.59
25/07/2013 01:15	205.05	144.47
25/07/2013 01:20	205.06	145.59
25/07/2013 01:24	205.06	132.27
25/07/2013 01:30	205.06	125.19
25/07/2013 01:35	205.07	115.21
25/07/2013 01:39	205.07	121.84
25/07/2013 01:44	205.07	121.7
25/07/2013 01:50	205.08	111.06
25/07/2013 01:55	205.08	109.04
25/07/2013 01:59	205.08	106.54
25/07/2013 02:05	205.09	97.46
25/07/2013 02:10	205.09	100.49
25/07/2013 02:15	205.09	84.98
25/07/2013 02:19	205.10	87.71
25/07/2013 02:25	205.10	94.06

Table 4.10 continued from previous page

Date	Julian Day	m^3/s
25/07/2013 02:30	205.10	82.36
25/07/2013 02:34	205.11	79.37
25/07/2013 02:39	205.11	86.48
25/07/2013 02:45	205.11	93.91
25/07/2013 02:50	205.12	94.85
25/07/2013 02:54	205.12	93.38
25/07/2013 03:00	205.13	92.46
25/07/2013 03:05	205.13	104.27
25/07/2013 03:09	205.13	91.78
25/07/2013 03:14	205.14	82.32
25/07/2013 03:20	205.14	86.2
25/07/2013 03:25	205.14	82.75
25/07/2013 03:29	205.15	88.09
25/07/2013 03:35	205.15	78.53
25/07/2013 03:40	205.15	86.19
25/07/2013 03:45	205.16	72.09
25/07/2013 03:49	205.16	85.8
25/07/2013 03:55	205.16	75.88
25/07/2013 04:00	205.17	75.29
25/07/2013 04:04	205.17	77.93
25/07/2013 04:09	205.17	78
25/07/2013 04:15	205.18	89.2
25/07/2013 04:20	205.18	81.02
25/07/2013 04:24	205.18	77.13
25/07/2013 04:30	205.19	71.65
25/07/2013 04:35	205.19	64.48
25/07/2013 04:39	205.19	76.02
25/07/2013 04:44	205.20	75.6
25/07/2013 04:50	205.20	79.93
25/07/2013 04:55	205.20	76.4
25/07/2013 04:59	205.21	77.48
25/07/2013 05:05	205.21	73.35
25/07/2013 05:10	205.22	71.26
25/07/2013 05:15	205.22	70.85
25/07/2013 05:19	205.22	71.56

Table 4.10 continued from previous page

Date	Julian Day	m^3/s
25/07/2013 05:25	205.23	73.57
25/07/2013 05:30	205.23	71.63
25/07/2013 05:34	205.23	70.2
25/07/2013 05:39	205.24	71.63
25/07/2013 05:45	205.24	68.31
25/07/2013 05:50	205.24	73.39
25/07/2013 05:54	205.25	68.3
25/07/2013 06:00	205.25	57.44
25/07/2013 06:05	205.25	62.3
25/07/2013 06:09	205.26	60.41
25/07/2013 06:14	205.26	68.67
25/07/2013 06:20	205.26	64.94
25/07/2013 06:25	205.27	70.73
25/07/2013 06:29	205.27	70.23
25/07/2013 06:35	205.27	69.35
25/07/2013 06:40	205.28	72.36
25/07/2013 06:45	205.28	74.21
25/07/2013 06:49	205.28	67.22
25/07/2013 06:55	205.29	71.62
25/07/2013 07:00	205.29	65.14
25/07/2013 07:04	205.30	65.13
25/07/2013 07:09	205.30	70.8
25/07/2013 07:15	205.30	72.54
25/07/2013 07:20	205.31	68.4
25/07/2013 07:24	205.31	75.42
25/07/2013 07:30	205.31	70.22
25/07/2013 07:35	205.32	68.76
25/07/2013 07:39	205.32	65.78
25/07/2013 07:44	205.32	60.59
25/07/2013 07:50	205.33	59.89
25/07/2013 07:55	205.33	56.21
25/07/2013 07:59	205.33	58.35
25/07/2013 08:05	205.34	56.82
25/07/2013 08:10	205.34	59.48
25/07/2013 08:15	205.34	58.43

Table 4.10 continued from previous page

Date	Julian Day	m^3/s
25/07/2013 08:19	205.35	59.11
25/07/2013 08:25	205.35	55.12
25/07/2013 08:30	205.35	59.53
25/07/2013 08:34	205.36	57.77
25/07/2013 08:39	205.36	57.81
25/07/2013 08:45	205.36	54.77
25/07/2013 08:50	205.37	55.71
25/07/2013 08:54	205.37	60.13
25/07/2013 09:00	205.38	58.46
25/07/2013 09:05	205.38	60.94
25/07/2013 09:09	205.38	54.95
25/07/2013 09:14	205.39	57.54
25/07/2013 09:20	205.39	54.9
25/07/2013 09:25	205.39	55.01
25/07/2013 09:29	205.40	55.39
25/07/2013 09:35	205.40	56.6
25/07/2013 09:40	205.40	55.2
25/07/2013 09:45	205.41	53.95
25/07/2013 09:49	205.41	53.85
25/07/2013 09:55	205.41	54.91
25/07/2013 10:00	205.42	52.2
25/07/2013 10:04	205.42	52.23
25/07/2013 10:09	205.42	54.68
25/07/2013 10:15	205.43	49.57
25/07/2013 10:20	205.43	49.93
25/07/2013 10:24	205.43	49.64
25/07/2013 10:30	205.44	54.62
25/07/2013 10:35	205.44	51.46
25/07/2013 10:39	205.44	53.94
25/07/2013 10:44	205.45	48.82
25/07/2013 10:50	205.45	50.19
25/07/2013 10:55	205.45	51.07
25/07/2013 10:59	205.46	50.13
25/07/2013 11:05	205.46	51.13
25/07/2013 11:10	205.47	51.3

Table 4.10 continued from previous page

Date	Julian Day	m^3/s
25/07/2013 11:15	205.47	49.71
25/07/2013 11:19	205.47	50.97
25/07/2013 11:25	205.48	49.4
25/07/2013 11:30	205.48	51.63
25/07/2013 11:34	205.48	50.42
25/07/2013 11:39	205.49	52.15
25/07/2013 11:45	205.49	51.53
25/07/2013 11:50	205.49	48.54
25/07/2013 11:54	205.50	52.59
25/07/2013 12:00	205.50	51.05
25/07/2013 12:05	205.50	50.69
25/07/2013 12:09	205.51	49.77
25/07/2013 12:14	205.51	49.24
25/07/2013 12:20	205.51	47.52
25/07/2013 12:25	205.52	50.14
25/07/2013 12:29	205.52	50.09
25/07/2013 12:35	205.52	51.58
25/07/2013 12:40	205.53	50.59
25/07/2013 12:45	205.53	52.15
25/07/2013 12:49	205.53	48.34
25/07/2013 12:55	205.54	50.88
25/07/2013 13:00	205.54	51.94
25/07/2013 13:04	205.55	51.6
25/07/2013 13:09	205.55	51.19
25/07/2013 13:15	205.55	51.49
25/07/2013 13:20	205.56	52.43
25/07/2013 13:24	205.56	51.19
25/07/2013 13:30	205.56	49.27
25/07/2013 13:35	205.57	52.03
25/07/2013 13:39	205.57	52.32
25/07/2013 13:44	205.57	49.8
25/07/2013 13:50	205.58	45.68
25/07/2013 13:55	205.58	46.65
25/07/2013 13:59	205.58	46.48
25/07/2013 14:05	205.59	45.96

Table 4.10 continued from previous page

Date	Julian Day	m^3/s
25/07/2013 14:10	205.59	45.33
25/07/2013 14:15	205.59	45.17
25/07/2013 14:19	205.60	45.42
25/07/2013 14:25	205.60	47.78
25/07/2013 14:30	205.60	45.82
25/07/2013 14:34	205.61	43.74
25/07/2013 14:39	205.61	47.92
25/07/2013 14:45	205.61	45.96
25/07/2013 14:50	205.62	45.92
25/07/2013 14:54	205.62	46.98
25/07/2013 15:00	205.63	46.89
25/07/2013 15:05	205.63	46.45
25/07/2013 15:09	205.63	47.03
25/07/2013 15:14	205.64	46.71
25/07/2013 15:20	205.64	46.57
25/07/2013 15:25	205.64	47.15
25/07/2013 15:29	205.65	43.2
25/07/2013 15:35	205.65	44.92
25/07/2013 15:40	205.65	44.43
25/07/2013 15:45	205.66	47.81
25/07/2013 15:49	205.66	46.28
25/07/2013 15:55	205.66	46.08
25/07/2013 16:00	205.67	48.24
25/07/2013 16:04	205.67	45.1
25/07/2013 16:09	205.67	45.91
25/07/2013 16:15	205.68	45.9
25/07/2013 16:20	205.68	45.06
25/07/2013 16:24	205.68	45.51
25/07/2013 16:30	205.69	46.63
25/07/2013 16:35	205.69	45.31
25/07/2013 16:39	205.69	45.59
25/07/2013 16:44	205.70	45.99
25/07/2013 16:50	205.70	44.8
25/07/2013 16:55	205.70	45.38
25/07/2013 16:59	205.71	44.2

Table 4.10 continued from previous page

Date	Julian Day	m^3/s
25/07/2013 17:05	205.71	41.53
25/07/2013 17:10	205.72	45.23
25/07/2013 17:15	205.72	43.88
25/07/2013 17:19	205.72	44.45
25/07/2013 17:25	205.73	42.9
25/07/2013 17:30	205.73	44.67
25/07/2013 17:34	205.73	44.2
25/07/2013 17:39	205.74	43.34
25/07/2013 17:45	205.74	41.92
25/07/2013 17:50	205.74	42.59
25/07/2013 17:54	205.75	41.25
25/07/2013 18:00	205.75	44.07

Table 4.11 – *2013 Khudi Khola rainfall data (From J. Lavé).*

Date	Time at Intake	T Intake (°C)	Intake Cumulative mm	Intake mm/10′
24/07/2013 12:00	24/07/2013 11:59	31.98	1242.8	0
24/07/2013 12:10	24/07/2013 12:09	32.19	1242.8	0
24/07/2013 12:20	24/07/2013 12:19	31.47	1242.8	0
24/07/2013 12:30	24/07/2013 12:29	30.46	1242.8	0
24/07/2013 12:40	24/07/2013 12:39	30.15	1242.8	0
24/07/2013 12:50	24/07/2013 12:49	30.96	1242.8	0
24/07/2013 13:00	24/07/2013 12:59	31.47	1242.8	0
24/07/2013 13:10	24/07/2013 13:09	31.17	1242.8	0
24/07/2013 13:20	24/07/2013 13:19	30.56	1242.8	0
24/07/2013 13:30	24/07/2013 13:29	29.95	1242.8	0
24/07/2013 13:40	24/07/2013 13:39	30.66	1242.8	0
24/07/2013 13:50	24/07/2013 13:49	30.66	1242.8	0
24/07/2013 14:00	24/07/2013 13:59	29.85	1242.8	0
24/07/2013 14:10	24/07/2013 14:09	28.85	1242.8	0
24/07/2013 14:20	24/07/2013 14:19	27.66	1243.2	0.4
24/07/2013 14:30	24/07/2013 14:29	26	1244.8	1.6
24/07/2013 14:40	24/07/2013 14:39	25.32	1245.2	0.4
24/07/2013 14:50	24/07/2013 14:49	25.22	1245.2	0
24/07/2013 15:00	24/07/2013 14:59	25.12	1245.2	0

Table 4.11 continued from previous page

Date	Time at Intake	T Intake (°C)	Intake Cumulative mm	Intake mm/10′
24/07/2013 15:10	24/07/2013 15:09	25.12	1245.2	0
24/07/2013 15:20	24/07/2013 15:19	25.12	1245.2	0
24/07/2013 15:30	24/07/2013 15:29	25.42	1245.2	0
24/07/2013 15:40	24/07/2013 15:39	25.32	1245.2	0
24/07/2013 15:50	24/07/2013 15:49	25.32	1245.2	0
24/07/2013 16:00	24/07/2013 15:59	25.51	1245.2	0
24/07/2013 16:10	24/07/2013 16:09	25.61	1245.2	0
24/07/2013 16:20	24/07/2013 16:19	25.9	1245.2	0
24/07/2013 16:30	24/07/2013 16:29	26.2	1245.2	0
24/07/2013 16:40	24/07/2013 16:39	26.39	1245.2	0
24/07/2013 16:50	24/07/2013 16:49	26.58	1245.2	0
24/07/2013 17:00	24/07/2013 16:59	26.58	1245.2	0
24/07/2013 17:10	24/07/2013 17:09	26.49	1245.2	0
24/07/2013 17:20	24/07/2013 17:19	25.8	1245.2	0
24/07/2013 17:30	24/07/2013 17:29	24.93	1245.2	0
24/07/2013 17:40	24/07/2013 17:39	24.74	1245.2	0
24/07/2013 17:50	24/07/2013 17:49	24.64	1245.2	0
24/07/2013 18:00	24/07/2013 17:59	24.26	1245.2	0
24/07/2013 18:10	24/07/2013 18:09	23.77	1245.2	0
24/07/2013 18:20	24/07/2013 18:19	23.48	1245.2	0
24/07/2013 18:30	24/07/2013 18:29	23.2	1245.2	0
24/07/2013 18:40	24/07/2013 18:39	23	1245.2	0
24/07/2013 18:50	24/07/2013 18:49	22.91	1245.2	0
24/07/2013 19:00	24/07/2013 18:59	22.81	1245.2	0
24/07/2013 19:10	24/07/2013 19:09	22.72	1245.2	0
24/07/2013 19:20	24/07/2013 19:19	22.52	1245.2	0
24/07/2013 19:30	24/07/2013 19:29	22.33	1245.2	0
24/07/2013 19:40	24/07/2013 19:39	22.14	1245.4	0.2
24/07/2013 19:50	24/07/2013 19:49	22.05	1245.8	0.4
24/07/2013 20:00	24/07/2013 19:59	21.95	1246	0.2
24/07/2013 20:10	24/07/2013 20:09	21.86	1246.2	0.2
24/07/2013 20:20	24/07/2013 20:19	21.66	1246.2	0
24/07/2013 20:30	24/07/2013 20:29	21.86	1247.6	1.4
24/07/2013 20:40	24/07/2013 20:39	21.95	1251.4	3.8
24/07/2013 20:50	24/07/2013 20:49	22.05	1253.4	2

Table 4.11 continued from previous page

Date	Time at Intake	T Intake (°C)	Intake Cumulative mm	Intake mm/10′
24/07/2013 21:00	24/07/2013 20:59	21.95	1256.2	2.8
24/07/2013 21:10	24/07/2013 21:09	21.86	1262.8	6.6
24/07/2013 21:20	24/07/2013 21:19	21.86	1266	3.2
24/07/2013 21:30	24/07/2013 21:29	21.86	1273.2	7.2
24/07/2013 21:40	24/07/2013 21:39	21.86	1280.2	7
24/07/2013 21:50	24/07/2013 21:49	21.76	1289.2	9
24/07/2013 22:00	24/07/2013 21:59	21.66	1291.6	2.4
24/07/2013 22:10	24/07/2013 22:09	21.47	1292.6	1
24/07/2013 22:20	24/07/2013 22:19	21.47	1295.2	2.6
24/07/2013 22:30	24/07/2013 22:29	21.38	1299.6	4.4
24/07/2013 22:40	24/07/2013 22:39	21.28	1302	2.4
24/07/2013 22:50	24/07/2013 22:49	21.28	1303.2	1.2
24/07/2013 23:00	24/07/2013 22:59	21.19	1304.2	1
24/07/2013 23:10	24/07/2013 23:09	21.09	1305.4	1.2
24/07/2013 23:20	24/07/2013 23:19	21.09	1310.4	5
24/07/2013 23:30	24/07/2013 23:29	21.09	1316.6	6.2
24/07/2013 23:40	24/07/2013 23:39	21	1319.2	2.6
24/07/2013 23:50	24/07/2013 23:49	20.9	1320.8	1.6
25/07/2013 00:00	24/07/2013 23:59	20.8	1322	1.2
25/07/2013 00:10	25/07/2013 00:09	20.71	1323	1
25/07/2013 00:20	25/07/2013 00:19	20.62	1324.4	1.4
25/07/2013 00:30	25/07/2013 00:29	20.62	1326.8	2.4
25/07/2013 00:40	25/07/2013 00:39	20.42	1329.8	3
25/07/2013 00:50	25/07/2013 00:49	20.52	1334.6	4.8
25/07/2013 01:00	25/07/2013 00:59	20.42	1340.6	6
25/07/2013 01:10	25/07/2013 01:09	20.52	1345.8	5.2
25/07/2013 01:20	25/07/2013 01:19	20.52	1350.6	4.8
25/07/2013 01:30	25/07/2013 01:29	20.52	1353.2	2.6
25/07/2013 01:40	25/07/2013 01:39	20.42	1354.4	1.2
25/07/2013 01:50	25/07/2013 01:49	20.23	1355	0.6
25/07/2013 02:00	25/07/2013 01:59	20.04	1355.8	0.8
25/07/2013 02:10	25/07/2013 02:09	19.95	1356.6	0.8
25/07/2013 02:20	25/07/2013 02:19	19.95	1356.8	0.2
25/07/2013 02:30	25/07/2013 02:29	19.85	1357.2	0.4
25/07/2013 02:40	25/07/2013 02:39	19.85	1357.6	0.4

Table 4.11 continued from previous page

Date	Time at Intake	T Intake (°C)	Intake Cumulative mm	Intake mm/10′
25/07/2013 02:50	25/07/2013 02:49	19.85	1357.8	0.2
25/07/2013 03:00	25/07/2013 02:59	19.85	1357.8	0
25/07/2013 03:10	25/07/2013 03:09	19.76	1357.8	0
25/07/2013 03:20	25/07/2013 03:19	19.66	1357.8	0
25/07/2013 03:30	25/07/2013 03:29	19.66	1357.8	0
25/07/2013 03:40	25/07/2013 03:39	19.76	1357.8	0
25/07/2013 03:50	25/07/2013 03:49	19.85	1358	0.2
25/07/2013 04:00	25/07/2013 03:59	19.85	1358.2	0.2
25/07/2013 04:10	25/07/2013 04:09	19.76	1358.4	0.2
25/07/2013 04:20	25/07/2013 04:19	19.66	1358.8	0.4
25/07/2013 04:30	25/07/2013 04:29	19.57	1359.2	0.4
25/07/2013 04:40	25/07/2013 04:39	19.57	1359.6	0.4
25/07/2013 04:50	25/07/2013 04:49	19.57	1359.8	0.2
25/07/2013 05:00	25/07/2013 04:59	19.57	1360.2	0.4
25/07/2013 05:10	25/07/2013 05:09	19.66	1360.8	0.6
25/07/2013 05:20	25/07/2013 05:19	19.66	1361.4	0.6
25/07/2013 05:30	25/07/2013 05:29	19.76	1362	0.6
25/07/2013 05:40	25/07/2013 05:39	19.76	1362.4	0.4
25/07/2013 05:50	25/07/2013 05:49	19.76	1362.8	0.4
25/07/2013 06:00	25/07/2013 05:59	19.76	1363.2	0.4
25/07/2013 06:10	25/07/2013 06:09	19.66	1363.8	0.6
25/07/2013 06:20	25/07/2013 06:19	19.66	1364.2	0.4
25/07/2013 06:30	25/07/2013 06:29	19.66	1364.8	0.6
25/07/2013 06:40	25/07/2013 06:39	19.66	1365.2	0.4
25/07/2013 06:50	25/07/2013 06:49	19.66	1365.4	0.2
25/07/2013 07:00	25/07/2013 06:59	19.57	1365.6	0.2
25/07/2013 07:10	25/07/2013 07:09	19.66	1365.8	0.2
25/07/2013 07:20	25/07/2013 07:19	19.76	1365.8	0
25/07/2013 07:30	25/07/2013 07:29	19.85	1365.8	0
25/07/2013 07:40	25/07/2013 07:39	20.04	1365.8	0
25/07/2013 07:50	25/07/2013 07:49	20.33	1365.8	0
25/07/2013 08:00	25/07/2013 07:59	20.71	1365.8	0
25/07/2013 08:10	25/07/2013 08:09	21	1365.8	0
25/07/2013 08:20	25/07/2013 08:19	21.38	1365.8	0
25/07/2013 08:30	25/07/2013 08:29	21.38	1365.8	0

Table 4.11 continued from previous page

Date	Time at Intake	T Intake (°C)	Intake Cumulative mm	Intake mm/10′
25/07/2013 08:40	25/07/2013 08:39	21.28	1365.8	0
25/07/2013 08:50	25/07/2013 08:49	21.38	1365.8	0
25/07/2013 09:00	25/07/2013 08:59	21.47	1365.8	0
25/07/2013 09:10	25/07/2013 09:09	21.57	1365.8	0
25/07/2013 09:20	25/07/2013 09:19	22.05	1365.8	0
25/07/2013 09:30	25/07/2013 09:29	23.77	1365.8	0
25/07/2013 09:40	25/07/2013 09:39	24.84	1365.8	0
25/07/2013 09:50	25/07/2013 09:49	26.2	1365.8	0
25/07/2013 10:00	25/07/2013 09:59	26.78	1365.8	0
25/07/2013 10:10	25/07/2013 10:09	27.76	1365.8	0
25/07/2013 10:20	25/07/2013 10:19	28.36	1365.8	0
25/07/2013 10:30	25/07/2013 10:29	28.66	1365.8	0
25/07/2013 10:40	25/07/2013 10:39	29.65	1365.8	0
25/07/2013 10:50	25/07/2013 10:49	30.46	1365.8	0
25/07/2013 11:00	25/07/2013 10:59	31.17	1365.8	0
25/07/2013 11:10	25/07/2013 11:09	30.76	1365.8	0
25/07/2013 11:20	25/07/2013 11:19	30.46	1365.8	0
25/07/2013 11:30	25/07/2013 11:29	30.46	1365.8	0
25/07/2013 11:40	25/07/2013 11:39	30.96	1365.8	0
25/07/2013 11:50	25/07/2013 11:49	30.96	1365.8	0
25/07/2013 12:00	25/07/2013 11:59	30.15	1365.8	0
25/07/2013 12:10	25/07/2013 12:09	28.85	1365.8	0
25/07/2013 12:20	25/07/2013 12:19	27.76	1365.8	0
25/07/2013 12:30	25/07/2013 12:29	27.17	1365.8	0
25/07/2013 12:40	25/07/2013 12:39	26.98	1365.8	0
25/07/2013 12:50	25/07/2013 12:49	26.78	1365.8	0
25/07/2013 13:00	25/07/2013 12:59	26.78	1365.8	0
25/07/2013 13:10	25/07/2013 13:09	26.88	1365.8	0
25/07/2013 13:20	25/07/2013 13:19	27.08	1365.8	0
25/07/2013 13:30	25/07/2013 13:29	27.37	1365.8	0
25/07/2013 13:40	25/07/2013 13:39	27.27	1365.8	0
25/07/2013 13:50	25/07/2013 13:49	27.08	1365.8	0
25/07/2013 14:00	25/07/2013 13:59	26.78	1365.8	0
25/07/2013 14:10	25/07/2013 14:09	26.78	1365.8	0
25/07/2013 14:20	25/07/2013 14:19	26.49	1365.8	0

Table 4.11 continued from previous page

Date	Time at Intake	T Intake (°C)	Intake Cumulative mm	Intake mm/10′
25/07/2013 14:30	25/07/2013 14:29	26.29	1365.8	0
25/07/2013 14:40	25/07/2013 14:39	26.2	1365.8	0
25/07/2013 14:50	25/07/2013 14:49	26.1	1365.8	0
25/07/2013 15:00	25/07/2013 14:59	26.1	1365.8	0
25/07/2013 15:10	25/07/2013 15:09	26.39	1365.8	0
25/07/2013 15:20	25/07/2013 15:19	26.78	1365.8	0
25/07/2013 15:30	25/07/2013 15:29	27.08	1365.8	0
25/07/2013 15:40	25/07/2013 15:39	27.27	1365.8	0
25/07/2013 15:50	25/07/2013 15:49	27.27	1365.8	0
25/07/2013 16:00	25/07/2013 15:59	27.27	1365.8	0
25/07/2013 16:10	25/07/2013 16:09	27.27	1365.8	0
25/07/2013 16:20	25/07/2013 16:19	27.37	1365.8	0
25/07/2013 16:30	25/07/2013 16:29	27.47	1365.8	0
25/07/2013 16:40	25/07/2013 16:39	26.88	1365.8	0
25/07/2013 16:50	25/07/2013 16:49	26.39	1365.8	0
25/07/2013 17:00	25/07/2013 16:59	26	1365.8	0
25/07/2013 17:10	25/07/2013 17:09	25.51	1365.8	0
25/07/2013 17:20	25/07/2013 17:19	25.22	1365.8	0
25/07/2013 17:30	25/07/2013 17:29	25.12	1365.8	0
25/07/2013 17:40	25/07/2013 17:39	24.54	1365.8	0
25/07/2013 17:50	25/07/2013 17:49	23.68	1366	0.2
25/07/2013 18:00	25/07/2013 17:59	23	1366.8	0.8

Table 4.12 – *2015 Rainfall and discharge data at Khudi Khola Intake (Calculated from pressure gauge by J. Lavé).*

Date	Rain/10′ (mm)	Date	m^3/s
29/7/15 11:45	0	29.45	13.03
29/7/15 12:15	0	29.4569	13.09
29/7/15 12:45	0	29.4639	13.06
29/7/15 13:15	0	29.4708	12.93
29/7/15 13:45	0	29.4778	12.76
29/7/15 14:45	0	29.4847	13
29/7/15 15:00	0	29.4917	12.58
29/7/15 15:15	0	29.4986	12.85

Table 4.12 continued from previous page

Date	Rain/10′ (mm)	Date	m^3/s
29/7/15 15:45	0.4	29.5056	13.06
29/7/15 15:55	0.4	29.5125	12.85
29/7/15 16:05	0	29.5194	12.57
29/7/15 16:15	0	29.5264	12.58
29/7/15 16:25	0	29.5333	12.73
29/7/15 16:35	0	29.5403	12.7
29/7/15 16:45	0	29.5472	12.99
29/7/15 16:55	0	29.5542	9.51
29/7/15 17:05	0	29.5611	10.29
29/7/15 17:15	0	29.5681	10.51
29/7/15 17:25	0	29.575	10.56
29/7/15 17:35	0	29.5819	10.72
29/7/15 17:45	0	29.5889	10.75
29/7/15 17:55	0	29.5958	10.53
29/7/15 18:05	0	29.6028	10.44
29/7/15 18:15	0	29.6097	10.33
29/7/15 18:25	0	29.6167	10.18
29/7/15 18:35	0	29.6236	10.17
29/7/15 18:45	0	29.6306	10.11
29/7/15 18:55	0	29.6375	9.95
29/7/15 19:05	0	29.6444	10.05
29/7/15 19:15	0	29.6514	10
29/7/15 19:25	0	29.6583	10.01
29/7/15 19:35	0	29.6653	10
29/7/15 19:45	0	29.6722	9.97
29/7/15 19:55	0	29.6792	9.99
29/7/15 20:05	0	29.6861	9.93
29/7/15 20:15	0	29.6931	9.93
29/7/15 20:25	0	29.7	9.97
29/7/15 20:35	0	29.7069	9.97
29/7/15 20:45	0	29.7139	9.97
29/7/15 20:55	0	29.7208	9.95
29/7/15 21:05	0	29.7278	9.99
29/7/15 21:15	0	29.7347	9.99
29/7/15 21:25	0	29.7417	9.96

Table 4.12 continued from previous page

Date	Rain/10′ (mm)	Date	m^3/s
29/7/15 21:35	0	29.7486	10
29/7/15 21:45	2	29.7556	10.01
29/7/15 21:55	4	29.7625	10.01
29/7/15 22:05	3.2	29.7694	10.01
29/7/15 22:15	4.4	29.7764	9.99
29/7/15 22:25	3.2	29.7833	10.01
29/7/15 22:35	3.2	29.7903	9.97
29/7/15 22:45	2	29.7972	10
29/7/15 22:55	2.8	29.8042	10.01
29/7/15 23:05	7.6	29.8111	10.07
29/7/15 23:15	10.8	29.8181	10.04
29/7/15 23:25	9.2	29.825	10.08
29/7/15 23:35	8	29.8319	10.08
29/7/15 23:45	4	29.8389	10.08
29/7/15 23:55	5.2	29.8458	10
30/7/15 0:05	2	29.8528	9.97
30/7/15 0:15	2.8	29.8597	10.37
30/7/15 0:25	3.6	29.8667	10.27
30/7/15 0:35	2.8	29.8736	10.38
30/7/15 0:45	2.4	29.8806	10.41
30/7/15 0:55	2	29.8875	10.27
30/7/15 1:05	2.4	29.8944	10.4
30/7/15 1:15	2.4	29.9014	10.52
30/7/15 1:25	2.8	29.9083	10.52
30/7/15 1:35	2	29.9153	10.66
30/7/15 1:45	0.8	29.9222	12.96
30/7/15 1:55	0	29.9292	12.93
30/7/15 2:05	0.4	29.9361	12.96
30/7/15 2:15	0.4	29.9431	12.04
30/7/15 2:25	0.4	29.95	11.86
30/7/15 2:35	0.4	29.9569	13.42
30/7/15 2:45	0	29.9639	20.74
30/7/15 2:55	0	29.9708	23.26
30/7/15 3:05	0	29.9778	20.49
30/7/15 3:15	0	29.9847	19.65

Table 4.12 continued from previous page

Date	Rain/10′ (mm)	Date	m^3/s
30/7/15 3:45	0	29.9917	16.27
30/7/15 4:15	0	29.9986	19.98
30/7/15 4:45	0	30.0056	30.79
30/7/15 5:15	0	30.0125	32.99
30/7/15 5:45	0	30.0194	32.41
30/7/15 6:15	0	30.0264	33.34
30/7/15 6:45	0	30.0333	35.17
30/7/15 7:15	0	30.0403	35.37
30/7/15 7:45	0	30.0472	35.78
30/7/15 8:15	0	30.0542	37.45
30/7/15 8:45	0	30.0611	35.73
30/7/15 9:15	0	30.0681	38.32
30/7/15 9:45	0	30.075	37.93
30/7/15 10:15	0	30.0819	39.68
30/7/15 10:45	0	30.0889	38.34
30/7/15 11:15	0	30.0958	35.11
30/7/15 11:45	0	30.1028	34.84
30/7/15 12:15	0	30.1097	34.47
30/7/15 12:25	0	30.1167	33.27
30/7/15 12:35	0	30.1236	31.92
30/7/15 12:45	2.8	30.1306	30.54
		30.1375	28.86
		30.1444	27.88
		30.1514	28.51
		30.1583	27.74
		30.1653	26.25
		30.1722	25.44
		30.1792	24.43
		30.1861	23.38
		30.1931	22.61
		30.2	21.98
		30.2069	21.52
		30.2139	21.19
		30.2208	19.82
		30.2278	20.29

Table 4.12 continued from previous page

Date	Rain/10′ (mm)	Date	m^3/s
		30.2347	19.26
		30.2417	18.96
		30.2486	17.84
		30.2556	18.63
		30.2625	20.08
		30.2694	19.93
		30.2764	19.62
		30.2833	19.08
		30.2903	19.35
		30.2972	18.82
		30.3042	18.1
		30.3111	18.01
		30.3181	17.4
		30.325	22.51
		30.3319	22.22
		30.3389	21.75
		30.3458	21.32
		30.3528	20.93
		30.3597	20.34
		30.3667	19.92
		30.3736	19.87
		30.3806	19.41
		30.3875	18.74
		30.3944	18.6
		30.4014	18.59
		30.4083	18.73
		30.4153	18.31
		30.4222	18.25
		30.4292	18.31
		30.4361	18.34
		30.4431	21.46
		30.45	21.36
		30.4569	21.41
		30.4639	21.53
		30.4708	21.22

Table 4.12 continued from previous page

Date	Rain/10′ (mm)	Date	m^3/s
		30.4778	21.06
		30.4847	20.77
		30.4917	20.85
		30.4986	20.78
		30.5056	20.71
		30.5125	20.24
		30.5194	20.64
		30.5264	20.66
		30.5333	20.47
		30.5403	18.83
		30.5472	18.82
		30.5542	19.05
		30.5611	18.77
		30.5681	19.04
		30.575	18.82
		30.5819	18.88
		30.5889	19.27
		30.5958	19.18
		30.6028	18.97
		30.6097	19.12
		30.6167	19.06
		30.6236	19.18
		30.6306	15.11
		30.6375	15.25
		30.6444	13.02
		30.6514	12.53
		30.6583	12.73
		30.6653	12.56
		30.6722	12.58
		30.6792	12.47
		30.6861	12.32
		30.6931	12.32
		30.7	12.04
		30.7069	12.38
		30.7139	12.42

Table 4.12 continued from previous page

Date	Rain/10′ (mm)	Date	m^3/s
		30.7208	12.21
		30.7278	12.25
		30.7347	12.43
		30.7417	12.36
		30.7486	12.52
		30.7556	12.49
		30.7625	12.18
		30.7694	12.27
		30.7764	12.18
		30.7833	12.21
		30.7903	12.34
		30.7972	12.58
		30.8042	12.61
		30.7903	12.34
		30.7972	12.58
		30.8042	12.61

Table 4.9 – *Average analytical data by session for the samples analyzed in this study.*

	$^{41}K/^{40}Ca$	Raw ratios (Line 1)			Line 2	Corrected ratios (static mode)			
		$^{40}Ca/^{44}Ca$	$^{42}Ca/^{44}Ca$	$^{43}Ca/^{44}Ca$	$^{40}Ca/^{42}Ca$	$^{40}Ca/^{44}Ca$ (ST)	± (2 S.D.)	$^{43}Ca/^{44}Ca$ (ST)	± (2 S.D.)
Session 1B (May 2014)	7.51E-04	46.40274	0.30976	0.06461		47.10575	2.80E-03	0.06486	5.01E-06
Session 2 (July 2014)	1.00E-03	46.37640	0.30969	0.06460		47.09675	2.75E-03	0.06486	5.23E-06
Session 6 (April 2015)	5.87E-04	46.39036	0.30973	0.06461		47.14327	2.53E-03	0.06486	6.15E-06
Session 6B (April 2015)	4.10E-04	46.35035	0.30958	0.06460		47.15059	2.89E-03	0.06487	6.04E-06
Session 7 (July 2015)	4.84E-04	46.35148	0.30959	0.06459		47.13892	2.94E-03	0.06487	6.34E-06
Session 8 (February 2016)	3.69E-03	46.39896	0.30974	0.06461		47.11998	9.76E-02	0.06487	1.37E-04
Three Year Averages (± 2 S.D.)		**46.37838**	**0.30968**	**0.06460**		**47.12588**	**1.86E-02**	**0.06487**	**2.76E-05**

	Corrected ratios multidynamic mode)					$\varepsilon^{40}Ca$ (I-MD)	± (2 S.D.)	$\varepsilon^{40}Ca$ (ST)	± (2S.D.)
	$^{40}Ca/^{42}Ca$ (MD)	$^{40}Ca/^{44}Ca$ (MD)	± (2S.D.)	$^{40}Ca/^{44}Ca$ (I-MD)	± (2S.D.)				
Session 1B (May 2014)	151.04263	47.15702	1.71E-03	47.15668	1.40E-03	1.10	2.97E-01	0.19	5.94E-01
Session 2 (July 2014)	151.02794	47.15243	1.67E-03	47.15241	1.42E-03	0.20	3.01E-01	-1.42	5.83E-01
Session 6 (April 2015)	151.03036	47.15319	1.79E-03	47.15299	1.46E-03	1.24	3.10E-01	1.59	5.36E-01
Session 6B (April 2015)	151.05425	47.16065	2.00E-03	47.16027	1.69E-03	1.29	3.59E-01	0.91	6.13E-01
Session 7 (July 2015)	151.04765	47.15859	1.84E-03	47.15844	1.55E-03	0.78	3.28E-01	0.76	6.24E-01
Session 8 (February 2016)	151.04875	47.15893	9.69E-02	47.15907	2.69E-03	1.03	5.70E-01	0.98	2.07E+01
Three Year Averages (± 2 S.D.)	**151.04193**	**47.15680**	**1.76E-02**	**47.15664**	**1.70E-03**	**0.94**	**3.61E-01**	**0.50**	**3.94E+00**

	$\varepsilon^{43}Ca$ (ST)	± (2S.D.)	Mass Fract. Factor (‰)	Mass Fract. Rate (ppm.s^{-1})	F	ΔR_C (ppm)
Session 1B (May 2014)	-0.47	7.72E-01	-3.92	0.19	1.000007	7.19
Session 2 (July 2014)	-0.10	8.06E-01	-4.03	0.19	1.000007	0.50
Session 6 (April 2015)	0.45	9.48E-01	-3.97	0.04	1.000001	4.14
Session 6B (April 2015)	0.51	9.31E-01	-4.21	0.10	1.000004	7.97
Session 7 (July 2015)	-0.07	9.77E-01	-4.20	0.15	1.000006	3.17
Session 8 (February 2016)	0.29	2.11E+01	-3.95	0.12	1.000005	-2.87
Three Year Averages (± 2 S.D.)	**0.10**	**4.26E+00**	**-4.05**	**0.13**	**1.000005**	**3.35**

CHAPTER 5

RADIOGENIC CA SYSTEMATICS IN THE NARAYANI BASIN, CENTRAL NEPAL

> Thus identified with astronomy, in proclaiming truths supposed to be hostile to Scripture, Geology has been denounced as the enemy of religion. The twin sisters of terrestrial and celestial physics have thus been joint - heirs of intolerance and persecution - unresisting victims in the crusade which ignorance and fanaticism are ever waging against science. When great truths are driven to make an appeal to reason, knowledge becomes criminal, and philosophers martyrs. Truth, however, like all moral powers, can neither be checked nor extinguished. When compressed, it but reacts the more. It crushes where it cannot expand—it burns where it is not allowed to shine. Human when originally divulged, it becomes divine when finally established. At first, the breath of a rage – at last it is the edict of a god. Endowed with such vital energy, astronomical truth has cut its way through the thick darkness of superstitious times, and, cheered by its conquests, Geology will find the same open path when it has triumphed over the less formidable obstacles of a civilized age.
>
> David Brewster *More Worlds Than One: The Creed of the Philosopher and the Hope of the Christian*

5.1 Introduction

Silicate weathering consumes CO_2 and thus plays an important role in determining the pCO_2 of the atmosphere over geological time periods (i.e., millions of years) (Walker et al., 1981; Berner et al., 2003). Overall, approximately 70% of CO_2 removal from the atmosphere occurs through silicate weathering processes, coupled with biogenic carbonate precipitation (Gaillardet et al., 1999), whereas the remaining 30% is consumed by the burial of organic carbon (Walker et al., 1981; Garrels, 1974; Lasaga et al., 1985; Berner, 1990). Knowledge of the magnitudes and sources of silicate and carbonate weathering is important because these two processes do not have the same effect on the global carbon cycle, river geochemistry, and geomorphology, especially in such a dynamic setting as the Himalaya. One of the best approaches to study silicate weathering is by using the dissolved load composition of rivers. However, to apply this approach it is essential to determine the proportion of the dissolved cations that derive from silicate, rather than carbonate, weathering.

Although scientists have discussed the links between silicate weathering and the long-term carbon cycle for more than 150 years (Ebelmen, 1845; Högbom, 1894; Chamberlin, 1899; Goudie and Viles, 2012), the complexity of these interactions at the Earth's surface has produced several, often conflicting, interpretations concerning the magnitude and characteristics of these processes over varying time-scales. Two main hypotheses exist that attempt to connect chemical weathering and the long-term carbon cycle: one that is controlled by climate and another that is controlled by tectonics. In the climate-controlled hypothesis, Berner and Raiswell (1983) and Kump et al. (2000) suggested that volcanic eruptions (i.e., increases in atmospheric CO_2) lead to higher temperatures, which enhance weathering rates, the consumption of CO_2, and finally decreases in temperature. Contrarily, in the tectonic-controlled hypothesis, Raymo and Ruddiman (1992) and Ruddiman et al. (1997) proposed that the uplift of mountain ranges increases the availability of fresh mineral surfaces, leading to increases in chemical weathering, and thus an increase in the consumption of CO_2 and a decrease in temperature. Despite these two hypotheses, there is still a lack of knowledge that complicates our understanding of the links and interactions between erosion, weathering, uplift, climate, and the long-term carbon cycle (Goudie and Viles, 2012). One of the biggest challenges in this field is the ability to quantify the feedbacks between chemical weathering and the carbon cycle. Goudie and Viles (2012) proposed that there is a need for better datasets of weathering rates that span the geomorphological diversity of global landscapes to aid in advancing our understanding of the links between chemical weathering and the long-term carbon cycle.

These issues and interactions are especially relevant to the Himalaya, the sole region of the world that is currently experiencing a combination of uplift, related to the Indian-Asian collision, and monsoonal precipitation. In order to understand these interactions in the Himalaya, however, we must first understand the sources and magnitudes of silicate and carbonate weathering. Many efforts have been made to do this in Himalayan rivers (Galy and France-Lanord, 1999; Galy et al., 1999; Bickle et al., 2001, 2005). A detailed review of these methods and budgets is presented in Chapter 1 of this thesis. Briefly, Berner and Raiswell (1983) estimated the areas and relative rates of weathering of silicate and carbonate rocks. Mackenzie et al. (1967) used modal mineral compositions to delineate between varying water compositions. Other authors have used estimates of the average major elemental ratios of silicate and carbonate rocks to constrain the relative contributions of these lithologies to water chemistry (Harris et al., 1998; Krishnaswami et al., 1999; Galy and France-Lanord, 1999; Gaillardet et al., 1999). More recently, several studies have used methods that estimate the proportion of the carbonate and silicate inputs to river waters using mixing arrays in Sr-Ca-Mg-Na-K-$^{87}Sr/^{86}Sr$ space (i.e., by solving two or more mass balance equations simultaneously for the weight fractions of the carbonate and silicate sources required to obtain the measured water composition) (Singh et al., 1998; West et al., 2002; Bickle et al., 2005, 2015). Non-traditional isotopic methods have also gained popularity, throughout the past 20 years, when trying to solve problems related to Himalayan erosion and weathering. These methods include the use of the stable isotopes of calcium and magnesium (Tipper et al., 2008) and lithium (Kısakűrek et al., 2005).

Another popular method used to determine the relative contributions of silicate and carbonate sources is the isotopes of Sr. Wadleigh et al. (1985) first suggested the possibility of using a combination of $^{87}Sr/^{86}Sr$ compositions and Ca/Sr ratios of river water to quantify the amount of silicate weathering and identify the sources of Ca^{2+} and Sr^{2+}. Erosion of Himalayan lithologies has given the dissolved load of Himalayan rivers unique strontium isotope and elemental characteristics (i.e., high Sr concentrations and highly radiogenic $^{87}Sr/^{86}Sr$ compositions compared with those of the world's largest rivers). This contrasts with what is observed in most non-Himalayan rivers (Gaillardet et al., 1997, 1999), which typically show anti-correlated $^{87}Sr/^{86}Sr$ ratios and Sr abundances, reflecting the normally unradiogenic nature of the Sr-rich carbonate end-member. Using $^{87}Sr/^{86}Sr$ ratios to trace Himalayan silicate weathering is not straightforward because (1) the formations of the Himalaya have different crustal ages, hence contrasting bulk $^{87}Sr/^{86}Sr$ compositions and (2) recent metamorphism redistributed radiogenic ^{87}Sr among silicate phases and towards carbonates (France-Lanord et al., 1993). Edmond (1992) and others (Palmer

and Edmond, 1989, 1992; Derry and France-Lanord, 1996) proposed that, during metamorphism, there was a redistribution of Sr between coexisting silicate phases. For example, the Sr isotopic composition of relatively resistant and very radiogenic biotites was redistributed to less resistant and radiogenic plagioclase. An even more important, complicating factor in studies of Himalayan rivers is that carbonates, during metamorphism, have inherited the Sr isotopic composition of silicates (France-Lanord et al., 1993). For this reason, the relative magnitudes of silicate and carbonate weathering cannot be simply inferred from the Sr isotopic composition of the dissolved load, as both rock types have very similar isotope signatures. Therefore, Sr isotopes cannot divulge unambiguous information on the magnitude of silicate weathering and the consumption of CO_2 in the Himalaya.

All of the methods described above have their own respective advantages and disadvantages. Despite the availability of several methods to estimate the relative contributions of carbonate and silicate weathering, there is not one, single method that stands out as the most accurate. For major elemental budgets, defining appropriate end-members for individual catchments and specific lithologies remains a problem. Determining the magnitude of silicate weathering in smaller catchments is problematic due to the occurrence of catchment specific geological processes such as landslides, physical erosion, and the presence of disseminated calcite, among others. On the other hand, larger basins average the variations in lithology and other factors across a large area and thus pose less of a problem when trying to calculate the magnitude of silicate weathering. Vegetation, specifically its potential to isotopically fractionate Ca, as well as the large variability in stable isotopic compositions in Himalayan rivers, poses problems for the application of stable Ca isotopes (Tipper et al., 2008). For Li isotopes, questions remain as to the extent of fractionation during weathering (i.e., differences in fractionation between the dissolved and suspended load) and its influence on Li isotopic compositions (Kısakűrek et al., 2005). Finally, a widespread complicating factor throughout the Himalaya, in our search to understand the sources and magnitude of silicate and carbonate weathering, is the process of secondary carbonate precipitation, observed in basins that are oversaturated with respect to calcite (Galy and France-Lanord, 1999; Galy et al., 1999; Jacobson et al., 2002; Bickle et al., 2005, 2015). Secondary carbonate precipitation leads to excesses of dissolved Mg and Sr relative to Ca. This process has less of an effect on small HHC or LH tributaries but is more significant for large tributaries such as the Kali Gandaki, Seti, Marsyandi, and Narayani whose resulting major elemental budgets do not reflect the lithology in each respective basin. This, and other problems, will be discussed later in this chapter.

This study develops a new application of the ^{40}K–^{40}Ca radiogenic isotope

system, in order to explore radiogenic calcium's potential to trace the signature of carbonate and silicate weathering in Himalayan rivers. The ^{40}K–^{40}Ca decay scheme has geochemical properties similar to those of the ^{87}Rb/^{87}Sr system. However, unlike Sr, calcium is a major element that plays a pivotal role in the global carbon cycle.

Potassium-40 has a branched decay scheme (λ = 5.543 x 10^{-10} year^{-1}) (White, 2013) in which 11% of the total decay comes from electron capture producing the decay of ^{40}K to ^{40}Ar (λ_e = 0.581 x 10^{-10} year^{-1}) (White, 2013), whereas 89% of the total decay can be attributed to the β^- decay of ^{40}K to ^{40}Ca (λ_B = 4.962 x 10^{-10} year^{-1}) (Nägler and Villa, 2000). Ultramafic rocks usually have low K/Ca ratios on the order of 0.01 and thus have radiogenic ingrowth of Ca that is well below the current detection limits (< 0.40 ε-units; see Chapter 3). Taylor and Blum (1995) estimate that the upper continental crust has a K/Ca (molar) ratio of approximately 0.95. If we assume that crustal growth began at 3.8 Ga, the decay of ^{40}K to ^{40}Ca would produce an approximate 2.5–3 ε-unit growth in the ε^{40}Ca composition of the upper continental crust (Caro et al., 2010). However, this value is just an average. The upper crust can contain certain felsic (silicate) lithologies, which have high K/Ca ratios between 1 and 4 (and greater), thus producing large abundances of ^{40}Ca (Caro et al., 2010). In contrast, Caro et al. (2010) has shown that the ^{40}Ca composition of marine carbonates and thus of seawater has remained constant and indistinguishable from the mantle value for > 3.5 Ga, testifying to a dominantly mantle source for the Ca in the ocean.

More recently, studies have questioned the hypothesis that the radiogenic Ca composition of the oceans has remained equivalent to that of the mantle (i.e., 0) (Antonelli et al., 2018). Antonelli et al. (2018) found that, relative to igneous rocks standards (i.e., the bulk silicate earth represented by oceanic basalts or meteorites), seawater and the standard SRM915a have radiogenic compositions, which implies that: 1) SRM915a is not an acceptable standard to estimate ^{40}Ca excesses and 2) that seawater may be slightly more radiogenic than the mantle over the past 3.5 Ga. However, radiogenic Ca analyses from Schiller et al. (2012) and Simon et al. (2009) show that the ε^{40}Ca values of several standards and basalts are identical to the value of the SRM915a standard. Despite these discrepancies, we can hypothesize that seawater has remained indistinguishable or slightly more radiogenic than the modern mantle over the past 3.5 Ga (Simon et al., 2009; Caro et al., 2010; Schiller et al., 2012; Antonelli et al., 2018). In either case, the definition of the bulk silicate Earth and its agreement with SRM915a has no influence on the interpretation of the results of this thesis.

Caro et al. (2010) hinted at the possibility of using ^{40}Ca as a tracer of silicate weathering based on analyses of the dissolved loads of the Ganga, Brahmaputra, Columbia, and Mississippi rivers because the Columbia (young basaltic rocks) and the Mississippi (predominantly carbonate) have unradiogenic water compositions

whereas Caro et al. (2010) observed that the Ganga and Brahmaputra have ^{40}Ca excesses. This led to the hypothesis that the radiogenic Ca system could be used to quantify the magnitude of carbonate and silicate weathering based on the distinct isotopic differences between rivers that drain carbonate and silicate lithologies from the main Himalayan formations of central Nepal (see below).

At present these are the only four published measurements of radiogenic Ca isotope ratios in rivers, and the controls on dissolved radiogenic Ca isotope ratios are therefore largely unconstrained. The central Himalayan survey presented here, mostly focused on the Narayani Basin, includes samples from all of the major formations of the central Himalaya (see below). We demonstrate that 1) radiogenic Ca isotope signatures, unlike Sr during recent metamorphic events, have not been significantly transferred from silicate to carbonate, 2) that carbonate bed rock and rivers dominated by carbonate input have no detectable radiogenic Ca signature, whereas silicate bedrock and rivers influenced by silicate lithologies have radiogenic signatures that depend on the age of the weathered source rock and its K/Ca ratio, and 3) radiogenic Ca systematics present a scenario in which catchments can be modeled by approximate two-component mixing trends between a carbonate and silicate source. This new data set allows us to shed light on silicate and carbonate weathering processes in the Narayani basin that was not attainable before now with more traditional methods of source tracing.

5.2 Geological Setting

The Himalayan range can be divided into three major litho-tectonic units, separated by detachment systems (Le Fort, 1989, 1999) (see Figures 5.1 and 5.2). Moving from Tibet to the Ganga plain in the south, they are:

1. The Tethyan Sedimentary Series (TSS). The TSS is a sedimentary terrain formed from deposition along the North Indian passive margin environment in the Tethys Ocean between the Cambrian and Eocene. The TSS contains clastic sediments, marls, and limestones metamorphosed to varying extents. For silicate rocks, $^{87}Sr/^{86}Sr \leq 0.720$ (Derry and France-Lanord, 1997; France-Lanord and Fort, 1988). The TSS accounts for approximately 30% (Department of Mines and Geology of Nepal) (Morin, 2015) of outcropping lithology in the Narayani basin.

2. The High Himalayan Crystalline series (HHC). The TSS is separated from the HHC by the Southern Tibetan Detachment System (STDS). The HHC is composed of highly metamorphosed metasediments and comprises dominant gneisses and migmatitic gneisses (Formation I), impure marbles (Formation II), and minor augen gneisses (Formation III). During the Miocene, partial melting of the HHC generated major leucogranite massifs such as Manaslu in Central Nepal (Le Fort, 1981). For silicate rocks in the HHC, $^{87}Sr/^{86}Sr$ is approximately 0.750 (Derry and France-Lanord, 1997). The HHC accounts for approximately 24% (Department of Mines and Geology of Nepal) (Morin, 2015) of outcropping lithology in the Narayani basin.

3. The Lesser Himalaya (LH). The Main Central Thrust (MCT) separates the HHC from the LH. The LH comprises medium to highly metamorphosed quartzite, quartzo-pelitic schists, minor black shales, and dolomitic limestones. Highly radiogenic strontium isotopic ratios are primarily indicative of the presence of high Rb/Sr lithologies (i.e., meta-pelites) rather than of particularly old crustal extraction ages, which are only slightly older than those of the HHC (Ahmad et al., 2000). Ahmad et al. (2000) confirm that LH formations are distinguishable from the HHC based on the LH's older source regions (i.e., T = ca. 2500 Ma). For silicate rocks in the LH, $^{87}Sr/^{86}Sr$ is > 0.850 (Derry and France-Lanord, 1997; France-Lanord and Fort, 1988). The LH accounts for approximately 46% (Department of Mines and Geology of Nepal) (Morin, 2015) of the outcropping lithology in the Narayani basin.

The Narayani River is the most important tributary of the Ganga in terms of discharge and sediment flux (Singh et al., 2008; Lupker et al., 2012; Andermann et al., 2012a). The Narayani drains an area of 32,000 km^2 and is supplied by five major tributaries, which are, from west to east, the Kali Gandaki, the Seti, the Marsyandi, the Bhuri Gandaki, and the Trisuli. The Narayani forms from the confluence of the Trisuli and the Kali Gandaki, whose basins traverse all three geological units mentioned above (see Figure 5.2). After traversing the Main Frontal Thrust (MFT), the Narayani descends to the Gangetic plain as the Gandak, eventually draining into the Ganga at Patna, 250 km downstream of the Himalayan front (Fig. 5.1).

The Indian Summer Monsoon (ISM) is a controlling factor on the hydrology and annual discharge of the Narayani basin. Beginning in mid-June and continuing until mid to late September, it represents approximately 80% of the 1,400 to 1,900 mm/yr of annual rainfall (Shrestha, 2000; Bookhagen and Burbank, 2010; Andermann et al., 2012b). Annual rainfall varies from approximately 50 mm in the Mustang region (NW part of the watershed) to approximately 5,000 mm in the Annapurna foothills (i.e., the boundary between the LH and HHC) at 3,000 m in the HHC (Putkonen, 2004). The precipitation dataset from the DHM (Department of Hydrology and Meteorology, Nepal) shows that this 5,000 m/yr is likely an upper limit and appears quite specific to several flanks of the southern Annapurna massive. This creates a scenario in which the HHC is characterized by massive erosion events associated with landslides, runoff, glaciers, and river incision (Lavé and Avouac, 2001), reflected in an annual erosion rate of 0.1 to 1.9 mm/yr (Gabet et al., 2008). Major erosional events of these types occur frequently in the Narayani, but are also quite common in other large basins, such as the Karnali and Kosi (Fig. 5.1). In contrast, the LH is characterized by lower erosion rates, between 0.1 and 0.5 mm/yr (Godard et al., 2012), and thus is more influenced by chemical weathering processes (West et al., 2005). Due to less pronounced relief and arid conditions, areas of the Marsyandi and Trisuli in the TSS have erosion rates (Fig. 5.2) (approximately 0.1 mm/yr) that are much lower than in the LH and HHC to the south (Gabet et al., 2008). Areas where the Kali and Seti drain the TSS (which include numerous glacial occurrences throughout the Annapurna and Dhaulagiri massifs), however, are much wetter and have higher runoff, and therefore have higher erosion rates than the Marsyandi and Trisuli TSS (Fig. 5.2). Recent studies have also shown that the Narayani basin exhibits the highest erosive activity in the central Himalaya (Andermann et al., 2012a; Lupker et al., 2012; Sinha and Friend, 1994).

5.3 Sampling

Figures 5.1 (Ganga-Brahmaputra system) and 5.2 (Narayani basin inset) show the location of samples analyzed in this study and Table 5.1 gives detailed information about the collection of each sample. While most of the 34 water samples analyzed in this study were collected from the Narayani basin, five water samples were also taken from other medium sized Himalayan front rivers in eastern (Kosi and Arun) and western (Karnali) Nepal for comparison. Water sampling includes: (1) the main tributaries of the Narayani in the Lesser Himalaya (i.e., the Seti, Kali Gandaki, and Trisuli), (2) detailed sampling of LH draining rivers including the Andi Khola and tributaries of the Trisuli, Darondi, and Bhuri Ghandaki, and (3) minor tributaries from elsewhere in the Narayani basin. In addition, four samples of impure marble were collected along the Madi Khola, Bhuri Gandaki, and Darondi Khola rivers (Galy and France-Lanord, 1999), while bank sediments were collected from the Marysandi (TSS) (Galy and France-Lanord, 1999), Khudi Khola (HHC) (Morin, 2015) and Isul Khola (LH) (Galy and France-Lanord, 1999). Two suspended load samples were also taken from the Ganga and Brahmaputra rivers north of their confluence in Bangladesh.

The goal of the sampling scheme was to determine the radiogenic Ca isotopic signatures of the different formations currently being eroded and their respective signatures in the dissolved load. In order to characterize the isotopic signature of each of the three main geological units we sampled river water from small watersheds draining a single formation, including the Khudi Khola (HHC) (see also Chapter 4), Chepe Khola (HHC), Jaran Khola (LH), and Isul Khola (LH), among others (see Table 5.1). Nevertheless, each Himalayan formation (TSS, LH, or HHC) comprises a large range of lithologies that vary significantly both in major elemental and isotopic compositions (see section above on the geology of each formation). Thus, dissolved load compositions even from the smaller watersheds reflect the mixture of these lithologies, unless a specific geological unit is the only formation present in a catchment, such as HHC FI in the Upper Khudi (see Chapter 4). In addition, samples were collected from larger rivers (e.g., the Trisuli, Narayani, and Kosi, among others; see Table 5.1) and include sediments from two or all three formations (TSS, HHC, and LH; see Table 5.1). The river water and bed loads, and carbonate and dolomitic rocks analyzed in this study were collected over numerous field seasons from 1974 to 2015.

Water samples were collected from the riverside, filtered through 0.2 mm nylon or PES filters, and stored in bottles free of air. One drop of concentrated HNO_3 was added to each bottle to acidify the water. The hydrogeochemistry of a number of the river water samples have been presented elsewhere (Galy and France-Lanord, 1999; Galy et al., 1999; France-Lanord et al., 2003; Morin, 2015) but will be briefly

summarized here (see Section 5 below).

Table 5.1 – *Sample Locations and descriptions for the samples analyzed in this study.*

Sample	River	Formation	Basin	Type	Date	Longitude	Latitude	Altitude (m)
PB9	Thini Khola	TSS	Thini	Water	7/7/05	83.72419	28.76688	2650
MO503[a]	Yankim Khola	TSS	Yankim	Water	7/26/98	83.64120	28.71120	2602
MO359	Chepe Khola	HHC	Marysandi	Water	7/15/98	84.66944	28.28500	1700
MO364[e]	Chepe Khola	HHC	Marysandi	Water	7/15/98	84.63611	28.18889	1063
MO58[c,d]	Chepe Khola	HHC	Marysandi	Water	5/7/97	84.64639	28.29528	3100
MO79[c,d]	Chepe Khola	HHC	Marysandi	Water	5/9/97	84.64844	28.21315	1700
CA15003	Chepe Khola	HHC	Marysandi	Water	7/28/15	84.64844	28.21315	1500
MO100[a,c,d]	Masel Khola	LH	Darondi	Water	5/11/97	84.66944	28.04111	590
MO383	Masel Khola	LH	Darondi	Water	7/18/98	84.66944	28.04111	590
MO107[a,c,d]	Maudi Khola	LH	Bhuri G.	Water	5/12/97	84.81333	28.04694	540
MO110[a,d]	Isul Khola	LH	Darondi	Water	5/12/97	84.81472	28.04694	520
MO119[a]	Anku Khola	LH	Bhuri G.	Water	5/13/97	84.81861	27.98611	455
MO380	Jaran Khola	LH	Darondi khola	Water	7/18/98	84.65400	28.05563	500
CA15032	Jaran Khola	LH	Darondi khola	Water	7/27/15	84.65400	28.05563	500
MO311[a,e]	Andi Khola	LH	Kali Gandaki	Water	7/8/98	83.79026	28.04288	750
CA15001	Anku Khola	LH	Bhuri G.	Water	7/27/15	84.553393	27.595911	600
CA15005	Chiti Khola	LH	Trisuli	Water	7/27/15	84.252285	28.112712	700
CA15008	Paundi Khola	LH	Trisuli	Water	8/10/15	84.255255	28.64415	515
CA15030	Darondi Khola	HHC+LH	Marsyandi	Water	8/10/15	84.382308	28.25079	530
CA15034	Maleku Khola	LH	Trisuli	Water	8/10/15	84.472169	27.49264	480
CA15036	Thopal Khola	LH	Trisuli	Water	8/10/15	84.502397	27.485297	369
CA11150	Seti	TSS+HHC+LH	Kali Gandaki	Water	8/7/12	84.46667	27.82917	227
MO304	Seti	TSS+HHC+LH	Kali Gandaki	Water	7/7/98	84.07500	28.05000	530
CA11149	Kali Gandaki	TSS+HHC+LH	Narayani	Water	8/7/12	84.42302	27.74353	200
LO760	Trisuli	TSS+HHC+LH	Narayani	Water	8/12/07	84.84445	27.80275	369
CA15038	Trisuli	TSS+HHC+LH	Narayani	Water	8/10/15	84.451832	27.484535	328
PB81	Karnali	TSS+HHC+LH	Ganga	Water	7/15/05	81.28324	28.64132	431
CA11169	Arun	TSS+HHC+LH	Ganga	Water	8/13/11	87.15487	26.92328	139
CA11167	Kosi	TSS+HHC+LH	Ganga	Water	8/13/11	87.14478	26.92743	142
PB71	Kosi	TSS+HHC+LH	Ganga	Water	7/13/05	87.15141	26.84702	125
LO764	Kosi	TSS+HHC+LH	Ganga	Water	8/16/07	87.15137	26.84815	125
PB53	Narayani	TSS+HHC+LH	Ganga	Water	7/11/05	84.42670	27.70330	180
CA11147	Narayani	TSS+HHC+LH	Ganga	Water	8/6/12	84.42558	27.70298	182
CA13130	Narayani	TSS+HHC+LH	Ganga	Water	7/28/13	84.418039	27.696499	180
AP75-867[d]	Madi Khola	LH	Madi Khola	Impure marble	1975	84.26	27.98	323
AP75-811[d]	Bhuri Gandaki	LH	Bhuri Gandaki	Impure marble	1975	85.10	28.18	723
AP75-865[d]	Madi Khola	LH	Madi Khola	Impure marble	1975	84.25	28.00	429
AP74-207[d]	Darondi Khola	LH	Darondi Khola	Impure marble	1975	84.71	28.18	468
MAR50[b]	Marsyandi	TSS	Marsyandi	Bank Sediment		84.30	28.53	2050
CA950[b]	Khudi Khola	HHC	Khudi Khola	Bank Sediment	11/11/09	84.28865	28.37559	2350
MO112[b]	Isul Khola	LH	Isul Khola	Bank Sediment	5/12/97	84.81472	28.04694	520
BR8218[b]	Ganga	TSS+HHC+LH	Ganga	Suspended Load	9/1/08	89.02313	24.05938	4
BR8203[b]	Brahmaputra	TSS+HHC+LH	Brahmaputra	Suspended Load	8/31/08	89.76459	24.37196	8

a: Chabaux et al. (2001)
b: Morin (2015)
c: Galy and France-Lanord (1999)
d: Galy et al. (1999)
e: France-Lanord et al. (2003)

5.3.1 *Whole Rocks and Sediments*

Table 5.2 displays the major elemental compositions for sediments and whole rocks analyzed in this study. The five sediment samples chosen for this study (MAR50, CA950, MO112, BR8203, and BR8218) were selected on the basis of their distinct Nd and Sr isotopic characteristics (Sr and Nd data for these sediment samples are from Galy et al. (1999) and Morin (2015), and are listed in Table 5.4). The LH, HHC, and TSS have distinct isotopic signatures related to differences in both lithology and crustal extraction ages (France-Lanord et al., 1993; Harris et al., 1998; Ahmad et al., 2000; Vidal et al., 1982; Deniel et al., 1987; Schärer et al., 1990; Petterson et al., 1993; Parrish and

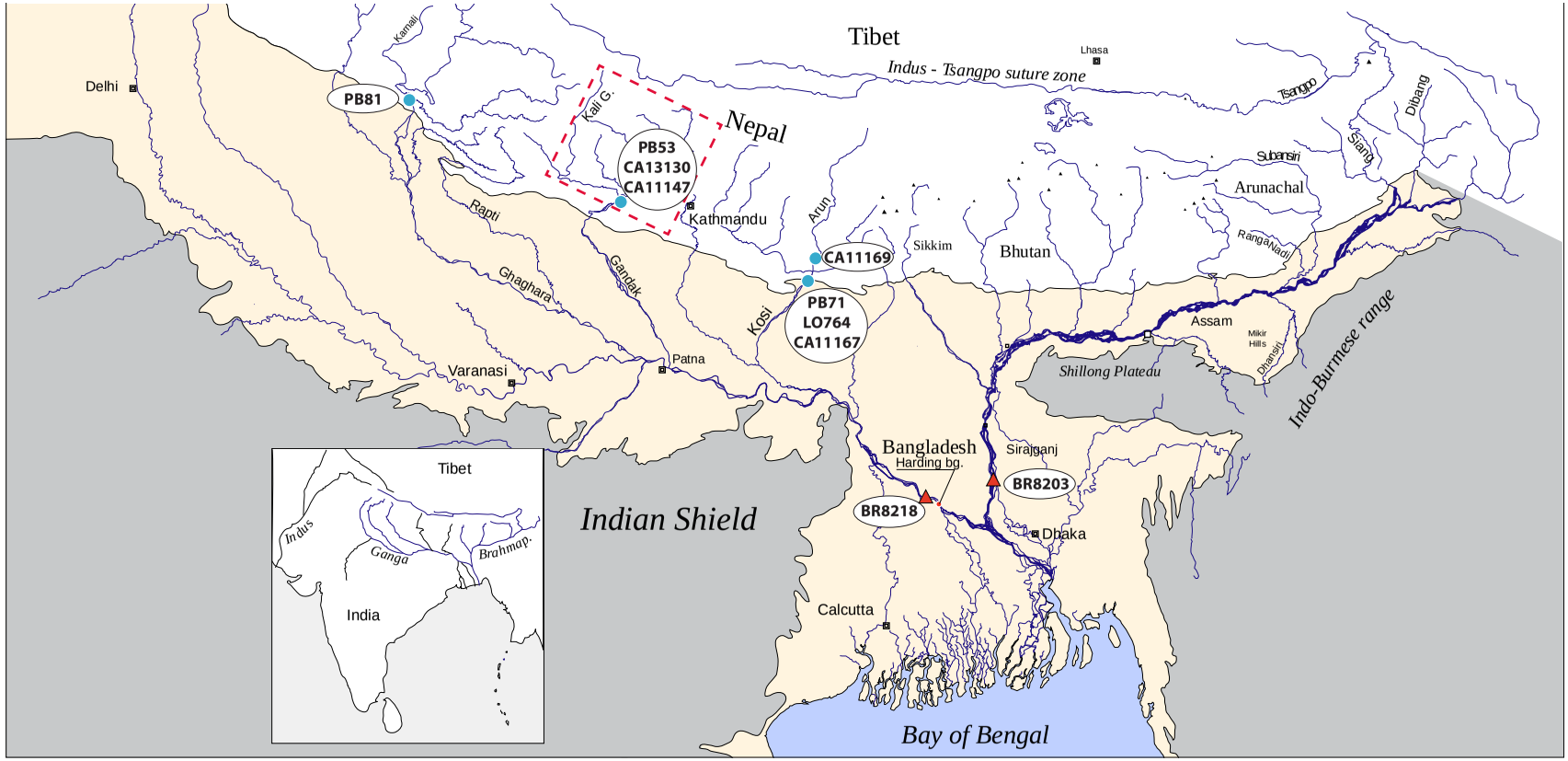

Figure 5.1 – *Map of the Ganga-Brahmaputra river system showing bed load and river water sample locations. The inset rectangle indicates the map area of Figure 5.2. The modern Gangetic Plain is shown in yellow.*

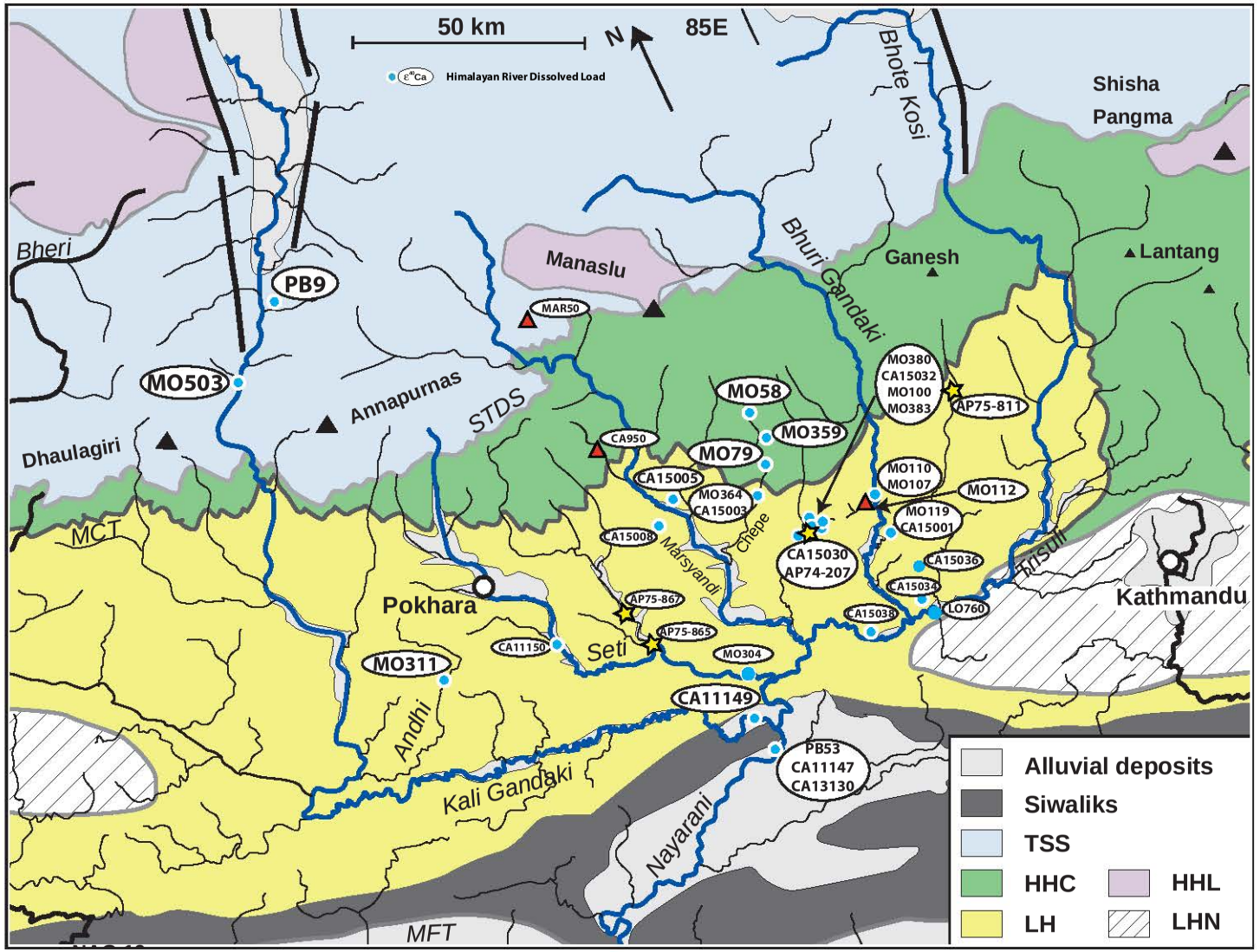

Figure 5.2 – *Geological map of the Narayani watershed showing bedload, bedrock, and river water sample locations recreated from Galy and France-Lanord (1999) and Colchen et al. (1986). Red triangles represent river bedload, yellow stars represent LH dolomites, and blue circles represent dissolved load samples. TSS: Tethyan Sedimentary Series, HHC: High Himalaya Crystalline, LH: Lesser Himalaya, HHL: High Himalaya Leucogranite, LHN: LH Nappe. MFT: Main Frontal Thrust, placing Mio-Pliocene Siwalik foreland basin sediments over the modern Gangetic Plain. MCT: Main Central Thrust, placing the HHC over the LH. STDZ: South Tibetan Detachment Zone, separating the TSS from the HHC.*

Hodges, 1996; Whittington et al., 1999; Robinson et al., 2001; Najman, 2006). This leads to well-defined domains in Sr–Nd isotopic space for each Himalayan lithological unit (see Figure 5.3).

Sample MAR50 is a bank sediment sample collected on the Upper Marysandi, located predominantly in the TSS, near the confluence with the Temang river upstream of Dharapani. It has a [Ca] (Ca concentration), Al/Si ratio, and carbonate content of 0.31 mol/100 g, 0.21 (mol:mol), and 28.8 wt. %, respectively (Table 5.2), and a [Sr] (Sr concentration) of 284.5 ppm. The $^{87}Sr/^{86}Sr$ composition of MAR50 is 0.73488 and 0.71372 for the silicate and carbonate fractions, respectively, with a bulk εNd of –17.3 (Sr and Nd data for this and other sediment samples given below from Galy et al. (1999); Morin (2015) and listed in Table 5.4). Due to the very low carbonate Nd concentration, we assume that the bulk Nd composition of this and other bed load samples derives essentially from the silicate fraction.

Sample CA950 is a bank sediment sample from the Khudi Khola upstream of an active landslide (the Saituti Landslide; see Chapter 4 or Morin (2015)) in Formation 1 of the HHC. It has a [Ca] and Al/Si ratio of 0.03 mol/100 g and 0.22 (mol:mol), respectively, and a [Sr] of 82.45 ppm. The $^{87}Sr/^{86}Sr$ composition of CA950 is 0.75880 and 0.752800 for the silicate and leachate (i.e., this sample is in an environment where, theoretically, no carbonate exists), respectively, with a bulk εNd of –16.

Sample MO112 is a bank sediment sample from the Isul Khola of the LH, a small tributary feeding the Bhuri Gandaki at Aarughat. It has a [Ca], Al/Si ratio, and carbonate content of 0.04 mol/100 g, 0.09 (mol:mol), and 4.26 wt. %, respectively, and a low [Sr] of 40.5 ppm. The $^{87}Sr/^{86}Sr$ composition of MO112 is 0.86060 and 0.833035 for the silicate and carbonate fractions, respectively, with a bulk εNd of –25.6.

Sample BR8218 is a suspended load sediment collected at Harding Bridge along the mainstem of the Ganga in Bangladesh in September of 2008 (Lupker et al., 2011). It has a [Ca] and Al/Si ratio of 0.07 mol/100 g and 0.26 (mol:mol), respectively, and a [Sr] of 103.4 ppm. The $^{87}Sr/^{86}Sr$ composition of BR8218 is 0.77000 and 0.73661 for the silicate and carbonate fractions, respectively, with an εNd of –17.9 for the silicate fraction. Sample BR8203 is a suspended load sediment collected at Jamuna Bridge along the mainstem of the Brahmaputra in August of 2008 (Lupker et al., 2013). It has a [Ca] and Al/Si ratio of 0.03 mol/100 g and 0.24 (mol:mol), respectively, and a [Sr] of 127.6 ppm. The $^{87}Sr/^{86}Sr$ composition of BR8203 is 0.74180 and 0.74364 for the silicate and carbonate fractions, respectively.

In addition to the sediments, whole rock dolomitic samples from the LH were selected to assess the degree of metamorphic redistribution of Ca isotopes between carbonates and silicate lithologies of the LH. Samples AP74-207, AP75-811, AP75-865, and AP75-867 are all Lesser Himalayan impure dolomitic marbles (Galy and France-

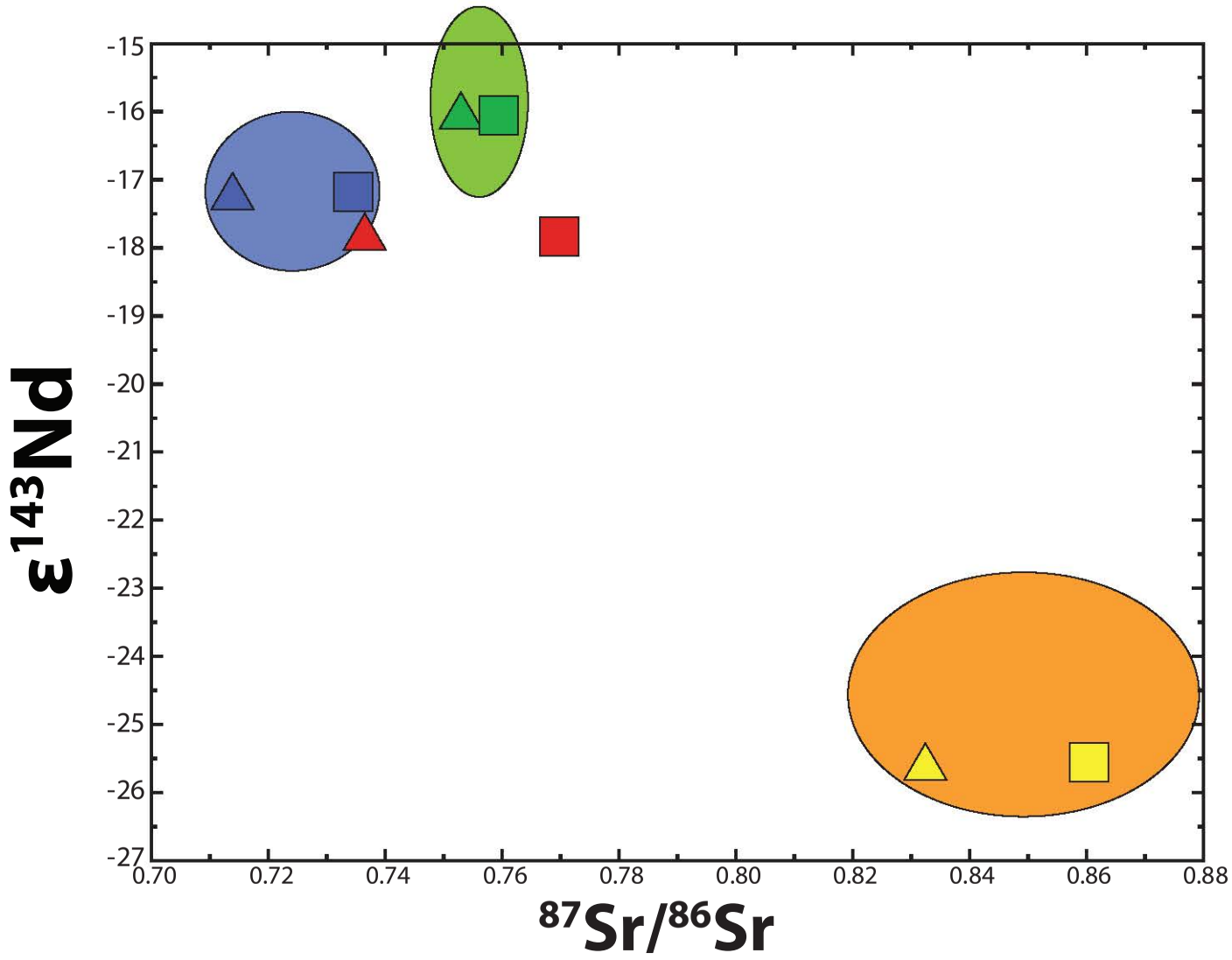

Figure 5.3 – *Sr and Nd isotopic compositions of the HHC (in green), LH (in yellow), and TSS (in blue) bank sediments from the Khudi Khola, Isul Khola, and Marysandi, respectively. Also included are suspended load sediments from the Ganga (shown in red) for comparison. Sr and Nd isotopic analyses show that these river sediments have quite a limited range in composition for each formation, and thus allow detailed provenance tracing. The silicate fraction of each sediment is shown by squares, whereas the carbonate fraction is shown by triangles. Sr and Nd isotopic compositions are from Galy et al. (1999); Singh and France-Lanord (2002); Morin (2015); Galy et al. (2010) and isotopic compositional fields are from Morin (2015).*

Lanord, 1999; Galy et al., 1999; Pecher, 1978). Sample AP74-207 was collected from a rock face adjacent to the Darondi just after its confluence with the Jaran Khola. Sample AP75-811 was collected on the Bhuri Gandaki northeast of Gorkha. Samples AP75-865 and -867 were collected along the Madi Khola just before its confluence with the Seti Khola. These samples have [Ca] ranging from 0.38–0.45 mol/100 g, Al/Si ratios ranging from 0.07–0.13, and [Sr] ranging from 34–55 ppm. The whole rock $^{87}Sr/^{86}Sr$ ranges from 0.73950–0.85722 (Galy and France-Lanord, 1999; Galy et al., 1999).

5.3.2 Major Element Geochemistry of the Dissolved Load

Chemical characteristics of the dissolved load strongly depend on the lithology of the watershed (i.e., carbonate versus silicate), the climate (e.g., dry, north flank rivers with high total dissolved solids (TDS) compared with wet, south flank rivers), and the season (i.e., monsoon samples are more dilute whereas dry season samples have higher concentrations). Figures 5.4 and 5.5 summarize the variations in the major element geochemistry of the water samples (listed in Table 5.3). Samples denoted by CA14XXX and CA15XXX are presented here for the first time and other samples were presented in Galy and France-Lanord (1999),Galy et al. (1999), France-Lanord et al. (2003), or Morin (2015) (Table 5.3 denotes where each water sample has been published). The major element geochemistry of the rivers of the Narayani Basin has been extensively documented by Galy and France-Lanord (1999), Galy et al. (1999), France-Lanord et al. (2003), and Bickle et al. (2015), among others. The new major cation and anion concentrations in our river water samples are in good agreement with those obtained in these previous studies, and confirm the general conclusions from major element data proposed for rivers in the Narayani Basin.

In their synthesis of Himalayan stream geochemistry, Jacobson et al. (2002) observed that Na/Ca and HCO_3/SiO_2 ratios of Himalayan streams fall between silicate and carbonate end members, but the stream geochemistry of very few HHC and LH rivers reflect the complete compositional range produced via silicate weathering (Jacobson et al., 2002). Globally, these authors found that most Himalayan streams are dominated by characteristically carbonate Na/Ca and HCO_3/SiO_2 ratios.

The geochemical budget of the dissolved load, in large rivers, with high contributions from carbonate dissolution show high concentrations of Mg (about 50% of Ca) suggesting extensive dissolution of dolomite. However, these rivers also have [Sr] in large excess to what LH dolomite dissolution could generate. Based also on the Sr isotopic composition, previous studies (Bickle et al., 2015, 2005; Galy et al., 1999) have concluded that the main source of dissolved Ca and Sr is the dissolution of TSS limestone, and that due to oversaturation with respect to calcite, precipitation of calcite poor in Sr and Mg tends to deplete the dissolved load in Ca relative to

Table 5.2 – *The geochemical compositions of the whole rocks and bank/suspended load sediments analyzed in this study.*

Sample	River	Formation	SiO_2	Al_2O_3	Fe_2O_3	MnO	MgO	CaO	Na_2O	K_2O	TiO_2	P_2O_5	L.O.I.	Total	[Ca] mol/100 g	Al/Si (mol:mol)	K/Ca (mol:mol)	Carbonate (wt%)	Sr ppm
			wt. %																
Whole Rocks - Dolomites																			
AP75-867[a]	Madi Khola	LH	13.91	1.22	0.6	0.06	17.88	25.08	0.12	0.36	0.12	–	39.41	98.76	0.45	0.100	0.02	–	34.00
AP75-811[a]	Bhuri Gandaki	LH	33.6	2.76	2.87	0.18	14.01	25.26	0.62	0.32	0.23	–	19.64	99.49	0.45	0.100	0.02	–	44.00
AP75-865[a]	Madi Khola	LH	24.93	1.57	2.83	0.1	14.32	21.05	–	0.72	0.2	–	32.91	98.63	0.38	0.070	0.04	–	51.00
AP74-207[a]	Darondi Khola	LH	27.15	3.1	1.12	0.1	14.95	21.79	0.02	1.68	0.02	–	29.5	99.43	0.39	0.130	0.09	–	55.00
Sediments																			
MAR50[b]	Marsyandi	TSS	50.97	9.13	2.95	0.03	1.58	17.24	1.46	2.31	0.38	0.06	13.42	99.53	0.31	0.210	0.16	28.80	284.50
CA950[b]	Khudi Khola	HHC	73.40	13.85	4.57	0.09	2.08	1.55	1.51	2.21	0.48	0.11	1.05	100.90	0.03	0.222	1.70	–	82.45
MO112[b]	Isul Khola	LH	79.89	6.36	3.88	0.08	1.74	2.41	0.68	1.40	0.50	0.11	2.80	99.85	0.04	0.094	0.69	4.26	40.48
BR8218[b]	Ganga	TSS+HHC+LH	62.24	13.90	5.50	0.08	2.36	4.13	1.13	2.95	0.70	0.14	7.55	100.67	0.07	0.260	0.85	7.20	103.40
BR8203[b]	Brahmaputra	TSS+HHC+LH	67.43	13.94	4.85	0.08	2.14	1.90	1.61	3.04	0.62	0.14	3.79	99.53	0.03	0.240	1.91	–	127.60

a: Galy et al. (1999)
b: Morin (2015)

Sr and Mg. At a small catchment scale, such as the Khudi or Chepe Khola, calcite precipitation has relatively small effects due to no significant presence of carbonate lithologies in these catchments. However, secondary calcite processes produce discordance in large Himalayan rivers resulting in complex river geochemistry whose elemental budget is more challenging to resolve.

Major elemental results obtained from Himalayan rivers show that there are a variety of sources of dissolved elements with highly varied concentrations. Unlike in most rivers (Gaillardet et al., 1997, 1999), carbonate and silicate sources do not define unique elemental end members (see Figure 5.5a, for example). Figure 5.5a shows that water from gneiss-dominated basins have compositions that vary from strongly Na + K dominated to strongly Ca dominated, probably due to the presence of trace carbonates in Formation I gneisses. Therefore, the problem may be not that the silicate source spans a wide elemental range, but rather that many of the basins described as "gneiss basins" in fact include carbonates (Jacobson et al., 2002).

5.3.2.1 The TSS

The major tributaries of the Narayani (i.e., the Seti, Kali Gandaki, Trisuli, Bhuri Gandaki) have their source in the TSS. The Kali Gandaki, Trisuli, and the Bhuri Gandaki have their source north of the High range, which is characterized by low precipitation (25 to 50 cm/year) and a cold, arid, desert-like climate. However, the TSS is not restricted to dry, desert-like areas, such as in the North flank. The Dhaulagiri and Annapurna massive contain large exposures of the TSS on the south flank with relatively high runoff and significant glacial presence. This is where the Seti has its source. TSS rivers rivers analyzed in this study, i.e., the Thini Khola (sample PB9) and Yankim Khola (sample MO503), are both tributaries of the Kali Gandaki and display highly elevated concentrations of SO_4 (610–730 µmol/L), Ca (890–1010 µmol/L), Sr (2.6–3.2 µmol/L), and Mg (415–670 µmol/L), and are characterized by highly elevated Sr/Ca ratios (Galy and France-Lanord, 1999; English et al., 2000; Bickle et al., 2015), whereas Si (45–170 µmol/L), Na (28–145 µmol/L), and K (30–40 µmol/L) have diminished concentrations. In Figures 5.4 and 5.5, TSS samples (blue circles) plot predominantly towards the carbonate signature pole and are consistent with analyses from a Marysandi TSS tributary (Bickle et al., 2015). Galy and France-Lanord (1999) and Turchyn et al. (2013) cite the presence of significant weathering and dissolution of $CaSO_4$ minerals and/or the oxidation of sulfide (i.e., pyrite) or sulfate (i.e., gypsum) minerals to explain the origin of high [SO_4]. Sulphide oxidation produces H_2SO_4, which promotes the aggressive dissolution of carbonates in certain catchments in the TSS, contributing to between 27 and 47% of the anionic charge (Galy and France-

Lanord, 1999; Turchyn et al., 2013). The dissolution of $CaSO_4$ minerals yields a neutral solution. Dissolved sulphate dominantly derives from sulphide oxidation and therefore represents an important source of acid. Furthermore, a demonstrated evaporitic component exists in the Mustang graben in the Triassic TSS (Narsing Khola), likely giving rise to the elevated Cl concentrations in TSS rivers.

5.3.2.2 The HHC

When crossing the high range into the HHC, runoff increases rapidly due to monsoon precipitation as compared with the north flank. HHC rivers in Figures 5.4 and 5.5 (green circles) plot between the carbonate and silicate poles, consistent with analyses from (Galy and France-Lanord, 1999). HHC rivers (samples from the Khudi and Chepe Khola, both tributaries of the Marysandi) are very dilute with relatively low concentrations of both cations and anions with the majority at or below 100 µmol/L, leading to a "Total Cation" concentration of normally less than 500 µmol/L. HHC rivers are characterized by a geochemical signature that reflects the weathering of significant amounts of gneiss (mainly high grade metamorphic silicates, as well as marbles in Formation II, i.e., elevated [Na]). Rivers that exclusively drain HHC Formation I, i.e., silicate bedrock, are dilute and have higher Na/Ca ratios. However, the rivers in this study have Na/Ca ratios lower than 1, significantly below the average Na/Ca ratio of the Formation I gneisses (Na/Ca = 1.5 to 2). One possible explanation for the disconnect between whole rock Na/Ca ratios and dissolved load Na/Ca ratios is the dissolution of trace carbonates that are present in Formation I gneisses, which decrease the Na/Ca ratios (Blum et al., 1998; Jacobson et al., 2002; Morin, 2015). Sulphide oxidation is not restricted to the TSS (see above) and is also active in the HHC leading to high $[SO_4]$, such as in springs in the upper Khudi Khola landslide (see Chapter 4).

5.3.2.3 The LH

The LH has significantly fewer steep slopes compared with the HHC, which favors chemical weathering processes over physical erosion. High [Ca] reflects the dual carbonate and silicate nature of the LH. However, the equally elevated Si and Na concentrations speak to significant weathering of schist. LH rivers, by contrast to those of the HHC, generally exhibit higher dissolved cation concentrations (> 300 µmol/L) and can be divided into two groups based on their Ca/Na ratios. This dichotomy can be seen in Figure 5.5b, where some samples plot closer to the "Silicate Springs" field and others plot closer to the "Limestone Springs" field. Furthermore, there is a geographic distribution between these two groups reflecting a lithological

control. Samples collected from the Kali Gandaki and its tributaries drain a higher proportion of carbonate material compared with samples collected from the Trisuli and its tributaries. In the west (i.e., the Seti and Kali Gandaki), the dissolved load is dominated by carbonates (including dolostones) producing streams with high [Ca]. Small catchments in the LH of the eastern Narayani are dominated by schists, gneisses, and quartzites decreasing the [Ca], while K contents are higher relative to the western basins (Galy and France-Lanord, 1999; Galy et al., 1999; English et al., 2000; Jacobson et al., 2002). In general, [Mg] is higher in the eastern basins, although some western LH basins with abundant dolomite also have high Mg contents.

Table 5.3 – *Dissolved load geochemistry of samples analyzed in this study.*

Sample	River	Formation	HCO_3^-	Cl^-	SO_4^{2-}	Si	Mg^{2+}	Ca^{2+}	Na^+	K^+	Sr^{2+}
							µmol/L				
PB9	Thini Khola	TSS	165.49	4.95	729.39	29.73	671.53	1007.73	143.71	38.11	3.24
MO503[a]	Yankim Khola	TSS	46.65	9.22	609.10	31.00	417.00	888.00	28.00	30.00	2.55
MO359	Chepe Khola	HHC	163.00	3.81	6.54	129.82	19.53	30.90	39.10	33.15	0.07
MO364[e]	Chepe Khola	HHC	104.72	4.29	31.54	144.45	16.84	44.24	39.35	22.65	0.12
MO58[c,d]	Chepe Khola	HHC	188.51	1.64	16.72	–	6.17	77.31	30.00	14.58	0.07
MO79[c,d]	Chepe Khola	HHC	431.08	3.30	30.73	–	34.16	154.36	68.75	67.52	0.13
CA15003	Chepe Khola	HHC	426.50	8.36	34.94	178.53	61.02	147.87	87.84	50.24	0.25
MO100[a,c,d]	Masel Khola	LH	756.64	17.15	16.96	–	60.08	139.90	234.58	48.85	0.30
MO383	Masel Khola	LH	419.39	12.95	11.05	213.84	43.95	62.34	140.25	37.65	0.28
MO107	Maudi Khola	LH	992.32	19.46	27.84	–	76.13	247.88	255.42	59.34	0.50
MO110[a,d]	Isul Khola	LH	2670.16	9.87	62.41	–	526.34	1231.92	137.92	107.67	0.64
MO119[a]	Anku Khola	LH	871.20	55.91	67.56	–	164.61	348.63	148.75	69.31	0.42
MO380	Jaran Khola	LH	327.99	16.93	39.90	208.43	43.25	62.64	130.46	51.53	0.55
CA15032	Jaran Khola	LH	782.45	27.55	48.28	316.59	82.70	139.08	272.41	94.52	0.41
MO311[a,e]	Andi Khola	LH	508.68	20.68	6.61	91.29	170.91	220.72	30.97	15.61	0.10
CA15001	Anku Khola	LH	669.89	17.90	45.23	134.00	130.63	264.72	95.05	76.42	0.24
CA15005	Chiti Khola	LH	698.69	29.92	9.85	226.98	58.66	193.51	153.47	24.56	0.30
CA15008	Paundi Khola	LH	663.47	32.55	9.51	249.95	50.63	141.69	179.68	39.50	0.36
CA15030	Darondi Khola	TSS+HHC+LH	1007.47	30.36	79.92	157.10	224.84	431.16	139.59	95.93	0.39
CA15034	Maleku Khola	LH	1739.13	15.89	229.29	235.80	268.99	949.96	197.24	122.17	1.04
CA15036	Thopal Khola	LH	325.87	15.75	2.63	161.83	44.73	57.43	91.34	26.71	0.10
CA11150	Seti	TSS+HHC+LH	693.30	20.00	265.76	–	341.04	627.50	75.82	73.73	0.83
MO304[e]	Seti	TSS+HHC+LH	1004.05	15.35	80.36	109.41	205.39	543.14	45.82	56.83	0.96
CA11149	Kali Gandaki	TSS+HHC+LH	1423.66	–	–	104.04	399.22	636.48	90.95	76.70	1.18
LO760	Trisuli	TSS+HHC+LH	559.01	9.26	112.78	94.70	75.44	350.05	75.34	36.68	0.51
CA15038	Trisuli	TSS+HHC+LH	771.05	15.04	83.20	116.08	101.60	385.40	98.24	43.38	0.59
PB81	Karnali	TSS+HHC+LH	1220.24	–	–	70.28	179.14	540.12	49.83	30.05	0.89
CA11169	Arun	TSS+HHC+LH	734.47	23.91	252.22	95.17	131.74	582.34	140.32	35.17	1.24
CA11167	Kosi	TSS+HHC+LH	589.62	9.00	61.56	–	81.22	290.42	70.51	42.76	0.27
PB71	Kosi	TSS+HHC+LH	483.02	9.75	105.51	98.06	69.92	303.34	71.93	39.36	0.25
LO764	Kosi	TSS+HHC+LH	683.52	7.58	84.60	105.00	69.05	372.94	70.50	40.82	0.23
PB53	Narayani	TSS+HHC+LH	1330.10	0.00	–	89.23	237.82	564.41	67.41	56.32	0.74
CA11147	Narayani	TSS+HHC+LH	898.47	20.18	159.65	98.20	239.29	579.84	74.64	58.21	0.83
CA13130	Narayani	TSS+HHC+LH	1290.93	–	–	112.23	221.64	520.98	92.04	54.76	0.72

a: Chabaux et al. (2001)
b: Morin (2015)
c: Galy and France-Lanord (1999)
d: Galy et al. (1999)
e: France-Lanord et al. (2003)

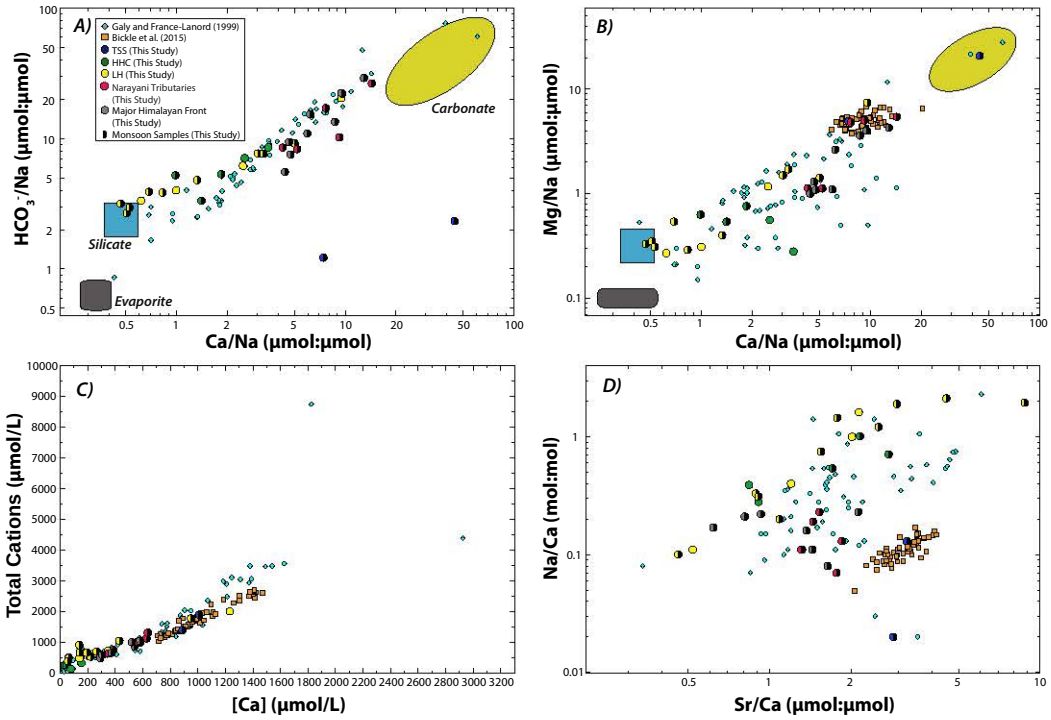

Figure 5.4 – *A) and B) Mixing diagrams using Na-normalized molar ratios in the dissolved phase of Himalayan rivers analyzed in this study as well as rivers analyzed in Galy and France-Lanord (1999) (light blue diamonds) and Bickle et al. (2015) from a Marysandi TSS tributary (orange squares). End-member reservoirs were estimated using data on small rivers draining one single lithology, i.e., carbonates, silicates, and evaporites, taken from Gaillardet et al. (1999). C) Total cations (µmol/L) plotted against [Ca], where we observe that the TSS and several LH rivers are the most concentrated with respect to Ca as well as Total Cations, whereas HHC and the majority of LH rivers are relatively dilute. D) The Na/Ca ratio plotted against the Sr/Ca ratio for samples analyzed in this study as well as rivers from Galy and France-Lanord (1999) and Bickle et al. (2015). Color scheme: blue circles – TSS rivers, green circles – HHC rivers, yellow circles – LH rivers, red circles – Narayani tributaries, grey circles – Major Himalayan Front rivers. Symbols with black half-circles represent samples collected during the monsoon. This color scheme will remain the same for the figures and graphs that follow in the chapter.*

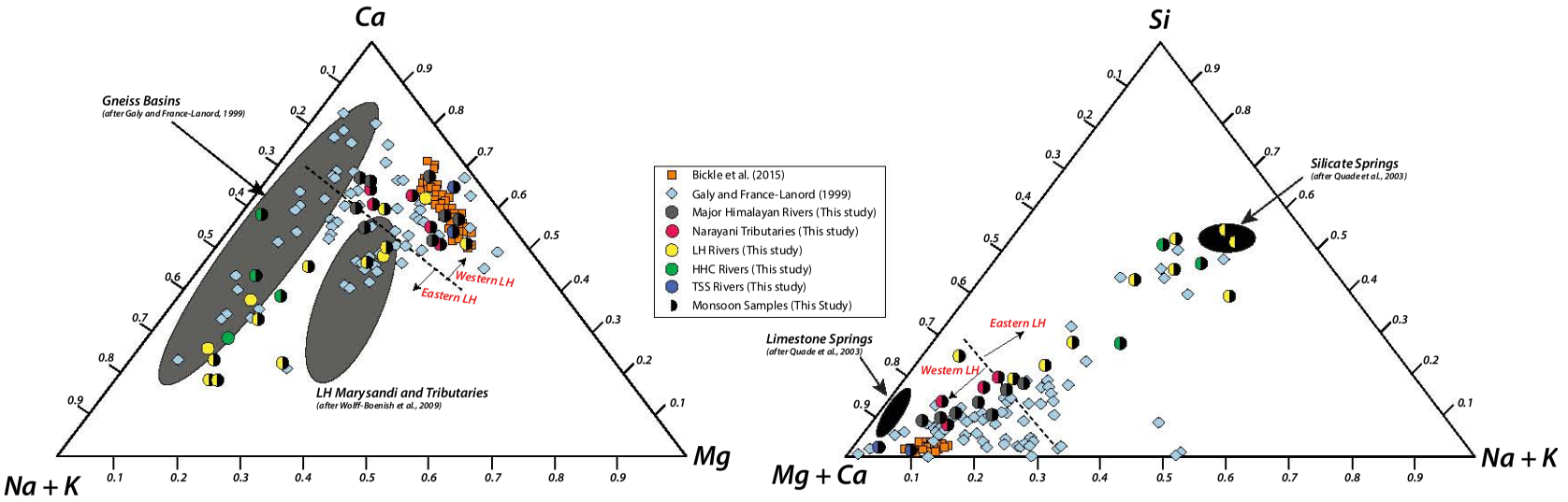

Figure 5.5 – *Triangular plots representing the relative abundance of major cations of Central Nepal rivers. Compositions are similar to other Nepalese rivers draining gneiss, silicates, and carbonates. Silicate and limestone spring compositions are from Quade (2003), Marsyandi water compositions from Wolff-Boenisch et al. (2009), and gneiss basin waters are from Galy and France-Lanord (1999). Calcium is the dominant cation and Mg remains low in silicate drainage. Symbols with black half-circles represent samples collected during the monsoon.*

5.4 Results

Sr and Ca isotope results are plotted in Figure 5.8 (sediments and whole rocks) and Figure 5.10 (river water) and summarized in Table 5.4 (sediments and whole rocks) and Table 5.5 (river water). Figures 5.6 and 5.7 also display the spatial variability of radiogenic Ca isotopic compositions throughout the field area. Following previously established conventions, we report $^{40}Ca/^{44}Ca$ measurements normalized to the NIST SRM915a standard, using the "epsilon" notation ($\varepsilon^{40}Ca$):

$$\varepsilon^{40}Ca = \left[\frac{^{40}Ca/^{44}Ca_{Sample}}{^{40}Ca/^{44}Ca_{Standard}} - 1 \right] \times 10^4 \tag{5.1}$$

Repeated analyses (N = 111) of the NIST SRM 915a standard over the three-year period of this study yielded $^{40}Ca/^{44}Ca_{SRM915a}$ = 47.15072 ± 0.00118 (2 S.D. = 40 ppm). Analytical techniques for major elemental and Sr and Ca isotopic analyses are presented in Chapter 3 and the Supplementary Materials (Tables 5.15, 5.16, and 5.17) contain a more extensive dataset for each sample Ca analysis in this study.

5.4.1 Whole Rocks and Sediments

The $\varepsilon^{40}Ca$ compositions of whole rock and sediment samples are shown in Figure 5.8 and plotted against their $^{87}Sr/^{86}Sr$ compositions in Figure 5.9. Results show that carbonate lithologies have homogeneous $\varepsilon^{40}Ca$ within analytical uncertainty of the present-day mantle and seawater compositions. LH dolomites have $\varepsilon^{40}Ca$ values ranging from –0.2 to 0 despite a wide range of Sr isotopic compositions (0.74–0.86), indicative of isotopic exchange with pelitic schists with high Rb/Sr and $^{87}Sr/^{86}Sr$ ratios. Likewise, carbonate fractions obtained by acid leaching of sediments from the HHC, LH, and TSS, as well as the Ganga and Brahmaputra have variable $^{87}Sr/^{86}Sr$ (0.71–0.84) but homogenous $\varepsilon^{40}Ca$ values ranging from 0 to +0.4. This result shows that carbonate sediments in the Himalayas are primarily unradiogenic in ^{40}Ca, despite having highly variable Sr isotopic compositions reflecting differing degrees of exchange with silicates. The presence of non-radiogenic carbonates within Himalayan sediments confirms the conclusions drawn by Caro et al. (2010), i.e., that carbonates have retained the $\varepsilon^{40}Ca$ signature of the mantle ($\varepsilon^{40}Ca$ = 0) over geological time, and that this signature is not easily modified during dolomitisation and metamorphism. This observation implies that carbonate weathering releases variably radiogenic Sr but unradiogenic Ca indistinguishable from that of both the mantle and seawater. The seawater-like composition of sediment leachates also demonstrates that the carbonate fraction represents primarily detrital material as opposed to secondary phases precipitated from the dissolved load as secondary carbonates would inherit the radiogenic ^{40}Ca composition of the riverine dissolved load (see below).

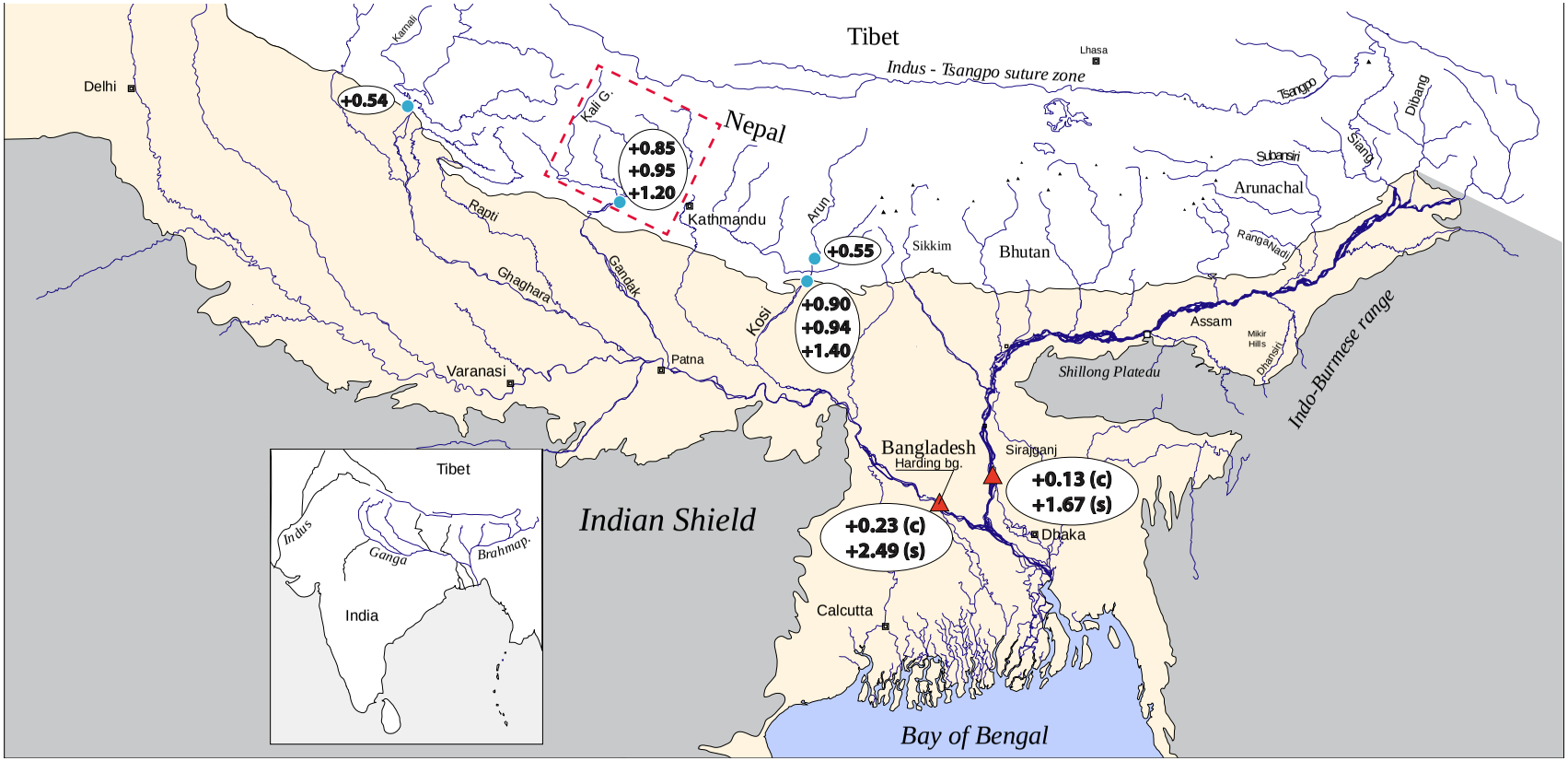

Figure 5.6 – *Map of the Ganga-Brahmaputra river system showing $\varepsilon^{40}Ca$ compositions of samples taken outside of the detailed Narayani basin sampling area, indicated by the rectangle. Red triangles represent river bed loads (with "c" and "s" indicating respectively carbonate and silicate fractions) and blue circles represent the river water samples.*

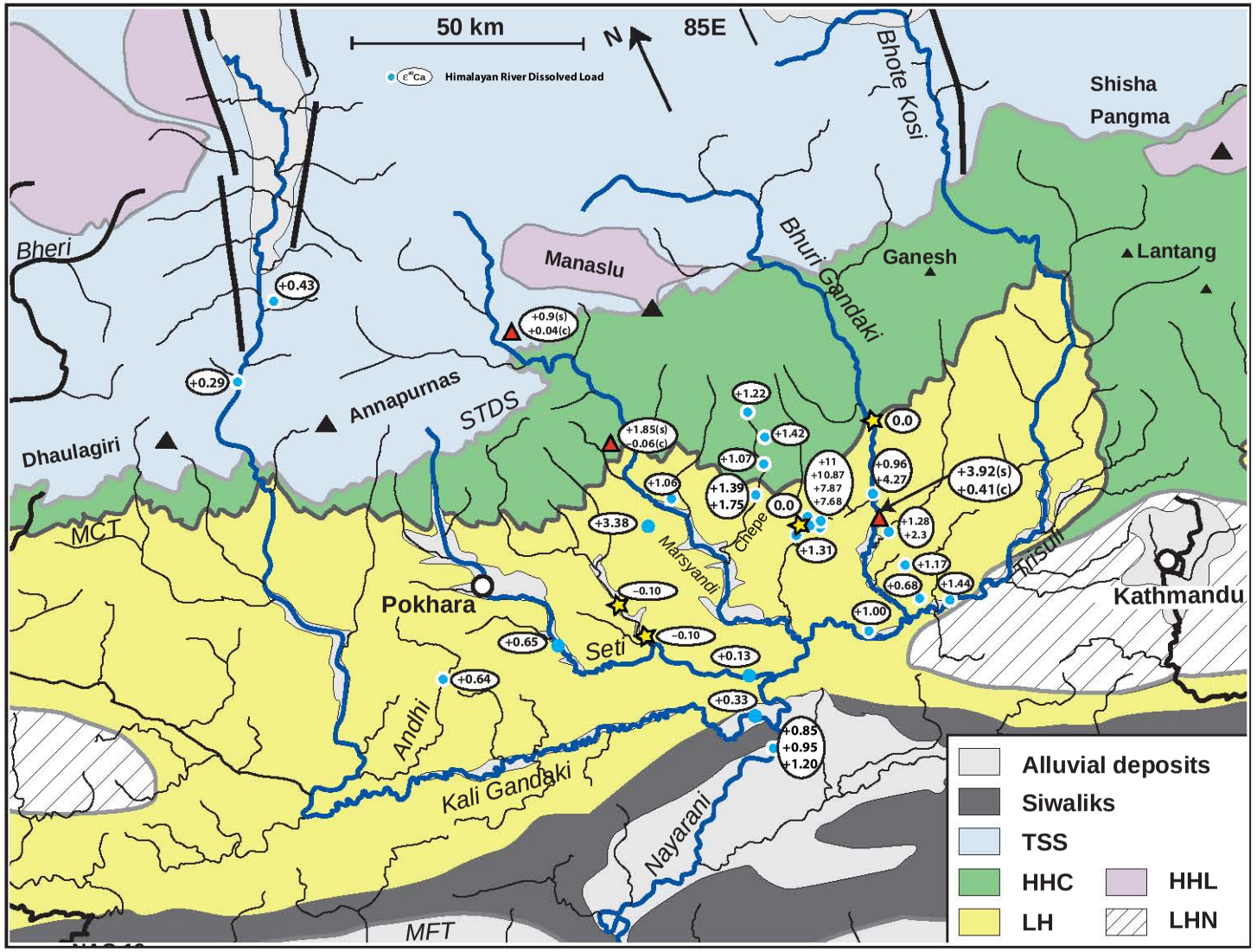

Figure 5.7 – *Geological map of the Narayani watershed showing the $\varepsilon^{40}Ca$ compositions. Red triangles represent river bed loads (with "c" and "s" indicating respectively carbonate and silicate fractions), yellow stars represent LH dolomites, and blue circles represent river water samples. TSS: Tethyan Sedimentary Series, HHC: HH Cristallines, LH: Lesser Himalaya, HHL: High Himalaya Leucogranite, LHN: LH Nappe.*

Table 5.4 – *$\varepsilon^{143}Nd$, $^{87}Sr/^{86}Sr$, and $\varepsilon^{40}Ca$ compositions of the whole rocks and bank/suspended load sediments.*

Sample	River	Formation	ε^{143}Nd	^{87}Sr/^{86}Sr WR	^{87}Sr/^{86}Sr Silicate	^{87}Sr/^{86}Sr Carbonate	ε^{40}Ca WR	± (ε-units)	ε^{40}Ca Silicate	± (ε-units)	ε40Ca Carbonate	± (ε-units)
Whole Rocks - Dolomites												
AP75-867[a]	Madi Khola	LH	–	0.73950	–	–	-0.1	0.20	–	–	–	–
AP75-811[a]	Bhuri Gandaki	LH	–	0.74639	–	–	-0.2	0.46	–	–	–	–
AP75-865[a]	Madi Khola	LH	–	0.75872	–	–	-0.1	0.25	–	–	–	–
AP74-207[a]	Darondi Khola	LH	–	0.85722	–	–	0.00	0.20	–	–	–	–
Sediments												
MAR50[b]	Marsyandi	TSS	-17.3	–	0.73488	0.71372	–	–	0.90	0.3	0.04	0.3
CA950[b]	Khudi Khola	HHC	-16	–	0.75880	0.75280	–	–	1.85	0.3	-0.06	0.3
MO112[b]	Isul Khola	LH	-25.6	–	0.86060	0.83304	–	–	3.92	0.3	0.41	0.3
BR8218[b]	Ganga	TSS+HHC+LH	-17.9	–	0.77000	0.73661	–	–	2.49	0.3	0.23	0.3
BR8203[b]	Brahmaputra	TSS+HHC+LH	–	–	0.74180	0.74364	–	–	1.67	0.3	0.13	0.3

a: Galy et al. (1999)
b: Morin (2015)

Table 5.5 – *$^{87}Sr/^{86}Sr$ and $\varepsilon^{40}Ca$ compositions of river water.*

Sample	River	Formation	$^{87}Sr/^{86}Sr$	$\varepsilon^{40}Ca$	± (ε-units)	Average $\varepsilon^{40}Ca$	± (ε-units)
PB9	Thini Khola	TSS	0.71513	0.43	0.27	–	–
MO503	Yankim Khola	TSS	0.72418	0.29	0.53	–	–
MO359	Chepe Khola	HHC	0.74703	1.42	0.29	–	–
MO364	Chepe Khola	HHC	0.74517	1.53	0.25	1.39	0.37
				1.25	0.27		
MO58	Chepe Khola	HHC	0.74310	1.22	0.24	–	–
MO79	Chepe Khola	HHC	0.74490	1.07	0.31	–	–
CA15003	Chepe Khola	HHC	–	1.75	0.38	–	–
MO100	Masel Khola	LH	0.79690	7.97	0.29	7.87	0.44
				7.77	0.33		
MO383	Masel Khola	LH	0.79830	7.74	0.39	7.68	0.53
				7.61	0.35		
MO107	Maudi Khola	LH	0.80300	3.98	0.29	4.27	0.42
				4.55	0.31		
MO110	Isul Khola	LH	0.77560	1.02	0.28	0.96	0.42
				0.89	0.31		
MO119	Anku Khola	LH	0.77636	2.30	0.39	–	–
MO380	Jaran Khola	LH	0.79875	10.98	0.54	11.00	0.66
				11.02	0.31		
CA15032	Jaran Khola	LH	0.82843	10.77	0.39	10.87	0.56
				10.97	0.40		
MO311	Andi Khola	LH	0.77198	0.42	0.31	0.64	0.59
				0.70	0.28		
				0.79	0.31		
CA15001	Anku Khola	LH	0.80160	1.28	0.44	–	–
CA15005	Chiti Khola	LH	0.74568	1.06	0.44	–	–
CA15008	Paundi Khola	LH	0.78591	3.38	0.37	–	–
CA15030	Darondi Khola	HHC+LH	0.76470	1.31	0.61	–	–
CA15034	Maleku Khola	LH	0.72680	0.68	0.35	–	–
CA15036	Thopal Khola	LH	0.82845	1.17	0.38	–	–
CA11150	Seti	TSS+HHC+LH	0.74566	0.65	0.15	0.39	0.22
MO304	Seti	TSS+HHC+LH	0.72438	0.13	0.16		
CA11149	Kali Gandaki	TSS+HHC+LH	0.73776	0.33	0.18	–	–
LO760	Trisuli	TSS+HHC+LH	0.73402	1.44	0.17	1.22	0.54
CA15038	Trisuli	TSS+HHC+LH	0.73467	1.00	0.44		
PB81	Karnali	TSS+HHC+LH	0.72483	0.54	0.16	–	–
CA11169	Arun	TSS+HHC+LH	0.71612	0.55	0.31	–	–
CA11167	Kosi	TSS+HHC+LH	0.77456	1.40	0.19	–	–
PB71	Kosi	TSS+HHC+LH	0.75714	0.94	0.24	–	–
LO764	Kosi	TSS+HHC+LH	0.74196	0.90	0.34	–	–
PB53	Narayani	TSS+HHC+LH	0.73662	0.68	0.26	1.20	0.56
				1.40	0.30		
				1.51	0.29		
CA11147	Narayani	TSS+HHC+LH	0.73730	0.85	0.23	–	–
CA13130	Narayani	TSS+HHC+LH	0.73723	0.95	0.28	–	–

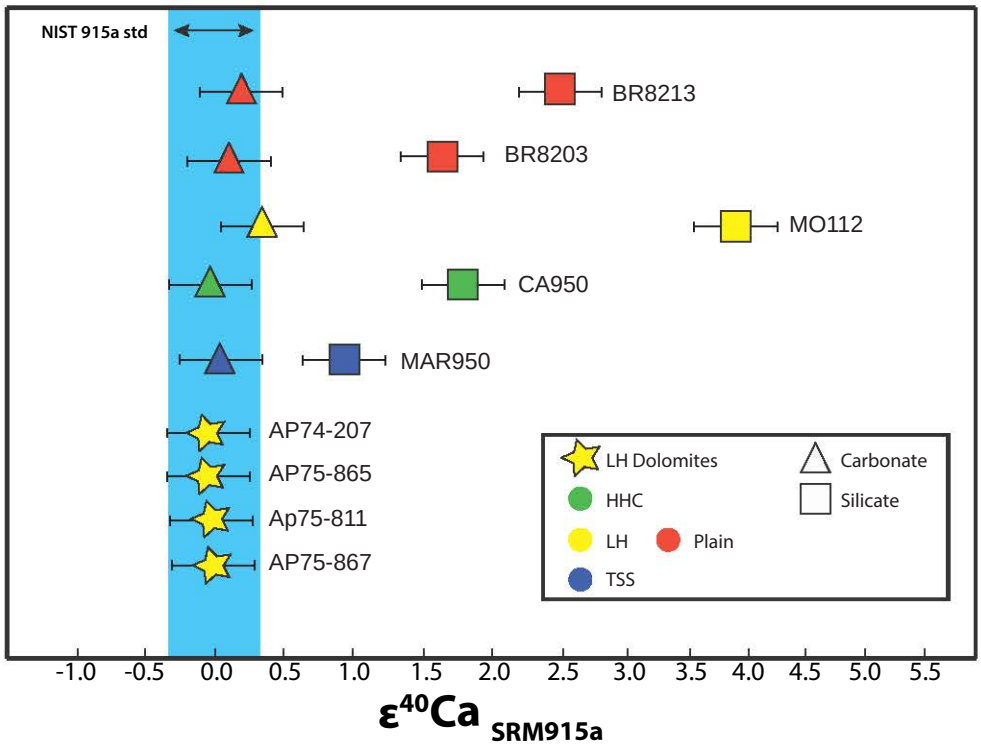

Figure 5.8 – *$\varepsilon^{40}Ca$ results for bedrock and sediment samples. Typical external reproducibility for sample analyses is 0.4 ε-unit (2 S.D.). Similar to the Archean and Proterozoic carbonates presented in Caro et al. (2010), carbonates (triangle symbols) and dolomites (yellow stars) presented here have $\varepsilon^{40}Ca$ indistinguishable from the mantle value and modern seawater. Silicate fractions of sediments (square symbols) have varying $\varepsilon^{40}Ca$ depending on their lithological origin. Yellow = LH, blue = TSS, green = HHC, and red = plain rivers.*

The silicate fractions of sediments show significant ^{40}Ca excesses, with $\varepsilon^{40}Ca$ = +0.9 in the TSS (MAR50), +1.85 in the HHC (CA950) and +3.96 in the LH (MO112). Sediments from the Ganga (BR8218) and Brahmaputra (BR8203) have intermediate $\varepsilon^{40}Ca$ compositions of +2.5 and +1.7, respectively. As shown in Figure 5.9, ^{40}Ca excesses are positively correlated with $^{87}Sr/^{86}Sr$, reflecting variations in both the crustal extraction ages and the compositions of silicate catchments exposed in the different litho-tectonic units of the Himalayas. In particular, the more radiogenic composition of LH silicates reflects both the older crustal extraction model age (T_{DM} = 2.5 Ga) compared with HHC and TSS silicates (T_{DM} = 2.2 Ga) (see discussion below) and the presence of high-K metapelitic rocks in the LH (Ahmad et al., 2000; Clift, 2017).

5.4.2 Dissolved Load

Figure 5.10 shows the variation of the $\varepsilon^{40}Ca$ composition in river water samples, while Figure 5.11 compares $\varepsilon^{40}Ca$ with $^{87}Sr/^{86}Sr$. In the TSS, $\varepsilon^{40}Ca$ values (+0.43

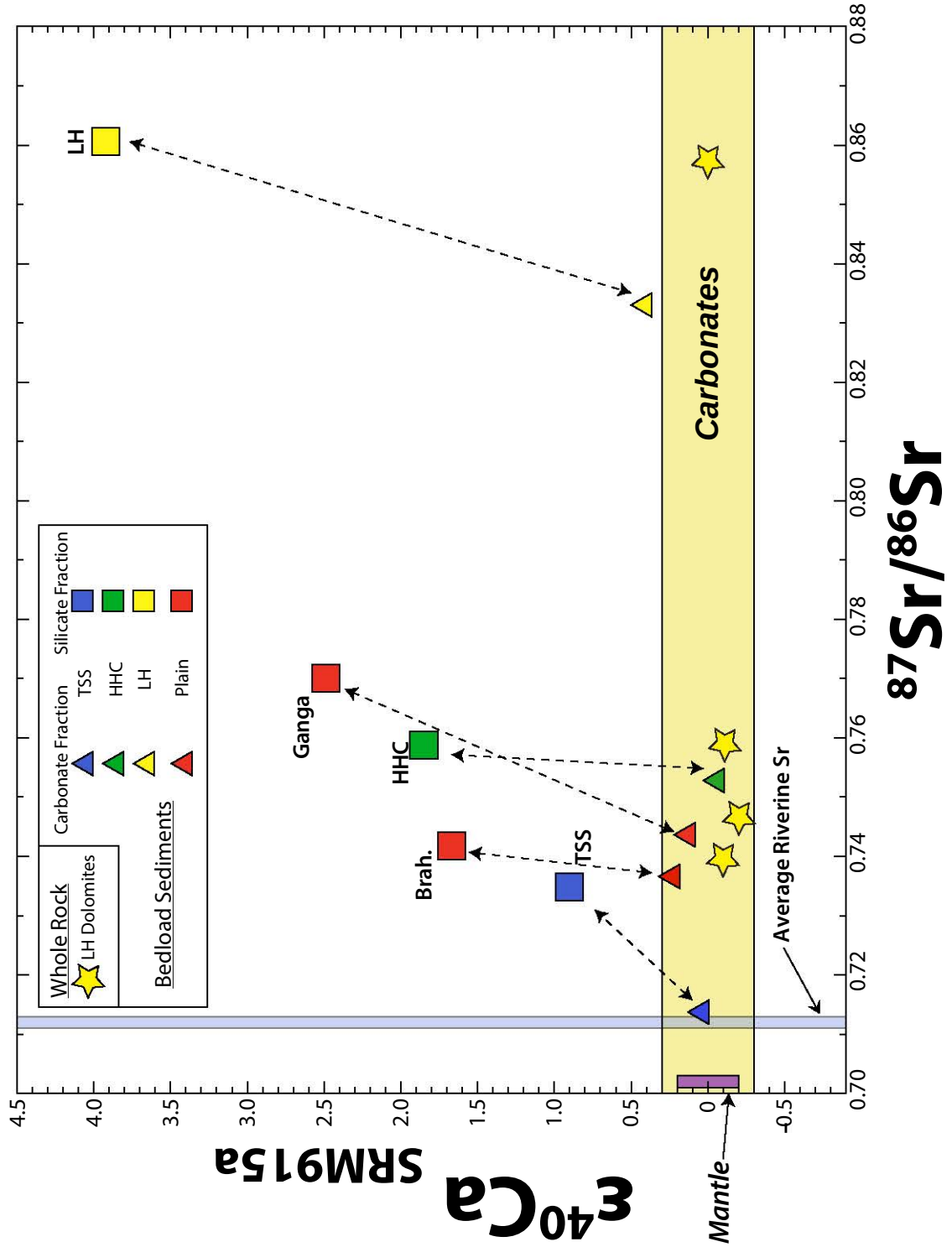

Figure 5.9 – *$\varepsilon^{40}Ca$ vs $^{87}Sr/^{86}Sr$ of carbonate and silicate fractions of sediments from the main lithological units of central Nepal (square for silicate, triangle for carbonate; Yellow = LH, blue = TSS, green = HHC, and red = plain rivers). For carbonates and dolomites, the $\varepsilon^{40}Ca$ remains at 0, within error, showing no detectable radiogenic enrichments despite significant variations in the $^{87}Sr/^{86}Sr$ of carbonates and dolomites. In contrast, silicate fractions show significant enrichments in $\varepsilon^{40}Ca$. The average riverine Sr value (Gaillardet et al., 1999) and the average Sr and Ca isotopic values for the mantle (Caro et al., 2010; McCulloch, 1994; Prokoph et al., 2008) are shown for comparison.*

and +0.29) are within analytical uncertainty of the marine limestone signature, and the $^{87}Sr/^{86}Sr$ ratios (0.71513 and 0.72418) are the lowest of the three units. This is consistent with the high abundance of Paleozoic carbonates in the basin (Galy et al., 1999). Rivers draining solely Formation I in the HHC (i.e., the Upper Khudi, see Chapter 4, and the Chepe Khola) have $\varepsilon^{40}Ca$ compositions that vary between +1.1 and +1.8 coupled with a relatively homogeneous and moderately radiogenic Sr isotopic composition ($^{87}Sr/^{86}Sr$ = 0.743–0.747), consistent with a predominantly silicate origin of dissolved Ca and Sr. LH rivers show the greatest variation, with $\varepsilon^{40}Ca$ ranging from +0.42 in the Andhi Khola (sample MO311) to +11 in the Jaran Khola (sample MO380 and CA15032), while $^{87}Sr/^{86}Sr$ ranges from 0.727 to 0.828. More radiogenic river water Ca compositions in the LH are due to the fact that LH lithologies are more radiogenic than lithologies in the HHC and TSS. There may be a possible correlation between Ca isotopic composition and geographic location among the small LH basins, with the more radiogenic basins found in the northeast, while the single small western LH basin analyzed has a less radiogenic composition (Fig. 5.7) but this is speculative and certainly needs to be confirmed via the analysis of more river water samples, especially smaller LH basins in the west. Figure 5.12 shows $\varepsilon^{40}Ca$ as a function of Ca^*/Na^* in the river waters (asterisk indicates concentrations corrected for precipitation, using rainwater values from Wolff-Boenisch et al. (2009)). Water from rivers with high Ca^*/Na^* ratios are radiogenic in Sr but unradiogenic in Ca, consistent with dolomitic input, whereas rivers with highly radiogenic Ca compositions have low Ca^*/Na^*, indicative of a dominantly radiogenic silicate end-member (Fig. 5.12). Though most tributaries to the Trisuli are highly radiogenic, one of the least radiogenic samples was collected from the Isul Khola, which is also a tributary to this river. The intermediate composition of the Trisuli also suggests that there must be a more unradiogenic signature in this region that contributes to the isotopic composition of Trisuli water.

Despite the apparent decoupling of $^{87}Sr/^{86}Sr$ and $\varepsilon^{40}Ca$ signatures in LH carbonate lithologies, the major tributaries of the Narayani and major Himalayan rivers (Figure 5.11) show a rough correlation between $\varepsilon^{40}Ca$ and $^{87}Sr/^{86}Sr$ dissolved load compositions. The Andhi Khola, Seti, and Kali Gandaki, which drain the LH in the western region of the Narayani, display non-radiogenic Ca isotopic signatures and high Ca^*/Na^* ratios indicative of a dominant carbonate (dolomite) input. In contrast, the Trisuli, which is fed by smaller, mostly highly radiogenic LH rivers with low Ca^*/Na^* ratios (e.g., the Darondi, Jaran Khola, Masel Khola, Mati Khola, etc.), exhibits a geochemical and isotopic signature influenced by radiogenic lithologies (see Figure 5.7), though some non-radiogenic tributaries (e.g., the Isul Khola and Maleku Khola) also contribute. The presence of ^{40}Ca excesses that couple with radiogenic

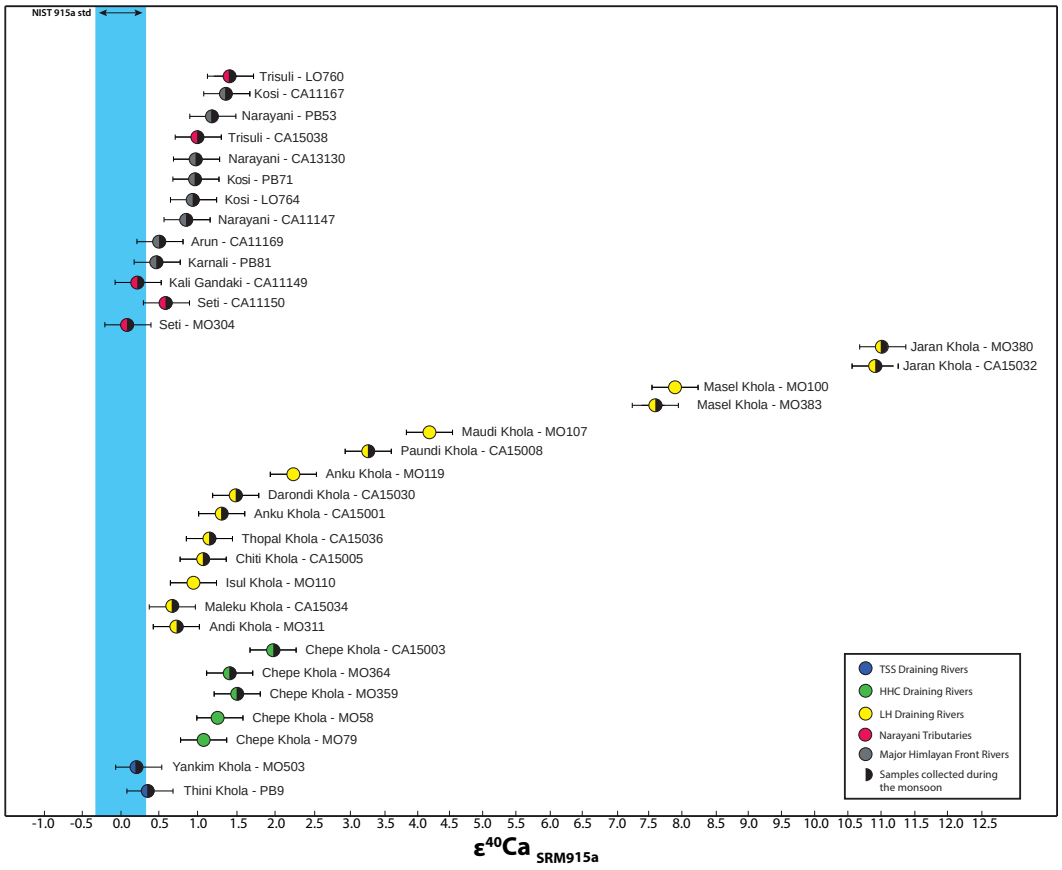

Figure 5.10 – *$\varepsilon^{40}Ca$ results for dissolved load samples analyzed in this study. Typical external reproducibility (used to define error bars) is 0.40 ε-unit (2 S.D.). Yellow = LH, blue = TSS, green = HHC, red = Narayani tributaries, and grey = major Himalayan front rivers. Symbols with black half-circles represent samples collected during the monsoon. There are significant variations in the $\varepsilon^{40}Ca$ of the dissolved load which reflects the lithology of the rivers being drained, i.e., LH rivers with large enrichments in $\varepsilon^{40}Ca$ are extremely small catchments draining solely silicate lithologies.*

^{87}Sr compositions suggests that this signature is inherited from weathering of silicate lithologies (metapelites) rather than dolomites. The headwaters of both the Kali Gandaki and Trisuli are in the TSS. The Kali Gandaki, however, traverses a larger area of the TSS compared with the Trisuli. Therefore, the Kali Gandaki drains a larger proportion of TSS limestones, phylites, and quartzites (English et al., 2000), which, together with the possibly less radiogenic composition of the western LH basin (which requires confirmation by future sampling and analyses), may give rise to the relatively unradiogenic ^{40}Ca isotopic compositions.

Figure 5.13 plots $\varepsilon^{40}Ca$ and $^{87}Sr/^{86}Sr$ of the dissolved load against, respectively, Na^*/Ca^* and $1/Ca^*$, and Na^*/Sr^* and $1/Sr^*$. Dilution affects only the $1/Sr^*$ and $1/Ca^*$ ratios but does not affect the Na^*/Sr^* and Na^*/Ca^* ratios, thus the latter plots allow mixing processes to be more easily identified (Blum et al., 1998; Jacobson et al., 2002). Broad correlations are observed in Figs. 5.13a and 5.13c, consistent with mixing between carbonate and silicate endmembers. However the ranges and the slopes of the correlations seem to vary between the formations, suggesting that the compositions of the silicate endmembers in the LH, HHC and TSS are distinct. Two distinct trends between $\varepsilon^{40}Ca$ and $1/Ca^*$ are also observed, though there is more scatter. Similarly, $^{87}Sr/^{86}Sr$ correlates with Na^*/Sr^*, and less well with $1/Sr^*$, with the latter plot showing two distinct trends. The greater scatter in the plots vs. $1/Ca^*$ and $1/Sr^*$ may be due to effects such as river dilution during the monsoon (i.e., sample points marked with a half black circle), which is removed when normalizing to [Na].

Major Himalayan Front rivers, including the Narayani, Arun, and Kosi, all drain the TSS, HHC, and LH, and thus exhibit a mixture of the geochemical and isotopic signatures discussed throughout this section, resulting in mostly non-radiogenic (e.g., the Arun) to slightly radiogenic Ca isotope compositions (e.g., the Kosi and Narayani) (Figs. 5.6 and 5.10).

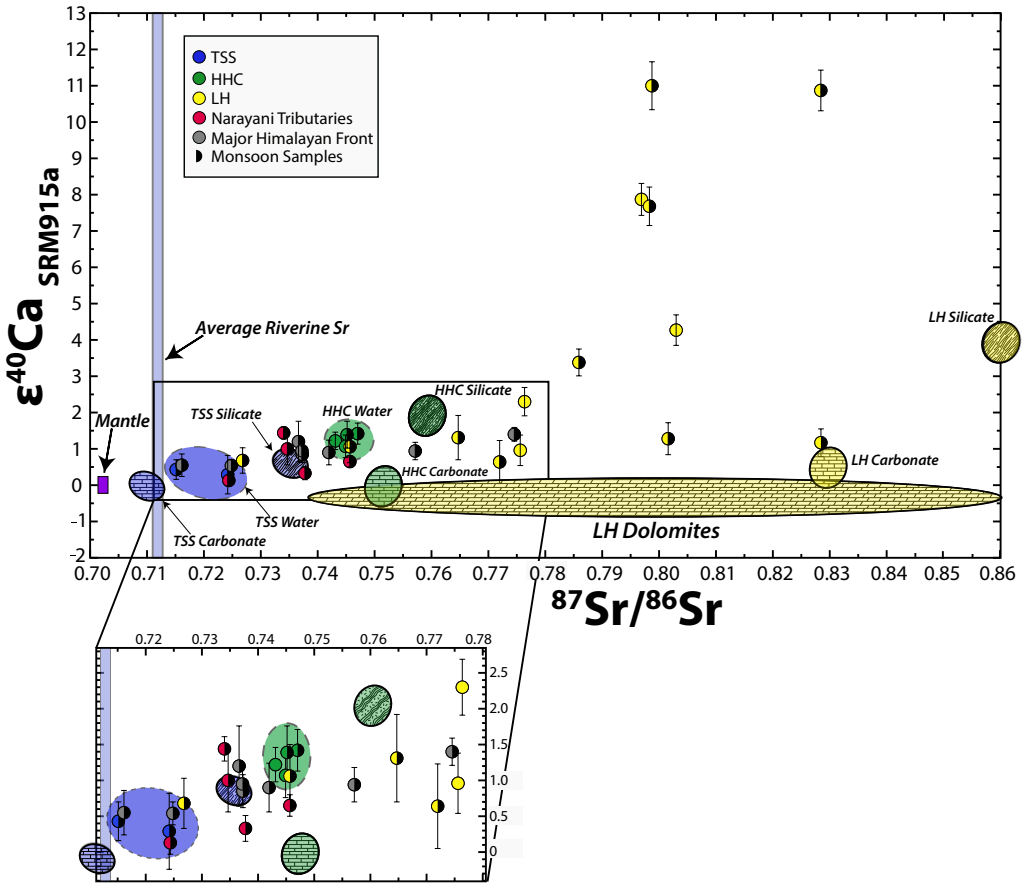

Figure 5.11 – *$\varepsilon^{40}Ca$ vs $^{87}Sr/^{86}Sr$ of the dissolved load from the main litho-tectonic units of central Nepal (Yellow = LH, yellow, blue = TSS, green = HHC, grey = major Himalayan front rivers, red = Narayani tributaries, and black half circles represent samples collected during the monsoon; the silicate and carbonate whole rock end-members deduced from the residues and leachates of bedload samples are denoted by fields with the respective colors of blue, green, and yellow for the TSS, HHC, and LH, and dissolved load fields for the TSS and HHC are denoted by dotted line borders). The average global river water $^{87}Sr/^{86}Sr$ value is shown as a blue vertical bar, while the approximate Sr and Ca isotopic composition of the mantle is indicated by a purple box. The inset (at the bottom of the main plot) shows a rough correlation between the $\varepsilon^{40}Ca$ and $^{87}Sr/^{86}Sr$ of major Himalayan rivers. Well-defined excesses of radiogenic ^{40}Ca are observed in Himalayan Rivers, which likely reflect mixing between calcium derived from non-radiogenic carbonates and radiogenic silicate metasediments.*

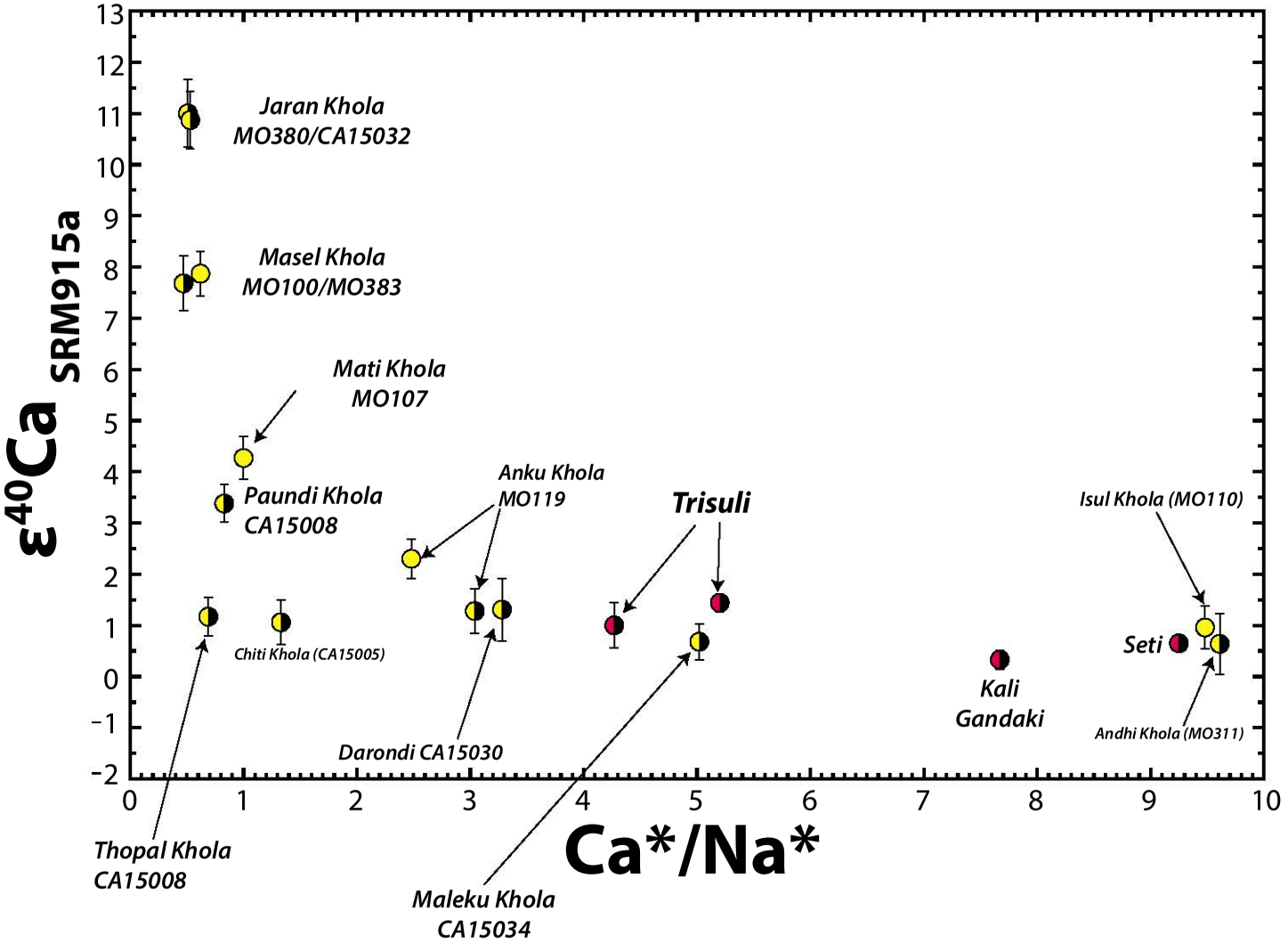

Figure 5.12 – *$\varepsilon^{40}Ca$ compositions versus Ca*/Na* ratios (* indicates that concentrations were corrected for the cyclic contribution) of dissolved load samples from the Narayani basin showing that waters derived from basins rich in carbonates (high Ca*/Na*) tend to be less radiogenic. Symbols with black half-circles represent samples collected during the monsoon.*

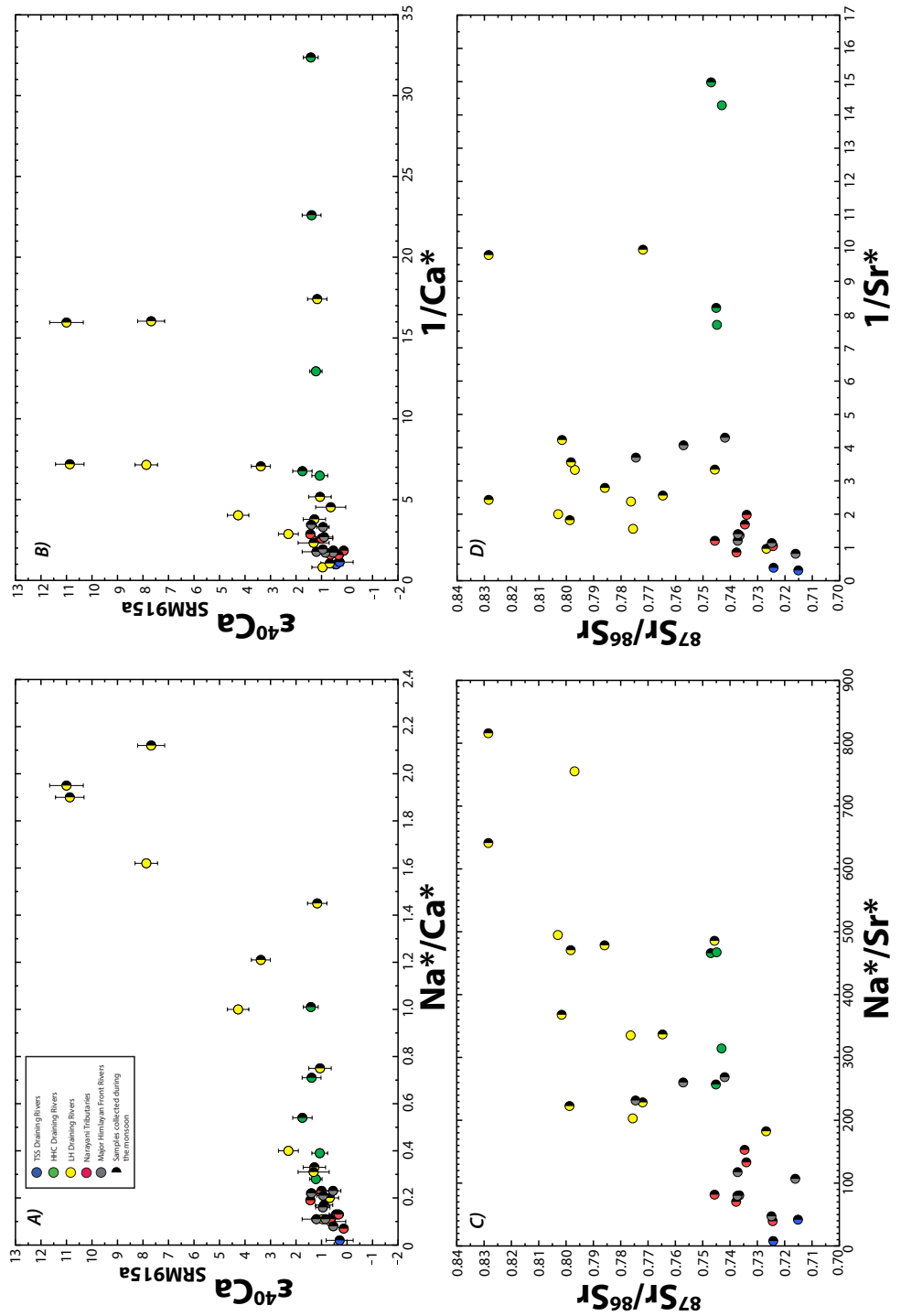

Figure 5.13 – *The relationship between the major element ratios corrected for cyclic contribution (*), and Sr and Ca isotope ratios in tributaries of the Narayani. (Yellow = LH, yellow and black = LH rivers from Monsoon 2015, blue = TSS, green = HHC, grey = major Himalayan front rivers and red = plain rivers). Symbols with black half-circles represent samples collected during the monsoon. A) ε^{40}Ca vs. Na*/Ca* showing an approximate two component mixing trend in river waters between carbonate rich and silicate rich endmembers. B) 1/Ca* shows similar trends but also possible effects of monsoon dilution where samples spread to the right of the carbonate–silicate mixing curve (e.g., HHC and LH samples collected during the monsoon). C) and D) Sr isotope compositions versus Na*/Sr* and 1/Sr* ratios, respectively. Sr isotopes display trends similar to those observed in Ca isotopes.*

5.5 Discussion

5.5.1 Divergence of Ca and Sr isotope behavior in sediments

One first order observation is that LH limestones are not radiogenic in Ca isotopes despite spanning a large range of Sr isotopic compositions. This is not only the case for LH dolomites, but also for the carbonate fraction of bank sediment from each of the three formations, as well as for suspended load sediments collected from the Ganga and Brahmaputra. The presence of non-radiogenic Himalayan carbonates confirms the conclusion made by Caro et al. (2010), i.e., that carbonates have retained the ε^{40}Ca value of the marine limestone signature (= 0) over geological time. This implies that, unlike for Sr isotopes, Ca isotopes in carbonates have not re-equilibrated with adjacent highly radiogenic silicate rocks during metamorphism related to Himalayan orogenesis. The reason for this is not immediately obvious. Both Ca and Sr are mobile elements, and both are affected by hydrothermal alteration and/or metamorphic fluids (Von Damm et al., 1985; Ghatak and Basu, 2011; Ludden et al., 1982). So it is not clear that fluid mobility can explain the difference in behavior observed here. It is possible that Sr and Ca diffuse at different rates during metamorphism, but there are few data allowing direct comparison between Sr and Ca diffusion coefficients under conditions relevant to Himalayan metamorphism.

Perhaps the most straightforward explanation is that mass balance causes Sr isotopes in carbonates to be more strongly influenced than Ca isotopes by reequilibration with silicates. In the LH, for example, the Ca/Sr ratio is approximately an order of magnitude higher in carbonates than in silicates (Deniel et al., 1987). This is consistent with what is observed when worldwide compilations of shale data are compared with those of carbonates (GERM website). In addition, preferential loss of Sr is a possible consequence of dolomitization, which could increase Ca/Sr ratios in Himalayan carbonates even further. As a result, Sr isotopes in carbonates are more easily perturbed than Ca isotopes by re-equilibration with silicates during metamorphism.

5.5.2 General observations concerning radiogenic Ca isotopes in the dissolved load

In the dissolved load, in general, from north (i.e., the TSS) to south (i.e., the LH), both the major elemental and $^{87}Sr/^{86}Sr$ and ε^{40}Ca isotopic values vary according to the range of lithologies drained, which reflects the age and composition of the silicate and carbonate catchments in each formation. Moving towards the south, the dissolved loads found in the small catchments become more radiogenic, and certain elements become more dilute (i.e., Ca and Sr) compared with other elements, reflecting, in general, a decreased carbonate contribution (Galy et al., 1999; Morin, 2015). This trend

is muted, but still exists, in larger rivers such as the Kali Gandaki, Trisuli, or Bhuri Gandaki, whose dissolved load concentrations reflect a mixture of smaller catchments from the three formations. We can also see a general consistency between the lithology of a basin and its ε^{40}Ca composition, i.e., basins rich in silicates have high ε^{40}Ca values. For example, rivers from the eastern LH, such as the Masel, Jaran, Mati, and Anku Khola all have high to extremely high ε^{40}Ca (approximately 1 to 11) and all drain basins that are predominantly silicate. Figure 5.14 shows that Masel and Jaran Khola, two of the most radiogenic rivers analyzed in this study, drain exclusively the Kuncha Formation and a garnetiferous schist lithology. In this region, the Kuncha Formation is composed of thick sequences of phyllite, phyllitic metasandstone, and quartzite. There are also frequent occurrences of garnet–biotite–muscovite schists, and augen and banded gneisses (Dhital, 2015). These lithologies seem to correlate with the highest radiogenic ^{40}Ca excesses and should be the target for future investigations into the upper limit of radiogenic Ca compositions in the central Himalaya.

Water from HHC rivers, which are predominantly silicate in nature, such as the upper Khudi (see Chapter 4) and Chepe Khola, also have moderately high ε^{40}Ca values (approximately 1 to 2). The lithology of river basins, such as the Thini and Yankim Khola (TSS) and the Andhi Khola (LH) are predominantly carbonate or sedimentary in nature and have low ε^{40}Ca values. Himalayan front rivers have intermediate values consistent with mixtures of highly radiogenic waters from silicate-dominated basins and less radiogenic waters from carbonate-dominated basins, including a strong contribution from the TSS.

5.5.3 Defining average silicate compositions of the LH, HHC, and TSS

In this section, we begin to define the average silicate end-member compositions of the LH, HHC, and TSS. Here, the goal is to find the average key major elemental ratios and Ca isotope compositions of each formation because this information is necessary to evaluate the fraction of cations in river water that derive from silicate weathering. These ratios and compositions are needed for the budget modeling that will be discussed in section 5.5.5, which is aimed at estimating the silicate weathering flux of central Nepalese rivers and its effect on CO_2 consumption. We have measured these ratios and isotopic compositions in three sediments that are representative of the TSS, HHC, and TSS. However, it is important to confirm whether these measured values are geologically reasonable in the context of the extreme heterogeneity that is characteristic of Himalayan lithologies.

In Supplementary Tables 5.18, 5.19, and 5.20, we have listed sediment compositions for the TSS, HHC, and LH. Supplementary Table 5.21 contains compositions for whole rocks from the LH. As much as possible, we use the sediment

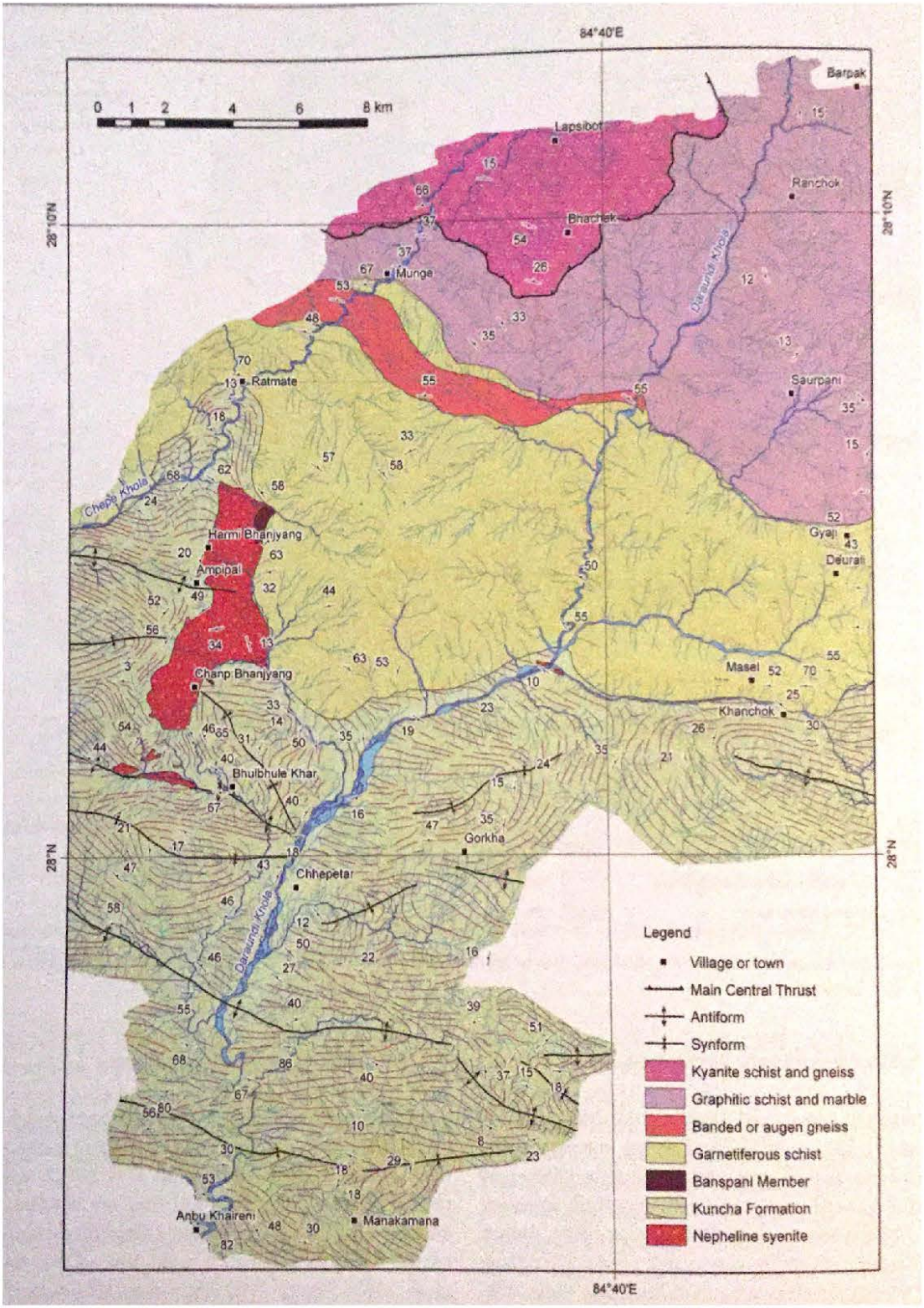

Figure 5.14 – *A geological map of the Gorkha–Ampipal region in the Lesser Himalaya of Central Nepal (taken from Dhital (2015), which was modified from Dhital (1995).*

data to estimate silicate rock compositions for each formation, as these integrate the crustal composition at the catchment scale, thus averaging out some of the heterogeneity seen in the whole rocks. We have calculated the average ratios for K/Ca, Ca/Na, and Mg/K by dividing the average elemental concentrations, instead of using the average or median of the individual ratios to avoid overweighting samples with outlier values. In addition to the problem of extreme heterogeneity, estimating the average silicate composition of each of the Himalayan formations is complicated by the abundance of carbonate. Himalayan samples that have more than 3 wt. % CaO most certainly have carbonate. This, however, does not imply that samples with less than 3% CaO do not contain carbonate. "Silicate" samples that derive from the TSS, with up to 20 wt. % CaO, are in fact impure marbles.

The following summarizes the methods we used to estimate the K/Ca, Ca/Na, and Mg/K ratios for the average silicate components of the TSS, HHC, and LH formations (see Supplementary Tables 5.18, 5.19, and 5.20 – for TSS, HHC, and LH river sediments, and Table 5.21 for LH bed rock data).

- TSS: In the TSS, we have 12 samples that contain large components of both calcite and dolomite. After correcting for carbonate, these samples yield a K/Ca ratio of 3.74 $\pm$ 2.57 (Supplementary Tables 5.18, 5.19, and 5.20). The standard deviation is high and there are large uncertainties associated with the carbonate correction because TSS samples typically contain 30 wt. % carbonate, i.e., more than 90 wt. % of the total CaO. The carbonate corrected and non-corrected K/Ca ratios are 2.39 $\pm$ 2.52 and 0.16 $\pm$ 0.06, respectively. These data yield average carbonate corrected and non-corrected Ca/Na ratios of 0.65 $\pm$ 0.71 and 0.10 $\pm$ 0.03, respectively, and a Mg/K ratio of 0.73 $\pm$ 0.31 (see Table 5.7 and Supplementary Tables 5.18, 5.19, and 5.20).

- HHC: Sediments derived from the Formation I in the Khudi Khola provide a good estimate of the HHC crust because (1) previous studies have measured numerous sediment samples from this basin that have very low carbonate contents (i.e., below 0.3 wt. %) (Morin, 2015) and (2) the intensity of chemical weathering is relatively low compared with that of the LH. The carbonate corrected and non-corrected K/Ca ratios are 2.65 $\pm$ 0.61 and 1.81 $\pm$ 0.83, respectively. These data yield average carbonate corrected and non-corrected Ca/Na ratios of 0.49 $\pm$ 0.07 and 0.62 $\pm$ 0.24, respectively, and a Mg/K ratio of 1.04 $\pm$ 0.36 (see Table 5.7 and Supplementary Tables 5.18, 5.19, and 5.20).

- LH: In the LH, we have only five sediment samples that have been analyzed for carbonate content (Supplementary Tables 5.18, 5.19, and 5.20), which poses

a problem because of the great compositional variability of the LH, at least compared with the HHC in the Khudi Khola (Chapter 4). The sediment data yield highly variable K/Ca ratios between 2.5 and 125. Using the bedrock database from Pecher (1978) is a possible alternative approach, but these data show even more variability than the sediment data (Supplementary Table 5.21). Using the sediment data, the carbonate corrected and non-corrected K/Ca ratios are 7.06 ± 6.73 and 1.78 ± 1.87, respectively. These data yield average carbonate corrected and non-corrected Ca/Na ratios of 0.21 ± 0.22 and 0.84 ± 0.99, respectively, and a Mg/K ratio of 1.03 ± 0.46 (see Table 5.7 and Supplementary Table 5.21).

5.5.4 *Estimating the average $\varepsilon^{40}Ca$ compositions of silicate rocks in the Himalayan formations*

Crustal extraction ages, which are model ages that represent the average amount of time that the material in a rock formation has resided in the continental crust, can be estimated using the Sm–Nd isotopic system. Based on the Sm-Nd isotopic analyses and Sm and Nd trace element concentrations of the sediments used in this study, we can calculate the model ages, τ_{DM}, for crustal extraction of each formation from the Depleted Mantle (DM) reservoir:

$$\tau_{DM} = \frac{1}{\lambda} \times \ln\left[\frac{^{143}Nd/^{144}Nd_{Sample} - ^{143}Nd/^{144}Nd_{DM}}{^{147}Sm/^{144}Nd_{Sample} - ^{147}Sm/^{144}Nd_{DM}} + 1\right] \tag{5.2}$$

where $^{143}Nd/^{144}Nd_{DM}$ and $^{147}Sm/^{144}Nd_{DM}$ are 0.51315 and 0.2137, respectively, and λ is the decay constant of ^{147}Sm (λ = 6.54 x 10^{-12}) (all values from White (2013)). Sm–Nd model ages were calculated using representative $^{143}Nd/^{144}Nd$ and $^{147}Sm/^{144}Nd$ values for each formation (Table 5.6), yielding ages of 2.53 Ga for the LH, 2.23 Ga for the HHC, and 2.23 Ga for the TSS, which are similar to the model ages for these formations obtained in previous studies (Ahmad et al., 2000).

We assume a simple three-stage ^{40}Ca growth model (schematically illustrated in Figure 5.15). In the first stage, which lasts until the time of crustal extraction (i.e., the Sm-Nd model age), a K/Ca ratio equivalent to the mantle value is assumed (for radiogenic Ca isotopes the primitive mantle is essentially equivalent to the depleted mantle). In the second stage, which lasts until the sedimentary age of the formation under consideration, an average crustal K/Ca ratio (0.95) is assumed. In the third stage, which lasts until the present-day, the K/Ca ratios estimated above for each formation are used. This model is a simplification, as it precludes the fact that these formations have experienced a number of crustal recycling and/or alteration events throughout the past 60 Ma, as well as earlier events, which may have perturbed the

K–Ca system and K/Ca ratios. Making these assumptions, the change in ε^{40}Ca since crustal extraction can be calculated from the following equations:

$$^{40}Ca/^{44}Ca_{PresentCrust} = ^{40}Ca/^{44}Ca_{PresentMantle} + ^{40}K/^{44}Ca_{PresentCrust} \times \beta \times \left(e^{\lambda \times T_{DM}} - 1\right) \quad (5.3)$$

$$^{40}Ca/^{44}Ca_{CrustatT_{sedimentary}} = ^{40}Ca/^{44}Ca_{PresentCrust} - ^{40}K/^{44}Ca_{PresentCrust} \times \beta \times \left(e^{\lambda \times T_{Sedimentary}} - 1\right) \quad (5.4)$$

$$^{40}Ca/^{44}Ca_{PresentFormation} = ^{40}Ca/^{44}Ca_{CrustatT_{sedimentary}} + ^{40}K/^{44}Ca_{PresentFormation} \times \beta \times \left(e^{\lambda \times T_{Sedimentary}} - 1\right) \quad (5.5)$$

$$\varepsilon^{40}Ca_{PresentFormation} = \frac{^{40}Ca/^{44}Ca_{PresentFormation}}{^{40}Ca/^{44}Ca_{Mantle}} \times 10^4 \quad (5.6)$$

where β = 0.8952, λ = 5.51 x 10^{-10}, $T_{Sedimentary}$ is the sedimentary age of each formation, and T_{DM} is the model age of crustal extraction. As the mantle ε^{40}Ca is approximately 0, the change in ε^{40}Ca calculated with equation 5.6 is equivalent to the ε^{40}Ca for the average silicate component of each formation: 1) ε^{40}Ca = 13.60 $\pm$ 12.31 for the LH, 2) ε^{40}Ca = 3.00 $\pm$ 0.21 for the HHC, and 3) ε^{40}Ca = 2.91 $\pm$ 0.86 for the TSS (Table 5.6; also shown, for comparison, are values calculated from a two-stage model). The very large uncertainties, especially for the LH, are related to the large uncertainty on the K/Ca ratio of each formation (see above). We use these ε^{40}Ca values to constrain the radiogenic Ca budget presented in section 5.5.5. We note that the calculated ε^{40}Ca values for each formation are, on average, more radiogenic than the measured ε^{40}Ca values of the corresponding sediment silicate fractions (see Table 5.6).

5.5.5 *Quantifying the contribution of silicate weathering products to Himalayan river waters*

Using the average elemental and Ca isotopic compositions of the silicate rocks of the three formations estimated above, we can now address the quantification of the silicate weathering flux in the Himalaya, and ultimately its effect on the carbon cycle and climate. To accomplish this task, we must first determine the fraction of cations in the dissolved load that derive from silicate weathering based on the major elemental and ^{40}Ca analyses presented in this study.

The soluble chemistry of a river can be described as the summation of atmospheric input and the weathering products of silicate, carbonate, sulfide, and

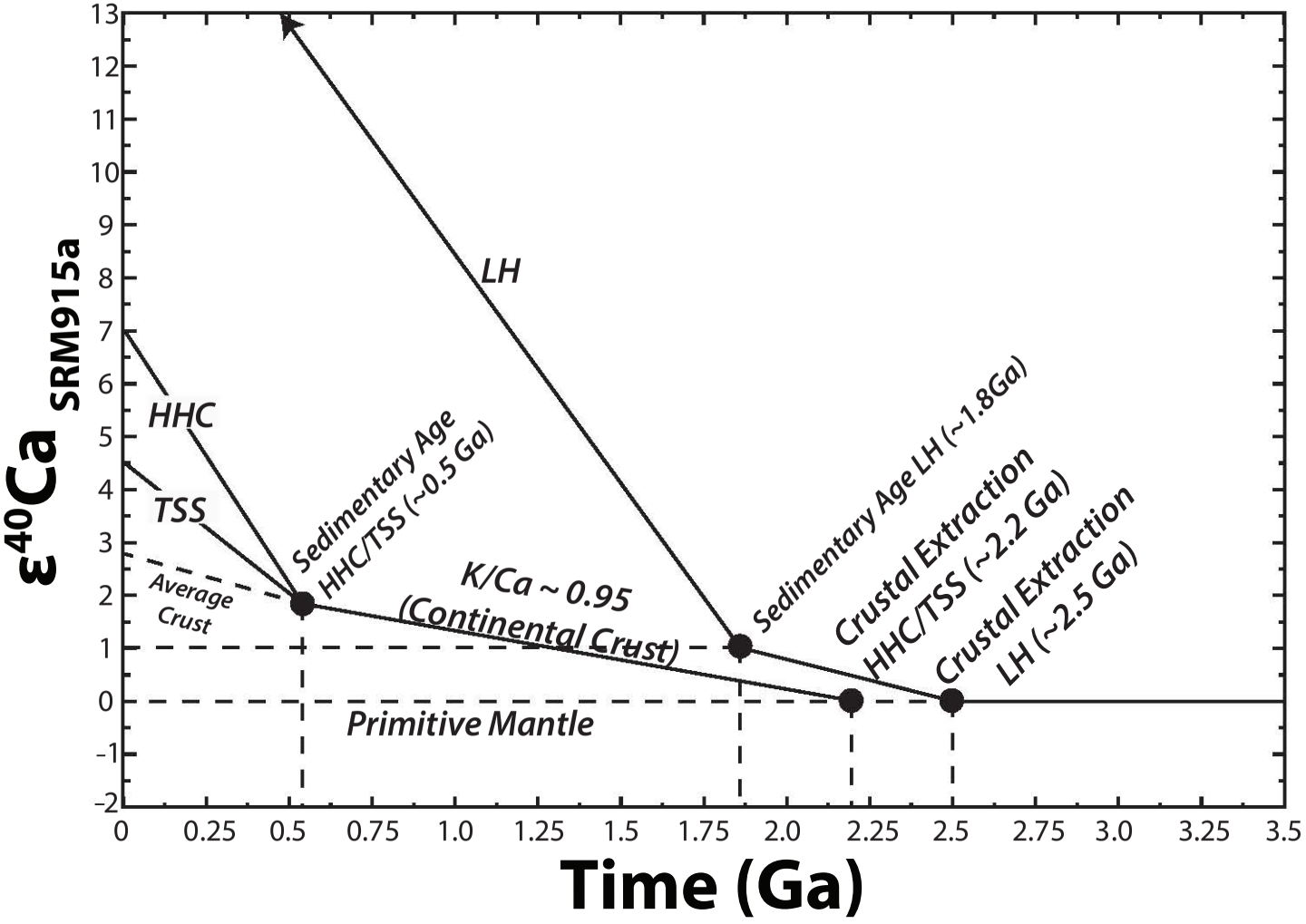

Figure 5.15 – *A schematic illustration of a three stage isotopic growth model that can be applied to TSS, HHC, and LH sediments. On the basis of the Sm-Nd T_{DM} ages, a crustal extraction age of 2.5 Ga is assumed for the LH and 2.2 Ga for the TSS and HHC. A sedimentary age of 1.8 Ga is assumed for the LH and 0.5 Ga for the TSS and HHC.*

Table 5.6 – *Sm–Nd model ages and K–Ca decay calculations.*

Sample	Formation	[Nd]	[Sm]	ε^{143}Nd (BULK)	^{143}Nd/^{144}Nd	^{147}Sm	^{147}Sm/^{144}Nd	T_{DM}	$T_{Sedimentary}$	^{40}K/^{44}Ca (formation silicate average)	Calculated formation ε^{40}Ca (Two-Stage Model τ_{DM})	Calculated formation ε^{40}Ca (Three-Stage Model τ_{DM})	Measured load ε^{40}Ca	bed
BR8218	Ganga	36.2	7.2	-17.8	0.511726	0.007183	0.12025	2.31E+09		–	–	–	–	
MO112	LH	45.2	7.8	-25.6	0.511326	0.007781	0.10433	2.53E+09	1.80E+09	0.04 ± 0.04	23.12 ± 22.04	13.60 ± 12.31	3.92	
CA950	HHC	25.1	5.1	-16	0.511818	0.005088	0.12285	2.23E+09	5.00E+08	0.015 ± 0.003	6.92 ± 1.59	3.00 ± 0.21	1.85	
MAR50	TSS	27.39	5.38	-17.2	0.511756	0.005367	0.11876	2.23E+09	5.00E+08	0.02 ± 0.04	6.24 ± 6.58	2.91 ± 0.86	0.9	

evaporitic material plus anthropogenic input (Galy and France-Lanord, 1999). This relationship can be summarized in terms of the concentration of element X of a specific river:

$$X_{river} = X_{cyclic} + X_{evaporite} + X_{carbonate} + X_{silicate} + X_{sulfide} + X_{anthropogenic} \tag{5.7}$$

Starting with this equation, forward modeling of the river chemistry with constraints from the major elemental chemistry of lithological units and stream sediments allows the fraction of the cation budget derived from silicate weathering to be determined. These constraints are determined from small catchments that contain single lithologies and can be used to define the contribution of silicate rock units to the dissolved load during weathering. For example, the upper Khudi or Chepe can be used to define the end-member of HHC lithologies or catchments such as the Jaran Khola or Masel Khola can be used to define the end-member composition of LH silicate lithologies (see section 5.5.3).

Knowledge of these compositions allows us to define R^{chem}, i.e., the fraction of the amount of dissolved cations derived from silicate weathering, which, in a general form, is as follows:

$$R^{chem} = \frac{X^*_{silicate}}{X^*_{silicate} + X^*_{evaporite} + X^*_{carbonate} + X^*_{sulfide} + X^*_{anthropogenic}} \tag{5.8}$$

Here, X^* represents the measured concentrations after subtraction of the estimated cyclic (rainwater) component (based on Galy and France-Lanord (1999) but using rain water values from Wolff-Boenisch et al. (2009)) and R represents the total cationic charge budget obtained from major elements (i.e., the superscript "chem"). We will consider only the major cations (Ca, Mg, Na, and K). Thus, equation 5.8 becomes:

$$R^{chem} = \frac{Na^{chem}_{sil} + K^{chem}_{sil} + 2 \times Ca^{chem}_{sil} + 2 \times Mg^{chem}_{sil}}{Na^* + K^* + 2 \times Ca^* + 2 \times Mg^*} \tag{5.9}$$

In equation 5.9, the factor of 2 derives from the equivalent cationic charge of Ca and Mg. The concentrations of Ca^*, Mg^*, Na^*, and K^* in equation 5.9 are the total dissolved load concentration for each element (corrected for the cyclic contribution; see Wolff-Boenisch et al. (2009) for the correction values used here), while the subscript "sil" represents the concentration of each element derived from silicate weathering (similarly, below the subscript "carb" represents the concentration of each element derived from carbonate weathering, while "evap" represents that from evaporite weathering). We also adopt here the assumptions of Galy and France-Lanord (1999) that contributions from sulfates and anthropogenic inputs are negligible

to the major cation budget, that carbonate dissolution does not contribute to sodium and potassium concentrations in the dissolved load, and that the evaporite load represents solely dissolved NaCl. Thus, after Galy and France-Lanord (1999):

$$Na_{evap}^{chem} = Cl_{evap}^{chem} = Cl^* \tag{5.10}$$

$$Na_{sil} = Na^* - Cl^* \tag{5.11}$$

$$K_{sil}^{chem} = K^* \tag{5.12}$$

$$Ca_{sil}^{chem} = Ca^* - Ca_{carb} \tag{5.13}$$

$$Mg_{sil}^{chem} = Mg^* - Mg_{carb} \tag{5.14}$$

In this method of modeling, the only parameters that must be known are the dissolved load concentrations of each element considered, their concentrations in precipitation, and the Mg/K and Ca/Na ratios released by weathering of the silicate rocks currently being eroded in each catchment. After Galy and France-Lanord (1999), we define Ca_{sil}^{chem} (in µmol/L) as:

$$Ca_{sil}^{chem} = (Na^* - Cl^*) \times \left(\frac{Ca}{Na}\right)_{DissolvedPureSilicate} \tag{5.15}$$

which is the concentration of Ca, from silicate weathering, in the dissolved load. Mg_{sil}^{chem} (in µmol/L), the concentration of Mg released during silicate weathering to the dissolved load, is defined as:

$$Mg_{sil}^{chem} = K^* \times \left(\frac{Mg}{K}\right)_{DissolvedPureSilicate} \tag{5.16}$$

Magnesium derived from silicates could alternatively be calculated using the Mg/Na ratio, but Morin (2015) showed that this choice does not significantly change the budget calculations, so we will use the Mg/K ratio here for simplicity. Plugging these expressions into equation 5.9 we obtain:

$$R^{chem} = \frac{(Na^* - Cl^*) + K^* + 2 \times (Na^* - Cl^*) \times \left(\frac{Ca}{Na}\right)_{DissolvedPureSilicate} + 2 \times K^* \times \left(\frac{Mg}{K}\right)_{DissolvedPureSilicate}}{Na^* + K^* + 2 \times Ca^* + 2 \times Mg^*} \tag{5.17}$$

where "DPS" represents "Dissolved Pure Silicate." Equation 5.17 can be rearranged to give:

$$R^{chem} = \frac{\left(1+2\left(\frac{Ca}{Na}_{DPS}\right)\right)\times Na^* - \left(1+2\left(\frac{Ca}{Na}_{DPS}\right)\right)\times Cl^* + \left(1+2\left(\frac{Mg}{K}_{DPS}\right)\right)\times K^*}{(Na^*-Cl^*)+K^*+2\times Ca^*+2\times Mg^*} \tag{5.18}$$

Here, R^{chem} is in fact the ratio of the silicate to the silicate plus carbonate fraction, as the evaporitic contribution is removed by the subtraction of Cl^* from Na^* in the denominator. This allows the budget to be viewed as a two component mixture.

The values calculated for R^{chem} will of course depend on the accuracy of each of the parameters in equation 5.18, which each have associated uncertainties. These include:

1. Measurement uncertainties: Uncertainties for major elemental analyses (ICP-OES, SARM, CRPG, Nancy, France) of the dissolved load vary between 2 and 5% for Ca, Na, Mg, and K. This does not introduce a significant amount of error into the budget calculations.

2. Variation in river water cation concentrations and cyclic contributions: Varying river concentrations are principally a factor associated with alternation between the monsoon and dry seasons. The amount of geochemical variation during the monsoon depends on a number of factors, such as basin location and the amount of precipitation, which varies significantly even between the Chepe and Khudi, for example. Taking into account these variations would require long-term monitoring such as that which has been done in the Khudi Khola (see Chapter 4). This is a source of uncertainty, but as it is difficult to quantify it is not taken into account in the budget models.

3. Uncertainties in the representative Ca/Na and Mg/K ratios used for each formation: Elemental and isotopic mixing relationships in river water allow us to identify end-members and the proportions to which each contributes to the river chemistry in a specific catchment. One difficulty in applying the forward modeling technique presented in Galy and France-Lanord (1999) is the uncertainties that arise when trying to define characteristic elemental ratios for the sources of weathering (see below). Characteristic values of Ca/Na and Mg/K for each of the three formations have been defined in previous studies (France-Lanord and Derry, 1997; Galy and France-Lanord, 1999; Quade, 2003; Wolff-Boenisch et al., 2009; Morin, 2015; Pecher, 1978; Brouand, 1989), as well as

in section 5.5.3. It is clear that uncertainties in end-member estimates translate to uncertainties in the mass balance calculations. The wide range of Mg/K ratios have a lesser, though non-negligible, effect on the budget of silicate to carbonate weathering than the range in Ca/Na, mainly because Ca constitutes most of the river cationic charge (see Galy and France-Lanord (1999). As Ca represents between 60 and 70% of cationic riverine charge, the uncertainties on the relative silicate and carbonate contributions to this flux are the main source of error for R^{chem} estimates.

R^{chem} is a ratio of the silicate to silicate + carbonate weathering budget. To be directly comparable with the budget estimates made with ε^{40}Ca compositions (see below), which is purely an estimate of the contribution of Ca derived from silicate weathering, we can define the parameter F_{Ca}^{chem} (F denotes an elemental budget from 0 to 100%), which takes into account only Ca delivered to the dissolved load via silicate weathering and will thus always be lower than R^{chem} (i.e., R^{chem} includes the amount of Na, K, and Mg, as well as Ca released from silicate weathering whereas F_{Ca}^{chem} includes only Ca from silicate weathering):

$$F_{Ca}^{chem} = \frac{Ca_{sil}^{chem}}{X_{Ca}} \tag{5.19}$$

where X_{Ca} refers to the Ca derived from both silicates and carbonates, i.e., the Ca^* in the dissolved load. R^{chem} and F_{Ca}^{chem} are not independent estimates, and there will never be a linear relationship between them. If R^{chem} = 0 or 1, then F_{Ca}^{chem} will also be 0 or 1, but if R^{chem} = 0.5, then F_{Ca}^{chem} will always be < 0.5 because F_{Ca}^{chem} only considers the weathering signature/flux derived from Ca silicate minerals, whereas R^{chem} takes into account the weathering signature/flux derived from Ca, Na, Mg, and K silicate minerals.

Using the radiogenic Ca data produced in this study, we can make similar budget calculations based on the balance between the ε^{40}Ca of the river and the silicate and carbonate end-members:

$$F_{Ca}^{iso} = \frac{\varepsilon^{40}Ca_{river} - \varepsilon^{40}Ca_{carb}}{\varepsilon^{40}Ca_{sil} - \varepsilon^{40}Ca_{carb}} \tag{5.20}$$

where F_{Ca}^{iso} is the fraction of calcium derived from silicate weathering, $\varepsilon^{40}Ca_{River}$ is the ε^{40}Ca composition of the river, $\varepsilon^{40}Ca_{carb}$ is the ε^{40}Ca value of the carbonate end-member, and $\varepsilon^{40}Ca_{sil}$ is the ε^{40}Ca value of the silicate end-member.

We can define the value Ca_{sil}^{iso} (in µmol/L), which is the concentration of Ca derived from silicate weathering in the dissolved load based on the calculated radiogenic Ca budget result:

$$Ca_{sil}^{iso} = F_{Ca}^{iso} \times Ca^{*} \tag{5.21}$$

Out of the three sources of error discussed above, the uncertainties on the Ca/Na and Mg/K contribute most to the total uncertainty on the major element budget. As discussed earlier, the Ca/Na and Mg/K ratios of representative silicate lithologies can be defined from the major element whole rock and mineral geochemistry of small eroding catchments, which Galy and France-Lanord (1999) defined as 0.2 for Ca/Na and 0.5 for the Mg/K. In section 5.5.3, we extended these estimates to 0.65 ± 0.71 for Ca/Na and 0.73 ± 0.31 for Mg/K in the TSS, 0.49 ± 0.07 for Ca/Na and 1.04 ± 0.36 for Mg/K in the HHC, and 0.21 ± 0.22 for Ca/Na and 1.03 ± 0.46 for Mg/K in the LH based on the database of sediment analyses of the TSS, HHC, and LH, respectively (these values are carbonate-corrected based on the calcite and dolomite wt. % within the sediments; see Supplementary Tables 5.18, 5.19, and 5.20, Table 5.7 in the main text, and section 5.5.3). These values and their associated uncertainties are used to calculate the R^{chem} values for each of the sampled rivers. In Tables 5.8, 5.9, and 5.10, the total uncertainties related to the range of silicate compositions for each lithology are calculated by first holding the Mg/K ratio constant while calculating the range in R^{chem} values corresponding to the range in Ca/Na ratios, then by holding the Ca/Na ratio constant while varying the Mg/K ratio, with the final uncertainty obtained by quadratic addition. The results of these calculations and associated errors are shown in Tables 5.8, 5.9, and 5.10 for all of the rivers analyzed in this study.

In the radiogenic Ca budget, similar to the chemical budget, we make the assumption that sulfates, evaporites, and anthropogenic inputs are negligible, leading to a budget that considers only carbonate and silicate input. Here, we define the ε^{40}Ca values of the sedimentary carbonate end-member to be 0 for all catchments. However, the choice of the silicate end-member composition is more difficult and leads to one of the largest sources of uncertainty. As discussed above, two different approaches were used to estimate this end-member. First, we used the measured ε^{40}Ca values from the silicate fractions of lithologically representative sediments from each basin (i.e., sample MAR50 for the TSS, ε^{40}Ca = +0.9, and sample CA950 for the HHC, ε^{40}Ca = 1.85). For LH rivers, of which several have large ^{40}Ca excesses, the radiogenic Ca sediment analysis of sample MO112 produced an ε^{40}Ca value of +3.92, which is significantly lower than the most radiogenic river water analyzed in the LH. To avoid obtaining nonsensical results, we used a silicate end-member ε^{40}Ca value of +11, corresponding to the signature of the most radiogenic river (i.e., the Jaran Kola). This value, however, may not be appropriate to calculate the silicate contribution for all LH basins.

The uncertainty listed in Tables 5.8, 5.9, and 5.10 for F_{Ca}^{iso} is based on the measurement uncertainty of the Ca analysis. However, a much greater problem is the representativity of the sediment samples used to represent each of the three formations and the potential effect on the calculated radiogenic Ca budget estimates. To try to take this into account, the radiogenic budget is also calculated using the estimated average silicate ε^{40}Ca values of each formation (section 5.5.4), obtained from the 3-stage K–Ca crustal and sedimentary extraction decay model and the average K/Ca ratios with their associated uncertainties (Table 5.6). This new budget estimate, known as F_{Ca}^{isoEMA} (for the Ca isotopic end-member model age value), is also listed in Tables 5.8, 5.9, and 5.10 and estimates using both endmembers (F_{Ca}^{iso} and F_{Ca}^{isoEMA}) are plotted in Figure 5.16 with the associated uncertainties. As can be seen from the magnitude of the uncertainties, this estimate takes into account the extreme compositional variation that exists within each formation, especially the LH. All end-member values used in the major element and isotopic budget models are listed in Table 5.7.

Finally, Ca_{sil}^{iso} (estimated from eq. 5.21, using sediment ε^{40}Ca values to calculate F_{Ca}^{iso}) was substituted into equation 5.9 (after correction for the evaporitic contribution to Na*) for Ca_{sil}^{chem} in order to compare these results with results obtained for the R^{chem} and F_{Ca}^{iso} methods. This fifth estimate of the silicate contribution will be referred to as R^{mix}, as it combines both chemical and isotopic estimates.

So, to sum up, we use five different methods to estimate the proportion of silicate input: 1) R^{chem} (the contribution of silicate derived elements in the dissolved load), 2) F_{Ca}^{chem} (considers only the Ca derived from silicate weathering), 3) F_{Ca}^{iso} (estimates based on ε^{40}Ca analyses of river waters using sediment ε^{40}Ca values for silicate end-members), 4) F_{Ca}^{isoEMA} (estimates also based on ε^{40}Ca analyses of river waters but calculated using modeled ε^{40}Ca values for silicate end-members, and 5) R^{mix} (where Ca_{sil}^{chem} is replaced by Ca_{sil}^{iso} in equation 5.9). Note that the three estimates denoted by "F" consider solely Ca abundances or isotopes, while the two denoted by "R" consider other major elements as well. Tables 5.8, 5.9, and 5.10 include the results and associated uncertainties for all of these estimates. Figure 5.16 plots the budget estimates against one another to visually illustrate the agreement or discordance of each of the budget estimation methods.

Table 5.7 – *Total and respective formation areas of the major basins analyzed in this study and their respective Ca/Na, Mg/K, and radiogenic Ca end-members.*

River	Formation	A_{Total}	A_{TSS}	A_{HHC}	A_{LH}	Ca/Na	±	Mg/K	±	ε^{40}Ca (Measured)	±	ε^{40}Ca (Estimated)	±	Flux (m^3/year)	Runoff (m/year)
		km^2													
Pure TSS	–	–	–	–	–	0.65	0.71	0.73	0.31	0.9	0.3	2.91	0.86	–	–
Pure HHC	–	–	–	–	–	0.49	0.07	1.04	0.36	1.85	0.3	3	0.21	–	–
Pure LH	–	–	–	–	–	0.21	0.22	1.03	0.46	11	0.3	13.6	12.31	–	–
Thini Khola	TSS	370	370	–	–	–	–	–	–	–	–	–	–	1.32E+09	0.42
Yankim Khola	TSS	55	55	–	–	–	–	–	–	–	–	–	–	1.32E+09	3.56
Jaran Khola	LH	25	–	–	25	–	–	–	–	–	–	–	–	1.09E+09	43.63
Masel Khola	LH	14	–	–	14	–	–	–	–	–	–	–	–	1.09E+09	77.91
Maudi Khola	LH	16	–	–	16	–	–	–	–	–	–	–	–	1.09E+09	68.17
Isul Khola	LH	52	–	–	53	–	–	–	–	–	–	–	–	1.09E+09	20.98
Chiti Khola	LH	3	–	–	3	–	–	–	–	–	–	–	–	1.09E+09	363.60
Paundi Khola	LH	87	–	–	87	–	–	–	–	–	–	–	–	1.09E+09	12.54
Maleku Khola	LH	5	–	–	5	–	–	–	–	–	–	–	–	1.09E+09	218.16
Thopal Khola	LH	224	–	–	224	–	–	–	–	–	–	–	–	1.09E+09	4.87
Andhi Khola	LH	712	–	–	712	–	–	–	–	–	–	–	–	1.09E+09	1.53
Anku Khola	HHC + LH	880	–	211	669	0.28	0.17	1.03	0.36	8.81	0.24	11.06	9.36	1.09E+09	1.24
Khudi Khola	HHC + LH	146	–	132	14	0.47	0.07	1.04	0.34	1.75	0.28	2.82	0.20	2.83E+08	1.94
Chepe Khola	HHC + LH	297	–	50	247	0.27	0.18	1.03	0.37	1.57	0.25	1.8	0.24	2.83E+08	0.95
Darondi	HHC + LH	720	–	117	603	0.25	0.19	1.03	0.39	9.536	0.26	11.904	10.34	8.14E+08	1.13
Seti	HHC + LH + TSS	2701	189	390	2122	0.28	0.18	1.01	0.37	9.01	0.24	11.37	9.73	3.29E+09	1.22
Kali Gandaki	HHC + LH + TSS	11653	3522	944	7187	0.77	0.58	0.94	0.30	7.24	0.21	9.55	7.64	8.08E+10	6.93
Trisuli	HHC + LH + TSS	21921	8169	5425	8327	0.44	0.28	0.92	0.23	4.98	0.18	6.99	4.69	8.08E+09	0.37
Narayani	HHC + LH + TSS	33574	10072	8058	15444	0.41	0.24	0.94	0.25	5.77	0.18	7.85	5.67	5.05E+10	1.50

Table 5.8 – *Budget model calculations based on major element geochemistry and $\varepsilon^{40}Ca$ isotopic compositions for all rivers. (1) Major Element Budget; Ca/Na of silicate end-member taken based on catchment area proportions listed in Table 5.7. (2) Ca elemental budget; Ca/Na of silicate end-member taken based on catchment area proportion listed in Table 5.7. (3) Error associated with Ca/Na uncertainty (see 1). (4) Error associated with Mg/K uncertainty (see 1). (5) Error associated with Ca/Na uncertainty.*

			$\mathbf{R}^{chem}$ **(1)**				$\mathbf{F}_{Ca}^{chem}$ **(2)**	
Sample	River	Formation	$\mathbf{R}^{chem}$ **(1)**	± (3)	± (4)	**Total Error** $\mathbf{R}^{chem}$	$\mathbf{F}_{Ca}^{chem}$	± **(5)**
PB9	Thini Khola	TSS	**0.11**	0.06	0.01	**1.29**	**0.08**	**0.09**
MO503	Yankim Khola	TSS	**0.04**	0.02	0.01	**1.25**	**0.006**	**0.007**
MO364	Chepe Khola	HHC + LH	**0.66**	0.16	0.09	**0.80**	**0.18**	**0.12**
MO79	Chepe Khola	HHC + LH	**0.58**	0.15	0.10	**0.81**	**0.10**	**0.07**
CA15003	Chepe Khola	HHC + LH	**0.49**	0.12	0.06	**0.80**	**0.13**	**0.09**
MO359	Chepe Khola	HHC	**1.03**	0.17	0.14	**0.43**	**0.54**	**0.08**
MO58	Chepe Khola	HHC	**0.39**	0.05	0.04	**0.41**	**0.13**	**0.02**
CA11206A	Khudi Khola	HHC	**0.64**	0.09	0.06	**0.41**	**0.29**	**0.04**
CA12w03	Khudi Khola	HHC	**0.53**	0.08	0.06	**0.42**	**0.21**	**0.03**
CA12w04	Khudi Khola	HHC	**0.23**	0.04	0.03	**0.44**	**0.06**	**0.01**
CA11103	Khudi Khola	HHC	**0.56**	0.10	0.08	**0.44**	**0.11**	**0.02**
CA15010	Khudi Khola	HHC	**1.43**	0.32	0.30	**0.48**	**0.06**	**0.01**

Table 5.8 continued from previous page

			R^{chem} (1)				F_{Ca}^{chem} (2)	
Sample	River	Formation	**R^{chem} (1)**	± (3)	± (4)	**Total Error R^{chem}**	**F_{Ca}^{chem}**	**± (5)**
CA15023	Khudi Khola	HHC	**0.73**	0.13	0.11	**0.44**	**0.15**	**0.02**
CA14009	Khudi Khola	HHC	**0.52**	0.09	0.07	**0.43**	**0.10**	**0.01**
CA14010	Khudi Khola	HHC	**0.38**	0.07	0.06	**0.45**	**0.07**	**0.01**
CA14014	Khudi Khola	HHC	**0.79**	0.13	0.10	**0.43**	**0.25**	**0.04**
CA14015	Khudi Khola	HHC	**0.98**	0.18	0.15	**0.44**	**0.28**	**0.04**
July 29 - 12:20-14:20	Khudi Khola	HHC	**0.73**	0.12	0.09	**0.43**	**0.11**	**0.02**
July 29 - 14:20-16:20	Khudi Khola	HHC	**0.73**	0.12	0.09	**0.43**	**0.11**	**0.02**
July 29 - 16:20-18:20	Khudi Khola	HHC	**0.74**	0.12	0.09	**0.43**	**0.12**	**0.02**
July 29 - 18:20-20:20	Khudi Khola	HHC	**0.73**	0.12	0.09	**0.43**	**0.11**	**0.02**
July 29 - 20:20-22:20	Khudi Khola	HHC	**0.74**	0.13	0.09	**0.43**	**0.12**	**0.02**
July 29 - 22:20-24:20	Khudi Khola	HHC	**0.78**	0.13	0.10	**0.43**	**0.11**	**0.02**
July 30 - 00:20-02:20	Khudi Khola	HHC	**1.33**	0.24	0.18	**0.44**	**0.12**	**0.02**
July 30 - 02:20-04:20	Khudi Khola	HHC	**0.88**	0.17	0.13	**0.44**	**0.08**	**0.01**
July 30 - 04:20-06:20	Khudi Khola	HHC	**0.82**	0.15	0.11	**0.44**	**0.09**	**0.01**
July 30 - 06:20-08:20	Khudi Khola	HHC	**0.81**	0.14	0.10	**0.43**	**0.10**	**0.01**
July 30 - 08:20-10:20	Khudi Khola	HHC	**0.84**	0.14	0.10	**0.43**	**0.09**	**0.01**
July 30 - 10:20-12:20	Khudi Khola	HHC	**0.77**	0.13	0.09	**0.43**	**0.10**	**0.01**
July 30 - 12:20-14:20	Khudi Khola	HHC	**0.82**	0.14	0.09	**0.43**	**0.11**	**0.02**
July 31 - 17:30-18:30	Khudi Khola	HHC	**1.51**	0.26	0.18	**0.43**	**0.26**	**0.04**
July 31 - 23:30-00:30	Khudi Khola	HHC	**1.58**	0.24	0.16	**0.42**	**0.29**	**0.04**

Table 5.8 continued from previous page

			R^{chem} (1)				F_{Ca}^{chem} (2)	
Sample	River	Formation	**R^{chem} (1)**	± (3)	± (4)	**Total Error R^{chem}**	**F_{Ca}^{chem}**	**± (5)**
August 1 - 5:30-06:30	Khudi Khola	HHC	**1.61**	0.28	0.19	**0.43**	**0.25**	**0.04**
August 1 - 9:30-10:30	Khudi Khola	HHC	**1.61**	0.28	0.19	**0.43**	**0.25**	**0.04**
July 29 - 11:00	Khudi Khola	LH+HHC	**0.41**	0.07	0.05	**0.41**	**0.09**	**0.01**
July 29 - 16:00	Khudi Khola	LH+HHC	**0.39**	0.06	0.05	**0.41**	**0.08**	**0.01**
July 29 - 21:00	Khudi Khola	LH+HHC	**0.39**	0.06	0.05	**0.41**	**0.08**	**0.01**
July 30 - 00:00	Khudi Khola	LH+HHC	**0.37**	0.07	0.05	**0.42**	**0.06**	**0.01**
July 30 - 01:00	Khudi Khola	LH+HHC	**0.37**	0.06	0.05	**0.42**	**0.06**	**0.01**
July 30 - 02:00	Khudi Khola	LH+HHC	**0.54**	0.10	0.08	**0.43**	**0.07**	**0.01**
July 30 - 03:00	Khudi Khola	LH+HHC	**0.54**	0.10	0.08	**0.43**	**0.07**	**0.01**
July 30 - 04:00	Khudi Khola	LH+HHC	**0.49**	0.09	0.07	**0.42**	**0.07**	**0.01**
July 30 - 05:00	Khudi Khola	LH+HHC	**0.49**	0.09	0.07	**0.42**	**0.06**	**0.01**
July 30 - 06:00	Khudi Khola	LH+HHC	**0.45**	0.08	0.07	**0.42**	**0.06**	**0.01**
July 30 - 07:00	Khudi Khola	LH+HHC	**0.45**	0.08	0.06	**0.42**	**0.07**	**0.01**
July 30 - 08:00	Khudi Khola	LH+HHC	**0.44**	0.08	0.06	**0.42**	**0.07**	**0.01**
July 30 - 09:00	Khudi Khola	LH+HHC	**0.44**	0.08	0.06	**0.42**	**0.07**	**0.01**
July 30 - 10:00	Khudi Khola	LH+HHC	**0.49**	0.08	0.06	**0.41**	**0.09**	**0.01**
July 30 - 11:00	Khudi Khola	LH+HHC	**0.53**	0.08	0.06	**0.40**	**0.08**	**0.01**
August 1 - 18:00-19:00	Khudi Khola	LH+HHC	**0.24**	0.04	0.03	**0.41**	**0.05**	**0.01**
August 2 - 00:00-01:00	Khudi Khola	LH+HHC	**0.24**	0.04	0.03	**0.41**	**0.05**	**0.01**

Table 5.8 continued from previous page

			R^{chem} (1)				F_{Ca}^{chem} (2)	
Sample	River	Formation	**R^{chem} (1)**	± (3)	± (4)	**Total Error R^{chem}**	F_{Ca}^{chem}	**± (5)**
August 2 - 07:00-08:00	Khudi Khola	LH+HHC	**0.25**	0.04	0.03	**0.41**	**0.05**	**0.01**
WKD34606 (July 24, 2013 16:50)	Khudi Khola	LH+HHC	**0.39**	0.07	0.06	**0.42**	**0.09**	**0.01**
WKD34701 (July 25, 2013 0:30)	Khudi Khola	LH+HHC	**0.74**	0.14	0.14	**0.44**	**0.09**	**0.01**
WKD34702 (July 25, 2013 2:45)	Khudi Khola	LH+HHC	**0.58**	0.11	0.11	**0.45**	**0.05**	**0.01**
WKD34703 (July 25, 2013 4:00)	Khudi Khola	LH+HHC	**0.51**	0.10	0.09	**0.44**	**0.05**	**0.01**
WKD34704 (July 25, 2013 5:20)	Khudi Khola	LH+HHC	**0.48**	0.09	0.09	**0.44**	**0.05**	**0.01**
WKD34707 (July 25, 201310:30)	Khudi Khola	LH+HHC	**0.48**	0.09	0.08	**0.43**	**0.08**	**0.01**
CA15013	Khudi Khola	LH+HHC	**0.98**	0.11	0.06	**0.37**	**0.85**	**0.12**
CA15014	Khudi Khola	LH+HHC	**1.51**	0.17	0.09	**0.38**	**4.28**	**0.61**
CA15016	Khudi Khola	LH+HHC	**0.95**	0.16	0.14	**0.42**	**0.27**	**0.04**
MO100	Masel Khola	LH	**0.71**	0.22	0.06	**1.18**	**0.33**	**0.35**
MO383	Masel Khola	LH	**0.81**	0.25	0.08	**1.19**	**0.45**	**0.47**
MO107	Maudi Khola	LH	**0.56**	0.18	0.05	**1.19**	**0.20**	**0.21**
MO110	Isul Khola	LH	**0.13**	0.04	0.03	**1.19**	**0.02**	**0.02**
MO119	Anku Khola	LH	**0.36**	0.12	0.05	**1.20**	**0.05**	**0.05**

Table 5.8 continued from previous page

			R^{chem} (1)				F_{Ca}^{chem} (2)	
Sample	River	Formation	**R^{chem} (1)**	± (3)	± (4)	**Total Error R^{chem}**	**F_{Ca}^{chem}**	**± (5)**
MO380	Jaran Khola	LH	**0.90**	0.28	0.12	**1.19**	**0.40**	**0.42**
CA15032	Jaran Khola	LH	**0.86**	0.27	0.11	**1.19**	**0.38**	**0.39**
MO311	Andi Khola	LH	**0.09**	0.03	0.01	**1.20**	**0.0003**	**0.0003**
CA15001	Anku Khola	LH	**0.41**	0.09	0.04	**1.16**	**0.10**	**0.07**
CA15005	Chiti Khola	LH	**0.43**	0.14	0.03	**1.19**	**0.13**	**0.13**
CA15008	Paundi Khola	LH	**0.65**	0.21	0.06	**1.19**	**0.22**	**0.23**
CA15034	Maleku Khola	LH	**0.23**	0.07	0.04	**1.19**	**0.04**	**0.04**
CA15036	Thopal Khola	LH	**0.65**	0.21	0.07	**1.19**	**0.28**	**0.29**
CA15030	Darondi	HHC+LH	**0.32**	0.09	0.05	**0.87**	**0.06**	**0.04**
CA11150	Seti	TSS+HHC+LH	**0.15**	0.04	0.02	**0.80**	**0.02**	**0.01**
MO304	Seti	TSS+HHC+LH	**0.14**	0.03	0.02	**0.80**	**0.01**	**0.01**
CA11149	Kali Gandaki	TSS+HHC+LH	**0.19**	0.06	0.02	**0.90**	**0.10**	**0.08**
LO760	Trisuli	TSS+HHC+LH	**0.23**	0.05	0.02	**0.71**	**0.07**	**0.05**
CA15038	Trisuli	TSS+HHC+LH	**0.26**	0.06	0.02	**0.72**	**0.09**	**0.05**

Table 5.8 continued from previous page

			$\mathbf{R}^{chem}$ **(1)**				$\mathbf{F}_{Ca}^{chem}$ **(2)**	
Sample	River	Formation	$\mathbf{R}^{chem}$ **(1)**	± (3)	± (4)	**Total Error** $\mathbf{R}^{chem}$	$\mathbf{F}_{Ca}^{chem}$	± **(5)**
PB81	Karnali	TSS+HHC+LH	**0.10**	0.02	0.01	**0.68**	**0.03**	**0.02**
CA11169	Arun	TSS+HHC+LH	**0.22**	0.05	0.01	**0.68**	**0.08**	**0.04**
CA11167	Kosi	TSS+HHC+LH	**0.27**	0.06	0.02	**0.68**	**0.07**	**0.04**
PB71	Kosi	TSS+HHC+LH	**0.26**	0.06	0.02	**0.68**	**0.07**	**0.04**
LO764	Kosi	TSS+HHC+LH	**0.22**	0.05	0.02	**0.68**	**0.06**	**0.03**
PB53	Narayani	TSS+HHC+LH	**0.15**	0.03	0.01	**0.68**	**0.04**	**0.02**
CA11147	Narayani	TSS+HHC+LH	**0.16**	0.04	0.02	**0.68**	**0.03**	**0.02**
CA13130	Narayani	TSS+HHC+LH	**0.18**	0.04	0.02	**0.68**	**0.07**	**0.04**

Table 5.9 – *Budget model calculations based on major element geochemistry and $\varepsilon^{40}Ca$ isotopic compositions for all rivers. (6) Ca isotopic budget, bed load end-members. (7) Error calculated based on the Ca isotopic measurement uncertainty. (8) Ca isotope budget, modeled average end-member for each formation. (9) Error from lithological uncertainty (see section 5.5.3 and 5.5.4 in main text).*

					F_{Ca}^{iso} (6)		F_{Ca}^{isoEMA} (8)		
Sample	River	Formation	ε^{40}Ca	±	F_{Ca}^{iso}	± (7)	F_{Ca}^{isoEMA} (8)	± (9)	**Total Error**
PB9	Thini Khola	TSS	0.43	0.27	**0.48**	**0.30**	**0.15**	**0.05**	**0.27**
MO503	Yankim Khola	TSS	0.29	0.53	**0.32**	**0.59**	**0.10**	**0.03**	**0.53**
MO364	Chepe Khola	HHC + LH	1.53	0.25	**0.83**	**0.14**	**0.51**	**0.04**	**0.25**
MO79	Chepe Khola	HHC + LH	1.07	0.31	**0.58**	**0.17**	**0.36**	**0.03**	**0.31**
CA15003	Chepe Khola	HHC + LH	1.75	0.38	**0.95**	**0.21**	**0.58**	**0.04**	**0.38**
MO359	Chepe Khola	HHC	1.42	0.29	**0.77**	**0.16**	**0.47**	**0.03**	**0.29**
MO58	Chepe Khola	HHC	1.22	0.24	**0.66**	**0.13**	**0.41**	**0.03**	**0.24**
CA11206A	Khudi Khola	HHC	1.62	0.32	**0.88**	**0.17**	**0.54**	**0.04**	**0.32**
CA12w03	Khudi Khola	HHC	0.84	0.40	**0.45**	**0.22**	**0.28**	**0.02**	**0.40**
CA12w04	Khudi Khola	HHC	0.50	0.65	**0.27**	**0.35**	**0.17**	**0.01**	**0.65**
CA11103	Khudi Khola	HHC	1.90	0.30	**1.03**	**0.16**	**0.63**	**0.04**	**0.30**
CA15010	Khudi Khola	HHC	1.08	0.29	**0.58**	**0.16**	**0.36**	**0.03**	**0.29**
CA15023	Khudi Khola	HHC	0.82	0.34	**0.44**	**0.18**	**0.27**	**0.02**	**0.34**
CA14009	Khudi Khola	HHC	0.44	1.03	**0.24**	**0.56**	**0.15**	**0.01**	**1.03**

Table 5.9 continued from previous page

					F_{Ca}^{iso} (6)		F_{Ca}^{isoEMA} (8)		
Sample	River	Formation	ε^{40}Ca	±	F_{Ca}^{iso}	± (7)	F_{Ca}^{isoEma} (8)	± (9)	Total Error
CA14010	Khudi Khola	HHC	0.95	0.45	**0.51**	**0.24**	**0.32**	**0.02**	**0.45**
CA14014	Khudi Khola	HHC	1.20	0.32	**0.65**	**0.17**	**0.40**	**0.03**	**0.32**
CA14015	Khudi Khola	HHC	0.61	0.39	**0.33**	**0.21**	**0.20**	**0.01**	**0.39**
July 29 - 12:20-14:20	Khudi Khola	HHC							
July 29 - 14:20-16:20	Khudi Khola	HHC							
July 29 - 16:20-18:20	Khudi Khola	HHC							
July 29 - 18:20-20:20	Khudi Khola	HHC							
July 29 - 20:20-22:20	Khudi Khola	HHC							
July 29 - 22:20-24:20	Khudi Khola	HHC							
July 30 - 00:20-02:20	Khudi Khola	HHC							
July 30 - 02:20-04:20	Khudi Khola	HHC							
July 30 - 04:20-06:20	Khudi Khola	HHC							
July 30 - 06:20-08:20	Khudi Khola	HHC							
July 30 - 08:20-10:20	Khudi Khola	HHC							
July 30 - 10:20-12:20	Khudi Khola	HHC							
July 30 - 12:20-14:20	Khudi Khola	HHC							
July 31 - 17:30-18:30	Khudi Khola	HHC							
July 31 - 23:30-00:30	Khudi Khola	HHC							
August 1 - 5:30-06:30	Khudi Khola	HHC							
August 1 - 9:30-10:30	Khudi Khola	HHC							

Table 5.9 continued from previous page

					F_{Ca}^{iso} (6)		F_{Ca}^{isoEMA} (8)		
Sample	River	Formation	ε^{40}Ca	±	F_{Ca}^{iso}	± (7)	F_{Ca}^{isoEma} (8)	± (9)	**Total Error**
July 29 - 11:00	Khudi Khola	LH+HHC							
July 29 - 16:00	Khudi Khola	LH+HHC							
July 29 - 21:00	Khudi Khola	LH+HHC							
July 30 - 00:00	Khudi Khola	LH+HHC							
July 30 - 01:00	Khudi Khola	LH+HHC							
July 30 - 02:00	Khudi Khola	LH+HHC							
July 30 - 03:00	Khudi Khola	LH+HHC							
July 30 - 04:00	Khudi Khola	LH+HHC							
July 30 - 05:00	Khudi Khola	LH+HHC							
July 30 - 06:00	Khudi Khola	LH+HHC							
July 30 - 07:00	Khudi Khola	LH+HHC							
July 30 - 08:00	Khudi Khola	LH+HHC							
July 30 - 09:00	Khudi Khola	LH+HHC							
July 30 - 10:00	Khudi Khola	LH+HHC							
July 30 - 11:00	Khudi Khola	LH+HHC							
August 1 - 18:00-19:00	Khudi Khola	LH+HHC							
August 2 - 00:00-01:00	Khudi Khola	LH+HHC							
August 2 - 07:00-08:00	Khudi Khola	LH+HHC							
WKD34606 (July 24, 2013 16:50)	Khudi Khola	LH+HHC	0.26	0.38	**0.15**	**0.22**	**0.09**	**0.01**	**0.38**

Table 5.9 continued from previous page

					F_{Ca}^{iso} (6)		F_{Ca}^{isoEMA} (8)		
Sample	River	Formation	ε^{40}Ca	±	F_{Ca}^{iso}	± (7)	F_{Ca}^{isoEma} (8)	± (9)	Total Error
WKD34701 (July 25, 2013 0:30)	Khudi Khola	LH+HHC	1.78	0.29	**1.02**	**0.17**	**0.59**	**0.04**	**0.29**
WKD34702 (July 25, 2013 2:45)	Khudi Khola	LH+HHC	1.35	0.26	**0.77**	**0.15**	**0.45**	**0.03**	**0.26**
WKD34703 (July 25, 2013 4:00)	Khudi Khola	LH+HHC	1.36	0.24	**0.78**	**0.14**	**0.45**	**0.03**	**0.24**
WKD34704 (July 25, 2013 5:20)	Khudi Khola	LH+HHC	0.98	0.47	**0.56**	**0.27**	**0.33**	**0.02**	**0.47**
WKD34707 (July 25, 201310:30)	Khudi Khola	LH+HHC	0.09	0.64	**0.05**	**0.37**	**0.030**	**0.002**	**0.64**
CA15013	Khudi Khola	LH+HHC	1.23	0.37	**0.70**	**0.21**	**0.41**	**0.03**	**0.37**
CA15014	Khudi Khola	LH+HHC	0.71	0.41	**0.41**	**0.23**	**0.24**	**0.02**	**0.41**
CA15016	Khudi Khola	LH+HHC	0.83	0.33	**0.47**	**0.19**	**0.28**	**0.02**	**0.33**
MO100	Masel Khola	LH	7.97	0.29	**0.72**	**0.03**	**0.59**	**3.31**	**3.32**
			7.77	0.33					
MO383	Masel Khola	LH	7.74	0.39	**0.70**	**0.04**	**0.57**	**3.22**	**3.24**
			7.61	0.35					
MO107	Maudi Khola	LH	3.98	0.29	**0.36**	**0.03**	**0.29**	**1.65**	**1.68**
			4.55	0.31					
MO110	Isul Khola	LH	1.02	0.28	**0.09**	**0.03**	**0.08**	**0.42**	**0.51**
			0.89	0.31					
MO119	Anku Khola	LH	2.30	0.39	**0.21**	**0.04**	**0.17**	**0.96**	**1.03**
MO380	Jaran Khola	LH	10.98	0.54	**1.00**	**0.05**	**0.81**	**4.56**	**4.59**
			11.02	0.31					

Table 5.9 continued from previous page

					F_{Ca}^{iso} (6)		F_{Ca}^{isoEMA} (8)		
Sample	River	Formation	ε^{40}Ca	±	F_{Ca}^{iso}	± (7)	F_{Ca}^{isoEma} (8)	± (9)	Total Error
CA15032	Jaran Khola	LH	10.77	0.39	**0.98**	**0.04**	**0.79**	**4.48**	**4.49**
			10.97	0.40					
MO311	Andi Khola	LH	0.42	0.31	**0.04**	**0.03**	**0.03**	**0.17**	**0.36**
			0.70	0.28					
			0.79	0.31					
CA15001	Anku Khola	LH	1.28	0.44	**0.15**	**0.05**	**0.03**	**0.04**	**0.44**
CA15005	Chiti Khola	LH	1.06	0.44	**0.10**	**0.04**	**0.08**	**0.44**	**0.62**
CA15008	Paundi Khola	LH	3.38	0.37	**0.31**	**0.03**	**0.25**	**1.40**	**1.45**
CA15034	Maleku Khola	LH	0.68	0.35	**0.06**	**0.03**	**0.05**	**0.28**	**0.45**
CA15036	Thopal Khola	LH	1.17	0.38	**0.11**	**0.03**	**0.09**	**0.48**	**0.62**
CA15030	Darondi	HHC+LH	1.31	0.61	**0.14**	**0.06**	**0.11**	**0.44**	**0.75**
CA11150	Seti	TSS+HHC+LH	0.65	0.15	**0.07**	**0.02**	**0.06**	**0.20**	**0.25**
MO304	Seti	TSS+HHC+LH	0.13	0.16	**0.01**	**0.02**	**0.01**	**0.04**	**0.16**
CA11149	Kali Gandaki	TSS+HHC+LH	0.33	0.18	**0.05**	**0.02**	**0.03**	**0.08**	**0.20**
LO760	Trisuli	TSS+HHC+LH	1.44	0.17	**0.29**	**0.03**	**0.21**	**0.27**	**0.32**
CA15038	Trisuli	TSS+HHC+LH	1.00	0.44	**0.20**	**0.09**	**0.14**	**0.19**	**0.48**
PB81	Karnali	TSS+HHC+LH	0.54	0.16	**0.09**	**0.03**	**0.07**	**0.11**	**0.20**

Table 5.9 continued from previous page

					F_{Ca}^{iso} (6)		F_{Ca}^{isoEMA} (8)		
Sample	River	Formation	ε^{40}Ca	±	F_{Ca}^{iso}	± (7)	F_{Ca}^{isoEma} (8)	± (9)	Total Error
CA11169	Arun	TSS+HHC+LH	0.55	0.31	**0.10**	**0.05**	**0.07**	**0.11**	**0.33**
CA11167	Kosi	TSS+HHC+LH	1.40	0.19	**0.24**	**0.03**	**0.18**	**0.29**	**0.35**
PB71	Kosi	TSS+HHC+LH	0.94	0.24	**0.16**	**0.04**	**0.12**	**0.20**	**0.31**
LO764	Kosi	TSS+HHC+LH	0.90	0.34	**0.16**	**0.06**	**0.11**	**0.19**	**0.39**
PB53	Narayani	TSS+HHC+LH	0.68	0.26	**0.12**	**0.05**	**0.09**	**0.14**	**0.30**
CA11147	Narayani	TSS+HHC+LH	0.85	0.23	**0.15**	**0.04**	**0.11**	**0.18**	**0.29**
CA13130	Narayani	TSS+HHC+LH	0.95	0.28	**0.16**	**0.05**	**0.12**	**0.20**	**0.34**

Table 5.10 – *Budget model calculations based on major element geochemistry and $\varepsilon^{40}Ca$ isotopic compositions for all rivers. (10) Combined radiogenic and elemental budget. (11) Error calculated based on the Ca isotopic measurement uncertainty. (12) Combined error from isotope measurements and Mg/K error. (13) Substitution calculations made to observe the required Ca/Na and radiogenic silicate end-member required to satisfy the major elemental and isotopic budget estimates. (14) The radiogenic Ca composition required to be equal with the estimate based on (2) (see equation in text). (15) The Ca/Na ratio required to be equal with the estimate based on (6) (see equation in text). (16) The fraction of the dissolved load that has a radiogenic carbonate signature (see equation 5.22 and 5.23 in text).*

			R^{mixed} (10)				Substition Balance Calculations (13)		Radiogenic Carbonate Fraction (16)
Sample	River	Formation	Ca^{iso}_{sil}	± (11)	R^{Mixed}	± (12)	Radiogenic Silicate EM (14)	Ca/Na (15)	
PB9	Thini Khola	TSS	477.65	299.92	**0.33**	**0.17**	**5.14**	**3.57**	**0.39**
MO503	Yankim Khola	TSS	283.56	518.22	**0.24**	**0.39**	**44.74**	**15.95**	**0.32**
MO364	Chepe Khola	HHC + LH	29.97	4.90	**0.95**	**0.07**	**8.32**	**1.02**	**0.64**
MO79	Chepe Khola	HHC + LH	84.65	24.53	**0.87**	**0.10**	**10.62**	**1.44**	**0.48**
CA15003	Chepe Khola	HHC + LH	132.53	28.73	**0.92**	**0.11**	**13.27**	**1.70**	**0.82**
MO359	Chepe Khola	HHC	17.58	3.59	**1.08**	**0.05**	**2.62**	**0.60**	**0.23**
MO58	Chepe Khola	HHC	45.70	8.99	**0.79**	**0.10**	**9.40**	**2.29**	**0.53**
CA11206A	Khudi Khola	HHC	121.35	23.97	**0.92**	**0.10**	**5.51**	**1.63**	**0.58**
CA12w03	Khudi Khola	HHC	94.47	44.99	**0.64**	**0.13**	**3.95**	**1.17**	**0.24**
CA12w04	Khudi Khola	HHC	631.44	820.87	**0.36**	**0.23**	**8.10**	**2.23**	**0.21**
CA11103	Khudi Khola	HHC	100.65	15.89	**1.11**	**0.11**	**17.27**	**12.58**	**0.92**
CA15010	Khudi Khola	HHC	25.33	6.80	**1.50**	**0.07**	**18.24**	**-2.60**	**0.52**
CA15023	Khudi Khola	HHC	39.09	16.21	**0.80**	**0.11**	**5.29**	**2.68**	**0.29**
CA14009	Khudi Khola	HHC	30.48	71.35	**0.53**	**0.41**	**4.29**	**2.55**	**0.14**
CA14010	Khudi Khola	HHC	277.04	131.23	**0.68**	**0.17**	**13.02**	**4.29**	**0.44**
CA14014	Khudi Khola	HHC	63.85	17.03	**0.91**	**0.10**	**4.77**	**1.90**	**0.40**
CA14015	Khudi Khola	HHC	32.62	20.86	**0.90**	**0.10**	**2.15**	**0.83**	**0.05**
July 29 - 12:20-14:20	Khudi Khola	HHC							
July 29 - 14:20-16:20	Khudi Khola	HHC							
July 29 - 16:20-18:20	Khudi Khola	HHC							
July 29 - 18:20-20:20	Khudi Khola	HHC							
July 29 - 20:20-22:20	Khudi Khola	HHC							
July 29 - 22:20-24:20	Khudi Khola	HHC							
July 30 - 00:20-02:20	Khudi Khola	HHC							
July 30 - 02:20-04:20	Khudi Khola	HHC							
July 30 - 04:20-06:20	Khudi Khola	HHC							
July 30 - 06:20-08:20	Khudi Khola	HHC							
July 30 - 08:20-10:20	Khudi Khola	HHC							
July 30 - 10:20-12:20	Khudi Khola	HHC							

Table 5.10 continued from previous page

			R^{mixed} (10)				Substition Balance Calculations (13)		Radiogenic Carbonate Fraction (16)
Sample	River	Formation	Ca^{iso}_{sil}	± (11)	R^{Mixed}	± (12)	Radiogenic Silicate EM (14)	Ca/Na (15)	
July 30 - 12:20-14:20	Khudi Khola	HHC							
July 31 - 17:30-18:30	Khudi Khola	HHC							
July 31 - 23:30-00:30	Khudi Khola	HHC							
August 1 - 5:30-06:30	Khudi Khola	HHC							
August 1 - 9:30-10:30	Khudi Khola	HHC							
July 29 - 11:00	Khudi Khola	LH+HHC							
July 29 - 16:00	Khudi Khola	LH+HHC							
July 29 - 21:00	Khudi Khola	LH+HHC							
July 30 - 00:00	Khudi Khola	LH+HHC							
July 30 - 01:00	Khudi Khola	LH+HHC							
July 30 - 02:00	Khudi Khola	LH+HHC							
July 30 - 03:00	Khudi Khola	LH+HHC							
July 30 - 04:00	Khudi Khola	LH+HHC							
July 30 - 05:00	Khudi Khola	LH+HHC							
July 30 - 06:00	Khudi Khola	LH+HHC							
July 30 - 07:00	Khudi Khola	LH+HHC							
July 30 - 08:00	Khudi Khola	LH+HHC							
July 30 - 09:00	Khudi Khola	LH+HHC							
July 30 - 10:00	Khudi Khola	LH+HHC							
July 30 - 11:00	Khudi Khola	LH+HHC							
August 1 - 18:00-19:00	Khudi Khola	LH+HHC							
August 2 - 00:00-01:00	Khudi Khola	LH+HHC							
August 2 - 07:00-08:00	Khudi Khola	LH+HHC							
WKD34606 (July 24, 2013 16:50)	Khudi Khola	LH+HHC	20.98	30.67	**0.42**	**0.13**	**2.79**	**0.81**	**0.06**
WKD34701 (July 25, 2013 0:30)	Khudi Khola	LH+HHC	204.55	33.33	**1.27**	**0.10**	**20.39**	**5.26**	**0.93**
WKD34702 (July 25, 2013 2:45)	Khudi Khola	LH+HHC	255.29	49.17	**1.04**	**0.10**	**26.26**	**6.66**	**0.72**
WKD34703 (July 25, 2013 4:00)	Khudi Khola	LH+HHC	214.71	37.89	**0.97**	**0.09**	**28.94**	**7.90**	**0.73**
WKD34704 (July 25, 2013 5:20)	Khudi Khola	LH+HHC	145.07	69.57	**0.79**	**0.17**	**20.18**	**5.69**	**0.51**
WKD34707 (July 25, 201310:30)	Khudi Khola	LH+HHC	9.10	64.71	**0.45**	**0.22**	**1.18**	**0.42**	**-0.02**
CA15013	Khudi Khola	LH+HHC	841.70	253.19	**0.87**	**0.08**	**1.45**	**0.34**	**-0.14**
CA15014	Khudi Khola	LH+HHC	256.43	148.08	**1.03**	**0.03**	**0.17**	**0.04**	**-3.88**
CA15016	Khudi Khola	LH+HHC	46.42	18.46	**0.97**	**0.08**	**3.05**	**0.81**	**0.20**
MO100	Masel Khola	LH	95.57	3.48	**0.84**	**0.01**	**24.13**	**0.44**	**0.39**
MO383	Masel Khola	LH	38.24	1.93	**0.85**	**0.01**	**17.07**	**0.30**	**0.25**
MO107	Maudi Khola	LH	86.79	6.32	**0.62**	**0.01**	**20.12**	**0.37**	**0.16**
MO110	Isul Khola	LH	113.49	31.15	**0.18**	**0.02**	**50.36**	**0.89**	**0.07**

Table 5.10 continued from previous page

				R^{mixed} (10)			Substition Balance Calculations (13)		Radiogenic Carbonate Fraction (16)
Sample	River	Formation	Ca^{iso}_{sil}	± (11)	R^{Mixed}	± (12)	Radiogenic Silicate EM (14)	Ca/Na (15)	
MO119	Anku Khola	LH	71.22	12.08	**0.37**	**0.02**	**45.03**	**0.78**	**0.16**
MO380	Jaran Khola	LH	54.54	2.68	**1.03**	**0.02**	**27.59**	**0.48**	**0.60**
CA15032	Jaran Khola	LH	128.34	4.65	**1.02**	**0.01**	**28.62**	**0.53**	**0.60**
MO311	Andi Khola	LH	8.12	5.99	**0.06**	**0.02**	**1428.87**	**0.87**	**0.04**
CA15001	Anku Khola	LH	37.32	12.83	**0.40**	**0.03**	**12.34**	**0.49**	**0.04**
CA15005	Chiti Khola	LH	17.88	7.42	**0.34**	**0.02**	**8.25**	**0.15**	**-0.03**
CA15008	Paundi Khola	LH	41.03	4.49	**0.60**	**0.02**	**15.67**	**0.28**	**0.09**
CA15034	Maleku Khola	LH	58.23	29.97	**0.24**	**0.02**	**17.80**	**0.32**	**0.02**
CA15036	Thopal Khola	LH	5.24	1.71	**0.52**	**0.01**	**4.19**	**0.07**	**-0.17**
CA15030	Darondi	HHC+LH	58.13	27.07	**0.33**	**0.04**	**21.92**	**0.54**	**0.08**
CA11150	Seti	TSS+HHC+LH	44.68	10.31	**0.17**	**0.01**	**31.39**	**0.82**	**0.05**
MO304	Seti	TSS+HHC+LH	7.80	9.37	**0.12**	**0.01**	**12.26**	**0.26**	**0.00**
CA11149	Kali Gandaki	TSS+HHC+LH	28.65	15.63	**0.16**	**0.01**	**3.34**	**0.35**	**-0.05**
LO760	Trisuli	TSS+HHC+LH	99.00	11.69	**0.37**	**0.03**	**19.84**	**1.52**	**0.22**
CA15038	Trisuli	TSS+HHC+LH	76.05	33.37	**0.31**	**0.06**	**11.67**	**0.93**	**0.12**
PB81	Karnali	TSS+HHC+LH	49.77	14.75	**0.14**	**0.02**	**17.63**	**1.25**	**0.06**
CA11169	Arun	TSS+HHC+LH	54.71	30.84	**0.20**	**0.04**	**7.25**	**0.47**	**0.02**
CA11167	Kosi	TSS+HHC+LH	68.48	9.29	**0.37**	**0.02**	**18.76**	**1.13**	**0.17**
PB71	Kosi	TSS+HHC+LH	48.08	12.28	**0.30**	**0.03**	**13.00**	**0.79**	**0.09**
LO764	Kosi	TSS+HHC+LH	56.88	21.49	**0.28**	**0.05**	**15.17**	**0.94**	**0.10**
PB53	Narayani	TSS+HHC+LH	65.53	25.06	**0.20**	**0.03**	**16.11**	**1.14**	**0.08**
CA11147	Narayani	TSS+HHC+LH	84.18	22.78	**0.21**	**0.03**	**26.71**	**1.57**	**0.12**
CA13130	Narayani	TSS+HHC+LH	84.40	24.88	**0.25**	**0.03**	**14.52**	**1.03**	**0.10**

5.5.5.1 Results of various budget calculations

TSS Catchments For TSS rivers, F_{Ca}^{iso} ranges from 0.32 ± 0.59 (Yankim Khola) to 0.48 ± 0.30 (Thini Khola) and F_{Ca}^{isoEMA} ranges from 0.10 ± 0.53 to 0.15 ± 0.27. When substituting Ca_{sil}^{iso} for Ca_{sil}^{chem} in equation 5.4 R^{mix} ranges from 0.24 ± 0.39 (Yankim Khola) to 0.33 ± 0.17 (Thini Khola). F_{Ca}^{chem} ranges from 0.006 ± 0.007 to 0.08 ± 0.09. Based on mass balance calculations for the TSS (Tables 5.8, 5.9, and 5.10), we see that estimations based on ε^{40}Ca are larger than the estimates from the major element budget. The ε^{40}Ca calculations are of limited usefulness for the TSS because of the similarity between the ε^{40}Ca values of the carbonate and silicate end-members and the measured value of the dissolved load. This produces large uncertainties, compared with those of the other formations, on the estimates of the silicate fraction in the dissolved load. Even small uncertainties in any of the values (measured dissolved load or silicate or carbonate end-member compositions) translate into a large uncertainty on the calculated silicate fraction in the dissolved load.

HHC Catchments For HHC rivers, F_{Ca}^{chem} ranges from 0.07 ± 0.01 (Khudi Khola) to 0.54 ± 0.08 (Chepe Khola). In the isotopic mass balance, the corresponding samples have F_{Ca}^{iso} values of 0.58 ± 0.16 and 0.77 ± 0.16, while the entire range of F_{Ca}^{iso} values vary from 0.24 ± 0.56 to 1.03 ± 0.16 (both Khudi Khola), and F_{Ca}^{isoEMA} ranges from 0.15 ± 1.03 to 0.63 ± 0.30 When substituting Ca_{iso}^{sil} for Ca_{sil}^{chem} in equation 5.4, R^{mix} ranges from 0.36 ± 0.23 to 1.5 ± 0.07 (both Khudi Khola).

Results from the HHC show clear disagreement between the budget calculation methods. As evident from Figure 5.16A and B, the fraction of the dissolved Ca load derived from silicate weathering calculated from cation abundances (F^{chem}) is in most cases lower than those estimated using Ca isotopes (F_{Ca}^{iso} and F_{Ca}^{isoEMA}).

We have already assessed the uncertainty on the Ca/Na ratio and taken these into account in the mass balance calculations. Thus, the apparent discrepancy between the budget calculations is probably not due to the uncertainty on Ca. Instead, discrepancies may be related to the specific characteristics of the Ca source(s) in the dissolved load. Some of this Ca may possibly originate from the redissolution of precipitated secondary carbonate or disseminated calcite within the HHC Formation I (Morin, 2015) biasing the values of F^{chem} towards the carbonate fraction. On the other hand, disseminated calcite should have the radiogenic ^{40}Ca composition of its silicate host rocks, which implies that this Ca would be counted as silicate for the purposes of the F_{Ca}^{iso} calculations. In other words, disseminated carbonate in HHC Formation I gneisses act as carbonate in the major element budget and as a silicate in the radiogenic Ca budget. This is because the estimated Ca/Na ratio of the silicate endmember ratio

does not include disseminated calcite. This issue is discussed in more detail in section 5.5.6.

LH Catchments For LH rivers, F_{Ca}^{chem} ranges from 0.0003 ± 0.0003 (Andhi Khola) to 0.45 ± 0.47 (Masel Khola). In the isotopic mass balance, F_{Ca}^{iso} ranges from 0.04 ± 0.03 (Andhi Khola) to 1.0 ± 0.05 (Jaran Khola) and F_{Ca}^{isoEMA} ranges from 0.03 ± 0.36 (Andhi Khola) to 0.81 ± 4.59 (Jaran Khola). When substituting Ca_{iso}^{sil} for Ca_{sil}^{chem} in equation 5.4, R^{mix} ranges from 0.06 ± 0.02 (Andhi Khola) to 1.03 ± 0.02 (Jaran Khola).

We have defined the ε^{40}Ca composition of the LH silicate end-member as +11 (see section 5.5.5), as this value is more radiogenic than those of all of the analyzed samples. The model silicate ε^{40}Ca composition of the LH, calculated in section 5.5.4, is +13.6 ± 12.31, a range that includes the most radiogenic LH river that we have analyzed (i.e., the Jaran Khola). In some catchments, the average silicate end-member may very well be +13.6 (or higher), but in this study we have not observed any evidence for the existence of such radiogenic rivers in the LH. Using the ε^{40}Ca value of both +11 and +13.6, results from LH rivers agree between the isotopic mass balance and major element budget, at least substantially more than results for the HHC (Figure 5.16). This could be a consequence of the more limited extent of physical erosion in LH catchments compared with HHC catchments where physical erosion is a more dominant process. As a result, silicate weathering in the LH has enough time to profoundly break down rocks, sediment, and minerals, releasing their constituent ions into the dissolved load.

Narayani Tributaries Defining the values of Ca/Na and Mg/K for the carbonate and silicate end-members, and the ε^{40}Ca for the carbonate and silicate end-members of each basin requires that all three formations be accounted for in the budget calculations. We defined the silicate end-member for the radiogenic Ca budget by calculating an area-weighted average of each of the end-members for the three Himalayan formations (i.e., ε^{40}Ca = +0.9 for the TSS, +1.85 for the HHC, and +11 for the LH combined with their respective exposure areas) (see Table 5.7 for basin areas). For the tributaries of the Narayani, i.e., the Seti, Trisuli, and Kali Gandaki, the end-members used in the mass balance calculations were estimated based on the area of each formation present in the basin, assuming that all lithologies weather at the same rate (see Table 5.7), which of course is an oversimplification.

Using the determined silicate end-member values for each basin, F_{Ca}^{chem} ranges from 0.01 ± 0.01 (Seti Khola) to 0.10 ± 0.08 (Kali Gandaki). In the isotopic mass balance, F_{Ca}^{iso} ranges from 0.01 ± 0.02 (Seti Khola) to 0.29 ± 0.03 (Trisuli) and F_{Ca}^{isoEMA}

ranges from 0.01 ± 0.06 (Seti Khola) to 0.21 ± 0.32 (Trisuli). When substituting Ca_{iso}^{sil} for Ca_{sil}^{chem} in equation 5.4, R^{mix} ranges from 0.12 ± 0.01 (Seti Khola) to 0.37 ± 0.02 (Trisuli).

For the Trisuli, values for R^{chem} and R^{mix} calculated in this study do not agree within error with values calculated in Galy and France-Lanord (1999), i.e., 0.24–0.27 ± 0.44 (R^{chem}) and 0.31–0.37 ± 0.03–0.06 (R^{mix}) in this study, compared with 0.19 ± 0.03 in Galy and France-Lanord (1999). On the other hand, it worth noting that the high value of R^{mix} may reflect the overestimation of the silicate contribution obtained from isotope mass balance in many HHC basins (see possible explanations for this overestimation below).

Himalayan Front Catchments As noted by Galy and France-Lanord (1999), larger catchments, which drain a large variety of lithologies under diverse hydrological conditions, yield more reliable results than small basins for the silicate to carbonate weathering budget modeling. This is because larger basins tend to average the chemical variations of bedrock formations, and have high TDS concentrations, such that cyclic contributions are relatively minor when all factors are considered. The formation area-weighted end-members used for the Narayani budget calculations are as follows: 1) Ca/Na = 0.41 ± 0.24, 2) Mg/K = 0.94 ± 0.25, 3) ε^{40}Ca (Measured) = +5.77 ± 0.18, and 4) ε^{40}Ca (Calculated) = +7.85 ± 5.67 (see Table 5.7). For the Arun, Kosi, and Karnali, we use the same end-members values used for Narayani calculations due to the unavailability of a geologic map for these basins.

For Himalayan Front rivers, F_{Ca}^{chem} ranges from 0.03 ± 0.02 (Narayani and Karnali) to 0.08 ± 0.04 (Arun). In the isotopic mass balance, F_{Ca}^{iso} ranges from 0.09 ± 0.03 (Karnali) to 0.24 ± 0.03 (Kosi) and F_{Ca}^{isoEMA} ranges from 0.07 ± 0.33 (Karnali and Arun) to 0.18 ± 0.35 (Kosi). When substituting Ca_{iso}^{sil} for Ca_{sil}^{chem} in equation 5.4, R^{mix} ranges from 0.14 ± 0.02 (Karnali) to 0.37 ± 0.02 (Kosi).

We've emphasized that there is significant disagreement between the silicate contribution obtained for HHC waters using the elemental mass balance for calcium (F_{Ca}^{chem}) and that obtained using the isotopic mass balance (F_{Ca}^{iso}). However, the chemical and isotopic methods tend to provide more consistent results for the LH (though there are some exceptions), major Narayani tributaries, and Himalayan Front Basins. This may reflect the greater proportion of carbonate in the LH compared with the HHC. Thus, the effect of disseminated carbonate in silicate, if present in the LH, would be diluted by the much stronger carbonate contribution. In addition, as discussed below, the radiogenic carbonate signature in the LH may be masked by more extensive silicate weathering.

This approach to basin-wide mass balance calculations assumes that chemical erosion is evenly distributed over the entire basin, and that the lithologies within

each geological formation do not vary throughout the TSS, LH, and HHC. These assumptions are unlikely to be true for several reasons:

1. It is difficult to accurately estimate the elemental and isotopic composition of the silicate endmember of the TSS because it is masked by the dominant carbonate contribution.

2. Drainage areas located north of the High range experience 1 to 5 times less rainfall than South flank areas. This affects both the major element and isotopic budgets because areas in the High range experience less chemical erosion and more physical erosion compared with areas in the South flank. This results in differences in the chemical budgets in which South flank regions generally indicate higher estimated silicate contributions than High range areas, even when the two areas contain similar proportions of silicates.

3. These estimates are also influenced by the fact that carbonate weathering is a much more rapid process than silicate weathering.

5.5.6 Linking the budgets of large and small rivers in Central Nepal

Table 5.11 shows the average dissolved load elemental concentrations for the major tributaries of the Narayani, their respective fluxes, and their sum for comparison to the concentrations and elemental fluxes of the Narayani. In Table 5.11, we observe that the summation of the concentrations and isotopic compositions for the three major tributaries of the Narayani (i.e., the Kali Gandaki, Trisuli, and Seti) closely resemble the compositions of the Narayani itself at Naryanghat. However, the fluxes of each element are significantly elevated compared with the flux of each element in the Narayani. This could be a consequence of combining concentration data from samples collected during the dry season with discharge data obtained during the monsoon.

5.5.7 The possible roles of disseminated calcite and secondary carbonate precipitation

It has been suggested that secondary carbonate precipitation may be a first order control on Himalayan river chemistry. Observational evidence for this process has been found throughout the Himalaya (Blum et al., 1998; Galy et al., 1999; Jacobson et al., 2002; Bickle et al., 2005, 2015). Several studies propose that up to 70% of dissolved Ca can be removed from the dissolved load, leading to high Sr/Ca and Mg/Ca river ratios (Galy et al., 1999; Jacobson et al., 2002; Bickle et al., 2005, 2015). For example, based on analyses of water from the Marysandi and its tributaries, Bickle et al. (2015) argue that between 50 and 80% of the original Ca in the river water reprecipitated as secondary carbonate (see Figure 5B in Bickle et al. (2015)). Secondary

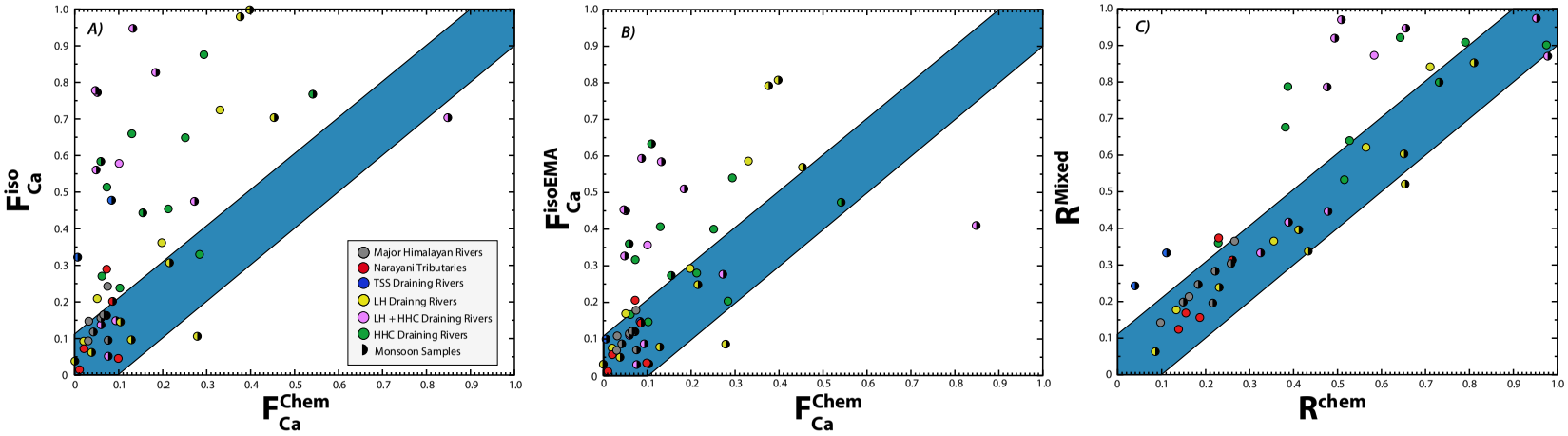

Figure 5.16 – *Results of budget modeling that compare chemically and isotopically based calculations, for both Ca-only and total cation budget calculations.* F^{chem}_{Ca} *plotted against* F^{iso}_{Ca} *(A) and* F^{chem}_{Ca} *(B), and* R^{chem} *plotted against* R^{Mix} *(C), for the dissolved load of the TSS (blue), LH (yellow), HHC (green), LH + HHC (pink), major Narayani tributaries (red), and Himalayan Front rivers (gray). The light blue field represents a 1:1 line (*2σ*), i.e., samples that fall along this line show agreement between the budget methods. Symbols with black half-circles represent samples collected during the monsoon. Error bars, which may be overestimated (see Tables 5.8, 5.9, and 5.10), have been left out to allow easier observation of the agreement and disagreement between the budget calculation methods.*

Table 5.11 – *Mixing calculations for the major tributarues of the Narayani.*

River	Discharge m^3/yr	HCO_3^-	Cl^-	SO_4	Na^+	K^+	Mg^{2+}	Ca^{2+}	Si^{2+}	Sr^{2+}	$\varepsilon^{40}Ca$	$^{87}Sr/^{86}Sr$
						µmol/L						
Seti	3.29E+09	1004.05	15.35	80.36	45.82	56.83	205.39	543.14	109.41	0.96	0.39	0.73502
Kali Gandaki	1.60E+10	1423.66			90.95	76.70	399.22	636.48	104.04	1.18	0.33	0.73776
Trisuli	8.08E+09	771.05	15.04	83.20	98.24	43.38	101.60	385.40	116.08	0.59	1.22	0.73435
Sum of tributaries	2.74E+10	1180.48	6.29	34.23	87.68	64.47	288.02	551.10	108.24	0.98	0.52	0.73683
Narayani	5.05E+10	1080.91	14.00	75.80	84.80	59.75	234.12	525.88	84.80	0.91	1.08	0.73705

calcite deposition has the opposite effect to that of the dissolution of hydrothermal calcite veins described by Blum et al. (1998), which adds Ca to the dissolved load.

Radiogenic Ca isotopes offer the possibility of testing the observation that there is an extensive amount of secondary carbonate precipitation in rivers. It is quite possible that carbonate precipitation would lead to mass dependent fractionation of Ca isotopes. However, even if this occurred, this would have no effect on the measured radiogenic composition because during radiogenic isotopic analysis, corrections are made for mass fractionation. These corrections remove both the artificial (mass spectrometry and column chemistry) and natural mass fractionation effects. This means that a river whose dissolved load is radiogenic in Ca will precipitate carbonate that exhibits the same radiogenic composition as the dissolved load, whereas the radiogenic Ca composition of detrital carbonates should be approximately 0. The limited number of sediment samples that have been analyzed in this study suggest that the radiogenic Ca composition of the carbonate fraction is near 0, implying that the carbonate is predominantly detrital. This is the case in all three formations, as well as in the Ganga and Brahmaputra (Table 5.4). If more analyses of the carbonate fractions of sediments confirm this unradiogenic composition, this should allow us to place strict upper limits on the amount of carbonate precipitation from river water that is occurring in the Himalaya.

Carbonate precipitation can affect major element mass balance calculations due to the removal of Ca but has no effect on isotopic budget calculations. This process would, however, increase the discrepancy between the isotopic and chemical budgets, i.e., the removal of Ca via the formation of secondary calcite will "artificially" increase F_{Ca}^{chem}, the fraction of the dissolved Ca estimated to be derived from silicate weathering. There is no evidence that this has occurred, as F_{Ca}^{chem} is almost never significantly greater than F_{Ca}^{iso} (Figure 5.16). This observation is consistent with the unradiogenic character of the sediment carbonate fraction and provides further evidence that carbonate precipitation in rivers is only a minor process.

Another phenomenon that can influence the results of the mass balance estimates is the presence of disseminated calcite as fine veins in the host rock, as has been previously documented in the HHC for Sr isotopes (Blum et al., 1998; Jacobson et al., 2002; Evans et al., 2001, 2004, 2008; Chamberlain et al., 2005). As disseminated calcite is formed by the reprecipitation of Ca originally dissolved from the silicate phases, it should have the radiogenic composition of the host rock. If such calcite is present even in small quantities (i.e., Chamberlain et al. (2005) estimate that the dissolution of as little as 3% vein calcite in a catchment can account for up to 60% of the dissolved riverine Sr flux), it can produce an inconsistency between the F_{Ca}^{iso} and F_{Ca}^{chem} values, as the F_{Ca}^{iso} value will reflect the reflect the radiogenic composition of the disseminated

calcite, while the F_{Ca}^{chem} value will simply reflect the fact that additional calcite is present.

Alternatively, it could be argued that the discrepancy between F_{Ca}^{iso} and F_{Ca}^{chem} is due simply to an inappropriate choice for the Ca/Na ratio or the ε^{40}Ca composition of the silicate endmember. However, this is unlikely, as the ε^{40}Ca silicate endmember values (listed in Tables 5.8, 5.9, and 5.10; $\varepsilon^{40}Ca_{end-member} = \left(\left(\frac{\varepsilon^{40}Ca_{river} - 0}{F_{Ca}^{chem}}\right) + 0\right)$, where 0 is the ε^{40}Ca value of the carbonate endmember) that would be required to bring strongly divergent F_{Ca}^{iso} and F_{Ca}^{chem} estimates into agreement greatly exceed both measured sediment ε^{40}Ca values and modeled estimates of the silicate ε^{40}Ca compositions. In other words, the radiogenic silicate endmember would need to be unreasonably radiogenic in order for F_{Ca}^{chem} to equal F_{Ca}^{iso}. There is also the possibility that the Ca/Na estimate of the silicate endmember is wrong, leading to F_{Ca}^{chem} estimates that are too low compared with the estimates for F_{Ca}^{iso}. In Tables 5.8, 5.9, and 5.10, we estimate the Ca/Na ratios required to bring the F_{Ca}^{iso} and F_{Ca}^{chem} values into agreement (i.e., $\frac{Ca}{Na} = \frac{F_{Ca}^{iso} \times X_{Ca}}{Na^* - Cl^*}$). For samples showing large discrepancies between the F_{Ca}^{iso} and F_{Ca}^{chem} values, notably those from the HHC, the required Ca/Na ratios of the silicate endmember are mostly > 1, more than double the Ca/Na ratio (0.49 $\pm$ 0.07) defined for the average HHC silicate composition on the basis of sediment analyses. This suggests that the divergence in the mass balance estimates obtained for some HHC and LH basins is not due to an inaccurate characterization of the Ca/Na or ε^{40}Ca values of the silicate component. Instead, we suggest that it may reflect the presence of disseminated radiogenic calcite.

To estimate the fraction of Ca introduced by disseminated calcite, we can construct a riverine Ca budget (after correction for precipitation):

$$1 = F_{sil}^{Ca} + F_{carb}^{Ca} + F_{Rad-Carb}^{Ca} \tag{5.22}$$

where $F_{Rad-Carb}^{Ca}$ is the fraction of the Ca in the dissolved load derived from radiogenic disseminated carbonate, while F_{Carb}^{Ca} is the fraction derived from non-radiogenic carbonate lithologies. Considering that $F_{sil}^{Ca} = F_{Ca}^{chem}$ and that $F_{Carb}^{Ca} = (1 - F_{Ca}^{iso})$ we can simplify equation 5.22 into equation 5.23 to calculate the amount of secondary carbonate formed or disseminated calcite that has contributed to the dissolved load:

$$F_{Rad-Carb}^{Ca} = F_{Ca}^{iso} - F_{Ca}^{chem} \tag{5.23}$$

The results, shown in Tables 5.8, 5.9, and 5.10 and Figures 5.17 and 5.18, indicate that up to 93% of the Ca in the dissolved load in some river waters may be derived

from disseminated calcite with radiogenic compositions. Figure 5.18 shows that high estimated radiogenic calcite contents are found essentially in rivers draining basins that are dominated by silicate weathering ($R^{chem} > 0.5$). From Figures 5.17 and 5.18, we observe that the highest fractions of radiogenic carbonate originate from the HHC and LH. This agrees with previous studies that have shown that the HHC is a quite substantial source of disseminated calcite (Blum et al., 1998). For example, Quade (2003) observed the dissolution of calcite-rich bands in gneiss pebbles from the HHC in the Arun watershed. Our results suggest that the LH may also include a significant amount of disseminated radiogenic carbonate in silicate rocks, although this does not seem to have been documented in the literature. However, hydrothermal systems occur all along the Himalayan Front (Chamberlain et al., 2005; Evans et al., 2001, 2004, 2008), which presents the possibility that disseminated calcite could exist as veins in the schists and gneisses of the LH.

5.5.8 Implications for Erosion and CO_2 Consumption in the Narayani

5.5.8.1 Erosion in the Narayani

Using the methods of Gaillardet et al. (1999), we can calculate the amount of silicate and carbonate erosion occurring in a catchment by using the parameters Mg_{sil} and Ca_{sil}, which are given by equations 5.13 and 5.14. Ca_{carb} and Mg_{carb} are then calculated by the subtraction of Mg_{sil} and Ca_{sil} from Ca^* and Mg^*, respectively. These values represent the concentrations of Ca and Mg in the dissolved load originating from carbonate and silicate weathering. Next, we can define the amount of erosion (C; in g/m^3) of major cations occurring in a catchment, for both carbonates and silicates:

$$C_{carbonate}(g/m^3) = \frac{Ca_{carb} \times 40.078 + Mg_{carb} \times 24.3}{1000} \tag{5.24}$$

$$C_{silicate}(g/m^3) = \frac{Na^{**} \times 22.99 + K^* \times 39.1 + Ca_{sil} \times 40.078 + Mg_{sil} \times 22.035}{1000} \tag{5.25}$$

where $C_{Carbonate}$ and $C_{Silicate}$ are the concentrations of the cations in the carbonate and silicate material that have been eroded, respectively; 40.078, 24.3, 22.99, and 39.1 are the atomic weights of Ca, Mg, Na, and K, respectively; and the factor of 1,000 converts moles into m^3.

Next, we can define ER (the Erosion Rate) in T/year as:

$$ER_{carbonate}(T/year) = \frac{F \times C_{carbonate}(g/m^3)}{1000000} \tag{5.26}$$

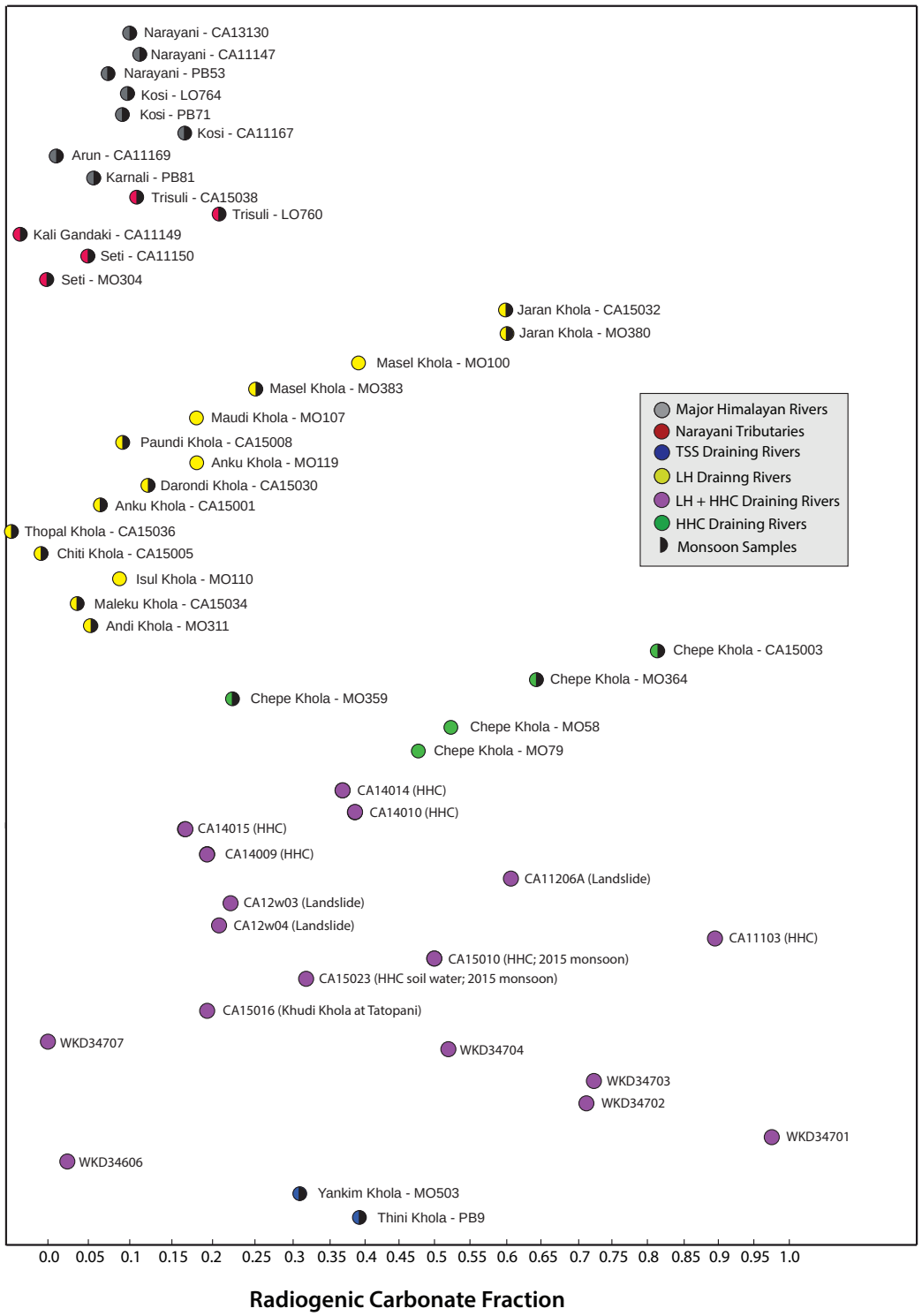

Figure 5.17 – *A plot showing the magnitude of the radiogenic carbonate fraction in the dissolved load of the TSS (blue), LH (yellow), HHC (green), LH + HHC (pink), major Narayani tributaries (red), and Himalayan Front rivers (gray). Symbols with black half-circles represent samples collected during the monsoon. Tables 5.8, 5.9, and 5.10 list the results of the calculations for the radiogenic carbonate fraction and silicate weathering magnitude calculations.*

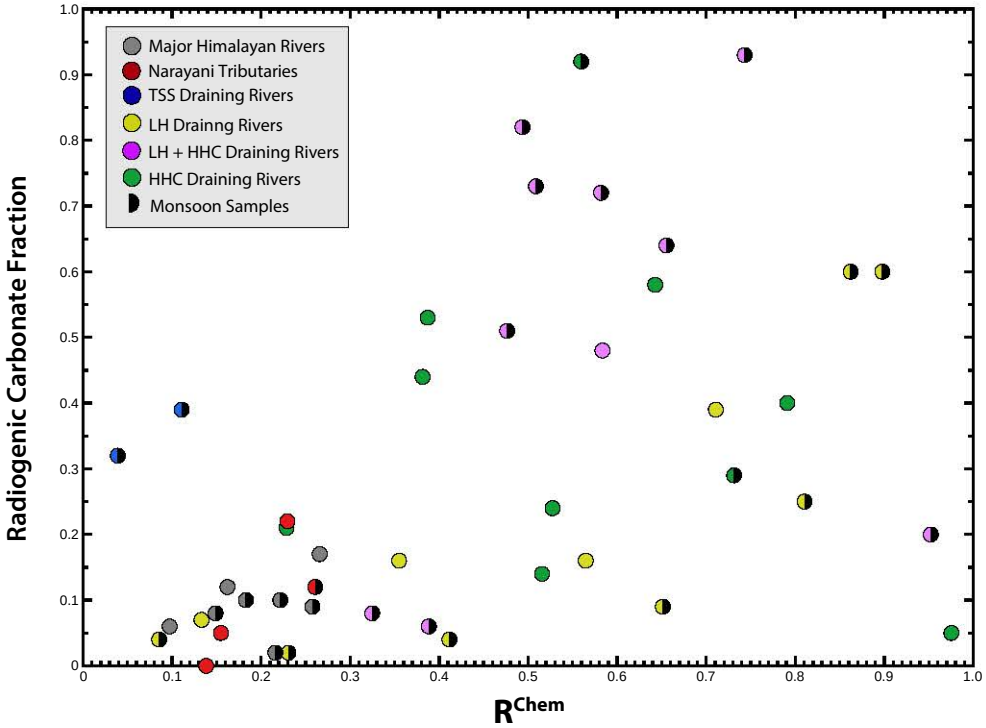

Figure 5.18 – *$F^{Ca}_{Rad-Carb}$ (the estimated fraction of Ca derived from weathering of radiogenic carbonate) as a function of R^{chem} (the fraction of the dissolved cations derived from silicate weathering) for the dissolved load of the TSS (blue), LH (yellow), HHC (green), LH + HHC (pink), major Narayani tributaries (red), and Himalayan Front rivers (gray). Symbols with black half-circles represent samples collected during the monsoon. Error bars are omitted for clarity. Tables 5.8, 5.9, and 5.10 list the results of the calculations for the $F^{Ca}_{Rad-Carb}$ and R^{chem} calculations.*

$$ER_{silicate}(T/year) = \frac{F \times C_{silicate}(g/m^3)}{1000000} \quad (5.27)$$

where F is the flux of the river in m^3/year (see Table 5.7) and the factor of 1,000,000 converts grams to tons. Finally, we can convert equation 5.26 and 5.27 into T/yr/km^2:

$$E_{Carbonate}(T/year/km^2) = \frac{ER_{carbonate}(T/year)}{A(km^2)} \quad (5.28)$$

$$E_{Silicate}(T/year/km^2) = \frac{ER_{silicate}(T/year)}{A(km^2)} \quad (5.29)$$

where A is the area of the catchment in km^2. We note that cationic silicate weathering rates are calculated here, but as shown by Gaillardet et al. (1999), these are proportional to the total silicate weathering rates.

Cationic erosion rates based on radiogenic Ca are calculated by replacing Ca_{Sil} with Ca^{sil}_{iso} in equation 5.24. For equation 5.25, Ca_{Carb} is equal to subtracting Ca^{sil}_{iso} from the river's [Ca] (cyclic corrected; Table 5.3). Tables 5.12, 5.13, and 5.14 list the silicate and carbonate erosion rates based on using major element concentrations and the radiogenic Ca compositions (i.e., Ca^{sil}_{iso} for the rivers analyzed in this study as well as the results of the calculations for Ca_{sil}, Mg_{sil}, and Ca^{sil}_{iso} (Table 5.7 includes river discharge data and basin areas necessary to calculate the values discussed above). The parameter Ca^{sil}_{iso}, however, must be viewed with caution due to the effects of the radiogenic carbonate fraction that were calculated and discussed earlier (see Tables 5.12, 5.13, and 5.14 and Figures 5.17 and 5.18). Since Ca^{sil}_{iso} is calculated based on the F^{iso}_{Ca} estimate, if a radiogenic carbonate signature exists in the dissolved load Ca^{sil}_{iso} will overestimate the Ca concentration derived from silicate weathering. Furthermore, as stressed earlier, substantial uncertainties exist on the radiogenic Ca isotope compositions of the silicate end-members and these vary significantly from catchment to catchment, which can translate into large uncertainties when calculating the rates of silicate and carbonate erosion based on ^{40}Ca.

Carbonate chemical erosion in the Narayani varies highly, from 0.96 to 35,860 t km^{-2} yr^{-1}. Some of the lowest rates of carbonate erosion occur in the Chepe Khola, upper Khudi Khola, Kali Gandaki, and Trisuli in agreement with estimates from France-Lanord et al. (2003). These rivers traverse very little or no carbonate formations (e.g., the Trisuli, where carbonates are restricted to a small area that drains the TSS and small carbonate patches in the LH). Other Narayani basin rivers have higher rates of carbonate chemical erosion, but are oversaturated with respect to carbonate, which presents a situation where carbonate erosion is limited by saturation and therefore

should correlate with runoff, as shown by France-Lanord et al. (2003) and which holds true for carbonate erosion estimates in this study. TSS rivers have relatively high carbonate erosion and runoff, which speaks to the large amount of carbonate bedrock in these catchments.

Estimates for the magnitude of carbonate chemical erosion based on radiogenic Ca compositions range from 0.18 (in the Chepe Khola) to 26,907 t km^{-2} yr^{-1} (in the Yankim Khola). Estimates for the magnitude of carbonate erosion based on radiogenic Ca compositions (Tables 5.12, 5.13, and 5.14) either are in relative agreement or underestimate carbonate chemical erosion rates calculated with major element concentrations because of the presence of a radiogenic carbonate fraction. For example, for the Seti Khola, which has an extremely low amount of dissolved Ca thought to be derived from radiogenic carbonate, major elements yield an $E_{carbonate}$ of 30.20 t km^{-2} yr^{-1} and radiogenic Ca yields 30.21 t km^{-2} yr^{-1}, in excellent agreement. On the other hand, sample CA15003 from the Chepe Khola has one of the highest radiogenic carbonate fractions (0.82), which produces discrepancies between the $E_{carbonate}$ estimate based on major elements (4.95 t km^{-2} yr^{-1}) and the radiogenic Ca estimate (0.59 t km^{-2} yr^{-1}).

Silicate chemical erosion rates in the Narayani based on major cation concentrations range between 0.63 (in the Kali Gandaki) and 2,972 t km^{-2} yr^{-1} (in the Maleku Khola), where most rivers fall in the range of silicate erosion rates proposed by France-Lanord et al. (2003) (i.e., between 5 and 42 t km^{-2} yr^{-1}). A number of factors are responsible for this variability in rates of silicate chemical erosion, such as precipitation, temperature, vegetation, and relief (associated with physical erosion) (France-Lanord et al., 2003). For example, the extremely high silicate erosion rates of the Maleku Khola and Chiti Khola result from their exceptionally high runoff rates coupled with their very small size. Catchments in the High Himalaya, such as the Khudi and Chepe Khola, have variable, yet relatively low rates of silicate chemical erosion, whereas rivers that drain exclusively the LH have variable, yet significantly higher rates of silicate chemical erosion. This is because High Himalayan basins have steep relief and are weathering-limited environments, characterized by high rates of denundation or physical erosion (4–6 mm/year) (France-Lanord et al., 2003), and therefore lower rates of silicate chemical erosion. LH rivers have smoother relief and lower rates of physical erosion, resulting in higher rates of silicate chemical erosion.

Calculated rates of silicate chemical erosion (cations only) based on radiogenic Ca composition vary between 0.31 (in the Kali Gandaki) and 9,938 t km^{-2} yr^{-1} (in the Yankim Khola). Similar to the estimates of carbonate chemical erosion, the estimates for the rates of silicate chemical erosion must be taken with caution due to large uncertainties, especially considering that the highest calculated rates derive from

the TSS, a region that is dominated by carbonate lithologies and weathering (it is important to note that even the estimate for the rate of silicate erosion based on major elements at 1,475 t km^{-2} yr^{-1} is significantly elevated). On the other hand, radiogenic Ca calculated values are either in relative agreement or are greater than values based on major element concentrations. For example, for the Kali Gandaki, major elements give an Esilicate of 0.63 t km^{-2} yr^{-1} and radiogenic Ca yields 0.31 t km^{-2} yr^{-1}, in near agreement. Silicate erosion rates estimated from radiogenic Ca are higher, in many cases, than the major elemental estimates probably because of a contribution from a radiogenic carbonate component (i.e., disseminated calcite).

Figure 5.19 plots the radiogenic carbonate fraction (Tables 5.8, 5.9, and 5.10) as a function of $E_{Silicate}$ (5.19A) and $E_{Carbonate}$ (5.19B) (Tables 5.12, 5.13, and 5.14). From Figure 5.19, we observe that basins with the lowest rates of silicate erosion have the highest radiogenic carbonate components and those same basins have quite low rates of carbonate erosion. These are predominantly HHC basins but also include several LH basins. These relationships imply two important points: 1) Logically, the radiogenic carbonate fraction weathers more easily and rapidly than the silicate lithologies contained within these basins and 2) as both silicate and non-radiogenic carbonate erosion rates are quite low in these basins, preferential erosion of radiogenic carbonates may significantly affect the composition and flux of the dissolved load of these basins. In areas where more intensive silicate erosion/weathering occurs, i.e., much of the LH, the radiogenic carbonate component is probably diluted by the release of calcium of silicate origin.

Figure 5.20, which plots the radiogenic carbonate fraction as a function of the [Ca] (in µmol/L) for each river water sample, confirms these relationships. We observe that rivers with low concentrations of Ca generally have the highest radiogenic carbonate fractions. This implies that the radiogenic carbonate fraction has a relatively minor influence on the elemental composition of a river because these rivers are geochemically and isotopically similar to rivers that are purely silicate, i.e., low [Ca] and radiogenic Ca compositions. Moreover, the Ca in the radiogenic carbonate fractions is inherited from their silicate host rocks, which, in general, have significantly lower Ca concentrations than purely carbonate lithologies. The radiogenic carbonate fractions do, however, significantly influence the silicate weathering budget estimates. Rivers with intermediate and elevated concentrations of Ca generally show less of an influence from this radiogenic carbonate component. As the total riverine flux will be dominated by the rivers with high Ca concentrations, this means that radiogenic carbonates should have little influence on the overall Himalayan weathering budgets.

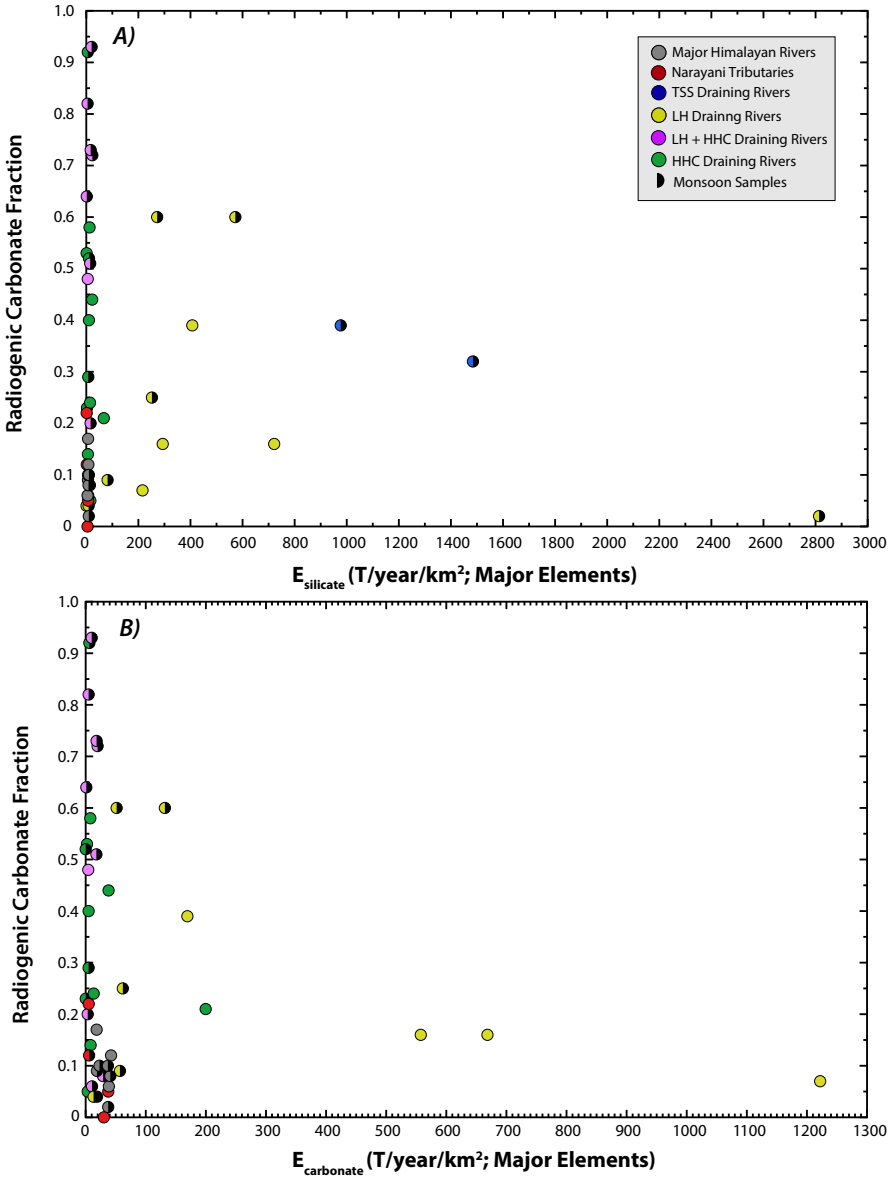

Figure 5.19 – *The radiogenic carbonate fraction as a function of $E_{silicate}$ (A) and $E_{Carbonate}$ (B) based on major elements (t km^{-2} yr^{-1}) for the dissolved load of the TSS (blue), LH (yellow), HHC (green), LH + HHC (pink), major Narayani tributaries (red), and Himalayan Front rivers (gray). Symbols with black half-circles represent samples collected during the monsoon. Tables 5.8, 5.9, and 5.10 list the results of the calculations for the radiogenic carbonate fraction and Tables 5.12, 5.13, and 5.14 list the results of the calculations to estimate the amount of silicate and carbonate erosion. We observe that basins with low silicate erosion rates show the highest proportions of radiogenic carbonates. This suggests that in areas of low intensity silicate weathering (i.e., the HHC) it is the radiogenic carbonates that weather first. It also implies that the radiogenic carbonate fraction will have little effect on the overall silicate weathering flux coming from the Narayani, and thus little influence on the CO_2 budget (see below).*

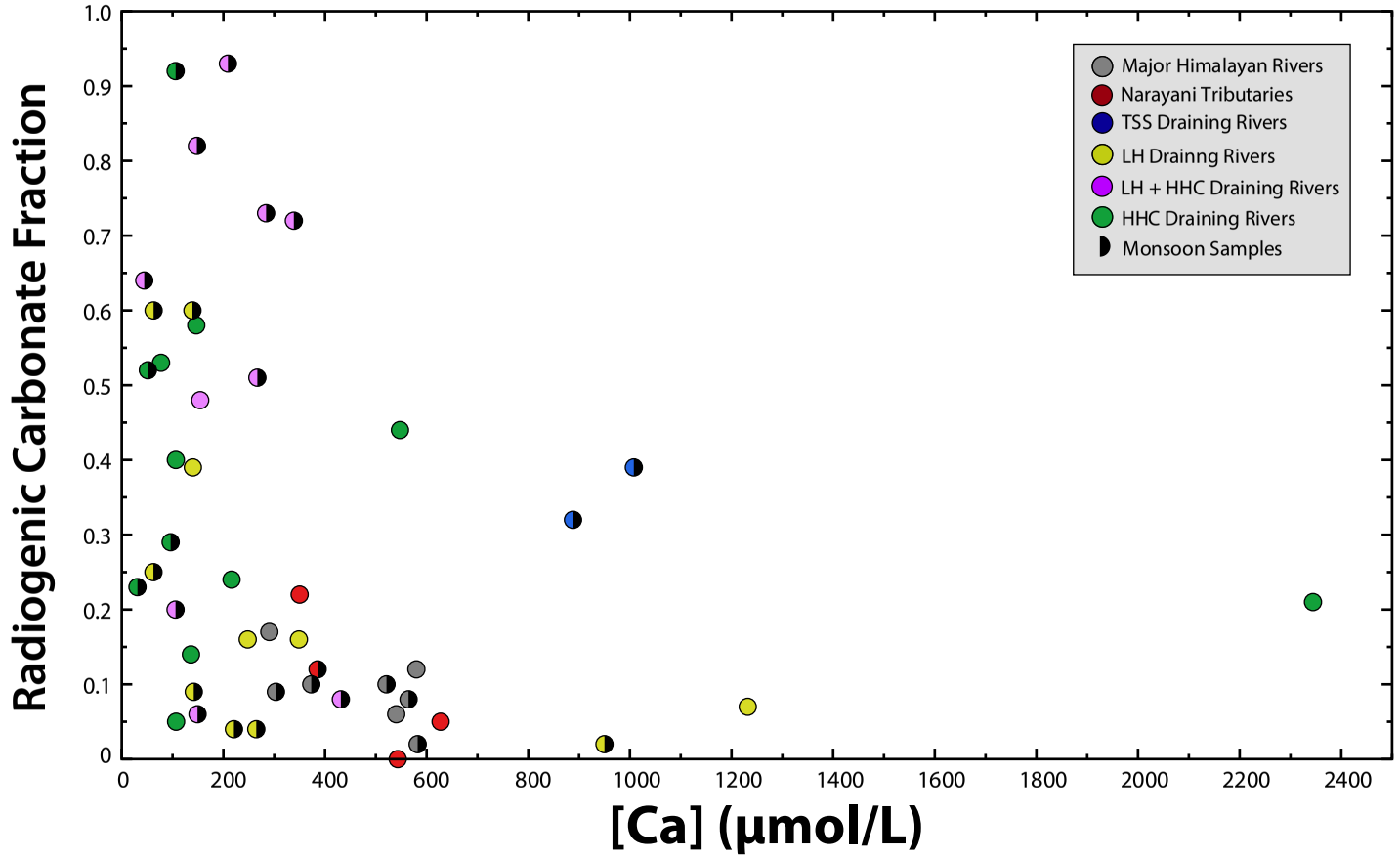

Figure 5.20 – *The radiogenic carbonate fraction plotted against the [Ca] (in µmol/L) for the dissolved load of the TSS (blue), LH (yellow), HHC (green), LH + HHC (pink), major Narayani tributaries (red), and Himalayan Front rivers (gray). Symbols with black half-circles represent samples collected during the monsoon. Table 5.3 lists the concentrations of Ca for each of the samples and Tables 5.8, 5.9, and 5.10 list the results of the calculations for the radiogenic carbonate fraction. This plot shows that rivers with an elevated radiogenic carbonate component have low concentrations of Ca, consistent with a dominantly silicate basin composition. Rivers with higher [Ca] are more likely influenced by non-radiogenic carbonates.*

5.5.8.2 CO_2 consumption in the Narayani

We can also calculate the rate of CO_2 consumption in the Narayani basin using the methods of Dessert et al. (2001, 2003):

$$R_{CO_2}(mol/year/km^2) = \frac{\left(\frac{Na^{**} + 2 \times Mg_{sil} + 2 \times Ca_{sil}}{1000}\right) \times \frac{F}{A}}{1000000} \tag{5.30}$$

where R_{CO_2} is the rate of consumption in mol/year/km^2. To estimate CO_2 consumption using the budget based on radiogenic Ca we substitute Ca_{iso}^{sil} for Ca_{sil} in equation 5.30.

Tables 5.12, 5.13, and 5.14 provide the results of the calculations for Ca_{sil}, Mg_{sil}, Ca_{iso}^{sil}, and the CO_2 consumption rate based on 1) major elemental concentrations and 2) the radiogenic Ca isotopic compositions (i.e., by using Ca_{iso}^{sil}) combined with other major elements. Figure 5.21 plots the rates of CO_2 consumption estimated by these two methods against each other.

The consumption of CO_2 in the Narayani Basin varies between 0.03 (in the Kali Gandaki) and 139 x 10^6 mol C yr^{-1} km^{-2} (in the Maleku Khola). These rates of consumption are in agreement with those published in Wolff-Boenisch et al. (2009) for small catchments along the Marysandi. For the majority of samples, R_{CO_2} estimates based on radiogenic Ca (plus other major element abundances) tend to be higher than estimates based on major elements. This is probably due to the radiogenic carbonate component that artificially increases the estimated fraction of silicate weathering due to its silicate isotopic signature, and thus leads to the overestimation of CO_2 in equation 5.30.

In Figure 5.21, at higher rates of CO_2 consumption we observe increased agreement between both major elements and radiogenic Ca + major elements. However, at lower rates of CO_2 consumption (see inset in Fig. 5.21), rates of CO_2 consumption based on radiogenic Ca plus major elements appear to overestimate the amount of CO_2 consumed compared with just major elemental calculations. It is important to note that the overestimation of CO_2 consumption occurs only in regions with low silicate weathering rates, and therefore has little effect on the overall CO_2 consumption.

Figure 5.22, which plots the radiogenic carbonate fraction as a function of CO_2 consumption rates from major elements, shows that this relationship between low silicate weathering and low consumption rates holds true. Rivers estimated to have very high fractions of Ca derived from radiogenic carbonate are the same rivers that have very low silicate weathering rates and therefore contribute very little to the consumption of CO_2. Logically, rivers with higher rates of silicate erosion, that are the

most efficient consumers of CO_2, have mostly lower estimated fractions of Ca derived from radiogenic carbonates.

In line with the conclusions drawn from Blum et al. (1998) and Chamberlain et al. (2005) based on Sr isotopes, we suggest that metamorphic conditions and hydrothermal fluid flow in the HHC and LH caused the precipitation of disseminated calcite veins that retained the radiogenic Ca isotopic composition of its host silicate rock, i.e., granites and gneisses. The dissolution/weathering of these veins, which is rapid, may represent a substantial, unconstrained flux of radiogenic Ca, similar to radiogenic Sr, that dominates the geochemical and isotopic signature of many central Nepal rivers (caution must be taken with Sr because there is also a substantial flux of radiogenic Sr from dolomites). This signature acts as a carbonate in major element weathering budgets, reducing the estimates of F_{Ca}^{chem}, and as a silicate in Ca isotope weathering budgets, increasing the value of F_{Ca}^{iso}, which in turn leads to the overestimation of the amount of CO_2 consumed in a particular region. Before radiogenic Ca isotopes can be used to reliably quantify the balance between silicate and carbonate weathering in the Himalaya and elsewhere, and by extension silicate erosion and CO_2 consumption rates, this flux of radiogenic carbonate must be clearly defined and better understood.

Table 5.12 – *Results of silicate and carbonate chemical erosion and CO_2 consumption calculations based on major elemental concentrations and radiogenic Ca isotopic compositions of the dissolved load in central Nepal. (1) The amount (in µmol/L) of Ca derived from silicate weathering based on the Ca/Na ratio of pure silicate rock (see equation 5.15 in text). (2) The amount (in µmol/L) of Mg derived from silicate weathering based on the Mg/K ratio of pure silicate rock (see equation 5.16 in text). (3) The amount (in µmol/L) of dissolved cations derived from silicate weathering based on Ca isotopic ratios (see equation 5.21 in text).*

Sample	River	Formation	Ca_{Sil} (1)	±	Mg_{Sil} (2)	±	Ca_{sil}^{iso}(3)	±
PB9	Thini Khola	TSS	83.70	91.42	24.17	10.26	477.65	299.92
MO503	Yankim Khola	TSS	5.70	6.23	18.25	21.41	283.56	518.22
MO364	Chepe Khola	HHC + LH	6.67	4.42	18.21	6.62	29.97	4.90
							24.49	5.29
MO79	Chepe Khola	HHC + LH	14.75	9.79	64.52	23.44	84.65	24.53
CA15003	Chepe Khola	HHC + LH	18.48	12.27	46.69	16.97	132.53	28.73
MO359	Chepe Khola	HHC	12.39	1.77	29.27	10.13	17.58	3.59
MO58	Chepe Khola	HHC	9.00	1.29	9.96	3.45	45.70	8.99
CA11206A	Khudi Khola	HHC	40.71	5.82	46.19	15.99	121.35	23.97
CA12w03	Khudi Khola	HHC	44.25	6.32	57.33	19.85	94.47	44.99
CA12w04	Khudi Khola	HHC	144.18	20.60	357.34	123.69	631.44	820.87
CA11103	Khudi Khola	HHC	10.78	1.54	32.24	11.16	100.65	15.89
CA15010	Khudi Khola	HHC	2.57	0.37	83.17	28.79	25.33	6.80

Table 5.12 continued from previous page

Sample	River	Formation	Ca_{Sil} (1)	±	Mg_{Sil} (2)	±	Ca_{sil}^{iso}(3)	±
CA15023	Khudi Khola	HHC	13.66	1.95	43.94	15.21	39.09	16.21
CA14009	Khudi Khola	HHC	13.13	1.88	33.38	11.56	30.48	71.35
CA14010	Khudi Khola	HHC	39.36	5.62	132.15	45.74	277.04	131.23
CA14014	Khudi Khola	HHC	24.74	3.53	49.52	17.14	63.85	17.03
CA14015	Khudi Khola	HHC	28.08	4.01	90.75	31.41	32.62	20.86
July 29 - 12:20-14:20	Khudi Khola	HHC	13.06	1.87	38.27	13.25		
July 29 - 14:20-16:20	Khudi Khola	HHC	11.68	1.67	34.88	12.08		
July 29 - 16:20-18:20	Khudi Khola	HHC	12.65	1.81	34.89	12.08		
July 29 - 18:20-20:20	Khudi Khola	HHC	11.95	1.71	35.12	12.16		
July 29 - 20:20-22:20	Khudi Khola	HHC	12.33	1.76	35.09	12.15		
July 29 - 22:20-24:20	Khudi Khola	HHC	10.71	1.53	34.68	12.00		
July 30 - 00:20-02:20	Khudi Khola	HHC	6.62	0.95	38.18	13.22		
July 30 - 02:20-04:20	Khudi Khola	HHC	7.25	1.04	45.31	15.69		
July 30 - 04:20-06:20	Khudi Khola	HHC	8.85	1.26	38.02	13.16		
July 30 - 06:20-08:20	Khudi Khola	HHC	9.17	1.31	34.00	11.77		
July 30 - 08:20-10:20	Khudi Khola	HHC	9.17	1.31	34.15	11.82		
July 30 - 10:20-12:20	Khudi Khola	HHC	10.26	1.47	33.78	11.69		
July 30 - 12:20-14:20	Khudi Khola	HHC	11.01	1.57	34.65	11.99		
July 31 - 17:30-18:30	Khudi Khola	HHC	11.27	1.61	39.40	13.64		
July 31 - 23:30-00:30	Khudi Khola	HHC	13.98	2.00	43.55	15.07		
August 1 - 5:30-06:30	Khudi Khola	HHC	10.25	1.46	37.70	13.05		

Table 5.12 continued from previous page

Sample	River	Formation	Ca_{Sil} (1)	±	Mg_{Sil} (2)	±	Ca_{sil}^{iso}(3)	±
August 1 - 9:30-10:30	Khudi Khola	HHC	10.70	1.53	38.01	13.16		
July 29 - 11:00	Khudi Khola	LH+HHC	17.91	2.55	53.51	17.32		
July 29 - 16:00	Khudi Khola	LH+HHC	17.36	2.47	51.29	16.60		
July 29 - 21:00	Khudi Khola	LH+HHC	17.02	2.42	49.97	16.17		
July 30 - 00:00	Khudi Khola	LH+HHC	10.58	1.51	52.49	16.99		
July 30 - 01:00	Khudi Khola	LH+HHC	10.55	1.50	50.87	16.46		
July 30 - 02:00	Khudi Khola	LH+HHC	9.60	1.37	57.61	18.64		
July 30 - 03:00	Khudi Khola	LH+HHC	9.69	1.38	57.78	18.70		
July 30 - 04:00	Khudi Khola	LH+HHC	11.19	1.59	58.22	18.84		
July 30 - 05:00	Khudi Khola	LH+HHC	10.41	1.48	57.55	18.62		
July 30 - 06:00	Khudi Khola	LH+HHC	10.88	1.55	52.56	17.01		
July 30 - 07:00	Khudi Khola	LH+HHC	12.28	1.75	54.03	17.49		
July 30 - 08:00	Khudi Khola	LH+HHC	12.54	1.78	53.19	17.21		
July 30 - 09:00	Khudi Khola	LH+HHC	12.82	1.82	52.29	16.92		
July 30 - 10:00	Khudi Khola	LH+HHC	16.36	2.33	57.22	18.52		
July 30 - 11:00	Khudi Khola	LH+HHC	15.89	2.26	57.19	18.51		
August 1 - 18:00-19:00	Khudi Khola	LH+HHC	16.24	2.31	50.43	16.32		
August 2 - 00:00-01:00	Khudi Khola	LH+HHC	15.12	2.15	48.11	15.57		
August 2 - 07:00-08:00	Khudi Khola	LH+HHC	13.52	1.92	44.35	14.35		
WKD34606 (July 24, 2013 16:50)	Khudi Khola	LH+HHC	13.17	1.87	40.84	13.22	20.98	30.67

Table 5.12 continued from previous page

Sample	River	Formation	Ca_{Sil} (1)	±	Mg_{Sil} (2)	±	Ca_{sil}^{iso}(3)	±
WKD34701 (July 25, 2013 0:30)	Khudi Khola	LH+HHC	17.54	2.49	145.17	46.98	204.55	33.33
WKD34702 (July 25, 2013 2:45)	Khudi Khola	LH+HHC	17.00	2.42	168.72	54.60	255.29	49.17
WKD34703 (July 25, 2013 4:00)	Khudi Khola	LH+HHC	12.97	1.85	122.31	39.58	214.71	37.89
WKD34704 (July 25, 2013 5:20)	Khudi Khola	LH+HHC	12.57	1.79	106.71	34.53	145.07	69.57
WKD34707 (July 25, 201310:30)	Khudi Khola	LH+HHC	13.45	1.91	71.71	23.21	9.10	64.71
CA15013	Khudi Khola	LH+HHC	1015.10	144.36	602.45	194.97	841.70	253.19
CA15014	Khudi Khola	LH+HHC	2705.20	384.71	1794.92	580.88	256.43	148.08
CA15016	Khudi Khola	LH+HHC	26.62	3.79	99.62	32.24	46.42	18.46
MO100	Masel Khola	LH	43.56	45.64	45.16	20.17	95.57	3.48
MO383	Masel Khola	LH	24.63	25.81	33.63	15.02	38.24	1.93
MO107	Maudi Khola	LH	47.45	49.71	55.97	24.99	86.79	6.32
MO110	Isul Khola	LH	24.79	25.97	105.75	47.23	113.49	31.15
MO119	Anku Khola	LH	17.40	18.22	66.24	29.58	71.22	12.08
MO380	Jaran Khola	LH	21.74	22.78	47.93	21.41	54.54	2.68
CA15032	Jaran Khola	LH	49.32	51.67	92.21	41.18	128.34	4.65

Table 5.12 continued from previous page

Sample	River	Formation	Ca_{Sil} (1)	±	Mg_{Sil} (2)	±	Ca_{sil}^{iso}(3)	±
MO311	Andi Khola	LH	0.06	0.07	10.93	4.88	8.12	5.99
CA15001	Anku Khola	LH	26.64	17.13	73.88	18.42	37.32	12.83
CA15005	Chiti Khola	LH	23.85	24.98	20.15	9.00	17.88	7.42
CA15008	Paundi Khola	LH	28.80	30.17	35.54	15.87	41.03	4.49
CA15034	Maleku Khola	LH	35.98	37.70	120.69	53.90	58.23	29.97
CA15036	Thopal Khola	LH	13.77	14.43	22.36	9.99	5.24	1.71
CA15030	Darondi Khola	HHC+LH	25.28	18.37	93.80	35.52	58.13	27.07
CA11150	Seti	TSS+HHC+LH	12.83	8.29	69.45	25.26	44.68	10.31
MO304	Seti	TSS+HHC+LH	5.73	3.71	52.37	19.05	7.80	9.37
CA11149	Kali Gandaki	TSS+HHC+LH	62.16	47.31	67.46	21.61	28.65	15.63
LO760	Trisuli	TSS+HHC+LH	24.83	15.49	29.19	7.21	99.00	11.69
CA15038	Trisuli	TSS+HHC+LH	32.41	20.22	35.37	8.74	76.05	33.37
PB81	Karnali	TSS+HHC+LH	16.30	9.42	23.61	6.18	49.77	14.75
CA11169	Arun	TSS+HHC+LH	43.54	25.16	28.43	7.44	54.71	30.84
CA11167	Kosi	TSS+HHC+LH	21.08	12.18	35.59	9.32	68.48	9.29
PB71	Kosi	TSS+HHC+LH	21.35	12.34	32.38	8.48	48.08	12.28

Table 5.12 continued from previous page

Sample	River	Formation	Ca_{Sil} (1)	±	Mg_{Sil} (2)	±	Ca^{iso}_{sil}(3)	±
LO764	Kosi	TSS+HHC+LH	21.66	12.51	33.76	8.84	56.88	21.49
PB53	Narayani	TSS+HHC+LH	23.49	13.57	48.36	12.66	65.53	25.06
CA11147	Narayani	TSS+HHC+LH	18.19	10.51	50.14	13.13	84.18	22.78
CA13130	Narayani	TSS+HHC+LH	33.57	19.40	46.90	12.28	84.40	24.88

Table 5.13 – *Results of silicate and carbonate chemical erosion and CO_2 consumption calculations based on major elemental concentrations and radiogenic Ca isotopic compositions of the dissolved load in central Nepal. (4) Silicate and carbonate erosion rates based on the major elemental and radiogenic Ca compositions of river water (see equations 5.28 and 5.29 and explanations in text).*

			Erosion (Major Elements) (4)				Erosion (Radiogenic Ca) (4)			
Sample	River	Formation	$E_{carbonate}$		$E_{silicate}$		$E_{carbonate}$		$E_{silicate}$	
			T/year/km^2	±	T/year/km^2	±	T/year/km^2	±	T/year/km^2	±
PB9	Thini Khola	TSS	6247.86	466.43	976.94	466.44	4365.99	1462.40	2442.41	1230.68
MO503	Yankim Khola	TSS	35845.56	609.50	1484.51	609.59	26916.74	17046.82	9928.64	17349.92
MO364	Chepe Khola	HHC + LH	1.08	0.32	1.88	0.32	0.18	0.34	1.95	0.28
MO79	Chepe Khola	HHC + LH	4.30	0.92	5.61	0.92	1.63	1.48	6.10	0.36
CA15003	Chepe Khola	HHC + LH	4.95	0.86	5.00	0.86	0.59	1.49	7.14	0.38
MO359	Chepe Khola	HHC	0.15	0.30	2.76	0.30	-0.05	0.37	1.97	0.43
MO58	Chepe Khola	HHC	2.19	0.13	1.33	0.13	0.79	0.42	2.19	0.17
CA11206A	Khudi Khola	HHC	7.73	1.21	12.42	1.21	1.46	2.62	13.60	1.27
CA12w03	Khudi Khola	HHC	13.34	1.43	14.35	1.43	9.43	4.43	12.51	1.08
CA12w04	Khudi Khola	HHC	199.65	7.43	67.25	7.43	161.76	69.66	81.28	50.44
CA11103	Khudi Khola	HHC	6.16	0.65	5.69	0.65	-0.83	1.76	10.73	0.37
CA15010	Khudi Khola	HHC	0.03	1.39	10.42	1.39	-1.74	1.89	9.46	0.95
CA15023	Khudi Khola	HHC	4.88	0.87	7.58	0.87	2.90	1.98	7.00	0.29
CA14009	Khudi Khola	HHC	8.19	0.69	6.23	0.69	6.85	6.09	5.38	4.46
CA14010	Khudi Khola	HHC	38.08	2.59	22.52	2.59	19.60	12.36	33.44	6.04
CA14014	Khudi Khola	HHC	4.87	1.08	10.12	1.08	1.83	2.13	9.42	0.89
CA14015	Khudi Khola	HHC	3.39	1.79	15.64	1.79	3.04	3.10	10.71	1.49
July 29 - 12:20-14:20	Khudi Khola	HHC	6.96	0.77	6.80	0.77				
July 29 - 14:20-16:20	Khudi Khola	HHC	6.57	0.70	6.16	0.70				
July 29 - 16:20-18:20	Khudi Khola	HHC	6.69	0.71	6.32	0.71				
July 29 - 18:20-20:20	Khudi Khola	HHC	6.72	0.71	6.24	0.71				
July 29 - 20:20-22:20	Khudi Khola	HHC	6.64	0.71	6.29	0.71				
July 29 - 22:20-24:20	Khudi Khola	HHC	6.16	0.68	5.97	0.69				
July 30 - 00:20-02:20	Khudi Khola	HHC	2.54	0.70	5.70	0.70				
July 30 - 02:20-04:20	Khudi Khola	HHC	5.58	0.82	6.67	0.82				
July 30 - 04:20-06:20	Khudi Khola	HHC	6.02	0.72	6.06	0.72				
July 30 - 06:20-08:20	Khudi Khola	HHC	5.99	0.66	5.63	0.66				
July 30 - 08:20-10:20	Khudi Khola	HHC	6.16	0.66	5.65	0.66				
July 30 - 10:20-12:20	Khudi Khola	HHC	6.69	0.67	5.79	0.67				
July 30 - 12:20-14:20	Khudi Khola	HHC	6.38	0.69	6.02	0.69				
July 31 - 17:30-18:30	Khudi Khola	HHC	1.77	0.77	6.63	0.77				

Table 5.13 continued from previous page

			Erosion (Major Elements) (4)				Erosion (Radiogenic Ca) (4)			
Sample	River	Formation	$E_{carbonate}$		$E_{silicate}$		$E_{carbonate}$		$E_{silicate}$	
			T/year/km^2	±	T/year/km^2	±	T/year/km^2	±	T/year/km^2	±
July 31 - 23:30-00:30	Khudi Khola	HHC	1.67	0.87	7.59	0.87				
August 1 - 5:30-06:30	Khudi Khola	HHC	1.66	0.73	6.26	0.73				
August 1 - 9:30-10:30	Khudi Khola	HHC	1.68	0.74	6.37	0.74				
July 29 - 11:00	Khudi Khola	LH+HHC	16.36	1.01	9.52	1.01				
July 29 - 16:00	Khudi Khola	LH+HHC	16.44	0.97	9.16	0.97				
July 29 - 21:00	Khudi Khola	LH+HHC	15.85	0.95	8.94	0.95				
July 30 - 00:00	Khudi Khola	LH+HHC	15.92	0.92	8.13	0.92				
July 30 - 01:00	Khudi Khola	LH+HHC	15.95	0.89	7.93	0.89				
July 30 - 02:00	Khudi Khola	LH+HHC	10.32	0.99	8.58	0.99				
July 30 - 03:00	Khudi Khola	LH+HHC	10.31	0.99	8.61	0.99				
July 30 - 04:00	Khudi Khola	LH+HHC	12.19	1.01	8.93	1.01				
July 30 - 05:00	Khudi Khola	LH+HHC	12.03	0.99	8.71	0.99				
July 30 - 06:00	Khudi Khola	LH+HHC	12.92	0.92	8.19	0.92				
July 30 - 07:00	Khudi Khola	LH+HHC	13.96	0.96	8.61	0.96				
July 30 - 08:00	Khudi Khola	LH+HHC	14.02	0.95	8.55	0.95				
July 30 - 09:00	Khudi Khola	LH+HHC	14.18	0.94	8.50	0.94				
July 30 - 10:00	Khudi Khola	LH+HHC	14.47	1.05	9.70	1.05				
July 30 - 11:00	Khudi Khola	LH+HHC	14.60	1.05	9.61	1.05				
August 1 - 18:00-19:00	Khudi Khola	LH+HHC	30.90	0.95	8.86	0.95				
August 2 - 00:00-01:00	Khudi Khola	LH+HHC	30.17	0.90	8.39	0.90				
August 2 - 07:00-08:00	Khudi Khola	LH+HHC	26.80	0.83	7.66	0.83				
WKD34606 (July 24, 2013 16:50)	Khudi Khola	LH+HHC	10.58	0.77	7.18	0.77	9.97	3.01	5.31	1.13
WKD34701 (July 25, 2013 0:30)	Khudi Khola	LH+HHC	10.04	2.41	20.47	2.41	-4.50	4.81	28.98	1.14
WKD34702 (July 25, 2013 2:45)	Khudi Khola	LH+HHC	19.84	2.76	23.21	2.76	1.31	6.40	35.05	0.27
WKD34703 (July 25, 2013 4:00)	Khudi Khola	LH+HHC	18.16	2.01	16.93	2.01	2.47	4.81	27.71	0.11
WKD34704 (July 25, 2013 5:20)	Khudi Khola	LH+HHC	17.84	1.77	14.99	1.77	7.54	7.04	20.89	2.86
WKD34707 (July 25, 201310:30)	Khudi Khola	LH+HHC	12.38	1.24	10.94	1.24	12.72	6.13	7.17	3.12
CA15013	Khudi Khola	LH+HHC	17.12	20.42	247.57	20.42	30.60	28.88	119.72	48.50
CA15014	Khudi Khola	LH+HHC	-185.75	57.30	682.53	57.31	4.67	38.90	181.62	168.89
CA15016	Khudi Khola	LH+HHC	3.39	1.81	16.56	1.81	1.85	2.96	12.58	1.93
MO100	Masel Khola	LH	169.23	101.19	406.95	101.19	78.29	27.47	259.00	126.78
MO383	Masel Khola	LH	61.84	61.05	252.10	61.05	38.05	19.29	135.27	74.00
MO107	Maudi Khola	LH	557.53	177.23	721.36	177.24	450.03	58.69	415.04	212.25
MO110	Isul Khola	LH	1221.99	45.91	215.90	45.91	1147.42	50.27	198.84	21.82

Table 5.13 continued from previous page

			Erosion (Major Elements) (4)				Erosion (Radiogenic Ca) (4)			
Sample	River	Formation	$E_{carbonate}$		$E_{silicate}$		$E_{carbonate}$		$E_{silicate}$	
			T/year/km^2	±	T/year/km^2	±	T/year/km^2	±	T/year/km^2	±
MO119	Anku Khola	LH	668.46	63.23	293.47	63.24	574.34	52.48	259.30	46.20
MO380	Jaran Khola	LH	51.51	62.53	272.09	62.53	-5.85	27.39	192.89	69.00
CA15032	Jaran Khola	LH	131.82	134.01	572.33	134.02	-6.35	51.79	412.00	154.28
MO311	Andi Khola	LH	18.98	0.19	1.06	0.19	1368.96	40.73	94.77	40.76
CA15001	Anku Khola	LH	13.11	1.41	8.92	1.41	12.58	1.19	6.11	1.48
CA15005	Chiti Khola	LH	2687.29	443.53	1752.81	443.55	2774.28	187.63	602.05	494.01
CA15008	Paundi Khola	LH	57.00	19.99	81.74	20.00	50.85	7.09	41.39	23.49
CA15034	Maleku Khola	LH	8702.11	615.33	2813.42	615.39	8507.60	547.78	1736.73	416.74
CA15036	Thopal Khola	LH	9.49	4.00	16.81	4.00	11.15	1.51	6.10	4.60
CA15030	Darondi Khola	HHC+LH	28.95	2.42	13.83	2.42	26.95	2.95	10.15	1.58
CA11150	Seti	TSS+HHC+LH	37.58	1.15	7.23	1.15	36.02	1.25	6.15	0.87
MO304	Seti	TSS+HHC+LH	30.31	0.74	4.87	0.74	30.20	1.02	3.38	0.28
CA11149	Kali Gandaki	TSS+HHC+LH	2.15	0.17	0.61	0.17	2.24	0.08	0.31	0.08
LO760	Trisuli	TSS+HHC+LH	5.09	0.29	1.56	0.29	4.00	0.24	1.99	0.23
CA15038	Trisuli	TSS+HHC+LH	5.68	0.38	1.97	0.38	5.04	0.57	1.77	0.17
PB81	Karnali	TSS+HHC+LH	38.54	0.83	4.93	0.83	36.42	1.17	4.96	0.58
CA11169	Arun	TSS+HHC+LH	37.48	1.88	9.56	1.88	36.78	2.23	5.64	1.20
CA11167	Kosi	TSS+HHC+LH	18.23	1.13	6.89	1.13	15.24	0.94	7.06	1.13
PB71	Kosi	TSS+HHC+LH	18.72	1.11	6.60	1.11	17.03	1.10	5.53	0.92
LO764	Kosi	TSS+HHC+LH	23.02	1.13	6.79	1.13	20.79	1.70	6.19	0.58
PB53	Narayani	TSS+HHC+LH	40.92	1.34	8.59	1.34	38.26	2.07	7.86	0.66
CA11147	Narayani	TSS+HHC+LH	42.22	1.17	7.97	1.17	38.04	1.94	9.17	0.51
CA13130	Narayani	TSS+HHC+LH	36.97	1.70	9.97	1.70	33.76	2.04	8.94	1.13

Table 5.14 – *Results of silicate and carbonate chemical erosion and CO_2 consumption calculations based on major elemental concentrations and radiogenic Ca isotopic compositions of the dissolved load in central Nepal. (5) The rate of CO_2 consumption based on the major elemental concentrations of the dissolved load (see equation 5.30 in the text). (6) The rate of CO_2 consumption based on the major elemental concentrations of the dissolved load and the amount of Ca derived from silicate weathering derived from Ca isotopic compositions.*

			Silicate CO_2 Consumtption			
Sample	River	Formation	RCO_2 (10^6 mol/year/km^2)			
			Major Elements (5)	±	Ca^{iso}_{sil} + Major Elements (6)	±
PB9	Thini Khola	TSS	45.01	10.61	138.92	60.28
MO503	Yankim Khola	TSS	65.50	42.36	511.07	862.71
MO364	Chepe Khola	HHC + LH	0.09	0.01	0.13	0.01
MO79	Chepe Khola	HHC + LH	0.26	0.04	0.40	0.07
CA15003	Chepe Khola	HHC + LH	0.23	0.01	0.45	0.04
MO359	Chepe Khola	HHC	0.13	0.01	0.14	0.02
MO58	Chepe Khola	HHC	0.06	0.01	0.13	0.01
CA11206A	Khudi Khola	HHC	0.58	0.04	0.90	0.04
CA12w03	Khudi Khola	HHC	0.68	0.04	0.87	0.13
CA12w04	Khudi Khola	HHC	3.18	0.37	5.07	3.43
CA11103	Khudi Khola	HHC	0.27	0.04	0.62	0.09

Table 5.14 continued from previous page

Sample	River	Formation	Silicate CO_2 Consumtption			
			RCO_2 (10^6 mol/year/km^2)			
			Major Elements (5)	±	Ca_{sil}^{iso} + Major Elements (6)	±
CA15010	Khudi Khola	HHC	0.50	0.19	0.59	0.21
CA15023	Khudi Khola	HHC	0.36	0.06	0.46	0.11
CA14009	Khudi Khola	HHC	0.29	0.03	0.36	0.30
CA14010	Khudi Khola	HHC	1.07	0.18	1.99	0.66
CA14014	Khudi Khola	HHC	0.48	0.04	0.63	0.08
CA14015	Khudi Khola	HHC	0.74	0.12	0.76	0.18
July 29 - 12:20-14:20	Khudi Khola	HHC	0.32	0.04		
July 29 - 14:20-16:20	Khudi Khola	HHC	0.29	0.04		
July 29 - 16:20-18:20	Khudi Khola	HHC	0.30	0.03		
July 29 - 18:20-20:20	Khudi Khola	HHC	0.30	0.04		
July 29 - 20:20-22:20	Khudi Khola	HHC	0.30	0.04		
July 29 - 22:20-24:20	Khudi Khola	HHC	0.28	0.04		
July 30 - 00:20-02:20	Khudi Khola	HHC	0.27	0.06		
July 30 - 02:20-04:20	Khudi Khola	HHC	0.32	0.08		
July 30 - 04:20-06:20	Khudi Khola	HHC	0.29	0.06		
July 30 - 06:20-08:20	Khudi Khola	HHC	0.27	0.05		
July 30 - 08:20-10:20	Khudi Khola	HHC	0.27	0.04		
July 30 - 10:20-12:20	Khudi Khola	HHC	0.27	0.04		
July 30 - 12:20-14:20	Khudi Khola	HHC	0.29	0.04		

Table 5.14 continued from previous page

			Silicate CO_2 Consumtption			
Sample	River	Formation	RCO_2 (10^6 mol/year/km^2)			
			Major Elements (5)	±	Ca_{sil}^{iso} + Major Elements (6)	±
July 31 - 17:30-18:30	Khudi Khola	HHC	0.31	0.05		
July 31 - 23:30-00:30	Khudi Khola	HHC	0.36	0.02		
August 1 - 5:30-06:30	Khudi Khola	HHC	0.30	0.05		
August 1 - 9:30-10:30	Khudi Khola	HHC	0.30	0.05		
July 29 - 11:00	Khudi Khola	LH+HHC	0.45	0.05		
July 29 - 16:00	Khudi Khola	LH+HHC	0.43	0.05		
July 29 - 21:00	Khudi Khola	LH+HHC	0.42	0.05		
July 30 - 00:00	Khudi Khola	LH+HHC	0.39	0.08		
July 30 - 01:00	Khudi Khola	LH+HHC	0.38	0.07		
July 30 - 02:00	Khudi Khola	LH+HHC	0.41	0.09		
July 30 - 03:00	Khudi Khola	LH+HHC	0.41	0.09		
July 30 - 04:00	Khudi Khola	LH+HHC	0.42	0.09		
July 30 - 05:00	Khudi Khola	LH+HHC	0.41	0.09		
July 30 - 06:00	Khudi Khola	LH+HHC	0.39	0.08		
July 30 - 07:00	Khudi Khola	LH+HHC	0.41	0.07		
July 30 - 08:00	Khudi Khola	LH+HHC	0.41	0.07		
July 30 - 09:00	Khudi Khola	LH+HHC	0.40	0.07		
July 30 - 10:00	Khudi Khola	LH+HHC	0.46	0.06		

Table 5.14 continued from previous page

Sample	River	Formation	Silicate CO_2 Consumtption			
			RCO_2 (10^6 mol/year/km^2)			
			Major Elements (5)	±	Ca_{sil}^{iso} + Major Elements (6)	±
July 30 - 11:00	Khudi Khola	LH+HHC	0.46	0.04		
August 1 - 18:00-19:00	Khudi Khola	LH+HHC	0.42	0.05		
August 2 - 00:00-01:00	Khudi Khola	LH+HHC	0.40	0.05		
August 2 - 07:00-08:00	Khudi Khola	LH+HHC	0.36	0.05		
WKD34606 (July 24, 2013 16:50)	Khudi Khola	LH+HHC	0.34	0.05	0.37	0.16
WKD34701 (July 25, 2013 0:30)	Khudi Khola	LH+HHC	0.97	0.26	1.70	0.38
WKD34702 (July 25, 2013 2:45)	Khudi Khola	LH+HHC	1.11	0.31	2.03	0.49
WKD34703 (July 25, 2013 4:00)	Khudi Khola	LH+HHC	0.81	0.23	1.59	0.36
WKD34704 (July 25, 2013 5:20)	Khudi Khola	LH+HHC	0.71	0.19	1.23	0.45
WKD34707 (July 25, 201310:30)	Khudi Khola	LH+HHC	0.52	0.12	0.50	0.35
CA15013	Khudi Khola	LH+HHC	11.59	2.65	10.92	2.23
CA15014	Khudi Khola	LH+HHC	31.97	6.93	22.47	7.85
CA15016	Khudi Khola	LH+HHC	0.79	0.12	0.86	0.18
MO100	Masel Khola	LH	18.71	2.75	23.24	6.41
MO383	Masel Khola	LH	11.63	1.15	12.81	3.22
MO107	Maudi Khola	LH	33.21	4.09	38.57	9.97

Table 5.14 continued from previous page

Sample	River	Formation	Silicate CO_2 Consumtption RCO_2 (10^6 mol/year/km^2)			
			Major Elements (5)	±	Ca_{sil}^{iso} + Major Elements (6)	±
MO110	Isul Khola	LH	10.11	1.67	13.83	1.87
MO119	Anku Khola	LH	13.72	0.75	18.42	0.23
MO380	Jaran Khola	LH	12.63	0.37	15.49	1.81
CA15032	Jaran Khola	LH	26.50	1.11	33.40	4.96
MO311	Andi Khola	LH	3.73	0.61	5.56	1.89
CA15001	Anku Khola	LH	0.42	0.04	0.45	0.03
CA15005	Chiti Khola	LH	80.39	18.49	76.05	31.25
CA15008	Paundi Khola	LH	3.77	0.55	4.07	1.20
CA15034	Maleku Khola	LH	131.30	15.05	141.01	12.08
CA15036	Thopal Khola	LH	0.78	0.07	0.69	0.19
CA15030	Darondi Khola	HHC+LH	0.65	0.06	0.75	0.09
CA11150	Seti	TSS+HHC+LH	0.34	0.06	0.42	0.06

Table 5.14 continued from previous page

Sample	River	Formation	Silicate CO_2 Consumtption			
			RCO_2 (10^6 mol/year/km^2)			
			Major Elements (5)	±	Ca_{sil}^{iso} + Major Elements (6)	±
MO304	Seti	TSS+HHC+LH	0.23	0.05	0.23	0.07
CA11149	Kali Gandaki	TSS+HHC+LH	0.03	0.01	0.02	0.00
LO760	Trisuli	TSS+HHC+LH	0.07	0.00	0.13	0.00
CA15038	Trisuli	TSS+HHC+LH	0.09	0.00	0.12	0.01
PB81	Karnali	TSS+HHC+LH	0.23	0.01	0.33	0.03
CA11169	Arun	TSS+HHC+LH	0.44	0.06	0.48	0.04
CA11167	Kosi	TSS+HHC+LH	0.32	0.02	0.47	0.01
PB71	Kosi	TSS+HHC+LH	0.31	0.01	0.39	0.01
LO764	Kosi	TSS+HHC+LH	0.31	0.01	0.43	0.04
PB53	Narayani	TSS+HHC+LH	0.40	0.04	0.53	0.07
CA11147	Narayani	TSS+HHC+LH	0.37	0.03	0.58	0.07
CA13130	Narayani	TSS+HHC+LH	0.46	0.02	0.62	0.04

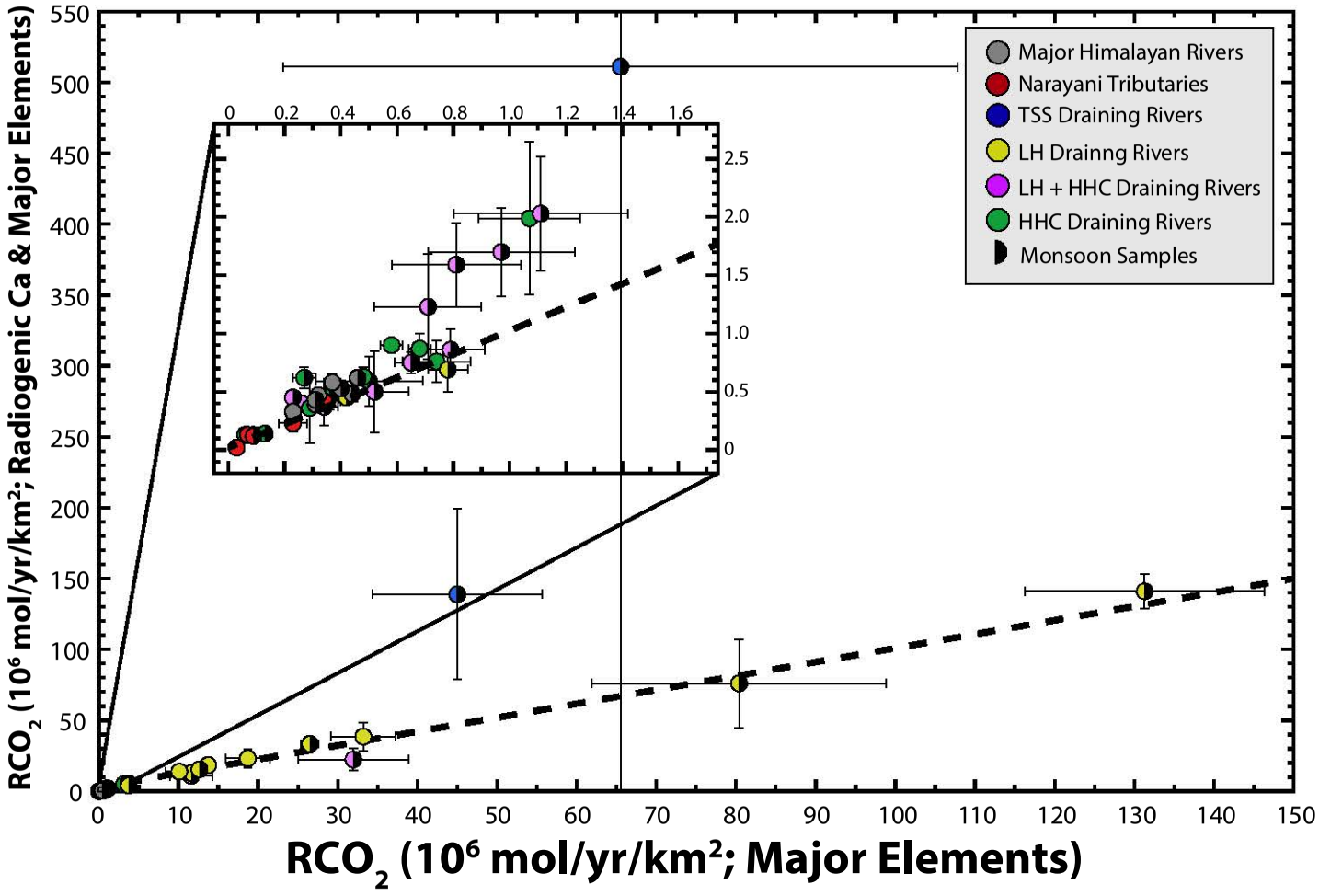

Figure 5.21 – *Estimates of CO_2 consumption (x 10^6 mol C yr^{-1} km^{-2}) based on calculations using solely major elements compared with the results based on radiogenic Ca compositions plus other major elements for the dissolved load of the TSS (blue), LH (yellow), HHC (green), LH + HHC (pink), major Narayani tributaries (red) and Himalayan Front rivers (gray). Symbols with black half-circles represent samples collected during the monsoon. The dotted line represents a 1:1 correlation line between the estimates, i.e., samples that fall along this line show agreement between both CO_2 consumption estimates. Tables 5.12, 5.13, and 5.14 list the rates of CO_2 consumption for the two methods discussed in the text. This plot shows that the overestimation of CO_2 consumption occurs only in regions with low silicate weathering rates (inset), and therefore has little effect on the overall CO_2 consumption (cf. Figure 5.22).*

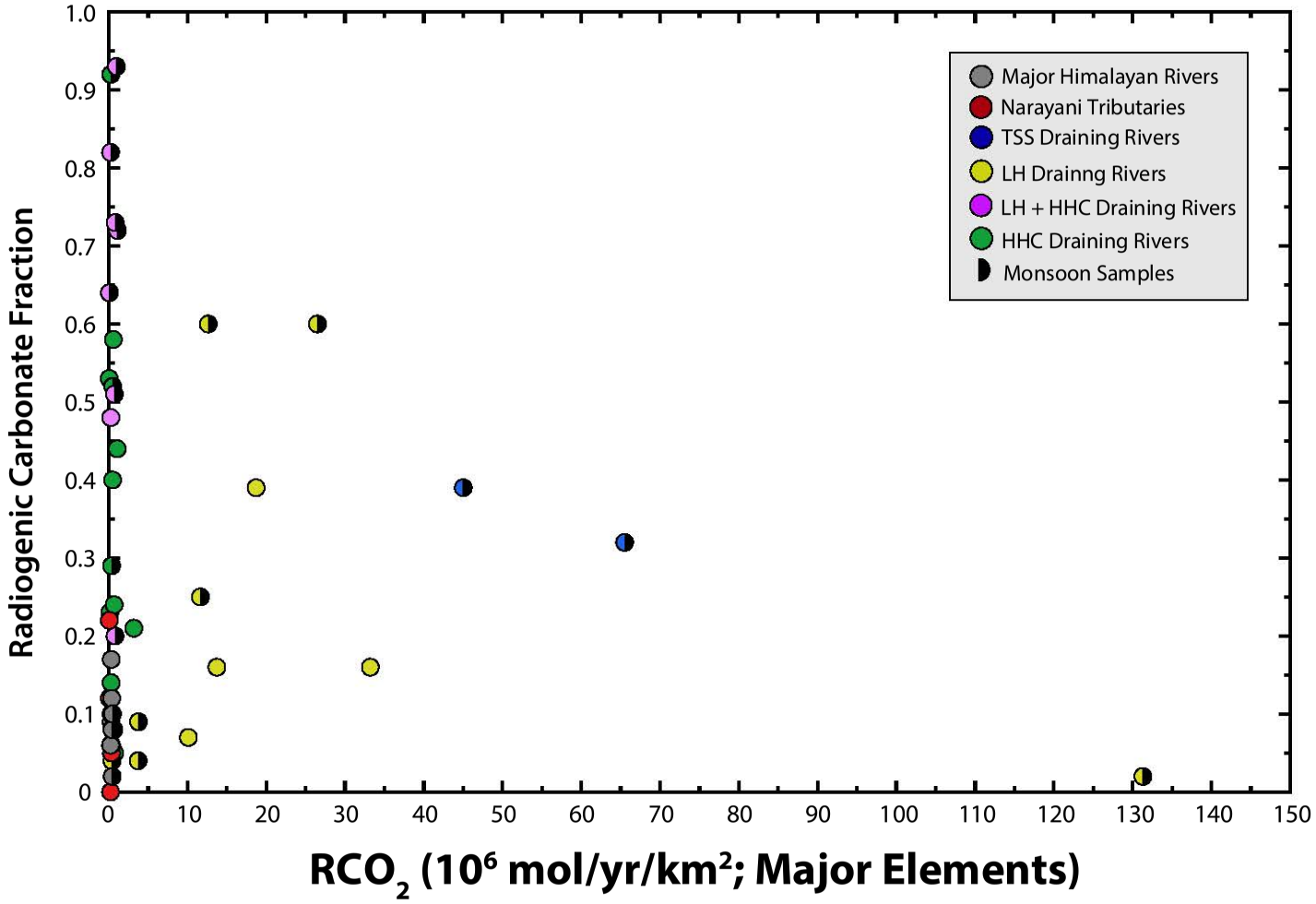

Figure 5.22 – *The radiogenic carbonate fraction as a function of the CO_2 consumption rate (based on major elements; x 10^6 mol C yr^{-1} km^{-2}) for the dissolved load of the TSS (blue), LH (yellow), HHC (green), LH + HHC (pink), major Narayani tributaries (red) and Himalayan Front rivers (gray). Symbols with black half-circles represent samples collected during the monsoon. Tables 5.8, 5.9, and 5.10 list the magnitude of the radiogenic carbonate component for each river and Tables 5.12, 5.13, and 5.14 list the rates of CO_2 consumption for each method discussed in the text. This plot shows that regions, such as the HHC and LH, with high amounts of radiogenic carbonate have very low consumption rates because, although this radiogenic carbonate component influences the silicate weathering budget, it is geochemically not silicate and therefore does not consume CO_2 and these regions have relatively small rates of silicate erosion.*

5.6 Conclusions

Radiogenic Ca isotopic compositions, as well as the Sr isotopic compositions and major elemental concentrations, have been measured in both small and large rivers draining each of the major Himalayan formations (i.e., the TSS, HHC, and LH) from central Nepal in the Narayani basin. Himalayan carbonate lithologies, both dolomite rock samples and carbonate fractions of sediments, have retained the ε^{40}Ca signature of marine limestone (= 0), which implies that, unlike for Sr isotopes, radiogenic Ca isotopes in carbonates have not re-equilibrated with adjacent highly radiogenic silicate rocks during metamorphism related to Himalayan orogenesis. On the contrary, the Ca isotopic composition of sediment in the silicate fraction exhibits enrichments in ^{40}Ca that correspond to the age and time-integrated K/Ca ratio of sediments. In the dissolved load, in general, from the north (i.e., the TSS) to the south (i.e., the LH), both the major elemental and ^{87}Sr/^{86}Sr and ε^{40}Ca isotopic values vary according to the range of lithologies drained. Rivers that drain purely carbonate lithologies, such as the Thini Khola, Yankim Khola, and the Seti, have unradiogenic compositions, i.e., +0–0.5 epsilon units. In contrast, rivers that drain predominantly or purely silicate lithologies have radiogenic Ca enrichments of up to +11 epsilon units, especially small LH rivers. This first radiogenic Ca survey of the central Nepal Himalaya allows us to establish limited constraints on the isotopic composition of each formation. It remains to be seen if these already highly radiogenic LH compositions are an upper limit or if more radiogenic isotopic values exist for river water and whole-rock in the Himalaya. Nevertheless, consideration of a simple three-stage ^{40}Ca isotope growth model, based on sedimentary and crustal extraction ages, suggests that the average silicate ε^{40}Ca compositions estimated for each formation on the basis of sediment analyses are not unreasonable.

One of the main objectives of this study was to determine the relative magnitudes of silicate and carbonate weathering that currently occurs in central Nepalese rivers. Based on budget modeling, we find that there is relatively good agreement between estimates based on Ca concentrations and estimates based on Ca isotopic compositions. Nevertheless there are some discrepancies, particularly in samples derived from rivers draining solely or partially the HHC formation, with estimates of the silicate contribution based on isotopic composition being sometimes higher than those based on Ca concentrations. These discrepancies cannot be attributed to secondary carbonate precipitation because this would lead to the opposite effect, i.e., higher estimates for the silicate contribution based on Ca concentrations. In fact, this observation, coupled with the determination that the carbonate fractions of the sediments have unradiogenic compositions, argues that secondary carbonate

precipitation in rivers is probably a relatively minor process. Instead, the most likely explanation for the discrepancies between the estimates is that the metamorphic silicate bedrocks contain trace amounts of disseminated carbonate with radiogenic compositions. This material will have a carbonate signature in budget calculations based on major elements, but a silicate signature in calculations based on isotopic composition.

Estimates of current silicate and carbonate erosion rates in the catchments of the Narayani based on major element geochemistry and radiogenic Ca isotopes generally agree but, in many cases, estimates based on the radiogenic Ca isotopic compositions are larger. As these calculations are based on the estimates of the fraction of Ca derived from silicate weathering, the observed discrepancies may also be attributed to the inferred presence of disseminated radiogenic calcite veinlets. These discrepancies are in turn reflected in the rates of CO_2 consumption based on cations derived from silicate weathering, and again most probably reflect the weathering of trace amounts of disseminated calcite.

Based on the results and interpretations of this study, we can draw the following four conclusions:

1. Radiogenic Ca isotope compositions suggest that secondary carbonate precipitation in rivers is only a minor process. This can be seen in two complementary ways: i) The unradiogenic composition of the sediment carbonate fraction implies that they have a detrital origin and ii) the fact that F_{Ca}^{chem} (i.e., the fraction of silicate-derived Ca estimated on the basis of Ca concentrations) is almost never greater than F_{Ca}^{iso} (i.e., the fraction of silicate-derived Ca estimated on the basis of Ca isotopes) implies that there has not been a loss of Ca via secondary carbonate precipitation processes.

2. Globally speaking, there is fairly good agreement between budget estimates based on Ca concentrations and those based on Ca isotopes of the proportion of Ca derived from silicate weathering. However, in many HHC basins and some LH basins, F_{Ca}^{iso} significantly exceeds F_{Ca}^{chem}. This may be due to the presence of disseminated calcite veins that have retained the radiogenic composition of their silicate host rocks.

3. The fraction of Ca estimated to derive from radiogenic carbonates is highest in basins with low silicate weathering rates. This suggests that, in regions that have less chemical weathering that occurs, such as the HHC, disseminated radiogenic calcite is preferentially weathered and dissolves faster than silicate lithologies because carbonates are characterized by fast dissolution kinetic properties.

4. Including radiogenic carbonates in the CO_2 consumption budget has little effect on the total CO_2 consumption in the Narayani because radiogenic carbonates are limited to areas with low silicate weathering rates.

5.7 Supplementary Figures

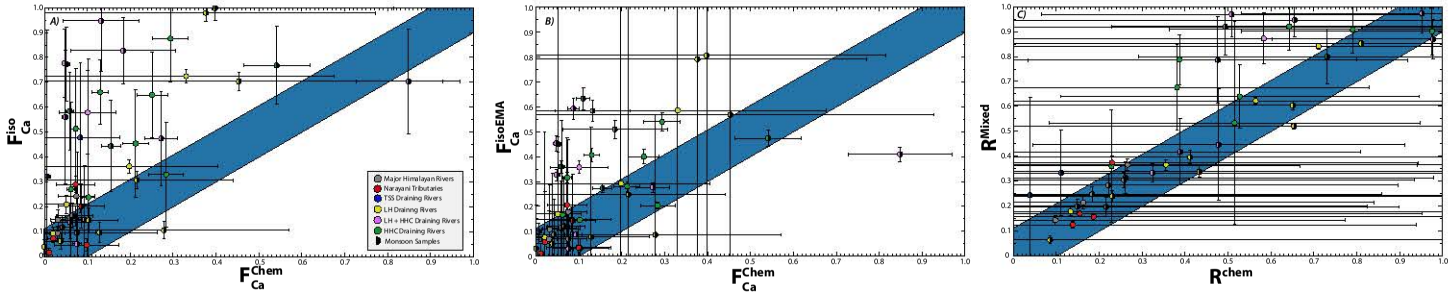

Figure 5.23 – *Results of budget modeling (see Figure 5.16) with error bars that compare chemically and isotopically based calculations, for both Ca-only and total cation budget calculations. F^{chem}_{Ca} plotted against F^{iso}_{Ca} (A) and F^{chem}_{Ca} (B), and R^{chem} plotted against R^{Mix} (C), for the dissolved load of the TSS (blue), LH (yellow), HHC (green), LH + HHC (pink), major Narayani tributaries (red), and Himalayan Front rivers (gray). The light blue field represents a 1:1 line (2σ), i.e., samples that fall along this line show agreement between the budget methods. Symbols with black half-circles represent samples collected during the monsoon. Error bars, which may be overestimated (see Tables 5.8, 5.9, and 5.10), have been left out to allow easier observation of the agreement and disagreement between the budget calculation methods.*

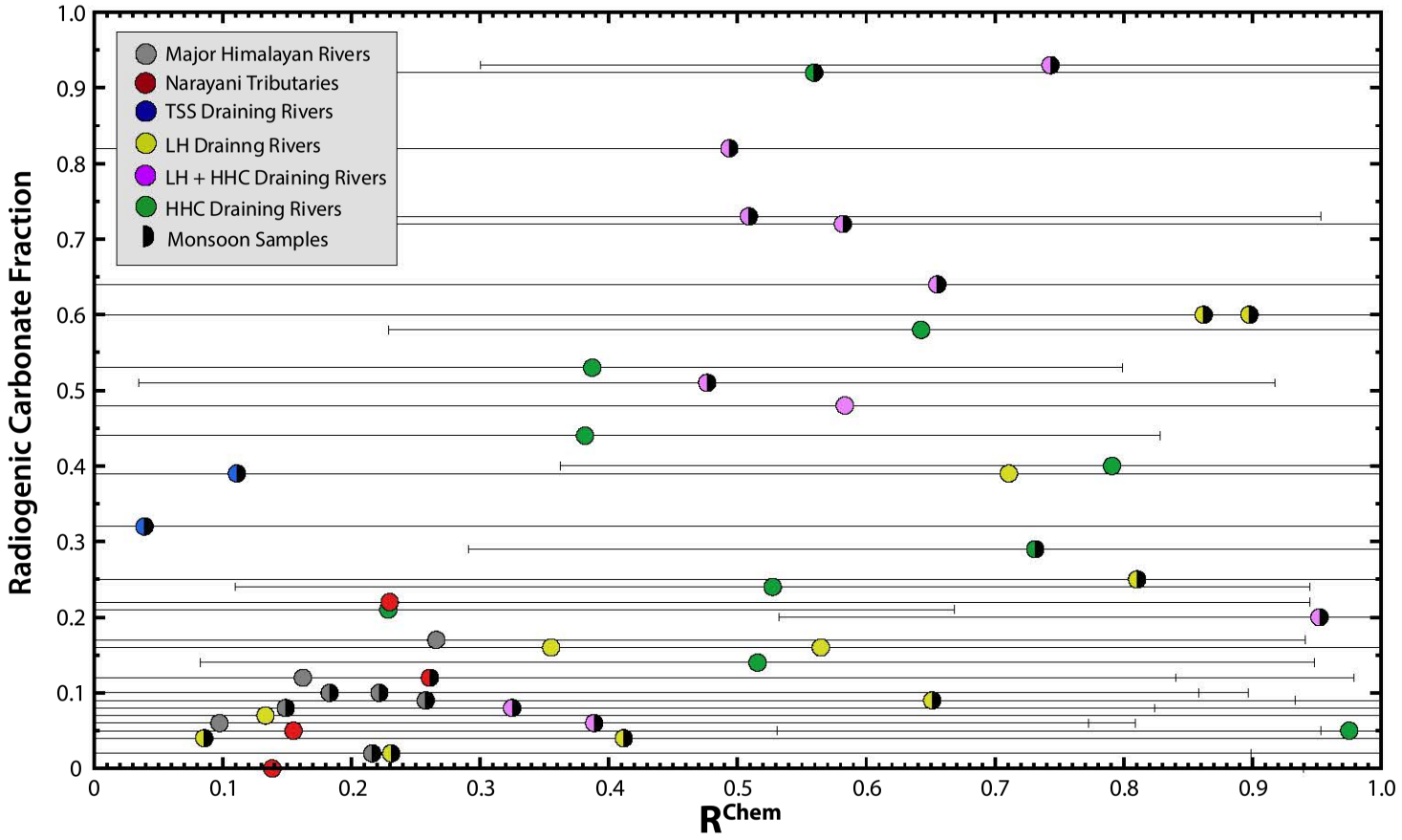

Figure 5.24 – *$F^{Ca}_{Rad-Carb}$ (the estimated fraction of Ca derived from weathering of radiogenic carbonate) as a function of R^{chem} (the fraction of the dissolved cations derived from silicate weathering) with error bars (see Figure 5.18) for the dissolved load of the TSS (blue), LH (yellow), HHC (green), LH + HHC (pink), major Narayani tributaries (red), and Himalayan Front rivers (gray). Symbols with black half-circles represent samples collected during the monsoon. Error bars are omitted for clarity. Tables 5.8, 5.9, and 5.10 list the results of the calculations for the $F^{Ca}_{Rad-Carb}$ and R^{chem} calculations.*

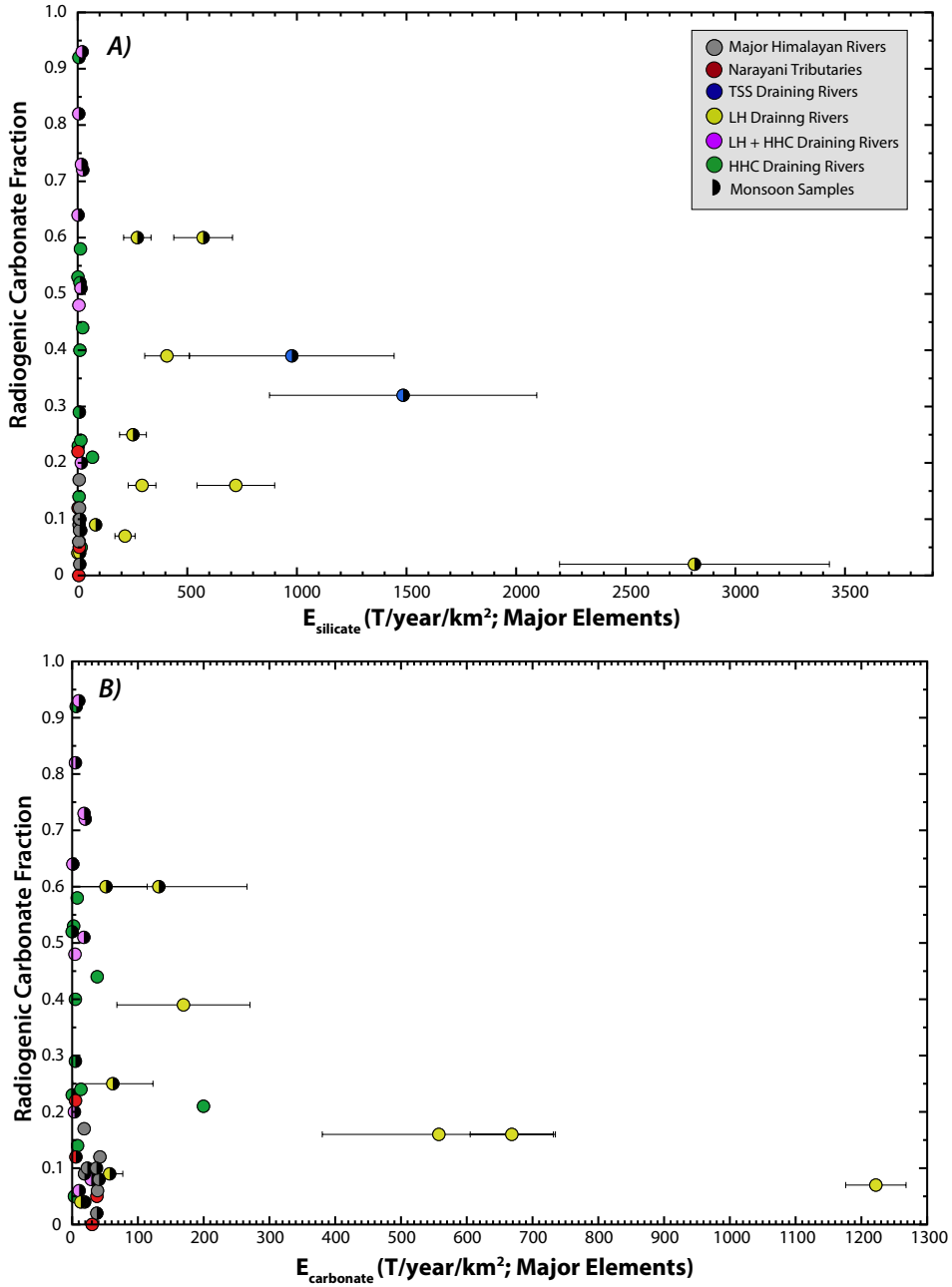

Figure 5.25 – *The radiogenic carbonate fraction as a function of $E_{silicate}$ (A) and $E_{Carbonate}$ (B) based on major elements with error bars (t km^{-2} yr^{-1}) (see Figure 5.19) for the dissolved load of the TSS (blue), LH (yellow), HHC (green), LH + HHC (pink), major Narayani tributaries (red), and Himalayan Front rivers (gray). Symbols with black half-circles represent samples collected during the monsoon. Tables 5.8, 5.9, and 5.10 list the results of the calculations for the radiogenic carbonate fraction and Tables 5.12, 5.13, and 5.14 list the results of the calculations to estimate the amount of silicate and carbonate erosion. We observe that basins with low silicate erosion rates show the highest proportions of radiogenic carbonates. This suggests that in areas of low intensity silicate weathering (i.e., the HHC) it is the radiogenic carbonates that weather first. It also implies that the radiogenic carbonate fraction will have little effect on the overall silicate weathering flux coming from the Narayani, and thus little influence on the CO_2 budget (see below).*

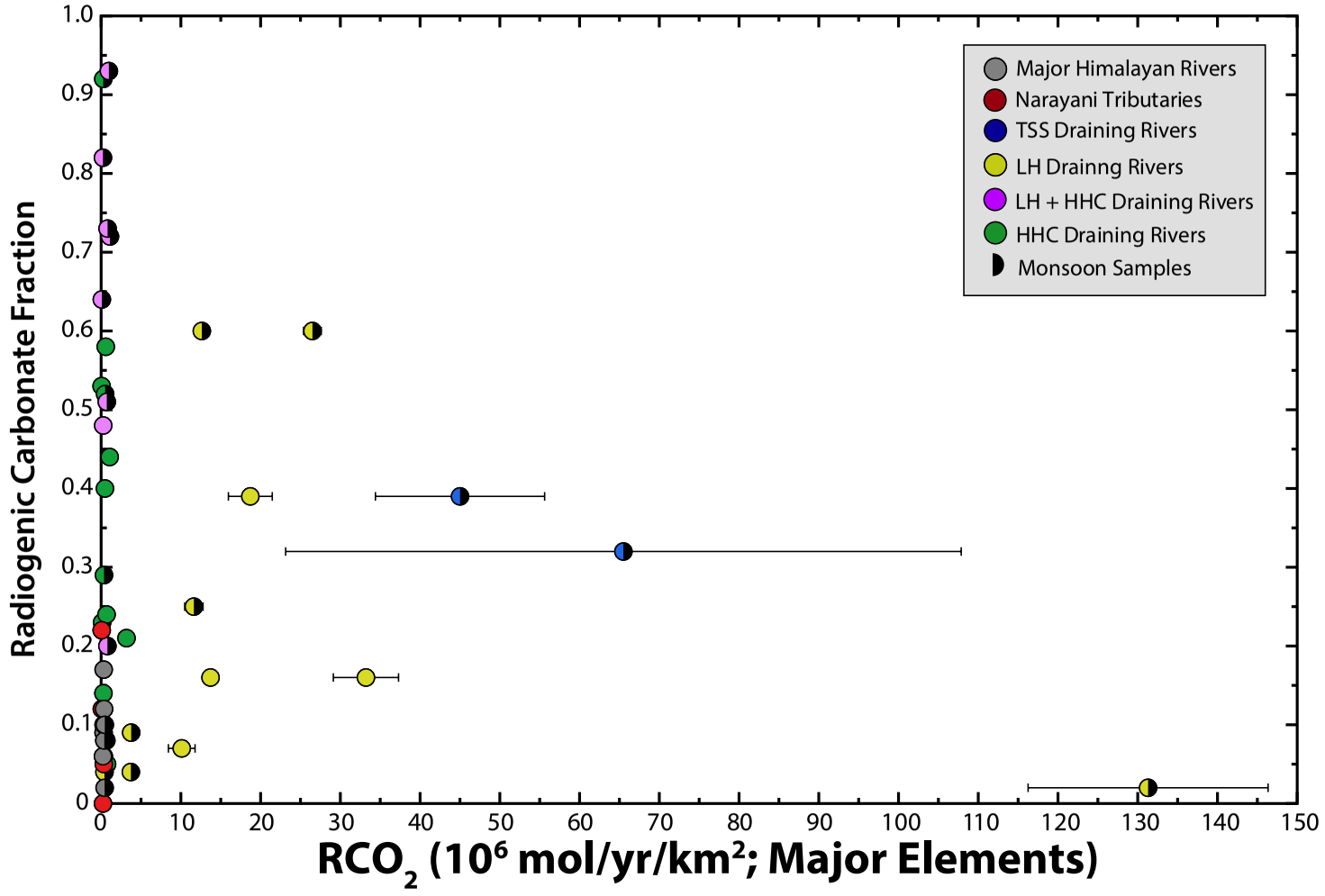

Figure 5.26 – *The radiogenic carbonate fraction as a function of the CO_2 consumption rate with error bars (based on major elements; x 10^6 mol C yr^{-1} km^{-2}) (see Figure 5.22) for the dissolved load of the TSS (blue), LH (yellow), HHC (green), LH + HHC (pink), major Narayani tributaries (red) and Himalayan Front rivers (gray). Symbols with black half-circles represent samples collected during the monsoon. Tables 5.8, 5.9, and 5.10 list the magnitude of the radiogenic carbonate component for each river and Tables 5.12, 5.13, and 5.14 list the rates of CO_2 consumption for each method discussed in the text. This plot shows that regions, such as the HHC and LH, with high amounts of radiogenic carbonate have very low consumption rates because, although this radiogenic carbonate component influences the silicate weathering budget, it is geochemically not silicate and therefore does not consume CO_2 and these regions have relatively small rates of silicate erosion.*

5.8 Supplementary Tables

Table 5.15 – *Individual analysis analytical data for each sample analyzed in this study.*

	# Cycles	^{42}Ca (V)	^{40}Ca (V)	Raw ratios (Line 1)			(Line 2)	Corrected ratios (static mode)			
				^{40}Ca/^{44}Ca	^{42}Ca/^{44}Ca	^{43}Ca/^{44}Ca	^{40}Ca/^{42}Ca	^{40}Ca/^{44}Ca (ST)	± (2 S.D.)	^{43}Ca/^{44}Ca (ST)	± (2 S.D.)
Session 1 May 2014											
2014_05_09_Ca-LO764-3	60	0.097492914	14.73427565	46.48733	0.31007	0.064627171	149.92383	47.09718	0.00283	0.06485	6.24E-06
2014_05_09_Ca-PB-71	120	0.095924268	14.52029668	46.36577	0.30968	0.064596198	149.72238	47.09590	0.00178	0.06486	4.13E-06
2014_05_10_Ca-PB-53	70	0.093163334	13.97697146	46.44740	0.30994	0.064611574	149.86037	47.09145	0.00262	0.06485	6.05E-06
2014_05_12_Ca-MO359	80	0.095196369	14.41666582	46.41383	0.30983	0.064605401	149.80430	47.09582	0.00223	0.06485	4.89E-06
2014_05_12_Ca-MO79	60	0.094747158	14.35611139	46.36396	0.30967	0.064581282	149.71948	47.09249	0.00236	0.06484	5.80E-06
Session 1B May 2014											
2014_05_18_Ca-MO311	90	0.094903188	5.86693E-06	46.39589	0.30975	0.064606173	149.78528	47.10737	0.00314	0.06486	5.88E-06
2014_05_18_Ca-MO311b	120	0.096248114	6.08921E-06	46.40370	0.30977	0.0646074	149.80049	47.10565	0.00269	0.06486	5.00E-06
2014_05_24_Ca-MO311	120	0.099206581	14.97411866	46.38840	0.30972	0.064601264	149.77458	47.10361	0.00244	0.06486	4.17E-06
Session 2 July 2014											
2014_07_05_Ca-PB9-1	120	0.100689065	15.28502181	46.37177	0.30967	0.064601793	149.74487	47.10564	0.00248	0.06487	4.22E-06
2014_07_07_Ca-CA11169-1	120	0.100583945	15.25803869	46.43310	0.30988	0.06462127	149.84096	47.10307	0.00245	0.06486	4.23E-06
2014_07_11_Ca-CA34606a	80	0.096854596	14.63486929	46.34957	0.30960	0.064586177	149.70613	47.09740	0.00290	0.06486	5.61E-06
2014_07_12_Ca-CA34606b	120	0.097273048	14.72436017	46.41139	0.30980	0.064619586	149.80905	47.09838	0.00227	0.06487	4.15E-06
2014_07_15_Ca-CA113130	120	0.099495939	15.10796543	46.42647	0.30984	0.064621272	149.83913	47.10806	0.00252	0.06487	4.27E-06
Session 3 September 2014											
2014_09_28_Ca-MO58-1	120	0.100670208	15.31007866	46.34476	0.30958	0.064596257	149.70321	47.12014	0.00265	0.06487	4.77E-06
2014_09_27_Ca-PB53-1	120	0.099955086	15.10599881	46.39120	0.30973	0.064607115	149.78145	47.11067	0.00271	0.06487	3.98E-06
2014_09_29_Ca-MO58-2	110	0.097489125	14.72103697	46.37613	0.30966	0.06460099	149.76334	47.10995	0.00275	0.06487	4.30E-06
2014_09_27_Ca-PB53-2	120	0.100649076	15.21744559	46.33807	0.30956	0.064588537	149.68857	47.11088	0.00233	0.06486	4.13E-06
2014_09_30_Ca-MO364-1	120	0.099589119	15.11100882	46.32825	0.30952	0.064589465	149.67812	47.11607	0.00259	0.06487	4.24E-06
2014_09_30_Ca-MO364-2	120	0.099257219	15.06268524	46.33731	0.30955	0.064587308	149.69159	47.11152	0.00253	0.06486	4.24E-06
Session 4 October 2014											
2014_10_03_Ca-PB53-3	110	0.10251429	15.45377642	46.39686	0.30974	0.064606447	149.79507	47.10421	0.00241	0.06486	4.70E-06
Session 6 April 2015											
2015_04_16_Ca-CA11103-2	120	0.079334532	11.95612257	46.35632	0.30961	0.06459548	149.72329	47.14632	0.00214	0.06487	5.24E-06
2015_04_20_Ca-CA111-69	120	0.063437461	9.630072442	46.35013	0.30961	0.064593444	149.70325	47.14319	0.00271	0.06486	6.72E-06
Session 7 July 2015											
2015_07_11_Ca-MO100	120	0.083554272	12.64522045	46.40752	0.30967	0.064598805	149.86354	47.16753	0.00271	0.06486	5.84E-06
2015_07_11_Ca-MO107	120	0.08855539	13.45002081	46.42067	0.30977	0.06460501	149.85702	47.15135	0.00284	0.06486	4.62E-06
2015_07_11_Ca-MO110	120	0.096399684	14.58888791	46.37723	0.30967	0.064599221	149.76297	47.13359	0.00257	0.06486	4.53E-06
2015_07_12_Ca-MO119	70	0.075956473	11.59045342	46.30493	0.30944	0.064574412	149.64267	47.13636	0.00466	0.06486	8.93E-06
2015_07_12_Ca-MO380	100	0.075928282	11.48053349	46.33559	0.30938	0.064568657	149.76690	47.18350	0.00440	0.06486	8.06E-06
2015_07_12_Ca-MO383	120	0.078528214	11.82435584	46.41598	0.30970	0.064604214	149.87611	47.16905	0.00307	0.06487	7.97E-06

Table 5.15 continued from previous page

	# Cycles	^{42}Ca (V)	^{40}Ca (V)	Raw ratios (Line 1)			(Line 2)	Corrected ratios (static mode)			
				^{40}Ca/^{44}Ca	^{42}Ca/^{44}Ca	^{43}Ca/^{44}Ca	^{40}Ca/^{42}Ca	^{40}Ca/^{44}Ca (ST)	± (2 S.D.)	^{43}Ca/^{44}Ca (ST)	± (2 S.D.)
2015_07_13_Ca-MO383	120	0.079993261	12.19308963	46.37993	0.30958	0.064594791	149.81603	47.16673	0.00315	0.06487	6.74E-06
2015_07_14_Ca-MO100	120	0.078637067	11.9241392	46.42668	0.30973	0.064612327	149.89352	47.16263	0.00261	0.06487	5.56E-06
2015_07_14_Ca-MO107	120	0.088688351	13.5884667	46.43598	0.30981	0.064612045	149.88625	47.15158	0.00274	0.06486	5.87E-06
2015_07_15_Ca-MO110	120	0.091588535	13.82498751	46.39502	0.30973	0.064596759	149.79263	47.12700	0.00261	0.06485	6.67E-06
2015_07_15_Ca-MO119	120	0.083685095	12.51135872	46.42695	0.30981	0.064614254	149.85599	47.13195	0.00271	0.06486	6.33E-06
2015_07_15_Ca-MO380	120	0.083821124	12.65721816	46.36887	0.30949	0.064583666	149.82231	47.18288	0.00307	0.06487	5.51E-06
Session 8 February 2016											
2016_02_07_Ca_MO503	120	0.079297822	12.08765878	46.37716	0.30968	0.064612217	149.75690	47.11749	0.00326	0.06487	7.91E-06
2016_02_19_Ca_CA15001	100	0.077387331	11.67902751	46.34839	0.30957	0.064609353	149.71675	47.11919	0.00392	0.06488	1.06E-05
2016_02_20_Ca_CA15005	110	0.069748219	10.59300709	46.43369	0.30986	0.064616681	149.85533	47.12060	0.00349	0.06486	9.35E-06
2016_02_21_Ca_CA15034	110	0.07442423	11.28420847	46.40114	0.30975	0.06460851	149.79979	47.11629	0.00310	0.06486	7.36E-06
2016_02_22_Ca_CA15008	110	0.070497774	10.73296123	46.35193	0.30955	0.064591726	149.73812	47.13131	0.00305	0.06487	8.24E-06
2016_02_22_Ca_CA15032	110	0.078263494	11.83316241	46.38579	0.30955	0.064584993	149.84782	47.16992	0.00293	0.06486	6.93E-06
2016_02_23_Ca_CA15036	110	0.081944897	12.43749907	46.43051	0.30984	0.064618009	149.85193	47.11585	0.00290	0.06486	6.97E-06
2016_03_01_Ca_CA15032	110	0.068714115	10.46318917	46.43443	0.30971	0.064609357	149.92954	47.16405	0.00315	0.06487	6.70E-06
2016_03_07_Ca_CA15030	80	0.075523555	11.43978905	46.37666	0.30966	0.064609286	149.76442	47.11764	0.00468	0.06487	7.83E-06

Table 5.16 – *Individual analysis analytical data for each sample analyzed in this study.*

	Corrected ratios (multidynamic mode)					ε^{40}Ca (I-MD)	± (2S.D.)
	$^{40}Ca/^{42}Ca$ (MD)	$^{40}Ca/^{44}Ca$ (MD)	± (2 S.D.)	$^{40}Ca/^{44}Ca$ (I-MD)	± (2 S.D.)		
Session 1 May 2014							
2014_05_09_Ca-LO764-3	151.00719	47.14595	1.96E-03	47.14513	1.59E-03	0.90	0.34
2014_05_09_Ca-PB-71	151.00569	47.14549	1.29E-03	47.14532	1.13E-03	0.94	0.24
2014_05_10_Ca-PB-53	151.01224	47.14753	1.82E-03	47.14752	1.39E-03	1.40	0.30
2014_05_12_Ca-MO359	151.01024	47.14691	1.62E-03	47.14762	1.37E-03	1.42	0.29
2014_05_12_Ca-MO79	151.00578	47.14552	1.99E-03	47.14593	1.47E-03	1.07	0.31
Session 1B May 2014							
2014_05_18_Ca-MO311	151.03269	47.15392	1.77E-03	47.15349	1.48E-03	0.42	0.31
2014_05_18_Ca-MO311b	151.03754	47.15543	1.70E-03	47.15520	1.48E-03	0.79	0.31
2014_05_24_Ca-MO311	151.03595	47.15493	1.51E-03	47.15479	1.34E-03	0.70	0.28
Session 2 July 2014							
2014_07_05_Ca-PB9-1	151.03168	47.15360	1.48E-03	47.15341	1.29E-03	0.41	0.27
2014_07_07_Ca-CA11169-1	151.02092	47.15024	1.45E-03	47.14977	1.20E-03	-0.36	0.25
2014_07_11_Ca-CA34606a	151.02741	47.15227	1.79E-03	47.15239	1.41E-03	0.19	0.30
2014_07_12_Ca-CA34606b	151.02905	47.15278	1.26E-03	47.15280	1.11E-03	0.28	0.23
2014_07_15_Ca-CA113130	151.03947	47.15603	1.46E-03	47.15586	1.30E-03	0.93	0.28
Session 3 September 2014							
2014_09_28_Ca-MO58-1	151.03778	47.15551	1.32E-03	47.15544	1.15E-03	1.17	0.24
2014_09_27_Ca-PB53-1	151.04101	47.15651	1.60E-03	47.15625	1.37E-03	1.35	0.29
2014_09_29_Ca-MO58-2	151.05498	47.16088	1.67E-03	47.16043	1.43E-03	2.23	0.30
2014_09_27_Ca-PB53-2	151.03029	47.15317	1.45E-03	47.15290	1.23E-03	0.63	0.26
2014_09_30_Ca-MO364-1	151.04250	47.15698	1.37E-03	47.15690	1.19E-03	1.48	0.25
2014_09_30_Ca-MO364-2	151.03933	47.15599	1.52E-03	47.15557	1.29E-03	1.20	0.27
Session 4 October 2014							
2014_10_03_Ca-PB53-3	151.04979	47.15926	1.60E-03	47.15892	1.37E-03	1.51	0.29
Session 6 April 2015							
2015_04_16_Ca-CA11103-2	151.03938	47.15600	1.66E-03	47.15624	1.43E-03	1.93	0.30
2015_04_20_Ca-CA111-69	151.01966	47.14985	1.91E-03	47.14986	1.46E-03	0.57	0.31
Session 7 July 2015							
2015_07_11_Ca-MO100	151.15480	47.19204	1.70E-03	47.19233	1.35E-03	7.97	0.29
2015_07_11_Ca-MO107	151.09649	47.17383	1.69E-03	47.17353	1.37E-03	3.98	0.29
2015_07_11_Ca-MO110	151.05048	47.15947	1.66E-03	47.15957	1.30E-03	1.02	0.28
2015_07_12_Ca-MO119	151.04864	47.15890	2.98E-03	47.15859	2.25E-03	0.81	0.48
2015_07_12_Ca-MO380	151.20082	47.20641	3.01E-03	47.20655	2.53E-03	10.98	0.54
2015_07_12_Ca-MO383	151.15141	47.19098	2.12E-03	47.19124	1.84E-03	7.74	0.39

Table 5.16 continued from previous page

	Corrected ratios (multidynamic mode)					ε^{40}Ca (I-MD)	± (2S.D.)
	$^{40}Ca/^{42}Ca$ (MD)	$^{40}Ca/^{44}Ca$ (MD)	± (2 S.D.)	$^{40}Ca/^{44}Ca$ (I-MD)	± (2 S.D.)		
2015_07_13_Ca-MO383	151.15016	47.19059	1.92E-03	47.19067	1.64E-03	7.61	0.35
2015_07_14_Ca-MO100	151.15134	47.19096	1.92E-03	47.19140	1.55E-03	7.77	0.33
2015_07_14_Ca-MO107	151.10464	47.17638	1.79E-03	47.17619	1.47E-03	4.55	0.31
2015_07_15_Ca-MO110	151.05105	47.15965	1.80E-03	47.15894	1.45E-03	0.89	0.31
2015_07_15_Ca-MO119	151.07295	47.16648	2.29E-03	47.16562	1.82E-03	2.30	0.39
2015_07_15_Ca-MO380	151.20139	47.20659	1.93E-03	47.20671	1.49E-03	11.02	0.31
Session 8 February 2016							
2016_02_07_Ca_MO503	151.03778	47.15551	2.69E-03	47.15554	2.48E-03	0.29	0.53
2016_02_19_Ca_CA15001	151.05350	47.16041	2.34E-03	47.16023	2.07E-03	1.28	0.44
2016_02_20_Ca_CA15005	151.04694	47.15837	2.48E-03	47.15919	2.06E-03	1.06	0.44
2016_02_21_Ca_CA15034	151.04494	47.15774	2.04E-03	47.15738	1.66E-03	0.68	0.35
2016_02_22_Ca_CA15008	151.08550	47.17040	2.07E-03	47.17049	1.74E-03	3.45	0.37
2016_02_22_Ca_CA15032	151.19655	47.20507	2.10E-03	47.20497	1.82E-03	10.77	0.39
2016_02_23_Ca_CA15036	151.05240	47.16007	1.96E-03	47.16007	1.77E-03	1.25	0.38
2016_03_01_Ca_CA15032	151.19534	47.20470	2.19E-03	47.20590	1.90E-03	10.97	0.40
2016_03_07_Ca_CA15030	151.05536	47.16099	3.48E-03	47.16036	2.88E-03	1.31	0.61

Table 5.17 – *Individual analysis analytical data for each sample analyzed in this study.*

	ε^{40}Ca (ST)	± (2 S.D.)	ε^{43}Ca (ST)	± (2 S.D.)	Mass Fract. Factor (‰)	Mass Fract. Rate (ppm s^{-1})	F	ΔR_C (ppm)
Session 1 May 2014								
2014_05_09_Ca-LO764-3	2.26	0.60	-0.51	0.96	0.14	0.14	1.000005	17.54
2014_05_09_Ca-PB-71	-1.90	0.38	-1.06	0.64	0.02	0.02	1.000001	3.59
2014_05_10_Ca-PB-53	-2.55	0.56	-2.61	0.93	0.04	0.04	1.000002	0.29
2014_05_12_Ca-MO359	-3.45	0.47	-1.85	0.75	-0.01	-0.01	1.000000	-15.01
2014_05_12_Ca-MO79	-4.23	0.50	-3.67	0.89	0.07	0.07	1.000003	-8.81
Session 1B May 2014								
2014_05_18_Ca-MO311	0.53	0.67	-0.66	0.91	0.25	0.27	1.000010	9.17
2014_05_18_Ca-MO311b	0.17	0.57	-0.81	0.77	0.21	0.23	1.000009	4.85
2014_05_24_Ca-MO311	-0.27	0.52	-0.97	0.64	0.12	0.12	1.000005	3.15
Session 2 July 2014								
2014_07_05_Ca-PB9-1	0.46	0.53	0.16	0.65	0.17	0.15	1.000006	4.10
2014_07_07_Ca-CA11169-1	-0.08	0.52	-0.22	0.65	0.24	0.22	1.000008	10.04
2014_07_11_Ca-CA34606a	-1.29	0.62	-1.16	0.86	0.25	0.22	1.000008	-2.68
2014_07_12_Ca-CA34606b	-1.08	0.48	0.79	0.64	0.22	0.20	1.000008	-0.39
2014_07_15_Ca-CA113130	0.98	0.53	0.43	0.66	0.19	0.17	1.000006	3.64
Session 3 September 2014								
2014_09_28_Ca-MO58-1	2.72	0.56	0.09	0.73	0.16	0.14	1.000006	1.39
2014_09_27_Ca-PB53-1	0.71	0.58	-0.62	0.61	0.31	0.28	1.000011	5.61
2014_09_29_Ca-MO58-2	0.56	0.58	-0.55	0.66	0.17	0.15	1.000006	9.44
2014_09_27_Ca-PB53-2	0.76	0.50	-0.87	0.64	0.15	0.13	1.000005	5.75
2014_09_30_Ca-MO364-1	1.86	0.55	-0.02	0.65	0.15	0.14	1.000005	1.71
2014_09_30_Ca-MO364-2	0.89	0.54	-0.88	0.65	0.27	0.24	1.000009	8.89
Session 4 October 2014								
2014_10_03_Ca-PB53-3	-1.67	0.51	-0.17	0.72	0.25	0.22	1.000009	7.05
Session 6 April 2015								
2015_04_16_Ca-CA11103-2	2.24	0.45	0.91	0.81	0.13	0.13	1.000005	-4.98
2015_04_20_Ca-CA111-69	1.57	0.58	0.59	1.04	-0.09	-0.08	0.999997	-0.33
Session 7 July 2015								
2015_07_11_Ca-MO100	6.83	0.58	-0.51	0.90	0.28	0.25	1.000010	-6.23
2015_07_11_Ca-MO107	3.40	0.60	-1.18	0.71	0.32	0.30	1.000011	6.51
2015_07_11_Ca-MO110	-0.37	0.55	-0.54	0.70	0.37	0.34	1.000013	-2.03
2015_07_12_Ca-MO119	0.22	0.99	-0.60	1.38	0.15	0.14	1.000005	6.43
2015_07_12_Ca-MO380	10.22	0.93	-0.66	1.24	1.04	0.95	1.000037	-2.93
2015_07_12_Ca-MO383	7.16	0.65	-0.16	1.23	-0.08	-0.08	0.999997	-5.54
2015_07_13_Ca-MO383	6.67	0.67	0.25	1.04	0.13	0.12	1.000004	-1.64

Table 5.17 continued from previous page

	ε^{40}Ca (ST)	± (2 S.D.)	ε^{43}Ca (ST)	± (2 S.D.)	Mass Fract. Factor (‰)	Mass Fract. Rate (ppm s^{-1})	F	ΔR_C (ppm)
2015_07_14_Ca-MO100	5.80	0.55	0.52	0.86	0.27	0.24	1.000009	-9.37
2015_07_14_Ca-MO107	3.45	0.58	-0.77	0.91	0.29	0.26	1.000010	3.95
2015_07_15_Ca-MO110	-1.77	0.55	-1.85	1.03	-0.26	-0.24	0.999991	15.02
2015_07_15_Ca-MO119	-0.71	0.58	-0.46	0.98	0.02	0.02	1.000001	18.37
2015_07_15_Ca-MO380	10.09	0.65	-0.07	0.85	0.16	0.14	1.000006	-2.65
Session 8 February 2016								
2016_02_07_Ca_MO503	0.45	0.69	1.11	1.22	0.19	-0.05	0.999998	-0.77
2016_02_19_Ca_CA15001	0.81	0.83	2.43	1.64	0.22	0.20	1.000008	3.84
2016_02_20_Ca_CA15005	1.11	0.74	-0.99	1.44	0.21	0.19	1.000007	-17.38
2016_02_21_Ca_CA15034	0.20	0.66	-0.61	1.13	0.19	0.17	1.000007	7.58
2016_02_22_Ca_CA15008	3.39	0.65	0.03	1.27	0.31	0.28	1.000011	-1.79
2016_02_22_Ca_CA15032	11.58	0.62	-1.00	1.07	0.07	0.07	1.000003	2.30
2016_02_23_Ca_CA15036	0.11	0.62	-0.56	1.07	0.41	0.38	1.000014	0.03
2016_03_01_Ca_CA15032	10.34	0.67	0.26	1.03	0.23	0.21	1.000008	-25.52
2016_03_07_Ca_CA15030	0.49	0.99	0.97	1.21	0.14	0.13	1.000005	13.36

Table 5.18 – *River sediment compositions from the TSS, HHC, and LH used to calculate formation K/Ca, Ca/Na, and Mg/K ratios.*

Sample	River	Type	SiO_2	Al_2O_3	Fe_2O_3	MnO	MgO	CaO	Na_2O	K_2O	TiO_2	P_2O_5	Pf	Total
HHC river sediments														
CA11212A <2mm	Khudi	Bank	73.94	11.51	3.80	0.05	1.77	1.86	1.90	2.03	0.43	0.13	2.49	99.92
CA10112B	Khudi	Bank	76.66	10.87	3.67	0.07	1.73	1.36	1.74	1.48	0.41	0.09	1.99	100.07
CA10112C	Khudi	Bank	67.40	14.64	7.33	0.21	2.13	2.29	1.29	2.08	0.52	0.23	1.82	99.96
CA952	Khudi	Bank (Lslide)	60.55	19.92	10.55	0.46	2.37	2.56	0.97	1.18	0.48	0.20	-0.05	99.16
CA950	Khudi	Bank (Lslide)	73.40	13.85	4.57	0.09	2.08	1.55	1.51	2.21	0.48	0.11	1.05	100.90
CA12005 <2mm	Khudi	Bank	73.07	12.82	4.31	0.07	1.90	1.46	1.64	2.14	0.46	0.10	1.15	99.12
CA947	Khudi	Bank (Lslide)	72.74	13.09	5.05	0.13	2.21	2.12	1.55	2.51	0.50	0.13	0.94	100.95
CA11103	Khudi	SL	64.40	14.87	6.62	0.08	3.41	1.98	1.40	3.59	0.82	0.19	2.93	100.28
CA970	Khudi	Bank (Cosmo)	72.01	11.45	4.72	0.06	2.94	1.31	1.56	1.99	0.61	0.12	3.39	100.14
CA 11007 B (sable)	Khudi	Bank	72.98	7.86	2.59	0.06	1.79	5.62	1.27	1.66	0.29	0.08	5.18	99.38
CA11204	Khudi	Bank	67.88	13.99	5.79	0.07	2.45	1.73	1.73	3.12	0.71	0.17	2.27	99.92
CA11011	Khudi	Bank	76.02	9.46	3.75	0.04	1.94	1.68	1.44	2.20	0.39	0.11	2.65	99.67
SKD10	Khudi	SL	58.64	16.95	7.94	0.08	3.82	1.57	1.54	4.20	0.96	0.17	4.11	99.98
SKD14	Khudi	SL	62.71	15.67	6.84	0.06	3.49	1.64	1.65	3.89	0.87	0.15	3.17	100.14
SKD20	Khudi	SL	71.58	12.62	4.40	0.04	2.18	1.49	1.58	2.73	0.57	0.10	1.92	99.21
SKD21	Khudi	SL	64.11	15.38	6.29	0.07	2.97	1.49	1.59	3.57	0.79	0.14	3.25	99.65
SKD22	Khudi	SL	68.49	13.42	5.36	0.06	2.75	1.46	1.50	3.14	0.70	0.10	2.34	99.32
SKD23	Khudi	SL	68.26	14.36	5.88	0.10	2.34	1.59	1.61	2.86	0.66	0.14	1.72	99.52
SKD24	Khudi	SL	66.37	14.94	6.02	0.07	2.67	1.46	1.68	3.37	0.76	0.14	2.15	99.63
SKD25	Khudi	SL	66.19	14.72	5.85	0.06	2.61	1.37	1.62	3.39	0.75	0.14	2.33	99.03
MAR-68	Khudi	BL	71.83	12.41	4.41	0.08	2.10	2.97	1.52	2.12	0.46	0.14	1.80	99.84
SKD30	Khudi	SL	70.74	12.62	4.74	0.08	2.13	1.33	1.47	2.51	0.55	0.09	2.36	98.62
SKD31	Khudi	SL	69.07	14.58	5.18	0.07	2.20	1.37	1.66	3.03	0.66	0.11	1.39	99.32
SKD32	Khudi	SL	69.09	14.49	5.30	0.07	2.29	1.38	1.69	3.01	0.68	0.11	1.41	99.52
SKD29	Khudi	SL	64.95	15.03	6.16	0.07	2.87	1.39	1.56	3.44	0.78	0.13	3.40	99.78
SKD34	Khudi	SL	64.64	15.03	6.39	0.07	3.03	1.52	1.57	3.37	0.79	0.14	2.83	99.38
SKD39F	Khudi	SL	67.29	14.36	5.71	0.07	2.64	1.50	1.61	3.19	0.71	0.13	2.55	99.76
SKD43	Khudi	SL	65.65	14.70	6.11	0.07	2.70	1.73	1.74	3.25	0.77	0.16	2.63	99.51
SKD51	Khudi	SL	68.61	13.94	5.34	0.07	2.42	1.52	1.49	2.91	0.67	0.12	2.14	99.23
SKD63	Khudi	SL	60.44	16.24	7.17	0.07	3.25	1.65	1.66	3.67	0.89	0.18	4.05	99.27
SKD70	Khudi	SL	65.75	14.51	5.90	0.07	2.70	1.73	1.72	3.13	0.76	0.16	2.65	99.08
SKD71	Khudi	SL	68.95	14.08	5.35	0.08	2.36	1.50	1.60	2.94	0.67	0.12	1.97	99.62
SKD79	Khudi	SL	69.16	13.92	5.45	0.10	2.32	1.61	1.57	2.64	0.62	0.11	1.78	99.28
SKD84	Khudi	SL	65.51	14.49	6.07	0.08	2.94	1.74	1.54	3.15	0.75	0.14	3.47	99.88
CA11100	Khudi	SL	67.77	14.06	5.74	0.08	2.55	2.00	1.62	3.13	0.69	0.19	1.95	99.78
CA11101	Khudi	SL	66.42	13.81	5.56	0.08	2.45	1.98	1.60	3.00	0.67	0.19	4.42	100.17
CA11102	Khudi	SL	68.40	14.05	5.73	0.09	2.51	2.03	1.62	3.07	0.68	0.18	2.25	100.60
CA11217	Khudi	Bank	73.42	12.60	4.77	0.11	1.62	1.80	1.55	2.09	0.45	0.13	1.27	99.79
CA15022 INT	Khudi	Bank	70.59	13.35	5.13	0.08	2.37	2.03	1.57	2.81	0.60	0.00	1.49	100.03
CA903	Khudi	Bank	69.36	14.34	7.16	0.26	1.72	2.00	1.46	1.68	0.42	0.16	0.62	99.17
CA11111	Khudi	SL	66.58	14.26	5.68	0.08	2.50	1.78	1.74	3.09	0.70	0.15	1.99	98.55

Table 5.18 continued from previous page

Sample	River	Type	SiO_2	Al_2O_3	Fe_2O_3	MnO	MgO	CaO	Na_2O	K_2O	TiO_2	P_2O_5	Pf	Total
CA11218 <2mm	Khudi	Bank	71.26	13.21	5.43	0.11	2.10	1.88	1.61	2.49	0.57	0.17	1.58	100.41
CA 934 <2mm	Khudi	Bank	74.06	12.24	4.44	0.05	1.97	1.23	1.51	2.29	0.47	0.10	1.74	100.09
CA 934 2-10mm	Khudi	Bank	66.96	13.80	6.50	0.07	3.16	1.29	1.47	3.27	0.73	0.14	1.79	99.18
CA 934 >10mm	Khudi	Bank	71.71	12.79	4.58	0.07	2.49	1.69	2.02	2.39	0.61	0.14	1.15	99.62
CA10111	Khudi	Bank	71.70	13.39	5.43	0.16	1.57	1.95	1.43	1.80	0.41	0.13	1.45	99.41
CA971	Khudi	Bank	78.28	9.46	2.94	0.03	1.65	1.06	1.67	1.23	0.39	0.09	2.00	98.81
CA11213A <2mm	Khudi	Bank	74.49	13.39	3.70	0.07	1.53	1.52	1.49	1.82	0.40	0.07	1.37	99.85
CA11215C	Khudi	Sand/Gravels	70.39	14.98	5.36	0.17	1.72	1.82	1.37	2.03	0.48	0.12	0.88	99.29
TSS from river sediments														
MAR-40	Sabche	BL	58.44	15.10	6.13	0.04	0.61	6.24	0.85	2.79	0.73	0.17	9.02	100.12
LO 100	Thini	Bank	44.76	10.10	3.94	0.03	1.95	19.24	0.72	2.16	0.53	0.14	16.14	99.70
NAG 25	Kali Gandaki	BL	44.62	11.92	4.51	0.03	1.15	16.97	0.71	2.20	0.61	0.16	16.85	99.73
LO 102	Kali Gandaki	BL	55.11	9.56	4.15	0.03	1.13	13.93	0.90	1.89	0.70	0.23	12.15	99.80
MO 501	Kali Gandaki	SL	38.06	9.97	3.55	0.03	1.76	22.66	0.87	2.22	0.47	0.21	20.14	99.94
NAG 29	Kali Gandaki	BL	49.24	6.48	3.30	0.07	1.07	21.03	0.82	1.40	0.33	0.15	15.89	99.78
NAG 31	Kali Gandaki	BL	53.40	7.41	2.52	0.02	1.01	18.09	0.99	1.78	0.30	0.12	14.03	99.67
NAG 33	Kali Gandaki	BL	51.15	8.12	3.21	0.02	1.29	17.96	0.96	1.79	0.43	0.13	14.67	99.73
NAG 36	Kali Gandaki	BL	42.35	10.89	3.87	0.03	1.59	19.37	0.92	2.34	0.48	0.14	17.77	99.75
NAG 22	Marsyandi	BL	43.33	15.41	5.60	0.04	2.10	13.07	0.51	3.72	0.80	0.16	14.95	99.69
MAR-50	Marsyandi	BL	50.97	9.13	2.95	0.03	1.58	17.24	1.46	2.31	0.38	0.06	13.42	99.53
MAR-51	Marsyandi	BL	54.41	11.65	3.83	0.03	1.97	14.26	1.84	2.77	0.46	0.09	8.54	99.85
LH from river sediments														
NAG 4	Bijaipur	BL	83.44	7.32	2.73	0.02	1.03	0.71	1.02	1.41	0.36	0.08	1.72	99.84
MO 112	Isul k.	BL	79.89	6.36	3.88	0.08	1.74	2.41	0.68	1.40	0.50	0.11	2.80	99.85
MO 102	Marsel k.	BL	81.82	8.82	2.98	0.00	1.25	0.02	0.82	1.96	0.33	0.08	1.80	99.89
MO 109	Mati k.	BL	85.18	7.19	2.34	0.02	1.04	0.10	1.07	1.60	0.27	0.17	1.00	99.88
MO 207	Andi	BL	78.27	6.04	2.66	0.06	2.46	2.49	0.16	2.19	0.39	0.13	5.15	100.00

Table 5.19 – *River sediment compositions from the TSS, HHC, and LH used to calculate formation K/Ca, Ca/Na, and Mg/K ratios.*

			mol/100g									
Sample	River	Type	Si	Al	Fe	Mn	Mg	Ca	Na	K	Ti	P
HHC river sediments												
CA11212A <2mm	Khudi	Bank	1.230282862	0.225686275	0.047534418	0.000768688	0.044019851	0.033190731	0.061322581	0.043142251	0.005394243	0.001832276
CA10112B	Khudi	Bank	1.275540765	0.213098039	0.045969962	0.000954866	0.043027295	0.024242424	0.05616129	0.031401274	0.005118899	0.001268499
CA10112C	Khudi	Bank	1.121464226	0.287058824	0.091727159	0.002954866	0.05292804	0.040891266	0.041741935	0.044203822	0.006533166	0.00324172
CA952	Khudi	Bank (Lslide)	1.007520799	0.390509804	0.132015019	0.006530324	0.058684864	0.045561497	0.031225806	0.025010616	0.005957447	0.002748414
CA950	Khudi	Bank (Lslide)	1.221364393	0.271529412	0.057133917	0.001260931	0.051712159	0.027682709	0.048774194	0.046963907	0.005982478	0.001508104
CA12005 <2mm	Khudi	Bank	1.215806988	0.251411765	0.053979975	0.001043724	0.047171216	0.025935829	0.053	0.045329087	0.005794743	0.001409443
CA947	Khudi	Bank (Lslide)	1.210232945	0.256686275	0.063204005	0.001813822	0.054888337	0.03771836	0.049903226	0.053227176	0.006220275	0.001832276
CA11103	Khudi	SL	1.071547421	0.291627451	0.082853567	0.001091678	0.084665012	0.035276292	0.04516129	0.076178344	0.010237797	0.002677942
CA970	Khudi	Bank (Cosmo)	1.198169717	0.224431373	0.05902378	0.00080677	0.073002481	0.023262032	0.050387097	0.042144374	0.007596996	0.001705426
CA 11007 B (sable)	Khudi	Bank	1.214309484	0.154098039	0.032377972	0.000860367	0.044292804	0.100178253	0.041064516	0.035244161	0.003617021	0.001127555
CA11204	Khudi	Bank	1.129450915	0.274352941	0.072465582	0.00103244	0.060843672	0.030909091	0.055870968	0.066305732	0.008911139	0.002396054
CA11011	Khudi	Bank	1.264891847	0.18545098	0.046908636	0.000593794	0.048114144	0.029946524	0.046387097	0.046794055	0.004831039	0.001550388
SKD10	Khudi	SL	0.975707155	0.332352941	0.099374218	0.00112835	0.094789082	0.02798574	0.049677419	0.089171975	0.012015019	0.002396054
SKD14	Khudi	SL	1.043427621	0.307254902	0.085607009	0.000846262	0.086600496	0.029233512	0.053225806	0.082590234	0.010888611	0.002114165
SKD20	Khudi	SL	1.191014975	0.24745098	0.055068836	0.000564175	0.054094293	0.026559715	0.050967742	0.057961783	0.007133917	0.001409443
SKD21	Khudi	SL	1.06672213	0.301568627	0.078723404	0.000987306	0.07369727	0.026559715	0.051290323	0.075796178	0.009887359	0.001973221
SKD22	Khudi	SL	1.139600666	0.263137255	0.067083855	0.000846262	0.068238213	0.026024955	0.048387097	0.066666667	0.008760951	0.001409443
SKD23	Khudi	SL	1.13577371	0.281568627	0.07359199	0.001410437	0.058064516	0.028342246	0.051935484	0.060721868	0.008260325	0.001973221
SKD24	Khudi	SL	1.104326123	0.292941176	0.07534418	0.000987306	0.066253102	0.026024955	0.054193548	0.071549894	0.00951189	0.001973221
SKD25	Khudi	SL	1.101331115	0.288627451	0.073216521	0.000846262	0.064764268	0.024420677	0.052258065	0.071974522	0.009386733	0.001973221
MAR-68	Khudi	BL	1.195174709	0.243333333	0.055193992	0.00112835	0.052109181	0.052941176	0.049032258	0.045010616	0.005757196	0.001973221
SKD30	Khudi	SL	1.17703827	0.24745098	0.059324155	0.00112835	0.052853598	0.023707665	0.047419355	0.05329087	0.006883605	0.001268499
SKD31	Khudi	SL	1.149251248	0.285882353	0.064831039	0.000987306	0.054590571	0.024420677	0.053548387	0.06433121	0.008260325	0.001550388
SKD32	Khudi	SL	1.149584027	0.284117647	0.066332916	0.000987306	0.056823821	0.02459893	0.054516129	0.063906582	0.008510638	0.001550388
SKD29	Khudi	SL	1.080698835	0.294705882	0.07709637	0.000987306	0.071215881	0.024777184	0.050322581	0.073036093	0.009762203	0.001832276
SKD34	Khudi	SL	1.075540765	0.294705882	0.079974969	0.000987306	0.075186104	0.027094474	0.050645161	0.071549894	0.009887359	0.001973221
SKD39F	Khudi	SL	1.119633943	0.281568627	0.07146433	0.000987306	0.065508685	0.026737968	0.051935484	0.067728238	0.008886108	0.001832276
SKD43	Khudi	SL	1.09234609	0.288235294	0.076470588	0.000987306	0.066997519	0.03083779	0.056129032	0.069002123	0.009637046	0.002255109
SKD51	Khudi	SL	1.141597338	0.273333333	0.066833542	0.000987306	0.060049628	0.027094474	0.048064516	0.061783439	0.008385482	0.001691332
SKD63	Khudi	SL	1.005657238	0.318431373	0.089737171	0.000987306	0.080645161	0.029411765	0.053548387	0.077919321	0.011138924	0.002536998
SKD70	Khudi	SL	1.094009983	0.284509804	0.073842303	0.000987306	0.066997519	0.03083779	0.055483871	0.066454352	0.00951189	0.002255109
SKD71	Khudi	SL	1.147254576	0.276078431	0.066958698	0.00112835	0.058560794	0.026737968	0.051612903	0.062420382	0.008385482	0.001691332
SKD79	Khudi	SL	1.150748752	0.272941176	0.068210263	0.001410437	0.057568238	0.028698752	0.050645161	0.056050955	0.0077597	0.001550388
SKD84	Khudi	SL	1.090016639	0.284117647	0.075969962	0.00112835	0.072952854	0.031016043	0.049677419	0.066878981	0.009386733	0.001973221
CA11100	Khudi	SL	1.127620632	0.275686275	0.071827284	0.001152327	0.063325062	0.035561497	0.052258065	0.066496815	0.008635795	0.002677942
CA11101	Khudi	SL	1.10515807	0.270784314	0.069599499	0.001122708	0.060719603	0.035276292	0.051677419	0.063715499	0.008385482	0.002677942
CA11102	Khudi	SL	1.138103161	0.275490196	0.07175219	0.001205924	0.062158809	0.036167558	0.052387097	0.065244161	0.008523154	0.002536998
CA11217	Khudi	Bank	1.221630616	0.247137255	0.059662078	0.001493653	0.040099256	0.032049911	0.049870968	0.044309979	0.005657071	0.001832276
CA15022 INT	Khudi	Bank	1.174542429	0.261686275	0.064242804	0.001174894	0.058883375	0.036185383	0.050741935	0.059660297	0.007484355	0
CA903	Khudi	Bank	1.154093178	0.281235294	0.089649562	0.003634697	0.042679901	0.035632799	0.046967742	0.035605096	0.005281602	0.002198732

Table 5.19 continued from previous page

			mol/100g									
Sample	River	Type	Si	Al	Fe	Mn	Mg	Ca	Na	K	Ti	P
CA11111	Khudi	SL	1.1078203	0.279607843	0.071126408	0.001080395	0.062084367	0.031693405	0.05616129	0.065583864	0.008760951	0.002114165
CA11218 <2mm	Khudi	Bank	1.185690516	0.258941176	0.06795995	0.001609309	0.052133995	0.033547237	0.051870968	0.052908705	0.007133917	0.002396054
CA 934 <2mm	Khudi	Bank	1.232279534	0.24	0.055519399	0.000760226	0.048833747	0.021889483	0.048774194	0.048683652	0.005882353	0.001409443
CA 934 2-10mm	Khudi	Bank	1.114143095	0.270627451	0.08135169	0.00100141	0.078337469	0.022959002	0.047548387	0.069341826	0.009186483	0.001973221
CA 934 >10mm	Khudi	Bank	1.193178037	0.250745098	0.057371715	0.000932299	0.0617866	0.030071301	0.065	0.050679406	0.00767209	0.001973221
CA10111	Khudi	Bank	1.193011647	0.262588235	0.067934919	0.002210155	0.038908189	0.03483066	0.045967742	0.038301486	0.005168961	0.001832276
CA971	Khudi	Bank	1.302545757	0.18554902	0.036770964	0.000466855	0.040918114	0.018966132	0.053741935	0.026178344	0.004906133	0.00124031
CA11213A <2mm	Khudi	Bank	1.239434276	0.262627451	0.046245307	0.000942172	0.037965261	0.027130125	0.048129032	0.038726115	0.005006258	0.00098661
CA11215C	Khudi	Sand/Gravels	1.171214642	0.293627451	0.067083855	0.002389281	0.042555831	0.032388592	0.044096774	0.043078556	0.005982478	0.001691332
TSS from river sediments												
MAR-40	Sabche	BL	0.972379368	0.296078431	0.076720901	0.000564175	0.015136476	0.111229947	0.027419355	0.059235669	0.009136421	0.002396054
LO 100	Thini	Bank	0.744758735	0.198039216	0.04931164	0.000423131	0.048387097	0.342959002	0.023225806	0.045859873	0.006633292	0.001973221
NAG 25	Kali Gandaki	BL	0.742429285	0.23372549	0.056445557	0.000423131	0.02853598	0.302495544	0.022903226	0.04670913	0.007634543	0.002255109
LO 102	Kali Gandaki	BL	0.917051465	0.187426789	0.051959735	0.000428455	0.028141214	0.248362155	0.029070879	0.040202267	0.008744443	0.003282504
MO 501	Kali Gandaki	SL	0.63327787	0.195490196	0.044430538	0.000423131	0.043672457	0.403921569	0.028064516	0.047133758	0.005882353	0.002959831
NAG 29	Kali Gandaki	BL	0.819301165	0.127058824	0.041301627	0.000987306	0.026550868	0.37486631	0.026451613	0.029723992	0.004130163	0.002114165
NAG 31	Kali Gandaki	BL	0.888519135	0.145294118	0.031539424	0.000282087	0.025062035	0.322459893	0.031935484	0.037791932	0.003754693	0.001691332
NAG 33	Kali Gandaki	BL	0.851081531	0.159215686	0.040175219	0.000282087	0.032009926	0.320142602	0.030967742	0.038004246	0.005381727	0.001832276
NAG 36	Kali Gandaki	BL	0.704658902	0.213529412	0.048435544	0.000423131	0.039454094	0.345276292	0.029677419	0.049681529	0.006007509	0.001973221
NAG 22	Marsyandi	BL	0.720965058	0.302156863	0.07008761	0.000564175	0.052109181	0.232976827	0.016451613	0.078980892	0.010012516	0.002255109
MAR-50	Marsyandi	BL	0.848086522	0.179019608	0.036921151	0.000423131	0.039205955	0.307308378	0.047096774	0.049044586	0.004755945	0.000845666
MAR-51	Marsyandi	BL	0.905324459	0.228431373	0.047934919	0.000423131	0.048883375	0.254188948	0.059354839	0.05881104	0.005757196	0.001268499
LH from river sediments												
NAG 4	Bijaipur	BL	1.388352745	0.143529412	0.03416771	0.000282087	0.025558313	0.012655971	0.032903226	0.029936306	0.004505632	0.001127555
MO 112	Isul k.	BL	1.329284526	0.124705882	0.048560701	0.00112835	0.043176179	0.042959002	0.021935484	0.029723992	0.006257822	0.001550388
MO 102	Marsel k.	BL	1.361397671	0.172941176	0.037296621	0	0.03101737	0.000356506	0.026451613	0.041613588	0.004130163	0.001127555
MO 109	Mati k.	BL	1.417304493	0.140980392	0.029286608	0.000282087	0.025806452	0.001782531	0.034516129	0.033970276	0.003379224	0.002396054
MO 207	Andi	BL	1.302329451	0.118431373	0.033291615	0.000846262	0.061042184	0.044385027	0.00516129	0.046496815	0.004881101	0.001832276

Table 5.20 – *River sediment compositions from the TSS, HHC, and LH used to calculate formation K/Ca, Ca/Na, and Mg/K ratios.*

Sample	River	Type	Ca/Na		Al/Si	Mg/K	K/Ca		CaO_{sil}	Ca_{sil}	CaO_{carb}	$CaCO_3$	Dol	Carb
			mol:mol						wt. %					
			No Carb Correction	Carb Correction			No Carb Correction	Carb Correction						
HHC river sediments														
CA11212A <2mm	Khudi	Bank	0.54		0.18	1.02	1.30							
CA10112B	Khudi	Bank	0.43		0.17	1.37	1.30							
CA10112C	Khudi	Bank	0.98		0.26	1.20	1.08							
CA952	Khudi	Bank (Lslide)	1.46		0.39	2.35	0.55							
CA950	Khudi	Bank (Lslide)	0.57		0.22	1.10	1.70							
CA12005 <2mm	Khudi	Bank	0.49		0.21	1.04	1.75							
CA947	Khudi	Bank (Lslide)	0.76		0.21	1.03	1.41							
CA11103	Khudi	SL	0.78		0.27	1.11	2.16							
CA970	Khudi	Bank (Cosmo)	0.46		0.19	1.73	1.81							
CA 11007 B (sable)	Khudi	Bank	2.44		0.13	1.26	0.35							
CA11204	Khudi	Bank	0.55		0.24	0.92	2.15							
CA11011	Khudi	Bank	0.65		0.15	1.03	1.56							
SKD10	Khudi	SL	0.56	0.52	0.34	1.06	3.19	3.42	1.46	0.03		0.12	0.14	
SKD14	Khudi	SL	0.55	0.52	0.29	1.05	2.83	3.01	1.54	0.03		0.11	0.13	
SKD20	Khudi	SL	0.52	0.48	0.21	0.93	2.18	2.36	1.38	0.02		0.13	0.13	0.04
SKD21	Khudi	SL	0.52	0.48	0.28	0.97	2.85	3.07	1.39	0.02		0.12	0.13	
SKD22	Khudi	SL	0.54	0.50	0.23	1.02	2.56	2.74	1.36	0.02		0.11	0.12	
SKD23	Khudi	SL	0.55	0.50	0.25	0.96	2.14	2.33	1.46	0.03		0.13	0.20	0.07
SKD24	Khudi	SL	0.48	0.45	0.27	0.93	2.75	2.95	1.36	0.02		0.11	0.13	0.03
SKD25	Khudi	SL	0.47	0.43	0.26	0.90	2.95	3.18	1.27	0.02		0.11	0.14	0.09
MAR-68	Khudi	BL	1.08	0.71	0.20	1.16	0.85	1.30	1.95	0.03		1.50	0.64	2.14
SKD30	Khudi	SL	0.50	0.49	0.21	0.99	2.25	2.29	1.31	0.02		0.03	0.02	0.09
SKD31	Khudi	SL	0.46	0.39	0.25	0.85	2.63	3.07	1.18	0.02		0.12	0.44	0.10
SKD32	Khudi	SL	0.45	0.43	0.25	0.89	2.60	2.71	1.32	0.02		0.03	0.14	
SKD29	Khudi	SL	0.49		0.27	0.98	2.95							
SKD34	Khudi	SL	0.53		0.27	1.05	2.64							
SKD39F	Khudi	SL	0.51		0.25	0.97	2.53							0.04
SKD43	Khudi	SL	0.55		0.26	0.97	2.24							
SKD51	Khudi	SL	0.56		0.24	0.97	2.28							
SKD63	Khudi	SL	0.55		0.32	1.03	2.65							
SKD70	Khudi	SL	0.56		0.26	1.01	2.15							0.04
SKD71	Khudi	SL	0.52		0.24	0.94	2.33							
SKD79	Khudi	SL	0.57		0.24	1.03	1.95							0.14
SKD84	Khudi	SL	0.62		0.26	1.09	2.16							
CA11100	Khudi	SL	0.68		0.24	0.95	1.87							0.13
CA11101	Khudi	SL	0.68		0.25	0.95	1.81							
CA11102	Khudi	SL	0.69		0.24	0.95	1.80							
CA11217	Khudi	Bank	0.64		0.20	0.90	1.38							

Table 5.20 continued from previous page

Sample	River	Type		Ca/Na		Al/Si	Mg/K	K/Ca		CaO_{sil}	Ca_{sil}	CaO_{carb}	$CaCO_3$	Dol	Carb
				mol:mol						wt. %					
				No Carb Correction	Carb Correction			No Carb Correction	Carb Correction						
CA15022 INT	Khudi	Bank		0.71		0.22	0.99	1.65							
CA903	Khudi	Bank		0.76		0.24	1.20	1.00							
CA11111	Khudi	SL		0.56		0.25	0.95	2.07							0.19
CA11218 <2mm	Khudi	Bank		0.65		0.22	0.99	1.58							
CA 934 <2mm	Khudi	Bank		0.45		0.19	1.00	2.22							
CA 934 2-10mm	Khudi	Bank		0.48		0.24	1.13	3.02							
CA 934 >10mm	Khudi	Bank		0.46		0.21	1.22	1.69							
CA10111	Khudi	Bank		0.76		0.22	1.02	1.10							
CA971	Khudi	Bank		0.35		0.14	1.56	1.38							
CA11213A <2mm	Khudi	Bank		0.56		0.21	0.98	1.43							
CA11215C	Khudi	Sand/Gravels		0.73		0.25	0.99	1.33							
			Average	**0.62**	***0.49***	**0.24**	***1.04***	**1.81**	***2.65***						
			STDEV	**0.24**	***0.07***	**0.05**	***0.36***	**0.83**	***0.61***						
			Median	**0.52**	***0.49***	**0.25**	***0.96***	**2.62**	***2.85***						
TSS river sediments															
MAR-40	Sabche	BL		4.06	0.24	0.30	0.26	0.53	8.91	0.37	0.01	6.34	9.58	1.74	11.32
LO 100	Thini	Bank		14.77	0.51	0.27	1.06	0.13	3.86	0.67	0.01	20.10	30.27	5.62	35.89
NAG 25	Kali Gandaki	BL		13.21	0.63	0.31	0.61	0.15	3.22	0.81	0.01	16.58	28.04	1.57	29.61
LO 102	Kali Gandaki	BL		8.54	0.33	0.20	0.70	0.16	4.21	0.54	0.01	13.92	22.92	1.94	24.86
MO 501	Kali Gandaki	SL		14.39	0.56	0.31	0.93	0.12	2.98	0.89	0.02	22.55	37.40	2.87	40.27
NAG 29	Kali Gandaki	BL		14.17	0.67	0.16	0.89	0.08	1.68	0.99	0.02	20.79	34.34	2.78	37.13
NAG 31	Kali Gandaki	BL		10.10	0.36	0.16	0.66	0.12	3.31	0.64	0.01	18.14	29.86	2.53	32.38
NAG 33	Kali Gandaki	BL		10.34	0.36	0.19	0.84	0.12	3.42	0.62	0.01	18.33	29.07	3.67	32.73
NAG 36	Kali Gandaki	BL		11.63	0.72	0.30	0.79	0.14	2.31	1.20	0.02	19.01	30.84	3.11	33.95
NAG 22	Marsyandi	BL		14.16	0.55	0.42	0.66	0.34	8.68	0.51	0.01	13.81	20.05	4.60	24.66
MAR-50	Marsyandi	BL		6.53	0.68	0.21	0.80	0.16	1.54	1.78	0.03	16.13	26.32	2.48	28.80
MAR-51	Marsyandi	BL		4.28	1.39	0.25	0.83	0.23	0.71	4.63	0.08	9.91	16.65	1.05	17.70
			Average	**0.10**	***0.65***	**0.26**	***0.73***	**0.16**	***2.39***						
			STDEV	**0.03**	***0.71***	**0.08**	***0.31***	**0.06**	***2.52***						
			Median	**10.99**	***0.56***	**0.26**	***0.80***	**0.15**	***3.27***						
LH river sediments															
NAG 4	Bijaipur	BL		0.38	0.24	0.10	0.85	2.37	3.81	0.44	0.01	0.37	0.30	0.36	0.65
MO 112	Isul k.	BL		1.96	0.55	0.09	1.45	0.69	2.47	0.68	0.01	2.38	1.86	2.39	4.26
MO 102	Marsel k.	BL		0.01	0.01	0.13	0.75	116.73	125.47	0.02	0.00	0.00	0.00	0.00	0.00
MO 109	Mati k.	BL		0.05	0.05	0.10	0.76	19.06	20.73	0.09	0.00	0.01	0.01	0.01	0.02
MO 207	Andi	BL		8.60	0.75	0.09	1.31	1.05	12.02	0.22	0.00	3.86	1.04	5.87	6.90
			Average	**0.84**	***0.21***	**0.10**	***1.03***	**1.78**	***7.06***						

Table 5.20 continued from previous page

Sample	River	Type		Ca/Na		Al/Si	Mg/K	K/Ca		CaO_{sil}	Ca_{sil}	CaO_{carb}	$CaCO_3$	Dol	Carb
				mol:mol						wt. %					
				No Carb Correction	Carb Correction			No Carb Correction	Carb Correction						
			STDEV	**0.99**	***0.22***	**0.01**	***0.46***	**1.87**	***6.73***						
			Median	**0.38**	***0.24***	**0.10**	***0.85***	**2.37**	***12.02***						

Table 5.21 – *Compositions of LH whoe rock.*

Sample	SiO_2	Al_2O3	Fe_2O_3	MnO	MgO	CaO	Na_2O	K_2O	TiO_2	P_2O_5	Pf	Total	Si	Al	Fe	Mn	Mg	Ca	Na	K	Ti	P	K/Ca	Ca/Na	Mg/K
							wt. %										mol/100g							mol:mol	
AP007	74.77	11.53	4.37	0.05	1.83	0.01	0.64	2.43	0.41	0.00	2.71	98.75	1.24	0.23	0.05	0.00	0.05	0.00	0.02	0.05	0.01	0.00	289.43	0.01	0.88
AP023	95.47	0.93	1.75	0.03	0.41	0.01	0.00	0.04	0.00	0.00	0.94	99.58	1.59	0.02	0.02	0.00	0.01	0.00	0.00	0.00	0.00	0.00	4.76		11.98
AP407	62.67	18.22	6.39	0.08	2.38	0.07	0.36	5.89	0.85	0.00	3.36	100.27	1.04	0.36	0.08	0.00	0.06	0.00	0.01	0.13	0.01	0.00	100.22	0.11	0.47
AP545	78.33	9.75	4.20	0.06	1.34	0.01	0.14	2.38	0.43	0.00	2.14	98.78	1.30	0.19	0.05	0.00	0.03	0.00	0.00	0.05	0.01	0.00	283.48	0.04	0.66
AP546	62.40	19.34	5.84	0.06	1.81	0.01	0.16	5.48	0.52	0.00	3.88	99.50	1.04	0.38	0.07	0.00	0.04	0.00	0.01	0.12	0.01	0.00	652.71	0.03	0.39
AP990	56.35	22.11	7.59	0.05	2.81	0.01	0.33	5.96	0.57	0.00	4.26	100.04	0.94	0.43	0.09	0.00	0.07	0.00	0.01	0.13	0.01	0.00	709.89	0.02	0.55
AP991	74.15	11.61	5.98	0.06	2.32	0.01	0.94	2.37	0.35	0.00	2.55	100.34	1.23	0.23	0.07	0.00	0.06	0.00	0.03	0.05	0.00	0.00	282.29	0.01	1.14
AP994	46.05	14.01	14.43	0.19	6.78	2.30	2.43	2.36	1.13	0.00	9.93	99.61	0.77	0.27	0.18	0.00	0.17	0.04	0.08	0.05	0.01	0.00	1.22	0.52	3.36
BE127	85.73	7.55	1.75	0.02	0.52	0.07	1.78	1.84	0.22	0.00	0.86	100.34	1.43	0.15	0.02	0.00	0.01	0.00	0.06	0.04	0.00	0.00	31.31	0.02	0.33
BE30	59.58	20.65	5.77	0.03	2.86	0.01	0.19	5.95	0.91	0.00	4.33	100.28	0.99	0.40	0.07	0.00	0.07	0.00	0.01	0.13	0.01	0.00	708.69	0.03	0.56
E206	66.49	16.26	5.71	0.03	1.94	0.19	0.74	3.35	0.56	0.00	3.22	98.49	1.11	0.32	0.07	0.00	0.05	0.00	0.02	0.07	0.01	0.00	21.00	0.14	0.68
L81	76.50	11.43	3.04	0.04	0.99	0.42	1.49	2.74	0.31	0.00	1.94	98.90	1.27	0.22	0.04	0.00	0.02	0.01	0.05	0.06	0.00	0.00	7.77	0.16	0.42
L82	53.18	23.87	5.81	0.06	2.29	0.01	0.68	7.08	0.50	0.00	4.50	97.98	0.88	0.47	0.07	0.00	0.06	0.00	0.02	0.15	0.01	0.00	843.29	0.01	0.38
LS108	56.22	22.25	7.72	0.15	2.71	1.43	1.37	3.72	0.75	0.00	3.85	100.17	0.94	0.44	0.10	0.00	0.07	0.03	0.04	0.08	0.01	0.00	3.10	0.58	0.85
LS126	57.53	17.11	9.47	0.10	3.01	2.89	0.97	4.44	0.85	0.00	2.47	98.84	0.96	0.34	0.12	0.00	0.07	0.05	0.03	0.09	0.01	0.00	1.83	1.65	0.79
LS131	84.03	4.30	3.17	0.03	3.99	0.04	0.00	0.41	0.36	0.00	2.09	98.42	1.40	0.08	0.04	0.00	0.10	0.00	0.00	0.01	0.00	0.00	12.21		11.37
LS151	57.60	17.77	11.93	0.09	1.88	0.76	1.05	5.02	1.29	0.00	2.77	100.16	0.96	0.35	0.15	0.00	0.05	0.01	0.03	0.11	0.02	0.00	7.87	0.40	0.44
LS152	71.37	8.06	8.72	0.07	5.39	0.17	0.12	0.69	0.85	0.00	3.18	98.62	1.19	0.16	0.11	0.00	0.13	0.00	0.00	0.01	0.01	0.00	4.83	0.78	9.13
LS153	59.18	16.54	10.49	0.14	3.04	1.82	1.12	2.98	0.89	0.00	2.96	99.16	0.98	0.32	0.13	0.00	0.08	0.03	0.04	0.06	0.01	0.00	1.95	0.90	1.19
LS22	73.25	13.14	3.25	0.03	2.61	0.46	5.03	0.26	0.56	0.00	1.78	100.37	1.22	0.26	0.04	0.00	0.06	0.01	0.16	0.01	0.01	0.00	0.67	0.05	11.73
NL4	53.60	24.36	6.95	0.05	2.55	0.01	0.29	6.78	0.72	0.25	4.55	100.11	0.89	0.48	0.09	0.00	0.06	0.00	0.01	0.14	0.01	0.00	807.55	0.02	0.44
NL3	80.71	9.33	2.59	0.04	0.51	0.25	1.11	3.53	0.35	0.10	1.23	99.75	1.34	0.18	0.03	0.00	0.01	0.00	0.04	0.07	0.00	0.00	16.82	0.12	0.17
75668	74.87	13.12	2.08	0.04	0.54	0.47	3.07	4.10	0.32	1.53	0.00	100.14	1.25	0.26	0.03	0.00	0.01	0.01	0.10	0.09	0.00	0.02	10.39	0.08	0.15
75836	73.77	15.10	1.60	0.02	0.42	0.85	5.32	2.08	0.20	0.60	0.00	99.96	1.23	0.30	0.02	0.00	0.01	0.02	0.17	0.04	0.00	0.01	2.91	0.09	0.24
75846	73.26	14.39	2.01	0.04	0.85	0.15	4.21	3.29	0.26	1.03	0.00	99.49	1.22	0.28	0.03	0.00	0.02	0.00	0.14	0.07	0.00	0.01	26.12	0.02	0.30
E015	73.46	12.84	2.37	0.06	0.35	0.89	2.51	5.08	0.26	1.26	0.00	99.08	1.22	0.25	0.03	0.00	0.01	0.02	0.08	0.11	0.00	0.02	6.80	0.20	0.08
E56	76.00	12.99	1.18	0.02	0.94	0.01	3.89	2.62	0.14	1.56	0.00	99.35	1.26	0.25	0.01	0.00	0.02	0.00	0.13	0.06	0.00	0.02	312.06	0.00	0.42
J09L	76.35	13.80	1.34	0.03	0.31	0.36	4.76	1.89	0.10	0.99	0.00	99.93	1.27	0.27	0.02	0.00	0.01	0.01	0.15	0.04	0.00	0.01	6.25	0.04	0.19
Lb5	73.42	12.87	2.11	0.01	0.64	0.40	2.62	5.33	0.26	1.57	0.00	99.23	1.22	0.25	0.03	0.00	0.02	0.01	0.08	0.11	0.00	0.02	15.87	0.08	0.14
U21	73.55	13.69	1.92	0.04	0.56	0.36	2.61	4.98	0.29	1.29	0.00	99.29	1.22	0.27	0.02	0.00	0.01	0.01	0.08	0.11	0.00	0.02	16.48	0.08	0.13
	77.92	12.85	0.99	0.02	0.54	0.01	4.88	1.70	0.12	1.12	0.00	100.15	1.30	0.25	0.01	0.00	0.01	0.00	0.16	0.04	0.00	0.02	202.48	0.00	0.37
AL049	80.69	9.05	2.64	0.04	1.14	0.08	1.52	2.06	0.45	0.00	1.61	99.28	1.34	0.18	0.03	0.00	0.03	0.00	0.05	0.04	0.01	0.00	30.67	0.03	0.65
AL068	84.56	7.13	1.85	0.03	0.56	0.11	1.03	2.31	0.31	0.00	1.17	99.06	1.41	0.14	0.02	0.00	0.01	0.00	0.03	0.05	0.00	0.00	25.01	0.06	0.28
AL071	86.80	5.76	1.83	0.06	0.31	0.07	0.61	1.94	0.31	0.00	1.06	98.75	1.44	0.11	0.02	0.00	0.01	0.00	0.02	0.04	0.00	0.00	33.01	0.06	0.19
AL185	84.58	7.64	1.89	0.04	0.45	0.15	1.12	2.43	0.42	0.00	1.04	99.76	1.41	0.15	0.02	0.00	0.01	0.00	0.04	0.05	0.01	0.00	19.30	0.07	0.22
AL39	82.01	8.86	2.40	0.03	1.16	0.57	1.67	1.49	0.40	0.00	1.40	99.99	1.36	0.17	0.03	0.00	0.03	0.01	0.05	0.03	0.01	0.00	3.11	0.19	0.91
AP167	77.16	10.69	3.04	0.03	1.34	0.15	1.62	1.91	0.63	0.00	2.70	99.27	1.28	0.21	0.04	0.00	0.03	0.00	0.05	0.04	0.01	0.00	15.17	0.05	0.82
AP198	85.35	7.72	1.67	0.07	0.91	0.21	1.11	1.84	0.48	0.00	1.11	100.47	1.42	0.15	0.02	0.00	0.02	0.00	0.04	0.04	0.01	0.00	10.44	0.10	0.58
AP440	84.78	6.89	1.88	0.05	0.44	0.39	1.16	1.92	0.36	0.00	0.92	98.79	1.41	0.14	0.02	0.00	0.01	0.01	0.04	0.04	0.00	0.00	5.86	0.19	0.27
AP454	81.28	9.55	2.45	0.08	1.15	0.35	1.25	2.12	0.40	0.00	1.52	100.15	1.35	0.19	0.03	0.00	0.03	0.01	0.04	0.05	0.01	0.00	7.21	0.15	0.63
AP834	80.10	9.76	3.20	0.02	0.80	0.01	1.46	2.55	0.50	0.00	1.10	99.50	1.33	0.19	0.04	0.00	0.02	0.00	0.05	0.05	0.01	0.00	303.73	0.00	0.37

Table 5.21 continued from previous page

Sample	SiO_2	Al_2O3	Fe_2O_3	MnO	MgO	CaO	Na_2O	K_2O	TiO_2	P_2O_5	Pf	Total	Si	Al	Fe	Mn	Mg	Ca	Na	K	Ti	P	K/Ca	Ca/Na	Mg/K
						wt. %											mol/100g							mol:mol	
AP835	79.17	10.33	2.79	0.03	0.43	0.55	1.58	3.37	TR	0.90	0.00	99.15	1.32	0.20	0.03	0.00	0.01	0.01	0.05	0.07	0.01	0.01	7.30	0.19	0.15
E68	85.29	7.64	1.69	0.03	0.25	0.25	1.23	2.62	0.28	0.00	0.83	100.11	1.42	0.15	0.02	0.00	0.01	0.00	0.04	0.06	0.00	0.00	12.48	0.11	0.11
AL169	77.79	10.95	3.95	0.03	1.27	0.01	0.22	3.05	0.47	0.00	2.44	100.18	1.29	0.21	0.05	0.00	0.03	0.00	0.01	0.06	0.01	0.00	363.28	0.03	0.49
AL214	65.89	16.23	4.80	0.02	1.99	0.01	0.06	4.98	0.72	0.00	3.89	98.59	1.10	0.32	0.06	0.00	0.05	0.00	0.00	0.11	0.01	0.00	593.16	0.09	0.47
AL44	75.02	12.98	3.93	0.05	1.39	0.27	0.80	3.12	0.45	0.00	2.48	100.49	1.25	0.25	0.05	0.00	0.03	0.00	0.03	0.07	0.01	0.00	13.76	0.19	0.52
AP13	81.03	9.69	2.53	0.03	1.40	0.01	0.14	3.03	0.37	0.00	1.97	100.20	1.35	0.19	0.03	0.00	0.03	0.00	0.00	0.06	0.00	0.00	360.90	0.04	0.54
AP136	82.88	7.78	2.31	0.02	0.75	0.01	0.26	3.00	0.35	0.00	1.33	98.69	1.38	0.15	0.03	0.00	0.02	0.00	0.01	0.06	0.00	0.00	357.32	0.02	0.29
AP385	62.47	19.35	6.94	0.02	1.89	0.01	0.52	5.19	0.46	0.00	3.26	100.11	1.04	0.38	0.09	0.00	0.05	0.00	0.02	0.11	0.01	0.00	618.17	0.01	0.43
AP390	64.69	18.09	5.44	0.02	1.51	0.01	0.18	4.88	0.56	0.00	4.72	100.10	1.08	0.35	0.07	0.00	0.04	0.00	0.01	0.10	0.01	0.00	581.25	0.03	0.36
AP537	77.06	10.29	4.84	0.07	0.97	0.01	0.35	3.08	0.42	0.00	2.15	99.24	1.28	0.20	0.06	0.00	0.02	0.00	0.01	0.07	0.01	0.00	366.85	0.02	0.37
AP843	72.95	13.18	4.82	0.03	2.03	0.01	0.80	3.48	0.41	0.00	2.20	99.91	1.21	0.26	0.06	0.00	0.05	0.00	0.03	0.07	0.01	0.00	414.50	0.01	0.68
AP857	82.78	8.84	2.45	0.03	0.87	0.01	0.48	2.60	0.38	0.00	1.27	99.71	1.38	0.17	0.03	0.00	0.02	0.00	0.02	0.06	0.00	0.00	309.68	0.01	0.39
AP888	72.20	14.44	4.32	0.03	1.79	0.10	1.02	3.36	0.50	0.00	2.71	100.47	1.20	0.28	0.05	0.00	0.04	0.00	0.03	0.07	0.01	0.00	40.02	0.05	0.62
AP9	81.13	8.52	3.11	0.02	1.58	0.01	0.05	2.32	0.21	0.00	2.14	99.09	1.35	0.17	0.04	0.00	0.04	0.00	0.00	0.05	0.00	0.00	276.33	0.11	0.80
AP826	97.85	1.04	0.49		0.11	0.01		0.30	0.16	0.00	0.28	100.24	1.63	0.02	0.01	0.00	0.00	0.00	0.00	0.01	0.00	0.00	35.73		0.43
AP828	90.14	4.46	2.32	0.02	0.82	0.01	0.00	1.04	0.27	0.00	0.83	99.91	1.50	0.09	0.03	0.00	0.02	0.00	0.00	0.02	0.00	0.00	123.87		0.92
AL54	47.70	14.48	12.80	0.13	13.26	0.23	0.02	0.52	2.57	0.00	8.30	100.01	0.79	0.28	0.16	0.00	0.33	0.00	0.00	0.01	0.03	0.00	2.69	6.35	29.80
AP425	44.69	14.97	13.73	0.06	14.81	0.01	0.01	0.44	1.94	0.00	7.97	98.63	0.74	0.29	0.17	0.00	0.37	0.00	0.00	0.01	0.02	0.00	52.41	0.55	39.34
AP559	58.42	19.26	10.08	0.13	1.93	0.01	0.36	3.97	1.12	0.00	4.58	99.86	0.97	0.38	0.13	0.00	0.05	0.00	0.01	0.08	0.01	0.00	472.86	0.02	0.57
AP589	63.49	14.59	9.73	0.04	2.71	0.02	0.16	4.60	1.09	0.00	3.05	99.48	1.06	0.29	0.12	0.00	0.07	0.00	0.01	0.10	0.01	0.00	273.95	0.07	0.69
AP590	61.84	16.63	3.95	0.05	7.16	0.04	0.15	4.05	1.18	0.00	4.82	99.87	1.03	0.33	0.05	0.00	0.18	0.00	0.00	0.09	0.01	0.00	120.60	0.15	2.07
AP603	57.35	17.41	11.29	0.04	3.22	0.10	0.18	5.14	1.26	0.00	3.58	99.57	0.95	0.34	0.14	0.00	0.08	0.00	0.01	0.11	0.02	0.00	61.22	0.31	0.73
E112	41.84	14.78	17.64	0.06	13.58	0.09	0.08	0.00	3.05	0.00	7.64	98.76	0.70	0.29	0.22	0.00	0.34	0.00	0.00	0.00	0.04	0.00	0.00	0.62	
AL174	62.45	19.76	5.57	0.03	2.10	0.01	0.33	5.42	0.61	0.00	3.77	100.05	1.04	0.39	0.07	0.00	0.05	0.00	0.01	0.12	0.01	0.00	645.57	0.02	0.45
AL212	75.50	11.46	4.26	0.02	1.54	0.01	0.02	3.21	0.48	0.00	3.06	99.56	1.26	0.22	0.05	0.00	0.04	0.00	0.00	0.07	0.01	0.00	382.34	0.28	0.56
AP199	53.81	23.32	9.86	0.15	2.23	1.04	0.98	4.75	1.14	0.00	2.96	100.24	0.90	0.46	0.12	0.00	0.06	0.02	0.03	0.10	0.01	0.00	5.44	0.59	0.55
AP334	56.99	22.56	7.72	0.11	2.45	0.08	0.97	4.79	0.66	0.00	3.84	100.17	0.95	0.44	0.10	0.00	0.06	0.00	0.03	0.10	0.01	0.00	71.32	0.05	0.60
AP375	73.56	13.55	4.25	0.02	1.32	0.48	0.92	3.39	0.13	0.00	2.15	99.77	1.22	0.27	0.05	0.00	0.03	0.01	0.03	0.07	0.00	0.00	8.41	0.29	0.46
AP417	54.42	23.47	6.34	0.07	0.95	0.01	0.33	6.99	0.37	0.00	5.48	98.43	0.91	0.46	0.08	0.00	0.02	0.00	0.01	0.15	0.00	0.00	832.57	0.02	0.16
AP447	54.48	22.63	6.71	0.05	3.62	0.25	1.06	4.99	0.52	0.00	5.04	99.35	0.91	0.44	0.08	0.00	0.09	0.00	0.03	0.11	0.01	0.00	23.77	0.13	0.85
AP524	56.22	22.18	8.56	0.11	2.65	0.01	0.70	5.44	0.70	0.00	3.78	100.35	0.94	0.43	0.11	0.00	0.07	0.00	0.02	0.12	0.01	0.00	647.95	0.01	0.57
AP657	57.77	21.98	7.76	0.09	2.80	0.23	0.64	4.98	0.70	0.00	2.67	99.62	0.96	0.43	0.10	0.00	0.07	0.00	0.02	0.11	0.01	0.00	25.79	0.20	0.66
AP874	55.39	24.47	5.77	0.06	1.55	0.01	0.49	6.96	0.50	0.00	4.81	100.01	0.92	0.48	0.07	0.00	0.04	0.00	0.02	0.15	0.01	0.00	828.99	0.01	0.26
AP969	64.35	17.80	6.12	0.04	1.61	0.01	0.09	4.55	0.63	0.00	4.06	99.26	1.07	0.35	0.08	0.00	0.04	0.00	0.00	0.10	0.01	0.00	541.94	0.06	0.41
AP972	64.09	16.91	8.29	0.03	1.61	0.01	0.04	4.21	0.89	0.00	4.42	100.50	1.07	0.33	0.10	0.00	0.04	0.00	0.00	0.09	0.01	0.00	501.45	0.14	0.45
E211	65.53	18.00	4.33	0.03	2.60	0.01	0.44	4.80	0.58	0.00	3.77	100.09	1.09	0.35	0.05	0.00	0.06	0.00	0.01	0.10	0.01	0.00	571.72	0.01	0.63
AP197	93.09	3.49	0.84	0.03	0.39	0.01	0.39	0.76	0.17	0.00	0.60	99.77	1.55	0.07	0.01	0.00	0.01	0.00	0.01	0.02	0.00	0.00	90.52	0.01	0.60
AP592	95.41	1.53	0.58	0.02	0.43	0.01	0.04	0.37	0.10	0.00	0.47	98.96	1.59	0.03	0.01	0.00	0.01	0.00	0.00	0.01	0.00	0.00	44.07	0.14	1.36
AP601	96.86	1.38	0.46	0.00	0.26	0.01	0.05	0.30	0.10	0.00	0.68	100.10	1.61	0.03	0.01	0.00	0.01	0.00	0.00	0.01	0.00	0.00	35.73	0.11	1.01
AP838	72.36	14.49	1.42	0.00	3.45	0.01	0.23	3.73	0.30	0.00	3.05	99.04	1.20	0.28	0.02	0.00	0.09	0.00	0.01	0.08	0.00	0.00	444.27	0.02	1.08
AP862	93.85	3.17	1.06	0.03	0.46	0.01	0.16	1.16	0.20	0.00	0.21	100.31	1.56	0.06	0.01	0.00	0.01	0.00	0.01	0.02	0.00	0.00	138.17	0.03	0.46
AP955	83.53	8.03	1.63	0.02	1.25	0.01	0.83	1.36	0.42	0.00	2.00	99.08	1.39	0.16	0.02	0.00	0.03	0.00	0.03	0.03	0.01	0.00	161.99	0.01	1.07

Table 5.21 continued from previous page

Sample	SiO_2	Al_2O3	Fe_2O_3	MnO	MgO	CaO	Na_2O	K_2O	TiO_2	P_2O_5	Pf	Total	Si	Al	Fe	Mn	Mg	Ca	Na	K	Ti	P	K/Ca	Ca/Na	Mg/K
						wt. %											mol/100g							mol:mol	
AP253	68.52	14.24	5.15	0.13	1.97	1.40	2.05	3.05	0.63	0.00	1.95	99.09	1.14	0.28	0.06	0.00	0.05	0.02	0.07	0.06	0.01	0.00	2.59	0.38	0.75
AP815	95.08	2.26	0.38	0.03	0.15	0.15	0.36	3.73	1.20	0.00	2.37	105.71	1.58	0.04	0.00	0.00	0.00	0.00	0.01	0.08	0.02	0.00	29.62	0.23	0.05
BE135	58.03	19.02	7.61	0.02	2.97	0.09	1.18	6.51	0.83	0.00	3.32	99.58	0.97	0.37	0.10	0.00	0.07	0.00	0.04	0.14	0.01	0.00	86.15	0.04	0.53
BE165	70.98	12.95	1.25	0.02	1.14	0.01	0.04	4.27	0.70	0.00	8.68	100.04	1.18	0.25	0.02	0.00	0.03	0.00	0.00	0.09	0.01	0.00	508.59	0.14	0.31
E196	74.45	14.06	1.09	0.03	0.40	0.20	6.62	0.92	0.50	0.00	1.00	99.27	1.24	0.28	0.01	0.00	0.01	0.00	0.21	0.02	0.01	0.00	5.48	0.02	0.51
E199	58.83	19.52	7.62	0.06	2.62	0.01	0.51	4.07	0.67	0.00	4.80	98.71	0.98	0.38	0.10	0.00	0.07	0.00	0.02	0.09	0.01	0.00	484.77	0.01	0.75
LS110	57.42	15.63	13.46	0.10	2.32	2.15	2.38	3.03	1.27	0.00	1.20	98.96	0.96	0.31	0.17	0.00	0.06	0.04	0.08	0.06	0.02	0.00	1.68	0.50	0.89
LS114	57.47	14.83	15.51	0.09	3.06	0.18	0.40	3.70	1.26	0.00	2.64	99.14	0.96	0.29	0.19	0.00	0.08	0.00	0.01	0.08	0.02	0.00	24.48	0.25	0.97
LS115	55.32	15.97	14.10	0.13	2.92	2.32	1.55	3.48	1.52	0.00	1.92	99.23	0.92	0.31	0.18	0.00	0.07	0.04	0.05	0.07	0.02	0.00	1.79	0.83	0.98
LS116	56.51	17.11	11.99	0.05	3.04	0.34	2.65	4.47	1.35	0.00	1.61	99.12	0.94	0.34	0.15	0.00	0.08	0.01	0.09	0.09	0.02	0.00	15.66	0.07	0.79
LS29	58.91	16.59	10.68	0.12	3.41	0.01	0.95	3.79	1.24	0.00	3.44	99.14	0.98	0.33	0.13	0.00	0.08	0.00	0.03	0.08	0.02	0.00	451.42	0.01	1.05
LS30	55.91	17.10	13.87	0.13	3.01	0.56	0.39	3.91	2.03	0.00	3.25	100.16	0.93	0.34	0.17	0.00	0.07	0.01	0.01	0.08	0.03	0.00	8.32	0.79	0.90
LS31	52.19	13.98	10.86	0.11	13.68	0.04	0.14	0.22	1.62	0.00	7.23	100.07	0.87	0.27	0.14	0.00	0.34	0.00	0.00	0.00	0.02	0.00	6.55	0.16	72.67
LS32	47.64	15.15	10.26	0.11	15.92	0.06	0.26	0.07	1.77	0.00	7.97	99.21	0.79	0.30	0.13	0.00	0.40	0.00	0.01	0.00	0.02	0.00	1.39	0.13	265.80
AP359	73.68	13.24	2.46	0.09	0.83	0.05	0.50	7.06	0.58	0.00	1.07	99.56	1.23	0.26	0.03	0.00	0.02	0.00	0.02	0.15	0.01	0.00	168.18	0.06	0.14
AP473	67.29	15.13	5.77	0.10	1.98	1.44	1.29	4.74	0.59	0.00	2.02	100.35	1.12	0.30	0.07	0.00	0.05	0.03	0.04	0.10	0.01	0.00	3.92	0.62	0.49
AP346	60.38	20.63	6.66	0.05	2.43	0.40	0.48	5.28	0.56	0.00	3.25	100.12	1.00	0.40	0.08	0.00	0.06	0.01	0.02	0.11	0.01	0.00	15.72	0.46	0.54
AP645	63.09	16.55	5.83	0.05	3.09	0.21	0.40	5.12	0.71	0.00	4.56	99.61	1.05	0.32	0.07	0.00	0.08	0.00	0.01	0.11	0.01	0.00	29.04	0.29	0.71
AP746	55.31	26.10	9.71	0.07	1.63	0.01	0.36	4.74	0.59	0.00	2.02	100.54	0.92	0.51	0.12	0.00	0.04	0.00	0.01	0.10	0.01	0.00	564.57	0.02	0.40
AP808	61.79	17.99	6.30	0.10	3.65	1.99	1.31	3.71	0.60	0.00	2.08	99.52	1.03	0.35	0.08	0.00	0.09	0.04	0.04	0.08	0.01	0.00	2.22	0.84	1.15
AP813	62.47	16.73	7.69	0.04	3.89	0.16	0.33	4.74	0.90	0.00	2.57	99.52	1.04	0.33	0.10	0.00	0.10	0.00	0.01	0.10	0.01	0.00	35.29	0.27	0.96
AP823	46.89	28.77	5.31	0.04	2.04	0.75	1.74	8.40	1.20	0.00	3.86	99.00	0.78	0.56	0.07	0.00	0.05	0.01	0.06	0.18	0.02	0.00	13.34	0.24	0.28
E97	61.91	13.75	6.16	0.02	5.21	1.85	0.31	5.05	0.64	0.00	5.19	100.09	1.03	0.27	0.08	0.00	0.13	0.03	0.01	0.11	0.01	0.00	3.25	3.30	1.21
AP807	65.59	9.94	4.64	0.06	3.80	1.88	0.77	1.46	0.40	0.00	10.95	99.49	1.09	0.19	0.06	0.00	0.09	0.03	0.02	0.03	0.01	0.00	0.92	1.35	3.04
AP825	68.21	12.41	2.46	0.03	2.12	0.56	0.78	2.62	0.57	0.00	10.59	100.35	1.13	0.24	0.03	0.00	0.05	0.01	0.03	0.06	0.01	0.00	5.57	0.40	0.95
E33	73.35	10.73	0.92	0.01	0.96	0.10	0.68	3.15	0.50	0.00	8.31	98.71	1.22	0.21	0.01	0.00	0.02	0.00	0.02	0.07	0.01	0.00	37.52	0.08	0.36
110L	57.42	15.63	13.46	0.10	2.32	2.15	2.38	3.03	1.27	0.00	1.20	98.96	0.96	0.31	0.17	0.00	0.06	0.04	0.08	0.06	0.02	0.00	1.68	0.50	0.89
114L	57.47	14.83	15.51	0.09	3.06	0.18	0.40	3.70	1.26	0.00	2.64	99.14	0.96	0.29	0.19	0.00	0.08	0.00	0.01	0.08	0.02	0.00	24.48	0.25	0.97
115L	55.32	15.97	14.10	0.13	2.92	2.32	1.55	3.48	1.52	0.00	1.92	99.23	0.92	0.31	0.18	0.00	0.07	0.04	0.05	0.07	0.02	0.00	1.79	0.83	0.98
116L	56.51	17.11	11.99	0.05	3.04	0.34	2.65	4.47	1.35	0.00	1.61	99.12	0.94	0.34	0.15	0.00	0.08	0.01	0.09	0.09	0.02	0.00	15.66	0.07	0.79
151L	57.60	17.77	11.93	0.09	1.88	0.76	1.05	5.02	1.29	0.00	2.77	100.16	0.96	0.35	0.15	0.00	0.05	0.01	0.03	0.11	0.02	0.00	7.87	0.40	0.44
153L	59.18	16.54	10.49	0.14	3.04	1.82	1.12	2.98	0.89	0.00	2.96	99.16	0.98	0.32	0.13	0.00	0.08	0.03	0.04	0.06	0.01	0.00	1.95	0.90	1.19
29L	58.91	16.59	10.68	0.12	3.41	0.01	0.95	3.79	1.24	0.00	3.44	99.14	0.98	0.33	0.13	0.00	0.08	0.00	0.03	0.08	0.02	0.00	451.42	0.01	1.05
30L	55.91	17.10	13.87	0.13	3.01	0.56	0.39	3.91	2.03	0.00	3.25	100.16	0.93	0.34	0.17	0.00	0.07	0.01	0.01	0.08	0.03	0.00	8.32	0.79	0.90
31L	52.19	13.98	10.86	0.11	13.68	0.04	0.14	0.22	1.62	0.00	7.23	100.07	0.87	0.27	0.14	0.00	0.34	0.00	0.00	0.00	0.02	0.00	6.55	0.16	72.67
32L	47.64	15.15	10.26	0.11	15.92	0.06	0.26	0.07	1.77	0.00	7.97	99.21	0.79	0.30	0.13	0.00	0.40	0.00	0.01	0.00	0.02	0.00	1.39	0.13	265.80
AP572	44.22	14.54	8.64	0.11	1.73	0.63	0.94	1.59	0.93	0.00	25.49	98.82	0.74	0.29	0.11	0.00	0.04	0.01	0.03	0.03	0.01	0.00	3.01	0.37	1.27
AP801	60.62	17.37	8.51	0.08	3.85	1.63	0.30	4.11	1.06	0.00	2.88	100.41	1.01	0.34	0.11	0.00	0.10	0.03	0.01	0.09	0.01	0.00	3.00	3.00	1.09
AP830	64.69	17.09	6.34	0.04	1.93	0.55	0.66	4.76	0.76	0.00	3.52	100.34	1.08	0.34	0.08	0.00	0.05	0.01	0.02	0.10	0.01	0.00	10.31	0.46	0.47
AL147	70.90	14.26	1.97	0.01	1.84	0.22	0.52	4.75	0.66	0.00	4.60	99.73	1.18	0.28	0.02	0.00	0.05	0.00	0.02	0.10	0.01	0.00	25.72	0.23	0.45
AL31	73.42	11.00	3.02	0.02	2.84	0.10	0.27	3.31	0.53	0.00	4.64	99.15	1.22	0.22	0.04	0.00	0.07	0.00	0.01	0.07	0.01	0.00	39.42	0.20	1.00
AP242	63.38	17.59	8.27	0.05	2.99	0.15	0.48	3.89	0.99	0.00	2.44	100.23	1.05	0.34	0.10	0.00	0.07	0.00	0.02	0.08	0.01	0.00	30.89	0.17	0.90

Table 5.21 continued from previous page

Sample	SiO_2	Al_2O3	Fe_2O_3	MnO	MgO	CaO	Na_2O	K_2O	TiO_2	P_2O_5	Pf	Total	Si	Al	Fe	Mn	Mg	Ca	Na	K	Ti	P		K/Ca	Ca/Na	Mg/K
						wt. %											mol/100g							mol:mol		
AP298	66.37	17.39	6.18	0.00	1.63	0.01	0.24	4.90	0.43	0.00	2.15	99.30	1.10	0.34	0.08	0.00	0.04	0.00	0.01	0.10	0.01	0.00		583.63	0.02	0.39
AP303	65.70	15.86	4.31	0.01	3.11	0.83	0.35	5.10	0.50	0.00	3.90	99.67	1.09	0.31	0.05	0.00	0.08	0.01	0.01	0.11	0.01	0.00		7.32	1.31	0.71
AP693	67.90	15.43	5.40	0.04	2.34	0.06	0.84	3.30	0.71	0.00	3.88	99.90	1.13	0.30	0.07	0.00	0.06	0.00	0.03	0.07	0.01	0.00		65.51	0.04	0.83
E46	73.52	12.50	1.60	0.01	1.14	0.09	1.53	3.14	0.55	0.00	5.98	100.06	1.22	0.25	0.02	0.00	0.03	0.00	0.05	0.07	0.01	0.00		41.56	0.03	0.42
AP025	44.69	14.94	13.73	0.06	14.81	0.01	0.01	0.44	1.94	0.00	7.97	98.60	0.74	0.29	0.17	0.00	0.37	0.00	0.00	0.01	0.02	0.00		52.41	0.55	39.34
NL1	66.51	10.13	2.36	0.02	0.93	0.01	0.06	5.83	0.42	0.00	12.90	99.17	1.11	0.20	0.03	0.00	0.02	0.00	0.00	0.12	0.01	0.00		694.40	0.09	0.19
NL506	70.47	12.62	6.81	0.02	1.49	0.11	2.07	2.39	0.77	0.14	1.69	98.58	1.17	0.25	0.09	0.00	0.04	0.00	0.07	0.05	0.01	0.00		25.88	0.03	0.73
BE130	69.04	12.94	5.65	0.09	2.71	0.63	1.91	2.76	0.80	0.00	2.09	98.62	1.15	0.25	0.07	0.00	0.07	0.01	0.06	0.06	0.01	0.00		5.22	0.18	1.15
BE241	65.58	16.58	5.11	0.03	2.06	0.16	1.58	3.78	0.63	0.00	3.08	98.59	1.09	0.33	0.06	0.00	0.05	0.00	0.05	0.08	0.01	0.00		28.14	0.06	0.64
BE246	65.42	16.64	7.24	0.03	2.18	0.29	0.89	3.62	0.62	0.00	3.13	100.06	1.09	0.33	0.09	0.00	0.05	0.01	0.03	0.08	0.01	0.00		14.87	0.18	0.70
BE41	48.14	16.02	9.11	0.09	15.29	0.01	0.54	1.04	2.26	0.00	7.66	100.16	0.80	0.31	0.11	0.00	0.38	0.00	0.02	0.02	0.03	0.00		123.87	0.01	17.18
AP009	81.13	8.52	3.11	0.02	1.58	0.01	0.05	2.32	0.21	0.00	2.14	99.09	1.35	0.17	0.04	0.00	0.04	0.00	0.00	0.05	0.00	0.00		276.33	0.11	0.80
NA424	73.41	13.82	1.09	0.08	0.04	1.77	2.47	6.53	0.08	0.15	0.24	99.68	1.22	0.27	0.01	0.00	0.00	0.03	0.08	0.14	0.00	0.00		4.39	0.40	0.01
NL007	79.72	9.16	2.97	0.01	2.47	0.17	0.20	2.91	0.36	0.00	1.66	99.63	1.33	0.18	0.04	0.00	0.06	0.00	0.01	0.06	0.00	0.00		20.39	0.47	0.99
NL017	84.24	7.69	2.22	0.00	1.02	0.26	0.73	2.52	0.34	0.00	1.08	100.10	1.40	0.15	0.03	0.00	0.03	0.00	0.02	0.05	0.00	0.00		11.54	0.20	0.47
																							Average	**160.02**	**0.31**	**6.69**
																							STDEV	**234.87**	**0.69**	**33.02**
																							Median	**26.00**	**0.11**	**0.63**

CHAPTER 6

CONCLUSIONS, PERSPECTIVES, AND FUTURE RESEARCH

> No Geologist worth anything is permanently bound to a desk or laboratory, but the charming notion that true science can only be based on unbiased observation of nature in the raw is mythology. Creative work, in geology and anywhere else, is interaction and synthesis: half-baked ideas from a bar room, rocks in the field, chains of thought from lonely walks, numbers squeezed from rocks in a laboratory, numbers from a calculator riveted to a desk, fancy equipment usually malfunctioning on expensive ships, cheap equipment in the human cranium, arguments before a road cut.
>
> — *Stephen Jay Gould, An Urchin in the Storm: Essays about Books and Ideas*

Calcium is an important element because of its abundance in the continental crust, its influence on the carbon cycle, and the fact that it is a major constituent in both carbonate and silicate minerals. Despite its limited use, numerous studies have shown the potential of the radiogenic Ca isotopic system as a petrogenetic tracer and geochronometer (Marshall and DePaolo, 1982; Marshall et al., 1986; Marshall and DePaolo, 1989; Fletcher et al., 1997b; Kreissig and Elliott, 2005; Caro et al., 2010). This thesis has presented new data and interpretations that also imply that the radiogenic Ca isotopic system has significant potential to trace silicate and carbonate weathering processes and geochemical cycles at the surface of the Earth. The ability to understand silicate weathering, the Ca cycle, the global carbon cycle, and how these processes affect climate change are important objectives in geochemistry and Earth Science. Understanding these processes and their interactions requires tracers of continental alteration. We have shown that the radiogenic Ca isotopic system provides such a tracer, though like all isotopic tracers it has its limitations. Improvements in the analytical capabilities of thermal ionization mass spectrometers (i.e., the Thermo Triton) and improvements to mass spectrometric methods (Chapter 3) enable the increasingly accurate and precise measurement of radiogenic Ca isotope compositions.

This thesis has presented more than 100 new measurements of radiogenic Ca isotope ratios in Himalayan waters, as well as about 15 analyses of bedrock, sediment and soil. These samples originate from across the Himalayan arc. In particular, we focused on the Narayani basin in central Nepal. At an even smaller scale, we selected the Khudi, a tributary of the Marysandi River, for detailed study. We used the Sr isotope and major element geochemistry of each of the rivers analyzed as a context and starting point for the interpretation of the Ca isotopic compositions obtained in this thesis, as well as to construct river budget models to explore the processes occurring in the rivers at the small and large scale. In general, the data and interpretations presented in this thesis show that the radiogenic Ca isotopic system is capable of providing information that is not available from major elements and Sr isotope compositions for the interpretation of riverine geochemistry. However, like with most geochemical tracers, Ca isotopes cannot stand alone but rather must be complemented by other tracers to improve our efforts to interpret and understand Himalayan and global weathering and erosion.

6.1 Summary of the major findings

6.1.1 Ca isotope ratios of bedrock and sediments

The analysis of Lesser Himalayan impure marbles revealed that carbonate lithologies in the Himalaya have homogeneous ε^{40}Ca compositions (ε^{40}Ca = –0.2 to 0), despite having highly variable Sr isotopic compositions (^{87}Sr/^{86}Sr = 0.74–0.86). Furthermore, we found that the carbonate fraction of bed load sediment from the HHC, LH, and TSS, as well as the Ganga and Brahmaputra, have ε^{40}Ca compositions identical within uncertainty to the mantle and seawater values (ε^{40}0Ca = 0 to +0.4), despite, again, having variable ^{87}Sr/^{86}Sr compositions (0.71–0.84). These analyses imply several important points:

1. The non-radiogenic nature of Himalayan carbonates confirms the conclusion made by Caro et al. (2010), i.e., that marine carbonates have retained a non-radiogenic composition (ε^{40}Ca = 0) over geological time.

2. Ca isotopes in carbonates have not re-equilibrated with adjacent highly radiogenic silicate rocks during metamorphism related to Himalayan orogenesis.

3. The seawater-like composition of bed load carbonate demonstrates that the carbonate fraction represents primarily detrital material as opposed to secondary phases precipitated from the dissolved load, as secondary carbonates would inherit the radiogenic ^{40}Ca composition of the riverine dissolved load.

The reason that Ca isotopes did not reequilibrate between silicate and carbonate lithologies is perhaps due to the fact that mass balance causes Sr isotopes in carbonates to be more strongly influenced than Ca isotopes by reequilibration with silicates or perhaps the fact that Ca is a major element locked into the crystalline structure of a rock/mineral while Sr is a trace element. In either case, as a result, Sr isotopes in carbonates are more easily perturbed than Ca isotopes by re-equilibration with silicates during metamorphism.

Contrary to Himalayan carbonates, analyses reveal that the silicate fractions of bed load sediment have radiogenic Ca compositions (ε^{40}Ca = +0.9 in the TSS to +3.96 in the LH) reflecting variations in both the crustal extraction ages and the compositions (specifically, the K/Ca ratios) of silicate catchments exposed in the different litho-tectonic units of the Himalayas. The fact that we see a dichotomy between the radiogenic Ca compositions of silicate and carbonate lithologies confirms our hypothesis that the properties of the K–Ca system can be used to trace silicate and carbonate weathering in the dissolved load.

6.1.2 *Ca isotope ratios of water*

From north to south across the Himalayan arc we see a general increase in the ε^{40}Ca isotopic values in small catchments of the TSS, HHC, and LH. TSS rivers are characterized by unradiogenic compositions (ε^{40}Ca = +0.29 to +0.42) due to the dominant presence of carbonate lithologies. Rivers in the HHC have intermediate radiogenic compositions varying between +0.5 and +2, which is in agreement with the analysis of sediment from the HHC. LH rivers are characterized by extreme variations in their radiogenic Ca compositions ranging from +0.42 to +11. Smaller catchments of the LH with purely silicate lithologies seem to correlate with the greatest radiogenic ^{40}Ca excesses and should be the target for future investigations into the upper limit of radiogenic Ca compositions in central Himalayan bedrock, sediment, and water. The tributaries of the Narayani and major Himalayan front rivers have intermediate values consistent with mixtures of highly radiogenic waters from silicate-dominated basins and less radiogenic waters from carbonate-dominated basins, including a strong contribution from the TSS.

6.1.3 *Implications for the Khudi Khola*

In this thesis, we undertook a detailed study of the Khudi Khola, a small catchment in the Narayani Basin of central Nepal. It was chosen because of its long history of investigation and its well-constrained nature in terms of lithology, weathering, erosion, climate, vegetation, and river dynamics. Based on this, we show that radiogenic Ca compositions of water are highly variable between the LH, below the MCT, and the HHC, above the MCT. In the LH, with the exception of samples collected during major storm events, water compositions are unradiogenic and reflect a source from the massive outcrops of dolostone and limestone that are situated below the MCT. Above the MCT in the HHC, radiogenic Ca compositions are elevated compared with the LH due to the silicate nature of the HHC. As proposed by previous studies, landslides in the HHC part of the Khudi basin represent a significant source of eroded material (Gallo and Lavé, 2014; Morin, 2015). Analyses of powders made from aggregated pebbles from the landslide show that the ε^{40}Ca values vary substantially but are in large part radiogenic.

In the Khudi, storm events during the monsoon yield high discharge and sediment load values, spikes in the concentrations of K, Ca, and SO_4, and generally turbulent riverine conditions (Morin, 2015; Morin et al., 2014). In the 2013 storm event, documented by Morin et al. (2014), we observe, along with the element concentration spikes, a sharp increase in the ε^{40}Ca values, from +0 to +1.78 at the peak of the storm. Based on the geology and structure of the Khudi, this radiogenic Ca signature can only originate from the HHC. Concurrent increases in the SO_4^{2-}, K, and Ca concentrations

during the 2013 storm event imply that these species may have been released via silicate weathering and associated sulfide oxidation.

Based on these observations and conclusions, we suggest that the breakdown and leaching/weathering of pebbles and gravel in the landslides and throughout the catchment is the most plausible explanation for the observed spikes in concentration and radiogenic Ca composition during storm events.

6.1.4 Implications for the Narayani

6.1.4.1 Weathering Budgets in the Narayani

One of the main goals of this thesis was to determine whether radiogenic Ca isotopes could be used to distinguish between carbonate and silicate weathering products in the dissolved loads of Himalayan rivers. This could in turn allow quantification of the silicate weathering flux from the Himalaya and its effect on CO_2 removal. To do this we compared mass balance budgets based on major elements with budgets based on radiogenic Ca isotopes in the dissolved load of the Narayani river and its tributaries. Past studies of the magnitude and flux of silicate and carbonate weathering in the Himalaya have emphasized the difficulties associated with defining the carbonate and silicate end-members used in weathering budgets (Galy and France-Lanord, 1999; West et al., 2002; Quade, 2003; Bickle et al., 2003, 2005, 2015). In this thesis, we defined our end-members (Ca/Na, Mg/K, and K/Ca ratios) based on a database of sediments from the TSS, HHC, and LH. For the isotopic budget, we used both the silicate fraction of bedload sediments and a three stage isotopic growth model to define the ε^{40}Ca composition of the silicate end-members of each formation.

Based on these end-members and the budget approaches discussed in Chapter 5, we addressed the quantification of the silicate weathering flux in the Himalaya, and ultimately its effect on erosion and the carbon cycle. We find that there is relatively good agreement between estimates based on Ca concentrations and estimates based on Ca isotopic compositions. Nevertheless there are some discrepancies, particularly in samples derived from the HHC and several in the LH, with estimates of the silicate contribution based on Ca isotopic composition being sometimes higher than those based on Ca concentrations. These discrepancies cannot be attributed to secondary carbonate precipitation because this would lead to the opposite effect, i.e., lower estimates for the silicate contribution based on Ca concentrations compared with estimates based on the isotopic compositions. In fact, this observation, coupled with the determination that the carbonate fractions of the sediments have unradiogenic compositions, argues that carbonate precipitation in rivers is probably a relatively minor process. Instead, the most likely explanation for the discrepancies between the estimates is that silicate bedrocks contain trace amounts of disseminated carbonate

veinlets with radiogenic Ca compositions. These veinlets will appear as a carbonate signature in budget calculations based on major elements but as a silicate signature in calculations based on Ca isotopic composition as was previously shown for Sr isotopes (Blum et al., 1998; Chamberlain et al., 2005).

6.1.4.2 Rates of erosion and CO_2 consumption

Estimates of current silicate and carbonate erosion rates in the catchments of the Narayani based on major element geochemistry and radiogenic Ca isotopes generally agree but, in many cases, estimates based on the radiogenic Ca isotopic compositions are larger. This is likely due to the presence of disseminated calcite veinlets, as discussed above. These discrepancies are also seen when calculating the rates of CO_2 consumption based on cations derived from silicate weathering, and again most probably reflects the weathering of disseminated calcite.

Based on the results of erosion and CO_2 consumption rate calculations, we observe that the fraction of Ca derived from radiogenic carbonates (i.e., a disseminated calcite source) is highest in basins with low silicate weathering rates. This suggests that, in regions that are characterized by lower rates of chemical weathering, such as the HHC, disseminated radiogenic calcite is preferentially weathered and dissolves faster than silicate lithologies because carbonates are characterized by fast dissolution kinetic properties. We also observe that the radiogenic carbonates have little effect on the total calculated CO_2 consumption in the Narayani because radiogenic carbonates are limited to areas with low silicate weathering rates.

6.2 Can we use ^{40}Ca to trace past changes in silicate weathering?

Until recently, it was thought that the radiogenic Ca composition of the oceans has remained equivalent to that of the mantle (i.e., 0) (Marshall and DePaolo, 1982; Caro et al., 2010). Furthermore, radiogenic Ca analyses from Schiller et al. (2012) and Simon et al. (2009) showed that the ε^{40}Ca values of several standards and basalts are identical to the value of the SRM915a standard and seawater.

Antonelli et al. (2018), however, found that, relative to igneous rock standards (i.e., the bulk silicate earth represented by oceanic basalts or meteorites), seawater and the SRM915a standard have radiogenic compositions, which implies that: 1) SRM915a is not an acceptable standard to estimate ^{40}Ca excesses and 2) that seawater may be slightly more radiogenic than the mantle over the past 3.5 Ga. Past studies have proposed that the flux and composition of oceanic hydrothermal systems have strongly dominated the radiogenic Ca budget of the oceans (Caro et al., 2010), resulting in a complete overprinting of the radiogenic signature derived from continental erosion. However, if seawater has not retained a composition identical to that of the mantle over the past 3.5 Ga, this raises the question of whether the ^{40}Ca marine record can be possibly used to trace past changes in the flux and intensity of silicate weathering. To answer this question, as discussed above, riverine and hydrothermal fluxes of radiogenic Ca must be constrained and more accurate and precise analyses of the composition of seawater must be made.

6.3 Future research

This thesis has presented an initial overview of the systematics of radiogenic Ca isotope ratios throughout the Himalaya. The ideas and interpretations presented in this thesis may provide a framework to better understand the behavior of radiogenic Ca isotope ratios but future ideas and modeling will benefit from further analyses of ^{40}Ca in bedrock, sediments, river water, hydrothermal fluids, and other terrestrial samples in both the Himalaya and throughout the globe.

Moving forward, more analyses are required to answer questions about both the large and small scale systematics of radiogenic Ca isotope ratios for its use as a geochemical tracer. Constraining the average riverine ε^{40}Ca and the compositions of the other fluxes in the radiogenic Ca global system are important for constraining the evolution of radiogenic Ca in the oceans. In order to better understand radiogenic Ca systematics in rivers, we must investigate well constrained catchments, such as the Khudi Khola, and use multi-proxy approaches. Coupling measurements of radiogenic Ca isotopes (sensitive to carbonate and silicate weathering) with other isotope systems, such Sr isotope ratios, has proven advantageous in this thesis. However, coupling radiogenic Ca isotopes with other isotopic systems, such as the Li and Si isotopic systems (sensitive to silicate, carbonate, and biological processes), may prove to be even more advantageous. Much work needs to be done but the data in this thesis confirm that radiogenic Ca isotopes, measured by TIMS, have the potential to provide insight into some of the most important questions in geochemistry and Earth Science: the interactions between climate, erosion, weathering, and the global carbon cycle.

Bibliography

Ahmad, T., Harris, N., Bickle, M., Chapman, H., Bunbury, J., and Prince, C. (2000). Isotopic constraints on the structural relationships between the lesser himalayan series and the high himalayan crystalline series, garhwal himalaya. *Geological Society of America Bulletin*, 112(3):467–477.

Ahrens, L. H. (1951). The feasibility of a calcium method for the determination of geological age. *Geochimica et Cosmochimica Acta*, 1(4-6):312–316.

Aitchison, J. C., Ali, J. R., and Davis, A. M. (2007). When and where did india and asia collide? *Journal of Geophysical Research: Solid Earth*, 112(B5).

Albarède, F., Michard, A., Minster, J., and G. Michard, G. (1981). $^{87}Sr/^{86}Sr$ ratios in hydrothermal waters and deposits from the east pacific rise at 21°n. *Earth and Planetary Science Letters*, 55(2):229–236.

Allègre, C. J., Louvat, P., Gaillardet, J., Meynadier, L., Rad, S., and Capmas, F. (2010). The fundamental role of island arc weathering in the oceanic sr isotope budget. *Earth and Planetary Science Letters*, 292(1-2):51–56.

Andermann, C., Crave, A., Gloaguen, R., Davy, P., and Bonnet, S. (2012a). Connecting source and transport: Suspended sediments in the nepal himalayas. *Earth and Planetary Science Letters*, 351:158–170.

Andermann, C., Longuevergne, L., Bonnet, S., Crave, A., Davy, P., and Gloaguen, R. (2012b). Impact of transient groundwater storage on the discharge of himalayan rivers. *Nature Geoscience*, 5(2):127–132.

Anders, A. M., Roe, G. H., Hallet, B., Montgomery, D. R., Finnegan, N. J., and Putkonen, J. (2006). Spatial patterns of precipitation and topography in the himalaya. *Geological Society of America Special Papers*, 398:39–53.

Antonelli, M., DePaolo, D., Brown, S., and Pester, N. (2018). Radiogenic ^{40}ca in seawater. In *Goldschidmt 2018*.

Armstrong, L. (1971). Glacial erosion and the variable isotopic composition of strontium in sea water. *Nature*, 230(14):132–133.

Asmerom, Y., Jacobsen, S., Knoll, A., Butterfield, N., and Swett, K. (1991). Strontium isotopic variations of neoproterozoic seawater: implications for crustal evolution. *Geochimica et Cosmochimica Acta*, 55(10):2883–2894.

Attal, M. and Lavé, J. (2006). Changes ofbedload characteristics along the marsyandi river (central nepal): Implications for understanding hillslope sediment supply, sediment load evolution along fluvial networks, and denudation in active orogenic belts. *Tectonics, climate, and landscape evolution*, 398:143.

Barbey, P., Brouand, M., Le Fort, P., and Pecher, A. (1996). Granite-migmatite genetic link: the example of the manaslu granite and tibetan slab migmatites in central nepal. *Lithos*, 38(1-2):63–79.

Basu, A. R., Jacobsen, S. B., Poreda, R. J., Dowling, C. B., and Aggarwal, P. K. (2001). Large groundwater strontium flux to the oceans from the bengal basin and the marine strontium isotope record. *Science*, 293(5534):1470–1473.

Beaumont, C., Jamieson, R. A., Nguyen, M., and Lee, B. (2001). Himalayan tectonics explained by extrusion of a low-viscosity crustal channel coupled to focused surface denudation. *Nature*, 414(6865):738.

Beaumont, C., Jamieson, R. A., Nguyen, M. H., and Medvedev, S. (2004). Crustal channel flows: 1. numerical models with applications to the tectonics of the himalayan-tibetan orogen. *Journal of Geophysical Research: Solid Earth*, 109(B6).

Beerling, D. J. and Royer, D. L. (2011). Convergent cenozoic co 2 history. *Nature Geoscience*, 4(7):418.

Berner, E., Berner, R., and Moulton, K. (2003). Plants and mineral weathering: present and past. *Treatise on geochemistry*, 5:169–188.

Berner, E. K. and Berner, R. A. (2012). *Global environment: water, air, and geochemical cycles*. Princeton University Press.

Berner, R. A. (1990). Atmospheric carbon dioxide levels over phanerozoic time. *Science*, 249(4975):1382–1386.

Berner, R. A. (2004). A model for calcium, magnesium and sulfate in seawater over phanerozoic time. *American Journal of Science*, 304(5):438–453.

Berner, R. A. (2006). Geocarbsulf: a combined model for phanerozoic atmospheric O_2 and CO_2. *Geochimica et Cosmochimica Acta*, 70(23):5653–5664.

Berner, R. A. et al. (1999). A new look at the long-term carbon cycle. *Gsa Today*, 9(11):1–6.

Berner, R. A. and Kothavala, Z. (2001). Geocarb iii: a revised model of atmospheric CO_2 over phanerozoic time. *American Journal of Science*, 301(2):182–204.

Berner, R. A. and Raiswell, R. (1983). Burial of organic carbon and pyrite sulfur in sediments over phanerozoic time: a new theory. *Geochimica et Cosmochimica Acta*, 47(5):855–862.

Besse, J., Courtillot, V., Pozzi, J., Westphal, M., and Zhou, Y. (1984). Palaeomagnetic estimates of crustal shortening in the himalayan thrusts and zangbo suture. *Nature*, 311(5987):621.

Bickle, M., Bunbury, J., Chapman, H., Harris, N., Fairchild, I., and Ahmad, T. (2003). Fluxes of sr into the headwaters of the ganges. *Geochimica et Cosmochimica Acta*, 67(14):2567–2584.

Bickle, M., Chapman, H., Bunbury, J., Harris, N., Fairchild, I., Ahmad, T., and Pomiès, C. (2005). Relative contributions of silicate and carbonate rocks to riverine sr fluxes in the headwaters of the ganges. *Geochimica et Cosmochimica Acta*, 69(9):2221–2240.

Bickle, M., Harris, N., Bunbury, J., Chapman, H., Fairchild, I., and Ahmad, T. (2001). Controls on the $^{87}Sr/^{86}Sr$ ratio of carbonates in the garhwal himalaya, headwaters of the ganges. *The Journal of Geology*, 109(6):737–753.

Bickle, M. J., Tipper, E., Galy, A., Chapman, H., and Harris, N. (2015). On discrimination between carbonate and silicate inputs to himalayan rivers. *American Journal of Science*, 315(2):120–166.

Blum, J., Gazis, C., Jacobson, A., and Chamberlain, C. (1998). Carbonate versus silicate weathering in the raikhot watershed within the high himalayan crystalline series. *Geology*, 26(5):411–414.

Bluth, G. J. and Kump, L. R. (1994). Lithologic and climatologic controls of river chemistry. *Geochimica et Cosmochimica Acta*, 58(10):2341–2359.

Blythe, A., Burbank, D., Carter, A., Schmidt, K., and Putkonen, J. (2007). Plio-quaternary exhumation history of the central nepalese himalaya: 1. apatite and zircon fission track and apatite [u-th]/he analyses. *Tectonics*, 26(3).

Bogard, D., Garrison, D., McKay, D., and Wentworth, S. (1992). The age of copernicus: New evidence for 800 $\pm$ 15 million years. In *Lunar and Planetary Science Conference*, volume 23.

Bogard, D., Garrison, D., Shih, C., and Nyquist, L. (1994). ^{39}ar-^{40}ar dating of two lunar granites: The age of copernicus. *Geochimica et cosmochimica acta*, 58:3093–3100.

Bookhagen, B. and Burbank, D. W. (2006). Topography, relief, and trmm-derived rainfall variations along the himalaya. *Geophysical Research Letters*, 33(8).

Bookhagen, B. and Burbank, D. W. (2010). Toward a complete himalayan hydrological budget: Spatiotemporal distribution of snowmelt and rainfall and their impact on river discharge. *Journal of Geophysical Research: Earth Surface*, 115(F3).

Bookhagen, B., Thiede, R. C., and Strecker, M. R. (2005a). Abnormal monsoon years and their control on erosion and sediment flux in the high, arid northwest himalaya. *Earth and Planetary Science Letters*, 231(1):131–146.

Bookhagen, B., Thiede, R. C., and Strecker, M. R. (2005b). Late quaternary intensified monsoon phases control landscape evolution in the northwest himalaya. *Geology*, 33(2):149–152.

Bouchez, J., Gaillardet, J., Lupker, M., Louvat, P., France-Lanord, C., Maurice, L., Armijos, E., and Moquet, J.-S. (2012). Floodplains of large rivers: Weathering reactors or simple silos? *Chemical Geology*, 332:166–184.

Bouchez, J., Métivier, F., Lupker, M., Maurice, L., Perez, M., Gaillardet, J., and France-Lanord, C. (2011). Prediction of depth-integrated fluxes of suspended sediment in the amazon river: Particle aggregation as a complicating factor. *Hydrological processes*, 25(5):778–794.

Brantley, S. L. and Lebedeva, M. (2011). Learning to read the chemistry of regolith to understand the critical zone. *Annual Review of Earth and Planetary Sciences*, 39:387–416.

Brass, G. (1976). The variation of the marine $^{87}Sr/^{86}Sr$ ratio during phanerozonic time: interpretation using a flux model. *Geochimica et Cosmochimica Acta*, 40(7):721–730.

Brouand, M. (1989). *Pétrogenèse des migmatites de la dalle du Tibet (Himalaya du Népal)*. PhD thesis, Institut National Polytechnique de Lorraine.

Burbank, D., Blythe, A., Putkonen, J., Pratt-Sitaula, B., Gabet, E., Oskin, M., Barros, A., and Ojha, T. (2003). Decoupling of erosion and precipitation in the himalayas. *Nature*, 426(6967):652–655.

Burbank, D. W. (1992). Causes of recent himalayan uplift deduced from deposited patterns in the ganges basin. *Nature*, 357(6380):680.

Burke, W., Denison, R., Hetherington, E., Koepnick, R., Nelson, H., and Otto, J. (1982). Variation of seawater $^{87}Sr/^{86}Sr$ throughout phanerozoic time. *Geology*, 10(10):516–519.

Calmels, D., Gaillardet, J., Brenot, A., and France-Lanord, C. (2007). Sustained sulfide oxidation by physical erosion processes in the mackenzie river basin: climatic perspectives. *Geology*, 35(11):1003–1006.

Caro, G., Bourdon, B., Birck, J.-L., and Moorbath, S. (2006). High-precision $^{142}Nd/^{144}Nd$ measurements in terrestrial rocks: constraints on the early differentiation of the earth's mantle. *Geochimica et Cosmochimica Acta*, 70(1):164–191.

Caro, G., Morino, P., Mojzsis, S., Cates, N., and Bleeker, W. (2017). Sluggish hadean geodynamics: Evidence from coupled ^{146,147}sm–^{142,143}nd systematics in eoarchean supracrustal rocks of the inukjuak domain (québec). *Earth and Planetary Science Letters*, 457:23–37.

Caro, G., Papanastassiou, D., and Wasserburg, G. (2010). ^{40}K-^{40}Ca isotopic constraints on the oceanic calcium cycle. *Earth and Planetary Science Letters*, 296(1):124–132.

Chabaux, F., Riotte, J., Clauer, N., and France-Lanord, C. (2001). Isotopic tracing of the dissolved u fluxes of himalayan rivers: implications for present and past u budgets of the ganges-brahmaputra system. *Geochimica et Cosmochimica Acta*, 65(19):3201–3217.

Chamberlain, C., Waldbauer, J., and Jacobson, A. (2005). Strontium, hydrothermal systems and steady-state chemical weathering in active mountain belts. *Earth and Planetary Science Letters*, 238(3):351–366.

Chamberlin, T. C. (1899). An attempt to frame a working hypothesis of the cause of glacial periods on an atmospheric basis. *The Journal of Geology*, 7(6):545–584.

Chaudhuri, S. and Clauer, N. (1986). Fluctuations of isotopic composition of strontium in seawater during the phanerozoic eon. *Chemical Geology: Isotope Geoscience section*, 59:293–303.

Chowdhury, M. R. and Ward, N. (2004). Hydro-meteorological variability in the greater ganges–brahmaputra–meghna basins. *International Journal of Climatology*, 24(12):1495–1508.

Clift, P. D. (2017). Cenozoic sedimentary records of climate-tectonic coupling in the western himalaya. *Progress in Earth and Planetary Science*, 4(1):39.

Clift, P. D., Giosan, L., Blusztajn, J., Campbell, I. H., Allen, C., Pringle, M., Tabrez, A. R., Danish, M., Rabbani, M., Alizai, A., et al. (2008). Holocene erosion of the lesser himalaya triggered by intensified summer monsoon. *Geology*, 36(1):79–82.

Colchen, M., Le Fort, P., and Pêcher, A. (1986). Notice explicative de la carte géologique annapurna-manaslu-ganesh (himalaya du népal) au 1:200,000 e (bilingue: Français-english). *Cent. Natl. de la Rech. Sci., Paris*.

Coleman, M. (1971). Potassium-calcium dates from pegmatitic micas. *Earth and Planetary Science Letters*, 12(4):399–405.

Copley, A., Avouac, J.-P., and Royer, J.-Y. (2010). India-asia collision and the cenozoic slowdown of the indian plate: Implications for the forces driving plate motions. *Journal of Geophysical Research: Solid Earth*, 115(B3).

Craddock, W. H., Burbank, D. W., Bookhagen, B., and Gabet, E. J. (2007). Bedrock channel geometry along an orographic rainfall gradient in the upper marsyandi river valley in central nepal. *Journal of Geophysical Research: Earth Surface*, 112(F3).

Dasch, E. and Biscaye, P. (1971). Isotopic composition of strontium in cretaceous-to-recent, pelagic foraminifera. *Earth and Planetary Science Letters*, 11(1):201–204.

Davenport, J., Caro, G., and France-Lanord, C. (2014). Tracing silicate weathering in the himalaya using the ^{40}K-^{40}Ca system: A reconnaissance study. *Procedia Earth and Planetary Science*, 10:238–242.

Davis, A. C., Bickle, M. J., and Teagle, D. A. (2003). Imbalance in the oceanic strontium budget. *Earth and Planetary Science Letters*, 211(1):173–187.

De La Rocha, C. and DePaolo, D. J. (2000). Isotopic evidence for variations in the marine calcium cycle over the cenozoic. *Science*, 289(5482):1176–1178.

DeCelles, P. and Giles, K. (1996). Foreland basin systems. *Basin research*, 8(2):105–123.

Dellinger, M., Gaillardet, J., Bouchez, J., Calmels, D., Galy, V., Hilton, R. G., Louvat, P., and France-Lanord, C. (2014). Lithium isotopes in large rivers reveal the cannibalistic nature of modern continental weathering and erosion. *Earth and Planetary Science Letters*, 401:359–372.

Demicco, R. V., Lowenstein, T. K., Hardie, L. A., and Spencer, R. J. (2005). Model of seawater composition for the phanerozoic. *Geology*, 33(11):877–880.

Deniel, C., Vidal, P., Fernandez, A., Le Fort, P., and Peucat, J.-J. (1987). Isotopic study of the manaslu granite (himalaya, nepal): inferences on the age and source of himalayan leucogranites. *Contributions to Mineralogy and Petrology*, 96(1):78–92.

DePaolo, D. and Ingram, B. (1985). High-resolution stratigraphy with strontium isotopes. *Science*, 227(4689):938–941.

Derry, L. and France-Lanord, C. (1996). Neogene himalayan weathering history and river $^{87}Sr/^{86}Sr$: Impact on the marine sr record. *Earth and Planetary Science Letters*, 142(1):59–74.

Derry, L. and France-Lanord, C. (1997). Himalayan weathering and erosion fluxes: climate and tectonic controls. In *Tectonic uplift and climate change*, pages 289–312. Springer.

Derry, L., Keto, L., Jacobsen, S., Knoll, A., and Swett, K. (1989). Sr isotopic variations in upper proterozoic carbonates from svalbard and east greenland. *Geochimica et Cosmochimica Acta*, 53(9):2331–2339.

Dessert, C., Dupré, B., François, L. M., Schott, J., Gaillardet, J., Chakrapani, d., and Bajpai, S. (2001). Erosion of deccan traps determined by river geochemistry: impact on the global climate and the $^{87}Sr/^{86}Sr$ ratio of seawater. *Earth and Planetary Science Letters*, 188(3):459–474.

Dessert, C., Dupré, B., Gaillardet, J., François, L. M., and Allegre, C. J. (2003). Basalt weathering laws and the impact of basalt weathering on the global carbon cycle. *Chemical Geology*, 202(3):257–273.

Dewey, J., Cande, S., and Pitman, W. (1989). The tectonic evolution of the india/eurasia collision zone. *Ecolgae Geologicae Helvetiae*, 82:717–734.

Dèzes, P. (1999). *Tectonic and metamorphic Evolution of the Central Himalayan Domain in Southeast Zanskar (Kashmir, India)*. PhD thesis, University of Lausanne, Lausanne, Switzerland.

Dhital, M. (1995). Geology and structure of the siwaliks and lesser himalaya in the surai khola-bardanda area, mid western nepal. *Bull. Dept. Geol., Tribhuvan Univ.*, 4:1–70.

Dhital, M. R. (2015). *Geology of the Nepal Himalaya: regional perspective of the classic collided orogen*. Springer.

Dosseto, A., Bourdon, B., and Turner, S. P. (2008). Uranium-series isotopes in river materials: insights into the timescales of erosion and sediment transport. *Earth and Planetary Science Letters*, 265(1):1–17.

Dowling, C. B., Poreda, R. J., and Basu, A. R. (2003). The groundwater geochemistry of the bengal basin: Weathering, chemsorption, and trace metal flux to the oceans. *Geochimica et Cosmochimica Acta*, 67(12):2117–2136.

Drever, J. I. (1997). *The geochemistry of natural waters*, volume 437. Prentice Hall Englewood Cliffs.

Dürr, S. B. (1996). Provenance of xigaze fore-arc basin clastic rocks (cretaceous, south tibet). *Geological Society of America Bulletin*, 108(6):669–684.

Ebelmen, J. (1845). Sur les produits de la decomposition des especes minerales de la famille des silicates. *Annales des Mines*, 7:66.

Edmond, J. (1992). Himalayan tectonics, weathering processes, and the strontium isotope record in marine limestones. *Science-New York then Washington-*, 258:1594–1594.

Edmond, J., Palmer, M., Measures, C., Brown, E., and Huh, Y. (1996). Fluvial geochemistry of the eastern slope of the northeastern andes and its foredeep in the drainage of the orinoco in colombia and venezuela. *Geochimica et Cosmochimica Acta*, 60(16):2949–2974.

Edmond, J. M. and Huh, Y. (2003). Non-steady state carbonate recycling and implications for the evolution of atmospheric pCO_2. *Earth and Planetary Science Letters*, 216(1):125–139.

Elderfield, H. and Gieskes, J. (1982). Sr isotopes in interstitial waters of marine sediments from deep sea drilling project cores. *Nature*.

Elderfield, H. and Schultz, A. (1996). Mid-ocean ridge hydrothermal fluxes and the chemical composition of the ocean. *Annual Review of Earth and Planetary Sciences*, 24:191–224.

Emberson, R., Galy, A., and Hovius, N. (2017). Combined effect of carbonate and biotite dissolution in landslides biases silicate weathering proxies. *Geochimica et Cosmochimica Acta*, 213:418–434.

Emberson, R., Hovius, N., Galy, A., and Marc, O. (2016a). Chemical weathering in active mountain belts controlled by stochastic bedrock landsliding. *Nature Geoscience*, 9(1):42.

Emberson, R., Hovius, N., Galy, A., and Marc, O. (2016b). Oxidation of sulfides and rapid weathering in recent landslides. *Earth Surface Dynamics*, 4(3):727–742.

English, N., Quade, J., DeCelles, P., and Garzione, C. (2000). Geologic control of sr and major element chemistry in himalayan rivers, nepal. *Geochimica et Cosmochimica Acta*, 64(15):2549–2566.

Esat, T., Spear, R., and Taylor, S. (1986). Isotope anomalies induced in laboratory distillation. *Nature*, 319(6054).

Evans, M., Derry, L., Anderson, S., and France-Lanord, C. (2001). Hydrothermal source of radiogenic sr to himalayan rivers. *Geology*, 29:803–806.

Evans, M., Derry, L., and France-Lanord, C. (2004). Geothermal fluxes of alkalinity in the narayani river system of central nepal. *Geochemistry, Geophysics, Geosystems*, 5(8):1–21.

Evans, M., Derry, L., and France-Lanord, C. (2008). Degassing of metamorphic carbon dioxide from the nepal himalaya. *Geochemistry, Geophysics, Geosystems*, 9(4):1–18.

Fantle, M. S. and Bullen, T. D. (2009). Essentials of iron, chromium, and calcium isotope analysis of natural materials by thermal ionization mass spectrometry. *Chemical Geology*, 258(1):50–64.

Faure, G., Hurley, P., and Powell, J. (1965). The isotopic composition of strontium in surface water from the north atlantic ocean. *Geochimica et Cosmochimica Acta*, 29(4):209–220.

Fielding, E., Isacks, B., Barazangi, M., and Duncan, C. (1994). How flat is tibet? *Geology*, 22(2):163–167.

Fletcher, I., Maggi, A., Rosman, K., and McNaughton, N. (1997a). Isotopic abundance measurements of k and ca using a wide-dispersion multi-collector mass spectrometer and low-fractionation ionisation techniques. *International Journal of Mass Spectrometry and Ion Processes*, 163(1):1 – 17.

Fletcher, I., McNaughton, N., Pidgeon, R., and Rosman, K. (1997b). Sequential closure of k–ca and rb–sr isotopic systems in archaean micas. *Chemical geology*, 138(3):289–301.

Foster, G. L. and Vance, D. (2006). Negligible glacial–interglacial variation in continental chemical weathering rates. *Nature*, 444(7121):918–921.

Foster, G. L., Vance, D., and Prytulak, J. (2007). No change in the neodymium isotope composition of deep water exported from the north atlantic on glacial-interglacial time scales. *Geology*, 35(1):37–40.

France-Lanord, C. and Derry, L. (1997). Organic carbon burial forcing of the carbon cycle from himalayan erosion. *Nature*, 390:65–67.

France-Lanord, C., Derry, L., and Michard, A. (1993). Evolution of the himalaya since miocene time: isotopic and sedimentological evidence from the bengal fan. *Geological Society, London, Special Publications*, 74(1):603–621.

France-Lanord, C., Evans, M., Hurtrez, J.-E., and Riotte, J. (2003). Annual dissolved fluxes from central nepal rivers: budget of chemical erosion in the himalayas. *Comptes Rendus Geoscience*, 335(16):1131–1140.

France-Lanord, C. and Fort, P. L. (1988). Crustal melting and granite genesis during the himalayan collision orogenesis. *Transactions of the Royal Society of Edinburgh: Earth Sciences*, 79(2-3):183–195.

François, L. and Goddéris, Y. (1998). Isotopic constraints on the cenozoic evolution of the carbon cycle. *Chemical Geology*, 145(3):177–212.

Gabet, E. J., Burbank, D. W., Pratt-Sitaula, B., Putkonen, J., and Bookhagen, B. (2008). Modern erosion rates in the high himalayas of nepal. *Earth and Planetary Science Letters*, 267(3):482–494.

Gabet, E. J., Burbank, D. W., Putkonen, J. K., Pratt-Sitaula, B. A., and Ojha, T. (2004). Rainfall thresholds for landsliding in the himalayas of nepal. *Geomorphology*, 63(3):131–143.

Gabet, E. J. and Mudd, S. M. (2009). A theoretical model coupling chemical weathering rates with denudation rates. *Geology*, 37(2):151–154.

Gadgil, S., Vinayachandran, P., Francis, P., and Gadgil, S. (2004). Extremes of the indian summer monsoon rainfall, enso and equatorial indian ocean oscillation. *Geophysical Research Letters*, 31(12).

Gaillardet, J., Dupre, B., Allegre, C. J., and Négrel, P. (1997). Chemical and physical denudation in the amazon river basin. *Chemical geology*, 142(3-4):141–173.

Gaillardet, J., Dupré, B., Louvat, P., and Allegre, C. (1999). Global silicate weathering and CO_2 consumption rates deduced from the chemistry of large rivers. *Chemical geology*, 159(1):3–30.

Gallo, F. (2014). *Glissements de terrain et érosion des chaînes de montagnes: étude de cas dans l'Himalaya central*. PhD thesis, Université de Lorraine.

Gallo, F. and Lavé, J. (2014). Evolution of a large landslide in the high himalaya of central nepal during the last half-century. *Geomorphology*, 223:20–32.

Galy, A. and France-Lanord, C. (1999). Weathering processes in the ganges–brahmaputra basin and the riverine alkalinity budget. *Chemical Geology*, 159(1):31–60.

Galy, A., France-Lanord, C., and Derry, L. (1999). The strontium isotopic budget of himalayan rivers in nepal and bangladesh. *Geochimica et Cosmochimica Acta*, 63:1905–1925.

Galy, V. (2007). *Source, transport et enfouissement du carbone organique lors de l'érosion continentale: l'exemple du système himalayen*. PhD thesis, Université de Lorraine.

Galy, V., France-Lanord, C., Peucker-Ehrenbrink, B., and Huyghe, P. (2010). Sr–nd–os evidence for a stable erosion regime in the himalaya during the past 12 myr. *Earth and Planetary Science Letters*, 290(3):474–480.

Gardner, R. and Walsh, N. (1996). Chemical weathering of metamorphic rocks from low elevations in the southern himalaya. *Chemical Geology*, 127(1-3):161–176.

Garrels, R. M. (1974). Cycling of carbon, sulfur, and oxygen through geologic time. *The sea.*, 5:303–336.

Garrels, R. M. (1983). The carbonate-silicate geochemical cycle and its effect on atmospheric carbon dioxide over the past 100 million years. *Am J Sci*, 283:641–683.

Garzanti, E., Vezzoli, G., Andò, S., Lavé, J., Attal, M., France-Lanord, C., and DeCelles, P. (2007). Quantifying sand provenance and erosion (marsyandi river, nepal himalaya). *Earth and Planetary Science Letters*, 258(3):500–515.

Georg, R., West, A., Vance, D., Newman, K., and Halliday, A. (2013). Is the marine osmium isotope record a probe for CO_2 release from sedimentary rocks? *Earth and Planetary Science Letters*, 367:28–38.

Ghatak, A. and Basu, A. R. (2011). Vestiges of the kerguelen plume in the sylhet traps, northeastern india. *Earth and Planetary Science Letters*, 308(1):52–64.

Godard, V., Bourlès, D. L., Spinabella, F., Burbank, D. W., Bookhagen, B., Fisher, G. B., Moulin, A., and Léanni, L. (2014). Dominance of tectonics over climate in himalayan denudation. *Geology*, 42(3):243–246.

Godard, V., Burbank, D., Bourlès, D., Bookhagen, B., Braucher, R., and Fisher, G. (2012). Impact of glacial erosion on 10be concentrations in fluvial sediments of the marsyandi catchment, central nepal. *Journal of Geophysical Research: Earth Surface*, 117(F3).

Goldstein, S. J. and Jacobsen, S. B. (1987). The nd and sr isotopic systematics of river-water dissolved material: Implications for the sources of nd and sr in seawater. *Chemical Geology: Isotope Geoscience section*, 66(3-4):245–272.

Goodbred, S. L. and Kuehl, S. A. (2000). Enormous ganges-brahmaputra sediment discharge during strengthened early holocene monsoon. *Geology*, 28(12):1083–1086.

Goudie, A. S. and Viles, H. A. (2012). Weathering and the global carbon cycle: geomorphological perspectives. *Earth-Science Reviews*, 113(1-2):59–71.

Guillot, S. and Le Fort, P. (1995). Geochemical constraints on the bimodal origin of high himalayan leucogranites. *Lithos*, 35(3-4):221–234.

Guillot, S., Le Fort, P., Pe^cher, A., Barman, M. R., and Aprahamian, J. (1995). Contact metamorphism and depth of emplacement of the manaslu granite (central nepal). implications for himalayan orogenesis. *Tectonophysics*, 241(1-2):99–119.

Gutjahr, M., Frank, M., Stirling, C. H., Keigwin, L. D., and Halliday, A. N. (2008). Tracing the nd isotope evolution of north atlantic deep and intermediate waters in the western north atlantic since the last glacial maximum from blake ridge sediments. *Earth and Planetary Science Letters*, 266(1):61–77.

Hardie, L. A. (1996). Secular variation in seawater chemistry: An explanation for the coupled secular variation in the mineralogies of marine limestones and potash evaporites over the past 600 my. *Geology*, 24(3):279–283.

Harris, N., Bickle, M., Chapman, H., Fairchild, I., and Bunbury, J. (1998). The significance of himalayan rivers for silicate weathering rates: evidence from the bhote kosi tributary. *Chemical Geology*, 144(3):205–220.

Harrison, T. M., Heizler, M. T., McKeegan, K. D., and Schmitt, A. K. (2010). In situ ^{40}k-^{40}ca double-plus sims dating resolves klokken feldspar ^{40}k-^{40}ar paradox. *Earth and Planetary Science Letters*, 299(3):426 – 433.

Hart, S. R. and Zindler, A. (1989). Isotope fractionation laws: a test using calcium. *International journal of mass spectrometry and ion processes*, 89(2-3):287–301.

Henderson, G., Martel, D., O'Nions, R., and Shackleton, N. (1994). Evolution of seawater ^{87}Sr/^{86}Sr over the last 400 ka: the absence of glacial/interglacial cycles. *Earth and Planetary Science Letters*, 128(3):643–651.

Hess, J., Bender, M., and Schilling, J. (1986). Evolution of the ratio of strontium-87 to strontium-86 in seawater from cretaceous to present. *Science*, 231(4741):979–984.

Heumann, K. and Lieser, K. (1973). Untersuchung von isotopenfeinvariationen des calciums in der natur an rezenten carbonaten und sulfaten. *Geochimica et Cosmochimica Acta*, 37(6):1463–1471.

Heumann, K. and Luecke, W. (1973). Calcium isotope ratios in natural carbonate rocks. *Earth and Planetary Science Letters*, 20(3):341–346.

Heumann, K. G., Kubassek, E., Schwabenbauer, W., and Stadler, I. (1979). Analytisches verfahren zur k/ca-altersbestimmung geologischer proben. *Fresenius' Zeitschrift für analytische Chemie*, 297(1):35–43.

Hinderer, M. (2001). Late quaternary denudation of the alps, valley and lake fillings and modern river loads. *Geodinamica Acta*, 14(4):231–263.

Hirt, B. and Epstein, S. (1964). A search for isotopic variations in some terrestrial and meteoritic calcium. *Trans. Am. Geophys. Union*, 45:113.

Hodell, D., Mueller, P., and Garrido, J. (1991). Variations in the strontium isotopic composition of seawater during the neogene. *Geology*, 19(1):24–27.

Hodell, D., Mueller, P., McKenzie, J., and Mead, G. (1989). Strontium isotope stratigraphy and geochemistry of the late neogene ocean. *Earth and Planetary Science Letters*, 92(2):165–178.

Hodges, K. V. (2000). Tectonics of the himalaya and southern tibet from two perspectives. *Geological Society of America Bulletin*, 112(3):324–350.

Högbom, A. (1894). Om sannolikheten för sekulära förändringar i atmosfärens kolsyrehalt. *Svensk kemisk tidskrift*, 4:169–177.

Holland, H. (2003). Treatise on geochemistry: volume 6 the oceans and marine geochemistry, ch. the geologic histiry of seawater, vol. 6.

Holland, H. D. (1984). *The chemical evolution of the atmosphere and oceans*. Princeton University Press.

Holland, H. D. (2005). Sea level, sediments and the composition of seawater. *American Journal of Science*, 305(3):220–239.

Holmden, C., Papanastassiou, D., Blanchon, P., and Evans, S. (2012). $\delta^{44/40}$Ca variability in shallow water carbonates and the impact of submarine groundwater discharge on ca-cycling in marine environments. *Geochimica et Cosmochimica Acta*, 83:179–194.

Holmes, A. (1932). The origin of igneous rocks. *Geological Magazine*, 69(12):543–558.

Horita, J., Zimmermann, H., and Holland, H. D. (2002). Chemical evolution of seawater during the phanerozoic: Implications from the record of marine evaporites. *Geochimica et Cosmochimica Acta*, 66(21):3733–3756.

Huyghe, P., Galy, A., Mugnier, J., and France-Lanord, C. (2001). Propagation of the thrust system and erosion in the lesser himalaya: Geochemical and sedimentological evidence. *Geology*, 29(11):1007–1010.

Jacobson, A., Blum, J., and Walter, L. (2002). Reconciling the elemental and sr isotope composition of himalayan weathering fluxes: insights from the carbonate geochemistry of stream waters. *Geochimica et Cosmochimica Acta*, 66(19):3417–3429.

Jaeger, J.-J., Courtillot, V., and Tapponnier, P. (1989). Paleontological view of the ages of the deccan traps, the cretaceous/tertiary boundary, and the india-asia collision. *Geology*, 17(4):316–319.

Jamieson, R. A., Beaumont, C., Nguyen, M., and Grujic, D. (2006). Provenance of the greater himalayan sequence and associated rocks: predictions of channel flow models. *Geological Society, London, Special Publications*, 268(1):165–182.

Jeandel, C. and Oelkers, E. H. (2015). The influence of terrigenous particulate material dissolution on ocean chemistry and global element cycles. *Chemical Geology*, 395:50–66.

Jones, C. and Jenkyns, H. (2001). Seawater strontium isotopes, oceanic anoxic events, and seafloor hydrothermal activity in the jurassic and cretaceous. *American Journal of Science*, 301(2):112–149.

Jones, M., Pearce, C., Jeandel, C., Gislason, S., Eiriksdottir, E., Mavromatis, V., and Oelkers, E. (2012). Riverine particulate material dissolution as a significant flux of strontium to the oceans. *Earth and Planetary Science Letters*, 355:51–59.

Jones, M. T., Gislason, S. R., Burton, K. W., Pearce, C. R., Mavromatis, V., von Strandmann, P. A. P., and Oelkers, E. H. (2014). Quantifying the impact of riverine particulate dissolution in seawater on ocean chemistry. *Earth and planetary science letters*, 395:91–100.

Kaufman, A., Jacobsen, S., and Knoll, A. (1993). The vendian record of sr and c isotopic variations in seawater: implications for tectonics and paleoclimate. *Earth and Planetary Science Letters*, 120(3):409–430.

Kısakűrek, B., James, R. H., and Harris, N. B. (2005). Li and δ^7li in himalayan rivers: Proxies for silicate weathering? *Earth and Planetary Science Letters*, 237(3-4):387–401.

Klootwijk, C., Sharma, M. L., Gergan, J., Shah, S., and Tirkey, B. (1984). The indus-tsangpo suture zone in ladakh, northwest himalaya: Further palaeomagnetic data and implications. *Tectonophysics*, 106(3-4):215–238.

Koepnick, R., Burke, W., Denison, R., Hetherington, E., Nelson, H., Otto, J., and Waite, L. (1985). Construction of the seawater 87sr86sr curve for the cenozoic and cretaceous: supporting data. *Chemical Geology: Isotope Geoscience section*, 58(1-2):55–81.

Kohn, M., Paul, S., and Corrie, S. (2010). The lower lesser himalayan sequence: A paleoproterozoic arc on the northern margin of the indian plate. *Geological Society of America Bulletin*, 122(3-4):323–335.

Kohn, M., Wieland, M., Parkinson, C., and Upreti, B. (2005). Five generations of monazite in langtang gneisses: implications for chronology of the himalayan metamorphic core. *Journal of Metamorphic Geology*, 23(5):399–406.

Kreissig, K. and Elliott, T. (2005). Ca isotope fingerprints of early crust-mantle evolution. *Geochimica et cosmochimica acta*, 69(1):165–176.

Krishnaswami, S., Singh, S., and Dalai, T. (1999). Silicate weathering in the himalaya: role in contributing to major ions and radiogenic sr to the bay of bengal. *Ocean Science, Trends and Future Directions*, pages 23–51.

Krishnaswami, S., Trivedi, J., Sarin, M., Ramesh, R., and Sharma, K. (1992). Strontium isotopes and rubidium in the ganga-brahmaputra river system: Weathering in the

himalaya, fluxes to the bay of bengal and contributions to the evolution of oceanic $^{87}Sr/^{86}Sr$. *Earth and Planetary Science Letters*, 109(1):243–253.

Kump, L. and Alley, R. B. (1994). Global chemical weathering on glacial time scales. *Material Fluxes on the Surface of the Earth*, pages 46–60.

Kump, L. R. (1989). Alternative modeling approaches to the geochemical cycles of carbon, sulfur, and strontium isotopes. *Am. J. Sci*, 289(4):390–410.

Kump, L. R., Brantley, S. L., and Arthur, M. A. (2000). Chemical weathering, atmospheric co_2, and climate. *Annual Review of Earth and Planetary Sciences*, 28(1):611–667.

Kunchithapadam, G., Macdougall, J., and Macisaac, C. (2007). High precision determination of $^{48}Ca/^{42}Ca$ ratio by tims for ca isotope fractionation studies. *Geostandards and Geoanalytical Research*, 31:227–236.

Lasaga, A. C., Berner, R. A., and Garrels, R. M. (1985). An improved geochemical model of atmospheric co_2 fluctuations over the past 100 million years. *The carbon cycle and atmospheric CO_2: natural variations Archean to present*, 32:397–411.

Lavé, J. and Avouac, J. (2001). Fluvial incision and tectonic uplift across the himalayas of central nepal. *Journal of Geophysical Research: Solid Earth*, 106(B11):26561–26591.

Le Fort, P. (1975). Himalayas: the collided range. present knowledge of the continental arc. *American Journal of Science*, 275(1):44.

Le Fort, P. (1981). Manaslu leucogranite: a collision signature of the himalaya: a model for its genesis and emplacement. *Journal of Geophysical Research: Solid Earth*, 86(B11):10545–10568.

Le Fort, P. (1986). Metamorphism and magmatism during the himalayan collision. *Geological Society, London, Special Publications*, 19(1):159–172.

Le Fort, P. (1989). The himalayan orogenic segment. In *Tectonic evolution of the Tethyan region*, pages 289–386. Springer.

Le Fort, P. (1999). Lesser himalayan crystalline nappes of nepal: Problems of their origin. *Himalaya and Tibet: mountain roots to mountain tops*, 328:225.

Le Fort, P., Cuney, M., Deniel, C., France-Lanord, C., Sheppard, S., Upreti, B., and Vidal, P. (1987). Crustal generation of the himalayan leucogranites. *Tectonophysics*, 134(1-3):39–57.

Lear, C., Elderfield, H., and Wilson, P. (2000). Cenozoic deep-sea temperatures and global ice volumes from mg/ca in benthic foraminiferal calcite. *Science*, 287(5451):269–272.

Leech, M. L. (2008). Does the karakoram fault interrupt mid-crustal channel flow in the western himalaya? *Earth and Planetary Science Letters*, 276(3-4):314–322.

Lehn, G. O. and Jacobson, A. D. (2015). Optimization of a ^{48}Ca–^{43}Ca double-spike mc-tims method for measuring ca isotope ratios ($\delta^{44/40}$Ca and $\delta^{44/42}$Ca): limitations from filament reservoir mixing. *Journal of Analytical Atomic Spectrometry*, 30(7):1571–1581.

Li, S.-L., Calmels, D., Han, G., Gaillardet, J., and Liu, C.-Q. (2008). Sulfuric acid as an agent of carbonate weathering constrained by δ^{13}C dic: examples from southwest china. *Earth and Planetary Science Letters*, 270(3):189–199.

Licht, A., Van Cappelle, M., Abels, H., Ladant, J.-B., Trabucho-Alexandre, J., France-Lanord, C., Donnadieu, Y., Vandenberghe, J., Rigaudier, T., Lécuyer, C., et al. (2014). Asian monsoons in a late eocene greenhouse world. *Nature*, 513(7519):501–506.

Lister, G., Forster, M., and Rawling, T. (2001). Episodicity during orogenesis. *Geological Society, London, Special Publications*, 184(1):89–113.

Lorphelin, L. (1986). Weathering of silt and clay in soils of a toposequence in the himalayas, nepal. *Geoderma*, 39(2):141–155.

Louvat, P. and Allègre, C. J. (1997). Present denudation rates on the island of reunion determined by river geochemistry: basalt weathering and mass budget between chemical and mechanical erosions. *Geochimica et Cosmochimica Acta*, 61(17):3645–3669.

Lowenstein, T. K., Timofeeff, M. N., Brennan, S. T., Hardie, L. A., and Demicco, R. V. (2001). Oscillations in phanerozoic seawater chemistry: Evidence from fluid inclusions. *Science*, 294(5544):1086–1088.

Ludden, J., Gélinas, L., and Trudel, P. (1982). Archean metavolcanics from the rouyn–noranda district, abitibi greenstone belt, quebec. 2. mobility of trace elements and petrogenetic constraints. *Canadian Journal of Earth Sciences*, 19(12):2276–2287.

Lupker, M., Blard, P.-H., Lave, J., France-Lanord, C., Leanni, L., Puchol, N., Charreau, J., and Bourlès, D. (2012). 10 be-derived himalayan denudation rates and sediment budgets in the ganga basin. *Earth and Planetary Science Letters*, 333:146–156.

Lupker, M., France-Lanord, C., Galy, V., Lavé, J., and Kudrass, H. (2013). Increasing chemical weathering in the himalayan system since the last glacial maximum. *Earth and Planetary Science Letters*, 365:243–252.

Lupker, M., France-Lanord, C., Lavé, J., Bouchez, J., Galy, V., Métivier, F., Gaillardet, J., Lartiges, B., and Mugnier, J.-l. (2011). A rouse-based method to integrate the chemical composition of river sediments: Application to the ganga basin. *Journal of Geophysical Research: Earth Surface*, 116(F4).

Mackenzie, F. T., Garrels, R. M., Bricker, O. P., and Bickley, F. (1967). Silica in sea water: control by silica minerals. *Science*, 155(3768):1404–1405.

Marshall, B. and DePaolo, D. (1982). Precise age determinations and petrogenetic studies using the k-ca method. *Geochimica et Cosmochimica Acta*, 46(12):2537–2545.

Marshall, B. and DePaolo, D. (1989). Calcium isotopes in igneous rocks and the origin of granite. *Geochimica et Cosmochimica Acta*, 53(4):917–922.

Marshall, B., Woodard, H., and DePaolo, D. (1986). K-ca-ar systematics of authigenic sanidine from waukau, wisconsin, and the diffusivity of argon. *Geology*, 14(11):936–938.

Martin, A. J., Gehrels, G. E., and DeCelles, P. G. (2007). The tectonic significance of (u, th)/pb ages of monazite inclusions in garnet from the himalaya of central nepal. *Chemical Geology*, 244(1-2):1–24.

McArthur, J., Howarth, R., and Bailey, T. (2001). Strontium isotope stratigraphy: Lowess version 3: Best fit to the marine sr-isotope curve for 0.509 ma and accompanying look-up table for deriving numerical age. *Journal of Geology*, 109:155–170.

McCauley, S. E. and DePaolo, D. J. (1997). The marine ^{87}sr/^{86}sr and δ^{18}o records, himalayan alkalinity fluxes, and cenozoic climate models. In *Tectonic uplift and climate change*, pages 427–467. Springer.

McCulloch, M. T. (1994). Primitive ^{87}sr/^{86}sr from an archean barite and conjecture on the earth's age and origin. *Earth and planetary science letters*, 126(1-3):1–13.

Meybeck, M. (1987). Global chemical weathering of surficial rocks estimated from river dissolved loads. *American Journal of Science*, 287(5):401–428.

Michael, H. A. and Voss, C. I. (2009a). Controls on groundwater flow in the bengal basin of india and bangladesh: regional modeling analysis. *Hydrogeology Journal*, 17(7):1561.

Michael, H. A. and Voss, C. I. (2009b). Estimation of regional-scale groundwater flow properties in the bengal basin of india and bangladesh. *Hydrogeology Journal*, 17(6):1329–1346.

Milliman, J. and Droxler, A. (1996). Neritic and pelagic carbonate sedimentation in the marine environment: ignorance is not bliss. *Geologische Rundschau*, 85(3):496–504.

Milliman, J. D. (1993). Production and accumulation of calcium carbonate in the ocean: budget of a nonsteady state. *Global Biogeochemical Cycles*, 7(4):927–957.

Millot, R., Gaillardet, J., Dupré, B., and Allègre, C. J. (2002). The global control of silicate weathering rates and the coupling with physical erosion: new insights from rivers of the canadian shield. *Earth and Planetary Science Letters*, 196(1):83–98.

Molnar, P. (1986). The geologic history and structure of the himalaya. *American Scientist*, 74(2):144–154.

Molnar, P. and Tapponnier, P. (1975). Cenozoic tectonics of asia: effects of a continental collision. *Science*, 189(4201):419–426.

Moore, W. S. (1997). High fluxes of radium and barium from the mouth of the ganges-brahmaputra river during low river discharge suggest a large groundwater source. *Earth and Planetary Science Letters*, 150(1-2):141–150.

Morin, G. (2015). *L'Érosion et L'Alteration en Himalaya et leur Évolution depuis le Tardi-Pleistocene: Analyse des Processus d'Érosion a partir de Sediments de Riviere Actuels et Passes au Nepal Central*. PhD thesis, Université de Lorraine.

Morin, G., France-Lanord, C., Gajurel, A., Gallo, F., and Lavé, J. (2014). High k and ca chemical erosion triggered by physical erosion in a watershed of the high himalaya of nepal. *Procedia Earth and Planetary Science*, 10:292–296.

Mukherjee, B. (1964). Clay minerals in argillaceous sediments of the himalayan zone. *Clay Minerals Bulletin*, 5(31):363–372.

Nägler, T. and Villa, I. (2000). In pursuit of the ^{40}K branching ratios: K-ca and ^{39}Ar–^{40}Ar dating of gem silicates. *Chemical Geology*, 169(1):5–16.

Najman, Y. (2006). The detrital record of orogenesis: A review of approaches and techniques used in the himalayan sedimentary basins. *Earth-Science Reviews*, 74(1-2):1–72.

Nakayama, K. and Ulak, P. (1999). Evolution of fluvial style in the siwalik group in the foothills of the nepal himalaya. *Sedimentary Geology*, 125(3):205–224.

Naumenko-Dèzes, M. O., Bouman, C., Nägler, T. F., Mezger, K., and Villa, I. M. (2015). Tims measurements of full range of natural ca isotopes with internally consistent fractionation correction. *International Journal of Mass Spectrometry*, 387:60–68.

Nelson, D. R. and McCulloch, M. T. (1989). Petrogenetic applications of the ^{40}K-^{40}Ca radiogenic decay scheme — a reconnaissance study. *Chemical Geology: Isotope Geoscience section*, 79(4):275–293.

Niederer, F. R. and Papanastassiou, D. (1984). Ca isotopes in refractory inclusions. *Geochimica et Cosmochimica Acta*, 48(6):1279–1293.

Niemi, N. A., Oskin, M., Burbank, D. W., Heimsath, A. M., and Gabet, E. J. (2005). Effects of bedrock landslides on cosmogenically determined erosion rates. *Earth and Planetary Science Letters*, 237(3):480–498.

Noble, S., Searle, M., and Walker, C. (2001). Age and tectonic significance of permian granites in western zanskar, high himalaya. *The Journal of Geology*, 109(1):127–135.

Oelkers, E., Gislason, S., Eiriksdottir, E., Jones, M., Pearce, C., and Jeandel, C. (2011). The role of riverine particulate material on the global cycles of the elements. *Applied Geochemistry*, 26:S365–S369.

Oliver, L., Harris, N., Bickle, M., Chapman, H., Dise, N., and Horstwood, M. (2003). Silicate weathering rates decoupled from the ^{87}Sr/^{86}Sr ratio of the dissolved load during himalayan erosion. *Chemical Geology*, 201(1):119–139.

Palmer, M. and Edmond, J. (1989). The strontium isotope budget of the modern ocean. *Earth and Planetary Science Letters*, 92(1):11–26.

Palmer, M. and Edmond, J. (1992). Controls over the strontium isotope composition of river water. *Geochimica et Cosmochimica Acta*, 56(5):2099–2111.

Papanastassiou, D. and Wasserburg, G. (1987). Rayleigh distillation constraints on mg isotopic compositions. In *Lunar and Planetary Science Conference*, volume 18.

Parrish, R. R. and Hodges, V. (1996). Isotopic constraints on the age and provenance of the lesser and greater himalayan sequences, nepalese himalaya. *Geological Society of America Bulletin*, 108(7):904–911.

Patriat, P. and Achache, J. (1984). India-eurasia collision chronology has implications for crustal shortening and driving mechanism of plates. *Nature*, 311:615–621.

Pačes, T. (1983). Rate constants of dissolution derived from the measurements of mass balance in hydrological catchments. *Geochimica et Cosmochimica Acta*, 47(11):1855–1863.

Pecher, A. (1978). *Déformations et métamorphisme associés à une zone de cisaillement. Exemple du grand Chevauchement Central Himalayen (M.C.T.), transversale des Anapurnas et du Manaslu (Népal)*. PhD thesis, Université Scientifique et Médicale de Grenoble.

Pegram, W., Krishnaswami, S., Ravizza, G., and Turekian, K. (1992). The record of sea water ^{187}os/^{186}os variation through the cenozoic. *Earth and Planetary Science Letters*, 113(4):569–576.

Peterman, Z., Hedge, C., and Tourtelot, H. (1970). Isotopic composition of strontium in sea water throughout phanerozoic time. *Geochimica et Cosmochimica Acta*, 34(1):105–120.

Petterson, M., Crawford, M., and Windley, B. (1993). Petrogenetic implications of neodymium isotope data from the kohistan batholith, north pakistan. *Journal of the Geological Society*, 150(1):125–129.

Peucker-Ehrenbrink, B. and Ravizza, G. (2000). The marine osmium isotope record. *Terra Nova*, 12(5):205–219.

Pin, C. and Bassin, C. (1992). Evaluation of a strontium-specific extraction chromatographic method for isotopic analysis in geological materials. *Analytica Chimica Acta*, 269(2):249–255.

Polevaya, N., Titov, N., Belyaev, V., and Sprintsson, V. (1958). Application of the ca method in the absolute age determination of sylvites. *Geochemistry*, 1958(8):897–906.

Porder, S., Hilley, G. E., and Chadwick, O. A. (2007). Chemical weathering, mass loss, and dust inputs across a climate by time matrix in the hawaiian islands. *Earth and Planetary Science Letters*, 258(3):414–427.

Pratt-Sitaula, B., Burbank, D. W., Heimsath, A. M., Humphrey, N. F., Oskin, M., and Putkonen, J. (2011). Topographic control of asynchronous glacial advances: A case study from annapurna, nepal. *Geophysical Research Letters*, 38(24).

Prokoph, A., Shields, G., and Veizer, J. (2008). Compilation and time-series analysis of a marine carbonate δ^{18}o, δ^{13}c, ^{87}sr/^{86}sr and δ^{34}s database through earth history. *Earth-Science Reviews*, 87(3-4):113–133.

Puchol, N., Lavé, J., Lupker, M., Blard, P.-H., Gallo, F., France-Lanord, C., Team, A., et al. (2014). Grain-size dependent concentration of cosmogenic ^{10}Be and erosion dynamics in a landslide-dominated himalayan watershed. *Geomorphology*, 224:55–68.

Putkonen, J. K. (2004). Continuous snow and rain data at 500 to 4400 m altitude near annapurna, nepal, 1999–2001. *Arctic, Antarctic, and Alpine Research*, 36(2):244–248.

Quade, J. (2003). Silicate versus carbonate weathering in the himalaya: a comparison of the arun and seti river watersheds. *Chemical Geology*, 202:275–296.

Quade, J., Roe, L., DeCelles, P., and Ojha, T. (1997). The late neogene ^{87}sr/^{86}sr record of lowland himalayan rivers. *Science*, 276(5320):1828–1831.

Ranen, M. and Jacobsen, S. (2008). Fractionation corrections for high-precision multi-collector thermal ionization mass spectrometry. In *Lunar and Planetary Science Conference*, volume 39, page 1966.

Rao, K. (1979). *India's water wealth*. Orient Blackswan.

Raymo, M. (1994). The himalayas, organic carbon burial, and climate in the miocene. *Paleoceanography*, 9(3):399–404.

Raymo, M. and Ruddiman, W. (1992). Tectonic forcing of late cenozoic climate. *Nature*, 359:117–122.

Raymo, M. E., Ruddiman, W. F., and Froelich, P. N. (1988). Influence of late cenozoic mountain building on ocean geochemical cycles. *Geology*, 16(7):649–653.

Richter, F. M., Rowley, D. B., and DePaolo, D. J. (1992). Sr isotope evolution of seawater: the role of tectonics. *Earth and Planetary Science Letters*, 109(1-2):11–23.

Ridgwell, A. and Edwards, U. (2007). 6 geological carbon sinks. *Greenhouse gas sinks*, 10:74.

Riebe, C. S., Kirchner, J. W., and Finkel, R. C. (2004). Erosional and climatic effects on long-term chemical weathering rates in granitic landscapes spanning diverse climate regimes. *Earth and Planetary Science Letters*, 224(3):547–562.

Riebe, C. S., Kirchner, J. W., Granger, D. E., and Finkel, R. C. (2001). Minimal climatic control on erosion rates in the sierra nevada, california. *Geology*, 29(5):447–450.

Robinson, D. M., DeCelles, P. G., Patchett, P. J., and Garzione, C. N. (2001). The kinematic evolution of the nepalese himalaya interpreted from nd isotopes. *Earth and Planetary Science Letters*, 192(4):507–521.

Roe, G. (2005). Orographic precipitation. *Annu. Rev. Earth Planet. Sci.*, 33:645–671.

Roth, A. S., Scherer, E. E., Maden, C., Mezger, K., and Bourdon, B. (2014). Revisiting the ^{142}Nd deficits in the 1.48 ga khariar alkaline rocks, india. *Chemical Geology*, 386:238–248.

Ruddiman, W. F., Raymo, M. E., Prell, W. L., and Kutzbach, J. E. (1997). The uplift-climate connection: a synthesis. In *Tectonic uplift and climate change*, pages 471–515. Springer.

Russell, W., Papanastassiou, D., and Tombrello, T. (1978). Ca isotope fractionation on the earth and other solar system materials. *Geochimica et Cosmochimica Acta*, 42(8):1075–1090.

Sarin, M. and Krishnaswami, S. (1984). Major ion chemistry of the ganga–brahmaputra river systems, india. *Nature*, 312(5994):538.

Sarin, M., Krishnaswami, S., Dilli, K., Somayajulu, B., and Moore, W. (1989). Major ion chemistry of the ganga-brahmaputra river system: Weathering processes and fluxes to the bay of bengal. *Geochimica et cosmochimica acta*, 53(5):997–1009.

Sarin, M., Krishnaswami, S., Trivedi, J., and Sharma, K. (1992). Major ion chemistry of the ganga source waters: weathering in the high altitude himalaya. *Proceedings of the Indian Academy of Sciences-Earth and Planetary Sciences*, 101(1):89–98.

Schärer, U., Copeland, P., Harrison, T. M., and Searle, M. P. (1990). Age, cooling history, and origin of post-collisional leucogranites in the karakoram batholith; a multi-system isotope study. *The Journal of Geology*, 98(2):233–251.

Schelling, D. and Arita, K. (1991). Thrust tectonics, crustal shortening, and the structure of the far-eastern nepal himalaya. *Tectonics*, 10(5):851–862.

Schiller, M., Paton, C., and Bizzarro, M. (2012). Calcium isotope measurement by combined hr-mc-icpms and tims. *Journal of Analytical Atomic Spectrometry*, 27(1):38–49.

Schopka, H. (2011). *Chemical weathering and consumption of atmospheric CO_2 in volcanic and ultramafic regions in the tropics*. PhD thesis, Cornell University.

Schopka, H., Derry, L., and Arcilla, C. (2011). Chemical weathering, river geochemistry and atmospheric carbon fluxes from volcanic and ultramafic regions on luzon island, the philippines. *Geochimica et Cosmochimica Acta*, 75(4):978–1002.

Searle, M., Waters, D., Dransfield, M., Stephenson, B., Walker, C., Walker, J., and Rex, D. (1999). Thermal and mechanical models for the structural and metamorphic evolution of the zanskar high himalaya. *Geological Society, London, Special Publications*, 164(1):139–156.

Searle, M., Waters, D., Rex, D., and Wilson, R. (1992). Pressure, temperature and time constraints on himalayan metamorphism from eastern kashmir and western zanskar. *Journal of the Geological Society*, 149(5):753–773.

Sharma, M., Balakrishna, K., Hofmann, A., and Shankar, R. (2007). The transport of osmium and strontium isotopes through a tropical estuary. *Geochimica et Cosmochimica Acta*, 71(20):4856–4867.

Shih, C., Nyquist, L., Bogard, D., and Wiesmann, H. (1994). K-ca and rb-sr dating of two lunar granites: Relative chronometer resetting. *Geochimica et cosmochimica acta*, 58(14):3101–3116.

Shrestha, A. B. (1998). *Physical and chemical climate in the Nepal Himalaya*. PhD thesis, University of New Hampshire.

Shrestha, M. (2000). Interannual variation of summer monsoon rainfall over nepal and its relation to southern oscillation index. *Meteorology and Atmospheric Physics*, 75(1):21–28.

Simon, J. I., DePaolo, D. J., and Moynier, F. (2009). Calcium isotope composition of meteorites, earth, and mars. *The Astrophysical Journal*, 702(1):707.

Singh, S. (2006). Spatial variability in erosion in the brahmaputra basin: causes and impacts. *Current Science*, 90(9):1272–1275.

Singh, S. and France-Lanord, C. (2002). Tracing the distribution of erosion in the brahmaputra watershed from isotopic compositions of stream sediments. *Earth and Planetary Science Letters*, 202(3):645–662.

Singh, S., Trivedi, J., K. Pande, R. R., and Krishnaswami, S. (1998). Chemical and strontium, oxygen, and carbon isotopic compositions of carbonates from the lesser himalaya: Implications to the strontium isotope composition of the source waters of the ganga, ghaghara, and the indus rivers. *Geochimica et Cosmochimica Acta*, 62(5):743–755.

Singh, S. K., Rai, S. K., and Krishnaswami, S. (2008). Sr and nd isotopes in river sediments from the ganga basin: sediment provenance and spatial variability in physical erosion. *Journal of Geophysical Research: Earth Surface*, 113(F3).

Singh, S. K., Sarin, M., and France-Lanord, C. (2005). Chemical erosion in the eastern himalaya: major ion composition of the brahmaputra and δ^{13}c of dissolved inorganic carbon. *Geochimica et Cosmochimica Acta*, 69(14):3573–3588.

Sinha, R. and Friend, P. F. (1994). River systems and their sediment flux, indo-gangetic plains, northern bihar, india. *Sedimentology*, 41(4):825–845.

Spooner, E. (1976). The strontium isotopic composition of seawater, and seawater-oceanic crust interaction. *Earth and Planetary Science Letters*, 31(1):167–174.

Stahl, W. (1968). Search for natural variations in calcium isotope abundances. *Earth and Planetary Science Letters*, 5:171–174.

Stahl, W. and Wendt, I. (1968). Fractionation of calcium isotopes in carbonate precipitation. *Earth and Planetary Science Letters*, 5:184–186.

Stallard, R. and Edmond, J. (1983). Geochemistry of the amazon: 2. the influence of geology and weathering environment on the dissolved load. *Journal of Geophysical Research: Oceans*, 88(C14):9671–9688.

Stallard, R. F. (1995). Tectonic, environmental, and human aspects of weathering and erosion: a global review using a steady-state perspective. *Annual Review of Earth and Planetary Sciences*, 23(1):11–39.

Taylor, A. and Blum, J. D. (1995). Relation between soil age and silicate weathering rates determined from the chemical evolution of a glacial chronosequence. *Geology*, 23(11):979–982.

Taylor, S. (1964). Abundance of chemical elements in the continental crust: a new table. *Geochimica et cosmochimica acta*, 28(8):1273–1285.

Taylor, S. and McLennan, S. (1985). *The continental crust. Its evolution and composition.* Black-Well Science.

Tera, F., Eugster, O., Burnett, D., and Wasserburg, G. (1970). Comparative study of li, na, k, rb, cs, ca, sr and ba abundances in achondrites and in apollo 11 lunar samples. *Geochimica et Cosmochimica Acta Supplement*, 1:1637.

Tipper, E., Gaillardet, J., Galy, A., Louvat, P., Bickle, M., and Capmas, F. (2010). Calcium isotope ratios in the world's largest rivers: a constraint on the maximum imbalance of oceanic calcium fluxes. *Global Biogeochemical Cycles*, 24(3).

Tipper, E. T., Galy, A., and Bickle, M. J. (2008). Calcium and magnesium isotope systematics in rivers draining the himalaya-tibetan-plateau region: Lithological or fractionation control? *Geochimica et Cosmochimica Acta*, 72(4):1057–1075.

Turchyn, A. V., Tipper, E. T., Galy, A., Lo, J.-K., and Bickle, M. J. (2013). Isotope evidence for secondary sulfide precipitation along the marsyandi river, nepal, himalayas. *Earth and Planetary Science Letters*, 374:36–46.

Upreti, B. (1999). An overview of the stratigraphy and tectonics of the nepal himalaya. *Journal of Asian Earth Sciences*, 17(5):577–606.

Urey, H. C. (1952). On the early chemical history of the earth and the origin of life. *Proceedings of the National Academy of Sciences*, 38(4):351–363.

Valdiya, K. S. (1993). Uplift and geomorphic rejuvenation of the himalaya in the quaternary period. *Current Science*, pages 873–885.

Vance, D. and Harris, N. (1999). Timing of prograde metamorphism in the zanskar himalaya. *Geology*, 27(5):395–398.

Vance, D., Teagle, D. A., and Foster, G. L. (2009). Variable quaternary chemical weathering fluxes and imbalances in marine geochemical budgets. *Nature*, 458(7237):493–496.

Veizer, J., Buhl, D., Diener, A., Ebneth, S., Podlaha, O. G., Bruckschen, P., Jasper, T., Korte, C., Schaaf, M., Ala, D., et al. (1997). Strontium isotope stratigraphy: potential resolution and event correlation. *Palaeogeography, Palaeoclimatology, Palaeoecology*, 132(1-4):65–77.

Veizer, J. and Compston, W. (1974). $^{87}Sr/^{86}Sr$ composition of seawater during the phanerozoic. *Geochimica et Cosmochimica Acta*, 38(9):1461–1484.

Veizer, J. and Compston, W. (1976). $^{87}Sr/^{86}Sr$ in precambrian carbonates as an index of crustal evolution. *Geochimica et Cosmochimica Acta*, 40(8):905–914.

Velbel, M. A. (1985). Geochemical mass balances and weathering rates in forested watersheds of the southern blue ridge. *American Journal of Science*, 285(10):904–930.

Velbel, M. A. (1993). Constancy of silicate-mineral weathering-rate ratios between natural and experimental weathering: implications for hydrologic control of differences in absolute rates. *Chemical Geology*, 105(1-3):89–99.

Vidal, P., Cocherie, A., and Le Fort, P. (1982). Geochemical investigations of the origin of the manaslu leucogranite (himalaya, nepal). *Geochimica et Cosmochimica Acta*, 46(11):2279–2292.

Viers, J., Dupré, B., and Gaillardet, J. (2009). Chemical composition of suspended sediments in world rivers: New insights from a new database. *Science of the total Environment*, 407(2):853–868.

Von Damm, K., Edmond, J., Grant, B., Measures, C., Walden, B., and Weiss, R. (1985). Chemistry of submarine hydrothermal solutions at 21°N, east pacific rise. *Geochimica et Cosmochimica Acta*, 49(11):2197–2220.

Wadleigh, M. A., Veizer, J., and Brooks, C. (1985). Strontium and its isotopes in canadian rivers: Fluxes and global implications. *Geochimica et Cosmochimica Acta*, 49(8):1727–1736.

Walker, C., Searle, M., and Waters, D. (2001). An integrated tectonothermal model for the evolution of the high himalaya in western zanskar with constraints from thermobarometry and metamorphic modeling. *Tectonics*, 20(6):810–833.

Walker, J., Hays, P., and Kasting, J. (1981). A negative feedback mechanism for the long-term stabilization of earth's surface temperature. *Journal of Geophysical Research: Oceans*, 86:9776–9782.

Wang, Q., Zhang, P.-Z., Freymueller, J. T., Bilham, R., Larson, K. M., Lai, X., You, X., Niu, Z., Wu, J., Li, Y., et al. (2001). Present-day crustal deformation in china constrained by global positioning system measurements. *Science*, 294(5542):574–577.

Wasserburg, G., Jacobsen, S., DePaolo, D., McCulloch, M., and Wen, T. (1981). Precise determination of sm/nd ratios, sm and nd isotopic abundances in standard solutions. *Geochimica et Cosmochimica Acta*, 45(12):2311–2323.

West, A. J., Bickle, M. J., Collins, R., and Brasington, J. (2002). Small-catchment perspective on himalayan weathering fluxes. *Geology*, 30(4):355–358.

West, A. J., Galy, A., and Bickle, M. (2005). Tectonic and climatic controls on silicate weathering. *Earth and Planetary Science Letters*, 235(1):211–228.

Whipp, D. M., Ehlers, T. A., Blythe, A. E., Huntington, K. W., Hodges, K. V., and Burbank, D. W. (2007). Plio-quaternary exhumation history of the central nepalese himalaya: 2. thermokinematic and thermochronometer age prediction model. *Tectonics*, 26(3).

White, A. F. and Blum, A. E. (1995). Effects of climate on chemical weathering in watersheds. *Geochimica et Cosmochimica Acta*, 59(9):1729–1747.

White, A. F. and Brantley, S. L. (2003). The effect of time on the weathering of silicate minerals: why do weathering rates differ in the laboratory and field? *Chemical Geology*, 202(3):479–506.

White, A. F., Bullen, T. D., Vivit, D. V., Schulz, M. S., and Clow, D. W. (1999). The role of disseminated calcite in the chemical weathering of granitoid rocks. *Geochimica et Cosmochimica Acta*, 63(13):1939–1953.

White, L. T. and Lister, G. S. (2012). The collision of india with asia. *Journal of Geodynamics*, 56:7–17.

White, W. M. (2013). *Geochemistry*. John Wiley & Sons.

Whittington, A., Foster, G., Harris, N., Vance, D., and Ayres, M. (1999). Lithostratigraphic correlations in the western himalaya—an isotopic approach. *Geology*, 27(7):585–588.

Wickman, F. (1948). Isotope ratios: a clue to the age of certain marine sediments. *The Journal of Geology*, pages 61–66.

Wieser, M. E. and Schwieters, J. B. (2005). The development of multiple collector mass spectrometry for isotope ratio measurements. *International Journal of Mass Spectrometry*, 242(2):97–115.

Wilhelm, H. G. and Ackermann, W. (1972). Altersbestimmung nach der k-ca-methode an sylvin des oberen zechsteines des werragebietes potassium. *Zeitschrift für Naturforschung A*, 27(8-9):1256–1259.

Wilkinson, B. H. and Algeo, T. J. (1989). Sedimentary carbonate record of calcium-magnesium cycling. *American Journal of Science*, 289(10):1158–1194.

Wolff-Boenisch, D., Gabet, E., Burbank, D., Langner, H., and Putkonen, J. (2009). Spatial variations in chemical weathering and co_2 consumption in nepalese high himalayan catchments during the monsoon season. *Geochimica Cosmochimica Acta*, 73:3148–3170.

Yin, A. (2006). Cenozoic tectonic evolution of the himalayan orogen as constrained by along-strike variation of structural geometry, exhumation history, and foreland sedimentation. *Earth-Science Reviews*, 76(1–2):1–131.

Zachos, J., Pagani, M., Sloan, L., Thomas, E., and Billups, K. (2001). Trends, rhythms, and aberrations in global climate 65 ma to present. *science*, 292(5517):686–693.

Zhu, H. L., Zhang, Z. F., Wang, G. Q., Liu, Y. F., Liu, F., Li, X., and Sun, W. D. (2015). Calcium isotopic fractionation during ion-exchange column chemistry and thermal ionisation mass spectrometry (tims) determination. *Geostandards and Geoanalytical Research*.

Appendices

APPENDIX A

APPENDIX A

Table A.1 – *Sample Locations and descriptions for the samples analyzed in the Ganga, Brahmaputra, Meghna System.*

Sample	River	Description	Date	Longitude	Latitude	Altitude
BR400	Brahmaputra	Sirajganj	12/07/2004	89.431089	24.61146	12
BGP79	Brahmaputra	Chilmari	07/03/1997	89.431807	25.361351	24
BR200	Brahmaputra	Jamuna Bridge	15/07/2002	89.474686	24.23561	9
BGP15	Brahmaputra	Chilmari	05/08/1996	89.431807	25.361351	24
BR410	Ganga Bangla	Harding Bridge	13/07/2004	89.105187	23.565492	12
BR942	Ganga Upper	Rishikesh		78.33044	30.12661	407
BR112	Ganga	Manihari	06/08/2001	87.36114	25.1857	25
BR212	Ganga	Harding Bridge	16/07/2002	89.13954	24.33792	4
BGP39	Meghna	Bhairab Bazar	13/08/1996	91.042	24.25934	4
BR221	Lower Meghna	Ganeshpura	18/07/2002	90.66667	22.80000	4
BR447	Lower Meghna		18/07/2004	90.463515	22.35006	7
BR531	Lower Meghna	Padma at Mawa	24/07/2005	90.25000	23.46693	3
BR936	Chambal			77.90255	26.65746	120
AK1	Alaknanda	Name of town: Muley Goen, small tributary of the Alaknanda river, right above the confluence of Alaknanda and Bhagirathi.	02/10/2014	78.38354	30.1127	595
AK11	Alaknanda	Main river sample	03/10/2014	78.58695	30.18132	651
AK16	Alaknanda	main Pindar River, downstream of Simli Gad.	04/10/2014	79.15374	30.13667	816
AK29	Alaknanda	Tributary Dhauli Ganga	09/10/2014	79.49497	30.37344	2628
AK53	Alaknanda	Vegetation plot in Rishikesh, soil is clayrich, but very high contamination (Ganga River)	15/10/2014	78.19898	30.07903	346
S16	Sutlej	Waterpump close to Rampur	16/09/2014	77.3726	31.24865	928
S17	Sutlej	Main Sutlej River	16/09/2014	77.37274	31.25037	940
S29	Sutlej	hot spring	17.09.2014	77.4688	31.31539	
S43	Sutlej	tributary Sutlej, close to the powerplant project (Whanga Gat)	17/09/2014	78.00741	31.32678	1537
S50	Sutlej	major tributary Baspa river	18/09/2014	78.21225	31.2329	3110
S59	Sutlej	tributary Baspa river, very clear water, so is not filtered.	18/09/2014	78.17.883	31.2503	2795
S68	Sutlej	main Baspa river, downstream of the dam, and just downstream of the landslide	19/09/2014	78.12695	31.26592	2144
S101	Sutlej	Pump	23/09/2014	78.12.340	32.05082	3454
S111	Sutlej	Waterpump	24/09/2014	78.05632	32.11159	3562

Table A.2 – *Dissolved load geochemistry of samples analyzed in the Ganga, Brahmaputra, Meghna System.*

Sample	River	Cl^-	SO_4	HCO_3^-	Si	Mg	Ca	Na	K	Sr	1/Sr	1/Ca	Ca^*/Na^*	Mg^*/Na^*	Ca^*/Sr	Sr/Na^*	Na^*/Ca^*	HCO_3^{-*}/Na^*
							µmol/L											
BR400	Brahmaputra	18.62	42.27	698.73	99.48	125.76	318.95	61.53	54.71	0.45	2.22	0.0031	6.19	2.44	706.79	8.76	0.16	13.56
BGP79	Brahmaputra	52.47	149.39	1208.71	–	214.36	589.82	195.74	75.45	0.90	1.11	0.0017	3.18	1.15	655.08	4.85	0.31	6.51
BR200	Brahmaputra	–	–	1082.00	126.58	120.29	432.99	77.02	61.97	–	–	0.0023	6.46	1.79	–	–	0.15	16.14
BGP15	Brahmaputra	24.54	–	1010.84	154.88	178.98	412.92	73.73	37.21	0.32	3.08	0.0024	6.48	2.81	1272.66	5.09	0.15	15.86
BR410	Ganga Bangla	73.91	69.54	1338.48	123.51	178.11	498.85	232.81	73.68	0.69	1.45	0.0020	2.24	0.80	722.98	3.10	0.45	6.01
BR942	Ganga Upper	4.95	144.21	715.59	70.74	142.00	477.30	61.90	59.90	0.55	1.83	0.0021	9.20	2.74	875.27	10.51	0.11	13.79
BR112	Ganga	51.90	63.61	1467.19	–	175.31	591.02	191	82.61	1.01	0.99	0.0017	3.26	0.97	585.81	5.56	0.31	8.08
BR213	Ganga	80.39	86.72	1414.39	158.30	192.76	590.05	200.35	84.35	–	–	0.0017	3.10	1.01	–	–	0.32	7.43
BGP39	Meghna	30.18	21.24	340.60	129.25	73.44	101.92	87.43	15.98	0.22	4.55	0.0098	1.32	0.95	463.79	2.84	0.76	4.40
BR221	Lower Meghna	–	–	1032.12	113.65	115.27	391.45	99.22	50.79	–	–	0.0026	4.39	1.29	–	–	0.23	11.57
BR447	Lower Meghna	31.59	55.28	967.81	116.75	136.05	438.55	92.86	60.79	0.62	1.62	0.0023	5.29	1.64	711.73	7.44	0.19	11.68
BR531	Lower Meghna	33.71	61.97	1270.29	121.80	170.10	536.50	152.80	68.20	–	–	0.0019	3.76	1.19	–	–	0.27	8.90
BR936	Chambal	245.42	166.56	2381.95	161.59	295.23	721.31	663.77	99.72	2.37	0.42	0.0014	1.10	0.45	304.92	3.62	0.91	3.64
AK1	Alaknanda	–	–	2987.61	282.90	488.40	922.15	549.85	31.18	3.02	0.33	0.0011	1.71	0.90	305.24	5.60	0.59	5.53
AK11	Alaknanda	–	–	1009.40	183.19	272.04	399.39	91.43	18.01	0.35	2.83	0.0025	4.90	3.34	1130.82	4.34	0.20	12.40
AK16	Alaknanda	–	–	1196.18	136.74	205.81	481.20	87.74	48.44	0.46	2.17	0.0021	6.19	2.65	1042.47	5.94	0.16	15.39
AK29	Alaknanda	–	–	1204.14	73.44	341.43	510.56	78.29	15.57	1.45	0.69	0.0020	7.48	5.00	351.29	21.28	0.13	17.63
AK53	Alaknanda	–	–	1153.11	109.71	180.09	435.03	113.64	45.67	0.69	1.44	0.0023	4.20	1.74	627.17	6.69	0.24	11.13
S16	Sutlej	126.20	620.31	2372.13	371.91	737.86	733.03	1107.78	538.39	3.66	0.27	0.0014	0.67	0.67	200.41	3.33	1.50	2.16
S17	Sutlej	61.10	260.64	459.38	98.39	155.82	453.73	139.85	43.05	1.68	0.60	0.0022	3.49	1.20	270.06	12.94	0.29	3.54
S29	Sutlej	40068.63	1747.50	74655.15	1359.39	687.41	3222.18	36338.91	747.56	18.51	0.05	0.0003	0.09	0.02	174.06	0.51	11.27	2.05
S43	Sutlej	19.08	157.14	291.76	123.61	72.12	263.27	87.69	51.42	0.44	2.27	0.0038	3.39	0.93	597.73	5.67	0.30	3.76
S50	Sutlej	10.01	361.94	-30.53	85.62	209.94	393.53	108.01	41.38	1.42	0.70	0.0025	4.02	2.14	276.41	14.53	0.25	-0.31
S59	Sutlej	7.59	183.88	232.23	162.10	43.00	282.42	88.28	32.88	0.20	5.00	0.0035	3.61	0.55	1412.79	2.55	0.28	2.97
S68	Sutlej	16.60	308.45	121.64	104.80	136.50	386.20	103.60	57.01	1.00	1.00	0.0026	4.13	1.46	387.87	10.64	0.24	1.30
S101	Sutlej	–	–	3369.79	80.56	831.70	1398.13	262.60	27.04	11.90	0.08	0.0007	5.53	3.29	117.50	47.10	0.18	13.34
S111	Sutlej	–	–	2655.72	83.42	844.30	1128.04	173.33	21.35	22.23	0.04	0.0009	6.91	5.17	50.74	136.11	0.14	16.26

Table A.3 – *$^{87}Sr/^{86}Sr$ and $\varepsilon^{40}Ca$ compositions of water samples from the Ganga, Brahmaputra, and Meghna system.*

Sample	River	$^{87}Sr/^{86}Sr$	$\varepsilon^{40}Ca$	$\pm$	$\varepsilon^{40}Ca$ (Average)	$\pm$ (Average)
BR400	Brahmaputra	0.73138	1.25	0.29		
			0.92	0.33	1.02	0.65
			0.88	0.32		
BGP79	Brahmaputra	0.72176	0.55	0.34	–	–
BR200	Brahmaputra	0.71785	0.23	0.35	–	–
BGP15	Brahmaputra	0.74130	-0.07	0.40	–	–
BR410	Ganga Bangla	0.73086	0.58	0.22	0.61	0.31
			0.65	0.21		
BR942	Ganga Upper	0.73065	-0.09	0.28		
			0.69	0.25	0.31	0.54
			0.31	0.29		
BR112	Ganga	0.73009	0.89	0.33	–	–
BR213	Ganga	0.73066	1.04	0.35	–	–
BGP39	Meghna	0.71595	-0.17	0.41	–	–
BR221	Lower Meghna	0.72323	0.19	0.38	–	–
BR447	Lower Meghna	0.72268	0.72	0.30	–	–
BR531	Lower Meghna	0.72445	0.34	0.30	–	–
BR936	Chambal	0.71101	0.32	0.21	0.27	0.32
			0.22	0.24		
AK1	Alaknanda	0.74652	1.79	0.38	1.99	0.93
			2.19	0.76		
AK11	Alaknanda	0.75305	1.17	0.33		
			1.57	0.31	1.42	0.71
			1.53	0.39		
AK16	Alaknanda	0.74168	0.71	0.41	0.57	0.56
			0.42	0.39		
AK29	Alaknanda	0.73103	0.24	0.56	0.45	0.73
			0.65	0.45		

Table A.3 continued from previous page

Sample	River	$^{87}Sr/^{86}Sr$	$\varepsilon^{40}Ca$	$\pm$	$\varepsilon^{40}Ca$ (Average)	$\pm$ (Average)
AK53	Alaknanda	0.73792	0.25	0.48	0.49	0.67
			0.72	0.47		
S16	Sutlej	0.73285	0.41	0.41	0.42	0.53
			0.43	0.32		
S17	Sutlej	0.71981	0.47	0.40		
			0.91	0.47	0.69	0.97
			0.69	0.48		
S29	Sutlej	0.76290	0.26	0.31	0.05	0.44
			-0.17	0.31		
S43	Sutlej	0.73143	0.96	0.34	0.81	0.48
			0.65	0.34		
S50	Sutlej	0.72797	0.45	0.56	0.39	0.83
			0.33	0.61		
S59	Sutlej	0.74882	0.53	0.74	0.15	0.92
			-0.23	0.43		
S68	Sutlej	0.73011	1.93	0.40	–	–
S101	Sutlej	0.70940	0.10	0.48	0.16	0.64
			0.22	0.41		
S111	Sutlej	0.70879	0.25	0.36	0.42	0.54
			0.58	0.40		

Table A.4 – *Budget model calculations based on major element geochemistry and $\varepsilon^{40}Ca$ isotopic compositions for water from the Ganga, Brahmaputra, and Meghna system.*

		R^{chem} (1)				F_{Ca}^{chem} (2)		F_{Ca}^{iso} (6)		F_{Ca}^{isoEMA} (8)			R^{mixed} (10)			Substition Balance Calculations (13)		Radiogenic Carbonate Fraction (16)
Sample	River	R^{chem} (1)	± (3)	± (4)	Total Error R^{chem}	F_{Ca}^{chem}	± (5)	F_{Ca}^{iso}	± (7)	F_{Ca}^{isoEMA}	± (9)	Ca_{sil}^{iso}	± (11)	R^{Mixed}	± (12)	Radiogenic Silicate EM (14)	Ca/Na (15)	
BR400	Brahmaputra	**0.27**	0.06	0.03	**0.68**	**0.06**	**0.03**	**0.18**	**0.11**	**0.13**	**0.21**	52.25	33.46	**0.32**	**0.07**	18.29	0.50	0.12
BGP79	Brahmaputra	**0.33**	0.08	0.02	**0.68**	**0.10**	**0.06**	**0.09**	**0.06**	**0.07**	**0.11**	53.81	33.27	**0.26**	**0.04**	5.40	0.03	-0.01
BR200	Brahmaputra	**0.24**	0.05	0.02	**0.67**	**0.07**	**0.04**	**0.04**	**0.06**	**0.03**	**0.05**	16.56	24.96	**0.24**	**0.04**	3.14	0.39	-0.03
BGP15	Brahmaputra	**0.19**	0.05	0.01	**0.68**	**0.05**	**0.03**	**-0.01**	**0.07**	**-0.01**	**0.01**	-4.62	27.08	**0.11**	**0.04**	-1.40	-0.09	-0.06
BR410	Ganga Bangla	**0.44**	0.11	0.02	**0.69**	**0.13**	**0.08**	**0.11**	**0.05**	**0.08**	**0.13**	50.73	25.28	**0.30**	**0.03**	4.58	0.28	-0.03
BR942	Ganga Upper	**0.20**	0.04	0.02	**0.67**	**0.05**	**0.03**	**0.05**	**0.09**	**0.04**	**0.06**	24.44	42.58	**0.21**	**0.07**	6.35	0.69	0.00
BR112	Ganga	**0.35**	0.09	0.02	**0.68**	**0.10**	**0.06**	**0.15**	**0.06**	**0.11**	**0.19**	88.15	32.05	**0.32**	**0.04**	9.08	0.58	0.06
BR213	Ganga	**0.38**	0.10	0.02	**0.69**	**0.08**	**0.05**	**0.18**	**0.06**	**0.13**	**0.22**	102.39	34.76	**0.33**	**0.04**	12.31	0.58	0.10
BR221	L. Meghna	**0.27**	0.06	0.02	**0.67**	**0.11**	**0.06**	**0.03**	**0.07**	**0.02**	**0.04**	12.34	24.02	**0.24**	**0.04**	1.80	0.22	-0.07
BR447	Lower Meghna	**0.28**	0.07	0.02	**0.68**	**0.06**	**0.03**	**0.12**	**0.05**	**0.09**	**0.15**	51.82	21.97	**0.27**	**0.04**	12.46	0.70	0.07
BR531	Lower Meghna	**0.31**	0.07	0.02	**0.68**	**0.09**	**0.05**	**0.06**	**0.05**	**0.04**	**0.07**	30.16	26.92	**0.24**	**0.03**	3.65	0.26	-0.03
BGP39	Meghna	**0.55**	0.15	0.02	**0.69**	**0.28**	**0.16**	**-0.03**	**0.07**	**-0.02**	**0.04**	-2.35	5.68	**0.25**	**0.03**	-0.61	-0.06	-0.31
BR936	Chambal	**0.67**	0.19	0.02	**0.69**	**0.24**	**0.14**	**0.05**	**0.06**	**0.03**	**0.06**	32.70	38.76	**0.31**	**0.03**	1.11	0.06	-0.20
AK1	Alaknanda	**0.25**	0.06	0.00	**0.68**	**0.25**	**0.14**	**0.34**	**0.16**	**0.25**	**0.41**	310.23	144.98	**0.30**	**0.07**	8.00	1.36	0.10
AK11	Alaknanda	**0.11**	0.03	0.00	**0.68**	**0.10**	**0.06**	**0.25**	**0.12**	**0.18**	**0.30**	92.81	46.41	**0.19**	**0.06**	14.74	2.71	0.15
AK16	Alaknanda	**0.13**	0.03	0.01	**0.67**	**0.08**	**0.04**	**0.10**	**0.10**	**0.07**	**0.12**	45.33	44.54	**0.15**	**0.04**	7.51	1.39	0.02
AK29	Alaknanda	**0.08**	0.02	0.00	**0.67**	**0.06**	**0.04**	**0.08**	**0.13**	**0.06**	**0.09**	38.08	61.77	**0.09**	**0.06**	7.10	1.31	0.01
AK53	Alaknanda	**0.17**	0.04	0.01	**0.67**	**0.11**	**0.06**	**0.08**	**0.12**	**0.06**	**0.10**	35.05	47.93	**0.17**	**0.05**	4.45	0.80	-0.03
S16	Sutlej	**0.83**	0.19	0.06	**0.68**	**0.56**	**0.33**	**0.07**	**0.09**	**0.05**	**0.09**	51.72	65.27	**0.60**	**0.03**	0.75	0.13	-0.49
S17	Sutlej	**0.21**	0.06	0.01	**0.69**	**0.07**	**0.04**	**0.12**	**0.17**	**0.09**	**0.14**	51.59	72.53	**0.16**	**0.08**	9.56	0.61	0.05
S29	Sutlej	**10.26**	3.71	0.04	**0.73**	**-0.48**	**0.28**	**0.01**	**0.08**	**0.01**	**0.01**	27.71	243.87	**-0.16**	**0.05**	-0.10	0.00	0.49
S43	Sutlej	**0.26**	0.06	0.02	**0.68**	**0.11**	**0.06**	**0.14**	**0.08**	**0.10**	**0.17**	33.85	20.06	**0.25**	**0.04**	7.23	0.85	0.03
S50	Sutlej	**0.18**	0.04	0.01	**0.68**	**0.11**	**0.06**	**0.07**	**0.14**	**0.05**	**0.08**	25.09	53.41	**0.16**	**0.06**	3.71	0.53	-0.04
S59	Sutlej	**0.20**	0.04	0.01	**0.68**	**0.12**	**0.07**	**0.03**	**0.16**	**0.02**	**0.03**	6.77	41.49	**0.15**	**0.07**	1.22	0.18	-0.10
S68	Sutlej	**0.21**	0.05	0.02	**0.68**	**0.09**	**0.05**	**0.33**	**0.07**	**0.25**	**0.40**	121.74	25.23	**0.30**	**0.03**	20.35	2.62	0.24
S101	Sutlej	**0.09**	0.02	0.00	**0.68**	**0.08**	**0.04**	**0.03**	**0.11**	**0.02**	**0.03**	38.13	152.53	**0.07**	**0.05**	2.07	0.32	-0.05
S111	Sutlej	**0.07**	0.02	0.00	**0.68**	**0.06**	**0.04**	**0.07**	**0.09**	**0.05**	**0.09**	80.45	103.44	**0.08**	**0.04**	6.65	1.07	0.01

(1) Major Element Budget; Ca/Na of silicate end-member of the Narayani used here.
(2) Ca elemental budget; Ca/Na of silicate end-member of the Narayani used here.
(3) Error associated with Ca/Na uncertainty (see 1).
(4) Error associated with Mg/K uncertainty (see 1).
(5) Error associated with Ca/Na uncertainty.
(6) Ca isotopic budget, bed load end-members.
(7) Error calculated based on the Ca isotopic measurement uncertainty.
(8) Ca isotope budget, modeled average end-member for each formation.
(9) Error from lithological uncertainty (see section 5.5.3 and 5.5.4 in Chapter 5.
(10) Combined radiogenic and elemental budget.
(11) Error calculated based on the Ca isotopic measurement uncertainty.

Table A.4 continued from previous page

		$\mathbf{R}^{chem}$ **(1)**				$\mathbf{F}_{Ca}^{chem}$ **(2)**		$\mathbf{F}_{Ca}^{iso}$ **(6)**		$\mathbf{F}_{Ca}^{isoEMA}$ **(8)**			$\mathbf{R}^{mixed}$ **(10)**		Substition Balance Calculations (13)		Radiogenic Carbonate Fraction (16)
Sample	River	$\mathbf{R}^{chem}$ **(1)**	$\pm$ (3)	$\pm$ (4)	**Total Error** $\mathbf{R}^{chem}$	$\mathbf{F}_{Ca}^{chem}$	$\pm$ **(5)**	$\mathbf{F}_{Ca}^{iso}$	$\pm$ **(7)**	$\mathbf{F}_{Ca}^{isoEMA}$	$\pm$ **(9)**	Ca_{sil}^{iso}	$\pm$ (11)	$\mathbf{R}^{Mixed}$	$\pm$ **(12)**	Radiogenic Silicate EM (14)	Ca/Na (15)	

(12) Combined error from isotope measurements and Mg/K error.

(13) Substitution calculations made to observe the required Ca/Na and radiogenic silicate end-member required to satisfy the major elemental and isotopic budget estimates.

(14) The radiogenic Ca composition required to be equal with the estimate based on (2) (see equation in Chapter 5).

(15) The Ca/Na ratio required to be equal with the estimate based on (6) (see equation in Chapter 5).

(16) The amount (%) of the dissolved load that has a radiogenic carbonate signature (see equation 5.22 and 5.23 in Chapter 5.

Table A.5 – *The Ganges-Brahmaputra Sr and radiogenic Ca isotopic balance and the global marine Sr and radiogenic Ca isotopic mass balance. The total mass of Sr in seawater is 1.25 x 10^{17} mol and the total mass of Ca in seawater is 1.4 x 10^{19} mol.*

	Water Flux (liter/year)		Concentration (μmol/liter)		J_i (μmol/year)		Isotope Ratio (α)		$J_i(\alpha_i-\alpha_{SW})$ (μmol/year)	
	Sr	Ca	Sr	Ca	Sr	Ca	$^{87}Sr/^{86}Sr$	$\varepsilon^{40}Ca$	$^{87}Sr/^{86}Sr$	$\varepsilon^{40}Ca$
Ganges-Brahmaputra										
River Water	1.07 x 10^{15}◊	8.76 x 10^{14}◊	0.83	527.15◊	0.89 x 10^{15}	4.62 x 10^{17}	0.71595	0.07§	6.01 x 10^{12}	3.23 x 10^{16}
							0.74130	1.04§	2.86 x 10^{13}	4.8 x 10^{17}
Groundwater	0.2 x 10^{15}○	2.0 x 10^{14}	4.5○	2747.0	0.90 x 10^{15}	0.55 x 10^{18}	0.7150	0.30§	5.22 x 10^{12}	1.65 x 10^{17}
							0.7200	0.60§	9.72 x 10^{12}	3.3 x 10^{17}
Total Flux	1.27 x 10^{15}	1.08 x 10^{15}	1.42	882.20	1.80 x 10^{15}	1.12 x 10^{18}	0.71548	0.19§	1.13 x 10^{13}	2.13 x 10^{17}
							0.73065	0.82§	3.86 x 10^{13}	9.18 x 10^{17}
Global										
River Water	4.24 x 10^{16}	3.74 x 10^{16}*	0.78	858*	3.3 x 10^{16}+	3.21 x 10^{19}	0.711+	0.1⊗	5.94 x 10^{13}	3.21 x 10^{18}
							–	2.5⊗	–	8.03 x 10^{19}
Groundwater	0.238 x 10^{16}○	1.19 x 10^{15}•	6.93○	13498.68	1.65 x 10^{16}+	1.6 x 10^{19}	0.711	0.1⊗	2.97 x 10^{13}	1.6 x 10^{18}
							–	2.5⊗	–	4 x 10^{19}
Total Continental Flux	4.48 x 10^{16}	3.93 x 10^{16}	1.11	7178.34	4.95 x 10^{16}+	4.81 x 10^{19}	0.711	1.3	8.91 x 10^{13}	6.25 x 10^{19}
Hydrothermal Water	1.095 x 10^{14}	–	91.3	–	1.0 x 10^{16}+	–	0.7035+	–	-5.7 x 10^{13}	–
Low-T		1.16 x 10^{16}*	–	10200*	–	1.63 x 10^{20}	–	-0.21⊗	–	-3.42 x 10^{19}
							–	-0.01⊗	–	-1.63 x 10^{18}
High-T		3 (± 1.5) x 10^{13}*	–	20000*	–	6 x 10^{17}	–	-0.21⊗	–	-1.26 x 10^{17}
							–	-0.01⊗	–	-6 x 10^{15}
Diagenetic Flux	3.29 x 10^{13}	–	91.3	–	0.3 x 10^{16}+	–	0.7084+	–	-2.4 x 10^{12}	–
Seawater	–	–	91.3	10000	–	–	0.7092+	0.0⊗	–	–

○ Values from Basu et al. (2001)
+ Values from Richter et al. (1992) based on Goldstein and Jacobsen (1987) and Palmer and Edmond (1992)
⊗ Values suggested by Caro et al. (2010)
* Values from Elderfield and Schultz (1996)
• Values from Holmden et al. (2012) based on estimates from Milliman (1993)
◊ Values from Galy and France-Lanord (1999) and Galy et al. (1999)
§ Values suggested by this study

Table A.6 – *Average analytical data by session for the samples analyzed in the Ganga, Brahmaputra, and Meghna system.*

	# Cycles	^{42}Ca (V)	^{40}Ca (V)	^{41}K/^{40}Ca	Raw ratios (Line 1)		(Line 2)	Corrected ratios (static mode)			
					^{40}Ca/^{44}Ca	^{42}Ca/^{44}Ca	^{40}Ca/^{42}Ca	^{40}Ca/^{44}Ca (ST)	± (2 S.D.)	^{43}Ca/^{44}Ca (ST)	± (2 S.D.)
Session 1B May 2014											
2014_05_16_Ca-BR410	120	9.3E-06	0.10	2.34E-03	46.37649	0.30968	149.75397	47.10347	2.31E-03	0.06486	4.27E-06
2014_05_17_Ca-BR400b	100	6.4E-06	0.09	2.02E-03	46.39793	0.30974	149.79456	47.10759	2.72E-03	0.06486	4.75E-06
2014_05_17_Ca-BR447	80	6.9E-06	0.10	2.22E-03	46.40407	0.30977	149.80055	47.10413	2.68E-03	0.06486	5.36E-06
2014_05_19_Ca-BR400a	120	8.2E-06	0.10	2.09E-03	46.43406	0.30987	149.85110	47.10362	2.87E-03	0.06487	4.86E-06
2014_05_23_Ca-BR400bis	60	1.5E+01	0.10	4.23E-04	46.42294	0.30983	149.83282	47.10793	3.69E-03	0.06486	5.36E-06
Session 2 July 2014											
2014_06_30_Ca-BR942-1	110	1.4E+01	0.10	1.55E-04	46.39441	0.30975	149.77832	47.10308	2.92E-03	0.06487	6.21E-06
2014_07_01_Ca-BR936-1	120	1.4E+01	0.10	2.82E-04	46.39230	0.30974	149.77777	47.09659	2.05E-03	0.06487	3.92E-06
2014_07_06_Ca-BR942-2	120	1.4E+01	0.09	4.16E-04	46.35449	0.30962	149.71564	47.10799	2.55E-03	0.06487	4.17E-06
2014_07_08_Ca-BR942-4	90	1.4E+01	0.09	2.12E-04	46.38874	0.30972	149.77476	47.10220	2.82E-03	0.06487	6.50E-06
2014_07_08_Ca-BR936-4	120	1.4E+01	0.09	2.27E-04	46.40741	0.30979	149.80216	47.09832	2.37E-03	0.06486	3.84E-06
2014_07_11_Ca-BR410a	60	1.5E+01	0.10	5.19E-04	46.35613	0.30962	149.71885	47.10589	3.67E-03	0.06486	6.20E-06
2014_07_12_Ca-BR410b	120	1.7E+01	0.11	1.04E-04	46.43065	0.30986	149.84364	47.10411	2.19E-03	0.06487	3.34E-06
Session 8 February 2016											
2016_02_07_Ca_BGP15	120	1.1E+01	0.07	6.56E-04	46.28108	0.30937	149.59603	47.11686	3.31E-03	0.06487	8.00E-06
2016_02_08_Ca-BGP65	110	1.2E+01	0.08	2.75E-05	46.40066	0.30976	149.79481	47.12830	2.87E-03	0.06487	6.24E-06
2016_02_08_Ca_BR112	120	1.2E+01	0.08	6.84E-06	46.40089	0.30975	149.80078	47.12393	2.57E-03	0.06486	6.07E-06
2016_02_08_Ca_BR221	120	1.1E+01	0.07	1.33E-03	46.30716	0.30947	149.63325	47.11705	2.83E-03	0.06487	6.96E-06
2016_02_09_Ca_BR213	120	1.2E+01	0.08	3.82E-05	46.37764	0.30967	149.76380	47.12111	2.97E-03	0.06487	7.19E-06
2016_02_10_Ca_BGP79	120	1.3E+01	0.08	4.47E-06	46.36842	0.30965	149.74448	47.11881	2.63E-03	0.06486	4.85E-06
2016_02_10_Ca_BR513	110	1.2E+01	0.08	7.26E-05	46.37920	0.30969	149.76138	47.11656	2.69E-03	0.06486	6.02E-06
2016_02_12_Ca-AK16	110	1.1E+01	0.07	1.66E-04	46.33069	0.30951	149.69241	47.12173	3.09E-03	0.06485	7.08E-06
2016_02_12_Ca_S68	110	1.2E+01	0.08	2.79E-04	46.36564	0.30962	149.75057	47.12811	3.07E-03	0.06485	6.97E-06
2016_02_13_Ca_AK11	110	1.2E+01	0.08	9.17E-05	46.39896	0.30974	149.79968	47.12330	2.90E-03	0.06488	6.61E-06
2016_02_14_Ca_BGP39	110	1.2E+01	0.08	5.82E-05	46.37770	0.30969	149.75430	47.11393	2.98E-03	0.06488	6.15E-06
2016_02_14_Ca_BR200	110	1.2E+01	0.08	2.73E-05	46.40249	0.30977	149.79806	47.11921	2.73E-03	0.06487	6.64E-06
2016_02_14_Ca_S17	110	1.2E+01	0.08	6.87E-05	46.34054	0.30956	149.69816	47.11616	2.95E-03	0.06487	5.95E-06
2016_03_04_Ca-BGP51	110	1.2E+01	0.08	2.52E-04	46.34019	0.30956	149.69464	47.11578	2.57E-03	0.06486	5.80E-06
2016_03_07_Ca_BR221	110	1.2E+01	0.08	1.28E-04	46.34501	0.30958	149.70310	47.11628	2.86E-03	0.06487	7.25E-06
2016_03_08_Ca-BGP39	110	1.2E+01	0.08	6.51E-05	46.35040	0.30959	149.71401	47.11396	3.03E-03	0.06487	6.19E-06
2016_03_08_Ca-BGP15	110	1.2E+01	0.08	9.56E-05	46.40690	0.30977	149.81182	47.11885	3.01E-03	0.06487	6.57E-06

Table A.7 – *Average analytical data by session for the samples analyzed in the Ganga, Brahmaputra, and Meghna system.*

	Corrected ratios (multidynamic mode)					ε^{40}Ca (I-MD)	± (2 S.D.)
	$^{40}Ca/^{42}Ca$ (MD)	$^{40}Ca/^{44}Ca$ (MD)	± (2 S.D.)	$^{40}Ca/^{44}Ca$ (I-MD)	± (2 S.D.)		
Session 1B May 2014							
2014_05_16_Ca-BR410	151.03386	47.15428	1.34E-03	47.15423	1.05E-03	0.58	0.22
2014_05_17_Ca-BR400b	151.04461	47.15764	1.70E-03	47.15741	1.39E-03	1.25	0.29
2014_05_17_Ca-BR447	151.03598	47.15494	1.72E-03	47.15488	1.44E-03	0.72	0.30
2014_05_19_Ca-BR400a	151.03810	47.15561	1.99E-03	47.15562	1.51E-03	0.88	0.32
2014_05_23_Ca-BR400bis	151.03871	47.15580	1.99E-03	47.15582	1.55E-03	0.92	0.33
Session 2 July 2014							
2014_06_30_Ca-BR942-1	151.02358	47.15107	1.60E-03	47.15098	1.32E-03	-0.11	0.28
2014_07_01_Ca-BR936-1	151.02958	47.15295	1.18E-03	47.15289	9.77E-04	0.30	0.21
2014_07_06_Ca-BR942-2	151.03031	47.15317	1.54E-03	47.15287	1.36E-03	0.29	0.29
2014_07_08_Ca-BR942-4	151.03554	47.15480	1.67E-03	47.15466	1.20E-03	0.67	0.25
2014_07_08_Ca-BR936-4	151.02843	47.15258	1.37E-03	47.15244	1.14E-03	0.20	0.24
2014_07_11_Ca-BR410a	151.03130	47.15348	2.29E-03	47.15323	1.98E-03	0.37	0.42
2014_07_12_Ca-BR410b	151.03483	47.15458	1.22E-03	47.15445	9.85E-04	0.63	0.21
Session 8 February 2016							
2016_02_07_Ca_BGP15	151.03394	47.15431	2.10E-03	47.15385	1.89E-03	-0.07	0.40
2016_02_08_Ca-BGP65	151.03631	47.15505	1.76E-03	47.15490	1.57E-03	0.15	0.33
2016_02_08_Ca_BR112	151.04789	47.15866	1.79E-03	47.15839	1.53E-03	0.89	0.33
2016_02_08_Ca_BR221	151.02149	47.15042	1.85E-03	47.15065	1.70E-03	-0.75	0.36
2016_02_09_Ca_BR213	151.05085	47.15959	1.93E-03	47.15908	1.67E-03	1.04	0.35
2016_02_10_Ca_BGP79	151.04243	47.15696	1.78E-03	47.15676	1.60E-03	0.54	0.34
2016_02_10_Ca_BR513	151.04051	47.15636	1.79E-03	47.15577	1.42E-03	0.33	0.30
2016_02_12_Ca-AK16	151.06367	47.16359	2.14E-03	47.16366	1.86E-03	2.01	0.39
2016_02_12_Ca_S68	151.06443	47.16383	2.12E-03	47.16327	1.87E-03	1.92	0.40
2016_02_13_Ca_AK11	151.05217	47.16000	1.80E-03	47.15971	1.54E-03	1.17	0.33
2016_02_14_Ca_BGP39	151.03101	47.15339	2.21E-03	47.15338	1.94E-03	-0.17	0.41
2016_02_14_Ca_BR200	151.03678	47.15519	1.96E-03	47.15527	1.65E-03	0.23	0.35
2016_02_14_Ca_S17	151.04193	47.15680	2.09E-03	47.15641	1.87E-03	0.47	0.40
2016_03_04_Ca-BGP51	151.03580	47.15489	1.81E-03	47.15486	1.54E-03	0.14	0.33
2016_03_07_Ca_BR221	151.03684	47.15521	1.98E-03	47.15509	1.77E-03	0.19	0.38
2016_03_08_Ca-BGP39	151.04101	47.15651	2.28E-03	47.15650	2.01E-03	0.49	0.43
2016_03_08_Ca-BGP15	151.05014	47.15936	1.80E-03	47.15925	1.54E-03	1.07	0.33

Table A.8 – *Average analytical data by session for the samples analyzed in the Ganga, Brahmaputra, and Meghna system.*

	ε^{40}Ca (ST)	± (2 S.D.)	ε^{43}Ca (ST)	± (2 S.D.)	Mass Fract. Factor (‰)	Mass Fract. Rate (ppm s^{-1})	F	ΔR_C (ppm)
Session 1B May 2014								
2014_05_16_Ca-BR410	-0.30	0.49	-0.49	0.66	-4.04	0.31	1.000012	0.97
2014_05_17_Ca-BR400b	0.58	0.58	-0.77	0.73	-3.95	0.20	1.000008	4.85
2014_05_17_Ca-BR447	-0.16	0.57	-1.03	0.83	-3.90	0.21	1.000008	1.35
2014_05_19_Ca-BR400a	-0.26	0.61	-0.08	0.75	-3.75	0.47	1.000018	-0.31
2014_05_23_Ca-BR400bis	0.65	0.78	-0.41	0.83	-3.81	0.21	1.000008	-0.61
Session 2 July 2014								
2014_06_30_Ca-BR942-1	-0.08	0.62	1.06	0.96	-3.93	0.11	1.000004	2.04
2014_07_01_Ca-BR936-1	-1.46	0.43	0.35	0.60	-3.95	0.14	1.000006	1.23
2014_07_06_Ca-BR942-2	0.96	0.54	1.12	0.64	-4.15	0.20	1.000008	6.38
2014_07_08_Ca-BR942-4	-0.27	0.60	0.31	1.00	-3.98	0.19	1.000007	3.14
2014_07_08_Ca-BR936-4	-1.09	0.50	-0.05	0.59	-3.87	0.23	1.000009	3.00
2014_07_11_Ca-BR410a	0.52	0.78	-0.66	0.96	-4.15	0.11	1.000004	5.48
2014_07_12_Ca-BR410b	0.14	0.47	0.26	0.52	-3.76	0.25	1.000010	2.87
Session 8 February 2016								
2016_02_07_Ca_BGP15	0.32	0.70	-0.22	1.23	-4.54	-0.09	0.999996	9.59
2016_02_08_Ca-BGP65	2.75	0.61	-0.15	0.96	-3.92	0.00	1.000000	3.18
2016_02_08_Ca_BR112	1.82	0.55	-0.87	0.94	-3.94	-0.05	0.999998	5.67
2016_02_08_Ca_BR221	0.36	0.60	0.39	1.07	-4.39	0.19	1.000007	-4.93
2016_02_09_Ca_BR213	1.22	0.63	-0.20	1.11	-4.06	0.24	1.000009	10.64
2016_02_10_Ca_BGP79	0.73	0.56	-1.51	0.75	-4.10	0.18	1.000007	4.26
2016_02_10_Ca_BR513	0.26	0.57	-0.75	0.93	-4.04	0.18	1.000007	12.45
2016_02_12_Ca-AK16	1.35	0.66	-2.43	1.09	-4.33	0.15	1.000006	-1.49
2016_02_12_Ca_S68	2.71	0.65	-2.19	1.07	-4.15	0.29	1.000011	11.78
2016_02_13_Ca_AK11	1.69	0.62	1.58	1.02	-3.96	0.28	1.000011	6.09
2016_02_14_Ca_BGP39	-0.30	0.63	1.29	0.95	-4.03	0.12	1.000005	0.24
2016_02_14_Ca_BR200	0.82	0.58	0.27	1.02	-3.91	0.11	1.000004	-1.67
2016_02_14_Ca_S17	0.17	0.63	1.10	0.92	-4.24	0.14	1.000005	8.26
2016_03_04_Ca-BGP51	0.09	0.55	-0.70	0.89	-4.24	0.16	1.000006	0.58
2016_03_07_Ca_BR221	0.20	0.61	0.64	1.12	-4.21	0.27	1.000010	2.67
2016_03_08_Ca-BGP39	-0.30	0.64	0.15	0.95	-4.19	0.29	1.000011	0.35
2016_03_08_Ca-BGP15	0.74	0.64	-0.21	1.01	-3.91	0.16	1.000006	2.38

APPENDIX B

THE EVOLUTION OF OCEANIC RADIOGENIC CA

B.1 Introduction

The weathering of silicate rocks exerts a long-term control on the global atmospheric CO_2 budget. There a number of processes by which atmospheric CO_2 concentrations are regulated, and as pointed out by Georg et al. (2013), these are carbon neutral, carbon producing, or carbon consuming. For example, the dissolution of carbonate rocks via carbonic acid is CO_2 neutral, neither producing nor consuming CO_2. However, the dissolution of Mg- and Ca-bearing silicate rocks consumes carbon (Georg et al., 2013; Garrels, 1983; Berner, 2006; Holland, 1984; Walker et al., 1981).

Despite the fact that we can obtain direct evidence of modern-day weathering rates and fluxes and their temporal variability, it is much more complicated to asses these parameters and their magnitude in the past, thus making it more difficult to understand CO_2 regulating processes. Using isotopic proxies of marine paleo-records, such as the radiogenic isotopes of Sr, Os, Hf, Nd, and Pb, may be one way to obtain indirect information on past chemical weathering fluxes (Foster and Vance, 2006; Foster et al., 2007; Gutjahr et al., 2008; Pegram et al., 1992; Peucker-Ehrenbrink and Ravizza, 2000; Raymo and Ruddiman, 1992; Raymo et al., 1988).

A possible proxy to trace these changes in the magnitude of silicate weathering may be the use of the ^{40}Ca isotope, a decay product of ^{40}K, and its marine paleo-record. The oceanic Ca budget is controlled by three main variables: continental weathering, ocean rock weathering/hydrothermal exchange, and carbonate sedimentation, all of which significantly affect the CO_2 cycle. Marine life is based on the use and uptake of calcium carbonate to produce skeletons. These skeletons accumulate on the ocean floor, forming a carbonate reservoir of Ca and carbon, which are at least five orders of magnitude larger than the ocean-atmosphere reservoir Ridgwell and Edwards (2007). Thus, the carbonate reservoir (and its large size) makes it a controlling factor for the balance between carbon in the solid Earth and carbon in the ocean-atmosphere system. On the continents, Ca is the fifth most abundant element in the crust (Taylor and McLennan, 1985) and is an essential nutrient in the continental biosphere. The high solubility of Ca^{2+} in water makes it one of the most concentrated cations in rivers (Drever, 1997). During weathering, Ca is released from silicate minerals from both

continental and oceanic crust and is transferred to the oceanic carbonate reservoir (Holland, 2003). This results in the sequestration of one mole of atmospheric CO_2 for one mole of silicate Ca consumed (Urey, 1952; Walker et al., 1981).

Although the role of Ca for both the biosphere and the carbon cycle is well established there is ongoing debate on the mass balance of Ca in the ocean (Milliman, 1993; Milliman and Droxler, 1996; De La Rocha and DePaolo, 2000; Tipper et al., 2010; Caro et al., 2010). Rivers are the main supplier of Ca to the oceans, but hydrothermal circulation also supplies Ca via alteration of continental and oceanic crust (Holland, 1984). The output of Ca is a function of its removal via carbonate precipitation and its subsequent accumulation on the seafloor (Milliman, 1993). Despite knowledge of the inputs and outputs in the oceanic Ca system, it is still unclear if this balance is currently or was at steady state in the geologic past. Milliman (1993) estimated, in a detailed review, that either the modern carbonate accumulation exceeds inputs by a factor of two or that groundwater supply of Ca must be significantly larger than currently acknowledged. Holland (2005), on the other hand, proposed modern Ca fluxes that imply that the Ca budget to steady state, but that overall in the Tertiary the output fluxes must have outweighed the input fluxes. Modeling approaches have produced contrasting results of oceanic Ca evolution (Berner and Kothavala, 2001; Berner, 2004; Demicco et al., 2005; Hardie, 1996; Wilkinson and Algeo, 1989) and data to constrain these assertions are insufficient. Although Ca concentrations, reconstructed from fluid inclusions, provide a valuable constraint (Horita et al., 2002; Lowenstein et al., 2001), they have low temporal resolution and relatively large uncertainty. The source of riverine Ca and the absolute magnitude of the continental flux of Ca are also subjects for debate. The source of Ca is important because although the weathering of silicate minerals consumes CO_2 over geological timescales, the weathering of carbonate minerals has no net influence on atmospheric CO_2 over longer timescales (Berner and Kothavala, 2001; Urey, 1952), though destruction of the carbonate reservoir by weathering can have consequences for the global carbon cycle over shorter timescales (Calmels et al., 2007; Li et al., 2008; Edmond and Huh, 2003). Partitioning riverine Ca^{2+} ions between lithological sources (carbonate, silicate, and evaporate) is complicated (Gaillardet et al., 1999). At a global scale, it is estimated that at least two-thirds of riverine Ca is derived from the weathering of carbonate rocks (Berner and Berner, 2012; Gaillardet et al., 1999; Meybeck, 1987) implying that the recycling of ancient carbonates dominates Ca weathering sources.

Compared with contributions from hydrothermal fluxes over much of Earth's history, the weathering input from shales and granitic sources has remained quite small. Mass balance models imply that the current Ca hydrothermal flux are greater, by an order of magnitude than fluxes from silicate weathering (Caro et al., 2010).

An order of magnitude indicates that processes at off-axis hydrothermal sites are much more important than previously thought (Caro et al., 2010) , which implies that hydrothermal exchanges between the oceanic crust and have dominated the oceanic Ca concentration and isotopic composition throughout the geological past. This is quite different when compared with the Sr isotopic composition of the oceans. For Sr, the riverine input of radiogenic Sr dominates the hydrothermal flux over the geological past, especially during the latter part of the Cenozoic Era. If the global, oceanic budget of Ca is dominated by unradiogenic hydrothermal fluxes (unradiogenic due to a mantle influence, see Caro et al. (2010)), then the signal of continental weathering will not fluctuate throughout the past 5 Ga. However, by modeling the radiogenic Ca isotopic budget of the ocean, we can place constraints on the magnitude of these hydrothermal fluxes. Here we explore the possibility that the radiogenic Ca isotope record of seawater may provide the possibility to constrain the fluxes of the low- and high-temperature hydrothermal sources of radiogenic Ca in the oceans and, as a side note, provide a 'yes' or 'no' answer to the applicability of using the radiogenic Ca seawater record to provide insights into long-term CO_2 consuming processes (i.e., silicate weathering).

B.2 Radiogenic Ca as a tracer of weathering?

B.2.1 Continental Sources of radiogenic Ca

Despite the relatively minuscule amount of material published on the ^{40}K–^{40}Ca system, a handful of pioneering publications established this system as useful in geochronologic studies (Russell et al., 1978; Marshall and DePaolo, 1982; Marshall et al., 1986; Marshall and DePaolo, 1989). Variations in the initial radiogenic ^{40}Ca can reveal the fractionation of potassium from calcium during igneous processes yielding useful information regarding the origin of ultra-potassic rocks and granites (Marshall and DePaolo, 1989). These workers have shown that some continental rocks have high degrees of enrichment in ^{40}Ca due to the decay of ^{40}K. For example, Marshall and DePaolo (1989) reported ε^{40}Ca (defined as the difference in ^{40}Ca/^{44}Ca in parts in 10,000 (ε-units) relative to the NIST SRM 915a standard) for Proterozoic crustal rocks ranging between +2 and +6, while Kreissig and Elliott (2005) reported values up to +8 in Archean TTGs (Tonalite–Trondhjemite–Granodiorite). Furthermore, felsic lithologies derived from the upper crust have elevated K/Ca ratios (approximately 1–4) and have developed large excesses of ε^{40}Ca. These ^{40}Ca excesses allow us to constrain continental versus mantle inputs in the oceanic calcium cycle.

B.2.2 Sources of non-radiogenic Ca

Ultramafic rocks typically have K/Ca ratios of 0.01, so that radiogenic growth in the mantle is approximately 0.13 ε-unit, well below detection limits (as defined by TIMS measurements; Chapter 3). Caro et al. (2010) analyzed the ^{40}Ca composition of a number of ancient and modern carbonate samples as well as seawater, showing that the ε^{40}Ca composition of modern seawater is indistinguishable from the mantle value. Similarly, Caro et al. (2010) found no significant ^{40}Ca excess detectable in carbonates, regardless of their age, depositional setting, or bulk composition. Furthermore, in a preliminary study of Himalayan silicate and carbonate sources, Davenport et al. (2014) showed that despite highly variable Sr isotopic compositions, carbonates, dolomites, and marbles show no significant excesses of radiogenic ^{40}Ca. These results demonstrate that the Ca isotopic composition of the oceans has remained constant over the past 3.5 Ga. There is no evidence of significant upper crustal contributions to seawater that can be measured at the current level of precision. It follows that marine carbonates reflect the value of the depleted mantle with no apparent enrichment due to inflow from weathering of upper crustal silicates.

Thus, Caro et al. (2010) inferred that the absence of any detectable excesses of ^{40}Ca must reflect the composition of seawater, and indicates that hydrothermal processes buffered the ^{40}Ca/^{44}Ca composition of seawater over most of geologic

time. This could be explained by the ongoing influence of low-T hydrothermal fluids characterized by high Ca/Sr ratios. This observation, therefore, represents a strong constraint for modeling the fluxes of Ca to the oceanic reservoir and quantifying elemental fluxes associated with hydrothermal circulation.

B.3 Model Parameters

The inverse modeling approach presented in the following requires three principle constraints; (i) a modern-day Ca mass balance, (ii) a paleo-data archive that contains information about fluctuations of the marine Ca composition over time and (iii) a numerical interpretation of the conceptual model to analyze the variability in the data archive. This model is based on and is a continuation of the work presented in Georg et al. (2013) on the Os oceanic cycle as a tracer of continental weathering and CO_2 producing processes.

B.3.1 The modern-day Ca cycle and mass balances

All data used for the following modeling have been previously published, and are summarized in Table B.1. The modern riverine Ca flux is approximately 12 x 10^{12} mol/year (Elderfield and Schultz, 1996), derived from an average riverine Ca concentration of approximately 300 µmol/L (Elderfield and Schultz, 1996) and a global river water flux (Q_{riv}) of 3.74 x 10^{16} kg/year (Gaillardet et al., 1999). This represents a continental flux of 1.12 x 10^{13} mol Ca/year. The riverine Ca flux was further split into the two major Ca sources, i.e., silicate derived Ca (10–15%) (Gaillardet et al., 1999; Berner and Berner, 2012) and Ca derived from carbonate weathering (85–90%). The silicate proportion was given an ε^{40}Ca ratio of +2.5, which is the average of the upper continental crust as estimated from loess samples (Caro et al., 2010), and the carbonate ε^{40}Ca ratio was set to 0.

Table B.1 – *Parameters used for model runs - See main text for references.*

River Component	Qriv = 3.74x10^{16} kg yr^{-1} C_{riv} = 3.0x10^{-4} moles L^{-1} F_{sil} = 0.3 F_{sed} = 1-F_{sil} F_{rivsil} = Q_{rivsil} x C_{riv} = (F_{sil} x Q_{riv}) x C_{riv} = 1.12 x 10^{12} moles yr^{-1} F^{rivsed} = Q_{rivsed} x C_{riv} = (1 - F_{sil} x Q_{riv}) x C_{riv} = 1.01 x 10^{13} moles yr^{-1} F_{rivtot} = F_{rivsil} + F_{rivsed} $\varepsilon^{40}Ca_{sil}$ = 2.5 $\varepsilon^{40}Ca_{sed}$ = 0.0
High-T Hydrothermal Component	Q_{HT} = 3 x 10^{13} kg yr^{-1} C_{HT} = 2 x 10^{-2} moles L^{-1} F_{HT} = Q_{HT} x C_{HT} = 6 x 10^{11} moles yr^{-1} $\varepsilon^{40}Ca_{HT}$ = 0.0
Low-T Hydrothermal Component	Q_{LT} = 7.35 x 10^{15} kg yr^{-1} (Average) CLT = 10.2 x 10^{-3} moles L^{-1} F_{LT} = Q_{LT} x C_{LT} = 1.18 x 10^{14} moles yr^{-1} $\varepsilon^{40}Ca_{LT}$ = 0.0

For Ca, hydrothermal fluxes are assumed to provide a more significant source of non-radiogenic Ca to the ocean. However, data are sparse and all estimates are

associated with significant uncertainties. Elderfield and Schultz (1996) estimated a total global hydrothermal flux of Ca to be between 4 and 15 x 10^{12} mol Ca/year. Thus, the model uses an estimate for the high-T hydrothermal component from Elderfield and Schultz (1996) with a best estimate for the high-T fluid flux (Q_{HT} = 3 $\pm$ 1.5 x 10^{13} kg/year) and a Ca concentration of 2 x 10^{-2} moles/L, which yields a high-T hydrothermal flux of 6 x 10^{11} mol Ca/year (equal to approximately 5% of the riverine Ca flux). We set the ε^{40}Ca composition to 0. The low-temperature (low-T) component of the hydrothermal flux (QLT) was explored using an average flux estimate of 1.16 x 10^{16} kg/year (Elderfield and Schultz, 1996), with a Ca concentration of 10.2 x 10^{-3} mol/L, and an isotopic composition of 0, which yields annual molar fluxes of 1.18 x 10^{14} mol Ca/year.

B.4 Modeling the Ca Cycle

B.4.1 Static Model

The oceanic mass balance for Ca can be expressed as two ordinary differential equations (Eqs. B.1 and B.2 below), which are solved simultaneously by iterating through a Runge–Kutta-4.5 algorithm using MathWorks Matlab non-discrete 'ode45' solver. The model consists of one main reservoir, the ocean, with a volume (V_{oc}) of 1.37 x 10^{21} L, the designated input fluxes (river, high-T fluids, low-T fluids, see Table B.1), and one main sink (output). The input fluxes, F_j, are the product of annual water fluxes, Q_j, and the average Ca concentration of component j. The isotopic parameter, R_j, of each component, is the product of the Ca flux F_j and its $^{40}Ca/^{44}Ca$ composition r_j, i.e., $R_j = F_j \times (r_j - r_{oc}) \times \left[\frac{(1+r_{oc})}{(1+r_j)}\right]$ (Kump, 1989). We assume that the Ca sink does not fractionate the Ca isotope composition of the ocean, such that the sink-term is eliminated by $R_{out} = F_{out} \times (r_{oc} - r_{oc}) \times \left[\frac{(1+r_{oc})}{(1+r_{oc})}\right] = 0$ (Brass, 1976; Kump, 1989; Sharma et al., 2007). The change in the ocean's Ca concentration (M_{oc} in moles), as well as its isotopic composition (r_{oc}), through time are given by the following ordinary differential equations:

$$\frac{dM_{oc}}{dt} = F_{sil} + F_{LT} + F_{HT} + F_{out} \tag{B.1}$$

$$\frac{dr_{oc}}{dt} = \frac{1}{M_{oc}} \times [R_{sil} + R_{LT} + R_{HT}] \tag{B.2}$$

Initial conditions for the initialization run were set to 0, i.e., the ocean does not contain any Ca at t = 0. The elemental Ca budget of the ocean was achieved via a balance of the output and inputs, and was not forced upon the system by using the modern ocean Ca inventory as an initial condition. All parameters were kept constant and the model was run until elemental steady state was achieved. Best estimates for hydrothermal fluxes require two scenarios to be tested, i.e., using the maximum and minimum estimates for the low-T hydrothermal fluxes (Elderfield and Schultz, 1996). We initiated the minimum hydrothermal flux scenario (Q_{LTmin} = 3.7 x 10^{15} kg/year), which resulted in a total low-T hydrothermal flux, F_{LT}, of 3.8 x 10^{14} mol/year. The maximum estimate for the low-T hydrothermal flux (Q_{LTmax} = 1.1 x 10^{16} kg/year) yielded a low-T hydrothermal flux of 1.12 x 10^{14} mol/year. The two different scenarios change the total Ca flux into the ocean by 2.68 x 10^{14} mol/year and the total isotope composition of fluxes into the ocean from +0.02 (max low-T flux) to +0.05 (min low-T flux).

The accuracy of the model was evaluated by comparing steady-state results with

known, modern-day conditions, e.g., a Ca concentration of approximately 10.27 mM and an ε^{40}Ca ratio of 0. Both low-T hydrothermal scenarios reproduce modern-day conditions, with Ca concentrations and Ca ratios well within the range observed in modern-day ocean basins (Caro et al., 2010) (see Figures B.1 and B.2). For the minimum Q_{LT} scenario, elemental steady state resulted in a mean Ca oceanic residence time, τ_{Ca}, of approximately 133,240 years. The steady-state Ca concentrations were 10.28 mM and an ε^{40}Ca isotope ratio of +0.03. The maximum QLT scenario had a shorter mean residence time of approximately 113,150 years. Further sensitivity tests on the effect of the magnitude of the low- and high-T and riverine Ca fluxes are performed later in the context of the dynamic model.

B.4.2 Dynamic Model – Varying the Friv and Rriv

The dynamic model used the same differential equations and parameters as the static model but introduced a temporal variation in both components of the continental Ca flux (i.e., riverine flux and the isotopic ratio of the flux) to explore responses to forcing during glacial-interglacial periods. The fluxes of radiogenic elements from the continents are dependent upon a number of factors, such as the occurrence of a glacial or interglacial period or if a certain region of the world is experiencing a combination of uplift and erosion coupled with increased precipitation. The fluxes of radiogenic (continental) Ca to the oceans increase during interglacial periods, i.e., intense periods of erosion, while the fluxes of radiogenic Ca decrease during glacial periods, when weathering is inhibited or the flux of radiogenic Ca is limited compared with interglacial periods (Raymo and Ruddiman, 1992). We vary the parameters F_{riv} and R_{riv} to reflect the changing conditions of erosion and weathering during interglacial and glacial periods.

B.4.2.1 Varying silicate weathering fluxes

As in Georg et al. (2013), we explore the potential impact that variations in physical weathering rates can have on glacial-interglacial weathering fluxes via the variable weathering term ϕ_{sil} (see Appendix A in Georg et al. (2013)). The rationale behind ϕ_{sil} is based on the common observation (Porder et al., 2007; Taylor and Blum, 1995; White and Brantley, 2003) that silicate-weathering rates exhibit a power law dependence on substrate age, with very fast weathering rates accompanying early soil formation and rates slowing thereafter. Glacial–interglacial cycles constantly produce fresh, unweathered substrates through glacial grinding. Foster and Vance (2006) presented a quantitative approach to modeling variable continental weathering fluxes based on these dynamics. In their model the average silicate weathering rate in high latitude glaciated regions is calculated from the exposure age of the weathering soils, e.g. the

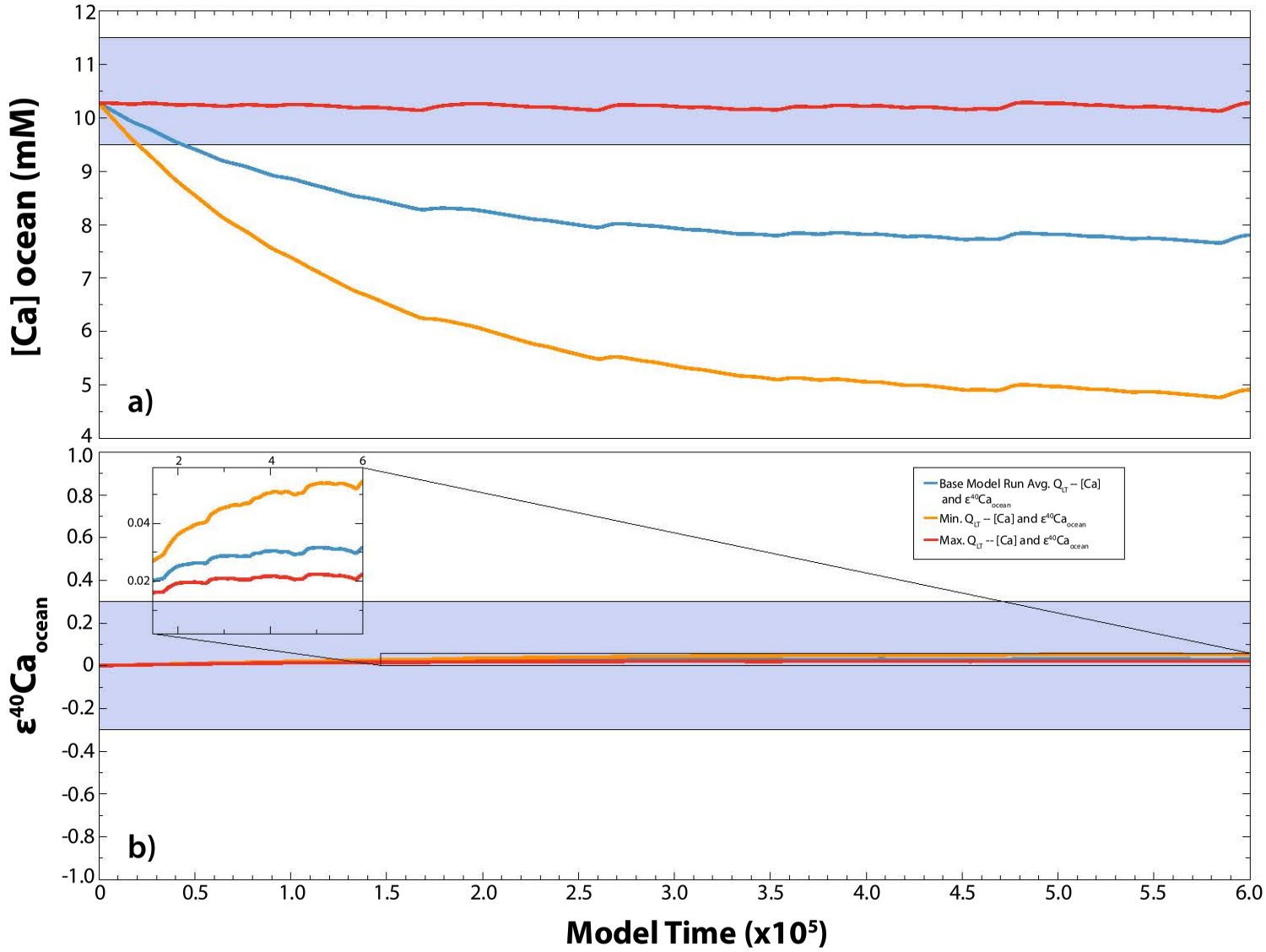

Figure B.1 – *The concentration of Ca (in mM) (top panel) and the $\varepsilon^{40}Ca$ composition of the oceans (bottom panel) plotted against time. The Ca model has been tested for two different input scenarios: 1) with minimum low-T hydrothermal fluxes (orange lines) and 2) maximum low-T hydrothermal fluxes (red lines). In both cases, the model reproduces modern-day seawater Ca concentration (in mM) (upper panel) and marine $\varepsilon^{40}Ca$ ratios (lower panel, see inset for detail). Model run time is 6 x 10^5 yr. Shaded areas represent the measured range of Ca concentrations (upper panel) and Ca isotope compositions (lower panel) in the modern ocean.*

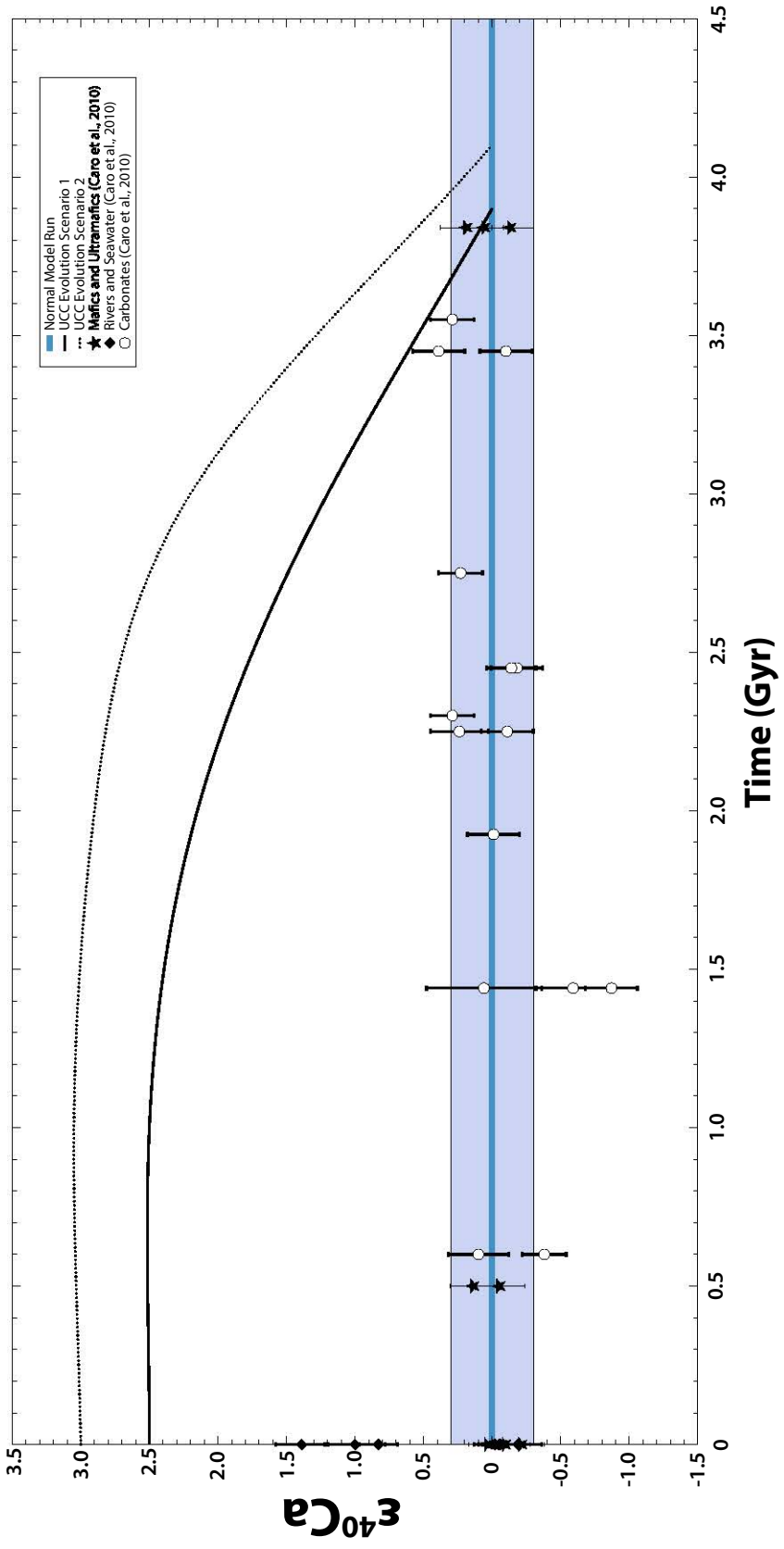

Figure B.2 – *$\varepsilon^{40}Ca$ plotted against time. A comparison of the model presented here (with time extended to 4 Ga; blue line) to $\varepsilon^{40}Ca$ isotopic ratios from ultramafics and mafics (black stars), rivers and seawater (black diamonds) and carbonates (open circles) all presented in Caro et al. (2010). Models for the radiogenic evolution of the upper continental crust (UCC) with a present-day average value of $\varepsilon^{40}Ca$ = +2.5 (black line) and $\varepsilon^{40}Ca$ = +3.0 (black dotted line). Within the limits of precision presented in this paper and that of Caro et al. (2010), the $\varepsilon^{40}Ca$ data and the model validate each other.*

time elapsed since surfaces were last covered by continental ice. According to this model, silicate weathering rates in glaciated continental areas vary between $\phi_{sil} = 0.06$ and 21.1 mmol m^{-2} kyr^{-1} during glacial cycles, with a high in interglacial periods, a low in glacial periods, and an average of 6.7 mmol m^{-2} yr^{-1} (Vance et al., 2009). This corresponds to weathering rates during interglacial periods that are 3 times the average and a reduction to 1% of the long-term average weathering rate at the height of glacial periods.

In Foster and Vance (2006), the quantification of variable past silicate weathering rates is only considered for 25% of the total continental area (Kump and Alley, 1994), i.e., regions at high latitudes that have been glaciated or covered in periglacial sediments at some stage during glacial cycles. Vance et al. (2009), however, suggested that the same variability may extend to silicate weathering in at least a part of the 75% of continental landmass that was not directly affected by large-scale glaciation. These authors compile evidence for variability in fresh sediment production in Alpine, Himalayan, and Andean basins (Goodbred and Kuehl, 2000; Hinderer, 2001) that closely matches ice volume changes in high-latitude regions. Taking into account these sediment production rates allows us to extend the idea of variable weathering to some of the remaining 75% landmass. On the other hand, chemical weathering in some major low land tropical rivers appears near equilibrium with the physical production of new fine-grained sediment (Dosseto et al., 2008), which implies that there is little temporal variation in chemical weathering, at least throughout the last deglaciation.

In the model presented here, the global silicate weathering flux is partitioned into these two regimes, and can be expressed as a mass balance of silicate weathering in regions affected by variable weathering rates (high-latitudes, low-latitude mountain belts) and those not (low-latitude low-land river basins):

$$Q_{rivsil}(t) = Q_{riv} \times \sigma \times (1 - f_{sil}) + [Q_{riv} \times \sigma \times f_{sil} \times \phi_{sil}(t)] \tag{B.3}$$

The term ϕ_{sil} is calculated from the variable silicate weathering rate σ_{sil}(t) by converting the deviations from the record's average into relative proportions (see Appendix A in Georg et al. (2013)). It is then applied to the proportion ϕ_{sil} of the global river water flux, which is allowed to vary. The proportion ϕ_{sil} was set to 0.1 and 0.15 to match estimates obtained from marine Sr records (Gaillardet et al., 1999; Vance et al., 2009). The term σ describes the proportion of the continental Ca flux designated as silicate weathering.

B.5 Dynamic Model Results

B.5.1 Responses to variable silicate weathering rates

Figure B.3 shows the model output as a response to variable silicate weathering rates. The low- and high-T components were kept constant in this scenario. Despite large changes in the silicate-derived Ca flux, the model displays no significant response. This invariant behavior is consistent with the riverine silicate component being the smaller continental flux compared with the riverine carbonate flux but is largely due to an isotope value similar to modern-day seawater (i.e., the isotopic value of the majority of continental flux has a Ca isotopic value of 0 or close to 0). Even large variations do not propagate large enough changes in overall flux characteristics and therefore have no impact on the isotope composition of the ocean. This result shows that the marine radiogenic Ca isotope record is unlikely to be driven by silicate weathering despite the postulated variability of silicate weathering throughout glacial–interglacial transitions (Vance et al., 2009) and effects related to large-scale mountain building events (Raymo and Ruddiman, 1992). For the purpose of this study this finding allows us to filter out any potential signal variability that may have arisen from variable silicate weathering, i.e., for the marine Ca isotopic evolution the weathering of silicates may simply be ignored.

In Figure B.3, we observe that the marine Ca isotope composition has no response to variations in silicate weathering rates. Depending on the size, location, and age of highly weatherable substrates (as well as other factors such as precipitation, rainfall, and lithology all of which effect weathering rates), this component can exhibit a relatively large flux of radiogenic Ca to the oceans. Despite this fact, variations of the highly radiogenic silicate component do not have any significant effect on the evolution of radiogenic Ca in the oceans. This in contrast to the records of Os and Sr, for example, where a combination of the size and isotopic composition of this component means that even small variations can have a significant impact on the marine isotope composition (Vance et al., 2009; Georg et al., 2013).

B.5.2 Responses to variable high- and low-T hydrothermal fluxes

Figures B.3 and B.4 show the model output as a response to varying low- and high-T hydrothermal fluxes. Figure B.3 varies the low-T flux between the minimum, mean, and maximum estimates (Elderfield and Schultz, 1996). Figure B.4 varies the low- and high-T fluxes from the mean to 1% and 10% of the mean flux and 3x the mean flux. Despite significant variations in the magnitude of the high-T hydrothermal, the model shows no response.

However, this is not the case when we vary the magnitude of the low-T

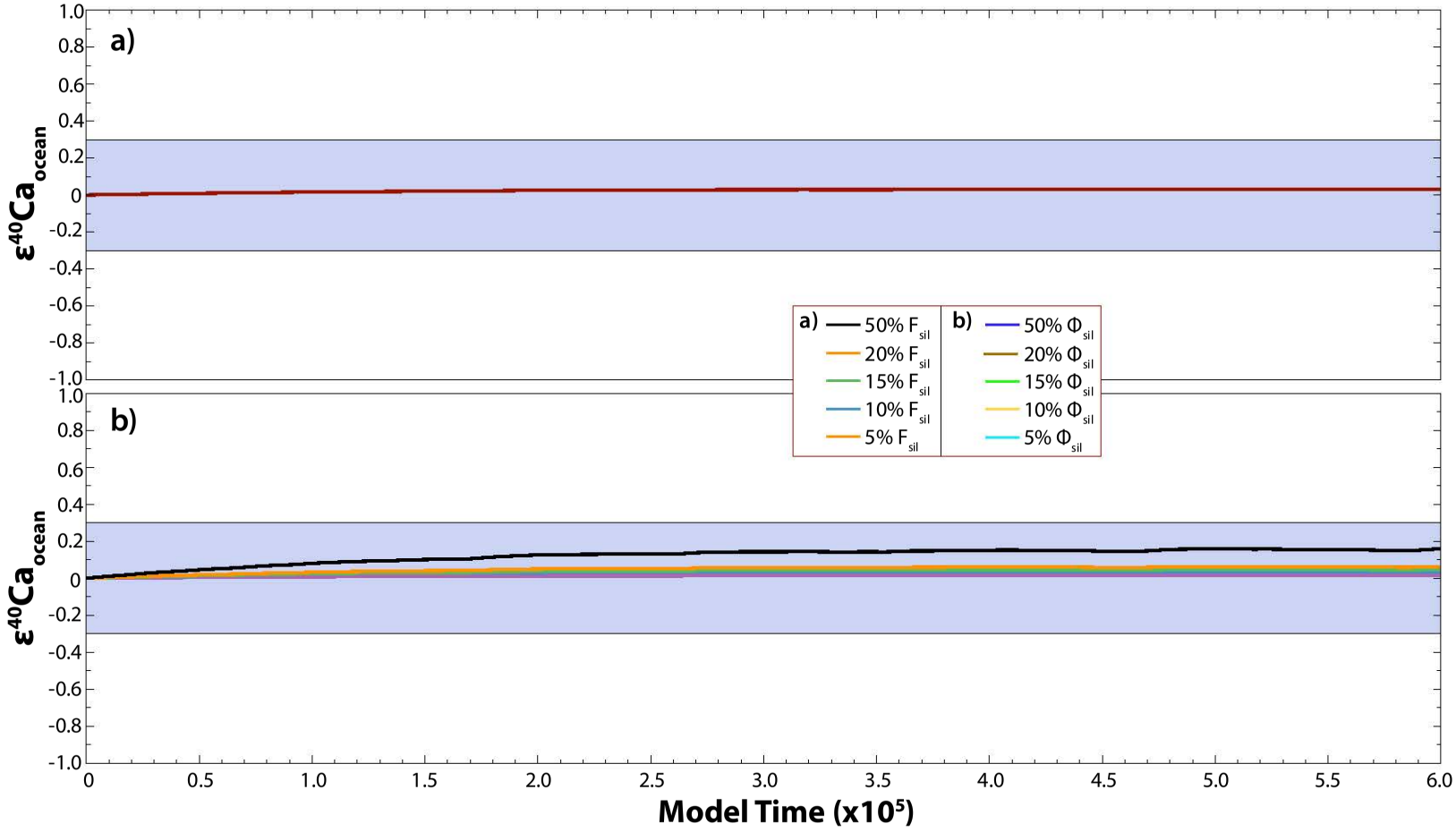

Figure B.3 – *The marine Ca record and its response to cyclic forcing. a) The output of the model in response to variable silicate weathering rates. Following Gaillardet et al. (1999) we assumed that 5–20% of the continental silicate-weathering budget might have varied in response to repeated glaciation-deglaciation cycles. We display the response to a F_{sil} = 50% to show the unrealistic nature of this scenario. b) Five scenarios in which ϕ_{sil} is given differing proportions of the silicate derived Ca fraction: (1) 5% of the silicate proportion, (2) 10% of the silicate proportion, (3) 15% of the silicate proportion, (4) 20% of the silicate proportion, and 5) 50% of the silicate proportion. The best match with the base model run is achieved in all five scenarios because the parameter ϕ_{sil} does not affect the proportion of silicate Ca derived from the continents. Shaded areas in a) and b) are the range of $\varepsilon^{40}Ca$ in modern-day seawater (i.e., the reproducibility presently capable during TIMS analysis, see Chapter 3).*

hydrothermal flux (Figures B.1 and B.6). In Figure B.4 we vary the low-T hydrothermal flux between the minimum, average, and maximum estimates of this flux and in Figure B.6 we model the evolution by increasing the flux to 3, 5, and 10 times the average estimate, as well as by decreasing the flux by 0.01, 0.1, 1, and 10% of the average estimate.

Varying the magnitude of the low-T flux not only significantly changes the isotopic composition of the oceans but the Ca concentration as well. However, as shown by Figure B.6, as the flux decreases or increases to a certain point, we obtain an asymptotic relationship, despite significant changes in magnitude and isotopic composition, which renders the model insensitive and subsequently is not characterized by large variations in the [Ca] or the oceanic ε^{40}Ca composition.

B.5.3 Responses to variable continental riverine fluxes

The above model makes a few assumptions about the magnitude of the fluxes. In particular, for the riverine (un- and radiogenic) fluxes to close the isotope balance for the Ca system. Here we test the sensitivity of the Ca model to various riverine fluxes (Figure B.5). As the following sensitivity analyses reveal, changing the absolute size of any of the invariant flux components shifts the model curve vertically, simply representing a shift in the isotope balance. This has a very little effect on the relative magnitude of the glacial–interglacial variability of the data output, and therefore very little effect on the fundamental conclusions of our study (Figures B.4 and B.5).

We obtained the riverine flux from the global oceanic water discharge and the average riverine Ca concentration. Both values have uncertainty. Therefore, it is necessary to test how sensitive the model is towards various estimates of the riverine Ca flux. Figure B.5 shows the model output for different riverine fluxes ($\pm$ 50%). Not only does the isotope balance shift (vertical curve shifting – Figure B.5), but changes to this flux also indicate that the system's response to forcing is either amplified or reduced, which is based on whether the absolute flux is reduced or increased. Increasing the riverine flux by 50% has more of an effect because, although not the dominant flux of Ca, the riverine component is the sole source of radiogenic Ca in the system and thus, when increased, this flux systemically increases the delivery of radiogenic Ca to the ocean and yields a more radiogenic oceanic composition. Reducing the riverine flux by 50% results in a hampered response and thus "flatter" Ca model curve. However, the model outputs based on modifying the riverine fluxes within a 50% envelope of published values are consistent with previously published work and the main conclusions do not change.

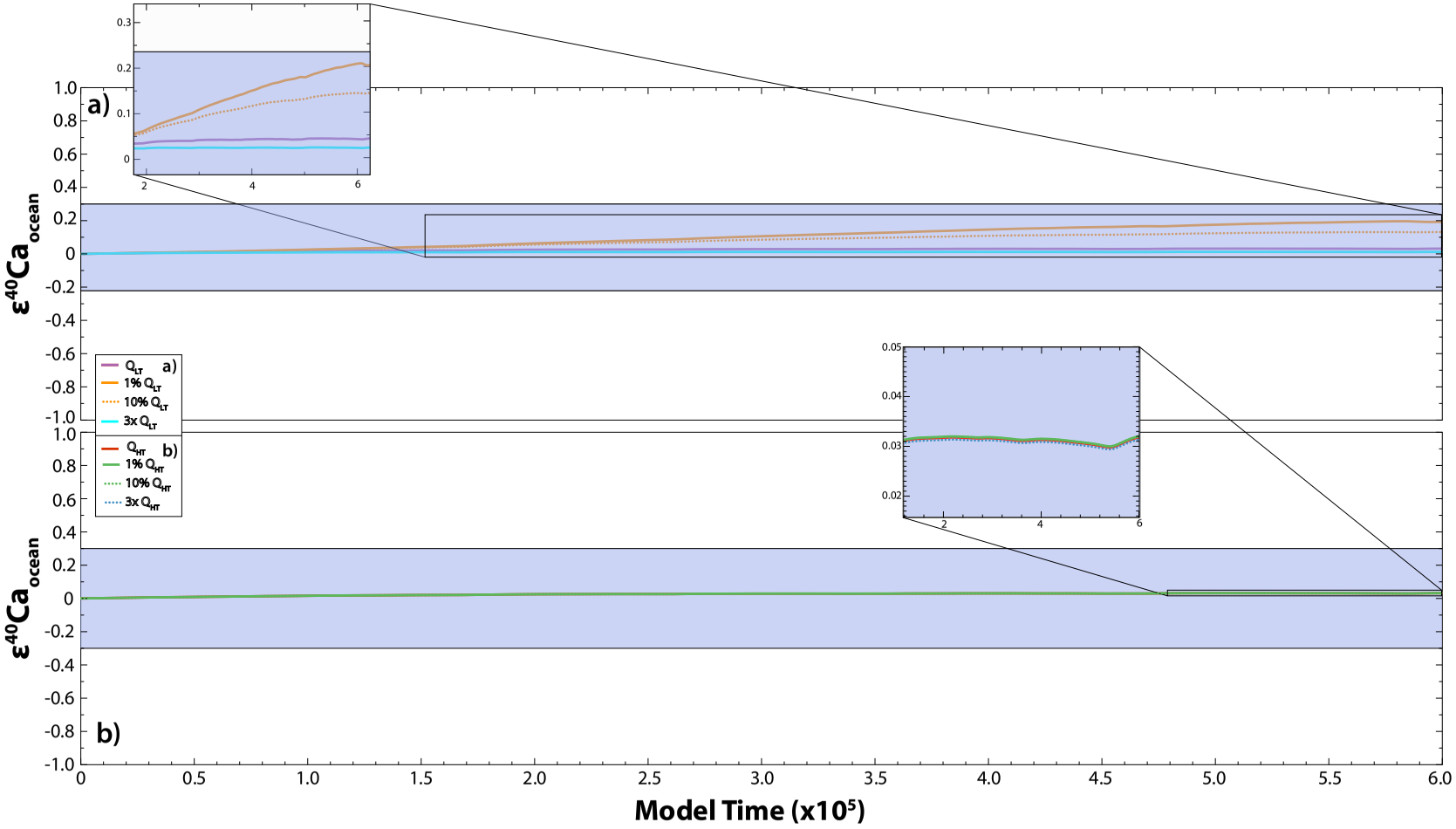

Figure B.4 – *a) The response of the Ca model to various low-T hydrothermal flux scenarios. Changing the size of the low-T hydrothermal flux significantly shifts the curve horizontally where lower estimates for the low-T hydrothermal increase the $\varepsilon^{40}Ca$ composition of the ocean. This displays the extreme influence that the low-T hydrothermal flux has on maintaining the oceanic mass balance, as well as its significance over the flux of radiogenic Ca from the continents. b) The response of the Ca model to various high-T hydrothermal flux scenarios. Unlike the low-T hydrothermal scenario, the $\varepsilon^{40}Ca$ composition of the ocean does not respond to changes in the high-T flux. The various high-T flux estimates have a very little effect on the relative pattern.*

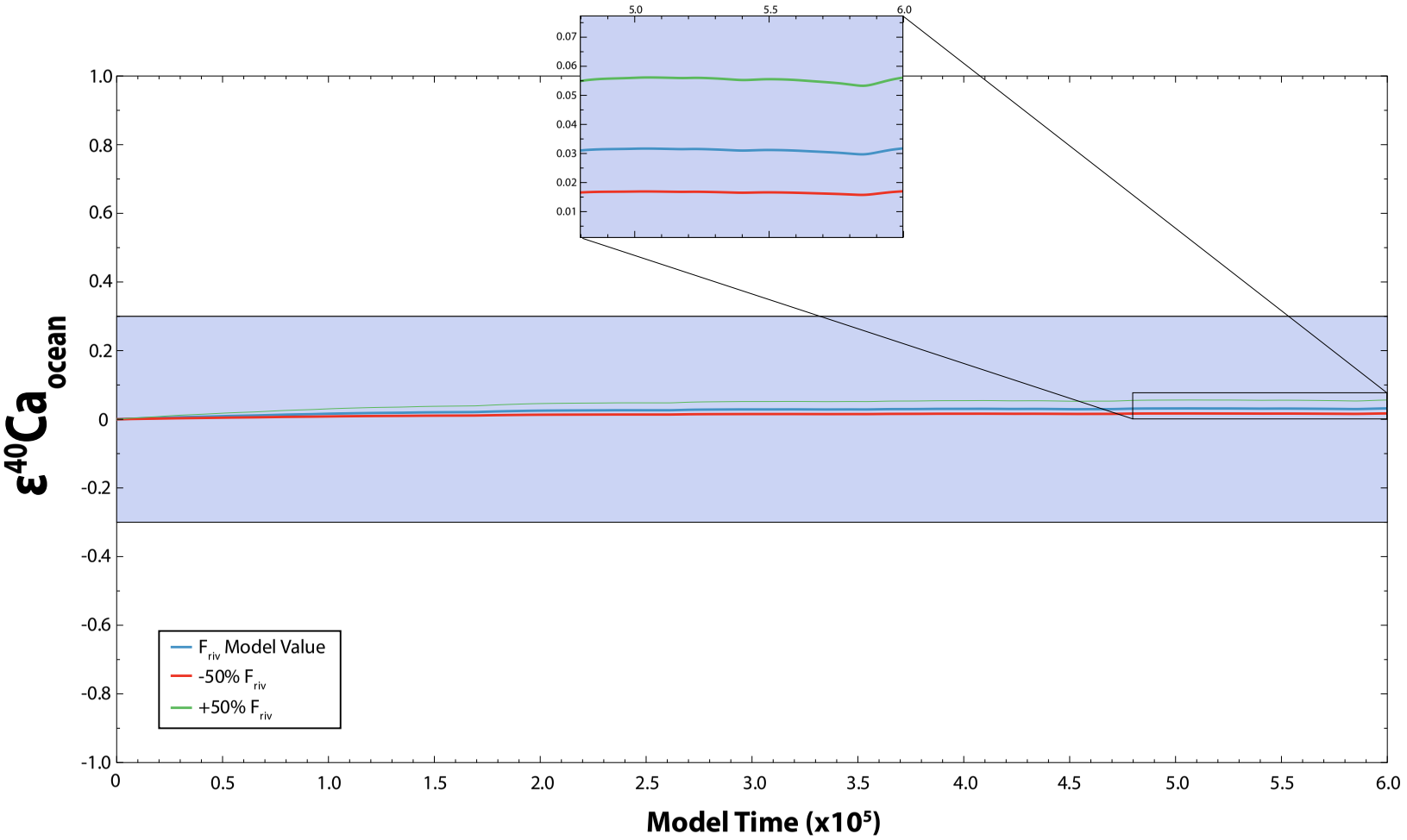

Figure B.5 – *The riverine flux is the variant component of this model and it is also the largest flux component. Therefore, it is important to test the sensitivity of the model with different flux estimates. Changing the magnitude of the riverine Ca flux shifts the isotope balance and therefore causes a vertical shift of the model output. Changing the magnitude of the flux either amplifies or reduces the response of the model to variable weathering rates. However, as long as the riverine flux is within ± 50% of the chosen value, the model output remains consistent with the few oceanic radiogenic Ca data that exist (Caro et al., 2010).*

B.6 Discussion

Overall, the Ca budget of seawater is governed either by hydrothermal exchange that occurs at spreading centers and their extensive flanks or is dominated by continental carbonates and evaporates, which implies this contribution is higher than current estimates and masks any contributions from upper continental crustal silicates.

However, the model presented here suggests that the marine radiogenic Ca budget response to silicate weathering is negligible in the context of the overall evolution of the radiogenic Ca oceanic system and is not related to changes in the increased contribution of carbonates, evaporates, and mafic rocks. Instead, it appears that the marine Ca record may reflect a response to variable Ca fluxes that are derived from the weathering and input of sea-floor basalt interactions and hydrothermal fluxes.

We can use the model presented here to further constrain the low-T hydrothermal fluxes in the oceanic Ca system. As mentioned earlier, Elderfield and Schultz (1996) constrained the Ca flux to a: 1) Minimum = 3.7 x 10^{15} kg/year, 2) Average = 7.35 x 10^{15} kg/year, and 3) Maximum = 1.16 x 10^{16} kg/year (Figure B.6). Table B.2 shows a simple mass balance where we have calculated the fluxes of high and low radiogenic continental Ca sources as well as the low- and high-T hydrothermal fluxes using the values mentioned above. Based on these calculations, we observe that there is a large gap between continental fluxes of Ca and hydrothermal sources, which is not taken into account by current hydrothermal flux estimates. To balance the total continental flux with the largest high-T flux we require a low-T flux that is at least 105 times greater than the maximum low-T flux previously proposed, i.e., a water flux of approximately 1.22 x 10^{18} L/year. This would, in turn, produce a Ca flux of approximately 1.24 x 10^{22} µmol/year. With an oceanic ε^{40}Ca composition of +0.03, this produces a radiogenic Ca flux of approximately 3.7 x 10^{20} µmol/year. This, combined with the maximum high-T hydrothermal Ca flux balances the continental input.

Conversely, we can perform the same calculation for the high-T hydrothermal flux. To balance the total continental flux with the highest low-T flux we need a high-T flux that is at least 12,800 times greater than the maximum high-T flux already proposed, i.e., a water flux of approximately 5.76 x 10^{17} L/year. This would, in turn, produce a Ca flux of approximately 1.15 x 10^{22} µmol/year. With an oceanic ε^{40}Ca composition at +0.032, this yields a radiogenic Ca flux of approximately 3.69 x 10^{20} µmol/year. This, combined with the maximum low-T Ca hydrothermal flux balances the continental input.

A low-T flux that is 105 times greater and a high-T flux that is 12,800 times greater than the literature value does not particularly seem feasible. Another test that can be

done is to lower the radiogenic Ca composition of continental input from +1.3 to +0.5 or +0.1. Even in this scenario, with a radiogenic Ca flux of 1.41 x 10^{20} µmol/year (for ε^{40}Ca = +0.5) or 2.82 x 10^{19} µmol/year (for ε^{40}Ca = +0.1), we need a low-T flux that is at least 40 or 8 times greater than literature values or a high-T flux that is at least 4,800 or 865 times greater than literature values for ε^{40}Ca = +0.5 and +0.1, respectively. Thus, we can propose a new minimum, average and maximum value of the low-T and high-T hydrothermal flux of Ca. For the low-T flux, we have a minimum of 9.41 x 10^{20} µmol/year, an average of 4.73 x 10^{21} µmol/year, and a maximum of 1.24 x 10^{22} µmol/year. For the high-T flux, we have a minimum of 7.79 x 10^{20} µmol/year, an average of 4.32 x 10^{21} µmol/year, and a maximum of 1.15 x 10^{22} mol/year.

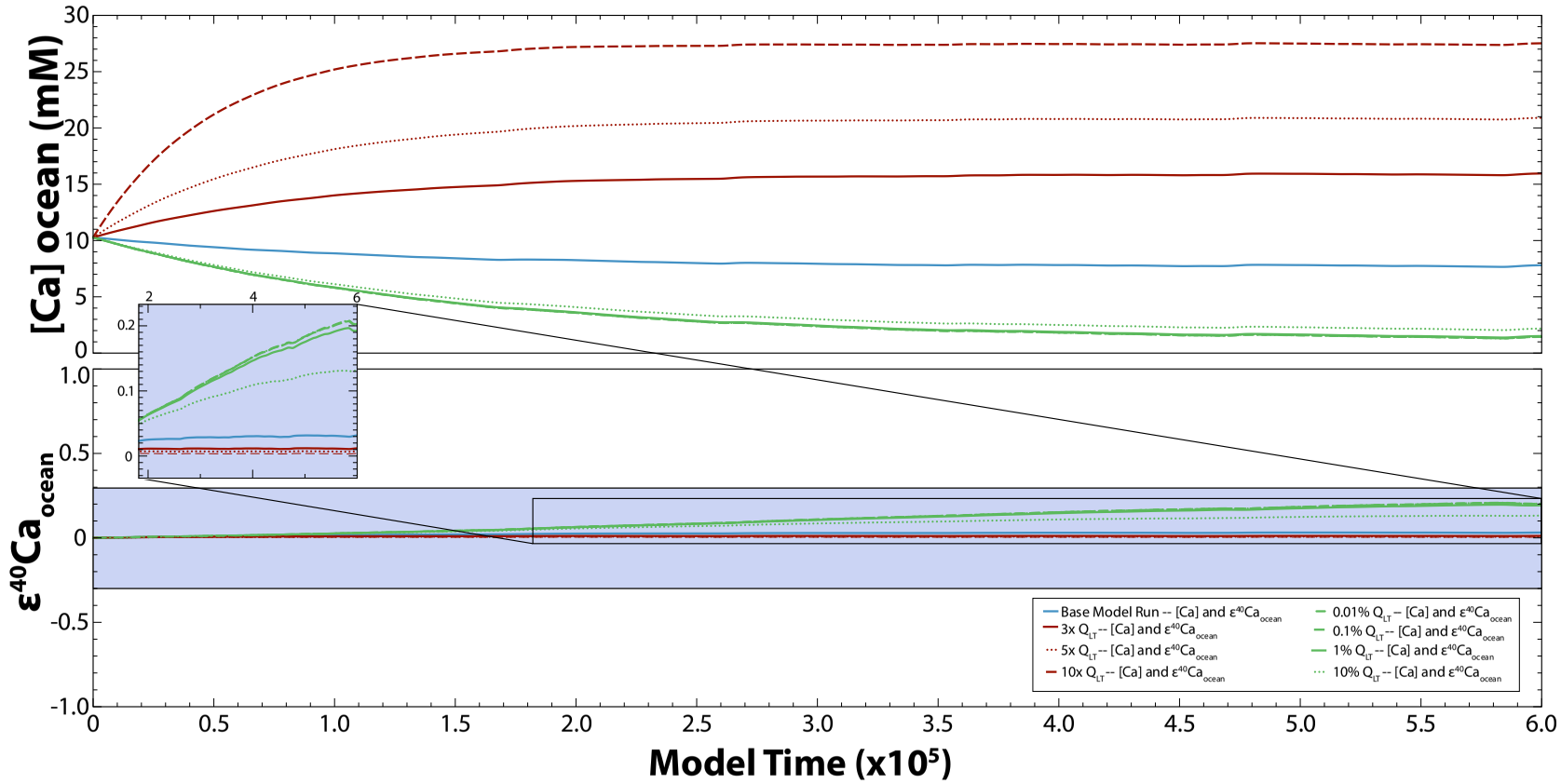

Figure B.6 – *The response of the Ca model to various low-T hydrothermal flux scenarios as in Figure 4, but a more detailed view. The base run is displayed in a light blue solid line, similar to previous figures. This figure displays the 3, 5, and 10 times the average low-T flux estimates in red with varying solid and dashed lines. The model values of 0.01, 0.1, 1, and 10% of the average low-T flux estimate are shown by green lines with varying solid and dashed lines. We observe that increasing the low-T flux lowers the radiogenic oceanic composition and the modeling scenario begins with elevated [Ca] that eventually reaching equilibrium. Conversely, decreasing the low-T flux drastically elevates the radiogenic composition of the oceans and decreases the [Ca].*

Table B.2 – *The radiogenic Ca global isotopic balance. The total mass of Ca in seawater is 1.4 x 10^{19} moles.*

		Water Flux (liter/year)	Concentration (µmol/liter) Ca	J_i (µmol/year) Ca	Isotope Ratio (α) ε^{40}Ca	$J_i(\alpha_i$-$\alpha_{SW})$ (µmol/year) ε^{40}Ca
Global						
River Water		3.74 x 10^{16}*	858*	3.21 x 10^{19}	0.1∞	3.21 x 10^{18}
					2.5∞	8.03 x 1019
Groundwater		1.19 x 10^{15}•	13498.68•	1.6 x 10^{19}	0.1∞	1.6 x 10^{18}
					2.5∞	4 x 10^{19}
Total Continental Flux		3.93 x 10^{16}	7178.34	2.82 x 10^{20}	1.3⫛	3.7 x 10^{20}
Hydrothermal Water						
	Low-T					
	Min	3.7 x 10^{15}*	10200*	3.8 x 10^{19}	0.05⫛	-1.9 x 10^{18}
	Average	7.35 x 10^{15}*	10200*	7.5 x 10^{19}	0.03⫛	-2.3 x 10^{18}
	Max	1.16 x 10^{16}*	10200*	1.63 x 10^{20}	0.02⫛	-3.3 x 10^{18}
	High-T					
	Min	1.5 x 10^{13}*	20000*	3 x 10^{17}	0.032⫛	-9.6 x 10^{15}
	Average	3 x 10^{13}*	20000*	6 x 10^{17}	0.032⫛	-1.9 x 10^{16}
	Max	4.5 x 10^{13}*	20000*	9 x 10^{17}	0.032⫛	-2.9 x 10^{16}
Seawater		–	10000*	–	0.0∞	–

*Values from Elderfield and Schultz (1996)
•Values from Holmden et al. (2012) based on estimates from Milliman (1993)
∞Values suggested by Caro et al. (2010)
⫛Values used in this study

B.7 Conclusions

The Ca model presented here shows that the marine radiogenic Ca record cannot provide information on variations in continental silicate weathering and CO_2 consuming processes throughout the geologic past. However, modeling of the radiogenic Ca marine record does allow us to place constraints on the compositions and fluxes of individual components of the oceanic Ca cycle. On shorter timescales, the marine Ca record does not seem to be sensitive to even large changes in low-T hydrothermal fluxes, but this is not the case, however, on longer timescales.

Overall, our modeling results indicate that ε^{40}Ca in seawater has remained constant and indistinguishable from the mantle composition for the past 3.5 Ga despite the influx of radiogenic calcium delivered via the weathering of high K/Ca components of the continental crust as indicated previously by Caro et al. (2010). Therefore, the weathering input from silicate sources has remained small compared with contributions from hydrothermal fluxes over much of Earth's history. Mass balance constraints require that the present hydrothermal flux of calcium exceeds the silicate weathering flux by at least one order of magnitude. This indicates that important exchanges of calcium take place at off-axis hydrothermal sites. Hydrothermal exchanges between oceanic crust and seawater appear to control oceanic Ca chemistry. We propose new estimates of the low- and high-T hydrothermal fluxes of Ca in the oceans based on the modeling presented here. For the low-T flux, we propose a minimum of 9.41 x 10^{20} µmol/year, an average of 4.73 x 10^{21} µmol/year, and a maximum of 1.24 x 10^{22} µmol/year. For the high-T flux, we propose a minimum of 7.79 x 10^{20} µmol/year, an average of 4.32 x 10^{21} µmol/year, and a maximum of 1.15 x 10^{22} µmol/year.

Available online at www.sciencedirect.com

ScienceDirect

Procedia Earth and Planetary Science 00 (2014) 000–000

Procedia
Earth and Planetary Science

www.elsevier.com/locate/procedia

Geochemistry of the Earth's Surface meeting, GES-10

Tracing silicate weathering in the Himalaya using the ^{40}K-^{40}Ca system: A reconnaissance study

Jesse Davenport*, Guillaume Caro, Christian France-Lanord

Centre des Recherches Petrographiques et Geochimiques (CNRS-CRPG), 15 rue Notre Dame des Pauvres, Vandœuvre-les-Nancy, France, 54500

Abstract

This study investigates the potential of the ^{40}K-^{40}Ca decay scheme as a tracer of silicate vs. carbonate weathering in the Himalayan erosional system. To this end, we present high precision ^{40}Ca data on river sediments, dissolved river loads and whole-rock carbonates representative of the main tectonic units of the Himalayas. Our results show that metamorphosed dolomites from the Lesser Himalaya (LH) exhibit no radiogenic ^{40}Ca excess despite highly variable $^{87}Sr/^{86}Sr$ signatures (0.73-0.85). In contrast, silicate material is radiogenic, with $\varepsilon^{40}Ca$ ranging between +1 in the TSS to +4 ε-units in the LH. Preliminary results obtained from a series of 27 Himalayan rivers show that $\varepsilon^{40}Ca$ in the dissolved load is significantly influenced by silicate lithologies, with $\varepsilon^{40}Ca$ ranging from +0.1 to +1.6 ε-units. Our results suggest that the ^{40}Ca signature of Himalayan rivers primarily reflects the lithological nature of their erosional source, and highlights the potential of the ^{40}K-^{40}Ca decay scheme as a tracer of silicate weathering.

Peer-review under responsibility of the Scientific Committee of GES-10.

Keywords: weathering; silicate; carbonate; Himalaya; calcium cycle; ^{40}K-^{40}Ca system

1. Introduction

The uplift and erosion of the Himalayan-Tibetan Plateau (HTP) has long been thought to play a key role in controlling the $^{87}Sr/^{86}Sr$ evolution of seawater throughout the geologic past [1-6]. Understanding the relative contribution of silicate versus carbonate weathering in the Himalaya is important for understanding the evolution of the CO_2 cycle and seawater chemistry [7]. However, Himalayan rivers have distinct characteristics, i.e. high Sr

* Corresponding author. Tel.: +33 03 83 59 42 42.
E-mail address: jessed@crpg.cnrs-nancy.fr

Peer-review under responsibility of the Scientific Committee of GES-10.

concentrations and radiogenic $^{87}Sr/^{86}Sr$, that exclude a simple mixing relationship between silicate and carbonate lithologies [8-10]. The use of $^{87}Sr/^{86}Sr$ signatures as a tracer of Himalayan weathering is not straightforward because (1) the formations of the Himalaya have different crustal aging, hence contrasted bulk $^{87}Sr/^{86}Sr$, and (2) the recent metamorphism redistributed radiogenic ^{87}Sr towards weatherable minerals such as feldspars and carbonates [5, 8-11].

This study investigates the potential use of the ^{40}K-^{40}Ca system as a tracer to better quantify the contributions of silicate and carbonate lithologies in the dissolved load of major Himalayan rivers [13-15]. Previous work showed that the ^{40}Ca budget of seawater is dominated by mantle inputs [15], so that marine carbonates display a homogeneous $\varepsilon^{40}Ca$ signature indistinguishable from the mantle value (i.e. $\varepsilon^{40}Ca=0$). In contrast, the silicate upper crust, with a K/Ca ratio of 1, is expected to have developed a radiogenic $\varepsilon^{40}Ca$ of ca. +2 ε -units. It was therefore anticipated that the ^{40}K-^{40}Ca system could yield robust constraints on the relative contribution of silicate vs. carbonate lithologies in dissolved river loads. Here, we present the first extensive investigation of ^{40}K-^{40}Ca systematics in the Himalayan erosional system. We show that during the collision of India with Asia, ^{40}Ca, unlike ^{87}Sr, remained remarkably resistant to metamorphism/dolomitization, allowing us to distinguish carbonate and silicate sources in the dissolved load of the major Himalayan rivers.

2. Samples

Three types of samples were investigated in this study. First, bedload sediments (Figure 1) were selected from rivers draining the main lithological and tectonic units of the Himalaya. These include the Marsyandi in the TSS, the Chepe in the HHC and the Isul in the LH, as well as sediments from the Ganga and Brahmaputra rivers. The silicate fractions of these sediments have $^{87}Sr/^{86}Sr$ compositions ranging from 0.72 (in the TSS) to 0.86 (in the LH) and εNd between -16 and -25.6 [9]. Based on Sr-Nd provenance work in [8], these samples fall into

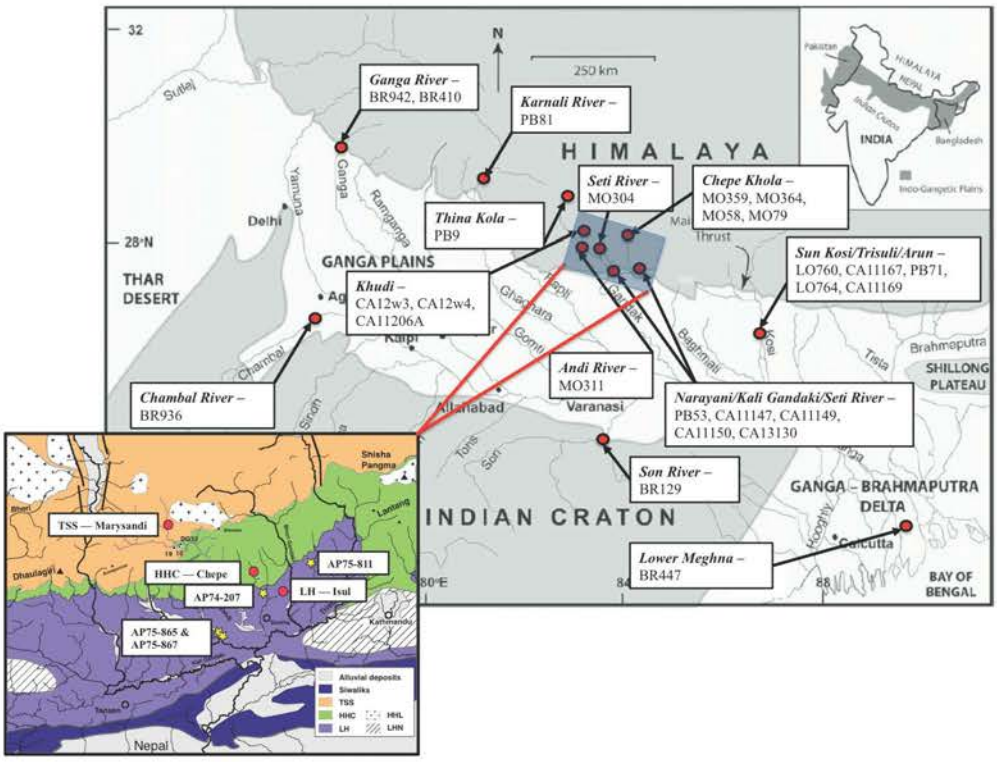

Figure 1. Map of the Ganges and Brahmaputra basin and major tributaries. Location of river samples is denoted by a red dot with the specific river and sample number also identified. The Main Frontal Thrust (MFT) is also denoted on the larger map. The MFT places Siwalik foreland basin sediments over the modern Gangetic plain, while the MCT places the HHC over the LH. The inset image shows an enhanced geological map view of the Narayani watershed and the location of bedload (red dots) and carbonate samples (yellow stars) analysed in this study.

compositional fields representative of the main tectonic units of the Himalayas and should therefore provide a general overview of $^{40}Ca/^{44}Ca$ variability in the Himalayan system.

Second, a suite of 27 river water samples (Figure 1) was selected to gain a clearer understanding of the contribution from main litho-tectonic units to the ^{40}Ca dissolved flux. The selected samples include the major tributaries of the Ganga (Upper Ganga, Narayani, Karnali, Kosi) as well as small rivers draining single lithologies (Khudi, Chepe). While this study is more strongly focused on the Narayani watershed, these samples cover most of the Sr isotope and major element variability observed in Himalayan rivers.

Lastly, a series of variably dolomitized impure marbles from the Lesser Himalaya were analyzed to assess the sensitivity of ^{40}Ca to post-depositional effects (dolomitization, metasomatism, metamorphism) (Figure 1, inset image). The marbles are characterized by a carbonate content of 60-80 wt% and a Mg/Ca ratio from 0.1 to 0.55 [9]. Their $^{87}Sr/^{86}Sr$ varies between 0.72 (for massive beds) and 0.86, reflecting extensive redistribution of ^{87}Sr between carbonates and the surrounding calc-silicate shists.

3. Methods

Relatively little work has been completed so far on the ^{40}K-^{40}Ca system due to the difficulty of measuring small radiogenic effects on the large ^{40}Ca isotope. Work in the 1980s using the Finnigan-MAT 262 reported external precisions of ±0.6-1.5 ε-units (2σ) [16-17]. More recently, using a Thermo-Finnigan Triton Thermal Ionization Mass Spectrometer (TIMS) to analyze samples from Archean cratons, Kreissig and Eliott [18] obtained a reproducibility of ±0.5 ε-units (2σ) and Caro et al. [15] reported $^{40}Ca/^{44}Ca$ data in marine carbonates with external precision of ±0.35 ε-units. This improvement was made possible by i) the measurement of larger ion beams on the Triton (<50V, against <10V using the MAT262), and ii) the implementation of multidynamic acquisition schemes using the "Zoom" optical system of the Triton. Thus, problems with the requisite sensitivity to analyze small variations in the abundant ^{40}Ca isotope (96.9%) can now be resolved using the Triton TIMS [15].

The mass spectrometric method implemented here is a multidynamic approach modified from [15]. Prior to analysis, ca.10 µg of Ca is loaded in concentrated HNO_3 onto the evaporation filament of a double rhenium filament assembly. Heating the ionization filament to about 3000 mA generates a stable signal during approximately 2-4 hours of analysis (15V on ^{40}Ca, 100 mV on ^{42}Ca). The multidynamic scheme involves the acquisition of ^{40}Ca, ^{42}Ca ^{43}Ca and ^{44}Ca on line 1 (L1) followed by ^{42}Ca and ^{44}Ca on line 2 (L2). The $^{40}Ca/^{42}Ca_{(L1)}$ ratio is corrected from instrumental mass fractionation using the exponential law with $^{42}Ca/^{44}Ca_{(L2)}=0.31221$ as a normalization ratio. Sample analyses were interspersed with measurements of the NIST SRM915a standard, whose $^{40}Ca/^{42}Ca$ value is identical within errors to both seawater and MORBs [15]. $^{40}Ca/^{42}Ca$ variations are normalized to the NIST value and expressed using the conventional $\varepsilon^{40}Ca$ notation. In-run internal precision is typically ±0.2-0.3 ε-units ($2\sigma_m$) and external precision in multi-dynamic mode is ±0.2-0.4 ε-units (2σ).

4. Results

Calcium and strontium isotopic results for bedrock, bedload sediments and rivers are presented in Figure 2. A major result of this study is the remarkably homogeneous $\varepsilon^{40}Ca$ signatures measured in both bedrock and bedload carbonates, which contrasts with their heterogeneous $^{87}Sr/^{86}Sr$ compositions (from ≈0.72 to ≈0.86). It is certainly plausible that despite isotopic exchange associated with Himalayan metamorphism, the high Ca content of carbonate rocks prevented any significant modification of their original signature (at $\varepsilon^{40}Ca=0$). In contrast, the silicate fractions in bedload sediments show significant ^{40}Ca excesses on the order of +0.9 ε-units in the TSS to +3.8 ε-units in the LH (±0.3 ε-units, 2σ), correlating with their $^{87}Sr/^{86}Sr$ ratios. In the Brahmaputra and Ganga sediments, $\varepsilon^{40}Ca$ average ca. +2 ε -units, similar to those measured in HHC bedloads. These $\varepsilon^{40}Ca$ values are consistent with the K/Ca and Nd model ages for their respective Himalayan formations. Therefore, the ^{40}K-^{40}Ca system offers a simple means of distinguishing carbonate vs. silicate sources in the dissolved river flux.

As shown in Figure 2, Himalayan rivers display a wide range of $\varepsilon^{40}Ca$ compositions, from +0.1 in rivers draining carbonate dominated catchments to +1.6 in HHC rivers draining predominantly silicate catchments. Given the limited magnitude of $\varepsilon^{40}Ca$ excesses measured in silicate rocks, this result implies that silicate weathering makes a significant contribution to the dissolved calcium budget of Himalayan rivers. Interestingly, rivers with the most radiogenic $^{87}Sr/^{86}Sr$ ratios are not necessarily associated with the highest $\varepsilon^{40}Ca$ values. For example, the Andi River,

which drains Lesser Himalayan lithologies, exhibits one of the highest $^{87}Sr/^{86}Sr$ signatures at 0.7720 and has a relatively low $\varepsilon^{40}Ca$ at +0.64 (±0.30 ε-units, 2σ). In contrast, the Khudi, which drains a HHC silicate catchment, has a lower $^{87}Sr/^{86}Sr$ of 0.74 but an $\varepsilon^{40}Ca$ signature that is far more radiogenic at +1.6 (±0.3 ε-units, 2σ). As mentioned above, such decoupling is expected from the presence in the LH of metamorphosed carbonates with high $^{87}Sr/^{86}Sr$ ratios but non-radiogenic $^{40}Ca/^{44}Ca$. Overall, the positive $\varepsilon^{40}Ca$ observed in Himalayan rivers seem to originate primarily from silicate catchments of the HHC, while their radiogenic ^{87}Sr budget is more strongly influenced by carbonates of the Lesser Himalaya. Since calcium is a major constituent in water and sediment, compared to strontium — a trace element, the calcium isotopic system might better represent the overall weathering budget and fluxes. This suggests that, with a more extensive knowledge of ^{40}Ca distribution in silicate catchments, the ^{40}K-^{40}Ca system could become a powerful tool to quantify silicate weathering in the Himalayan system.

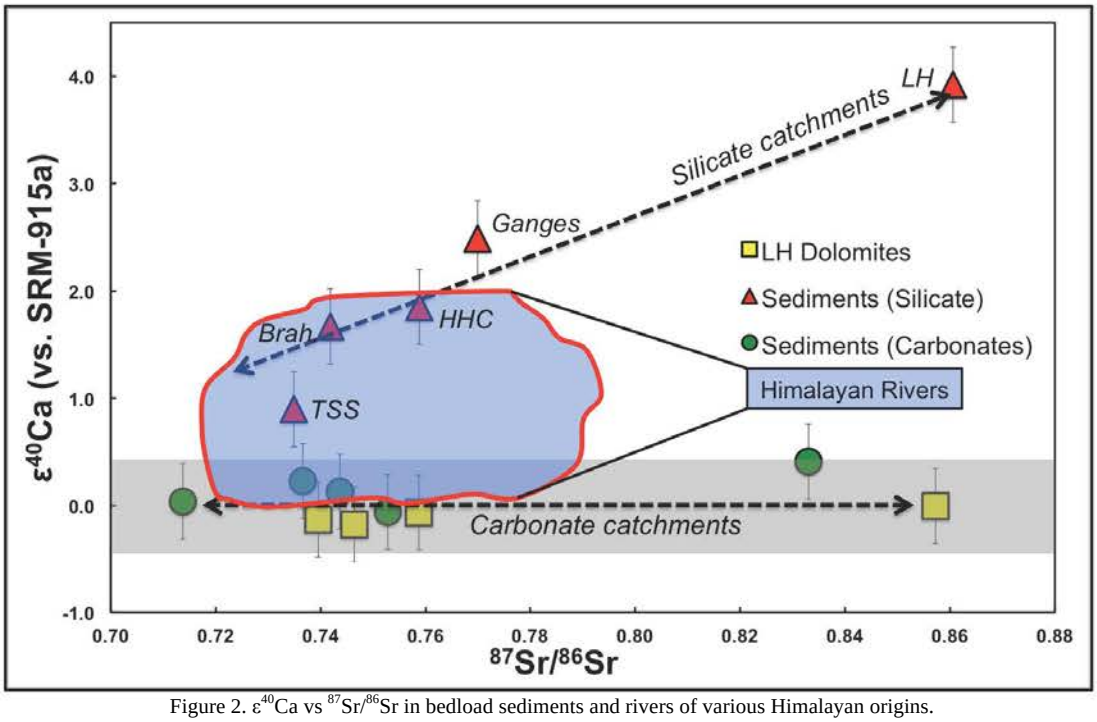

Figure 2. $\varepsilon^{40}Ca$ vs $^{87}Sr/^{86}Sr$ in bedload sediments and rivers of various Himalayan origins.

5. Conclusions

High precision ^{40}Ca analyses using the Triton TIMS enable the use of ^{40}K-^{40}Ca as a tracer of silicate weathering in the Himalaya as well as other complex erosional systems. To the contrary, unlike with strontium, calcium isotopic compositions in carbonates appear to be remarkably resistant to metamorphism and thus no radiogenic effect was found in carbonates from the main Himalayan formations. In contrast, radiogenic ^{40}Ca excesses are found in dissolved river loads with a composition intermediate between non-radiogenic carbonate and radiogenic silicate HHC sources. These results suggests that silicate catchments make a major contribution to the dissolved Ca budget of major Himalayan rivers.

Acknowledgements

We thank Dr. Lin Ma, Dr. Albert Galy for insightful reviews, comments and discussion as well as Catherine Zimmerman, Christiane Parmentier, Damien Cividini and Aimeryc Schumacher for technical and laboratory assistance. This study benefited from sampling of the ANR Blanc Calimero project, and is supported in the framework of the Marie Curie Initial Training Network (ITN) of Investigating Tectonism Erosion Climate

Couplings (iTECC) an inter-European research group. The analytical development on the ^{40}K-^{40}Ca system was supported by CNRS program SYSTER. This is CRPG Contribution No. 2326.

References

1. Palmer M.R., Edmond J.M. The Strontium isotope budget of the modern ocean. *Earth and Planetary Science Letters* 1989;**92**:11-26.
2. Hodell D.A., Mead G.A., Mueller P.A. Variation in the strontium isotopic composition of seawater (8 Ma to present): Implications for chemical weathering rates and dissolved fluxes to the ocreans. *Chemical Geology (Isotope Geosciences Section)* 1990;**80**: 291-307.
3. Richter F.M., Rowley D.B., DePaolo D.J. Sr isotope evolution of seawater: the role of tectonics. *Earth and Planetary Science Letter* 1992;109: 11-23.
4. Palmer M.R., Edmond J.M. Controls over the strontium isotope composition of river water. *Geochimica et Cosmochimica Acta* 1992;**56**: 2099-2111.
5. Edmond J.M. Himalayan Tectonics, Weathering Processes, and the Strontium Isotope Record in Matine Limestones. *Science* 1992;**258**: 1594-1597.
6. Krishnaswami S., Trivedi J.R., Sarin M.M., Ramesh R., Sharma K.K. Strontium isotopes and rubidium in the Ganga-Brahmaputra river system: Weathering in the Himalaya, fluxes to the Bay of Bengal and contributions to the evolution of oceanic ^{87}Sr/^{86}Sr. *Earth and Planetary Science Letters* 1992;**109**: 243-253.
7. Jacobson A.D., Blum J.D., Walter L.M. Reconciling the elemental and Sr isotope composition of Himalayan weathering fluxes: Insights from the carbonate geochemistry of stream waters. *Geochimica et Cosmochimica Acta* 2002;**66**: 3417-3429.
8. Derry L.A., France-Lanord C. Neogene Himalayan weathering history and river ^{87}Sr/^{86}Sr: impact on the marine Sr record. *Earth and Planetary Science Letter* 1996;**142**: 59-74.
9. Galy A., France-Lanord C., Derry L.A. The Strontium isotopic budget of Himalayan Rivers in Nepal and Bangladesh. *Geochimica et Cosmochimica Acta* 1999;**63**: 1905-1925.
10. Quade J., English N., DeCelles P.G. Silicate versus carbonate weathering in the Himalayas: a comparison of the Arun and Seti Watersheds. *Chemical Geology (Isotope Geoscience Section)* 2003;**202**: 275-296.
11. Bickle M.J., Chapman H.J., Bunbury J., Harris N.B.W., Fairchild I.J., Ahmad T., Pomies C. Relative contributions of silicate and carbonate rocks to riverine Sr fluxes in the headwaters of the Ganges. *Geochimica et Cosmochimica Acta* 2005;**69**: 2221-2240.
12. Bickle M.J., Harris N.B.W., Bunbury J., Chapman H.J., Fairchild I.J., Ahmad T. Controls on the ^{87}Sr/^{86}Sr of carbonates in the Garwal Himalaya, heawaters of the Ganges. *J. Geol.* 2001;**109**: 737-753.
13. Caro G., France-Lanord C. ^{40}K-^{40}Ca constraints on the source of dissolved calcium in Himalayan Rivers. *Goldschmidt 2013*;**Abstract**: 828.
14. Caro G., Papanastassiou D.A., Wasserburg G.J., Schopf J.W. ^{40}K-^{40}Ca isotopic systematics of marine carbonates: a record of continental crust evolution since 3.5 Gyr. *American Geophysical Union, Fall Meeting* 2006;**Abstract**.
15. Caro G., Papanastassiou D.A., Wasserburg G.J. ^{40}K-^{40}Ca isotopic constraints on the oceanic calcium cycle. *Earth and Planetary Science Letters* 2010;**296**: 124-132.
16. Marshall B.D., DePaolo D.J. Calcium isotopes in igneous rocks and the origin of granite. *Geochimica et Cosmochimica Acta* 1989;**53**: 917-922.
17. Nelson D.R., McCulloch M.T. Petrogenetic applications of the ^{40}K-^{40}Ca radiogenic decay scheme — A reconnaissance study. *Chemical Geology (Isotope Geoscience Section)* 1989;**79**: 275-293.
18. Kreissig K. Elliot T. Ca isotope fingerprints of early crust-mantle evolution. *Geochimica et Cosmochimica Acta* 2005;**69**: 165-176.

THE GEOLOGICAL SOCIETY OF AMERICA®

Timing and mechanism of the rise of the Shillong Plateau in the Himalayan foreland

G. Govin[1†], Y. Najman[1], A. Copley[2], I. Millar[3], P. van der Beek[4], P. Huyghe[4], D. Grujic[5], and J. Davenport[6]
[1]Lancaster Environment Centre, Lancaster University, Lancaster LA1 4YQ, UK
[2]Department of Earth Sciences, Cambridge University, Cambridge CB2 3EQ, UK
[3]NERC Isotope Geosciences Laboratory, British Geological Survey, Keyworth, Nottingham NG12 5GG, UK
[4]ISTerre, Université Grenoble Alpes, 38058 Grenoble Cedex 9, France
[5]Department of Earth Sciences, Dalhousie University, Halifax B3H 4R2, Canada
[6]Centre de Recherches Pétrographiques et Géochimiques (CRPG), 54500 Vandœuvre-Lès-Nancy, France

ABSTRACT

The Shillong Plateau (northeastern India) constitutes the only significant topography in the Himalayan foreland. Knowledge of its surface uplift history is key to understanding topographic development and unraveling tectonic–climate–topographic coupling in the eastern Himalaya. We use the sedimentary record of the Himalayan foreland basin north of the Shillong Plateau to show that the paleo-Brahmaputra river was redirected north and west by the rising plateau at 5.2–4.9 Ma. We suggest that onset of plateau uplift is a result of increased fault-slip rates in response to stresses caused by the Indian lithosphere bending beneath the Himalaya.

INTRODUCTION

Unraveling the topographic evolution of mountain ranges remains a challenge. We address this question in the Shillong Plateau (SP), a 1600-m-high fault-bounded basement uplift in the Himalayan foreland (northeastern India; Fig. 1), the uplift history of which is linked to both orographic rainfall patterns and strain partitioning in the eastern Himalaya (Clark and Bilham, 2008; Coutand et al., 2014; Grujic et al., 2006).

Low-temperature thermochronology data indicate that exhumation of the SP initiated between ca. 9 and 15 Ma (Biswas et al., 2007; Clark and Bilham, 2008), whereas surface uplift of sufficient magnitude to create local flexural loading of the Indian plate is only observed by ca. 2–3.5 Ma (Najman et al., 2016). Surface uplift is therefore decoupled from exhumation for much of the plateau's history, and occurred after a period when rock uplift was compensated by surface erosion (Biswas et al., 2007). The causes and timing of the initiation of surface uplift remain uncertain.

Here, we establish the first direct estimate for the timing of onset of surface uplift, deduce a causal mechanism, and examine the relative roles of tectonics and erosion in the temporal evolution of topography in the SP. Our work advances the discussion regarding the relative importance of strain partitioning (Clark and Bilham, 2008; Coutand et al., 2014) versus orographic precipitation linked to SP uplift (Grujic et al., 2006) in influencing Himalayan exhumation rates to its north, and provides a framework for interpreting the present-day crustal structure of the SP and flanking regions (e.g., Mitra et al., 2005; Singh et al., 2016). Additionally, we provide new insights into the behavior of basement-cored foreland uplifts applicable to other orogens (e.g., Jordan and Allmendinger, 1986; Kober et al., 2013), as well as to older ranges where early records of uplift have been destroyed.

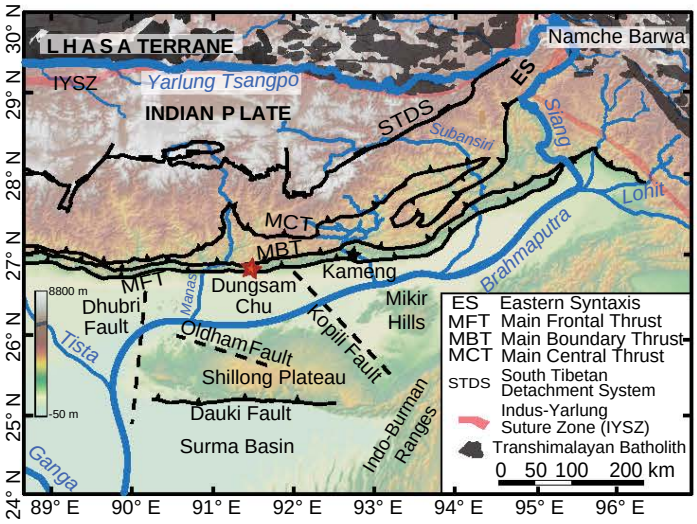

Figure 1. Main geologic features of the eastern Himalaya (from Lang and Huntington, 2014; Long et al., 2011). Red and black stars represent the Dungsam Chu (DC) and Kameng sections, respectively.

GEOLOGICAL CONTEXT AND APPROACH

The SP and adjacent Mikir Hills expose Proterozoic-Paleozoic basement overlain by outliers of Cenozoic sedimentary rocks (Mitra and Mitra, 2001). The plateau is bounded by two active crustal-scale reverse faults (Mitra et al., 2005): the Oldham and Dauki faults (Fig. 1). The latter juxtaposes basement against the Cenozoic sediments of the Surma Basin to the south, with a vertical offset of ~10 km (Biswas et al., 2007). The SP has been uplifted either as a symmetric pop-up (England and Bilham, 2015), along the Dauki fault acting as a north-dipping thrust connected to the Himalayan orogen (Seeber and Armbruster, 1981), as a crustal-scale fault-propagation fold (Clark and Bilham, 2008), or as an asymmetric basement-cored uplift (Biswas et al., 2007). Surface uplift of the SP, along with westward propagation of the Indo-Burman Ranges (IBR) (Fig. 1), diverted the Brahmaputra River northward from a south-southwest course, to flow between the Himalaya and the SP (Chirouze et al., 2013; Johnson and Alam, 1991; Najman et al., 2016; Uddin and Lundberg, 1999). Therefore, the first occurrence of paleo-Brahmaputra deposits in the basin directly north of the SP allows the initiation of surface uplift to be dated. Because only limited topographic uplift is required before river diversion occurs, this approach dates initiation of SP uplift more sensitively than flexural modeling (Najman et al., 2016), for which a significant load must be established.

Brahmaputra deposits are readily identified in the sedimentary record because the river's upstream continuation, the Yarlung River, drains the Indus-Yarlung suture zone and Transhimalayan batholiths of the Asian

†Deceased

Lhasa terrane. In contrast, Himalayan rivers only drain Indian plate rocks to the south (Bracciali et al., 2015; Cina et al., 2009; Gehrels et al., 2011). Transhimalayan detritus in dated Siwalik sediments of the eastern Himalaya shows that the Yarlung and Brahmaputra were connected by 13 Ma; connection through the Siang River (Fig. 1) was established by at least 7 Ma (Bracciali et al., 2016; Chirouze et al., 2013; Cina et al., 2009; Govin, 2017; Lang and Huntington, 2014; Lang et al., 2016).

Using new and published provenance analyses from Himalayan foreland-basin rocks, we reconstruct Brahmaputra drainage from Late Miocene to present, and determine when the river was deflected due to the initiation of uplift of the SP. By combining this work with a model for the regional stress field, we assess the cause of the transition from exhumation to surface uplift.

RESULTS: PROVENANCE ANALYSIS

We report detrital zircon U-Pb data from the Dungsam Chu (DC) section in Bhutan, located directly north of the SP (Figs. 1 and 2). We can identify paleo-Brahmaputra input to the sediments because Transhimalayan zircons are typically of Cretaceous–Eocene age. In contrast, zircons derived from Indian-plate Himalayan drainages are dominated by >400 Ma and Miocene ages (e.g., Bracciali et al., 2016; Cina et al., 2009; Gehrels et al., 2011; Lang and Huntington, 2014; Fig. 2).

Zircons from eight sandstones from the DC section (see the GSA Data Repository[1]), magnetostratigraphically dated between 7 and 1 Ma (Coutand et al., 2016), were U-Pb dated using ion-microprobe and inductively coupled plasma–mass spectrometry (ICPMS) techniques (see Data Repository sections 2–6). Samples ≤4.9 Ma show 13%–22% Cretaceous–Cenozoic grains, which we interpret as being derived from the Transhimalaya (Fig. 2). In contrast, samples ≥5.2 Ma do not contain grains of such age (Fig. 2). These data therefore show a shift to Brahmaputra-type values at 5.2–4.9 Ma. Rutile U-Pb dating of sample SJ8 (depositional age 4.9 Ma) returned 25 out of 92 ages unique to the syntaxis (U-Pb ages <9 Ma; Bracciali et al., 2016; Data Repository sections 2 and 7), also demonstrating that these deposits are sourced from the Siang River.

DISCUSSION

Brahmaputra Paleo-Drainage

We combine our new sediment provenance results with existing studies from northeast, northwest, and south of the SP to form an evolutionary model of Brahmaputra drainage (Fig. 3). Our combined zircon and rutile U-Pb age-dating provides an unambiguous signature of the paleo-Brahmaputra draining through the Siang and axially along the foreland, rather than a hypothetical transverse drainage (Cina et al., 2009). Moreover, documentation of Transhimalayan-derived detritus upstream (east) of the location of the hypothesized transverse drainage (Govin, 2017; Lang and Huntington, 2014) invalidates the Cina et al. (2009) model. Therefore, the arrival of Transhimalayan detritus at DC at 5.2–4.9 Ma reflects northwest diversion of the paleo-Brahmaputra River to this locality. Prior to this time, DC sediments were sourced exclusively by rivers draining the southern Himalaya. Because of its location relative to the SP, encroachment of the Brahmaputra to the DC section likely occurred due to uplift of the SP. The timing of uplift is consistent with a recent estimate based on incision rates in the SP (Rosenkranz et al., 2018).

Prior to 7 Ma, the Brahmaputra flowed directly south-southwest to the Bengal Fan (Fig. 3A; Uddin and Lundberg, 1999). By 7 Ma, provenance

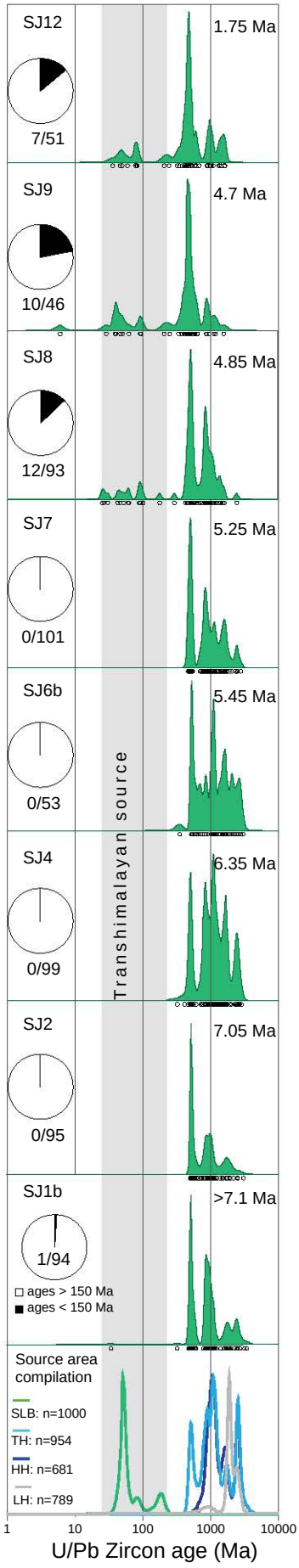

Figure 2. Kernel density plots (Vermeesch, 2012) of detrital zircon U-Pb ages from the Dungsam Chu (DC) section in the Himalaya. Depositional ages (numbers in top right) are from Coutand et al. (2016), location information is provided in the Data Repository (see footnote 1). Source area compilation is from Hu et al. (2012, and references therein). SLB—South Lhasa Block, TH, HH and LH—Tethyan, Higher, and Lesser Himalaya, respectively. Pie charts show proportion of zircons <150 Ma, x/xx is number of <150 Ma grains after data screening/total number of grains. Gray band shows ages characteristic of Transhimalaya of the SLB. Although grains in the range 30–50 Ma occur both in the Transhimalaya (commonly) and Indian plate Himalaya (uncommonly) (e.g., Lang and Huntington, 2014), the fact that none of our Indian-derived samples (SJ1 to SJ7) contain any grains of such age indicates that the 30–50 Ma population is also Transhimalayan-derived at DC.

[1]GSA Data Repository item 2018078, analytical and stress calculation methods and supplementary figures; sample locations (Table DR1); zircon U-Pb ages from source-areas compilation (Table DR2); zircon U-Pb ion probe data and standard (Tables DR3 and DR4); zircon U-Pb laser ablation data and standard (Tables DR5 and DR6); and rutile U-Pb laser ablation data and standard (Table DR7), is available online at http://www.geosociety.org/datarepository/2018/ or on request from editing@geosociety.org.

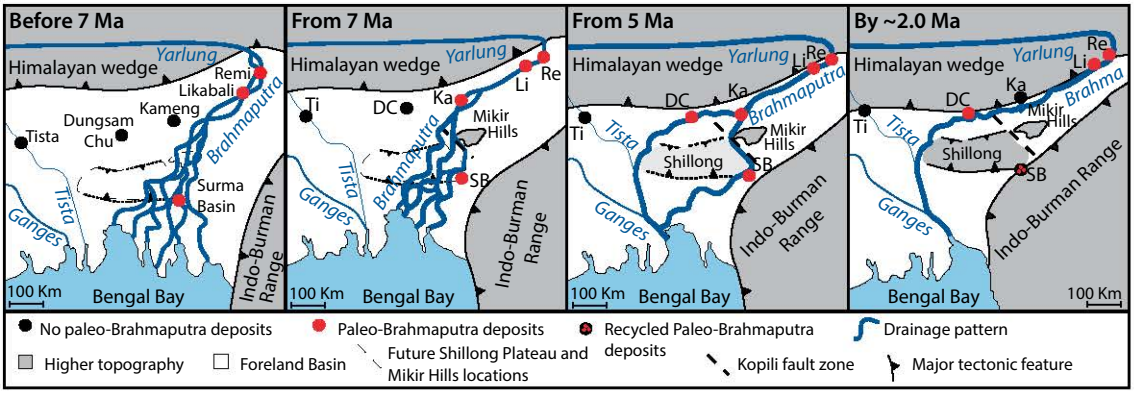

Figure 3. Brahmaputra paleodrainage evolution (modified from Chirouze et al., 2013), constructed using provenance studies from various sedimentary sections: Dungsam Chu (DC, this study); Likabali (Li) (Lang and Huntington, 2014); Remi (Re) (Govin, 2017), Tista (Ti) (Cina et al., 2009) Kameng (Ka) (Chirouze et al., 2013), and Surma Basin (SB) (Bracciali et al., 2015). Position of coastline is ill-constrained and thus the modern position is shown; DC sediments >5 Ma are deltaic (Coutand et al., 2016).

data indicate that the Brahmaputra reached the location of the Kameng section, northeast of the SP (Chirouze et al., 2013; Fig. 3), perhaps due to uplift in the Mikir Hills deflecting the river northward.

Between 4.9 and 5.2 Ma, the Brahmaputra reached DC due to the uplift of the SP deflecting the river northward and westward. However, coeval paleo-Brahmaputra deposits, not recycled from older units (thermochronological ages young up-section), are also found in the Surma Basin to the south of the SP (Bracciali et al., 2015). This can be explained by temporal and spatial variations of displacements on the Oldham and Dauki faults (Biswas et al., 2007), resulting in non-uniform uplift, and repeated switching of the Brahmaputra to courses east and west of the rising plateau.

By ca. 2 Ma, the Brahmaputra course east of the plateau closed due to the combination of westward propagation of the Indo-Burman Ranges and plateau rise (Najman et al., 2016). Since then, the river has flowed exclusively to the north and west of the SP, with Himalayan thrusting deflecting the river progressively south to its current location.

Causes of the Transition from Rock Uplift to Surface Uplift

The time lag between exhumation and surface uplift of the SP has previously been proposed to result from exhumation of basement rocks from beneath the more erodible Cenozoic sediment cover, leading to a decrease in erosion rate (Biswas et al., 2007). However, it was not until after ca. 1.5 Ma that SP basement rocks became the primary contributor to the Surma Basin (Najman et al., 2012; Bracciali et al. 2016). Thus, there appears to be an ~3.5 m.y. lag between our inferred onset of surface uplift (5.2–4.9 Ma) and the time of transition from predominantly cover to basement erosion (after 1.5 Ma), suggesting that the latter is not the dominant factor responsible for the change from exhumation to surface uplift of the SP.

A possible tectonic driver for this change involves an increase in slip rates of the faults bounding the plateau, such that surface denudation could no longer keep pace with rock uplift. Because the SP lies in the foreland being overridden by the Himalaya, the stresses acting on the faults bounding the plateau will have changed through time. Copley et al. (2011) calculated the stress state in the Indian plate due to far-field tectonic forces and bending of the Indian lithosphere beneath the Himalaya, using a model in which the Indian crust is broken by faults (see Data Repository section 2c). Copley et al. (2011) showed that the maximum differential stresses on the faults, and in the upper part of the ductile mantle, increase by a factor of ~1.5 as the Indian lithosphere bends beneath the Himalaya.

Fault-slip rates are thought to be nonlinearly related to the stress state at the base of the seismogenic layer, either through nonlinearity in the rate-state friction equations that describe the loading of faults by aseismic creep on their down-dip extensions (Marone, 1998), or by stress accumulation due to dislocation creep immediately beneath the seismogenic layer (Zoback and Townend, 2001). The nonlinear relationship between applied stress and fault loading rate for both possible mechanisms means that an increase in differential stress near the brittle-ductile transition by a factor of ~1.5 could result in a slip-rate increase by a factor of ≥2 (see Data Repository section 2c). Such an increase in slip rate is a plausible cause for the onset of surface uplift in the SP. The apparent twofold or larger increase in slip rate on the faults bounding the SP in the past ~10 m.y. suggested by Vernant et al., (2014), inferred from comparing modern and Miocene-Pliocene slip rates (Biswas et al., 2007; Clark and Bilham, 2008), provides support for this model.

The time scale for such a change depends on how long it takes the plateau to be transported through the region affected by bending stresses as India underthrusts the Himalaya (the east-west stresses due to loading by the Indo-Burman Ranges affect only the intermediate principal stress, so will not affect the fault-slip rates). The negative gravity anomaly associated with the foreland basin farther west indicates that the region subject to significant bending stresses is ~300 km wide (see Data Repository section 2c). The complex geometry of faults and basins makes this distance difficult to pinpoint in the SP region. However, we assume that the bending stresses occur over a similar distance from the Himalayan front in the SP region as farther west, based upon the similar depth distribution of earthquakes in these two regions (Craig et al., 2012). This logic implies that the SP has been transported ~100–200 km into the region affected by stresses resulting from bending of the Indian lithosphere beneath the Himalaya. At a convergence rate of ~15 mm/yr between the SP and southern Tibet (Vernant et al., 2014), this distance is consistent with the onset timing of exhumation (9–15 Ma) and surface uplift (ca. 5.2–4.9 Ma) in the SP.

Our results imply that the decrease in shortening rate in the Bhutan Himalaya, as a consequence of an increasing proportion of the overall convergence being accommodated by the SP, is likely to have occurred close to the most recent limit of the time range suggested by McQuarrie et al. (2014). The onset of rotation of the Brahmaputra valley relative to the Indian subcontinent described by Vernant et al. (2014) must have begun earlier, in order to allow the shortening that led to exhumation in the SP at 9–15 Ma, but to have accelerated at ca. 5 Ma. Our results imply that the presence and rate of this rotation are controlled not only by far-field tectonic stresses and pre-existing lithospheric structure (such as the transition from continental to thinned continental or oceanic crust, which coincides with the location of the SP), but also by bending of the foreland lithosphere beneath the Himalaya.

CONCLUSIONS

We date the initiation of topographic growth of the Shillong Plateau to between 4.9 and 5.2 Ma. Rock uplift in the plateau was balanced by surface erosion between 9 and 15 Ma and 5.2–4.9 Ma, such that no topography was created. We link plateau uplift to accelerated displacement along the Dauki fault, caused by bending stresses resulting from northward underthrusting of the Indian plate beneath Tibet. By incorporating the full

range of available observations, we have pinpointed the transition from exhumation balanced by erosion to topographic growth, and suggest this previously unrecognized mechanism for the transition.

ACKNOWLEDGMENTS

This work was supported by the European Union Executive Agency For Research FP7 MC ITN "iTECC" (Investigating Tectonics Erosion Climate Couplings) grant 316966 and Natural Environment Research Council Isotope Geosciences Laboratory FSC grant IP-1500–1114. We thank six reviewers and editor J. Schmitt for comments. Gwladys Govin died while this paper was in review; final edits were carried out by the co-authors.

REFERENCES CITED

Biswas, S., Coutand, I., Grujic, D., Hager, C., Stockli, D., and Grasemann, B., 2007, Exhumation and uplift of the Shillong Plateau and its influence on the eastern Himalayas: New constraints from apatite and zircon (U-Th-[Sm])/He and apatite fission track analysis: Tectonics, v. 26, TC6013, https://doi.org/10.1029/2007TC002125.

Bracciali, L., Najman, Y., Parrish, R.R., Akhter, S.H., and Millar, I., 2015, The Brahmaputra tale of tectonics and erosion: Early Miocene river capture in the Eastern Himalaya: Earth and Planetary Science Letters, v. 415, p. 25–37, https://doi.org/10.1016/j.epsl.2015.01.022.

Bracciali, L., Parrish, R.R., Najman, Y., Smye, A., Carter, A., and Wijbrans, J.R., 2016, Plio-Pleistocene exhumation of the eastern Himalayan syntaxis and its domal 'pop-up': Earth-Science Reviews, v. 160, p. 350–385, https://doi.org/10.1016/j.earscirev.2016.07.010.

Chirouze, F., Huyghe, P., van der Beek, P., Chauvel, C., Chakraborty, T., Dupont-Nivet, G., and Bernet, M., 2013, Tectonics, exhumation, and drainage evolution of the eastern Himalaya since 13 Ma from detrital geochemistry and thermochronology, Kameng River Section, Arunachal Pradesh: Geological Society of America Bulletin, v. 125, p. 523–538, https://doi.org/10.1130/B30697.1.

Cina, S.E., Yin, A., Grove, M., Dubey, C.S., Shukla, D.P., Lovera, O.M., Kelty, T.K., Gehrels, G.E., and Foster, D.A., 2009, Gangdese arc detritus within the eastern Himalayan Neogene foreland basin: Implications for the Neogene evolution of the Yalu-Brahmaputra River system: Earth and Planetary Science Letters, v. 285, p. 150–162, https://doi.org/10.1016/j.epsl.2009.06.005.

Clark, M.K., and Bilham, R., 2008, Miocene rise of the Shillong Plateau and the beginning of the end for the Eastern Himalaya: Earth and Planetary Science Letters, v. 269, p. 337–351, https://doi.org/10.1016/j.epsl.2008.01.045.

Copley, A., Avouac, J.P., Hollingsworth, J., and Leprince, S., 2011, The 2001 Mw 7.6 Bhuj earthquake, low fault friction, and the crustal support of plate driving forces in India: Journal of Geophysical Research. Solid Earth, v. 116, B08405, 10.1029/2010JB008137.

Coutand, I., Barrier, L., Govin, G., Grujic, D., Hoorn, C., Dupont-Nivet, G., and Najman, Y., 2016, Late Miocene-Pleistocene evolution of India-Eurasia convergence partitioning between the Bhutan Himalaya and the Shillong Plateau: New evidences from foreland basin deposits along the Dungsam Chu section, eastern Bhutan: Tectonics, v. 35, p. 2963–2994, https://doi.org/10.1002/2016TC004258.

Coutand, I., Whipp, D.M., Grujic, D., Bernet, M., Fellin, M.G., Bookhagen, B., Landry, K.R., Ghalley, S.K., and Duncan, C., 2014, Geometry and kinematics of the Main Himalayan Thrust and Neogene crustal exhumation in the Bhutanese Himalaya derived from inversion of multithermochronologic data: Journal of Geophysical Research: Solid Earth, v. 119, p. 1446–1481, https://doi.org/10.1002/2013JB010891.

Craig, T.J., Copley, A., and Jackson, J., 2012, Thermal and tectonic consequences of India underthrusting Tibet: Earth and Planetary Science Letters, v. 353–354, p. 231–239, https://doi.org/10.1016/j.epsl.2012.07.010.

England, P.C., and Bilham, R., 2015, The Shillong Plateau and the great 1897 Assam Earthquake: Tectonics, v. 34, p. 1792–1812, https://doi.org/10.1002/2015TC003902.

Gehrels, G., Kapp, P., DeCelles, P., Pullen, A., Blakey, R., Weislogel, A., Ding, L., Guynn, J., Martin, A., and McQuarrie, N., 2011, Detrital zircon geochronology of pre-Tertiary strata in the Tibetan-Himalayan orogen: Tectonics, v. 30, TC5016, https://doi.org/10.1029/2011TC002868.

Govin, G., 2017, Tectonic-Erosion Interactions: Insights from the palaeo-drainage of the Brahmaputra River [Ph.D. thesis]: Lancaster, UK, Lancaster University, 331 p., https://doi.org/10.17635/lancaster/thesis/116.

Grujic, D., Coutand, I., Bookhagen, B., Bonnet, S., Blythe, A., and Duncan, C., 2006, Climatic forcing of erosion, landscape and tectonics in the Bhutan Himalayas: Geology, v. 34, p. 801–804, https://doi.org/10.1130/G22648.1.

Hu, X., Sinclair, H.D., Wang, J., Jiang, H., and Wu, F., 2012, Late Cretaceous-Palaeogene stratigraphic and basin evolution in the Zhepure Mountain of southern Tibet: Implications for the timing of India-Asia initial collision: Basin Research, v. 24, p. 520–543, https://doi.org/10.1111/j.1365-2117.2012.00543.x.

Johnson, S.Y., and Alam, A.M.N., 1991, Sedimentation and tectonics of the Sylhet trough, Bangladesh: Geological Society of America Bulletin, v. 103, p. 1513–1527, https://doi.org/10.1130/0016-7606(1991)103<1513:SATOTS>2.3.CO;2.

Jordan, T.E., and Allmendinger, R.W., 1986, The Sierras Pampeanas of Argentina—A modern analogue of Rocky-mountain foreland deformation: American Journal of Science, v. 286, p. 737–764, https://doi.org/10.2475/ajs.286.10.737.

Kober, M., Seib, N., Kley, J., and Voigt, T., 2013, Thick-skinned thrusting in the northern Tien Shan foreland, Kazakhstan: Structural inheritance and polyphase deformation: Geological Society of London Special Publications, v. 377, p. 19–42, https://doi.org/10.1144/SP377.7.

Lang, K.A., and Huntington, K.W., 2014, Antecedence of the Yarlung-Siang-Brahmaputra River, eastern Himalaya: Earth and Planetary Science Letters, v. 397, p. 145–158, https://doi.org/10.1016/j.epsl.2014.04.026.

Lang, K.A., Huntington, K.W., Burmester, R., and Housen, B., 2016, Rapid exhumation of the eastern Himalayan syntaxis since the Late Miocene: Geological Society of America Bulletin, v. 128, p. 1403–1422, https://doi.org/10.1130/B31419.1.

Long, S., McQuarrie, N., Tobgay, T., Grujic, D., and Hollister, L.S., 2011, Geological map of Bhutan: Journal of Maps, v. 7, p. 184–192, https://doi.org/10.4113/jom.2011.1159.

Marone, C., 1998, Laboratory-derived friction laws and their application to seismic faulting: Annual Review of Earth and Planetary Sciences, v. 26, p. 643–696, https://doi.org/10.1146/annurev.earth.26.1.643.

McQuarrie, N., Tobgay, T., Long, S., Reiners, P., and Cosca, M., 2014, Variable exhumation rates and variable displacement rates: Documenting recent slowing of Himalayan shortening in western Bhutan: Earth and Planetary Science Letters, v. 386, p. 161–174, https://doi.org/10.1016/j.epsl.2013.10.045.

Mitra, S., and Mitra, S., 2001, Tectonic setting of the Precambrian of the northeastern India (Meghalaya Plateau) and age of the Shillong Group of rocks: Geological Survey of India Special Publication, v. 64, p. 653–658.

Mitra, S., Priestley, K., Bhattacharyya, A.K., and Gaur, V., 2005, Crustal structure and earthquake focal depths beneath northeastern India and southern Tibet: Geophysical Journal International, v. 160, p. 227–248, https://doi.org/10.1111/j.1365-246X.2004.02470.x.

Najman, Y., Allen, R., Willett, E., Carter, A., Barfod, D., Garzanti, E., Wijbrans, J., Bickle, M., Vezzoli, G., and Ando, S., 2012, The record of Himalayan erosion preserved in the sedimentary rocks of the Hatia Trough of the Bengal Basin and the Chittagong Hill Tracts, Bangladesh: Basin Research, v. 24, p. 499–519, https://doi.org/10.1111/j.1365-2117.2011.00540.x.

Najman, Y., Bracciali, L., Parrish, R.R., Chisty, E., and Copley, A., 2016, Evolving strain partitioning in the Eastern Himalaya: The growth of the Shillong Plateau: Earth and Planetary Science Letters, v. 433, p. 1–9, https://doi.org/10.1016/j.epsl.2015.10.017.

Rosenkranz, R., Schildgen, T., Wittmann, H., and Spiegel, C., 2018, Coupling erosion and topographic development in the rainiest place on Earth: Reconstructing the Shillong Plateau uplift history with in-situ cosmogenic ^{10}Be: Earth and Planetary Science Letters, v. 483, p. 39–51, https://doi.org/10.1016/j.epsl.2017.11.047.

Seeber, L., and Armbruster, J.G., 1981, Great detachment earthquakes along the Himalayan Arc and long-term forecasting, *in* Simpson, D.W., and Richards, P.G., eds., Earthquake Prediction: An International Review: American Geophysical Union, Maurice Ewing Series, v. 4, p. 259–277, https://doi.org/10.1029/ME004p0259.

Singh, A., Bhushan, K., Singh, C., Steckler, M.S., Akhter, S.H., Seeber, L., Kim, W.Y., Tiwari, A.K., and Biswas, R., 2016, Crustal structure and tectonics of Bangladesh: New constraints from inversion of receiver functions: Tectonophysics, v. 680, p. 99–112, https://doi.org/10.1016/j.tecto.2016.04.046.

Uddin, A., and Lundberg, N., 1999, A paleo-Brahmaputra? Subsurface lithofacies analysis of Miocene deltaic sediments in the Himalayan–Bengal system, Bangladesh: Sedimentary Geology, v. 123, p. 239–254, https://doi.org/10.1016/S0037-0738(98)00134-1.

Vermeesch, P., 2012, On the visualisation of detrital age distributions: Chemical Geology, v. 312–313, p. 190–194, https://doi.org/10.1016/j.chemgeo.2012.04.021.

Vernant, P., Bilham, R., Szeliga, W., Drupka, D., Kalita, S., Bhattacharyya, A., Gaur, V., Pelgay, P., Cattin, R., and Berthet, T., 2014, Clockwise rotation of the Brahmaputra Valley relative to India: Tectonic convergence in the eastern Himalaya, Naga Hills, and Shillong Plateau: Journal of Geophysical Research: Solid Earth, v. 119, p. 6558–6571, https://doi.org/10.1002/2014JB011196.

Zoback, M.D., and Townend, J., 2001, Implications of hydrostatic pore pressures and high crustal strength for the deformation of intraplate lithosphere: Tectonophysics, v. 336, p. 19–30, https://doi.org/10.1016/S0040-1951(01)00091-9.

Manuscript received 3 November 2017
Revised manuscript received 23 December 2017
Manuscript accepted 27 December 2017

Printed in USA

GSA Data Repository 2018078

Govin et al., 2018, Timing and mechanism of the rise of the Shillong Plateau in the Himalayan foreland: Geology, https://doi.org/10.1130/G39864.1.

Analytical and stress calculation methods and supplementary figures

Table DR1: sample locations

Table DR2: zircon U-Pb ages from source-areas compilation

Tables DR3 and DR4: zircon U-Pb ion probe data and standard

Tables DR5 and DR6: zircon U-Pb laser ablation data and standard

Table DR7: rutile U-Pb laser ablation data and standard

TABLE DR1a: LOCATIONS OF SAMPLES FROM DUNGSANG CHU SECTION (Coutand et al 2016)

Sample no	Depositional age (Ma)	Strat height (m) up section	Latitude (°N)	Longitude (°E)
SJ12	1.75±0.05	2136	26.83164	91.48105
SJ9	4.70±0.05	1610	26.82300	91.48179
SJ8	4.85±0.05	1394	26.82036	91.48350
SJ7	5.20±0.05	1205	26.81966	91.48624
SJ6b	5.45±0.10	1047	26.81930	91.48952
SJ4	6.35±0.05	620	26.81198	91.49379
SJ2	7.05±0.05	74	26.80851	91.50233
SJ1b	>7.10±n/a	-150	26.80052	91.50239

TABLE DR1b: SOURCE AREA COMPILATION U-Pb ZIRCON

Source area	Age (Ma)	Error ± 1σ	Reference
Southern Lhasa	183	2	Chu et al., 2006
Southern Lhasa	185	3	Chu et al., 2006
Southern Lhasa	193	3	Chu et al., 2006
Southern Lhasa	181	3	Chu et al., 2006
Southern Lhasa	187	3	Chu et al., 2006
Southern Lhasa	190	3	Chu et al., 2006
Southern Lhasa	195	3	Chu et al., 2006
Southern Lhasa	191	3	Chu et al., 2006
Southern Lhasa	188	3	Chu et al., 2006
Southern Lhasa	187	3	Chu et al., 2006
Southern Lhasa	190	3	Chu et al., 2006
Southern Lhasa	194	4	Chu et al., 2006
Southern Lhasa	181	4	Chu et al., 2006
Southern Lhasa	188	4	Chu et al., 2006
Southern Lhasa	197	4	Chu et al., 2006
Southern Lhasa	199	4	Chu et al., 2006
Southern Lhasa	191	4	Chu et al., 2006
Southern Lhasa	191	4	Chu et al., 2006
Southern Lhasa	189	5	Chu et al., 2006
Southern Lhasa	195	6	Chu et al., 2006
Southern Lhasa	52	1	Ji et al., 2009
Southern Lhasa	49	1	Ji et al., 2009
Southern Lhasa	45	1	Ji et al., 2009
Southern Lhasa	46	1	Ji et al., 2009
Southern Lhasa	51	1	Ji et al., 2009
Southern Lhasa	49	1	Ji et al., 2009
Southern Lhasa	50	1	Ji et al., 2009
Southern Lhasa	50	1	Ji et al., 2009
Southern Lhasa	62	1	Ji et al., 2009
Southern Lhasa	63	1	Ji et al., 2009
Southern Lhasa	64	1	Ji et al., 2009
Southern Lhasa	62	1	Ji et al., 2009
Southern Lhasa	62	1	Ji et al., 2009
Southern Lhasa	64	1	Ji et al., 2009
Southern Lhasa	64	1	Ji et al., 2009
Southern Lhasa	65	1	Ji et al., 2009
Southern Lhasa	54	1	Ji et al., 2009
Southern Lhasa	53	1	Ji et al., 2009
Southern Lhasa	58	1	Ji et al., 2009
Southern Lhasa	55	1	Ji et al., 2009
Southern Lhasa	53	1	Ji et al., 2009
Southern Lhasa	52	1	Ji et al., 2009
Southern Lhasa	58	1	Ji et al., 2009
Southern Lhasa	58	1	Ji et al., 2009
Southern Lhasa	56	1	Ji et al., 2009
Southern Lhasa	57	1	Ji et al., 2009
Southern Lhasa	55	1	Ji et al., 2009
Southern Lhasa	56	1	Ji et al., 2009
Southern Lhasa	56	1	Ji et al., 2009
Southern Lhasa	57	1	Ji et al., 2009
Southern Lhasa	58	1	Ji et al., 2009

Southern Lhasa	55	1	Ji et al., 2009
Southern Lhasa	58	1	Ji et al., 2009
Southern Lhasa	53	1	Ji et al., 2009
Southern Lhasa	47	1	Ji et al., 2009
Southern Lhasa	51	1	Ji et al., 2009
Southern Lhasa	50	1	Ji et al., 2009
Southern Lhasa	50	1	Ji et al., 2009
Southern Lhasa	51	1	Ji et al., 2009
Southern Lhasa	52	1	Ji et al., 2009
Southern Lhasa	51	1	Ji et al., 2009
Southern Lhasa	51	1	Ji et al., 2009
Southern Lhasa	57	1	Ji et al., 2009
Southern Lhasa	51	1	Ji et al., 2009
Southern Lhasa	53	1	Ji et al., 2009
Southern Lhasa	53	1	Ji et al., 2009
Southern Lhasa	53	1	Ji et al., 2009
Southern Lhasa	55	1	Ji et al., 2009
Southern Lhasa	53	1	Ji et al., 2009
Southern Lhasa	50	1	Ji et al., 2009
Southern Lhasa	50	1	Ji et al., 2009
Southern Lhasa	48	1	Ji et al., 2009
Southern Lhasa	49	1	Ji et al., 2009
Southern Lhasa	51	1	Ji et al., 2009
Southern Lhasa	53	1	Ji et al., 2009
Southern Lhasa	52	1	Ji et al., 2009
Southern Lhasa	52	1	Ji et al., 2009
Southern Lhasa	52	1	Ji et al., 2009
Southern Lhasa	50	1	Ji et al., 2009
Southern Lhasa	52	1	Ji et al., 2009
Southern Lhasa	49	1	Ji et al., 2009
Southern Lhasa	54	1	Ji et al., 2009
Southern Lhasa	52	1	Ji et al., 2009
Southern Lhasa	51	1	Ji et al., 2009
Southern Lhasa	52	1	Ji et al., 2009
Southern Lhasa	51	1	Ji et al., 2009
Southern Lhasa	50	1	Ji et al., 2009
Southern Lhasa	50	1	Ji et al., 2009
Southern Lhasa	52	1	Ji et al., 2009
Southern Lhasa	53	1	Ji et al., 2009
Southern Lhasa	52	1	Ji et al., 2009
Southern Lhasa	52	1	Ji et al., 2009
Southern Lhasa	50	1	Ji et al., 2009
Southern Lhasa	50	1	Ji et al., 2009
Southern Lhasa	52	1	Ji et al., 2009
Southern Lhasa	49	1	Ji et al., 2009
Southern Lhasa	50	1	Ji et al., 2009
Southern Lhasa	50	1	Ji et al., 2009
Southern Lhasa	52	1	Ji et al., 2009
Southern Lhasa	53	1	Ji et al., 2009
Southern Lhasa	53	1	Ji et al., 2009
Southern Lhasa	48	1	Ji et al., 2009
Southern Lhasa	51	1	Ji et al., 2009
Southern Lhasa	53	1	Ji et al., 2009
Southern Lhasa	50	1	Ji et al., 2009
Southern Lhasa	52	1	Ji et al., 2009
Southern Lhasa	50	1	Ji et al., 2009
Southern Lhasa	48	1	Ji et al., 2009
Southern Lhasa	52	1	Ji et al., 2009
Southern Lhasa	50	1	Ji et al., 2009
Southern Lhasa	50	1	Ji et al., 2009
Southern Lhasa	49	1	Ji et al., 2009
Southern Lhasa	51	1	Ji et al., 2009
Southern Lhasa	49	1	Ji et al., 2009
Southern Lhasa	51	1	Ji et al., 2009
Southern Lhasa	51	1	Ji et al., 2009
Southern Lhasa	49	1	Ji et al., 2009
Southern Lhasa	50	1	Ji et al., 2009
Southern Lhasa	51	1	Ji et al., 2009
Southern Lhasa	50	1	Ji et al., 2009
Southern Lhasa	51	1	Ji et al., 2009
Southern Lhasa	46	1	Ji et al., 2009

Southern Lhasa	50	1	Ji et al., 2009
Southern Lhasa	51	1	Ji et al., 2009
Southern Lhasa	52	1	Ji et al., 2009
Southern Lhasa	52	1	Ji et al., 2009
Southern Lhasa	45	1	Ji et al., 2009
Southern Lhasa	50	1	Ji et al., 2009
Southern Lhasa	50	1	Ji et al., 2009
Southern Lhasa	50	1	Ji et al., 2009
Southern Lhasa	54	1	Ji et al., 2009
Southern Lhasa	45	1	Ji et al., 2009
Southern Lhasa	46	1	Ji et al., 2009
Southern Lhasa	52	1	Ji et al., 2009
Southern Lhasa	50	1	Ji et al., 2009
Southern Lhasa	48	1	Ji et al., 2009
Southern Lhasa	49	1	Ji et al., 2009
Southern Lhasa	50	1	Ji et al., 2009
Southern Lhasa	49	1	Ji et al., 2009
Southern Lhasa	48	1	Ji et al., 2009
Southern Lhasa	49	1	Ji et al., 2009
Southern Lhasa	49	1	Ji et al., 2009
Southern Lhasa	48	1	Ji et al., 2009
Southern Lhasa	51	1	Ji et al., 2009
Southern Lhasa	50	1	Ji et al., 2009
Southern Lhasa	50	1	Ji et al., 2009
Southern Lhasa	48	1	Ji et al., 2009
Southern Lhasa	50	1	Ji et al., 2009
Southern Lhasa	52	1	Ji et al., 2009
Southern Lhasa	50	1	Ji et al., 2009
Southern Lhasa	51	1	Ji et al., 2009
Southern Lhasa	49	1	Ji et al., 2009
Southern Lhasa	50	1	Ji et al., 2009
Southern Lhasa	53	1	Ji et al., 2009
Southern Lhasa	52	1	Ji et al., 2009
Southern Lhasa	47	1	Ji et al., 2009
Southern Lhasa	51	1	Ji et al., 2009
Southern Lhasa	48	1	Ji et al., 2009
Southern Lhasa	52	1	Ji et al., 2009
Southern Lhasa	48	1	Ji et al., 2009
Southern Lhasa	48	1	Ji et al., 2009
Southern Lhasa	51	1	Ji et al., 2009
Southern Lhasa	52	1	Ji et al., 2009
Southern Lhasa	48	1	Ji et al., 2009
Southern Lhasa	55	1	Ji et al., 2009
Southern Lhasa	53	1	Ji et al., 2009
Southern Lhasa	54	1	Ji et al., 2009
Southern Lhasa	53	1	Ji et al., 2009
Southern Lhasa	53	1	Ji et al., 2009
Southern Lhasa	54	1	Ji et al., 2009
Southern Lhasa	54	1	Ji et al., 2009
Southern Lhasa	52	1	Ji et al., 2009
Southern Lhasa	51	1	Ji et al., 2009
Southern Lhasa	52	1	Ji et al., 2009
Southern Lhasa	43	1	Ji et al., 2009
Southern Lhasa	43	1	Ji et al., 2009
Southern Lhasa	46	1	Ji et al., 2009
Southern Lhasa	45	1	Ji et al., 2009
Southern Lhasa	48	1	Ji et al., 2009
Southern Lhasa	50	1	Ji et al., 2009
Southern Lhasa	42	1	Ji et al., 2009
Southern Lhasa	40	1	Ji et al., 2009
Southern Lhasa	40	1	Ji et al., 2009
Southern Lhasa	43	1	Ji et al., 2009
Southern Lhasa	43	1	Ji et al., 2009
Southern Lhasa	43	1	Ji et al., 2009
Southern Lhasa	43	1	Ji et al., 2009
Southern Lhasa	40	1	Ji et al., 2009
Southern Lhasa	43	1	Ji et al., 2009
Southern Lhasa	42	1	Ji et al., 2009
Southern Lhasa	43	1	Ji et al., 2009
Southern Lhasa	41	1	Ji et al., 2009
Southern Lhasa	41	1	Ji et al., 2009

Southern Lhasa	43	1	Ji et al., 2009
Southern Lhasa	43	1	Ji et al., 2009
Southern Lhasa	41	1	Ji et al., 2009
Southern Lhasa	43	1	Ji et al., 2009
Southern Lhasa	41	1	Ji et al., 2009
Southern Lhasa	42	1	Ji et al., 2009
Southern Lhasa	42	1	Ji et al., 2009
Southern Lhasa	43	1	Ji et al., 2009
Southern Lhasa	39	1	Ji et al., 2009
Southern Lhasa	41	1	Ji et al., 2009
Southern Lhasa	40	1	Ji et al., 2009
Southern Lhasa	41	1	Ji et al., 2009
Southern Lhasa	43	1	Ji et al., 2009
Southern Lhasa	41	1	Ji et al., 2009
Southern Lhasa	42	1	Ji et al., 2009
Southern Lhasa	43	1	Ji et al., 2009
Southern Lhasa	44	1	Ji et al., 2009
Southern Lhasa	40	1	Ji et al., 2009
Southern Lhasa	41	1	Ji et al., 2009
Southern Lhasa	42	1	Ji et al., 2009
Southern Lhasa	41	1	Ji et al., 2009
Southern Lhasa	40	1	Ji et al., 2009
Southern Lhasa	43	1	Ji et al., 2009
Southern Lhasa	41	1	Ji et al., 2009
Southern Lhasa	42	1	Ji et al., 2009
Southern Lhasa	47	1	Ji et al., 2009
Southern Lhasa	44	1	Ji et al., 2009
Southern Lhasa	43	1	Ji et al., 2009
Southern Lhasa	42	1	Ji et al., 2009
Southern Lhasa	43	1	Ji et al., 2009
Southern Lhasa	42	1	Ji et al., 2009
Southern Lhasa	52	1	Ji et al., 2009
Southern Lhasa	52	1	Ji et al., 2009
Southern Lhasa	53	1	Ji et al., 2009
Southern Lhasa	50	1	Ji et al., 2009
Southern Lhasa	53	1	Ji et al., 2009
Southern Lhasa	51	1	Ji et al., 2009
Southern Lhasa	50	1	Ji et al., 2009
Southern Lhasa	52	1	Ji et al., 2009
Southern Lhasa	50	1	Ji et al., 2009
Southern Lhasa	51	1	Ji et al., 2009
Southern Lhasa	51	1	Ji et al., 2009
Southern Lhasa	55	1	Ji et al., 2009
Southern Lhasa	51	1	Ji et al., 2009
Southern Lhasa	49	1	Ji et al., 2009
Southern Lhasa	51	1	Ji et al., 2009
Southern Lhasa	49	1	Ji et al., 2009
Southern Lhasa	51	1	Ji et al., 2009
Southern Lhasa	52	1	Ji et al., 2009
Southern Lhasa	52	1	Ji et al., 2009
Southern Lhasa	53	1	Ji et al., 2009
Southern Lhasa	52	1	Ji et al., 2009
Southern Lhasa	53	1	Ji et al., 2009
Southern Lhasa	54	1	Ji et al., 2009
Southern Lhasa	55	1	Ji et al., 2009
Southern Lhasa	54	1	Ji et al., 2009
Southern Lhasa	54	1	Ji et al., 2009
Southern Lhasa	54	1	Ji et al., 2009
Southern Lhasa	57	1	Ji et al., 2009
Southern Lhasa	47	1	Ji et al., 2009
Southern Lhasa	48	1	Ji et al., 2009
Southern Lhasa	46	1	Ji et al., 2009
Southern Lhasa	47	1	Ji et al., 2009
Southern Lhasa	48	1	Ji et al., 2009
Southern Lhasa	50	1	Ji et al., 2009
Southern Lhasa	50	1	Ji et al., 2009
Southern Lhasa	49	1	Ji et al., 2009
Southern Lhasa	48	1	Ji et al., 2009
Southern Lhasa	52	1	Ji et al., 2009
Southern Lhasa	51	1	Ji et al., 2009
Southern Lhasa	52	1	Ji et al., 2009

Southern Lhasa	49	1	Ji et al., 2009
Southern Lhasa	50	1	Ji et al., 2009
Southern Lhasa	52	1	Ji et al., 2009
Southern Lhasa	53	1	Ji et al., 2009
Southern Lhasa	49	1	Ji et al., 2009
Southern Lhasa	52	1	Ji et al., 2009
Southern Lhasa	49	1	Ji et al., 2009
Southern Lhasa	54	1	Ji et al., 2009
Southern Lhasa	67	2	Ji et al., 2009
Southern Lhasa	63	2	Ji et al., 2009
Southern Lhasa	68	2	Ji et al., 2009
Southern Lhasa	66	2	Ji et al., 2009
Southern Lhasa	66	2	Ji et al., 2009
Southern Lhasa	67	2	Ji et al., 2009
Southern Lhasa	62	2	Ji et al., 2009
Southern Lhasa	64	2	Ji et al., 2009
Southern Lhasa	67	2	Ji et al., 2009
Southern Lhasa	67	2	Ji et al., 2009
Southern Lhasa	69	2	Ji et al., 2009
Southern Lhasa	68	2	Ji et al., 2009
Southern Lhasa	63	2	Ji et al., 2009
Southern Lhasa	65	2	Ji et al., 2009
Southern Lhasa	67	2	Ji et al., 2009
Southern Lhasa	65	2	Ji et al., 2009
Southern Lhasa	68	2	Ji et al., 2009
Southern Lhasa	63	2	Ji et al., 2009
Southern Lhasa	68	2	Ji et al., 2009
Southern Lhasa	67	2	Ji et al., 2009
Southern Lhasa	66	2	Ji et al., 2009
Southern Lhasa	65	2	Ji et al., 2009
Southern Lhasa	67	2	Ji et al., 2009
Southern Lhasa	64	2	Ji et al., 2009
Southern Lhasa	66	2	Ji et al., 2009
Southern Lhasa	66	2	Ji et al., 2009
Southern Lhasa	66	2	Ji et al., 2009
Southern Lhasa	67	2	Ji et al., 2009
Southern Lhasa	55	2	Ji et al., 2009
Southern Lhasa	59	2	Ji et al., 2009
Southern Lhasa	52	2	Ji et al., 2009
Southern Lhasa	62	2	Ji et al., 2009
Southern Lhasa	57	2	Ji et al., 2009
Southern Lhasa	62	2	Ji et al., 2009
Southern Lhasa	60	2	Ji et al., 2009
Southern Lhasa	58	2	Ji et al., 2009
Southern Lhasa	50	2	Ji et al., 2009
Southern Lhasa	57	2	Ji et al., 2009
Southern Lhasa	56	2	Ji et al., 2009
Southern Lhasa	59	2	Ji et al., 2009
Southern Lhasa	58	2	Ji et al., 2009
Southern Lhasa	57	2	Ji et al., 2009
Southern Lhasa	55	2	Ji et al., 2009
Southern Lhasa	55	2	Ji et al., 2009
Southern Lhasa	60	2	Ji et al., 2009
Southern Lhasa	54	2	Ji et al., 2009
Southern Lhasa	56	2	Ji et al., 2009
Southern Lhasa	54	2	Ji et al., 2009
Southern Lhasa	53	2	Ji et al., 2009
Southern Lhasa	55	2	Ji et al., 2009
Southern Lhasa	56	2	Ji et al., 2009
Southern Lhasa	57	2	Ji et al., 2009
Southern Lhasa	65	2	Ji et al., 2009
Southern Lhasa	53	2	Ji et al., 2009
Southern Lhasa	57	2	Ji et al., 2009
Southern Lhasa	54	2	Ji et al., 2009
Southern Lhasa	53	2	Ji et al., 2009
Southern Lhasa	54	2	Ji et al., 2009
Southern Lhasa	54	2	Ji et al., 2009
Southern Lhasa	56	2	Ji et al., 2009
Southern Lhasa	54	2	Ji et al., 2009
Southern Lhasa	53	2	Ji et al., 2009
Southern Lhasa	52	2	Ji et al., 2009

Southern Lhasa	52	2	Ji et al., 2009
Southern Lhasa	53	2	Ji et al., 2009
Southern Lhasa	53	2	Ji et al., 2009
Southern Lhasa	49	2	Ji et al., 2009
Southern Lhasa	53	2	Ji et al., 2009
Southern Lhasa	51	2	Ji et al., 2009
Southern Lhasa	49	2	Ji et al., 2009
Southern Lhasa	50	2	Ji et al., 2009
Southern Lhasa	50	2	Ji et al., 2009
Southern Lhasa	51	2	Ji et al., 2009
Southern Lhasa	58	2	Ji et al., 2009
Southern Lhasa	53	2	Ji et al., 2009
Southern Lhasa	54	2	Ji et al., 2009
Southern Lhasa	52	2	Ji et al., 2009
Southern Lhasa	55	2	Ji et al., 2009
Southern Lhasa	56	2	Ji et al., 2009
Southern Lhasa	53	2	Ji et al., 2009
Southern Lhasa	52	2	Ji et al., 2009
Southern Lhasa	56	2	Ji et al., 2009
Southern Lhasa	53	2	Ji et al., 2009
Southern Lhasa	50	2	Ji et al., 2009
Southern Lhasa	51	2	Ji et al., 2009
Southern Lhasa	50	2	Ji et al., 2009
Southern Lhasa	53	2	Ji et al., 2009
Southern Lhasa	53	2	Ji et al., 2009
Southern Lhasa	51	2	Ji et al., 2009
Southern Lhasa	51	2	Ji et al., 2009
Southern Lhasa	53	2	Ji et al., 2009
Southern Lhasa	53	2	Ji et al., 2009
Southern Lhasa	52	2	Ji et al., 2009
Southern Lhasa	51	2	Ji et al., 2009
Southern Lhasa	53	2	Ji et al., 2009
Southern Lhasa	52	2	Ji et al., 2009
Southern Lhasa	52	2	Ji et al., 2009
Southern Lhasa	54	2	Ji et al., 2009
Southern Lhasa	58	2	Ji et al., 2009
Southern Lhasa	54	2	Ji et al., 2009
Southern Lhasa	55	2	Ji et al., 2009
Southern Lhasa	53	2	Ji et al., 2009
Southern Lhasa	54	2	Ji et al., 2009
Southern Lhasa	57	2	Ji et al., 2009
Southern Lhasa	57	2	Ji et al., 2009
Southern Lhasa	56	2	Ji et al., 2009
Southern Lhasa	56	2	Ji et al., 2009
Southern Lhasa	52	2	Ji et al., 2009
Southern Lhasa	56	2	Ji et al., 2009
Southern Lhasa	54	2	Ji et al., 2009
Southern Lhasa	57	2	Ji et al., 2009
Southern Lhasa	57	2	Ji et al., 2009
Southern Lhasa	59	2	Ji et al., 2009
Southern Lhasa	58	2	Ji et al., 2009
Southern Lhasa	50	2	Ji et al., 2009
Southern Lhasa	48	2	Ji et al., 2009
Southern Lhasa	53	2	Ji et al., 2009
Southern Lhasa	49	2	Ji et al., 2009
Southern Lhasa	49	2	Ji et al., 2009
Southern Lhasa	52	2	Ji et al., 2009
Southern Lhasa	52	2	Ji et al., 2009
Southern Lhasa	49	2	Ji et al., 2009
Southern Lhasa	54	2	Ji et al., 2009
Southern Lhasa	53	2	Ji et al., 2009
Southern Lhasa	54	2	Ji et al., 2009
Southern Lhasa	48	2	Ji et al., 2009
Southern Lhasa	50	2	Ji et al., 2009
Southern Lhasa	54	2	Ji et al., 2009
Southern Lhasa	61	2	Ji et al., 2009
Southern Lhasa	46	2	Ji et al., 2009
Southern Lhasa	45	2	Ji et al., 2009
Southern Lhasa	45	2	Ji et al., 2009
Southern Lhasa	42	2	Ji et al., 2009
Southern Lhasa	43	2	Ji et al., 2009

Southern Lhasa	45	2	Ji et al., 2009
Southern Lhasa	46	2	Ji et al., 2009
Southern Lhasa	45	2	Ji et al., 2009
Southern Lhasa	46	2	Ji et al., 2009
Southern Lhasa	44	2	Ji et al., 2009
Southern Lhasa	48	2	Ji et al., 2009
Southern Lhasa	44	2	Ji et al., 2009
Southern Lhasa	43	2	Ji et al., 2009
Southern Lhasa	41	2	Ji et al., 2009
Southern Lhasa	46	2	Ji et al., 2009
Southern Lhasa	44	2	Ji et al., 2009
Southern Lhasa	44	2	Ji et al., 2009
Southern Lhasa	49	2	Ji et al., 2009
Southern Lhasa	46	2	Ji et al., 2009
Southern Lhasa	46	2	Ji et al., 2009
Southern Lhasa	45	2	Ji et al., 2009
Southern Lhasa	45	2	Ji et al., 2009
Southern Lhasa	45	2	Ji et al., 2009
Southern Lhasa	47	2	Ji et al., 2009
Southern Lhasa	46	2	Ji et al., 2009
Southern Lhasa	49	2	Ji et al., 2009
Southern Lhasa	45	2	Ji et al., 2009
Southern Lhasa	51	2	Ji et al., 2009
Southern Lhasa	48	2	Ji et al., 2009
Southern Lhasa	49	2	Ji et al., 2009
Southern Lhasa	43	2	Ji et al., 2009
Southern Lhasa	47	2	Ji et al., 2009
Southern Lhasa	51	2	Ji et al., 2009
Southern Lhasa	47	2	Ji et al., 2009
Southern Lhasa	45	2	Ji et al., 2009
Southern Lhasa	43	2	Ji et al., 2009
Southern Lhasa	42	2	Ji et al., 2009
Southern Lhasa	45	2	Ji et al., 2009
Southern Lhasa	44	2	Ji et al., 2009
Southern Lhasa	43	2	Ji et al., 2009
Southern Lhasa	53	2	Ji et al., 2009
Southern Lhasa	54	2	Ji et al., 2009
Southern Lhasa	57	2	Ji et al., 2009
Southern Lhasa	55	2	Ji et al., 2009
Southern Lhasa	54	2	Ji et al., 2009
Southern Lhasa	62	2	Ji et al., 2009
Southern Lhasa	57	2	Ji et al., 2009
Southern Lhasa	60	2	Ji et al., 2009
Southern Lhasa	53	2	Ji et al., 2009
Southern Lhasa	49	2	Ji et al., 2009
Southern Lhasa	50	2	Ji et al., 2009
Southern Lhasa	50	2	Ji et al., 2009
Southern Lhasa	51	2	Ji et al., 2009
Southern Lhasa	51	2	Ji et al., 2009
Southern Lhasa	53	2	Ji et al., 2009
Southern Lhasa	51	2	Ji et al., 2009
Southern Lhasa	52	2	Ji et al., 2009
Southern Lhasa	52	2	Ji et al., 2009
Southern Lhasa	53	2	Ji et al., 2009
Southern Lhasa	51	2	Ji et al., 2009
Southern Lhasa	50	2	Ji et al., 2009
Southern Lhasa	53	2	Ji et al., 2009
Southern Lhasa	52	2	Ji et al., 2009
Southern Lhasa	50	2	Ji et al., 2009
Southern Lhasa	51	2	Ji et al., 2009
Southern Lhasa	58	2	Ji et al., 2009
Southern Lhasa	61	2	Ji et al., 2009
Southern Lhasa	54	2	Ji et al., 2009
Southern Lhasa	54	2	Ji et al., 2009
Southern Lhasa	59	2	Ji et al., 2009
Southern Lhasa	56	2	Ji et al., 2009
Southern Lhasa	56	2	Ji et al., 2009
Southern Lhasa	55	2	Ji et al., 2009
Southern Lhasa	54	2	Ji et al., 2009
Southern Lhasa	58	2	Ji et al., 2009
Southern Lhasa	55	2	Ji et al., 2009

Southern Lhasa	51	2	Ji et al., 2009
Southern Lhasa	52	2	Ji et al., 2009
Southern Lhasa	55	2	Ji et al., 2009
Southern Lhasa	53	2	Ji et al., 2009
Southern Lhasa	56	2	Ji et al., 2009
Southern Lhasa	56	2	Ji et al., 2009
Southern Lhasa	56	2	Ji et al., 2009
Southern Lhasa	55	2	Ji et al., 2009
Southern Lhasa	59	2	Ji et al., 2009
Southern Lhasa	57	2	Ji et al., 2009
Southern Lhasa	55	2	Ji et al., 2009
Southern Lhasa	56	2	Ji et al., 2009
Southern Lhasa	56	2	Ji et al., 2009
Southern Lhasa	57	2	Ji et al., 2009
Southern Lhasa	59	2	Ji et al., 2009
Southern Lhasa	58	2	Ji et al., 2009
Southern Lhasa	59	2	Ji et al., 2009
Southern Lhasa	56	2	Ji et al., 2009
Southern Lhasa	60	2	Ji et al., 2009
Southern Lhasa	61	2	Ji et al., 2009
Southern Lhasa	58	2	Ji et al., 2009
Southern Lhasa	57	2	Ji et al., 2009
Southern Lhasa	57	2	Ji et al., 2009
Southern Lhasa	58	2	Ji et al., 2009
Southern Lhasa	50	2	Ji et al., 2009
Southern Lhasa	60	2	Ji et al., 2009
Southern Lhasa	57	2	Ji et al., 2009
Southern Lhasa	60	2	Ji et al., 2009
Southern Lhasa	61	2	Ji et al., 2009
Southern Lhasa	50	2	Ji et al., 2009
Southern Lhasa	51	2	Ji et al., 2009
Southern Lhasa	52	2	Ji et al., 2009
Southern Lhasa	51	2	Ji et al., 2009
Southern Lhasa	52	2	Ji et al., 2009
Southern Lhasa	58	2	Ji et al., 2009
Southern Lhasa	56	2	Ji et al., 2009
Southern Lhasa	65	2	Ji et al., 2009
Southern Lhasa	64	2	Ji et al., 2009
Southern Lhasa	63	2	Ji et al., 2009
Southern Lhasa	63	2	Ji et al., 2009
Southern Lhasa	61	2	Ji et al., 2009
Southern Lhasa	57	2	Ji et al., 2009
Southern Lhasa	60	2	Ji et al., 2009
Southern Lhasa	60	2	Ji et al., 2009
Southern Lhasa	63	2	Ji et al., 2009
Southern Lhasa	61	2	Ji et al., 2009
Southern Lhasa	60	2	Ji et al., 2009
Southern Lhasa	60	2	Ji et al., 2009
Southern Lhasa	66	2	Ji et al., 2009
Southern Lhasa	61	2	Ji et al., 2009
Southern Lhasa	62	2	Ji et al., 2009
Southern Lhasa	61	2	Ji et al., 2009
Southern Lhasa	59	2	Ji et al., 2009
Southern Lhasa	61	2	Ji et al., 2009
Southern Lhasa	59	2	Ji et al., 2009
Southern Lhasa	57	2	Ji et al., 2009
Southern Lhasa	57	2	Ji et al., 2009
Southern Lhasa	57	2	Ji et al., 2009
Southern Lhasa	56	2	Ji et al., 2009
Southern Lhasa	55	2	Ji et al., 2009
Southern Lhasa	56	2	Ji et al., 2009
Southern Lhasa	56	2	Ji et al., 2009
Southern Lhasa	55	2	Ji et al., 2009
Southern Lhasa	58	2	Ji et al., 2009
Southern Lhasa	56	2	Ji et al., 2009
Southern Lhasa	55	2	Ji et al., 2009
Southern Lhasa	59	2	Ji et al., 2009
Southern Lhasa	49	2	Ji et al., 2009
Southern Lhasa	50	2	Ji et al., 2009
Southern Lhasa	48	2	Ji et al., 2009
Southern Lhasa	46	2	Ji et al., 2009

Southern Lhasa	52	2	Ji et al., 2009
Southern Lhasa	47	2	Ji et al., 2009
Southern Lhasa	48	2	Ji et al., 2009
Southern Lhasa	48	2	Ji et al., 2009
Southern Lhasa	52	2	Ji et al., 2009
Southern Lhasa	50	2	Ji et al., 2009
Southern Lhasa	49	2	Ji et al., 2009
Southern Lhasa	46	2	Ji et al., 2009
Southern Lhasa	56	2	Ji et al., 2009
Southern Lhasa	53	2	Ji et al., 2009
Southern Lhasa	50	2	Ji et al., 2009
Southern Lhasa	55	2	Ji et al., 2009
Southern Lhasa	53	2	Ji et al., 2009
Southern Lhasa	53	2	Ji et al., 2009
Southern Lhasa	54	2	Ji et al., 2009
Southern Lhasa	51	2	Ji et al., 2009
Southern Lhasa	56	2	Ji et al., 2009
Southern Lhasa	54	2	Ji et al., 2009
Southern Lhasa	54	2	Ji et al., 2009
Southern Lhasa	50	2	Ji et al., 2009
Southern Lhasa	51	2	Ji et al., 2009
Southern Lhasa	55	2	Ji et al., 2009
Southern Lhasa	55	2	Ji et al., 2009
Southern Lhasa	53	2	Ji et al., 2009
Southern Lhasa	54	2	Ji et al., 2009
Southern Lhasa	91	2	Ji et al., 2009
Southern Lhasa	90	2	Ji et al., 2009
Southern Lhasa	85	2	Ji et al., 2009
Southern Lhasa	85	2	Ji et al., 2009
Southern Lhasa	88	2	Ji et al., 2009
Southern Lhasa	87	2	Ji et al., 2009
Southern Lhasa	87	2	Ji et al., 2009
Southern Lhasa	90	2	Ji et al., 2009
Southern Lhasa	83	2	Ji et al., 2009
Southern Lhasa	82	2	Ji et al., 2009
Southern Lhasa	82	2	Ji et al., 2009
Southern Lhasa	89	2	Ji et al., 2009
Southern Lhasa	90	2	Ji et al., 2009
Southern Lhasa	155	2	Ji et al., 2009
Southern Lhasa	156	2	Ji et al., 2009
Southern Lhasa	159	2	Ji et al., 2009
Southern Lhasa	154	2	Ji et al., 2009
Southern Lhasa	150	2	Ji et al., 2009
Southern Lhasa	150	2	Ji et al., 2009
Southern Lhasa	151	2	Ji et al., 2009
Southern Lhasa	69	3	Ji et al., 2009
Southern Lhasa	64	3	Ji et al., 2009
Southern Lhasa	53	3	Ji et al., 2009
Southern Lhasa	56	3	Ji et al., 2009
Southern Lhasa	52	3	Ji et al., 2009
Southern Lhasa	46	3	Ji et al., 2009
Southern Lhasa	43	3	Ji et al., 2009
Southern Lhasa	45	3	Ji et al., 2009
Southern Lhasa	56	3	Ji et al., 2009
Southern Lhasa	59	3	Ji et al., 2009
Southern Lhasa	53	3	Ji et al., 2009
Southern Lhasa	55	3	Ji et al., 2009
Southern Lhasa	61	3	Ji et al., 2009
Southern Lhasa	62	3	Ji et al., 2009
Southern Lhasa	52	3	Ji et al., 2009
Southern Lhasa	50	3	Ji et al., 2009
Southern Lhasa	52	3	Ji et al., 2009
Southern Lhasa	57	3	Ji et al., 2009
Southern Lhasa	58	3	Ji et al., 2009
Southern Lhasa	49	3	Ji et al., 2009
Southern Lhasa	49	3	Ji et al., 2009
Southern Lhasa	52	3	Ji et al., 2009
Southern Lhasa	46	3	Ji et al., 2009
Southern Lhasa	55	3	Ji et al., 2009
Southern Lhasa	51	3	Ji et al., 2009
Southern Lhasa	49	3	Ji et al., 2009

Southern Lhasa	50	3	Ji et al., 2009
Southern Lhasa	53	3	Ji et al., 2009
Southern Lhasa	54	3	Ji et al., 2009
Southern Lhasa	52	3	Ji et al., 2009
Southern Lhasa	50	3	Ji et al., 2009
Southern Lhasa	58	3	Ji et al., 2009
Southern Lhasa	52	3	Ji et al., 2009
Southern Lhasa	56	3	Ji et al., 2009
Southern Lhasa	51	3	Ji et al., 2009
Southern Lhasa	51	3	Ji et al., 2009
Southern Lhasa	56	3	Ji et al., 2009
Southern Lhasa	51	3	Ji et al., 2009
Southern Lhasa	49	3	Ji et al., 2009
Southern Lhasa	81	3	Ji et al., 2009
Southern Lhasa	85	3	Ji et al., 2009
Southern Lhasa	85	3	Ji et al., 2009
Southern Lhasa	152	3	Ji et al., 2009
Southern Lhasa	157	3	Ji et al., 2009
Southern Lhasa	153	3	Ji et al., 2009
Southern Lhasa	178	3	Ji et al., 2009
Southern Lhasa	166	3	Ji et al., 2009
Southern Lhasa	157	3	Ji et al., 2009
Southern Lhasa	161	3	Ji et al., 2009
Southern Lhasa	164	3	Ji et al., 2009
Southern Lhasa	163	3	Ji et al., 2009
Southern Lhasa	160	3	Ji et al., 2009
Southern Lhasa	154	3	Ji et al., 2009
Southern Lhasa	152	3	Ji et al., 2009
Southern Lhasa	152	3	Ji et al., 2009
Southern Lhasa	152	3	Ji et al., 2009
Southern Lhasa	153	3	Ji et al., 2009
Southern Lhasa	153	3	Ji et al., 2009
Southern Lhasa	150	3	Ji et al., 2009
Southern Lhasa	150	3	Ji et al., 2009
Southern Lhasa	151	3	Ji et al., 2009
Southern Lhasa	151	3	Ji et al., 2009
Southern Lhasa	153	3	Ji et al., 2009
Southern Lhasa	151	3	Ji et al., 2009
Southern Lhasa	150	3	Ji et al., 2009
Southern Lhasa	107	3	Ji et al., 2009
Southern Lhasa	107	3	Ji et al., 2009
Southern Lhasa	106	3	Ji et al., 2009
Southern Lhasa	109	3	Ji et al., 2009
Southern Lhasa	109	3	Ji et al., 2009
Southern Lhasa	109	3	Ji et al., 2009
Southern Lhasa	108	3	Ji et al., 2009
Southern Lhasa	107	3	Ji et al., 2009
Southern Lhasa	109	3	Ji et al., 2009
Southern Lhasa	108	3	Ji et al., 2009
Southern Lhasa	107	3	Ji et al., 2009
Southern Lhasa	112	3	Ji et al., 2009
Southern Lhasa	110	3	Ji et al., 2009
Southern Lhasa	60	4	Ji et al., 2009
Southern Lhasa	53	4	Ji et al., 2009
Southern Lhasa	56	4	Ji et al., 2009
Southern Lhasa	59	4	Ji et al., 2009
Southern Lhasa	43	4	Ji et al., 2009
Southern Lhasa	53	4	Ji et al., 2009
Southern Lhasa	48	4	Ji et al., 2009
Southern Lhasa	54	4	Ji et al., 2009
Southern Lhasa	56	4	Ji et al., 2009
Southern Lhasa	83	4	Ji et al., 2009
Southern Lhasa	80	4	Ji et al., 2009
Southern Lhasa	205	4	Ji et al., 2009
Southern Lhasa	191	4	Ji et al., 2009
Southern Lhasa	203	4	Ji et al., 2009
Southern Lhasa	201	4	Ji et al., 2009
Southern Lhasa	190	4	Ji et al., 2009
Southern Lhasa	191	4	Ji et al., 2009
Southern Lhasa	193	4	Ji et al., 2009
Southern Lhasa	198	4	Ji et al., 2009

Southern Lhasa	201	4	Ji et al., 2009
Southern Lhasa	212	4	Ji et al., 2009
Southern Lhasa	211	4	Ji et al., 2009
Southern Lhasa	208	4	Ji et al., 2009
Southern Lhasa	196	4	Ji et al., 2009
Southern Lhasa	204	4	Ji et al., 2009
Southern Lhasa	209	4	Ji et al., 2009
Southern Lhasa	209	4	Ji et al., 2009
Southern Lhasa	198	4	Ji et al., 2009
Southern Lhasa	159	4	Ji et al., 2009
Southern Lhasa	156	4	Ji et al., 2009
Southern Lhasa	163	4	Ji et al., 2009
Southern Lhasa	154	4	Ji et al., 2009
Southern Lhasa	180	4	Ji et al., 2009
Southern Lhasa	184	4	Ji et al., 2009
Southern Lhasa	182	4	Ji et al., 2009
Southern Lhasa	111	4	Ji et al., 2009
Southern Lhasa	110	4	Ji et al., 2009
Southern Lhasa	109	4	Ji et al., 2009
Southern Lhasa	57	5	Ji et al., 2009
Southern Lhasa	53	5	Ji et al., 2009
Southern Lhasa	54	5	Ji et al., 2009
Southern Lhasa	188	5	Ji et al., 2009
Southern Lhasa	183	5	Ji et al., 2009
Southern Lhasa	190	5	Ji et al., 2009
Southern Lhasa	190	5	Ji et al., 2009
Southern Lhasa	199	5	Ji et al., 2009
Southern Lhasa	190	5	Ji et al., 2009
Southern Lhasa	204	5	Ji et al., 2009
Southern Lhasa	203	5	Ji et al., 2009
Southern Lhasa	211	5	Ji et al., 2009
Southern Lhasa	215	5	Ji et al., 2009
Southern Lhasa	176	5	Ji et al., 2009
Southern Lhasa	174	5	Ji et al., 2009
Southern Lhasa	174	5	Ji et al., 2009
Southern Lhasa	176	5	Ji et al., 2009
Southern Lhasa	174	5	Ji et al., 2009
Southern Lhasa	174	5	Ji et al., 2009
Southern Lhasa	178	5	Ji et al., 2009
Southern Lhasa	174	5	Ji et al., 2009
Southern Lhasa	174	5	Ji et al., 2009
Southern Lhasa	173	5	Ji et al., 2009
Southern Lhasa	173	5	Ji et al., 2009
Southern Lhasa	194	5	Ji et al., 2009
Southern Lhasa	176	5	Ji et al., 2009
Southern Lhasa	176	5	Ji et al., 2009
Southern Lhasa	172	5	Ji et al., 2009
Southern Lhasa	114	5	Ji et al., 2009
Southern Lhasa	103	5	Ji et al., 2009
Southern Lhasa	110	5	Ji et al., 2009
Southern Lhasa	63	1	Lee et al., 2007
Southern Lhasa	64	1	Lee et al., 2007
Southern Lhasa	64	1	Lee et al., 2007
Southern Lhasa	57	1	Lee et al., 2007
Southern Lhasa	60	1	Lee et al., 2007
Southern Lhasa	56	1	Lee et al., 2007
Southern Lhasa	55	1	Lee et al., 2007
Southern Lhasa	59	1	Lee et al., 2007
Southern Lhasa	55	1	Lee et al., 2007
Southern Lhasa	60	2	Lee et al., 2007
Southern Lhasa	59	2	Lee et al., 2007
Southern Lhasa	58	2	Lee et al., 2007
Southern Lhasa	65	2	Lee et al., 2007
Southern Lhasa	64	2	Lee et al., 2007
Southern Lhasa	59	2	Lee et al., 2007
Southern Lhasa	55	2	Lee et al., 2007
Southern Lhasa	61	2	Lee et al., 2007
Southern Lhasa	59	2	Lee et al., 2007
Southern Lhasa	54	2	Lee et al., 2007
Southern Lhasa	55	1	Lee et al., 2008
Southern Lhasa	56	1	Lee et al., 2009

Southern Lhasa	180	2	Zhang et al. 2007a
Southern Lhasa	180	2	Zhang et al. 2007a
Southern Lhasa	178	2	Zhang et al. 2007a
Southern Lhasa	178	2	Zhang et al. 2007a
Southern Lhasa	179	2	Zhang et al. 2007a
Southern Lhasa	178	2	Zhang et al. 2007a
Southern Lhasa	178	2	Zhang et al. 2007a
Southern Lhasa	179	2	Zhang et al. 2007a
Southern Lhasa	180	2	Zhang et al. 2007a
Southern Lhasa	177	2	Zhang et al. 2007a
Southern Lhasa	177	2	Zhang et al. 2007a
Southern Lhasa	180	2	Zhang et al. 2007a
Southern Lhasa	177	2	Zhang et al. 2007a
Southern Lhasa	127	2	Zhu et al., 2009
Southern Lhasa	135	2	Zhu et al., 2009
Southern Lhasa	135	2	Zhu et al., 2009
Southern Lhasa	135	3	Zhu et al., 2009
Southern Lhasa	138	3	Zhu et al., 2009
Southern Lhasa	136	3	Zhu et al., 2009
Southern Lhasa	141	3	Zhu et al., 2009
Southern Lhasa	139	3	Zhu et al., 2009
Southern Lhasa	132	4	Zhu et al., 2009
Southern Lhasa	134	4	Zhu et al., 2009
Southern Lhasa	119	4	Zhu et al., 2009
Southern Lhasa	131	4	Zhu et al., 2009
Southern Lhasa	138	5	Zhu et al., 2009
Southern Lhasa	43	0	Zhu et al., 2011
Southern Lhasa	43	0	Zhu et al., 2011
Southern Lhasa	45	0	Zhu et al., 2011
Southern Lhasa	44	1	Zhu et al., 2011
Southern Lhasa	44	1	Zhu et al., 2011
Southern Lhasa	45	1	Zhu et al., 2011
Southern Lhasa	51	1	Zhu et al., 2011
Southern Lhasa	80	1	Zhu et al., 2011
Southern Lhasa	79	1	Zhu et al., 2011
Southern Lhasa	78	1	Zhu et al., 2011
Southern Lhasa	44	1	Zhu et al., 2011
Southern Lhasa	52	1	Zhu et al., 2011
Southern Lhasa	51	1	Zhu et al., 2011
Southern Lhasa	51	1	Zhu et al., 2011
Southern Lhasa	49	1	Zhu et al., 2011
Southern Lhasa	49	1	Zhu et al., 2011
Southern Lhasa	49	1	Zhu et al., 2011
Southern Lhasa	49	1	Zhu et al., 2011
Southern Lhasa	50	1	Zhu et al., 2011
Southern Lhasa	51	1	Zhu et al., 2011
Southern Lhasa	52	1	Zhu et al., 2011
Southern Lhasa	54	1	Zhu et al., 2011
Southern Lhasa	54	1	Zhu et al., 2011
Southern Lhasa	80	1	Zhu et al., 2011
Southern Lhasa	79	1	Zhu et al., 2011
Southern Lhasa	82	1	Zhu et al., 2011
Southern Lhasa	80	1	Zhu et al., 2011
Southern Lhasa	44	1	Zhu et al., 2011
Southern Lhasa	50	1	Zhu et al., 2011
Southern Lhasa	51	1	Zhu et al., 2011
Southern Lhasa	51	1	Zhu et al., 2011
Southern Lhasa	51	1	Zhu et al., 2011
Southern Lhasa	52	1	Zhu et al., 2011
Southern Lhasa	51	1	Zhu et al., 2011
Southern Lhasa	51	1	Zhu et al., 2011
Southern Lhasa	52	1	Zhu et al., 2011
Southern Lhasa	81	1	Zhu et al., 2011
Southern Lhasa	54	1	Zhu et al., 2011
Southern Lhasa	55	1	Zhu et al., 2011
Southern Lhasa	79	1	Zhu et al., 2011
Southern Lhasa	79	1	Zhu et al., 2011
Southern Lhasa	79	1	Zhu et al., 2011
Southern Lhasa	83	1	Zhu et al., 2011
Southern Lhasa	82	1	Zhu et al., 2011
Southern Lhasa	44	1	Zhu et al., 2011

Southern Lhasa	52	1	Zhu et al., 2011
Southern Lhasa	51	1	Zhu et al., 2011
Southern Lhasa	52	1	Zhu et al., 2011
Southern Lhasa	51	1	Zhu et al., 2011
Southern Lhasa	50	1	Zhu et al., 2011
Southern Lhasa	50	1	Zhu et al., 2011
Southern Lhasa	49	1	Zhu et al., 2011
Southern Lhasa	52	1	Zhu et al., 2011
Southern Lhasa	51	1	Zhu et al., 2011
Southern Lhasa	52	1	Zhu et al., 2011
Southern Lhasa	52	1	Zhu et al., 2011
Southern Lhasa	52	1	Zhu et al., 2011
Southern Lhasa	83	1	Zhu et al., 2011
Southern Lhasa	82	1	Zhu et al., 2011
Southern Lhasa	55	1	Zhu et al., 2011
Southern Lhasa	84	1	Zhu et al., 2011
Southern Lhasa	81	1	Zhu et al., 2011
Southern Lhasa	80	1	Zhu et al., 2011
Southern Lhasa	83	1	Zhu et al., 2011
Southern Lhasa	84	1	Zhu et al., 2011
Southern Lhasa	83	1	Zhu et al., 2011
Southern Lhasa	52	1	Zhu et al., 2011
Southern Lhasa	52	1	Zhu et al., 2011
Southern Lhasa	54	1	Zhu et al., 2011
Southern Lhasa	53	1	Zhu et al., 2011
Southern Lhasa	52	1	Zhu et al., 2011
Southern Lhasa	51	1	Zhu et al., 2011
Southern Lhasa	51	1	Zhu et al., 2011
Southern Lhasa	52	1	Zhu et al., 2011
Southern Lhasa	51	1	Zhu et al., 2011
Southern Lhasa	51	1	Zhu et al., 2011
Southern Lhasa	50	1	Zhu et al., 2011
Southern Lhasa	50	1	Zhu et al., 2011
Southern Lhasa	49	1	Zhu et al., 2011
Southern Lhasa	50	1	Zhu et al., 2011
Southern Lhasa	52	1	Zhu et al., 2011
Southern Lhasa	51	1	Zhu et al., 2011
Southern Lhasa	51	1	Zhu et al., 2011
Southern Lhasa	79	1	Zhu et al., 2011
Southern Lhasa	81	1	Zhu et al., 2011
Southern Lhasa	80	1	Zhu et al., 2011
Southern Lhasa	80	1	Zhu et al., 2011
Southern Lhasa	80	1	Zhu et al., 2011
Southern Lhasa	80	1	Zhu et al., 2011
Southern Lhasa	77	1	Zhu et al., 2011
Southern Lhasa	51	1	Zhu et al., 2011
Southern Lhasa	49	1	Zhu et al., 2011
Southern Lhasa	51	1	Zhu et al., 2011
Southern Lhasa	50	1	Zhu et al., 2011
Southern Lhasa	50	1	Zhu et al., 2011
Southern Lhasa	50	1	Zhu et al., 2011
Southern Lhasa	59	1	Zhu et al., 2011
Southern Lhasa	58	1	Zhu et al., 2011
Southern Lhasa	64	1	Zhu et al., 2011
Southern Lhasa	62	1	Zhu et al., 2011
Southern Lhasa	61	1	Zhu et al., 2011
Southern Lhasa	60	1	Zhu et al., 2011
Southern Lhasa	62	1	Zhu et al., 2011
Southern Lhasa	63	1	Zhu et al., 2011
Southern Lhasa	55	1	Zhu et al., 2011
Southern Lhasa	55	1	Zhu et al., 2011
Southern Lhasa	53	1	Zhu et al., 2011
Southern Lhasa	54	1	Zhu et al., 2011
Southern Lhasa	53	1	Zhu et al., 2011
Southern Lhasa	54	1	Zhu et al., 2011
Southern Lhasa	55	1	Zhu et al., 2011
Southern Lhasa	54	1	Zhu et al., 2011
Southern Lhasa	54	1	Zhu et al., 2011
Southern Lhasa	54	1	Zhu et al., 2011
Southern Lhasa	80	1	Zhu et al., 2011
Southern Lhasa	78	1	Zhu et al., 2011

Southern Lhasa	80	1	Zhu et al., 2011
Southern Lhasa	79	1	Zhu et al., 2011
Southern Lhasa	80	1	Zhu et al., 2011
Southern Lhasa	82	1	Zhu et al., 2011
Southern Lhasa	84	1	Zhu et al., 2011
Southern Lhasa	84	1	Zhu et al., 2011
Southern Lhasa	82	1	Zhu et al., 2011
Southern Lhasa	81	1	Zhu et al., 2011
Southern Lhasa	83	1	Zhu et al., 2011
Southern Lhasa	88	1	Zhu et al., 2011
Southern Lhasa	88	1	Zhu et al., 2011
Southern Lhasa	89	1	Zhu et al., 2011
Southern Lhasa	91	1	Zhu et al., 2011
Southern Lhasa	90	1	Zhu et al., 2011
Southern Lhasa	85	1	Zhu et al., 2011
Southern Lhasa	84	1	Zhu et al., 2011
Southern Lhasa	90	1	Zhu et al., 2011
Southern Lhasa	87	1	Zhu et al., 2011
Southern Lhasa	85	1	Zhu et al., 2011
Southern Lhasa	88	1	Zhu et al., 2011
Southern Lhasa	89	1	Zhu et al., 2011
Southern Lhasa	87	1	Zhu et al., 2011
Southern Lhasa	90	1	Zhu et al., 2011
Southern Lhasa	84	1	Zhu et al., 2011
Southern Lhasa	89	1	Zhu et al., 2011
Southern Lhasa	86	1	Zhu et al., 2011
Southern Lhasa	90	1	Zhu et al., 2011
Southern Lhasa	91	1	Zhu et al., 2011
Southern Lhasa	51	2	Zhu et al., 2011
Southern Lhasa	52	2	Zhu et al., 2011
Southern Lhasa	52	2	Zhu et al., 2011
Southern Lhasa	52	2	Zhu et al., 2011
Southern Lhasa	52	2	Zhu et al., 2011
Southern Lhasa	80	2	Zhu et al., 2011
Southern Lhasa	78	2	Zhu et al., 2011
Southern Lhasa	84	2	Zhu et al., 2011
Southern Lhasa	85	2	Zhu et al., 2011
Southern Lhasa	84	2	Zhu et al., 2011
Southern Lhasa	85	2	Zhu et al., 2011
Southern Lhasa	85	2	Zhu et al., 2011
Southern Lhasa	85	2	Zhu et al., 2011
Southern Lhasa	84	2	Zhu et al., 2011
Southern Lhasa	191	2	Zhu et al., 2011
Southern Lhasa	192	2	Zhu et al., 2011
Southern Lhasa	192	2	Zhu et al., 2011
Southern Lhasa	192	2	Zhu et al., 2011
Southern Lhasa	192	2	Zhu et al., 2011
Southern Lhasa	191	2	Zhu et al., 2011
Southern Lhasa	202	2	Zhu et al., 2011
Southern Lhasa	205	2	Zhu et al., 2011
Southern Lhasa	202	2	Zhu et al., 2011
Southern Lhasa	201	2	Zhu et al., 2011
Southern Lhasa	200	2	Zhu et al., 2011
Southern Lhasa	205	2	Zhu et al., 2011
Southern Lhasa	200	2	Zhu et al., 2011
Southern Lhasa	201	2	Zhu et al., 2011
Southern Lhasa	201	2	Zhu et al., 2011
Southern Lhasa	199	2	Zhu et al., 2011
Southern Lhasa	199	2	Zhu et al., 2011
Southern Lhasa	199	2	Zhu et al., 2011
Southern Lhasa	200	2	Zhu et al., 2011
Southern Lhasa	92	2	Zhu et al., 2011
Southern Lhasa	89	2	Zhu et al., 2011
Southern Lhasa	85	2	Zhu et al., 2011
Southern Lhasa	86	2	Zhu et al., 2011
Southern Lhasa	89	2	Zhu et al., 2011
Southern Lhasa	88	2	Zhu et al., 2011
Southern Lhasa	87	2	Zhu et al., 2011
Southern Lhasa	85	2	Zhu et al., 2011
Southern Lhasa	52	3	Zhu et al., 2011
Southern Lhasa	82	3	Zhu et al., 2011

Southern Lhasa	85	3	Zhu et al., 2011
Southern Lhasa	83	3	Zhu et al., 2011
Southern Lhasa	201	3	Zhu et al., 2011
Southern Lhasa	192	3	Zhu et al., 2011
Southern Lhasa	191	3	Zhu et al., 2011
Southern Lhasa	191	3	Zhu et al., 2011
Southern Lhasa	192	3	Zhu et al., 2011
Southern Lhasa	202	3	Zhu et al., 2011
Southern Lhasa	204	3	Zhu et al., 2011
Southern Lhasa	208	3	Zhu et al., 2011
Southern Lhasa	202	3	Zhu et al., 2011
Southern Lhasa	206	3	Zhu et al., 2011
Southern Lhasa	200	3	Zhu et al., 2011
Southern Lhasa	201	3	Zhu et al., 2011
Southern Lhasa	199	3	Zhu et al., 2011
Southern Lhasa	84	3	Zhu et al., 2011
Southern Lhasa	82	4	Zhu et al., 2011
Southern Lhasa	190	4	Zhu et al., 2011
Southern Lhasa	192	4	Zhu et al., 2011
Southern Lhasa	190	4	Zhu et al., 2011
Southern Lhasa	190	4	Zhu et al., 2011
Southern Lhasa	206	4	Zhu et al., 2011
Southern Lhasa	200	4	Zhu et al., 2011
Southern Lhasa	200	4	Zhu et al., 2011
Southern Lhasa	206	5	Zhu et al., 2011
Southern Lhasa	203	5	Zhu et al., 2011
Lesser Himalaya	474	33	Gehrels et al., 2008
Lesser Himalaya	525	8	Gehrels et al., 2008
Lesser Himalaya	537	14	Gehrels et al., 2008
Lesser Himalaya	542	9	Gehrels et al., 2008
Lesser Himalaya	542	15	Gehrels et al., 2008
Lesser Himalaya	550	8	Gehrels et al., 2008
Lesser Himalaya	552	6	Gehrels et al., 2008
Lesser Himalaya	553	3	Gehrels et al., 2008
Lesser Himalaya	555	3	Gehrels et al., 2008
Lesser Himalaya	560	19	Gehrels et al., 2008
Lesser Himalaya	561	13	Gehrels et al., 2008
Lesser Himalaya	563	13	Gehrels et al., 2008
Lesser Himalaya	578	15	Gehrels et al., 2008
Lesser Himalaya	585	6	Gehrels et al., 2008
Lesser Himalaya	590	14	Gehrels et al., 2008
Lesser Himalaya	594	9	Gehrels et al., 2008
Lesser Himalaya	599	21	Gehrels et al., 2008
Lesser Himalaya	620	6	Gehrels et al., 2008
Lesser Himalaya	644	14	Gehrels et al., 2008
Lesser Himalaya	650	30	Gehrels et al., 2008
Lesser Himalaya	655	21	Gehrels et al., 2008
Lesser Himalaya	662	12	Gehrels et al., 2008
Lesser Himalaya	663	4	Gehrels et al., 2008
Lesser Himalaya	674	6	Gehrels et al., 2008
Lesser Himalaya	684	15	Gehrels et al., 2008
Lesser Himalaya	686	8	Gehrels et al., 2008
Lesser Himalaya	691	4	Gehrels et al., 2008
Lesser Himalaya	749	9	Gehrels et al., 2008
Lesser Himalaya	752	10	Gehrels et al., 2008
Lesser Himalaya	754	5	Gehrels et al., 2008
Lesser Himalaya	766	9	Gehrels et al., 2008
Lesser Himalaya	773	77	Gehrels et al., 2008
Lesser Himalaya	785	16	Gehrels et al., 2008
Lesser Himalaya	789	14	Gehrels et al., 2008
Lesser Himalaya	792	13	Gehrels et al., 2008
Lesser Himalaya	797	14	Gehrels et al., 2008
Lesser Himalaya	800	7	Gehrels et al., 2008
Lesser Himalaya	810	12	Gehrels et al., 2008
Lesser Himalaya	812	14	Gehrels et al., 2008
Lesser Himalaya	822	17	Gehrels et al., 2008
Lesser Himalaya	825	19	Gehrels et al., 2008
Lesser Himalaya	830	6	Gehrels et al., 2008
Lesser Himalaya	838	15	Gehrels et al., 2008
Lesser Himalaya	841	17	Gehrels et al., 2008
Lesser Himalaya	841	13	Gehrels et al., 2008

Lesser Himalaya	843	16	Gehrels et al., 2008
Lesser Himalaya	843	7	Gehrels et al., 2008
Lesser Himalaya	864	16	Gehrels et al., 2008
Lesser Himalaya	869	14	Gehrels et al., 2008
Lesser Himalaya	873	42	Gehrels et al., 2008
Lesser Himalaya	906	9	Gehrels et al., 2008
Lesser Himalaya	910	11	Gehrels et al., 2008
Lesser Himalaya	929	6	Gehrels et al., 2008
Lesser Himalaya	929	9	Gehrels et al., 2008
Lesser Himalaya	932	12	Gehrels et al., 2008
Lesser Himalaya	936	7	Gehrels et al., 2008
Lesser Himalaya	941	20	Gehrels et al., 2008
Lesser Himalaya	953	15	Gehrels et al., 2008
Lesser Himalaya	953	23	Gehrels et al., 2008
Lesser Himalaya	959	19	Gehrels et al., 2008
Lesser Himalaya	962	8	Gehrels et al., 2008
Lesser Himalaya	967	33	Gehrels et al., 2008
Lesser Himalaya	969	16	Gehrels et al., 2008
Lesser Himalaya	969	19	Gehrels et al., 2008
Lesser Himalaya	974	12	Gehrels et al., 2008
Lesser Himalaya	977	18	Gehrels et al., 2008
Lesser Himalaya	979	10	Gehrels et al., 2008
Lesser Himalaya	979	10	Gehrels et al., 2008
Lesser Himalaya	979	12	Gehrels et al., 2008
Lesser Himalaya	984	10	Gehrels et al., 2008
Lesser Himalaya	986	14	Gehrels et al., 2008
Lesser Himalaya	993	17	Gehrels et al., 2008
Lesser Himalaya	993	16	Gehrels et al., 2008
Lesser Himalaya	994	16	Gehrels et al., 2008
Lesser Himalaya	999	22	Gehrels et al., 2008
Lesser Himalaya	1008	7	Gehrels et al., 2008
Lesser Himalaya	1010	21	Gehrels et al., 2008
Lesser Himalaya	1014	11	Gehrels et al., 2008
Lesser Himalaya	1016	10	Gehrels et al., 2008
Lesser Himalaya	1016	12	Gehrels et al., 2008
Lesser Himalaya	1025	9	Gehrels et al., 2008
Lesser Himalaya	1044	25	Gehrels et al., 2008
Lesser Himalaya	1052	9	Gehrels et al., 2008
Lesser Himalaya	1065	11	Gehrels et al., 2008
Lesser Himalaya	1079	25	Gehrels et al., 2008
Lesser Himalaya	1081	14	Gehrels et al., 2008
Lesser Himalaya	1082	18	Gehrels et al., 2008
Lesser Himalaya	1101	32	Gehrels et al., 2008
Lesser Himalaya	1111	12	Gehrels et al., 2008
Lesser Himalaya	1136	16	Gehrels et al., 2008
Lesser Himalaya	1139	9	Gehrels et al., 2008
Lesser Himalaya	1147	13	Gehrels et al., 2008
Lesser Himalaya	1153	6	Gehrels et al., 2008
Lesser Himalaya	1164	53	Gehrels et al., 2008
Lesser Himalaya	1303	24	Gehrels et al., 2008
Lesser Himalaya	1372	42	Gehrels et al., 2008
Lesser Himalaya	1458	19	Gehrels et al., 2008
Lesser Himalaya	1470	12	Gehrels et al., 2008
Lesser Himalaya	1528	82	Gehrels et al., 2008
Lesser Himalaya	1560	7	Gehrels et al., 2008
Lesser Himalaya	1599	15	Gehrels et al., 2008
Lesser Himalaya	1604	22	Gehrels et al., 2008
Lesser Himalaya	1611	36	Gehrels et al., 2008
Lesser Himalaya	1614	50	Gehrels et al., 2008
Lesser Himalaya	1615	25	Gehrels et al., 2008
Lesser Himalaya	1622	6	Gehrels et al., 2008
Lesser Himalaya	1625	14	Gehrels et al., 2008
Lesser Himalaya	1629	58	Gehrels et al., 2008
Lesser Himalaya	1638	12	Gehrels et al., 2008
Lesser Himalaya	1640	20	Gehrels et al., 2008
Lesser Himalaya	1644	26	Gehrels et al., 2008
Lesser Himalaya	1661	46	Gehrels et al., 2008
Lesser Himalaya	1661	23	Gehrels et al., 2008
Lesser Himalaya	1673	16	Gehrels et al., 2008
Lesser Himalaya	1673	25	Gehrels et al., 2008
Lesser Himalaya	1682	60	Gehrels et al., 2008

Lesser Himalaya	1684	38	Gehrels et al., 2008
Lesser Himalaya	1686	7	Gehrels et al., 2008
Lesser Himalaya	1687	3	Gehrels et al., 2008
Lesser Himalaya	1698	17	Gehrels et al., 2008
Lesser Himalaya	1699	36	Gehrels et al., 2008
Lesser Himalaya	1715	18	Gehrels et al., 2008
Lesser Himalaya	1716	5	Gehrels et al., 2008
Lesser Himalaya	1717	4	Gehrels et al., 2008
Lesser Himalaya	1717	14	Gehrels et al., 2008
Lesser Himalaya	1718	48	Gehrels et al., 2008
Lesser Himalaya	1721	10	Gehrels et al., 2008
Lesser Himalaya	1725	27	Gehrels et al., 2008
Lesser Himalaya	1726	28	Gehrels et al., 2008
Lesser Himalaya	1728	4	Gehrels et al., 2008
Lesser Himalaya	1732	16	Gehrels et al., 2008
Lesser Himalaya	1733	2	Gehrels et al., 2008
Lesser Himalaya	1733	7	Gehrels et al., 2008
Lesser Himalaya	1737	6	Gehrels et al., 2008
Lesser Himalaya	1744	11	Gehrels et al., 2008
Lesser Himalaya	1745	5	Gehrels et al., 2008
Lesser Himalaya	1750	95	Gehrels et al., 2008
Lesser Himalaya	1750	6	Gehrels et al., 2008
Lesser Himalaya	1752	9	Gehrels et al., 2008
Lesser Himalaya	1757	14	Gehrels et al., 2008
Lesser Himalaya	1759	10	Gehrels et al., 2008
Lesser Himalaya	1763	7	Gehrels et al., 2008
Lesser Himalaya	1769	3	Gehrels et al., 2008
Lesser Himalaya	1770	6	Gehrels et al., 2008
Lesser Himalaya	1771	5	Gehrels et al., 2008
Lesser Himalaya	1777	26	Gehrels et al., 2008
Lesser Himalaya	1777	4	Gehrels et al., 2008
Lesser Himalaya	1779	6	Gehrels et al., 2008
Lesser Himalaya	1780	4	Gehrels et al., 2008
Lesser Himalaya	1780	4	Gehrels et al., 2008
Lesser Himalaya	1782	8	Gehrels et al., 2008
Lesser Himalaya	1784	6	Gehrels et al., 2008
Lesser Himalaya	1785	8	Gehrels et al., 2008
Lesser Himalaya	1788	6	Gehrels et al., 2008
Lesser Himalaya	1789	7	Gehrels et al., 2008
Lesser Himalaya	1790	5	Gehrels et al., 2008
Lesser Himalaya	1791	6	Gehrels et al., 2008
Lesser Himalaya	1792	14	Gehrels et al., 2008
Lesser Himalaya	1794	16	Gehrels et al., 2008
Lesser Himalaya	1797	15	Gehrels et al., 2008
Lesser Himalaya	1797	9	Gehrels et al., 2008
Lesser Himalaya	1798	3	Gehrels et al., 2008
Lesser Himalaya	1798	56	Gehrels et al., 2008
Lesser Himalaya	1799	5	Gehrels et al., 2008
Lesser Himalaya	1804	7	Gehrels et al., 2008
Lesser Himalaya	1804	10	Gehrels et al., 2008
Lesser Himalaya	1807	6	Gehrels et al., 2008
Lesser Himalaya	1810	5	Gehrels et al., 2008
Lesser Himalaya	1811	10	Gehrels et al., 2008
Lesser Himalaya	1817	9	Gehrels et al., 2008
Lesser Himalaya	1817	6	Gehrels et al., 2008
Lesser Himalaya	1818	4	Gehrels et al., 2008
Lesser Himalaya	1818	6	Gehrels et al., 2008
Lesser Himalaya	1820	4	Gehrels et al., 2008
Lesser Himalaya	1822	3	Gehrels et al., 2008
Lesser Himalaya	1824	24	Gehrels et al., 2008
Lesser Himalaya	1824	5	Gehrels et al., 2008
Lesser Himalaya	1826	5	Gehrels et al., 2008
Lesser Himalaya	1827	5	Gehrels et al., 2008
Lesser Himalaya	1827	13	Gehrels et al., 2008
Lesser Himalaya	1828	5	Gehrels et al., 2008
Lesser Himalaya	1830	9	Gehrels et al., 2008
Lesser Himalaya	1830	4	Gehrels et al., 2008
Lesser Himalaya	1832	7	Gehrels et al., 2008
Lesser Himalaya	1834	30	Gehrels et al., 2008
Lesser Himalaya	1834	12	Gehrels et al., 2008
Lesser Himalaya	1835	6	Gehrels et al., 2008

Lesser Himalaya	1836	20	Gehrels et al., 2008
Lesser Himalaya	1836	5	Gehrels et al., 2008
Lesser Himalaya	1836	5	Gehrels et al., 2008
Lesser Himalaya	1837	11	Gehrels et al., 2008
Lesser Himalaya	1839	8	Gehrels et al., 2008
Lesser Himalaya	1839	10	Gehrels et al., 2008
Lesser Himalaya	1839	7	Gehrels et al., 2008
Lesser Himalaya	1840	4	Gehrels et al., 2008
Lesser Himalaya	1841	22	Gehrels et al., 2008
Lesser Himalaya	1841	39	Gehrels et al., 2008
Lesser Himalaya	1841	4	Gehrels et al., 2008
Lesser Himalaya	1842	16	Gehrels et al., 2008
Lesser Himalaya	1843	20	Gehrels et al., 2008
Lesser Himalaya	1843	5	Gehrels et al., 2008
Lesser Himalaya	1844	5	Gehrels et al., 2008
Lesser Himalaya	1844	6	Gehrels et al., 2008
Lesser Himalaya	1845	6	Gehrels et al., 2008
Lesser Himalaya	1845	12	Gehrels et al., 2008
Lesser Himalaya	1846	14	Gehrels et al., 2008
Lesser Himalaya	1847	12	Gehrels et al., 2008
Lesser Himalaya	1847	16	Gehrels et al., 2008
Lesser Himalaya	1847	14	Gehrels et al., 2008
Lesser Himalaya	1847	4	Gehrels et al., 2008
Lesser Himalaya	1847	4	Gehrels et al., 2008
Lesser Himalaya	1848	4	Gehrels et al., 2008
Lesser Himalaya	1849	5	Gehrels et al., 2008
Lesser Himalaya	1849	7	Gehrels et al., 2008
Lesser Himalaya	1849	32	Gehrels et al., 2008
Lesser Himalaya	1849	5	Gehrels et al., 2008
Lesser Himalaya	1850	7	Gehrels et al., 2008
Lesser Himalaya	1850	3	Gehrels et al., 2008
Lesser Himalaya	1851	18	Gehrels et al., 2008
Lesser Himalaya	1852	2	Gehrels et al., 2008
Lesser Himalaya	1852	3	Gehrels et al., 2008
Lesser Himalaya	1852	5	Gehrels et al., 2008
Lesser Himalaya	1853	11	Gehrels et al., 2008
Lesser Himalaya	1855	9	Gehrels et al., 2008
Lesser Himalaya	1855	5	Gehrels et al., 2008
Lesser Himalaya	1855	4	Gehrels et al., 2008
Lesser Himalaya	1856	2	Gehrels et al., 2008
Lesser Himalaya	1856	4	Gehrels et al., 2008
Lesser Himalaya	1856	5	Gehrels et al., 2008
Lesser Himalaya	1856	4	Gehrels et al., 2008
Lesser Himalaya	1858	16	Gehrels et al., 2008
Lesser Himalaya	1858	2	Gehrels et al., 2008
Lesser Himalaya	1858	8	Gehrels et al., 2008
Lesser Himalaya	1858	14	Gehrels et al., 2008
Lesser Himalaya	1858	5	Gehrels et al., 2008
Lesser Himalaya	1859	12	Gehrels et al., 2008
Lesser Himalaya	1859	4	Gehrels et al., 2008
Lesser Himalaya	1860	10	Gehrels et al., 2008
Lesser Himalaya	1861	12	Gehrels et al., 2008
Lesser Himalaya	1861	4	Gehrels et al., 2008
Lesser Himalaya	1862	14	Gehrels et al., 2008
Lesser Himalaya	1862	10	Gehrels et al., 2008
Lesser Himalaya	1863	5	Gehrels et al., 2008
Lesser Himalaya	1865	12	Gehrels et al., 2008
Lesser Himalaya	1865	4	Gehrels et al., 2008
Lesser Himalaya	1865	4	Gehrels et al., 2008
Lesser Himalaya	1865	4	Gehrels et al., 2008
Lesser Himalaya	1865	12	Gehrels et al., 2008
Lesser Himalaya	1866	18	Gehrels et al., 2008
Lesser Himalaya	1866	18	Gehrels et al., 2008
Lesser Himalaya	1866	2	Gehrels et al., 2008
Lesser Himalaya	1866	6	Gehrels et al., 2008
Lesser Himalaya	1866	4	Gehrels et al., 2008
Lesser Himalaya	1866	5	Gehrels et al., 2008
Lesser Himalaya	1867	9	Gehrels et al., 2008
Lesser Himalaya	1867	10	Gehrels et al., 2008
Lesser Himalaya	1868	1	Gehrels et al., 2008
Lesser Himalaya	1868	7	Gehrels et al., 2008

Lesser Himalaya	1868	5	Gehrels et al., 2008
Lesser Himalaya	1868	9	Gehrels et al., 2008
Lesser Himalaya	1868	4	Gehrels et al., 2008
Lesser Himalaya	1869	10	Gehrels et al., 2008
Lesser Himalaya	1869	18	Gehrels et al., 2008
Lesser Himalaya	1869	8	Gehrels et al., 2008
Lesser Himalaya	1869	3	Gehrels et al., 2008
Lesser Himalaya	1870	16	Gehrels et al., 2008
Lesser Himalaya	1870	4	Gehrels et al., 2008
Lesser Himalaya	1871	9	Gehrels et al., 2008
Lesser Himalaya	1872	2	Gehrels et al., 2008
Lesser Himalaya	1872	7	Gehrels et al., 2008
Lesser Himalaya	1873	5	Gehrels et al., 2008
Lesser Himalaya	1874	2	Gehrels et al., 2008
Lesser Himalaya	1875	6	Gehrels et al., 2008
Lesser Himalaya	1876	2	Gehrels et al., 2008
Lesser Himalaya	1876	3	Gehrels et al., 2008
Lesser Himalaya	1876	5	Gehrels et al., 2008
Lesser Himalaya	1876	4	Gehrels et al., 2008
Lesser Himalaya	1876	6	Gehrels et al., 2008
Lesser Himalaya	1877	6	Gehrels et al., 2008
Lesser Himalaya	1877	8	Gehrels et al., 2008
Lesser Himalaya	1877	10	Gehrels et al., 2008
Lesser Himalaya	1877	4	Gehrels et al., 2008
Lesser Himalaya	1878	4	Gehrels et al., 2008
Lesser Himalaya	1878	5	Gehrels et al., 2008
Lesser Himalaya	1879	3	Gehrels et al., 2008
Lesser Himalaya	1879	2	Gehrels et al., 2008
Lesser Himalaya	1880	5	Gehrels et al., 2008
Lesser Himalaya	1880	4	Gehrels et al., 2008
Lesser Himalaya	1880	2	Gehrels et al., 2008
Lesser Himalaya	1881	3	Gehrels et al., 2008
Lesser Himalaya	1881	2	Gehrels et al., 2008
Lesser Himalaya	1881	5	Gehrels et al., 2008
Lesser Himalaya	1881	3	Gehrels et al., 2008
Lesser Himalaya	1882	15	Gehrels et al., 2008
Lesser Himalaya	1882	44	Gehrels et al., 2008
Lesser Himalaya	1882	5	Gehrels et al., 2008
Lesser Himalaya	1882	5	Gehrels et al., 2008
Lesser Himalaya	1882	5	Gehrels et al., 2008
Lesser Himalaya	1883	2	Gehrels et al., 2008
Lesser Himalaya	1883	3	Gehrels et al., 2008
Lesser Himalaya	1883	4	Gehrels et al., 2008
Lesser Himalaya	1883	4	Gehrels et al., 2008
Lesser Himalaya	1883	4	Gehrels et al., 2008
Lesser Himalaya	1884	8	Gehrels et al., 2008
Lesser Himalaya	1884	4	Gehrels et al., 2008
Lesser Himalaya	1884	4	Gehrels et al., 2008
Lesser Himalaya	1884	8	Gehrels et al., 2008
Lesser Himalaya	1884	6	Gehrels et al., 2008
Lesser Himalaya	1884	5	Gehrels et al., 2008
Lesser Himalaya	1885	7	Gehrels et al., 2008
Lesser Himalaya	1886	2	Gehrels et al., 2008
Lesser Himalaya	1887	27	Gehrels et al., 2008
Lesser Himalaya	1887	5	Gehrels et al., 2008
Lesser Himalaya	1888	26	Gehrels et al., 2008
Lesser Himalaya	1888	2	Gehrels et al., 2008
Lesser Himalaya	1888	2	Gehrels et al., 2008
Lesser Himalaya	1888	8	Gehrels et al., 2008
Lesser Himalaya	1888	4	Gehrels et al., 2008
Lesser Himalaya	1888	6	Gehrels et al., 2008
Lesser Himalaya	1888	3	Gehrels et al., 2008
Lesser Himalaya	1889	5	Gehrels et al., 2008
Lesser Himalaya	1890	3	Gehrels et al., 2008
Lesser Himalaya	1890	7	Gehrels et al., 2008
Lesser Himalaya	1891	6	Gehrels et al., 2008
Lesser Himalaya	1891	3	Gehrels et al., 2008
Lesser Himalaya	1892	28	Gehrels et al., 2008
Lesser Himalaya	1892	5	Gehrels et al., 2008
Lesser Himalaya	1892	2	Gehrels et al., 2008
Lesser Himalaya	1892	8	Gehrels et al., 2008

Lesser Himalaya	1892	4	Gehrels et al., 2008
Lesser Himalaya	1892	7	Gehrels et al., 2008
Lesser Himalaya	1892	6	Gehrels et al., 2008
Lesser Himalaya	1892	5	Gehrels et al., 2008
Lesser Himalaya	1893	4	Gehrels et al., 2008
Lesser Himalaya	1893	7	Gehrels et al., 2008
Lesser Himalaya	1894	18	Gehrels et al., 2008
Lesser Himalaya	1895	3	Gehrels et al., 2008
Lesser Himalaya	1895	6	Gehrels et al., 2008
Lesser Himalaya	1896	8	Gehrels et al., 2008
Lesser Himalaya	1896	5	Gehrels et al., 2008
Lesser Himalaya	1896	5	Gehrels et al., 2008
Lesser Himalaya	1897	7	Gehrels et al., 2008
Lesser Himalaya	1897	4	Gehrels et al., 2008
Lesser Himalaya	1897	3	Gehrels et al., 2008
Lesser Himalaya	1898	7	Gehrels et al., 2008
Lesser Himalaya	1898	3	Gehrels et al., 2008
Lesser Himalaya	1900	6	Gehrels et al., 2008
Lesser Himalaya	1900	4	Gehrels et al., 2008
Lesser Himalaya	1901	14	Gehrels et al., 2008
Lesser Himalaya	1901	11	Gehrels et al., 2008
Lesser Himalaya	1902	23	Gehrels et al., 2008
Lesser Himalaya	1902	6	Gehrels et al., 2008
Lesser Himalaya	1903	3	Gehrels et al., 2008
Lesser Himalaya	1904	5	Gehrels et al., 2008
Lesser Himalaya	1904	3	Gehrels et al., 2008
Lesser Himalaya	1906	3	Gehrels et al., 2008
Lesser Himalaya	1907	4	Gehrels et al., 2008
Lesser Himalaya	1907	6	Gehrels et al., 2008
Lesser Himalaya	1907	4	Gehrels et al., 2008
Lesser Himalaya	1910	16	Gehrels et al., 2008
Lesser Himalaya	1910	4	Gehrels et al., 2008
Lesser Himalaya	1912	6	Gehrels et al., 2008
Lesser Himalaya	1913	28	Gehrels et al., 2008
Lesser Himalaya	1913	5	Gehrels et al., 2008
Lesser Himalaya	1913	7	Gehrels et al., 2008
Lesser Himalaya	1914	4	Gehrels et al., 2008
Lesser Himalaya	1914	12	Gehrels et al., 2008
Lesser Himalaya	1914	3	Gehrels et al., 2008
Lesser Himalaya	1915	3	Gehrels et al., 2008
Lesser Himalaya	1915	2	Gehrels et al., 2008
Lesser Himalaya	1916	12	Gehrels et al., 2008
Lesser Himalaya	1916	6	Gehrels et al., 2008
Lesser Himalaya	1916	6	Gehrels et al., 2008
Lesser Himalaya	1917	6	Gehrels et al., 2008
Lesser Himalaya	1917	9	Gehrels et al., 2008
Lesser Himalaya	1917	6	Gehrels et al., 2008
Lesser Himalaya	1918	5	Gehrels et al., 2008
Lesser Himalaya	1919	3	Gehrels et al., 2008
Lesser Himalaya	1921	6	Gehrels et al., 2008
Lesser Himalaya	1922	6	Gehrels et al., 2008
Lesser Himalaya	1923	5	Gehrels et al., 2008
Lesser Himalaya	1923	6	Gehrels et al., 2008
Lesser Himalaya	1923	2	Gehrels et al., 2008
Lesser Himalaya	1925	4	Gehrels et al., 2008
Lesser Himalaya	1925	4	Gehrels et al., 2008
Lesser Himalaya	1926	6	Gehrels et al., 2008
Lesser Himalaya	1927	7	Gehrels et al., 2008
Lesser Himalaya	1927	5	Gehrels et al., 2008
Lesser Himalaya	1927	4	Gehrels et al., 2008
Lesser Himalaya	1928	16	Gehrels et al., 2008
Lesser Himalaya	1928	5	Gehrels et al., 2008
Lesser Himalaya	1928	7	Gehrels et al., 2008
Lesser Himalaya	1928	10	Gehrels et al., 2008
Lesser Himalaya	1929	2	Gehrels et al., 2008
Lesser Himalaya	1929	2	Gehrels et al., 2008
Lesser Himalaya	1931	7	Gehrels et al., 2008
Lesser Himalaya	1932	5	Gehrels et al., 2008
Lesser Himalaya	1932	4	Gehrels et al., 2008
Lesser Himalaya	1932	3	Gehrels et al., 2008
Lesser Himalaya	1933	16	Gehrels et al., 2008

Lesser Himalaya	1933	14	Gehrels et al., 2008
Lesser Himalaya	1933	4	Gehrels et al., 2008
Lesser Himalaya	1933	48	Gehrels et al., 2008
Lesser Himalaya	1934	4	Gehrels et al., 2008
Lesser Himalaya	1935	14	Gehrels et al., 2008
Lesser Himalaya	1935	2	Gehrels et al., 2008
Lesser Himalaya	1936	14	Gehrels et al., 2008
Lesser Himalaya	1936	3	Gehrels et al., 2008
Lesser Himalaya	1936	9	Gehrels et al., 2008
Lesser Himalaya	1936	5	Gehrels et al., 2008
Lesser Himalaya	1937	5	Gehrels et al., 2008
Lesser Himalaya	1938	5	Gehrels et al., 2008
Lesser Himalaya	1938	8	Gehrels et al., 2008
Lesser Himalaya	1939	100	Gehrels et al., 2008
Lesser Himalaya	1939	3	Gehrels et al., 2008
Lesser Himalaya	1939	5	Gehrels et al., 2008
Lesser Himalaya	1940	5	Gehrels et al., 2008
Lesser Himalaya	1940	7	Gehrels et al., 2008
Lesser Himalaya	1942	16	Gehrels et al., 2008
Lesser Himalaya	1942	5	Gehrels et al., 2008
Lesser Himalaya	1942	4	Gehrels et al., 2008
Lesser Himalaya	1944	14	Gehrels et al., 2008
Lesser Himalaya	1945	5	Gehrels et al., 2008
Lesser Himalaya	1946	6	Gehrels et al., 2008
Lesser Himalaya	1947	24	Gehrels et al., 2008
Lesser Himalaya	1947	5	Gehrels et al., 2008
Lesser Himalaya	1948	10	Gehrels et al., 2008
Lesser Himalaya	1948	2	Gehrels et al., 2008
Lesser Himalaya	1949	5	Gehrels et al., 2008
Lesser Himalaya	1950	8	Gehrels et al., 2008
Lesser Himalaya	1950	7	Gehrels et al., 2008
Lesser Himalaya	1950	7	Gehrels et al., 2008
Lesser Himalaya	1950	6	Gehrels et al., 2008
Lesser Himalaya	1951	8	Gehrels et al., 2008
Lesser Himalaya	1951	5	Gehrels et al., 2008
Lesser Himalaya	1951	6	Gehrels et al., 2008
Lesser Himalaya	1952	6	Gehrels et al., 2008
Lesser Himalaya	1953	32	Gehrels et al., 2008
Lesser Himalaya	1954	6	Gehrels et al., 2008
Lesser Himalaya	1954	5	Gehrels et al., 2008
Lesser Himalaya	1955	5	Gehrels et al., 2008
Lesser Himalaya	1955	10	Gehrels et al., 2008
Lesser Himalaya	1955	6	Gehrels et al., 2008
Lesser Himalaya	1955	4	Gehrels et al., 2008
Lesser Himalaya	1955	24	Gehrels et al., 2008
Lesser Himalaya	1956	3	Gehrels et al., 2008
Lesser Himalaya	1957	7	Gehrels et al., 2008
Lesser Himalaya	1957	5	Gehrels et al., 2008
Lesser Himalaya	1959	4	Gehrels et al., 2008
Lesser Himalaya	1960	34	Gehrels et al., 2008
Lesser Himalaya	1960	9	Gehrels et al., 2008
Lesser Himalaya	1960	7	Gehrels et al., 2008
Lesser Himalaya	1961	16	Gehrels et al., 2008
Lesser Himalaya	1961	4	Gehrels et al., 2008
Lesser Himalaya	1963	12	Gehrels et al., 2008
Lesser Himalaya	1964	5	Gehrels et al., 2008
Lesser Himalaya	1966	20	Gehrels et al., 2008
Lesser Himalaya	1966	10	Gehrels et al., 2008
Lesser Himalaya	1967	14	Gehrels et al., 2008
Lesser Himalaya	1968	4	Gehrels et al., 2008
Lesser Himalaya	1969	5	Gehrels et al., 2008
Lesser Himalaya	1969	5	Gehrels et al., 2008
Lesser Himalaya	1969	2	Gehrels et al., 2008
Lesser Himalaya	1969	7	Gehrels et al., 2008
Lesser Himalaya	1970	4	Gehrels et al., 2008
Lesser Himalaya	1971	4	Gehrels et al., 2008
Lesser Himalaya	1974	5	Gehrels et al., 2008
Lesser Himalaya	1976	22	Gehrels et al., 2008
Lesser Himalaya	1976	17	Gehrels et al., 2008
Lesser Himalaya	1976	28	Gehrels et al., 2008
Lesser Himalaya	1977	6	Gehrels et al., 2008

Lesser Himalaya	1977	6	Gehrels et al., 2008
Lesser Himalaya	1977	6	Gehrels et al., 2008
Lesser Himalaya	1980	11	Gehrels et al., 2008
Lesser Himalaya	1980	5	Gehrels et al., 2008
Lesser Himalaya	1980	5	Gehrels et al., 2008
Lesser Himalaya	1981	3	Gehrels et al., 2008
Lesser Himalaya	1982	4	Gehrels et al., 2008
Lesser Himalaya	1986	3	Gehrels et al., 2008
Lesser Himalaya	1986	10	Gehrels et al., 2008
Lesser Himalaya	1986	4	Gehrels et al., 2008
Lesser Himalaya	1987	11	Gehrels et al., 2008
Lesser Himalaya	1988	30	Gehrels et al., 2008
Lesser Himalaya	1989	4	Gehrels et al., 2008
Lesser Himalaya	1992	6	Gehrels et al., 2008
Lesser Himalaya	1994	2	Gehrels et al., 2008
Lesser Himalaya	1995	6	Gehrels et al., 2008
Lesser Himalaya	1997	9	Gehrels et al., 2008
Lesser Himalaya	2001	9	Gehrels et al., 2008
Lesser Himalaya	2001	1	Gehrels et al., 2008
Lesser Himalaya	2004	8	Gehrels et al., 2008
Lesser Himalaya	2004	9	Gehrels et al., 2008
Lesser Himalaya	2005	5	Gehrels et al., 2008
Lesser Himalaya	2006	4	Gehrels et al., 2008
Lesser Himalaya	2006	5	Gehrels et al., 2008
Lesser Himalaya	2006	8	Gehrels et al., 2008
Lesser Himalaya	2006	6	Gehrels et al., 2008
Lesser Himalaya	2009	3	Gehrels et al., 2008
Lesser Himalaya	2010	3	Gehrels et al., 2008
Lesser Himalaya	2011	7	Gehrels et al., 2008
Lesser Himalaya	2012	6	Gehrels et al., 2008
Lesser Himalaya	2016	3	Gehrels et al., 2008
Lesser Himalaya	2017	9	Gehrels et al., 2008
Lesser Himalaya	2018	7	Gehrels et al., 2008
Lesser Himalaya	2018	6	Gehrels et al., 2008
Lesser Himalaya	2019	9	Gehrels et al., 2008
Lesser Himalaya	2019	4	Gehrels et al., 2008
Lesser Himalaya	2021	7	Gehrels et al., 2008
Lesser Himalaya	2022	25	Gehrels et al., 2008
Lesser Himalaya	2022	4	Gehrels et al., 2008
Lesser Himalaya	2025	7	Gehrels et al., 2008
Lesser Himalaya	2026	4	Gehrels et al., 2008
Lesser Himalaya	2026	8	Gehrels et al., 2008
Lesser Himalaya	2028	6	Gehrels et al., 2008
Lesser Himalaya	2034	2	Gehrels et al., 2008
Lesser Himalaya	2035	3	Gehrels et al., 2008
Lesser Himalaya	2035	8	Gehrels et al., 2008
Lesser Himalaya	2036	3	Gehrels et al., 2008
Lesser Himalaya	2037	10	Gehrels et al., 2008
Lesser Himalaya	2039	2	Gehrels et al., 2008
Lesser Himalaya	2040	11	Gehrels et al., 2008
Lesser Himalaya	2042	2	Gehrels et al., 2008
Lesser Himalaya	2046	18	Gehrels et al., 2008
Lesser Himalaya	2046	4	Gehrels et al., 2008
Lesser Himalaya	2046	4	Gehrels et al., 2008
Lesser Himalaya	2050	3	Gehrels et al., 2008
Lesser Himalaya	2051	14	Gehrels et al., 2008
Lesser Himalaya	2056	18	Gehrels et al., 2008
Lesser Himalaya	2062	2	Gehrels et al., 2008
Lesser Himalaya	2065	4	Gehrels et al., 2008
Lesser Himalaya	2074	9	Gehrels et al., 2008
Lesser Himalaya	2075	5	Gehrels et al., 2008
Lesser Himalaya	2080	7	Gehrels et al., 2008
Lesser Himalaya	2084	7	Gehrels et al., 2008
Lesser Himalaya	2085	9	Gehrels et al., 2008
Lesser Himalaya	2085	11	Gehrels et al., 2008
Lesser Himalaya	2087	3	Gehrels et al., 2008
Lesser Himalaya	2088	5	Gehrels et al., 2008
Lesser Himalaya	2100	10	Gehrels et al., 2008
Lesser Himalaya	2100	5	Gehrels et al., 2008
Lesser Himalaya	2101	2	Gehrels et al., 2008
Lesser Himalaya	2102	6	Gehrels et al., 2008

Lesser Himalaya	2103	3	Gehrels et al., 2008
Lesser Himalaya	2106	24	Gehrels et al., 2008
Lesser Himalaya	2108	2	Gehrels et al., 2008
Lesser Himalaya	2116	3	Gehrels et al., 2008
Lesser Himalaya	2127	5	Gehrels et al., 2008
Lesser Himalaya	2137	2	Gehrels et al., 2008
Lesser Himalaya	2137	2	Gehrels et al., 2008
Lesser Himalaya	2138	2	Gehrels et al., 2008
Lesser Himalaya	2142	3	Gehrels et al., 2008
Lesser Himalaya	2149	7	Gehrels et al., 2008
Lesser Himalaya	2149	8	Gehrels et al., 2008
Lesser Himalaya	2151	4	Gehrels et al., 2008
Lesser Himalaya	2151	6	Gehrels et al., 2008
Lesser Himalaya	2154	14	Gehrels et al., 2008
Lesser Himalaya	2154	3	Gehrels et al., 2008
Lesser Himalaya	2156	36	Gehrels et al., 2008
Lesser Himalaya	2157	1	Gehrels et al., 2008
Lesser Himalaya	2159	4	Gehrels et al., 2008
Lesser Himalaya	2160	14	Gehrels et al., 2008
Lesser Himalaya	2167	4	Gehrels et al., 2008
Lesser Himalaya	2176	14	Gehrels et al., 2008
Lesser Himalaya	2180	3	Gehrels et al., 2008
Lesser Himalaya	2186	32	Gehrels et al., 2008
Lesser Himalaya	2189	9	Gehrels et al., 2008
Lesser Himalaya	2193	6	Gehrels et al., 2008
Lesser Himalaya	2199	12	Gehrels et al., 2008
Lesser Himalaya	2201	17	Gehrels et al., 2008
Lesser Himalaya	2208	19	Gehrels et al., 2008
Lesser Himalaya	2215	4	Gehrels et al., 2008
Lesser Himalaya	2217	4	Gehrels et al., 2008
Lesser Himalaya	2217	5	Gehrels et al., 2008
Lesser Himalaya	2218	1	Gehrels et al., 2008
Lesser Himalaya	2222	5	Gehrels et al., 2008
Lesser Himalaya	2224	3	Gehrels et al., 2008
Lesser Himalaya	2226	1	Gehrels et al., 2008
Lesser Himalaya	2228	6	Gehrels et al., 2008
Lesser Himalaya	2231	19	Gehrels et al., 2008
Lesser Himalaya	2231	3	Gehrels et al., 2008
Lesser Himalaya	2233	6	Gehrels et al., 2008
Lesser Himalaya	2234	4	Gehrels et al., 2008
Lesser Himalaya	2235	3	Gehrels et al., 2008
Lesser Himalaya	2236	3	Gehrels et al., 2008
Lesser Himalaya	2238	14	Gehrels et al., 2008
Lesser Himalaya	2238	2	Gehrels et al., 2008
Lesser Himalaya	2242	7	Gehrels et al., 2008
Lesser Himalaya	2243	5	Gehrels et al., 2008
Lesser Himalaya	2251	3	Gehrels et al., 2008
Lesser Himalaya	2251	3	Gehrels et al., 2008
Lesser Himalaya	2263	19	Gehrels et al., 2008
Lesser Himalaya	2264	2	Gehrels et al., 2008
Lesser Himalaya	2270	3	Gehrels et al., 2008
Lesser Himalaya	2275	4	Gehrels et al., 2008
Lesser Himalaya	2277	6	Gehrels et al., 2008
Lesser Himalaya	2280	4	Gehrels et al., 2008
Lesser Himalaya	2282	39	Gehrels et al., 2008
Lesser Himalaya	2287	8	Gehrels et al., 2008
Lesser Himalaya	2288	3	Gehrels et al., 2008
Lesser Himalaya	2297	2	Gehrels et al., 2008
Lesser Himalaya	2298	2	Gehrels et al., 2008
Lesser Himalaya	2305	2	Gehrels et al., 2008
Lesser Himalaya	2312	1	Gehrels et al., 2008
Lesser Himalaya	2314	10	Gehrels et al., 2008
Lesser Himalaya	2314	2	Gehrels et al., 2008
Lesser Himalaya	2316	9	Gehrels et al., 2008
Lesser Himalaya	2328	4	Gehrels et al., 2008
Lesser Himalaya	2333	6	Gehrels et al., 2008
Lesser Himalaya	2345	12	Gehrels et al., 2008
Lesser Himalaya	2349	7	Gehrels et al., 2008
Lesser Himalaya	2355	10	Gehrels et al., 2008
Lesser Himalaya	2357	2	Gehrels et al., 2008
Lesser Himalaya	2358	32	Gehrels et al., 2008

Lesser Himalaya	2362	6	Gehrels et al., 2008
Lesser Himalaya	2363	4	Gehrels et al., 2008
Lesser Himalaya	2366	3	Gehrels et al., 2008
Lesser Himalaya	2368	3	Gehrels et al., 2008
Lesser Himalaya	2368	3	Gehrels et al., 2008
Lesser Himalaya	2373	14	Gehrels et al., 2008
Lesser Himalaya	2375	3	Gehrels et al., 2008
Lesser Himalaya	2381	4	Gehrels et al., 2008
Lesser Himalaya	2392	4	Gehrels et al., 2008
Lesser Himalaya	2395	2	Gehrels et al., 2008
Lesser Himalaya	2397	3	Gehrels et al., 2008
Lesser Himalaya	2398	14	Gehrels et al., 2008
Lesser Himalaya	2400	2	Gehrels et al., 2008
Lesser Himalaya	2400	5	Gehrels et al., 2008
Lesser Himalaya	2403	3	Gehrels et al., 2008
Lesser Himalaya	2406	20	Gehrels et al., 2008
Lesser Himalaya	2406	2	Gehrels et al., 2008
Lesser Himalaya	2418	5	Gehrels et al., 2008
Lesser Himalaya	2420	12	Gehrels et al., 2008
Lesser Himalaya	2423	2	Gehrels et al., 2008
Lesser Himalaya	2427	2	Gehrels et al., 2008
Lesser Himalaya	2429	12	Gehrels et al., 2008
Lesser Himalaya	2432	5	Gehrels et al., 2008
Lesser Himalaya	2432	10	Gehrels et al., 2008
Lesser Himalaya	2434	14	Gehrels et al., 2008
Lesser Himalaya	2435	9	Gehrels et al., 2008
Lesser Himalaya	2435	5	Gehrels et al., 2008
Lesser Himalaya	2436	4	Gehrels et al., 2008
Lesser Himalaya	2451	17	Gehrels et al., 2008
Lesser Himalaya	2451	33	Gehrels et al., 2008
Lesser Himalaya	2453	15	Gehrels et al., 2008
Lesser Himalaya	2454	12	Gehrels et al., 2008
Lesser Himalaya	2454	4	Gehrels et al., 2008
Lesser Himalaya	2455	5	Gehrels et al., 2008
Lesser Himalaya	2456	38	Gehrels et al., 2008
Lesser Himalaya	2461	3	Gehrels et al., 2008
Lesser Himalaya	2465	22	Gehrels et al., 2008
Lesser Himalaya	2467	5	Gehrels et al., 2008
Lesser Himalaya	2468	6	Gehrels et al., 2008
Lesser Himalaya	2469	10	Gehrels et al., 2008
Lesser Himalaya	2472	5	Gehrels et al., 2008
Lesser Himalaya	2476	10	Gehrels et al., 2008
Lesser Himalaya	2480	17	Gehrels et al., 2008
Lesser Himalaya	2480	14	Gehrels et al., 2008
Lesser Himalaya	2480	1	Gehrels et al., 2008
Lesser Himalaya	2486	3	Gehrels et al., 2008
Lesser Himalaya	2493	3	Gehrels et al., 2008
Lesser Himalaya	2494	5	Gehrels et al., 2008
Lesser Himalaya	2494	6	Gehrels et al., 2008
Lesser Himalaya	2495	7	Gehrels et al., 2008
Lesser Himalaya	2495	2	Gehrels et al., 2008
Lesser Himalaya	2498	7	Gehrels et al., 2008
Lesser Himalaya	2499	2	Gehrels et al., 2008
Lesser Himalaya	2500	3	Gehrels et al., 2008
Lesser Himalaya	2501	22	Gehrels et al., 2008
Lesser Himalaya	2502	12	Gehrels et al., 2008
Lesser Himalaya	2504	6	Gehrels et al., 2008
Lesser Himalaya	2510	12	Gehrels et al., 2008
Lesser Himalaya	2516	2	Gehrels et al., 2008
Lesser Himalaya	2516	3	Gehrels et al., 2008
Lesser Himalaya	2516	4	Gehrels et al., 2008
Lesser Himalaya	2518	13	Gehrels et al., 2008
Lesser Himalaya	2520	5	Gehrels et al., 2008
Lesser Himalaya	2523	9	Gehrels et al., 2008
Lesser Himalaya	2523	12	Gehrels et al., 2008
Lesser Himalaya	2524	4	Gehrels et al., 2008
Lesser Himalaya	2524	7	Gehrels et al., 2008
Lesser Himalaya	2524	2	Gehrels et al., 2008
Lesser Himalaya	2529	24	Gehrels et al., 2008
Lesser Himalaya	2534	6	Gehrels et al., 2008
Lesser Himalaya	2534	3	Gehrels et al., 2008

Lesser Himalaya	2534	3	Gehrels et al., 2008
Lesser Himalaya	2535	3	Gehrels et al., 2008
Lesser Himalaya	2537	4	Gehrels et al., 2008
Lesser Himalaya	2538	2	Gehrels et al., 2008
Lesser Himalaya	2540	5	Gehrels et al., 2008
Lesser Himalaya	2541	4	Gehrels et al., 2008
Lesser Himalaya	2543	16	Gehrels et al., 2008
Lesser Himalaya	2543	1	Gehrels et al., 2008
Lesser Himalaya	2543	1	Gehrels et al., 2008
Lesser Himalaya	2544	3	Gehrels et al., 2008
Lesser Himalaya	2545	17	Gehrels et al., 2008
Lesser Himalaya	2546	3	Gehrels et al., 2008
Lesser Himalaya	2546	5	Gehrels et al., 2008
Lesser Himalaya	2548	2	Gehrels et al., 2008
Lesser Himalaya	2551	4	Gehrels et al., 2008
Lesser Himalaya	2552	3	Gehrels et al., 2008
Lesser Himalaya	2553	7	Gehrels et al., 2008
Lesser Himalaya	2554	3	Gehrels et al., 2008
Lesser Himalaya	2555	3	Gehrels et al., 2008
Lesser Himalaya	2555	3	Gehrels et al., 2008
Lesser Himalaya	2556	7	Gehrels et al., 2008
Lesser Himalaya	2556	2	Gehrels et al., 2008
Lesser Himalaya	2556	3	Gehrels et al., 2008
Lesser Himalaya	2562	7	Gehrels et al., 2008
Lesser Himalaya	2563	3	Gehrels et al., 2008
Lesser Himalaya	2564	26	Gehrels et al., 2008
Lesser Himalaya	2564	8	Gehrels et al., 2008
Lesser Himalaya	2565	5	Gehrels et al., 2008
Lesser Himalaya	2566	2	Gehrels et al., 2008
Lesser Himalaya	2567	4	Gehrels et al., 2008
Lesser Himalaya	2568	1	Gehrels et al., 2008
Lesser Himalaya	2569	9	Gehrels et al., 2008
Lesser Himalaya	2569	9	Gehrels et al., 2008
Lesser Himalaya	2569	5	Gehrels et al., 2008
Lesser Himalaya	2569	2	Gehrels et al., 2008
Lesser Himalaya	2572	3	Gehrels et al., 2008
Lesser Himalaya	2573	2	Gehrels et al., 2008
Lesser Himalaya	2573	2	Gehrels et al., 2008
Lesser Himalaya	2575	3	Gehrels et al., 2008
Lesser Himalaya	2576	3	Gehrels et al., 2008
Lesser Himalaya	2579	6	Gehrels et al., 2008
Lesser Himalaya	2579	5	Gehrels et al., 2008
Lesser Himalaya	2579	7	Gehrels et al., 2008
Lesser Himalaya	2580	2	Gehrels et al., 2008
Lesser Himalaya	2581	11	Gehrels et al., 2008
Lesser Himalaya	2581	2	Gehrels et al., 2008
Lesser Himalaya	2581	3	Gehrels et al., 2008
Lesser Himalaya	2590	2	Gehrels et al., 2008
Lesser Himalaya	2592	8	Gehrels et al., 2008
Lesser Himalaya	2593	4	Gehrels et al., 2008
Lesser Himalaya	2596	6	Gehrels et al., 2008
Lesser Himalaya	2597	2	Gehrels et al., 2008
Lesser Himalaya	2600	19	Gehrels et al., 2008
Lesser Himalaya	2602	1	Gehrels et al., 2008
Lesser Himalaya	2607	27	Gehrels et al., 2008
Lesser Himalaya	2616	2	Gehrels et al., 2008
Lesser Himalaya	2619	10	Gehrels et al., 2008
Lesser Himalaya	2621	6	Gehrels et al., 2008
Lesser Himalaya	2627	3	Gehrels et al., 2008
Lesser Himalaya	2629	3	Gehrels et al., 2008
Lesser Himalaya	2629	3	Gehrels et al., 2008
Lesser Himalaya	2635	7	Gehrels et al., 2008
Lesser Himalaya	2636	1	Gehrels et al., 2008
Lesser Himalaya	2645	4	Gehrels et al., 2008
Lesser Himalaya	2653	4	Gehrels et al., 2008
Lesser Himalaya	2663	4	Gehrels et al., 2008
Lesser Himalaya	2671	3	Gehrels et al., 2008
Lesser Himalaya	2674	3	Gehrels et al., 2008
Lesser Himalaya	2680	1	Gehrels et al., 2008
Lesser Himalaya	2687	6	Gehrels et al., 2008
Lesser Himalaya	2689	2	Gehrels et al., 2008

Lesser Himalaya	2690	9	Gehrels et al., 2008
Lesser Himalaya	2690	3	Gehrels et al., 2008
Lesser Himalaya	2693	3	Gehrels et al., 2008
Lesser Himalaya	2693	2	Gehrels et al., 2008
Lesser Himalaya	2718	6	Gehrels et al., 2008
Lesser Himalaya	2720	2	Gehrels et al., 2008
Lesser Himalaya	2720	3	Gehrels et al., 2008
Lesser Himalaya	2723	4	Gehrels et al., 2008
Lesser Himalaya	2728	1	Gehrels et al., 2008
Lesser Himalaya	2730	4	Gehrels et al., 2008
Lesser Himalaya	2739	14	Gehrels et al., 2008
Lesser Himalaya	2753	10	Gehrels et al., 2008
Lesser Himalaya	2759	14	Gehrels et al., 2008
Lesser Himalaya	2764	3	Gehrels et al., 2008
Lesser Himalaya	2769	8	Gehrels et al., 2008
Lesser Himalaya	2774	5	Gehrels et al., 2008
Lesser Himalaya	2779	3	Gehrels et al., 2008
Lesser Himalaya	2779	2	Gehrels et al., 2008
Lesser Himalaya	2782	5	Gehrels et al., 2008
Lesser Himalaya	2788	2	Gehrels et al., 2008
Lesser Himalaya	2793	3	Gehrels et al., 2008
Lesser Himalaya	2813	8	Gehrels et al., 2008
Lesser Himalaya	2845	1	Gehrels et al., 2008
Lesser Himalaya	2846	1	Gehrels et al., 2008
Lesser Himalaya	2850	3	Gehrels et al., 2008
Lesser Himalaya	2860	3	Gehrels et al., 2008
Lesser Himalaya	2900	33	Gehrels et al., 2008
Lesser Himalaya	2901	2	Gehrels et al., 2008
Lesser Himalaya	2925	2	Gehrels et al., 2008
Lesser Himalaya	2943	2	Gehrels et al., 2008
Lesser Himalaya	2955	2	Gehrels et al., 2008
Lesser Himalaya	2966	13	Gehrels et al., 2008
Lesser Himalaya	2991	7	Gehrels et al., 2008
Lesser Himalaya	3002	3	Gehrels et al., 2008
Lesser Himalaya	3171	3	Gehrels et al., 2008
Lesser Himalaya	3232	1	Gehrels et al., 2008
Lesser Himalaya	3267	7	Gehrels et al., 2008
Lesser Himalaya	3268	2	Gehrels et al., 2008
Lesser Himalaya	3301	1	Gehrels et al., 2008
Lesser Himalaya	3348	1	Gehrels et al., 2008
Lesser Himalaya	3352	3	Gehrels et al., 2008
Lesser Himalaya	3455	12	Gehrels et al., 2008
Lesser Himalaya	3526	7	Gehrels et al., 2008
Greater Himalaya	555	56	Gehrels et al., 2008
Greater Himalaya	575	58	Gehrels et al., 2008
Greater Himalaya	621	10	Gehrels et al., 2008
Greater Himalaya	623	29	Gehrels et al., 2008
Greater Himalaya	630	9	Gehrels et al., 2008
Greater Himalaya	639	24	Gehrels et al., 2008
Greater Himalaya	640	14	Gehrels et al., 2008
Greater Himalaya	653	8	Gehrels et al., 2008
Greater Himalaya	663	8	Gehrels et al., 2008
Greater Himalaya	683	8	Gehrels et al., 2008
Greater Himalaya	693	41	Gehrels et al., 2008
Greater Himalaya	709	3	Gehrels et al., 2008
Greater Himalaya	710	9	Gehrels et al., 2008
Greater Himalaya	715	9	Gehrels et al., 2008
Greater Himalaya	718	9	Gehrels et al., 2008
Greater Himalaya	720	13	Gehrels et al., 2008
Greater Himalaya	727	38	Gehrels et al., 2008
Greater Himalaya	727	73	Gehrels et al., 2008
Greater Himalaya	728	21	Gehrels et al., 2008
Greater Himalaya	734	22	Gehrels et al., 2008
Greater Himalaya	747	75	Gehrels et al., 2008
Greater Himalaya	752	22	Gehrels et al., 2008
Greater Himalaya	752	56	Gehrels et al., 2008
Greater Himalaya	756	8	Gehrels et al., 2008
Greater Himalaya	757	76	Gehrels et al., 2008
Greater Himalaya	759	8	Gehrels et al., 2008
Greater Himalaya	767	9	Gehrels et al., 2008
Greater Himalaya	767	77	Gehrels et al., 2008

Greater Himalaya	770	29	Gehrels et al., 2008
Greater Himalaya	776	24	Gehrels et al., 2008
Greater Himalaya	789	19	Gehrels et al., 2008
Greater Himalaya	807	46	Gehrels et al., 2008
Greater Himalaya	808	10	Gehrels et al., 2008
Greater Himalaya	808	10	Gehrels et al., 2008
Greater Himalaya	813	12	Gehrels et al., 2008
Greater Himalaya	815	21	Gehrels et al., 2008
Greater Himalaya	816	4	Gehrels et al., 2008
Greater Himalaya	821	14	Gehrels et al., 2008
Greater Himalaya	831	9	Gehrels et al., 2008
Greater Himalaya	833	10	Gehrels et al., 2008
Greater Himalaya	833	26	Gehrels et al., 2008
Greater Himalaya	834	22	Gehrels et al., 2008
Greater Himalaya	843	55	Gehrels et al., 2008
Greater Himalaya	846	23	Gehrels et al., 2008
Greater Himalaya	848	6	Gehrels et al., 2008
Greater Himalaya	848	25	Gehrels et al., 2008
Greater Himalaya	850	33	Gehrels et al., 2008
Greater Himalaya	858	9	Gehrels et al., 2008
Greater Himalaya	862	41	Gehrels et al., 2008
Greater Himalaya	863	11	Gehrels et al., 2008
Greater Himalaya	864	13	Gehrels et al., 2008
Greater Himalaya	865	5	Gehrels et al., 2008
Greater Himalaya	866	8	Gehrels et al., 2008
Greater Himalaya	869	11	Gehrels et al., 2008
Greater Himalaya	870	35	Gehrels et al., 2008
Greater Himalaya	870	39	Gehrels et al., 2008
Greater Himalaya	871	42	Gehrels et al., 2008
Greater Himalaya	872	11	Gehrels et al., 2008
Greater Himalaya	873	23	Gehrels et al., 2008
Greater Himalaya	875	13	Gehrels et al., 2008
Greater Himalaya	876	7	Gehrels et al., 2008
Greater Himalaya	877	7	Gehrels et al., 2008
Greater Himalaya	879	14	Gehrels et al., 2008
Greater Himalaya	879	18	Gehrels et al., 2008
Greater Himalaya	884	21	Gehrels et al., 2008
Greater Himalaya	887	11	Gehrels et al., 2008
Greater Himalaya	888	20	Gehrels et al., 2008
Greater Himalaya	888	11	Gehrels et al., 2008
Greater Himalaya	888	17	Gehrels et al., 2008
Greater Himalaya	894	21	Gehrels et al., 2008
Greater Himalaya	894	11	Gehrels et al., 2008
Greater Himalaya	895	22	Gehrels et al., 2008
Greater Himalaya	895	10	Gehrels et al., 2008
Greater Himalaya	895	7	Gehrels et al., 2008
Greater Himalaya	898	12	Gehrels et al., 2008
Greater Himalaya	899	11	Gehrels et al., 2008
Greater Himalaya	899	4	Gehrels et al., 2008
Greater Himalaya	899	54	Gehrels et al., 2008
Greater Himalaya	900	22	Gehrels et al., 2008
Greater Himalaya	900	26	Gehrels et al., 2008
Greater Himalaya	902	5	Gehrels et al., 2008
Greater Himalaya	902	17	Gehrels et al., 2008
Greater Himalaya	905	11	Gehrels et al., 2008
Greater Himalaya	907	11	Gehrels et al., 2008
Greater Himalaya	908	11	Gehrels et al., 2008
Greater Himalaya	910	13	Gehrels et al., 2008
Greater Himalaya	910	7	Gehrels et al., 2008
Greater Himalaya	910	8	Gehrels et al., 2008
Greater Himalaya	912	21	Gehrels et al., 2008
Greater Himalaya	916	15	Gehrels et al., 2008
Greater Himalaya	916	19	Gehrels et al., 2008
Greater Himalaya	917	14	Gehrels et al., 2008
Greater Himalaya	918	13	Gehrels et al., 2008
Greater Himalaya	920	11	Gehrels et al., 2008
Greater Himalaya	922	4	Gehrels et al., 2008
Greater Himalaya	924	30	Gehrels et al., 2008
Greater Himalaya	924	21	Gehrels et al., 2008
Greater Himalaya	925	7	Gehrels et al., 2008
Greater Himalaya	925	30	Gehrels et al., 2008

Greater Himalaya	927	20	Gehrels et al., 2008
Greater Himalaya	930	13	Gehrels et al., 2008
Greater Himalaya	935	5	Gehrels et al., 2008
Greater Himalaya	936	21	Gehrels et al., 2008
Greater Himalaya	936	13	Gehrels et al., 2008
Greater Himalaya	939	25	Gehrels et al., 2008
Greater Himalaya	941	20	Gehrels et al., 2008
Greater Himalaya	942	11	Gehrels et al., 2008
Greater Himalaya	942	5	Gehrels et al., 2008
Greater Himalaya	946	21	Gehrels et al., 2008
Greater Himalaya	946	21	Gehrels et al., 2008
Greater Himalaya	947	10	Gehrels et al., 2008
Greater Himalaya	947	8	Gehrels et al., 2008
Greater Himalaya	950	11	Gehrels et al., 2008
Greater Himalaya	950	33	Gehrels et al., 2008
Greater Himalaya	950	19	Gehrels et al., 2008
Greater Himalaya	952	23	Gehrels et al., 2008
Greater Himalaya	953	35	Gehrels et al., 2008
Greater Himalaya	955	13	Gehrels et al., 2008
Greater Himalaya	956	6	Gehrels et al., 2008
Greater Himalaya	956	96	Gehrels et al., 2008
Greater Himalaya	958	5	Gehrels et al., 2008
Greater Himalaya	959	13	Gehrels et al., 2008
Greater Himalaya	962	25	Gehrels et al., 2008
Greater Himalaya	963	14	Gehrels et al., 2008
Greater Himalaya	964	21	Gehrels et al., 2008
Greater Himalaya	964	8	Gehrels et al., 2008
Greater Himalaya	968	12	Gehrels et al., 2008
Greater Himalaya	968	3	Gehrels et al., 2008
Greater Himalaya	970	15	Gehrels et al., 2008
Greater Himalaya	970	5	Gehrels et al., 2008
Greater Himalaya	971	11	Gehrels et al., 2008
Greater Himalaya	971	51	Gehrels et al., 2008
Greater Himalaya	972	23	Gehrels et al., 2008
Greater Himalaya	972	12	Gehrels et al., 2008
Greater Himalaya	973	11	Gehrels et al., 2008
Greater Himalaya	974	21	Gehrels et al., 2008
Greater Himalaya	976	13	Gehrels et al., 2008
Greater Himalaya	978	9	Gehrels et al., 2008
Greater Himalaya	982	21	Gehrels et al., 2008
Greater Himalaya	982	7	Gehrels et al., 2008
Greater Himalaya	982	43	Gehrels et al., 2008
Greater Himalaya	982	44	Gehrels et al., 2008
Greater Himalaya	986	30	Gehrels et al., 2008
Greater Himalaya	988	69	Gehrels et al., 2008
Greater Himalaya	988	10	Gehrels et al., 2008
Greater Himalaya	989	28	Gehrels et al., 2008
Greater Himalaya	990	12	Gehrels et al., 2008
Greater Himalaya	993	6	Gehrels et al., 2008
Greater Himalaya	994	37	Gehrels et al., 2008
Greater Himalaya	994	45	Gehrels et al., 2008
Greater Himalaya	999	15	Gehrels et al., 2008
Greater Himalaya	1002	14	Gehrels et al., 2008
Greater Himalaya	1002	32	Gehrels et al., 2008
Greater Himalaya	1004	12	Gehrels et al., 2008
Greater Himalaya	1005	79	Gehrels et al., 2008
Greater Himalaya	1006	23	Gehrels et al., 2008
Greater Himalaya	1010	21	Gehrels et al., 2008
Greater Himalaya	1011	21	Gehrels et al., 2008
Greater Himalaya	1012	21	Gehrels et al., 2008
Greater Himalaya	1013	19	Gehrels et al., 2008
Greater Himalaya	1015	20	Gehrels et al., 2008
Greater Himalaya	1017	17	Gehrels et al., 2008
Greater Himalaya	1018	20	Gehrels et al., 2008
Greater Himalaya	1019	21	Gehrels et al., 2008
Greater Himalaya	1019	34	Gehrels et al., 2008
Greater Himalaya	1019	50	Gehrels et al., 2008
Greater Himalaya	1023	8	Gehrels et al., 2008
Greater Himalaya	1024	22	Gehrels et al., 2008
Greater Himalaya	1027	20	Gehrels et al., 2008
Greater Himalaya	1027	23	Gehrels et al., 2008

Greater Himalaya	1027	18	Gehrels et al., 2008
Greater Himalaya	1030	20	Gehrels et al., 2008
Greater Himalaya	1030	4	Gehrels et al., 2008
Greater Himalaya	1030	25	Gehrels et al., 2008
Greater Himalaya	1030	17	Gehrels et al., 2008
Greater Himalaya	1032	20	Gehrels et al., 2008
Greater Himalaya	1032	15	Gehrels et al., 2008
Greater Himalaya	1032	19	Gehrels et al., 2008
Greater Himalaya	1034	31	Gehrels et al., 2008
Greater Himalaya	1036	25	Gehrels et al., 2008
Greater Himalaya	1036	38	Gehrels et al., 2008
Greater Himalaya	1036	19	Gehrels et al., 2008
Greater Himalaya	1036	32	Gehrels et al., 2008
Greater Himalaya	1037	20	Gehrels et al., 2008
Greater Himalaya	1038	21	Gehrels et al., 2008
Greater Himalaya	1042	33	Gehrels et al., 2008
Greater Himalaya	1042	23	Gehrels et al., 2008
Greater Himalaya	1043	20	Gehrels et al., 2008
Greater Himalaya	1043	21	Gehrels et al., 2008
Greater Himalaya	1043	21	Gehrels et al., 2008
Greater Himalaya	1043	8	Gehrels et al., 2008
Greater Himalaya	1044	20	Gehrels et al., 2008
Greater Himalaya	1044	20	Gehrels et al., 2008
Greater Himalaya	1045	21	Gehrels et al., 2008
Greater Himalaya	1045	23	Gehrels et al., 2008
Greater Himalaya	1045	29	Gehrels et al., 2008
Greater Himalaya	1047	22	Gehrels et al., 2008
Greater Himalaya	1049	21	Gehrels et al., 2008
Greater Himalaya	1049	4	Gehrels et al., 2008
Greater Himalaya	1049	75	Gehrels et al., 2008
Greater Himalaya	1052	27	Gehrels et al., 2008
Greater Himalaya	1052	20	Gehrels et al., 2008
Greater Himalaya	1054	27	Gehrels et al., 2008
Greater Himalaya	1055	20	Gehrels et al., 2008
Greater Himalaya	1056	20	Gehrels et al., 2008
Greater Himalaya	1057	20	Gehrels et al., 2008
Greater Himalaya	1057	20	Gehrels et al., 2008
Greater Himalaya	1057	4	Gehrels et al., 2008
Greater Himalaya	1060	57	Gehrels et al., 2008
Greater Himalaya	1060	35	Gehrels et al., 2008
Greater Himalaya	1060	20	Gehrels et al., 2008
Greater Himalaya	1060	20	Gehrels et al., 2008
Greater Himalaya	1060	31	Gehrels et al., 2008
Greater Himalaya	1061	21	Gehrels et al., 2008
Greater Himalaya	1063	22	Gehrels et al., 2008
Greater Himalaya	1063	17	Gehrels et al., 2008
Greater Himalaya	1063	12	Gehrels et al., 2008
Greater Himalaya	1066	20	Gehrels et al., 2008
Greater Himalaya	1067	21	Gehrels et al., 2008
Greater Himalaya	1068	21	Gehrels et al., 2008
Greater Himalaya	1068	21	Gehrels et al., 2008
Greater Himalaya	1069	20	Gehrels et al., 2008
Greater Himalaya	1069	21	Gehrels et al., 2008
Greater Himalaya	1069	20	Gehrels et al., 2008
Greater Himalaya	1073	25	Gehrels et al., 2008
Greater Himalaya	1073	15	Gehrels et al., 2008
Greater Himalaya	1075	22	Gehrels et al., 2008
Greater Himalaya	1077	21	Gehrels et al., 2008
Greater Himalaya	1082	20	Gehrels et al., 2008
Greater Himalaya	1085	20	Gehrels et al., 2008
Greater Himalaya	1085	20	Gehrels et al., 2008
Greater Himalaya	1085	17	Gehrels et al., 2008
Greater Himalaya	1086	25	Gehrels et al., 2008
Greater Himalaya	1089	30	Gehrels et al., 2008
Greater Himalaya	1089	22	Gehrels et al., 2008
Greater Himalaya	1089	18	Gehrels et al., 2008
Greater Himalaya	1090	20	Gehrels et al., 2008
Greater Himalaya	1090	12	Gehrels et al., 2008
Greater Himalaya	1091	20	Gehrels et al., 2008
Greater Himalaya	1091	20	Gehrels et al., 2008
Greater Himalaya	1091	4	Gehrels et al., 2008

Greater Himalaya	1093	72	Gehrels et al., 2008
Greater Himalaya	1093	28	Gehrels et al., 2008
Greater Himalaya	1097	105	Gehrels et al., 2008
Greater Himalaya	1098	22	Gehrels et al., 2008
Greater Himalaya	1100	28	Gehrels et al., 2008
Greater Himalaya	1106	20	Gehrels et al., 2008
Greater Himalaya	1107	41	Gehrels et al., 2008
Greater Himalaya	1109	26	Gehrels et al., 2008
Greater Himalaya	1110	15	Gehrels et al., 2008
Greater Himalaya	1111	20	Gehrels et al., 2008
Greater Himalaya	1112	22	Gehrels et al., 2008
Greater Himalaya	1113	45	Gehrels et al., 2008
Greater Himalaya	1113	19	Gehrels et al., 2008
Greater Himalaya	1113	5	Gehrels et al., 2008
Greater Himalaya	1114	42	Gehrels et al., 2008
Greater Himalaya	1114	13	Gehrels et al., 2008
Greater Himalaya	1114	37	Gehrels et al., 2008
Greater Himalaya	1117	32	Gehrels et al., 2008
Greater Himalaya	1118	79	Gehrels et al., 2008
Greater Himalaya	1120	20	Gehrels et al., 2008
Greater Himalaya	1120	5	Gehrels et al., 2008
Greater Himalaya	1125	20	Gehrels et al., 2008
Greater Himalaya	1126	5	Gehrels et al., 2008
Greater Himalaya	1127	20	Gehrels et al., 2008
Greater Himalaya	1129	18	Gehrels et al., 2008
Greater Himalaya	1132	20	Gehrels et al., 2008
Greater Himalaya	1132	23	Gehrels et al., 2008
Greater Himalaya	1135	21	Gehrels et al., 2008
Greater Himalaya	1137	20	Gehrels et al., 2008
Greater Himalaya	1137	15	Gehrels et al., 2008
Greater Himalaya	1137	20	Gehrels et al., 2008
Greater Himalaya	1137	5	Gehrels et al., 2008
Greater Himalaya	1138	20	Gehrels et al., 2008
Greater Himalaya	1138	20	Gehrels et al., 2008
Greater Himalaya	1140	15	Gehrels et al., 2008
Greater Himalaya	1141	15	Gehrels et al., 2008
Greater Himalaya	1142	10	Gehrels et al., 2008
Greater Himalaya	1143	20	Gehrels et al., 2008
Greater Himalaya	1144	24	Gehrels et al., 2008
Greater Himalaya	1145	16	Gehrels et al., 2008
Greater Himalaya	1146	7	Gehrels et al., 2008
Greater Himalaya	1147	26	Gehrels et al., 2008
Greater Himalaya	1148	20	Gehrels et al., 2008
Greater Himalaya	1152	11	Gehrels et al., 2008
Greater Himalaya	1153	20	Gehrels et al., 2008
Greater Himalaya	1154	38	Gehrels et al., 2008
Greater Himalaya	1154	32	Gehrels et al., 2008
Greater Himalaya	1155	57	Gehrels et al., 2008
Greater Himalaya	1156	44	Gehrels et al., 2008
Greater Himalaya	1157	20	Gehrels et al., 2008
Greater Himalaya	1162	20	Gehrels et al., 2008
Greater Himalaya	1162	20	Gehrels et al., 2008
Greater Himalaya	1162	37	Gehrels et al., 2008
Greater Himalaya	1164	28	Gehrels et al., 2008
Greater Himalaya	1164	22	Gehrels et al., 2008
Greater Himalaya	1164	28	Gehrels et al., 2008
Greater Himalaya	1166	35	Gehrels et al., 2008
Greater Himalaya	1166	28	Gehrels et al., 2008
Greater Himalaya	1167	20	Gehrels et al., 2008
Greater Himalaya	1167	20	Gehrels et al., 2008
Greater Himalaya	1169	24	Gehrels et al., 2008
Greater Himalaya	1169	24	Gehrels et al., 2008
Greater Himalaya	1171	20	Gehrels et al., 2008
Greater Himalaya	1171	22	Gehrels et al., 2008
Greater Himalaya	1171	5	Gehrels et al., 2008
Greater Himalaya	1174	7	Gehrels et al., 2008
Greater Himalaya	1174	16	Gehrels et al., 2008
Greater Himalaya	1176	20	Gehrels et al., 2008
Greater Himalaya	1176	3	Gehrels et al., 2008
Greater Himalaya	1177	25	Gehrels et al., 2008
Greater Himalaya	1178	17	Gehrels et al., 2008

Greater Himalaya	1179	20	Gehrels et al., 2008
Greater Himalaya	1179	15	Gehrels et al., 2008
Greater Himalaya	1181	24	Gehrels et al., 2008
Greater Himalaya	1181	24	Gehrels et al., 2008
Greater Himalaya	1182	21	Gehrels et al., 2008
Greater Himalaya	1188	22	Gehrels et al., 2008
Greater Himalaya	1188	10	Gehrels et al., 2008
Greater Himalaya	1188	32	Gehrels et al., 2008
Greater Himalaya	1193	20	Gehrels et al., 2008
Greater Himalaya	1198	21	Gehrels et al., 2008
Greater Himalaya	1198	9	Gehrels et al., 2008
Greater Himalaya	1199	23	Gehrels et al., 2008
Greater Himalaya	1199	23	Gehrels et al., 2008
Greater Himalaya	1201	64	Gehrels et al., 2008
Greater Himalaya	1203	21	Gehrels et al., 2008
Greater Himalaya	1203	20	Gehrels et al., 2008
Greater Himalaya	1203	21	Gehrels et al., 2008
Greater Himalaya	1205	35	Gehrels et al., 2008
Greater Himalaya	1208	25	Gehrels et al., 2008
Greater Himalaya	1208	25	Gehrels et al., 2008
Greater Himalaya	1208	38	Gehrels et al., 2008
Greater Himalaya	1209	8	Gehrels et al., 2008
Greater Himalaya	1211	57	Gehrels et al., 2008
Greater Himalaya	1215	25	Gehrels et al., 2008
Greater Himalaya	1215	25	Gehrels et al., 2008
Greater Himalaya	1215	29	Gehrels et al., 2008
Greater Himalaya	1218	11	Gehrels et al., 2008
Greater Himalaya	1220	20	Gehrels et al., 2008
Greater Himalaya	1220	20	Gehrels et al., 2008
Greater Himalaya	1220	4	Gehrels et al., 2008
Greater Himalaya	1220	3	Gehrels et al., 2008
Greater Himalaya	1222	24	Gehrels et al., 2008
Greater Himalaya	1226	21	Gehrels et al., 2008
Greater Himalaya	1226	11	Gehrels et al., 2008
Greater Himalaya	1234	20	Gehrels et al., 2008
Greater Himalaya	1241	20	Gehrels et al., 2008
Greater Himalaya	1250	18	Gehrels et al., 2008
Greater Himalaya	1252	25	Gehrels et al., 2008
Greater Himalaya	1256	20	Gehrels et al., 2008
Greater Himalaya	1256	6	Gehrels et al., 2008
Greater Himalaya	1258	36	Gehrels et al., 2008
Greater Himalaya	1261	21	Gehrels et al., 2008
Greater Himalaya	1261	24	Gehrels et al., 2008
Greater Himalaya	1261	21	Gehrels et al., 2008
Greater Himalaya	1261	13	Gehrels et al., 2008
Greater Himalaya	1269	41	Gehrels et al., 2008
Greater Himalaya	1269	36	Gehrels et al., 2008
Greater Himalaya	1271	42	Gehrels et al., 2008
Greater Himalaya	1271	9	Gehrels et al., 2008
Greater Himalaya	1271	37	Gehrels et al., 2008
Greater Himalaya	1273	55	Gehrels et al., 2008
Greater Himalaya	1274	23	Gehrels et al., 2008
Greater Himalaya	1274	11	Gehrels et al., 2008
Greater Himalaya	1282	20	Gehrels et al., 2008
Greater Himalaya	1288	22	Gehrels et al., 2008
Greater Himalaya	1292	22	Gehrels et al., 2008
Greater Himalaya	1292	10	Gehrels et al., 2008
Greater Himalaya	1293	4	Gehrels et al., 2008
Greater Himalaya	1296	37	Gehrels et al., 2008
Greater Himalaya	1300	6	Gehrels et al., 2008
Greater Himalaya	1301	7	Gehrels et al., 2008
Greater Himalaya	1311	7	Gehrels et al., 2008
Greater Himalaya	1314	50	Gehrels et al., 2008
Greater Himalaya	1316	4	Gehrels et al., 2008
Greater Himalaya	1321	23	Gehrels et al., 2008
Greater Himalaya	1323	18	Gehrels et al., 2008
Greater Himalaya	1325	14	Gehrels et al., 2008
Greater Himalaya	1328	14	Gehrels et al., 2008
Greater Himalaya	1345	56	Gehrels et al., 2008
Greater Himalaya	1370	20	Gehrels et al., 2008
Greater Himalaya	1379	19	Gehrels et al., 2008

Greater Himalaya	1383	20	Gehrels et al., 2008
Greater Himalaya	1383	20	Gehrels et al., 2008
Greater Himalaya	1383	15	Gehrels et al., 2008
Greater Himalaya	1394	21	Gehrels et al., 2008
Greater Himalaya	1395	3	Gehrels et al., 2008
Greater Himalaya	1401	21	Gehrels et al., 2008
Greater Himalaya	1401	21	Gehrels et al., 2008
Greater Himalaya	1402	42	Gehrels et al., 2008
Greater Himalaya	1408	10	Gehrels et al., 2008
Greater Himalaya	1415	55	Gehrels et al., 2008
Greater Himalaya	1415	52	Gehrels et al., 2008
Greater Himalaya	1415	16	Gehrels et al., 2008
Greater Himalaya	1415	4	Gehrels et al., 2008
Greater Himalaya	1417	26	Gehrels et al., 2008
Greater Himalaya	1440	36	Gehrels et al., 2008
Greater Himalaya	1440	30	Gehrels et al., 2008
Greater Himalaya	1450	126	Gehrels et al., 2008
Greater Himalaya	1452	20	Gehrels et al., 2008
Greater Himalaya	1460	7	Gehrels et al., 2008
Greater Himalaya	1468	20	Gehrels et al., 2008
Greater Himalaya	1468	20	Gehrels et al., 2008
Greater Himalaya	1485	26	Gehrels et al., 2008
Greater Himalaya	1489	11	Gehrels et al., 2008
Greater Himalaya	1497	19	Gehrels et al., 2008
Greater Himalaya	1497	5	Gehrels et al., 2008
Greater Himalaya	1509	28	Gehrels et al., 2008
Greater Himalaya	1511	19	Gehrels et al., 2008
Greater Himalaya	1511	19	Gehrels et al., 2008
Greater Himalaya	1511	6	Gehrels et al., 2008
Greater Himalaya	1517	19	Gehrels et al., 2008
Greater Himalaya	1517	19	Gehrels et al., 2008
Greater Himalaya	1518	49	Gehrels et al., 2008
Greater Himalaya	1539	24	Gehrels et al., 2008
Greater Himalaya	1539	15	Gehrels et al., 2008
Greater Himalaya	1542	19	Gehrels et al., 2008
Greater Himalaya	1544	15	Gehrels et al., 2008
Greater Himalaya	1548	10	Gehrels et al., 2008
Greater Himalaya	1549	19	Gehrels et al., 2008
Greater Himalaya	1549	4	Gehrels et al., 2008
Greater Himalaya	1551	21	Gehrels et al., 2008
Greater Himalaya	1551	9	Gehrels et al., 2008
Greater Himalaya	1554	8	Gehrels et al., 2008
Greater Himalaya	1556	6	Gehrels et al., 2008
Greater Himalaya	1573	19	Gehrels et al., 2008
Greater Himalaya	1573	19	Gehrels et al., 2008
Greater Himalaya	1574	3	Gehrels et al., 2008
Greater Himalaya	1586	16	Gehrels et al., 2008
Greater Himalaya	1589	6	Gehrels et al., 2008
Greater Himalaya	1594	19	Gehrels et al., 2008
Greater Himalaya	1594	4	Gehrels et al., 2008
Greater Himalaya	1595	16	Gehrels et al., 2008
Greater Himalaya	1607	20	Gehrels et al., 2008
Greater Himalaya	1607	20	Gehrels et al., 2008
Greater Himalaya	1609	38	Gehrels et al., 2008
Greater Himalaya	1610	23	Gehrels et al., 2008
Greater Himalaya	1610	13	Gehrels et al., 2008
Greater Himalaya	1615	7	Gehrels et al., 2008
Greater Himalaya	1621	12	Gehrels et al., 2008
Greater Himalaya	1625	10	Gehrels et al., 2008
Greater Himalaya	1626	9	Gehrels et al., 2008
Greater Himalaya	1629	6	Gehrels et al., 2008
Greater Himalaya	1630	44	Gehrels et al., 2008
Greater Himalaya	1639	6	Gehrels et al., 2008
Greater Himalaya	1641	5	Gehrels et al., 2008
Greater Himalaya	1641	15	Gehrels et al., 2008
Greater Himalaya	1641	13	Gehrels et al., 2008
Greater Himalaya	1652	20	Gehrels et al., 2008
Greater Himalaya	1652	10	Gehrels et al., 2008
Greater Himalaya	1653	12	Gehrels et al., 2008
Greater Himalaya	1657	19	Gehrels et al., 2008
Greater Himalaya	1657	4	Gehrels et al., 2008

Greater Himalaya	1662	64	Gehrels et al., 2008
Greater Himalaya	1663	80	Gehrels et al., 2008
Greater Himalaya	1664	13	Gehrels et al., 2008
Greater Himalaya	1664	8	Gehrels et al., 2008
Greater Himalaya	1666	21	Gehrels et al., 2008
Greater Himalaya	1666	19	Gehrels et al., 2008
Greater Himalaya	1666	49	Gehrels et al., 2008
Greater Himalaya	1666	21	Gehrels et al., 2008
Greater Himalaya	1666	19	Gehrels et al., 2008
Greater Himalaya	1667	19	Gehrels et al., 2008
Greater Himalaya	1669	12	Gehrels et al., 2008
Greater Himalaya	1673	14	Gehrels et al., 2008
Greater Himalaya	1682	81	Gehrels et al., 2008
Greater Himalaya	1690	5	Gehrels et al., 2008
Greater Himalaya	1691	12	Gehrels et al., 2008
Greater Himalaya	1694	19	Gehrels et al., 2008
Greater Himalaya	1696	8	Gehrels et al., 2008
Greater Himalaya	1698	28	Gehrels et al., 2008
Greater Himalaya	1704	18	Gehrels et al., 2008
Greater Himalaya	1706	29	Gehrels et al., 2008
Greater Himalaya	1707	21	Gehrels et al., 2008
Greater Himalaya	1707	19	Gehrels et al., 2008
Greater Himalaya	1707	11	Gehrels et al., 2008
Greater Himalaya	1707	4	Gehrels et al., 2008
Greater Himalaya	1715	8	Gehrels et al., 2008
Greater Himalaya	1745	19	Gehrels et al., 2008
Greater Himalaya	1745	19	Gehrels et al., 2008
Greater Himalaya	1747	9	Gehrels et al., 2008
Greater Himalaya	1751	20	Gehrels et al., 2008
Greater Himalaya	1752	19	Gehrels et al., 2008
Greater Himalaya	1754	12	Gehrels et al., 2008
Greater Himalaya	1759	4	Gehrels et al., 2008
Greater Himalaya	1760	24	Gehrels et al., 2008
Greater Himalaya	1762	5	Gehrels et al., 2008
Greater Himalaya	1777	8	Gehrels et al., 2008
Greater Himalaya	1782	22	Gehrels et al., 2008
Greater Himalaya	1782	12	Gehrels et al., 2008
Greater Himalaya	1787	18	Gehrels et al., 2008
Greater Himalaya	1791	19	Gehrels et al., 2008
Greater Himalaya	1791	19	Gehrels et al., 2008
Greater Himalaya	1807	8	Gehrels et al., 2008
Greater Himalaya	1813	23	Gehrels et al., 2008
Greater Himalaya	1814	33	Gehrels et al., 2008
Greater Himalaya	1814	33	Gehrels et al., 2008
Greater Himalaya	1815	24	Gehrels et al., 2008
Greater Himalaya	1831	18	Gehrels et al., 2008
Greater Himalaya	1832	18	Gehrels et al., 2008
Greater Himalaya	1843	6	Gehrels et al., 2008
Greater Himalaya	1851	35	Gehrels et al., 2008
Greater Himalaya	1853	8	Gehrels et al., 2008
Greater Himalaya	1870	11	Gehrels et al., 2008
Greater Himalaya	1889	16	Gehrels et al., 2008
Greater Himalaya	1900	18	Gehrels et al., 2008
Greater Himalaya	1900	5	Gehrels et al., 2008
Greater Himalaya	1904	3	Gehrels et al., 2008
Greater Himalaya	1905	18	Gehrels et al., 2008
Greater Himalaya	1905	5	Gehrels et al., 2008
Greater Himalaya	1914	7	Gehrels et al., 2008
Greater Himalaya	1962	18	Gehrels et al., 2008
Greater Himalaya	1969	19	Gehrels et al., 2008
Greater Himalaya	1982	18	Gehrels et al., 2008
Greater Himalaya	2017	20	Gehrels et al., 2008
Greater Himalaya	2017	9	Gehrels et al., 2008
Greater Himalaya	2028	18	Gehrels et al., 2008
Greater Himalaya	2062	3	Gehrels et al., 2008
Greater Himalaya	2072	18	Gehrels et al., 2008
Greater Himalaya	2072	6	Gehrels et al., 2008
Greater Himalaya	2075	16	Gehrels et al., 2008
Greater Himalaya	2109	19	Gehrels et al., 2008
Greater Himalaya	2109	7	Gehrels et al., 2008
Greater Himalaya	2122	23	Gehrels et al., 2008

Greater Himalaya	2123	18	Gehrels et al., 2008
Greater Himalaya	2199	11	Gehrels et al., 2008
Greater Himalaya	2234	17	Gehrels et al., 2008
Greater Himalaya	2309	19	Gehrels et al., 2008
Greater Himalaya	2319	21	Gehrels et al., 2008
Greater Himalaya	2319	13	Gehrels et al., 2008
Greater Himalaya	2338	17	Gehrels et al., 2008
Greater Himalaya	2359	4	Gehrels et al., 2008
Greater Himalaya	2361	17	Gehrels et al., 2008
Greater Himalaya	2384	17	Gehrels et al., 2008
Greater Himalaya	2388	6	Gehrels et al., 2008
Greater Himalaya	2403	11	Gehrels et al., 2008
Greater Himalaya	2407	26	Gehrels et al., 2008
Greater Himalaya	2412	8	Gehrels et al., 2008
Greater Himalaya	2413	5	Gehrels et al., 2008
Greater Himalaya	2422	4	Gehrels et al., 2008
Greater Himalaya	2426	11	Gehrels et al., 2008
Greater Himalaya	2435	18	Gehrels et al., 2008
Greater Himalaya	2439	21	Gehrels et al., 2008
Greater Himalaya	2439	12	Gehrels et al., 2008
Greater Himalaya	2441	21	Gehrels et al., 2008
Greater Himalaya	2441	5	Gehrels et al., 2008
Greater Himalaya	2441	13	Gehrels et al., 2008
Greater Himalaya	2442	32	Gehrels et al., 2008
Greater Himalaya	2449	18	Gehrels et al., 2008
Greater Himalaya	2451	17	Gehrels et al., 2008
Greater Himalaya	2451	5	Gehrels et al., 2008
Greater Himalaya	2455	6	Gehrels et al., 2008
Greater Himalaya	2456	17	Gehrels et al., 2008
Greater Himalaya	2456	17	Gehrels et al., 2008
Greater Himalaya	2456	18	Gehrels et al., 2008
Greater Himalaya	2458	18	Gehrels et al., 2008
Greater Himalaya	2464	17	Gehrels et al., 2008
Greater Himalaya	2469	3	Gehrels et al., 2008
Greater Himalaya	2471	17	Gehrels et al., 2008
Greater Himalaya	2471	4	Gehrels et al., 2008
Greater Himalaya	2478	3	Gehrels et al., 2008
Greater Himalaya	2481	10	Gehrels et al., 2008
Greater Himalaya	2483	8	Gehrels et al., 2008
Greater Himalaya	2486	7	Gehrels et al., 2008
Greater Himalaya	2488	17	Gehrels et al., 2008
Greater Himalaya	2488	5	Gehrels et al., 2008
Greater Himalaya	2489	17	Gehrels et al., 2008
Greater Himalaya	2496	17	Gehrels et al., 2008
Greater Himalaya	2496	22	Gehrels et al., 2008
Greater Himalaya	2501	9	Gehrels et al., 2008
Greater Himalaya	2504	17	Gehrels et al., 2008
Greater Himalaya	2510	17	Gehrels et al., 2008
Greater Himalaya	2510	5	Gehrels et al., 2008
Greater Himalaya	2511	11	Gehrels et al., 2008
Greater Himalaya	2517	11	Gehrels et al., 2008
Greater Himalaya	2520	17	Gehrels et al., 2008
Greater Himalaya	2520	6	Gehrels et al., 2008
Greater Himalaya	2521	17	Gehrels et al., 2008
Greater Himalaya	2521	17	Gehrels et al., 2008
Greater Himalaya	2527	32	Gehrels et al., 2008
Greater Himalaya	2528	6	Gehrels et al., 2008
Greater Himalaya	2529	17	Gehrels et al., 2008
Greater Himalaya	2532	17	Gehrels et al., 2008
Greater Himalaya	2532	5	Gehrels et al., 2008
Greater Himalaya	2533	30	Gehrels et al., 2008
Greater Himalaya	2534	17	Gehrels et al., 2008
Greater Himalaya	2534	5	Gehrels et al., 2008
Greater Himalaya	2536	23	Gehrels et al., 2008
Greater Himalaya	2537	17	Gehrels et al., 2008
Greater Himalaya	2537	17	Gehrels et al., 2008
Greater Himalaya	2537	17	Gehrels et al., 2008
Greater Himalaya	2539	17	Gehrels et al., 2008
Greater Himalaya	2539	17	Gehrels et al., 2008
Greater Himalaya	2541	21	Gehrels et al., 2008
Greater Himalaya	2542	17	Gehrels et al., 2008

Greater Himalaya	2542	17	Gehrels et al., 2008
Greater Himalaya	2542	17	Gehrels et al., 2008
Greater Himalaya	2543	17	Gehrels et al., 2008
Greater Himalaya	2543	17	Gehrels et al., 2008
Greater Himalaya	2544	12	Gehrels et al., 2008
Greater Himalaya	2549	6	Gehrels et al., 2008
Greater Himalaya	2551	17	Gehrels et al., 2008
Greater Himalaya	2551	4	Gehrels et al., 2008
Greater Himalaya	2559	10	Gehrels et al., 2008
Greater Himalaya	2560	17	Gehrels et al., 2008
Greater Himalaya	2560	4	Gehrels et al., 2008
Greater Himalaya	2564	17	Gehrels et al., 2008
Greater Himalaya	2574	17	Gehrels et al., 2008
Greater Himalaya	2579	14	Gehrels et al., 2008
Greater Himalaya	2584	17	Gehrels et al., 2008
Greater Himalaya	2591	17	Gehrels et al., 2008
Greater Himalaya	2591	17	Gehrels et al., 2008
Greater Himalaya	2610	17	Gehrels et al., 2008
Greater Himalaya	2615	17	Gehrels et al., 2008
Greater Himalaya	2615	6	Gehrels et al., 2008
Greater Himalaya	2616	3	Gehrels et al., 2008
Greater Himalaya	2620	1	Gehrels et al., 2008
Greater Himalaya	2625	20	Gehrels et al., 2008
Greater Himalaya	2632	3	Gehrels et al., 2008
Greater Himalaya	2632	15	Gehrels et al., 2008
Greater Himalaya	2637	17	Gehrels et al., 2008
Greater Himalaya	2639	2	Gehrels et al., 2008
Greater Himalaya	2640	17	Gehrels et al., 2008
Greater Himalaya	2640	4	Gehrels et al., 2008
Greater Himalaya	2641	17	Gehrels et al., 2008
Greater Himalaya	2641	6	Gehrels et al., 2008
Greater Himalaya	2646	2	Gehrels et al., 2008
Greater Himalaya	2648	24	Gehrels et al., 2008
Greater Himalaya	2648	24	Gehrels et al., 2008
Greater Himalaya	2662	7	Gehrels et al., 2008
Greater Himalaya	2667	18	Gehrels et al., 2008
Greater Himalaya	2669	6	Gehrels et al., 2008
Greater Himalaya	2685	19	Gehrels et al., 2008
Greater Himalaya	2695	23	Gehrels et al., 2008
Greater Himalaya	2695	16	Gehrels et al., 2008
Greater Himalaya	2707	6	Gehrels et al., 2008
Greater Himalaya	2725	17	Gehrels et al., 2008
Greater Himalaya	2735	10	Gehrels et al., 2008
Greater Himalaya	2738	3	Gehrels et al., 2008
Greater Himalaya	2744	17	Gehrels et al., 2008
Greater Himalaya	2744	6	Gehrels et al., 2008
Greater Himalaya	2749	1	Gehrels et al., 2008
Greater Himalaya	2753	16	Gehrels et al., 2008
Greater Himalaya	2768	3	Gehrels et al., 2008
Greater Himalaya	2771	2	Gehrels et al., 2008
Greater Himalaya	2773	17	Gehrels et al., 2008
Greater Himalaya	2834	16	Gehrels et al., 2008
Greater Himalaya	2834	4	Gehrels et al., 2008
Greater Himalaya	2862	8	Gehrels et al., 2008
Greater Himalaya	2902	22	Gehrels et al., 2008
Greater Himalaya	2911	14	Gehrels et al., 2008
Greater Himalaya	2920	22	Gehrels et al., 2008
Greater Himalaya	2920	15	Gehrels et al., 2008
Greater Himalaya	2953	18	Gehrels et al., 2008
Greater Himalaya	2953	8	Gehrels et al., 2008
Greater Himalaya	2960	16	Gehrels et al., 2008
Greater Himalaya	2977	16	Gehrels et al., 2008
Greater Himalaya	2977	6	Gehrels et al., 2008
Greater Himalaya	3023	18	Gehrels et al., 2008
Greater Himalaya	3051	16	Gehrels et al., 2008
Greater Himalaya	3051	7	Gehrels et al., 2008
Greater Himalaya	3121	16	Gehrels et al., 2008
Greater Himalaya	3175	16	Gehrels et al., 2008
Greater Himalaya	3175	16	Gehrels et al., 2008
Greater Himalaya	3212	9	Gehrels et al., 2008
Greater Himalaya	3221	16	Gehrels et al., 2008

Greater Himalaya	3221	7	Gehrels et al., 2008
Greater Himalaya	3262	12	Gehrels et al., 2008
Greater Himalaya	3264	16	Gehrels et al., 2008
Greater Himalaya	3308	1	Gehrels et al., 2008
Greater Himalaya	3446	19	Gehrels et al., 2008
Greater Himalaya	3446	11	Gehrels et al., 2008
Greater Himalaya	3457	16	Gehrels et al., 2008
Greater Himalaya	3457	5	Gehrels et al., 2008
Greater Himalaya	3463	16	Gehrels et al., 2008
Greater Himalaya	3463	16	Gehrels et al., 2008
Greater Himalaya	3499	2	Gehrels et al., 2008
Greater Himalaya	3943	15	Gehrels et al., 2008
Greater Himalaya	3976	15	Gehrels et al., 2008
Greater Himalaya	4760	15	Gehrels et al., 2008
Tethys Himalaya	420	15	Gehrels et al., 2008
Tethys Himalaya	474	15	Gehrels et al., 2008
Tethys Himalaya	481	10	Gehrels et al., 2008
Tethys Himalaya	484	7	Gehrels et al., 2008
Tethys Himalaya	485	8	Gehrels et al., 2008
Tethys Himalaya	485	6	Gehrels et al., 2008
Tethys Himalaya	485	8	Gehrels et al., 2008
Tethys Himalaya	486	6	Gehrels et al., 2008
Tethys Himalaya	486	8	Gehrels et al., 2008
Tethys Himalaya	489	4	Gehrels et al., 2008
Tethys Himalaya	490	9	Gehrels et al., 2008
Tethys Himalaya	490	6	Gehrels et al., 2008
Tethys Himalaya	491	14	Gehrels et al., 2008
Tethys Himalaya	491	5	Gehrels et al., 2008
Tethys Himalaya	495	12	Gehrels et al., 2008
Tethys Himalaya	495	9	Gehrels et al., 2008
Tethys Himalaya	495	13	Gehrels et al., 2008
Tethys Himalaya	496	7	Gehrels et al., 2008
Tethys Himalaya	496	6	Gehrels et al., 2008
Tethys Himalaya	496	5	Gehrels et al., 2008
Tethys Himalaya	496	7	Gehrels et al., 2008
Tethys Himalaya	496	4	Gehrels et al., 2008
Tethys Himalaya	497	11	Gehrels et al., 2008
Tethys Himalaya	497	6	Gehrels et al., 2008
Tethys Himalaya	497	4	Gehrels et al., 2008
Tethys Himalaya	497	6	Gehrels et al., 2008
Tethys Himalaya	498	6	Gehrels et al., 2008
Tethys Himalaya	499	7	Gehrels et al., 2008
Tethys Himalaya	500	13	Gehrels et al., 2008
Tethys Himalaya	501	11	Gehrels et al., 2008
Tethys Himalaya	502	6	Gehrels et al., 2008
Tethys Himalaya	504	6	Gehrels et al., 2008
Tethys Himalaya	504	29	Gehrels et al., 2008
Tethys Himalaya	504	10	Gehrels et al., 2008
Tethys Himalaya	504	12	Gehrels et al., 2008
Tethys Himalaya	504	17	Gehrels et al., 2008
Tethys Himalaya	505	11	Gehrels et al., 2008
Tethys Himalaya	506	8	Gehrels et al., 2008
Tethys Himalaya	506	5	Gehrels et al., 2008
Tethys Himalaya	508	6	Gehrels et al., 2008
Tethys Himalaya	508	8	Gehrels et al., 2008
Tethys Himalaya	509	6	Gehrels et al., 2008
Tethys Himalaya	510	11	Gehrels et al., 2008
Tethys Himalaya	510	13	Gehrels et al., 2008
Tethys Himalaya	511	9	Gehrels et al., 2008
Tethys Himalaya	511	18	Gehrels et al., 2008
Tethys Himalaya	514	6	Gehrels et al., 2008
Tethys Himalaya	514	8	Gehrels et al., 2008
Tethys Himalaya	515	8	Gehrels et al., 2008
Tethys Himalaya	515	7	Gehrels et al., 2008
Tethys Himalaya	516	7	Gehrels et al., 2008
Tethys Himalaya	516	12	Gehrels et al., 2008
Tethys Himalaya	516	12	Gehrels et al., 2008
Tethys Himalaya	516	4	Gehrels et al., 2008
Tethys Himalaya	517	14	Gehrels et al., 2008
Tethys Himalaya	518	6	Gehrels et al., 2008
Tethys Himalaya	519	10	Gehrels et al., 2008

Tethys Himalaya	519	9	Gehrels et al., 2008
Tethys Himalaya	519	6	Gehrels et al., 2008
Tethys Himalaya	520	8	Gehrels et al., 2008
Tethys Himalaya	521	5	Gehrels et al., 2008
Tethys Himalaya	521	13	Gehrels et al., 2008
Tethys Himalaya	522	10	Gehrels et al., 2008
Tethys Himalaya	522	31	Gehrels et al., 2008
Tethys Himalaya	523	10	Gehrels et al., 2008
Tethys Himalaya	524	12	Gehrels et al., 2008
Tethys Himalaya	524	11	Gehrels et al., 2008
Tethys Himalaya	524	9	Gehrels et al., 2008
Tethys Himalaya	524	6	Gehrels et al., 2008
Tethys Himalaya	524	6	Gehrels et al., 2008
Tethys Himalaya	525	13	Gehrels et al., 2008
Tethys Himalaya	525	7	Gehrels et al., 2008
Tethys Himalaya	525	8	Gehrels et al., 2008
Tethys Himalaya	526	12	Gehrels et al., 2008
Tethys Himalaya	526	12	Gehrels et al., 2008
Tethys Himalaya	526	12	Gehrels et al., 2008
Tethys Himalaya	527	6	Gehrels et al., 2008
Tethys Himalaya	527	9	Gehrels et al., 2008
Tethys Himalaya	527	10	Gehrels et al., 2008
Tethys Himalaya	528	6	Gehrels et al., 2008
Tethys Himalaya	528	12	Gehrels et al., 2008
Tethys Himalaya	529	7	Gehrels et al., 2008
Tethys Himalaya	529	11	Gehrels et al., 2008
Tethys Himalaya	530	12	Gehrels et al., 2008
Tethys Himalaya	530	12	Gehrels et al., 2008
Tethys Himalaya	530	8	Gehrels et al., 2008
Tethys Himalaya	531	14	Gehrels et al., 2008
Tethys Himalaya	531	7	Gehrels et al., 2008
Tethys Himalaya	532	12	Gehrels et al., 2008
Tethys Himalaya	532	5	Gehrels et al., 2008
Tethys Himalaya	532	13	Gehrels et al., 2008
Tethys Himalaya	533	7	Gehrels et al., 2008
Tethys Himalaya	534	13	Gehrels et al., 2008
Tethys Himalaya	535	5	Gehrels et al., 2008
Tethys Himalaya	535	9	Gehrels et al., 2008
Tethys Himalaya	535	8	Gehrels et al., 2008
Tethys Himalaya	536	4	Gehrels et al., 2008
Tethys Himalaya	537	7	Gehrels et al., 2008
Tethys Himalaya	539	12	Gehrels et al., 2008
Tethys Himalaya	539	6	Gehrels et al., 2008
Tethys Himalaya	540	11	Gehrels et al., 2008
Tethys Himalaya	542	6	Gehrels et al., 2008
Tethys Himalaya	542	11	Gehrels et al., 2008
Tethys Himalaya	542	7	Gehrels et al., 2008
Tethys Himalaya	545	12	Gehrels et al., 2008
Tethys Himalaya	546	8	Gehrels et al., 2008
Tethys Himalaya	546	7	Gehrels et al., 2008
Tethys Himalaya	549	10	Gehrels et al., 2008
Tethys Himalaya	550	7	Gehrels et al., 2008
Tethys Himalaya	551	6	Gehrels et al., 2008
Tethys Himalaya	552	12	Gehrels et al., 2008
Tethys Himalaya	557	10	Gehrels et al., 2008
Tethys Himalaya	560	7	Gehrels et al., 2008
Tethys Himalaya	560	3	Gehrels et al., 2008
Tethys Himalaya	562	12	Gehrels et al., 2008
Tethys Himalaya	562	6	Gehrels et al., 2008
Tethys Himalaya	563	24	Gehrels et al., 2008
Tethys Himalaya	564	14	Gehrels et al., 2008
Tethys Himalaya	567	6	Gehrels et al., 2008
Tethys Himalaya	568	22	Gehrels et al., 2008
Tethys Himalaya	568	6	Gehrels et al., 2008
Tethys Himalaya	569	6	Gehrels et al., 2008
Tethys Himalaya	571	8	Gehrels et al., 2008
Tethys Himalaya	572	13	Gehrels et al., 2008
Tethys Himalaya	572	9	Gehrels et al., 2008
Tethys Himalaya	581	8	Gehrels et al., 2008
Tethys Himalaya	582	6	Gehrels et al., 2008
Tethys Himalaya	582	21	Gehrels et al., 2008

Tethys Himalaya	583	14	Gehrels et al., 2008
Tethys Himalaya	586	28	Gehrels et al., 2008
Tethys Himalaya	588	25	Gehrels et al., 2008
Tethys Himalaya	595	25	Gehrels et al., 2008
Tethys Himalaya	596	14	Gehrels et al., 2008
Tethys Himalaya	596	18	Gehrels et al., 2008
Tethys Himalaya	598	10	Gehrels et al., 2008
Tethys Himalaya	601	48	Gehrels et al., 2008
Tethys Himalaya	602	6	Gehrels et al., 2008
Tethys Himalaya	607	7	Gehrels et al., 2008
Tethys Himalaya	608	15	Gehrels et al., 2008
Tethys Himalaya	609	8	Gehrels et al., 2008
Tethys Himalaya	614	12	Gehrels et al., 2008
Tethys Himalaya	617	8	Gehrels et al., 2008
Tethys Himalaya	620	14	Gehrels et al., 2008
Tethys Himalaya	622	9	Gehrels et al., 2008
Tethys Himalaya	626	5	Gehrels et al., 2008
Tethys Himalaya	627	17	Gehrels et al., 2008
Tethys Himalaya	632	13	Gehrels et al., 2008
Tethys Himalaya	634	13	Gehrels et al., 2008
Tethys Himalaya	637	18	Gehrels et al., 2008
Tethys Himalaya	641	4	Gehrels et al., 2008
Tethys Himalaya	643	15	Gehrels et al., 2008
Tethys Himalaya	645	16	Gehrels et al., 2008
Tethys Himalaya	646	32	Gehrels et al., 2008
Tethys Himalaya	652	6	Gehrels et al., 2008
Tethys Himalaya	653	15	Gehrels et al., 2008
Tethys Himalaya	654	26	Gehrels et al., 2008
Tethys Himalaya	654	5	Gehrels et al., 2008
Tethys Himalaya	657	8	Gehrels et al., 2008
Tethys Himalaya	659	7	Gehrels et al., 2008
Tethys Himalaya	659	5	Gehrels et al., 2008
Tethys Himalaya	669	6	Gehrels et al., 2008
Tethys Himalaya	669	4	Gehrels et al., 2008
Tethys Himalaya	671	7	Gehrels et al., 2008
Tethys Himalaya	675	10	Gehrels et al., 2008
Tethys Himalaya	680	7	Gehrels et al., 2008
Tethys Himalaya	682	19	Gehrels et al., 2008
Tethys Himalaya	691	25	Gehrels et al., 2008
Tethys Himalaya	694	12	Gehrels et al., 2008
Tethys Himalaya	695	10	Gehrels et al., 2008
Tethys Himalaya	695	3	Gehrels et al., 2008
Tethys Himalaya	696	3	Gehrels et al., 2008
Tethys Himalaya	697	13	Gehrels et al., 2008
Tethys Himalaya	704	18	Gehrels et al., 2008
Tethys Himalaya	705	15	Gehrels et al., 2008
Tethys Himalaya	708	12	Gehrels et al., 2008
Tethys Himalaya	722	6	Gehrels et al., 2008
Tethys Himalaya	723	12	Gehrels et al., 2008
Tethys Himalaya	725	27	Gehrels et al., 2008
Tethys Himalaya	730	23	Gehrels et al., 2008
Tethys Himalaya	734	9	Gehrels et al., 2008
Tethys Himalaya	734	15	Gehrels et al., 2008
Tethys Himalaya	736	12	Gehrels et al., 2008
Tethys Himalaya	740	14	Gehrels et al., 2008
Tethys Himalaya	742	18	Gehrels et al., 2008
Tethys Himalaya	746	4	Gehrels et al., 2008
Tethys Himalaya	747	26	Gehrels et al., 2008
Tethys Himalaya	751	9	Gehrels et al., 2008
Tethys Himalaya	752	4	Gehrels et al., 2008
Tethys Himalaya	754	11	Gehrels et al., 2008
Tethys Himalaya	756	20	Gehrels et al., 2008
Tethys Himalaya	759	11	Gehrels et al., 2008
Tethys Himalaya	761	59	Gehrels et al., 2008
Tethys Himalaya	762	10	Gehrels et al., 2008
Tethys Himalaya	763	9	Gehrels et al., 2008
Tethys Himalaya	764	10	Gehrels et al., 2008
Tethys Himalaya	769	15	Gehrels et al., 2008
Tethys Himalaya	770	29	Gehrels et al., 2008
Tethys Himalaya	770	31	Gehrels et al., 2008
Tethys Himalaya	770	5	Gehrels et al., 2008

Tethys Himalaya	771	10	Gehrels et al., 2008
Tethys Himalaya	772	4	Gehrels et al., 2008
Tethys Himalaya	773	29	Gehrels et al., 2008
Tethys Himalaya	773	9	Gehrels et al., 2008
Tethys Himalaya	778	10	Gehrels et al., 2008
Tethys Himalaya	780	20	Gehrels et al., 2008
Tethys Himalaya	780	18	Gehrels et al., 2008
Tethys Himalaya	780	6	Gehrels et al., 2008
Tethys Himalaya	785	24	Gehrels et al., 2008
Tethys Himalaya	785	7	Gehrels et al., 2008
Tethys Himalaya	786	5	Gehrels et al., 2008
Tethys Himalaya	789	6	Gehrels et al., 2008
Tethys Himalaya	789	7	Gehrels et al., 2008
Tethys Himalaya	791	16	Gehrels et al., 2008
Tethys Himalaya	794	9	Gehrels et al., 2008
Tethys Himalaya	795	6	Gehrels et al., 2008
Tethys Himalaya	796	18	Gehrels et al., 2008
Tethys Himalaya	796	14	Gehrels et al., 2008
Tethys Himalaya	797	21	Gehrels et al., 2008
Tethys Himalaya	798	15	Gehrels et al., 2008
Tethys Himalaya	799	5	Gehrels et al., 2008
Tethys Himalaya	800	9	Gehrels et al., 2008
Tethys Himalaya	801	20	Gehrels et al., 2008
Tethys Himalaya	802	7	Gehrels et al., 2008
Tethys Himalaya	803	13	Gehrels et al., 2008
Tethys Himalaya	806	5	Gehrels et al., 2008
Tethys Himalaya	809	17	Gehrels et al., 2008
Tethys Himalaya	812	11	Gehrels et al., 2008
Tethys Himalaya	812	4	Gehrels et al., 2008
Tethys Himalaya	814	20	Gehrels et al., 2008
Tethys Himalaya	814	5	Gehrels et al., 2008
Tethys Himalaya	815	4	Gehrels et al., 2008
Tethys Himalaya	816	10	Gehrels et al., 2008
Tethys Himalaya	816	5	Gehrels et al., 2008
Tethys Himalaya	819	12	Gehrels et al., 2008
Tethys Himalaya	821	26	Gehrels et al., 2008
Tethys Himalaya	821	11	Gehrels et al., 2008
Tethys Himalaya	821	7	Gehrels et al., 2008
Tethys Himalaya	823	15	Gehrels et al., 2008
Tethys Himalaya	826	22	Gehrels et al., 2008
Tethys Himalaya	827	13	Gehrels et al., 2008
Tethys Himalaya	829	18	Gehrels et al., 2008
Tethys Himalaya	829	11	Gehrels et al., 2008
Tethys Himalaya	831	11	Gehrels et al., 2008
Tethys Himalaya	832	10	Gehrels et al., 2008
Tethys Himalaya	832	30	Gehrels et al., 2008
Tethys Himalaya	835	10	Gehrels et al., 2008
Tethys Himalaya	835	4	Gehrels et al., 2008
Tethys Himalaya	836	30	Gehrels et al., 2008
Tethys Himalaya	837	14	Gehrels et al., 2008
Tethys Himalaya	837	4	Gehrels et al., 2008
Tethys Himalaya	838	5	Gehrels et al., 2008
Tethys Himalaya	839	9	Gehrels et al., 2008
Tethys Himalaya	840	11	Gehrels et al., 2008
Tethys Himalaya	840	25	Gehrels et al., 2008
Tethys Himalaya	841	5	Gehrels et al., 2008
Tethys Himalaya	842	11	Gehrels et al., 2008
Tethys Himalaya	845	11	Gehrels et al., 2008
Tethys Himalaya	846	29	Gehrels et al., 2008
Tethys Himalaya	846	12	Gehrels et al., 2008
Tethys Himalaya	846	8	Gehrels et al., 2008
Tethys Himalaya	849	9	Gehrels et al., 2008
Tethys Himalaya	851	25	Gehrels et al., 2008
Tethys Himalaya	854	19	Gehrels et al., 2008
Tethys Himalaya	854	43	Gehrels et al., 2008
Tethys Himalaya	857	22	Gehrels et al., 2008
Tethys Himalaya	861	12	Gehrels et al., 2008
Tethys Himalaya	862	16	Gehrels et al., 2008
Tethys Himalaya	862	8	Gehrels et al., 2008
Tethys Himalaya	863	20	Gehrels et al., 2008
Tethys Himalaya	864	20	Gehrels et al., 2008

Tethys Himalaya	866	41	Gehrels et al., 2008
Tethys Himalaya	869	18	Gehrels et al., 2008
Tethys Himalaya	869	10	Gehrels et al., 2008
Tethys Himalaya	870	22	Gehrels et al., 2008
Tethys Himalaya	872	21	Gehrels et al., 2008
Tethys Himalaya	874	22	Gehrels et al., 2008
Tethys Himalaya	874	12	Gehrels et al., 2008
Tethys Himalaya	876	14	Gehrels et al., 2008
Tethys Himalaya	877	21	Gehrels et al., 2008
Tethys Himalaya	877	17	Gehrels et al., 2008
Tethys Himalaya	878	10	Gehrels et al., 2008
Tethys Himalaya	878	16	Gehrels et al., 2008
Tethys Himalaya	879	25	Gehrels et al., 2008
Tethys Himalaya	879	8	Gehrels et al., 2008
Tethys Himalaya	880	12	Gehrels et al., 2008
Tethys Himalaya	881	14	Gehrels et al., 2008
Tethys Himalaya	882	12	Gehrels et al., 2008
Tethys Himalaya	882	16	Gehrels et al., 2008
Tethys Himalaya	886	82	Gehrels et al., 2008
Tethys Himalaya	887	8	Gehrels et al., 2008
Tethys Himalaya	889	58	Gehrels et al., 2008
Tethys Himalaya	889	11	Gehrels et al., 2008
Tethys Himalaya	889	3	Gehrels et al., 2008
Tethys Himalaya	890	21	Gehrels et al., 2008
Tethys Himalaya	890	22	Gehrels et al., 2008
Tethys Himalaya	890	25	Gehrels et al., 2008
Tethys Himalaya	893	11	Gehrels et al., 2008
Tethys Himalaya	894	12	Gehrels et al., 2008
Tethys Himalaya	894	6	Gehrels et al., 2008
Tethys Himalaya	895	6	Gehrels et al., 2008
Tethys Himalaya	897	5	Gehrels et al., 2008
Tethys Himalaya	898	15	Gehrels et al., 2008
Tethys Himalaya	900	21	Gehrels et al., 2008
Tethys Himalaya	901	13	Gehrels et al., 2008
Tethys Himalaya	902	16	Gehrels et al., 2008
Tethys Himalaya	904	10	Gehrels et al., 2008
Tethys Himalaya	905	22	Gehrels et al., 2008
Tethys Himalaya	905	27	Gehrels et al., 2008
Tethys Himalaya	907	23	Gehrels et al., 2008
Tethys Himalaya	907	17	Gehrels et al., 2008
Tethys Himalaya	908	33	Gehrels et al., 2008
Tethys Himalaya	908	35	Gehrels et al., 2008
Tethys Himalaya	908	4	Gehrels et al., 2008
Tethys Himalaya	910	13	Gehrels et al., 2008
Tethys Himalaya	914	7	Gehrels et al., 2008
Tethys Himalaya	916	51	Gehrels et al., 2008
Tethys Himalaya	917	20	Gehrels et al., 2008
Tethys Himalaya	917	34	Gehrels et al., 2008
Tethys Himalaya	917	6	Gehrels et al., 2008
Tethys Himalaya	917	16	Gehrels et al., 2008
Tethys Himalaya	918	23	Gehrels et al., 2008
Tethys Himalaya	918	7	Gehrels et al., 2008
Tethys Himalaya	918	7	Gehrels et al., 2008
Tethys Himalaya	919	9	Gehrels et al., 2008
Tethys Himalaya	920	12	Gehrels et al., 2008
Tethys Himalaya	921	6	Gehrels et al., 2008
Tethys Himalaya	921	6	Gehrels et al., 2008
Tethys Himalaya	924	13	Gehrels et al., 2008
Tethys Himalaya	924	15	Gehrels et al., 2008
Tethys Himalaya	925	11	Gehrels et al., 2008
Tethys Himalaya	929	28	Gehrels et al., 2008
Tethys Himalaya	930	14	Gehrels et al., 2008
Tethys Himalaya	930	24	Gehrels et al., 2008
Tethys Himalaya	932	12	Gehrels et al., 2008
Tethys Himalaya	932	4	Gehrels et al., 2008
Tethys Himalaya	932	5	Gehrels et al., 2008
Tethys Himalaya	935	12	Gehrels et al., 2008
Tethys Himalaya	935	11	Gehrels et al., 2008
Tethys Himalaya	935	9	Gehrels et al., 2008
Tethys Himalaya	937	37	Gehrels et al., 2008
Tethys Himalaya	937	14	Gehrels et al., 2008

Tethys Himalaya	939	18	Gehrels et al., 2008
Tethys Himalaya	939	8	Gehrels et al., 2008
Tethys Himalaya	940	21	Gehrels et al., 2008
Tethys Himalaya	940	22	Gehrels et al., 2008
Tethys Himalaya	940	22	Gehrels et al., 2008
Tethys Himalaya	943	21	Gehrels et al., 2008
Tethys Himalaya	943	13	Gehrels et al., 2008
Tethys Himalaya	944	14	Gehrels et al., 2008
Tethys Himalaya	945	11	Gehrels et al., 2008
Tethys Himalaya	947	8	Gehrels et al., 2008
Tethys Himalaya	949	14	Gehrels et al., 2008
Tethys Himalaya	950	6	Gehrels et al., 2008
Tethys Himalaya	951	11	Gehrels et al., 2008
Tethys Himalaya	952	12	Gehrels et al., 2008
Tethys Himalaya	953	8	Gehrels et al., 2008
Tethys Himalaya	954	20	Gehrels et al., 2008
Tethys Himalaya	955	10	Gehrels et al., 2008
Tethys Himalaya	956	8	Gehrels et al., 2008
Tethys Himalaya	961	31	Gehrels et al., 2008
Tethys Himalaya	963	22	Gehrels et al., 2008
Tethys Himalaya	965	23	Gehrels et al., 2008
Tethys Himalaya	965	21	Gehrels et al., 2008
Tethys Himalaya	967	9	Gehrels et al., 2008
Tethys Himalaya	968	12	Gehrels et al., 2008
Tethys Himalaya	968	14	Gehrels et al., 2008
Tethys Himalaya	969	19	Gehrels et al., 2008
Tethys Himalaya	972	22	Gehrels et al., 2008
Tethys Himalaya	972	44	Gehrels et al., 2008
Tethys Himalaya	973	13	Gehrels et al., 2008
Tethys Himalaya	975	17	Gehrels et al., 2008
Tethys Himalaya	976	14	Gehrels et al., 2008
Tethys Himalaya	978	6	Gehrels et al., 2008
Tethys Himalaya	979	12	Gehrels et al., 2008
Tethys Himalaya	983	22	Gehrels et al., 2008
Tethys Himalaya	983	44	Gehrels et al., 2008
Tethys Himalaya	983	16	Gehrels et al., 2008
Tethys Himalaya	985	9	Gehrels et al., 2008
Tethys Himalaya	985	16	Gehrels et al., 2008
Tethys Himalaya	986	26	Gehrels et al., 2008
Tethys Himalaya	989	49	Gehrels et al., 2008
Tethys Himalaya	998	5	Gehrels et al., 2008
Tethys Himalaya	1002	31	Gehrels et al., 2008
Tethys Himalaya	1003	29	Gehrels et al., 2008
Tethys Himalaya	1004	9	Gehrels et al., 2008
Tethys Himalaya	1005	14	Gehrels et al., 2008
Tethys Himalaya	1005	52	Gehrels et al., 2008
Tethys Himalaya	1009	27	Gehrels et al., 2008
Tethys Himalaya	1010	16	Gehrels et al., 2008
Tethys Himalaya	1010	20	Gehrels et al., 2008
Tethys Himalaya	1015	38	Gehrels et al., 2008
Tethys Himalaya	1017	22	Gehrels et al., 2008
Tethys Himalaya	1020	12	Gehrels et al., 2008
Tethys Himalaya	1022	21	Gehrels et al., 2008
Tethys Himalaya	1024	63	Gehrels et al., 2008
Tethys Himalaya	1025	33	Gehrels et al., 2008
Tethys Himalaya	1027	33	Gehrels et al., 2008
Tethys Himalaya	1027	36	Gehrels et al., 2008
Tethys Himalaya	1027	5	Gehrels et al., 2008
Tethys Himalaya	1030	21	Gehrels et al., 2008
Tethys Himalaya	1030	88	Gehrels et al., 2008
Tethys Himalaya	1031	4	Gehrels et al., 2008
Tethys Himalaya	1031	6	Gehrels et al., 2008
Tethys Himalaya	1034	22	Gehrels et al., 2008
Tethys Himalaya	1037	31	Gehrels et al., 2008
Tethys Himalaya	1039	4	Gehrels et al., 2008
Tethys Himalaya	1040	48	Gehrels et al., 2008
Tethys Himalaya	1042	8	Gehrels et al., 2008
Tethys Himalaya	1042	10	Gehrels et al., 2008
Tethys Himalaya	1045	5	Gehrels et al., 2008
Tethys Himalaya	1050	47	Gehrels et al., 2008
Tethys Himalaya	1052	8	Gehrels et al., 2008

Tethys Himalaya	1052	18	Gehrels et al., 2008
Tethys Himalaya	1053	25	Gehrels et al., 2008
Tethys Himalaya	1053	12	Gehrels et al., 2008
Tethys Himalaya	1056	23	Gehrels et al., 2008
Tethys Himalaya	1056	28	Gehrels et al., 2008
Tethys Himalaya	1056	86	Gehrels et al., 2008
Tethys Himalaya	1058	40	Gehrels et al., 2008
Tethys Himalaya	1058	26	Gehrels et al., 2008
Tethys Himalaya	1060	5	Gehrels et al., 2008
Tethys Himalaya	1061	4	Gehrels et al., 2008
Tethys Himalaya	1062	21	Gehrels et al., 2008
Tethys Himalaya	1062	32	Gehrels et al., 2008
Tethys Himalaya	1063	24	Gehrels et al., 2008
Tethys Himalaya	1063	7	Gehrels et al., 2008
Tethys Himalaya	1064	25	Gehrels et al., 2008
Tethys Himalaya	1065	21	Gehrels et al., 2008
Tethys Himalaya	1065	30	Gehrels et al., 2008
Tethys Himalaya	1065	4	Gehrels et al., 2008
Tethys Himalaya	1066	21	Gehrels et al., 2008
Tethys Himalaya	1066	24	Gehrels et al., 2008
Tethys Himalaya	1070	12	Gehrels et al., 2008
Tethys Himalaya	1070	6	Gehrels et al., 2008
Tethys Himalaya	1070	11	Gehrels et al., 2008
Tethys Himalaya	1071	21	Gehrels et al., 2008
Tethys Himalaya	1071	7	Gehrels et al., 2008
Tethys Himalaya	1071	10	Gehrels et al., 2008
Tethys Himalaya	1072	63	Gehrels et al., 2008
Tethys Himalaya	1073	20	Gehrels et al., 2008
Tethys Himalaya	1074	25	Gehrels et al., 2008
Tethys Himalaya	1074	19	Gehrels et al., 2008
Tethys Himalaya	1075	16	Gehrels et al., 2008
Tethys Himalaya	1076	54	Gehrels et al., 2008
Tethys Himalaya	1077	5	Gehrels et al., 2008
Tethys Himalaya	1078	67	Gehrels et al., 2008
Tethys Himalaya	1078	4	Gehrels et al., 2008
Tethys Himalaya	1079	21	Gehrels et al., 2008
Tethys Himalaya	1079	29	Gehrels et al., 2008
Tethys Himalaya	1079	4	Gehrels et al., 2008
Tethys Himalaya	1079	4	Gehrels et al., 2008
Tethys Himalaya	1082	35	Gehrels et al., 2008
Tethys Himalaya	1087	33	Gehrels et al., 2008
Tethys Himalaya	1087	20	Gehrels et al., 2008
Tethys Himalaya	1087	6	Gehrels et al., 2008
Tethys Himalaya	1088	30	Gehrels et al., 2008
Tethys Himalaya	1088	35	Gehrels et al., 2008
Tethys Himalaya	1088	12	Gehrels et al., 2008
Tethys Himalaya	1089	22	Gehrels et al., 2008
Tethys Himalaya	1090	35	Gehrels et al., 2008
Tethys Himalaya	1090	24	Gehrels et al., 2008
Tethys Himalaya	1090	6	Gehrels et al., 2008
Tethys Himalaya	1090	19	Gehrels et al., 2008
Tethys Himalaya	1092	20	Gehrels et al., 2008
Tethys Himalaya	1094	23	Gehrels et al., 2008
Tethys Himalaya	1094	26	Gehrels et al., 2008
Tethys Himalaya	1094	12	Gehrels et al., 2008
Tethys Himalaya	1095	68	Gehrels et al., 2008
Tethys Himalaya	1096	20	Gehrels et al., 2008
Tethys Himalaya	1096	20	Gehrels et al., 2008
Tethys Himalaya	1097	21	Gehrels et al., 2008
Tethys Himalaya	1097	77	Gehrels et al., 2008
Tethys Himalaya	1101	23	Gehrels et al., 2008
Tethys Himalaya	1101	13	Gehrels et al., 2008
Tethys Himalaya	1102	38	Gehrels et al., 2008
Tethys Himalaya	1104	38	Gehrels et al., 2008
Tethys Himalaya	1105	34	Gehrels et al., 2008
Tethys Himalaya	1107	22	Gehrels et al., 2008
Tethys Himalaya	1108	37	Gehrels et al., 2008
Tethys Himalaya	1108	43	Gehrels et al., 2008
Tethys Himalaya	1109	13	Gehrels et al., 2008
Tethys Himalaya	1110	11	Gehrels et al., 2008
Tethys Himalaya	1111	5	Gehrels et al., 2008

Tethys Himalaya	1112	6	Gehrels et al., 2008
Tethys Himalaya	1112	7	Gehrels et al., 2008
Tethys Himalaya	1114	13	Gehrels et al., 2008
Tethys Himalaya	1116	17	Gehrels et al., 2008
Tethys Himalaya	1117	45	Gehrels et al., 2008
Tethys Himalaya	1117	9	Gehrels et al., 2008
Tethys Himalaya	1118	20	Gehrels et al., 2008
Tethys Himalaya	1120	23	Gehrels et al., 2008
Tethys Himalaya	1120	6	Gehrels et al., 2008
Tethys Himalaya	1121	8	Gehrels et al., 2008
Tethys Himalaya	1124	32	Gehrels et al., 2008
Tethys Himalaya	1125	8	Gehrels et al., 2008
Tethys Himalaya	1127	10	Gehrels et al., 2008
Tethys Himalaya	1127	7	Gehrels et al., 2008
Tethys Himalaya	1128	34	Gehrels et al., 2008
Tethys Himalaya	1129	20	Gehrels et al., 2008
Tethys Himalaya	1129	22	Gehrels et al., 2008
Tethys Himalaya	1129	30	Gehrels et al., 2008
Tethys Himalaya	1132	34	Gehrels et al., 2008
Tethys Himalaya	1134	28	Gehrels et al., 2008
Tethys Himalaya	1136	32	Gehrels et al., 2008
Tethys Himalaya	1138	22	Gehrels et al., 2008
Tethys Himalaya	1140	16	Gehrels et al., 2008
Tethys Himalaya	1140	46	Gehrels et al., 2008
Tethys Himalaya	1142	20	Gehrels et al., 2008
Tethys Himalaya	1144	30	Gehrels et al., 2008
Tethys Himalaya	1145	24	Gehrels et al., 2008
Tethys Himalaya	1147	55	Gehrels et al., 2008
Tethys Himalaya	1148	21	Gehrels et al., 2008
Tethys Himalaya	1148	32	Gehrels et al., 2008
Tethys Himalaya	1148	8	Gehrels et al., 2008
Tethys Himalaya	1149	22	Gehrels et al., 2008
Tethys Himalaya	1150	24	Gehrels et al., 2008
Tethys Himalaya	1152	4	Gehrels et al., 2008
Tethys Himalaya	1153	16	Gehrels et al., 2008
Tethys Himalaya	1154	95	Gehrels et al., 2008
Tethys Himalaya	1155	22	Gehrels et al., 2008
Tethys Himalaya	1156	32	Gehrels et al., 2008
Tethys Himalaya	1158	69	Gehrels et al., 2008
Tethys Himalaya	1159	16	Gehrels et al., 2008
Tethys Himalaya	1160	90	Gehrels et al., 2008
Tethys Himalaya	1160	6	Gehrels et al., 2008
Tethys Himalaya	1161	20	Gehrels et al., 2008
Tethys Himalaya	1161	5	Gehrels et al., 2008
Tethys Himalaya	1163	20	Gehrels et al., 2008
Tethys Himalaya	1164	20	Gehrels et al., 2008
Tethys Himalaya	1167	36	Gehrels et al., 2008
Tethys Himalaya	1168	3	Gehrels et al., 2008
Tethys Himalaya	1169	3	Gehrels et al., 2008
Tethys Himalaya	1170	13	Gehrels et al., 2008
Tethys Himalaya	1172	34	Gehrels et al., 2008
Tethys Himalaya	1172	19	Gehrels et al., 2008
Tethys Himalaya	1174	5	Gehrels et al., 2008
Tethys Himalaya	1174	7	Gehrels et al., 2008
Tethys Himalaya	1176	12	Gehrels et al., 2008
Tethys Himalaya	1176	8	Gehrels et al., 2008
Tethys Himalaya	1178	7	Gehrels et al., 2008
Tethys Himalaya	1178	4	Gehrels et al., 2008
Tethys Himalaya	1179	26	Gehrels et al., 2008
Tethys Himalaya	1181	23	Gehrels et al., 2008
Tethys Himalaya	1181	24	Gehrels et al., 2008
Tethys Himalaya	1182	6	Gehrels et al., 2008
Tethys Himalaya	1184	14	Gehrels et al., 2008
Tethys Himalaya	1185	10	Gehrels et al., 2008
Tethys Himalaya	1186	40	Gehrels et al., 2008
Tethys Himalaya	1188	51	Gehrels et al., 2008
Tethys Himalaya	1188	26	Gehrels et al., 2008
Tethys Himalaya	1189	33	Gehrels et al., 2008
Tethys Himalaya	1190	21	Gehrels et al., 2008
Tethys Himalaya	1194	20	Gehrels et al., 2008
Tethys Himalaya	1194	24	Gehrels et al., 2008

Tethys Himalaya	1196	32	Gehrels et al., 2008
Tethys Himalaya	1197	32	Gehrels et al., 2008
Tethys Himalaya	1198	18	Gehrels et al., 2008
Tethys Himalaya	1200	30	Gehrels et al., 2008
Tethys Himalaya	1200	6	Gehrels et al., 2008
Tethys Himalaya	1203	7	Gehrels et al., 2008
Tethys Himalaya	1203	7	Gehrels et al., 2008
Tethys Himalaya	1204	23	Gehrels et al., 2008
Tethys Himalaya	1205	27	Gehrels et al., 2008
Tethys Himalaya	1205	39	Gehrels et al., 2008
Tethys Himalaya	1205	8	Gehrels et al., 2008
Tethys Himalaya	1208	34	Gehrels et al., 2008
Tethys Himalaya	1209	20	Gehrels et al., 2008
Tethys Himalaya	1213	34	Gehrels et al., 2008
Tethys Himalaya	1213	28	Gehrels et al., 2008
Tethys Himalaya	1214	5	Gehrels et al., 2008
Tethys Himalaya	1215	7	Gehrels et al., 2008
Tethys Himalaya	1216	36	Gehrels et al., 2008
Tethys Himalaya	1217	21	Gehrels et al., 2008
Tethys Himalaya	1219	29	Gehrels et al., 2008
Tethys Himalaya	1223	19	Gehrels et al., 2008
Tethys Himalaya	1223	3	Gehrels et al., 2008
Tethys Himalaya	1224	31	Gehrels et al., 2008
Tethys Himalaya	1225	20	Gehrels et al., 2008
Tethys Himalaya	1225	41	Gehrels et al., 2008
Tethys Himalaya	1225	26	Gehrels et al., 2008
Tethys Himalaya	1225	20	Gehrels et al., 2008
Tethys Himalaya	1226	20	Gehrels et al., 2008
Tethys Himalaya	1227	59	Gehrels et al., 2008
Tethys Himalaya	1228	24	Gehrels et al., 2008
Tethys Himalaya	1229	32	Gehrels et al., 2008
Tethys Himalaya	1231	33	Gehrels et al., 2008
Tethys Himalaya	1234	33	Gehrels et al., 2008
Tethys Himalaya	1234	19	Gehrels et al., 2008
Tethys Himalaya	1235	8	Gehrels et al., 2008
Tethys Himalaya	1236	30	Gehrels et al., 2008
Tethys Himalaya	1236	34	Gehrels et al., 2008
Tethys Himalaya	1237	20	Gehrels et al., 2008
Tethys Himalaya	1239	20	Gehrels et al., 2008
Tethys Himalaya	1239	90	Gehrels et al., 2008
Tethys Himalaya	1240	29	Gehrels et al., 2008
Tethys Himalaya	1246	21	Gehrels et al., 2008
Tethys Himalaya	1246	25	Gehrels et al., 2008
Tethys Himalaya	1246	8	Gehrels et al., 2008
Tethys Himalaya	1247	28	Gehrels et al., 2008
Tethys Himalaya	1247	23	Gehrels et al., 2008
Tethys Himalaya	1251	10	Gehrels et al., 2008
Tethys Himalaya	1256	7	Gehrels et al., 2008
Tethys Himalaya	1257	20	Gehrels et al., 2008
Tethys Himalaya	1259	17	Gehrels et al., 2008
Tethys Himalaya	1265	20	Gehrels et al., 2008
Tethys Himalaya	1267	20	Gehrels et al., 2008
Tethys Himalaya	1267	32	Gehrels et al., 2008
Tethys Himalaya	1272	16	Gehrels et al., 2008
Tethys Himalaya	1274	20	Gehrels et al., 2008
Tethys Himalaya	1274	22	Gehrels et al., 2008
Tethys Himalaya	1274	16	Gehrels et al., 2008
Tethys Himalaya	1275	27	Gehrels et al., 2008
Tethys Himalaya	1285	11	Gehrels et al., 2008
Tethys Himalaya	1287	8	Gehrels et al., 2008
Tethys Himalaya	1288	12	Gehrels et al., 2008
Tethys Himalaya	1291	12	Gehrels et al., 2008
Tethys Himalaya	1295	10	Gehrels et al., 2008
Tethys Himalaya	1297	6	Gehrels et al., 2008
Tethys Himalaya	1305	32	Gehrels et al., 2008
Tethys Himalaya	1312	23	Gehrels et al., 2008
Tethys Himalaya	1312	27	Gehrels et al., 2008
Tethys Himalaya	1319	21	Gehrels et al., 2008
Tethys Himalaya	1320	38	Gehrels et al., 2008
Tethys Himalaya	1322	34	Gehrels et al., 2008
Tethys Himalaya	1325	26	Gehrels et al., 2008

Tethys Himalaya	1327	9	Gehrels et al., 2008
Tethys Himalaya	1330	35	Gehrels et al., 2008
Tethys Himalaya	1332	19	Gehrels et al., 2008
Tethys Himalaya	1332	21	Gehrels et al., 2008
Tethys Himalaya	1333	16	Gehrels et al., 2008
Tethys Himalaya	1335	20	Gehrels et al., 2008
Tethys Himalaya	1338	26	Gehrels et al., 2008
Tethys Himalaya	1341	33	Gehrels et al., 2008
Tethys Himalaya	1346	12	Gehrels et al., 2008
Tethys Himalaya	1349	29	Gehrels et al., 2008
Tethys Himalaya	1352	5	Gehrels et al., 2008
Tethys Himalaya	1356	25	Gehrels et al., 2008
Tethys Himalaya	1360	35	Gehrels et al., 2008
Tethys Himalaya	1364	19	Gehrels et al., 2008
Tethys Himalaya	1365	18	Gehrels et al., 2008
Tethys Himalaya	1368	17	Gehrels et al., 2008
Tethys Himalaya	1370	20	Gehrels et al., 2008
Tethys Himalaya	1372	21	Gehrels et al., 2008
Tethys Himalaya	1376	8	Gehrels et al., 2008
Tethys Himalaya	1376	20	Gehrels et al., 2008
Tethys Himalaya	1380	22	Gehrels et al., 2008
Tethys Himalaya	1381	20	Gehrels et al., 2008
Tethys Himalaya	1388	19	Gehrels et al., 2008
Tethys Himalaya	1390	21	Gehrels et al., 2008
Tethys Himalaya	1392	26	Gehrels et al., 2008
Tethys Himalaya	1398	20	Gehrels et al., 2008
Tethys Himalaya	1400	12	Gehrels et al., 2008
Tethys Himalaya	1418	19	Gehrels et al., 2008
Tethys Himalaya	1423	12	Gehrels et al., 2008
Tethys Himalaya	1433	25	Gehrels et al., 2008
Tethys Himalaya	1439	6	Gehrels et al., 2008
Tethys Himalaya	1445	62	Gehrels et al., 2008
Tethys Himalaya	1447	8	Gehrels et al., 2008
Tethys Himalaya	1454	19	Gehrels et al., 2008
Tethys Himalaya	1459	14	Gehrels et al., 2008
Tethys Himalaya	1474	5	Gehrels et al., 2008
Tethys Himalaya	1490	19	Gehrels et al., 2008
Tethys Himalaya	1496	20	Gehrels et al., 2008
Tethys Himalaya	1515	19	Gehrels et al., 2008
Tethys Himalaya	1519	37	Gehrels et al., 2008
Tethys Himalaya	1521	19	Gehrels et al., 2008
Tethys Himalaya	1534	20	Gehrels et al., 2008
Tethys Himalaya	1537	23	Gehrels et al., 2008
Tethys Himalaya	1539	27	Gehrels et al., 2008
Tethys Himalaya	1553	6	Gehrels et al., 2008
Tethys Himalaya	1562	5	Gehrels et al., 2008
Tethys Himalaya	1581	12	Gehrels et al., 2008
Tethys Himalaya	1591	3	Gehrels et al., 2008
Tethys Himalaya	1593	4	Gehrels et al., 2008
Tethys Himalaya	1611	5	Gehrels et al., 2008
Tethys Himalaya	1612	6	Gehrels et al., 2008
Tethys Himalaya	1615	29	Gehrels et al., 2008
Tethys Himalaya	1618	11	Gehrels et al., 2008
Tethys Himalaya	1628	19	Gehrels et al., 2008
Tethys Himalaya	1628	19	Gehrels et al., 2008
Tethys Himalaya	1629	23	Gehrels et al., 2008
Tethys Himalaya	1631	7	Gehrels et al., 2008
Tethys Himalaya	1636	48	Gehrels et al., 2008
Tethys Himalaya	1638	19	Gehrels et al., 2008
Tethys Himalaya	1644	4	Gehrels et al., 2008
Tethys Himalaya	1646	21	Gehrels et al., 2008
Tethys Himalaya	1664	12	Gehrels et al., 2008
Tethys Himalaya	1671	3	Gehrels et al., 2008
Tethys Himalaya	1672	6	Gehrels et al., 2008
Tethys Himalaya	1681	58	Gehrels et al., 2008
Tethys Himalaya	1685	47	Gehrels et al., 2008
Tethys Himalaya	1693	4	Gehrels et al., 2008
Tethys Himalaya	1700	10	Gehrels et al., 2008
Tethys Himalaya	1706	12	Gehrels et al., 2008
Tethys Himalaya	1708	5	Gehrels et al., 2008
Tethys Himalaya	1714	5	Gehrels et al., 2008

Tethys Himalaya	1720	19	Gehrels et al., 2008
Tethys Himalaya	1723	6	Gehrels et al., 2008
Tethys Himalaya	1730	27	Gehrels et al., 2008
Tethys Himalaya	1731	23	Gehrels et al., 2008
Tethys Himalaya	1731	7	Gehrels et al., 2008
Tethys Himalaya	1732	18	Gehrels et al., 2008
Tethys Himalaya	1734	22	Gehrels et al., 2008
Tethys Himalaya	1734	20	Gehrels et al., 2008
Tethys Himalaya	1735	19	Gehrels et al., 2008
Tethys Himalaya	1735	20	Gehrels et al., 2008
Tethys Himalaya	1735	26	Gehrels et al., 2008
Tethys Himalaya	1743	27	Gehrels et al., 2008
Tethys Himalaya	1744	18	Gehrels et al., 2008
Tethys Himalaya	1748	27	Gehrels et al., 2008
Tethys Himalaya	1751	11	Gehrels et al., 2008
Tethys Himalaya	1756	10	Gehrels et al., 2008
Tethys Himalaya	1757	24	Gehrels et al., 2008
Tethys Himalaya	1757	4	Gehrels et al., 2008
Tethys Himalaya	1762	32	Gehrels et al., 2008
Tethys Himalaya	1763	41	Gehrels et al., 2008
Tethys Himalaya	1768	19	Gehrels et al., 2008
Tethys Himalaya	1771	18	Gehrels et al., 2008
Tethys Himalaya	1771	18	Gehrels et al., 2008
Tethys Himalaya	1775	8	Gehrels et al., 2008
Tethys Himalaya	1776	9	Gehrels et al., 2008
Tethys Himalaya	1783	20	Gehrels et al., 2008
Tethys Himalaya	1783	8	Gehrels et al., 2008
Tethys Himalaya	1784	21	Gehrels et al., 2008
Tethys Himalaya	1785	28	Gehrels et al., 2008
Tethys Himalaya	1787	5	Gehrels et al., 2008
Tethys Himalaya	1791	28	Gehrels et al., 2008
Tethys Himalaya	1796	23	Gehrels et al., 2008
Tethys Himalaya	1798	6	Gehrels et al., 2008
Tethys Himalaya	1800	31	Gehrels et al., 2008
Tethys Himalaya	1800	19	Gehrels et al., 2008
Tethys Himalaya	1801	25	Gehrels et al., 2008
Tethys Himalaya	1802	39	Gehrels et al., 2008
Tethys Himalaya	1813	27	Gehrels et al., 2008
Tethys Himalaya	1824	8	Gehrels et al., 2008
Tethys Himalaya	1835	16	Gehrels et al., 2008
Tethys Himalaya	1850	30	Gehrels et al., 2008
Tethys Himalaya	1862	33	Gehrels et al., 2008
Tethys Himalaya	1862	4	Gehrels et al., 2008
Tethys Himalaya	1867	19	Gehrels et al., 2008
Tethys Himalaya	1878	9	Gehrels et al., 2008
Tethys Himalaya	1895	15	Gehrels et al., 2008
Tethys Himalaya	1908	30	Gehrels et al., 2008
Tethys Himalaya	1912	19	Gehrels et al., 2008
Tethys Himalaya	1913	26	Gehrels et al., 2008
Tethys Himalaya	1919	35	Gehrels et al., 2008
Tethys Himalaya	1920	5	Gehrels et al., 2008
Tethys Himalaya	1948	4	Gehrels et al., 2008
Tethys Himalaya	1963	18	Gehrels et al., 2008
Tethys Himalaya	1964	27	Gehrels et al., 2008
Tethys Himalaya	1969	18	Gehrels et al., 2008
Tethys Himalaya	1980	14	Gehrels et al., 2008
Tethys Himalaya	1981	6	Gehrels et al., 2008
Tethys Himalaya	2005	42	Gehrels et al., 2008
Tethys Himalaya	2006	32	Gehrels et al., 2008
Tethys Himalaya	2013	9	Gehrels et al., 2008
Tethys Himalaya	2019	9	Gehrels et al., 2008
Tethys Himalaya	2082	28	Gehrels et al., 2008
Tethys Himalaya	2084	18	Gehrels et al., 2008
Tethys Himalaya	2093	20	Gehrels et al., 2008
Tethys Himalaya	2096	39	Gehrels et al., 2008
Tethys Himalaya	2104	9	Gehrels et al., 2008
Tethys Himalaya	2105	18	Gehrels et al., 2008
Tethys Himalaya	2116	22	Gehrels et al., 2008
Tethys Himalaya	2134	5	Gehrels et al., 2008
Tethys Himalaya	2141	6	Gehrels et al., 2008
Tethys Himalaya	2171	18	Gehrels et al., 2008

Tethys Himalaya	2217	3	Gehrels et al., 2008
Tethys Himalaya	2226	10	Gehrels et al., 2008
Tethys Himalaya	2252	5	Gehrels et al., 2008
Tethys Himalaya	2270	18	Gehrels et al., 2008
Tethys Himalaya	2299	26	Gehrels et al., 2008
Tethys Himalaya	2333	26	Gehrels et al., 2008
Tethys Himalaya	2345	18	Gehrels et al., 2008
Tethys Himalaya	2362	19	Gehrels et al., 2008
Tethys Himalaya	2377	12	Gehrels et al., 2008
Tethys Himalaya	2390	4	Gehrels et al., 2008
Tethys Himalaya	2410	53	Gehrels et al., 2008
Tethys Himalaya	2413	24	Gehrels et al., 2008
Tethys Himalaya	2420	19	Gehrels et al., 2008
Tethys Himalaya	2429	12	Gehrels et al., 2008
Tethys Himalaya	2453	17	Gehrels et al., 2008
Tethys Himalaya	2454	17	Gehrels et al., 2008
Tethys Himalaya	2454	5	Gehrels et al., 2008
Tethys Himalaya	2457	24	Gehrels et al., 2008
Tethys Himalaya	2458	19	Gehrels et al., 2008
Tethys Himalaya	2461	17	Gehrels et al., 2008
Tethys Himalaya	2462	3	Gehrels et al., 2008
Tethys Himalaya	2463	29	Gehrels et al., 2008
Tethys Himalaya	2465	8	Gehrels et al., 2008
Tethys Himalaya	2466	18	Gehrels et al., 2008
Tethys Himalaya	2466	23	Gehrels et al., 2008
Tethys Himalaya	2467	17	Gehrels et al., 2008
Tethys Himalaya	2470	23	Gehrels et al., 2008
Tethys Himalaya	2476	21	Gehrels et al., 2008
Tethys Himalaya	2477	17	Gehrels et al., 2008
Tethys Himalaya	2477	44	Gehrels et al., 2008
Tethys Himalaya	2478	14	Gehrels et al., 2008
Tethys Himalaya	2479	18	Gehrels et al., 2008
Tethys Himalaya	2480	17	Gehrels et al., 2008
Tethys Himalaya	2481	4	Gehrels et al., 2008
Tethys Himalaya	2484	17	Gehrels et al., 2008
Tethys Himalaya	2487	17	Gehrels et al., 2008
Tethys Himalaya	2491	29	Gehrels et al., 2008
Tethys Himalaya	2497	17	Gehrels et al., 2008
Tethys Himalaya	2499	27	Gehrels et al., 2008
Tethys Himalaya	2501	17	Gehrels et al., 2008
Tethys Himalaya	2502	18	Gehrels et al., 2008
Tethys Himalaya	2503	6	Gehrels et al., 2008
Tethys Himalaya	2504	20	Gehrels et al., 2008
Tethys Himalaya	2506	17	Gehrels et al., 2008
Tethys Himalaya	2506	7	Gehrels et al., 2008
Tethys Himalaya	2507	17	Gehrels et al., 2008
Tethys Himalaya	2508	30	Gehrels et al., 2008
Tethys Himalaya	2509	17	Gehrels et al., 2008
Tethys Himalaya	2510	5	Gehrels et al., 2008
Tethys Himalaya	2511	23	Gehrels et al., 2008
Tethys Himalaya	2511	5	Gehrels et al., 2008
Tethys Himalaya	2511	8	Gehrels et al., 2008
Tethys Himalaya	2512	17	Gehrels et al., 2008
Tethys Himalaya	2513	6	Gehrels et al., 2008
Tethys Himalaya	2515	11	Gehrels et al., 2008
Tethys Himalaya	2517	17	Gehrels et al., 2008
Tethys Himalaya	2519	5	Gehrels et al., 2008
Tethys Himalaya	2520	17	Gehrels et al., 2008
Tethys Himalaya	2522	18	Gehrels et al., 2008
Tethys Himalaya	2522	4	Gehrels et al., 2008
Tethys Himalaya	2523	17	Gehrels et al., 2008
Tethys Himalaya	2530	18	Gehrels et al., 2008
Tethys Himalaya	2534	23	Gehrels et al., 2008
Tethys Himalaya	2534	17	Gehrels et al., 2008
Tethys Himalaya	2535	3	Gehrels et al., 2008
Tethys Himalaya	2543	17	Gehrels et al., 2008
Tethys Himalaya	2543	5	Gehrels et al., 2008
Tethys Himalaya	2544	17	Gehrels et al., 2008
Tethys Himalaya	2545	24	Gehrels et al., 2008
Tethys Himalaya	2558	4	Gehrels et al., 2008
Tethys Himalaya	2562	5	Gehrels et al., 2008

Tethys Himalaya	2563	6	Gehrels et al., 2008
Tethys Himalaya	2569	8	Gehrels et al., 2008
Tethys Himalaya	2570	3	Gehrels et al., 2008
Tethys Himalaya	2570	5	Gehrels et al., 2008
Tethys Himalaya	2572	30	Gehrels et al., 2008
Tethys Himalaya	2572	5	Gehrels et al., 2008
Tethys Himalaya	2574	5	Gehrels et al., 2008
Tethys Himalaya	2574	2	Gehrels et al., 2008
Tethys Himalaya	2575	6	Gehrels et al., 2008
Tethys Himalaya	2576	6	Gehrels et al., 2008
Tethys Himalaya	2582	6	Gehrels et al., 2008
Tethys Himalaya	2585	8	Gehrels et al., 2008
Tethys Himalaya	2587	8	Gehrels et al., 2008
Tethys Himalaya	2587	5	Gehrels et al., 2008
Tethys Himalaya	2588	5	Gehrels et al., 2008
Tethys Himalaya	2592	4	Gehrels et al., 2008
Tethys Himalaya	2593	5	Gehrels et al., 2008
Tethys Himalaya	2596	4	Gehrels et al., 2008
Tethys Himalaya	2597	17	Gehrels et al., 2008
Tethys Himalaya	2597	4	Gehrels et al., 2008
Tethys Himalaya	2599	6	Gehrels et al., 2008
Tethys Himalaya	2601	24	Gehrels et al., 2008
Tethys Himalaya	2601	5	Gehrels et al., 2008
Tethys Himalaya	2606	30	Gehrels et al., 2008
Tethys Himalaya	2606	27	Gehrels et al., 2008
Tethys Himalaya	2607	7	Gehrels et al., 2008
Tethys Himalaya	2607	14	Gehrels et al., 2008
Tethys Himalaya	2607	5	Gehrels et al., 2008
Tethys Himalaya	2615	5	Gehrels et al., 2008
Tethys Himalaya	2625	8	Gehrels et al., 2008
Tethys Himalaya	2625	22	Gehrels et al., 2008
Tethys Himalaya	2626	17	Gehrels et al., 2008
Tethys Himalaya	2627	6	Gehrels et al., 2008
Tethys Himalaya	2632	29	Gehrels et al., 2008
Tethys Himalaya	2632	5	Gehrels et al., 2008
Tethys Himalaya	2632	3	Gehrels et al., 2008
Tethys Himalaya	2641	24	Gehrels et al., 2008
Tethys Himalaya	2644	7	Gehrels et al., 2008
Tethys Himalaya	2648	62	Gehrels et al., 2008
Tethys Himalaya	2649	3	Gehrels et al., 2008
Tethys Himalaya	2652	17	Gehrels et al., 2008
Tethys Himalaya	2653	7	Gehrels et al., 2008
Tethys Himalaya	2654	24	Gehrels et al., 2008
Tethys Himalaya	2654	14	Gehrels et al., 2008
Tethys Himalaya	2655	29	Gehrels et al., 2008
Tethys Himalaya	2655	5	Gehrels et al., 2008
Tethys Himalaya	2659	25	Gehrels et al., 2008
Tethys Himalaya	2668	6	Gehrels et al., 2008
Tethys Himalaya	2668	6	Gehrels et al., 2008
Tethys Himalaya	2680	17	Gehrels et al., 2008
Tethys Himalaya	2681	5	Gehrels et al., 2008
Tethys Himalaya	2685	4	Gehrels et al., 2008
Tethys Himalaya	2686	6	Gehrels et al., 2008
Tethys Himalaya	2687	27	Gehrels et al., 2008
Tethys Himalaya	2687	8	Gehrels et al., 2008
Tethys Himalaya	2696	5	Gehrels et al., 2008
Tethys Himalaya	2698	6	Gehrels et al., 2008
Tethys Himalaya	2699	19	Gehrels et al., 2008
Tethys Himalaya	2703	1	Gehrels et al., 2008
Tethys Himalaya	2706	7	Gehrels et al., 2008
Tethys Himalaya	2710	17	Gehrels et al., 2008
Tethys Himalaya	2725	16	Gehrels et al., 2008
Tethys Himalaya	2731	6	Gehrels et al., 2008
Tethys Himalaya	2737	17	Gehrels et al., 2008
Tethys Himalaya	2741	5	Gehrels et al., 2008
Tethys Himalaya	2746	5	Gehrels et al., 2008
Tethys Himalaya	2760	6	Gehrels et al., 2008
Tethys Himalaya	2760	5	Gehrels et al., 2008
Tethys Himalaya	2769	9	Gehrels et al., 2008
Tethys Himalaya	2772	6	Gehrels et al., 2008
Tethys Himalaya	2790	6	Gehrels et al., 2008

Tethys Himalaya	2801	18	Gehrels et al., 2008
Tethys Himalaya	2805	23	Gehrels et al., 2008
Tethys Himalaya	2812	6	Gehrels et al., 2008
Tethys Himalaya	2828	37	Gehrels et al., 2008
Tethys Himalaya	2830	16	Gehrels et al., 2008
Tethys Himalaya	2836	17	Gehrels et al., 2008
Tethys Himalaya	2839	28	Gehrels et al., 2008
Tethys Himalaya	2841	16	Gehrels et al., 2008
Tethys Himalaya	2842	3	Gehrels et al., 2008
Tethys Himalaya	2843	18	Gehrels et al., 2008
Tethys Himalaya	2853	11	Gehrels et al., 2008
Tethys Himalaya	2860	16	Gehrels et al., 2008
Tethys Himalaya	2875	5	Gehrels et al., 2008
Tethys Himalaya	2877	16	Gehrels et al., 2008
Tethys Himalaya	2889	22	Gehrels et al., 2008
Tethys Himalaya	2916	5	Gehrels et al., 2008
Tethys Himalaya	2944	5	Gehrels et al., 2008
Tethys Himalaya	2953	16	Gehrels et al., 2008
Tethys Himalaya	2955	16	Gehrels et al., 2008
Tethys Himalaya	2970	5	Gehrels et al., 2008
Tethys Himalaya	3043	29	Gehrels et al., 2008
Tethys Himalaya	3083	16	Gehrels et al., 2008
Tethys Himalaya	3103	19	Gehrels et al., 2008
Tethys Himalaya	3119	16	Gehrels et al., 2008
Tethys Himalaya	3137	16	Gehrels et al., 2008
Tethys Himalaya	3145	3	Gehrels et al., 2008
Tethys Himalaya	3156	16	Gehrels et al., 2008
Tethys Himalaya	3257	30	Gehrels et al., 2008
Tethys Himalaya	3264	33	Gehrels et al., 2008
Tethys Himalaya	3280	4	Gehrels et al., 2008
Tethys Himalaya	3291	23	Gehrels et al., 2008
Tethys Himalaya	3310	7	Gehrels et al., 2008
Tethys Himalaya	3311	16	Gehrels et al., 2008
Tethys Himalaya	3318	43	Gehrels et al., 2008
Tethys Himalaya	3320	4	Gehrels et al., 2008
Tethys Himalaya	3372	6	Gehrels et al., 2008
Tethys Himalaya	3446	19	Gehrels et al., 2008
Tethys Himalaya	3452	18	Gehrels et al., 2008
Tethys Himalaya	3457	16	Gehrels et al., 2008
Tethys Himalaya	3533	2	Gehrels et al., 2008
Tethys Himalaya	3538	16	Gehrels et al., 2008
Tethys Himalaya	3755	5	Gehrels et al., 2008
Tethys Himalaya	3785	15	Gehrels et al., 2008
Tethys Himalaya	4042	6	Gehrels et al., 2008
Tethys Himalaya	4082	6	Gehrels et al., 2008

Chu, M.-F., Chung, S.-L., Song, B., Liu, D., O'Reilly, S. Y., Pearson, N. J., Ji, J., and Wen, D.-J., 2006, Zircon U-Pb and Hf isotope constraints on the Mesozoic tectonics and crustal evolution of southern Tibet: Geology, v. 34, no. 9, p. 745-748, doi: 10.1130/G22725.1.

Gehrels, G. E., Valencia, V. A., and Ruiz, J., 2008, Enhanced precision, accuracy, efficiency, and spatial resolution of U-Pb ages by laser ablation–multicollector–inductively coupled plasma–mass spectrometry: Geochemistry, Geophysics, Geosystems, v. 9, no. 3, doi: 10.1029/2007GC001805.

Ji, W.-Q., Wu, F.-Y., Chung, S.-L., Li, J.-X., and Liu, C.-Z., 2009, Zircon U–Pb geochronology and Hf isotopic constraints on petrogenesis of the Gangdese batholith, southern Tibet: Chemical Geology, v. 262, no. 3, p. 229-245, doi: 10.1016/j.chemgeo.2009.01.020.

Lee, H., Chung, S., Wang, Y., Zhu, D., Yan, J., Song, B., and Liu, D., 2007, Age, Petrogenesis and Geological Significance of the Linzizong Volcanic Successions in the Linzhou Basin, Southern Tibet: Evidence from Zircon U–Pb Dates and Hf Isotopes, Volume 23, Acta Petrologica Sinica, p. 493-500.

Zhang, R., Xu, W., Guo, J., Zong, K., Cai, H., and Yuan, H., 2007, Zircon U-Pb and Hf isotopic composition of deformed granite in the southern margin of the Gangdese belt, Tibet: Evidence for Early Jurassic subduction of Neo-Tethyan oceanic slab: Acta Petrologica Sinica, v. 23, no. 6, p. 1347-1353, doi: 10.1016/j.chemgeo.2009.09.008.

Zhu, D.-C., Mo, X.-X., Niu, Y., Zhao, Z.-D., Wang, L.-Q., Liu, Y.-S., and Wu, F.-Y., 2009, Geochemical investigation of Early Cretaceous igneous rocks along an east–west traverse throughout the central Lhasa Terrane, Tibet: Chemical Geology, v. 268, no. 3, p. 298-312.

Zhu, D.-C., Zhao, Z.-D., Niu, Y., Mo, X.-X., Chung, S.-L., Hou, Z.-Q., Wang, L.-Q., and Wu, F.-Y., 2011, The Lhasa Terrane: record of a microcontinent and its histories of drift and growth: Earth and Planetary Science Letters, v. 301, no. 1, p. 241-255, doi: 10.1016/j.epsl.2010.11.005.

DR2: ANALYTICAL AND NUMERICAL METHODS

DR2a: Zircon U-Pb dating methods

Six medium-grained sandstones were selected at regular intervals throughout the Dungsam Chu section of Siwalik sedimentary rocks (SJ1b, SJ2, SJ4, SJ6b, SJ9 and SJ12) and analyzed at GRPG, Nancy (France). Two further samples of similar grain size were selected once the change in provenance had been detected, within the relevant gap (i.e. between samples SJ6b and SJ9, where the change in provenance is observed). These samples were analyzed at NIGL, Keyworth (UK).

Prior to analysis, samples were dried and sieved to extract the <500-µm fraction at Lancaster University. Heavy minerals were extracted at NIGL, BGS Keyworth (UK) by wet separation on a Haultain superpanner, and di-iodomethane heavy liquid (with a density of 3.3). Magnetic separation was kept to a minimum to avoid biasing mineral populations. Zircon grains were handpicked, taking special care to select all grain types with respect to morphology, color and grain size, within a particular fraction of the separate. The zircons were mounted in epoxy, polished and photographed to help identify the analyzed grains. They were also imaged by cathodo-luminescence using an FEI Scanning Electron Microscope to ensure suitable areas were targeted during analysis. Each analysis corresponds to a different zircon grain.

The zircons mounts of samples SJ1b, SJ2, SJ4, SJ6b, SJ9 and SJ12, were subsequently gold-plated at CRPG, Nancy (France). U-Pb zircon dating for these samples was performed using the CAMECA IMS 1270 E7 ion microprobe facility at CRPG. The analyzed masses were: 203.5 (background noise, measured for 4 sec), Zr_2O (4 sec), ^{204}Pb (8 sec), ^{206}Pb (4 sec), ^{207}Pb (16 sec), ^{208}Pb (4 sec), ^{238}U (4 sec), $^{238}U^{16}O$ (3 sec) and $^{238}U^{16}O_2$ (3 sec). Counting was performed in mono-collection using an electron multiplier. Each analysis consists of 12 or 16 iterative cycles over each mass. The mass resolution was about 6000, which is sufficient to separate the molecular interferences. The primary current was ca. 5 nA using the duoplasmatron (oxygen source). The O^{2-} primary beam is a projected beam of about 20 µm in diameter (corresponding to the projection of a diaphragm of 200 µm). Before each measurement, there is a 120-second pre-sputtering with a 10 µm x 10 µm raster, a centering of the secondary beam within the field aperture, the contrast aperture and the energy slit and a centering of the mass on Zr_2O.

The zircon reference material 91500, with an age of 1064 Ma (Wiedenbeck et al., 1995), was analyzed at regular intervals and was used for determination of the correlation line between $^{206}Pb/^{238}U$ and UO/U in order to correct data for instrumental fractionation. The age calculations were based on the isotope ratios corrected for background noise and common lead (using ^{204}Pb). The U and Pb abundances are

calculated on the basis of the Zr_2O and UO correlation for the standard, and the isotope ratio $^{238}U/^{206}Pb$. The $^{207}Pb/^{206}Pb$ ratio is directly derived from each spot analysis.

U-Pb dating of zircons from samples SJ7 and SJ8 was performed using a Nu Instruments AttoM single-collector inductively coupled plasma mass spectrometer (SC-ICP-MS). The instrument was tuned such that oxides of U and Th represented less than 0.4% of the signal obtained from the metal ion peaks. The Nu AttoM SC-ICP-MS was used in peak-jumping mode with measurement on a MassCom secondary electron multiplier. The analyzed masses in each sweep were: ^{202}Hg, $^{204}Pb+Hg$, ^{206}Pb, ^{207}Pb, and ^{235}U. Each data integration records 100 sweeps of the measured masses, which roughly equates to 0.22 seconds. Dwell times on each mass are 400 µs on ^{207}Pb and ^{235}U, and 200 µs on all other masses; the switching between masses takes 40µs. ^{238}U is calculated using $^{238}U/^{235}U = 137.818$. Laser ablation was performed with a NewWave UP193SS solid-state laser ablation system. Ablation parameters were optimized to suit the Pb and U contents of the material and parameters adopted were a frequency of 10 Hz, with a fluence of 1.8 to 2.5 J/cm^2, a 30 second ablation time, and a 25-µm spot size. Three zircon reference materials (91500, GJ-1 and Plesovice; Jackson et al., 2004; Sláma et al., 2008; Wiedenbeck et al., 1995) were analyzed at regular intervals in order to correct data for instrumental fractionation. The average bias of the $^{207}Pb/^{206}Pb$ and $^{206}Pb/^{238}U$ ratios from preferred values derived by TIMS analysis are used for normalization. $^{206}Pb/^{238}U$ and $^{207}Pb/^{206}Pb$ uncertainties were propagated in the manner advocated by Horstwood (2008), utilizing the measurement uncertainty and the reproducibility of the ablation reference material used.

For the two sets of samples, respective in-house Excel spreadsheets were used for data reduction and error propagation, and Density Plotter (Vermeesch, 2012) was used for data presentation. Data reduction was undertaken with the age filters summarized in the following screening procedure table.

Table: Data screening procedure

1	Failed	Discarded
2	$^{206}Pb/^{238}U$ age > 100 Ma, uncertainty >10%	Discarded
3	> 10% discordant	Discarded
4	$^{206}Pb/^{238}U$ age 100 – 1200 Ma, >5% discordant	Discarded
5	Young grain - $^{206}Pb/^{238}U$ age < 100 Ma, < 10% discordant	$^{206}Pb/^{238}U$ age used
6	$^{206}Pb/^{238}U$ age 100 – 1200 Ma, < 5% discordant	$^{206}Pb/^{238}U$ age used
7	$^{206}Pb/^{238}U$ age > 1200 Ma, < 10% discordant	$^{207}Pb/^{206}Pb$ age used

Concordant ages within the limits defined in this table were accepted. It is important to consider that young zircon grains contain low levels of radiogenic Pb, which means that even low levels of common

Pb may lead to discordance. Many of the young analyzed grains in this study have been discarded in order for robustness of the ages to prevail. Data are presented in DR 3-6. Concordia diagrams for each sample are presented in Figure DR2a-1, below.

Dr2b: Rutile U-Pb dating method

Prior to analysis, the sample was dried, sieved (fraction < 500 μm) and washed with tap water at Lancaster University. Heavy minerals were extracted by wet separation on a Haultain superpanner, standard di-iodomethane heavy liquid (density of 3.3), and magnetic separation, which was kept to a minimum to avoid biasing mineral populations, at the NERC Isotope Geosciences Laboratory, Keyworth, UK (NIGL). Rutile grains were hand-picked, taking special care to select all grain types with respect to morphology, colour and grain size, within a particular fraction of the separate.

The rutiles were mounted in epoxy, polished, and photographed to help identify the analysed grains. U-Pb rutile dating was performed using a Nu Instruments AttoM single-collector inductively coupled plasma mass spectrometer (SC-ICP-MS) at NIGL. The instrument was tuned to ensure that ThO and UO were less than 0.4%. The Nu Attom SC-ICP-MS was used in peak-jumping mode with measurement on a MassCom secondary electron multiplier. The analysed masses in each sweep were: ^{202}Hg, ^{204}Pb+Hg, ^{206}Pb, ^{207}Pb, and ^{235}U. Each data integration records 100 sweeps of the measured masses, which roughly equates to 0.22 seconds. Dwell times on each mass are 400 μs on ^{207}Pb and ^{235}U, and 200 μs on all other masses; the switching between masses takes 40 μs. ^{238}U is calculated using ^{238}U/^{235}U = 137.818.

Laser ablation was performed using a New Wave Research UP193SS laser ablation system, with a low-volume cell (Horstwood et al., 2003). This cell has a washout to less than 1% of the peak signal in less than one second. Ablation parameters were optimized to suit the Pb and U contents with a frequency of 5Hz, a fluence of 1.5 to 3.0 J/cm^2, a 30 second ablation time, and a 30 to 35 μm spot size.
Four rutile reference materials, Sugluk-4, PCA-S207 (Bracciali et al., 2013) and R10 (Luvizotto et al., 2009) were analysed at regular intervals in order to correct data for instrumental fractionation. The average bias of the ^{207}Pb/^{206}Pb and ^{206}Pb/^{238}U ratios from preferred values derived by TIMS analysis are used for normalization. ^{206}Pb/^{238}U and ^{207}Pb/^{206}Pb uncertainties were propagated in the manner advocated by Horstwood (2008), utilising the measurement uncertainty and the reproducibility of the ablation reference material used.

Rutile commonly incorporates a significant amount of common Pb during crystallisation, and as a result is typically discordant in the U-Pb isotope system. Following the approach of Chew et al. (2011),

a ^{207}Pb-based correction was employed, using an iterative approach to obtain a ^{207}Pb/^{206}Pb intercept value based on a starting estimate generated from the terrestrial Pb evolution model of Stacey and Kramers (1975). This was used to calculate rutile ^{207}Pb-corrected ^{206}Pb/ ^{238}Uages.

Data reduction of rutile measurements was undertaken with the age filters summarised in the following screening procedure table.

Table: U-Pb rutile data screening procedure

	Failed	Discarded
	^{207}Pb-corr. age > 100 Ma, uncertainty > 10 %	Discarded
	^{207}Pb-corr. age 10-100 Ma, uncertainty > 20 %	Discarded
	^{207}Pb-corr. age < 10 Ma, uncertainty > 25 %	Discarded
	All other ages	Accepted

The analytical results are presented in Data Repository 7 and the accepted ages are plotted in figure DR2b-1 below.

References cited

Bracciali, L., Parrish, R. R., Horstwood, M. S., Condon, D. J., and Najman, Y., 2013, U Pb LA-(MC)-ICP-MS dating of rutile: New reference materials and applications to sedimentary provenance: Chemical Geology, v. 347, p. 82-101.

Chew, D. M., Sylvester, P. J., and Tubrett, M. N., 2011, U–Pb and Th–Pb dating of apatite by LA-ICPMS: Chemical Geology, v. 280, no. 1, p. 200-216.

Horstwood, M., 2008, Data reduction strategies, uncertainty assessment and resolution of LA-(MC-) ICP-MD isotope data, Mineralogical Association of Canada, v. 40.

Horstwood, M. S., Foster, G. L., Parrish, R. R., Noble, S. R., and Nowell, G. M., 2003, Common-Pb corrected in situ U–Pb accessory mineral geochronology by LA-MC-ICP-MS: Journal of Analytical Atomic Spectrometry, v. 18, no. 8, p. 837-846.

Luvizotto, G., Zack, T., Meyer, H., Ludwig, T., Triebold, S., Kronz, A., Münker, C., Stockli, D., Prowatke, S., and Klemme, S., 2009, Rutile crystals as potential trace element and isotope mineral standards for microanalysis: Chemical Geology, v. 261, no. 3, p. 346-369.

Stacey, J. t., and Kramers, J., 1975, Approximation of terrestrial lead isotope evolution by a two-stage model: Earth and planetary science letters, v. 26, no. 2, p. 207-221.

Vermeesch, P., 2012, On the visualisation of detrital age distributions: Chemical Geology, v. 312, p. 190-194.

DR2C: Stress calculation

Here we summarize the steps Copley et al. (2011) used to calculate the distribution of stress in the Indian lithosphere. Earthquakes and active faults have been observed where the Indian lithosphere bends beneath the Himalaya, and also further south within the Indian shield. Copley et al. (2011) therefore assumed that the stress within the lithosphere is limited to what can be supported by the faults before they break in earthquakes. Two independent estimates of the force balance were then used to estimate the stress distribution within the Indian plate: the locations, mechanisms, and stress drops of earthquakes within the Indian lithosphere (which give an increase in differential stress with depth of ~5 MPa km^{-1}), and the net force transmitted through the Indian plate (estimated from the motion of the plate and the forces exerted between India and Tibet; 5.5±1.5 TN m^{-1} along-strike).

If the stress drops in the earthquakes are summed over the seismogenic layer, the total force supported by the faults can be estimated to be approximately the same as the independent estimate of the total force transmitted through the Indian plate. This result has two implications: (1) the majority of the force transmitted through the Indian plate is supported by stresses on faults, and (2) the stress drops in the earthquakes represent close to the total pre-earthquake shear stresses on the faults. Point (2) means that the variation of stress drop with depth gives an estimate of the total stress distribution within the Indian plate, south of the region of bending beneath the Ganges foreland basin.

Beneath the Ganges foreland basin, the far-field tectonic compression is still present, but there are additional stresses related to the bending of the Indian plate beneath the Himalaya. This results in shallow normal faulting, and deeper thrust faulting. The depth of the transition from normal- to thrust-faulting is at 25±5 km. Copley et al. (2011) used this transition depth, along with the constraint that the net force transmitted through the lithosphere should match the far-field tectonic driving stresses, to calculate the variation of stress with depth within the Indian lithosphere underlying the foreland basin. They found that, in order to match the depth of transition from normal faulting to thrust faulting, and to also obtain the correct net force transmitted through the lithosphere, the faults underlying the foreland basin must have similar coefficients of friction to those further south within the Indian shield. In this foreland region, faults that cut through the entire seismogenic layer (e.g. the Oldham Fault on the northern margin of the Shillong Plateau that ruptured in a M8 earthquake in 1897) have resolved stresses that result in thrust motion. Faults that only cut the upper part of the seismogenic layer slip in a normal sense, and those that cut only the lower part slip as thrusts (see focal mechanisms in Figure DR2C(a)).

The variation of stress with depth suggests that differential stresses at the brittle-ductile transition are ~1.5 times higher in the foreland basin than further south within the Indian shield. These estimates therefore provide a picture of the changes in stress distribution as an area of the Indian Plate moves

northwards towards the Tibetan Plateau, and becomes affected by the stresses related to bending beneath the Himalaya.

In models of dislocation creep, the relationship between stress and strain-rate is of the form $\dot{\varepsilon} \propto \sigma^3$ where $\dot{\varepsilon}$ is strain rate, and S is stress. For rate-dependent fault creep, a change in shear stress would result in a change in sliding velocity by a factor of $exp(\Delta\sigma/aN)$, where $\Delta\sigma$ is the change in stress, a is the rate-dependent frictional parameter, and N is the effective normal stress. In either of these rheological laws, a change in the driving stress by a factor of 1.5 would result in a change in the fault-loading rate by a factor of 2 or more.

In these calculations we neglect local effects relating to erosion, deposition, isostatic balance, and strain accumulation in the hangingwalls and footwalls of the faults. As displacement accumulates on a thrust fault, the difference in gravitational potential energy across the fault increases, which acts to inhibit motion. This effect can be decreased is material is eroded from the hangingwall and deposited in the footwall, and if vertical motions occur to maintain isostatic equilibrium. Our inference that the slip rates on the faults on the margins of the Shillong Plateau has through time, rather than decreased, implies that these local effects on faulting are small compared to the imposed far-field compressive and bending stresses.

References cited:

Copley, A., Avouac, J. P., Hollingsworth, J., and Leprince, S., 2011, The 2001 Mw 7.6 Bhuj earthquake, low fault friction, and the crustal support of plate driving forces in India: Journal of Geophysical Research: Solid Earth, v. 116, no. B8, doi: 10.1029/2010JB008137.

Förste, C., Bruinsma, S., Flechtner, F., Marty, J., Lemoine, J., Dahle, C., Abrikosov, O., Neumayer, H., Biancale, R., and Barthelmes, F., A preliminary update of the Direct approach GOCE Processing and a new release of EIGEN-6C, *in* Proceedings AGU Fall Meeting Abstracts2012, Volume 1, p. 0923.

Horstwood, M., 2008, Data reduction strategies, uncertainty assessment and resolution of LA-(MC-) ICP-MS isotope data, Mineralogical Association of Canada, v. 40.

Jackson, S. E., Pearson, N. J., Griffin, W. L., and Belousova, E. A., 2004, The application of laser ablation-inductively coupled plasma-mass spectrometry to in situ U–Pb zircon geochronology: Chemical Geology, v. 211, no. 1, p. 47-69, doi: 10.1016/j.chemgeo.2004.06.017.

Ludwig, K. R., 2003, User's manual for Isoplot 3.00: a geochronological toolkit for Microsoft Excel, Kenneth R. Ludwig, v. 4.

Sláma, J., Košler, J., Condon, D. J., Crowley, J. L., Gerdes, A., Hanchar, J. M., Horstwood, M. S., Morris, G. A., Nasdala, L., and Norberg, N., 2008, Plešovice zircon—a new natural reference material for U–Pb and Hf isotopic microanalysis: Chemical Geology, v. 249, no. 1, p. 1-35, doi: 10.1016/j.chemgeo.2007.11.005.

Vermeesch, P., 2012, On the visualisation of detrital age distributions: Chemical Geology, v. 312, p. 190-194, doi: 10.1016/j.chemgeo.2012.04.021.

Wiedenbeck, M., Alle, P., Corfu, F., Griffin, W., Meier, M., Oberli, F., Quadt, A. v., Roddick, J., and Spiegel, W., 1995, Three natural zircon standards for U-Th-Pb, Lu-Hf, trace element and REE analyses: Geostandards newsletter, v. 19, no. 1, p. 1-23.

Supplementary figure captions:

Fig. DR2a-1: Zircon U-Pb concordia diagrams of samples from the Dungsam Chu section. Data are plotted as Wetherill concordia diagrams, using the Isoplot v. 4.14 add-in for Microsoft Excel (Ludwig, 2003), after data screening. The dotted dark blue line is the concordia curve where ages are indicated in Ma. Data point ellipses are at the 2σ level.

Fig. DR2b-1: Detrital rutile U-Pb ages for the sample SJ8 from the Dungsam Chu section, plotted as adaptive Kernel density plots (Vermeesch, 2012) with overlying histograms; n=number of dated grains. Inset: rutile U-Pb data from modern rivers draining the Himalayan syntaxis (solid line,n=138) and Himalaya outwith the syntaxis (dashed line, n=282). Note the uniquely short lag time for syntaxial rivers (from Bracciali et al 2016 and refs therein).

Fig. DR2C: (a) Topography and focal mechanisms for the India-Tibet region. Black focal mechanisms are thrust and normal earthquakes within the Indian lithosphere, labeled with their centroid depth in km and moment magnitude (see Copley et al. (2011) for details). Thrust faulting occurs throughout the seismogenic layer in central India. Beneath the foreland basin, shallow normal faulting is underlain by deeper thrust faulting. The red focal mechanism corresponds to the Bhuj earthquake (case study of Copley et al., 2011). SP, Shillong Plateau; RK, Rann of Kachchh. (b) Free-air gravity anomaly in the same region as shown in (a), from the EIGEN-6C gravity model (Förste et al., 2012). The contour interval is 50 mGal. The yellow dashed line shows the southern edge of the negative anomaly representing the foreland basin in the central and western part of the Himalayan arc. The Shillong Plateau is the positive anomaly marked 'SP'. (c) and (e) show profiles of differential stress against depth form locations in central India, and in the foreland basin, as shown schematically in (d) (calculations from Copley et al., 2011).

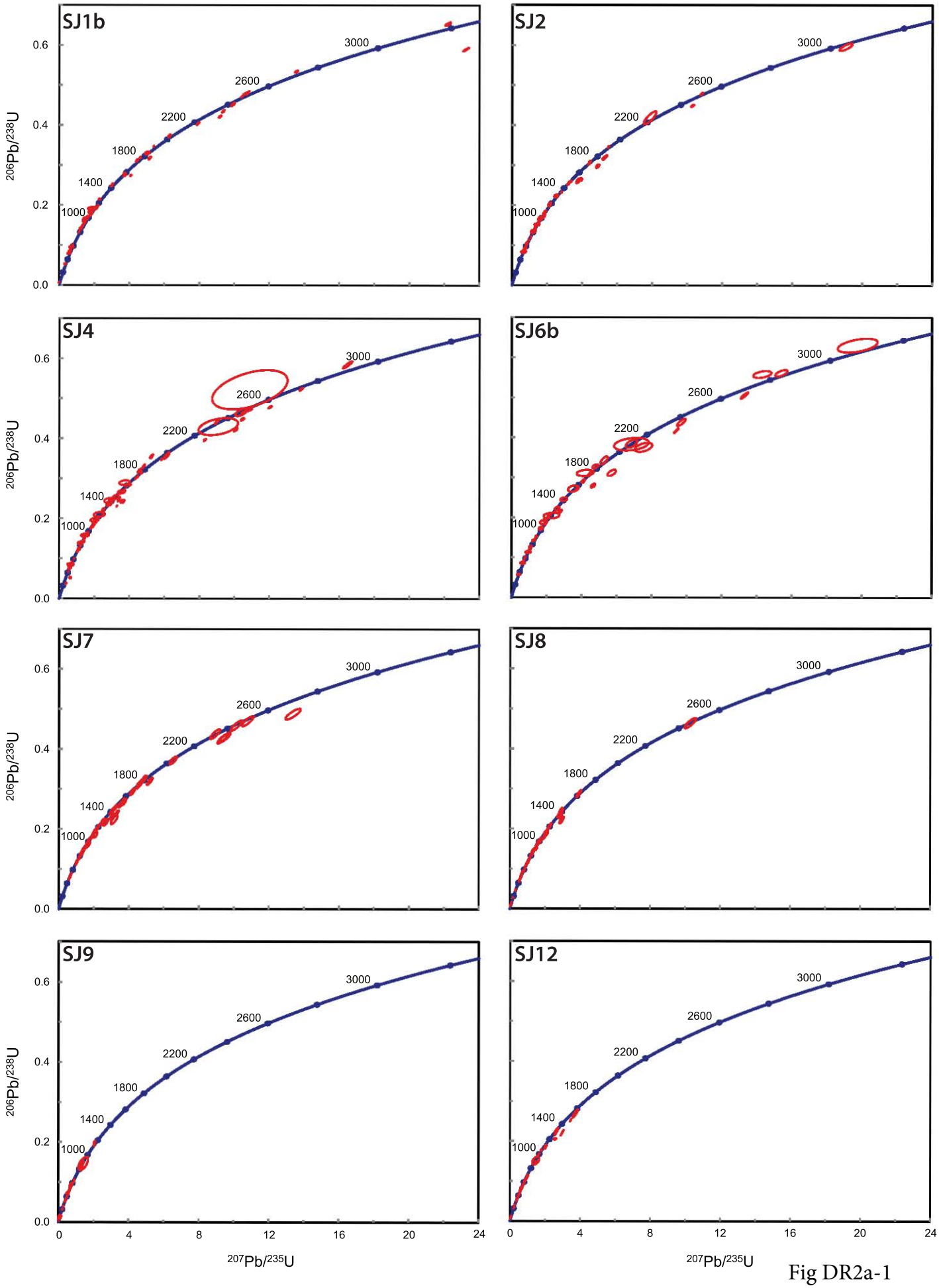
SJ1b
SJ2
SJ4
SJ6b
SJ7
SJ8
SJ9
SJ12
1000
1400
1800
2200
2600
3000
$^{206}Pb/^{238}U$
$^{207}Pb/^{235}U$
0.0
0.2
0.4
0.6
0
4
8
12
16
20
24

Fig DR2a-1

DC section Sample SJ8, depositional age 4.9 Ma

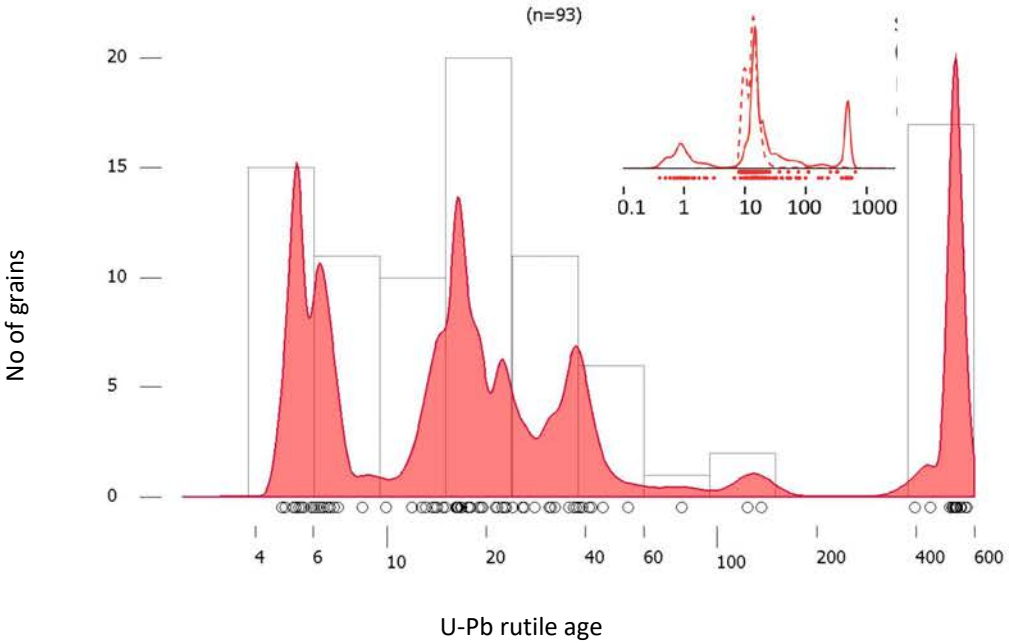

Fig DR2b-1

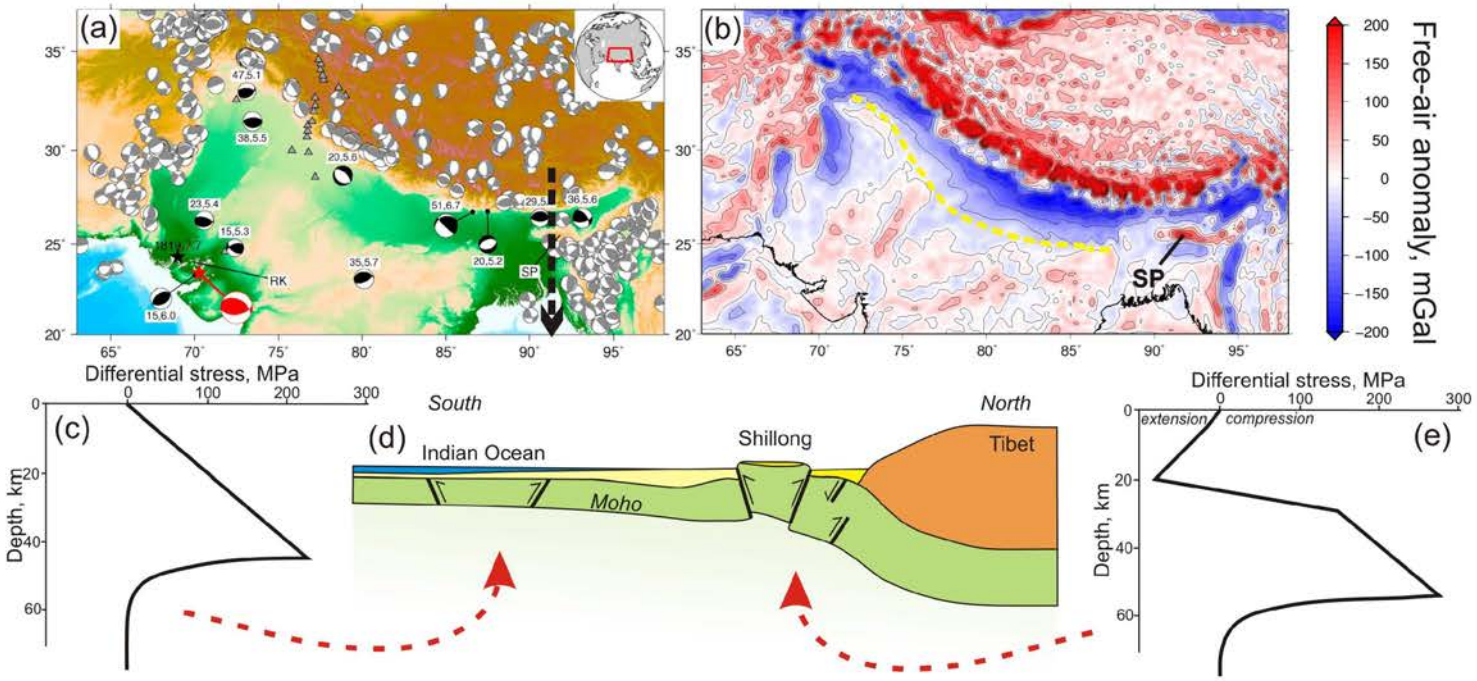
(a)
(b)
(c)
(d)
(e)
47,5,1
38,5,5
20,5,6
23,5,4
15,5,3
18,1,7
RK
15,6,0
35,5,7
51,6,7
29,5
36,5,6
20,5,2
SP
Differential stress, MPa
Depth, km
South
North
Indian Ocean
Shillong
Tibet
Moho
extension
compression
Free-air anomaly, mGal

Fig DR2c

TABLE S3: ION PROBE ZIRCON U-Pb DATA

Sample #	Grain #	$^{207}Pb/^{206}Pb$	$^{204}Pb/^{206}Pb$	$^{208}Pb/^{206}Pb$	Contents (ppm)			Data for Tera-Wasserburg plot				Data for Normal - Wetherill plot				Ages (Ma)				Disc.	Preferred Age		
					Pb	U	Th	$^{238}U/^{206}Pb$	1σ %	$^{207}Pb/^{206}Pb$	1σ %	$^{207}Pb/^{235}U$	1σ %	$^{206}Pb/^{238}U$	1σ %	ρ	$^{207}Pb/^{206}Pb$	2σ	$^{206}Pb/^{238}U$	2σ	$^{207}Pb/^{235}U$	2σ	6-38/ 7-35 (%)	Age (Ma)	2σ	Exp.
SJ1b	68	0.187	0.010	0.336	1	174	0	188.679	2.7	0.047	0.4	0.034	43.1	0.005	2.7	0.06	29	1586	34	2	34	28	0.0	34	2	5
SJ1b	50	0.078	0.002	0.187	4	98	27	19.380	1.5	0.054	0.1	0.384	9.0	0.052	1.5	0.17	372	376	324	10	330	50	1.8	324	10	6
SJ1b	103	0.059	0.000	0.222	51	773	510	12.970	0.5	0.057	0.0	0.604	0.9	0.077	0.5	0.58	485	32	479	4	480	6	0.2	479	4	6
SJ1b	14	0.078	0.002	0.120	49	737	197	12.887	1.1	0.057	0.1	0.612	10.1	0.078	1.1	0.11	499	414	482	10	485	76	0.6	482	10	6
SJ1b	59	0.060	0.000	0.143	28	410	174	12.453	0.6	0.056	0.0	0.616	1.2	0.080	0.6	0.50	438	46	498	6	487	10	-2.3	498	6	6
SJ1b	71	0.059	0.000	0.154	15	209	102	12.285	0.6	0.057	0.0	0.644	1.0	0.081	0.6	0.57	506	36	505	6	505	8	0.0	505	6	6
SJ1b	26	0.060	0.001	0.450	46	656	866	12.195	0.6	0.058	0.0	0.658	1.0	0.082	0.6	0.55	537	36	508	6	513	8	1.0	508	6	6
SJ1b	16	0.066	0.001	0.159	15	215	95	12.136	0.7	0.058	0.0	0.654	2.8	0.082	0.7	0.24	513	118	510	6	511	22	0.2	510	6	6
SJ1b	43	0.060	0.000	0.035	70	984	74	12.121	0.4	0.055	0.0	0.625	1.0	0.083	0.4	0.41	412	40	511	4	493	8	-3.7	511	4	6
SJ1b	112	0.064	0.001	0.192	20	278	156	12.092	0.5	0.057	0.0	0.654	1.9	0.083	0.5	0.26	505	80	512	4	511	16	-0.2	512	4	6
SJ1b	96	0.067	0.001	0.205	14	203	121	12.063	0.7	0.057	0.0	0.653	2.7	0.083	0.7	0.25	497	114	513	6	510	22	-0.6	513	6	6
SJ1b	10	0.068	0.001	0.156	49	668	321	12.077	0.4	0.059	0.0	0.672	2.7	0.083	0.4	0.14	562	112	513	4	522	22	1.7	513	4	6
SJ1b	116	0.067	0.001	0.255	24	337	250	12.063	0.7	0.057	0.0	0.654	2.0	0.083	0.7	0.35	501	80	513	6	511	16	-0.4	513	6	6
SJ1b	70	0.064	0.001	0.165	14	196	94	12.048	0.6	0.055	0.0	0.625	2.5	0.083	0.6	0.25	395	104	514	6	493	20	-4.3	514	6	6
SJ1b	33	0.074	0.001	0.251	38	528	362	12.034	0.6	0.056	0.1	0.636	6.0	0.083	0.6	0.10	434	254	514	6	500	46	-2.8	514	6	6
SJ1b	92	0.067	0.001	0.276	10	140	115	12.005	0.5	0.057	0.0	0.652	2.4	0.083	0.5	0.19	482	102	516	4	510	20	-1.2	516	4	6
SJ1b	31	0.063	0.000	0.252	38	529	499	12.005	0.5	0.058	0.0	0.665	2.8	0.083	0.5	0.18	528	118	516	4	518	22	0.4	516	4	6
SJ1b	118	0.059	0.000	0.193	41	568	357	11.990	0.5	0.057	0.0	0.659	0.9	0.083	0.5	0.54	503	30	516	4	514	6	-0.4	516	4	6
SJ1b	74	0.059	0.000	0.187	45	623	369	11.990	0.5	0.056	0.0	0.646	0.8	0.083	0.5	0.58	466	30	517	4	507	6	-2.0	517	4	6
SJ1b	67	0.063	0.001	0.214	27	373	243	11.962	0.5	0.056	0.0	0.645	1.6	0.084	0.5	0.32	449	64	518	4	505	12	-2.6	518	4	6
SJ1b	88	0.060	0.000	0.316	31	432	431	11.947	0.5	0.058	0.0	0.664	1.2	0.084	0.5	0.39	512	48	518	4	517	10	-0.2	518	4	6
SJ1b	95	0.059	0.000	0.156	49	668	321	11.891	0.4	0.057	0.0	0.659	1.0	0.084	0.4	0.42	485	38	520	4	514	8	-1.2	520	4	6
SJ1b	79	0.074	0.001	0.314	28	367	341	11.834	0.7	0.058	0.0	0.674	5.0	0.085	0.7	0.13	523	210	523	6	523	40	0.0	523	6	6
SJ1b	86	0.059	0.000	0.123	75	1029	402	11.806	0.4	0.057	0.0	0.663	0.8	0.085	0.4	0.48	484	32	524	4	517	6	-1.4	524	4	6
SJ1b	48	0.059	0.000	0.089	68	921	253	11.723	0.4	0.057	0.0	0.670	0.8	0.085	0.4	0.47	499	32	528	4	520	6	-1.5	528	4	6
SJ1b	105	0.058	0.000	0.121	142	1910	707	11.587	0.3	0.057	0.0	0.677	0.6	0.086	0.3	0.55	488	22	533	4	525	4	-1.5	533	4	6
SJ1b	34	0.063	0.000	0.335	28	375	388	11.468	0.5	0.059	0.0	0.704	1.6	0.087	0.5	0.31	549	66	539	6	541	14	0.4	539	6	6
SJ1b	69	0.059	0.000	0.169	50	658	362	11.312	0.5	0.057	0.0	0.697	0.9	0.088	0.5	0.57	500	32	546	6	537	8	-1.7	546	6	6
SJ1b	64	0.061	0.000	0.179	38	486	277	11.038	0.6	0.057	0.0	0.714	1.3	0.091	0.6	0.47	497	50	559	6	547	12	-2.2	559	6	6
SJ1b	61	0.058	0.001	0.983	30	368	263	10.650	1.4	0.057	0.1	0.740	11.2	0.094	1.4	0.13	498	454	578	16	562	94	-2.8	578	16	6
SJ1b	115	0.066	0.001	0.305	11	139	129	10.471	0.9	0.060	0.0	0.787	2.6	0.096	0.9	0.34	594	106	588	10	589	24	0.2	588	10	6
SJ1b	53	0.068	0.000	0.042	33	394	42	10.288	1.1	0.058	0.0	0.782	1.7	0.097	1.1	0.64	543	58	598	12	586	16	-2.0	598	12	6
SJ1b	113	0.062	0.000	0.265	50	595	505	10.256	0.3	0.059	0.0	0.799	1.2	0.098	0.3	0.29	583	48	600	4	596	10	-0.7	600	4	6
SJ1b	6	0.062	0.000	0.074	51	599	131	10.091	0.3	0.060	0.0	0.821	1.0	0.099	0.3	0.35	605	40	609	4	608	8	-0.2	609	4	6
SJ1b	51	0.067	0.000	0.226	63	561	446	7.657	0.4	0.065	0.0	1.177	0.8	0.131	0.4	0.54	786	28	791	6	790	8	-0.1	791	6	6
SJ1b	89	0.069	0.000	0.128	35	295	116	7.273	0.6	0.066	0.0	1.251	0.8	0.138	0.6	0.74	806	22	831	8	824	8	-0.8	831	8	6
SJ1b	94	0.068	0.000	0.057	84	702	119	7.215	0.5	0.067	0.0	1.283	0.8	0.139	0.5	0.64	842	26	837	8	838	10	0.1	837	8	6
SJ1b	21	0.072	0.001	0.126	28	235	87	7.143	0.4	0.064	0.0	1.240	1.9	0.140	0.4	0.22	749	78	845	6	819	22	-3.2	845	6	6
SJ1b	63	0.071	0.000	0.375	27	225	272	7.123	0.4	0.066	0.0	1.280	1.6	0.140	0.4	0.22	810	64	847	6	837	18	-1.2	847	6	6
SJ1b	57	0.069	0.000	0.121	30	251	96	7.123	0.4	0.066	0.0	1.286	1.0	0.140	0.4	0.43	821	36	847	6	840	12	-0.8	847	6	6
SJ1b	81	0.068	0.000	0.125	54	445	178	7.123	0.4	0.067	0.0	1.294	0.7	0.140	0.4	0.51	834	24	847	6	843	8	-0.5	847	6	6
SJ1b	53	0.068	0.000	0.211	67	559	389	7.123	0.4	0.066	0.0	1.271	0.7	0.140	0.5	0.63	796	24	847	8	833	8	-1.7	847	8	6
SJ1b	35	0.077	0.001	0.113	16	131	37	7.097	0.7	0.066	0.0	1.281	2.4	0.141	0.7	0.29	803	94	850	12	837	28	-1.6	850	12	6
SJ1b	30	0.068	0.000	0.487	104	858	1360	7.062	0.4	0.067	0.0	1.295	0.6	0.141	0.4	0.59	822	20	852	6	844	8	-0.9	852	6	6
SJ1b	41	0.067	0.000	0.227	71	585	436	7.007	0.4	0.066	0.0	1.289	0.7	0.142	0.4	0.59	808	22	853	6	841	8	-1.4	853	6	6
SJ1b	83	0.068	0.000	0.080	83	677	172	7.013	0.4	0.066	0.0	1.292	0.7	0.143	0.4	0.53	797	24	859	6	842	8	-2.0	859	6	6
SJ1b	120	0.069	0.000	0.150	55	442	212	6.949	0.6	0.067	0.0	1.332	1.0	0.144	0.6	0.57	841	34	867	10	860	12	-0.8	867	10	6
SJ1b	44	0.067	0.000	0.033	228	1831	191	6.887	0.3	0.067	0.0	1.337	0.4	0.145	0.3	0.74	831	12	874	6	862	6	-1.4	874	6	6
SJ1b	24	0.091	0.002	0.265	46	366	242	6.775	0.8	0.068	0.0	1.391	1.9	0.148	0.8	0.41	879	70	887	12	885	22	-0.2	887	12	6
SJ1b	76	0.073	0.000	0.186	39	300	174	6.588	0.5	0.069	0.0	1.445	1.1	0.152	0.5	0.45	900	42	911	8	908	14	-0.3	911	8	6
SJ1b	39	0.069	0.000	0.047	110	833	118	6.510	0.5	0.068	0.0	1.437	0.7	0.154	0.5	0.77	864	18	921	8	904	8	-1.9	921	8	6
SJ1b	109	0.071	0.000	0.051	120	902	158	6.452	0.6	0.070	0.0	1.493	0.7	0.155	0.6	0.86	924	16	929	10	928	8	-0.1	929	10	6
SJ1b	2	0.075	0.000	0.409	24	176	229	6.427	1.1	0.069	0.0	1.480	2.1	0.156	1.1	0.52	898	72	932	20	922	26	-1.1	932	20	6
SJ1b	12	0.072	0.000	0.125	51	383	156	6.423	1.0	0.069	0.0	1.482	2.1	0.156	1.0	0.50	900	72	933	18	923	24	-1.1	933	18	6
SJ1b	52	0.077	0.001	0.143	49	363	143	6.382	0.5	0.070	0.0	1.515	1.4	0.157	0.5	0.35	931	52	939	8	938	16	-0.3	938	8	6
SJ1b	4	0.073	0.000	0.030	81	593	42	6.297	0.5	0.070	0.0	1.540	0.6	0.159	0.5	0.79	939	14	950	8	947	8	-0.3	950	8	6
SJ1b	7	0.073	0.000	0.092	85	621	175	6.285	0.5	0.070	0.0	1.528	0.9	0.159	0.5	0.58	918	30	952	10	942	12	-1.1	952	10	6
SJ1b	49	0.091	0.002	0.222	15	104	56	6.165	2.5	0.069	0.0	1.484	4.4	0.162	2.5	0.56	818	148	969	44	924	52	-4.9	969	44	6
SJ1b	46	0.076	0.000	0.066	82	577	107	6.075	0.7	0.072	0.0	1.641	1.4	0.165	0.7	0.47	994	50	982	12	986	18	0.4	982	12	6
SJ1b	104	0.078	0.000	0.052	34	237	33	5.999	0.7	0.073	0.0	1.676	1.3	0.167	0.7	0.50	1011	46	994	12	999	16	0.5	994	12	6
SJ1b	80	0.074	0.000	0.252	49	343	283	5.967	0.4	0.071	0.0	1.650	0.9	0.168	0.4	0.43	968	34	999	8	989	12	-1.0	999	8	6
SJ1b	13	0.076	0.000	0.058	115	796	139	5.956	0.5	0.073	0.0	1.695	0.7	0.168	0.5	0.68	1020	20	1000	8	1007	8	0.7	1000	8	6
SJ1b	22	0.081	0.001	0.300	136	940	868	5.845	0.4	0.072	0.0	1.659	0.6	0.168	0.4	0.59	972	20	1002	6	993	8	-0.9	1002	6	6
SJ1b	101	0.075	0.000	0.120	59	401	150	5.875	0.5	0.072	0.0	1.686	0.9	0.170	0.5	0.61	982	28	1013	10	1003	12	-1.0	1013	10	6
SJ1b	85	0.077	0.000	0.028	83	553	43	5.721	1.3	0.076	0.0	1.829	1.7	0.175	1.3	0.76	1093	44	1036	24	1056	22	1.7	1036	24	6
SJ1b	108	0.081	0.000	0.196	18	115	69	5.596	1.8	0.077	0.0	1.901	2.5	0.179	1.8	0.72	1125	70	1060	38	1081	34	1.9	1060	38	6
SJ1b	37	0.086	0.001	0.414	14	90	111	5.525	0.7	0.077	0.0	1.773	1.7	0.181	0.7	0.39	959	62	1072	12	1036	22	-3.5	1072	12	6
SJ1b	82	0.077	0.000	0.168	45	288	158	5.444	0.7	0.075	0.0	1.883	1.0	0.184	0.7	0.70	1062	30	1087	14	1079	14	-0.7	1087	14	6
SJ1b	107	0.076	0.000	0.053	57	356	61	5.342	0.7	0.074	0.0	1.922	0.9	0.187	0.7	0.83	1053	20	1106	14	1089	12	-1.6	1106	14	6
SJ1b	58	0.078	0.000	0.114	64	394	145	5.274	0.5	0.075	0.0	1.965	0.6	0.190	0.5	0.77	1074	14	1119	10	1104	8	-1.4	1119	10	6
SJ1b	75	0.113	0.003	0.299	16	100	70	5.263	1.2	0.074	0.1	1.944	8.8	0.190	1.2	0.14	1047	332	1121	24	1096	114	-2.3	1121	24	6
SJ1b	99	0.077	0.000	0.178	165	996	591	5.189	0.4	0.076	0.0	2.024	0.4	0.193	0.4	0.82	1100	10	1136	8	1124	6	-1.1	1136	8	6
SJ1b	87	0.086	0.001	0.148	79	467	212	5.099	0.7	0.083	0.0	2.247	1.0	0.196	0.7	0.72	1272	30	1154	14	1196	14	3.5	1154	14	6
SJ1b	90	0.087	0.001	0.335	18	98	105	4.693	0.5	0.080	0.0	2.357	1.3	0.213	0.5	0.38	1203	46	1245	12	1230	18	-1.2	1203	46	7
SJ1b	54	0.093	0.000	0.233	27	128	99	4.019	1.1	0.089	0.0	3.061	1.2	0.249	1.1	0.86	1409	22	1432	28	1423	18	-0.6	1409	22	7
SJ1b	76	0.099	0.000	0.407	95	498	544	3.591	0.4	0.098	0.0	3.754	0.8	0.279	0.4	0.53	1582	26	1584	12	1583	12	-0.1	1582	26	8
SJ1b	11	0.113	0.001	0.204	126	535	303	3.655	0.8	0.100	0.0	3.760	1.4	0.274	0.8	0.56	1628	42	1559	22	1588	22	1.8	1628	42	8
SJ1b	65	0.113	0.001	0.231	66	247	182	3.226	0.6	0.105	0.0	4.474	0.8	0.310	0.6	0.76	1708	20	1741	18	1726	14	-0.9	1708	20	8
SJ1b	9	0.107	0.000	0.190	84	310	199	3.153	0.4	0.104	0.0	4.655	0.5	0.317	0.4	0.72	1739	14	1776	12	1759	8	-1.0	1739	14	8
SJ1b	36	0.111	0.000	0.066	139	592	137	3.068	0.4	0.110	0.0	4.134	0.6	0.273	0.4	0.70	1799	14	1554	10	1681	8	6.4	1799	14	8
SJ1b	19	0.123	0.001	0.290	26	91	82	3.039	0.7	0.112	0.0	5.072	1.7	0.329	0.7	0.42	1828	56	1834	24	1831	28	-0.2	1828	56	8
SJ1b	98	0.114	0.000	0.068	410	1380	325	2.891	0.3	0.114	0.0	5.438	0.3	0.346	0.3	0.94	1864	4	1915	10	1891	6	-1.3	1864	4	8
SJ1b	91	0.122	0.002	0.042	70	257	35	3.162	0.8	0.119	0.0	5.210	0.9	0.316	0.8	0.89	1949	14	1771	24	1854	16	4.5	1949	14	8
SJ1b	47	0.125	0.000	0.249	63	196	168	2.688	0.6	0.123	0.0	6.329	0.7	0.372	0.6	0.80	2006	16	2039	20	2023	12	-0.8	2006	16	8
SJ1b	106	0.144	0.000	0.184	168	484	612	2.484	0.6	0.144	0.0	7.972	0.7	0.402	0.6	0.94	2271	8	2181	22	2228	12	2.1	2271	8	8
SJ1b	5	0.157	0.000	0.155	959	2574	1342	2.307	0.5	0.157	0.0	9.401	0.5	0.434	0.5	0.84	2427	10	2322	18	2378	10	2.4	2427	10	8
SJ1b	73	0.160	0.000	0.189	93	259	175	2.381	0.4	0.159	0.0	9.215	0.5	0.420	0.4	0.80	2446	10	2260	16	2360	10	4.2	2446	10	8
SJ1b	27	0.161	0.000	0.261	85	220	206	2.219	0.6	0.160	0.0	9.952	0.7	0.451	0.6	0.87	2457	12	2398	24	2430	12	1.3	2457	12	8
SJ1b	17	0.164	0.000	0.248	165	406	354	2.115	0.7	0.161	0.0	10.523	0.7	0.473	0.7	0.98	2470	4	2496	30	2482	14	-0.6	2470	4	8
SJ1b	66	0.164	0.000	0.151	136	331	184	2.089	0.4	0.162	0.0	10.720	0.4	0.479	0.4	0.93	2481	6	2522	16	2499	8	-0.9	2481	6	8
SJ1b	32	0.164	0.000	0.153	82	199	107	2.085	0.6	0.163	0.0	10.789	0.6	0.480	0.6	0.94	2489	8	2525	24	2505	12	-0.8	2489	8	8
SJ1b	117	0.185	0.000	0.184	134	293	194	1.877	0.3	0.185	0.0	13.572	0.4	0.533	0.3	0.75	2696	10	2753	14	2720	8	-1.2	2696	10	8
SJ1b	97	0.249	0.000	0.279	52	93	97	1.533	0.4	0.247	0.0	22.220	0.5	0.652	0.4	0.85	3166	8	3237	22	3193	10	-1.4	3166	8	8
SJ1b	18	0.287	0.000	0.223	403	796	663	1.698	0.5	0.286	0.0	23.253	0.5	0.589	0.5	0.97	3398	4	2984	24	3238	10	7.8	3398	4	8
SJ1b	29	0.145	0.007	0.940	3	11	20	1.691	2.8	0.054	0.3	0.672	32.1	0.091	2.8	0.09	391	350	1210	561	522	250	-7.5	N.D.	N.D.	4
SJ1b	119	0.073	0.002	0.692	6	84	174	12.005	0.7	0.053	0.2	0.607	2.5	0.084	0.7	0.28	322	106	516	6	482	18	-7.1	N.D.	N.D.	4
SJ1b	42	0.071	0.001	0.424	7	92	113	11.891	1.0	0.052	0.0	0.606	4.6	0.084	1.0	0.22	296	198	521	10	481	34	-8.3	N.D.	N.D.	4
SJ1b	62	0.070	0.001	0.081	16	216	247	11.834	0.9	0.054	0.0	0.632	3.8	0.085	0.9	0.24	380	162	523	10	497	30	-5.2	N.D.	N.D.	4
SJ1b	20	0.070	0.001	0.326	17	258	239	13.089	5.9	0.054	0.1	0.676	7.6	0.076	5.9	0.78	749	194	474	54	524	62	9.5	N.D.	N.D.	4
SJ1b	110	0.124	0.004	0.196	32	307	62	8.278	1.6	0.069	0.1	1.155	10.1	0.121	1.6	0.15	908	388	735	22	780	108	5.8	N.D.	N.D.	4
SJ1b	56	0.135	0.006	0.230	39	542	70	11.834	2.8	0.053	0.3	0.618	32.1	0.085	2.8	0.09	333	1194	523	28	489	234	-7.0	N.D.	N.D.	4
SJ1b	72	0.072	0.002	0.627	4	57	107	11.682	1.0	0.049	0.1	0.577	5.8	0.086	1.0	0.17	144	258	529	10	463	42	-14.3	N.D.	N.D.	3
SJ1b	93	0.072	0.002	0.307	6	91	76	12.315	1.1	0.049	0.0	0.550	4.9	0.081	1.1	0.22	154	216	503	10	445	34	-13.0	N.D.	N.D.	3
SJ1b	114	0.086	0.002	0.598	6	39	70	6.013	0.9	0.062	0.0	1.415	4.6	0.166	0.9	0.20	665	186	991	16	895	54	-10.7	N.D.	N.D.	3
SJ1b	77	0.069	0.001	0.170	8	116	126	11.808	0.5	0.051	0.0	0.595	3.7	0.085	0.5	0.28	236	162	524	10	474	28	-10.5	N.D.	N.D.	4
SJ1b	84	0.076	0.000	0.075	59	1004	115	14.577	1.0	0.074	0.0	0.699	1.2	0.069	1.0	0.84	1039	26	428	8	538	10	20.4	N.D.	N.D.	3
SJ1b	102	0.155	0.000	0.104	77	256	81	2.841	0.7	0.154	0.0	7.484	0.9	0.352	0.7	0.83	2393	16	1944	24	2171	16	10.5	N.D.	N.D.	4
SJ1b	40	0.115	0.001	0.200	108	926	648	7.342	0.7	0.107	0.0	2.016	0.9	0.136	0.7	0.88	1755	20	823	12	1121	12	26.6	N.D.	N.D.	4
SJ1b	3	0.881	0.052	2.264	N.D.	N.D.	N.D.	N.D.	N.D.	N.D.	N.D.	N.D.	N.D.	N.D.	N.D.	N.D.	N.D.	N.D.	N.D.	N.D.	N.D.	N.D.	N.D.	N.D.	N.D.	4
SJ1b	15	N.D.	N.D.	N.D.	N.D.	N.D.	N.D.	N.D.	N.D.	N.D.	N.D.	N.D.	N.D.	N.D.	N.D.	N.D.	N.D.	N.D.	N.D.	N.D.	N.D.	N.D.	N.D.	N.D.	N.D.	4
SJ1b	23	0.173	0.000	0.073	N.D.	N.D.	N.D.	N.D.	N.D.	N.D.	N.D.	N.D.	N.D.	N.D.	N.D.	N.D.	N.D.	N.D.	N.D.	N.D.	N.D.	N.D.	N.D.	N.D.	N.D.	4
SJ1b	25	0.601	0.045	1.297	N.D.	N.D.	N.D.	N.D.	N.D.	N.D.	N

SJ4	95	0.059	0.000	0.426	40	570	775	12.151	0.6	0.056	0.0	0.639	1.0	0.082	0.6	0.55	464	38	510	6	501	8	-1.8	510	6	6
SJ4	16	0.101	0.003	0.443	28	389	447	12.086	1.8	0.055	0.1	0.625	13.6	0.083	1.8	0.13	402	553	512	17	493	103	-4.0	512	17	6
SJ4	84	0.060	0.000	0.159	13	183	88	12.034	0.7	0.057	0.0	0.652	1.3	0.083	0.7	0.53	489	48	514	6	510	10	-0.8	514	6	6
SJ4	103	0.060	0.000	0.331	47	666	696	12.048	0.5	0.057	0.0	0.645	0.8	0.083	0.5	0.68	477	26	514	6	507	6	-1.4	514	6	6
SJ4	120	0.058	0.000	0.172	71	985	534	11.990	1.0	0.057	0.0	0.652	1.2	0.083	1.0	0.83	479	30	516	10	510	10	-1.2	516	10	6
SJ4	107	0.060	0.000	0.263	27	366	306	11.848	0.4	0.058	0.0	0.671	1.3	0.084	0.4	0.33	517	54	523	4	522	10	-0.2	523	4	6
SJ4	78	0.058	0.000	0.078	233	3170	791	11.710	0.5	0.057	0.0	0.675	0.5	0.085	0.5	0.89	503	10	528	4	524	4	-0.8	528	4	6
SJ4	24	0.147	0.006	0.527	23	313	326	11.708	2.2	0.055	0.2	0.647	18.4	0.085	2.2	0.12	408	728	528	23	506	142	-4.3	528	23	6
SJ4	83	0.064	0.001	0.220	10	133	88	11.547	1.0	0.055	0.0	0.658	1.8	0.087	1.0	0.52	416	68	535	10	513	14	-4.3	535	10	6
SJ4	33	0.063	0.000	0.345	41	527	546	10.973	0.9	0.057	0.0	0.722	1.5	0.091	0.9	0.61	509	51	562	10	552	13	-1.9	562	10	6
SJ4	77	0.062	0.000	0.100	53	611	190	9.980	0.3	0.061	0.0	0.658	0.5	0.100	0.3	0.71	628	14	615	4	618	4	0.5	615	4	6
SJ4	61	0.085	0.002	0.311	32	311	268	9.446	1.1	0.064	0.0	1.038	2.2	0.118	1.1	0.61	729	78	721	16	723	22	0.3	721	16	6
SJ4	86	0.081	0.001	0.203	15	140	74	8.137	0.6	0.066	0.0	1.123	2.8	0.123	0.6	0.22	816	112	747	8	765	30	2.4	747	8	6
SJ4	44	0.096	0.000	0.042	111	1027	83	7.985	0.9	0.063	0.0	1.081	1.2	0.125	0.9	0.80	695	30	761	13	744	12	-2.2	761	13	6
SJ4	59	0.069	0.000	0.130	46	420	163	7.899	0.6	0.065	0.0	1.132	0.7	0.127	0.6	0.83	769	16	769	8	769	8	0.0	769	8	6
SJ4	70	0.070	0.000	0.226	20	177	128	7.587	0.4	0.068	0.0	1.233	0.9	0.132	0.4	0.44	865	32	798	6	816	10	2.2	798	6	6
SJ4	121	0.070	0.000	0.166	21	179	92	7.289	0.5	0.067	0.0	1.274	0.8	0.137	0.5	0.69	849	28	829	8	834	6	0.6	829	8	6
SJ4	50	0.069	0.000	0.292	35	300	288	7.273	0.5	0.066	0.0	1.250	1.1	0.136	0.5	0.47	804	38	830	8	823	12	-0.9	830	8	6
SJ4	72	0.069	0.000	0.138	43	368	151	7.278	0.5	0.066	0.0	1.250	0.8	0.137	0.5	0.54	805	30	830	8	823	10	-0.9	830	8	6
SJ4	106	0.071	0.000	0.149	23	197	88	7.257	0.6	0.065	0.0	1.239	1.1	0.138	0.6	0.56	782	38	832	10	819	12	-1.6	832	10	6
SJ4	18	0.085	0.001	0.188	57	477	236	7.194	1.2	0.065	0.0	1.243	4.7	0.139	1.2	0.26	770	187	839	19	820	53	-2.3	839	19	6
SJ4	20	0.094	0.002	0.236	53	441	258	7.185	1.5	0.063	0.0	1.204	7.9	0.139	1.5	0.19	699	314	840	24	802	86	-4.7	840	24	6
SJ4	54	0.068	0.000	0.047	52	433	60	7.163	0.5	0.066	0.0	1.279	0.9	0.140	0.5	0.54	822	30	842	8	837	10	-0.6	842	8	6
SJ4	67	0.068	0.000	0.247	79	652	537	7.123	0.4	0.066	0.0	1.285	0.8	0.140	0.4	0.45	819	30	847	6	839	10	-1.0	847	6	6
SJ4	97	0.074	0.000	0.151	52	427	190	6.993	0.5	0.072	0.0	1.411	1.5	0.143	1.0	0.62	972	48	862	16	893	18	3.5	862	16	6
SJ4	105	0.067	0.000	0.009	440	3564	101	6.954	0.5	0.067	0.0	1.320	0.5	0.144	0.5	0.91	824	8	866	8	854	6	-1.4	866	8	6
SJ4	71	0.124	0.003	0.469	83	526	601	6.914	0.4	0.076	0.0	1.442	0.6	0.150	0.5	0.87	921	12	900	8	906	8	0.7	900	8	6
SJ4	56	0.079	0.000	0.136	202	1270	578	5.411	0.4	0.078	0.0	1.995	0.4	0.185	0.4	0.94	1155	6	1093	8	1114	6	-1.9	1093	8	6
SJ4	116	0.077	0.000	0.040	108	672	86	5.348	0.7	0.078	0.0	1.958	0.7	0.187	0.7	0.93	1093	10	1105	14	1101	10	-0.4	1105	14	6
SJ4	96	0.077	0.000	0.044	68	421	57	5.322	0.4	0.078	0.0	1.966	0.5	0.188	0.4	0.72	1092	16	1110	8	1104	8	-0.5	1110	8	6
SJ4	9	0.098	0.002	0.187	239	1450	774	5.206	1.4	0.076	0.0	2.020	4.0	0.192	1.4	0.35	1102	145	1133	28	1122	53	-0.9	1133	28	6
SJ4	114	0.078	0.000	0.352	61	368	432	5.176	0.5	0.076	0.0	2.012	0.9	0.193	0.5	0.59	1082	28	1139	10	1120	12	-1.7	1139	10	6
SJ4	41	0.078	0.000	0.113	75	452	148	5.164	0.9	0.075	0.0	2.000	1.3	0.194	0.9	0.71	1066	36	1141	19	1116	17	-2.3	1141	19	6
SJ4	34	0.099	0.002	0.386	45	272	280	5.151	1.0	0.076	0.0	1.989	1.9	0.194	1.0	0.51	1050	65	1144	20	1112	26	-2.9	1144	20	6
SJ4	27	0.113	0.002	0.272	41	245	166	5.088	1.3	0.074	0.1	2.000	7.5	0.197	1.3	0.17	1036	284	1157	27	1115	99	-3.7	1157	27	6
SJ4	82	0.082	0.000	0.747	16	93	230	5.033	0.5	0.077	0.0	2.112	1.2	0.199	0.5	0.45	1124	42	1168	12	1153	16	-1.3	1168	12	6
SJ4	30	0.120	0.003	0.212	44	242	110	4.759	1.9	0.079	0.2	2.285	9.2	0.210	1.9	0.21	1168	336	1229	43	1208	126	-1.8	1168	336	6
SJ4	98	0.086	0.001	0.513	17	101	168	4.948	1.0	0.078	0.0	2.181	1.7	0.202	1.0	0.57	1154	56	1187	22	1175	24	-1.0	1187	22	6
SJ4	36	0.098	0.001	0.351	27	143	142	4.483	1.0	0.082	0.0	2.510	1.6	0.223	1.0	0.61	1236	51	1298	23	1275	24	-1.8	1298	23	6
SJ4	81	0.084	0.000	0.213	61	320	223	4.509	0.4	0.082	0.0	2.520	0.7	0.222	0.4	0.60	1255	20	1291	10	1278	10	-1.0	1255	20	6
SJ4	76	0.085	0.001	0.171	57	306	178	4.581	0.6	0.083	0.0	2.488	0.7	0.218	0.6	0.84	1261	16	1273	14	1268	10	-0.4	1261	16	6
SJ4	17	0.121	0.003	0.191	49	234	88	4.078	1.6	0.094	0.1	2.832	6.3	0.245	1.6	0.25	1287	229	1414	41	1364	93	-3.6	1287	229	6
SJ4	38	0.091	0.000	0.165	39	191	95	4.245	1.1	0.085	0.0	2.747	1.6	0.236	1.1	0.71	1306	43	1364	27	1341	23	-1.7	1306	43	6
SJ4	74	0.085	0.000	0.089	103	562	169	4.690	0.8	0.085	0.0	2.487	0.8	0.213	0.8	0.91	1307	14	1246	18	1268	12	1.7	1307	14	6
SJ4	21	0.092	0.002	0.310	244	1155	1249	4.072	0.9	0.085	0.0	2.880	1.5	0.246	0.9	0.64	1455	20	1430	20	1447	22	2.8	1317	44	6
SJ4	26	0.102	0.001	0.240	92	453	324	4.214	1.4	0.087	0.0	2.836	3.6	0.237	1.4	0.40	1353	123	1373	35	1365	53	-0.5	1353	123	6
SJ4	66	0.091	0.000	0.037	112	523	64	4.106	0.5	0.085	0.0	2.590	0.7	0.221	0.5	0.71	1421	14	1436	10	1430	8	-0.4	1421	14	6
SJ4	92	0.095	0.000	0.275	20	93	84	4.026	0.8	0.091	0.0	3.130	0.9	0.248	0.8	0.83	1455	20	1430	20	1440	14	0.7	1455	20	6
SJ4	29	0.109	0.001	0.070	110	504	57	3.940	1.4	0.092	0.0	3.217	3.4	0.254	1.4	0.40	1466	116	1458	36	1461	52	0.2	1466	116	6
SJ4	23	0.122	0.002	0.289	57	228	188	3.448	1.3	0.093	0.1	3.724	5.2	0.290	1.3	0.25	1490	186	1542	38	1577	82	-4.1	1490	186	6
SJ4	15	0.117	0.002	0.557	92	401	695	3.758	1.1	0.095	0.0	3.485	2.7	0.266	1.1	0.40	1527	94	1521	30	1524	43	0.2	1527	94	6
SJ4	11	0.100	0.000	0.155	41	168	86	3.554	0.4	0.098	0.0	3.806	0.6	0.281	0.4	0.67	1588	16	1599	10	1594	10	-0.3	1588	16	6
SJ4	22	0.108	0.001	0.338	167	725	795	3.732	1.1	0.099	0.0	3.669	1.8	0.268	1.1	0.61	1611	51	1530	29	1565	28	2.2	1611	51	6
SJ4	31	0.104	0.000	0.093	104	437	137	4.037	1.4	0.099	0.0	3.394	1.4	0.248	1.4	0.95	1613	16	1426	34	1503	22	5.1	1613	16	6
SJ4	68	0.103	0.000	0.140	79	323	153	3.516	0.5	0.103	0.0	4.031	0.8	0.284	0.5	0.67	1675	22	1613	16	1640	12	1.6	1675	22	6
SJ4	91	0.104	0.000	0.232	302	1519	1259	4.327	0.4	0.103	0.0	3.285	0.4	0.231	0.4	0.98	1681	4	1340	10	1478	6	9.3	1681	4	6
SJ4	39	0.116	0.001	0.182	64	235	118	3.132	1.0	0.104	0.0	4.560	1.2	0.319	1.0	0.79	1689	28	1786	30	1742	21	-2.5	1689	28	6
SJ4	104	0.106	0.000	0.157	101	393	231	3.328	0.3	0.105	0.0	4.359	0.4	0.301	0.3	0.79	1718	10	1694	10	1705	8	0.6	1718	10	6
SJ4	42	0.109	0.000	0.166	74	262	138	3.025	0.9	0.105	0.0	4.804	1.0	0.331	0.9	0.92	1721	14	1841	29	1786	16	-3.1	1721	14	6
SJ4	53	0.107	0.000	0.147	153	582	345	3.278	0.5	0.106	0.0	4.472	0.5	0.305	0.5	0.90	1737	8	1717	14	1726	6	0.5	1737	8	6
SJ4	109	0.109	0.000	0.187	79	292	188	3.167	0.4	0.107	0.0	4.667	0.5	0.316	0.4	0.83	1752	10	1769	12	1761	6	-0.5	1752	10	6
SJ4	45	0.111	0.000	0.249	86	283	233	2.813	0.9	0.107	0.0	5.261	1.1	0.356	0.9	0.82	1755	23	1961	31	1863	19	-5.3	1755	23	6
SJ4	113	0.110	0.000	0.224	41	195	144	4.115	1.1	0.107	0.0	3.601	2.0	0.243	1.1	0.55	1757	62	1402	28	1550	32	9.5	1757	62	6
SJ4	57	0.110	0.000	0.130	44	164	72	3.183	0.4	0.108	0.0	4.677	0.6	0.314	0.4	0.70	1766	14	1761	12	1763	10	0.1	1766	14	6
SJ4	60	0.122	0.000	0.044	114	382	57	2.868	0.4	0.121	0.0	5.841	0.5	0.349	0.4	0.90	1978	8	1828	14	1952	6	1.2	1978	8	6
SJ4	37	0.125	0.000	0.037	381	1239	130	2.796	1.5	0.124	0.0	6.124	1.8	0.358	1.5	0.87	2017	30	1971	52	1994	30	1.1	2017	30	6
SJ4	48	0.149	0.000	0.277	116	311	275	2.257	0.9	0.147	0.0	8.988	1.0	0.443	0.9	0.97	2313	8	2364	36	2337	17	-1.2	2313	8	6
SJ4	13	0.208	0.004	0.209	134	299	111	1.913	6.2	0.151	0.1	10.861	13.1	0.523	6.2	0.47	2354	369	2711	271	2511	230	-8.0	2354	369	6
SJ4	117	0.152	0.000	0.359	59	172	219	2.520	0.4	0.152	0.0	8.297	0.5	0.397	0.4	0.85	2365	10	2154	16	2264	10	4.9	2365	10	6
SJ4	7	0.219	0.005	0.385	40	108	90	2.324	3.3	0.153	0.1	9.062	8.2	0.430	3.3	0.40	2377	246	2607	127	2344	145	1.6	2377	246	6
SJ4	6	0.177	0.001	0.304	230	573	667	2.144	1.4	0.161	0.0	10.379	2.2	0.466	1.4	0.65	2470	55	2468	58	2469	40	0.0	2470	55	6
SJ4	62	0.163	0.000	0.259	201	503	467	2.150	0.4	0.163	0.0	10.435	0.4	0.465	0.4	0.95	2484	4	2463	14	2474	6	0.4	2484	4	6
SJ4	115	0.166	0.000	0.173	178	438	338	2.111	0.6	0.165	0.0	10.793	1.2	0.474	0.6	0.51	2511	36	2499	28	2505	22	0.2	2511	36	6
SJ4	75	0.173	0.000	0.111	25	64	25	2.229	0.5	0.169	0.0	10.440	0.6	0.449	0.5	0.76	2546	14	2389	18	2475	12	3.5	2546	14	6
SJ4	102	0.173	0.000	0.081	83	230	104	2.366	0.6	0.173	0.0	10.060	0.7	0.423	0.6	0.87	2583	12	2272	24	2440	14	6.9	2583	12	6
SJ4	65	0.182	0.000	0.112	238	578	233	2.089	0.4	0.182	0.0	12.013	0.5	0.479	0.4	0.88	2671	8	2522	16	2605	8	3.2	2671	8	6
SJ4	64	0.192	0.000	0.089	124	276	89	1.909	0.5	0.191	0.0	13.786	0.5	0.524	0.5	0.94	2751	6	2716	22	2734	6	0.7	2751	6	6
SJ4	40	0.208	0.001	0.201	40	80	53	1.709	1.0	0.204	0.0	16.443	1.1	0.585	1.0	0.94	2856	12	2970	49	2903	21	-2.3	2856	12	6
SJ4	118	0.058	0.000	0.222	6	196	67	12.376	0.5	0.055	0.0	0.283	2.7	0.081	0.5	0.90	402	52	237	12	253	12	6.3	N.D.	N.D.	4
SJ4	43	0.129	0.004	0.277	12	85	34	5.855	1.4	0.067	0.0	1.583	3.7	0.171	1.4	0.38	845	139	1017	26	964	45	-5.5	N.D.	N.D.	4
SJ4	25	0.139	0.006	0.370	41	632	348	13.141	1.5	0.050	0.2	0.530	15.1	0.076	1.5	0.10	217	633	413	43	432	104	-9.6	N.D.	N.D.	4
SJ4	3	0.120	0.003	0.486	43	318	361	6.366	2.7	0.062	0.2	1.341	20.0	0.157	2.7	0.14	671	751	941	47	864	220	-8.9	N.D.	N.D.	4
SJ4	4	0.120	0.003	0.517	59	345	527	5.041	2.3	0.071	0.1	1.951	10.8	0.198	2.3	0.21	967	404	1166	49	1099	140	-8.2	N.D.	N.D.	4
SJ4	28	0.081	0.002	0.056	96	860	42	7.711	1.1	0.058	0.1	1.037	5.3	0.130	1.1	0.21	530	217	786	16	723	54	-8.8	N.D.	N.D.	4
SJ4	32	0.092	0.002	0.181	101	577	272	4.928	1.0	0.089	0.0	2.498	1.3	0.203	1.0	0.84	1410	29	1191	22	1272	18	6.3	N.D.	N.D.	4
SJ4	46	0.422	0.027	1.056	2	102	35	44.208	2.7	0.026	0.5	0.081	45.4	0.023	2.7	0.06	0	0	144	8	79	68	-81.7	N.D.	N.D.	4
SJ4	2	0.345	0.019	0.107	17	63	36	3.772	7.2	0.078	0.4	3.307	36.9	0.315	7.2	0.20	1097	1185	757	221	1483	106	-19.1	N.D.	N.D.	4
SJ4	1	0.211	0.013	0.470	18	235	38	11.534	6.1	0.017	1.7	0.203	170.1	0.087	6.1	0.04	0	0	536	62	188	513	-185.6	N.D.	N.D.	4
SJ4	12	0.365	0.023	0.842	20	1730	36	73.304	28.4	0.017	2.5	0.032	249.7	0.014	28.4	0.11	0	1216	67	32	154	-169.0	N.D.	N.D.	4
SJ4	8	0.150	0.007	0.331	43	728	425	14.699	2.0	0.045	0.3	0.420	33.2	0.068	2.0	0.06	0	1183	424	17	356	190	-18.1	N.D.	N.D.	4
SJ4	10	0.136	0.007	0.233	52	436	95	7.148	2.7	0.032	0.4	0.618	36.3	0.140	2.7	0.06	0	0	844	43	488	264	-72.9	N.D.	N.D.	4
SJ4	31	0.103	0.000	0.193	64	389	312	5.240	0.9	0.057	0.2	2.599	1.1	0.191	0.9	0.85	1601	21	1126	19	1300	16	13.4	N.D.	N.D.	4
SJ4	55	0.147	0.000	0.092	76	336	75	3.797	0.5	0.146	0.0	5.302	0.9	0.263	0.5	0.56	2300	26	1507	14	1869	16	19.4	N.D.	N.D.	4
SJ4	5	0.081	0.001	0.149	195	2444	1494	10.747	1.1	0.069	0.0	0.882	3.6	0.093	1.1	0.30	891	140	574	12	642	34	10.7	N.D.	N.D.	4
SJ4	14	0.195	0.009	0.544	27	347	277	10.904	11.8	0.063	0.5	0.796	54.4	0.092	11.8	0.22	707	1698	566	127	595	439	4.9	N.D.	N.D.	4
SJ4	11	0.124	0.004	0.383	63	773	948	10.480	13.5	0.071	0.1	0.936	17.6	0.095	13.5	0.77	962	429	588	151	671	166	12.4	N.D.	N.D.	4
SJ4	35	0.775	0.053	1.871	9791	43986	1764	3.860	68.4	0.303	0.3	73.5	10.823	73.5	0.259	68.4	0.93	0	1485	1699	N.D.	0.0	N.D.	N.D.	N.D.	4
SJ4	119	0.074	0.000	0.154	N.D.	N.D.	N.D.	N.D.	N.D.	N.D.	N.D.	N.D.	N.D.	N.D.	N.D.	N.D.	N.D.	N.D.	N.D.	N.D.	N.D.	N.D.	N.D.	N.D.	N.D.	N.D.	N.D.
SJ6b	85	0.106	0.004	0.372	53	1106	640	17.854	1.8	0.054	0.1	0.417	15.0	0.056	1.8	0.12	371	607	351	12	354	88	0.7	351	12	6
SJ6b	43	0.066	0.001	0.370	71	978	1053	11.879	1.1	0.055	0.0	0.643	2.7	0.084	1.1	0.40	429	110	521	11	504	22	-3.3	521	11	6
SJ6b	10	0.061	0.001	0.223	14	195	113	11.769	1.1	0.055	0.0	0.648	4.7	0.085	1.1	0.24	425	197	526	11	507	37	-3.6	526	11	6
SJ6b	51	0.100	0.003	0.340	41	555	466	11.730	1.8	0.055	0.1	0.641	13.7	0.085	1.8	0.13	395	559	527	18	503	106	-4.8	527	18	6
SJ6b	19	0.066	0.001	0.243	33	442	311	11.552	0.9	0.055	0.0	0.660	2.1	0.087	0.9	0.44	423	84	535	10	514	17	-4.0	535	10	6
SJ6b	25	0.064	0.001	0.194	40	536	309	11.542	1.1	0.056	0.0	0.672	2.6	0.087	1.1	0.41	462	103	536	11	522	21	-2.7	536	11	6
SJ6b	21	0.061	0.000	0.252	62	824	648	11.399	1.0	0.056	0.0	0.680	1.5	0.088	1.0	0.66	461	51	542	10	527	12	-2.9	542	10	6
SJ6b	9	0.060	0.000	0.144	61	805	358	11.355	0.9	0.056	0.0	0.683	1.2	0.088	0.9	0.78	463	32	544	9	529	10	-2.9	544	9	6
SJ6b	41	0.059	0.000	0.189	165	2160	1311	11.238	0.9	0.057	0.0	0.694	1.1	0.089	0.9	0.85	475	25	550	10	535	9	-2.6	550	10	6
SJ6b	9	0.061	0.000	0.206	58	729	461	10.758	0.9	0.057	0.0	0.736	1.2	0.093	0.9	0.73	507	37	573	10	560	11	-2.3	573	10	6
SJ6b	8	0.059	0.000	0.038	253	2964	338	11.069	0.9	0.057	0.0	0.785	1.1	0.099	0.9	0.84	503	26	610	10	588	10	-3.8	610	10	6
SJ6b	11	0.058	0.000	0.089	354	4084	1151	9.912	0.9	0.057	0.0	0.796	1.0	0.101	0.9	0.94	501	15	620	11	595	9	-4.2	620	11	6
SJ6b	78	0.108	0.003	0.148	69	710	90	8.907	1.4	0.062	0.1	0.954	10.6	0.112	1.4	0.14	660	420	688	19	680	102	-0.9	686	19	6
SJ6b	16	0.075	0.001	0.207	17	180	89	8.834	1.0	0.059	0.0	0.927	3.4	0.113	1.0	0.29	580	139	691	13	668	33	-3.8	691	13	6
SJ6b	33	0.069	0.001	0.092	82	804	160	8.415	1.1	0.063	0.0	1.029	2.1	0.119	1.1	0.52	702	75	724	15	719	21	-0.7	724	15	6
SJ6b	20	0.

SJ9	16	0.062	0.000	0.019	125	1497	80	10.288	2.3	0.062	0.0	0.828	2.3	0.097	2.3	1.00	667	10	598	26	613	22	2.4	598	26	6
SJ9	7	0.069	0.000	0.085	26	298	64	9.681	2.0	0.084	0.0	0.913	2.0	0.103	2.0	0.98	745	18	634	24	659	20	3.8	634	24	6
SJ9	14	0.064	0.000	0.053	75	815	116	9.398	0.5	0.063	0.0	0.922	0.5	0.106	0.5	0.89	704	10	652	6	663	6	1.7	652	6	6
SJ9	21	0.074	0.000	0.116	18	149	44	6.968	4.4	0.069	0.0	1.365	4.9	0.144	4.4	0.89	898	90	864	70	874	57	1.1	864	70	6
SJ9	20	0.071	0.000	0.093	35	285	80	6.947	1.3	0.069	0.0	1.370	1.4	0.144	1.3	0.92	899	22	887	21	876	16	1.1	867	21	6
SJ9	81	0.090	0.001	0.114	24	193	40	6.831	7.2	0.071	0.1	1.430	12.5	0.146	7.2	0.58	953	390	881	118	902	144	2.3	881	118	6
SJ9	18	0.079	0.000	0.163	14	100	51	6.206	0.8	0.076	0.0	1.691	0.9	0.161	0.8	0.86	1098	19	963	15	1005	12	4.2	963	15	6
SJ9	35	0.078	0.000	0.046	127	767	112	5.177	0.9	0.077	0.0	2.063	1.0	0.193	0.9	0.97	1133	9	1138	19	1137	13	-0.2	1138	19	6
SJ9	69	0.080	0.000	0.139	68	511	244	5.001	1.0	0.075	0.0	2.074	1.2	0.200	1.0	0.78	1074	32	1175	21	1140	17	-3.1	1175	21	6
SJ9	1	0.097	0.000	0.129	184	881	360	4.107	0.7	0.097	0.0	3.250	0.8	0.243	0.7	0.95	1564	9	1405	18	1469	12	4.4	1564	9	7
SJ9	63	0.087	0.002	0.275	15	218	148	12.613	1.5	0.052	0.1	0.568	9.8	0.079	1.5	0.15	283	416	492	14	457	71	-7.7	N.D	N.D	4
SJ9	61	0.110	0.003	0.460	21	125	173	5.139	1.2	0.072	0.1	1.919	7.2	0.195	1.2	0.17	973	276	1146	26	1088	94	-5.4	N.D	N.D	4
SJ9	83	0.067	0.001	0.133	26	923	159	30.429	10.4	0.056	0.1	0.253	12.5	0.033	10.4	0.83	448	296	208	43	229	51	9.1	N.D	N.D	4
SJ9	77	0.064	0.001	0.095	27	612	107	19.428	4.5	0.057	0.0	0.402	4.7	0.051	4.5	0.94	476	69	324	28	343	27	5.6	N.D	N.D	4
SJ9	55	0.088	0.002	0.088	36	1956	28	46.544	4.5	0.052	0.1	0.154	28.9	0.021	4.5	0.42	292	420	137	12	146	29	6.0	N.D	N.D	4
SJ9	39	0.070	0.001	0.048	50	1987	29	33.901	9.7	0.054	0.1	0.219	11.4	0.029	9.7	0.96	360	256	187	36	201	41	6.6	N.D	N.D	4
SJ9	84	0.062	0.000	0.038	53	896	41	14.553	4.0	0.059	0.0	0.560	4.2	0.069	4.0	0.96	570	52	428	33	451	30	5.1	N.D	N.D	4
SJ9	70	0.180	0.009	0.324	57	1390	28	21.009	4.0	0.049	0.5	0.323	46.6	0.048	4.0	0.09	158	1659	300	23	284	219	-5.5	N.D	N.D	4
SJ9	21	0.060	0.000	0.054	58	1385	129	20.576	2.5	0.057	0.0	0.380	2.7	0.049	2.5	0.92	484	46	306	16	327	16	6.4	N.D	N.D	4
SJ9	40	0.068	0.000	0.048	76	1026	88	11.673	7.3	0.065	0.0	0.773	7.3	0.086	7.3	1.00	789	26	530	74	582	64	8.9	N.D	N.D	4
SJ9	32	0.061	0.000	0.117	97	2318	501	20.577	0.9	0.057	0.0	0.385	1.1	0.049	0.9	0.83	508	27	306	5	331	6	7.5	N.D	N.D	4
SJ9	65	0.068	0.001	0.131	119	1814	599	13.052	1.2	0.053	0.0	0.561	4.0	0.077	1.2	0.30	332	168	476	11	452	29	-5.3	N.D	N.D	4
SJ9	24	0.281	0.010	0.515	0	121	0	921.001	4.9	0.191	0.1	0.029	13.2	0.001	4.9	0.37	2751	377	7	1	29	7	75.6	N.D	N.D	3
SJ9	8	0.435	0.000	1.009	0	95	21	388.982	7.8	-0.214	-0.3	-0.076	32.4	0.003	7.8	0.24	0	0	17	3	-80	-55	120.6	N.D	N.D	3
SJ9	45	0.306	0.017	0.766	0	39	12	72.461	8.0	0.083	0.6	0.157	57.8	0.014	8.0	0.14	1261	1672	88	14	148	153	40.4	N.D	N.D	3
SJ9	41	0.506	0.033	1.140	1	271	4	331.834	58.4	-0.005	-46.1	-0.002	4809.1	0.003	58.4	0.01	0	5980	19	23	-2	-201	1077.3	N.D	N.D	3
SJ9	7	0.167	0.000	0.273	1	14	0	17.696	1.3	0.083	0.1	0.644	8.8	0.057	1.3	0.14	1261	323	354	9	505	69	29.8	N.D	N.D	3
SJ9	59	0.525	0.037	1.217	1	272	1	262.047	22.5	-0.098	-0.7	-0.051	78.2	0.004	22.5	0.29	0	0	25	11	-54	-88	145.7	N.D	N.D	3
SJ9	89	0.260	0.016	0.453	1	365	9	334.290	57.1	0.022	2.9	0.009	282.8	0.003	57.1	0.19	0	2670	19	22	9	53	-108.3	N.D	N.D	3
SJ9	47	0.415	0.026	0.979	1	414	1	253.902	13.0	0.036	1.3	0.020	128.0	0.004	13.0	0.10	0	2533	25	7	20	50	-27.3	N.D	N.D	3
SJ9	51	0.562	0.044	1.378	2	661	28	272.610	43.0	-0.609	-0.2	-0.308	48.4	0.004	43.0	0.89	0	0	24	20	-374	-493	106.3	N.D	N.D	3
SJ9	53	0.668	0.044	1.575	2	4141	4	1550.382	24.5	-0.060	-1.1	-0.005	116.1	0.001	24.5	0.21	0	0	4	2	-5	-13	176.2	N.D	N.D	3
SJ9	46	0.197	0.011	0.524	3	329	172	94.389	2.3	0.038	0.3	0.055	31.4	0.011	2.3	0.07	0	369	68	3	55	33	-24.1	N.D	N.D	3
SJ9	82	0.071	0.001	0.272	4	541	388	126.564	1.3	0.053	0.1	0.058	5.8	0.008	1.3	0.23	350	244	51	1	58	6	11.8	N.D	N.D	3
SJ9	19	0.101	0.000	0.260	4	46	44	8.801	1.7	0.090	0.1	1.414	7.5	0.114	1.7	0.23	1432	267	694	22	695	87	22.5	N.D	N.D	3
SJ9	42	0.346	0.022	0.755	5	370	4	69.025	41.4	0.010	14.4	0.020	1437.4	0.014	41.4	0.03	0	4735	33	76	20	499	-367.0	N.D	N.D	3
SJ9	19	0.095	0.000	0.221	5	43	39	7.998	4.7	0.082	0.1	1.413	9.4	0.125	4.7	0.50	1245	303	759	68	894	109	15.1	N.D	N.D	3
SJ9	60	0.244	0.014	0.476	5	172	2	30.064	8.0	0.030	1.5	0.139	149.7	0.033	8.0	0.05	0	2158	211	33	132	340	-60.0	N.D	N.D	3
SJ9	52	0.130	0.007	0.215	6	1890	20	275.804	3.4	0.022	0.7	0.011	67.9	0.004	3.4	0.05	0	0	23	2	11	15	-111.0	N.D	N.D	3
SJ9	64	0.201	0.014	0.387	10	3937	50	340.572	3.2	-0.014	-2.6	-0.006	255.6	0.003	3.2	0.01	0	0	19	1	-6	-30	430.1	N.D	N.D	3
SJ9	67	0.287	0.019	0.630	12	1775	188	127.915	3.1	-0.012	-1.6	-0.013	164.0	0.008	3.1	0.02	0	0	50	3	-13	-44	480.1	N.D	N.D	3
SJ9	30	0.106	0.003	0.187	13	1035	51	69.302	24.0	0.057	0.3	0.114	37.8	0.014	24.0	0.64	505	1078	92	44	110	77	15.8	N.D	N.D	3
SJ9	15	0.093	0.000	0.120	13	1974	8	131.003	23.6	0.087	0.1	0.092	26.0	0.008	23.6	0.91	1360	387	49	23	89	44	44.9	N.D	N.D	3
SJ9	73	0.100	0.004	0.267	15	109	71	6.176	1.3	0.040	0.1	0.903	7.6	0.162	1.3	0.17	0	0	967	24	653	72	-48.1	N.D	N.D	3
SJ9	17	0.073	0.000	0.076	15	297	25	16.685	3.6	0.070	0.0	0.577	5.5	0.060	3.6	0.65	524	168	375	26	463	41	18.9	N.D	N.D	3
SJ9	38	0.060	0.000	0.086	22	1671	80	64.434	13.2	0.057	0.0	0.121	13.3	0.016	13.2	1.00	481	58	99	26	116	29	14.7	N.D	N.D	3
SJ9	76	0.125	0.006	0.363	28	1159	283	35.934	10.4	0.032	0.5	0.123	50.6	0.028	10.4	0.20	0	182	177	36	118	109	-50.5	N.D	N.D	3
SJ9	74	0.132	0.005	0.146	28	3027	491	91.837	11.9	0.060	0.2	0.090	20.5	0.011	11.9	0.58	599	651	70	17	87	34	20.1	N.D	N.D	3
SJ9	78	0.065	0.000	0.204	28	1134	288	34.381	7.7	0.060	0.0	0.242	7.9	0.029	7.7	0.98	619	74	185	28	220	31	16.1	N.D	N.D	3
SJ9	26	0.079	0.002	0.175	35	836	246	20.560	1.4	0.046	0.1	0.310	6.9	0.049	1.4	0.20	8	311	306	8	274	33	-11.7	N.D	N.D	3
SJ9	27	0.059	0.000	0.058	36	1358	100	32.566	1.4	0.058	0.0	0.244	1.5	0.031	1.4	0.92	513	25	195	5	221	6	12.0	N.D	N.D	3
SJ9	50	0.131	0.003	0.178	57	377	90	5.719	4.5	0.095	0.1	2.290	9.9	0.175	4.5	0.45	1528	316	1039	86	1209	136	14.1	N.D	N.D	3
SJ9	68	0.078	0.003	0.135	74	1390	268	16.042	1.3	0.033	0.0	0.280	4.7	0.062	1.3	0.29	0	0	390	10	251	21	-55.6	N.D	N.D	3
SJ9	22	0.093	0.000	0.122	108	978	3332	7.771	2.2	0.089	0.0	1.588	2.4	0.129	2.2	0.90	1415	40	780	32	965	30	19.2	N.D	N.D	3
SJ9	4	0.631	0.000	0.071	560	222	1021	0.340	10.2	0.623	0.0	252.359	10.2	2.940	10.2	0.99	4562	31	8839	941	5620	197	-57.3	N.D	N.D	3
SJ9	49	0.350	0.033	0.886	17	746	103	37.700	15.2	-0.409	-0.1	-1.497	16.5	0.027	15.2	0.92	0	0	169	50	N.D	0	N.D	N.D	N.D	3
SJ9	10	0.058	0.000	0.089	19	493	61	22.447	15.6	0.053	0.0	0.327	15.6	0.045	15.6	1.00	341	36	281	85	288	77	2.3	N.D	N.D	2
SJ9	43	0.069	0.001	0.265	31	1016	387	28.267	13.6	0.056	0.0	0.274	14.4	0.035	13.6	0.94	455	212	224	60	246	62	8.7	N.D	N.D	2
SJ9	72	0.070	0.001	0.247	46	1594	496	29.752	11.0	0.054	0.1	0.251	13.1	0.034	11.0	0.84	379	309	213	48	227	53	6.3	N.D	N.D	2
SJ9	37	0.082	0.002	0.084	61	2904	45	41.113	23.6	0.051	0.2	0.172	33.9	0.024	23.6	0.70	258	961	155	72	161	99	4.0	N.D	N.D	2
SJ9	71	0.073	0.001	0.080	72	2086	170	24.730	13.2	0.063	0.0	0.354	13.9	0.040	13.2	0.85	725	173	256	66	308	72	17.0	N.D	N.D	2
SJ9	3	0.057	0.000	0.136	90	2225	566	21.218	11.8	0.056	0.0	0.366	11.9	0.047	11.8	1.00	467	39	297	68	317	64	6.3	N.D	N.D	2
SJ9	66	0.630	0.041	1.683	-9	7458	10	-719.802	22.6	0.207	0.5	-0.040	57.0	-0.001	22.6	0.40	2886	1330	-9	-4	-41	-48	78.2	N.D	N.D	3
SJ9	87	0.319	0.032	0.880	5	-1967	0	-336.225	50.8	-0.141	-0.9	0.058	105.0	-0.003	50.8	0.48	0	0	-19	-20	57	113	133.8	N.D	N.D	3
SJ9	29	0.088	0.002	0.146	39	1154	62	-25.621	10.9	0.063	0.1	-0.337	14.3	-0.039	10.9	0.76	696	375	-257	-57	-418	-154	38.5	N.D	N.D	3
SJ9	1	0.058	0.000	0.031	N.D	N.D	N.D	N.D	N.D	N.D	N.D	N.D	N.D	N.D	N.D	N.D	N.D	N.D	N.D	N.D	N.D	N.D	N.D	N.D	N.D	1
SJ9	11	0.073	0.000	0.120	N.D	N.D	N.D	N.D	N.D	N.D	N.D	N.D	N.D	N.D	N.D	N.D	N.D	N.D	N.D	N.D	N.D	N.D	N.D	N.D	N.D	1
SJ9	12	0.081	0.003	0.077	N.D	N.D	N.D	N.D	N.D	N.D	N.D	N.D	N.D	N.D	N.D	N.D	N.D	N.D	N.D	N.D	N.D	N.D	N.D	N.D	N.D	1
SJ9	13	0.059	0.000	0.191	N.D	N.D	N.D	N.D	N.D	N.D	N.D	N.D	N.D	N.D	N.D	N.D	N.D	N.D	N.D	N.D	N.D	N.D	N.D	N.D	N.D	1
SJ9	15	0.051	0.000	0.012	N.D	N.D	N.D	N.D	N.D	N.D	N.D	N.D	N.D	N.D	N.D	N.D	N.D	N.D	N.D	N.D	N.D	N.D	N.D	N.D	N.D	1
SJ9	19	0.156	0.000	0.142	N.D	N.D	N.D	N.D	N.D	N.D	N.D	N.D	N.D	N.D	N.D	N.D	N.D	N.D	N.D	N.D	N.D	N.D	N.D	N.D	N.D	1
SJ9	20	0.515	0.034	1.244	N.D	N.D	N.D	N.D	N.D	N.D	N.D	N.D	N.D	N.D	N.D	N.D	N.D	N.D	N.D	N.D	N.D	N.D	N.D	N.D	N.D	1
SJ9	9	0.072	0.000	0.120	N.D	N.D	N.D	N.D	N.D	N.D	N.D	N.D	N.D	N.D	N.D	N.D	N.D	N.D	N.D	N.D	N.D	N.D	N.D	N.D	N.D	1
SJ12	102	0.053	0.000	0.008	23	4880	6	179.199	0.6	0.050	0.0	0.038	1.2	0.006	0.6	0.49	172	48	36	0	38	1	5.5	36	0	5
SJ12	70	0.056	0.001	0.105	3	434	114	138.834	1.0	0.049	0.0	0.049	1.8	0.007	1.0	0.56	157	68	46	1	48	2	4.5	46	1	5
SJ12	22	0.055	0.001	0.142	7	1017	95	130.609	13.7	0.049	0.0	0.049	13.8	0.008	13.7	0.99	0	56	49	13	48	13	-2.6	49	13	5
SJ12	115	0.064	0.000	0.143	13	1582	108	108.106	24.9	0.045	0.0	0.057	25.2	0.009	24.9	0.99	0	27	59	29	56	27	-5.8	59	29	5
SJ12	71	0.052	0.000	0.052	4	417	60	82.752	1.0	0.048	0.0	0.081	1.3	0.012	1.0	0.71	117	44	77	1	79	2	-1.6	77	1	5
SJ12	4	0.056	0.001	0.073	76	6970	915	78.527	4.8	0.043	0.0	0.076	6.6	0.013	4.8	0.72	0	0	82	8	74	9	-9.9	82	8	5
SJ12	82	0.060	0.001	0.173	2	212	92	78.153	0.9	0.047	0.0	0.083	4.3	0.013	0.9	0.21	40	193	82	1	81	7	-1.7	82	1	6
SJ12	107	0.052	0.000	0.035	31	1108	6	30.703	0.7	0.049	0.0	0.222	1.1	0.033	0.7	0.92	199	40	207	3	204	4	-1.5	207	3	6
SJ12	40	0.055	0.000	0.024	50	1518	67	25.874	4.9	0.050	0.0	0.268	5.0	0.039	4.9	0.99	205	33	244	23	241	21	-1.5	244	23	6
SJ12	27	0.058	0.000	0.108	21	467	107	19.527	2.2	0.055	0.0	0.390	2.3	0.051	2.2	0.97	419	26	322	14	334	13	3.6	322	14	6
SJ12	80	0.057	0.000	0.144	58	1231	419	18.184	6.0	0.057	0.0	0.429	6.1	0.055	6.0	1.00	474	19	345	41	362	37	4.7	345	41	6
SJ12	3	0.057	0.000	0.115	29	550	181	16.516	2.8	0.056	0.0	0.466	2.9	0.061	2.8	0.97	444	33	379	21	388	19	2.4	379	21	6
SJ12	49	0.057	0.000	0.131	34	616	224	15.429	1.8	0.054	0.0	0.478	1.8	0.065	1.8	0.98	351	18	405	14	397	12	-2.0	405	14	6
SJ12	21	0.058	0.000	0.104	59	1058	351	15.349	2.4	0.057	0.0	0.515	2.4	0.065	2.4	0.98	505	19	407	19	422	17	3.6	407	19	6
SJ12	84	0.058	0.000	0.145	23	402	156	14.743	0.9	0.057	0.0	0.533	1.1	0.068	0.9	0.80	493	30	423	8	434	8	2.5	423	8	6
SJ12	67	0.059	0.000	0.008	54	912	16	14.408	4.8	0.058	0.0	0.554	4.9	0.069	4.8	0.98	526	42	433	40	448	35	3.4	433	40	6
SJ12	62	0.058	0.000	0.003	12	206	1	14.316	3.3	0.058	0.0	0.557	3.4	0.070	3.3	0.96	525	40	435	28	450	25	3.2	435	28	6
SJ12	52	0.057	0.000	0.107	33	535	191	13.876	0.7	0.057	0.0	0.563	1.0	0.072	0.7	0.93	477	33	449	6	453	8	1.0	449	6	6
SJ12	18	0.058	0.000	0.028	86	1381	111	13.728	0.7	0.057	0.0	0.572	0.7	0.073	0.7	0.98	491	7	453	6	460	5	1.4	453	6	6
SJ12	11	0.058	0.000	0.177	33	522	281	13.634	2.8	0.057	0.0	0.578	2.8	0.073	2.8	0.99	499	17	456	25	463	21	1.5	456	25	6
SJ12	55	0.056	0.000	0.013	174	2691	103	13.253	3.9	0.055	0.0	0.573	4.0	0.075	3.9	0.99	414	28	469	35	460	29	-2.0	469	35	6
SJ12	45	0.057	0.000	0.203	25	390	246	13.177	1.1	0.054	0.0	0.568	1.3	0.076	1.1	0.86	384	28	472	10	457	9	-3.2	472	10	6
SJ12	117	0.060	0.000	0.019	43	660	30	13.048	1.1	0.058	0.0	0.608	1.4	0.077	1.1	0.78	511	40	476	10	482	11	1.3	476	10	6
SJ12	104	0.059	0.000	0.004	25	379	4	12.980	1.1	0.055	0.0	0.587	1.3	0.077	1.1	0.86	424	30	478	10	469	10	-2.0	478	10	6
SJ12	93	0.059	0.000	0.414	16	238	322	12.924	0.5	0.054	0.0	0.573	1.0	0.077	0.5	0.50	359	39	480	5	460	7	-4.5	480	5	6
SJ12	85	0.059	0.000	0.010	17	251	5	12.924	0.8	0.059	0.0	0.627	1.0	0.077	0.8	0.84	559	22	480	7	494	7	2.8	480	7	6
SJ12	98	0.059	0.000	0.012	35	517	14	12.613	0.8	0.057	0.0	0.623	1.0	0.079	0.8	0.78	490	28	492	7	492	8	-0.1	492	7	6
SJ12	96	0.059	0.000	0.278	26	383	334	12.599	0.7	0.056	0.0	0.609	1.2	0.079	0.7	0.57	439	45	492	7	483	10	-1.9	492	7	6
SJ12	53	0.059	0.000	0.066	91	1330	311	12.530	0.6	0.056	0.0	0.620	0.7	0.080	0.6	0.92	466	12	495	6	490	5	-1.0	495	6	6
SJ12	48	0.056	0.000	0.004	82	1147	12	12.072	2.0	0.056	0.0	0.638	2.1	0.083	2.0	0.96	447	26	513	19	501	16	-2.4	513	19	6
SJ12	61	0.057	0.000	0.045	177	2445	349	11.865	0.6	0.057	0.0	0.665	0.6	0.084	0.6	0.91	500	11	522	6	518	5	-0.8	522	6	6
SJ12	26	0.058	0.000	0.021	136	1672	124	11.845	1.3	0.057	0.0	0.666	1.3	0.084	1.3	0.98	501	11	522	13	519	11	-0.8	522	13	6
SJ12	17	0.055	0.000	0.002	38	517	2	11.801	0.7	0.055	0.0	0.642	2.6	0.085	0.7	0.25	409	111	524	7	503	21	-4.2	524	7	6
SJ12	73	0.061	0.000	0.045	26	349	40	11.515	5.2	0.061	0.0	0.733	5.4	0.087	5.2	0.96	548	65	537	54	559	46	3.9	537	54	6
SJ12	76	0.063	0.001	0.051	75	918	119	10.466	4.6	0.063	0.0	0.832	4.6	0.096	4.6	1.00	713	9	568	52	615	42	4.3	588	52	6
SJ12	64	0.061	0.000	0.001	107	1252	2	10.079	0.7	0.061	0.0	0.836	0.8	0.099	0.7	0.83	642	19	610	8	617	7	1.1	610	8	6
SJ12	6	0.071	0.001	0.088	23	269	52	9.927	4.6	0.063	0.0	0.872	4.7	0.101	4.6	0.98	700	44	619	54	637	44	2.8	619	54	6
SJ12	81	0.066	0.000	0.126	58	615	202	9.038	3.9	0.065	0.0	0.994	4.2	0.111	3.9	0.93	780	65	676	50	701	42	3.5	676	50	6
SJ12	87	0.075	0.000	0.013	184	1451	82	6.778	1.6	0.074	0.0	1.508	2.7	0.148	1.6	0.59	1045	86	887	26	934	32	5.0	887	26	6
SJ12	60	0.091	0.001	0.205	46	3562	190	6.606	4.3	0.071	0.1	1.492	9.1	0.151	4.3	0.47	971	310	909	73	927	107	2.0	909	73	6
SJ12	41	0.072	0.000	0.036	169	1205	147	6.132	0.6	0.072	0.0	1.615	0.6	0.163	0.6	0.88	981	12	974	10	976	8	0.2	974	10	6
SJ12	88	0.072	0.000	0.139	103	735	350	6.106	0.6	0.071	0.0	1.606	0.8	0.164	0.6	0.71	961	23	978	10	973	10	-0.5	978	10	6
SJ12	112	0.073	0.000	0.043	86	1995	90	5.944	0.7	0.072	0.0	1.676	1.0	0.168	0.7

TABLE S4: ION PROBE ZIRCON U-Pb STANDARD

Analysis #	Contents (ppm)			$^{204}Pb/^{206}Pb$	Data for Tera-Wasserburg plot				Data for Normal - Wetherill plot					Ages (Ma)				
	Pb	U	Th		$^{238}U/^{206}Pb$	1σ %	$^{207}Pb/^{206}Pb$	1σ %	$^{207}Pb/^{235}U$	1σ %	$^{206}Pb/^{238}U$	1σ %	ρ	$^{207}Pb/^{206}Pb$	2σ	$^{206}Pb/^{238}U$	2σ	$^{207}Pb/^{235}U$	2σ
91500@21	12	80	28	0.000	5.662	0.6	0.076	1.9	1.849	2.0	0.177	0.6	0.28	1094	76	1048	11	1063	26
91500@10	15	95	34	0.002	5.436	1.3	0.078	3.7	1.985	3.9	0.184	1.3	0.32	1154	144	1089	25	1110	52
91500@11	14	92	33	0.001	5.525	1.6	0.077	8.7	1.922	8.8	0.181	1.6	0.18	1121	330	1072	32	1089	115
91500@12	13	82	29	0.001	5.483	0.9	0.074	2.5	1.858	2.7	0.182	0.9	0.35	1038	99	1080	19	1066	35
91500@13	12	80	28	0.001	5.547	0.7	0.073	3.7	1.808	3.8	0.180	0.7	0.18	1007	148	1069	14	1048	49
91500@14	13	80	28	0.001	5.447	1.0	0.075	4.2	1.890	4.3	0.184	1.0	0.24	1059	164	1087	20	1078	56
91500@15	13	81	29	0.001	5.560	0.7	0.072	3.9	1.797	3.9	0.180	0.7	0.18	999	154	1066	14	1044	51
91500@16	13	81	29	0.002	5.550	1.6	0.068	8.2	1.688	8.4	0.180	1.6	0.19	867	323	1068	32	1004	104
91500@17	14	92	32	0.001	5.522	1.3	0.072	4.3	1.799	4.5	0.181	1.3	0.29	987	172	1073	26	1045	58
91500@18	14	87	30	0.001	5.504	1.2	0.080	7.5	2.016	7.6	0.182	1.2	0.15	1208	282	1076	23	1121	100
91500@19	13	84	29	0.001	5.508	1.2	0.072	5.0	1.813	5.1	0.182	1.2	0.24	997	196	1075	24	1050	66
91500@2	12	78	28	0.000	5.564	0.9	0.075	1.3	1.864	1.6	0.180	0.9	0.57	1074	52	1066	18	1068	21
91500@20	14	89	32	0.000	5.503	0.9	0.074	2.5	1.848	2.7	0.182	0.9	0.33	1035	100	1078	18	1063	35
91500@21	14	90	31	0.002	5.547	1.6	0.080	10.5	1.979	10.6	0.180	1.6	0.15	1187	388	1068	32	1108	138
91500@22	12	76	26	0.001	5.513	1.3	0.074	3.5	1.856	3.8	0.181	1.3	0.33	1047	140	1075	25	1065	49
91500@3	12	77	27	0.000	5.623	1.2	0.074	1.6	1.826	2.0	0.178	1.2	0.58	1055	66	1055	23	1055	26
91500@4	12	78	28	0.000	5.542	0.6	0.075	1.2	1.878	1.4	0.180	0.6	0.46	1082	48	1069	12	1073	18
91500@5	12	79	28	0.001	5.666	0.9	0.078	4.6	1.896	4.7	0.177	0.9	0.20	1144	178	1048	18	1080	62
91500@6	12	78	28	0.000	5.748	0.8	0.074	0.8	1.774	1.2	0.174	0.8	0.72	1040	33	1034	16	1036	15
91500@8	15	92	34	0.000	5.468	0.9	0.073	2.6	1.850	2.8	0.183	0.9	0.33	1024	103	1083	18	1063	36
91500@9	15	94	34	0.000	5.469	0.6	0.074	2.6	1.869	2.7	0.183	0.6	0.22	1045	104	1082	10	1070	35
91500@23	13	86	30	0.000	5.560	0.7	0.076	2.3	1.878	2.4	0.180	0.7	0.28	1088	91	1066	13	1073	32
91500@24	14	89	31	0.000	5.523	0.7	0.077	1.4	1.923	1.5	0.181	0.7	0.45	1122	54	1073	14	1089	20
91500@25	12	82	29	0.001	5.537	0.7	0.076	3.6	1.894	3.7	0.181	0.7	0.20	1097	142	1070	14	1079	49
91500@27	13	80	28	0.000	5.400	1.0	0.075	1.7	1.904	2.0	0.185	1.0	0.50	1057	69	1095	20	1083	28
91500@28	12	80	28	0.001	5.526	0.6	0.073	3.5	1.820	3.6	0.181	0.6	0.16	1013	139	1072	11	1053	46
91500@29	12	80	29	0.000	5.536	1.0	0.077	2.7	1.918	2.9	0.181	1.0	0.34	1122	105	1070	19	1087	38
91500@30	12	81	29	0.000	5.556	0.9	0.076	2.8	1.892	2.9	0.180	0.9	0.29	1101	109	1067	17	1078	38
91500@31	13	80	28	0.001	5.465	0.9	0.075	3.7	1.880	3.9	0.183	0.9	0.23	1056	147	1083	18	1074	50
91500@32	13	80	29	0.001	5.478	1.3	0.070	6.0	1.773	6.1	0.183	1.3	0.21	942	235	1081	25	1036	78
91500@33	13	83	29	0.001	5.581	0.7	0.074	4.9	1.834	5.0	0.179	0.7	0.14	1048	192	1062	14	1058	64
91500@34	13	79	28	0.001	5.406	1.3	0.077	3.7	1.966	3.9	0.185	1.3	0.32	1123	145	1094	25	1104	52
91500@37	13	78	27	0.000	5.348	0.9	0.077	2.8	1.974	3.0	0.187	0.9	0.31	1110	110	1105	19	1107	39
91500@38	13	80	28	0.001	5.452	1.0	0.074	4.4	1.877	4.5	0.183	1.0	0.22	1051	171	1084	19	1073	58
91500@39	11	72	25	0.001	5.568	1.0	0.075	3.8	1.862	3.9	0.180	1.0	0.24	1073	148	1065	19	1068	51
91500@40	11	72	25	0.001	5.611	0.5	0.075	4.1	1.849	4.2	0.178	0.5	0.13	1075	161	1057	11	1063	54
91500@44	12	80	29	0.001	5.516	0.8	0.075	3.0	1.869	3.1	0.181	0.8	0.26	1062	117	1074	16	1070	40
91500@46	13	83	29	0.001	5.608	0.5	0.075	2.8	1.843	2.9	0.178	0.5	0.18	1067	111	1058	10	1061	37
91500@47	12	78	28	0.000	5.585	0.6	0.077	2.6	1.890	2.6	0.179	0.6	0.23	1110	100	1062	12	1078	35
91500@48	14	89	31	0.001	5.519	1.0	0.074	4.9	1.851	5.0	0.181	1.0	0.19	1044	192	1074	19	1064	65
91500@49	13	83	29	0.001	5.587	0.7	0.075	2.1	1.842	2.2	0.179	0.7	0.33	1059	84	1061	14	1060	29
91500@50	14	90	32	0.000	5.572	0.7	0.076	1.7	1.878	1.8	0.179	0.7	0.39	1092	66	1064	14	1073	24
91500@52	13	84	29	0.001	5.599	0.9	0.074	3.0	1.830	3.2	0.179	0.9	0.27	1050	121	1059	17	1056	41
91500@53	12	76	26	0.001	5.606	0.5	0.079	3.5	1.946	3.5	0.178	0.5	0.14	1176	134	1058	9	1097	46
91500@54	12	80	28	0.000	5.622	0.8	0.076	2.6	1.863	2.8	0.178	0.8	0.29	1094	104	1055	16	1068	36
91500@55	13	84	28	0.003	5.604	1.1	0.072	9.5	1.766	9.6	0.178	1.1	0.11	982	365	1058	21	1034	121
91500@56	12	78	28	0.001	5.622	0.6	0.076	3.4	1.870	3.4	0.178	0.6	0.16	1102	132	1055	11	1070	45
91500@57	12	78	28	0.001	5.576	1.4	0.074	4.8	1.825	5.0	0.179	1.4	0.29	1036	188	1063	28	1054	65
91500@58	12	79	28	0.001	5.601	0.9	0.072	2.7	1.764	2.8	0.179	0.9	0.31	976	108	1059	17	1032	36
91500@59	12	79	28	0.001	5.517	0.6	0.074	2.0	1.850	2.1	0.181	0.6	0.28	1042	81	1074	12	1064	28
91500@60	12	80	29	0.000	5.573	0.7	0.076	2.3	1.883	2.4	0.179	0.7	0.29	1088	91	1064	14	1075	32
91500@61	12	83	29	0.000	5.693	0.8	0.073	1.9	1.775	2.1	0.176	0.8	0.39	1022	77	1043	16	1036	27
91500@62	13	83	29	0.001	5.681	1.0	0.075	2.5	1.809	2.7	0.176	1.0	0.36	1056	99	1045	18	1049	35
91500@63	13	83	29	0.000	5.646	0.6	0.075	3.2	1.838	3.3	0.177	0.6	0.18	1076	127	1051	11	1059	43
91500@64	12	81	28	0.000	5.669	0.8	0.076	1.8	1.841	1.9	0.176	0.8	0.41	1088	69	1047	15	1060	25
91500@65	12	82	28	0.001	5.887	0.7	0.073	2.8	1.699	2.9	0.170	0.7	0.23	1002	113	1011	12	1008	37
91500@66	13	85	29	0.000	5.747	0.8	0.076	1.8	1.820	2.0	0.174	0.8	0.38	1091	73	1034	15	1053	26
91500@67	12	82	28	0.000	5.686	0.8	0.074	2.4	1.801	2.6	0.176	0.8	0.31	1049	97	1044	15	1046	33
91500@68	12	78	26	0.000	5.667	0.7	0.075	2.1	1.817	2.2	0.176	0.7	0.34	1060	82	1048	14	1052	29
91500@69	12	80	27	0.000	5.667	0.6	0.076	2.0	1.844	2.1	0.176	0.6	0.28	1090	78	1048	11	1061	27
91500@74	11	77	27	0.000	5.758	0.9	0.075	2.4	1.797	2.6	0.174	0.9	0.34	1070	96	1032	17	1044	33
91500@75	11	73	25	0.001	5.712	0.6	0.076	2.6	1.830	2.7	0.175	0.6	0.22	1090	102	1040	11	1056	35
91500@76	12	75	26	0.000	5.598	0.8	0.075	2.0	1.835	2.1	0.178	0.8	0.38	1055	78	1060	16	1058	28
91500@77	13	82	29	0.000	5.610	0.6	0.075	0.9	1.841	1.1	0.178	0.6	0.52	1066	36	1057	11	1060	14
91500@78	12	75	27	0.000	5.507	0.7	0.076	1.2	1.902	1.4	0.182	0.7	0.48	1094	49	1076	13	1082	19
91500@79	12	77	27	0.000	5.531	0.5	0.076	1.3	1.903	1.4	0.181	0.5	0.38	1104	52	1071	11	1082	19
91500@80	12	77	27	0.000	5.642	0.5	0.075	1.3	1.828	1.4	0.177	0.5	0.37	1063	51	1052	10	1055	18
91500@81	12	76	27	0.000	5.557	0.8	0.075	1.1	1.859	1.4	0.180	0.8	0.57	1067	44	1067	15	1067	18
91500@85	11	77	27	0.000	6.078	0.8	0.075	1.5	1.700	1.7	0.165	0.8	0.49	1067	59	982	15	1009	22
91500@86	11	77	28	0.000	6.111	0.6	0.074	1.6	1.666	1.8	0.164	0.6	0.36	1037	66	977	11	996	22
91500@01	13	79	28	0.000	5.225	1.0	0.075	1.3	1.967	1.6	0.191	1.0	0.58	1056	53	1129	20	1104	22
91500@02	13	79	28	0.000	5.261	1.2	0.075	2.0	1.966	2.4	0.190	1.2	0.52	1069	80	1122	25	1104	32
91500@03	13	79	28	0.000	5.212	1.1	0.076	1.6	1.999	1.9	0.192	1.1	0.56	1084	62	1132	22	1115	25
91500@04	13	79	28	0.000	5.126	1.0	0.074	1.1	2.002	1.5	0.195	1.0	0.68	1054	45	1149	22	1116	21
91500@05	13	78	28	0.000	5.199	1.1	0.075	1.1	1.983	1.5	0.192	1.1	0.69	1062	45	1134	22	1110	21
91500@06	13	80	29	0.000	5.420	0.9	0.076	1.2	1.950	1.6	0.185	0.9	0.60	1105	49	1095	19	1098	21
91500@07	13	83	30	0.000	5.575	1.2	0.075	1.4	1.847	1.8	0.179	1.2	0.64	1060	55	1063	23	1062	24
91500@08	13	84	30	0.000	5.744	1.2	0.072	2.6	1.732	2.8	0.174	1.2	0.43	990	102	1035	23	1021	36
91500@09	13	83	30	0.000	5.689	1.2	0.078	1.3	1.881	1.8	0.176	1.2	0.68	1136	51	1044	23	1074	23
91500@10	12	83	30	0.000	5.771	1.2	0.075	1.4	1.790	1.8	0.173	1.2	0.65	1066	56	1030	23	1042	24
91500@11	12	84	30	0.000	5.809	1.3	0.072	1.3	1.712	1.9	0.172	1.3	0.71	989	53	1024	25	1013	24
91500@12	12	83	30	0.000	5.726	1.0	0.074	1.5	1.778	1.9	0.175	1.0	0.56	1038	61	1038	20	1038	24
91500@13	13	84	30	0.000	5.636	1.3	0.074	1.5	1.811	2.0	0.177	1.3	0.65	1042	59	1053	25	1049	25
91500@14	13	82	29	0.000	5.341	1.3	0.077	1.3	1.986	1.9	0.187	1.3	0.69	1120	53	1106	26	1111	25
91500@15	13	81	29	0.000	5.456	1.0	0.075	1.7	1.898	2.0	0.183	1.0	0.50	1071	67	1085	20	1080	26
91500@16	13	81	29	0.000	5.394	1.2	0.074	1.4	1.884	1.8	0.185	1.2	0.63	1033	57	1096	23	1075	24
91500@17	13	81	29	0.000	5.381	1.1	0.076	1.2	1.956	1.6	0.186	1.1	0.65	1104	49	1099	21	1100	22
91500@18	13	80	29	0.000	5.497	1.2	0.075	1.5	1.869	1.9	0.182	1.2	0.62	1056	59	1077	23	1070	25
91500@19	13	81	29	0.001	5.484	1.2	0.072	3.0	1.799	3.2	0.182	1.2	0.37	973	120	1080	24	1045	42
91500@20	13	82	30	0.000	5.462	1.1	0.076	2.3	1.929	2.6	0.183	1.1	0.45	1106	90	1084	23	1091	34
91500@21	13	83	30	0.000	5.621	1.3	0.076	2.4	1.858	2.7	0.178	1.3	0.47	1088	95	1055	25	1066	36
91500@22	12	81	29	0.000	5.677	1.1	0.075	1.8	1.832	2.2	0.176	1.1	0.53	1080	72	1046	22	1057	28
91500@23	12	82	29	0.000	5.785	1.4	0.084	2.7	1.996	3.0	0.173	1.4	0.46	1287	103	1028	27	1114	41
91500@24	12	80	29	0.000	5.741	1.0	0.077	0.9	1.855	1.3	0.174	1.0	0.76	1127	34	1035	19	1065	18
91500@25	12	79	28	0.000	5.774	1.0	0.075	1.3	1.799	1.7	0.173	1.0	0.60	1078	52	1030	19	1045	21
91500@26	11	76	28	0.001	6.413	1.3	0.075	4.0	1.607	4.2	0.156	1.3	0.31	1061	156	934	23	973	52
91500@27	12	79	28	0.001	5.707	1.3	0.074	2.2	1.798	2.5	0.175	1.3	0.50	1052	87	1041	24	1045	**33**
91500@28	13	82	29	0.000	5.514	1.3	0.076	1.9	1.892	2.3	0.181	1.3	0.56	1086	75	1074	25	1078	30
91500@29	13	84	29	0.000	5.430	1.3	0.076	1.1	1.919	1.7	0.184	1.3	0.76	1094	44	1090	26	1088	22
91500@30	11	80	28	0.001	6.103	1.4	0.075	5.0	1.699	5.2	0.164	1.4	0.28	1074	196	978	26	1008	66
91500@31	12	87	31	0.000	5.879	1.3	0.076	3.1	1.773	3.4	0.170	1.3	0.38	1084	122	1013	24	1036	43
91500@32	13	82	31	0.003	5.498	1.5	0.072	10.2	1.803	10.3	0.182	1.5	0.15	983	389	1077	30	1046	130
91500@33	13	88	33	0.003	6.041	1.9	0.069	12.3	1.568	12.4	0.166	1.9	0.16	889	470	987	36	957	149
91500@34	13	82	29	0.005	5.534	1.5	0.072	9.6	1.803	9.7	0.181	1.5	0.15	997	369	1071	29	1047	123
91500@36	13	85	32	0.003	5.590	1.9	0.078	9.7	1.936	9.9	0.179	1.9	0.20	1159	363	1061	38	1094	128
91500@37	12	82	31	0.002	5.675	2.3	0.070	12.9	1.706	13.1	0.176	2.3	0.17	935	488	1046	44	1011	161
91500@38	14	91	32	0.001	5.719	1.9	0.074	7.9	1.775	8.1	0.175	1.9	0.23	1031	302	1039	36	1036	102
91500@39	13	88	31	0.001	5.650	1.5	0.071	6.4	1.743	6.6	0.177	1.5	0.23	969	252	1050	29	1024	83
91500@40	13	85	30	0.002	5.424	1.8	0.074	8.4	1.869	8.6	0.184	1.8	0.21	1028	324	1091	36	1070	111
91500@41	14	92	33	0.001	5.468	1.2	0.074	1.7	1.882	2.1	0.183	1.2	0.56	1037	69	1083	23	1068	27
91500@42	13	83	29	0.000	5.412	1.1	0.074	2.8	1.891	3.0	0.185	1.1	0.36	1048	110	1093	22	1078	39
91500@43	12	76	25	0.000	5.405	1.1	0.076	1.3	1.946	1.7	0.185	1.1	0.65	1103	51	1094	22	1097	23
91500@44	12	83	30	0.000	5.832	4.5	0.075	2.9	1.778	5.4	0.171	4.5	0.84	1074	116	1020	85	1037	69
91500@45	12	83	29	0.000	5.814	1.0	0.078	2.4	1.839	2.6	0.172	1.0	0.37	1135	93	1023	18	1060	33
91500@46	11	84	31	0.000	6.443	1.2	0.078	2.5	1.682	2.8	0.155	1.2	0.43	1139	99	930	21	994	35
91500@48	13	81	29	0.001	5.415	1.1	0.073	4.3	1.857	4.5	0.185	1.1	0.25	1012	170	1092	22	1066	58
91500@49	13	82	28	0.001	5.613	1.1	0.073	3.7	1.805	3.8	0.178	1.1	0.29	1027	145	1057	22	1047	50
91500@50	13	83	29	0.000	5.564	1.2	0.079	3.0	1.953	3.3	0.180	1.2	0.37	1168	118	1065	24	1100	43
91500@51	12	82	29	0.001	6.054	1.3	0.071	4.2	1.609	4.4	0.165	1.3	0.30	947	166	985	24	974	54
91500@52	11	79	28	0.001	6.421	1.4	0.072	4.0	1.545	4.2	0.156	1.4	0.34	984	157	933	25	948	51
91500@53	11	82	29	0.001	6.383	1.5	0.075	5.0	1.620	5.2	0.157	1.5	0.28	1068	194	938	26	978	64
91500@54	11	77	28	0.001	6.141	1.3	0.075	4.7	1.684	4.9	0.163	1.3	0.27	1069	185	972	24	1003	62
91500@55	10	81	29	0.001	6.814	1.2	0.073	3.2	1.473	3.4	0.147	1.2	0.36	1009	127	883	20	919	41
91500@56	12	80	29	0.002	6.265	1.4	0.070	9.4	1.548	9.5	0.160	1.4	0.15	939	363	955	25	950	114
91500@58	13	82	28	0.008	5.411	5.9	0.040	73.3	1.022	73.5	0.185	5.9	0.08	0	1826	1093	118	715	641
91500@59	12	81	29	0.005	5.752	4.1	0.070	30.0	1.674	30.3	0.174	4.1	0.13	923	1038	1033	78	999	353
91500@60	13	80	27	0.009	5.461	5.1	0.078	42.4	1.960	42.7	0.183	5.1	0.12	1138	1343	1084	101	1102	506
91500@61	12	80	28	0.009	5.672	7.3	0.052	81.6	1.256	81.9	0.176	7.3	0.09	271	2468	1047	140	826	763
91500@62	13	88	30	0.008	5.630	4.4	0.054	54.6	1.325	54.8	0.176	4.4	0.08	375	1819	1054	86	857	552
91500@67	11	81	27	0.012	6.133	10.7	0.076	79.7	1.713	80.4	0.163	10.7	0.13	1100	2177	974	192	1014	834
91500@70	13	80	28	0.005	5.309	3.4	0.059	32.4	1.538	32.6	0.188	3.4	0.11	575	1164	1112	70	946	366
91500@71	13	81	29	0.005	5.171	5.1	0.072	28.9	1.930	29.4	0.193	5.1	0.17	997	996	1140	107	1092	359
91500@72	13	77	28	0.006	5.205	4.2	0.071	30.6	1.870	30.9	0.192	4.2	0.14	946	1052	1133	87	1071	373
91500@73	13	79	27	0.007	5.135	5.6	0.073	41.0	1.968	41.4	0.195	5.6	0.14	1022	1327	1147	118	1105	493
91500@74	13	80	27	0.000	5.223	1.2	0.075	1.5	1.991	1.9	0.191	1.2	0.62	1079	59	1129	24	1112	25
91500@75	13	82	28	0.000	5.469	1.0	0.076	0.7	1.911	1.2	0.183	1.0	0.81	1087	27	1084	19	1085	16
91500@76	14	81	27	0.001	5.057	1.1	0.072	4.5	1.971	4.6	0.198	1.1	0.24	994	176	1163	24	1106	61
91500@77	13	81	26	0.001	5.264	1.5	0.074	4.0	1.942	4.3	0.190	1.5	0.35	1046	159	1121	31	1096	57
91500@78	14	82	28	0.001	5.062	1.1	0.074	2.2	2.022	2.5	0.198	1.1	0.44	1049	87	1162	24	1123	33
91500@79	14	84	30	0.001	5.337	1.4	0.075	2.6	1.942	3.0	0.187	1.4	0.48	1073	104	1107	29	1096	40
91500@80	14	85	29	0.001	5.070	1.0	0.077	4.1	2.082	4.2	0.199	1.0	0.23	1110	158	1161	21	1143	56
91500@81	11	68	22	0.001	5.302	1.4	0.072	6.1	1.863	6.2	0.189	1.4	0.22	976	238	1114	28	1068	81
91500@82	10	64	20	0.002	5.336	1.2	0.075	4.7	1.943	4.9	0.187	1.2	0.25	1073	184	1107	25	1096	64
91500@83	12	71	23	0.002	5.292	1.3	0.076	7.9	2.018	8.0	0.192	1.3	0.17	1099	299	1133	27	1122	105
91500@0	12	82	29	0.000	5.790	0.8	0.077	1.0	1.842	1.3	0.173	0.8	0.63	1130	39	1027	15	1060	17
91500@01	12	78	28	0.000	5.389	1.

91500@51	10	73	27	0.000	6.441	0.6	0.082	0.9	1.754	1.1	0.155	0.6	0.52	1244	36	930	10	1029	14
91500@44	10	74	28	0.000	6.411	0.9	0.081	1.1	1.749	1.4	0.156	0.9	0.63	1229	42	934	15	1027	18
91500@53	10	71	27	0.000	6.252	0.8	0.081	1.2	1.792	1.4	0.160	0.8	0.55	1227	46	957	14	1042	18
91500@43	10	72	27	0.000	6.244	0.8	0.085	1.9	1.870	2.0	0.160	0.8	0.39	1309	71	958	14	1071	26

P = correlation coefficient

TABLE S5: LASER ABLATION ZIRCON U-Pb DATA

Sample #	Grain #	^{206}Pb (cps)	^{207}Pb (cps)	^{208}Pb (cps)	^{232}Th (cps)	^{238}U (cps)	Th/U	Contents (ppm) Th	U	Data for Tera-Wasserburg plot $^{238}U/^{206}Pb$ %	1σ	$^{207}Pb/^{206}Pb$ %	1σ	Data for Normal - Wetherill plot $^{207}Pb/^{206}Pb$	1σ	$^{207}Pb/^{235}U$ %	1σ	ρ	$^{206}Pb/^{238}U$	2σ	Ages (Ma) $^{207}Pb/^{235}U$	2σ	$^{206}Pb/^{238}U$	2σ	Discordance (%) 6-38/ 7-35	6-38/ 7-35 (Mo)	Preferred Age Age	2σ	Exp.
SJ7	119	123600	7320	14100	505000	2213000	0.6	519	333	55	13.344	1.8	0.058	1.2	0.600	2.2	0.075	1.8	0.83	535	55	466	16	477	17	12.9	2.3	466	16	6
SJ7	93	526000	30410	87400	2915000	9120000	0.9	2157	2453	354	13.130	1.8	0.057	1.1	0.597	2.1	0.076	1.8	0.85	493	50	473	16	475	16	4.0	0.4	473	16	6
SJ7	98	1097000	64300	213000	6570000	18790000	0.9	4350	5340	858	13.089	2.1	0.057	1.0	0.603	2.3	0.076	2.1	0.90	506	45	475	19	478	18	6.1	0.7	475	19	6
SJ7	62	8100000	46900	28500	945000	13980000	0.2	4160	844	125	12.835	1.7	0.057	1.1	0.611	2.0	0.078	1.7	0.85	492	44	484	16	484	16	1.7	0.1	484	16	6
SJ7	92	6180000	35400	59800	1807000	10300000	0.5	2450	1529	243	12.636	1.8	0.056	1.1	0.615	2.1	0.079	1.8	0.84	468	48	491	17	486	16	-4.9	-1.0	491	17	6
SJ7	104	252000	14750	26700	711000	4190000	0.5	956	547	107	12.610	1.9	0.058	1.1	0.625	2.2	0.079	1.9	0.88	518	49	492	18	493	17	5.0	0.1	492	18	6
SJ7	89	146300	8470	20600	422000	2490000	0.5	554	340	69	12.596	1.8	0.057	1.0	0.622	2.0	0.079	1.8	0.87	486	50	493	17	491	17	-1.3	-0.3	493	17	6
SJ7	14	80000	4710	23400	772000	1309000	1.5	76.6	188.1	89	12.516	1.9	0.058	1.2	0.638	2.2	0.080	1.9	0.86	526	51	495	18	501	17	5.8	1.1	495	18	6
SJ7	2	1100600	6530	46000	1467000	1857000	1.9	138.1	413	169	12.473	1.8	0.058	1.4	0.652	2.1	0.080	1.8	0.84	524	58	497	17	509	17	5.1	2.4	497	17	6
SJ7	102	27200	1650	21300	570000	1450000	3.6	103.4	449	85	12.453	2.0	0.059	1.6	0.653	2.5	0.080	2.0	0.79	503	70	498	19	509	20	11.6	2.2	498	19	6
SJ7	42	238000	14100	41000	1200000	3940000	0.8	836	7080	174	12.438	1.8	0.059	1.3	0.648	2.2	0.080	1.8	0.81	542	53	499	17	507	18	8.0	1.6	499	17	6
SJ7	75	1048000	61200	173200	1439000	7740000	0.4	4240	1228	162	12.436	1.7	0.058	1.0	0.644	2.1	0.080	1.7	0.83	516	44	499	17	505	17	3.4	1.2	499	17	6
SJ7	103	194700	11380	37300	1057000	3190000	0.9	729	821	149	12.416	1.8	0.058	1.1	0.644	2.2	0.081	1.8	0.83	540	50	499	18	506	18	7.5	1.3	499	18	6
SJ7	61	53600	3170	38100	1176000	885000	3.7	265.2	1051	167	12.407	1.9	0.058	1.3	0.650	2.2	0.081	1.9	0.83	547	55	500	18	508	18	8.6	1.6	500	18	6
SJ7	79	79700	4630	5200	215000	1330000	0.4	327.4	779	27.5	12.346	1.9	0.058	1.2	0.644	2.2	0.081	1.9	0.88	511	56	502	18	505	18	1.7	0.7	502	18	6
SJ7	86	455600	26720	94500	2736000	7520000	1.0	1719	2189	409	12.340	1.8	0.058	1.0	0.641	2.1	0.081	1.8	0.85	509	47	502	17	503	16	1.3	0.2	502	17	6
SJ7	85	146000	8530	19300	1152000	2394000	1.4	550	927	170	12.323	1.8	0.058	1.2	0.648	2.2	0.081	1.8	0.86	513	54	503	18	507	17	2.0	0.8	503	18	6
SJ7	53	230000	13200	61900	1522000	3730000	1.1	801	1920	267	12.306	1.8	0.057	1.1	0.641	2.1	0.081	1.8	0.85	489	48	504	18	504	16	-3.0	0.1	504	18	6
SJ7	91	926000	54000	92500	2760000	15060000	0.5	3900	2350	376	12.250	1.8	0.058	1.0	0.647	2.1	0.082	1.8	0.88	513	46	506	18	506	17	1.4	0.1	506	18	6
SJ7	37	200300	11470	54700	1750000	3490000	0.4	688	N.D.	63	12.255	1.8	0.057	1.1	0.647	2.1	0.082	1.8	0.88	497	49	506	18	507	17	-1.8	0.2	506	18	6
SJ7	52	128000	7440	76200	1690000	2100000	2.2	447	2300	328	12.240	1.9	0.057	1.2	0.646	2.2	0.082	1.9	0.88	501	52	506	18	507	18	-1.1	-0.1	506	18	6
SJ7	117	471000	27480	138300	3970000	7740000	1.4	1797	2674	545	12.223	1.8	0.057	1.1	0.644	2.1	0.082	1.8	0.85	500	50	507	17	505	17	3.4	-0.4	507	17	6
SJ7	9	436000	26050	121500	3640000	7030000	1.2	435	911	454	12.225	1.8	0.058	1.1	0.656	2.2	0.082	1.8	0.83	540	50	507	18	512	18	6.1	0.9	507	18	6
SJ7	27	184300	10750	41500	983000	3000000	0.8	235.7	301	162	12.210	1.9	0.058	1.1	0.651	2.1	0.082	1.9	0.88	522	51	507	18	510	17	2.8	0.5	507	18	6
SJ7	44	72400	4410	17200	462000	1153000	1.0	242.9	1650	73	12.189	1.9	0.057	1.3	0.670	2.3	0.082	1.9	0.82	597	56	508	19	520	19	14.9	2.4	508	19	6
SJ7	23	61700	3570	20500	572000	996700	1.5	65.1	154	79	12.180	1.9	0.057	1.5	0.654	2.4	0.082	1.9	0.80	493	66	509	19	511	19	-3.1	0.4	509	19	6
SJ7	73	77600	4560	15200	1225000	1350000	1.3	331.6	502	95	12.048	1.8	0.058	1.2	0.662	2.3	0.083	1.9	0.81	547	54	514	18	515	19	0.6	0.3	514	18	6
SJ7	24	134300	7640	7900	221000	2130000	0.3	144	61.1	30.8	12.031	1.8	0.057	1.1	0.656	2.1	0.083	1.8	0.84	480	52	515	18	512	17	-7.2	-0.6	515	18	6
SJ7	5	146200	8780	68400	2760000	2290000	2.9	154.8	727	253	12.019	1.9	0.059	1.3	0.662	2.5	0.083	1.9	0.77	579	51	515	19	527	20	11.0	2.3	515	19	6
SJ7	21	2540000	14980	28600	748000	3970000	0.5	247	194.4	112	11.969	1.8	0.058	1.0	0.666	2.1	0.084	1.8	0.85	519	48	517	18	518	17	0.3	0.1	517	18	6
SJ7	58	122700	7350	15500	364000	1966000	0.5	448	352	67	11.905	1.8	0.059	1.3	0.682	2.3	0.084	1.8	0.81	577	60	520	18	519	18	9.9	1.4	520	19	6
SJ7	68	157900	9380	33800	970000	2500000	0.4	706	793	148	11.899	1.8	0.058	1.1	0.672	2.1	0.084	1.8	0.84	544	48	520	18	522	17	4.4	0.3	520	18	6
SJ7	16	162100	9650	71900	2060000	2530000	2.0	1477	503	273	11.715	1.8	0.059	1.1	0.686	2.1	0.085	1.8	0.86	567	50	528	18	530	17	6.9	0.4	528	18	6
SJ7	26	405000	24300	69000	1750000	6500000	0.7	480	513	271	11.677	1.8	0.058	1.0	0.681	2.1	0.086	1.8	0.85	512	47	530	18	527	18	-3.5	-0.5	530	18	6
SJ7	38	694000	42370	254000	4510000	10670000	0.1	2307	6	107	11.473	1.8	0.059	1.1	0.711	2.1	0.087	1.8	0.87	581	46	539	19	546	17	7.3	1.3	539	19	6
SJ7	41	196500	12900	24600	380000	2313000	0.4	492	1100	104	8.811	1.9	0.064	1.2	1.006	2.2	0.114	1.9	0.85	752	49	693	24	707	22	7.9	1.9	693	24	6
SJ7	22	65100	4320	7900	132000	770000	0.5	41.8	94.8	30.1	8.554	2.1	0.063	1.3	0.999	2.6	0.117	2.1	0.84	700	56	712	29	701	26	-1.7	-1.6	712	29	6
SJ7	49	215300	13950	24100	375000	2470000	0.4	520	662	103	8.482	2.2	0.064	1.1	1.049	2.5	0.118	2.2	0.89	752	48	718	30	728	26	4.5	1.4	718	30	6
SJ7	59	532000	35600	49300	768000	5710000	0.4	1326	710	213	7.930	1.9	0.066	1.1	1.139	2.2	0.126	1.9	0.87	804	44	765	28	775	24	4.9	1.3	765	28	6
SJ7	114	108700	7420	16200	227000	1115000	0.5	256.2	157	40	7.764	1.9	0.068	1.2	1.192	2.2	0.129	1.9	0.87	859	50	781	28	786	24	9.1	1.9	781	28	6
SJ7	112	309900	20770	24000	359000	3108000	0.3	711	254	95	7.502	1.9	0.067	1.1	1.222	2.1	0.133	1.9	0.88	822	47	806	28	813	23	1.9	0.6	806	28	6
SJ7	1	401000	28800	60500	1132000	3626000	1.0	831	833	357	6.911	1.9	0.069	1.2	1.370	2.2	0.145	1.9	0.79	882	47	858	31	855	25	3.1	1.6	858	31	6
SJ7	7	200000	13630	9800	159000	1838000	0.2	146.9	6840	19.9	6.840	1.9	0.068	1.3	1.374	2.2	0.146	1.9	0.85	883	51	879	31	878	26	-1.9	-0.2	879	31	6
SJ7	40	375000	26980	47200	472000	3261000	0.4	987	1930	180	6.689	1.8	0.071	1.1	1.462	2.1	0.150	1.8	0.87	951	45	898	30	915	25	5.6	1.8	898	30	6
SJ7	20	108200	7800	16800	261000	906000	0.7	55.2	66.3	64.5	6.394	2.0	0.072	1.2	1.539	2.2	0.156	2.0	0.87	979	48	937	34	945	27	4.3	0.8	937	34	6
SJ7	107	382000	29500	60400	882000	3270000	0.7	745	659	241	6.386	1.9	0.075	1.5	1.621	2.5	0.157	1.9	0.77	1069	54	938	33	976	30	12.3	3.9	938	33	6
SJ7	108	141700	10270	30000	521000	1164000	1.2	265.1	384	119	6.173	1.9	0.072	1.3	1.591	2.2	0.162	1.9	0.87	973	45	968	34	967	26	0.5	-0.1	968	34	6
SJ7	13	117500	8960	5500	44900	964000	0.1	56.8	11	20.8	6.158	1.9	0.077	1.2	1.729	2.2	0.162	1.9	0.87	1126	46	970	34	1020	29	13.9	4.9	970	34	6
SJ7	57	199600	14540	52800	1454000	3120000	0.9	367	532	192	6.151	1.9	0.071	1.1	1.596	2.2	0.163	1.9	0.87	968	44	974	34	970	28	-0.6	-0.5	974	34	6
SJ7	25	419000	30120	54300	853000	3330000	0.3	235.1	185	210	6.039	1.8	0.071	1.1	1.627	2.1	0.166	1.8	0.88	957	44	983	34	980	26	-2.5	1.2	983	34	6
SJ7	94	94600	7050	13200	224000	744000	0.8	175	188	53	5.814	1.9	0.073	1.2	1.720	2.2	0.172	1.9	0.86	1023	46	1023	36	1015	28	0.0	-0.8	1023	36	6
SJ7	3	162100	7870	17600	294000	741000	1.0	53.1	80.1	65.4	5.546	1.9	0.076	1.1	1.877	2.2	0.180	1.9	0.86	1083	47	1068	37	1072	29	1.4	0.4	1068	37	6
SJ7	60	571000	46900	13100	123000	4140000	0.1	1251	110	58	5.385	2.7	0.080	1.6	2.090	3.8	0.186	2.7	0.70	1188	64	1095	56	1127	52	7.8	2.8	1095	56	6
SJ7	97	121600	9390	33600	1014000	1158000	1.3	199.4	345	136	5.308	1.9	0.076	1.3	1.968	2.2	0.188	1.9	0.87	1092	44	1113	39	1105	29	-1.9	-0.7	1113	39	6
SJ7	115	23800	1858	9700	140000	164600	2.1	37.9	96.1	38	5.230	2.2	0.077	1.6	2.019	2.7	0.191	2.2	0.82	1119	63	1127	46	1118	36	-0.7	-0.8	1127	46	6
SJ7	100	394700	30680	18300	244000	2728000	0.2	628	197	74	5.187	1.8	0.077	1.1	2.023	2.1	0.193	1.8	0.85	1114	44	1138	37	1124	28	-2.2	-1.3	1138	37	6
SJ7	80	398000	31500	47600	647000	2710000	0.6	659	537	207	5.149	1.8	0.078	1.1	2.088	2.1	0.194	1.9	0.88	1137	45	1144	39	1144	29	-0.6	0.0	1144	39	6
SJ7	19	352000	27400	52600	677000	2380000	0.7	143	170	202	5.086	1.8	0.078	1.1	2.107	2.1	0.197	1.8	0.85	1140	43	1158	37	1151	29	-1.6	-0.6	1158	37	6
SJ7	76	830000	64500	124000	1038000	5270000	0.7	2391	1226	927	5.076	1.8	0.078	1.2	2.119	2.2	0.197	1.9	0.84	1142	45	1159	39	1156	29	-1.5	-0.3	1159	39	6
SJ7	4	109600	10730	34000	368000	548000	1.7	38.1	104.1	125	3.830	1.9	0.097	1.2	3.520	2.1	0.261	1.9	0.90	1571	43	1495	52	1530	35	4.8	2.3	1571	43	7
SJ7	18	122500	12180	31900	346000	708000	1.2	41.9	85.9	122	4.374	1.9	0.097	1.1	3.064	2.3	0.229	1.9	0.84	1572	41	1326	46	1426	34	15.6	7.0	1572	41	7
SJ7	111	2290000	52300	65000	1481000	4230000	0.3	889	5140	1579	4.324	1.9	0.098	1.3	3.527	2.4	0.262	1.9	0.79	1590	50	1497	52	1532	40	5.8	2.3	1590	50	7
SJ7	78	1195000	119200	195400	1571000	5990000	0.8	1492	1318	851	3.722	1.8	0.099	1.1	3.642	2.1	0.269	1.8	0.85	1595	39	1534	49	1558	33	3.8	1.6	1595	39	7
SJ7	54	415000	41600	59900	630000	2029000	0.6	503	750	258	4.179	2.0	0.100	1.1	3.313	2.3	0.239	2.0	0.87	1619	39	1382	49	1482	36	14.6	6.7	1619	39	7
SJ7	32	123800	12940	18300	177000	908000	0.7	137.5	76	74.0	3.741	2.1	0.100	1.2	3.720	2.4	0.267	2.1	0.85	1627	41	1526	56	1574	41	6.2	3.0	1627	41	7
SJ7	45	1115000	111900	56300	473000	7200000	0.2	1510	1390	240	4.484	3.1	0.101	1.2	3.160	4.0	0.223	3.1	0.79	1630	45	1293	72	1425	59	20.7	9.3	1630	45	7
SJ7	15	87700	9180	16000	82900	393000	0.5	22.92	27.9	14.9	3.408	1.9	0.103	1.2	4.207	2.3	0.293	1.9	0.83	1676	39	1658	54	1673	36	1.1	0.9	1676	39	7
SJ7	109	76400	8280	16500	163000	325700	1.3	74.2	118.9	66	3.190	1.9	0.106	1.3	4.620	2.4	0.314	1.9	0.80	1723	46	1762	58	1751	40	-2.3	-0.6	1723	46	7
SJ7	120	235000	25800	47300	355000	1027000	0.9	242	229	188	3.221	1.9	0.107	1.1	4.593	2.2	0.311	1.9	0.89	1755	39	1742	57	1747	35	0.7	0.3	1755	39	7
SJ7	30	318100	34960	22000	136500	1301000	0.4	298.5	784	97	3.033	1.8	0.108	1.2	4.861	2.2	0.325	1.8	0.85	1770	40	1814	59	1796	37	-2.5	-1.0	1770	40	7
SJ7	35	785000	93200	23300	149500	3250000	0.1	718	97	39	3.133	1.9	0.118	1.1	5.185	2.1	0.319	1.9	0.89	1919	38	1786	57	1849	36	6.9	3.4	1919	38	7
SJ7	6	316600	40600	26700	412000	1120000	0.6	179.3	69.3	199	2.689	1.7	0.127	1.1	6.528	2.1	0.372	1.7	0.81	2048	33	2035	63	2049	37	0.5	0.5	2048	37	8
SJ7	84	764000	115300	41100	280000	2350000	0.3	548	226	178	2.284	1.8	0.148	1.1	8.920	2.1	0.438	1.8	0.86	2328	38	2340	71	2331	38	-0.5	0.4	2328	38	7
SJ7	101	354000	56400	59200	333000	1108000	0.8	254	264	238	2.345	1.9	0.159	1.1	9.350	2.1	0.426	1.9	0.88	2448	38	2289	71	2372	39	6.5	3.5	2448	38	7
SJ7	74	189400	32580	27700	158000	823000	0.7	162.7	134	130	2.329	1.9	0.160	1.2	9.490	2.2	0.429	1.9	0.86	2453	36	2308	70	2385	40	5.9	3.2	2453	36	7
SJ7	115	1115000	111900	56300	473000	7200000	0.2	1510	1390	240	4.484	3.1	0.101	1.2	3.160	4.0	0.223	3.1	0.79	1630	45	1293	72	1425	59	20.7	9.3	1630	45	7
SJ7	15	87700	9180	16000	82900	393000	0.5	22.92	27.9	14.9	3.408	1.9	0.103	1.2	4.207	2.3	0.293	1.9	0.83	1676	39	1658	54	1673	36	1.1	0.9	1676	39	7
SJ7	109	76400	8280	16500	163000	325700	1.3	74.2	118.9	66	3.190	1.9	0.106	1.3	4.620	2.4	0.314	1.9	0.80	1723	46	1762	58	1751	40	-2.3	-0.6	1723	46	7
SJ7	120	235000	25800	47300	355000	1027000	0.9	242	229	188	3.221	1.9	0.107	1.1	4.593	2.2	0.311	1.9	0.89	1755	39	1742	57	1747	35	0.7	0.3	1755	39	7
SJ7	30	318100	34960	22000	136500	1301000	0.4	298.5	784	97	3.033	1.8	0.108	1.2	4.861	2.2	0.325	1.8	0.85	1770	40	1814	59	1796	37	-2.5	-1.0	1770	40	7
SJ7	35	785000	93200	23300	149500	3250000	0.1	718	97	39	3.133	1.9	0.118	1.1	5.185	2.1	0.319	1.9	0.89	1919	38	1786	57	1849	36	6.9	3.4	1919	38	7
SJ7	6	316600	40600	26700	412000	1120000	0.6	179.3	69.3	199	2.689	1.7	0.127	1.1	6.528	2.1	0.372	1.7	0.81	2048	33	2035	63	2049	37	0.5	0.5	2048	37	8
SJ7	84	764000	115300	41100	280000	2350000	0.3	548	226	178	2.284	1.8	0.148	1.1	8.920	2.1	0.438	1.8	0.86	2328	38	2340	71	2331	38	-0.5	0.4	2328	38	7
SJ7	101	354000	56400	59200	333000	1108000	0.8	254	264	238	2.345	1.9	0.159	1.1	9.350	2.1	0.426	1.9	0.88	2448	38	2289	71	2372	39	6.5	3.5	2448	38	7
SJ7	74	189400	32580	27700	158000	823000	0.7	162.7	134	130	2.329	1.9	0.160	1.2	9.490	2.2	0.429	1.9	0.86	2453	36	2308	70	2385	40	5.9	3.2	2453	36	7
SJ7	115	312100	51340	51900	298000	3090000	0.9	207.3	216	206	2.177	1.9	0.161	1.1	10.140	2.1	0.459	1.9	0.87	2462	37	2436	75	2449	39	1.1	0.5	2462	37	7
SJ7	64	870000	148900	78000	2457000	9	717	695	605	2.129	1.8	0.166	1.0	10.778	2.1	0.470	1.8	0.87	2516	34	2487	76	2505	38	1.2	0.7	2516	34	7
SJ7	72	268000	53800	35500	189000	733000	0.7	196	163.8	155	2.050	1.8	0.199	1.1	13.360	2.2	0.488	1.8	0.85	2816	38	2561	78	2705	40	9.1	5.3	2816	38	7
SJ7	28	77200	6070	24000	271000	658000	1.0	55.5	86.8	94	6.406	2.7	0.077	1.2	1.657	2.9	0.156	2.7	0.92	1116	47	933	46	986	37	16.4	5.4	N.D.	N.D.	4
SJ7	39	91200	5850	18200	578000	1540000	1.0	330	1500	77	12.771	1.9	0.063	2.6	0.692	3.9	0.078	1.9	0.53	766	115	615	18	615	18	21.5	5.6	N.D.	N.D.	4
SJ7	43	304000	23700	21000	271000	2810000	0.3	593	1220	89	6.949	1.9	0.077	1.1	1.532	2.2	0.144	1.9	0.86	1116	42	867	30	946	27	22.3	8.3	N.D.	N.D.	4
SJ7	47	23950	1603	16500	444000	350000	3.4	91.1	27.1	73.4	6.400	1.9	0.066	1.6	0.829	2.6	0.091	2.0	0.78	797	69	562	23	613	23	29.5	8.3	N.D.	N.D.	4
SJ7	55	472000	44200	16900	144000	3160000	0.1	692	160	73	5.023	2.0	0.093	2.9	2.600	4.2	0.199	2.0	0.48	1480	110	1170	44	1277	58	20.9	8.4	N.D.	N.D.	4
SJ7	65	485500	35400	54200	1218000	5185000	0.2	1498	1083	237	8.052	1.9	0.071	1.0	1.230	2.2	0.124	1.9	0.86	968	43	754	27	813	25	22.1	7.3	N.D.	N.D.	4
SJ7	82	41630	2650	18200	530000	658000	2.2	157	435	79	11.962	1.9	0.063	1.6	0.724	2.6	0.084	1.9	0.75	693	67	517	19	552	21	25.3	6.3	N.D.	N.D.	4
SJ7	83	84000	6540	19000	284000	760000	1.0	179	231	83	6.789	1.9	0.077	1.4	1.561	2.3	0.147	1.9	0.80	1115	53	886	31	955	28	20.5	7.2	N.D.	N.D.	4
SJ7	70	345

SJ8	59	17970	3270	10500	297000	400000	1.9	93.6	180.5	39	16.529	2.2	0.177	1.4	1.488	2.5	0.061	2.2	0.89	2623	44	378	16	923	30	85.6	59.0	N.D.	N.D.	3
SJ8	98	32100	3380	-2100	9400	496000	0.1	105.6	8	N.D.	11.990	2.0	0.103	1.4	1.206	2.3	0.083	2.0	0.87	1664	50	517	20	802	25	69.0	35.6	N.D.	N.D.	3
SJ8	19	42	21	-4300	-2000	-1610	N.D.	N.D.	N.D.	N.D.	N.D.	N.D.	N.D.	N.D.	N.D.	N.D.	N.D.	N.D.	N.D.	N.D.	N.D.	N.D.	N.D.	N.D.	N.D.	N.D.	N.D.	N.D.	N.D.	1
SJ8	40	15	6.7	-1400	-2600	-360	N.D.	N.D.	N.D.	N.D.	N.D.	N.D.	N.D.	N.D.	N.D.	N.D.	N.D.	N.D.	N.D.	N.D.	N.D.	N.D.	N.D.	N.D.	N.D.	N.D.	N.D.	N.D.	N.D.	1
SJ8	96	-3	-20.7	-3200	-9400	-2000	N.D.	N.D.	N.D.	N.D.	N.D.	N.D.	N.D.	N.D.	N.D.	N.D.	N.D.	N.D.	N.D.	N.D.	N.D.	N.D.	N.D.	N.D.	N.D.	N.D.	N.D.	N.D.	N.D.	1
SJ8	107	-7	-15.4	-4400	-3300	200	N.D.	N.D.	N.D.	N.D.	N.D.	N.D.	N.D.	N.D.	N.D.	N.D.	N.D.	N.D.	N.D.	N.D.	N.D.	N.D.	N.D.	N.D.	N.D.	N.D.	N.D.	N.D.	N.D.	1

P = correlation coefficient
Exp. = screening explanation
N.D. = not determined

TABLE S6: LASER ABLATION ZIRCON U-Pb STANDARD

Analysis #	^{206}Pb (cps)	^{207}Pb (cps)	^{208}Pb (cps)	^{232}Th (cps)	^{238}U (cps)	Th/U	Contents (ppm)			Data for Tera-Wasserburg plot				Data for Normal - Wetherill plot						Ages (Ma)						Discordance (%)	
							Pb	Th	U	$^{238}U/^{206}Pb$	1σ %	$^{207}Pb/^{206}Pb$	1σ %	$^{207}Pb/^{235}U$	1σ %	$^{206}Pb/^{238}U$	1σ %	ρ	$^{207}Pb/^{206}Pb$	2σ	$^{206}Pb/^{238}U$	2σ	$^{207}Pb/^{235}U$	2σ	6-38/ 7-6	6-38/ 7-35
91500																											
Z_91500_0	68500	5210	4800	99100	480000	0.42	79	31	15	5.473	2.0	0.075	1.2	1.889	2.2	0.183	2.0	0.89	1081	47	1084	38	1076	30	-0.3	0.7
Z_91500_1	70900	5364	5800	95300	503000	0.38	84	31	18	5.534	1.9	0.075	1.2	1.873	2.2	0.181	1.9	0.86	1065	50	1071	37	1072	29	-0.6	-0.1
Z_91500_2	63800	4709	4000	78200	452000	0.35	76	27	13	5.519	1.9	0.073	1.2	1.842	2.2	0.181	1.9	0.84	1017	46	1073	37	1059	29	-5.5	1.3
Z_91500_3	68800	5240	6800	91200	505000	0.37	82	33	22	5.528	2.0	0.076	1.2	1.881	2.3	0.181	2.0	0.85	1080	49	1071	39	1073	31	0.8	-0.2
Z_91500_4	45940	3459	5300	50700	335300	0.32	80	31	18	5.552	2.0	0.074	1.2	1.828	2.3	0.180	2.0	0.87	1037	50	1067	39	1056	29	-2.9	1.0
Z_91500_5	43940	3276	2800	48500	314900	0.26	80	29	10	5.559	1.9	0.074	1.2	1.847	2.2	0.180	1.9	0.85	1037	49	1066	37	1061	29	-2.8	0.5
Z_91500_6	62200	4780	4100	85200	467000	0.45	84	42	16	5.714	1.9	0.076	1.1	1.836	2.2	0.175	1.9	0.85	1092	46	1039	36	1057	29	4.9	-1.7
Z_91500_7	44180	3419	3900	43300	322300	0.31	73	24	16	5.537	2.0	0.076	1.3	1.874	2.3	0.181	2.0	0.86	1089	50	1070	39	1070	30	1.7	0.0
Z_91500_8	45480	3482	4300	51400	341800	0.35	83	32	17	5.669	2.0	0.075	1.3	1.824	2.3	0.176	2.0	0.86	1068	53	1047	38	1052	30	2.0	-0.5
Z_91500_9	37670	2907	2100	35500	283700	0.37	80	29	9	5.714	2.0	0.076	1.3	1.812	2.3	0.175	2.0	0.85	1087	50	1039	38	1052	30	4.4	-1.2
Z_91500_10	36530	2778	1500	41200	270100	0.36	79	34	7	5.559	2.0	0.075	1.4	1.856	2.4	0.180	2.0	0.84	1067	54	1066	40	1063	32	0.1	0.3
Z_91500_11	35990	2706	3000	32600	268600	0.38	80	27	13	5.593	2.0	0.075	1.3	1.824	2.4	0.179	2.0	0.85	1070	54	1060	40	1052	31	0.9	0.8
Z_91500_12	38460	2912	4100	37600	298300	0.32	80	30	17	5.774	1.9	0.074	1.3	1.771	2.3	0.173	1.9	0.86	1049	54	1029	37	1034	29	1.9	-0.5
Z_91500_13	37520	2822	7500	40500	286900	0.30	79	32	31	5.682	1.9	0.074	1.4	1.793	2.3	0.176	1.9	0.83	1033	55	1045	37	1045	30	-1.2	0.0
Z_91500_14	38010	2895	300	36100	292600	0.25	80	29	1	5.760	2.0	0.074	1.3	1.780	2.5	0.174	2.0	0.81	1047	54	1031	38	1037	33	1.5	-0.6
Z_91500_15	37540	2824	4500	51500	267500	0.42	80	30	17	5.444	2.0	0.075	1.5	1.913	2.4	0.184	2.0	0.85	1077	59	1087	40	1088	33	-0.9	-0.1
Z_91500_16	36310	2732	3500	53000	260400	0.42	80	31	13	5.336	2.1	0.074	1.4	1.906	2.5	0.187	2.1	0.85	1031	56	1106	43	1080	33	-7.3	2.4
Z_91500_17	35780	2808	8900	50400	262900	0.43	80	29	34	5.459	2.1	0.076	1.3	1.919	2.4	0.183	2.1	0.86	1106	53	1083	42	1089	32	2.1	-0.6
Z_91500_18	39000	2968	4800	50000	289200	0.38	81	31	18	5.574	2.1	0.076	1.3	1.875	2.4	0.179	2.1	0.87	1078	53	1063	40	1070	32	1.4	-0.7
Z_91500_19	37480	2885	1900	47100	270100	0.35	79	30	7	5.453	1.9	0.077	1.3	1.925	2.3	0.183	1.9	0.85	1106	53	1088	37	1091	32	1.6	-0.3
Z_91500_20	38040	2873	1700	44800	274500	0.34	81	29	6	5.461	2.0	0.075	1.3	1.904	2.4	0.183	2.0	0.86	1069	55	1086	41	1084	33	-1.6	0.2
Z_91500_21	37900	2903	7900	51600	283700	0.34	80	31	30	5.708	2.0	0.076	1.4	1.837	2.4	0.175	2.0	0.86	1076	54	1040	39	1057	31	3.3	-1.6
Z_91500_22	36550	2768	6000	50300	270700	0.39	80	30	23	5.596	2.0	0.076	1.3	1.840	2.4	0.179	2.0	0.85	1067	52	1059	39	1060	30	2.6	-0.1
Z_91500_23	35950	2767	4400	49600	265500	0.38	80	30	17	5.612	2.0	0.075	1.4	1.848	2.4	0.178	2.0	0.85	1062	55	1057	39	1060	31	0.5	-0.3
Z_91500_24	38120	2921	3500	55100	285700	0.37	80	30	13	5.605	2.0	0.074	1.2	1.809	2.4	0.178	2.0	0.86	1044	51	1057	40	1049	32	-1.2	0.8
Z_91500_25	37620	2914	5700	56100	278800	0.39	80	31	22	5.593	2.0	0.076	1.4	1.862	2.4	0.179	2.0	0.84	1106	56	1060	39	1067	31	4.2	-0.7
Z_91500_26	38100	2871	200	50600	275100	0.36	80	29	1	5.525	2.0	0.075	1.4	1.844	2.4	0.181	2.0	0.83	1063	57	1072	39	1061	32	-0.8	1.0
Z_91500_27	35680	2737	4100	45100	271000	0.22	80	31	16	5.663	2.0	0.075	1.3	1.833	2.4	0.177	2.0	0.85	1066	52	1050	40	1055	31	1.5	-0.5
Z_91500_28	34240	2593	1900	49800	251700	0.31	80	34	8	5.634	2.1	0.075	1.3	1.829	2.4	0.178	2.1	0.88	1056	55	1052	41	1054	31	0.4	-0.2
Z_91500_29	33030	2519	400	37700	243300	0.27	80	25	2	5.621	2.0	0.076	1.3	1.858	2.4	0.178	2.0	0.83	1081	50	1055	39	1064	32	2.4	-0.8
Z_91500_30	65000	4990	7400	108900	468000	0.38	81	33	30	5.565	1.9	0.074	1.2	1.859	2.2	0.180	1.9	0.85	1051	50	1065	37	1065	30	-1.3	0.0
Z_91500_31	60900	4587	5200	100500	438000	0.39	79	30	21	5.504	2.0	0.074	1.2	1.867	2.3	0.182	2.0	0.86	1027	48	1076	39	1068	30	-4.8	0.7
Z_91500_32	59200	4440	2900	96400	433000	0.37	80	28	12	5.528	2.0	0.074	1.2	1.842	2.2	0.181	2.0	0.89	1035	48	1071	39	1059	29	-3.5	1.1
GJ1																											
Z_GJ1_0	121700	7380	-170	29900	1596000	0.04	249	11	N.D.	10.132	1.8	0.060	1.1	0.812	2.2	0.099	1.8	0.85	596	48	607	22	603	19	-1.9	0.7
Z_GJ1_1	125700	7680	-110	25300	1643000	0.03	248	10	N.D.	10.070	1.8	0.061	1.2	0.824	2.1	0.099	1.8	0.85	619	49	610	21	610	19	1.4	0.0
Z_GJ1_2	129100	7890	-70	25000	1699000	0.03	251	10	N.D.	10.040	1.8	0.060	1.1	0.830	2.1	0.100	1.8	0.86	614	48	612	21	614	19	0.3	-0.3
Z_GJ1_3	128700	7950	650	31200	1695000	0.04	248	13	2	10.062	1.8	0.061	1.1	0.828	2.1	0.099	1.8	0.86	624	47	611	21	612	19	2.1	-0.3
Z_GJ1_4	129400	7790	860	28800	1722000	0.03	458	17	3	10.187	1.8	0.060	1.2	0.806	2.2	0.098	1.8	0.82	586	49	604	21	600	19	-3.0	0.6
Z_GJ1_5	133000	8080	1300	28500	1762000	0.04	487	17	5	10.152	1.8	0.060	1.2	0.818	2.1	0.099	1.8	0.83	609	50	606	21	607	19	0.6	-0.2
Z_GJ1_6	125600	7700	5200	32600	1709000	0.03	418	23	21	10.384	1.8	0.061	1.2	0.805	2.2	0.096	1.8	0.84	628	51	593	21	600	20	5.6	-1.1
Z_GJ1_7	128900	7770	2700	26800	1761000	0.03	433	22	11	10.267	1.8	0.060	1.2	0.803	2.1	0.097	1.8	0.85	589	50	599	21	598	19	-1.7	0.2
Z_GJ1_8	129900	7850	2200	27700	1769000	0.03	436	26	9	10.267	1.8	0.060	1.2	0.802	2.1	0.097	1.8	0.87	588	51	599	21	599	20	-1.9	0.1
Z_GJ1_9	114500	6970	-100	20700	1594000	0.02	480	17	N.D.	10.460	1.9	0.060	1.2	0.796	2.1	0.096	1.9	0.88	609	51	588	21	594	19	3.4	-1.0
Z_GJ1_10	111200	6840	1700	16400	1548000	0.02	470	14	8	10.428	1.8	0.061	1.2	0.801	2.2	0.096	1.8	0.84	615	52	590	21	597	20	4.1	-1.1
Z_GJ1_11	116100	7140	-1500	26100	1622000	0.09	496	22	N.D.	10.515	1.8	0.060	1.3	0.785	2.2	0.095	1.8	0.85	600	55	586	20	590	20	2.4	-0.7
Z_GJ1_12	103300	6320	2400	24100	1495000	0.04	407	20	10	10.823	1.8	0.060	1.2	0.765	2.2	0.092	1.8	0.85	605	50	570	20	576	19	5.9	-1.2
Z_GJ1_13	103400	6340	0	26700	1449000	0.04	390	22	0	10.537	1.8	0.060	1.2	0.785	2.1	0.095	1.8	0.88	606	49	584	21	588	19	3.6	-0.6
Z_GJ1_14	108900	6670	1000	23500	1516000	0.04	404	19	4	10.431	1.8	0.060	1.2	0.794	2.1	0.096	1.8	0.85	614	51	590	20	593	19	3.9	-0.5
Z_GJ1_15	104500	6460	1800	39700	1385000	0.06	420	23	7	9.862	1.8	0.060	1.2	0.836	2.1	0.101	1.8	0.87	611	50	623	22	617	20	-1.9	0.9
Z_GJ1_16	105100	6340	-6400	30500	1381000	0.03	416	18	N.D.	9.775	1.9	0.059	1.2	0.830	2.2	0.102	1.9	0.86	586	51	628	22	614	20	-7.2	2.3
Z_GJ1_17	110800	6730	2700	43700	1439000	0.06	429	25	11	9.709	1.8	0.060	1.1	0.846	2.1	0.103	1.8	0.87	583	49	632	22	622	20	-8.4	1.5
Z_GJ1_18	113000	6760	600	37900	1482000	0.05	434	25	2	9.940	1.9	0.059	1.2	0.814	2.1	0.101	1.9	0.88	575	50	618	22	605	20	-7.5	2.1
Z_GJ1_19	116200	7040	4500	49200	1525000	0.06	443	34	17	9.891	1.8	0.060	1.1	0.826	2.1	0.101	1.8	0.86	591	49	621	22	611	20	-5.1	1.6
Z_GJ1_20	116000	7010	-2200	36400	1502000	0.06	434	26	N.D.	9.891	1.8	0.059	1.2	0.832	2.2	0.101	1.8	0.85	570	52	621	22	614	20	-8.9	1.1
Z_GJ1_21	110600	6680	7500	41400	1473000	0.07	454	25	28	10.152	1.8	0.060	1.2	0.815	2.1	0.099	1.8	0.85	612	52	606	21	606	19	1.0	0.0
Z_GJ1_22	108100	6630	6400	41800	1460000	0.06	458	25	24	10.320	1.9	0.060	1.2	0.807	2.2	0.097	1.9	0.86	607	51	596	21	601	20	1.8	-0.7
Z_GJ1_23	111200	6730	3800	41000	1459000	0.06	464	24	14	9.970	1.8	0.059	1.2	0.823	2.2	0.100	1.8	0.84	561	50	616	22	609	20	-9.9	1.2
Z_GJ1_24	110000	6590	3800	31600	1458000	0.04	429	18	15	10.204	1.8	0.059	1.2	0.805	2.2	0.098	1.8	0.84	574	54	604	22	600	20	-5.2	0.7
Z_GJ1_25	103000	6290	1800	38100	1360000	0.05	404	23	7	10.030	1.8	0.060	1.2	0.827	2.2	0.100	1.8	0.83	600	54	613	21	614	20	-2.1	-0.1
Z_GJ1_26	101900	6200	-600	27500	1359000	0.04	406	17	N.D.	10.142	1.9	0.059	1.2	0.809	2.1	0.099	1.9	0.89	583	53	606	21	602	19	-3.9	0.7
Z_GJ1_27	109700	6690	7800	35700	1416000	0.04	469	23	31	10.030	1.9	0.060	1.2	0.827	2.2	0.100	1.9	0.85	599	50	613	22	613	19	-2.3	0.0
Z_GJ1_28	109400	6550	3300	37500	1399000	0.03	452	23	13	9.881	1.9	0.059	1.2	0.828	2.2	0.101	1.9	0.86	567	50	621	22	612	20	-9.6	1.5
Z_GJ1_29	109800	6650	2400	31700	1460000	0.03	454	19	10	10.111	1.9	0.060	1.2	0.808	2.2	0.099	1.9	0.86	584	49	608	22	602	20	-4.0	0.9
Z_GJ1_30	109300	6670	-1800	34500	1442000	0.04	242	12	N.D.	10.225	1.8	0.060	1.2	0.816	2.1	0.098	1.8	0.86	589	52	601	21	606	19	-2.1	-0.7
Z_GJ1_31	112000	6670	4800	35500	1461000	0.04	244	11	19	10.081	1.9	0.059	1.3	0.821	2.1	0.099	1.9	0.87	558	53	611	22	608	20	-9.4	0.4
Z_GJ1_32	110100	6640	1700	39200	1444000	0.06	243	12	7	10.040	1.8	0.060	1.2	0.824	2.2	0.100	1.8	0.83	583	51	612	21	611	20	-5.0	0.2
Plesovice																											
Z_Plesovice_0	204600	11050	10300	481000	4900000	0.22	711	210	33	18.495	1.8	0.053	1.1	0.399	2.1	0.054	1.8	0.82	340	51	340	12	341	12	0.1	-0.4
Z_Plesovice_1	156300	8410	3500	286000	3770000	0.17	547	130	11	18.379	1.8	0.053	1.1	0.401	2.1	0.054	1.8	0.87	345	48	342	12	343	12	1.0	-0.4
Z_Plesovice_2	185000	9920	8000	376000	4420000	0.19	646	176	26	18.212	1.8	0.053	1.1	0.398	2.1	0.055	1.8	0.85	321	50	345	12	340	12	-7.4	1.4
Z_Plesovice_3	182300	9890	5700	353000	4330000	0.18	640	171	19	18.262	1.7	0.053	1.0	0.402	2.1	0.055	1.7	0.82	345	48	344	12	343	12	0.4	0.3
Z_Plesovice_4	186200	10140	5200	211800	4590000	0.10	1294	125	18	18.832	1.8	0.054	1.1	0.395	2.2	0.053	1.8	0.83	369	49	334	12	338	12	9.6	-1.4
Z_Plesovice_5	195900	10550	5300	207000	4760000	0.10	1354	122	18	18.420	1.7	0.053	1.0	0.396	2.1	0.054	1.7	0.82	335	47	341	12	339	11	-1.7	0.6
Z_Plesovice_6	176300	9460	4900	183000	4400000	0.10	1089	201	20	18.879	1.8	0.054	1.2	0.391	2.2	0.053	1.8	0.82	353	50	333	12	335	12	5.8	-0.6
Z_Plesovice_7	150300	8200	4600	142100	3848000	0.09	951	182	19	19.073	1.8	0.054	1.1	0.389	2.1	0.052	1.8	0.88	363	51	329	11	333	12	9.3	-1.2
Z_Plesovice_8	177400	9550	4200	176000	4370000	0.10	1080	277	17	18.671	1.8	0.053	1.1	0.394	2.2	0.054	1.8	0.82	341	52	336	12	337	12	1.4	-0.3
Z_Plesovice_9	163400	8820	1700	189000	4150000	0.12	1277	163	7	19.102	1.8	0.053	1.2	0.383	2.2	0.052	1.8	0.82	330	57	329	12	330	12	0.3	-0.2
Z_Plesovice_10	167000	8980	1600	171000	4170000	0.11	1286	149	7	18.619	1.8	0.053	1.1	0.391	2.0	0.054	1.8	0.86	324	51	337	12	335	12	-4.1	0.6
Z_Plesovice_11	167200	9010	900	188000	4200000	0.12	1302	164	4	18.972	1.8	0.054	1.1	0.390	2.0	0.053	1.8	0.88	354	50	331	12	335	12	6.5	-1.0
Z_Plesovice_12	142300	7570	7300	281000	3608000	0.22	952	236	30	19.095	1.8	0.053	1.1	0.382	2.1	0.052	1.8	0.87	329	54	329	12	329	13	0.0	-0.1
Z_Plesovice_13	134200	7320	5300	186000	3440000	0.14	899	156	22	18.975	1.8	0.053	1.1	0.386	2.1	0.053	1.8	0.87	339	50	331	12	331	12	2.3	0.0
Z_Plesovice_14	143600	7890	5500	259000	3623000	0.19	937	219	23	19.011	1.8	0.054	1.2	0.393	2.2	0.053	1.8	0.83	368	52	330	12	336	12	10.2	-1.7
Z_Plesovice_15	155700	8320	200	238000	3770000	0.16	1112	137	1	18.096	1.8	0.053	1.1	0.400	2.1	0.055	1.8	0.85	316	54	347	12	341	12	-9.7	1.6
Z_Plesovice_16	91000	4880	3900	187000	2157000	0.20	628	107	15	18.116	1.8	0.053	1.1	0.402	2.1	0.055	1.8	0.86	335	51	346	12	343	12	-3.4	1.0
Z_Plesovice_17	136400	7550	2200	195000	3340000	0.14	958	112	9	18.332	1.8	0.054	1.3	0.402	2.2	0.055	1.8	0.82	374	53	342	12	343	13	8.4	-0.1
Z_Plesovice_18	185600	10030	11000	460000	4670000	0.25	1338	330	41	19.001	1.8	0.053	1.1	0.386	2.1	0.053	1.8	0.87	334	49	331	12	331	12	1.0	-0.1
Z_Plesovice_19	151200	8130	4100	377000	3760000	0.25	1067	275	16	19.001	1.8	0.053	1.1	0.383	2.1	0.053	1.8	0.86	312	55	331	12	329	12	-6.0	0.4
Z_Plesovice_20	122500	6640	-1500	177000	3088000	0.14	868	131	N.D.	18.801	1.9	0.053	1.2	0.392	2.2	0.053	1.9	0.87	326	56	334	12	336	13	-2.5	-0.5
Z_Plesovice_21	139600	7660	6800	336000	3390000	0.23	1093	198	26	18.389	1.8	0.054	1.1	0.401	2.1	0.054	1.8	0.87	369	52	341	12	342	12	7.5	-0.3
Z_Plesovice_22	159000	8590	6600	296000	3799000	0.19	1237	174	25	18.238	1.8	0.053	1.2	0.404	2.1	0.055	1.8	0.87	341	54	344	12	344	12	-0.9	-0.1
Z_Plesovice_23	148300	8010	5200	261000	3610000	0.18	1182	153	19	18.474	1.8	0.053	1.1	0.398	2.1	0.054	1.8	0.87	344	53	340	12	340	12	1.2	-0.1
Z_Plesovice_24	143300	7800	3000	208000	3540000	0.13	1062	129	12	18.997	1.8	0.053	1.2	0.389	2.2	0.053	1.8	0.83	352	56	331	12	333	12	6.1	-0.8
Z_Plesovice_25	139900	7560	2400	196000	3363000	0.13	1009	123	9	18.349	1.8	0.053	1.1	0.399	2.1	0.055	1.8	0.86	332	54	342	12	341	12	-3.0	0.5
Z_Plesovice_26	142900	7680	2500	209000	3530000	0.13	1057	133	10	18.667	1.8	0.054	1.1	0.392	2.2	0.054	1.8	0.82	351	48	336	12	336	12	4.2	0.1
Z_Plesovice_27	84600	4709	1600	152000	2012000	0.14	587	85	6	18.488	1.8	0.054	1.2	0.406	2.2	0.054	1.8	0.83	371	55	340	12	347	13	8.5	-2.0
Z_Plesovice_28	173000	9340	5900	306000	4140000	0.14	1132	162	23	18.512	1.8	0.053	1.1	0.394	2.2	0.054	1.8	0.82	309	51	339	12	338	12	-9.7	0.4
Z_Plesovice_29	167700	9050	4400	302000	4110000	0.14	1044	151	18	18.793	1.8	0.053	1.0	0.388	2.1	0.053	1.8	0.86	307	48	334	12	333	12	-8.9	0.5
Z_Plesovice_30	146800	7860	-1100	232000	3619000	0.12	666	88	N.D.	19.055	1.8	0.053	1.1	0.386	2.1	0.052	1.8	0.87	333	53	330	12	332	12	1.0	-0.6
Z_Plesovice_31	104300	5670	2600	164000	2568000	0.12	452	60	11	19.059	1.8	0.054	1.1	0.393	2.2	0.052	1.8	0.84	353	53	330	12	337	12	6.6	-2.1
Z_Plesovice_32	94400	5040	-1600	131000	2340000	0.10	400	45	N.D.	19.117	1.8	0.052	1.2	0.379	2.2	0.052	1.8	0.81	291	57	329	12	326	12	-13.0	0.7

P = correlation coefficient

Journal of Geochemical Exploration 185 (2018) 33–51

Contents lists available at ScienceDirect

Journal of Geochemical Exploration

journal homepage: www.elsevier.com/locate/gexplo

Sources, enrichment, and redistribution of As, Cd, Cu, Li, Mo, and Sb in the Northern Atacama Region, Chile: Implications for arid watersheds affected by mining

Tapia J.[a,*], Davenport J.[b], Townley B.[c], Dorador C.[d], Schneider B.[e], Tolorza V.[a], von Tümpling W.[f]

[a] Instituto de Ciencias de la Tierra, Facultad de Ciencias, Universidad Austral de Chile, Chile
[b] Université de Lorraine CNRS-CRPG, Vandœuvre-lés-Nancy, France
[c] Departamento de Geología y Advanced Mining Technology Center, Facultad de Ciencias Físicas y Matemáticas, Universidad de Chile, Chile
[d] Departamento de Biotecnología, Facultad de Ciencias del Mar y Recursos Biológicos e Instituto Antofagasta, Universidad de Antofagasta, Chile
[e] Montgomery & Associates, Vitacura 2771, Las Condes, Santiago, Chile
[f] Helmholtz Centre for Environmental Research – UFZ, Central Laboratory for Water Analytics & Chemometrics, Brückstrasse 3a, 39114 Magdeburg, Germany

ABSTRACT

Long-established and widespread mining activities in the Northern Atacama Region of Chile have historically impacted the environment. Most notably, the Potrerillos and El Salvador mines, until 1976, were responsible for dumping over $150 \cdot 10^6$ tons of tailings into the El Salado River, discharging directly into the bay of Chañaral on the coast. Water resources in the Northern Atacama Region are scarce; the few include the El Salado River and the Pedernales, Maricunga, and Laguna Verde basins. This region also contains two highly sensitive national parks: the Pan de Azúcar on the coast and the Nevado de Tres Cruces in the Andes.

Protecting available water resources in this inherently dry region is critical and environmental degradation that has occurred has not been reported in terms of the most important superficial pollutants. In order to specifically evaluate the metals and metalloids polluting superficial water and fluvial sediments, a 3 year-long survey was carried out in the basins of the Northern Atacama Region. Additionally, impacts of the El Salado River flood in March 2015 were evaluated.

When compared to the average concentrations of dissolved elements in river water worldwide, the most enriched elements of the Northern Atacama Region are, in decreasing order: Li, As, Mo, ± Cd, Sb, and Cu. In the case of fluvial sediments, compared to the composition of the upper continental crust, samples are enriched in the following elements (in decreasing order): As, Cu, Mo, Li, ± Cd and Sb. In surface waters, dissolved As, Li, Mo and Cd are naturally enriched, concentrations of Cu and Sb are inferred to be related to mining activities. In fluvial sediments, concentrations of As, Li and Cd are of natural origin while Cu, Mo and Sb are related to the exploitation and mineral treatment of porphyry copper deposits.

During the intense March 2015 flood event, contaminant elements were remobilized in the Andes Mountains and El Salado Alto Basin, and concentrations increased in the El Salado Bajo Basin predominantly due to the creation of a hydrologic connection between adjacent basins. Despite the presence of world-class porphyry Cu-Mo and iron oxide copper-gold deposits in the region, some of which have been mined since the end of the 19th century, concentrations of dissolved Cu are lower than previously reported. This is likely related to circumneutral pH and the complexation of Cu as a cation in contrast to As and Mo which might be stable as $HAsO_4^{2-}$ and MoO_4^{2-}, respectively, in solution over long distances.

1. Introduction

The Northern Atacama Region of Chile, specifically located between 26 and 27°S, is one of the most inhospitable places in the Atacama Desert. Despite arid to hyper arid conditions since the Late Triassic (Clarke, 2006), there are a few available water resources. Sources of extractable groundwater include the El Salado, Pedernales, Maricunga, and Laguna Verde basins, in which two highly sensitive National Parks exist, the Nevado Tres Cruces in the Andes (Earle et al., 2003) and the Pan de Azúcar on the coast (Thompson et al., 2003). The El Salado

* Corresponding author.
E-mail address: joseline.tapia@uach.cl (J. Tapia).

https://doi.org/10.1016/j.gexplo.2017.10.021
Received 17 May 2017; Received in revised form 6 October 2017; Accepted 26 October 2017
Available online 31 October 2017

River drains into the Pacific Ocean and is the only superficial water system in the Northern Atacama Region. In particular, groundwater is a valuable resource that is supplied predominantly by precipitation and surface water infiltration; aside from potable water use, it is estimated that 70% of extracted groundwater is utilized for mining operations (Neary and García-Chevesich, 2008).

The Northern Atacama Region also hosts important mineral deposits. Since 1894, the seams and veins of the El Salvador porphyry copper deposit, in the Potrerillos district, were mined by selective methods followed by block caving methods (Olson, 1989). More recently, other deposit types explored and exploited in this region consist of stratabound (Espinoza, 1990), iron oxide copper-gold (IOCG) and iron oxide-apatite (IOA) deposits along the Coastal Cordillera (Benavides et al., 2007) as well as epithermal Cu-Au deposits in the Andes (Sillitoe, 1997). Additionally, Li has become an important commodity, especially in the Pedernales and Maricunga salt flats (Gajardo, 2014). As a result of the economic potential and large-scale mining efforts, the El Salado River has been affected by intense and often uncontrolled mining activities during the 20th and 21st century (Ramírez et al., 2005).

To date, no geochemical baseline analysis has been conducted for contaminants in surface water and fluvial sediments in the Northern Atacama Region of Chile, in non-storm conditions or as a function of storm events which are infrequent but powerful in regard to their impacts on inhabitants of the region and the environment (i.e. flooding and distribution of water sources). A comprehensive understanding of contaminant sources, in addition to their distribution and redistribution, is critical in the Atacama Desert due to water scarcity and the importance of sustaining current ecosystems. In the case of groundwater that is recharged by surface water such as the El Salado River, its quality impacts consumption and utilization for mining as the concentrations of contaminants such as As in water affect the production and processing of copper concentrate (International Mining, 2016). In addition, although infrequent, flood events can potentially create a connection between areas of the region not normally linked hydrologically. This connection, which forms as a function of higher water levels in upgradient areas, can act as a conduit for the flow and transport of potential contaminants to areas downgradient where such species may not be present under normal, non-storm conditions.

Through conducting a 3-year long survey of surface water and fluvial sediments in the Northern Atacama Region, this study aims to: (i) identify and evaluate the main contaminants and probable sources, (ii) establish a local geochemical background of the naturally and otherwise anthropogenically enriched elements in surface water and fluvial sediments, and (iii) document the influence of the March 2015 storm event and mudflow in the Northern Atacama Region on the redistribution of contaminant elements. In regard to the flooding of the El Salado River which caused the March 2015 mudflow, metallic contaminants of surface water and fluvial sediments in the region were characterized and compared before, two months after, and one year after the event. As such, the presented results, discussions, and conclusions can have broader implications in comparable arid, high altitude watersheds outside of the immediate study area.

2. Study area

2.1. Physiography and climate

The physiography of the Northern Atacama Region is comprised of several features, including the coastal range (or *Cordillera de la Costa*) separated from the Precordillera by the Central Depression. Pre-Andean basins separate the Precordillera from the Andes (Valero-Garcés et al., 2003). The specific study area encompasses basins of the Andes Mountains, which include Pedernales, Maricunga, and Laguna Verde, as well as the El Salado Bajo, Chañaral, and El Salado Alto basins (Fig. 1a). The highest volcano in the world, the Nevado Ojos del Salado (6893 m s.n.m.; Stern, 2004), closes the Laguna Verde basin to the south (Risacher et al., 1999; Fig. 1a) and marks the southern limit of the central volcanic zone (CVZ) (Stern, 2004).

The Köppen climate classification (Rioseco and Tesser, 2016) indicates that this area within the Atacama Desert is composed of, from west to east: a coastal desert (BWn), normal desert (BWk), cold desert (BWk'), and a dry, steppe-like Andean climate (ETH (ws); Fig. 1b). Additionally, the Andean study area is classified as the *Desert Andes* (north of 31°S), within the *Dry Andes* (north of 35°S). Here, due to limited precipitation and high elevation, only permanent snow patches and small glaciers are found (Lliboutry, 1988 and references therein).

In the Northern Atacama Region, precipitation is scarce. Since 1984, the average precipitation rate in the El Salado River (Las Vegas Station; 26°40′41″ S, 69°39′56″ E) has been 31 mm year^{-1}, with a maximum of 174 mm and 115 mm in 1987 and 2015 respectively. Furthermore, in 2003 and 2007, there was no record of precipitation (MOP, 2017).

2.2. Hydrology

The Northern Atacama Region has four main hydrologic basins, two of which contain hot springs. From west to east these correspond to the El Salado Basin (which is divided into the smaller El Salado Bajo, Chañaral, and El Salado Alto basins) and the naturally endorheic Pedernales, Maricunga, and Laguna Verde basins located within the Puna (Fig. 1a).

The El Salado River originates west of the Andes and its natural headwaters are located downgradient of the Pedernales Basin in a different basin; both are separated by a distance of approximately 200 m (Fig. 1a). The El Salado River drains naturally into the Pacific Ocean at Chañaral. However, in the mid-1970s, it was channeled 10 km to the north of Chañaral, at Caleta Palito (Ramírez et al., 2005; Fig. 1a).

The Pedernales Basin and salt flat, located at 3370 m a.s.l., are the largest of the Atacama Region. There are two hot springs located in this basin: (i) Juncalito, at 4180 m a.s.l., with temperatures ranging between 30 and 40 °C (Hauser, 1997a) and (ii) Río Negro, at 4150 m a.s.l., with an average temperature of 35 °C (Hauser, 1997a; Fig. 1a). The Maricunga Basin and salt flat are located at 3760 m a.s.l. and, after Pedernales, this basin is the second largest in the Northern Atacama Region (Fig. 1a). The Laguna Verde Basin, located within the Puna near the Argentina border at 4350 m a.s.l. (Fig. 1a), is a salty lagoon fed by rivers located generally to the south and west of the basin (Risacher et al., 1999, 2003). The Laguna Verde hot spring, located in the Laguna Verde Basin, is characterized by an average temperature of 40.5 °C (Risacher et al., 1999).

2.3. March 2015 storm event

Despite the aridity of the Northern Atacama Region, intense rain events typically occur once every few years. However, the frequency of storms with the potential to cause flooding in some areas of the Atacama Desert is within the interdecadal (Vargas et al., 2000) to 50 year (Hauser, 1997b) range. Between March 24th and 26th, 2015, the Atacama Region experienced an intense precipitation event resulting from unusual oceanic and atmospheric conditions that produced an inward bound low-pressure cut-off system. Reported rainfall, in the affected areas, ranged between 10 mm on the coast to > 85 mm in the Andes Mountains. Snowfall was also observed over a broad area above 3600 m a.s.l. (Jordan et al., 2015; Fig. 1c).

At the Las Vegas hydro-meteorological station located in the El Salado Alto Basin, reported precipitation within the three-day period was on the order of 80 mm (MOP, 2017). Concentrated, warm, and intense storms resulted in the flooding of the El Salado River (Wilcox et al., 2016). Wilcox et al. (2016) suggested that the March 2015 event was the heaviest and most extensive documented rainfall event within the Northern Atacama Region, producing the largest documented floods compared to adjacent regions. The floods were particularly unusual due

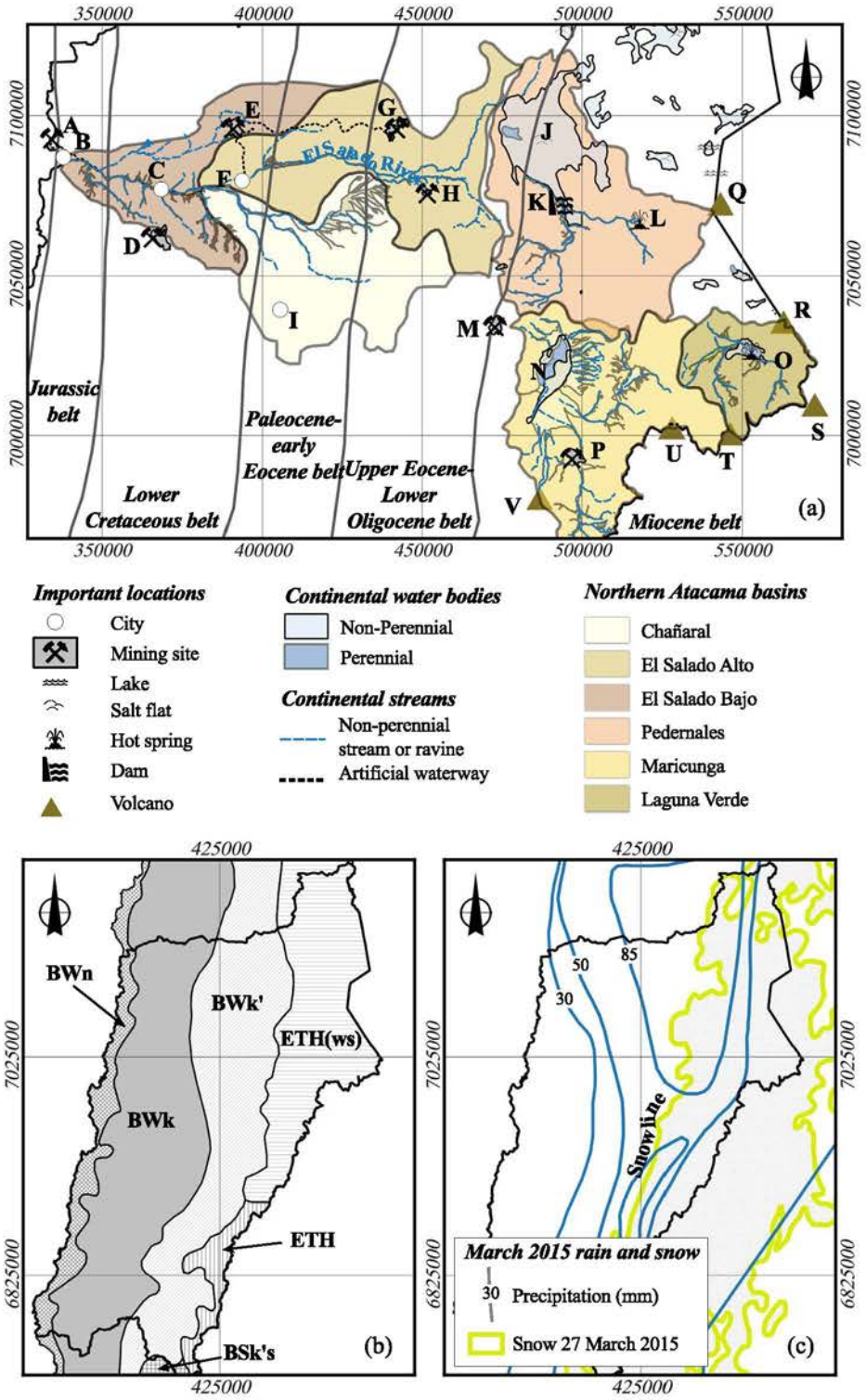

Fig. 1. The Northern Atacama Region. (a) Metallogenic belts (from Sillitoe, 2012; Sillitoe and Perelló, 2005) and basins (from Contreras et al., 2015). The uppercase labels indicate: A. Caleta Palito; B. Chañaral; C. El Salado; D. Manto Verde; E. Pampa Austral Tailings Dam; F. Diego de Almagro; G. El Salvador; H. Potrerillos; I. Inca de Oro; J. Pedernales; K. La Ola Dam; L. Río Negro hot spring; M. La Coipa Mine; N. Maricunga; O. Laguna Verde lake and hot spring; P. Marte Mine; Q: Sierra Nevada de Lagunas Bravas; R: Falso azufre; S: Nevado de Incahuasi; T: Nevado Ojos del Salado; U: El Solo; V: Copiapó Volcano. (b) Climatic zones of the Atacama Region: BWn - coastal desert, BWk - normal desert, BWk' - cold desert, ETH(ws) - cold steppe-like and dry climate of the Andes, ETH - cold steppe-like, and BSk's - cold, semi-arid with winter rain. (c) Precipitation and snow cover during March 27th 2015 (from Jordan et al., 2015).

to their magnitude and high sediment supply, producing highly concentrated sediment flows and extensive mud deposition in urban areas, especially at Diego de Almagro and Chañaral (Fig. 1a). As a result, the aftermath comprised 31 deaths, 16 disappearances, and 30,000 displaced people (Wilcox et al., 2016 and references therein).

2.4. Regional geology and ore deposits

Basement geology, in the distinct physiographic units, is composed of Mesozoic igneous and sedimentary rocks in the *Cordillera de la Costa* as well as Mesozoic to Eocene intrusive and volcanic rocks in the Precordillera; Oligocene to Pliocene basin fill sediments occupy the Central Depression (Clarke, 2006; Fig. 2). At least since 60 Ma, regional geology has been controlled by the CVZ, which is related to subduction of the Nazca plate below the South American plate at a current rate of 7–9 cm year^{-1} (Stern, 2004). In this zone, the continental crust is ≥ 70 km thick and basement ages range from Late Pre-Cambrian to Paleozoic (Stern, 2004; Fig. 2). Cenozoic volcanism in the Atacama Region is related to a number of recent geologic events: (i) Early Miocene to Pleistocene andesite-dacite main arc stratovolcanoes, (ii) early

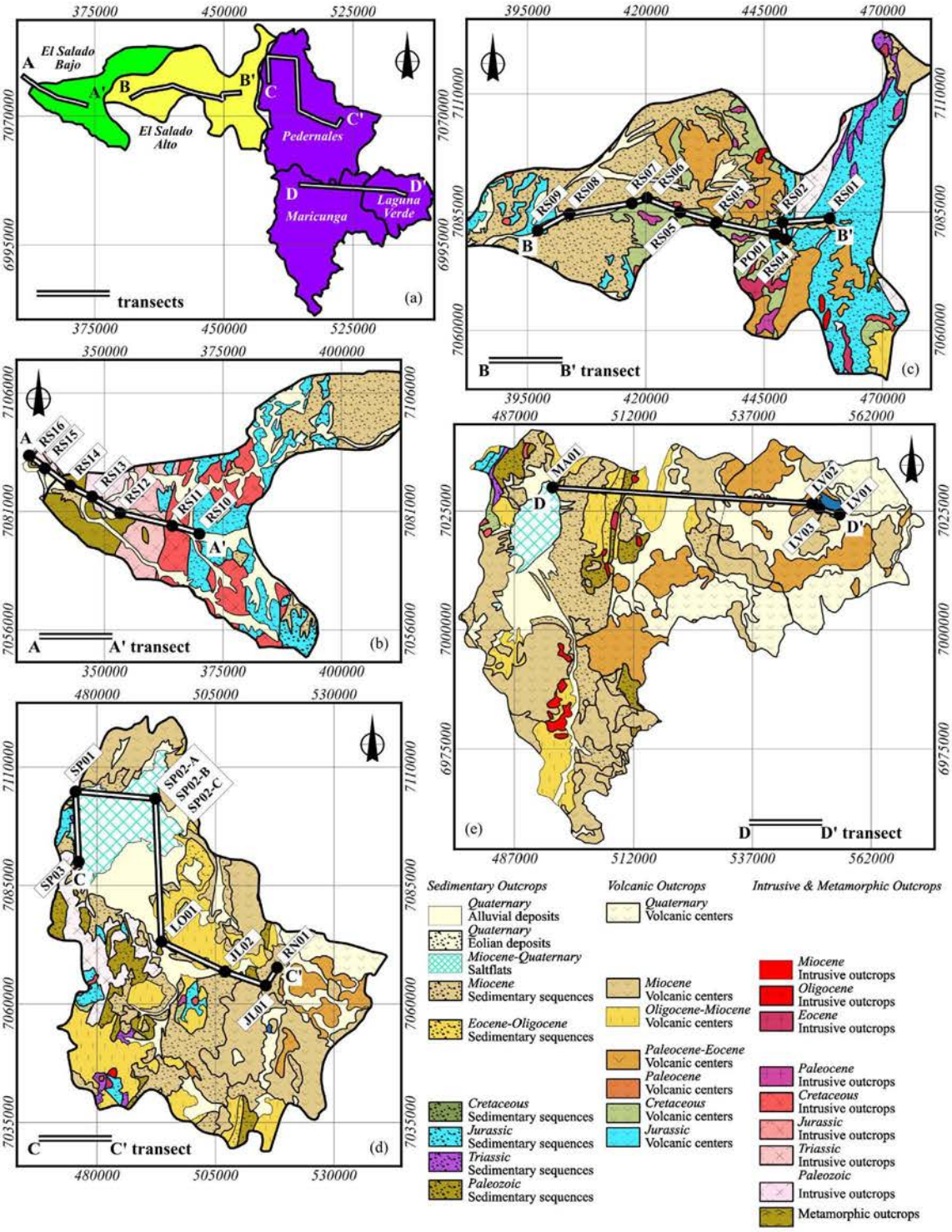

Fig. 2. Geologic maps, sampling sites, and transects. (a) General location map with the basins; (b) El Salado Bajo Basin; (c) El Salado Alto Basin; (d) Pedernales Basin; (e) Maricunga and Laguna Verde basins.

Miocene to Pliocene silicic ignimbrite deposits, and (iii) the formation of lava domes present in both main arc and back-arc regions as well as small Pliocene to Pleistocene basaltic centers in the back arc (Schnurr et al., 2007; Fig. 2).

Ore deposits in the Northern Atacama Region have been classified as longitudinal N-S trending metallogenic belts (Fig. 1a) which, from west to east, correspond to: (i) IOCG and IOA deposits, (ii) Cu-Mo porphyries, and (iii) Au-epithermal and porphyry deposits. Numerous Mesozoic IOCG and IOA ore deposits are hosted in the *Cordillera de la Costa* of northern Chile and are specifically contained within the Upper Jurassic-Lower Cretaceous metallogenic sub-province of the Central Andes (Sillitoe, 2003; Fig. 1a). These deposits include magnetite-dominated, sulfide-poor deposits of the Chilean Iron Belt (Cerro Negro-La Florida; Espinoza, 1990) and productive iron oxide Cu-Au deposits (e.g., Candelaria-Punta del Cobre and Mantoverde districts; Benavides et al., 2007; Fig. 1a). Continuing to the east, Paleocene-Early Oligocene (Sillitoe and Perelló, 2005) and Eocene-Oligocene metallogenic belts are present; in the region, the former holds the Relincho porphyry

copper deposit and the latter holds the Potrerillos (40–32 Ma) and the El Salvador (42–41 Ma) porphyry Cu-Mo deposits. The El Salvador (Fig. 1a) forms part of the major Cu-Mo porphyries in Chile (Cornejo et al., 1997). Farther east, the Miocene metallogenic belt, known as the Maricunga belt, is located in the Andes between 26 and 28°S. Mineralization includes porphyry-type Au and Au-Cu, epithermal Au and Ag-Au high sulfidation, and acid–sulfate-type deposits (Sillitoe et al., 1991). In addition, salt flats located in the Altiplano-Puna plateau, such as the Maricunga and Pedernales, have an estimated Li reserve of 280,000 and 240,000 tons respectively (Gajardo, 2014). The Maricunga salt flat is composed of a halite and gypsum crust where an ulexite ($NaCaB_5O_9{\cdot}8H_2O$) deposit is hosted (Risacher et al., 1999).

2.5. Anthropogenic activities and historical contamination of the El Salado River

The primary anthropogenic activities in the study area include the exploration, exploitation, and smelting of ores. The exploitation of seams and veins in the Potrerillos district, from 1894 to 1940, began the first of a series of anthropogenic developments in the region (Biblioteca Nacional de Chile, 2017; Olson, 1989). Activity continued in 1959 with the exploitation of the El Salvador porphyry copper deposit, producing an average of 81 thousand metric tons of copper per year between 1960 and 2015 (SONAMI, 2017).

In the 1930s, a tunnel was drilled to divert salty water from the Pedernales into the El Salado River (Risacher et al., 1999), transforming a naturally non-endorheic Pedernales Basin into an artificially exorheic basin (Risacher et al., 1999; Fig. 3a). Between 1938 and 1975, mining activities linked to Potrerillos and El Salvador resulted in the disposal of nearly $150{\cdot}10^6$ tons of tailings without treatment into the El Salado River flowing directly into Chañaral Bay, creating approximately 3.6 km^2 of artificial beach. This artificial feature extends nearly 5 km N-S and is 0.40 to 0.88 km wide (*E*–W) with an approximate thickness of 9 m at the center (Castilla, 1983 and references therein). In 1976, the El Salado was routed, via an artificial waterway, to Caleta Palito, a rocky beach located approximately 10 km north of Chañaral (Fig. 3b) and 10 km south of the Pan de Azúcar National Park. Between 1976 and 1990, $126{\cdot}10^6$ to $150{\cdot}10^6$ tons of solid waste were discharged forming a second artificial beach at Caleta Palito. Analyses of mine tailing waste water exhibited total Cu concentrations between 6 and 7 $mg\,L^{-1}$ (Castilla, 1983 and references therein). In March 1990, the Supreme Court of Chile ruled that discharging waste from the El Salvador Mine into the El Salado River was to be prohibited. Consequently, the mining company was required to build a tailings dam at Pampa Austral (Fig. 1a). Currently, this dam is only permitted to discharge "clean water" into the El Salado River that contains < 2 $mg\,L^{-1}$ total Cu (Castilla, 1996).

Presently, the Potrerillos facilities function as a copper smelter (Fig. 3c) and the largest mining operations are being developed simultaneously at sites in the *Cordillera de la Costa* and in the Andes. For example, in the *Cordillera de la Costa*, Mantos Copper (formerly Anglo American Norte) has produced, on average, 124 thousand metric tons of copper per year between 1990 and 2015 (SONAMI, 2017). Recent exploration activities in the Andes have permitted the discovery of Caspiche and Cerro Maricunga (COCHILCO, 2016) as well as the estimation of Li reserves in salt flats (Gajardo, 2014).

3. Analytical methods

3.1. Sampling

Superficial water and fluvial sediments were sampled within the El Salado basins (RS01 to RS16 and PO01; Fig. 2a,b,c), the Pedernales Basin (Fig. 2a,d), and the Maricunga and Laguna Verde basins (Fig. 2a,e). For more details, Fig. 2 is further separated into the respective basins sampled (b–e).

The El Salado River was sampled approximately every 5 km along its course in an *E*–W trending, downstream direction. The Pedernales

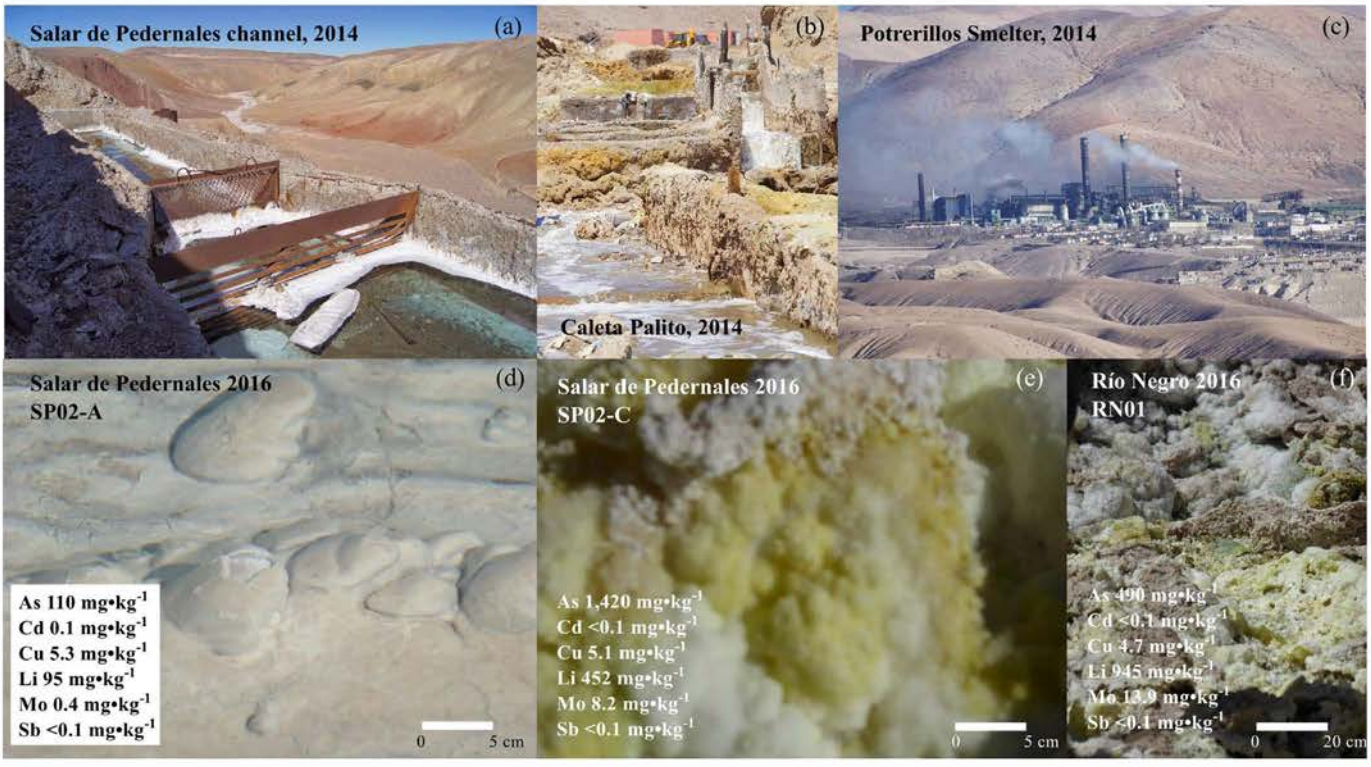

Fig. 3. Important locations and chemical deposits in the Northern Atacama Region. (a) Channel of the Pedernales salt flat in 2014; (b) Caleta Palito in 2014; (c) Potrerillos Smelter in 2014. (d) Chemical precipitate in the Pedernales salt flat, found in 2014 and 2016 and sampled in 2016; (e) Chemical precipitate in the Pedernales salt flat, found in 2016; (f) Chemical precipitate in the Río Negro hot spring, found in 2016.

Basin was sampled in the man-made outlet (SP01; Fig. 3a), the eastern lake of the Pedernales salt flat (SP02), the southwest border of the Pedernales salt flat (SP03), the La Ola Dam (LO01), the Juncal River (JL01 and JL02), and the Río Negro hot spring (RN01). Maricunga was sampled in the northern limit (MA01) and Laguna Verde was sampled along the eastern and western borders (LV01 and LV02) as well as in the hot spring (LV03).

At each site, pH was measured using a field pH-meter. All water samples were taken in the upper 5 cm of the river using a previously homogenized syringe. 100 mL were filtered through an acetate syringe filter (0.22 μm) into a previously acid-cleaned polypropylene vial. Previous tests made with water samples of this area showed that there was no significant difference in the concentration of the studied elements using 0.22 or 0.45 μm filters. In addition, work conducted by Leybourne and Cameron (2008) in the Spence Deposit, north of the sampling sites, indicated that there is no difference in the concentrations of filtered versus unfiltered trace elements in the area. Therefore the metal and metalloid species identified in this study are the dissolved (0.22 μm filter) and particulate (< 63 μm) fractions. Samples were acidified in the field (pH ~2 with suprapure HNO_3) and were stored at 4 °C until analysis.

At sites with available sediments, approximately 500 g were retrieved from the top 5 cm of 1 m^2 representative areas using acid-cleaned plastic instruments. In addition, in 2016 two precipitates were collected at Pedernales (SP01-A and SP02-C; Figs. 3d,e) and one was collected at Río Negro (RN01; Fig. 3f). Despite the fact that sediments from Potrerillos site (PO01) were sampled during all field campaigns (2014–2016), samples from 2014 and 2015 were misplaced and therefore not analyzed. After collection, these samples were stored in sealed sampling bags at 4 °C until analysis. The sampled sediments were dried in the laboratory at 50 °C. Afterwards, 2014 sediments were homogenized with an agate mortar, and 2015–2016 sediments were sieved (63 μm) for geochemical quantification.

The easternmost basins, i.e. Pedernales, Laguna Verde, and Maricunga, were not sampled during 2015 due to difficulties accessing these sites after the flooding of the El Salado River.

3.2. Water and sediment analyses

Geochemical analyses of water samples collected in 2014 were performed using a quadrupole ICP-MS at the GET Laboratory (Toulouse, France) and elemental concentrations were certified by the SLRS-5 water standard. Water samples collected during the 2015 and 2016 field campaigns were analyzed at the Helmholtz Centre for Environmental Research in Magdeburg, Germany.

For trace elements, river sediments were digested with an aqua regia solution according to the norm ISO 15587-1 (2002). Measurements of the diluted (2015 and 2016) and digested solutions were determined using an ICP-MS (Varian 8800) following the methods described in EN ISO 17294-2 (2016).

Independently measured sediment standards were incorporated in the daily procedure during each analysis for quality assurance. Independent from the certified reference material LGC6187 Batch 01, sample 0192 (river sediment – extractable metals) was used to verify that recovery rates for the analyzed elements were within the given certified range. The performed ongoing annual method validation established a minimum level of quantification in addition to the maintenance of calibration curve linearity and homoscedasticity of variance within the working range. Successful participation in a yearly inter-laboratory test, organized by r-concept, assured quality data production with the analytical methods used in this study. Element concentrations of all sediments and precipitates were quantified at the Helmholtz Centre for Environmental Research in Magdeburg, Germany.

3.3. Element selection, local geochemical background, and environmental indices

Before data treatment, all values below the detection limit (DL) were recalculated as the DL divided by 2. Samples SP02A-2016 (Fig. 3c), SP02C-2016 (Fig. 3d), and RN01-2016 (Fig. 3e) were not included in the statistical analysis of fluvial sediments as they correspond to chemical precipitates. Subsequently, the comparison of analyzed elements in the sampled fluvial water with average global concentrations of worldwide rivers (Gaillardet et al., 2003) demonstrated that As, Li, Mo, and to a lesser extent Cd, Cu and Sb are elevated. A comparison between the analyzed elements in the sediments and elemental concentrations in the upper continental crust (UCC; Rudnick and Gao, 2003) demonstrates that As, Cu, Li, Mo, and Sb are elevated with respect to the UCC. Therefore, As, Cd, Cu, Li, Mo, and Sb were selected in an effort to accomplish the objectives presented in the introduction.

Previous research from State Chilean Agencies has concluded that the concentration of certain elements in northern Chile in the dissolved form, namely As, tends to remain constant (DGA, 2014). Therefore, the goal of this study was to calculate the normal concentration of the selected elements in fluvial water and sediments of the Northern Atacama Region, including the geogenic and anthropogenic signatures, which here is referred to as the *local geochemical background*. To calculate the local geochemical background within this region for the dissolved and particulate form, two previously used methodologies were employed: percentiles (Tapia et al., 2012) and the iterative 2σ technique (Gałuszka et al., 2015; Matschullat et al., 2000). For the percentile method, values within the 0.25–0.75 percentile were considered the local geochemical background. For the iterative 2σ technique, the average and standard deviation (σ) were obtained. Afterwards all values beyond the ± 2σ level were discarded and a new average and σ were obtained; subsequently, a ± 2σ range using the reduced data was calculated. This procedure was repeated until all values lied within this range, i.e. until they approached a normal distribution (Gałuszka et al., 2015).

To infer water quality, recommendations of the World Health Organization (WHO, 2011), the United States Environmental Protection Agency (US EPA, 2009), and Chilean Guidelines (NCH 409, 2006) were employed. In the case of Li, despite the absence of a guideline, Aral and Vecchio-Sadus (2008) indicate that concentrations > 20 mg L^{-1} might entail a risk of death. To infer sediments quality, current Chilean regulations have not established guidelines for element concentrations. Due to the lack of these values, sediment concentrations were compared to the interim sediment quality guideline (ISQG) and probable effect level (PEL) of the Canadian legislation (Canadian Council of Ministers of the Environment, 2001), where there are guidelines for As, Cu and Cd. Sediment quality for Li, Mo and Sb were not studied.

To infer the degree of contamination and probable sources of As, Cd, Cu, Li, Mo, and Sb in sediments, geo-accumulation indices (Eq. 1, I_{geo}; Muller, 1979) and enrichment factors (Eq. 2, EFs; Zoller et al., 1974) were calculated using the following local background values: the average concentration of Atacama regolith from 30 cm depth (López, 2014), rocks from the La Negra (andesites to basaltic andesites; López, 2014; Oliveros et al., 2007) and Punta del Cobre (López, 2014) Formations, the Llano San Pedro volcanic sequence (López, 2014), ignimbrites (López, 2014), and the chemical precipitates obtained from the field campaign (Fig. 3d to f). All these materials (regolith, rocks and precipitates) belong to the Northern Atacama Region, rocks and regolith are specifically located in the Chañaral Basin (Fig. 1a), within a 100 km radius of the study area.

$$I_{geo} = \log_2\left(\frac{C_n}{1.5 \times B_n}\right) \quad (1)$$

In Eq. 1, C_n corresponds to the measured concentration of metal *n* in the sediment, and B_n is the local background value for the metal *n*. The

factor 1.5 is used for possible variations of the local background due to variable lithologies (Muller, 1979; Nowrouzi and Pourkhabbaz, 2014). For each sediment sample, the I_{geo} index indicates the following:

i. $I_{geo} \leq 0$, the sample is not contaminated.
ii. $0 < I_{geo} \leq 1$, the sample is non-to-slightly contaminated.
iii. $1 < I_{geo} \leq 2$, the sample is moderately contaminated.
iv. $2 < I_{geo} \leq 3$, the sample is moderately to highly contaminated.
v. $3 < I_{geo} \leq 4$, the sample is highly contaminated.
vi. $4 < I_{geo} \leq 5$, the sample is highly to extremely contaminated.
vii. $I_{geo} > 5$, the sample is extremely contaminated.

$$EF = \frac{M_{sample}/Fe_{sample}}{M_{background}/Fe_{background}} \quad (2)$$

In Eq. 2, M_{sample}/Fe_{sample} corresponds to the ratio of the concentration of the metal (of interest) to iron in the sample and $M_{background}/Fe_{background}$ is the ratio of the local background concentration of the metal to the local background concentration of iron (Zoller et al., 1974).

To infer possible sources, calculated EF values near 1 indicate that the trace metal originates from crustal contributions, is not enriched (Chen et al., 2007; Zhang and Liu, 2002), and could originate from the same rock, regolith, or precipitate with which it was calculated (Zoller et al., 1974). High values signify that the sample does not originate from that Earth material. Regarding EFs, Fe was used as the normalizing element because local background concentrations are readily provided in the literature for rocks of the Atacama Region (López, 2014; Oliveros et al., 2007).

4. Results

Results are presented for the various sampling areas as a function of surface elevation and are grouped as follows: the Andes Mountain basins (i.e. the Pedernales, Maricunga and Laguna Verde basins), the El Salado Alto Basin, and the El Salado Bajo Basin. Surface elevations are the highest in the Andes Mountains and they decrease toward the coast. The average site elevation within the studied basins of the Andes Mountains is 3832 m a.s.l. In contrast, the average surface elevations in the El Salado Alto and El Salado Bajo basins are 1583 and 191 m a.s.l., respectively.

4.1. Andes Mountains basins

4.1.1. Area-specific geology

The Andes Mountains contain the Pedernales (Fig. 2d), Maricunga and Laguna Verde (Fig. 2e) basins. This environment is mostly constituted by Eocene to Miocene continental, marine, and volcanic sedimentary sequences as well as Paleocene to Quaternary volcanic complexes, volcanic centers, and ignimbrites. Paleozoic to Cretaceous outcrops are very scarce in this area when compared to the El Salado Alto and Bajo basins, respectively, and Cenozoic outcrops are predominant (Fig. 2). The Pedernales Basin contains a mixture of sediments originating from volcanic and intrusive rocks (Risacher et al., 1999). The Maricunga Basin includes a mixture of volcanic formations, plutonic rocks, and sediments (Risacher et al., 1999).

4.1.2. Enriched elements in water and sediments

In these basins, the most enriched elements in superficial water when compared to the average concentration of worldwide rivers (from Gaillardet et al., 2003; Table 1) correspond to Li (44,135 times global average) > As (9444 times global average) > Mo (861 times global average) and to a lesser extent Sb, Cd and Cu (24, 21 and 2 times global average, respectively).

In fluvial sediments, the most enriched elements when compared to the upper continental crust (from Rudnick and Gao, 2003; Table 2) correspond to As (35 times global average) > Mo (33 times global average) > Cd (14 times global average) and to a lesser extent Li and Cu (7 and 6 times the global average respectively); Sb is not enriched.

4.1.3. Elements and regulations

In the Andes Mountains, 100% of the samples present surficial water values above the recommendations of the WHO, US EPA, and Chilean Guidelines for As; 73% of the values are above the WHO recommendation for Mo and 40% of the samples exhibit concentrations over the literature recommendation for Li (Fig. 4). On the contrary, only 13% of the samples have higher values than the WHO and EPA recommendations and no samples are above the NCH 409 for Cd. Only 6% of the samples are above the WHO and US EPA recommendations for Sb and all values of Cu are well below national and international recommendations for water (Fig. 4).

In the case of sediments, all As values are above the ISQG, while 88% of the samples are above the PEL; for Cd, 47% of the samples are above the ISQG and 6% above the PEL, and for Cu, 47% of the values are above the ISQG and 29% are above the PEL (Fig. 5).

4.1.4. Local geochemical background for water and sediments, contaminant elements, and probable sources

In the Andes, using the 0.75 percentile (Tapia et al., 2012) and iterative 2σ techniques (Gałuszka et al., 2015; Matschullat et al., 2000), in surface water the highest local geochemical background was observed for As, and depending on the statistical method used, Li and Mo (Table 3a). In sediments, the maximum values of local geochemical background using the 0.75 percentile and iterative 2σ methods are found in the Andes Mountains basins for As, Cd, and Li (Table 3b).

In relation to probable contaminant elements in the Andes Mountains basins, I_{geo} index indicate that Cu corresponds to a contaminant of this environment, especially during 2016 (Fig. 6); As, Cd, Li, and Sb are not considered contaminants in this area. Regarding Mo, in 2014 it was not considered a contaminant; however, in 2016 it became one. In general, the level of contamination tended to increase from 2014 to 2016 (Fig. 6).

In relation to the sources of the studied elements, except for Cu, EFs indicate that these elements might have originated from local precipitates obtained from remote areas of the Andes; the Atacama regolith might also be a source of Cd and Sb. Other Atacama rocks from the Chañaral Basin do not indicate that they could be the source of these elements (Fig. 7).

4.2. El Salado Alto basin

4.2.1. Area-specific geology

Geology at the location of El Salado Alto Basin is constituted by Jurassic marine and continental sedimentary sequences, Jurassic, Cretaceous and Paleocene-Eocene volcanic centers, domes and ignimbrites, and Miocene marine and continental sedimentary sequences. Mesozoic and Cenozoic rocks are predominant (Fig. 2c).

4.2.2. Enriched elements in water and sediments

In this basin, the most enriched elements in surficial water when compared to worldwide rivers (from Gaillardet et al., 2003; Table 1) are Li (78,662 times global average) > As (2787 times global average) > Mo (680 times global average) > Sb (72 times global average) and to a lesser extent Cd and Cu (17 and 14 times global average, respectively).

Sediments compared to the average respective concentrations of the UCC (from Rudnick and Gao, 2003; Table 2) indicate that in the El Salado Alto Basin they are enriched as follows (in decreasing order): Cu (50 times global average) > As (23 times global average) > Mo (19 times global average) and to a lesser extent Sb, Li, and Cd (7, 4.5, and 3.6 times the global averages, respectively). The Potrerillos sample collected in 2016 shows the highest concentrations of As, Cd, Cu, Mo,

Table 1
Basic statistics for water concentration values in all samples collected in the Andes Mountains and El Salado Alto and El Salado Bajo basins for As, Cd, Cu, Li, Mo and Sb. Also shown: the average concentration for these elements worldwide (Gaillardet et al., 2003) and the concentration for drinkable water recommended by the World Health Organization (WHO, 2011), the US Environmental Protection Agency (US EPA, 2009), Chilean regulations (NCH 409, 2006), and Aral and Vecchio-Sadus (2008).

All samples of Northern Atacama Region						Andes mountains						El Salado Alto						El Salado Bajo					
As	Cd	Cu	Li	Mo	Sb	As	Cd	Cu	Li	Mo	Sb	As	Cd	Cu	Li	Mo	Sb	As	Cd	Cu	Li	Mo	Sb
$\mu g \cdot L^{-1}$	$\mu g \cdot L^{-1}$	$\mu g \cdot L^{-1}$	$mg \cdot L^{-1}$	$\mu g \cdot L^{-1}$	$\mu g \cdot L^{-1}$	$\mu g \cdot L^{-1}$	$\mu g \cdot L^{-1}$	$\mu g \cdot L^{-1}$	$mg \cdot L^{-1}$	$\mu g \cdot L^{-1}$	$\mu g \cdot L^{-1}$	$\mu g \cdot L^{-1}$	$\mu g \cdot L^{-1}$	$\mu g \cdot L^{-1}$	$mg \cdot L^{-1}$	$\mu g \cdot L^{-1}$	$\mu g \cdot L^{-1}$	$\mu g \cdot L^{-1}$	$\mu g \cdot L^{-1}$	$\mu g \cdot L^{-1}$	$mg \cdot L^{-1}$	$\mu g \cdot L^{-1}$	$\mu g \cdot L^{-1}$
N																							
65	65	65	22	65	65	16	16	16	5	16	16	28	28	28	10	28	28	21	21	21	7	21	21
Average																							
2039	1.24	9.62	87	248	2.79	5502	1.48	0.93	81	397	2.00	1513	1.31	12.64	145	283	4.67	103	0.96	12.22	10	86	0.88
Standard deviation (σ)																							
4461	1.36	14.55	92	335	9.27	8001	2.47	1.15	110	594	6.05	1126	0.83	18.60	78	180	13.24	158	0.55	11.39	1.7	56	1.32
Median																							
618	1.04	2.35	12	161	0.35	900	0.59	0.25	2.9	230	0.43	1040	1.42	2.01	163	229	0.51	19	1.06	6.58	9	92	0.25
Maximum																							
24,751	8.49	60.97	228	2404	65	24,751	8.49	3.98	225	2404	24.65	4035	3.11	60.97	228	571	64.75	495	1.76	42.18	13	214	5.65
Minimum																							
2	0.10	0.25	1.5	0.25	0.07	79	0.10	0.25	1.5	0.25	0.25	75	0.10	0.25	5.1	10	0.20	2	0.15	0.25	8.6	18	0.07
Correlation coefficient element-elevation																							
0.41	0.09	−0.30	0.16	0.34	0.12	−0.24	−0.44	−0.25	−0.95	0.13	0.18	0.13	0.08	−0.02	−0.20	−0.12	0.29	−0.13	−0.07	−0.59	0.94	−0.06	0.03
World average																							
0.62	0.08	1.48	0.002	0.42	0.07																		
WHO recommendations																							
10	3	2000	–	70	20																		
US EPA guideline																							
10	5	1300	–	–	6																		
Chilean regulation																							
10	10	2000	–	–	–																		
Aral and Vecchio-Sadus (2008)																							
–	–	–	20	–	–																		

Table 2
Basic statistics for fluvial sediment compositions, namely of As, Cd, Cu, Li, Mo and Sb in all samples collected in the Andes Mountains, the El Salado Alto Basin, and the El Salado Bajo Basin. The average composition of the UCC (Rudnick and Gao, 2003), the Canadian interim sediment quality guideline of Canada (ISQG), and the Canadian probable effects level (PEL; Canadian Council of Ministers of the Environment, 2001).

All samples of Northern Atacama Region						Andes mountains						El Salado Alto						El Salado Bajo					
As	Cd	Cu	Li	Mo	Sb	As	Cd	Cu	Li	Mo	Sb	As	Cd	Cu	Li	Mo	Sb	As	Cd	Cu	Li	Mo	Sb
$\mu g \cdot g^{-1}$	$\mu g \cdot g^{-1}$	$\mu g \cdot g^{-1}$	$\mu g \cdot g^{-1}$	$\mu g \cdot g^{-1}$	$\mu g \cdot g^{-1}$	$\mu g \cdot g^{-1}$	$\mu g \cdot g^{-1}$	$\mu g \cdot g^{-1}$	$\mu g \cdot g^{-1}$	$\mu g \cdot g^{-1}$	$\mu g \cdot g^{-1}$	$\mu g \cdot g^{-1}$	$\mu g \cdot g^{-1}$	$\mu g \cdot g^{-1}$	$\mu g \cdot g^{-1}$	$\mu g \cdot g^{-1}$	$\mu g \cdot g^{-1}$	$\mu g \cdot g^{-1}$	$\mu g \cdot g^{-1}$	$\mu g \cdot g^{-1}$	$\mu g \cdot g^{-1}$	$\mu g \cdot g^{-1}$	$\mu g \cdot g^{-1}$
N																							
42	42	42	42	42	42	14	14	14	14	14	14	20	20	20	20	20	20	8	8.0	8	8	8	8
Average																							
121	0.6	932	127	29	2.0	170	1.3	178	155	37	0.2	109	0.3	1387	94	21	3.0	66.1	0.3	1114	163	37	2.8
Standard deviation (σ)																							
117	1.2	2396	148	67	5.5	151	2.0	207	207	97	0.2	103	0.3	3256	46	46	7.3	24.5	0.0	1734	195	52	4.9
Median																							
74	0.3	233	78	4.4	0.5	162	0.9	95	69	1.9	0.1	73	0.3	182	90	4.4	0.5	60.2	0.3	393	78.3	8.5	0.8
Maximum																							
571	7.7	14,600	799	345	33	571	7.7	643	799	345	1	463	1.5	14,600	202	210	33	117.0	0.3	5340	630	155	15
Minimum																							
8	0.1	7	19	0.2	0.1	8	0.1	7	19	0.2	0.1	18	0.1	17	29	0.9	0.1	38.1	0.2	235	58.3	5.2	0.6
Correlation coefficient element-elevation																							
0.37	0.27	− 0.14	− 0.01	− 0.002	− 0.15	− 0.03	− 0.58	− 0.41	− 0.47	− 0.49	− 0.04	0.41	0.30	0.18	0.08	0.21	0.20	− 0.80	− 0.33	− 0.47	− 0.41	− 0.48	− 0.52
UCC																							
4.8	0.09	28	21	1.1	0.4																		
ISQG																							
5.9	0.6	35.7	–	–	–																		
PEL																							
17	3.5	197	–	–	–																		

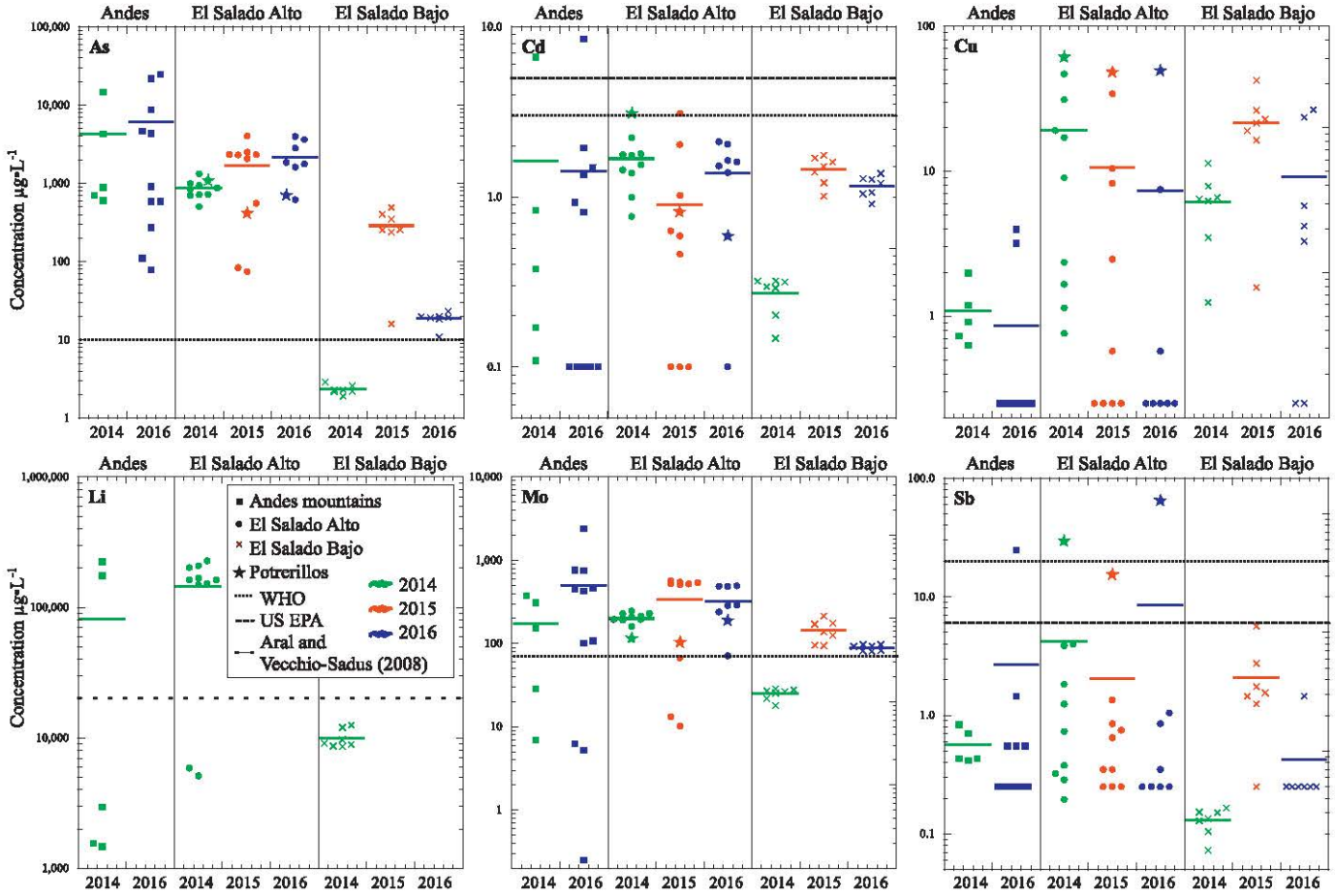

Fig. 4. Element concentrations as a function of the sample year in surface water from the Andes Mountains and El Salado Alto and El Salado Bajo basins. Continuous lines represent the average element concentration of surface water in each area and dashed lines represent concentrations suggested as drinkable by the US EPA (As, Sb; US EPA, 2009), WHO (As, Cd, Mo; WHO, 2011), Chilean regulation (As; NCH 409, 2006), and Aral and Vecchio-Sadus (2008; Li).

and Sb in collected sediments of El Salado Alto Basin (Fig. 8).

4.2.3. Elements and regulations

In El Salado Alto Basin, dissolved As concentrations are above the WHO, US EPA, and NCH 409 in all samples. For Mo, 89% of the samples are above the WHO recommendation and 80% of the samples are above the Aral and Vecchio-Sadus (2008) recommendation for Li (Fig. 4). In the case of Cd, only 7% of the samples are above the WHO recommendation and no samples are above the US EPA and Chilean regulations. For Sb, 7% and 11% are above the WHO and US EPA regulations, respectively, and Cu is below all normatives (Fig. 4).

In sediments, 100% of the samples are above the PEL for As. In the case of Cd, just 5% are above the ISQG and none above the PEL. For Cu, 95% of the samples are above the ISQG and 45% are above the PEL (Fig. 5).

4.2.4. Local geochemical background for water and sediments, contaminant elements, and probable sources

The highest local geochemical background for dissolved Cd is found in El Salado Alto, and depending on the employed statistical method, Li and Mo as well (Table 3a). In sediments, the highest local geochemical background is not present in this basin for any of the studied elements (Table 3b).

Regarding the probable contaminants of El Salado Alto Basin, the I_{geo} index indicates that Cu and Mo might be contaminants (Fig. 6).

In relation to probable sources, local precipitates can explain the presence of As and Li; the Punta del Cobre Formation could explain the concentration of As, and the Atacama regolith might explain the values of Cd and Sb (Fig. 7). None of the local background precipitates, rocks, and regolith used to calculate EFs can explain the elevated I_{geo} index for Cu and Mo. This enhances the idea that these elements correspond to contaminants of the El Salado Alto Basin (Fig. 7).

4.3. El Salado Bajo basin

4.3.1. Area-specific geology

El Salado Bajo Basin is constituted mostly of Jurassic sedimentary and volcanic sequences, Cretaceous, Jurassic and Paleozoic intrusive rocks, and metamorphic Paleozoic outcrops. Younger outcrops are scarce, and are comprised of Miocene sedimentary sequences and Quaternary alluvial and eolian deposits (Fig. 2b).

4.3.2. Enriched elements in water and sediments

In fluvial water, the most enriched elements in comparison to rivers worldwide (from Gaillardet et al., 2003; Table 1) are Li (5398 times global average) > Mo (206 times global average) > As (167 times global average) and to a lesser extent Sb, Cd, and Cu (14, 13, and 9 times global average, respectively).

Sediments compared to the average respective concentrations of the UCC (from Rudnick and Gao, 2003; Table 2) indicate that in the El Salado Bajo, elements are enriched as follows (in decreasing order): Cu (40 times global average) > Mo (33 times global average) > As (14 times global average) and to a lesser extent Li, Sb and Cd (8, 7 and 3 times global average, respectively).

As shown, enrichments of fluvial water and sediments are in general lower in this basin compared to the Andes Mountains and El Salado Alto

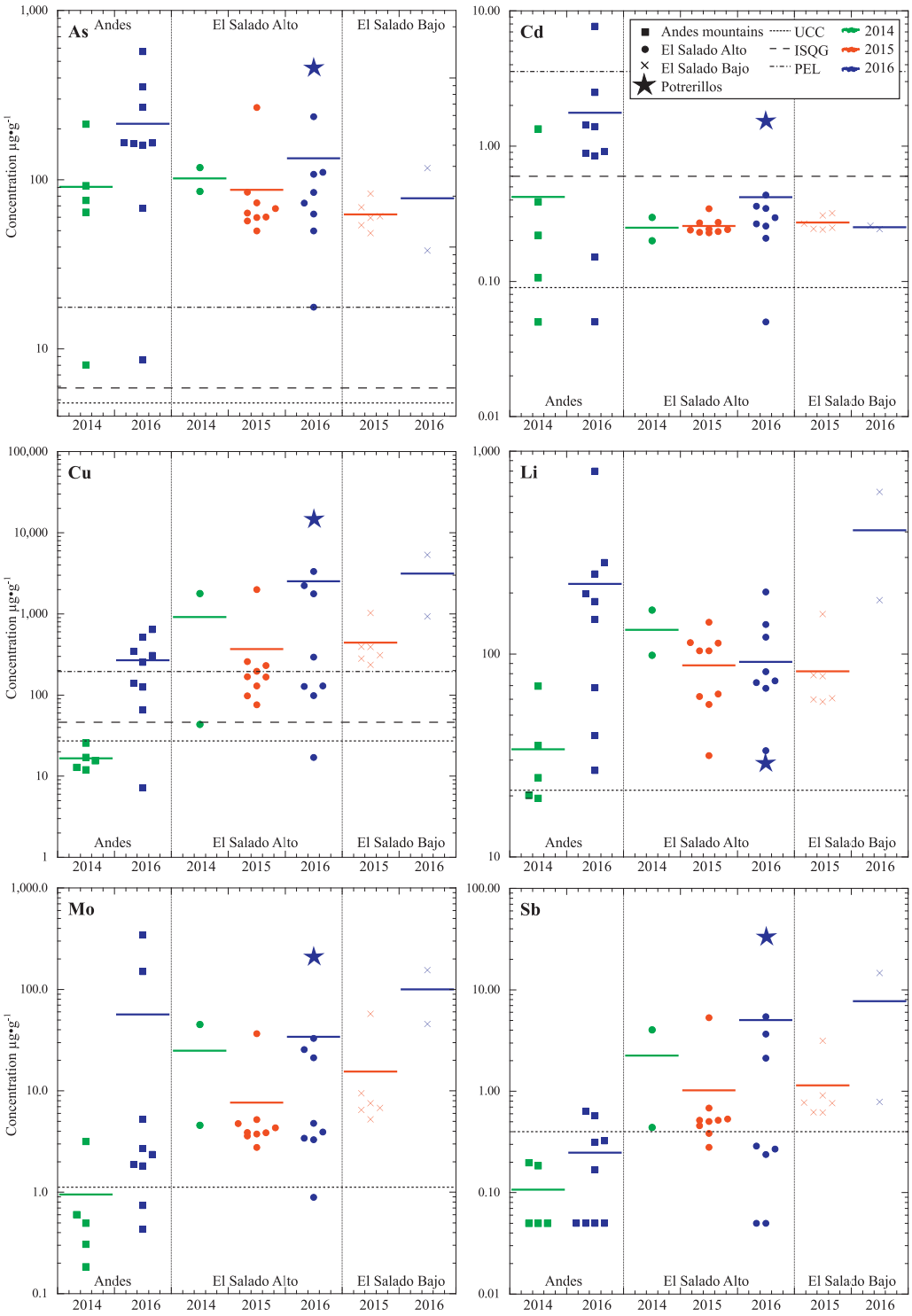

Fig. 5. Element concentrations as a function of the sample year in fluvial sediments of the Andes Mountains and El Salado Alto and El Salado Bajo basins. Continuous lines represent the average concentrations of sediments within each basin. UCC: Upper continental crust (Rudnick and Gao, 2003); ISQG: Canadian interim sediment quality guideline from Canada; PEL: Canadian probable effects level (Canadian Council of Ministers of the Environment, 2001).

basins.

4.3.3. Elements and regulations

For As and Mo, 63% of water samples present concentrations above the WHO, US EPA, or Chilean regulations. All samples with values below recommendations were taken during 2014, before the Atacama storm event and landslide. In addition, all samples values are below the national and international recommendations for Cd, Cu, Li, and Sb (Fig. 4).

In the case of sediments, for As and Cu, all samples show values above the ISQG and PEL. For Cd, all are below the ISQG and PEL (Fig. 5).

4.3.4. Local geochemical background for water and sediments, contaminant elements, and probable sources

The highest local geochemical background for dissolved Cu was obtained in this basin in addition to Sb when using the 0.75 percentile (Table 3a). In sediments, the highest local geochemical background was obtained in El Salado Bajo Basin for Cu, Mo, and Sb (Table 3b).

In relation to probable contaminants, I_{geo} index indicates that Cu, Mo, and Sb might be considered contaminants in this basin in contrast to As, Cd, and Li (Fig. 6).

Table 3
Local geochemical background of mining sites worldwide. (a) Dissolved water in Oruro; (b) Lake sediments in Oruro, fluvial sediments in Chalkidiki and the Northern Atacama Region basins, and soil in the Miedzianka Mountains. P 0.75: percentile 0.75; 2σ: maximum value of iterative 2σ technique (Gałuszka et al., 2015). Oruro (Tapia et al., 2012; Tapia and Audry, 2013; Li and Mo concentrations in pore water and sediments are unpublished data); Miedzianka Mountains (Gałuszka et al., 2015); Chalkidiki (Kelepertzis et al., 2010).

(a)

		Oruro, Bolivia		All samples of Northern Atacama Region		Andes mountains		El Salado Alto		El Salado Bajo	
		P 0.75	2σ	P 0.75	2σ	P 0.75	2σ	P 0.75	2σ	P 0.75	2σ
As	$\mu g \cdot L^{-1}$	740	902	1857	1032	5659	5073	2316	2832	238	28
Cd	$\mu g \cdot L^{-1}$	0.03	0.04	1.60	2.28	1.38	1.53	1.78	2.55	1.37	2.05
Cu	$\mu g \cdot L^{-1}$	0.74	0.86	11.35	0.61	0.98	0.25	18	0.57	21	29
Li	$mg \cdot L^{-1}$	0.04	0.06	167	272	175	301	194	300	11	13
Mo	$\mu g \cdot L^{-1}$	21	31	307	259	459	795	489	643	97	178
Sb	$\mu g \cdot L^{-1}$	10	12	1.24	0.36	0.59	0.71	1.27	0.86	1.45	0.32

(b)

		Oruro, Bolivia		Miedzianka Mt., Poland		Chalkidiki, Greece		All samples of Northern Atacama Region		Andes mountains		El Salado Alto		El Salado Bajo	
		P 0.75	2σ	P 0.75	2σ	P 0.75	2σ	P 0.75	2σ	P 0.75	2σ	P 0.75	2σ	P 0.75	2σ
As	$\mu g \cdot g^{-1}$	56	62	278	36	214	1138	161	89	201	240	92	118	67	88
Cd	$\mu g \cdot g^{-1}$	0.45	0.48	2.14	2.01	2.60	1.66	0.37	0.30	1.38	1.70	0.28	0.36	0.30	0.33
Cu	$\mu g \cdot g^{-1}$	53	61	1337	52	82	91	319	400	295	350	266	304	394	1167
Li	$\mu g \cdot g^{-1}$	75	82	–	–	–	–	145	125	194	286	126	166	79	201
Mo	$\mu g \cdot g^{-1}$	1.4	1.6	–	–	–	–	6.57	6.94	3.05	3.38	4.89	5.39	8.99	63.7
Sb	$\mu g \cdot g^{-1}$	12	13	–	–	32	12	0.63	0.84	0.29	0.33	0.57	0.74	0.88	0.97

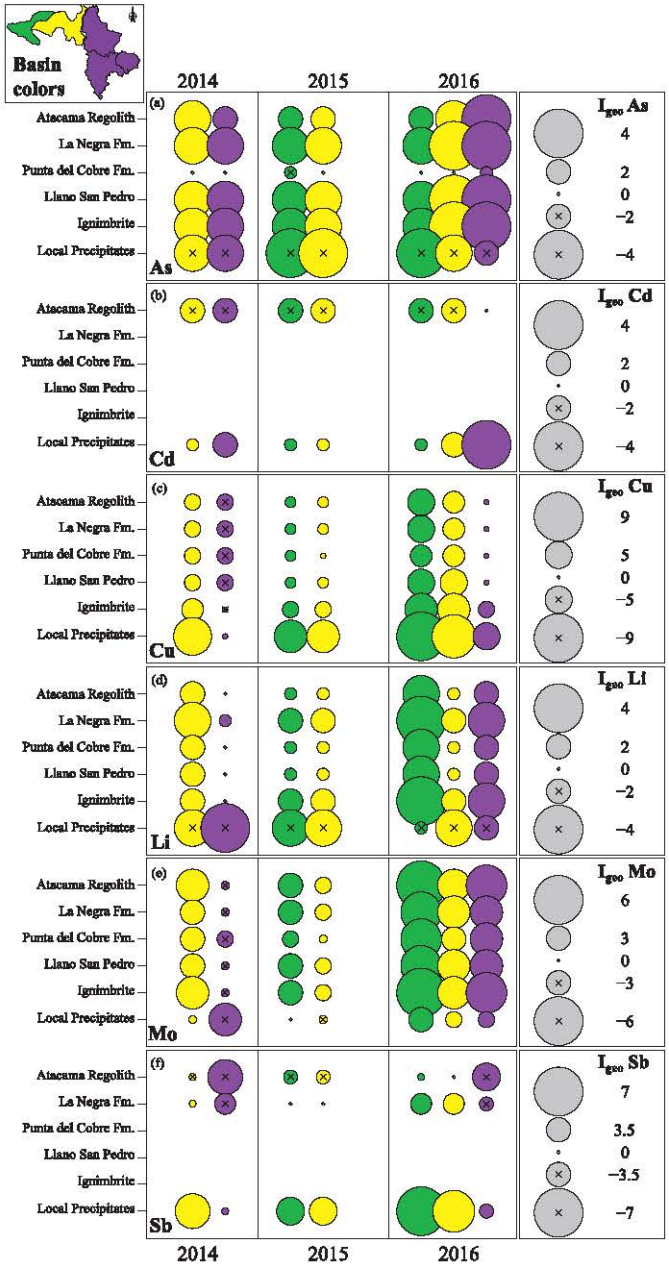

Fig. 6. Geo-accumulation index (I_{geo}) for selected elements. The materials used to calculate this index are: andesites to basaltic andesites of La Negra Formation (López, 2014; Oliveros et al., 2007), andesitic lavas of Punta del Cobre Formation (López, 2014), dacites of the Llano San Pedro volcanic complex (López, 2014), ignimbrites of dacitic composition (López, 2014), Atacama regolith from 30 cm depth (López, 2014), and chemical precipitates collected during this study from remote areas of the Andes.

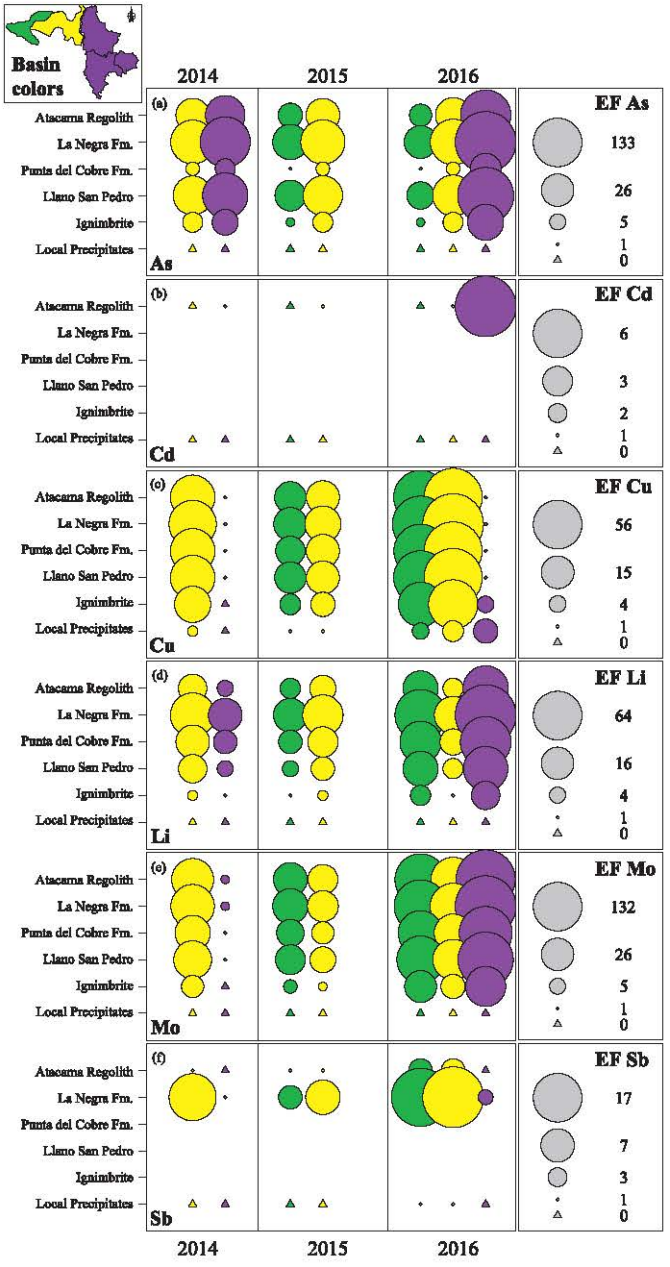

Fig. 7. Enrichment Factors (EFs) for selected elements. The materials used to calculate this index are: andesites to basaltic andesites of La Negra Formation (López, 2014; Oliveros et al., 2007), andesitic lavas of Punta del Cobre Formation (López, 2014), dacites of the Llano San Pedro volcanic complex (López, 2014), ignimbrites of dacitic composition (López, 2014), Atacama regolith from 30 cm depth (López, 2014), and chemical precipitates collected during this study from remote areas of the Andes.

In relation to probable sources, except for Cu, precipitates from the Andes could explain the high concentrations of the studied elements. However, the large distance between the basin and precipitates indicates that this material is not likely the source for elements in the El Salado Bajo Basin. Other rocks such as those found in the Punta del Cobre Formation, the Atacama regolith, and Ignimbrites could instead be the sources of As, Cd, Li and Sb (Fig. 7).

5. Discussion

Based on the conducted analyses, results obtained, and expected concentrations of each sample area, relevant observations, comparisons, and interpretations (such as possible sources) regarding the studied elements are summarized below in relation to the geology, anthropogenic activities, and geochemical anomalies (Section 5.1). A profile displaying the spatial variation of the average concentration of each of the studied elements at the sampling sites, between 2014 and 2016, is provided in Fig. 8 and the exact transect locations are shown in Fig. 2. Natural impacts on the redistribution of the studied elements is discussed in Section 5.2 and the temporal variation of concentration values at the sampling sites is highlighted as a function of the large-scale 2015 storm and flood event. Subsequently, applications to other similar environments are discussed in Section 5.3.

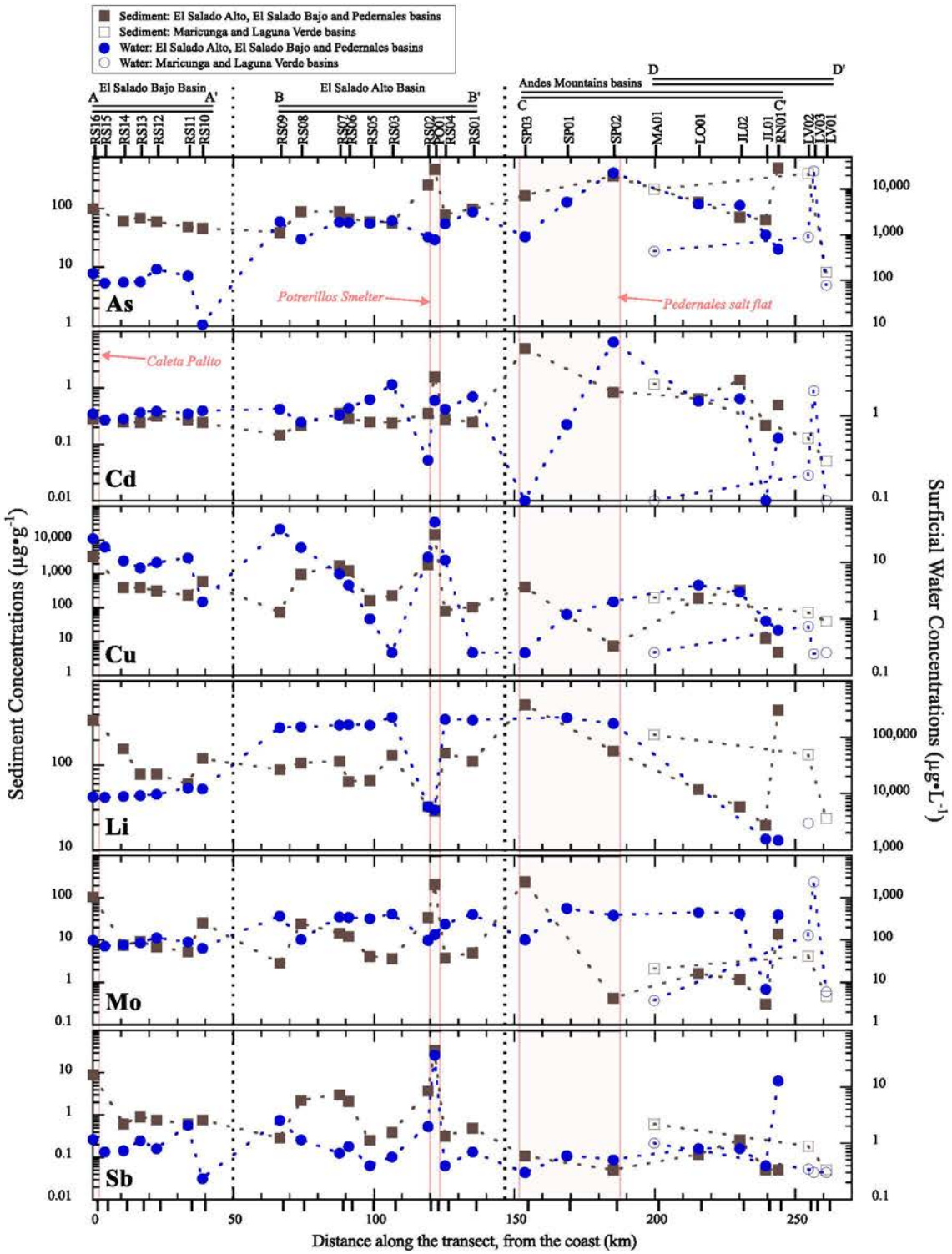

Fig. 8. Spatial distribution of average concentrations (2014 to 2016). Transect locations are provided in plan view in Fig. 2. For the Maricunga and Laguna Verde basins, due to their similar longitude and distinct latitude in relation to the Pedernales Basin, their symbols differ.

5.1. Geology, anthropogenic activities, and geochemical anomalies

5.1.1. Arsenic

The highest local geochemical background concentration for As in fluvial water and sediments is located in the Andes Mountains (Table 3) where the dominant geology corresponds to Cenozoic volcanic deposits and sedimentary sequences (Fig. 2d,e). Despite the fact that the As concentration is generally above the consulted regulations and recommendations for water and sediments (Figs. 4 and 5), in the studied basins, As is not considered a contaminant (Fig. 6a).

Increased natural concentrations of dissolved As in the Andes Mountains are a consequence of the presence of As-rich hot springs at Río Negro, Juncalito, and Laguna Verde (Aguirre and Clavero, 2000; Risacher et al., 1999; Tapia and Verdejo, 2015). Similar enrichments have also been observed at the El Tatio geysers, 500 km north of the study area. There, elevated concentrations provide an additional source

of dissolved As to the El Loa River (Romero et al., 2003).

High As local geochemical background concentrations are comparable to other mining sites worldwide (Oruro, Bolivia; Tapia et al., 2012; Tapia and Audry, 2013; Miedzianka, Poland; Gałuszka et al., 2015; Chalkidiki, Greece; Kelepertzis et al., 2010; Table 3b). However, in the case of the Northern Atacama Region, this local geochemical background is likely associated with natural sources of As present in large-scale evaporite belts of the Neogene Central Andes, which contain anomalous concentration of Li, As, Sr, and K (Alonso et al., 1991). Also, As is found in the Maricunga Metallogenic belt. This belt is rich in high-sulfidation gold deposits (Sillitoe et al., 1991) that are associated with elevated As concentrations (White and Hedenquist, 1995). In addition, and as determined in this study, precipitates from remote areas of the Andes and geologic formations similar to Punta del Cobre, a Jurassic to Cretaceous outcrop rich in andesites that bears the mineralization of the Inca de Oro District (Fig. 1a; Soto, 2010), are important sources of As for the Andes and El Salado Alto basins, respectively (Fig. 7a). It is also apparent from Fig. 8 that the concentration of As increases near the Potrerillos Smelter, attributable to the mining activities present there.

5.1.2. Cadmium

The highest local geochemical background of Cd concentration in fluvial water and sediments is found in the El Salado Alto and the Andes Mountains basins, respectively (Table 3). Despite the fact that this element is enriched when compared to fluvial water and sediment average global concentrations, in general it is not above water (Fig. 4) and sediment (Fig. 5) recommended values and is not considered a contaminant in any of the studied basins (Fig. 6b).

In relation to the origin of this element, in the Andes area, precipitates could be a source of Cd (Fig. 7b). In the El Salado Alto and Bajo basins, the Atacama Regolith might be an important source of Cd (Fig. 7b). It is also clear from Fig. 8 that the concentration of dissolved Cd is high in the eastern border of the Pedernales salt flat, and in sediments and water increases abruptly near the Potrerillos Smelter, attributable to the mining activities present there.

5.1.3. Copper

The highest local geochemical background concentration for Cu in fluvial water and sediments is found in El Salado Bajo Basin (Table 3). Copper concentrations are below national and international regulations for water (Fig. 4), yet Cu is importantly concentrated in sediments and is above the Canadian recommended values (Fig. 5). This element was classified as a contaminant in all the studied basins (Fig. 6c).

El Salado River is located in a well-known Cu-rich metallogenic province (Sillitoe, 2012; Sillitoe and Perelló, 2005) composed of Jurassic-Lower Cretaceous, Paleocene-Lower Eocene, and Upper Eocene-Lower Oligocene metallogenic belts (Fig. 1a). The Upper Eocene-Lower Oligocene and the Jurassic-Lower Cretaceous belts are recognized worldwide for the presence of large-scale porphyry Cu deposits (Sillitoe and Perelló, 2005) and IOCG deposits (Sillitoe, 2003), respectively.

Due to the Cu richness in this area, historically, the El Salado River has been significantly affected by mining activities, especially through the disposal of mining waste directly into the river over an approximate time period of 40 years (Castilla, 1983). This anthropogenic influence is evidenced by the fact that the highest elemental concentrations of Cu in fluvial water were found at the Potrerillos site during the three-year long sampling (Figs. 4 and 8). Additionally, sediments close to the Potrerillos Smelter and in the discharge area at Caleta Palito have the highest values of Cu (Fig. 8), supporting the idea that mining activities are an important source of anthropogenic Cu in the Northern Atacama Region.

Therefore it is likely that the natural presence of Cu-rich metallogenic belts, in addition to uncontrolled mining activities, have a direct relation to Cu contamination in the studied sediments.

5.1.4. Lithium

The highest local geochemical background concentration for Li in fluvial water is found in the Andes Mountains and El Salado Alto basins; for sediments, it is found in the Andes (Table 3). This element is above the recommended concentration for water as suggested by Aral and Vecchio-Sadus, 2008; (Fig. 4), and despite the fact that there are no regulations in Chile or Canada for its concentration in sediments, in this study it was found that Li is not considered a contaminant in any of the studied basins (Fig. 6d).

Dissolved Li concentrations are observed to be at their highest values in the Pedernales and El Salado Alto basins (Fig. 8). Brines from salt flats, in the Altiplano-Puna region, are known for their Li resources (Chong, 1988; Ericksen and Salas, 1990; Gajardo, 2014). In addition, Neogene Puna evaporites have anomalous concentrations of Li because of their closed drainages and position adjacent to the volcanic arc; thus, this basin can capture all the product of thermal activity there (Alonso et al., 1991). As suggested in this study, precipitates from remote areas of the Andes are also enriched in this element (Fig. 7d).

Therefore, the enrichment of Li in the Northern Atacama Region might be explained by natural sources of the Altiplano-Puna in addition to the transport of Li in fluvial water due to anthropogenic channelization of the Pedernales salt flat in the 1930s (Fig. 3a).

5.1.5. Molybdenum

Results from this study indicate that Mo presents the highest local geochemical background concentration for water in the Andes and El Salado Alto basins (Table 3a), and for sediments, the highest local geochemical background is present in the El Salado Bajo Basin (Table 3b). In water, for > 60% of the collected samples, the concentration of Mo is above the WHO recommendation (Fig. 4). Additionally, Mo is considered a contaminant in sediments of El Salado Alto and El Salado Bajo basins (Fig. 6e).

Natural high concentration of dissolved Mo has been found in groundwater from the Spence porphyry Cu deposit (Leybourne and Cameron, 2008), and as determined in this study, the highest local geochemical background for Mo in fluvial water is in the Andes and El Salado Alto basins (Fig. 8). Thus, natural Mo-rich brines and porphyry copper deposits related groundwater could be the source for Mo in water.

In the case of sediments, the highest local geochemical background of Mo is in El Salado Bajo Basin. The precipitates from remote areas of the Andes do not explain the high concentration of this element as do other rocks of the Chañaral Basin (Fig. 7e). Due to the fact that Mo is strongly correlated to Cu (Table 4), it is assumed that it originates from the processing of porphyry Cu-Mo deposits, suggesting an anthropogenic source for Mo in sediments. Therefore, Mo shows a geogenic origin in fluvial water and an anthropogenic origin in sediments.

5.1.6. Antimony

The highest local geochemical background concentration for Sb is present in El Salado Bajo Basin for fluvial water and sediments (Table 3). This element presents < 11% of water samples above the US EPA and WHO recommendations and any of these sample locations are in El Salado Bajo Basin (Fig. 4). In the case of sediments, there are no guidelines for Sb, however in this study it was shown that Sb is considered a contaminant in the El Saldo Bajo Basin (Fig. 6f).

In a similar manner to Cu, this element shows the highest values for fluvial water and sediments in the Potrerillos site (Figs. 4, 5, and 8). This is strongly correlated to Cu and Mo (Table 4), suggesting that mining activities could be the most important source for Sb in fluvial water and sediments of the El Salado River.

5.2. Natural element redistribution

Based on Table 4, all studied elements present strong positive correlations in the El Salado Alto and El Salado Bajo basins, except for Li in

Table 4
Correlation coefficients between elements of surface water (a) and fluvial sediments (b).

(a) Water

	All samples of Northern Atacama Region					Andes					El Salado Alto					El Salado Bajo				
	As	Cd	Cu	Li	Mo	As	Cd	Cu	Li	Mo	As	Cd	Cu	Li	Mo	As	Cd	Cu	Li	Mo
Cd	0.67					0.76					0.35					0.69				
Cu	− 0.19	0.04				0.01	0.14				− 0.35	0.04				0.70	0.54			
Li	0.34	0.48	− 0.07			0.69	0.56	0.74			− 0.89	− 0.21	− 0.67			− 0.68	− 0.90	− 0.84		
Mo	0.74	0.26	− 0.16	0.88		0.73	0.19	− 0.04	0.94		0.87	0.29	− 0.35	0.94		0.87	0.94	0.61	− 0.90	
Sb	− 0.08	0.01	0.55	− 0.18	0.01	− 0.19	− 0.06	− 0.15	− 0.10	0.15	− 0.21	0.00	0.67	− 0.72	− 0.22	0.76	0.64	0.55	− 0.85	0.71

(b) Sediments

	All samples of Northern Atacama Region					Andes					El Salado Alto					El Salado Bajo				
	As	Cd	Cu	Li	Mo	As	Cd	Cu	Li	Mo	As	Cd	Cu	Li	Mo	As	Cd	Cu	Li	Mo
As	0.18					− 0.03					0.87					0.18				
Cd	0.44	0.09				− 0.06	0.62				0.88	0.97				0.85	− 0.07			
Cu	0.14	0.30	0.05			0.27	0.37	0.28			− 0.51	− 0.37	− 0.43			0.75	− 0.20	0.97		
Li	0.29	0.81	0.52	0.46		0.00	0.95	0.52	0.49		0.91	0.96	0.99	− 0.43		0.82	0.00	0.97	0.91	
Mo	0.44	0.06	0.99	0.08	0.51	0.27	− 0.08	0.19	0.21	− 0.21	0.88	0.97	0.99	− 0.42	0.99	0.90	− 0.01	0.99	0.94	0.96

the El Salado Alto Basin and Cd in the El Salado Bajo Basin. These correlations suggest that besides mining there are likely other controls on the redistribution of elements.

5.2.1. *Redistribution in the Andes Mountains*

From the collected data, there was a systematic increase in the average concentration of dissolved Cu, Sb, and Mo. Concentrations of As and Cd remained constant. In fluvial sediments, the average concentration of all analyzed elements increased in 2016. Comparing specific sites (RN01 and SP02), there is a clear increase of Mo and Sb in the dissolved fraction however this is not observed for Cu. With respect to fluvial sediments, specific sites (LV01, LV02, JL02, LO01) showed a marked increase in Cu and Mo concentrations (contaminants of the El Salado Alto Basins), followed by Li and As, and to a lesser extent Cd and Sb. In 2016, saline precipitate samples from Pedernales (SP02-C; 3361 m a.s.l.) and Río Negro (RN01; 4118 m a.s.l.) showed a yellow coloration that was not present in 2014. These samples have the highest concentrations of As and Li in all the surveyed basins (Fig. 3e and f).

With the initiation of the March 2015 mudflow, recent research indicates that snow covered a wide area above 3600 m a.s.l. (Jordan et al., 2015; Fig. 1c), which is in agreement with information from local border agents in the field (personal communication, 2015). Studies performed in Scotland have demonstrated that there is an increase in concentration of dissolved Al, Cd, Cu, Fe, Mn, and Pb after snow melt (Abrahams et al., 1989). Previous research in the Arctic has additionally shown that polar environments are especially sensitive to these types of changes, of which, some would have direct effects on the role of snow in contaminant scavenging (Macdonald et al., 2005). The Desert Andes are characterized by permanent snow patches and small glaciers (Lliboutry, 1988). Therefore it is suggested that snow cover, above 3600 m a.s.l., and subsequent melting could have played an important role in the transport of elements from the west (the Cu-Mo rich metallogenic belt). This transport would have acted as a catalyst increasing the concentrations of Cu, Mo, and Sb in the dissolved fraction and Cu, Mo and (to a lesser extent) Li, As, Cd and Sb in fluvial sediments. Transport could have also produced enrichment of As and Li in saline crusts within the Andes Mountains of the Northern Atacama Region.

5.2.2. *Redistribution in the El Salado Alto basin*

From 2014 to 2015, the El Salado Alto Basin experienced a dilution in Cd, Cu, and Sb concentrations; this effect was not observed for As and Mo (Fig. 4). For Cu and Sb, the highest values were always found in Potrerillos (Fig. 4). Intense rainfall in the El Salado Alto Basin (80 mm; MOP, 2017) diluted these elements, diminishing their concentration in the dissolved fraction. As previously proposed, dissolved As and Mo originate in the Andes Mountains and the Altiplano-Puna plateau. Any increase in their concentration is related to the transport of these elements from their source area. For Cd, dilution is more complex. Although, in general, the highest concentrations of particulate and dissolved Cd are found in the Andes Mountains, this was not the case in 2014 when the highest Cd concentration found in the El Salado Alto Basin was at Potrerillos (Fig. 4). This suggests that dilution of this source caused the decreased concentrations in 2015. In the El Salado Alto Basin, most elements (As, Cu, Li, Mo, and Sb) in fluvial sediments show decreases in concentration in 2015 (Fig. 5), which is likely related to transport downstream during the flooding (Jordan et al., 2015; Wilcox et al., 2016).

5.2.3. *Redistribution in the El Salado Bajo basin*

Despite the redistribution of elements in the Andes Mountains and El Salado Alto Basin, the most notable changes of this type occur in the El Salado Bajo Basin. Dissolved elements from El Salado Bajo show higher concentrations of As, Cd, Cu, Mo, and Sb just after the 2015 storm and mudflow, with the lowest values in 2014 (Fig. 4). A possible explanation for this phenomenon is that, during 2014, the El Salado

Alto Basin was not hydrologically connected to the El Salado Bajo Basin, but rather the surface water flow ended 10 km west of Diego de Almagro (Fig. 1a). In 2015, the El Salado Alto, Chañaral and El Salado Bajo basins became connected hydrologically due to the El Salado River flood. This connection was observed two months after the flooding during the field campaign, that is, surficial flow with a notable amount of suspended matter at locations between Diego de Almagro and the first site of the El Salado Bajo Basin (Fig. 2b).

In spite of the pronounced 2015 storm event, hydrologic conditions reverted in 2016 as the El Salado Alto Basin terminated 20 km east of Diego de Almagro (Fig. 1a and Fig. 2c; water not present at RS08 and RS09), and furthermore, as in 2014, surficial water of the El Salado Alto Basin was not connected to the Chañaral and El Salado Bajo Basins. These normal conditions where water of the El Salado Alto and El Salado Bajo basins were confined to their respective areas, as of 2016, is capable of explaining the decrease in analyzed element concentrations when compared to those of 2015 (Fig. 4). For sediments collected in 2016, available samples show that Li, Mo, Cu, and Sb represent respectively, 7, 5, 4, and 3 times the 2015 concentrations. Arsenic and Cd do not exhibit significant changes in concentration at these sites (Fig. 5).

5.3. The case of copper and applications to other dry areas of the world

5.3.1. Copper in the El Salado Alto and El Salado Bajo basins

Large-scale porphyry copper deposits and mining activities are scattered throughout the El Salado Alto and El Salado Bajo basins. Average dissolved concentrations of Cu were 10, 42, and 27 μg L^{-1} in 2014, 2015, and 2016 respectively, which is approximately 6 times greater than the worldwide average for riverine Cu (Table 1; Gaillardet et al., 2003) as well as approximately 2 orders of magnitude lower than the concentration recommended for safe drinking water (Table 1; NCH 409, 2006; US EPA, 2009; WHO, 2011). Maximum concentrations for dissolved Cu were found at the Potrerillos stream and were 59, 48, and 50 μg L^{-1} in 2014, 2015, and 2016 respectively (Figs. 4 and 8).

Previous studies at Caleta Palito (Figs. 1a and 3b) showed an increased concentration of dissolved Cu in the disposal channel, of 2390 μg L^{-1} (Castilla, 1996). During the field campaigns of this study, values obtained at the same site are 2 orders of magnitude lower than previously reported. An explanation for these large differences could be the construction of the Pampa Austral tailing dam in the late 1990s, which helped to control and restrict concentrations of dissolved Cu entering the main stream. No important changes in concentrations of dissolved Cu were observed in studies with pH ≥ 6 (Atkinson et al., 2007). Therefore, these lower than expected values are reasonable because the El Salado Alto and El Salado Bajo basins were characterized by circumneutral to alkaline pH values thereby preventing the dissolution of Cu in the basins and sampling years of this study. Furthermore, the presence of carbonate rocks is limited to the Jurassic marine sequences which are found in the headwaters (RS01; Fig. 2c) as well as to the west of Diego de Almagro (sites RS09 to RS10; Figs. 2b,c), therefore, this type of rock is probably not controlling pH. Additionally, Leybourne and Cameron (2008) determined that in the Spence porphyry copper deposit, under circumneutral pH and high salinity conditions similar to those found in the present study (Aguirre and Clavero, 2000; Risacher et al., 1999), the concentrations of porphyry copper deposit-associated metal and metalloid species in groundwater are stable in solution for relatively long transport distances (> 1 km) in contrast to Cu which complexes as a cation (< 1 km). In the studied sites, it was found that dissolved and particulate Cu and Sb have elevated concentrations in the vicinity of Potrerillos. However, the same result was not reported downstream or in the Andes, suggesting that Cu and Sb complex as cations in the proximity of their source location. On the contrary, As and Mo migrate downstream long distances from their source. Considering average pH (8.6) and Eh (− 0.09 V) conditions during the 2016 sampling campaign as well as Eh-pH diagrams for aqueous As (Smedley and Kinniburgh, 2002) and Mo (Anbar, 2004), it is inferred that these elements are transported as $HAsO_4^{2-}$ and MoO_4^{2-}, respectively.

5.3.2. Applications to other dry areas of the world

Consequences of the exploitation of Cu have been studied in select locations of the Atacama Desert, Chile (Castilla, 1983, 1996; Ramírez et al., 2005). Nevertheless, at present there are other similar dry regions in which porphyry copper deposits are exploited. One of these locations is the Oyu Tolgoi porphyry Cu-Au-Mo deposit located in the southern part of the Gobi Desert, Mongolia. Modern exploration of this area started in the 1980s, and the first copper concentrate was produced and exported in 2013 (Porter, 2016), resulting in an improvement of their economy (The World Bank, 2017). The Gobi region is a cold desert and a snow cover is formed between November and February (Batima et al., 2005). As shown from this study, snowmelt can facilitate the remobilization of contaminant elements in this type of environment especially if mining activities are unregulated.

Likewise, Iran is related to the central Iranian volcano-plutonic Cu belt in which the Sarcheshmeh porphyry deposit is located, the most important Cu-Mo mine in Iran (Atapour and Aftabi, 2007). This mine is located 60 km NW from Kerman, the nearest city, and the Sarcheshmeh Cu smelter plant started operations in 1981. Conducted studies close to this facility have shown that mining activities have resulted in soil contamination (Khorasanipour and Aftabi, 2011). At Sarcheshmeh, the average annual precipitation varies from 300 to 550 mm, the temperature ranges from + 35 °C to − 20 °C, and the area is covered with snow 3 to 4 months per year (Ardejani et al., 2008). Generally, rainfall in Iran occurs from January to April (Weather Online, 2017); however, in a similar manner to the Atacama Desert, recently in August 2017, a vast area of northern Iran approximately 500 km north of Kerman was affected by heavy rains and flash floods, resulting in at least 12 fatalities, 2 missing people, and over 2000 affected individuals (Davies, 2017). As illustrated in this study, remobilization of mining-related contaminants could also occur in this arid to semiarid environment due to flash floods or snow melt.

6. Conclusions

Analyses of surface water and fluvial sediments of the Northern Atacama Region of Chile, as presented herein, have aided in the assessment of the main regional contaminants and probable sources, the establishment of a local geochemical background, and the assessment of the redistribution of contaminant elements as a result of the large-scale March 2015 Atacama flood event and mudflow. This analysis and evaluation aids in the goal of better understanding contaminant sources and impacts due to natural and anthropogenic factors in regions with scarce water resources.

In regard to the central subjects of this study, the following conclusions are summarized below and could be applicable to other similar geologic and hydrologic systems outside of the immediate research area:

6.1. Sources and contaminant elements

Samples obtained in the Northern Atacama Region indicate that Li, As, Mo, Cd, Sb, and Cu all exhibit higher concentrations in surface water and fluvial sediments when compared to worldwide averages in rivers and the UCC, respectively. In particular, concentrations of Li, As, and Mo are orders of magnitude greater in surface water when compared to worldwide averages in rivers. Despite elemental enrichment in the analyzed dissolved load samples, it is concluded that dissolved As, Cd, Li, and Mo originate from natural sources, whereas dissolved Cu and Sb are considered mining-related contaminants. In the particulate fraction, it is inferred that As, Li, and Cd enrichment is natural, originating from salt flats, Neogene evaporites, and epithermal deposits of

the Andes Mountains. Nevertheless, enrichment in Cu, Mo, and Sb is related to fluvial contamination from mining activities. The obtained local geochemical background is mainly reflecting geology for As, Cd and Li in fluvial water and sediments, however this is not concluded for Cu, Mo and Sb which reflect the combination of anthropogenic activities and geology. When comparing concentrations in surface water and sediments from the Northern Atacama Region to other sites impacted by mining activities such as Oruro, Bolivia, of the studied elements, only Sb exhibits higher values in the dissolved fraction outside of the studied region while concentrations in sediments are comparable. Aside from natural enrichment and human-induced contamination, remobilization of elements has occurred as the result of floods and snowmelt in the El Salado River basins (El Salado Alto and El Salado Bajo) and Andes Mountain basins, respectively.

6.2. March 2015 Flooding

In the Andes Mountains, the March 2015 massive flood event spurred an increase of Cu, Mo and Sb in the dissolved fraction as well as an increase of Cu, Mo, and, to a lesser extent, Li, As, Cd and Sb in fluvial sediments. Flooding also led to an enrichment of As and Li in saline crusts of the Andes Mountains. From 2014 to 2015, the El Salado Alto Basin samples exhibited a dilution of dissolved concentrations in Cd, Cu, and Sb due to increased precipitation. A major portion of the analyzed elements in the particulate fraction decreased in concentration just after the event and subsequently increased 1 year after the flood. The El Salado Bajo Basin showed the most significant changes in concentration in the dissolved fraction. Just after the 2015 event, concentrations increased due to the creation of a hydrologic connection between the El Salado Alto and El Salado Bajo basins.

6.3. Copper

Despite the fact that this region has been affected by intense mining activities, concentrations of Cu in the dissolved fraction are lower than previously reported. This is likely related to circumneutral to alkaline pH and the complexation of Cu as a cation.

Acknowledgements

This survey would not be possible without the economic support provided by a grant from the Universidad de Antofagasta, the use of laboratory facilities provided by Domingo Román, Pedro Cortés, and Juan Ávila of the Chemistry Department and Jorge Valdés and Sue Ellen Vega from the Instituto de Investigaciones Oceanológicas, at the Universidad de Antofagasta. We thank Verónica Oliveros for providing unpublished data of As, Mo, and Sb of La Negra Formation and two anonymous reviewers for their valuable suggestions and contributions. In addition we appreciate the help of Sergio Villagrán during the sampling campaigns, Stephane Audry during the 2014 sampling campaign, and the GET laboratory during water sample analyses of 2014. We would also like to thank undergraduate students Francisca Verdejo and Carlos Acuña (Universidad Católica del Norte). The March 2016 sampling campaign was funded by a grant entitled Programa de Inserción en la Academia (PAI) 79150070.

References

Abrahams, P.W., Tranter, M., Davies, T.D., Blackwood, I.L., 1989. Geochemical studies in a remote Scottish upland catchment II. Streamwater chemistry during snow-melt. Water Air Soil Pollut. 43, 231–248. http://dx.doi.org/10.1007/BF00279194.

Aguirre, I., Clavero, J., 2000. Antecedentes Fisicoquímicos Preliminares de Cuerpos de Agua Superficial del Altiplano de la III Región de Atacama, Chile, in: Sesión Temática 1. Presented at the IX Congreso Geológico Chileno, Puerto Varas, Chile. pp. 1–5.

Alonso, R.N., Jordan, T.E., Tabbutt, K.T., Vandervoort, D.S., 1991. Giant evaporate belts of the Neogene central Andes. Geology 19, 401–404. http://dx.doi.org/10.1130/0091-7613(1991)019<0401:GEBOTN>2.3.CO;2.

Anbar, A., 2004. Molybdenum stable isotopes: observations, interpretations and directions|reviews in mineralogy and geochemistry. Rev. Mineral. Geochem. 55, 429–454. http://dx.doi.org/10.2138/gsrmg.55.1.429.

Aral, H., Vecchio-Sadus, A., 2008. Toxicity of lithium to humans and the environment—a literature review. Ecotoxicol. Environ. Saf. 70, 349–356. http://dx.doi.org/10.1016/j.ecoenv.2008.02.026.

Ardejani, F., Karami, G., Assadi, A., Dehghan, R., 2008. Hydrogeochemical investigations of the Shour River and groundwater affected by acid mine drainage in Sarcheshmeh porphyry copper mine. In: Preceedings 2008 Mine Water and the Environment. Presented at the 10th International Mine Water Association Congress, Karlsbad, Czech Republic, pp. 235–238.

Atapour, H., Aftabi, A., 2007. The geochemistry of gossans associated with Sarcheshmeh porphyry copper deposit, Rafsanjan, Kerman, Iran: implications for exploration and the environment. J. Geochem. Explor. 93 (1), 47–65.

Atkinson, C.A., Jolley, D.F., Simpson, S.L., 2007. Effect of overlying water pH, dissolved oxygen, salinity and sediment disturbances on metal release and sequestration from metal contaminated marine sediments. Chemosphere 69, 1428–1437. http://dx.doi.org/10.1016/j.chemosphere.2007.04.068.

Batima, P., Natsagdorj, L., Gombluudev, P., Erdenetsetseg, B., 2005. Observed climate change in Mongolia. In: AIACC Working Papers. 12. pp. 1–26. http://www.start.org/Projects/AIACC_Project/working_papers/Working%20Papers/AIACC_WP_No013.pdf.

Benavides, J., Kyser, T.K., Clark, A.H., Oates, C.J., Zamora, R., Tarnovschi, R., Castillo, B., 2007. The Mantoverde iron oxide-copper-gold district, III Región, Chile: the role of regionally derived, nonmagmatic fluids in chalcopyrite mineralization. Econ. Geol. 102, 415–440. http://dx.doi.org/10.2113/gsecongeo.102.3.415.

Biblioteca Nacional de Chile, 2017. “Mineral de potrerillos”, en: Origen de la Gran Minería del Cobre (1904–1930) www.memoriachilena.cl (web archive link, 17 January 2017). URL http://www.memoriachilena.cl/602/w3-article-96522.html (accessed 1.17.17).

Canadian Council of Ministers of the Environment, 2001. Canadian Sediment Quality Guidelines for the Protection of Aquatic Life. Environment Canada Guidelines and Standards Division, Canada.

Castilla, J.C., 1983. Environmental impact in sandy beaches of copper mine tailings at Chañaral. Chile. Mar. Pollut. Bull. 14, 459–464. http://dx.doi.org/10.1016/0025-326X(83)90046-2.

Castilla, J.C., 1996. Copper mine tailing disposal in northern Chile rocky shores: *Enteromorpha compressa* (Chlorophyta) as a sentinel species. Environ. Monit. Assess. 40, 171–184. http://dx.doi.org/10.1007/BF00414390.

Chen, C.-W., Kao, C.-M., Chen, C.-F., Dong, C.-D., 2007. Distribution and accumulation of heavy metals in the sediments of Kaohsiung Harbor, Taiwan. Chemosphere 66, 1431–1440. http://dx.doi.org/10.1016/j.chemosphere.2006.09.030.

Chong, G., 1988. The Cenozoic saline deposits of the Chilean Andes between 18°00′ and 27°00′ south latitude. In: Bahlburg, D.H., Breitkreuz, P.D.D.C., Giese, P.D.P. (Eds.), The Southern Central Andes, Lecture Notes in Earth Sciences. Springer, Berlin Heidelberg, pp. 137–151. http://dx.doi.org/10.1007/BFb0045179.

Clarke, J.D.A., 2006. Antiquity of aridity in the Chilean Atacama Desert. Geomorphology 73, 101–114. http://dx.doi.org/10.1016/j.geomorph.2005.06.008.

COCHILCO, 2016. Franjas Metalogénicas de los Andes Centrales: Blancos Clave Para la Exploración Minera.

Contreras, J.P., Ramírez, C., Garrido, N., Núñez, G., 2015. Caracterización hídrica y geológica de los aluviones del 25 y 26 de marzo de 2015 en la cuenca del Río El Salado, Región de Atacama, Chile. In: Geología Para El Siglo XXI. Presented at the XIV Congreso Geológico Chileno, La Serena, Chile, pp. 785–788.

Cornejo, P., Tosdal, R.M., Mpodozis, C., Tomlinson, A.J., Rivera, O., Fanning, C.M., 1997. El Salvador, Chile porphyry copper deposit revisited: geologic and geochronologic framework. Int. Geol. Rev. 39, 22–54. http://dx.doi.org/10.1080/00206819709465258.

Davies, R., 2017. Iran – 12 killed in flash floods in North – FloodList, floodlist.com (web archive link, 13 August 2017). http://floodlist.com/asia/iran-flash-floods-august-2017, Accessed date: 5 October 2017.

DGA, 2014. Simposio Avances y Desafíos en la Problemática del Arsénico en Aguas de Chile y el Mundo.

Earle, L.R., Warner, B.G., Aravena, R., 2003. Rapid development of an unusual peat-accumulating ecosystem in the Chilean Altiplano. Quat. Res. 59, 2–11. http://dx.doi.org/10.1016/S0033-5894(02)00011-X.

EN ISO 17294-2, 2016. Water Quality - Application of Inductively Coupled Plasma Mass Spectrometry (ICP-MS) - Part 2: Determination of Selected Elements Including Uranium Isotopes.

Ericksen, G.E., Salas, R., 1990. Geology and Resources of Salars in the Central Andes.

Espinoza, S., 1990. The Atacama-Coquimbo Ferriferous Belt, Northern Chile. In: Fontboté, P.D.L., Amstutz, P.D.G.C., Cardozo, P.D.M., Cedillo, P.D.E., Frutos, P.D.J. (Eds.), Stratabound Ore Deposits in the Andes, Special Publication No. 8 of the Society for Geology Applied to Mineral Deposits. Springer Berlin Heidelberg, pp. 353–364.

Gaillardet, J., Viers, J., Dupré, B., 2003. 5.09 - trace elements in river waters. In: Turekian, H.D.H.K. (Ed.), Treatise on Geochemistry. Pergamon, Oxford, pp. 225–272.

Gajardo, A., 2014. Potencial de Litio en Salares del Norte de Chile.

Gałuszka, A., Migaszewski, Z.M., Dołęgowska, S., Michalik, A., Duczmal-Czernikiewicz, A., 2015. Geochemical background of potentially toxic trace elements in soils of the historic copper mining area: a case study from Miedzianka Mt., Holy Cross Mountains, south-central Poland. Environ. Earth Sci. 74, 4589–4605. http://dx.doi.org/10.1007/s12665-015-4395-6.

Hauser, A., 1997a. Catastro y Caracterización de las Fuentes de Aguas Minerales y Termales de Chile.

Hauser, A., 1997b. Los Aluviones del 18 de Junio de 1991 en Antofagasta: un Análisis Crítico, a 5 Años del Desastre. SERNAGEOMIN, Santiago.

International Mining, 2016. High-arsenic copper concentrates. www.im-mining.com (web archive link, 23 February 2016). http://im-mining.com/2016/02/23/high-arsenic-

copper-concentrates/, Accessed date: 9 May 2017.
ISO 15587-1, 2002. Water Quality - Digestion for the Determination of Selected Elements in Water - Part 1: Aqua Regia Digestion.
Jordan, T., Riquelme, R., González, G., Herrera, C., Godfrey, L., Colucci, S., Gironás, J., Gamboa, C., Urrutia, J., Tapia, L., Centella, K., Ramos, H., 2015. Hydrological and geomorphological consequences of the extreme precipitation event of 24–26 March 2015, Chile. In: Geología Para El Siglo XXI. Presented at the XIV Congreso Geológico Chileno, La Serena, Chile, pp. 777–780.
Kelepertzis, E., Argyraki, A., Daftsis, E., Ballas, D., 2010. Quality characteristics of surface waters at Asprolakkas river basin, N.E. Chalkidiki, Greece. Bull. Geol. Soc. Greece 1–10.
Khorasanipour, M., Aftabi, A., 2011. Environmental geochemistry of toxic heavy metals in soils around Sarcheshmeh porphyry copper mine smelter plant, Rafsanjan, Kerman, Iran. Environ. Earth Sci. 62 (3), 449–465.
Leybourne, M.I., Cameron, E.M., 2008. Source, transport, and fate of rhenium, selenium, molybdenum, arsenic, and copper in groundwater associated with porphyry–Cu deposits, Atacama Desert, Chile. Chem. Geol. 247, 208–228. http://dx.doi.org/10.1016/j.chemgeo.2007.10.017.
Lliboutry, L., 1988. Glaciers of Chile and Argentina, glaciers of the Dry Andes. In: Satellite Image Atlas of Glaciers of the World, South America, Professional Paper United States Geological Survey, pp. 109–147.
López, L.F., 2014. Exploraciones Geoquímicas de Yacimientos Bajo Cobertura Transportada en el Distrito de Inca de Oro, Atacama, Chile: Evolución de Regolito y Paisaje e Impactos en Métodos Geoquímicos Indirectos (Magíster en Ciencias Mención Geología). Universidad de Chile, Santiago.
Macdonald, R.W., Harner, T., Fyfe, J., 2005. Recent climate change in the Arctic and its impact on contaminant pathways and interpretation of temporal trend data. Sci. Total Environ. 342, 5–86. Sources, Occurrence, Trends and Pathways of Contaminants in the Arctic Bidleman SI. https://doi.org/10.1016/j.scitotenv.2004.12.059.
Matschullat, J., Ottenstein, R., Reimann, C., 2000. Geochemical background – can we calculate it? Environ. Geol. 39, 990–1000. http://dx.doi.org/10.1007/s002549900084.
MOP, 2017. Servicios Hidrometeorológicos. Minist. Obras Públicas - Dir. Gen. Aguas. http://www.dga.cl/productosyservicios/servicioshidrometeorologicos/Paginas/default.aspx, Accessed date: 16 January 2017.
Muller, G., 1979. Schwermetalle in den Sedimenten des Rheins - Veränderungen seit. Umschau 79, 778–783.
NCH 409, 2006. NCH 409/1 Norma Calidad del Agua Potable, NCH. 409. pp. 1.
Neary, D., García-Chevesich, P., 2008. Hydrology and erosion impacts of mining derived coastal sand dunes, Chañaral Bay, Chile. Hydrology and Water Resources in Arizona and the Southwest. 38. pp. 47–52.
Nowrouzi, M., Pourkhabbaz, A., 2014. Application of geoaccumulation index and enrichment factor for assessing metal contamination in the sediments of Hara Biosphere Reserve, Iran. Chem. Speciat. Bioavailab. 26, 99–105. http://dx.doi.org/10.3184/095422914X13951584546986.
Oliveros, V., Morata, D., Aguirre, L., Féraud, G., Fornari, M., 2007. Magmatismo asociado a subducción del Jurásico a Cretácico Inferior en la Cordillera de la Costa del norte de Chile (18°30′–24°S): geoquímica y petrogenesis. Rev. Geol. Chile 34, 209–232. http://dx.doi.org/10.4067/S0716-02082007000200003.
Olson, S., 1989. The stratigraphic and structural setting of the Potrerillos porphyry copper district, Northern Chile. Rev. Geológica Chile 16, 3–39.
Porter, T.M., 2016. The geology, structure and mineralisation of the Oyu Tolgoi porphyry copper-gold-molybdenum deposits, Mongolia: a review. Geosci. Front. 7 (3), 375–407.
Ramírez, M., Massolo, S., Frache, R., Correa, J.A., 2005. Metal speciation and environmental impact on sandy beaches due to El Salvador copper mine, Chile. Mar. Pollut. Bull. 50, 62–72. http://dx.doi.org/10.1016/j.marpolbul.2004.08.010.
Rioseco, R., Tesser, C., 2016. Cartografía interactiva de los climas de Chile: antecedentes generales. http://www7.uc.cl/sw_educ/geografia/cartografiainteractiva/Inicio/Paginas/UntitledFrameset-1.htm, Accessed date: 9 May 2016.
Risacher, F., Alonzo, H., Salazar, C., 1999. Geoquímica de Aguas en Cuencas Cerradas: I, II y III regiones - Chile.
Risacher, F., Alonso, H., Salazar, C., 2003. The origin of brines and salts in Chilean salars: a hydrochemical review. Earth-Sci. Rev. 63, 249–293. http://dx.doi.org/10.1016/S0012-8252(03)00037-0.
Romero, L., Alonso, H., Campano, P., Fanfani, L., Cidu, R., Dadea, C., Keegan, T., Thornton, I., Farago, M., 2003. Arsenic enrichment in waters and sediments of the Rio Loa (Second Region, Chile). Appl. Geochem. 2001 (18), 1399–1416. Arsenic Geochemistry-selected papers from the 10th Water-Rock Interaction Symposium, Villasimius, Italy, 10–15 June. https://doi.org/10.1016/S0883-2927(03)00059-3.
Rudnick, R.L., Gao, S., 2003. 3.01 - composition of the continental crust. In: Turekian, H.D.H.K. (Ed.), Treatise on Geochemistry. Pergamon, Oxford, pp. 1–64.
Schnurr, W.B.W., Trumbull, R.B., Clavero, J., Hahne, K., Siebel, W., Gardeweg, M., 2007. Twenty-five million years of silicic volcanism in the southern central volcanic zone of the Andes: geochemistry and magma genesis of ignimbrites from 25 to 27°S, 67 to 72°W. J. Volcanol. Geotherm. Res. 166, 17–46. http://dx.doi.org/10.1016/j.jvolgeores.2007.06.005.
Sillitoe, R.H., 1997. Characteristics and controls of the largest porphyry copper-gold and epithermal gold deposits in the circum-Pacific region. Aust. J. Earth Sci. 44, 373–388. http://dx.doi.org/10.1080/08120099708728318.
Sillitoe, R.H., 2003. Iron oxide-copper-gold deposits: an Andean view. Mineral. Deposita 38, 787–812. http://dx.doi.org/10.1007/s00126-003-0379-7.
Sillitoe, R., 2012. Copper provinces. Soc. Econ. Geol. Publ. 16, 1–18 Special Publication No.
Sillitoe, R., Perelló, J., 2005. Andean copper province: tectonomagmatic settings, deposit types, metallogeny, exploration, and discovery. Econ. Geol. 845–890 100th Anniversary Volume.
Sillitoe, R.H., McKee, E.H., Vila, T., 1991. Reconnaissance K-Ar geochronology of the Maricunga gold-silver belt, northern Chile. Econ. Geol. 86, 1261–1270. http://dx.doi.org/10.2113/gsecongeo.86.6.1261.
Smedley, P.L., Kinniburgh, D.G., 2002. A review of the source, behaviour and distribution of arsenic in natural waters. Appl. Geochem. 17, 517–568. http://dx.doi.org/10.1016/S0883-2927(02)00018-5.
SONAMI Estadísticas de producción de cobre, oro, plata, molibdeno y combustibles, www.sonami.cl (web archive link, 2017). http://www.sonami.cl/site/estadisticas-de-produccion/, Accessed date: 17 January 2017.
Soto, C., 2010. Hidrogeología e Hidroquímica de Aguas Sugterráneas en el Distrito Inca de Oro, Región de Atacama: Procesos de Interacción Agua-Roca y Dispersión Geoquímica (Tesis Para Optar al Grado de Magíster en Ciencias Mención Geología). Universidad de Chile, Santiago.
Stern, C.R., 2004. Active Andean volcanism: its geologic and tectonic setting. Rev. Geol. Chile 31, 161–206. http://dx.doi.org/10.4067/S0716-02082004000200001.
Tapia, J., Audry, S., 2013. Control of early diagenesis processes on trace metal (Cu, Zn, Cd, Pb and U) and metalloid (As, Sb) behaviors in mining- and smelting-impacted lacustrine environments of the Bolivian Altiplano. Appl. Geochem. 31, 60–78. http://dx.doi.org/10.1016/j.apgeochem.2012.12.006.
Tapia, J., Verdejo, F., 2015. Metal(loid)s distribution in northern Atacama Region hydrological basins. In: Presented at the 27th International Applied Geochemistry Symposium, Tucson, Estados Unidos.
Tapia, J., Audry, S., Townley, B., Duprey, J.L., 2012. Geochemical background, baseline and origin of contaminants from sediments in the mining-impacted Altiplano and Eastern Cordillera of Oruro, Bolivia. Geochem. Explor. Environ. Anal. 12, 3–20. http://dx.doi.org/10.1144/1467-7873/10-RA-049.
The World Bank, 2017. Mongolia | Data https://data.worldbank.org (web archive link, 2017). https://data.worldbank.org/country/mongolia, Accessed date: 4 October 2017.
Thompson, M., Palma, B., Knowless, J., Holbrook, M., 2003. Multi-annual climate in Parque Nacional Pan de Azúcar, Atacama Desert, Chile. Rev. Chil. Hist. Nat. 76, 235–254.
US EPA, 2009. Drinking WATER Contaminants. WWW Document. http://water.epa.gov/drink/contaminants/, Accessed date: 26 January 2015.
Valero-Garcés, B.L., Delgado-Huertas, A., Navas, A., Edwards, L., Schwalb, A., Ratto, N., 2003. Patterns of regional hydrological variability in central-southern Altiplano (18°–26°S) lakes during the last 500 years. Palaeogeogr. Palaeoclimatol. Palaeoecol. 194, 319–338. Late-quaternary palaeoclimates of the southern tropical Andes and adjacent regions. https://doi.org/10.1016/S0031-0182(03)00284-0.
Vargas, G., Ortlieb, L., Rutllant, J., 2000. Aluviones históricos en Antofagasta y su relación con eventos El Niño/Oscilación del Sur. Rev. Geol. Chile 27, 157–176. http://dx.doi.org/10.4067/S0716-02082000000200002.
Weather Online, 2017. Climate of the World: Iran | weatheronline.co.uk (web archive link, 2017). http://www.weatheronline.co.uk/reports/climate/Iran.htm, Accessed date: 5 October 2017.
White, N., Hedenquist, J.W., 1995. Epithermal gold deposits styles, characteristics and exploration. SEG Newsl. 23, 9–13.
WHO, 2011. WHO|Guidelines for Drinking-Water Quality, fourth edition. WHO, URL WWW Document. http://www.who.int/water_sanitation_health/publications/2011/dwq_guidelines/en/, Accessed date: 27 January 2015.
Wilcox, A.C., Escauriaza, C., Agredano, R., Mignot, E., Zuazo, V., Otárola, S., Castro, L., Gironás, J., Cienfuegos, R., Mao, L., 2016. An integrated analysis of the March 2015 Atacama floods. Geophys. Res. Lett. 43, 2016. (GL069751). https://doi.org/10.1002/2016GL069751.
Zhang, J., Liu, C.L., 2002. Riverine composition and estuarine geochemistry of particulate metals in China—weathering features, anthropogenic impact and chemical fluxes. Estuar. Coast. Shelf Sci. 54, 1051–1070. http://dx.doi.org/10.1006/ecss.2001.0879.
Zoller, W.H., Gladney, E.S., Duce, R.A., 1974. Atmospheric concentrations and sources of trace metals at the south pole. Science 183, 198–200. http://dx.doi.org/10.1126/science.183.4121.198.

DAVENPORT Jesse

Titre : Traçage isotopique de l'altération du silicate et du carbonate dans le système érosif de l'Himalaya

Title: Isotopic tracing of silicate and carbonate weathering in the Himalayan erosional system

Mot-clés : altération, érosion, silicate, carbonate, Himalaya, ^{40}K–^{40}Ca, Ca radiogénique, géochimie des isotopes, spectrométrie de masse à ionisation thermique

Key-words: weathering, erosion, silicate, carbonate, Himalaya, ^{40}K–^{40}Ca, radiogenic Ca, isotope geochemistry, thermal ionization mass spectrometry

Résumé

Au cours de la dernière partie de l'ère cénozoïque, l'altération des lithologies himalayennes a potentiellement impacté un certain nombre de cycles géochimiques et biogéochimiques, qui constituent ensemble le cycle global du carbone. Pour pouvoir contraindre et comprendre les processus qui se sont produits dans l'Himalaya et qui ont affecté ces cycles, nous devons être en mesure de distinguer les signatures de l'altération du silicate et du carbonate dans la charge dissoute des fleuves de l'Himalaya. Des études antérieures ont tenté de le faire en utilisant diverses méthodes, qui incluent la modélisation du budget en isotopes des éléments majeurs et Sr, ainsi que des techniques isotopiques non traditionnelles. Cependant, il n'existe toujours pas de consensus clair sur l'ampleur et le flux de l'altération du silicate dans l'Himalaya. Cette thèse propose l'utilisation du ^{40}Ca, un produit de désintégration de ^{40}K, comme traceur pouvant améliorer la quantification du flux d'altération du silicate et du carbonate dans la charge dissoute des rivières himalayennes. Des travaux antérieurs ont montré que le budget de l'eau de mer ^{40}Ca est dominé par une source de manteau, de sorte que les carbonates marins ont une signature homogène de $\varepsilon^{40}Ca$ indiscernable ou légèrement élevée par rapport à la valeur du manteau (c'est-à-dire $\varepsilon^{40}Ca = 0$). En revanche, la croûte supérieure de silicate, avec un rapport K/Ca d'environ 1, devrait avoir développé une composition radiogénique d'environ +2–3 ε-units. La différence entre la signature en Ca radiogénique des lithologies de carbonate et de silicate peut donc être utilisée pour différencier l'altération du carbonate et du silicate dans la charge dissoute des rivières.

Nous présentons ici une étude géochimique comprenant des analyses de Ca radiogénique des rivières drainant les principales unités lithologiques de l'Himalaya, ainsi que des résultats provenant de sédiments, de substrat rocheux, de sol et de gravier. Nos résultats montrent que les carbonates/dolomites de l'Himalaya ne présentent pas d'excès de ^{40}Ca radiogénique ($\varepsilon^{40}Ca = 0$) malgré des signatures très variables $^{87}Sr/^{86}Sr$ (0.73–0.85), alors que les sédiments et les roches sédimentaires sont radiogènes ($\varepsilon^{40}Ca$ = +0.9 à +4). Ceci suggère que pour Ca, contrairement à Sr, l'échange isotopique entre les lithologies silicate et carbonate a été minime. La composition en Ca radiogène de l'eau des rivières va de +0.1 dans les captages à prédominance carbonatée à +11 unités dans les rivières drainant des bassins versants silicatés. Pour les grandes rivières, les estimations du budget relatives à l'altération du silicate et du carbonate sur la base des éléments principaux et la composition en Ca radiogénique tendent à concorder. Cependant, pour certaines rivières plus petites, en particulier celles drainant des bassins à dominance silicatée dans les formations cristallines de l'Himalaya supérieur (HHC) et du Petit Himalaya (LH), certaines divergences sont observées. Celles-ci ne peuvent pas être

attribuées à une définition imprécise de la composition chimique ou radiogénique en Ca des pôles de mélange utilisés pour la modélisation budgétaire, car les valeurs requises pour résoudre le modèle ne sont pas raisonnables. Ils ne peuvent pas non plus être expliqués par la précipitation de carbonates secondaires dans les rivières car la composition non radiogénique de la fraction de carbonates dans les sédiments suggère que ce processus n'est que mineur. Au contraire, ces différences peuvent être dues à la dissolution/altération des traces de calcite radiogénique contenues dans les lithologies de silicate HHC et LH. Semblable à ce qui a été suggéré précédemment pour Sr, le vieillissement de ce matériau, qui ne représente qu'une infime partie de la surface du captage du silicate, pourrait produire une proportion substantielle du Ca radiogénique et pourrait ainsi avoir une influence significative sur le calcul des budgets de ces bassins à partir des données isotopiques. Néanmoins, comme cet effet est observé principalement dans les bassins à faible taux d'érosion des silicates, son influence sur les estimations du flux global de vieillissement du silicate sera mineure. Plus généralement, les résultats de cette thèse impliquent que le système $^{40}K–^{40}Ca$ permet une résolution de problématiques qui ne peuvent pas être approfondies avec succès à l'aide d'isotopes Sr dans l'Himalaya. Des travaux supplémentaires sont nécessaires pour définir la gamme complète des compositions de Ca radiogénique dans l'Himalaya afin de répondre clairement aux questions concernant les flux d'altération des silicates.

Abstract

During the latter part of the Cenozoic Era, weathering of Himalayan lithologies potentially impacted a number of geochemical and biogeochemical cycles, which together comprise the global carbon cycle. To be able to constrain and understand the processes that occurred in the Himalayas that affected these cycles, we must be able to distinguish between the signatures of silicate and carbonate weathering in the dissolved load of Himalayan rivers. Previous studies have attempted to do this using a variety of methods, which include major element and Sr isotope budget modeling as well as more non-traditional isotopic techniques. However, there is still not a clear consensus on the magnitude and flux of silicate weathering in the Himalaya. This thesis proposes the use of ^{40}Ca, a decay product of ^{40}K, as a tracer that could improve the quantification of the silicate and carbonate weathering flux in the dissolved load of Himalayan rivers. Previous work has shown that the ^{40}Ca budget of seawater is dominated by a mantle source, such that marine carbonates have a homogeneous $\varepsilon^{40}Ca$ signature indistinguishable, or slightly elevated, from the mantle value (i.e., $\varepsilon^{40}Ca = 0$). In contrast, the upper silicate crust, with a K/Ca ratio of approximately 1, is expected to have developed a radiogenic composition of approximately +2–3 ε-units. The difference between the radiogenic Ca signature of carbonate and silicate lithologies can be therefore used to differentiate between carbonate and silicate weathering in the dissolved load of rivers.

Here, we present a geochemical survey, including radiogenic Ca analyses, of rivers draining the main lithological units of the Himalaya, as well as results from sediments, bedrock, soil, and gravel. Our results show that Himalayan carbonates/dolomites exhibit no radiogenic ^{40}Ca excesses (i.e., $\varepsilon^{40}Ca = 0$) despite highly variable $^{87}Sr/^{86}Sr$ signatures (0.73–0.85), whereas silicate bed rock and sediments are variably radiogenic ($\varepsilon^{40}Ca = +0.9$ to $+4$). This suggests that for Ca, unlike for Sr, isotopic exchange between the silicate and carbonate lithologies has been minimal. The radiogenic Ca composition of river water ranges from +0.1 in carbonate dominated catchments to +11 ε-units in rivers draining silicate catchments. For large rivers, silicate and carbonate weathering budget estimates based on major elements and radiogenic

Ca compositions tend to agree. However, for some smaller rivers, especially those draining silicate dominated basins in the High Himalayan Crystalline (HHC) and Lesser Himalaya (LH) formations, some discrepancies are observed. These cannot be attributed to poor definition of the chemical or radiogenic Ca composition of the endmembers used for budget modeling, as the values required to bring the estimates into agreement are unreasonable. They also cannot be explained by precipitation of secondary carbonates in the rivers as the non-radiogenic composition of the carbonate fraction of sediments suggests that this process is only minor. Rather, these discrepancies may be due to the dissolution/weathering of trace amounts of radiogenic calcite contained within HHC and LH silicate lithologies. Similar to what has previously been suggested for Sr, the weathering of such material, which represents only a tiny fraction of the area of the silicate catchment, could yield a substantial proportion of the radiogenic Ca and may thus have a significant influence on the isotopically based weathering budgets of these basins. Nevertheless, as this effect is observed primarily in basins with low silicate erosion rates, its influence on estimates of the overall silicate weathering flux will be minor. More generally, the results of this thesis imply that the ^{40}K–^{40}Ca system can resolve issues that cannot be successfully addressed using Sr isotopes in the Himalaya. Further work is needed to define the full range of radiogenic Ca compositions in the Himalaya in order to clearly answer questions regarding silicate weathering fluxes.

Résumé Élargi

On pense depuis longtemps que le soulèvement et l'érosion du plateau himalayen-tibétain jouent un rôle clé dans la modification de l'évolution de l'eau de mer à travers le passé géologique. Cela pourrait être dû: 1) à l'augmentation de la composition isotopique du Sr dans l'eau transmise aux océans en raison de la nature radiogénique des lithologies de silicate et de carbonate dans l'Himalaya ou 2) à un flux accru de Sr dans les océans à partir du Orogène himalayen. Il est important de distinguer entre le flux de charge dissous dans l'Himalaya et l'altération du silicate ou du carbonate pour tenter de comprendre les interactions entre altération, érosion, climat et géomorphologie, mais aussi pour le cycle à long terme CO_2 et chimie de l'eau de mer. Toutefois, les rivières himalayennes présentent des caractéristiques distinctes, c'est-à-dire des concentrations de Sr élevées et des signatures radiogéniques $^{87}Sr/^{86}Sr$, qui excluent une simple relation de mélange entre les lithologies de silicate et de carbonate, car les silicates et les carbonates radiogenic ^{87}Sr, et donc, ces signatures sont difficiles à différencier dans la charge dissoute. Des études antérieures ont tenté de le faire en utilisant diverses méthodes, qui incluent une modélisation majeure du budget isotopique élémentaire et Sr, ainsi que des techniques isotopiques non traditionnelles. Cependant, il n'existe toujours pas de consensus clair sur l'ampleur et le flux de l'altération du silicate dans l'Himalaya.

Cette thèse propose l'utilisation de ^{40}Ca, un produit de désintégration de ^{40}K, comme traceur pour potentiellement améliorer la quantification du flux d'altération du silicate et du carbonate dans la charge dissoute des rivières himalayennes. Des études analytiques antérieures utilisant le système ^{40}K-^{40}Ca étaient gênées par plusieurs limitations géochimiques et analytiques qui réduisaient considérablement la précision et la reproductibilité des analyses de Ca radiogénique. Cependant, avec le spectromètre de masse à ionisation thermique Thermo Triton (TIMS), nous pouvons effectuer des mesures isotopiques de Ca radiogénique de haute précision (environ 30 ppm S.D.), ce qui représente une amélioration d'un facteur de 3 à 5 par rapport aux précédentes études et génération d'instruments.

Le schéma de désintégration ^{40}K-^{40}Ca a des propriétés géochimiques similaires à celles du $^{87}Rb/^{87}Sr$ et présente un intérêt similaire pour l'étude de l'altération du silicate car K, similaire à Rb, est un élément incompatible lors des processus d'extraction de la croûte et se concentre donc dans la croûte continentale supérieure,

où il se désintègre en Ca. Des travaux antérieurs ont montré que le budget de l'eau de mer ^{40}Ca est dominé par une source mantellique, de sorte que les carbonates marins ont une signature homogène ε^{40}Ca indiscernable, ou légèrement surélevée, de la valeur de manteau (c'est-à-dire ε^{40}Ca = 0). En revanche, la croûte supérieure de silicate, avec un rapport K/Ca d'environ 1, devrait avoir développé une composition radiogénique d'approximativement + 2 à 3 unités. Des études antérieures ont montré que cette dichotomie entre le silicate et le carbonate existait également dans l'eau des rivières, par exemple les rivières Mississippi (dominée par les carbonates) et Columbia (jeunes basaltes) avaient une composition en eau non radiogène, tandis que les rivières Ganga et Brahmaputra avaient une composition en Ca radiogène. Par conséquent, la différence entre la signature Ca radiogénique des lithologies de carbonate et de silicate peut être utilisée pour différencier l'altération du carbonate et du silicate dans la charge dissoute des rivières. Nous pouvons également contourner les problèmes associés au système Rb–Sr lors de la quantification des bilans climatiques dus à la redistribution métamorphique du Sr radiogénique entre silicates et carbonates dans l'Himalaya.

Malgré son potentiel en tant que traceur dans le cycle du Ca exogène, le système ^{40}K-^{40}Ca reste peu utilisé en raison de la difficulté analytique à mesurer les enrichissements radiogéniques sur l'isotope ^{40}Ca. Cela est dû en partie à l'abondance des isotopes pertinents du Ca (^{40}Ca: 96,94%; ^{42}Ca: 0,647%; ^{44}Ca: 2,086%), c'est-à-dire que l'isotope ^{40}Ca domine le système, ce qui rend difficile la mesure des isotopes moins abondants de Ca. Il est important de minimiser les erreurs sur les petits faisceaux d'ions ^{42}Ca et ^{44}Ca, car le rapport mesuré de ^{42}Ca/^{44}Ca est utilisé pour la correction du fractionnement en masse instrumentale. À l'aide du Finnigan MAT-262, des études antérieures indiquaient une précision externe de $\pm$ 0,6 à 1,5 ε-unités (2σ). Les spectromètres de masse à ionisation thermique (TIMS) plus modernes, notamment le Thermo Triton, permettent l'analyse de variations radiogéniques moins importantes sur l'isotope ^{40}Ca. En utilisant le Triton pour analyser des échantillons de cratons archéens, une étude a permis d'obtenir une reproductibilité de $\pm$ 0,5 ε-unité (2σ) et des données ^{40}Ca/^{44}Ca rapportées plus récemment dans des carbonates marins avec une précision externe de $\pm$ 0,35 ε-unité. Ces progrès en précision résultent de deux améliorations apportées à la nouvelle génération de TIMS: 1) la possibilité de mesurer des faisceaux d'ions plus importants par rapport aux instruments TIMS antérieurs (< 50 V contre < 10 V avec le MAT262) et 2) la possibilité d'utiliser le Système optique "Zoom" du Triton pour analyser les isotopes de calcium en mode multidynamique.

Le fractionnement instrumental en masse au cours d'une analyse TIMS a un impact significatif sur la composition isotopique mesurée de Ca. Par conséquent, il est important d'utiliser une loi de fractionnement appropriée pour corriger ce

fractionnement. La plupart des chercheurs ont conclu que la loi exponentielle convenait mieux à la correction du fractionnement instrumental. Cependant, plusieurs études ont signalé un comportement non exponentiel, en particulier à des niveaux élevés de fractionnement en masse. Les mesures isotopiques du calcium peuvent donc être gênées par des corrections de fractionnement de masse inappropriées dues à des écarts par rapport à la loi exponentielle. Cela pourrait résulter d'un certain nombre de processus comprenant l'évaporation de différents domaines ou régions du filament qui se sont fractionnés à des degrés différents avant ou pendant une analyse ou une transmission incomplète des ions Ca du filament aux collecteurs.

Dans cette thèse, nous rapportons les résultats d'analyses répétées du standard SRM915a du NIST effectuées au CRPG sur une période de trois ans en utilisant une approche spectrométrique de masse multi-dynamique. Nous décrivons également une technique de chargement améliorée qui élimine essentiellement 1) les phénomènes de mélange de "réservoir" de filament précédemment signalés lors des analyses TIMS des isotopes de Ca et 2) des effets de fractionnement massique important au cours d'une mesure individuelle. Ces améliorations techniques et les niveaux de reproductibilité nous permettent d'appliquer le système de Ca radiogénique au système d'érosion de l'Himalaya.

Cette thèse est la première du genre à mener une enquête approfondie sur la systématique ^{40}K-^{40}Ca dans le système d'érosion himalayen. Nous montrons qu'au cours du métamorphisme himalayen, ^{40}Ca, contrairement à ^{87}Sr, est resté remarquablement résistant au métamorphisme/dolomitisation. Les analyses révèlent que les roches et les sédiments carbonatés ont des signatures de Ca non radioactives, tandis que les sédiments des roches et des sédiments silicatés présentent des excès de ^{40}Ca qui dépendent de leur âge et de leurs rapports K/Ca, ce qui nous permet de distinguer les sources de carbonate et de silicate dans les sources dissoutes. charge des principaux fleuves himalayens. Cette dichotomie s'applique donc aux rivières, c'est-à-dire que les rivières qui drainent principalement des lithologies carbonatées ont des signatures non radiogènes, alors que les rivières qui drainent principalement des lithologies silicatées ont des signatures radiogéniques.

Ici, nous présentons un levé géochimique, incluant des analyses de Ca radiogénique, des rivières drainant les principales unités lithologiques de l'Himalaya, ainsi que des résultats de sédiments, de substrat rocheux, de sol et de gravier. Nos résultats montrent que les carbonates/dolomites de l'Himalaya ne présentent pas d'excès radiogéniques ^{40} Ca (c'est-à-dire que ε^{40}Ca = 0) malgré des variables très variables ^{87}Sr/^{86}Sr (0,73–0,85), alors que les roches et les sédiments de silicate sont radiogènes de façon variable (+0,9 à +4). Ceci suggère que pour Ca, contrairement

à Sr, l'échange isotopique entre les lithologies silicate et carbonate a été minime. La composition en Ca radiogénique de l'eau des rivières va de +0,1 dans les captages à prédominance carbonatée à +11 ε-unités dans les rivières drainant des captages de silicate.

Dans cette thèse, nous avons entrepris une étude détaillée de Khudi Khola, un petit bassin versant situé dans le bassin de Narayani, au centre du Népal. Il a été choisi en raison de sa longue histoire d'investigation et de sa nature contraignante en termes de lithologie, d'intempéries, d'érosion, de climat, de végétation et de dynamique des rivières. Sur cette base, nous montrons que les compositions d'eau radiogénique en Ca varient fortement entre la LH, en dessous du MCT, et le HHC, au-dessus du MCT. Dans la LH, à l'exception des échantillons prélevés lors d'importantes tempêtes, la composition de l'eau est non radioactive et reflète une source provenant des affleurements massifs de dolomie et de calcaire situés sous le MCT. Au-dessus du MCT dans le HHC, les compositions de Ca radiogénique sont plus élevées que le LH en raison de la nature silicate du HHC. Comme le proposaient des études antérieures, les glissements de terrain dans la partie HHC du bassin de Khudi représentent une source importante de matériaux érodés. Les analyses de poudres faites de cailloux agrégés provenant du glissement de terrain montrent que les valeurs de ε^{40}Ca varient considérablement mais sont en grande partie radiogènes. Dans le Khudi, les tempêtes de la mousson ont donné des valeurs de décharge et de charge en sédiments élevées, des pics de concentration de K, Ca, et de SO_4 et des conditions fluviales généralement turbulentes. Lors de la tempête de 2013, documentée par des études précédentes, nous observons, avec les pics de concentration d'éléments, une forte augmentation des valeurs de ε^{40}Ca, de +0 à +1,78 au plus fort de la tempête. Sur la base de la géologie et de la structure du Khudi, cette signature de Ca radiogénique ne peut provenir que du HHC. L'augmentation concomitante des concentrations de SO_4^{2-}, de K, et de Ca au cours de la tempête de 2013 implique que ces espèces ont peut-être été relâchées par l'altération du silicate et l'oxydation des sulfures associée. Sur la base de ces observations et conclusions, nous suggérons que la décomposition et le lessivage/vieillissement des cailloux et du gravier dans les glissements de terrain au HHC constituent l'explication la plus plausible des pics de concentration et de la composition radiogène en Ca observés pendant les tempêtes.

Pour les grandes rivières, les estimations budgétaires du vieillissement en silicate et en carbonate basées sur les éléments principaux et les compositions de Ca radiogénique ont tendance à concorder. Cependant, pour certaines rivières plus petites, en particulier celles drainant des bassins à dominance silicatée dans les formations cristallines de l'Himalaya supérieur (HHC) et de l'Himalaya inférieur (LH), certaines différences sont observées. Celles-ci ne peuvent pas être attribuées

à une définition médiocre de la composition chimique ou radiogénique en Ca des membres finaux utilisés pour la modélisation budgétaire, car les valeurs requises pour mettre les estimations en accord sont déraisonnables. Ils ne peuvent pas non plus être expliqués par la précipitation de carbonates secondaires dans les rivières car la composition non radiogénique de la fraction de carbonate des sédiments suggère que ce processus est seulement mineur. Au contraire, ces différences sont probablement dues à la dissolution/dégradation des veines minuscules de calcite hydrothermale contenues dans les lithologies de silicate HHC et LH. Semblable à ce qui a été observé précédemment pour Sr, l'altération de ces veines, qui ne représente qu'une infime fraction de la surface du captage de silicate, peut générer une proportion potentiellement importante de Ca radiogénique et va donc dominer les budgets de vieillissement basés sur l'isotope ces bassins. Néanmoins, cet effet étant observé principalement dans les bassins à faible taux d'érosion du silicate, son influence sur les estimations du flux global d'altération du silicate sera mineure.

Plus généralement, les résultats de cette thèse impliquent que le système ^{40}K-^{40}Ca peut résoudre des problèmes qui ne peuvent pas être traités avec succès à l'aide d'isotopes Sr dans l'Himalaya. Néanmoins, des travaux supplémentaires sont nécessaires pour définir la gamme complète des compositions de Ca radiogénique dans l'Himalaya afin de répondre clairement aux questions concernant les flux d'altération des silicates. Cette thèse présente un premier aperçu de la systématique des rapports isotopiques de Ca radiogénique dans l'Himalaya. Les idées et interprétations présentées dans cette thèse peuvent fournir un cadre pour mieux comprendre le comportement des rapports isotopiques de Ca radiogénique, mais les idées et la modélisation futures bénéficieront d'analyses plus poussées du ^{40}Ca dans le substrat rocheux, les sédiments, l'eau de rivière, les fluides hydrothermaux et d'autres échantillons terrestres dans l'Himalaya et dans le monde entier.

À l'avenir, davantage d'analyses sont nécessaires pour répondre aux questions concernant la systématique et la réduction à grande échelle des rapports isotopiques de Ca radiogénique pour son utilisation en tant que traceur géochimique. La contrainte du ^{40}Ca fluvial moyen et la composition des autres flux du système global de Ca radiogénique sont importantes pour limiter l'évolution du Ca radiogénique dans les océans. Afin de mieux comprendre la systématique de Ca radiogénique dans les rivières, nous devons étudier des bassins versants bien limités, tels que Khudi Khola, et utiliser des approches multi-proxy. Le couplage des mesures d'isotopes radiogènes de Ca (sensibles au vieillissement carbonaté et silicaté) avec d'autres systèmes isotopiques, tels que les rapports isotopiques Sr, s'est révélé avantageux dans cette thèse. Cependant, le couplage des isotopes radiogènes de Ca avec d'autres systèmes isotopiques, tels que les systèmes isotopiques de Li et Si (sensibles aux

procédés au silicate, au carbonate et aux processus biologiques), pourrait s'avérer encore plus avantageux. Beaucoup de travail reste à faire, mais les données de cette thèse confirment que les isotopes radiogéniques de Ca, mesurés par TIMS, pourraient potentiellement éclairer certaines des questions les plus importantes de la géochimie et des sciences de la Terre: les interactions entre climat, érosion, intempéries, etc. et le cycle global du carbone.